SATELLITE AND AERIAL IMAGING IN CHARACTERIZATION, HYDROLOGIC ANALYSIS AND MODELING OF INLAND WATERSHEDS AND STREAMS

By

GREGG N. TEASDALE

A dissertation to be submitted in partial fulfillment of
the requirements for the degree of

DOCTOR OF PHILOSOPHY
(Civil Engineering)

WASHINGTON STATE UNIVERSITY
Department of Civil and Environmental Engineering

December 2005

To the Faculty of Washington State University:

The members of the Committee appointed to examine the dissertation of **GREGG N. TEASDALE** find it satisfactory and recommend that it be accepted.

_____

Michael E. Barber, P. E., Ph.D, Chair

_____

William H. Funk, Ph.D.

_____

Richard T. Jacobsen, P.E., Ph.D.

_____

David R. Yonge, Ph.D.

ACKNOWLEDGEMENTS

I wish to acknowledge funding received in related, but separate, work for the Northwest Power Planning Council, Columbia River Basin Fish and Wildlife Program through the Bonneville Power Administration. The satellite and aerial imagery datasets acquired for that work contributed much to context of the dissertation. The value of satellite and aerial imaging in monitoring and managing precious resources was made startlingly clear.

The Idaho Department of Environmental Quality, an agency for which I once worked, provided initial funding and a venue for operational testing of the techniques of aerial assessment of ephemeral gully erosion. Resulting political controversy was clearly painful for the public servants involved. The unintended controversy, not the validity or efficacy of the method, is regretted.

Much of the work in the dissertation would not be possible without satellite imagery and geospatial data produced by the National Aeronautics and Space Administration and the U.S. Geological Survey. While no direct funding was received from these agencies, their very efficient and reliable data distribution systems greatly facilitated the research.

SATELLITE AND AERIAL IMAGING IN CHARACTERIZATION, HYDROLOGIC ANALYSIS AND MODELING OF INLAND WATERSHEDS AND STREAMS

Abstract

By Gregg N. Teasdale, P.E., Ph.D.
Washington State University
December 2005

Chair: Michael E. Barber

Satellite and Aerial images provide spatial, spectral and temporal information necessary to observe, characterize and parameterize the physical nature of watersheds and streams. Aerial views give a perspective that makes clear the spatial continuity and dependency of distributive physical and ecological systems—a perspective difficult to obtain otherwise.

This dissertation explores, examines and demonstrates the use of satellite and aerial imagery in the characterization and hydrologic analysis of inland Pacific Northwest watersheds and streams. Over 2000 stream miles and hundreds of square kilometers of high resolution digital natural color and color infrared aerial imagery were acquired during a period of seven years in watersheds throughout the Columbia River Basin. The imagery datasets clearly show that hydrologically relevant watershed and stream characteristics can be efficiently monitored and evaluated with a variety of remote sensing methods. These data and parameterizations in turn support a wide range of environmental assessment and hydrologic modeling work. The data and information derived by remote sensing methods presented are useful in both engineering research and practice.

The dissertation assembles the most relevant details of operational land surface imaging satellites in a form useful to environmental scientists and water resource engineers. Essential remote sensing principles are discussed and sources cited for further and supporting information. Satellite and aerial data preparation and analysis techniques are illustrated with hundreds of color images that convey the benefit and power of remote sensing methods. Fundamental principles are detailed for a highly efficient and unrecognized method of water resources investigation – analytical aerial survey. This method is demonstrated in practical applications and may be the most significant contribution of the research.

Beyond fundamentals, the dissertation demonstrates how satellite and aerial remote sensing methods are applied in the analysis of critical water resources issues: best practice hydrologic modeling, soil erosion, sediment delivery, fluvial morphology, and sediment transport. New engineering models of morphological sediment transport and watershed ephemeral gully erosion are proposed and demonstrated. Numerous opportunities for further research are noted throughout the dissertation.

TABLE OF CONTENTS

LIST OF FIGURES

LIST OF TABLES

Dedication

This dissertation is dedicated foremost to my wife, Jean, whose support and encouragement never failed in the entirety of the work. It exists because of her.

Secondly, to my uncle William G. Courtright, a life long educator who believed that academic achievement when applied for the betterment of humanity is among the worthiest of endeavors. Perhaps he knows he rescued this work from the abyss.

Lastly, to the aviators who flew and perished in pursuit of scientific and engineering knowledge – the world may not know you, but I understand.

1. Introduction

The dissertation work endured over a period of seven years and grew beyond even a liberal imagining of expectations. An astonishing number of opportunities arose during the course of the research to evaluate aerial and satellite imagery in practical applications related to transportation engineering, water resource engineering, water quality assessment, stream temperature modeling, hydrologic modeling, stream morphology assessment, forest land assessment, agricultural land assessment, soil erosion assessment, upland habitat analysis, fisheries habitat assessment, invasive species monitoring, and conservation planning. Work using satellite and aerial imagery was performed throughout the Columbia River basin, and in Wisconsin, Puerto Rico, and the country of Jordan. The work has at various times been praised, cursed and ignored. The dissertation document reveals a part, but certainly not all, of this broad scope of investigation. As intended, the dissertation emphasizes satellite and aerial imagery use in watershed characterization, hydrologic modeling and stream morphological assessment.

The primary motivation for the dissertation research was, and remains, the unending need for accurate data about the physical environment for environmental assessment and hydrologic modeling. Physical data is acquired and recorded according to diverse objectives and extend across broad areas and over long periods of time. It is essential in scientific study and engineering design that physical data accurately represent characteristics of the real environment.

Physical spatial data is an encompassing term that describes spatially distributed data about physical phenomena. Examples of physical spatial data cover the full range

of environmental assessment and hydrologic characterization: weather and precipitation data, land cover data, hydrography, transportation networks, demography, habitat delineations, and topographic data. A vast quantity of human effort and resources is expended in its acquisition. Expenditures for just one environmental assessment effort, the U.S. EPA Total Maximum Daily Load (TMDL) program, are expected to be approximately $90 million *annually* for data collection and TMDL plan development (EPA 2001a).

Data acquisition techniques, sources of information and data distribution systems evolve over time. Scientific research and practice demands vigilance to assess new sources of information and critically review the efficacy of existing approaches. Remote sensing appears to be perceived by some as an intractable and vaguely threatening technology that has yet to be proven. The literature review and practical experience provided motivating evidence to the contrary. It is hoped that the research and practical demonstrations presented in the documents encourage other scientists and engineers to view remote sensing technology and assessment methods as viable, practical and accessible sources of physical spatial data.

1.1 Dissertation Objectives

This dissertation is primarily motivated by the desire to better understand and incorporate the realities of physical spatial data into contemporary engineering analysis of hydrologic systems. It starts with the premise that the availability and accessibility of valid physical spatial data, rather than analytical sophistication, is generally the prevailing factor that limits applied engineering hydrologic analysis. If true, this

premise warrants the sustained attention of environmental and engineering research to maximize environmental and social benefits. While this premise it is not altogether possible to prove, the literature review showed it to be sufficiently true to justify the objectives of the dissertation.

The literature review and previous experience indicated that a significant and useful contribution to hydrological science should result from research emphasizing the use of satellite and aerial imaging techniques in watershed hydrologic characterization and assessment of stream morphology. Remote sensing is an under-exploited source of geospatial data that characterizes land and water resources across multiple scales. High temporal-low spatial resolution satellite imagery can be augmented with targeted high-resolution aerial imagery to enable development of hydrologic and environmental models that are more physically realistic than those developed from highly abstracted cartographic information and limited field sampling. Direct association of the analyst and modeler with primary source imagery improves understanding of environmental conditions, exposes uncertainty in analysis techniques, and promotes a more ecologically effective response to environmental problems.

Further refined, the dissertation objectives emphasized the application of satellite and aerial imagery in environmental assessment and hydrological modeling of watersheds and streams within the inland Pacific Northwest. Specific objectives of the research included:

- Identify geospatial parameters and physical spatial data important for hydrologic and environmental modeling that can be determined from satellite and aerial imagery;

- Evaluate the capabilities of operational satellite and aerial imaging to acquire the identified geospatial parameters and physical spatial data;
- Identify appropriate methods of extracting spatial data from satellite and aerial imagery for hydrologic and environmental modeling;
- Demonstrate the use of satellite and aerial imaging for acquiring geospatial information and physical spatial data for selected assessment protocols and environmental models;
- Demonstrate how geospatial information and physical spatial data acquired with satellite and aerial imaging complements and may potentially replace conventional sources of spatial data used in operational hydrologic and water quality models;
- Initiate development of new engineering models that are designed to utilize geospatial information and physical spatial data acquired from satellite and aerial imagery.

1.2 Accomplishments of the Dissertation Research

This dissertation is organized along the main lines of investigation and is purposely written so that sections are relatively independent. The section-subject organization should direct the attention of the reader to the topic most related to his or her particular interest and is organized in a manner that should be adaptable for electronic distribution.

Remote sensing is an observational and analytical science largely comprised of computer-based techniques operating upon and producing digital data. The dissertation document makes prolific use of remote sensing and geographic information system images to illustrate the process and products of remote sensing analysis. Remote

sensing concepts and capabilities are difficult to convey in a convincing manner when removed from visual context. The corollary to this is that the full scope and continuity of the beneficial material cannot be easily reduced to standard journal articles that must emphasize specific lines of research . The dissertation, therefore, must be able to stand on its own.

The reader needs a "road map" to help introduce the material. Brief summaries of the main content and accomplishments of the research are below.

1.2.1 Satellite and Aerial Imaging Resources

Section 2 introduces the types and sources of operational satellite and aerial imagery data and related geospatial data sources. It captures the main findings of the literature review related to remote sensing and gives an overview of the potential uses of satellite and aerial imagery in watershed and surface water characterization. Section 2 also references remote sensing data and educational materials produced for the Bonneville Power Administration (BPA) in related but separate work. The reader is directed to that source, which is distributed by the BPA office in Portland, Oregon (800-282-3713), for a much broader introduction to the potential use of satellite and aerial imagery in aquatic resource assessment and habitat characterization.

1.2.2 Aerial Imaging

Section 3 is a comprehensive review of the use of low-altitude high-resolution aerial imagery in hydrologic assessment. It describes the most important aerial image characteristics and principles of photogrammetry in context of the dissertation research. Theories and techniques of photogrammetry and remote sensing are mature, yet this

research revealed many opportunities for advanced investigations with photogrammetric analysis of high-resolution digital aerial imaging in hydrologic characterization and fluvial morphology.

Many examples demonstrate the practical use of aerial images to derive physical data for hydrological and stream analysis such as the determination of the slope and length of an empheral gully channel in Figure 1.1. The treatment is unlike any found elsewhere in the water resources and remote sensing literature and should help investigators and practitioners more easily utilize high-resolution aerial imagery in research, teaching and professional work.

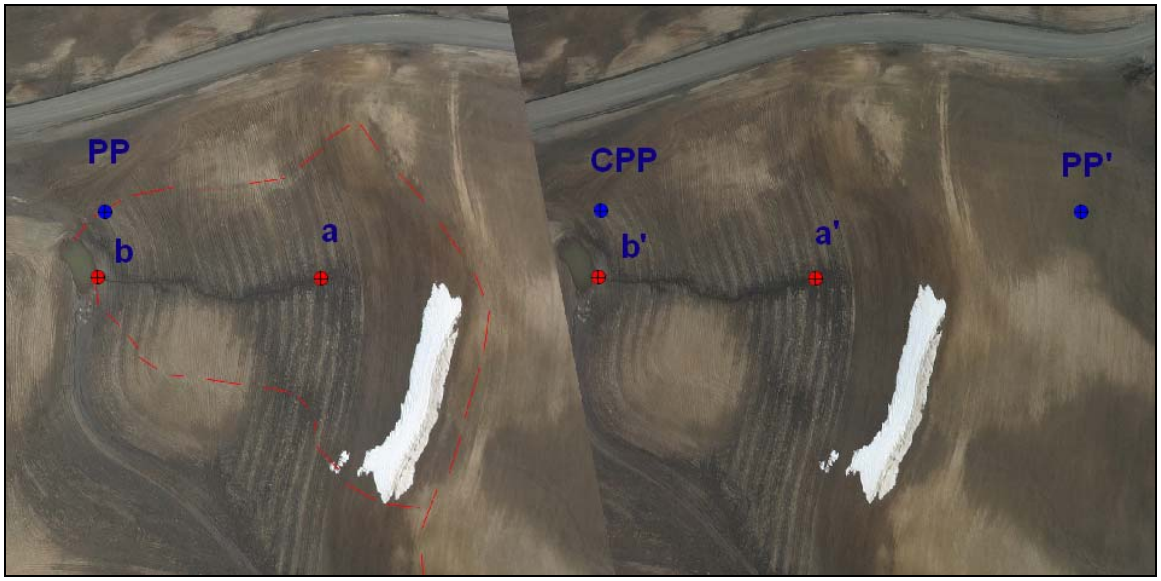

Figure 1.1 Parallax measurement of channel slope in digital aerial stereo pair.

1.2.3 Analytical Aerial Survey

Section 4 is a unique and original contribution to watershed hydrologic assessment. It presents fundamental principles of acquiring data with aerial transect surveys and demonstrates how to measure many attributes of watershed assessment at an appropriate level of accuracy over an extensive area. Aerial transects, especially when

combined with simultaneous acquisition of high-resolution aerial imagery reveal watershed and stream characteristics impractical to quantify by other means. For example, an estimate of the total lengths of streams and ephemeral gully channels in the Little Potlatch Creek basin in Figure 1.2 are derived from a statistical analysis of channels observed in the swaths of aerial images. The analysis techniques are very efficient and cost effective. With proper understanding and recognition, aerial survey should become a routine method to verify and derive catchment characteristics for hydrologic modeling.

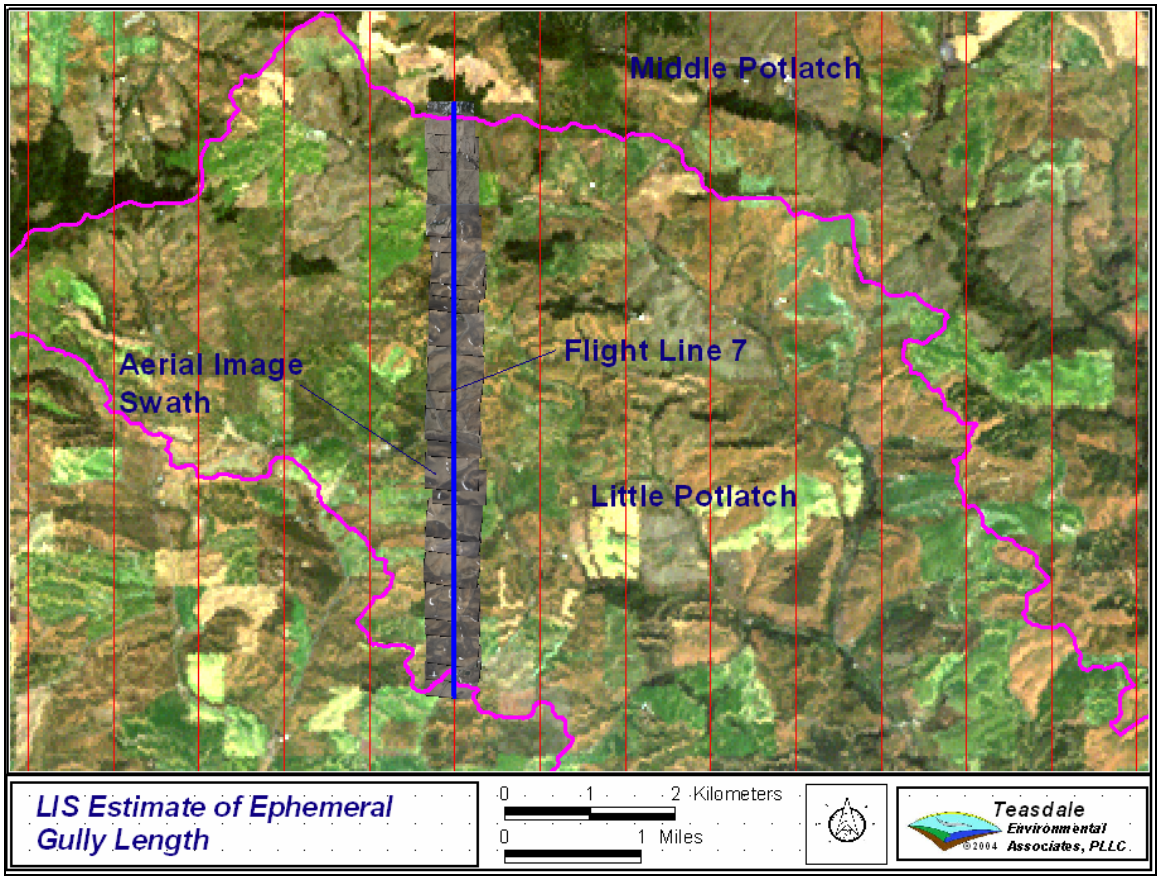

Figure 1.2 Aerial transect across the Little Potlatch Creek basin.

1.2.4 Satellite imagery in Hydrologic Assessment

Satellite imagery gives the hydrologist, environmental scientist and water resources engineer a view and perspective of the physical watershed that is nearly impossible to obtain otherwise. Previously difficult analytical characterizations such as the acreage of canyonland exposed by wildfire in a sensitive watershed can now be made with almost trivial ease. There is much opportunity for practical application and applied research related to satellite imagery in watershed science. Section 5 of the dissertation research explores a few of the possibilities and demonstrates that satellite imagery is indispensable in contemporary hydrologic analysis.

Practical and regionally important applications demonstrate the use of satellite imagery in watershed characterization. The first develops an erosion potential index derived from Landsat 7 imagery. This index characterizes the potential for soil loss and water quality degradation of large watersheds. The end product of this analysis is a land cover Erosion Potential Index (EPI) such as in (Figure 1.3) that integrates ground surface slope (S), soil erodibility (K) and a normalized difference image index (NDI) derived from seasonal Landsat 7 satellite imagery.

The second application produces a grid dataset of hydrologically relevant land cover with combined use of Landsat 7 imagery and high-resolution aerial imagery. A dataset of this type is a prerequisite for best-practice modeling of watershed hydrologic response.

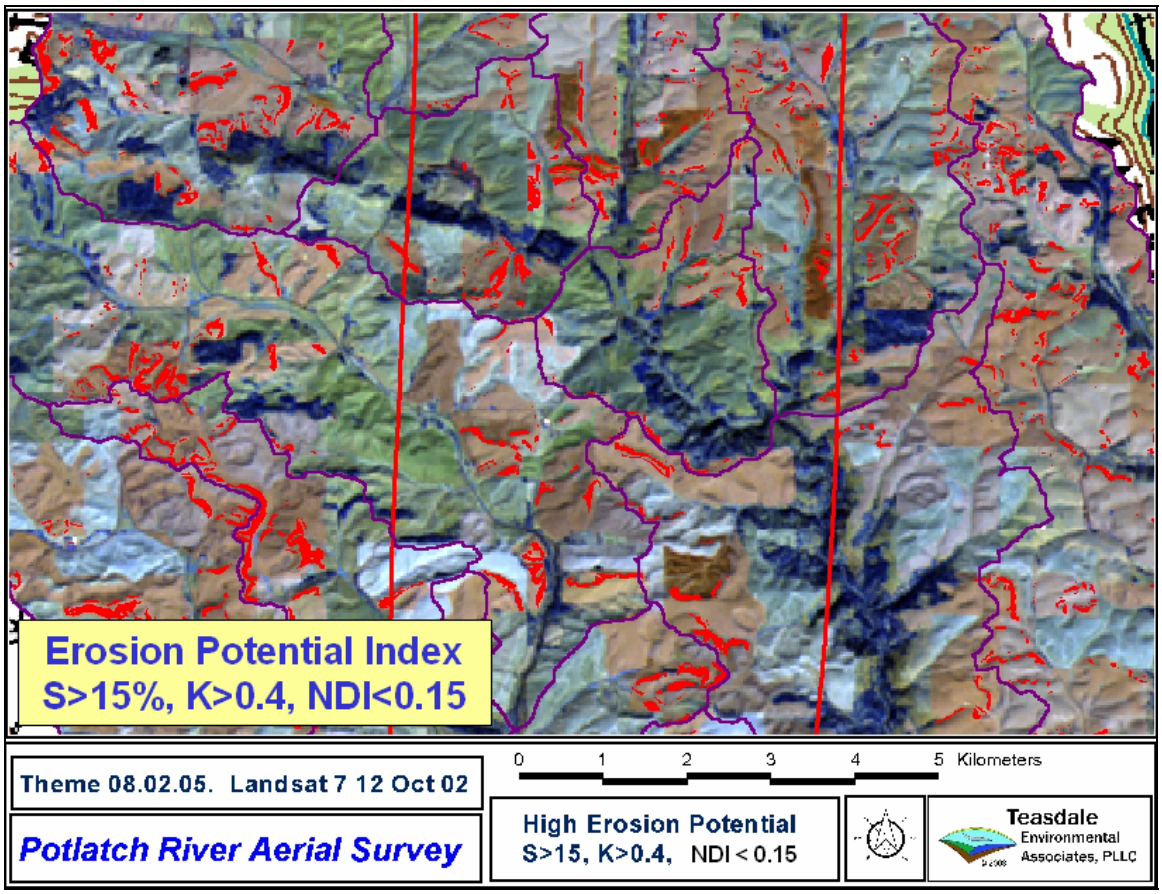

Figure 1.3 Erosion potential index in the Middle Potlatch Creek basin.

1.2.5 Assessment of Stream Morphology with Aerial Imagery

Over 2000 stream miles of natural color and color infrared aerial images were acquired within the Columbia River Basin in Washington, Idaho and Oregon during the research. Section 6 presents the main findings of this extensive evaluation and demonstrates practical use of aerial imagery in the assessment of rivers and streams. It is a unique contribution to literature of water resources, sediment transport and geomorphology. It should clearly demonstrate to researchers and practitioners that opportune acquisition of high-resolution aerial imagery is practical, and in many situations, the only means to acquire stream morphological data.

Many applications of stream morphology assessment are demonstrated such as the assessment of channel meander migration of the Palouse River in Figure 1.4. A previously unrecognized, perhaps controversial, reach scale morphological structure is proposed based on the research. Many opportunities for further research are suggested.

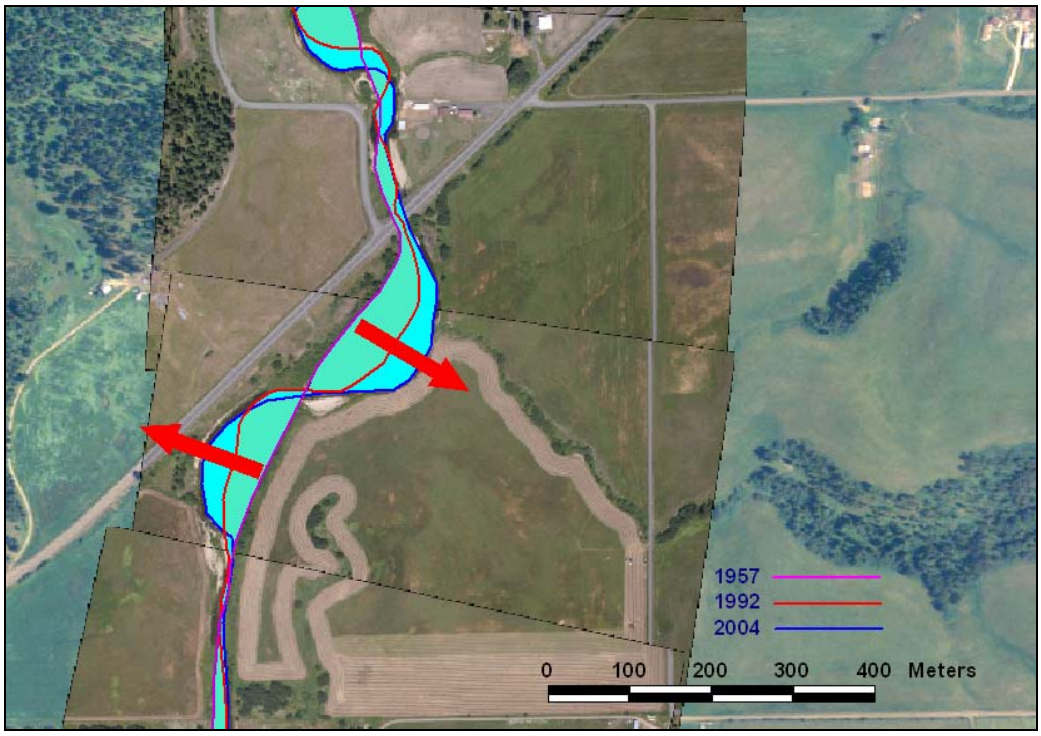

Figure 1.4 Channel change 1957-2004 on the upper Palouse River near Harvard, ID.

1.2.6 Assessment of Soil Erosion with Aerial Imagery

It is surprising that organized soil conservation makes little use of aerial survey and high-resolution aerial imagery in soil conservation planning and erosion assessment. Section 7 evaluates the status of operational soil erosion modeling and demonstrates how aerial imagery can be applied in best-practice soil loss estimation. Estimating soil loss over extensive areas is difficult by conventional methods. Much of the data necessary for computation of soil loss (Figure 1.5) including slope profile, land surface condition and pathways of concentrated flow can be derived from high-resolution aerial imagery.

High-resolution aerial imagery augments existing digital soils and elevation data in an enhancement of the soil loss computation technology developed by the U.S. Department of Agriculture such as the updated Revised Universal Soil Loss Estimation method (RUSLE2). The imagery based procedure is practical, efficient and provides direct observational evidence of soil erosion to validate soil loss computations. Several opportunities for further research are suggested.

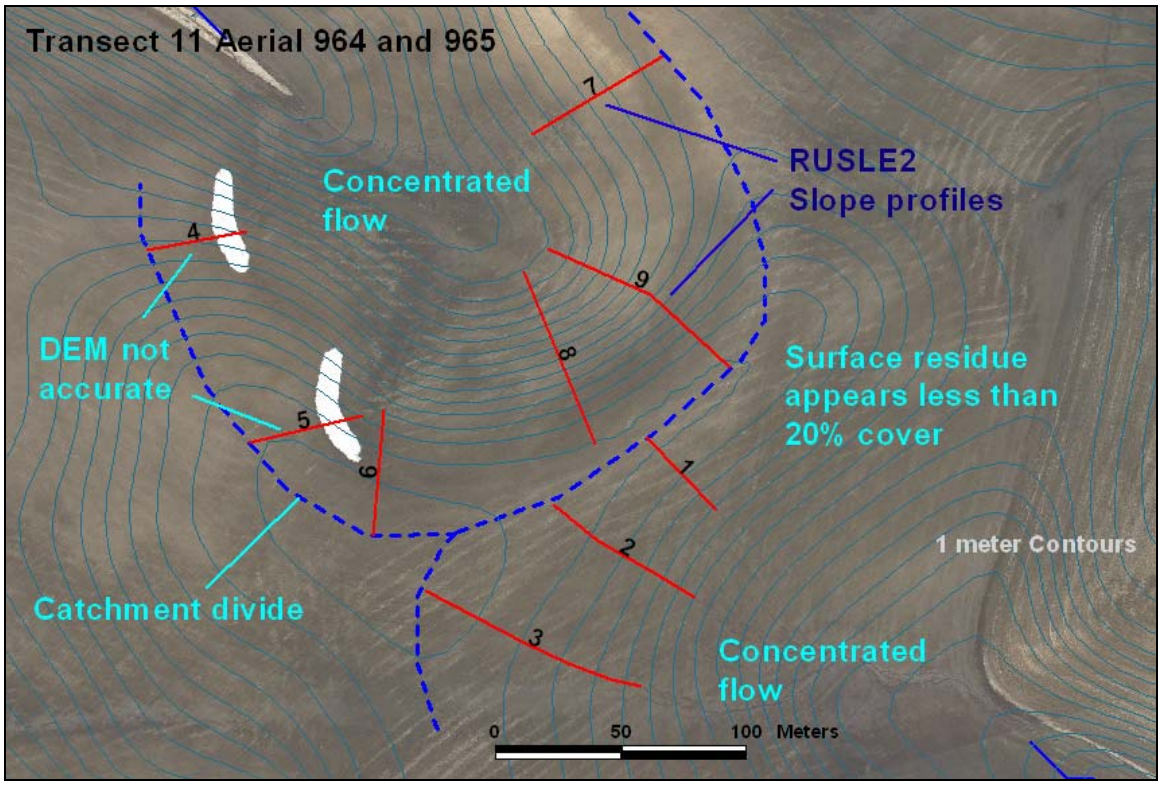

Figure 1.5 Potential RUSLE2 Profiles in a March 16, 2004 aerial image.

1.2.7 Analysis of Ephemeral Gullies with Digital Aerial Imagery

Conventional techniques of reconnaissance and field measurement of gully position, length and volume are appropriate for small catchments, but extensive field survey of ephemeral gullies is logistically difficult, costly, intrusive of private property,

and not synoptic. Aerial survey is the only practical alternative for monitoring and assessing ephemeral gully erosion for entire watersheds.

Section 8 discusses in detail the principles and procedures of measuring ephemeral gully erosion with high-resolution aerial imagery (Figure 1.6). An original physically-based ephemeral gully model is developed and demonstrated. This component of the dissertation work has immediate practical value and much potential for future research.

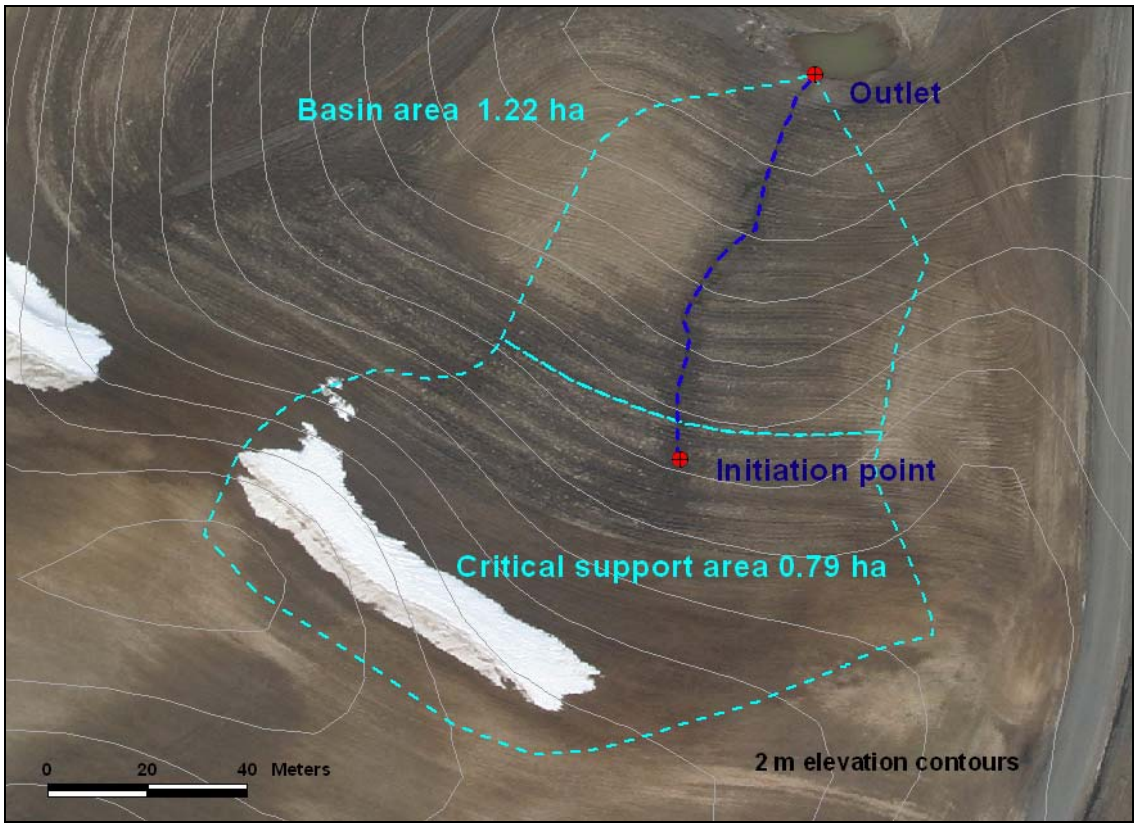

Figure 1.6 Digitized ephemeral gully and catchment parameters.

1.2.8 Reader Synopsis

Together Sections 2 through 8 form the most comprehensive and consistent demonstration of the application of satellite and aerial remote sensing methods to inland watershed hydrologic characterization and stream morphology assessment available in the technical and academic literature. Environmental scientists and water resource engineers who desire to apply remote sensing techniques in research and practice will likely find the insights and examples of immediate value. Readers new to remote sensing, especially graduate students engaged in hydrologic research, should find the technical discussions and cited literature an effective means to gain an accelerated knowledge of operational remote sensing techniques. Both groups of readers were kept in mind while preparing this document. It is my hope and belief that this work opens doors to unexplored hydrologic research and provides much practical help to those endeavoring to become familiar with operational satellite and aerial imaging assessment methods.

2. Operational Satellite and Aerial Imagery

Remote sensing is the science and art of obtaining information about an object, area, or phenomenon through analysis of data acquired by a sensor that is not in direct contact with the target of investigation (Lillesand and Kieffer 1994). The practice of remote sensing encompasses many instruments, platforms and data processes. Remote sensing is a well-developed science that has proven useful in many fields of earth science and engineering. Remote sensing is a powerful tool that aids understanding of the functioning of ecosystems and research in the application of remote sensing techniques should be a high national priority (NAS 2001).

Remote sensing is a mature science. Lueder (1959) reports characterization of landforms and hydrography with aerial remote sensing began soon after development of the airplane. Perhaps the earliest scientific journal article of the remote sensing of water resources in the North American literature is by Jones in *Science* (1920) that describes the aerial topographic and hydrographic mapping work of the U.S. Army and Navy aerial services. The rich and varied history of aerial remote sensing provides context and motivation for the dissertation research. It reveals that the application of remote sensing in watershed science is mostly unexplored and offers much potential to the innovative researcher. New and improved remote sensing technology and data distribution systems continually advance the potential for new lines of research and furtherance of existing investigations.

This dissertation research is concerned mostly with the techniques and capabilities of operational remotes sensing as applied to hydrologic analysis of watersheds and assessment of stream morphology. The object of operational land remote sensing is to

produce data or analyses of the condition or status of the earth surface for purposes other than the testing and development of remote sensing equipment or capabilities. Operational remote sensing technology must be proven and available to a non-exclusive body of civilian users. A user of operational remote sensing data should have a reasonable expectation that similar or better data can be obtained in future work through a well established and reliable procurement process. Most of the technology and sources described in this section are firmly established in operational remote sensing or appear likely to become operational within a short time.

No one field of science dominates the application of remote sensing. A review of university curricula in natural sciences, engineering and sociology reveals that remote sensing and spatial analysis are important parts of many professional educations. The potential literature base is very broad. A review of websites related to remote sensing in early 2001 identified over 150 remote sensing organizations in North America, over 120 organizations in Europe, approximately 5 in South America, 15 in the Pacific, 20 in Asia, and 6 in Africa. The number of organizations involved in remote sensing should continue to grow in parallel to the growth in the use of geographic information systems.

2.1 Use of Satellite and Aerial Imagery by Natural Resource Agencies

Many federal and state agencies routinely acquire remote sensing imagery and aerial photography to support resource management and environmental analysis. Among these are the National Aeronautics and Space Administration (NASA), U.S. Geological Survey (USGS), U.S. Forest Service (USFS), U.S. Bureau of Land Management (BLM), U.S. Army Corps of Engineers (COE), U.S. Fish and Wildlife Service (USFWS),

National Oceanic and Atmospheric Administration (NOAA), Federal Emergency Management Agency (FEMA), and U.S. Environmental Protection Agency (EPA). State agencies include natural resource departments, forestry departments, water resource agencies, environmental quality agencies, and fish and wildlife departments. Many Native American tribes have remote sensing departments.

International counterparts are found in many other countries. Those with active remote sensing programs include Canada, the United Kingdom, Australia, the Netherlands, France, Germany, Russia, Norway, Sweden, Finland, and Japan. Service organizations sponsored by the United Nations also use remote sensing data in core activities and publish guidance documents (Green et al. 2000). This summary emphasizes the U.S. contribution.

2.1.1 U.S. Geological Survey

The U.S. Geological Survey is the largest producer of remote sensing data and geospatial products for land surface assessment in the U.S. and possibly the world. Publications of the USGS describe satellite and aerial photography products, topographic mapping procedures, topographic mapping products and geospatial data products. USGS maintains an Aerial Photography Summary Record System (APSR) that records current and past aerial photography projects in the U.S. (USGS 1998). Numerous bulletins and fact sheets by USGS describe practical aspects of ordering and using satellite and aerial imagery obtained from USGS. Many fact sheets are available online at websites linked to the main USGS website at http://www.usgs.gov.

USGS archives the data from many of the U.S. remote sensing systems at the Earth Resources Observation System (EROS) Data Center or EDC. Holdings can be

searched and ordered through the USGS EarthExplorer web access at http://earthexplorer.usgs.gov. The EarthExplorer access replaced USGS's initial web access system, Global Land Information System (GLIS), in 2001. Data sets searchable through EarthExplorer include:

- Landsat Multi Spectral Scanner (MSS, Landsat 1-5)
- Thematic Mapper (TM, Landsat 4-5)
- Enhanced Thematic Mapper (ETM, Landsat 7)
- Corona (declassified satellite imagery)
- DOQs (digital orthophoto quads)
- NAPP (National Aerial Photography Program)
- NHAP (National High-altitude Aerial Photography)
- Digital elevation models
- USGS Paper Maps

EDC also maintains the National Satellite Land Remote Sensing Data Archive. Required by Congress, it provides a permanent and comprehensive record of the earth's land surface derived from almost 40 years of satellite remote sensing (USGS 2000). The archive holds data from:

- The Advanced Very High Resolution Radiometer (AVHRR)
- 880,000 declassified intelligence satellite photographs.
- Landsat 7
- MODIS
- ASTER
- The Shuttle Radar Topography Mission (SRTM)

- LightSAR, a NASA synthetic-aperture radar instrument
- NASA's Small Spacecraft Technology Initiative, or SSTI

USGS provides access to NASA remote sensing data sets through the Distributed Active Archive Center (DAAC). DAAC was established as part of NASA's Earth Observing System (EOS) Data and Information System (EOSDIS). Data is accessed through the EOS Data Gateway web-based query system. Data sets include:

- Landsat 7 ETM+
- Terra ASTER
- Terra MODIS
- Landsat Pathfinder
- AVHRR
- Global 30 Arc-Second Elevation Data Set
- Global Land Cover Characterization
- Airborne Imagery
- SIR-C

2.1.2 U.S. Bureau of Land Management

The U.S. Department of Interior, Bureau of Land Management (BLM) is required to maintain a continuous inventory of the lands it administers by the Federal Land Policy and Management Act of 1976. BLM maintains extensive spatial data sets as part of the agency GIS. Much of the data is available to the public through web access to the various BLM offices. BLM recognizes riparian zones as important and unique components of ecosystems in the western U.S. Riparian inventory procedures

developed by BLM utilize color infrared aerial photography to help determine the location and condition of riparian-wetland areas (Clemmer 1994; Clemmer et al. 1999).

2.1.3 U.S. Forest Service

Aerial photography and remote sensing are a primary means to acquire spatial information for extensive lands managed by public and private forestry organizations. The U.S. Forest Service (USFS) has been a leader in development of remote sensing techniques in natural resource management since the 1920's, and expects imagery use to continue to grow (Dull 1992). The Forest Service acquires aerial photography, satellite imagery and aerial videography to aid in many of its land management activities including monitoring forest plans, vegetation mapping and range allotment mapping (Lachowski 1992).

Many USFS remote sensing and GIS publications apply to watersheds in the Pacific Northwest. Aldrich (1979) authored a classic summary of remote sensing use in forestry that is often cited in USFS publications, and is still a relevant introduction. More recently, Lachowski et al. (1995) reviewed uses and characteristics of satellite imagery and developed guidelines for mapping vegetation with digital imagery. Detection of land use change and variation of hydrologic condition is discussed in recent reports recent reports (Hall 2001; Robichaud et al. 2000; Skovlin et al. 2001)

The U.S. Department of Agriculture (USDA) Aerial Photography Field Office (APFO) is the primary repository of historic and current aerial photography acquired by the U.S. Forest Service, Farm Services Agency and the Natural Resources Conservation

Service (NRCS). Catalogs of aerial photography holdings are available on the APFO website, http://www.apfo.usda.gov/.

2.1.4 Natural Resources Conservation Service

The NRCS National Engineering Handbook suggests the use of aerial photography to characterize watersheds when developing hydrologic analyses (Woodward 1999). It notes that aerial survey may be the only practical means to characterize stream reaches for hydraulic modeling in difficult or remote terrain (Woodward 1998).

2.1.5 U.S. Fish and Wildlife Service

Historic aerial photos are examined to characterize the state of channel equilibrium in the Instream Flow Incremental Methodology developed by the U.S. Fish and Wildlife Service (Bovee 1982). National Wetlands Inventory documents produced by the USFWS include guidelines for the use of aerial photography in classifying wetlands and riparian mapping (Cowardin et al. 1979; Dall et al. 1997).

2.1.6 U.S. Army Corps of Engineers

Detailed spatial data is necessary for the U.S. Army Corps of Engineers (USACE) to design, construct and manage its extensive water resource projects. USACE incorporates guidance for spatial data acquisition in its engineering manuals and circulars. In particular, engineering manual EM 1110-1-1000 provides detailed standard procedures, minimum accuracy requirements, equipment requirements, and quality

control criteria for photogrammetric mapping (USACE 1993). This document is intended as a guide specification for the acquisition on contracted aerial mapping services.

The USACE participates in the development of military applications of remote sensing. Terrain modeling research conducted by the USACE Army Topographic Engineering Center may have applications in the civilian sector. An analysis of the military applications of remote sensing is beyond the scope of this review.

USACE regulates dredge and fill activities in navigable waters and administers the Clean Water Act 404 permit program. The USACE Wetlands Delineation Manual (USACE 1987) recommends the use of aerial photography and remote sensing as a starting point to identify the location and extent of wetlands.

2.1.7 National Oceanic and Atmospheric Administration

The National Oceanic and Atmospheric Administration (NOAA) is the primary agency that collects and distributes remotely sensed hydrologic information. It operates an array of weather satellites through the National Environmental Satellite, Data, and Information Service (NESDIS). NOAA polar orbiting satellites carry the Advanced Very High Resolution Radiometer (AVHRR) which acquires spectral data useful for land surface characterization. Hastings and Emery (Hastings and Emery 1998) give an overview of the AVHRR system and capabilities. The NOAA Polar Orbiter Data User's Guide describes the orbital and spacecraft characteristics, instruments, data formats, etc. of the TIROS-N, NOAA-6 through NOAA-14 polar orbiter series of satellites (Kidwell 1998).

The NOAA National Weather Service (NWS) collects ground based weather data and conducts aircraft based remote sensing through the National Operational Hydrologic

Remote Sensing Center (NOHRSC). Each fall and winter HOHRSC flies gamma radiation snow surveys across the U.S. (Carroll 2001) and processes satellite snow cover imagery to determine snowpack water content. The snowpack data is a primary hydrologic variable in flood predictions made the NWS River Forecast Centers. The NWS also operates the NEXRAD weather radar system and distributes gridded precipitation data for use in hydrologic modeling by many government and private entities. A guide to NOAA products and services is available (Lott et al. 2001).

The NOAA National Ocean Service (NOS) Center for Coastal Monitoring and Assessment (CCMA) conducts research monitoring, surveys and assessments of coastal environmental quality. The Coastal Change Analysis Program (C-CAP) of NOAA's Coastal Remote Sensing (CRS) Program acquires and distributes regional landscape cover/change data in the coastal zone with remote sensing technology. C-CAP developed guidelines and standards for digital regional land cover and land cover change maps along the nation's coastal zone. C-CAP cover types include forested areas, urban areas, and wetlands. The Benthic Habitat Mapping program with C-CAP developed recent guidelines and standards for mapping submerged aquatic vegetation and other nearshore bottom cover types from aerial photography. Benthic habitat mapping products and beach topography (LIDAR) data sets for the Pacific Northwest may be access through the C-CAP website at http://www.csc.noaa.gov/crs/ccap_index.html.

2.1.8 Federal Emergency Management Administration

The Federal Emergency Management Administration (FEMA) administers the national flood insurance program and coordinates disaster relief. Both activities require the acquisition and evaluation of detailed geospatial data in very short time frames.

Remote sensing data is primary data source. FEMA personnel routinely evaluate satellite imagery of weather systems and report the progress of major storms on the agency website (http://www.fema.gov/storm/trop.shtm).

FEMA issues instructions to contractors involved in its flood hazard program to standardize the preparation of flood zone maps for flood insurance studies. These instructions include detailed specifications for determining flood plain cross sections with photogrammetry and Airborne LIght Detection And Ranging (FEMA 1999).

2.1.9 National Aeronautics and Space Administration

The National Aeronautics and Space Administration (NASA) is the primary U.S. federal agency for deployment of civilian spaced-base remote sensing platforms. NASA produces many technical documents related to a broad range of remote sensing topics. Only publications most relevant to remote sensing for watershed characterization will be reviewed here. NASA has several ongoing space-based earth imaging programs that acquire land and ocean imagery useful for environmental analysis, including the Landsat program, the Terrra mission and imagery acquired from manned space flights.

NASA and USGS share joint responsibilities for management of the Landsat 7 program with NASA primarily responsible for satellite operations and USGS provides data archiving and distribution (NASA and USGS 1999). In cooperation with USGS, NASA prepared several documents for users working with Landsat 7 imagery. The online Landsat 7 Science Data Users Handbook (USGS 1998) describes the satellite system and its data products. NASA maintains a website of its technical documents related to Landsat at http://landsat.gsfc.nasa.gov/main/documentation.html.

NASA participates in a multi-agency effort to develop national and global land cover data for global climate change research. One remote sensing system used for land cover assessment is the synthetic aperture radar (SAR). SAR data is used for classification of land cover, measurement of above-ground woody biomass and delineation of water bodies and wetlands, and estimates of soil moisture. NASA describes the theory and applications of SAR in a report available on the Jet Propulsion Laboratory website (NASA 1995).

NASA's conducts an international earth remote sensing study called the Earth Science Enterprise. The earth imagery acquisition component of the study is the Earth Observing System (EOS) consisting of several satellites designed to study global change. Other components are a data distribution system called EOSDIS and international teams of scientists who will study the data. The first satellite in this system, called Terra, was launched on August 18, 2000. It carries five main sensors (NASA 2001b):

- ASTER, or Advanced Spaceborne Thermal Emission and Reflection Radiometer
- CERES, or Clouds and Earth's Radiant Energy System
- MISR, or Multi-angle Imaging Spectroradiometer
- MODIS, or Moderate-resolution Imaging Spectroradiometer
- MOPITT, or Measurements of Pollution in the Troposphere.

These sensors acquire data for global climate research. Three sensors have potential applications in characterization of large watersheds: MODIS, ASTER, and MISR.

MODIS began acquiring continuous global coverage multispectral imagery in 2000. It is a successor to the AVHRR system and images in 36 spectral bands from 0.4

to 14.4 μm with a GSD of up to 250 meters. It has proven capabilities in land cover analysis. Technical documents describing the data processing algorithms for the Terra instruments are available at a NASA website (NASA 2001a). Figure 2.1 is a portion of a MODIS natural color image of a forest fire near Twisp, WA acquired on July 9, 2001. Lake Chelan is in the center of the image. Smoke from the fire is drifting northward.

Figure 2.1 MODIS Image of Forest Fire Near Twisp,WA.

ASTER is a tasking sensor that acquires images with resolutions between 15 and 90 GPR in 14 spectral bands across visible to thermal infrared wavelengths. ASTER images provide data on land and water surface temperature, emissivity, reflectance, and elevation. ASTER's higher resolution helps calibrate and validate other Terra sensors. ASTER collects an average of 8 minutes of data per orbit. ASTER has three telescopes:

visible near infrared (VNIR), short wave infrared (SWIR) and thermal infrared (TIR). Each is pointable in the crosstrack direction, increasing the effective revisit time for the sensor. ASTER can produce stereoscopic images and detailed terrain height models. The images produced by ASTER are considered operational because they are unrestricted and available through an efficient distribution system. A general user cannot easily procure custom ASTER coverages, but can order custom products produced from ASTER imagery such as DEM's for specific areas.

MISR images are acquired with visible and infrared cameras pointed at nine different angles to give oblique views that help determine land surface characteristics. The earth's surface is successively imaged by all nine cameras, each in four wavelengths. Global coverage is acquired about once every 9 days. MISR operates only during the daylight portion of an orbit. MISR can acquire image data in two different spatial resolution modes. In Local Mode, selected targets 300 km long are observed at the maximum resolution of 275 meters (pixel to pixel) in all cameras (250 meters across track for the nadir camera.) The data transmission rate would be excessive if the instrument worked continuously at this maximum resolution (NASA 2001c). Typically six high resolution targets are imaged each day.

NASA launched a second satellite in the EOS series in 2002 called Aqua. Several instruments are designed for global hydrology studies including the Advanced Microwave Scanning Radiometer (AMSR). This is a twelve channel, six frequency total power passive microwave radiometer system which can measure soil moisture content over large land areas. Other satellites in the EOS series are scheduled for launch. A general NASA website with details on EOS is at http://earthobservatory.nasa.gov/.

NASA and USGS provide public access to their large online data archives through the EOS Data Gateway web-based query system. This information management system provides access to a variety of data sets. Data sets are described in online documentation. Some data sets have reduced-resolution images to preview products. All data may be ordered directly from the web. The EOS Data Gateway is located at http://edcimswww.cr.usgs.gov/pub/imswelcome/.

2.1.10 National Imagery and Mapping Agency

The National Imagery and Mapping Agency (NIMA) was established in 1996 to consolidate administration of imagery, imagery intelligence, and geospatial information for the Department of Defense (DoD). It also provides public access to some data and imaging information. In cooperation with NASA, NIMA produced a high-resolution (30 m) global digital elevation data set based on radar coverage obtained by the Space Shuttle Mission STS-99 in February 2000. The final version of the 30 meter (1 arc second) SRTM data set was released in May 2005. USGS and NASA are also participating in processing and distribution of the shuttle elevation data through the seamless data distribution system at http://seamless.usgs.gov/website/seamless/index.asp.

2.1.11 U.S. Environmental Protection Agency

The U.S. Environmental Protection Agency is a primary user of geospatial data for analysis of environmental conditions of the land, air and water. EPA seems to have developed few published documents that directly address remote sensing use in environmental evaluation, but remote sensing use is implied in many of its programs and projects. General guidelines for selection of aerial photography for evaluation nonpoint

source controls are included in EPA monitoring guidance (Dressing 1997). Remote sensing is recommended for monitoring compliance with wetland water quality standards (EPA 1990). EPA and NASA participated in a joint workshop to discuss the state-of-the-art in remote sensing of water resources (EPA 1999b). The participants recommended increased use of remote sensing in EPA's water programs and development of improved remote sensing techniques for evaluating aquatic environments.

Some broad programmatic initiatives support the use and development of remotely-sensed spatial data. Five federal environmental monitoring programs including that of EPA have formed a partnership with the EROS Data Center (USGS) to development comprehensive land characteristics information for the United States (Homer et al. 2004). An overview of the program including current remote sensing derived land cover GIS data is available at the EPA website http://www.epa.gov/mrlc/. This effort is part of EPA's response to the National Environmental Monitoring Initiative which calls for linking of large-scale survey information and remote sensing data with ecological process research at intensive monitoring areas. One of the objectives of the monitoring initiative is to increase the use of remotely sensed data for detecting and evaluating environmental status and change (EPA 1997).

2.2 International and Commercial Satellite Imagery Providers

Satellite imagery for routine and operational use produced by U.S. agencies may be obtained directly from the USGS and NASA imagery ordering systems described above. International and commercial satellite imagery providers also offer a variety of historic and current imagery products useful for operational work. Many have online

imagery ordering systems and provide user support for products. Private sector companies are competing strongly to deploy high-resolution earth imaging satellites and are developing aggressive marketing campaigns.

2.2.1 International Earth Observation Satellite Imagery

Several international agencies and companies have satellites that acquire imagery over the continental U.S. The French Space Agency Centre National d'Etudes Spatiales (CNES) created the commercial SPOT image company in 1982 in cooperation with Belgium and Sweden. Worldwide commercial operations distribute the SPOT (Satellite Probatoire d'Observation de la Terre) satellite imagery: SPOT Image Corporation in the United States, SPOT Image in France, SATIMAGE in Sweden. Three SPOT satellites are operational. Each satellite carries two High Resolution Visible (HRV) sensors that provide 20 m resolution multispectral and 10 m resolution panchromatic images. The SPOT constellation allows stereo image acquisition. The newest and highest resolution satellite, SPOT 5, was launched in 2002. It has 2.5 meter and 5 meter resolution in the panchromatic mode. Multispectral imagery is 10 and 20 meter resolutions. Information about SPOT imagery and an online image ordering system is found at the SPOT website at http://www.spot.com/html/SICORP/_401_.php.

The European Space Agency launched its Earth Resource Satellites (ERS) in 1991, 1995 and 2000. The ERS satellites carry Synthetic Aperture Radar (SAR) sensors, a radar altimeter, a scatterometer, and Along Track Scanning Radiometer (ATSR). The SAR sensors acquires radar images at 30 m resolution. ATSR scans in the infrared range at 1 km resolution. The European Space Agency Centre (ESRIN), located in Italy, is

primary distributor of ERS data. Data catalogs may be accessed at http://earthnet.esrin.esa.it/.

The National Space Development Agency of Japan (NASDA) has developed several weather and earth observation satellites. JERS-1 was launched in 1992. It carried two optical sensors and a SAR with ground resolutions of 18 m. The JERS-1 mission was terminated in 1998. SAR and optical data from JERS-1 is available from international distributors. The Advanced Earth Observing Satellite (ADEOS) was launched in 1996 but failed prematurely in 1997. In its instrument package was an Advanced Visible Near Infrared Radiometer (AVNIR) and ocean monitoring instruments. ADEOS-II is scheduled for launch in 2001. In 2003, NASDA will launch the Advanced Land Observing Satellite (ALOS) as a successor to JERS-1 it will carry optical and SAR sensors with resolutions down to 2.5 m. Information about NASDA satellites is at http://www.nasda.go.jp/index-e.html.

India has an active earth resources observation program. The Indian Remote Sensing satellite IRS-1A was launched in 1988 by the former Soviet Union. It carried simple panchromatic and color infrared sensors. A similar satellite, IRS-1B, was launched in 1991. This was followed with the more advanced IRS-1C in 1995. IRS-1C carries three sensor systems: a panchromatic camera (PAN), a mulitspectral Linear Imaging and Self Scanning Sensor (LISS-III), and Wide Field Sensor (WiFS). The panchromatic sensor has a ground resolution of 5.8 m. Resolution of the LISS-III is 20.5 and 70.5 m depending on the spectral band. A similar satellite IRS-1D was launched in 1997. Another satellite, IRS-P6 the latest in a series of IRS-P satellites, was launch in 2003. It carries an advanced LISS-IV sensor that will provide 5.8 m ground resolution in

either panchromatic or multi spectral mode. The latest IRS satellite, launched in May 2005, is the high-resolution (2.5 m GPR) panchromatic tasking IRS-P5 satellite. It is equipped with forward and backward viewing telescopes for acquiring stereo images. Space Imaging Corporation distributes Indian Resource Satellite data products. Information about the Indian earth observation program is at the Indian National Remote Sensing Agency website at http://www.nrsa.gov.in/.

The Canadian Space Agency (CSA) launched its first satellite, RADARSAT-1, in 1995. RADARSAT carries a SAR sensor that gives a ground resolution of 8 m. A commercial company, RADARSAT International, distributes Radarsat data through a network of authorized resellers. RADARSAT-2 is being designed to acquired SAR imagery with spatial resolution from three meters to 100 meters. RADARSAT International also distributes JERS-1, ERS and IRS imagery. Descriptions of the satellites and imagery is at the company website at http://www.rsi.ca/.

The Russian remote sensing agency, SOVINFORMSPUTNIK, distributes earth imagery collected by the Russian space mapping system, KOMETA. This system acquires topographic stereographic film photography and high-resolution panoramic photography of the earth surface. A deployed satellite orbits for 45 days while photographing approximately 10.5 million square kilometers. The entire system is then retrieved from orbit and landed on the Russian mainland. The film is scanned to produce digital images of about 1 m resolution. Areas of the U.S. may have been photographed as recently as 2000. Inquiries about image availability may be made at the agency website http://www.sovinformsputnik.com/.

2.2.2 High Resolution Commercial Satellite Imagery

Commercial satellite companies now provide global coverage high-resolution satellite imagery. Users are able to order relatively low cost imagery as georectified products at resolutions previously only available from contracted aerial photography. The unprecedented spatial and temporal coverage and unrestricted availability of this imagery is changing the remote sensing industry (Baker et al. 2001; Fritz 1999). Unrestricted commercial access to high-resolution satellite imagery has caused concern for national defense (Baker and Johnson 2001; Hays 2001; Lidov et al. 2000) and may promote unethical use (Baker 2001). Potential for abuse and concern for the ethical use of remote sensing information is not new (Estep 1973).

In 1984, the Land Remote-Sensing Commercialization Act authorized NOAA to solicit commercial bids to manage the existing Landsat satellites, and build and operate future systems with government subsidies. This law proved flawed and did not satisfy Congress' intent (Lauer et al. 1997). The 1992 Land Remote Sensing Policy Act law reversed the 1984 decision to commercialize the Landsat system. This Act authorized the U.S. Department of Commerce to license private companies to operate private remote sensing space systems. The Commercial Space Act of 1998 streamlines government approval of commercial remote sensing systems. NOAA administers licensing of commercial remote sensing systems under rules published in the Code of Federal Records (NOAA 2001). These rules give NOAA authority to restrict availability of images (shutter control) and limit resolution.

Orbimage Corporation has launched two earth observation satellites: the OrbView-1 atmospheric imaging satellite in 1995 and the OrbView-2 ocean and land

imaging satellite in 1997. OrbView-3, launched in June 2003, provides one-meter panchromatic and four-meter multispectral digital imagery. Orbimage describes its satellites and imagery at http://www.orbimage.com/.

Space Imaging Corporation of Thornton Colorado launched the current Ikonos satellite in October 1999. Ikonos carries a 1 m resolution panchromatic and 4 m multispectral sensor. SpaceImaging also distributes imagery from the Indian Resource Satellite (IRS). An online imagery system and descriptions of Space Imaging products is at http://www.spaceimaging.com/.

EarthWatch launched its first satellite, EarlyBird-1, in 1997 on board a Russian Start-1 rocket. It failed in orbit after four days. The launch of EarlyBird-2 was cancelled. EarthWatch launched QuickBird-2 in 2001 from Vandenburg Air Force Base. QuickBird-2 acquires 61 cm resolution panchromatic and 2.44 m multispectral imagery. Information about the QuickBird-2 satellite and the EarthWatch imagery distribution system is available at http://www.digitalglobe.com/.

2.3 Airborne Remote Sensing Systems

At best, current civilian satellites produce imagery with a ground resolution of about 60 cm (e.g. QuickBird-2). This resolution is not yet sufficient for some applications such as large-scale mapping and highly detailed photointerpretation. Large-scale mapping projects, such as for highway design projects, require precise imagery that can be orthorectified to positional accuracies of a few centimeters. High accuracy photogrammetric applications rely on large-format aerial photography acquired by high-quality calibrated aerial mapping cameras. Satellite orbital geometry and ground

resolutions cannot meet the accuracy standards expected for calibrated aerial photography.

Moreover, temporal coverage of satellites is constrained by orbit geometry and a limited ability to direct sensors to off-nadir (sideways) views. Seasonal cloud coverage greatly limits optical satellite imaging for large portions of the earth and may be near continuous is some areas (Lillesand and Kieffer 1994). Current civilian satellites do not provide high-resolution hyperspectral imagery.

Given the practical limitations of satellite imagery, remote sensing systems carried by airborne platforms remain the primary source for applications that require high-resolution imagery of small to medium project areas. The literature of remote sensing reveals a wide variety of remote sensing aircraft from fixed wing airplanes and jet aircraft to helicopters, balloons, and unmanned aerial vehicles. Remote sensing systems are even more varied ranging from conventional film photography systems to radar and hyperspectral imaging systems. The ASPRS Manual of Remote Sensing (Morain and Budge 1997) details 161 airborne remote sensing systems. Not all are currently operating and many are designed primarily for research.

Relatively few commercial and agency airborne remote sensing systems are available for routine civilian work or for use where research objectives are not development or testing of remote sensing systems. Operational airborne remote sensing systems may be classified as:

- Large Format Aerial Photography and Digital Imaging
- Small Format Aerial Imaging (Film and Digital)
- Multispectral Imaging Systems

- Hyperspectral Imaging Systems
- Thermal Imaging Systems
- Radar Imaging systems
- Light detection and ranging systems (LIDAR)

2.3.1 Large Format Aerial Photography and Large Format Digital Imaging

Large format aerial photography is a dominant source of high-resolution imagery for precision photogrammetry and large area reconnaissance. Large format aerial photographs are produced from film negatives that measure 23 cm by 23 cm. Smaller films, typically with negatives measuring 70 mm or less, are classified as small format aerial imagery. The handheld film camera industry designates film sizes between 35 mm and 70 mm as medium format, but this distinction is not adopted in the aerial photography literature.

Many technical references describe the theory, procedures and applications of large format aerial photography. Nearly all the remote sensing texts devote several chapters to large format optical fundamentals, film characteristics, photogrammetric measurements, photo mission planning, lens and filter selection, camera operations, film processing, and applications. Texts by (Campbell 1996; Lillesand and Kieffer 1994; Mikhail et al. 2001; Wolf and Dewitt 2000)) are good references. Though becoming dated and under revision, the industry standard reference is the American Society for Photogrammetry and Remote Sensing (ASPRS) Manual of Photogrammetry by the (Slama et al. 1980) including the more recent digital photogrammetry addendum (Greve 1996).

Aerial film photography is a mature and commercial technology. Technical advances in large format aerial photographic equipment originate primarily in private sector organizations. Acquisition of nearly all large format civil aerial photography archived and distributed by U.S. federal agencies is contracted to private firms. Draft consensus standards for large format aerial photography have been developed by ASPRS in cooperation with industry representatives (ASPRS 1995). The Management Association for Private Photogrammetric Surveyors (MAPPS) offers national representation for private firms that provide aerial mapping and remote sensing services http://www.mapps.org/.

Relatively few manufacturers dominate the large format aerial camera market. Specifications in USACE photogrammetric mapping guidance (USACE 1993) require that aerial cameras "be of like/similar quality to" just six camera models made by three manufacturers: Wild, Zeiss, and Jena. In part, this is because of the exacting standards developed by USGS (Light 1992; USGS 1998b) for aerial camera calibration. These standards are adopted by many agencies to ensure the photogrammetric quality of large format photography. The USGS Optical Sciences Laboratory calibrates large format aerial mapping cameras and maintains a database of calibration parameters for cameras employed in the National Aerial Photography Program. Camera calibration data is available at http://edclxs22.cr.usgs.gov/osl/index.html.

Digital aerial mapping cameras offer an alternative to aerial film cameras for many aerial imaging tasks, but do not yet possess the resolution and frame coverage produced by large format film cameras (Caylor 2000; Light 1996; Mikhail 1999). Precision digital aerial cameras are being developed and may achieve the image quality

of large format film cameras, but not for 10 to 15 years (ASPRS 2000). Currently available models are manufactured by Z/I imaging (Carl Zeiss and Intergraph Corporation) http://www.ziimaging.com of Huntsville, Alabama and Leica Geosystems http://www.leica-geosystems.com. Descriptions of these cameras are available at the corporate websites.

2.3.2 Small Format Aerial Imaging

Acquisition of aerial imagery with small format cameras is well established in natural resource monitoring and environmental analysis. Small format cameras are generally described as light weight film or digital full frame photographic cameras, usually designed for handheld use, that produce images much smaller than large format aerial mapping cameras. Prior to digital cameras, small format cameras typically used 35 mm and 70 mm film. High quality digital cameras have replaced film cameras in small format aerial imaging work.

A wide variety of cameras have served this function ranging from precision metric cameras (e.g. Rolliflex) to consumer 35 mm film cameras and video camcorders. Suitability of camera equipment depends on the intended use of the small format imagery (Warner 1994; Warner et al. 1996). Meyer (1997) reviews the history of small format aerial imaging (SFAA) and its contribution to natural resource management in the U.S. Zsilinszky (1997) provides a similar review of Canadian aerial imaging work. The remote sensing literature shows that just about any quality film or digital camera can be suitable for SFAA under appropriate circumstances.

Much of the dissertation research imagery was acquired with small format digital aerial cameras. The dissertation work would have been impossible without this

capability. Most sections in the dissertation describe, demonstrate and evaluate the application of small format high-resolution digital aerial imagery in land surface and stream characterization. Applications and methods of small format aerial imaging were detailed in the literature review for the dissertation.

2.4 Satellite and Aerial Imagery Use in Watershed and Stream Assessment

Aerial imaging has been a valuable tool in the investigations of water resources and watershed characteristics for many years. This section summarizes a few of the applications described in the English language literature and cites sources for further information. A more detailed summary is in the dissertation literature review. Applications are organized by general resource types, but many techniques and imaging objectives overlap.

2.4.1 Watersheds and Uplands

Classification of current land cover over extensive areas would be a practical impossibility without satellite imagery. High altitude aerial imagery and Landsat imagery enabled development of the first digital land cover databases for the U.S. (Anderson et al. 1976). Landsat images and aerial imagery from the National Aerial Photography Program were the primary data sources for development of the 1992 National Land Cover Dataset (Vogelmann et al. 2001). An updated national land cover dataset is now being developed from Landsat imagery of the late 1990's and early 2000's (Yang et al. 2001).

Land use practices can be identified with aerial imagery. Stafford and Nettles et al. (1976) provides an early review in the civil engineering literature. Investigators use aerial photos to document abandoned mine sites (Berger 1980), agricultural conservation practices (Pelletier and Griffin 1988), and hazardous waste sites (Lyon 1987).

Soil erosion may be detected and measured with large scale aerial photography. Numerous papers report this is a useful and cost effective technique (Frazier and McCool 1981; Frazier et al. 1983; Johannsen and Barney 1981; Morgan et al. 1978; Ritchie 2000; Welch et al. 1984). Satellite imagery has also been applied in investigations of soil erosion (Fraser et al. 1995; Frazier and Cheng 1989)

Large scale videography and GPS provides supplemental information to validate vegetation maps produced from smaller scale satellite imagery. An example is the GAP analysis program in Arizona and New England (Slaymaker 1996). GIS analysis of digital orthophotos expedites the production of vegetation maps (Duhaime et al. 1997).

The USDA Agricultural Research Service has an active program to research the use of remote sensing techniques in crop and soil management. The Hydrology and Remote Sensing Laboratory in Beltsville, MD (Parry 2001) has several projects including the use of LIDAR to measure landscape terrain, estimating crop residue cover with high-resolution VNIR imagery, measurement of soil moisture with L-band microwave, measurement of crop yield with AVHRR data, and the use of color infrared (CIR) aerial photography to determine the spatial variability of crop growth.

The U.S. Forest Service acquires aerial videography for a variety of resource management data collection tasks including forest pest surveys (Myhre and Silvey 1992) and updating forest inventories (Evans and Beltz 1992).

Arnold (1992) compares aerial photography and videography in an environmental assessment of a drinking water supply watershed in the Ipswich River basin in Massachusetts. Land use and land cover were documented with low oblique 35 mm CIR and color videography. Complete basin coverage was acquired with vertical 70mm panchromatic photography and supplemented with color videography. Large format National High Altitude Photography (NHAP) program photos were purchased for a historic comparison.

Veregin et al. (1995) acquired color video imagery of an urban watershed in Ohio to develop a detailed ground cover classification for stormwater runoff modeling with SWMM. Imagery with a ground resolution of 1 meter was acquired with a Sony video camera and recorded in Super VHS format. Image position was logged with onboard GPS equipment and a video encoder. Classifications were physically-based (as opposed to use-based classifications such as "residential") and included grass-stubble, grass, asphalt, concrete, shingle roof, water, deciduous, and shadow. Supervised classifications were performed with decision tree and nearest neighbor classifiers. Shadow effects could not be removed with band ratios.

The USFS Remote Sensing Applications Center acquired digital color infrared imagery of a 1996 forest burn area in the Mendocino National Forest with a Kodak DCS 420 camera. Digital images with a ground resolution between 1 and 3 meters were georeferenced to SPOT 10 meter resolution orthocorrected satellite imagery to create an imagery data layer for GIS analysis. Burn area assessments were improved when the imagery was used in addition to conventional sketch mapping techniques.

Ahmed and Neile (1997) estimated crop water demand for irrigation scheduling from multispectral video imagery acquired with the Utah State University videography system. Soil adjusted vegetation index (SAVI) was correlated with crop water demand coefficients. Water allocation could be scheduled based on the imagery model and routine weather data rather than on field soil moisture and crop canopy measurements.

Chewings et al. (1997) verified the accuracy of a Landsat derived PD54 vegetation index with high-resolution multspectral videography. The PD54 is computed from green and red bands of Landsat TM. This index indicates the amount of vegetative cover in arid rangelands. Video cameras equipped with blue and red bandpass filters acquired imagery in approximately the same bands as Landsat TM. PD54 vegetation indices were computed from the high-resolution imagery and aggregated to 30 m pixels to verify the Landsat derived indices. The multispectral video imagery was acquired with the SpecTerra airborne imaging system at a ground resolution of 1 meter.

2.4.2 Rivers and Streams

Aerial imaging has aided pollution monitoring and water quality assessment. Researchers tracked effluent dispersion with a handheld camera onboard a helicopter in an early application in Canada (LeDrew and Franklin 1983). Remote sensing monitoring of effluent plumes is also useful in coastal applications (Davies and Neves 1997). The Tennessee Valley Authority was an early user of aerial photography for identifying dispersed (nonpoint) pollution sources (Perchalski and Higgins 1988).

Aerial photography was a useful source of spatial information for water resource evaluation. Neill and Galay (1967) mapped channel widths and profiles with aerial photography in an evaluation of river regime. Many investigators evaluated temporal

sequences of aerial photos or digital images to document stream channel change (Beeson and Doyle 1995; Odgaard 1984; Winterbottom 2000; Wolman 1959). Komura (1986) computed flood profiles from photogrammetric measurements of a time series of aerial photographs. Others attempted measurements of water velocity with a series of aerial photographs (Cameron 1960; Kim 1987).

The U.S. Bureau of Reclamation (BOR) identified habitat for native fisheries on the Green River below Flaming Gorge Dam with aerial photography and videography (Pucherelli et al. 1992). Backwater area from the aerial imagery was correlated with river flows to evaluate habitat availability for endangered native fish. BOR undertook the remote sensing approach after the simulation methods of the Instream Flow Incremental Methodology (IFIM) proved inadequate. Quality of the Aerial videography was adequate for habitat monitoring for the objectives of the study and judged to be cost effective.

Mesoscale hydraulic features were delineated from multispectral videography acquired by the USU system of the Green River. Hydraulic features included turbulent reaches, ruffles, shoals, shallow areas, runs and pools (Anderson et al. 1993). Hydraulic features delineated by classification algorithms compared favorably with classification determined on the ground. Turbid water can impair the ability to delineate hydraulic structure, but useful information may still be extracted (Panja et al. 1993).

Thermal refugia and Chinook Salmon habitat were mapped on the North Fork of the John Day River with aerial thermal videography (Torgersen et al. 2001; Torgerson et al. 1995). Thermal videography was acquired with an AGEMA Thermovision 800 FLIR (forward-looking infrared) instrument carried at low altitude onboard a helicopter. Ground resolution of the 140 x 140 pixel thermal images was 0.2 – 0.4 meter.

HoboTemp digital data loggers recorded instream temperature data for comparison. The geographic track of the imagery flight line was logged with onboard GPS equipment and matched to time information in the thermal image files. Locations of cool water inflows were readily detected and were not necessarily associated with riparian vegetation or channel morphology. Spatial temperature characteristics were cooler and more uniform in forested reaches.

Neale et al. (1995) developed a GIS model of bank erosion potential with multispectral aerial images of stream corridors as a primary input. Digital aerial imagery with a ground resolution of 0.2 meter was acquired with the USU aerial videography system. GIS themes included soils, vegetation density, stream curvature, and stream slope. Soil erodibility was ranked as high, medium and low based upon subjective analysis of existing soil information. Aerial imagery of bank vegetation was classified as dense, medium, low and bare exposed bank soil. Stream water surface profile and flow velocity were classified from the aerial imagery of hydraulic stream structure and some field measurement. Erosive weights 1, 2, and 3 were assigned to pools, runs and riffle classes. Curvature of stream segments measured on the georectified aerial imagery were assigned to subjective curvature erosion potential classes. A comparison of the GIS estimated erosion potential and field measurement of bank erosion was inconclusive.

General discussions of remote bathymetry reveal a variety of physically-based and empirical approaches for determining water depth from aerial photography and multispectral imagery (Ji et al. 1992; Lyon et al. 1992; Lyzenga 1981). Shallow river bathymetry was mapped with color infrared multispectral video imagery and small format aerial photography in streams in British Columbia (Roberts et al. 1995).

Regression analysis of aerial image pixel brightness (DN) of imaged underwater targets and measured stream depth exhibited a reasonable correlation (r^2 = 0.87). Water turbidity, the presence of spawning fish, and high scene contrast when banks were snow covered all inhibited the DN: depth relationship.

2.4.3 Lakes and Reservoirs

An early study by Funk and Flaherty (1972) demonstrated the advantages of small format aerial photography, including infrared film photography, in lake and watershed assessment. Aerial photographs gave investigators a synoptic view of the lake environment including identification of surface outlets, aquatic growth, possible nutrient sources and size of the basin in relation to other hydrographic features of the area.

Macrophytes in lakes, reservoirs and large rivers can be mapped with aerial imagery (Benton et al. 1980; Marshall and Lee 1994; Wile 1973). A good example is the mapping of submersed macrophytes in the St. Clair and Detroit rivers connecting Lake Huron with Lake Erie (Schloesser and Manny 1986; Schloesser et al. 1988). Presence of submersed macrophytes was detected on color aerial photography with about 80% accuracy compared to field data. Results were dependent on water clarity, relative density of the macrophytes, and skill of the interpreter.

Everitt et al. (2000) mapped the distribution of waterhyacinth and hydrilla in the Rio Grande with color infrared videography integrated with GPS and GIS. CIR photography was also used for detecting giant salvinia infestations. Reflectance measurements showed the macrophytes had unique spectral characteristics that facilitated their detection on aerial imagery.

2.4.4 Wetlands and Riparian Vegetation

Numerous investigations demonstrate aerial imagery can be analyzed to locate riparian and wetland boundaries, classify vegetation and assess temporal change (Barrette et al. 2000; Civco et al. 1986; Knott et al. 1997; Seher and Tueller 1973).

Frazier et al. (1993) acquired 35 mm color aerial photography of wetlands in Washington State to identify infestations of Purple Loosestrife. An interpretability test of several commercial films showed Fuji Velvia to give slightly better color discrimination of Purple Loosestrife blossoms than Kodachrome 64 and Extachrome 100. Photo negative scale was 1:5000.

Color video aerial imagery of a wetland was acquired with a Panasonic GP-KR412 Super-VHS video camera (Johnston et al. 1996; Sersland et al. 1995). Image locations were logged with an onboard Motorola LGT1000 GPS. Summer and fall images exhibited seasonal phenological changes. Images captured with a Targa frame grabber were georeferenced, rectified, mosaicked, and composited into a multi-temporal image. Vegetation was classified using a supervised classification algorithm. Comparison of the classified video image with the Thiessen polygon maps developed from ground data showed a 60% correspondence. Maps developed using field data provided more detailed classification of plant community types, but the airborne video maps provided a more detailed spatial depiction of their distribution.

Franklin et al. (1997) applied linear discriminant analysis to multispectral video imagery of riparian vegetation in the Lake Tahoe Basin. Riparian classes included deciduous riparian, coniferous riparian, moist meadow, wet meadow, emergent, and nonriparian. Imagery with 1.6-1.8 meter ground resolution was acquired with the

commercial SpecTerra digital multispectral video system for spectral bands centered at 450, 550, 650 and 770 nm. The video images were georeferenced to a USGS digital orthophoto quadrangle (DOQ). A statistical comparison of riparian classes determined from the multispectral imagery showed good accuracy (75%) with the linear discriminant analysis.

2.4.5 Hydrology and Hydrologic Modeling

Remote sensing technology is changing the practice of hydrologic analysis. The link between hydrologic analysis and remote sensing is clear: practical hydrologic analysis requires an abundance of geospatial information that usually must be developed by remote sensing techniques for projects larger than a few hectares. Remote sensing provides a perspective of broad-scale, dynamic patterns that can be difficult to discern using only point measurements.

Schultz and Engman (2000) recently edited an overview of remote sensing applications in hydrology and water management. Contributing writers discuss basic remote sensing principles, image processing, remote sensing in hydrologic modeling, precipitation measurement with radar, determination of land use and land cover characteristics, estimation of evapotranspiration, measurement of soil moisture, surface water extent and depth, snow and ice cover, general aspects of remote sensing in water management, irrigation and drainage, and detection of land cover change.

Hydrologists have sustained an effort to develop hydrologic models with remote sensing data. Early work predicts soil runoff coefficients with data from passive microwave measurement of soil properties (Blanchard et al. 1975). Engman (1982)

describes early approaches in runoff prediction, snow hydrology, flood mapping, wetlands delineation, and soil moisture assessment. Other early studies found satellite imagery useful for general water management (McGinnis et al. 1980), surface water inventory (Thiruvengadachari et al. 1980), verification of hydrodynamic models (Graham and John 1983), and flood prediction (Tao and Kouwen 1989).

Satellite and aerial imagery is used to develop land surface characteristics for hydrologic models (Bondelid et al. 1982; Ragan 1975). Chery and Jensen (1982) developed a lumped water balance model for a 15 km^2 watershed in southern Georgia with Landsat derived land cover data. Rango et al. (1983) developed input parameters for the HEC1 model from Landsat imagery. Similar applications have been developed by others (Franz and Lieu 1981; Smith and Bedient 1981; Trolier and Philipson 1986).

Hydrological models are not often designed to readily accept remote sensing data as input variables, but some are adaptable such as the U.S. Army Corps Engineers Streamflow Synthesis and Reservoir Regulation (SSARR) and the Snowmelt-Runoff Model (SRM). There is strong motive to adapt existing models: Landsat derived land cover data costs about one third that of conventional assessment techniques for basins larger than 25 km^2 (Rango and Martinec 1995). A U.S. Army Corps of Engineers Technical Paper (USACE 1980) recommends procedures for determining land use from satellite imagery. Hourani (1998) gives a practical example of hydrologic analysis with remote sensing data. Fortin et al. (2001) discuss development of hydrologic models compatible with remote sensing data.

Remote sensing of soil moisture is a promising area of research (Schumugge and Jackson 1996). Lin, Wood et al. (1994) compared soil moisture estimates from a

microwave radiometer and a synthetic aperture radar (SAR) with field-measured values. Remote sensing of soil moisture is the subject of a theme issue of the *Journal of Hydrology* in which Ulaby et al. (1996) give an overview of mapping soil moisture with radar. Contributing authors provide an overview of passive microwave techniques and discuss aerial acquisition of passive microwave data. Landsat thermal infrared data can also indicate soil moisture (Shih and Jordan 1993).

Bates et al. (1997) examines recent progress in remote sensing of flood hydrology and suggests an approach to calibration of high resolution flood hydraulic models based on remote sensing data. Useful properties include spatially-distributed boundary friction values, direct measurement of water surface level, measurement of rainfall rates and distribution, sediment concentrations and inundation field extent. A comparison of flood-extent predictions from a two-dimensional high-resolution channel model of the Missouri River with Landsat imagery for a steady flow discharge showed good similarity.

2.4.6 Water Quality

Optical properties of water are altered by the presence of suspended and dissolved materials. Correlation of optical characteristics with constituent concentration is the basis for some forms of laboratory measurement of water quality. Freshwater lakes and streams are optically complex because of the presence of phytoplankton, dissolved organic materials, and suspended sediment (Lathrop 1992; Wetzel 1983). Optical properties of freshwater streams and lakes may vary seasonally or in a matter of minutes with flow rates, turbidity levels, algae concentration, and solar angle. Quantitative remote sensing analysis of waterbodies is challenging because of the highly variable optical properties of water with location and time. Still, this variability, when combined

with the science of image spectroscopy, forms the basis of water quality evaluation by optical remote sensing.

Remote sensing offers a means to extend the coverage of point sample water quality data based upon physical characteristics of the waterbody. Some of the earliest applications of remote sensing in water quality investigations are found in international conference proceedings (Grew 1973; Johnson 1969; Lund 1978). Recently, Ritchie and Schiebe (2000) reviewed the remote sensing of the water quality characteristics and found the most often examined characteristics to be suspended sediments, chlorophyll, temperature, and surface oils.

In an early study, Whitlock et al. (1982) examined multispectral techniques as a possible tool for measuring total suspended sediment (TSS) concentrations. Best correlations of spectral response with TSS concentration were obtained in the near infrared band. The authors also recommended maximum depths of TSS sampling for near infrared remote sensing correlations, all less than 50 centimeters with lower values for high TSS concentrations.

Han (1997) conducted laboratory spectrometer tests to examine the effect of algae concentration on TSS reflectance in the visible and near infrared range. Algae reduced spectral reflectance in the visible range (400-700 nm), but had minimal effects on near infrared reflectance (720-900 nm).

Khorram and Cheshire (1985) conducted in-stream sampling of the Neuse River Estuary simultaneously with an overpass of the Landsat Multispectral Scanner and acquisition of color aerial photography (70 mm) by the U.S. EPA Enviropod. Regression models of salinity, chlorophyll, turbidity, and total suspended solids (TSS) were

developed with reasonably good results for salinity, chlorophyll and turbidity (R^2 values of 0.82, 0.70 and 0.76). The R^2 value for total suspended solids was 0.64.

Lathrop and Lillesand (1989) evaluated water quality parameters in Green Bay with SPOT multispectral imagery. Linear regression of MSS reflectance with log transformed secchi depth, turbidity and total suspended solids were good with R^2 values of 0.83, 0.88 and 0.93 respectively. A separate correlation of chlorophyll was difficult because of highly turbid conditions. Cross correlation analysis showed high intercorrelation of suspended sediment concentration, dissolved organic matter and chlorophyll with reflectance in the three SPOT spectral bands (green, red and near infrared).

Lathrop (1992) also developed TSS and Secchi depth regressions for Green Bay and Lake Yellowstone in Wyoming with Landsat reflectances. Power law expressions of band reflectance ratios yielded the best regression fits (R^2 from 0.82 to 0.94). Different relationships were developed for Green Bay and Lake Yellowstone.

Liedtke et al. (1995) measured suspended sediment concentration in the Fraser River with airborne multispectral imagery. Simple linear regressions with green and red spectral bands were reasonable predictors of suspended sediment concentration. MSS imagery should be corrected for sun angle and atmospheric influences for improved predictions.

Land and water surface temperatures are routinely measured by satellite remote sensing of thermal infrared radiation. NASA and NOAA develop global sea and land surface temperature datasets as standard products from MODIS and AVHRR sensors. Resolution of these data sets is too coarse for measuring temperatures of rivers, reservoirs

and all but the largest lakes. Higher spatial resolution water surface temperature measurements can be made with Landsat TM and airborne infrared sensors. Lathrop and Lillesand (1987) demonstrated that accurate temperature estimates of Lake Michigan (standard error < 0.1 °C) could be made from band 6 (10.4 to 12.5 μm) of Landsat 5 TM when calibrated with representative ground temperature measurements. Radiant temperatures computed from blackbody characteristics were accurate to within 1 °C, even without atmospheric correction. Satellite derived temperature maps were very useful in characterizing the circulation pattern of the lake.

Measurement of stream and river water surface temperature is a relatively new development in operational remote sensing. Torgerson et al. (2001), acquired thermal airborne Forward Looking Infrared (FLIR) digital imagery for several Oregon basins. Thermal sensing of stream and rivers appears to have become operational before being firmly supported by environmental and engineering research. This may be evidence that this capability is highly desired by water resource managers.

2.5 Satellite and Aerial Imagery Demonstration and Guidance

The examples cited above demonstrate that the extensive literature of remote sensing is an invaluable resource for researchers contemplating the application of remote sensing techniques in water resource investigations. However, the literature is much dispersed and difficult for many potential users to access and do not demonstrate important practical aspects of remote sensing. During the course of the dissertation research, I developed a comprehensive and extensive demonstration satellite and aerial imagery datasets in separate, but related work for the Bonneville Power Administration

(BPA). These materials are available directly from the BPA office in Portland, Oregon (800-282-3713). The BPA datasets are too general to describe in detail in the dissertation, but many new users would likely find the practical summary of operational imagery sources and demonstrations produced in this work a beneficial starting point for further study. These products are briefly referenced here.

The datasets were developed for 25 demonstration sites in various watershed and water resource settings throughout the Columbia River Basin. Most project datasets include:

- Current and historic Landsat satellite imagery
- ASTER satellite imagery
- High-resolution digital natural color or color infrared imagery
- USGS geospatial products including digital orthophotoquadrangles, digital raster graphic topographic maps, digital elevation data, and national land cover data.

Some project areas also include Ikonos satellite imagery and multispectral datasets from the Department of Energy Multispectral Thermal Imager (MTI). The datasets are only available from BPA.

Project areas were selected to demonstrate practical application of remote sensing technology and methods in the assessment of aquatic resources. Investigations included aquatic macrophyte monitoring, various watershed land cover assessments, and various stream and riparian assessments. Educational materials were produced from the project datasets that demonstrate and guide basic remote sensing imagery selection, processing and analysis. Satellite and imagery characteristics are summarized in spreadsheet tables

that suggest typical uses in aquatic assessment. Imagery and geospatial sources are organized by assessment category (watershed, rivers and streams, lakes, wetlands) and by general resolution of the imagery or geospatial data type (low, medium, high). These tables are intended to guide selection of imagery and geospatial data.

The guidance tables and other educational material from the BPA provide a practical introduction to operational remote sensing data for users interested in water resource applications. An excerpt from the table of suggested medium resolution data sources for watershed assessment is in Table 2.1. Other tables in the spreadsheet describe sources of the imagery (Table 2.2) and suggest literature references for further information on particular applications (Table 2.3). The satellite and aerial imagery use guidance spreadsheet is included in the digital resource compact disc accompanying the dissertation.

2.0	Medium Scale Medium Resolution	No.	Assessment Task Description	Imagery or Theme Name	Resolution or Scale
2.1	**Watersheds**	2.1.1.a	Topographic information	USGS 1:24,000 Digtal Raster Graphic (DRG)	1:24,000
		2.1.2.a	Online viewing of topographic information	USGS 1:24,000 Digtal Raster Graphic (DRG)	1:24,000
		2.1.3.a	Historic Land cover - land use type (Anderson Level II)	National Land Cover Dataset	30 meter grid
		2.1.3.b	Historic Land cover - land use type (Anderson Level II)	Online viewing of the National Land Cover Dataset	30 meter grid
		2.1.4.a	Initial vegetation cover type	GAP Vegetation Cover	30 meter grid
		2.1.5.a	Current land cover condition	Landsat 7 ETM+ Images	30 meter pixel
		2.1.5.b	Current land cover condition	ASTER Images	15 meter pixel
		2.1.6.a	Seasonal land cover variation	Landsat 7 ETM+ Images, Multiple season	30 meter pixel
		2.1.7.a	Land cover change analysis	Landsat 7 ETM+ Images, Multiple years	30 meter pixel
		2.1.8.a	Landscape metrics (Landscape ecology)	Landsat 7 ETM+ Images	30 meter pixel
		2.1.8.b	Landscape metrics (Landscape ecology)	ASTER Images	15 meter pixel
		2.1.8.c	Landscape metrics (Landscape ecology)	National Land Cover Dataset	30 meter grid
		2.1.8.d	Landscape metrics (Landscape ecology)	GAP Vegetation Cover	30 meter grid
		2.1.9.a	Wildland fire burn-area delineation	Landsat 7 ETM+ Images	30 meter pixel
		2.1.10.a	Burn-area regeneration monitoring	Landsat 7 ETM+ Images	30 meter pixel
		2.1.11.a	Agricultural and forest resource monitoring for significant changes in hydrologic condition	Landsat 7 ETM+ Images	30 meter pixel
		2.1.12.a	Surface soil properties	SSURGO	1:24,000
		2.1.13.a	Land surface elevation data	National Elevation Dataset (NED)	30 meter grid
		2.1.13.b	Land surface elevation data	National Elevation Dataset (1/3 NED)	10 meter grid
		2.1.14.a	Drainage area delineation and watershed topographic characteristics	National Elevation Dataset (1/3 NED)	10 meter grid
		2.1.15.a	Analysis of impervious surface	Landsat 7 ETM+ Images	30 meter pixel
		2.1.15.b	Analysis of impervious surface	ASTER Images	15 meter pixel

Table 2.1 Excerpt from the satellite and aerial imagery guidance spreadsheet tables.

Source Identification	Organization	Description	Internet URL
USEPA[1]	U.S. Enironmental Protection Agency	GIRAS is included with the EPA BASINS software and dataset	http://www.epa.gov/OST/BASINS/
NOAA[1]	National Oceanic and Atmospheric Adminstration	AVHRR data is available through the Comprehensive Large Array-data Stewardship System	http://www.saa.noaa.gov/cocoon/nsaa/products/welcome
NASA[1]	National Aeronautics and Space Adminstration	MODIS data is available through the Earth Observing System Data Gateway	http://edcimswww.cr.usgs.gov/pub/imswelcome/
USGS[1]	U.S. Geological Survey	National Land Cover Data and digital elevation model data may be downloaed in ESRI Grid format and Geotif format from the The National Map Seamless Data Distribution System	http://seamless.usgs.gov/
USGS[2]	U.S. Geological Survey	The Earth Explorer internet distribution system is the main online source to query and order satellite images, aerial photographs, and cartographic products through the U.S. Geological Survey	http://edcsns17.cr.usgs.gov/EarthExplorer/
University of Idaho[1]	U.S. Geological Survey	Gap Analysis Program	http://www.gap.uidaho.edu/
NASA-UMD	NASA Goddard Space Flight Centre (GSFC) and the University of Maryland (UMD).	Web Fire Mapper displays active fires detected by the MODIS Rapid Response System. Active fires can be viewed for the Continental U.S. and other regions of the world. Shapefiles of active fires can be downloaded.	http://maps.geog.umd.edu/default.asp
SpaceImaging	Space Imaging	Source for new and archived IKONOS high resolution satellite imagery	http://www.spaceimaging.com/default.htm

Table 2.2 Excerpt from the satellite and aerial imagery source spreadsheet tables.

Reference No.	Reference	Online Source
1	Lahlou, M., L. Shoemaker, et al. (1998). Better Assessment Science Integrating Point and Nonpoint Sources BASINS, Version 2.0, EPA-823-R-98-006. Washington, D.C., Office of Water, U.S. Environmental Protection Agency: 349.	http://www.epa.gov/waterscience/basins/bsnsdocs.html
2	GIRAS Landuse/Landcover data for the Conterminous United States by quadrangles at scale 1:250,000	http://geo-nsdi.er.usgs.gov/metadata/other/epa/giras-lulc/sdd/metadata.html
3	Hastings, D. A. and W. J. Emery (1998). The Advanced Very High Resolution Radiometer (AVHRR): A Brief Reference Guide NOAA National Data Centers, NGDC National Oceanic and Atmospheric Administration. 2001.	http://www.ngdc.noaa.gov/seg/globsys/avhrr4.shtml
4	Kidwell, K. B. (1997). NOAA Global Vegetation Index User's Guide. Suitland, MD, National Oceanic and Atmospheric Administration National Environmental Satellite, Data, and Information Service.	http://www2.ncdc.noaa.gov/docs/gviug/index.htm
5	Yin, Z. and T. H. L. Williams (1996). "Obtaining Spatial and Temporal Vegetation Data from Landsat MSS and AVHRR/NOAA Satellite Images for a Hydrologic Model." Photogrammetric Engineering and Remote Sensing 63(1).	
6	MODIS Surface Reflectance User's Guide	http://modis-land.gsfc.nasa.gov/mod09/html/surfref.htm
7	MODIS Vegetation Index User's Guide	http://tbrs.arizona.edu/project/MODIS/UserGuide_doc.php
8	MODIS MOD12 Land Cover and Land Cover Dynamics Products User	http://geography.bu.edu/landcover/userguidelc/
9	MODIS Land Surface Temperature Products	http://www.icess.ucsb.edu/modis/LstUsrGuide/usrguide.html
10	National Land Cover Characterization	http://landcover.usgs.gov/natllandcover.asp
11	Vogelmann, J.E., S.M. Howard, L. Yang, C.R. Larson, B.K. Wylie and N. Van Driel. 2001. Completion of the 1990s National Land Cover Data Set for the Conterminous United States from Landsat Thematic Mapper Data and Ancillary Data Sources. Photogrammetric Engineering and Remote Sensing Vol. 67 (6):650-662.	

Table 2.3 Excerpt from the satellite and aerial imagery reference spreadsheet tables.

References for Section 2

Ahmed, R. H., and Neale, C. M. U. "Estimating irrigation district water demand using remote sensing and GIS." *Proceedings of the 16th Biennial Workshop on Color Aerial Photography and Videography in Resource Assessment*, Weslaco, Texas, 167-178.

Aldrich, R. C. (1979). *Remote Sensing of Wildland Resources: A State-of-the-Art Review, Gen. Tech. Rep. RM-71*, Rocky Mountain Forest and Range Experiment Station, Forest Service, U.S. Department of Agriculture, Fort Collins, CO.

Anderson, J. R., Hardy, E. E., Roach, J. T., and Witmer, R. E. (1976). *A Land Use and Land Cover Classification System for Use with Remote Sensor Data*, U.S. Geological Survey, Washington D.C.

Anderson, P. C., Hardy, T. B., and Neale, C. M. U. "Application of multispectral videography for the delineation of riverine depths and mesoscale hydraulic features." *Proceedings of the 14th Biennial Workshop on Color Aerial Photography and Videography for Resource Monitoring*, Logan, UT, 154-163.

Arnold, R. H. "Aerial photography and videography as the basis of environmental planning and analysis of a small New England watershed." *13th Biennial Workshop on Videography & Color Photography in Plant Sciences*, Orlando, FL, 51-58.

ASPRS. (1995). *1995 DRAFT Standards for Aerial Photography, Online at http://www.asprs.org/asprs/resources/standards.html*, ASPRS Professional Practice Division Specifications and Standards Committee, American Society of Photogrammetry and Remote Sensing, Bethesda, ML.

ASPRS. (2000). *ASPRS Camera Calibration Panel Report*, ASPRS, Bethesda, MD.

Baker, J. C. (2001). "New Users and established experts: bridging the knowledge gap in interpreting commercial satellite imagery." Commercial Observation Satellites: at the Leading Edge of Global Transparency, Rand, Santa Monica, CA, 533-557.

Baker, J. C., and Johnson, D. J. (2001). "Security Implications of Commercial Satellite Imagery." Commercial Observation Satellites: at the Leading Edge of Global Transparency, Rand, Santa Monica, CA, 101-133.

Baker, J. C., O'Connel, K. M., and Williamson, R. A. (2001). *Commercial Observation Satellites: at the leading edge of global transparency*, Rand, Santa Monica, CA.

Barrette, J., August, P., and Golet, F. (2000). "Accuracy Assessment of Wetland Boundary Delineation Using Aerial Photography and Digital Orthophotography." *Photogrammetric Engineering and Remote Sensing*, 66(4), 409-416.

Bates, P. D., Horritt, M. S., Smith, C. N., and Mason, D. (1997). "Integrating remote sensing observations of flood hydrology and hydraulic modelling." *Hydrological Processes*, 11(14), 1777-1795.

Beeson, C. E., and Doyle, P. F. (1995). "Comparison of bank erosion at vegetated and non-vegetated channel bends." *Water Resources Bulletin*, 31(6), 983-990.

Benton, A. R., Jr., Snell, W. W., and Clark, C. A. (1980). "Monitoring Aquatic Plants in Reservoirs." *Transportation Engineering Journal*, 106(4), 453-470.

Berger, J. P. (1980). "High Altitude Photos for Inactive Mines." *Journal of the Surveying and Mapping Division*, 106(1), 27-34.

Blanchard, B. J., Rouse, J. R., Jr., and Schmugge, T. J. (1975). "Classifying storm runoff potential with passive microwave measurement." *Water Resouces Bulletin*, 11(5), 892-907.

Bondelid, T. R., Jackson, T. J., and McCuen, R. H. (1982). "Estimating runoff curve numbers using remote sensing data." Applied Modeling in Catchment Hydrology, V. P. Singh, ed., Water Resources Publications, Littleton, CO, 511-528.

Bovee, K. D. (1982). *Guide to Stream Habitat Analysis Using the Instream Flow Incremental Methodology*, U.S. Fish and Wildlife Service, Washington, D.C.

Cameron, H. L. (1960). "Water current measurement and time-lapse air photography." *Photogrammetric Engineering and Remote Sensing*, 26(5), 158-163.

Campbell, J. B. (1996). *Introduction to Remote Sensing*, The Guilford Press, New York.

Carroll, T. (2001). *Airborne gamma radiation airborne gamma radiation snow survey program snow survey program: A User's Guide A User's Guide Version 5.0*, National Operational Hydrologic Remote Sensing Center, Office of Climate, Water, and Weather Services, National Weather Service, NOAA, Chanhassen, MN.

Caylor, J. (2000). "Aerial photography in the next decade." *Journal of Forestry*, 48(6), 17-19.

Chery, D. L., Jr., and Jensen, J. R. (1982). "Lumped water balance mode using cover areas determined by Landsat remote sensing." Applied Modeling in Catchment Hydrology, V. P. Singh, ed., Water Resources Publications, Littleton, CO, 529-544.

Chewings, V. H., Bastin, G. N., and Pearce, G. "Using airborne videography to calibrate high resolution satellite data." *Proceedings of the 16th Biennial Workshop on Color Aerial Photography and Videography in Resource Assessment*, Weslaco, Texas, 508-512.

Civco, D. L., Kennard, W. C., and Lefor, M. W. (1986). "Changes in Connecticut salt-marsh vegetation as revealed by historical aerial photographs and computer-assisted catographics." *Environmental Management*, 10(2), 229-239.

Clemmer, P. (1994). *Riparian Area Management: The Use of Aerial Photography to Manage Riparian-Wetland Areas*, U.S. Bureau of Land Management, Denver, CO.

Clemmer, P., Gorges, M., Meyer, G., Shumac, K., Myman, S., and Miller, M. (1999). *Riparian Area Management: Using Aerial Photography to Assess Proper Functioning Condition of Riparian-Wetland Areas*, U.S. Bureau of Land Management, Denver, CO.

Cowardin, L. M., Carter, V., Golet, F. C., and LaRoe, E. T. (1979). *Classification of wetlands and deepwater habitats of the United States. FWS/OBS-79-31*, USDI Fish and Wildlife Service, Washington, DC.

Dall, D., Elliott, C., Peters, D., and Usfws, U. S. F. a. W. S. (1997). *A System for Mapping Riparian Areas in the Western United States*, U.S. Fish and Wildlife Service.

Davies, P. A., and Neves, M. J. V. "Remote Sensing Investigations and Modelling of Wastewater Plumes." *Environmental and Coastal Hydraulics: Protecting the Aquatic Habitat*, San Francisco, 341-346.

Dressing, S. (1997). *Techniques for tracking, evaluating, and reporting the implementation of nonpoint source control measures, EPA/841-B-97-010*, Nonpoint Source Pollution Control Branch, Office of Water, U.S. Environmental Protection Agency, Washington, D.C.

Duhaime, R. J., August, P. V., and Wright, W. R. (1997). "Automated Vegetation Mapping Using Digital Orthophotography." *Photogrammetric Engineering and Remote Sensing*, 63(11).

Dull, C. W. "Overview of Forest Service Remote Sensing Activities." *Remote Sensing & Natural Resource Management*, Orlando, FL, 18-23.

EPA. (1990). "National Guidance: Water Quality Standards for Wetlands, Appendix B to Chapter 2 - General Program Guidance." Water Quality Standards Handbook, Office of Wetlands, Office of Water Regulations and Standards Protection, U.S. Environmental Protection Agency, Washington, D.C.

EPA. (1997). *National Science and Technology Council Committee on Environment and Natural Resources Framework for the National Environmental Monitoring Initiative: A Proposed Framework, online at http://www.epa.gov/cludygxb/pubs.html*, The Environmental Monitoring Team, Committee on Environment and Natural Resources, National Science and Technology Council, Executive Office of the President, Washington, D.C.

EPA. (1999b). *Remotely monitoring water resources: an EPA/NASA workshop, EPA841-B99-06*, Office of Water, U.S. Environmental Protection Agency, Washington D.C.

Estep, S. D. (1973). "Legal and Social Policy Ramifications of Remote Sensing Techniques." The Surveillant Science: Remote Sensing of the Environment, R. K. Holz, ed., Houghton Mifflin, Boston, 362-374.

Evans, D. L., and Beltz, R. C. "Aerial video and associated technologies for forest assessments." *Remote Sensing & Natural Resource Management*, Orlando, FL, 301-304.

Everitt, J. H., Yang, C., Escobar, D. E., Helton, R. J., Hartmann, L. H., and Davis, M. R. "Using spatial information technologies for detecting and mapping three aquatic weeds in Texas waterways." *Remote Sensing and Geospatial Technologies for the New Millennium*, Salt Lake City, UT, 14.

FEMA. (1999). *Guidelines and Specifications for Study Contractors*, Federal Emergency Management Agency, Washington, D.C.

Fortin, J.-P., Turcotte, R., Massicotte, S., Moussa, R., Fitzback, J., and Villeneuve, J.-P. (2001). "A Distributed Watershed Model Compatible with Remote Sensing and GIS Data. I: Description of Model." *Journal of Hydrologic Engineering*, 6(2), 91-99.

Franklin, A. J., Tueller, P. T., Ayers, M., and Swanson, S. R. "Preparation and analysis of multspectral videography and digital orthophotoquads for riparian vegetation mapping." *Proceedings of the 16th Biennial Workshop on Color Aerial Photography and Videography in Resource Assessment*, Weslaco, Texas, 346-357.

Franz, D. D., and Lieu, S. M. (1981). *Evaluation of Remote Sensing Data for Input into Hydrological Simulation Program-Fortran (HSPF), EPA-600/S3-81-037*, U.S. Environmental Protection Agency, Washington, D.C.

Fraser, R. H., Warren, M. V., and Barten, P. K. (1995). "Comparative evaluation of land cover data sources for erosion prediction." *Water Resources Bulletin*, 31(6), 991-1000.

Frazier, B. E., and Cheng, Y. (1989). "Remote sensing of soils in the Eastern Palouse Region with Landsat Thematic Mapper." *Remote Sensing of Environment*, 28, 317-325.

Frazier, B. E., Hanrahan, T., and Moore, B. C. "Color aerial slide photography for detection of Lythrum Salicaria, Purple Loosestrife in wetland environments in Washington." *Proceedings of the 14th Biennial Workshop on Color Aerial Photography and Videography for Resource Monitoring*, Logan, UT, 37-47.

Frazier, B. E., and McCool, D. K. (1981). "Aerial Photography to Detect Rill Erosion." *Transactions of the ASAE*, 24(5), 1168-1171.

Frazier, B. E., McCool, D. K., and Engle, C. F. (1983). "Soil Erosion in the Palouse: An Aerial Perspective." *Journal of Soil and Water Conservation*, 38(2), 70-74.

Fritz, L. W. (1999). "High Resolution Commercial Remote Sensing Satellites and Spatial Information Systems." *ISPRS Highlights online* http://www.isprs.org/publications/, 4(2).

Funk, W. H., and Flaherty, D. C. (1972). "The Use of Photography in Water Quality Research." *Photographic applications in science, technology and medicine*, 7(5), 20-22.

Graham, D. S., and John, M. H. (1983). "Landsat and Water Quality Model Verification." *Journal of Transportation Engineering*, 109(5), 640-650.

Green, E. P., Mumby, P. J., Edwards, A. J., Clark, C. D., and Edwards, A. J. (2000). *Remote Sensing Handbook for Tropical Coastal Management*, United Nations Educational, Scientific and Cultural Organization.

Greve, C. (1996). "Digital Photogrammetry--An Addendum to the Manual of Photgrammetry." American Society for Photogrammetry and Remote Sensing, Bethesda, ML, 247.

Grew, G. W. "Remote detection of water pollution with MOCS: an imaging multispectral scanner, Proceedings." *Conference on Environmental Quality Sensors*, Las Vegas, 17-39.

Hall, F. C. (2001). *Ground-based photographic monitoring. Gen. Tech. Rep. PNW-GTR-503*, U.S. Department of Agriculture, Forest Service, Pacific Northwest Research Station, Portland, OR.

Han, L. (1997). "Spectral reflectance with varying suspended sediment concentrations in clear and algae laden waters." *Photogrammetric Engineering and Remote Sensing*, 63(6), 701-705.

Hastings, D. A., and Emery, W. J. (1998). "The Advanced Very High Resolution Radiometer (AVHRR): A Brief Reference Guide, online at http://www.ngdc.noaa.gov/seg/globsys/avhrr4.shtml." NOAA National Data Centers, NGDC National Oceanic and Atmospheric Administration.

Hays, L. C. P. L. "Transparency, stability, and deception: military implications of commercial high resolution imaging satellites in theory and practice." *International Studies Association Annual Convention*, Chicago, 26.

Homer, C., Huang, C., Yang, L., Wylie, B., and Coan, M. (2004). " Development of a 2001 National Landcover Database for the United States." *Photogrammetric Engineering and Remote Sensing*, 70(7), 829-840.

Hourani, N. M. "Watershed Modeling Using Remote Sensing." *Water Resources and the Urban Environment*, Chicago, 757-762.

Ji, W., Civco, D. L., and Kennard, W. C. (1992). "Satellite remote bathymetry: A new mechanism for modeling." *Photogrammetric Engineering and Remote Sensing*, 58(5), 545-549.

Johannsen, C. J., and Barney, T. W. (1981). "Remote Sensing Applications for Resource Management." *Journal of Soil and Water Conservation*, 26(3), 128-131.

Johnson, P. L. "Remote Sensing in Ecology." *Proceedings of a joint Conference by the Ecological Society of America and the American Society of Limnology and Oceanography*, Madison, Wis.

Johnston, C. A., Sersland, C. A., Bonde, J., Pomroy-Petry, D., and Meysembourg, P. "Constructing detailed vegetation databases from field data and airborne videography." *Third International Conference/Workshop on Integrating GIS and Environmental Modeling*, Santa Fe, New Mexico, USA.

Jones, E. L. (1920). "Surveying from the Air." *Science*, 52(1355), 574-575.

Khorram, S., and Cheshire, H. M. (1985). "Remote sensing of water quality in the Neuse River Estuary, North Carolina." *Photogrammetric Engineering and Remote Sensing*, 51(3), 329-341.

Kidwell, K. B. (1998). "NOAA Polar Orbiter Data User's Guide, online at http://www2.ncdc.noaa.gov/docs/intro.htm." National Oceanic and Atmospheric Administration.

Kim, B. G. (1987). "Surface Water Velocity Measurements on Delavan Lake Using Aerial Photographs." *Photogrammetric Engineering and Remote Sensing*, 53(6), 605-607.

Knott, D. M., Wenner, E. L., and Wendth, P. H. (1997). "Effects of pipeline construction on the vegetation and macrofauna of two South Carolina, USA salt marshes." *Wetlands*, 17(1), 65-81.

Komura, S. (1986). "Method for Computing Bed Profiles during Floods." *Journal of Hydraulic Engineering*, 112(9), 833-846.

Lachowski, H. M. "Intergration of remote sensing into resource data collection: an overview." *Remote Sensing & Natural Resource Management*, Orlando, FL, 34-40.

Lachowski, H. M., Maus, M., Golden, J., Johnson, J., Landrum, V., Powell, J., Varner, V., Wirth, T., Gonzales, J., and Bain, S. (1995). *Guidelines for the use of digital imagery for vegetation mapping. U.S. Dep. Agr. For. Serv., EM-7140-25*, USDA Forest Service, Washington, DC.

Lathrop, R. G., Jr. (1992). "Landsat thematic mapper monitoring of turbid inland water quality." *Photogrammetric Engineering and Remote Sensing*, 58(4), 465-470.

Lathrop, R. G., and Lillesand, T. M. (1987). "Calibration of Thematic Mapper Thermal Data for Water Surface Temperature Mapping: Case Study on the Great Lakes." *Remote Sensing of Environment*, 22(2), 297-307.

Lathrop, R. G., and Lillesand, T. M. (1989). "Monitoring Water Quality and River Plume Transport in Green Bay, Lake Michigan with Spot-1 Imagery." *Photogrammetric Engineering and Remote Sensing*, 55(3), 349-54.

Lauer, D. T., Morain, S. A., and Salomonson, V. V. (1997). "The Landsat Program: Its Origins, Evolution, and Impacts." *Photogramm. Eng. Remote Sens.*, 63(7), 831-838.

LeDrew, E. F., and Franklin, S. E. (1983). "Small Format, Hand Held Helicopter Based Photography for Monitoring Industrial Water Effluent Plumes." *Canadian Water Resources Journal*, 8(3), 26-38.

Lidov, L., Miller, R., Wormer, D. M., and Tilley, K. A. (2000). "Understanding the Future of Commercial Remote Sensing." *Photogrammetric Engineering and Remote Sensing*, 66(1), 5-14.

Liedtke, J., Roberts, A., and Luternauer, J. (1995). "Practical remote sensing of suspended sediment concentrations." *Photogrammetric Engineering and Remote Sensing*, 61(2), 167-175.

Light, D. L. (1992). "The new camera calibration system at the U.S. Geological Survey." *Photogrammetric Engineering and Remote Sensing*, 58(2), 185-188.

Light, D. L. (1996). "Film Cameras or Digital Sensors? The Challenge Ahead for Aerial Imaging." *Photogrammetric Engineering and Remote Sensing*, 62(3), 285-291.

Lillesand, T. M., and Kieffer, R. W. (1994). *Remote Sensing and Image Interpretation*, John Wiley and Sons, Inc., New York.

Lin, D. S., Wood, E. F., Troch, P. A., Mancini, M., and Jackson, T. J. (1994). "Comparisons of remotely sensed and model-simulated soil moisture over a heterogeneous watershed." *Remote Sensing of Environment*, 48(2), 159-171.

Lott, N., Ross, T., and Graumann, A. (2001). *Products and Services Guide*, National Climate Data Center, NOAA, Asheville, NC.

Lueder, D. R. (1959). *Aerial Photographic Interpretation*, McGraw-Hill, New York.

Lund, T. "Surveillance of environmental pollution and resources by electromagnetic waves." *NATO Advanced Study Institute*, Spatind, Norway.

Lyon, J. G. (1987). "Use of maps, aerial photographs, and other remote sensor data for practical evaluations of hazardous waste sites." *Photogrammetric Engineering and Remote Sensing*, 53(5), 515-519.

Lyon, L. J., Lunneta, R. S., and Williams, R. S. (1992). "Airborne multispectral scanner data for evaluating bottom sediment types and water depths in the St. Marys River Michigan." *Photogrammetric Engineering and Remote Sensing*, 57, 951-956.

Lyzenga, D. R. (1981). "Remote sensing of bottom reflectance and water attenuation parameters in shallow water using aircraft and Landsat data." *International Journal of Remote Sensing*, 2, 71-82.

Marshall, T. R., and Lee, P. F. (1994). "Mapping aquatic macrophytes through digital image analysis of aerial photographs: An assessment." *Journal of Aquatic Plant Management*, 32, 61-66.

McGinnis, D. F., Jr., Berg, C. P., and Scofield, R. A. (1980). "Satellites as Aid to Water Resource Managers." *Journal of the Water Resources Planning and Management Division*, 106(1), 1-19.

Meyer, M. P. "History of small format aerial photography." *First North American Symposium on Small Format Aerial Photography*, Cloquet, MN, 3-7.

Mikhail, E. M. (1999). "Is Photogrammetry Still Relevant?" *Photogrammetric Engineering and Remote Sensing*, 65(7), 740 -751.

Mikhail, E. M., Bethel, J. S., and McGlone, J. C. (2001). *Introduction to Modern Photogrammetry*, Wiley, New York.

Morain, S. A., and Budge, A. M. (1997). "Earth Observing Platforms & Sensors." The Manual of Remote Sensing, 3rd edition, R. A. Ryerson, ed., American Society for Photogrammetry and Remote Sensing, Bethesda, MD.

Morgan, K. M., Lee, G. B., Kiefer, R. W., Daniel, T. C., and Bubenzer, G. D. (1978). "Prediction of Soil Loss on Cropland with Remote Sensing." *Journal of Soil and Water Conservation*, 13(6), 291-293.

Myhre, R. J., and Silvey, B. "An airborne video system development within Forest Pest Management - status and activities." *Remote Sensing & Natural Resource Management: Proceedings of the Fourth Forest Service Remote Sensing Applications Conference*, Orlando, FL, 291-300.

NAS. (2001). "Grand Challenges in Environmental Sciences." National Academy of Sciences

Committee on Grand Challenges in Environmental SciencesNational Academy Press, Washington DC.

NASA. (1995). "Spaceborne Synthetic Aperture Radar: Current Status and Future Directions, NASA Technical Memorandum 4679, http://southport.jpl.nasa.gov/nrc." National Aeronautics and Space Administration, Jet Propulsion Laboratory, Pasadena, CA.

NASA. (2001a). "Terra Publications Index, http://terra.nasa.gov/Publications." National Aeronautics and Space Administration.

NASA. (2001b). *Science Writers' Guide to TERRA*, Earth Observing System Project Science Office NASA Goddard Space Flight Center National Aeronautics and Space Administration, Greenbelt, MD.

NASA. (2001c). "The MISR Instrument, Online at http://www-misr.jpl.nasa.gov/mission/minst.html." Jet Propulsion Laboratory, National Aeronautics and Space Administration.

NASA, and USGS. (1999). *Management Plan for the Landsat Program*, National Aeronautics and Space Administration, Washington, D.C.

Neale, C. M. U., Vest, G. K., and O'Neill, M. P. "Monitoring streambank erosion using multispectral video imagery in a GIS." *Proceedings of the 15 th Biennial Workshop on Color Photography and Videography in Resource Assessment*, Terre Haute, IN, 210-223.

Neill, C. R., and Galay, V. J. (1967). "Systematic evaluation of river regime." *Journal of the Waterways and Harbors Division*, 93(WW1), 25-53.

NOAA. (2001). "Licensing of Commercial Remote Sensing Satellite Systems, online http://www.licensing.noaa.gov." National Oceanic and Atmospheric Administration, Department of Commerce.

Odgaard, A. J. (1984). "Bank Erosion Contribution to Stream Sediment Load."

Panja, K. V., Hardy, T. B., and Neale, C. M. U. "Comparison of meso-scale hydraulic features at different discharges in a turbid river system using multispectral videography." *Proceedings of the 14th Biennial Workshop on Color Aerial Photography and Videography for Resource Monitoring*, Logan, UT, 164-173.

Parry, R. (2001). "Remote Sensing Research at the USDA ARS BARC, http://hydrolab.arsusda.gov/RSatBARC/rsatbarc.html." USDA Agricultural Research Service, Hydrology and Remote Sensing Laboratory.

Pelletier, R. E., and Griffin, R. H., II. (1988). "An evaluation of photographic scale in aerial photography for identification of conservation practices." *Journal of Soil and Water Conservation*, 43(4), 333-337.

Perchalski, F. R., and Higgins, J. M. (1988). "Pinpoint Nonpoint Pollution." *Civil Engineering*, 58(2), 62-64.

Pucherelli, M. J., Fenton, K. H., and Clark, R. "The utility of aerial photography and airborne videography to quantify and monitor river habitats as the relate to endangered fish." *13th Biennial Workshop on Videography & Color Photography in Plant Sciences*, Orlando, FL, 59-67.

Ragan, R. M. (1975). "Use of Satellite Data in Urban Hydrologic Models." *Journal of Hydraulic Division*, 101(12), 1469-1475.

Rango, A., Feldman, A., George, T., and Ragan, R. M. (1983). "Effective Use of Landsat in Hydrologic Models." *Water Resources Bulletin*, 19(2), 165-174.

Rango, A., and Martinec, J. (1995). "Revisiting the degree-day method for snowmelt computations." *Water Resources Bulletin*, 31(4), 657-670.

Ritchie, J. C. (2000). "Soil Erosion." Remote Sensing in Hydrology and Water Management, G. A. Schultz and E. T. Engman, eds., SpringerVerlag, Berlin, 271-286.

Ritchie, J. C., and Schiebe, F. R. (2000). "Water Quality." Remote Sensing in Hydrology and Water Management, G. A. Schultz and E. T. Engman, eds., SpringerVerlag, Berlin, 289-303.

Roberts, A., Bach, K., and Williams, I. "Digital MSV and SAP remote sensing of shallow water bathymetry." *Proceedings of the 15 th Biennial Workshop on Color*

Photography and Videography in Resource Assessment, Terre Haute, IN, 224-230.

Robichaud, P. R., Beyers, J. L., and Neary, D. G. (2000). *Evaluating the effectiveness of postfire rehabilitation treatments. Gen. Tech. Rep. RMRS-GTR-63*, U.S. Department of Agriculture, Forest Service, Rocky Mountain Research Station., Fort Collins, CO.

Schloesser, D., and Manny, B. (1986). "Distribution of submersed macrophytes in the St. Clair-Detroit River system, 1978." *Journal of Freshwater Ecology*, 3(4), 537-544.

Schloesser, D. W., Brown, C. L., and Manny, B. A. (1988). "Use of Aerial Photography to Inventory Aquatic Vegetation." *Journal of Aerospace Engineering*, 1(3), 142-150.

Schultz, G. A., and Engman, E. T. (2000). "Remote Sensing in Hydrology and Water Management." Springer, New York, 483.

Schumugge, T. J., and Jackson, T. J. (1996). "Soil moisture variability." Scaling up in Hydrology using Remote Sensing, J. B. Stewart, E. T. Engman, R. A. Feddes, and Y. Kerr, eds., Wiley, New York, 183-192.

Seher, J. S., and Tueller, P. T. (1973). "Color aerial photos for marshland." *Photogrammetric Engineering*, 39, 489-499.

Sersland, C. A., Johnston, C. A., and Bonde, J. "Assessing wetland vegetation with gps-linked color video image mosaics." *15th Biennial Workshop on Videography and Color Photography in Resource Assessment*, Terre Haute, Indiana, 23-29.

Skovlin, J. M., Strickler, G. S., Peterson, J. L., and Sampson, A. W. (2001). *Interpreting landscape change in high mountains of northeastern Oregon from long-term repeat, PNW-GTR-505*, U.S. Department of Agriculture, Forest Service, Pacific Northwest Research Station, Portland, OR.

Slama, C. C., Theurer, C., and Henricksen, S. W. (1980). "Manual of Photogrammetry." American Society of Photogrammetry, Bethesda, MD.

Slaymaker, D. M. K. M. L. J. C. R. G. a. J. T. F. (1996). "Mapping deciduous forests in Southern New England using aerial videography and hyperclustered multi-temporal Landsat TM imagery." Gap Analysis: A Landscape Approach to Biodiversity Planning, T. H. T. a. F. W. D. J.M. Scott, ed., American Society of Photogrammetry and Remote Sensing, Bethesda, MD.

Smith, D. P., and Bedient, P. B. (1981). "Preliminary Model of an Urban Floodplain Under Changing Land Use." *Journal of Hydrology*, 51(1-4), 179-185.

Stafford, D. B., Nettles, M. E., and Ligon, J. T. (1976). "Measuring Watershed Land-Use Changes with Airphotos." *Transportation Engineering Journal*, 102(1), 117-129.

Tao, T., and Kouwen, N. (1989). "Remote Sensing and Fully Distributed Modeling for Flood Forecasting." *Journal of Water Resources Planning and Management*, 115(6), 809-823.

Thiruvengadachari, S., Rao, K. R., and Rao, P. S. (1980). "Surface Water Inventory through Satellite Sensing." *Journal of the Water Resources Planning and Management Division*, 106(2), 493-502.

Torgersen, C. E., Faux, R. N., McIntosh, B. A., Poage, N. J., and Norton, D. J. (2001). "Airborne thermal remote sensing for water temperature assessment in rivers and streams." *Remote Sensing of Environment*.

Torgerson, C. E., Price, D. M., Li, H. W., and McIntosh, B. A. "Thermal refugia and chinook salmon habitat in Oregon: applications of airborne thermal videography." *Proceedings of the 15 th Biennial Workshop on Color Photography and Videography in Resource Assessment*, Terre Haute, IN, 167-171.

Trolier, L. J., and Philipson, W. R. (1986). "Visual Analysis of Landsat Thematic Mapper Images for Hydrologic Land Use and Cover." *Photogrammetric Engineering and Remote Sensing*, 52(9), 1531-1538.

Ulaby, F. T., Dubois, P. C., and Van Zyl, J. (1996). "Radar mapping of surface soil moisture." *Journal of Hydrology*, 184(1-2), 57-84.

USACE. (1980). *Determination of land use from satellite imagery for input into hydrologic models, Technical Paper no. 71*, U.S. Army Corps of Engineers, Davis, CA.

USACE. (1987). *Corps of Engineers Wetlands Delineation Manual, Technical Report Y-87-1*, Environmental Laboratory U.S. Army Corps of Engineers Waterways Experiment Station, Vicksburg, MS.

USACE. (1993). *Photogrammetic Mapping, Engineer Manual No. 1110-1-1000*, Department of the Army, U.S. Army Corps of Engineers, Washington, D.C.

USGS. (1998). *Aerial Photography Summary Record System, online* http://mac.usgs.gov/mac/isb/pubs, U.S. Geological Survey, Reston, VA.

USGS. (1998). "Landsat 7 Science Data Users Handbook." U.S. Geological Survey and National Aeronautics and Space Administration.

USGS. (1998b). *USGS Aerial Camera Specifications, Online at http://mac.usgs.gov/mac/tsb/osl/acspecs.html*, U.S. Geological Survey, Optical Science Laboratory, Reston, VA.

Veregin, H., Sincak, P., Gregory, K., and Davis, L. "Integration of high-resolution video imagery and urban stormwater runoff modeling." *Proceedings of the 15 th Biennial Workshop on Color Photography and Videography in Resource Assessment*, Terre Haute, IN, 182-191.

Vogelmann, J. E., Howard, S. M., Yang, L., Larson, C. R., Wylie, B. K., and Driel, N. V. (2001). "Completion of the 1990s National Land Cover Data Set for the Conterminous United States from Landsat Thematic Mapper Data and Ancillary Data Sources." *Photogrammetric Engineering and Remote Sensing*, 67(6), 650-662.

Warner, W. S. (1994). "Evaluating a low cost non metric aerial mapping system for waste site investigators." *Photogrammetric Engineering and Remote Sensing*, 60(8), 983-988.

Warner, W. S., Graham, R. W., and Read, R. E. (1996). *Small Format Aerial Photography*, Whittles Publishing Services, Caithness, Scotland, UK.

Welch, R., Jordan, T. R., and Thomas, A. W. (1984). "Photogrammetric Technique for Measuring Soil Erosion." *Journal of Soil and Water Conservation*, 39(3), 191-194.

Wetzel, R. G. (1983). *Limnology*, Harcourt Brace Jovanovich College Publishers, New York.

Whitlock, C. H., Witte, W. G., Talay, T. A., Morris, W. D., Usry, J. W., and Poole, L. R. (1982). "Research for reliable quantifications of water sediment concentrations from multispectral scanner remote sensing data." Applied Modeling in Catchment Hydrology, V. P. Singh, ed., Water Resources Publications, Littleton, CO, 495-510.

Wile, I. "Use of remote sensing for mapping of aquatic vegetation in the Kawartha Lakes." *17th Conference Remote Sensing and Water Resources Management*, Minneapolis, MN.

Winterbottom, S. J. (2000). "Medium and short-term channel planform changes on the Rivers Tay and Tummel, Scotland." *Geomorphology*, 34(3-4), 195-208.

Wolf, P. R., and Dewitt, B. A. (2000). *Elements of Photogrammetry*, McGraw-Hill, New York.

Wolman, M. G. (1959). "Factors influencing erosion of a cohesive river bank." *American Journal of Science*, 257, 204-216.

Woodward, D. E. (1998). "Stream Reaches and Hydrologic Units, Chapter 6." National Engineering Handbook, Part 630 Hydrology, U.S. Department of Agriculture, Natural Resources Conservation Service, Washington, D.C., 6-1.

Woodward, D. E. (1999). "Preliminary Investigations, Chapter 3." National Engineering Handbook, Part 630 Hydrology, U.S. Department of Agriculture, Natural Resources Conservation Service, Washington, D.C., 3-1 - 3-8.

Yang, L., Stehman, S. V., Smith, J. H., and Wickham, J. D. (2001). "Thematic accuracy of MRLC land cover for the eastern United States." *Remote Sensing of Environment*, 76(3), 418-422.

Zsilinszky, V. G. "History of small format aerial photography." *First North American Symposium on Small Format Aerial Photography*, Cloquet, MN, 8-16.

3. High-Resolution Low-Altitude Aerial Imagery

Spatial information derived from aerial images for engineering and environmental assessment must be useful, reliable, repeatable, and founded on sound physical principles. This section explores the principles and techniques of extracting qualitative and quantitative spatial information from low-altitude high-resolution digital aerial imagery. Theory and techniques from throughout remote sensing have been assembled and placed in context of the aerial imagery acquired in the dissertation research. Beneficial research possibilities are suggested throughout the section.

Technically, this section is about photogrammetry. Photogrammetry is the art, science, and technology of obtaining reliable information about physical objects and the environment through processes of recording, measuring, and interpreting images and patterns of electromagnetic radiant energy and other phenomena (ASPRS 1995). This section describes the most important image characteristics and principles of photogrammetry in context of the dissertation research. Theories and techniques of photogrammetry are quite mature, yet the research revealed many opportunities for advanced investigations into the photogrammetric analysis of high-resolution digital aerial imaging in hydrologic characterization and fluvial morphology.

Much more could and should be written, and many examples might be added to amplify insights gained from the research. Still, this summary is unlike any found elsewhere in the literature and should help investigators and practitioners recognize the benefits of aerial imagery assessment and more easily utilize high-resolution aerial imagery in research, teaching and professional work.

Some sections assume a working knowledge of calculus and linear algebra. Needless description and demonstration of routine GIS and image processing operations are avoided. Many other works describe these aspects of remote sensing admirably. Several appendices are included that provide details of mathematical derivations and computer code that would have been distractive if included in the main presentation.

3.1 Optics of Digital Aerial Imagery

Aerial digital sensors and film cameras are optical sensors—they acquire and record reflected light energy to form an image that carries spatial and qualitative information about the imaged scene. Terrestrial and aerial images share many common characteristics, but there are some differences and technical concerns. This section discusses the most important principles and relationships of optical physics that must be understood to use aerial imagery effectively.

3.1.1 Refraction

Propagation of light through a transparent medium or vacuum is described by the electromagnetic wave equation:

$$c = f\lambda \qquad 3.1$$

where c is the speed of light in a vacuum (2.998 x 108 m s^{-1}), f is the wave frequency (hz), and λ is the wavelength (m).

Light emitted from an infinitesimally small point source is modeled as a bundle of light rays traveling in straight lines in all directions. The speed of light through a transparent medium is expressed by the refractive index,

$$n = \frac{c}{V} \tag{3.2}$$

where n is the refractive index of the material, c is the speed of light in a vacuum, and V is the speed of light in the lens material. The indexes of refraction of atmospheric air and clean surface water are approximately 1.0003 and 1.33. Optical lens glass has an index of refraction between 1.2 and 2.0.

Refraction causes light rays to bend when passing through an interface between transparent media. The index of refraction is somewhat dependent on wavelength; the index of refraction for ultraviolet light in glass is about one percent greater than for red light. The change in the direction of the light is related by Snell's law:

$$n_1 \sin \phi_i = n_2 \sin \phi_r \tag{3.3}$$

where n_1 is the refractive index of the medium before the lens (air, water, vacuum), n_2 is the refractive index of the material across the interface (e.g. glass, water), ϕ_i is the angle of incidence, and ϕ_r is the angle of refraction. The angles of incidence and refraction are measured with respect to a line perpendicular to the media interface.

3.1.2 Refraction and Water Depth

The effect of refraction is substantial across the air-water interface and should be considered in optical methods of estimating water depth by photogrammetric analysis. Snell's law yields the following general relationship for estimating the true depth of an object in water and the apparent depth observed above the surface:

$$D_a = \frac{D_o \tan \phi_i}{\tan\left[\sin^{-1}\left(\frac{n_{air} \sin \phi_i}{n_{water}}\right)\right]} \tag{3.4}$$

where D_a is the actual object depth, D_o is the observed water depth, ϕ_t is the angle of incidence (observed angle), n_{air} is the index of refraction in air (1.0003), and n_{water} is the index of fraction in water (1.33). For near vertical angles of incidence, sin ϕ_t approximately equals tan ϕ_t so the actual object depth is approximately:

$$D_a = D_o \frac{n_{water}}{n_{air}} = 1.33 D_o \qquad 3.5$$

Equations 3.4 and Equation 3.5 show that channels below the surface of clear water are approximately one third deeper than observed. This difference is significant when estimating channel dimensions for hydraulic analysis with photogrammetric methods.

3.1.3 Lens Optics

A lens is a transparent object that alters the shape of wave-fronts of light that pass through it. A lens having outwardly curving surfaces (converging lens), refracts incoming light and focuses it at a distance on the opposite side of the lens. A simple optical glass lens has either two spherical surfaces or a spherical surface and a flat surface. Lens surfaces need not be spherical. Aspherical (non-spherical) lenses are shaped to avoid some types of distortion that occur with spherical lenses.

Light rays originating at an infinite distance are parallel when the strike the forward surface of a lens. In a single lens, the parallel light rays are refracted by the glass to coincide at the plane of infinite focus (focal plane). The distance from the optical center of a lens to the focal plane is the focal length. Light from all directions in the field of view of the lens is focused across the focal plane to an image of the scene. Light rays from an object relatively close to the lens are no longer parallel and are focused slightly

behind the focal plane. For a single thin lens the distance to the focused image is related to focal length and object distance by the lens equation:

$$\frac{1}{f} = \frac{1}{i} + \frac{1}{o} \qquad 3.6$$

where f is the focal length, i is the distance from the center of the lens to the point of focus and o is the distance from the center of the lens to the object. This relationship shows that for the large object distances involved in aerial imagery the image will be focused at a distance equal to the focal length of the lens. This is a fundamental assumption in the development of the geometric relationships of aerial imagery.

The focal length of a single lens depends on the index of refraction n of its material relative to that of the surrounding medium (air, water, vacuum), and upon the radii of the lens surfaces R_1 and R_2. This relationship is expressed in the thin lens lensmaker's equation:

$$\frac{1}{f} = (n-1)\left(\frac{1}{R_1} + \frac{1}{R_2}\right) \qquad 3.7$$

Most modern hand held film and digital (small format) camera lenses are composed of several lens elements that act in sequence to improve sharpness and reduce distortion. Lenses for large format aerial mapping cameras are composed of numerous elements (e.g. 12 or more elements in 153 mm lens of the Leica Geosystems (Wilde) RC 30 camera) and are of excellent quality.

Optical design and fabrication is a highly refined engineering science that has experienced much recent technological advancement. A basic understanding of the principles of lens design and a practical knowledge of optical design software is very helpful when designing small format aerial imaging systems. Commercial lens design

software allow users to quickly develop lens prototypes and generate ray-trace diagrams for comparative analysis. Figure 3.1 is an example of a ray-trace diagram for a typical triplet lens configuration. The ray concept of light transmission and refraction is the fundamental model of light propagation employed throughout optical remote sensing – from lens design to development to complex photogrammetric analytical matrix solutions.

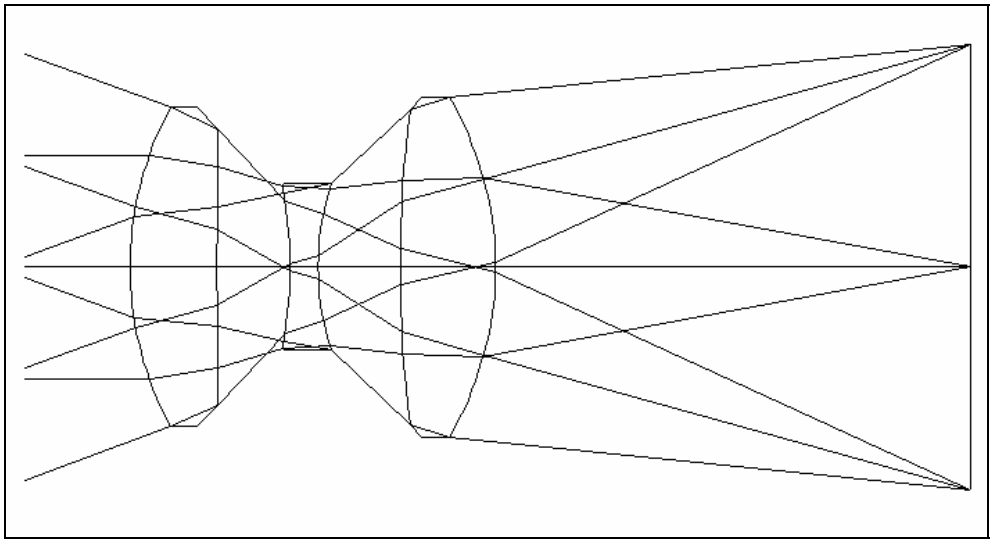

Figure 3.1 Triplet lens ray-trace produced by commercial lens design software.

Standard references of photogrammetry and remote sensing have limited coverage of optical principles and lens design, yet it is a key element of the science. Many good references on optical physics and design are available (Lipson et al. 1995; Ray 2002; Shannon 1997). The remote sensing community would benefit from a well researched compilation of recent technology. A somewhat dated discussion of lenses used in large format film aerial photography is given in Slama et al. (1980).

3.1.4 Illuminance

Illuminance is the amount of light received per unit area on the image plane during exposure. Illuminance is proportional to the square of the diameter of the lens opening (aperture) d^2 and varies with the square of the image distance i^2 (focal length at infinity) according to the inverse square law. The combined effect of aperture and image distance on illuminance is proportional to d/f. This relationship may be expressed as the brightness factor (Wolf and Dewitt 2000):

$$\sqrt{\frac{d^2}{f^2}} = \frac{d}{f} = \text{brightness factor} \qquad 3.8$$

where

f = lens focal length
d = diameter of the lens opening (aperture)

The more common expression is the *f* number (*f* stop) defined as:

$$f \text{ number} = \frac{f}{d} \qquad 3.9$$

The amount of illuminance at the image plane is equivalent for all combinations focal length and aperture having the same *f* number.

The amount of light energy acquired at the image plane is measured by the exposure of the image. Exposure is the product of illuminance and time. Exposure is varied by changing the aperture opening or the amount of time (shutter speed) that light is allowed to illuminate the image plane. The required exposure for maximum information recording and communication is a property of the image media. Many handheld cameras are indexed for *f* number settings that vary the amount of light reaching the image plane by a factor of two (*f*-1.0, *f*-1.4, *f*-2.0, *f*-2.8, *f*-4.0, *f*-5.6, *f*-8.0, *f*-11, *f*-16, *f*-22).

Aperture and *f* number are automatically controlled by many modern film and digital cameras according to an exposure program established by the manufacturer.

3.1.5 Lens Aberration and Distortion

Images produced by optical lenses are all transformed to varying degree by non-ideal refraction. Lens aberration is the displacement, blurring and chromatic separation of the image, particularly around the edges of the field. Aberrations develop because of the curvature of the lens surface. Monchromatic aberrations include spherical aberration, coma, astigmatism, curvature of field, and distortion (Ray 2002). Dependency of the refractive index on wavelength results in longitudinal and transverse chromatic aberration.

Spherical aberration, coma and astigmatism describe blurring of the image point. Spherical aberration is the radially symmetric blurring of an image point caused by the curvature of the surface of the lens. Blurring caused by coma (comet shaped) aberration is asymmetrical about the optical axis. Astigmatism is blurring caused by differential focus of light rays that strike the surface of the lens at points off the optical axis. Curvature of field and distortion describe the position and magnitude of distortion of the point of best image focus referenced to the image plane. Curvature of field identifies how far the best point of focus is ahead or behind the image plane. Distortion describes the differential enlargement of points across the image field. Aberrations are precisely defined mathematically in terms of the position of the actual image field compared to the position of an ideal wavefront (Lipson et al. 1995).

The amount of aberration depends on lens curvature, thickness, refractive index, and aperture (stop) position. Aberration is corrected by the combined effect of a series of

elements in a compound lens. Except for distortion, uncorrected aberration results in lost image information that cannot be recovered. Modern high quality lenses nearly eliminate uncorrected aberration.

Aberration is analyzed through ray tracing. Ray tracing repeatedly applies Snell's law (Equation 3.3) along a ray through the assembly of lens elements. The sine function in the ray trace model is approximated by the power Taylor series expansion of the sine function:

$$\sin\phi = \phi - \frac{\phi^3}{3!} + \frac{\phi^5}{5!} - \cdots \qquad 3.10$$

In Gaussian or paraxial optics the sin ϕ is approximated by ϕ (radians) and is adequate only to describe image formation for thin lenses of small aperture. Higher order terms are necessary for analyzing lenses with larger apertures and wider fields of view. Lens designers reference aberration correction to the order of the sign approximation. Modern lenses may be corrected to fifth or seventh order (Ray 2002).

Low altitude small format aerial imagery often is acquired with short focal length wide angle lenses to maximize ground field of view. It would be possible to fly higher with a longer focal length lens that produces less distortion to obtain desired coverage, but as will be discussed later, this reduces the stereo viewing effect and accuracy of parallax elevation measurement. Acquiring imagery with lenses that produce distortion is acceptable practice if lens distortion can be corrected with image processing software and other aberration is negligible for the intended use of the imagery. Lens distortion and correction is therefore of key concern.

Lens distortion alters the geometry or positional accuracy of the image but does not reduce information content. Lens distortion may be recovered by analysis of the lens

geometry and rectification of the image with image processing software. Lens distortion is separated into radial and tangential components. Radial distortion is symmetrical around the axis of the lens and is described by the shape of the displacement field, most commonly as either barrel or pincushion distortion. Tangential distortion may be called asymmetric or decentering distortion. Figure 3.1 is an unprocessed image of a brick wall acquired with a 17 mm focal length lens. The orthogonal lines of the brick layers are distorted radially outwards from the center of the image (barrel distortion). The magnitude of distortion is non-linear across the image and is most noticeable near the edges. There is almost no distortion near the center of the image.

Decentering distortion occurs when the lens assembly is misaligned along the optical axis during manufacture so that lens distortion is asymmetric about the center of the image plane. This is usually not a significant problem with modern high quality lenses unless damaged. Decentering distortion may be noticeable in images produced with some consumer quality lenses. There is no noticeable decentering distortion in Figure 3.2.

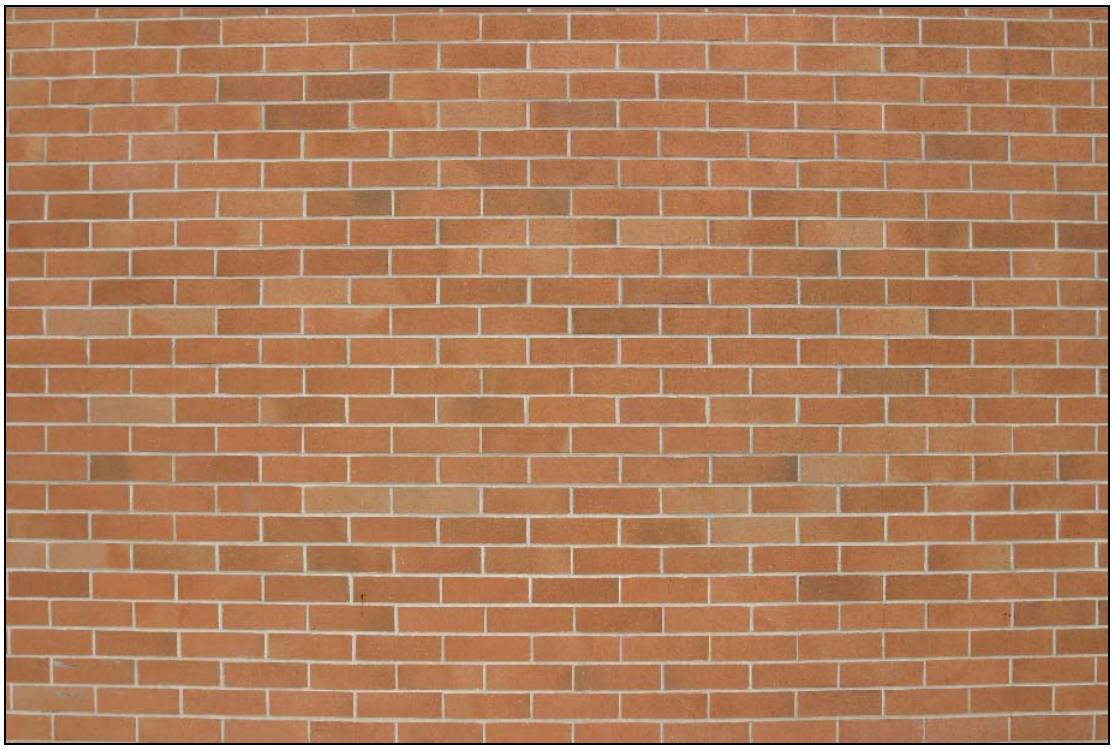

Figure 3.2 Radial distortion in a digital image captured with a 17 mm lens.

Evaluation and correction of geometric distortion are common tasks of image processing in optical remote sensing. Very small discrepancies in image measurements (around 0.01 mm) can produce large errors in height estimates in stereoscopic analysis. The geometric precision of aerial mapping cameras has historically been an important concern in photogrammetric engineering. Modern high quality aerial mapping cameras produce images with no noticeable lens distortion. Displacements caused by all lens distortion on large format aerial image negatives are typically less than 5 μm and are usually only corrected for precise analytical photogrammetry work (Clarke. and Wang 1998; Wolf and Dewitt 2000). U.S. Geological Survey standards for 6 inch (153 mm) aerial cameras require that radial distortion be less than ± 0.010 mm and a decentering distortion of less than 0.008 mm at any point on the image.

When necessary, an image is geometrically rectified by remapping pixels from the original image to a new image in a manner that reduces distortion to an acceptable amount. For radial distortion, each pixel is shifted in the radial direction from the center of the image as determined by a lens correction equation. Lens correction equations are determined from regression analysis of one or more test images. A common form of the lens equation is a polynomial of increasing order with up to four coefficients:

$$\Delta r = k_1 r + k_2 r^2 + k_3 r^3 + k_4 r^7 \qquad 3.11$$

where Δr is the radial lens distortion, r is the radial distance from the center of the image (principal point), and k_1, k_2, k_3, k_4 are coefficients. Other forms of polynomials and non linear equations with trigonometric terms may be employed (Fryer and Goodin 1989; Heikkila 2000; Light 1992). The coefficient on the seventh order term is often near zero in rigorously calibrated images from digital cameras and omitted (Heikkila 2000). The set of coefficients is unique to each camera and lens configuration and will change throughout the range of variable zoom lenses.

Decentering distortion may be included in rigorous calibration of images. The relationship most often found in the literatures of photogrammetry and machine vision originates in the work of Brown (1966; 1971). Brown's relationship in his 1966 paper was expressed as,

$$\begin{aligned} \Delta x &= \left[2k_1 xy + k_2\left(r^2 + 2x^2\right)\right]\left(1 + k_3 r^2 + k_4 r^4 + \cdots\right) \\ \Delta y &= \left[k_2\left(r^2 + 2y^2\right) + 2k_1 xy\right]\left(1 + k_3 r^2 + k_4 r^4 + \cdots\right) \end{aligned} \qquad 3.12$$

where r is the radial distance from the center of the image, Δx is the tangential distortion in the x direction, Δy is the tangential distortion in the y direction, and k_1, k_2, k_3, k_4 are different coefficients than those in Equation 3.5.

Optimal sets of coefficients for Equations 3.11 and 3.12 are best obtained by least squares analysis of carefully imaged orthogonal grids. Figure 3.3 is the brick wall image corrected for radial distortion. Image geometric rectification can be performed with most photogrammetric and remote sensing software packages. The level of correction in Figure 3.3 is sufficient for georeferencing of aerial images and low to moderate precision stereoscopic analysis.

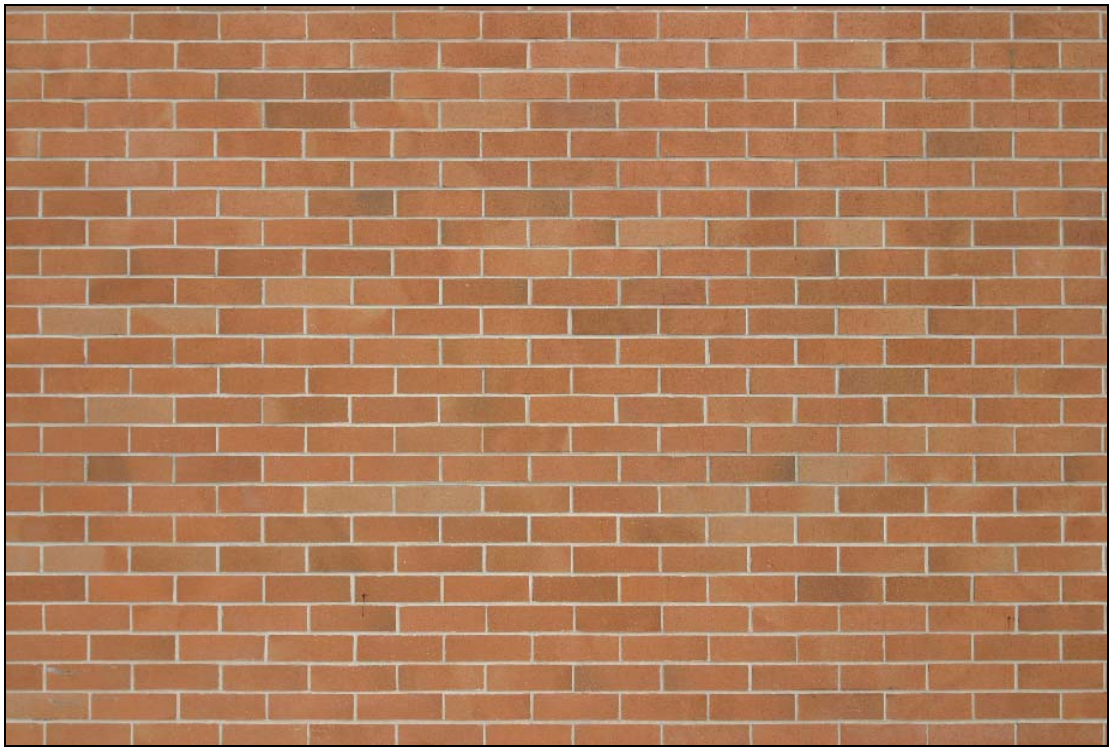

Figure 3.3 Digital image captured with a 17 mm lens corrected for radial distortion.

Practical application of a lens correction model is best illustrated with an example that does not rely on sophisticated adjustment of multiple images. Figure 3.4 is an image

of a calibration grid constructed from engineering grid paper glued to a flat laminate board. The 28 mm consumer grade lens produced significant radial distortion that is particularly noticeable along the visible left edge of the paper. Fourteen unevenly distributed control points in Figure 3.5 were measured both in image pixel coordinates and the true orthogonal grid locations. The diagonal lines identify the approximate location of the center of the image and the origin of the measurement grids for computation purposes.

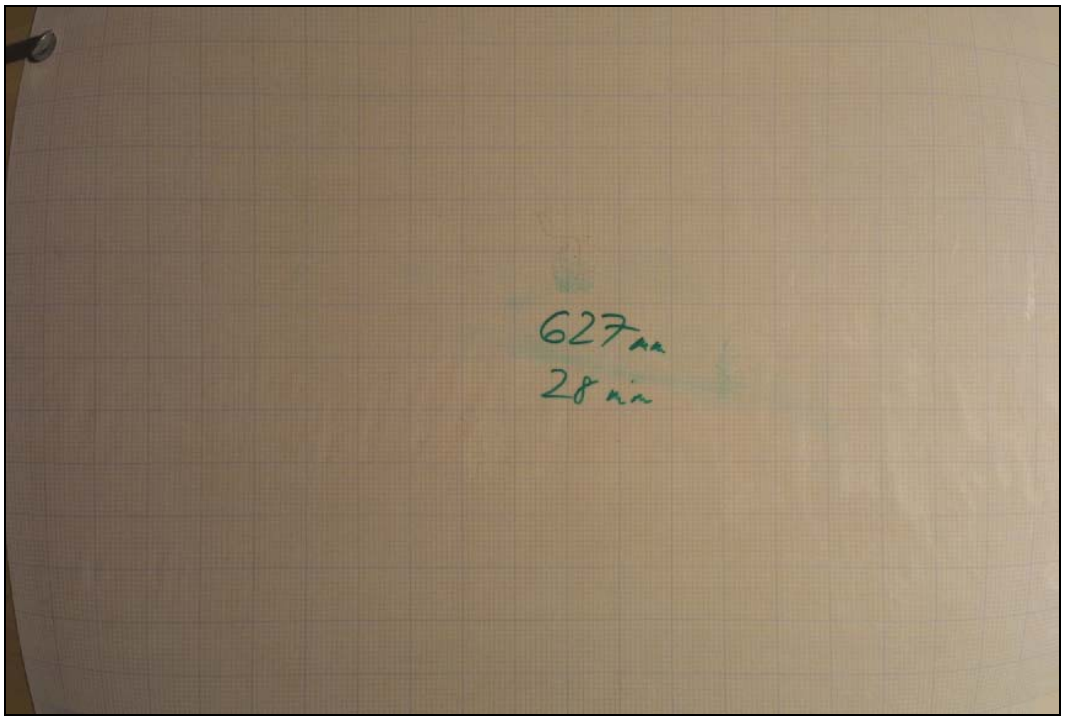

Figure 3.4 Original digital image of a calibration board.

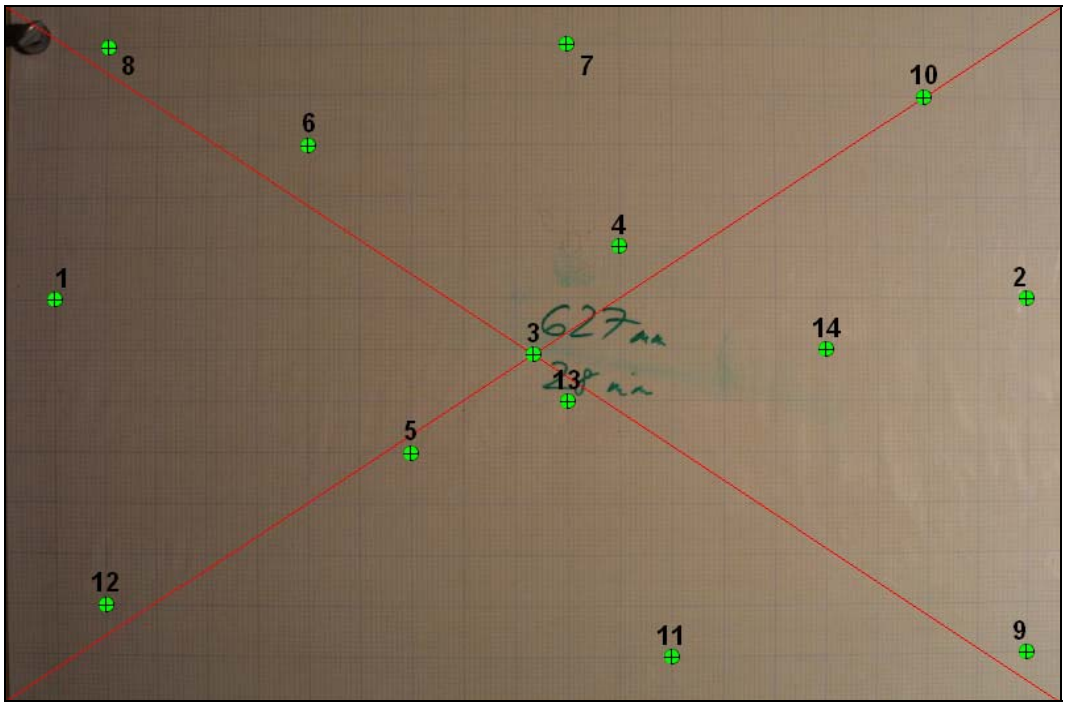

Figure 3.5 Control point locations.

Radial distances from the center of the original image in pixel units to each control point are listed in Table 3.1. The data in Table 3.1 will be used calibrate the coefficients of the Equation 3.11 by least squares analysis. Each control point in the table is referred to as an observation in the terminology of least squares analysis in photogrammetry and geomatics.

ID	Radius, r pixels	Shift, Δr pixels
1	980.44	16.61
2	1012.50	22.56
3	0.00	0.00
4	283.22	1.70
5	321.54	-2.23
6	627.43	4.69
7	643.65	7.47
8	1069.89	25.68
9	1177.85	27.25
10	957.14	21.86
11	685.63	3.89
12	1011.35	15.17
13	119.97	0.74
14	598.41	5.20

Table 3.1 Observations of control point radii and radial shifts.

The radial correction Equation 3.11 may be written for each observation (control point). A minimum of four control points would be necessary to solve for the unknown coefficients k_1, k_2, k_3, k_4. The 14 control points provide a reasonable level of redundancy. The algebraic lens correction observation equation with residual (Equation 3.12) is expressed in matrix form to facilitate the least squares solution:

$$k_1 r + k_2 r^3 + k_3 r^5 + k_4 r^7 = \Delta r + v \qquad 3.13$$

$$_m\mathbf{A}^n{}_n\mathbf{X}^1 =_m \mathbf{L}^1 +_m \mathbf{V}^1 \qquad 3.14$$

where **A** is the coefficient 14×1 matrix composed of the known values of r, r^3, r^5, *and* r^7; X is the 4×1 matrix of unknown lens correction parameters; **L** is the 14×1 matrix of observed radial shifts; and **V** is the 14×1matrix of residuals. The **A** matrix (Equation 3.15) was conditioned by dividing each radius value by 1000 because k_3 and k_4 are extremely large numbers when based on the original pixel values. The least squares solution is obtained from the matrix equation:

$$X = \left(A^T A\right)^{-1}\left(A^T L\right) \qquad 3.15$$

where $\mathbf{A}^T$ is the transpose of the **A** matrix. The matrix form of least squares analysis is used frequently in photogrammetry and geomatics. Development and illustration of the least squares matrix equation is in Appendix 3.1. Equation 3.15 is easily solved in Excel or with a mathematical computation package such as Matlab. Manual computation for a solution of Equation 3.15 is in Appendix 3.1.

$$\mathbf{A} = \begin{bmatrix} 0.9804 & 0.9425 & 0.9060 & 0.8709 \\ 1.0125 & 1.0380 & 1.0641 & 1.0908 \\ 0.0000 & 0.0000 & 0.0000 & 0.0000 \\ 0.2832 & 0.0227 & 0.0018 & 0.0001 \\ 0.3215 & 0.0332 & 0.0034 & 0.0004 \\ 0.6274 & 0.2470 & 0.0972 & 0.0383 \\ 0.6437 & 0.2667 & 0.1105 & 0.0458 \\ 1.0699 & 1.2247 & 1.4018 & 1.6046 \\ 1.1779 & 1.6341 & 2.2670 & 3.1451 \\ 0.9571 & 0.8769 & 0.8033 & 0.7359 \\ 0.6856 & 0.3223 & 0.1515 & 0.0712 \\ 1.0113 & 1.0344 & 1.0580 & 1.0822 \\ 0.1200 & 0.0017 & 0.0000 & 0.0000 \\ 0.5984 & 0.2143 & 0.0767 & 0.0275 \end{bmatrix} \qquad 3.16$$

Values of the lens correction parameters from the least squares solution are k_1 = -1.226, k_2 = 21.583, k_3 = 5.772, and k_4 = -6.157. A comparison of the observed and computed values of radial shift is in Table 3.2. The root mean squared error (RMSE) is 2.4 pixels or about 0.6 mm at the scale of the image.

ID	Radius, r pixels	r/1000	Shift, Δr pixels	Computed Shift, Δr	Residual Pixels
1	980.44	0.98	16.61	19.01	-2.39
2	1012.50	1.01	22.56	20.59	1.97
3	0.00	0.00	0.00	0.00	0.00
4	283.22	0.28	1.70	0.15	1.55
5	321.54	0.32	-2.23	0.34	-2.57
6	627.43	0.63	4.69	4.89	-0.20
7	643.65	0.64	7.47	5.32	2.15
8	1069.89	1.07	25.68	23.33	2.35
9	1177.85	1.18	27.25	27.54	-0.29
10	957.14	0.96	21.86	17.86	4.00
11	685.63	0.69	3.89	6.55	-2.66
12	1011.35	1.01	15.17	20.53	-5.36
13	119.97	0.12	0.74	-0.11	0.85
14	598.41	0.60	5.20	4.17	1.04

Table 3.2 Comparison of observed and computed values of radial shift.

The full image is transformed with image processing software by direct mapping of pixels with Equation 3.10 and the lens correction parameters from the least squares analysis. The final image corrected for radial lens distortion is in Figure 3.6. Additional control points could be measured to verify accuracy of the image. A visual assessment is normally sufficient for georeferencing of aerial images.

This example shows that even a modest calibration effort can remove a significant amount of radial lens distortion. The calibration only need be performed once for a particular lens and camera combination. Other images may be processed, typically in batch mode, with the derived lens correction parameters. In general, small format digital cameras and lenses used for aerial imaging and other photogrammetry work should be calibrated. The required effort is reasonable and the results worthwhile.

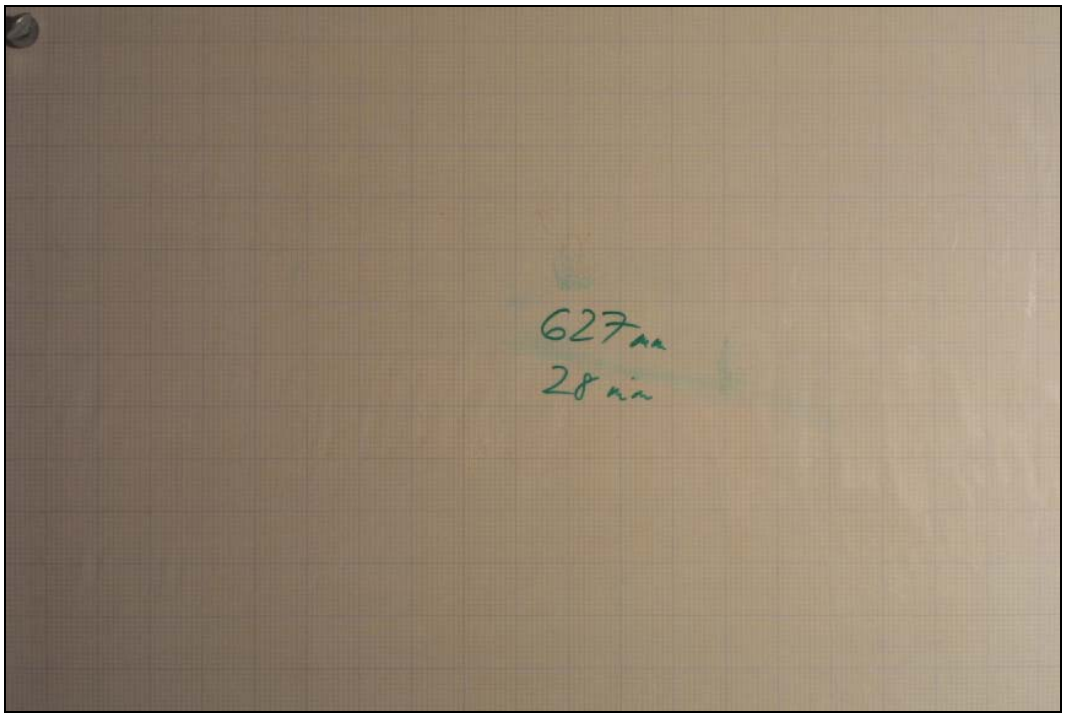

Figure 3.6 Final image corrected for radial lens distortion.

It is good practice to check the initial calibration and periodically recalibrate any camera and lens used in aerial imaging. The literature indicates that some non-metric digital cameras and lenses become misaligned with use or may not be optically aligned to an acceptable degree when manufactured (Clarke. and Wang 1998; Shortis et al. 1998). My experience tends to support these findings. Understandably, an exhaustive analysis of the numerous digital camera digital lens combinations is lacking. A good review of digital camera calibration and calibration models is given by Clarke and Fryer (1998). An evolving body of literature discusses methods of digital camera calibration and particular camera systems (Clarke and Fryer 1998; Fraser 1997; Tsai 1987; Zhang 1999; Zhang 2000).

Aerial mapping cameras are subject to flight stresses that may disturb the alignment of lens assemblies. Federal aerial mapping contracts require that aerial cameras be recalibrated by the U.S. Geological Survey Optical Sciences Laboratory (OSL) every three years. I visited the Optical Sciences Laboratory in Reston, VA early in my investigations and observed the camera calibration process. Many, if not most, aerial mapping cameras are found to be significantly out of calibration when arriving at the lab (MacCue 2001). Users of archived aerial imagery for precision photogrammetry should keep in mind that geometric calibration coefficients found in camera calibration may not adequately represent the actual internal camera and lens geometry.

Lens distortion may be accommodated directly in least squares adjustment methods of analytical photogrammetry along with determination of all the parameters of internal and external sensor orientation. This will be discussed in Section 3.4.2.

3.1.6 Field of View

The angular field of view determines the ground resolution and coverage of a particular camera and lens combination (Figure 3.7). Horizontal field of view (HFOV) may be determined from the relationship:

$$W_t = w_t \frac{H}{f} \tag{3.17}$$

where W_t is the transverse horizontal field of view on the ground (distance A to B), w_t is the width of the digital sensor array or film negative (distance a to b), f is the lens focal length, and H is the sensor height above terrain. A similar equation may be written for the longitudinal direction. Angular field of view may be determined from the expression:

$$\alpha_t = 2\tan^{-1}\left(\frac{w_t}{2f}\right) \tag{3.18}$$

where α_t is the angular field of view in the transverse direction.

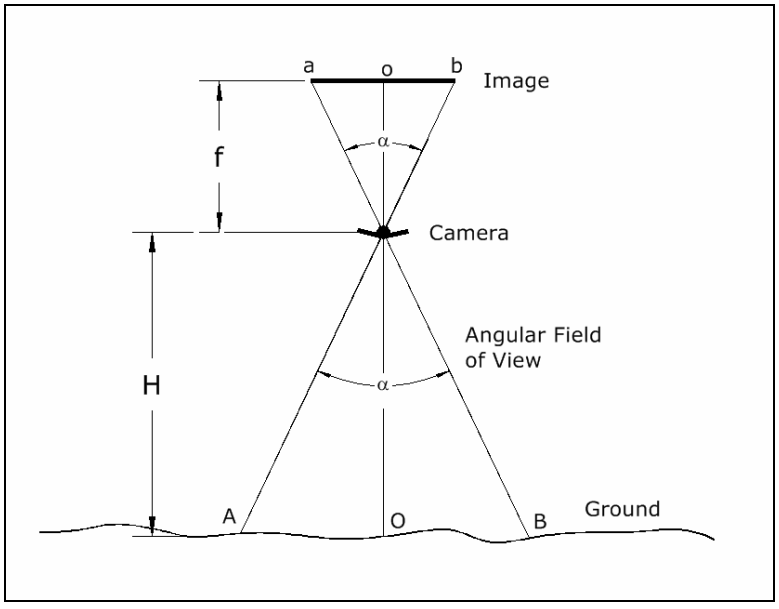

Figure 3.7 Field of view of an aerial sensor.

3.1.7 Assessment of Image Resolution

Resolving power (resolution) is the ability of the lens, camera and display media to convey detail to an observer. Resolving power of an optical system has been represented as the sum of the resolving power of its components (Philipson 1997):

$$\frac{1}{RP_{system}} = \frac{1}{RP_{lens}} + \frac{1}{RP_{film}} + \frac{1}{RP_{filter}} + \cdots \qquad 3.19$$

Defining the resolving power of each component is subjective and depends on the ability of the human observer. Equation 3.19 is mostly conceptual, but places the following discussion of numeric resolution in proper context. Image producers (and marketers) sometimes emphasize numeric resolution as if it is the only pertinent image characteristic. Resolution is of primary importance, but other factors such image contrast, sun angle, color accuracy, and time of year contribute greatly to an image's usefulness.

Various terms represent spatial resolution in the image (image space) and with reference to the ground (object space). Spatial resolution to most users simply means the ground distance covered by the width of a pixel in the final georeferenced or orthorectified image. Spatial resolution in this context is called ground sampling distance (GSD) from a sensor point of view or ground pixel resolution (GPR) from an image use point of view. The two terms are equivalent for practical purposes, but it should be understood that image GPR may be altered by image processing in a manner that does not represent the true GSD of the sensor.

It is implied in common usage that an analyst has ability to discern ground objects down to about the nominal GSD. This is generally true, but not guaranteed. A user learns by experience what may be resolved in a particular type of imagery at a specific

numeric resolution. A user of 1-meter GSD Ikonos 11-bit panchromatic satellite imagery will have a much different impression of resolving power than a user of 8-bit NAPP aerial images scanned at the same resolution. In practice the simple numeric sensor and image definitions of resolution are usually sufficient and understandable, and most often adopted by imagery producers. True image resolution – the ability to discern discrete objects in an image, is more complex and must be analyzed with photogrammetric relationships and signal theory.

A conceptual understanding of true image resolution is gained by recognizing that it takes at least two pixels, a light one and a dark one, to record the edge of a feature. All reflected light from an area the size of the GSD is aggregated into a single brightness value. No further information may be extracted from the pixel, though some techniques infer subpixel characteristics from the spatial arrangement of surrounding pixels. A stated GSD for a given type of sensor does not automatically mean that objects near this size can be discerned in a particular image. A blurred aerial photograph may be scanned to produce a GPR of 0.5 m, but objects many times this size may be too indistinct to identify. Conversely, original NAPP aerial image diapositives (transparency) often contain more detail than apparent in digital orthophoto quadrangles made from NAPP scans.

An image scanned at a resolution finer than discernible detail is said to be over-sampled, however, over sampling is generally wasteful of computer storage and image processing resources. Over sampling is not always undesirable. I often re-photograph features of interest from archived aerial imagery at high magnification to be certain to capture all discernible detail. It may be that future intelligent scanners and digital sensors

will have the ability to vary image resolution and bit depth to optimize detail retention and storage. Choice of scan resolution for the present is a subjective judgment.

Methods have been developed to link numeric resolution with objective measures of resolving power. A conventional technique is to image a precisely printed chart containing repetitive groups of contrasting elements of decreasing size. The chart in Figure 3.8, originally developed for the U.S. Air Force, has been in use for decades. In practice, a precisely printed version of the chart is imaged with a given sensor configuration (lens, recording media, focal length, target distance, illumination, aperture) for examination under magnification to determine the smallest triplet of elements clearly discernible. Each group in the chart contains six elements that decrease in size by a factor of $2^{1/6}$. A table (Table 3.3) is usually printed on the chart that gives the nominal resolution in line pairs per millimeter (lp/mm or *LPM*) by group and element at unit magnification.

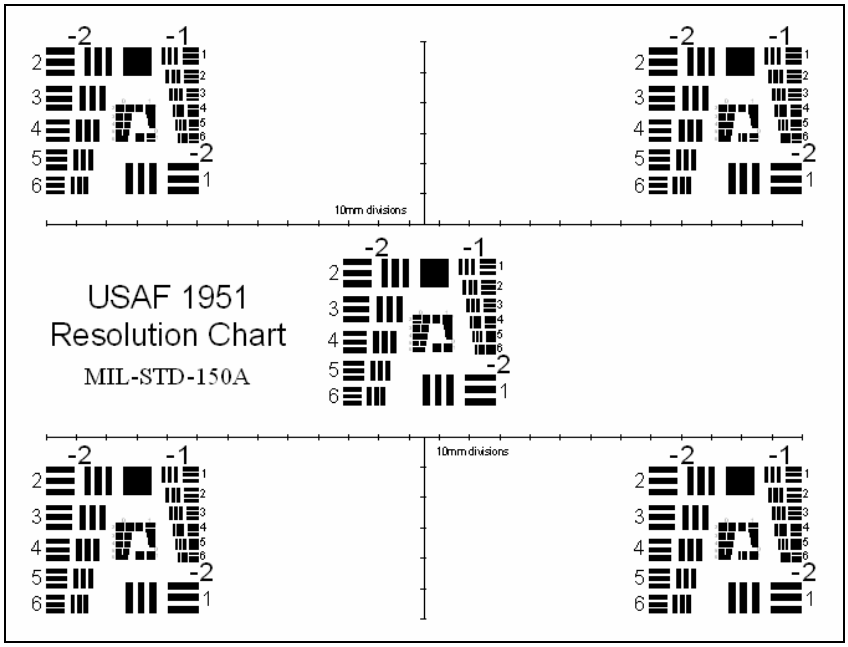

Figure 3.8 U.S. Air Force resolution chart.

Number of Lines/mm				
	Group Number			
Element	-2	-1	0	1
1	0.250	0.500	1.00	2.00
2	0.280	0.561	1.12	2.24
3	0.315	0.630	1.26	2.52
4	0.353	0.707	1.41	2.83
5	0.397	0.793	1.59	3.17
6	0.445	0.891	1.78	3.56

Table 3.3 Line pair resolution for the U.S. Air Force Resolution Chart.

The nominal resolution of the chart may be adjusted to the reduced image produced by a typical camera lens configuration by application of lens Equation 3.6 to give:

$$LPM_{image} = LPM_{chart}\left(\frac{o-f}{f}\right) \qquad 3.20$$

where LPM_{image} is the line pairs per mm (lp/mm) resolved in the image, LPM_{chart} is the lp/mm tabulated on the chart, o is the distance from the center of the lens (actually front nodal point if known), and f is the lens focal length.

An analyst typically examines several locations in the imaged chart and computes an area-weighted average resolution (AWAR). Resolution in lp/mm corresponding to the numbered chart triplets is shown in Table 3.3. Judging which triplet is the smallest discernible is a subjective assessment. Contrast between dark elements and white space significantly influences selection of the least discernible triplet.

The most widely accepted and objective quantitative method is the sensor modulation transfer function (MTF) (Slama et al. 1980, Lillesand and Kieffer 1994, Campbell 1996, Wolf and Dewitt 2000). The MTF avoids observer subjectivity by incorporating the effect of contrast variation in the analysis of the detectable spatial

frequency of chart elements. MTF borrows its terminology and theory from electronic signal processing. Measurements are quantitative. Typically, image processing software analyzes a scan of a precisely printed test pattern and generates MTF plotting values. Test patterns are composed of patterns of variable contrast lines of varying width spaced according to a sign function of decreasing wavelength (Lillesand and Kieffer 1994). Figure 3.9 is an example of one type of MTF test pattern. MTF analysis results are plotted as a MTF curve. Figure 3.10 is the author's interpretation of a published MTF curve for Kodak 2444 color aerial film.

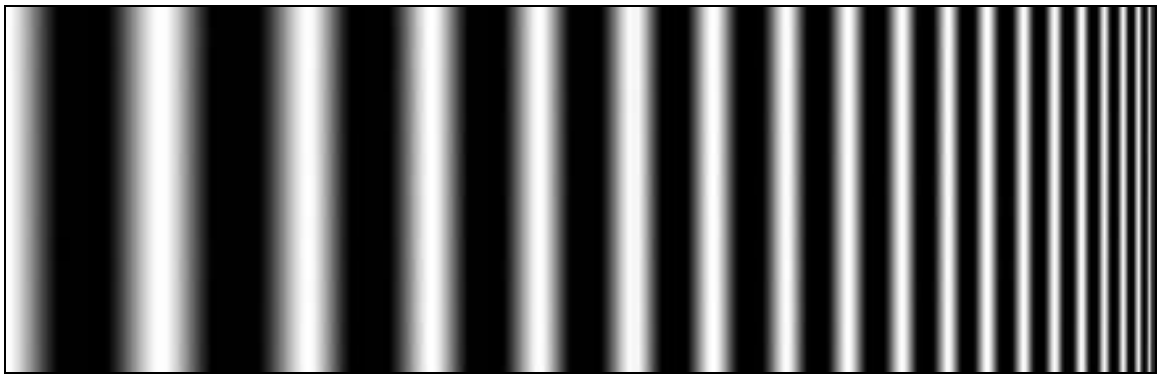

Figure 3.9 Resolution Test Chart for the Modulation Transfer Function.

MTF curves offer a quick visual check on the resolution capabilities of sensor configurations. Manufacturer's MTF plots are produced under near ideal conditions and normally do not represent the actual field configuration of the sensor and lens assembly. The vertical axis of the MTF plot indicates how well the sensor records the contrast of the target. A value of 100% MTF is perfect representation. Spatial resolution in terms of spatial frequency is indicated along the horizontal axis. Spatial frequency in cycles/mm is numerically equivalent to the units of line pairs per millimeter of the more subjective resolution chart test. Figure 3.10 shows a trade-off between MTF contrast response and

spatial resolution. Smaller features could be discerned in the image, but are less distinctive than larger features. The contrast response of the blue dye layer at a spatial frequency of 75 cycles/mm is about 50%. This means that black lines spaced at 0.01 mm on the test target would appear 50% lighter on the image than large black lines spaced further apart. Interestingly, the MTF response for the color aerial film is greater than 100 percent at low spatial frequencies. This likely indicates that the color dyes are designed to over saturate strong color features.

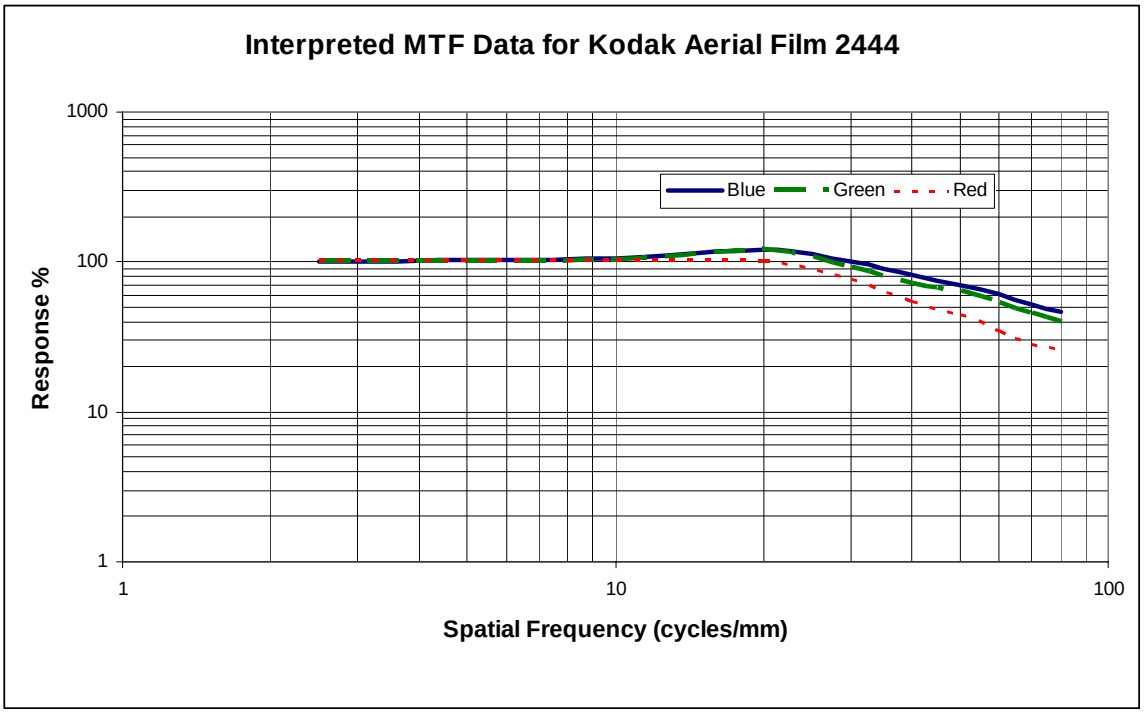

Figure 3.10 Modulation Transfer Function for Kodak 2444 Color Aerial Film.

The resolution chart and MTF analyses are of practical interest because they offer a means to evaluate the utility of archived aerial imagery prior to purchase. Resolved spatial frequency is reported in USGS aerial mapping camera calibration reports. Figure 3.11 is an excerpt from the calibration report for the aerial camera that produced the 1998 National Aerial Photography Program (NAPP) aerial photos of the Potlatch River basin. It reports an area weighted average resolution (AWAR) of 89 cycles/mm. Image MTF

spatial frequency is converted to ground spatial resolution from the lens focal length and sensor height above terrain. The nominal ground scale of a NAPP aerial image is 1:40,000, so the nominal static resolution of the NAPP aerial image is computed:

$$\text{Nominal Static Resolution} = \frac{40{,}000 \text{ scale}}{89 \text{ cycles/mm} \times 1000 \text{mm/m}} = 0.45 \text{ m} \qquad 3.21$$

Under near ideal conditions objects about one 0.5 meter wide should be discernible in NAPP images. Aircraft motion, atmospheric haze, and misadjusted lenses all contribute to lower resolution under actual flight conditions. Digital orthophoto quadrangles produced from NAPP imagery by USGS are scanned to give a ground pixel resolution of 1.0 meter. This results in a working resolution of about 2.0 meters. The AWAR reported in the camera calibration reports indicates that finer detail can be observable in original NAPP aerial photos than in digital orthophoto quadrangle images.

III. Lens Resolving Power in cycles/mm

Area-weighted average resolution: 89

Field angle:	0°	7.5°	15°	22.7°	30°	35°	40°
Radial Lines	95	113	113	67	95	95	95
Tangential lines	95	95	95	80	95	80	80

The resolving power is obtained by photographing a series of test bars and examining the resultant image with appropriate magnification to find the spatial frequency of the finest pattern in which the bars can be counted with reasonable confidence. The series of patterns has spatial frequencies from 5 to 268 cycles/mm in a geometric series having a ratio of the 4th root of 2. Radial lines are parallel to a radius from the center of the field, and tangential lines are perpendicular to a radius.

Figure 3.11 Lens resolving power from a USGS calibration report.

The resolving power of the lens reported in Figure 3.11 reaches its lowest value at a field angle of 22.7 degrees. Resolving power should typically decrease monotonically with increasing field angle. This particular calibration report indicates that one of the

lens elements in the lens assembly is likely slightly misaligned. The resolution still exceeds the USGS acceptance standard of 57 lp/mm at 22.7 degrees for a 153 mm focal length lens.

While MTF analysis provides an objective means to measure spatial frequency response of an imaging system, a working definition for spatial resolution in satellite and aerial imagery analysis remains subjective. It is interesting that the defense intelligence community has pursued a different approach. Defense analysts rank the suitability of images at various resolutions according to the ability to discern detail of military concern. The ranking criterion includes image snippets and narrative descriptions along the lines of a photointerpretation key. A narrative resolution key for civilian applications has evolved from this work. I followed a similar approach in my compilation of satellite and aerial imagery examples for the BPA project.

3.1.8 Theoretical Limits of Resolution

Two aspects of resolution that are more applicable to satellite remote sensing should be mentioned. The Nyquist sampling theorem from signal processing requires that a waveform be sampled at a spatial frequency of one half the smallest constituent wavelength to resolve all frequencies within the signal. A typical CCD sensor is composed of pixel elements that are 8 to 10 micrometers in size. The largest wavelength an 8 micrometer pixel array could sample is 16 micrometers. Since this wavelength is well into the far infrared region of the electromagnetic spectrum, the Nyquist sampling limit is of little concern in digital aerial imaging of optical wavelengths. The effect of sensor color pixel configurations on resolution will be discussed in a later section.

Light diffraction due to a finite aperture ultimately limits resolution in an ideal lens. A mathematical description of the diffraction of a circular aperture evolves from an analysis of Fraunhofer diffraction of a slit and can be approximated by the relationship (Rees 2001):

$$\alpha_c = \frac{w}{z} = \frac{\lambda}{d} \qquad 3.22$$

where α_c is the limiting angular resolution (field of view) of the sensor (radians), w is the minimum resolved width (object or image plane) approximated by the arc subtended by the very small angle, z is the distance from the lens to the object (or focal length), λ is the wavelength to be sampled, and d is aperture diameter of the lens. Equation 3.22 is valid if the distance from the lens to the object is greater than the Fresnel distance:

$$z > \frac{d^2}{2\lambda} \qquad 3.23$$

This relationship indicates that the Landsat 7 satellite orbiting 705 km above the surface of the earth must have an effective lens aperture of at least 3 cm to produced 15 meter resolution pancromatic images composed of light down to a wavelength of 0.5 μm (blue):

$$d \approx \frac{\lambda}{\alpha_c} = \frac{(705{,}000\,\text{m})(0.5\times10^{-6})}{15\,\text{m}} = 0.024\,\text{m}$$

The Landsat 7 imaging telescope has an internal clear aperture of 16.66 cm so it does not encroach on the diffraction limit in the visible bands. A similar computation for the 60 m resolution thermal band at 12.5 μm indicates a minimum aperture of 14.7 cm, close to the reported value. The Fresnel distance by Equation 3.23 is 576 m so Equation 3.22 is valid.

A variation of Equation 3.22 in optical engineering references and physics texts is (Beiser 1973):

$$\sin \alpha_c = 1.22 \frac{\lambda}{d} \qquad 3.24$$

This is essentially the same relationship as Equation 3.21 with a multiplier that develops from the first root of Fraunhofer analysis (i.e. the Airy disk of astronomy). Equations 3.22 and 3.24 are different because of different simplifications to the Fraunhofer analysis. The 22 percent difference is not significant in practical use of the equations. Equation 3.22 or 3.24 may be recast to provide the limiting resolution on the focal plane as a check on optical system design. At small angles the sine may be replaced by the angle in radians. Since arc length is the radius multiplied by the subtended angle, the minimum resolvable width from Equation 3.24 becomes:

$$w = 1.22 \lambda \frac{f}{d} \qquad 3.25$$

where w is the resolved width on the image plane, f is the focal length of the lens, and d is the lens diameter. The ratio f/d is seen to be the f number of the exposure (Equation 3.9). The more conservative Equation 3.21 provides a means to check the suitability of a digital sensor for high-resolution imaging work. For example, a typical exposure of a sunlit aerial scene during the middle of summer would be f 6.7 at 1/1000 second. Substituting this f number and a blue light wavelength of 0.5 μm into Equation 3.25, the minimum resolvable width due to diffraction at the aperture is:

$$w = 1.22 \lambda \frac{f}{d} = 1.22 \lambda \times f\text{stop} = 1.22(0.5\,\mu\text{m})(6.7) = 4.1\,\mu\text{m}$$

Most high quality digital cameras have sensors with pixel elements at least twice this size.

Manufacturers are well aware of diffraction effects and design camera and lenses to avoid this limitation. It appears that diffraction may be of concern for high *f* number settings. However, at constant illumination, higher *f* numbers (smaller aperture) require slower shutter speeds than would be used in aerial imaging. The trend in digital camera design is towards larger pixel arrays with pixel element size remaining relatively constant. Resolution limitation due to light diffraction through the lens aperture is not a significant concern in aerial imaging work performed with high quality digital cameras and lenses. Sensor designers, of course, must bear in mind the diffraction limits when selecting optical components.

3.1.9 Image Motion

Objects in the field of view of an aerial sensor are in constant relative motion because of forward aircraft velocity and momentary angular movements about the aircraft flight axis caused by air turbulence and manipulation of the flight controls. Large format aerial mapping cameras are typically equipped with forward motion compensation and gyroscopically stabilized camera mounts. Small format aerial imaging equipment is normally not equipped with motion compensating mounts. Image blurring in passively mounted imaging systems is reduced by maintaining high shutter speeds in optical-mechanical cameras or short sensor integration times in fully electronic systems.

The potential for image blurring may be evaluated by comparing the relative motion of an object on the ground during image capture with the size of the pixel element in the sensor array.

$$vt < \frac{H}{f} w \qquad 3.26$$

where v is the forward velocity of the aircraft (m s^{-1}), t is the shutter speed (s), H is the aircraft height above terrain (m), f is the lens focal length (m), and w is the sensor pixel element size (m). The right side of Equation 3.26 is equivalent to the ground sampling distance (GSD) of the sensor (m).

For example, parameters for a typical aerial imaging flight would be at a velocity of 44.7 m s^{-1} (100 mph) and an altitude of 800 m, with a camera having a 28 mm focal length lens set at a shutter speed of 1/1000 s and having a CCD with an 8 μm pixel element. Assuming these values Equation 3.26 becomes:

$$vt = 44.7 \text{ ms}^{-1} \frac{1}{1000 \text{ s}} = 0.0447 \approx 5 \text{ cm}$$

$$\frac{H}{f} w = \frac{800 \text{ m}}{.028 \text{ m}} \left(8 \times 10^{-6} \text{ m}\right) = 0.23 \text{ m} = 23 \text{ cm}$$

Aircraft motion is much less than the nominal GSD so blurring should be minimized. The relationship with shutter speed is linear so shutter speed could be reduced to 1/500 s in non-turbulent flight conditions. Air turbulence will cause abrupt and momentary movements of the aircraft pitch and roll. These are unavoidable, so it is usually best to use the fastest shutter speed possible (maximum aperture) within the limits of the lens and equivalent film speed of the camera.

3.1.10 Depth of Field

Depth of field is the range of distance from the lens in which an object will be in focus. Acceptable limits for blurring at the near and far distances of the depth of field is somewhat subjective and may be defined in terms of a circle of confusion c. The circle of confusion may be visualized as the spreading of a point on the image plane as the camera

is adjusted out of focus. The depth of field of lenses focused at infinity is defined by the hyper focal distance (Ray 2002):

$$p_H = \frac{f^2}{c\frac{f}{d}} + f = \frac{f^2}{c(f\ \text{number})} + f \qquad 3.27$$

where, P_H is the hyper focal distance, p is the distance of the object from the lens, f is the focal length, c is the diameter of the circle of confusion, and d is the lens aperture. Any object located further than the hyper focal distance from the lens will be in focus. The depth of field actually extends halfway from the hyper focal distance back to the lens. The circle of confusion is typically assumed to be around 0.03 mm based on the ability of the human eye to resolve point objects in 35 mm film images. A minimum value of c would be the size of the pixel element in a CCD sensor. Equation 3.27 provides a check on depth of field effects in aerial imaging for which lenses are set to focus at infinity. Assuming the typical flight parameters in the previous example, an f number of 6.7 and a c value of 8 μm, the hyperfocal distance is:

$$p_H = \frac{(.028\,\text{m})^2}{(8\times10^{-6})\,\text{m}\,(6.7)} + 0.028\,\text{m} = 14.6\,\text{m}$$

The hyperfocal length is very much less than the 800 m aircraft height above terrain, thus the depth of field does not affect the focus of aerial images.

Near and far points of acceptable focus may be computed for close range imaging with the relationship (Mikhail et al. 2001):

$$p_{N,F} = \frac{p}{1 \pm (p - f)c\frac{f\ \text{number}}{f^2}} \qquad 3.28$$

where P_N and P_F are the near and far limits of the depth of field, p is the distance of the object from the lens, f is the focal length, c is the diameter of the circle of confusion, and f number is the lens aperture setting.

3.1.11 Image Exposure

Exposure is the amount of energy accumulated at the surface of the sensor while light is admitted to the sensor when the shutter is open. Exposure is computed with the relationship:

$$H_{sensor} = \frac{\pi TLtd^2 \cos^4 \theta}{4f^2} = \frac{\pi TLt \cos^4 \theta}{4N^2} \qquad 3.29$$

where H is the image exposure (J), T is the transmittance of the lens material, L is scene reflected irradiance (W m^{-2}), d is the diameter of the lens aperture (m), t is the exposure time (s), f is the lens focal length (m), N is the f number (dimensionless), and θ is the angle from the optical axis to a specific point on the image surface. Appendix 3.3 includes the development of Equation 3.29 from lens geometry and a more complete discussion of the parameters.

According to Equation 3.29 exposure time and aperture may be varied to produce an image of equivalent brightness. Two images produced by the same lens configuration will have equivalent brightness if:

$$\left[\frac{t}{(f\text{number})^2}\right]_{image\ 1} = \left[\frac{t}{(f\text{number})^2}\right]_{image\ 2} \qquad 3.30$$

Values of Equation 3.30 are very small for practical values of shutter speed and f number. The exposure relationship in Equation 3.30 is more conveniently expressed as an exposure value EV:

$$EV = \log_2\left(\frac{t}{(f\text{number})^2}\right)$$
$$EV = \frac{1}{\log_{10}(2)}\log_{10}\left(\frac{t}{(f\text{number})^2}\right) = 3.32\log_{10}\left(\frac{t}{(f\text{number})^2}\right) \quad 3.31$$

The base-two logarithm is used in Equation 3.31 so that camera adjustments may be computed easily. Increasing the aperture *f* number by one full stop and holding film speed constant increases the exposure value by 1.0

3.1.12 Exposure Falloff

Exposure falloff (vignetting) is a lens property that reduces the intensity of light in a radial direction from the lens center. This can impair image interpretation or analytical analysis of images. Equation 3.29 shows that exposure falloff is a function of the fourth power of the cosine of the angle from the optical axis to a point on the image:

$$H_\theta = H_o \cos^4\theta \quad 3.32$$

where H_θ is the exposure at angle θ from the optical axis and H_o is the exposure on the optical axis or center of the image. The reduction in exposure is less than 1% for moderate focal length lenses. Exposure falloff may be noticeable in some wide angle lenses. In film photography falloff may be compensated by special filters or by print exposure adjustments. Gradient contrast enhancement algorithms can be applied in digital image processing and may be combined with lens distortion correction. High quality lenses are constructed to reduce exposure falloff to negligible amounts. The exponent on the cosine term in Equation 3.32 varies from 1.5 to 4 for corrected lenses(Ray 2002). Exposure falloff may be evaluated subjectively in overlapping aerial images by comparing matching areas. Figure 3.12 abuts matching sections of unaltered

overlapping images of the Palouse River floodplain. Falloff is not observable or detectable in pixel brightness values. If exposure falloff were significant, the brightness of the relatively uniform grass field would contrast markedly where the two images abut in Figure 3.12

Figure 3.12 Image falloff detection in high-resolution digital aerial images.

3.1.13 Spectral Sensitivity

Photogrammetric measurements are normally made from color or panchromatic images of reflected light produced by optical remote sensing techniques. Photogrammetry is not necessarily restricted to reflected light images. Photogrammetric principles are applied throughout remote sensing in such fields as medical imaging, radar imaging and sonar analysis. Spectral characteristics of images need not be precisely quantified for photogrammetric work – there are no geometric relationships that are

wavelength dependent. The only necessary restriction is that light reflection and transmission be adequately modeled by straight-line ray analysis.

In a broad sense, spectral characteristics determine the usability of aerial images for feature interpretation and photogrammetric measurements. Earth imaging instruments are classified as optical sensors if they image in the region of the solar spectrum from 0.3 to 14 μm where energy may be reflected and refracted with lenses and mirrors (Lillesand and Kieffer 1994). Most earth imaging sensors detect reflective and emitted energy in the visible and infrared range (Figure 3.13). Some sensors are designed to respond to a broad band of radiation, such as panchromatic film, while others may only image a narrow slice of the spectrum, as in the case of hyperspectral imagers.

Conventional panchromatic aerial photography records reflected energy across the visible range and portions of the ultra violet and near infrared bands. Manufacturers of aerial film publish spectral sensitivity charts such as that for the Kodak panchromatic aerial film in Figure 3.14. Film sensitivity is not designed haphazardly. Plots of the standard solar spectrum for air mass 1.5 (Figure 3.15) show that the Kodak aerial film is designed to be sensitive to visible and near infrared light region where solar energy at the surface is greatest. The film is also sensitive to ultraviolet which often must be removed by a lens filter to reduce ultraviolet haze caused by Rayleigh scattering.

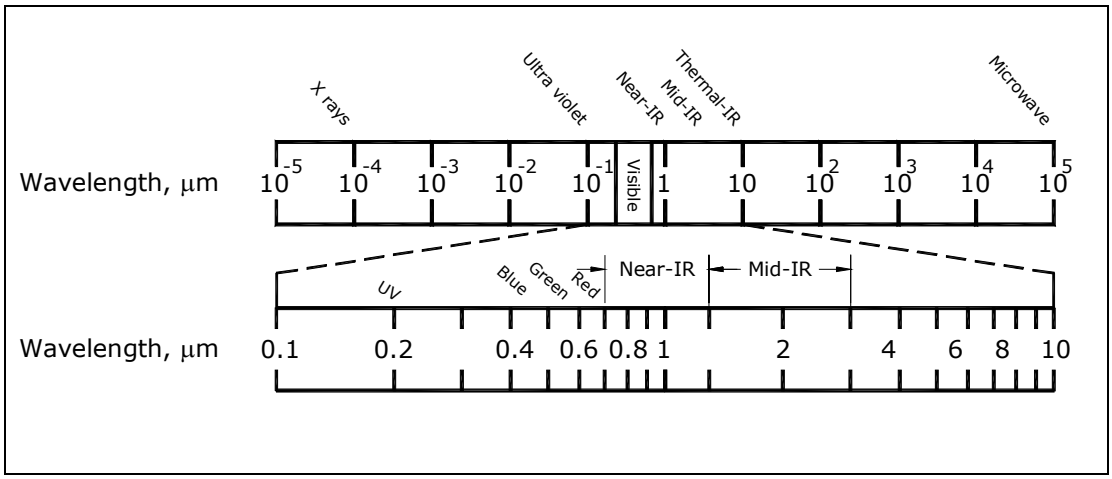

Figure 3.13 Partial electromagnetic spectrum.

Spectral response of an image scene is recorded in panchromatic film by photochemical conversion of silver halide crystals to dark silver grains (after development) in proportion to the amount and wavelength of light energy reflected from the target to the camera. Prints or transparencies produced from the film negative record relative reflectance as graytone (black and white) images and cannot generally quantify the amount of reflected energy. Panchromatic film and prints may be converted to grayscale digital images by scanning for use with GIS systems or image analysis software. During scanning the continuous gray tone of the film image is quantized into digital numbers depending on the bit depth of the scanner. Most scanners produce an eight-bit image resulting in 256 possible digital numbers from 0 to 255. Satellite imagery is sometimes quantized with bit depths of ten (1024 DN's) or twelve (4096 DN's).

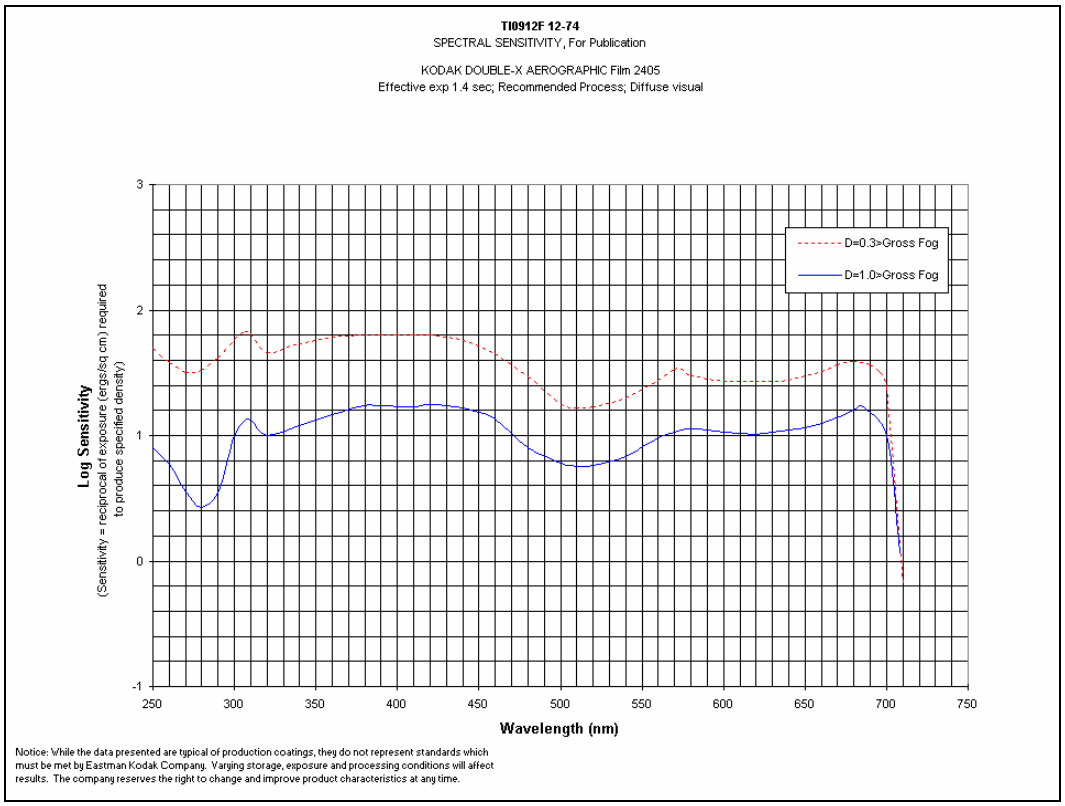

Figure 3.14 Spectral sensitivity of Kodak Double X Aerographic Film 2405 (Kodak)

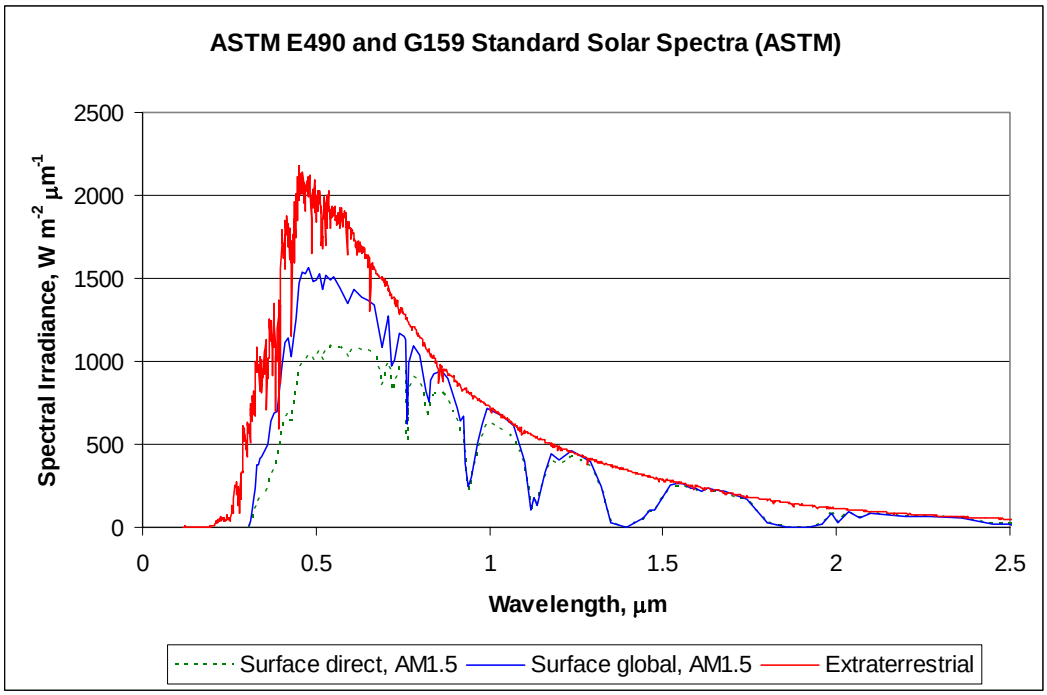

Figure 3.15 Standard Air Mass 1.5 solar spectra (Astm 1998).

Electronic sensors are sensitive to a wide band of electromagnetic radiation and can exceed the spectral range of panchromatic film. Silicon based charge couple device (CCD) sensors possess an efficiency of conversion of incident photons to image signal (quantum efficiency) of about 10% in the blue (380-430nm), about 40-60% in the far red/beginning of the near-IR (680-800nm), and about 10% in the near-IR at 900-1000nm (King 1995). Some CCD sensors may produce grayscale images with equivalent or better radiometric characteristics than panchromatic film (Campbell 1996). Spectral sensitivity of a silicon sensor is typified by the Kodak CCD plot in Figure 3.16. Enhanced sensitivity of the silicon sensor in the near infrared region compared to film improves the ability of digital sensors to acquire useful aerial imagery under lower light conditions.

Sensors made with other photoconductive materials exhibit different sensitivities. Silicon metal and PbO (lead oxide) are the most common detector materials for the visible light range. Photoconductor materials sensitive to near infrared include PbS (lead sulphide) and InAs (indium-arsenic). Photoconductors made with InSb (indium antimonide) respond to mid infrared (3-6 μm). The most common detector material for the far infrared range (8-14 μm) is Hg-Cd-Te (mercury-cadmium-tellurium) (Short 1998).

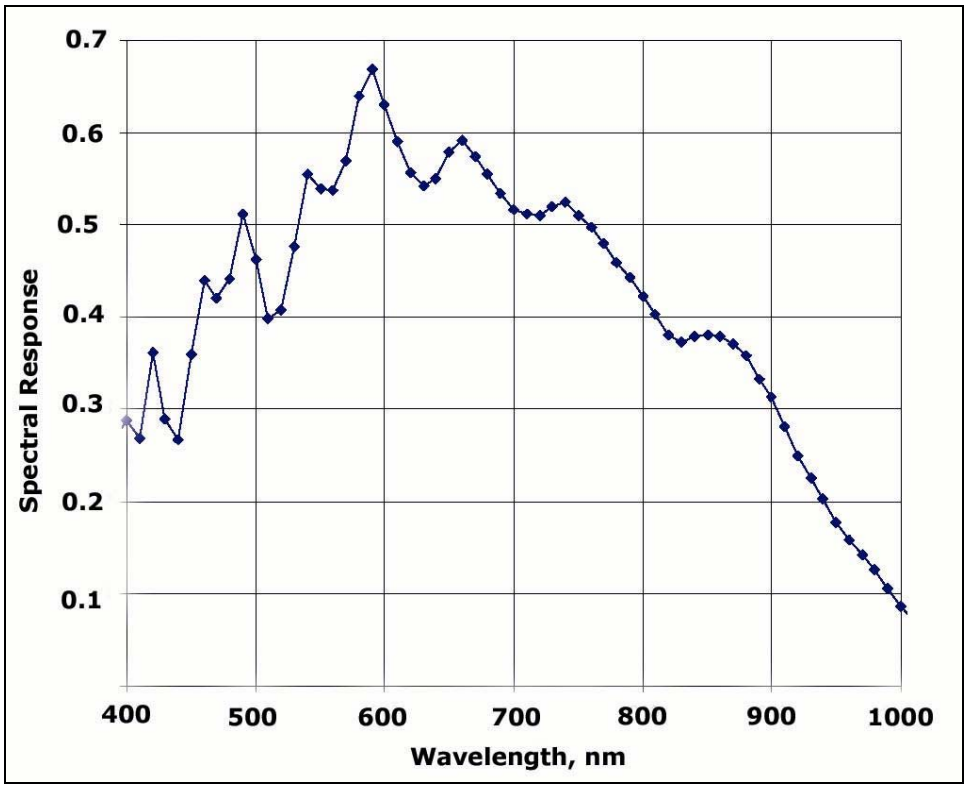

Figure 3.16 Spectral response curve for the Kodak KAF-0261E CCD.

Silicon detectors transform light energy to electrical current in a process called the photovoltaic effect. Light excites the movement of electrons from the valence band to the conduction band in the silicon metal. The accumulated charge flows to an attached electrical circuit to produce a response signal. Thermal energy also excites valence electrons to produce an electrical (dark) current. Non light related current results in electrical noise in the signal response (image) of the detector. The ratio of the signal output to the noise level is known as the signal to noise ratio (S/N), an important criteria for sensor designers.

Electronic sensors may be filtered and calibrated to measure reflected energy flux for specific wavelength bands. In general this requires an empirical correlation (calibration) of the sensor output with known amounts of reflected or emitted energy.

Calibration curves may be provided by the manufacturer of the sensor or determined by independent analysis. Relative sensitivities of the Ikonos satellite sensor bands are plotted in Figure 3.17. SpaceImaging, LLC also provides radiometric calibration values. Radiometric calibration is not necessary for photogrammetric analysis of aerial imagery. Radiometric calibration of satellite imagery is discussed in more detail in Section 5.

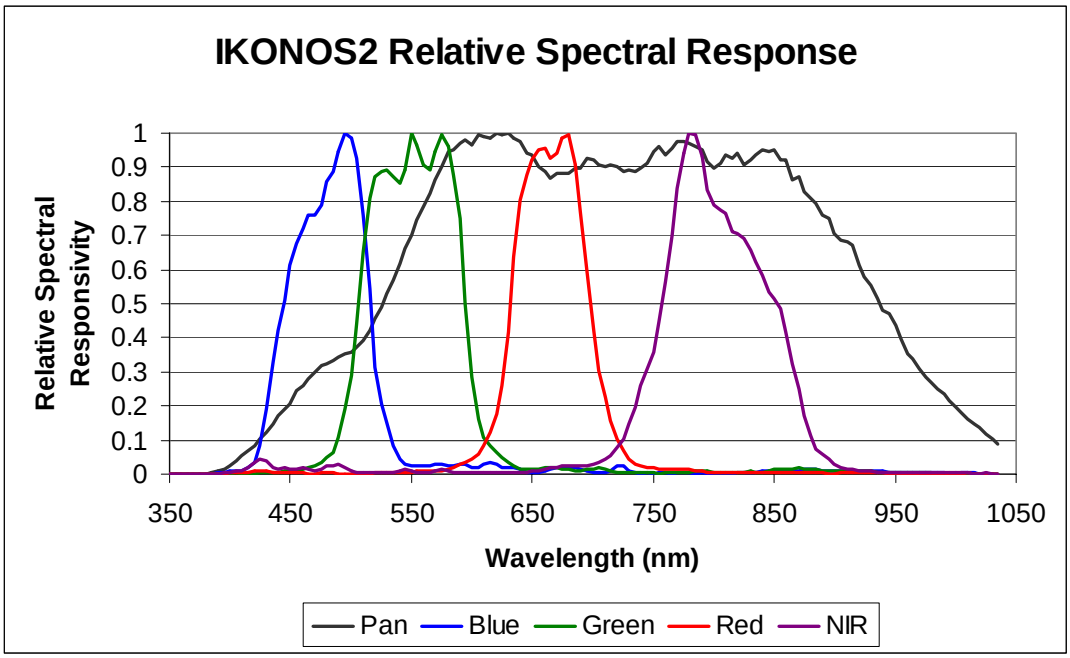

Figure 3.17 Ikonos satellite sensor spectral response (source SpaceImaging, LLC).

3.1.14 Image Color

Color is a semi-qualitative spectral aspect of imagery that is inseparable from physiological and psychological characteristics of human vision. The major advantage of the use of color in aerial imagery is that the human eye can discriminate many more shades of color than tones of gray (Lillesand and Kieffer 1994). Color perception is an element of the science of photometry. Some aspects of photometry are discussed in Appendix 3.3. Most models of perceived color contain three components: hue,

saturation, and lightness. In the CIE L*a*b* model, color is modeled as a sphere, with lightness being the linear variation from white to black along the axis of the sphere, and hues modeled as opposing pairs along the circumference, with saturation being the distance from the lightness axis. There are many other color space models employed in the well developed field of color science.

Color is reproduced in aerial and satellite images as the combination of the brightness values from three spectral bands. In natural color imagery the recorded spectral bands center on the perceived colors of blue, green and red. Human vision perceives infrared imagery as a mapping of green, red and infrared light to the blue, green and red color. The rather amazing result is that after minor acclimation most people have little difficulty recognizing features in the visible-near infrared spectrum. Typical satellite and aerial images are quantized to give 256 possible brightness values in each band (8 bits). Even at this modest quantization level the total number of possible shades of color is 256^3 or about 16 million. Color discrimination is an almost indispensable clue for photointerpretation, leading to a strong preference for color aerial imagery.

The aerial imaging system used in this research was not radiometrically calibrated in a strict sense, but image colors closely and dependably match observed colors of soil and vegetation. Photographic digital cameras mimic the sensitivity of human vision by collecting more green light than red or blue light. A CCD sensor in a typical digital camera has twice as many green activated pixel elements as blue and red (Bayer pattern) in a distributed array across the sensor. The importance of this arrangement is discussed in Appendix 3.3.

The accuracy of color capture can be judged by comparison of images with standard color charts such as that in Figure 3.18. Colors of most silt loam soils in the Potlatch basin study area are within the range of the Munsell 10YR color chart. Visual accuracy of a digital color reproduction (such as in this document) also depends on the quality and calibration of computer monitors and display software. It is again rather amazing that even poor color reproduction, such as in some satellite images, does not substantially impair the ability to interpret many color supported features such as vegetation types within the limits allowed by the image resolution.

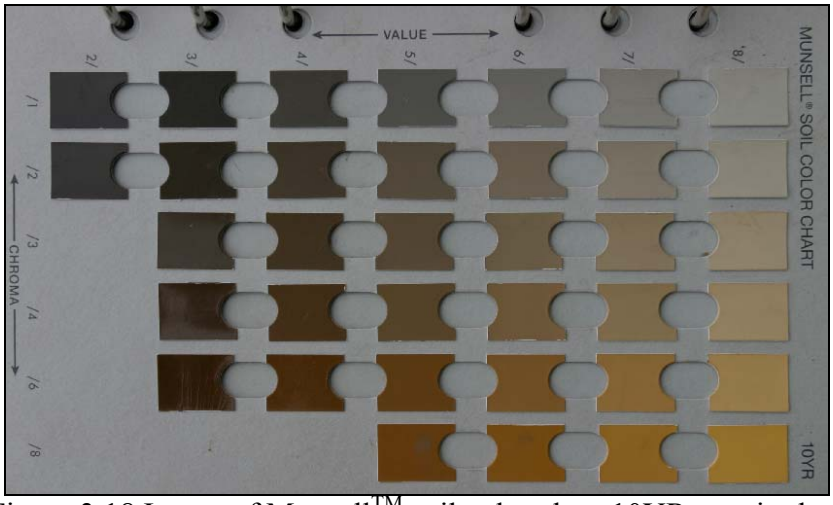

Figure 3.18 Image of Munsell™ soil color chart 10YR acquired with the TEA aerial imaging system.

Color representation is not essential for photogrammetric measurements of dimension. Object resolution and contrast are the most important characteristics for dimensional measurements as indicated by the discussion of resolution charts and spatial frequency. Figure 3.19 is a section of stereo pair created from overlapping natural color aerial images of a gravel bar on the Potlatch River acquired on September 27, 2003. The color image was converted to a grayscale image in Figure 3.20. There is no reduction of stereo fidelity between the images. In fact, the slight smoke haze evident in the color

image was diminished in the grayscale image. The conversion algorithm slightly enhances the green band (maximum solar energy) and diminishes the blue band that manifests most of the haze.

Figure 3.19 Natural color stereo pair of the Potlatch River, September 27, 2003.

Figure 3.20 Grayscale color stereo pair of the Potlatch River, September 27, 2003.

3.1.15 Surface Reflectance

Natural scenes are illuminated by two sources of light: direct rays of the sun and diffuse solar radiation scattered by the atmosphere, clouds and adjacent terrain. Direct solar rays are essentially parallel and propagated from a direction defined by the elevation and azimuth of the sun. Direct solar rays are well represented by a vector with definite direction and intensity. Diffuse light propagates from the general direction of the emitting area or volume source and impinges upon the surface from a range of directions with relatively constant intensity. Surface objects selectively reflect, transmit and absorb incoming light rays to varying degrees. A portion of absorbed radiation is re-emitted as thermal radiation. Surface light reflection is selective in direction, intensity and wavelength. The nature of the illuminating source and the characteristics of the reflecting surface greatly affect the suitability of aerial images for interpretive and photogrammetric tasks.

Surface reflectance is characterized by two idealized models – diffuse (lambertian) reflection and specular reflection (Figure 3.21). These models are useful for qualitative assessment of light effects in imagery. Diffuse reflection of a level surface scatters light evenly in all directions above the surface of the hemisphere. Diffuse reflection presents no particular problem in aerial imaging as long as there is sufficient light to record a useful image. Diffuse surfaces are identified in aerial images by their consistent brightness as the sensor position changes with respect to a point on the ground.

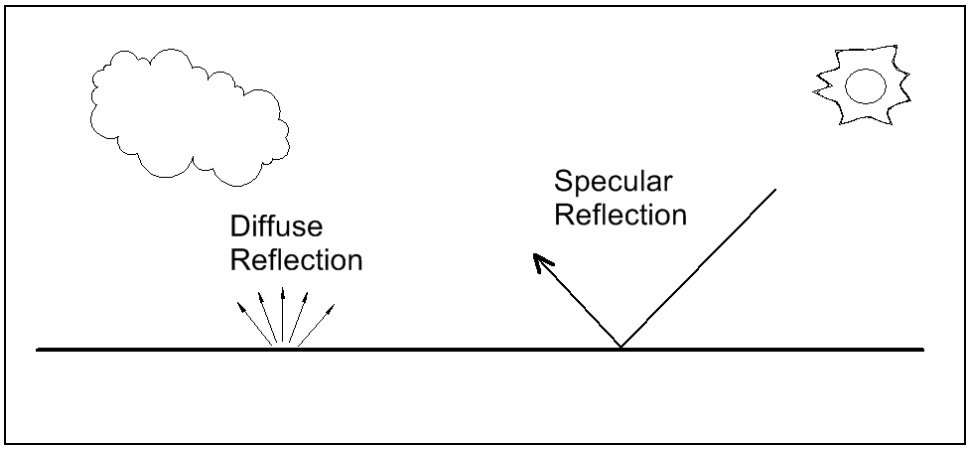

Figure 3.21 Surface reflectance models.

3.1.16 Specular Reflection

Light reflected from a specular surface is more or less coherent in a single direction. The most obvious example is sun reflection from the surface of the water as in Figure 3.22. Specular reflections off of smooth water surfaces will be seen in images when the sun zenith angle is equal to, or less than, one half the sensor angular field of view as seen in the geometrical relationships in Figure 3.23.

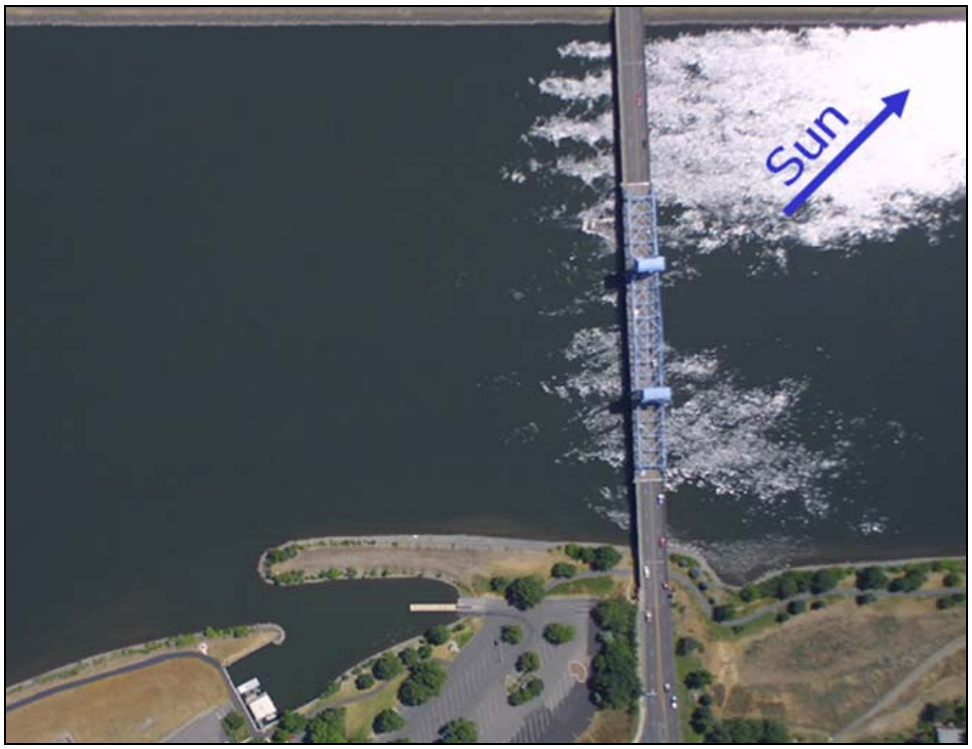

Figure 3.22 Specular reflection of the Clearwater River, June 22, 2001.

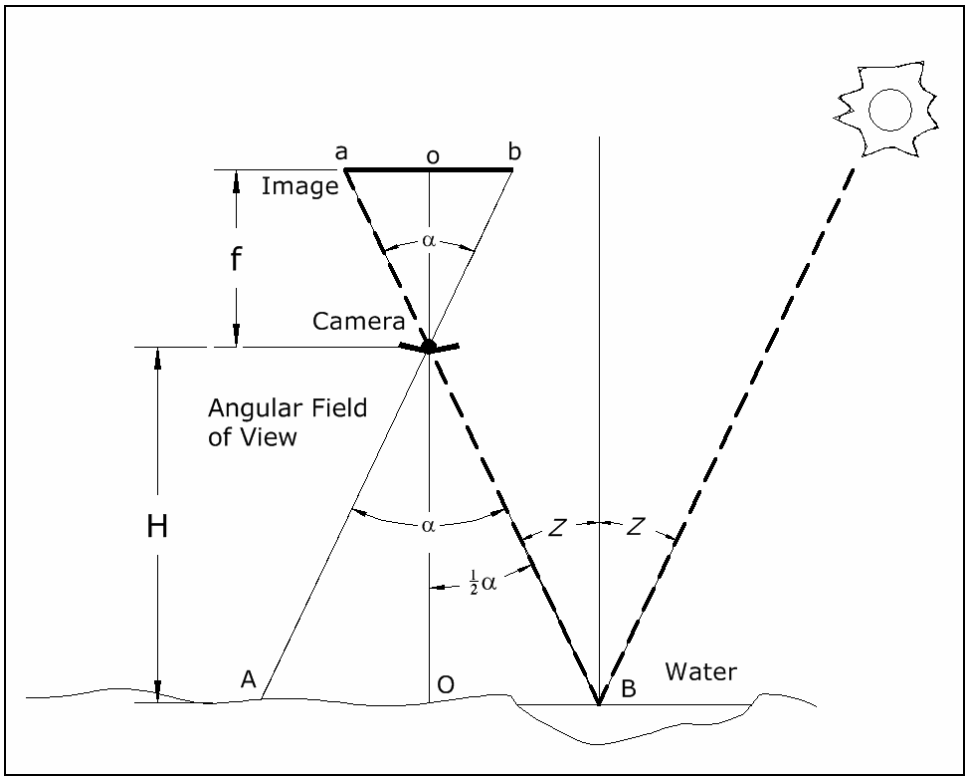

Figure 3.23 Geometry of specular reflection.

Specular reflections reduce the useful area in an image scene and are most prevalent for images acquired in late June and early July around the time of the summer solstice (northern mid latitudes). Specular reflection, while present, is generally not a problem in overlapping sequential images of rivers and streams because of the multiple views of the same channel section from different angles. Specular reflection is usually eliminated from one or more of the overlapping images as the position of the camera changes with respect to the ground point. For non overlapping images, flights may be conducted earlier or later in the day when sun angle is lower. A possible remedy, as indicated by Equation 3.17, is to reduce specular reflection by using a longer focal length lens. Locating flight lines along the sun-side of rivers and shorelines, if possible, will also reduce specular reflection.

Specular reflections also occur on non horizontal surfaces such as metal roofs and can be useful indicators of surface water turbulence and wet soil. For example, specular reflectance caused by wind wave action increases image pixel brightness in some portions of the surface of the pond in July 21, 2004 aerial image of Camp Grizzly Scout Camp on the Palouse River in Figure 3.24. Wind direction is clearly indicated by the lack of specular reflection on the lee side of the island and shoreline. Similarly, specular reflectance identifies a small riffle in the river to the right of the pond.

Figure 3.24 Specular reflectance caused by water waves.

3.1.17 Analytical Reflectance

Reflectance is quantified as a ratio of the radiation energy scattered away from the surface to the amount of incoming radiation. A common expression for reflectance is:

$$\rho_{s,\lambda} = \frac{\pi \cdot L_{s,\lambda}}{E_{dir,\lambda} + E_{dif,\lambda}} \qquad 3.33$$

where $L_{s,\lambda}$ is the reflected energy expressed as radiance (W m^{-2} sr^{-1} μm^{-1}), $E_{dir,\lambda}$ is the incoming direct irradiance (W m^{-2} μm^{-1}), and $E_{dif,\lambda}$ is the incoming diffuse irradiance. Radiance is converted to irradiance by multiplying by π in the numerator (Appendix 3.2). Equation 3.33 finds much use in computing reflectance from radiometrically calibrated satellite imagery and is discussed further in Section 5.

Many surfaces exhibit both diffuse and spectral reflectance characteristics that change with sun angle and the relative position of the sensor. Anisotropic surface

reflectance is assessed quantitatively with the bidirectional reflectance distribution function (BRDF) of the surface (Hapke 1981). An alternative is to express anisotropic reflectance as a bidirectional reflectance factor (BDF) – the ratio of actual reflected energy to the reflectance of an ideal diffuse surface (lambertian) at a specific viewing geometry and illumination. The BRDF relationship is expressed (Rees 2001):

$$R = \frac{L_1}{E} \qquad 3.34$$

where E is the down welling irradiance of the surface (W m^{-2}), L_1 is the radiance (W m^{-2} sr^{-1}) and R is the value of the BRDF (sr^{-1}). The subscript *1* indicates a direction of reflection. In general the reflected radiance L_1 is a function of zenith and azimuthal directions in the semi-hemisphere of irradiance. The geometry of irradiance is discussed in Appendix 3.2. One of the simplest models of the BRDF is the Minnaert model (Rees 2001):

$$R \propto \left(\cos\theta_o \cos\theta_1\right)^{\kappa-1} \qquad 3.35$$

where θ_o and θ_1 are the angles of incidence and reflectance, and κ is an empirical coefficient.

Bidirectional reflectance is seen in some aerial images acquired in this research including those of wet soil, snow and forested terrain. A hint of bidirectional reflectance is in the subtle variation in tone and color of conifer canopies at the match lines of the mosaic of aerial images in Figure 3.25. Bispectral reflectance of grass-covered open space is almost undetectable indicating the importance of canopy structure and shadow presentation on the BRDF.

Figure 3.25 Bidirectional reflectance of conifer canopies in an aerial image mosaic.

Bidirectional reflectance effects are important in image classification, extraction of biophysical variables, and the investigation of energy transfer of the land surface and vegetative canopies with remote sensing methods. It is the subject of continued research (Asner et al. 1998; Dymond et al. 2001; Pinty et al. 1989; Sandmeier; Susaki et al. 2004; Walthall et al. 1985). Preliminary investigations indicate that the BRDF can be estimated for many surfaces from high-resolution aerial images with an appropriate radiometric normalization of the image scene, calibration of the exterior camera geometry, and computation of solar vectors. Results are too preliminary to report. The BRDF need not be quantified for most photogrammetric analysis.

A reflectance phenomena observed in some satellite and aerial images is the opposition or hotspot effect (Figure 3.26). A hotspot is a localized area of increased image brightness near a point on the ground that is collinear with the aircraft and sun. In other words, the hotspot surrounds the shadow of the aircraft if it is within the field of view of the sensor. Hotspots are caused by two mechanisms (Hapke et al. 1996): self shadowing and coherent backscatter. Self shadowing is the primary mechanism in most

terrestrial surfaces and occurs when objects on the ground hide their own shadows from the view of the sensor. This increases the number of brightly illuminated pixels relative to darker shadowed pixels. Coherent backscatter occurs when a particulate media with grains about the same size as the wavelength of light (e.g. fine soil) scatters light back towards the sun and sensor in a process of constructive interference. Hapke et al. (1996) indicate coherent backscatter is the dominant hotspot mechanism observed in astronomic imagery. Hotspot reflectance is generally not observed in the near vertical imagery acquired in this research because aircraft shadows are seldom visible unless images are extremely tilted.

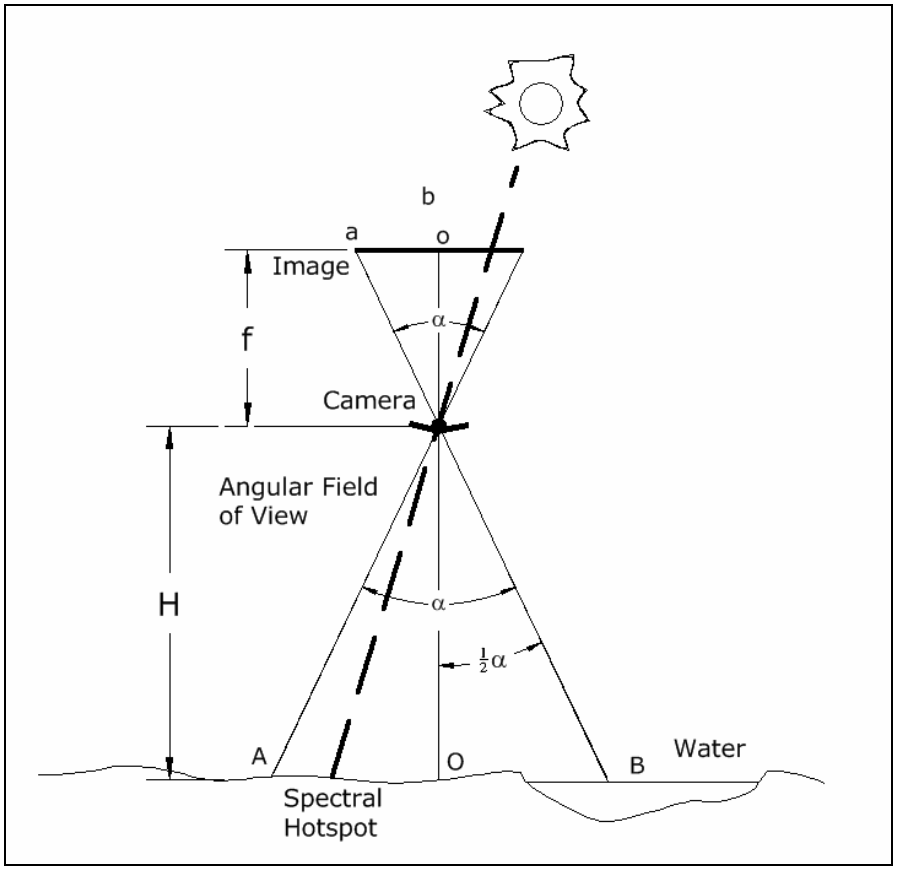

Figure 3.26 Geometry of the spectral hotspot.

3.1.18 Radiometric Camera Calibration

Equation 3.29 can be augmented as explained in Appendix 3.3 to include properties of the recording media (film or CCD). It can be rearranged to calculate scene reflected irradiance (radiant exitance) from recorded camera settings.

$$L = \frac{KN^2}{tS} \tag{3.36}$$

where t is exposure time, N is the f number, S is sensitivity (film speed) of the sensor, and K is a constant composed of lens and recording media parameters:

$$K = \frac{4kH_0}{\pi T \cos^4 \theta} \tag{3.37}$$

Doubling sensitivity (film speed) in Equation 3.36 requires a compensating reduction in aperture area by decreasing aperture diameter by the multiplicative factor $\sqrt{1/2}$ or reducing the exposure time by half.

Digital camera controls are conveniently scaled so that permissible adjustments of aperture, exposure time (shutter speed) and film speed produce doubling or halving of the amount of light on the focal plane (full stops). For example, if the exposure time of a camera set at f number 8.0 is reduced from 1/250 to 1/500 s the f number must be to $\sqrt{1/2}(8.0) = 5.7$. Most cameras are adjustable to one half or one third stops.

Equation 3.36 is a useful result. It relates camera settings to scene luminance with an empirical constant K. Measured luminance or radiance should plot as a straight line with N^2/tS. In general it is expected that for constant lens parameters and media sensitivity a camera calibration equation will have the form:

$$E = a\left(\frac{N^2}{t}\right) + b \tag{3.38}$$

An experiment was conducted to test whether a digital camera can be calibrated to measure reflected light with Equation 3.38. If so, it might be possible to estimate radiant exitance from digital aerial images and recorded camera settings. Radiant exitance is the power of reflected light energy per unit of surface area. The ability to easily measure radiant exitance would be very useful for determination of scene reflectance, albedo and energy balance.

The resolution chart in Figure 3.27 was imaged numerous times with a tripod mounted digital camera at various times during a partly cloudy day. Lens focal length and ISO film speed were kept constant.

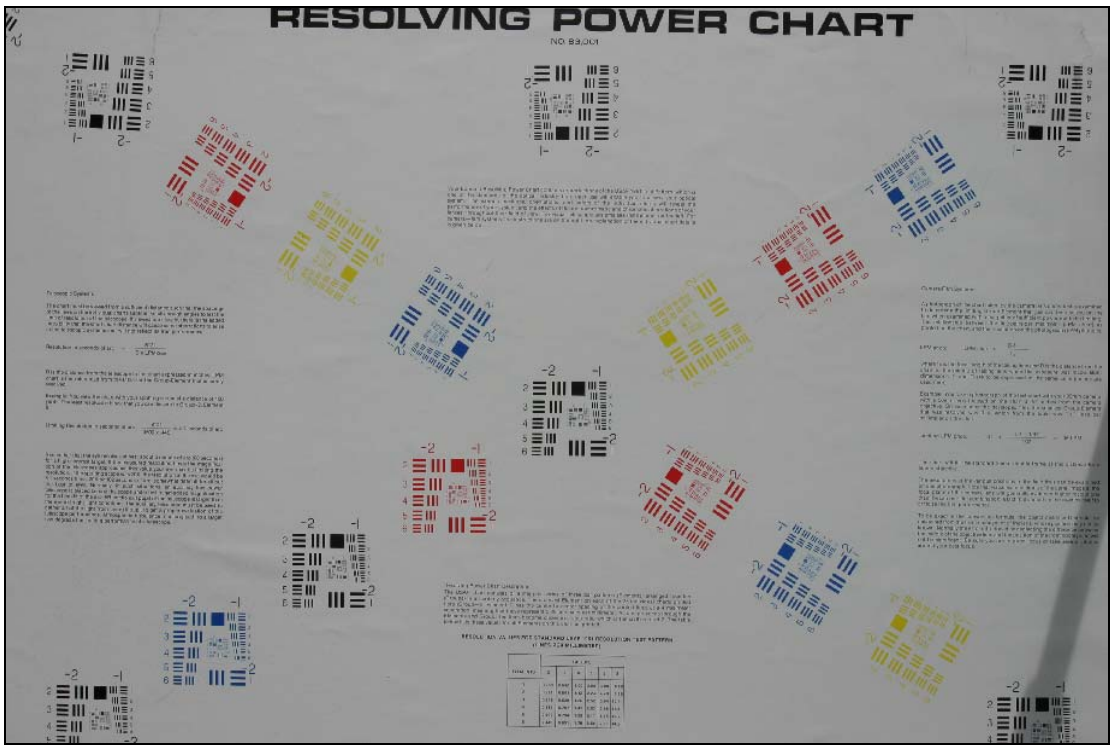

Figure 3.27 Resolution chart image.

Reflected solar irradiance (radiant exitance) was measured with a commercial silicon pyranometer before and after image acquisition. Table 3.4 lists the shutter speeds, *f* numbers and measured reflected irradiance.

Shutter Speed $1/t$ s^{-1}	*f* number N	Exposure Factor N^2/t s^{-1}	Reflected Solar Irradiance W m^{-2}
180	9.5	16,245	61
250	9.5	22,563	78
350	11.0	42,350	322
350	11.0	42,350	299
500	8.0	32,000	221
250	11.0	30,250	215
1000	5.6	31,360	207
250	13.0	42,250	286
250	11.0	30,250	201
350	13.0	59,150	474

Table 3.4 Camera calibration data.

The measured reflected irradiance values are plotted against the camera exposure factors N^2/t in Figure 3.28. As expected from Equation 3.38, the plotted values follow a linear trend. Regression of the data produced the equation:

$$E = 0.0098\left(\frac{N^2}{t}\right) - 104.73 \qquad \text{x.39}$$

where E is radiant exitance in W m^{-2}, t is in seconds and N is the dimensionless *f* number. It should be emphasized this is a radiometric quantity not a photometric value so it can be used in radiometric computations of reflectance and albedo. I have not seen a calibration of this type performed for a digital camera before in the remote sensing literature. Some scatter of the data is caused by incremental adjustment of aperture setting not observable

in the camera controls or image metadata. Also the pyranometer used in the experiment is not a scientific quality instrument.

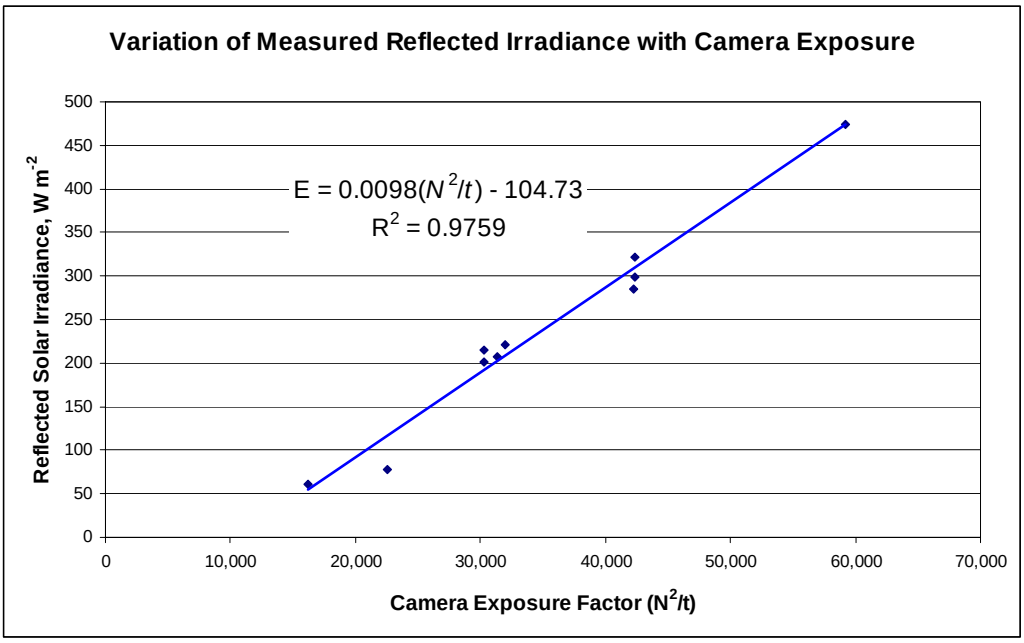

Figure 3.28 Plot of measured reflected irradiance with camera exposure factor.

The calibration parameters from this test are specific to the image calibration board because the wavelength distribution of the reflected light is not known with certainty. As discussed in Appendix 3.3, wavelength (spectral) information is not directly recoverable from images captured by digital cameras designed on photometric principles. Thus each image calibration is unique to the spectral reflectance characteristics of the scene. It would not be appropriate to apply the calibration equation of this light colored artificial image to natural aerial scenes of vegetative cover because the constituent wavelengths would be much different than the predominantly white colored resolution target.

Some calibration data for grass, Portland cement concrete and asphalt concrete were collected and plotted on Figure 3.29. The additional plots show dependency of the regression parameters on spectral reflectance characteristics. The resolution chart, Portland cement concrete and asphalt concrete are predominantly gray in color so would reflect nearly equal percentages of blue, green and red light (Figure 3.30). Regression slopes of the gray colored materials are nearly parallel, though the position varies depending on the amount of reflected light. The relatively small amount of blue, red and yellow color in the resolution chart surface may have steepened the regression slope slightly. The regression slope of the grass surface is much steeper indicating a much different reflected wavelength. The relatively low exposure factors for the grass surface show that more light on the sensor is required to produce an acceptable grass image.

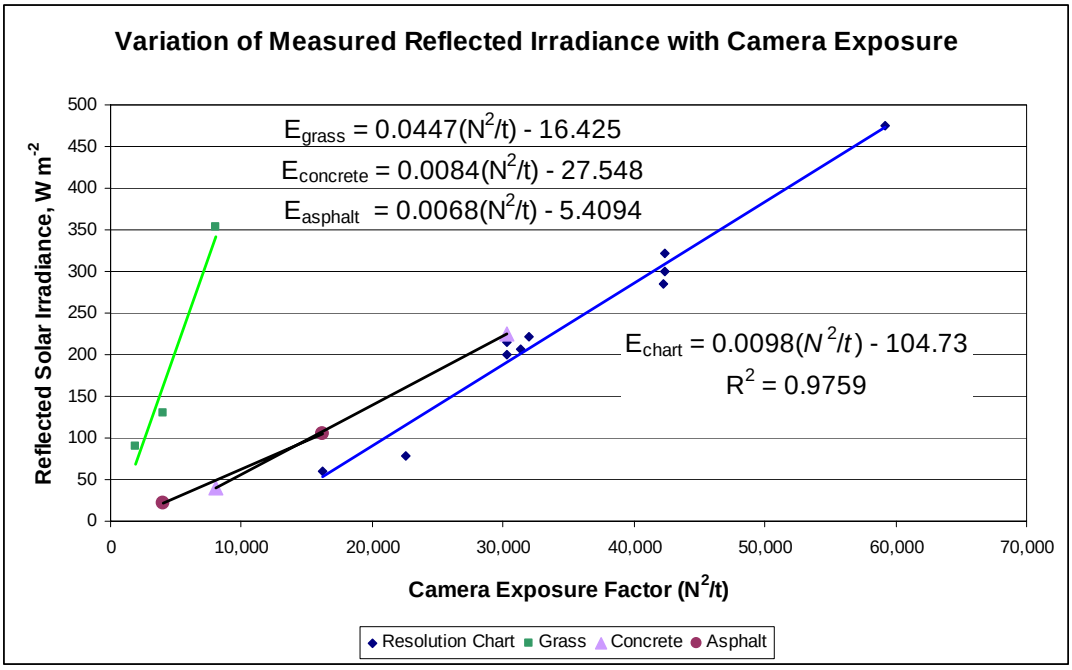

Figure 3.29 Measured reflected irradiance with camera exposure factor for selected materials.

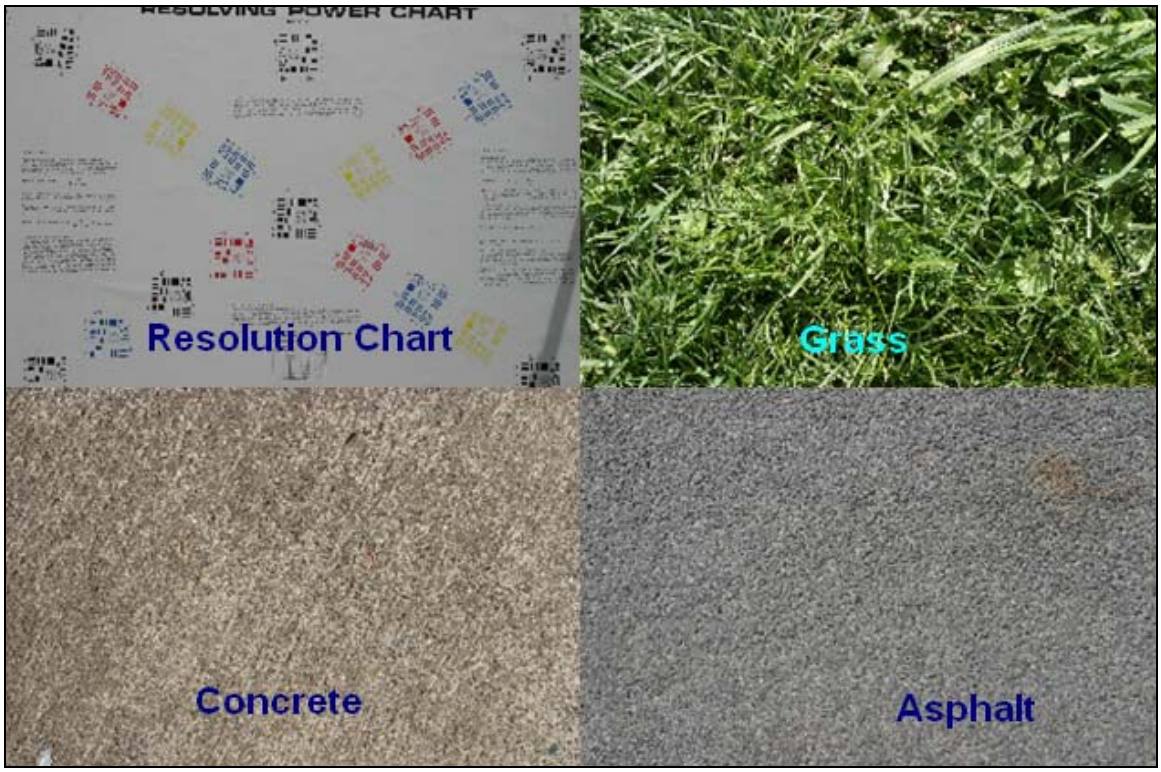

Figure 3.30 Surface types in reflected irradiance measurement tests.

While these tests are preliminary, the regression slope parameter of Equation 3.38 seems to be a measure of reflected wavelength while the intercept parameter is an indicator of the reflectance of a particular wavelength. These are the two most sought after parameters when verifying (ground truthing) satellite imagery and correcting for atmospheric effects. They are also desirable for computing some imagery based biophysical indices and subpixel spectral mixing analysis of satellite imagery. In this test, there may be some effect due to the imaging distance because of the bidirectional reflectance distribution. Operational calibrations should ideally be performed for flight conditions.

The relative ease of obtaining a good linear fit to the resolution chart data signifies a fairly robust technique. It appears it is possible to develop a functional

relationship between color, exposure setting and quantifiable spectral radiance. Given the relatively low cost and high quality of photographic digital cameras further investigation of radiometric camera calibration is warranted and likely beneficial to aerial and terrestrial assessment of land and water resources.

3.1.19 Aerial Image Estimate of the Albedo of Snow

Use of the radiometric camera calibration equation may be demonstrated with a practical example. Two of the most difficult snowmelt parameters to determine for realistic spatially distributed energy balance snowmelt simulation are snow depth and albedo. Snow albedo is measured by the MODIS satellite, but skies are seldom clear in the Pacific Northwest during times when snowmelt estimates are most desired. A reliable and cost effective technique to determine snow depth and albedo under cloudy skies would benefit snowmelt modeling for flood prediction. Radiometric camera calibration equations such as those developed above provide such a technique.

Figure 3.31 is an image of snow covered Palouse Prairie agricultural land acquired on February 22, 2004 at 3:15 pm under sunny conditions. The camera shutter speed was 1/750 second and the *f* number was 9.5. Snow cover radiant exitance should be reasonably represented by the camera calibration equation (Equation 3.39) for the predominantly white and moderately glossy surface of the resolution chart. An adjustment for media sensitivity is necessary. The resolution chart calibration was developed from images acquired at a film speed of ISO 100, while the aerial image was acquired at ISO 200. The image exposure factor value for the aerial image must be adjusted to the ISO 100 curve. A film speed of ISO 200 is twice as sensitive to light as

ISO 100 so it takes half as much light energy to produce an equivalent exposure. Equation 3.18 is modified to account for ISO setting by multiplying the exposure factor value by the ratio of the sensitivity factors (ISO speeds):

$$E = a\left(\frac{N^2}{t}\frac{S_{cal}}{S_{image}}\right) + b \qquad 3.40$$

where S_{cal} is the ISO value of the calibration curve and S_{image} is the ISO value of the acquired image.

Figure 3.31 Aerial image of snow covered agricultural land, February 22, 2004.

Entering the camera exposure settings and ISO values into the adjusted calibration equation gives:

$$E = 0.0098\left(\frac{N^2}{t}\frac{S_{cal}}{S_{image}}\right) - 104.73$$

$$E = 0.0098\left(\frac{(9.5)^2}{1/750}\frac{100}{200}\right) - 104.73 = 227 \text{ W m}^{-2}$$

The reflected (upwelling) irradiance from the surface of the snow measured from the camera exposure value is 227 W m^{-2}. Global solar irradiance (downwelling) was measured with a nearby ground level pyranometer during the flight. The pyranometer has an accuracy of plus or minus 10 W m^{-2}. Downwelling irradiance values were 358 W m^{-2} at 3:00 pm, 321 W m^{-2} at 3:15 pm, and 283 W m^{-2} at 3:30 pm. The average of the values for 3:00 pm and 3:30 pm is 321 W m^{-2}, so the 3:15 pm value is acceptable.

Snow albedo (reflectance) is the ratio of the upwelling and downwelling irradiances:

$$\rho_{snow} = \frac{227 \text{ W m}^{-2}}{321 \text{ W m}^{-2}} = 0.71$$

This is a reasonable average albedo for an aged and optically thin snowpack. This particular camera was set to adjust at 1/2 *f* stops, so the measured reflectance could be between 0.55 and 0.91, computed from plus or minus 1/4 *f* stops. The camera could have been set to adjust at 1/3 *f* stops in which case the reflectance estimate would likely have been between 0.55 to 0.78 (plus or minus 1/6 *f* stops). In either case a more precise estimate of reflectance is obtained by acquiring bracketed images and interpolating reflectance from pixel brightness of the scene and calibration images.

The spatial variation of albedo across a watershed can be determined by computing the average albedo for additional images along the aerial transect. An individual aerial image contains an abundance of information about the spatial variability of albedo among topographic features. The variation of snow albedo in an optically thin

snowpack is a direct indicator of snow depth. Figure 3.32 is a contrast enhanced view of the brightness channel extracted from the aerial image in Figure 3.31 after converting the RGB image to Lab color space. Subtle variations of albedo are enhanced revealing the topographic dependence of snow reflectance and areas of thin snowpack. Snow drift lines are seen along the left center of the image. Tillage marks are clearly expressed in the microrelief of the snow surface indicating that snow depth is mostly less than about 15 cm – enough for several days of significant runoff under rapid snowmelt conditions.

Figure 3.32 Enhanced image of snow albedo variation.

The example demonstrates the practical usefulness of radiometric camera calibration. Additional experimentation with several cameras and lenses from leading manufacturers should be conducted under controlled conditions with scientific grade instruments and a variety of surface types.

Inversing of the color information in a photographic digital image to spectral reflectance is not a simple task because there is no unique relationship between values in human vision color space and spectral reflectances. Even given known color space coordinates, illuminant properties and device spectral sensitivities; the inverse of color formation is generally an underdetermined set of linear equations with a potentially infinite set of solutions (Morovic and Morovic 2003). This phenomenon is known as metamerism and denotes the existence of a set of possible spectral reflectance values for any given photometric color value. Constraints necessary for the realistic transformation of color values to spectral radiance likely involves the development of a camera model: a current line of color science research (Barnard and Funt 2002; Hong et al. 2001; Lenz et al. 1999). Results of the simple experiment above suggest that a reasonable approach is to develop camera model constraints with aerial calibration tests involving simultaneous collection of spectroradiometer data and digital color imagery. There are aspects of this inversing problem that seem not to be recognized in the remote sensing literature. Details are best left for future research.

3.2 Geometry of Vertical Aerial Images

Object dimensions can be determined from an image by analysis of the optical geometry of the lens and imaging media. Object and image dimensions are related by an image scale factor and relief displacement. Scale factors and relief displacement vary throughout an image because of lens properties, imaging height, object height and topographic relief. Geometric relationships between terrain and image points are diagrammed in Figure 3.33. The figure shows the geometry of both the actual (negative)

and inverted (positive) images. The spatial relationships of the inverted image are the same as the actual image. Subsequent diagrams will adopt the inverted image convention to help clarify geometric relationships.

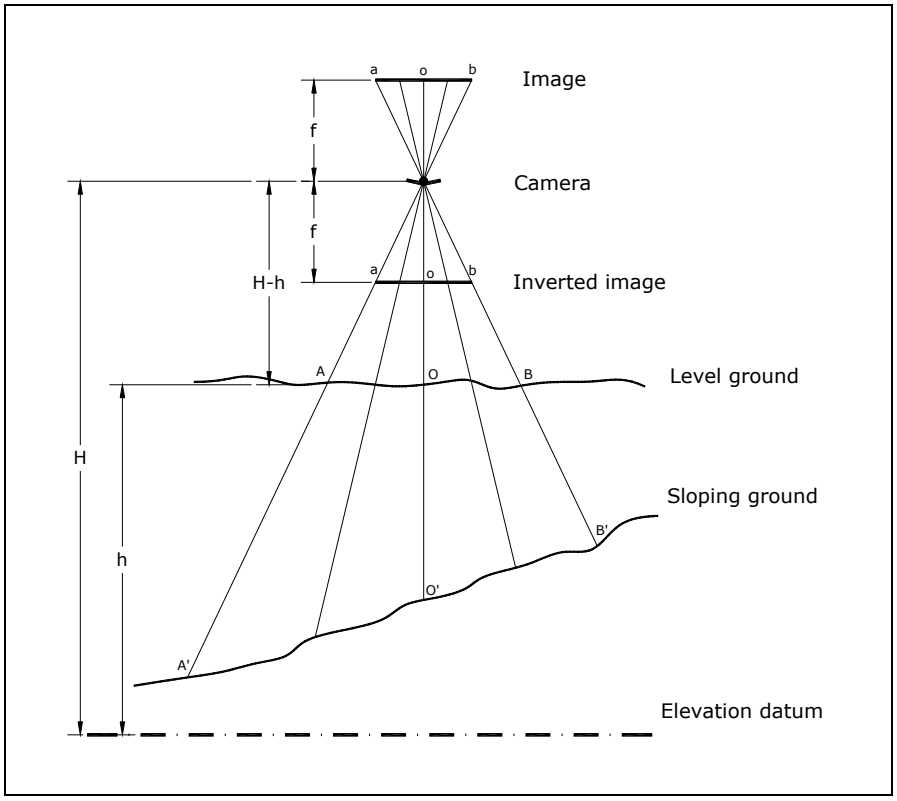

Figure 3.33 Actual and inverted vertical aerial images.

Aerial images are generally described by the orientation of the camera and lens optical axis. A truly vertical image is one in which the optical axis, the gravitational plumb line and the image media center (isocenter) are coincident. The actual image produced lies in a plane perpendicular to the plumb (or nadir) line. Oblique aerial images are tilted away from the plumb line. The discussion here relates mostly to vertical or near vertical aerial images.

The geometry of a true vertical image of a stream channel is diagrammed in Figure 3.34. Terrain points *C* and *D* in Figure 3.34 are located at the edge of the water

surface and lie at the same elevation. The distance between *C* and *D* corresponds to the distance between image points *c* and *d*. The scale factor relating distance *CD* to dimension *cd* is the ratio of the lens focal length *f* to the sensor height above terrain *H:*

$$S = \frac{\overline{cd}}{\overline{CD}} = \frac{f}{H} = \frac{1}{PSR} \qquad 3.41$$

where

S is the image scale

f is the lens focal length

H is the height of the sensor above the terrain point

$\overline{CD}$ is the distance between two points on the ground

$\overline{cd}$ is the distance between the same two points on the image

PSR = photo (image) scale reciprocal

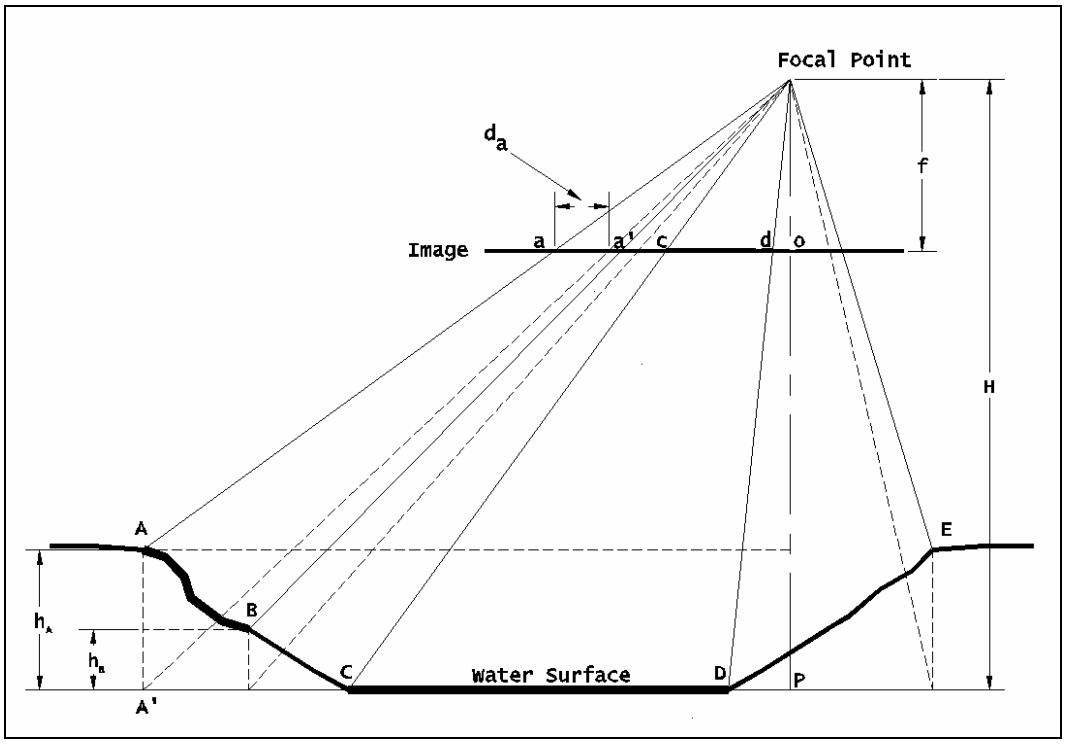

Figure 3.34 Vertical aerial image of stream channel.

3.2.1 Linear Measurement in an Aerial Image

Equation 3.41 is a simple, but very useful relationship that is best illustrated with an example from the research work. Very high-resolution digital aerial images of the Potlatch River corridor were acquired on September 27, 2003. Weather was sunny with a slight smoke haze. The image in Figure 3.35 is centered on the softball field in the City of Juliaetta, Idaho Centennial Park.

The objective of the example is to compute image scale and determine the length of the side of the rectangular play area at location *A* in Figure 3.35 with data from Table 3.5.

Figure 3.35 Aerial image of Juliaetta Centennial Park acquired September 27, 2003.

Flight, Image and Terrain Data	
Aircraft altitude recorded by flight navigation GPS	1242 m
Elevation of play area from 7.5 min topographic quadrangle	317 m
Sensor focal length	35 mm
Sensor CCD pixel size	7.4 μm
Length of sand retainer in image	91 pixels
Measured length of sand retainer on ground (as check)	17.59 m

Table 3.5 Aerial image data and dimensions.

The measurement and computations proceed in a series of steps:

1. View the unrectified aerial image with image processing or GIS software such as ArcView with the Image Analysis extension. Zoom to the play area and measure the number of pixels (91) along the length of the sand retainer at location A in Figure 3.36.

Figure 3.36 Measurement of sand retainer length.

2. Compute the image scale factor.

$$S = \frac{f}{H} = \frac{0.035 \cdot \text{m}}{(1242 - 317) \cdot \text{m}} = 3.784 \times 10^{-5}$$

$$PSR = \frac{1}{S} = \frac{1}{3.784 \times 10^{-5}} = 26{,}428$$

3. Compute the length of the sand retainer.

$$L = 91\,\text{pixels} \times \frac{7.4\,\mu\text{m}}{\text{pixel}} \times 10^{-6}\,\frac{\text{m}}{\mu\text{m}} \times 26428\,\frac{\text{m}}{\text{m}} = 17.8\,\text{m}$$

4. Compute the ground pixel resolution of the image at point A.

$$GPR = \frac{17.8}{91} = 0.20\,\frac{\text{m}}{\text{pixel}}$$

Computations are summarized in Table 3.36. The length of the sand retainer measured in the image agrees with the actual length of the retainer within one pixel.

Dimension	Actual	Maximum Height Difference	Minimum Height Difference
GPS Flight altitude, MSL, m	1242	1252	1232
Elevation of terrain point, m	317	311	323
focal length, m	35	35	35
Sensor pixel size, μm	7.4	7.4	7.4
Sensor height above terrain, H, m	925	941	909
Image scale, f/H	3.78398E-05	3.719E-05	3.851E-05
Scale reciprocal	26,427	26,887	25,967
Length of object on image, pixels	91	91	91
μm	673	673	673
m	0.000673	0.000673	0.000673
Length of object on ground, m	17.8	18.1	17.5
Ground pixel resolution, m	0.20	0.20	0.19
Measured length of object on ground, m	17.59	17.59	17.59
Length difference, m	0.21	0.52	-0.10
Percent difference from measured	1.19%	2.95%	-0.57%

Table 3.6 Computation summary for length measurement example.

The length of the sand retainer wall estimated from image measurements likely falls within a range of 17.5 and 18.1 meters depending primarily on the accuracy of the height-above-terrain measurement. Experience shows the altitude accuracy range of the flight navigation GPS is plus or minus 10 meters of the true altitude under most flight conditions. National Map Accuracy Standards require that ground elevations interpolated from contours on USGS 7.5 minute topographic quadrangles be within one-half contour interval, about 20 feet (6.10 m) for the 40 contour intervals on the Juliaetta quadrangle. Relatively minor errors in image length estimates arise because of fixed sensor geometric bias and the imprecision of image analysis techniques. A formal measurement error analysis is not possible for this procedure because it is not feasible to determine the error distribution of elevations for a specific USGS contour map. Nonetheless, an estimate of object length by the procedure illustrated above is appropriate for most natural resources and environmental reconnaissance investigations. An adaptation of this procedure might be employed to obtain an error distribution of USGS contour and digital elevation model elevations.

The above example shows that accurate measurements of linear dimensions, such as stream width and stream macrostructure dimensions can be made from unrectified (non-georeferenced) high-resolution digital aerial imagery with scale factors developed from aerial GPS and USGS 7.5 minute topographic quadrangles. The geographic coordinates of the approximate center of each aerial image in the overlapping sequence of images is known from the aerial GPS so the location of features can be readily determined. For many stream and riparian studies it is often only necessary to know the approximate location of a feature along the centerline distance of a stream. Precise

geographic positions accurate to within a few meters are normally not required for most environmental survey work. These results contradict a common misunderstanding among many GIS practitioners that aerial imagery is only useful for dimensional measurement if the image is orthorectified or georeferenced. A more accurate method of image measurement is described in the discussion of analytical photogrammetry in Section 3.4.

3.2.2 Measurement of Elevation Differences in Stereo Images

Topographic relief changes the apparent planimetric position of objects in an aerial image. This effect is especially noticeable in low altitude images. Aerial images must be scaled and rectified to remove topographic displacement to support precise photogrammetric measurement. In a rectification process all image points are adjusted to a constant scale referenced to a common elevation datum. Figure 3.34 shows that the apparent positions of terrain points above the common datum are displaced radially inward towards the isocenter of the image from true horizontal location referenced to the elevation of the water surface. Terrain points below the datum are displaced radially outward (none shown on diagram).

Terrain points *C* and *D* lie on the datum so corresponding image points, *c* and *d* are in true relative horizontal positions on the image. Points *A, B* and *E* lie above the datum so appear displaced towards the center of the image. The dashed lines projecting from the image focal point to the horizontal location of the terrain points intersect the image at a distance from the image point proportional to the relief displacement. The imaginary image point a' is the displaced location of image point a.

Relief displacement in an image provides a means to measure elevation differences between terrain points. An analysis of similar triangles in Figure 3.34 provides the relationships:

$$\frac{r}{R} = \frac{f}{H - h_a} \tag{3.42}$$

and

$$\frac{r'}{R} = \frac{f}{H} \tag{3.43}$$

where

h_A is the height of terrain point A above the datum

d_a is the relief displacement of image point *a*

H is the height of the sensor focal point above the datum

r is the radial distance *ao* of image point *a* from the isocenter of the image

r' is the radial distance *a'o* of image point *a'* from the isocenter of the image

R is the radial distance *AP* of terrain point *A* from the center (nadir) of the scene

Equations 3.8 and 3.9 are equated and d_a substituted for *r*-*r'* to yield

$$h_A = \frac{d_a H}{r} \tag{3.44}$$

Equation 3.44 gives the height of a terrain point above the datum from the relief displacement of the point. The measurement of relief displacement requires that the true horizontal location of the terrain point be known or visible in the image. Use of Equation 3.44 in a single image is normally limited to measurement of differential heights, such as heights of trees and buildings where both top and bottom of the objects are visible.

Elevation differences can be computed from parallax measurements of stereo images. Parallax is the apparent change in planimetric position due to sensor view angle. Geometric relationships for parallax are developed fully in photogrammetry texts (Wolf and Dewitt 2000). A very useful relationship is the elevation difference equation:

$$h_a = \frac{\Delta p H}{p_a} \tag{3.45}$$

where h_a is the height of a point a above the reference datum, p_a is the parallax of point a, Δp is the parallax difference between point a and a point on the reference datum, and H is the height of the sensor above the reference datum. Parallax differences in Equation 3.45 can be measured monoscopically in aerial images oriented along a line through the image centers (principal points) and the conjugate principal points of both images. Use of this equation is illustrated with an example.

Overlapping natural color aerial images of an ephemeral gully system and sedimentation basin in Figure 3.37 were acquired on March 15, 2004. The images have been oriented so that the principle points (PP) and conjugate principle points (CPP) are aligned in the horizontal x direction. The CCP on the left image is hidden by the overlapping right image. Points a and b were positioned at the top and bottom of the gully channel stereoscopically using the floating-mark technique. The stereo pair and floating marks are can be created with commercial image processing software such as Adobe Photoshop™. Only the x-distances between the points are needed for parallax computations if the image is aligned properly.

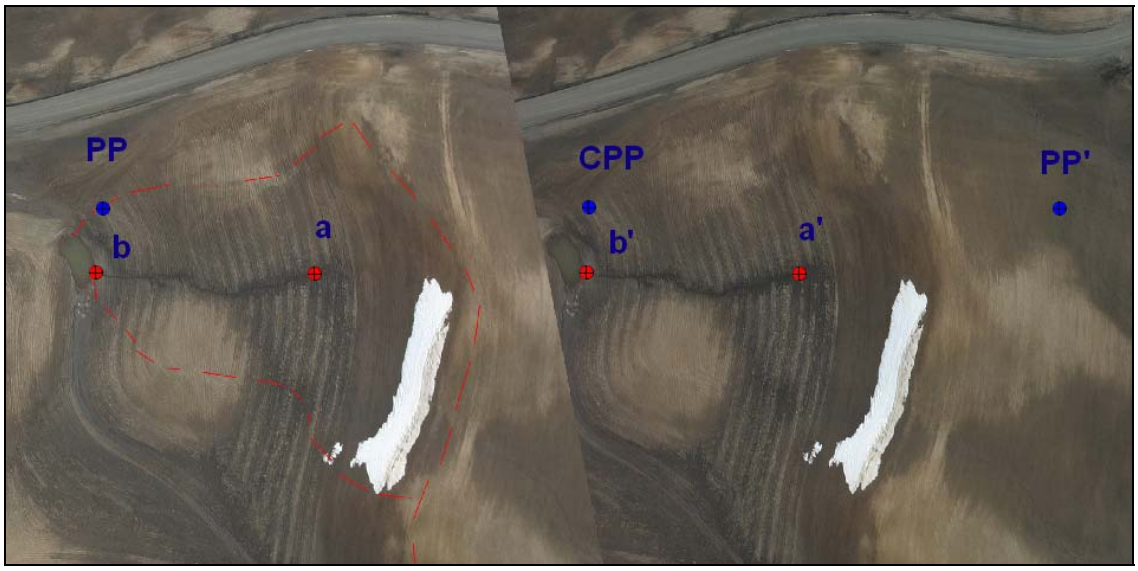

Figure 3.37 Parallax measurement with an aerial image stereo pair.

The parallax measurements for point *a* and *b* are computed:

$$p_a = \overline{PP\ PP'} - \overline{a\ a'} = 1906 - 964 = 942 \text{ pixels} \qquad 3.46$$

$$p_b = \overline{PP\ PP'} - \overline{b\ b'} = 1906 - 978 = 928 \text{ pixels} \qquad 3.47$$

where the bars over the point identifier indicate the distances between the image points.

If one or both of the images are georeferenced to ground control points with elevations of about that of point *b*, the height of the sensor above the ground surface can be computed from the lens focal length, sensor pixel size and the GPR obtained from the image georeferencing statistics:

$$H = \frac{f \times GPR}{d} = \frac{0.028 \text{ m} \times 0.1925 \text{ m}}{7.4 \times 10^{-6} \text{ m}} = 728 \text{ m} \qquad 3.48$$

where *f* is the lens focal length (28 mm), the *GPR* is 0.1925 m, and the sensor pixel size *d* is 7.4 μm. The elevation of point *a* above the datum is computed from Equation 3.45:

$$h_a = \frac{\Delta pH}{p_a} = \frac{(942 - 928)(728\,\text{m})}{942} = 10.82\,\text{m} \Rightarrow 11\,\text{m} \qquad 3.49$$

The elevation of point *a* is approximately 11 meters above point *b*. The measured value compares reasonably well with the 12.6 m elevation difference between points *a* and *b* measured in the USGS 10-meter DEM.

The height difference computation is relatively insensitive to the assumption of elevation for point *b*. If point *a* is assumed to lie at the elevation computed from the georeferencing information then the height difference (point *a* down to point *b*) is computed as:

$$h_b = \frac{\Delta pH}{p_b} = \frac{(928 - 942)(728)}{928} = -10.98\,\text{m} \Rightarrow -11\,\text{m} \qquad 3.50$$

In this case, the elevation difference between points *a* and *b* is about 11 meters, not a significant difference for approximate computations. Uncertainty also arises from the GPR obtained by georeferencing and the stereoscopic placement of the parallax measurement points.

Sensitivity of the elevation difference measurement to the image pixel measurement can be approximated by Equation 3.49. Substituting a one pixel difference in parallax measurement into Equation 3.49 gives:

$$\Delta h = \frac{\Delta pH}{p_a} = \frac{(1)(728\,\text{m})}{942} = 0.77\,\text{m} \qquad 3.51$$

Elevation measurements in this example can be no more precise than a nominal error of 0.8 m. This assumes all other sources of error are negligible, and that the images are

truly vertical and corrected for terrain relief. These conditions are not completely satisfied in this example. Actual error may be twice the nominal value.

This example shows that approximate elevation differences for natural resource surveys can be measured from non-metric digital aerial images by applying uncomplicated photogrammetric relationships to parallax distances measured with relatively inexpensive image processing software. Preparation of the stereo pair images becomes tedious if more than a few elevations must be measured. Aerial mapping firms use geometrically precise (metric) large format aerial mapping cameras and commercial digital photogrammetric software to increase the efficiency and accuracy of elevation measurements. Image elevation measurements are much improved with the techniques of analytical photogrammetry discussed in Section 3.4.

3.3 Georeferencing and Orthorectification

Georeferencing is a two-dimensional image rectification process that seeks an optimal fit of the original aerial image to an existing map, orthophoto image or matrix of ground control points in geographic coordinates. Georeferencing is sometimes described as a rectification process, but rectification in photogrammetry is reserved for correction of sensor tilt effects (Wolf and Dewitt 2000). Approximate distances, lengths and areas may be measured directly in a georeferenced aerial image with GIS software. The georeferencing process is mostly dismissed in the photogrammetric literature. Georeferenced aerial images were utilized throughout the dissertation research. Main points of the georeferencing process and accuracy assessment are discussed.

The most important aspect of georeferencing is its difference from orthorectification. Users must recognize that georeferenced aerial images are not corrected for perspective (orientation) and scale difference due to terrain relief. All georeferenced aerial images contain spatial error that is poorly defined and can be significant. Increased accuracy is obtained when aerial images are orthorectified with a three dimensional rectification process that corrects for sensor orientation and relief displacement. Orthorectification is preferred when measurements must be precise and have definable errors.

Orthorectification adjusts all image points to a constant scale. Orthoimages have dimensional properties similar to a topographic map. Measurements may be made anywhere on the orthoimage with nearly equal accuracy, though scale errors may still exist depending on the quality of the terrain information employed in rectifying the image. Orthorectfication of high-resolution aerial images requires a correspondingly dense digital elevation model (DEM) that accurately depict low order terrain variation (Manzer 1996) . High accuracy DEMs are seldom available and must be derived with analytical photogrammetry techniques as described in Section 3.4.

Digital orthoimages are processed with sophisticated photogrammetric software and require a relatively high level of expertise to produce. Advances in automatic collection of camera orientation (Mostafa and Schwarz 2001; Schwarz et al. 1993) and image block adjustment algorithms (Heipke 1997; Mikhail et al. 2001; Wolf and Dewitt 2000) have semi-automated the production of digital orthoimages, but the cost and effort is still not justifiable for much reconnaissance and environmental assessment work.

Direct viewing of aerial images and use of georeferenced aerial images are often the only cost-effective alternatives.

Given the importance of georeferenced images to much legitimate aerial survey work, it is surprising to find no comprehensive and authoritative treatment of the georeferencing of high-resolution digital aerial images. A detailed treatment of georeferencing could easily comprise a substantial part of a text dedicated to the remote sensing of low altitude high-resolution digital aerial imagery. The main aspects of georeferencing that are most relevant to the dissertation research are discussed below.

3.3.1 Georeferencing Guidelines

Visual georeferencing to a DOQ is an uncomplicated procedure whereby ground level features observed in the aerial image are matched to corresponding features in the DOQ. When faced with the need to georeference many images it is best to adopt procedures that expedite production while maintaining acceptable accuracy. Experience has shown that the following guidelines usually produce acceptable results.

- Examine the DOQ in the vicinity of the coverage of the aerial image(s) and identify prominent ground level point features that can serve as image match points (ground control).

- Select at least three, but usually no more than five ground control points spread throughout the image, preferably at the elevation of the main feature of interest such as an ephemeral gully or channel system. Selecting ground

control points close to the elevation of the gully system will produce an image scale that is most accurate along the gully or channel line. Avoid selecting ground control points on ridge tops because these tend to increase scale distortion in low altitude aerial imagery.

- Good ground control points include:
  - Building corners at ground level
  - Well defined fence corners
  - Bridge piers and railings
  - Transverse joints in asphalt and concrete pavement surfaces
  - Isolated small trees and shrubs
  - Exposed well defined rock outcrops
  - Culvert crossings at roads

- Less desirable, but often serviceable ground control points include
  - Bases of large trees inferred by shadow marks
  - Persistent high angle bends in streams and channels
  - Bends in field drainage ways
  - Corners of road intersections
  - Points and corners of persistent tillage obstructions
  - Distinct points on persistent and high contrast features such woodlots, shrub patches, road curves, and ponds.

- As a last resort, with practice, images can be georeferenced by matching terrain patterns and linear features (roads, field boundaries, fences, patch perimeters) by trial and error selection of assumed ground control points. With this technique it helps to repeatedly switch the visibility of the aerial image on and off while observing the DOQ base image. Most observers can readily detect significant scale differences and misalignment from a mismatch.

- When four or more good ground control points are available and well distributed, delete the worst ground control point and visually check the improvement by the visual pattern matching technique.

- When serviceable ground control points do not exist in the aerial image to be georeferenced, as is often the case in the center of large homogeneous fields, examine the preceding or subsequent aerial images for ground control points. Extend ground control into the sparse area by georeferencing one or both of the adjacent (anchor) images.

3.3.2 Georeferencing Procedure

An application of the guidelines is demonstrated for georeferencing aerial images of a gully system in the Middle Potlatch Creek basin acquired on March 13, 2004. Aerial images were georeferenced with ESRI ArcView 3.3™ and the Leica Geosystems Image Analysis™ extension. Potential ground control in the USGS DOQ is indicated in Figure 3.38. Control is sparse between the highway to the north and the county road to the

south. The red line through the center of the DOQ image depicts the flight line. Aerial images of the highway and county road each showed three good control points (small trees, culvert crossings and abrupt changes in waterway alignment). Ground control was extended to the middle image by georeferencing the adjacent images (Figure 3.39). Intermediate aerial images in Figure 3.40 were georeferenced with ground control points observed in the "anchor" images. Accuracy of the intermediate images was verified by visually matching the pattern of the DOQ. Skewed (crabbed) orientation of the images indicates a strong crosswind (typical for fair weather in March on the Palouse), but does not impair the usefulness or quality of the images. Ground pixel resolution of the georeferenced aerial images is about 0.2 meters. Overlap between images is about 50 percent, providing stereo coverage for most of the area.

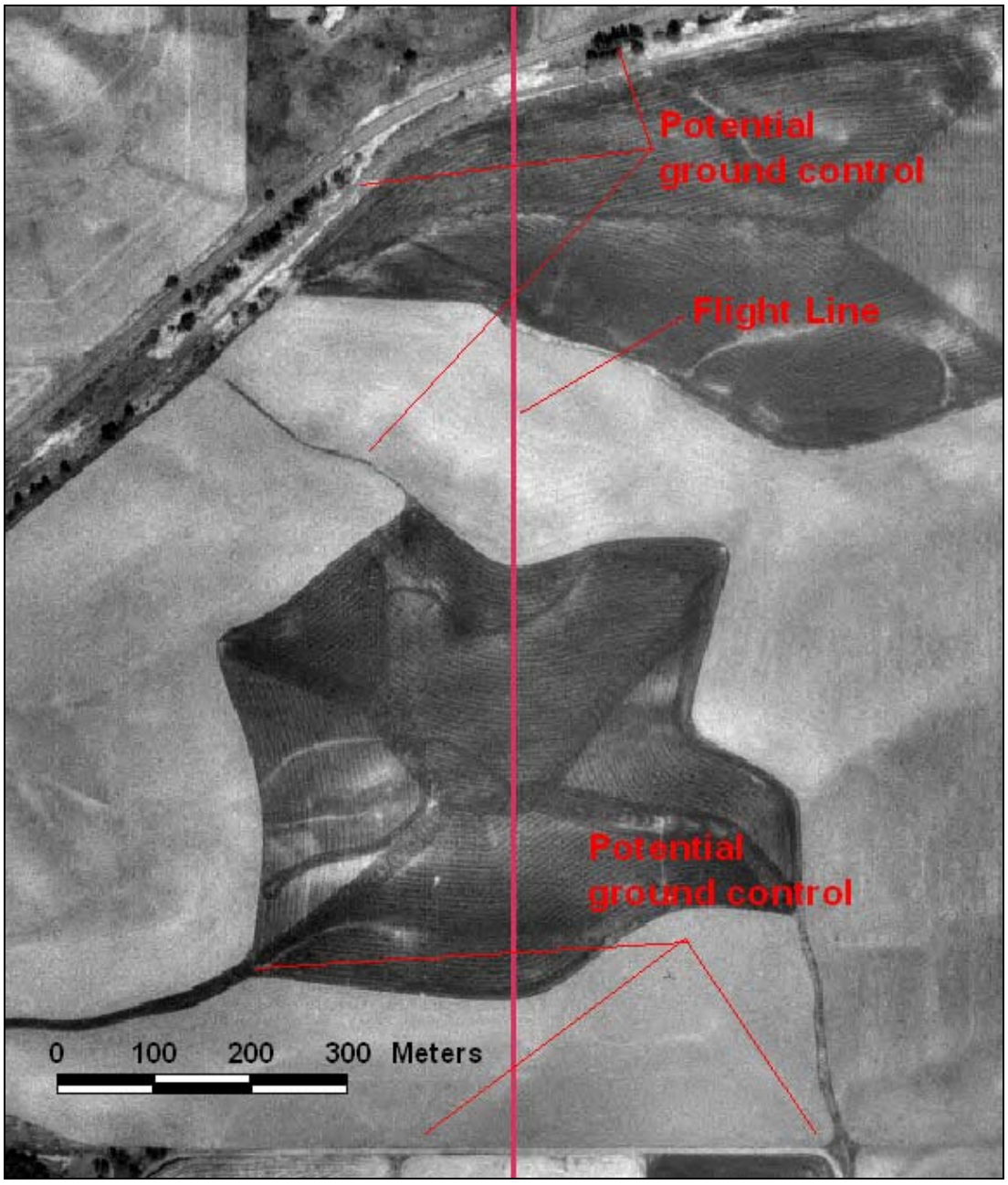

Figure 3.38 Potential ground control observed in a USGS Digital Orthophoto Quadrangle.

Figure 3.39 Georeferenced anchor images that extend ground control into central area.

Figure 3.40 Completed sequence of georeferenced aerial images.

3.3.3 Accuracy of Georeferencing

Georeferencing attempts to minimize, but cannot completely eliminate differences in the spatial correspondence between pixels in an image and the imaged surface (Wolf and Dewitt 2000). Spatial errors of georeferenced and orthorectified images are commonly expressed in terms of an overall root mean square error (RMSE) of the differences between ground control points (GCP) and corresponding image points. This is a meaningful statistic only when sufficient GCPs are available to give a reasonable level of redundancy in the mathematic transformation of the image. Most of the images along an aerial transect are georeferenced with only three or four GCPs observable in the DOQQ base image. Section 3.3.4 will show that three ground control points are necessary for a two-dimensional coordinate transformation used in georeferencing the aerial image. Additional ground control points are necessary to provide redundancy for an estimation of georeferencing error. However, georeferencing error statistics are without firm mathematical basis when GCPs are obtained from DOQQs that also possess an unknown degree of spatial uncertainty.

It would be possible to select a random sample of georeferenced images and verify spatial accuracy with a GPS field survey, but this is costly and seldom performed in natural resource survey type work. A more efficient and meaningful measure of georeferencing accuracy is to examine the effect of the expected limits of spatial error in an aerial image having minimal ground control. The following procedure and sequence of images demonstrates how this can be done.

Figure 3.41 is a representative aerial image of several ephemeral gully systems acquired in March 2004. Ground control observed in the 1992 USGS DOQQ is marked and identified by point number in Figure 3.42.

Figure 3.41Original aerial image, March 13, 2004.

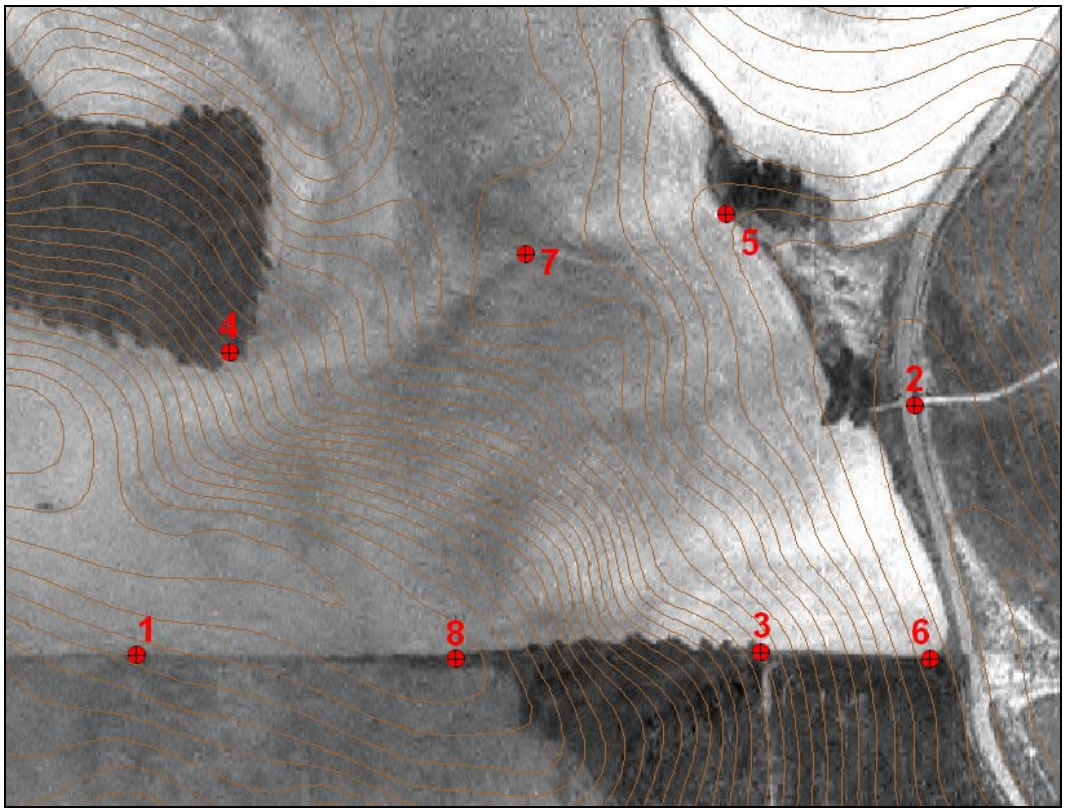

Figure 3.42 Potential ground control points.

Overall spatial error is greatest when only two ground control points are available. In the transformation, the image is simply scaled and rotated. Spatial relationships between pixels are not changed by the resampling process. In Figure 3.42, point 1, an isolated shrub, and point 2, a corner of a road intersection, are selected for the georeferencing. Point 1 is at an elevation of 929 m and point 2 is at 881 m, a difference of 48 m. The image georeferenced with these two points is in Figure 3.43.

Figure 3.43 Georeferenced image with two control points.

The ground distance between point 1 and point 2 measured on the DOQQ is 464.6 m. The pixel distance between these points measured on the original image is 2513 pixels. The mean GPR between these two points is 464.4/2513 or 0.185 m/pixel. This would be the GPR reported in the georeferencing statistics for the image. The accuracy of the georeferencing can be evaluated by comparing distances measured on the georeferenced image to those measured on the DOQQ. Three test distances (red) are shown on Figure 3.44. Channel centerlines of the three ephemeral gullies (blue) are digitized to determine their length. Differences between georeferenced image distances and DOQQ distances are summarized in Table 3.7. Selected widths along gully 2 were measured at locations in Figure 3.45 and also listed in Table 3.7.

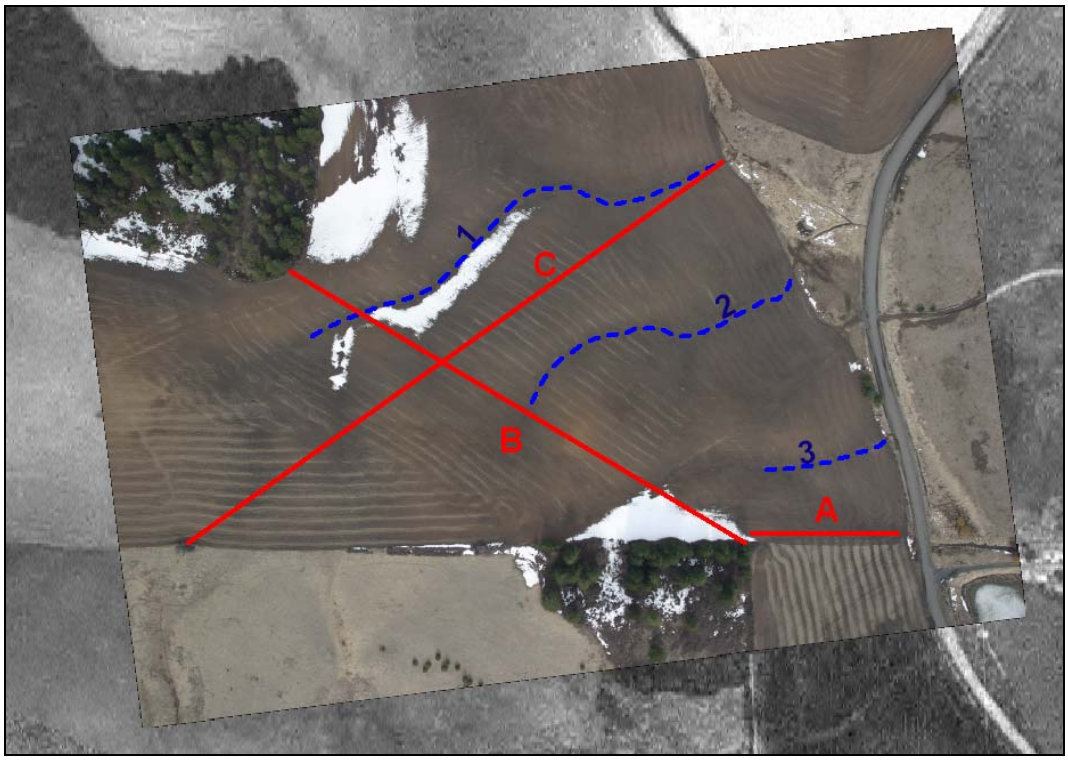

Figure 3.44 Measured distances for accuracy comparison.

Distance A, a short line in the lower elevation of the image, has the largest error at -4.2 percent. The longer lines B and C are along steeper gradients so are more similar to the conditions georeferencing solution. They have absolute errors less than 1%.

Line	Image Distance m	DOQ Distance m	Difference
GCP	464.6	464.6	0%
A	91	95	-4.2%
B	338	340	-0.6%
C	421	419	0.5%
Gully 1	302	na	
Gully 2	202	na	
Gully 3	80	na	
Width 1	1.1	na	
Width 2	1.1	na	
Width 3	1.0	na	

Table 3.7 Distance and error summary for image georeferencing accuracy.

Figure 3.45 Measured ephemeral gully width points (gully 2).

An error map can be constructed from elevation data in the DEM. Differences between the GPR for particular points and the GPR reported in the georeferencing statistics is directly proportional to the elevation difference between the particular point and the mean elevation of the points selected for georeferencing. Figure 3.46 is a contour map of scale variation generated from the DEM data. Maximum scale variation is about 5 percent.

It is evident from this comparison that even sparse georeferencing of a small footprint aerial image has minimal effect on estimates of relative distances and lengths. Estimates of ephemeral gully erosion in Section 8 are based on aerial image measurements of ephemeral gully channel length. Assuming no errors in the USGS DOQ and correct interpretation of endpoints, measured ephemeral gully lengths will be within 5 percent of their actual values. Nominal widths of ephemeral gully channels will be

also be within 5 percent. A 5 percent error is well within the normal uncertainty of hydrologic and soil loss estimates.

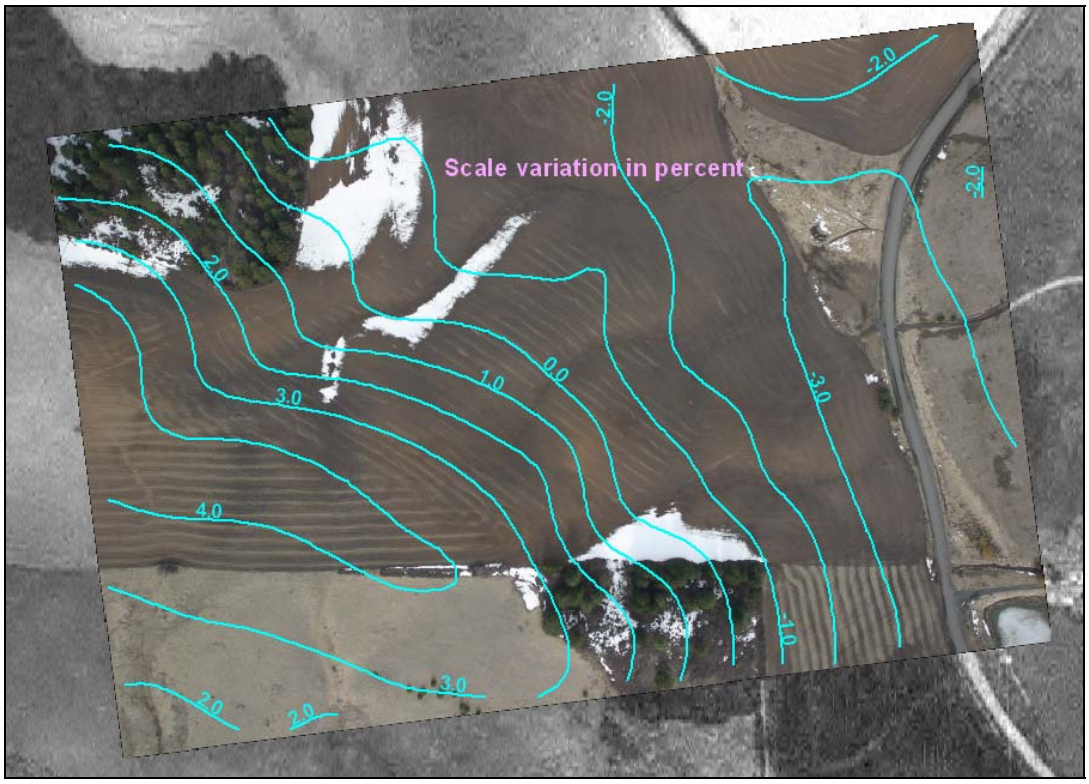

Figure 3.46 Contours of scale variation.

3.3.4 Two-Dimensional Coordinate Transformation

I have delayed discussion of the mathematics of georeferencing until now because it is entirely internal to commercial image processing software and tends to obscure the importance of the subjective aspects of georeferencing. By far, subjective selection of ground control points has the greatest effect on the accuracy of georeferenced aerial images. The choice of mathematical transformation is secondary and mostly of little concern to the normal user.

In context of the discussion of measurement accuracy, a more rigorous evaluation is to be had by extracting georeferencing statistics from the mathematical transformation of the image. Images are typically georeferenced with two-dimensional conformal coordinate transformations (Mikhail et al. 2001; Wolf and Dewitt 2000) . The highest possible order of transformation depends on the number of ground control points available and selected. Experience shows that reasonable results can be obtained with a six-parameter transformation. Ground position coordinates are computed with the algebraic equations:

$$X = a_0 + a_1 x + a_2 y \qquad 3.52$$

$$Y = b_0 + b_1 x + b_2 y \qquad 3.53$$

where X and Y are the real-world coordinates of a ground control point; x and y are the corresponding image coordinates; and a_0, a_1, a_2, b_0, b_1, b_2 are coefficients of scale and rotation. This system of equations in matrix form is,

$$\mathbf{L} = \mathbf{AX} \qquad 3.54$$

where **L** is the single column array of measured ground coordinates corresponding the **A** array of measured image coordinates. The **A** array has six columns. The number of rows in **L** and **A** are two times the number of ground control points. The **X** array is the single column of the six transformation parameters.

The transformation parameters are obtained by least squares analysis of ground control points. The matrix form for least squares analysis is,

$$\mathbf{AX} = \mathbf{L} + \mathbf{V} \qquad 3.55$$

where **V** is the single column array of residuals that has the same number of rows as **L**. Expanded, the arrays become,

$$\begin{bmatrix} X_1 \\ Y_1 \\ X_2 \\ Y_2 \\ \vdots \\ X_n \\ Y_n \end{bmatrix} \approx \begin{bmatrix} 1 & x_1 & y_1 & 0 & 0 & 0 \\ 0 & 0 & 0 & 1 & x_1 & y_1 \\ 1 & x_2 & y_2 & 0 & 0 & 0 \\ 0 & 0 & 0 & 1 & x_2 & y_2 \\ \vdots & \vdots & \vdots & \vdots & \vdots & \vdots \\ 1 & x_n & y_n & 0 & 0 & 0 \\ 0 & 0 & 0 & 1 & x_n & y_n \end{bmatrix} \begin{bmatrix} a_0 \\ a_1 \\ a_2 \\ b_0 \\ b_1 \\ b_2 \end{bmatrix} \qquad 3.56$$

The least squares matrix solution is,

$$\mathbf{X} = \left(\mathbf{A}^T\mathbf{A}\right)^{-1}\left(\mathbf{A}^T\mathbf{L}\right) \qquad 3.57$$

This matrix computation is easily computed in Matlab or Excel. Three ground control points providing two equations for each point are the minimum necessary to compute the six transformation parameters. Additional points provide redundancy for the least squares solution. The matrix form of the least squares solution is developed in Appendix 3.1.

An example illustrates analytical georeferencing and error evaluation. A total of fifteen ground control points and image points were measured in an aerial image of Genesee, ID acquired on February 22, 2004 (Figure 3.47). The ground control data and corresponding image point measurements are listed in Table 3.8

Point ID	Image X Pixels	Image Y Pixels	Ground UTM East m	Ground UTM North m
1	105.7	-1946.9	504918.4	5154939.1
2	1669.8	-1834.1	505529.4	5155007.7
3	2802.4	-1932.7	505991.8	5154973.7
4	2668.0	-1566.9	505917.7	5155124.8
5	1912.8	-1340.9	505609.2	5155206.8
6	1013.8	-1257.0	505272.2	5155228.5
7	336.4	-1500.8	505013.5	5155122.9
8	254.1	-770.9	504986.2	5155398.2
9	993.6	-636.6	505260.2	5155458.5
10	1793.3	-707.7	505550.2	5155443.1
11	2255.3	-991.3	505733.4	5155346.0
12	2877.4	-1167.1	505991.1	5155286.5
13	2649.6	-224.1	505856.6	5155632.4
14	1834.8	-105.6	505556.4	5155661.1
15	272.6	-250.3	504995.9	5155584.2

Table 3.8 Ground control point and image point data.

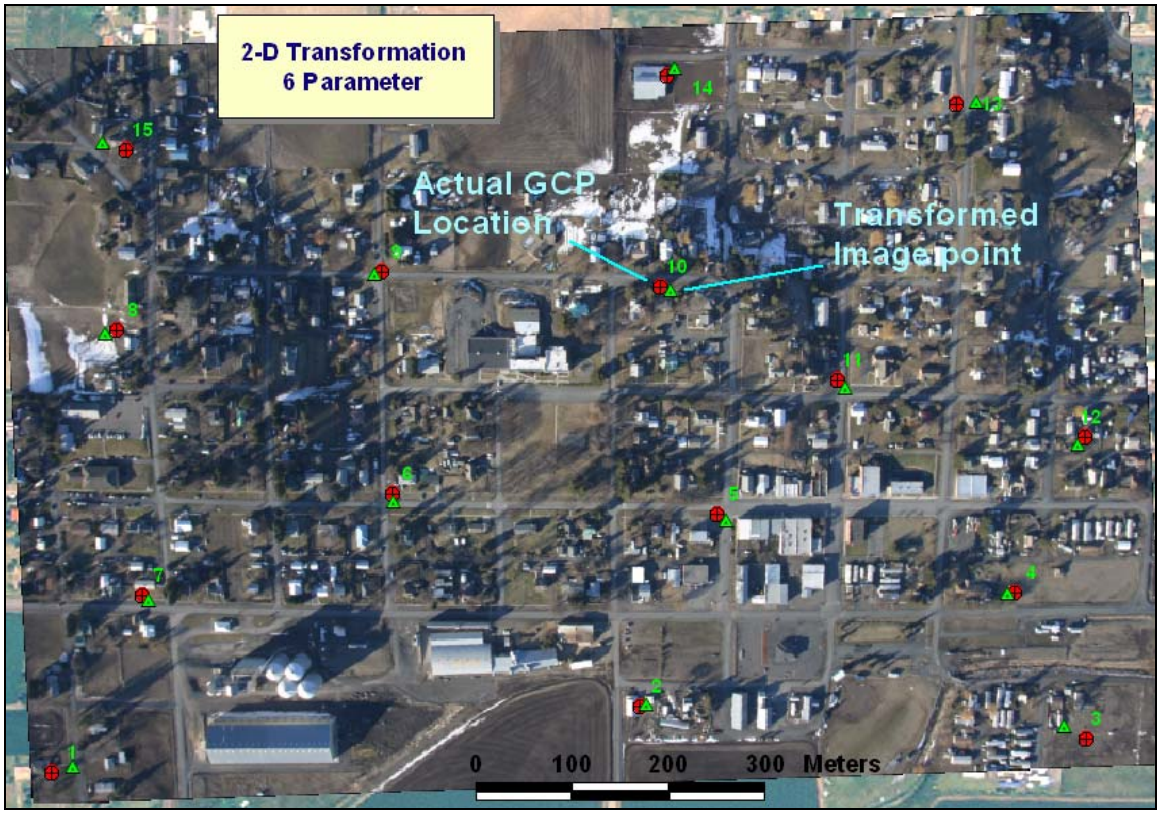

Figure 3.47 Aerial image georeferenced with 6 parameter 2D transformation.

The **A** and **L** matrices were developed from the point data and written to text files named A_maxtrix.ext and A_matrix.ext. The least squares solution was computed with

the Matlab code in Figure 3.48. The computed transformation parameters of the **X** array are:

a_0 = 504862.03	UTM east coordinate of the upper left corner of the image
a_1 = 0.3815	Scale parameter, ground pixel resolution in east direction
a_2 = -0.0191	Rotation parameter
b_0 = 5155684.61	UTM north coordinate of the upper left corner of the image
b_1 = 0.0135	Rotation parameter
b_2 = 0.3802	Scale parameter, ground pixel resolution in north direction

The Matlab code computes residual statistics. The root mean square errors (RSME) in the east and north directions are 9.56 m and 4.68 m. The total RSME is 10.64 m computed as the square root of the sum of the squares of the east and north RSMEs. The average residual distance is 6.65 computed as the average of the translation distances for each point. The average ground pixel resolution is 0.38 m.

The residual error in the 2D transformation is substantial because of topographic relief and lens distortion. Elevation varies from 842 meters in the west (right) side of the image to 808 m the southeast portion of the image. The image was acquired with a 17 mm lens producing noticeable radial barrel distortion.

```
% Transform2d6
% Computation of 2D-Transformation
% Six parmaeter affine transformation
% Load the A matrix text file of image coordinates
   load A_matrix.ext;
   A = A_matrix;
% Load the L matrix text file of measured ground control point coordinates
   load L_matrix.ext;
   L = L_matrix;
   n = length(L);
% Compute the least squares solution
%    Note that the single quote charcter is the transpose operator in Matlab
   X = (A'*A)^-1*(A'*L)
% Compute the residuals matrix
   V = L - A*X;
% Compute the mean squared error for X, Y, and residual distance
   sumx2 = 0;
   sumy2 = 0;
   residsum = 0;
for i = 1:2:n
   sumx2 = sumx2 + V(i)^2;
   sumy2 = sumy2 + V(i+1)^2;
   residsum = residsum + (V(i)^2+V(i+1)^2)^0.5;
end
   MSEx = (sumx2/n)^0.5
   MSEy = (sumy2/n)^0.5
   Total_RMSE = (MSEx^2 + MSEy^2)^0.5
   Average_residual = residsum/
   Average_resolution = (X(2)+X(6))/2
```

Figure 3.48 Matlab code for six parameter two-dimensional image transformation.

Accuracy statements based on the transformation error of ground control points are well accepted in general practice, but they can be manipulated and are subject to error by careless selection of image points. For example, if all ground control points were selected from about the same elevation, terrain relief would have little effect on how well the transformed points match the originals. A better fit is obtained with more ground control points and a higher order transformation, such as that available in the ESRI ArcMap georeferencing tool. Although higher order transformations may reduce error statistics, they can greatly distort the image boundary making the image unappealing and difficult to mosaic. Error statistics for individual georeferenced images, while easily

calculated, tell relatively little about the usability of the image. I prefer a use-oriented approach to evaluation of images as demonstrated above.

Selection of a georeferencing transformation and level of effort is a matter of choice and resources. My experience has been that use of more than 4 or 5 ground control points in each image when georeferencing a large volume of images contributes little to measurement accuracy and strains time resources. There is an almost irresistible temptation to spend an inordinate amount of time adjusting ground control points to obtain a good edge match when producing a mosaic or continuous strip of georeferenced images. Creating an aerial mosaic from georeferenced images is more art than science. Results can be quite good with care, but the ultimate quality of the mosaic is seldom known before completion. Most engineering work requires a more dependable technique. Aerial images should be orthorectified (at much greater cost and effort) if higher accuracy and a seamless appearance in the mosaic are required. Orthorectification of aerial images is discussed more in Section 3.4.

The georeferencing procedures discussed above are mostly applicable when measurements are desired throughout the coverage of the image. Georeferencing of stream corridor and shoreline images should be approached differently. Elevation variation is normally least along the stream course, so it is preferable to select ground control points as near the stream or shore as possible to increase the accuracy of morphology measurements (reach length, channel width, area of sediment deposition structures). It makes little sense to select ground control points at higher elevations, such as on canyon slopes, because doing so decreases accuracy of the stream morphology measurements.

When processing sequential stream images, I typically select one or two match points near the edge of the preceding georeferenced aerial image on both sides of the stream, then select one or two new ground control points from the base orthoimage near the stream near the forward limit of the current image. Edge match between images at the waterline is usually very good. Image edge match of higher terrain on either side of the stream will often be poor, but will not significantly affect morphology measurements. Occasionally this requires use of the control point extension technique described previously. This is the fastest way to georeference a large volume of stream or corridor images. With diligent effort, about one hundred aerial images can be manually georeferenced in this manner in an eight to ten hour period. Numerous examples of georeferenced aerial images of streams appear throughout this dissertation.

3.3.5 Georeferencing World Files

All remote sensing and GIS software packages require coordinate transformation information to properly display a georeferenced image. There are many methods to convey this information. Image files may have embedded geographic and transformation data such the proprietary image formats ERDAS Imagine and MrSID or the open architecture image formats such as geoTIFF, and more recently geoJPEG. Prior to the use of geographically intelligent images, the most common method to convey coordinate information was with a separate metadata file called the worldfile. Virtually all remote sensing and GIS software packages can read world files.

An example of a world file is shown in Figure 3.49. The world file is a separate ASCII text file that has a filename that corresponds to the name of the image file it represents. For example, a georeferenced aerial image in standard tif format named

"Aerial_15feb05.tif" would have an associated world file called "Aerial_15feb05.tfw". The suffix "tfw" announces the presence of the world file for this aerial image to the GIS or remote sensing software. The world file is usually (or must be) placed in the same directory as the image file. A georeferenced JPEG image would have a world file with a ".jgw" suffix.

The world file text file consists of six unformatted values separated by spaces or tabs or on individual lines. The first and fourth values are the ground width of a single pixel (GPR) in the x (easting) and y (northing) direction, 0.3817 and -0.3817 meters in this example. The northing GPR is a negative number because the image array is read from top to bottom. The second and third values are transformation rotation parameters, and are normally zero since most images are georeferenced to true north. Many GIS software packages cannot process rotated georeferenced images, the exception being some CAD software. The fifth and sixth values in the world file are the easting and northing coordinates of the upper left corner of the aerial image.

The information in the world file is sufficient for the software to position and orientate the aerial image in a rectangular coordinate system. Dimensional units and geographic datum are not defined by the worldfile. The user must specify this in the display software independent of the image. It is this aspect of the world file that has caused errors and frustration among users and is leading to its slow demise.

```
0.3817
0.0000
0.0000
-0.3817
504861
5155726
```

Figure 3.49 Aerial image worldfile.

Despite its limitations the worldfile offers a convenient means to rapidly index an aerial image to its approximate location with flight and terrain data.

3.4 Analytical Photogrammetry

The manual photogrammetric measurements become unwieldy, tedious and prone to blunders when more than a few measurements must be made or if the ultimate objective is to produce a digital elevation model and orthorectify a block of many images. Historically, elaborate electro-mechanical systems were employed to develop contour maps and orthorectified photomaps from hardcopy film images (1980). Now, nearly all photogrammetry is performed with image processing software on softcopy (digital) computer workstations.

The transition from analog to digital photogrammetry was made possible by availability of low cost computing power and advances in analytical photogrammetry. Analytical photogrammetry mathematically models the three-dimensional object and image spaces in the area of stereo overlap. True planimetric positions and elevations may then be made directly from on-screen images within the software system. Construction of the digital stereo model in general requires simultaneous solution of a large number of matrix equations of corresponding points in image and object space. The mathematical solution techniques have proven to be reliable and accurate. Commercial photogrammetry software semi-automates rectification of large numbers of aerial images. A full exposition of analytical photogrammetry is not possible here. Relationships and

processes essential to the understanding of the performance of photogrammetric software and its use in the dissertation research will be introduced below.

3.4.1 Collinearity Equations – External Geometry

The determination of the camera position and pointing angle from an image is called *resection*. A fundamental relationship in analytical photogrammetry that determines the geometry of resection is the system of *Collinearity* equations. It is best to begin the discussion of collinearity with a single tilted aerial image as depicted in Figure 3.50. Collinearity is the condition that the sensor (exposure station), any real world object point and the image of the object all lie along a straight line in three-dimensional space. The two-dimensional position of single point *a* in the image is related to its real world three-dimensional position by Equations 3.58 and 3.59.

$$x_a = x_o - f\left[\frac{m_{11}(X_A - X_L) + +m_{12}(Y_A - Y_L) + m_{13}(Z_A - Z_L)}{m_{31}(X_A - X_L) + +m_{32}(Y_A - Y_L) + m_{33}(Z_A - Z_L)}\right] \qquad 3.58$$

$$y_a = y_o - f\left[\frac{m_{21}(X_A - X_L) + +m_{22}(Y_A - Y_L) + m_{23}(Z_A - Z_L)}{m_{31}(X_A - X_L) + +m_{32}(Y_A - Y_L) + m_{33}(Z_A - Z_L)}\right] \qquad 3.59$$

where

$$m_{11} = \cos\phi\cos\kappa$$

$$m_{12} = \sin\omega\sin\phi\cos\kappa + \cos\omega\sin\kappa$$

$$m_{13} = -\cos\omega\sin\phi\cos\kappa + \sin\omega\sin\kappa$$

$$m_{21} = -\cos\phi\sin\kappa$$

$$m_{22} = -\sin\omega\sin\phi\sin\kappa + \cos\omega\cos\kappa$$

$$m_{23} = \cos\omega\sin\phi\sin\kappa + \sin\omega\cos\kappa$$

$$m_{31} = \sin\phi$$

$$m_{32} = -\sin\omega\cos\phi$$

$$m_{33} = \cos\omega\cos\phi$$

and

X_A is the ground coordinate of point A in the *x* direction

X_L is the ground coordinate of the sensor in the *x* direction

Y_A is the ground coordinate of point A in the *y* direction

Y_L is the ground coordinate of the sensor in the *y* direction

Z_A is the ground elevation of point A

Z_L is the ground elevation of the sensor

x_a is the image coordinate of point A in the *x* direction

y_a is the image coordinate of point A in the *y* direction

ω is the rotation of the image plane about the *x* axis

ϕ is the rotation of the image plane about the once rotated *y* axis

κ is the rotation of the image plane about the twice rotated *z* axis

f is the lens focal length, equivalent (z_a equals -*f*).

The rotation angles may seem a bit strange compared to direction cosines of standard engineering vectors. Total rotation movement of the camera is a sequential accumulation of rotation about the *x, y* and *z* axis of a coordinate system fixed to the camera. The standard sequence is to rotate angle omega, *ω,* about the *x*-axis, rotate angle phi, *ϕ,* about the once rotated *y* axis, and rotate angle kappa, *κ,* about the twice rotated *z* axis. The direction of positive rotation is according to the right-hand rule, meaning the

rotation will appear counter-clockwise when viewed from the positive end of the axis. The matrix of *m* coefficients is called the rotation matrix.

The collinearity equations develop directly from similar triangle relationships of image points and ground points in Figure 3.50 with rotation and translation. This involves a *three-dimensional conformal coordinate transformation* that is rather long to describe and illustrate, but is fully developed and well illustrated in photogrammetry and surveying texts. Particularly well described developments of the collinearity equations are by Wolf and Dewitt (2000) and Mikhail et al. (2001).

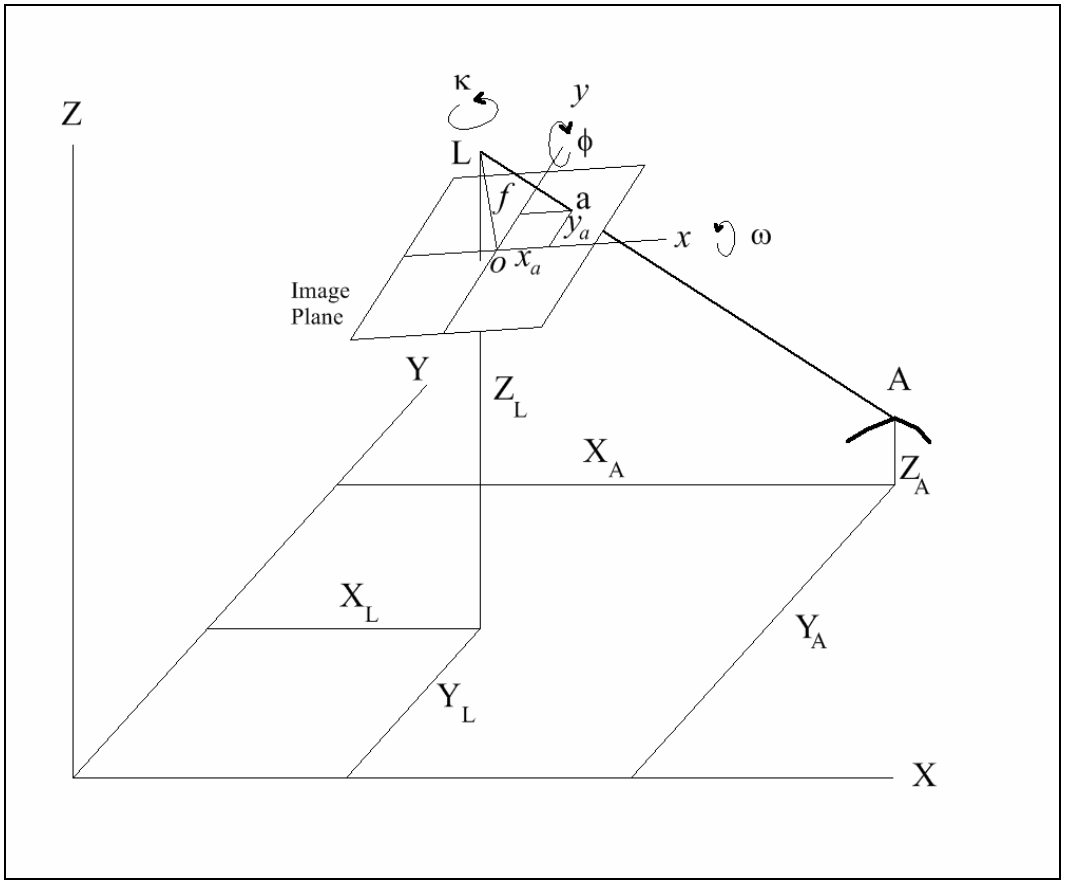

Figure 3.50 Geometry of a tilted aerial image.

Attention is more profitably directed to implementation of the collinearity equations. In general, the rotation parameters (ω,ϕ,κ) and sensor (exposure station)

coordinates (X_L,Y_L,Z_L) are not known because the precise geographic position and attitude (tilt, roll, yaw) of the sensor (camera) is not recorded at the instant of exposure. A fundamental task of analytical photogrammetry is to determine reliable values for the rotation and position of the exposure station from analysis of corresponding image and ground control points. This process is called the determination of *exterior orientation*.

The exterior orientation of a camera and sensor establishes the perspective of the image and is essential for computing the correspondence of measurements made in images and real world dimensions. Exterior orientation parameters must be determined for each aerial image in continuous strips or blocks of images to allow elevation measurement by stereo parallax. Given their importance in analytical photogrammetry, determination of exterior orientation from the collinearity equations will be developed more fully.

A minimum of three ground control points with X, Y, and Z coordinates are required to determine the six unknown parameters of exterior orientation. The collinearity equations are linearized with Taylor's Theorem to facilitate a least squares solution. Initial approximations of the orientation parameters are necessary because of the linearization. A practical initial assumption is that the sensor is pointed vertically at the ground (ϕ and ω are zero). Elevation of the exposure station Z_L is initially approximated with Equation 3.41 using at least two control points (with image coordinates and ground coordinates) and the lens focal length. Initial approximations for the remaining parameters are developed from an extension of the parallax relationships of a vertical image.

Following development of the initial approximations, the least squares solution is iterated until corrections to the linearized equations are less than a specified error. Manual solution of the least squares equations is tedious and unnecessary, as they are readily solved by computer algorithms in matrix form. An overview of the least squares matrix solution of the collinearity equations is given in some photogrammetry texts (Mikhail et al. 2001; Wolf and Dewitt 2000).

Adopting notation in Wolf and Dewitt (2000), Equation 3.58 and 3.59 can be expressed:

$$F = x_o - f\frac{r}{q} = x_a \tag{3.60}$$

$$G = y_a - f\frac{s}{q} = y_a \tag{3.61}$$

where

$$q = m_{31}(X_A - X_L) + m_{32}(Y_A - Y_L) + m_{33}(Z_A - Z_L) \tag{3.62}$$

$$r = m_{11}(X_A - X_L) + m_{12}(Y_A - Y_L) + m_{13}(Z_A - Z_L) \tag{3.63}$$

$$s = m_{21}(X_A - X_L) + m_{22}(Y_A - Y_L) + m_{23}(Z_A - Z_L) \tag{3.64}$$

By the Taylor theorem (Campbell and Dierker 1978), linear approximations of Equations 3.60 and 3.61 are the sum of partial derivatives with respect to the unknown rotation parameters and sensor coordinates:

$$\begin{aligned} &F_o + \left(\frac{\partial F}{\partial \omega}\right)_o d\omega + \left(\frac{\partial F}{\partial \phi}\right)_o d\phi + \left(\frac{\partial F}{\partial \kappa}\right)_o d\kappa + \left(\frac{\partial F}{\partial X_L}\right)_o dX_L + \left(\frac{\partial F}{\partial Y_L}\right)_o dY_L \\ &+ \left(\frac{\partial F}{\partial Z_L}\right)_o dZ_L + \left(\frac{\partial F}{\partial X_A}\right)_o dX_A + \left(\frac{\partial F}{\partial Y_A}\right)_o dY_A + \left(\frac{\partial F}{\partial Z_A}\right)_o dZ_A = x_a \end{aligned} \tag{3.65}$$

$$G_o + \left(\frac{\partial G}{\partial \omega}\right)_o d\omega + \left(\frac{\partial G}{\partial \phi}\right)_o d\phi + \left(\frac{\partial G}{\partial \kappa}\right)_o d\kappa + \left(\frac{\partial G}{\partial X_L}\right)_o dX_L + \left(\frac{\partial G}{\partial Y_L}\right)_o dY_L + \left(\frac{\partial G}{\partial Z_L}\right)_o dZ_L + \left(\frac{\partial G}{\partial X_A}\right)_o dX_A + \left(\frac{\partial G}{\partial Y_A}\right)_o dY_A + \left(\frac{\partial G}{\partial Z_A}\right)_o dZ_A = y_a \quad 3.66$$

where subscript *o* indicates the term is evaluated with an initial approximation of the unknowns and the full differentials ($d\omega$, $d\phi$, $d\kappa$, …) are unknown corrections that make the equations exactly equal to the measured image distances x_a and y_a. Higher order terms of the Taylor series are dropped and are not necessary for the iterative solution.

Equations 3.65 and 3.66 for the single image point *a* are expressed in computational form for a least squares solution as:

$$b_{11}d\omega + b_{12}d\phi + b_{13}d\kappa + b_{14}dX_L + b_{15}dY_L + b_{16}dZ_L = J + v_{x_a} \quad 3.67$$

$$b_{21}d\omega + b_{22}d\phi + b_{23}d\kappa + b_{24}dX_L + b_{25}dY_L + b_{26}dZ_L = K + v_{y_a} \quad 3.68$$

where the *b* coefficients form the Jacobian of partial derivatives, *J* is ($x_a - F_o$), *K* is ($y_a - G_o$). Residual terms v_{xa} and v_{ya} are added to make the approximate equations consistent. One set of equations is formed for each of the *n* control point. These equations differ slightly from those in Wolf and Dewitt (2000) in that all terms are positive, leaving the partial derivatives to convey a change in sign.

Equations for each of the *b* coefficients are obtained by differentiating *q*, *r* and *s* with respect to the unknown parameters. For example, by the quotient rule the b_{14} coefficient of the sensor position term X_L is:

$$\frac{\partial}{\partial X_L}\left(-f\frac{r}{q}\right) = -f\frac{q\frac{dr}{dX_L} - r\frac{dq}{dX_L}}{q^2} = -\frac{f}{q^2}\left(rm_{31} - qm_{11}\right) \quad 3.69$$

where m_{31} and m_{11} are coefficients of the rotation matrix.

Other *b* coefficients of partial derivatives develop similarly and are summarized below. Some of the expressions cannot be easily expressed in terms of rotation matrix coefficients, so reveal the trigonometric functions that compose the partial derivatives. Each coefficient expression given here retains negative signs in the *b* coefficient equation. Readers comparing these equations to those by Wolf and Dewitt (2000) should note the sign on the matrix of *b* coefficients of example 11-1 on page 239 of their text to confirm validity of the differences.

$$b_{11} = \frac{f}{q^2}\left[r\left(-m_{33}\Delta Y + m_{32}\Delta Z\right) + q\left(m_{13}\Delta Y - m_{12}\Delta Z\right)\right] \qquad 3.70a$$

$$b_{12} = \frac{f}{q^2}\left[\begin{array}{l} r\left(\cos\phi\Delta X + \sin\omega\sin\phi\Delta Y - \cos\omega\sin\phi\Delta Z\right) \\ \quad + q\left(\sin\phi\cos\kappa\Delta X - \sin\omega\cos\phi\cos\kappa\Delta Y + \cos\omega\cos\phi\cos\kappa\Delta Z\right) \end{array}\right] \qquad 3.70b$$

$$b_{13} = \frac{f}{q}\left(-m_{21}\Delta X - m_{22}\Delta Y - m_{23}\Delta Z\right) \qquad 3.70c$$

$$b_{14} = \frac{f}{q^2}\left(-rm_{31} + qm_{11}\right) \qquad 3.70d$$

$$b_{15} = \frac{f}{q^2}\left(-rm_{32} + qm_{12}\right) \qquad 3.70e$$

$$b_{16} = \frac{f}{q^2}\left(-rm_{33} + qm_{13}\right) \qquad 3.70f$$

$$b_{21} = \frac{f}{q^2}\left[s\left(-m_{33}\Delta Y + m_{32}\Delta Z\right) + q\left(m_{23}\Delta Y - m_{22}\Delta Z\right)\right] \qquad 3.70g$$

$$b_{22} = \frac{f}{q^2}\left[\begin{array}{l} s\left(\cos\phi\Delta X + \sin\omega\sin\phi\Delta Y - \cos\omega\sin\phi\Delta Z\right) \\ \quad + q\left(-\sin\phi\sin\kappa\Delta X + \sin\omega\cos\phi\sin\kappa\Delta Y - \cos\omega\cos\phi\sin\kappa\Delta Z\right) \end{array}\right] \qquad 3.70h$$

$$b_{23} = \frac{f}{q}\left(m_{11}\Delta X + m_{12}\Delta Y + m_{13}\Delta Z\right) \qquad 3.70i$$

$$b_{24} = \frac{f}{q^2}\left(-sm_{31} + qm_{21}\right) \qquad 3.70j$$

$$b_{25} = \frac{f}{q^2}\left(-sm_{32} + qm_{22}\right) \qquad 3.70k$$

$$b_{26} = \frac{f}{q^2}\left(-sm_{33} + qm_{23}\right) \qquad 3.70l$$

where

$$\Delta X = X_A - X_L$$

$$\Delta Y = Y_A - Y_L$$

$$\Delta Z = Z_A - Z_L$$

In computations *K* and *J* are evaluated for the current iteration as:

$$J = x_a - x_o + f\frac{r}{q} \qquad 3.71$$

$$K = y_a - y_o + f\frac{s}{q} \qquad 3.72$$

The system of Equations 3.67 and 3.68 written for each of the *n* control points in matrix equation form is:

$$\mathbf{B}\Delta = \varepsilon + \mathbf{V} \qquad 3.73$$

where **B** is the 2*n* by 6 matrix of *b* coefficients (two rows for each control point), Δ is the 6 by 1 single column matrix of the unknown adjustments to the external orientation parameters, ε is the 2*n* by 1 matrix of *J* and *K* values for each point, and **V** is the 2*n* by 1 matrix of residuals of the *x* and *y* image coordinates.

Least squares estimates of the external orientation parameters are obtained from the matrix equation:

$$\Delta = \left(\mathbf{B}^T\mathbf{B}\right)^{-1}\left(\mathbf{B}^T\varepsilon\right) \qquad 3.74$$

The solution proceeds iteratively with new estimates of the external orientation parameters formed by adding values of the Δ matrix to the initial estimates until the Δ matrix values change less than a specified amount.

It was surprising to find no complete public domain code for practical implementation of the least squares analysis of external orientation for Matlab or other mathematical software. Mikhail et al. (2001) provide some Matlab code, but while compact and efficient, the code is specific to an image and partitioned to three separate code files. Readers unfamiliar with photogrammetry or least squares matrix analysis might find their code difficult to follow. It also does not provide an initial approximation of parameters and uses a numerical approximation of the normal equation derivative coefficients different from that explained above.

A flexible and reasonably well annotated Matlab code *Exgeo.m* is included in Appendix 3.4. It computes the external orientation parameters for a single aerial image by the least squares method discussed above. The code is presented in Matlab rather than Fortran or C because it allows concise matrix manipulation and text like syntax that clarifies the computational algorithm. Matlab is well accepted in the engineering and scientific community as an alternative to conventional programming languages. Many recent text books and journal articles reference Matlab code. It is hoped that the code will promote understanding of the collinearity equations for engineers and scientists not specifically trained in photogrammetry and provide a practical means of computing the external orientation of digital aerial imagery.

Initial approximations of the external orientation parameters are computed in the code based on an assumption of a vertical image. The user provides the lens focal length

and at least three ground control points in real world coordinates and image coordinates. Any number of ground control points may be added to increase the strength of the least squares solution.

The code lacks some of the hallmarks of good programming technique, such as error trapping, but these were considered secondary to its instructive intent and omitted for sake of clarity. The user could easily modify the code to include such artifacts. If the matrix operations in the code fail, the probable cause is poor initial approximations of the orientation parameters. The initial approximations can be modified for other camera orientations such as those typical in close-range terrestrial and architectural imaging.

Computation of external geometry with the code is demonstrated with the data from the February 22, 2004 aerial image of Genesee. Nine well distributed ground control points were selected from the image overlap area (Figure 3.51). Table 3.9 lists the coordinates of the ground control points in image and object space. The image coordinates are in millimeters referenced to an origin at the image center. The real-world coordinates are projected in UTM 11 NAD83 and are in meters. Elevations were obtained from the USGS 10 meter digital elevation model. Lens focal length is 17 mm, and the image was corrected for radial lens distortion.

The UTM coordinate system is not a right-hand coordinate system with respect to the direction of flight for flight lines flown in a north-south direction. This is important because it establishes the positive direction of rotation of angles in the rotation matrix assumed in the Matlab code. The code will work if the image-centered coordinates also increase in the downward direction along the y-axis for images rotated so that the right edges of the images are towards the north. This adjustment produces a consistent

direction of positive rotation in the image coordinate system and the UTM system. The code could be modified to check and adjust for this orientation, but would significantly expand the code and obscure its educational value. New users might find it easier to measure ground control coordinates relative to a local right-hand coordinate rectangular coordinates system.

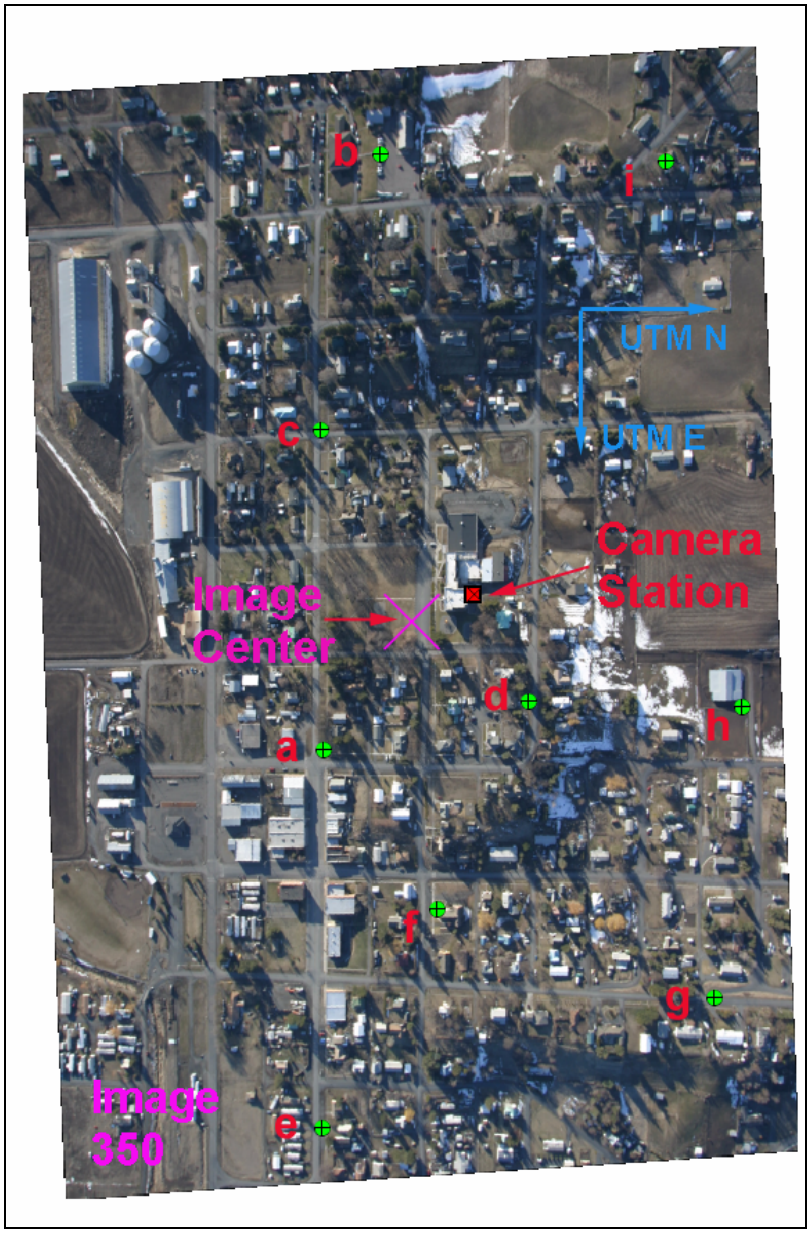

Figure 3.51 Location of the camera station in Genesee aerial image.

	Image 350		Image 350		
	x	y	UTM X (N)	UTM Y (E)	Elevation
ID	mm	mm	m	m	m
a	-1.70	-3.82	5155228.8	505272.4	813.33
b	-0.29	-9.62	5155289.6	504989.6	838.38
c	-1.83	2.55	5155232.2	505600.4	818.66
d	2.30	1.87	5155442.8	505550.6	842.58
e	-2.13	9.89	5155229.8	505989.8	813.12
f	0.25	5.86	5155349.2	505764.6	818.42
g	5.97	8.31	5155632.9	505856.1	844.38
h	6.77	2.20	5155661.1	505556.7	830.42
i	5.78	-9.46	5155583.5	504996.2	841.50

Table 3.9 Ground control point data for Genesee aerial image 350.

The ground control point data was copied into a text file of the same format as Table 3.9 with no column header lines. The name of the data file "genesee.dat" and the focal length were entered into the Matlab code, and the code was saved and run. The solution converged rapidly in three iterations. Table 3.10 lists the results of the collinearity equation least squares computation displayed on screen in the Matlab environment.

Parameter	**Least Squares Estimate**
Omega (roll) ω	4.14 degrees
Phi (pitch) ϕ	1.46 degrees
Kappa (yaw) κ	-2.47 degrees
Camera X_L (UTM E)	505,442 m
Camera Y_L (UTM N)	5,155,386 m
Camera Z_L (Elevation)	1685 m

Table 3.10 External orientation parameters for aerial image 350.

The largest angular rotation in the horizontal plane was ω (roll) at 4.14 degrees, not unusual for low altitude aerial imagery from a fixed wing aircraft with passively stabilized camera mounts. The rotation angle about the pitch axis of the aircraft ϕ was 1.46 degrees. Yaw rotation about the vertical axis κ was -2.47 degrees. The horizontal location of the camera station relative to the image center is indicated in Figure 3.51.

Elevation of the camera was 1685 meters, an altitude of approximately 870 (2850 ft) m above the ground.

Determination of the external orientation parameters is a necessary step in further photogrammetric analysis of the aerial image. External orientation parameters are useful in remote sensing whenever sensor orientation is important, such as in the analysis of the bispectral reflectance properties of an image. I routinely use external orientation computations in qualitative assessment of aerial imagery. Large rotation angles usually indicate images that will be difficult to edge match in a mosaic of georeferenced images because of scale variation due to camera perspective. Perspective transformations based on the external geometry are possible when alternative images are not available.

There are geometric alternatives for determining camera external geometry, such as the equations of *coplanarity*, but their use is not common in aerial photogrammetry. Other methods such as the *direct linear transform* (DLT) are applied in terrestrial close-range imaging. Descriptions of these approaches are found in photogrammetry texts.

3.4.2 Analytical Interior Orientation

The computations of external orientation above assume a perfectly orthogonal image with a provision in the equations to accommodate a small offset of the image center (principal point). It is known from the discussion of lenses that non-linear distortion is generally present in an uncorrected image. In addition, most cameras, both film and electronic, have physical irregularities that slightly skew the image axes, produce differential scaling of the *x* and *y* directions, and cause unevenness in the surface of the image plane (Fraser 1997). Most of this interior geometry bias is constant and can be corrected in a process known as *analytical interior orientation* or *analytical self-*

calibration (Wolf and Dewitt 2000). Analysis of interior orientation is often called *camera calibration* in terrestrial photogrammetry. Correction of the interior geometric bias is important for high precision photogrammetric measurements.

The interior orientation geometry of a camera is modeled by adding parameters to the lens distortion and decentering equations discussed previously. A ten parameter camera calibration model is currently judged the best conventional approach (Fraser 1997). Parameters include principal distance (calibrated focal length), principal point offset, correction terms for radial and decentering distortion, and two terms for in-plane distortion. The model parameters can be highly correlated. There is presently no method to correct for unevenness of a CCD sensor, though it appears that this effect can be neglected for all but high precision measurements (in excess of 1 part in 100,000). It also appears that image plane x and y orthogonal distortion is negligible in CCD sensors (Fraser 1997).

Analytic interior orientation for aerial imaging may include the effects of atmospheric refraction. The refraction index of the atmosphere changes with density, thus with altitude. Atmospheric refraction bends light rays away from the center of a vertical image in a manner similar to radial lens distortion. The amount of radial displacement depends on atmospheric conditions, but an approximate correction to image coordinates may be computed by assuming standard atmospheric conditions and knowing the altitudes of the sensor and terrain. The magnitude of the atmospheric correction for low altitude aerial imagery is less than half a pixel width and can be neglected in moderate precision work. Empirical equations for atmospheric correction are described in remote sensing texts (Mikhail et al. 2001; Wolf and Dewitt 2000).

Camera calibration may be combined with the simultaneous analysis of ground control points and exterior orientations for multiple images in a process called self-calibrated bundle block adjustment. Some parameters of the camera calibration model are strongly correlated and the degree of correlation affects the success of the adjustment process (Mikhail et al. 2001). Bundle block adjustment greatly increases the accuracy and precision of photogrammetric measurements and will be discussed more below.

3.4.3 Analytical Photogrammetry of an Aerial Image Stereo Pair

Collinear analysis can be extended to overlapping aerial images in a simultaneous least squares solution as depicted in Figure 3.52. Point **A** in the area of stereo overlap is captured in both images. The two camera stations L_1, L_2 and ground point **A** form an *epipolar plane.* The differential position of point *a* with respect to the two image centered coordinate systems allows a measurement of parallax. Elevation of point **A** can be computed from the parallax measurement and the orientation parameters of the two camera stations L_1 and L_2. This concept is similar to the approximate elevation measurement techniques discussed previously, but extends the analysis to arbitrarily oriented aerial images without sacrificing accuracy. This analysis is called *space intersection* by collinearity.

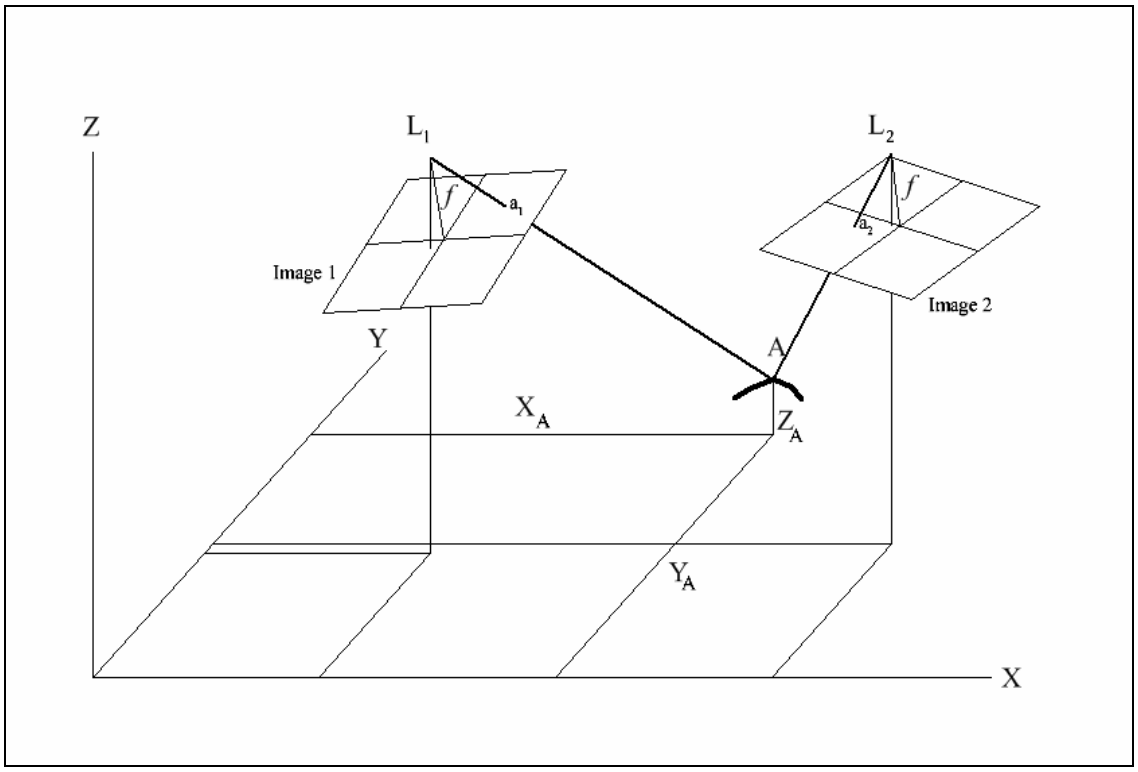

Figure 3.52 Geometry of stereo aerial images.

Space intersection by collinearity is extremely useful. It allows the determination of elevations and elevation differences throughout the area of overlap between two images with known exterior orientation. The preceding section showed that exterior orientation can be determined from camera data and as few as three measured ground control points. Space intersection of aerial images provides the ability to determine accurate three-dimensional coordinates of points in areas that are inaccessible or too costly to survey.

To implement space intersection, the collinearity Equations 3.58 and 3.59 are written for the *x* and *y* coordinates of target point **A** in each image, then the four equations are solved simultaneously with least squares analysis to yield the three unknown *X*, *Y* and *Z* real world coordinates. The Taylor Theorem least squares analysis is linearized with the same coefficients derived for the analysis of exterior orientation:

$$b_{14}dX_A + b_{15}dY_A + b_{16}dZ_A = J + v_{x_a} \quad 3.75$$

$$b_{24}dX_A + b_{25}dY_A + b_{26}dZ_A = K + v_{y_a} \quad 3.76$$

At first glance Equations 3.75 and 3.76 appear improperly reduced compared to Equations 3.67 and 3.68. The dω, dϕ, dκ terms are dropped because the Taylor Theorem linearization operates on the partial derivatives of the original collinearity equations; elements of orientation that do not change need not be represented. The terms dX_A, dY_A and dZ_A are retained because X_A, Y_A and Z_A are unknown and change ΔX, ΔY, ΔZ in the set of equations presented as Equation 3.70 (a-l). Following this simplification, the least squares solution of Equations 3.75 and 3.76 is developed much as it was for the analysis of exterior orientation.

The linearization again requires initial approximations for the unknown ground coordinates of the target point. These are developed from the simplified parallax equations for an assumed true vertical aerial image discussed previously. It is necessary to transform image centered coordinates of the simplified parallax analysis into the real world coordinate system that encompasses both aerial images as defined by the datum (UTM in this case) adopted for the external orientation parameters.

Again, there appears to be no public domain code of space intersection by collinearity for Matlab or other mathematical software. Moreover, useful examples are omitted from photogrammetry text books. The reason for this is probably because aerial mapping operates at a larger scale involving simultaneous solution of large blocks of images. This scaled-up approach may discourage potential users from outside the geomatics field from applying photogrammetry in less extensive applications. I have

found single stereo models of low altitude digital aerial images very useful and cost effective for the measurement of stream morphology and watershed analysis.

A Matlab code *Spaceintersect.m* that computes the three-dimensional coordinates of a single target point from a stereo pair is included in Appendix 3.4. As will be demonstrated, application of the code does not require the ability to observe the images in stereo or expensive photogrammetric software to achieve results of moderate accuracy. This code and the code for determination of exterior orientation should enable a motivated engineer or environmental scientist to test the usefulness of analytical photogrammetry for a particular application without a major commitment of time or resources. The usual cautions and disclaimers apply. No guarantee is made as to the suitability of the codes for any particular application. Their intent is purely educational.

3.4.4 Measurement of Elevation Difference by Space Intersection

Analytical space intersection is demonstrated with aerial images of Genesee acquired on February 22, 2004. Overlapped images 350 and 351 presented in Figure 3.53. Ground control points and the edges of overlap are superimposed on the images. Stereo overlap is approximately 65%. The images were acquired with a 17 mm focal length lens and corrected for radial lens distortion. Mean ground pixel resolution is approximately 0.38 m. Real world UTM coordinates of the ground control points were determined by visual matching of object points to the USGS/State of Idaho 2004 DOQ. Elevations were determined from the USGS 10-meter DEM. Points *P1* and *P2* are selected for photogrammetric measurement. Image coordinate measurements in pixels were made in ArcView GIS with the Image Analyst extension, but could have been made with digital photo editing software. Pixel coordinates were converted to image

coordinates in millimeters with a sensor pixel size of 7.39 μm. The image coordinate system in each image has its origin at the center of the image. Principal point offsets are assumed to be zero. Table 3.11 lists the image coordinates of the nine ground control points in the area of overlap.

	Left Image 350		Right Image 351		Left Image 350		Right Image 351		
	x	y	x	y	UTM X (N)	UTM Y (E)	UTM X (N)	UTM Y (E)	Elevation
ID	mm	mm	mm	mm	m	m	m	m	m
a	-1.70	-3.82	-6.30	-3.28	5155228.8	505272.4	5155228.8	505272.4	813.33
b	-0.29	-9.62	-4.96	-8.83	5155289.6	504989.6	5155289.6	504989.6	838.38
c	-1.83	2.55	-6.60	2.97	5155232.2	505600.4	5155232.2	505600.4	818.66
d	2.30	1.87	-2.73	2.40	5155442.8	505550.6	5155442.8	505550.6	842.58
e	-2.13	9.89	-7.05	10.28	5155229.8	505989.8	5155229.8	505989.8	813.12
f	0.25	5.86	-4.68	6.30	5155349.2	505764.6	5155349.2	505764.6	818.42
g	5.97	8.31	0.68	8.92	5155632.9	505856.1	5155632.9	505856.1	844.38
h	6.77	2.20	1.64	2.82	5155661.1	505556.7	5155661.1	505556.7	830.42
i	5.78	-9.46	0.80	-8.56	5155583.5	504996.2	5155583.5	504996.2	841.50

Table 3.11 Ground control points for aerial images of Genesee, February 22, 2004.

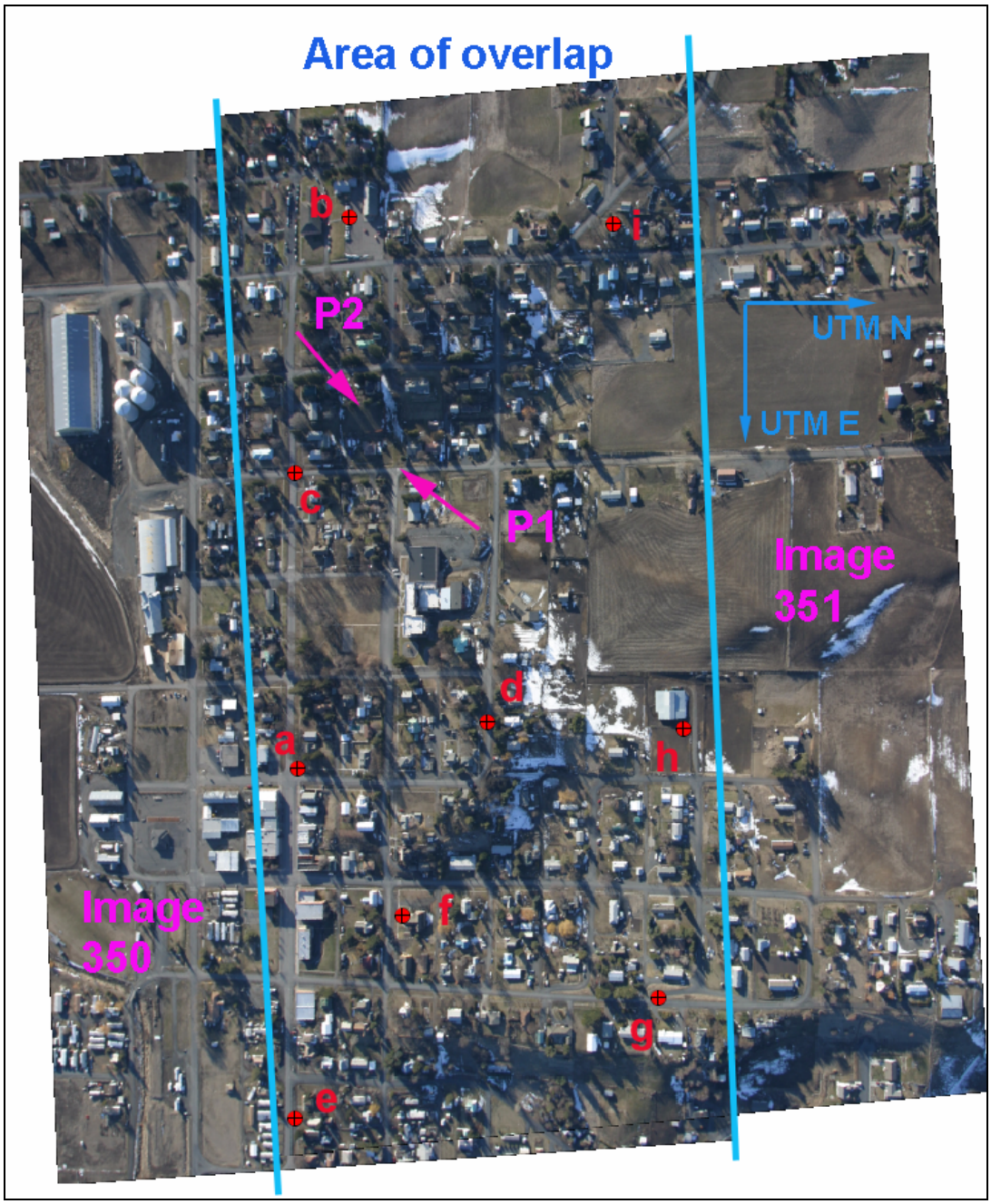

Figure 3.53 Stereo images of Genesee, ID, February 22, 2004.

The aerial images have been rotated so that the flight axis is approximately oriented with the *x*-direction from left to right. The images were acquired on a south to north flight line so the UTM northing direction coincides with the *x*-axis in the figure. The image coordinate system defined by the flight axis is adjusted with a two-

dimensional conformal transform in the space intersection code, so does not need to be parallel with the UTM grid.

Exterior orientation of both aerial images was computed from the nine control points with the Matlab code *Exgeo.m.* The computed exterior orientation parameters are listed in Table 3.12.

Image	Omega deg	Phi deg	Kappa deg	Camera E m	Camera N m	Camera Z m
Left 350	4.1434	1.4562	-2.4665	505,441.9	5,155,385.5	1685.39
Right 351	4.4604	0.3349	-3.7325	505,416.6	5,155,637.1	1680.78

Table 3.12 Exterior orientation parameters of aerial images 350 and 351.

Target points are selected for measurement. Points *P1* and *P2* in Figure 3.54 are the corner of the crosswalk stripe indicated and a small white marker panel, respectively. Figure 3.54 was rotate 90 degrees counter clockwise from Figure 3.53 for presentation purposes. The terrain slopes from *P1* to *P2*. It is important that ground points be clearly identified in both images so that the monoscopic image measurements are as precise as possible. Stereo viewing adds precision, especially when ground points are partially obscured. The *x* and *y* pixel location of each target point in each image is recorded and converted to millimeters referenced to the center of the image, defined as one half the image height and width. Target point coordinates for each image are listed in Table 3.13.

Image	Point	*x* coordinate mm	*y* coordinate mm
350 (left)	P1	0.587	-3.955
	P2	-0.201	-5.374
351 (right)	P1	-4.107	-3.364
	P2	-4.883	-4.759

Table 3.13 Target point image coordinates.

Figure 3.54 Locations of target points.

The exterior orientation parameters and target point coordinates are copied into three separate ASCII text file with the following forms.

Exterior geometry file *Gen_exgeo.dat*:

```
a   1.4562   4.1434   -2.4665   5155385.513    505441.8627   1685.3926
b   0.3349   4.4604   -3.7325   5155637.124   505416.621     1680.7846
```

Target point *P1* file *Gen_target1*.dat:

```
p1L   0.587    -3.955
p1R  -4.107    -3.364
```

Target point *P2* file *Gen_target2*.dat:

```
p2L   -0.201   -5.374
p2R   -4.883   -4.759
```

It is important to list values for the left image first in the text files as this is the order assumed by the arrays in the code. As discussed in Section 3.4.1, the y-axis of the image centered coordinate system for this particular set of images must increase in the downward direction because the UTM easting coordinate increases in the downward direction in the rotated images.

The Matlab code *spaceintersect.m* is modified to include the files as named and the proper lens focal length, 17 mm in this case. The code is run twice, once for P1 and once for P2. The computed real world coordinates for the point are displayed on screen after each run. Results of the space intersection computations are in Table 3.14.

Points	UTM E m	UTM N m	Elevation m
P1	505260.9	5155344.0	814.35
P2	505192.8	5155301.7	824.11

Table 3.14 Real world coordinates UTM and elevations of the target points.

The points are separated by a horizontal distance of 80.2 m and an elevation difference of 9.76 m. The actual horizontal distance measured with a cloth tape corrected for slope was 79.3 meters and the elevation difference was 8.66 m when determined by a slope angle measured with a one-minute transit. The elevation error is 1.06 m assuming correct transit and tape measurements.

A definite conclusion about the accuracy of this particular stereo model is not possible with a single measurement, but it is evident that the analytical photogrammetric methods are capable of moderate precision with a cost-effective level of effort. It is important to emphasize that none of the ground control point UTM coordinates or elevations were measured in the field. All coordinate and elevation data was obtained from the DOQ and DEM. The USGS 10-meter DEM elevations of the points were 815.2 m and 825.0 m, a difference of 9.8 m, relatively close agreement with the elevations measured from the stereo model.

The accuracy of the photogrammetric computations is dependent on the accuracy, number and distribution of ground control points. Results from the Genesee example are better than can be expected for some field settings encountered in this research. There is

both science and art in the selection of ground control points from USGS DOQs and DEM to maximize the accuracy of photogrammetric measurements made in high-resolution digital aerial imagery. This would be a beneficial area of future research.

3.4.5 Reported Accuracy of Elevation Measurements with Stereo Digital Aerial Images

Impressive values of accuracy have been reported for non metric photographic digital cameras in stereoscopic aerial applications using the methods of analytical photogrammetry. Journal articles report accuracies within 0.3 m RMS horizontal and 0.5 m RMS vertical in tests with good ground control (Fraser 1997; Mason et al. 1997; Mostafa and Schwarz 2001). Literature related to camera calibration and the determination of relative orientation consistently cite sub-pixel analytical accuracies under controlled conditions (Fraser 1997; Habib and Kelle 2001; Heipke 1997; Krupnik and Schenk 1997; Tang et al. 1997). While the statistics are indeed impressive, critical studies of the photogrammetric accuracy of digital photographic cameras are far from exhaustive. Concerns remain about flexing, shifting and unevenness of CCD arrays leading to image distortion and inconsistent interior orientation (Clarke. and Wang 1998; Shortis et al. 1998). Practical accuracy assessment of stereo digital aerial images under varying flight and terrain conditions appears to be a beneficial and relatively open area of applied research.

3.4.6 Photogrammetry in Other Disciplines

Other disciplines show growing interest in the photogrammetric capabilities of relatively low-cost high-quality photographic digital cameras. Photogrammetry is widely applied in close-range terrestrial imaging, architectural photography, archeology, vision metrology, machine vision, computer vision, and medical imaging. The related literature shows analytical sophistication and three dimensional accuracies moving towards that described in the aerial imaging literature. See for example Robson and Shortis (1998), Wang and Clarke (2001) and Chandler et al.(2005). Doubt is expressed whether close-range techniques can achieve the accuracy proven and expected in high precision aerial photogrammetry (Mikhail et al. 2001).

3.4.7 Analytical Relative Orientation

In the examples above, exterior orientation of the aerial images was determined independently with analytical space resection. It is often desirable to perform the orientation analysis simultaneously for both images in the stereo model without the need for ground control in real-world coordinates. The parameters of external orientation for one camera are defined relative to the other to form a relative *stereo model* in a process called *analytical relative orientation*.

Once camera rotation angles and relative center positions are known, the relative stereo model can be scaled with real world ground control points to enable the measurement of three dimensional coordinates of virtually any point visible in both images. At least five inter-visible ground points are necessary to develop the relative

stereo model. Six or more points allow least squares solution of the orientation parameters (Wolf and Dewitt 2000).

Initial approximations must be estimated for the parameters of relative orientation. A reasonable assumption is that the left image of the stereo pair and the principal distance of the left image (distance from the rear node of the lens to the image plane) is equal to the nominal focal length.

Analytical relative orientation is demonstrated with the aerial images of Genesee in Figure 3.53. The same ground control points are utilized, but only the image coordinates are necessary for the relative orientation (Table 3.15).

	Left Image 350		Right Image 351	
	x	y	x	y
ID	mm	mm	mm	mm
a	-1.70	-3.82	-6.30	-3.28
b	-0.29	-9.62	-4.96	-8.83
c	-1.83	2.55	-6.60	2.97
d	2.30	1.87	-2.73	2.40
e	-2.13	9.89	-7.05	10.28
f	0.25	5.86	-4.68	6.30
g	5.97	8.31	0.68	8.92
h	6.77	2.20	1.64	2.82
i	5.78	-9.46	0.80	-8.56

Table 3.15 Image coordinate data for analytical relative orientation.

A least squares analysis of the analytical relative orientation was performed by matrix analysis of the nine ground control points. Computational results are summarized in Table 3.16.

Parameter	Left Image		Right Image	
Omega ω, degrees		0		-1.3398
Phi ϕ, degrees		0		0.5420
Kappa κ, degrees		0		-1.3270
Camera X, mm		0		4.9244
Camera Y, mm		0		-0.2085
Camera Z, mm		17		17.2657
Control Point	**x residual mm**	**y residual mm**	**x residual mm**	**y residual mm**
a	-0.0001	-0.0026	0.0001	0.0026
b	0	-0.0001	0	0.0001
c	0.0001	0.0034	0	-0.0035
d	0.0001	0.0032	0	-0.0032
e	0	-0.0015	0	0.0015
f	0	-0.0019	0	0.0020
g	0	0.0026	0	-0.0026
h	-0.0002	-0.0046	0	0.0046
i	0.0001	0.0012	-0.0001	-0.0013
Root mean square	0.0001	0.0027	0.0001	0.0027

Table 3.16 Results of least squares analysis of relative orientation.

The largest relative angular rotation (ω) between the sensors in the horizontal plane is -1.34 degrees. The principal distance for the right image is 17.3 mm. The distance between camera sensor centers in the x direction is 4.9 mm in image space. This distance is approximately equal to the photobase. The ratio of photobase to the principal distance is 3.73 and is an indicator of stereo exaggeration. Residuals of the ground control points in the *x* direction are low because this is the direction of flight and *x*-parallax determines elevation difference in the collinear analysis. Residuals in the *y* direction are an indicator of unwanted *y*-parallax and potentially uncomfortable stereo viewing. A root mean square of the *y*-parallax residuals less than 5 μm (.005 mm) indicates a good relative orientation solution (Wolf and Dewitt 2000). The root mean square of the *y* residuals in Table 3.16 is 3 μm, a reasonably good solution.

An analysis of relative orientation was repeated with the original aerial images that were not corrected for radial lens distortion. The root mean square of the *y* residuals was 9 μm, indicating the importance and effectiveness of the lens correction model.

Analysis of relative orientation provides a good check on the effectiveness of the distribution of control points prior to field work when ground control is collected from natural points. It is also essential in extending an efficient form of collinearity analysis to multiple images along a flight line or a large block of images.

3.4.8 Analytical Photogrammetry of Multiple Stereo Aerial Images

Aerial topographic mapping and production of large digital orthoimages requires the analysis of many, possibly hundreds of aerial images. While it possible to construct a number of sequential stereo pair models to cover a larger area, the process becomes cumbersome and expensive. Individual stereo pair models require a minimum of two ground control points with three dimensional coordinates and a third point with at least elevation data. Field survey control for a large aerial mapping project is a substantial portion of total project cost and greatly increases the time required to develop a topographic coverage. Better methods were sought and developed.

The space intersection example above demonstrated how real world coordinates of a ground point can be determined by photogrammetry. *Aerotriangulation* extends the collinearity intersection analysis to multiple points across many images. There are different methods to perform aerotriangulation. A few are of historical interest from the days of mechanically based analog photogrammetry. Descriptions of analog techniques are found in photogrammetry text books (Wolf and Dewitt 2000, Mikhail et al. 2001).

The two prevalent current methods are simultaneous block adjustment of independent stereo models and simultaneous bundle block adjustment. Terminology varies among writers, but adjustment means the final correction of the relative orientation of a group of images into absolute coordinates of the real world coordinate system.

Triangulation and adjustment applies only to discrete points in the area of overlap between adjacent stereo pairs and the narrow fringe of overlap between flight lines. Aerotriangulation is not equivalent to image processing; it is more like land surveying. Image rectification, as in production of an orthorectified aerial mosaic, is performed based on parameters obtained from the adjusted ground control points in a manner similar to that demonstrated for correction of lens distortion. A possible layout of stereo models and shared control points readied for aerotriangulation is given in Figure 3.55. Note that the rectangular regions in Figure 3.55 are only the areas of overlap and not the outlines of the full images.

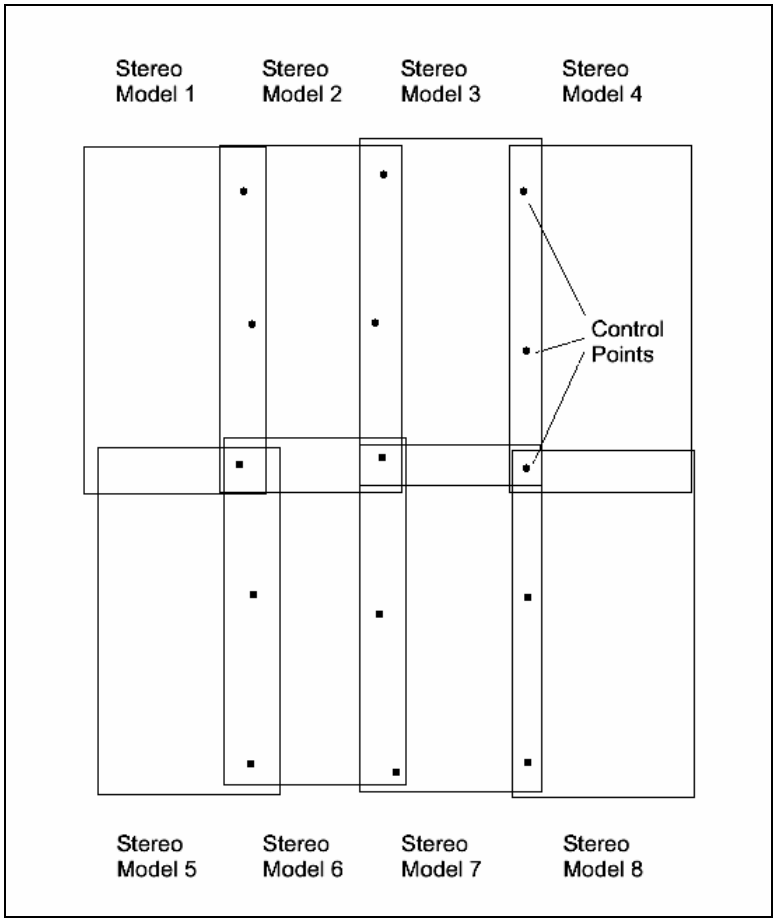

Figure 3.55 Block of independent stereo models.

Figure 3.55 represents eight independent stereo models. If three full ground control points were available for the first model, it would be computationally possible to sequentially pass real world coordinates along the strip and through the block. This is not a good practice because small errors accumulate to warp the solution. A better solution is to simultaneously adjust the block of contiguous stereo models. This called simultaneous block adjustment.

The mathematical basis of the simultaneous block adjustment is the three-dimensional conformal coordinate transformation:

$$\begin{aligned} X &= s\left(m_{11}x + m_{21}y + m_{31}z\right) + T_X \\ Y &= s\left(m_{12}x + m_{22}y + m_{32}z\right) + T_Y \\ Z &= s\left(m_{13}x + m_{23}y + m_{33}z\right) + T_Z \end{aligned} \qquad 3.77$$

where X, Y, Z are the transformed real world coordinates of image space coordinates x, y, z; the m coefficients are elements of the rotation matrix previously defined; s is a scale parameter; and T_X, T_Y, T_Z are translation parameters. For any particular stereo model, there are seven unknowns: the rotation angles ω, ϕ, κ ; the three translation parameters; and the scale factor. Thus, the block of eight stereo models in Figure 3.55 would have 56 unknowns in the simultaneous solution.

In theory, solution of Equations 3.77 is obtained with two control points with three real world dimensional coordinates and another vertical control point for the entire block. The additional observation equations needed for the solution come from the common *pass points* between the independent stereo models along a strip and the perspective centers (camera station) of each model. Points common to adjacent strips in a block of images are *tie points*. In practice, additional real ground control points allow a

least squares solution of a Taylor series linearization of the normal equations. The solution approach is conceptually similar to that demonstrated for determination of exterior orientation, but is greatly expanded because of the additional stereo models. This block adjustment method may be partially performed with analog (mechanical) stereoplotting instruments. More complete descriptions of the mathematical adjustment process are given in Wolf and Dewitt (2000); and Mikhail et al. (2001).

3.4.9 Simultaneous Bundle Block Adjustment

More accurate solutions are possible with a process called simultaneous bundle block adjustment, currently the state of the art in photogrammetry. A bundle is the projection of light rays from real world objects through the projection center to the image sensor. Bundle block methods treat the bundles of each aerial image as the computational element.

Wolf and Dewitt (2000) report routine horizontal accuracies of 1:15,000 of flying height and vertical accuracies of 1:10,000 of flying height with large format aerial mapping cameras. Accuracies as high as 1:350,000 horizontal and 1:180,000 vertical have been achieved. The routine accuracies of a typical NAPP aerial image flown at 6000 m (20,000 ft) above terrain processed by simultaneous bundle block adjustment would be 0.4 m horizontal and 0.6 m vertical.

The bundle block simultaneous solution is completely analytical and can accommodate any flying height, focal length and orientation. Most methods are based on the collinearity equations augmented with additional parameters to adjust for systematic camera bias (interior orientation). The full computational procedure is more complex and

lengthy than the previous methods, but generally consists of two phases: relative orientation in model space and absolute orientation in the real world coordinate system.

Ultimately, the mathematics of bundle block adjustment derives from the basic computational procedures of exterior orientation (space resection), interior orientation (camera calibration), space intersection, and relative orientation. Further refinements are necessary to assure validity of the computations. A weighting scheme of image coordinates is applied in the least squares solution and matrices are manipulated for efficient computation. Statistics of the computations must be evaluated to judge the precision of the final solution. Accuracy of the computed ground control coordinates must be ascertained by comparison with *check point* data not used in the adjustment process. Wolf and Dewitt (2000); and Mikhail et al. (2001) describe the overall approach to bundle block adjustment. A particularly good overview article is by Heipke (1997). Many details of computational algorithms in commercial photogrammetric software are proprietary.

Ease of implementation of the bundle block adjustment process from the viewpoint of the user is of practical interest because it directly influences the cost of producing a photogrammetric product and would influence its use in applied research. Most of the analyst's effort is in selection of ground control points and pass points between stereo models. This is done while viewing the models in stereo with photogrammetric software. In general, a greater number of well-distributed control points and pass points increases accuracy of the least squares solution. A good solution may require hundreds of individual pass points. Digitizing so many points is costly and

subject to blunders. Fortunately, operator effort can be greatly reduced in many situations by automated selection of pass points.

Some form of automatic image matching (image correlation) technique is implemented in most commercial photogrammetric software. Image correlation algorithms examine the pixel structures in matching images to identify groups of pixels that have a high probability of correspondence. An automatic pass point is set when a match exceeds a specified threshold criterion. Image matching may be based on area, features (points and edges) or the structure of relationships between features. Image matching is an area of academic research (Hannah 1989; Mustaffar and Mitchell 2001; Wang 1998).

3.4.10 GPS/IMU Aided Bundle Block Adjustment

Field survey of ground control points is a large part of aerial mapping cost even with bundle block adjustment. Ground survey may be prohibited in some areas because of legal access restrictions. The collinearity equations for space intersection reveal a very useful and technologically viable alternative: positions of ground points can be triangulated from the real world coordinates and rotation angles of airborne camera stations. The theory of triangulation from moving airborne platforms has been known for some time (Schwarz et al. 1993), but is now more practical because of advances in kinematic geographic global positioning (GPS) and inertial measurement unit system (IMU) equipment. Positions interpolated from the GPS antenna become observed quantities in the bundle adjustment. A GPS antenna is typically located on the exterior of the aircraft so an adjustment must be made from the antenna position to the projection center (camera station). Kinematic GPS has revolutionized many types of engineering

survey. The theory of kinematic GPS and inertial navigation is explained and well illustrated in monographs (Farrell and Barth 1999) and land surveying texts (Wolf and Brinker 1994).

Camera rotation angles are recorded by the inertial measurement unit (IMU). An IMU is a combination of microelectronic gyros and accelerometers. Gyros report the attitude (angular orientation) of the sensor at high accuracy and frequency. Accelerometers measure instantaneous accelerations in the orthogonal directions. Twice integrating the acceleration data gives the distance traveled during a sampling interval. Accelerometer distance information is combined with GPS data to resolve positional ambiguities caused by temporary loss of GPS signals. Integral IMU computations are subject to drift and cannot reliably determine position over long distances. The joint GPS/IMU solution has proven to be highly reliable. Resulting sensor position and orientation at the instant of camera exposure are applied in the least squares bundle block adjustment. Direct georeferencing of images with GPS/IMU data without supplemental ground control is possible and reported to achieve accuracies of around 0.2 m (Jacobsen and Mostafa 2001). Due to high cost, kinematic GPS and IMU equipment were not tested or applied in the dissertation research.

3.4.11 Analytical Photogrammetry Software

In the course of the research I have used digital photogrammetry software products of varying capabilities from several commercial vendors, but there are many I have not experienced. I am reluctant to describe the operation of any product or recommend any particular package. There are many fine products and virtually all will perform the relatively simple tasks demonstrated below. Unlike GIS software which is

dominated by a single vendor, numerous equally competent digital photogrammetry software packages are available from vendors in North America, Europe and Australia. Functionality, efficiency of use, and the quality of the documentation and training support are contingent upon product price which can exceed $10,000 for reasonably functional systems. To this must be added the cost of computer workstations, high quality digital printers, and stereo viewing equipment. Persons or institutions wishing to invest in photogrammetry software should understand that pre-purchase evaluation is not a small or effortless task.

Operational details vary between photogrammetric products, but the sequence of operations is consistent. Development and measurement of a stereo model involves the following steps:

- Define the project area: enter identify project information, define datums, specify location of images, define directory structure for working files, and other data.
- Prepare the images: select the best image sequence if multiple passes were made over the target area, apply lens correction for independent stereo model adjustment (not necessary for block bundle adjustment), possibly rotate and convert color images to grayscale to speed processing.
- Define camera properties: specify focal length, coordinates of fiducial marks and principal point offsets.
- Interior orientation of the images: manually digitize the locations of fiducial marks in the images.

- Exterior orientation of images: manually digitize ground control coordinates and specify point elevations.
- Identify the strip or block of images to process and possibly manually select representative pass points to localize the automatic image matching search areas.
- Perform automated pass point identification.
- Perform bundle block adjustment.
- Examine and critique the bundle block adjustment statistics.
- Load the stereo model created by the bundle block adjustment into the stereo image display program.
- Make manual measurements of object point horizontal coordinates and elevations while viewing the images in stereo.

In addition to the above, many photogrammetric software products perform stereo correlation throughout the area of overlap and automatically extract elevations to produce a digital terrain model (DTM). An orthoimage mosaic can then be constructed from rectified images of the stereo model.

Analytical photogrammetry was applied in many aspects of the dissertation research from validation of sensor geometric accuracy, determination of overland flow slope for stormwater runoff and erosion modeling, preliminary storm drainage design, accuracy assessment of published elevation data, solar radiation modeling for snowmelt, assessment of stream morphology, and small area terrain modeling. Each would require a full section in the dissertation document to fully describe. Three examples will

demonstrate a few of the possible applications and give the reader an impression of the efficiency, benefits and limitations of the techniques.

3.4.12 Measurement of Point Elevations with Analytical Photogrammetry

Bundle block adjustment was performed on images 349, 350 and 351 of the now familiar February 22, 2004 aerial images of Genesee, Idaho. Ground control points were the same as those in the space intersection example above plus three additional ground points in image 349. The adjustment process produced parameters for stereo models of the area of overlap area of images 349 and 350 and 350 and 351. This allowed stereo measurements throughout image 350. The stereo model 349-350 was viewed on screen with the stereo display module of the photogrammetric software. Figures 3.56 and 3.57 are screen "captures" from the onscreen display showing the stereo cursor placed on point *P1*. Figure 3.56 is a grayscale stereo view and Figure 3.57 is a red-left, blue-right anaglyph image. Some *y*-direction parallax is evident outside the immediate area of the stereo cursor in the anaglyph. The y-parallax is adjusted automatically as the stereo cursor is moved to different locations in the model.

Figure 3.56 Grayscale view of stereo model 149-150.

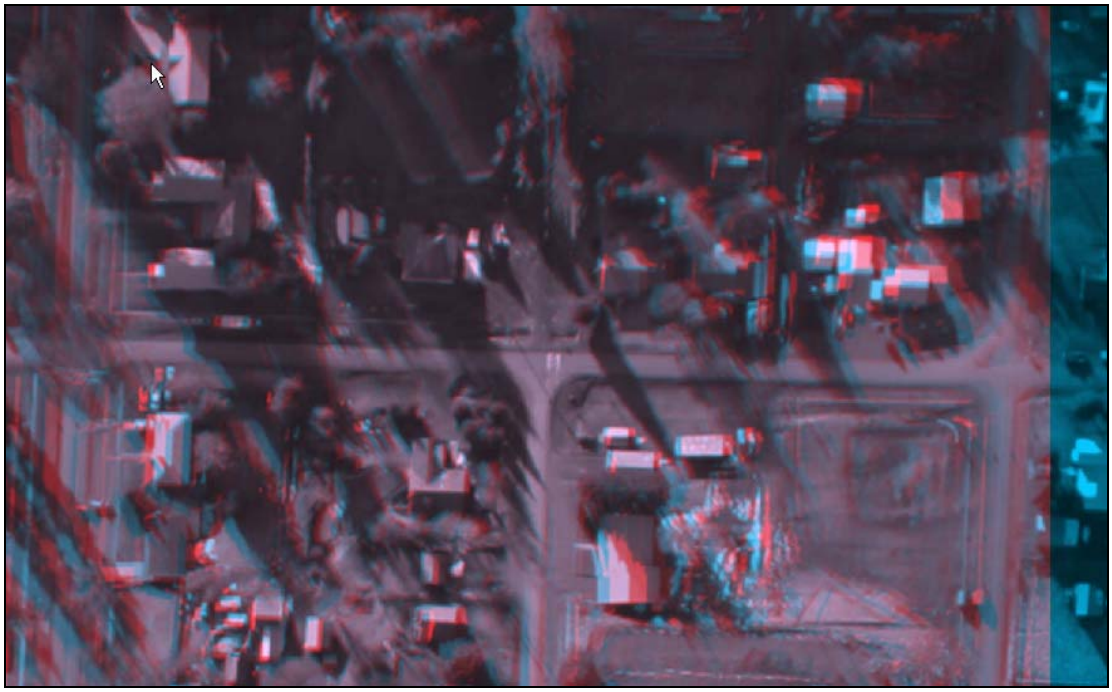

Figure 3.57 Red blue anaglyph view of stereo model 149-150.

Points *P*1 and *P2* of the space intersection example were measured by placing the floating stereo cursor on each point and recording the displayed three dimensional

coordinates displayed by the photogrammetric software. Point coordinates measured in the bundle block adjusted stereo model are compared with the coordinates obtained from the manual space intersection measurement in Table 3.17. Elevation difference from the bundle block adjustment method was 8.82 m while the manual method elevation difference was 9.76 m. The elevation difference measured with the one-minute transit was 8.66 m. As expected, the bundle block adjustment method provides a more accurate measurement of the elevation difference. Again, it should be stated that the horizontal coordinates and elevations of the ground control points were estimated from the 1994 DOQ and USGS 10-meter DEM. The accuracy of the bundle block adjustment will depend on the accuracy of the ground control points and the methods to estimate them.

	Manual Space Intersection			Bundle Block Adjustment		
	UTM E	UTM N	Elevation	UTM E	UTM N	Elevation
Points	m	m	m	m	m	m
P1	505260.9	5155344.0	814.35	505261.9	5155341.5	819.51
P2	505192.8	5155301.7	824.11	505193.4	5155303.1	828.33

Table 3.17 Comparison of target point coordinates measurements.

Stereo depth perception of digital displays of aerial imagery is a skill that takes considerable work to acquire and refine. Skill levels will vary among operators. It is advisable for new stereo analysts engaged in making critical measurements to be trained and supervised by experienced operators until achieving an acceptable level of competence. Measurement by stereo observation is always somewhat subjective. Whenever possible, stereo measurements of elevation should be compared to field measurements.

3.4.13 Measurement of Stream Channel Cross Sections for Flow Modeling

Analysis of alluvial stream morphology was a main research topic in the dissertation (Section 6). Stereo high-resolution digital aerial images of alluvial channels and floodplains and photogrammetric software are very useful for detecting and analyzing morphological change. Many streams in the Pacific Northwest are dangerous to access, logistically difficult, or practically impossible to survey with field techniques. Even when feasible, ground surveying takes considerable time. Following floods it is often desirable to assess the impact and potential hazard of changed alluvial morphology on private property, infrastructure and habitat throughout a region. The following example demonstrates that a stereo model of moderate precision can be developed from aerial reconnaissance imagery in a few hours without field ground control.

High-resolution digital aerial images of the Potlatch River at Centennial Park near Juliaetta, Idaho were acquired on October 27, 2004 at a discharge of 64 $ft^3\ s^{-1}$ (1.8 $m^3\ s^{-1}$). Overlapping images in Figure 3.58 provide stereo coverage at a ground pixel resolution of 0.28 m. Most of the channel is exposed at this flow. The water was clear so below-surface depths could be visually estimated.

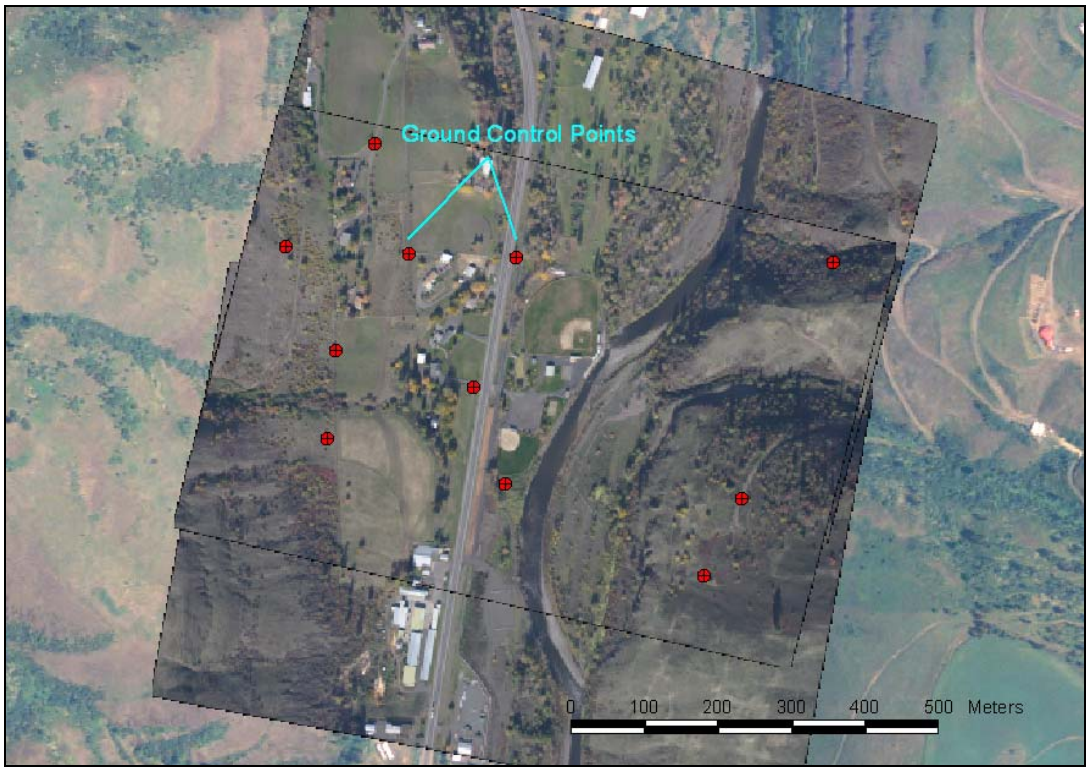

Figure 3.58 Stereo aerial imagery of Centennial Park October 27, 2004.

At high discharge the flow in the main channel impinges upon the softball field. Historic aerial images show that the main channel once occupied the ball field area. City officials are concerned the ball field will be eroded by floodwaters and had the channel bank reinforced with shotcrete riprap (Figures 3.59 and 3.60). Moderate discharges are constrained between the relatively immovable bank reinforcement and the steep canyon slope on the opposite side of the channel. Hydraulic head must build to force flows through the constriction causing deposition of cobble and gravel.

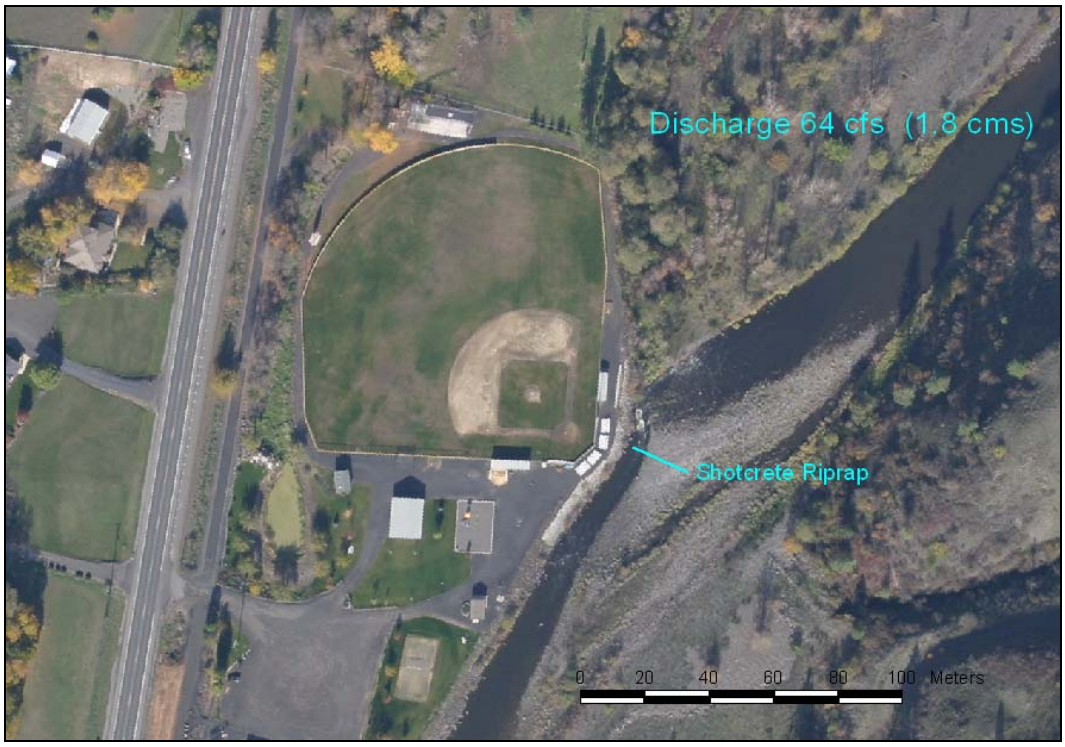

Figure 3.59 Channel bank reinforcement at the softball field (aerial).

Three-dimensional coordinates of the ground control points in Figure 3.58 were obtained from the 1994 USGS/State of Idaho DOQ and the USGS 10-meter DEM. No ground control points were field surveyed. Stereo models were developed by bundle block adjustment and ground points measured at break points along the cross section lines in Figure 3.61. Spacing of the cross sections is about 50 meters. The cross section at station 102.9 is in Figure 3.62. Cross sections are viewed facing downstream.

Figure 3.60 Channel bank reinforcement at the softball field (ground).

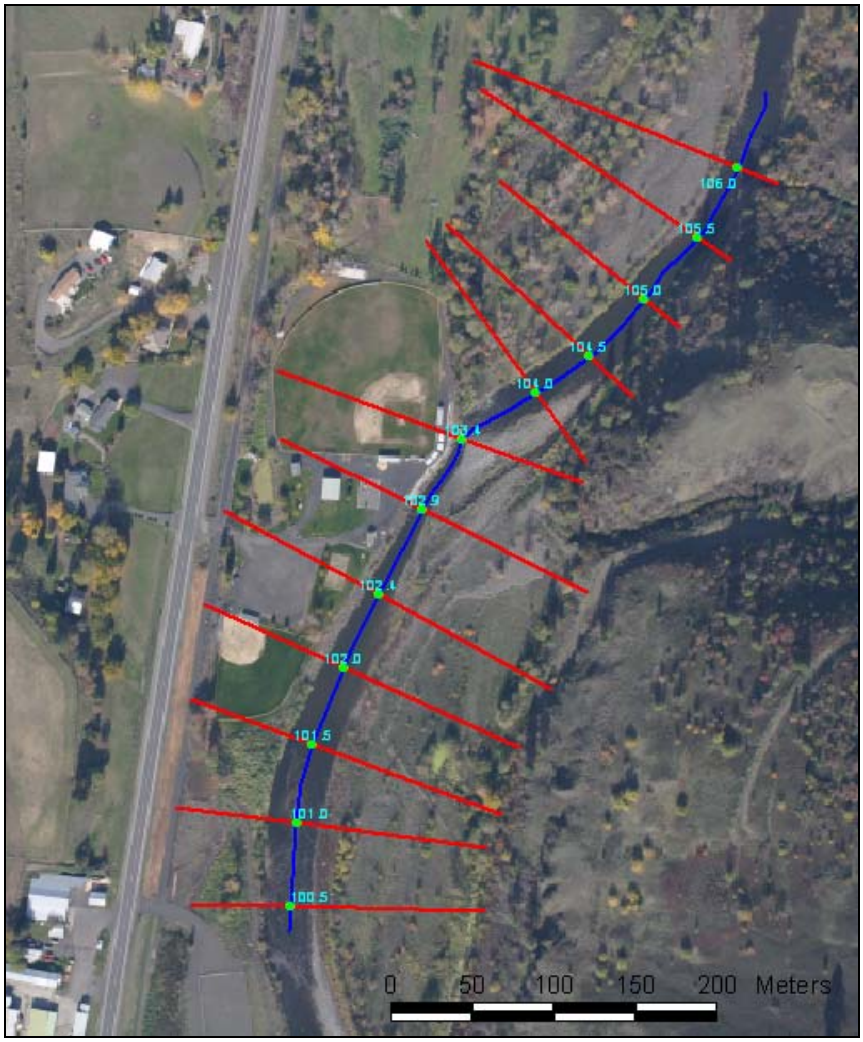

Figure 3.61 Stream channel and floodplain cross section locations.

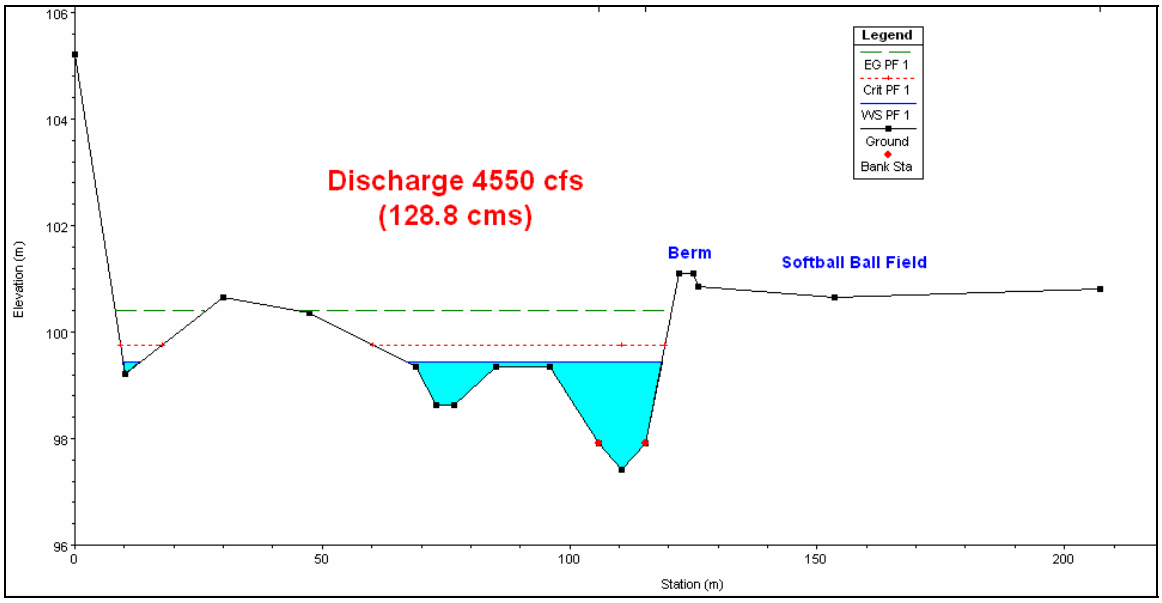

Figure 3.62 Channel cross section at Station 102.9

Photogrammetric methods generally lack the precision necessary to estimate water surface slopes of moderate gradient channels. An error of 0.5 meter over a 500 meter length of channel produces a 0.001 change in slope which is hydraulically significant for streams of moderate slope. Channel slope must be estimated by another technique.

A simple, though effective, method of estimating channel slope with no field survey data is as follows:

- Determine the overall mean channel slope in the vicinity of the target reach from contour intervals on the USGS topographic quadrangle map or USGS 10-meter DEM. A reach length of between 1 and 2 km is sufficient. Avoid measuring across obvious channel discontinuities such as falls or chutes. The aerial image sequence will help identify discontinuities not noted on the USGS topographic

quadrangle. Base high and low estimates of channel slope on the standard accuracy of one-half contour interval.

- Apply the mean channel slope to the model reach and compute a preliminary edge-of-water longitudinal profile. Begin and end the model reach at similar morphological structures; for example the midpoint of riffles as in Figure 3.61. Determine the overall elevation drop across the reach.
- Observe the aerial images in stereo and identify significant breaks in channel slope such as the downstream face of transverse bars or the channel construction in Figure 3.61. Measure the edge-of-water elevation difference across the relatively abrupt change in slope. It does not matter if the elevation difference measurement is highly accurate. What matters is the relative elevation difference among channel segments. The intent is to identify the segments of the reach that comprise most of the total elevation drop. Bar faces and riffles are steeper than pools or glides so will consume most of the elevation drop in a low flow reach. The result of this analysis will be tabulation of the relative elevation drops for each segment along the reach. These may be called relative elevation drops or parallax weights in recognition that the actual measured elevations may not be sufficiently accurate for direct computation of channel slope.
- Partition the total reach elevation drop among the segments based on the parallax weights observed in the aerial images.

- Recompute the edge-of-water profile with the weighted elevation drops. Adjust the cross section data measured in the stereo images so the edge of water elevation in the cross section is equal to the computed water surface profile.
- Visually estimate the water depth in the stereo images and adjust the channel bottom midpoint depth down from the edge-of-water elevation. Generally there is insufficient observable detail for a parallax measurement in the bottom of the channel, but changes of color and surface turbulence give visual clues that enable a reasonable estimate of depth. Morphological methods may also be applied.

The overall mean slope in the vicinity of the Centennial Park reach obtained from the USGS 10-meter DEM was about 0.006 plus or minus 0.001 over a distance of 1750 m. A value of 0.0051 was assumed in the profile computation for a conservative analysis of flood hazard. The model reach length is 550 m so the total elevation drop was 2.83 m. The low flow channel observed in the aerial imagery is significantly steeper at the transverse bar near the constriction. Relative segment weights in Table 3.18 were applied to compute the final edge-of-water profile plotted in Figure 3.63. It is best to avoid being overly analytical in assignment of segment weights. This is a subjective engineering judgment that depends on an ability to visualize flow patterns at higher discharges. As will be seen, high discharge aerial images are a valuable check on model assumptions.

Station	Parallax Weights	Elevation Change m	EOW Elevation m
106.0			99.83
105.5	0.0636	0.18	99.65
105.0	0.0601	0.17	99.48
104.5	0.0636	0.18	99.30
104.0	0.1201	0.34	98.96
103.4	0.1943	0.55	98.41
102.9	0.1767	0.50	97.91
102.4	0.0742	0.21	97.70
102.0	0.0601	0.17	97.53
101.5	0.0636	0.18	97.35
101.0	0.0601	0.17	97.18
100.5	0.0636	0.18	97.00
Total	1.0000	2.83	

Table 3.18 Segment weights and edge-of-water profile elevations.

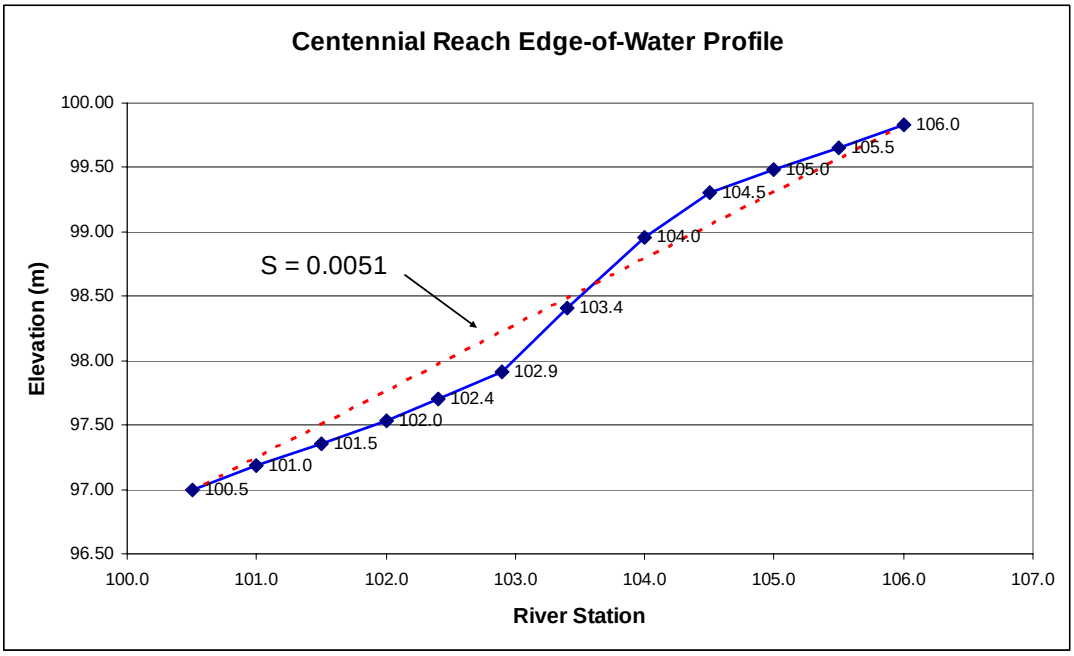

Figure 3.63 Edge-of-water profile for the Centennial Reach.

Cross channel changes in elevations are not as subtle as those along the channel. Hydraulic computations are dependent on the section properties of wetted perimeter, hydraulic radius and cross section area. Each of these elements depends on horizontal measurements as well as depth. Horizontal position measurements in stereo models may be assumed to be accurate because the relatively small horizontal error (around 0.5 meter)

has little effect on the computed section factor of moderately sized streams. Stereo measurements of depth are usually more accurate outside the wetted channel because details for stereo observation of height difference are more prevalent. Errors in parallax measurements are reduced and tend to offset one another across the cross section line. This conclusion is based on qualitative assessment. Additional research could formally test the assertion.

Cross section point elevations measured in the stereo imagery were adjusted to the edge-of-water profile. A mid channel bottom elevation was computed by subtracting the apparent water depth from the edge-of-water elevation. No water depths observed in the low flow imagery were greater than 1 meter. The data for the 12 cross sections was entered into the Corps of Engineers Hydraulic Engineering Center River Analysis System (HECRAS) model and a range of stream steady flow discharges were evaluated assuming rigid channel boundaries and a mixed flow regime. A typical Mannings *n* value of 0.032 was assumed for cross sections and not varied. Use and operation of the HECRAS model is described in Corps of Engineers documentation provided with the model (USACE 1995).

The initial run of the model was at a steady flow discharge of 1820 $ft^3\ s^{-1}$ (51.5 $m^3\ s^{-1}$), the discharge of the Potlatch River during a hydrologic reconnaissance flight on January 31, 2004. Edge-of-water lines were extracted from the HECRAS data summary and superimposed on the high-resolution digital aerial image in Figure 3.64. The water surface area and edge-of-water location is predicted reasonably well by the model. The-edge-of water line does not fully represent the flow around the mid channel bar. Figure 3.65 from HECRAS cross section display shows flow in the lateral channel

at 1820 ft^3 s^{-1} as observed in the aerial image. The width of flow is somewhat overestimated near station 100.5, but the dark tone of the lateral bar indicates that it was recently inundated at a slightly higher flow. It is important to realize that there has been no calibration of the model and that the elevation data was determined solely from the stereo images augmented with elevation data from the existing USGS DEM and topographic quadrangle. There was no field survey work involved.

Figure 3.64 Aerial image of the Centennial Reach, January 31, 2004.

The water surface profile for the 1820 ft^3 s^{-1} discharge in Figure 3.66 passes through critical flow at the constriction. Supercritical velocities are dissipated in a gradual hydraulic jump as the channel slope becomes less steep downstream. The aerial image in Figure 3.64 clearly shows the turbulent water surface at the transition through critical depth and the dissipation of energy through the jump. Flow patterns observed in

the high discharge aerial image provide an independent check on the ability of the model to represent real flows.

Several parameters important for water quality modeling and sediment transport can be extracted from HECRAS results. Reach travel time at a discharge of 1820 $ft^3\ s^{-1}$ is 4.9 minutes and reach average velocity is 2.17 m s^{-1} (7.11 ft s^{-1}). Average bed shear stress is 76.7 N m^{-2} and average stream power is 271 N $m^{-1}\ s^{-1}$.

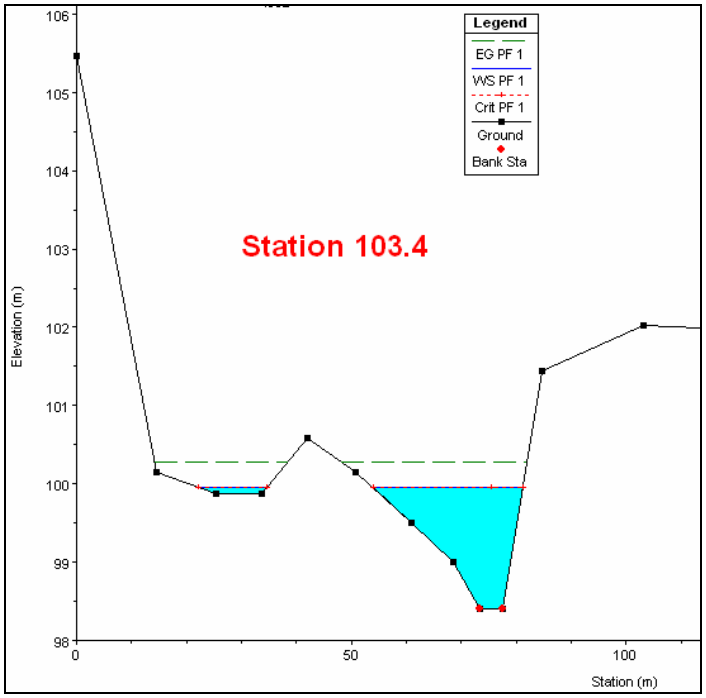

Figure 3.65 Cross section at station 103.4 for discharge of 1850 cfs.

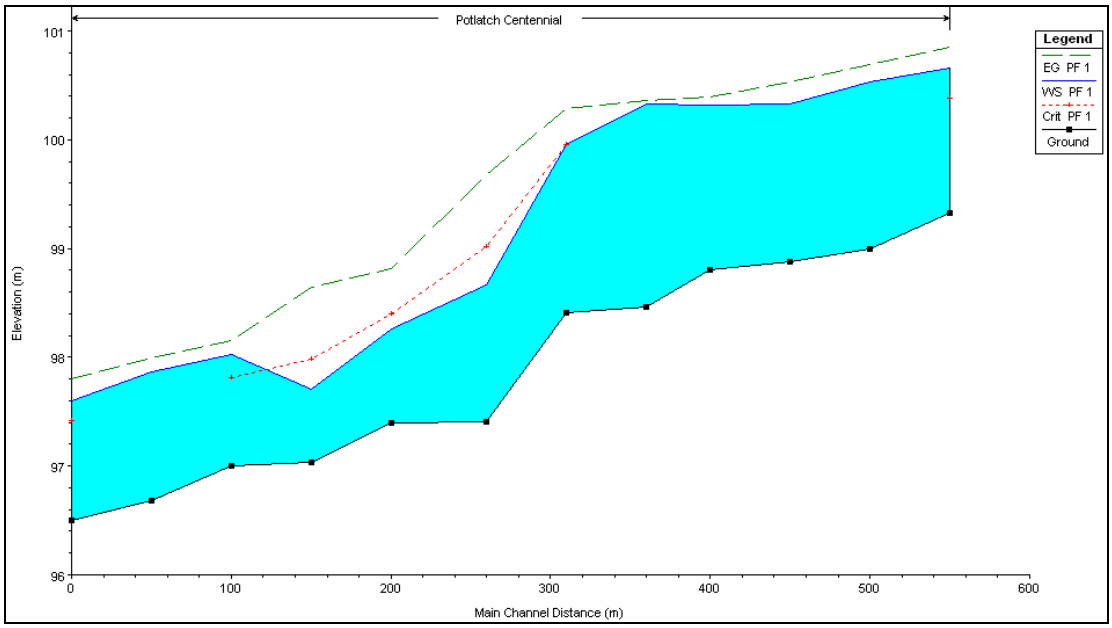

Figure 3.66 Water surface profile for the Centennial Reach at a discharge of 1850 cfs.

The length of the jump is overestimated by the model. Additional interpolated sections should be added to the model to satisfy suggested modeling criteria and clear warning statements from the model recitation. This was not done in this example to demonstrate the usefulness of the uncalibrated model. The model could be calibrated to better match the observed flow surface by adjusting the computed channel slope, channel depth, cross section spacing, and roughness. Several high flow aerial images would provide further information to fine tune the cross section elevations. Development of a formal least squares adjustment process of model parameters utilizing imagery data will likely be pursued in future research.

The uncalibrated model of the Centennial Reach was run again at a steady flow discharge of 4550 $ft^3\ s^{-1}$ (129 $m^3\ s^{-1}$). This discharge was observed (Figure 3.67) at Centennial Park on March 31, 2005. The photo faces upstream along the reinforced channel bank. A three-dimensional depiction of the flow surface from the HECRAS display is in Figure 3.68. The water level observed in the image is 4 to 5 feet (1.5 m)

below the top of the riprap berm and does not encroach on the ball field. Model results predict the water surface is 1.5 m below the top of the berm at station 103.4 and 1.7 below the top of the berm at station 102.9.

Figure 3.67 Centennial Reach at a discharge of 4550 cfs on March 31, 2005.

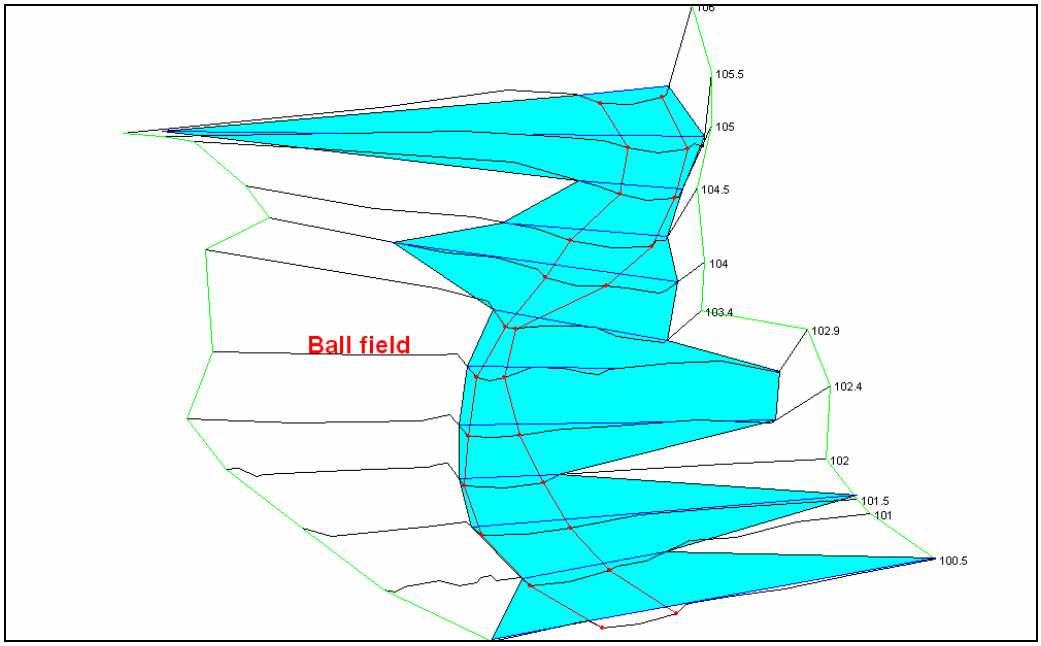

Figure 3.68 HECRAS water surface of Centennial Reach at a discharge of 4550 cfs.

Water inundates the mid channel gravel bar in Figure 3.69 at a discharge 4550 ft^3 s^{-1} as predicted by the model. The model also predicts that water encroaches into lower ground along the high flow side channel upstream of the ball field. This partially flooded area is observed in the photo of Figure 3.70.

Figure 3.69 Inundated mid channel bar at a discharge of 4550 cfs on March 31, 2005.

Figure 3.70 Flooded side channel at a discharge of 4550 cfs on March 31, 2005.

The Potlatch River experienced an extreme flood on February 9, 1996. Analysis of the lower Clearwater River hydrograph indicates that discharge of the lower Potlatch River was around 30,000 $ft^3\ s^{-1}$ (850 $m^3\ s^{-1}$). Model results (Figure 3.71) indicate complete inundation of the ball field area. The uncalibrated model in Figure 3.72 indicates flooding of the ball field area begins at a discharge of approximately 23,000 $ft^3\ s^{-1}$ (651 $m^3\ s^{-1}$).

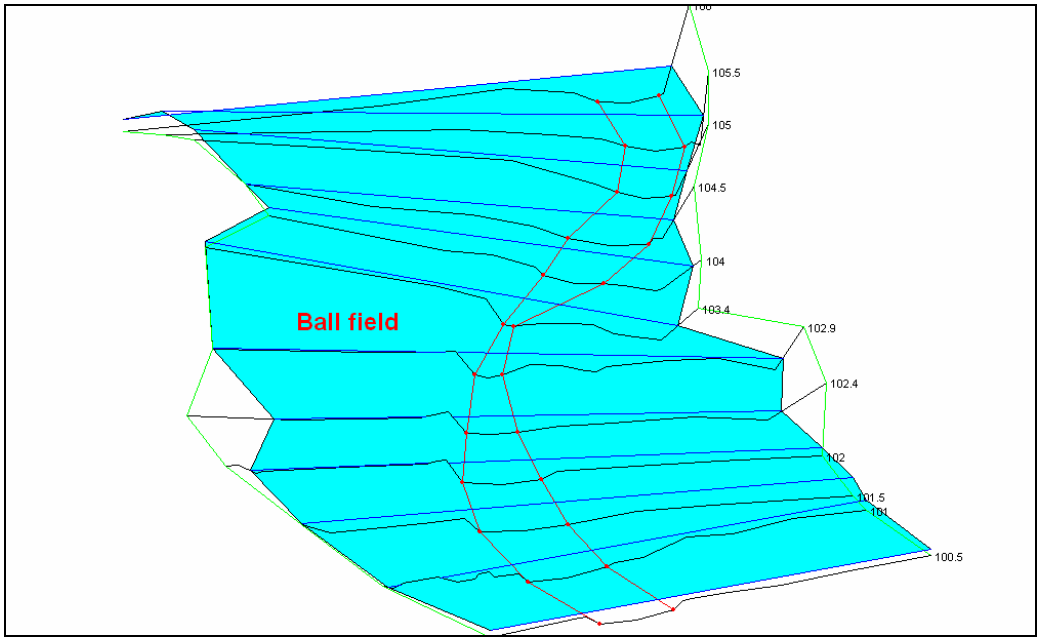

Figure 3.71 HECRAS water surface of Centennial Reach at a discharge of 30,000 cfs.

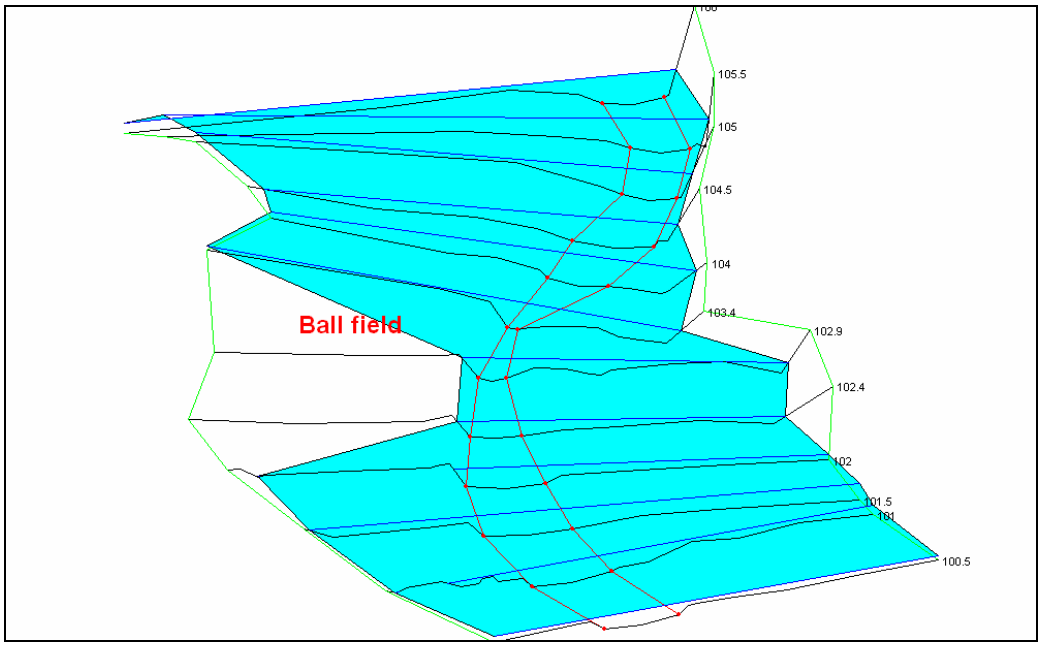

Figure 3.72 HECRAS water surface of Centennial Reach at a discharge of 23,000 cfs.

The uncalibrated HECRAS model ignores the effects of sediment transport and changes in stream morphology at high discharge. Hydraulic roughness was not varied to account for changes in relative submergence or floodplain roughness. In real application, it is difficult to judge whether these two hard-to-determine effects are cumulative or compensating. Clearly at some point surface roughness due to woody vegetation and interim deposits are overcome and mobilized to reduce overall roughness. High discharge aerial imagery could help determine a rational basis for estimating flood response at extreme discharge and would be a beneficial area of research.

Uncalibrated hydraulic models should not be used for engineering design or final determination of flood hazard where property and life are at risk. Despite this, there are many applications in preliminary hazard identification, flood response and habitat assessment that would be well served by the rapid, cost effective and fundamentally sound approach described.

3.4.14 Small Catchment Terrain Modeling

Shadow and tillage patterns in high-resolution digital aerial images of the Palouse consistently show that standard USGS 10-meter digital elevation model (DEM) data does not completely represent the large scale (high-resolution) variation of Palouse topography. This generally includes first order ephemeral gully catchments that are critical terrain structures in soil erosion modeling. Analytical photogrammetry and stereo high-resolution digital aerial imagery provide a means to augment the USGS DEM data to better model the erosion surface.

High-resolution digital aerial images were acquired along a north-south flight line in the Middle Potlatch Creek basin on March 31, 2005. A stereo model was produced by bundle block adjustment of the three overlapping images and ground control points in Figure 3.73. Three-dimensional coordinates of the ground control points were obtained from the 2004 USGS/State of Idaho DOQ and USGS 10-meter resolution DEM. No ground control points were field surveyed. Ground pixel resolution of the aerial images is about 0.22 m.

The stereo model was displayed in with photogrammetric software and elevations manually measured on a 10 meter by 10 meter grid. Elevation points closely follow the terrain in the red-blue anaglyph image of Figure 3.74. Manual measurement of elevation points is tedious, but was the only technique that produced a good quality DEM for the homogeneous surface of the planted agricultural field. An attempt to extract elevation data by automated image correlation with the available software produced very marginal results.

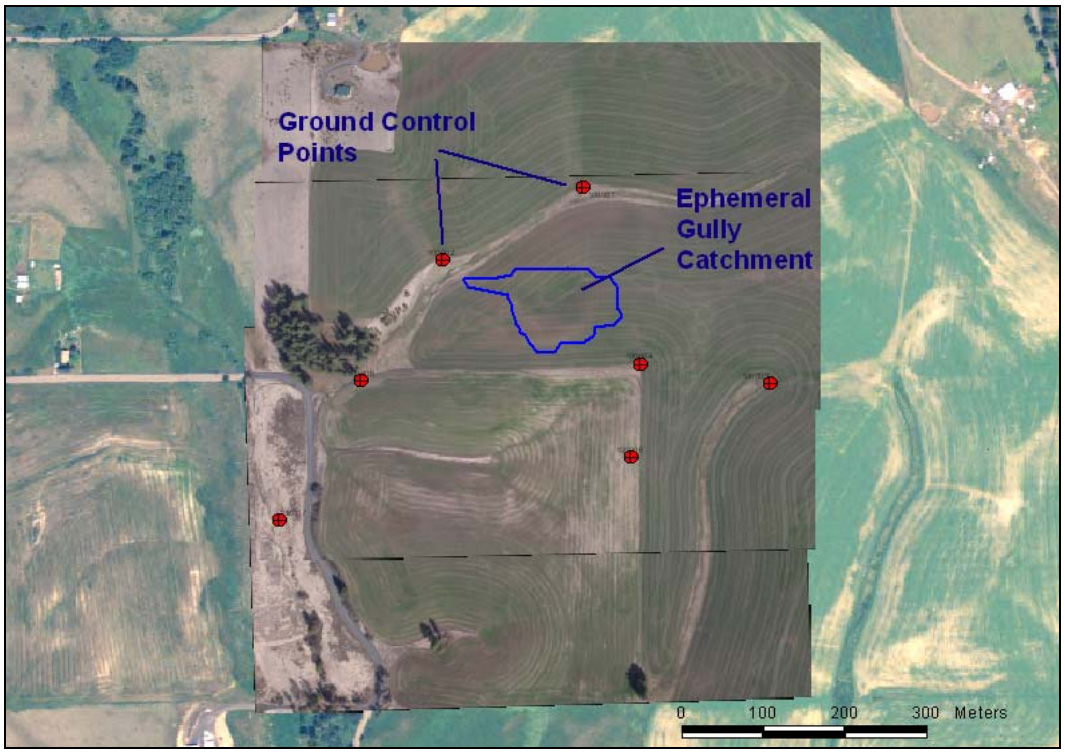

Figure 3.73 March 31, 2005 stereo aerial images and ground control points

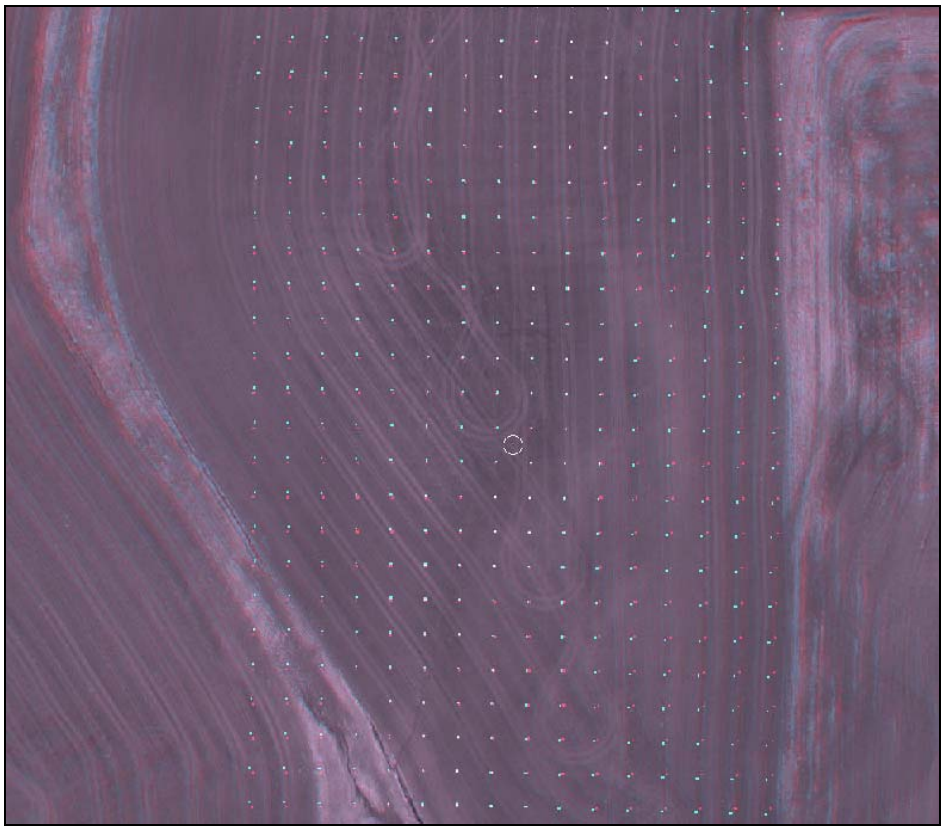
Figure 3.74 Anaglyph image of DEM points.

Automated stereo correlation techniques work reasonably well with aerial image scenes of spatially varied and contrasting objects, but less well with scenes of relatively homogeneous or patterned content such as agricultural fields. I have conducted considerable aerial imaging research trying to improve the success of image correlation by varying the resolution, season and daylight conditions of imagery acquisition. To the best of my knowledge this is a novel and original approach that should be the subject of future research. Results are too preliminary to report, but it should not be too surprising that some of the better results are obtained when the ground is covered with patchy snow.

The DEM data measured in the aerial image was imported into ArcView and converted to an ESRI grid. Elevation contours at 0.5 meter intervals were derived with the Spatial Analyst Extension. The catchment boundary of the first order ephemeral gully was extracted with the ESRI Hydro v1.1 extension. Drainage boundary, contours and DEM points are superimposed on the aerial image in Figure 3.75. Total catchment area was 1.15 ha (2.83 ac). Drainage area to the beginning of observed ephemeral gully channel (critical support area) is 1.07 ha (2.64 ac). The longest overland flow distance to the beginning of the ephemeral gully is 146 m. The average slope of the ephemeral gully is 9.05 percent.

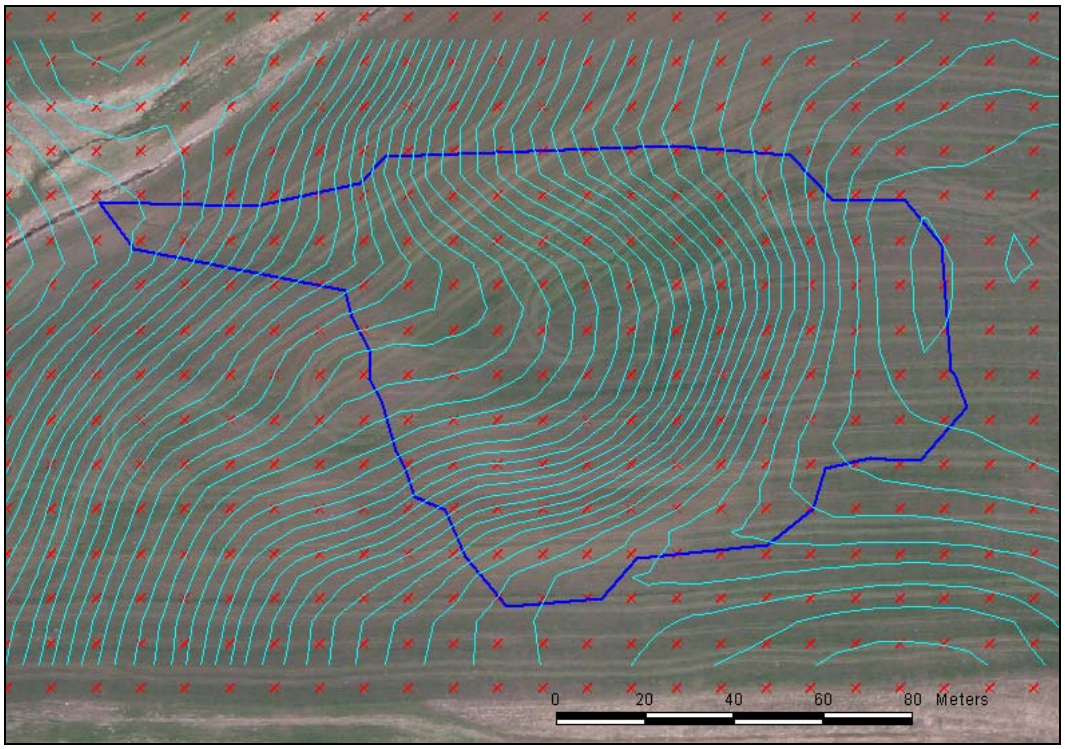

Figure 3.75 Ephemeral gully catchment area.

The 10 meter spacing of the aerial image DEM is the same as the USGS DEM. Figure 3.76 contrasts contour lines derived from the USGS DEM with the contours of the aerial image DEM. Both contour intervals are 0.5 meter. The contours show that the USGS DEM ignores low order variation in the terrain and almost completely obliterates the ephemeral gully catchment.

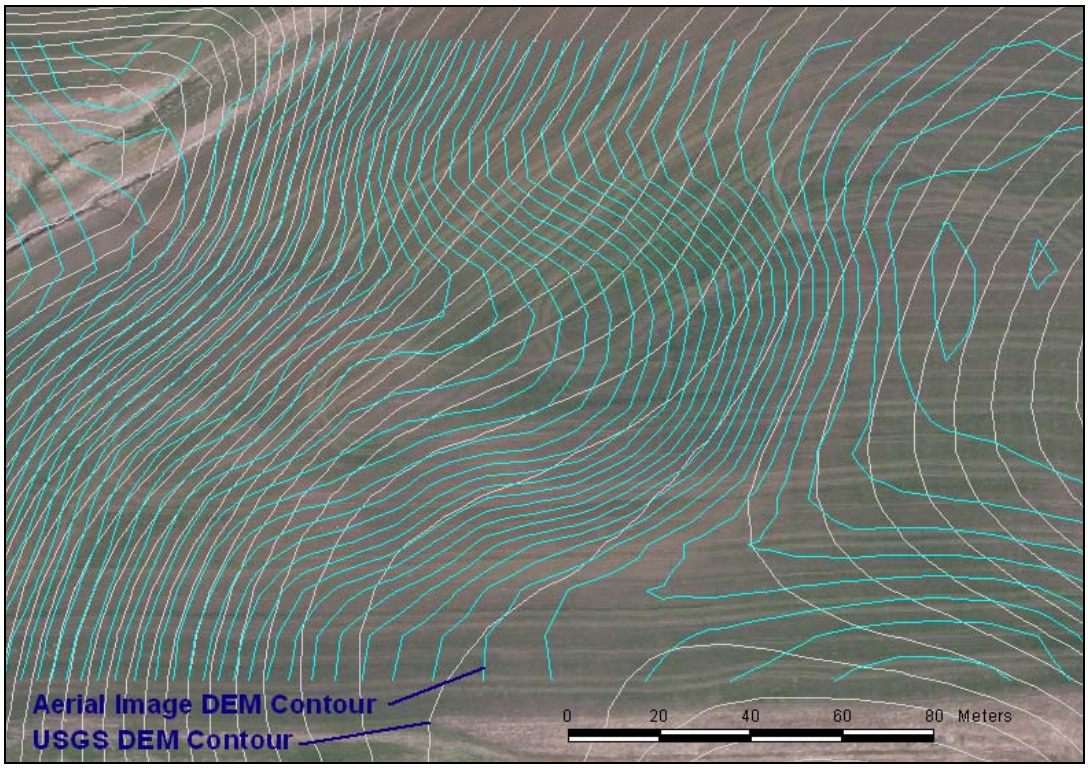

Figure 3.76 Comparison of USGS and aerial image DEM contours.

The USGS 10-meter DEM does not adequately represent many first order ephemeral gully basins in typical Palouse topography. The ephemeral gully parameters derived from the aerial image DEM are important for accurate analysis and modeling of ephemeral gully formation. There is virtually no other practical way to obtain precise measurements of ephemeral gully parameters over an extensive area on an unbiased statistical basis than with high-resolution stereo aerial imagery. Extensive field measurements are impractical and economically unfeasible even if access was freely granted by landowners. Elevation data from LIDAR is a possibility, but remains prohibitively expensive for most soil erosion studies.

Again, it is important to remind the reader that no field survey was required to produce elevation measurements of moderate precision with analytical photogrammetric techniques. The three examples above demonstrate but a few of the possible applications

of analytical photogrammetry in the assessment of streams and watersheds. Numerous opportunities exist for applied research that would benefit hazard identification, water quality modeling and soil erosion assessment.

3.5 Summary

This section described the fundamental principals and techniques of extracting spatial information from low altitude high-resolution digital aerial imagery. Practical examples illustrate insights gained from the dissertation research and emphasize problems of interest in water resources engineering and watershed assessment.

The dissertation research journeyed outside the normal bounds of water resources engineering and watershed assessment many times into subjects more closely related to the fields of environmental geology, soil mechanics (landslide analysis), transportation engineering, forestry, and demography. The reader is perhaps appreciative to be excused from a review of these applications. Nonetheless, the use of high-resolution aerial imagery is at least as beneficial in these fields as in water resource engineering.

References for Section 3

Asner, G. P., Braswell, B. H., Schimel, D. S., and Wessman, C. A. (1998). "Ecological research needs from multiangle remote sensing data." *Remote Sensing of Environment*, 63(2), 155-165.

ASPRS. (1995). *1995 DRAFT Standards for Aerial Photography, Online at http://www.asprs.org/asprs/resources/standards.html*, ASPRS Professional Practice Division Specifications and Standards Committee, American Society of Photogrammetry and Remote Sensing, Bethesda, ML.

ASTM. (1998). *G159-98 Standard Tables for References Solar Spectral Irradiance at Air Mass 1.5: Direct Normal and Hemispherical for a 37° Tilted Surface*, Committee G03 on Weathering and Durability, American Society for Testing and Materials International, Bethesda, MD.

Barnard, K., and Funt, B. (2002). "Camera characterization for color research." *Color Research and Application*, 27(3), 152-163.

Beiser, A. (1973). *Physics*, Cummings, Menlo Park, CA.

Brown, D. C. (1966). "Decentering Distortion of Lenses." *Photogrammetric Engineering*, 32(3), 444-463.

Brown, D. C. (1971). "Close range camera calibration." *Photogrammetric Engineering*, 37(8), 855-866.

Campbell, H. E., and Dierker, P. F. (1978). *Calculus with Analytic Geometry*, Prindle, Weber and Schmidt, Inc, Boston.

Campbell, J. B. (1996). *Introduction to Remote Sensing*, The Guilford Press, New York.

Chandler, J. H., Fryer, J. G., and Jack, A. (2005). "Metric capabilities of low-cost digital cameras for close range surface measurement." *Photogrammetric Record*, 20(109).

Clarke, T. A., and Fryer, J. G. (1998). "The development of camera calibration methods and models." *Photogrammetric Record*, 16 (91), 51-66.

Clarke., T. A., and Wang, X. (1998). "The principal point and CCD cameras." *Photogrammetric Record*, 16(92), 293-312.

Dymond, J. R., Shepherd, J. D., and Qi, J. (2001). "A Simple Physical Model of Vegetation Reflectance for Standardising Optical Satellite Imagery." *Remote Sensing of Environment*, 77(2), 230-239.

Farrell, J. A., and Barth, M. (1999). *The global positioning system and inertial navigation*, McGraw-Hill, New York.

Fraser, C. S. (1997). "Digital camera self-calibration." *ISPRS Journal of Photogrammetry and Remote Sensing*, 52(4), 149-159.

Fryer, J. G., and Goodin, H. J. (1989). "In-flight aerial camera calibration from photography of linear features." *Photogrammetric Engineering and Remote Sensing*, 55(12), 1751-1754.

Habib, A., and Kelle, D. (2001). "Automatic relative orientation of large scale imagery over urban areas using Modified Iterated Hough Transform." *ISPRS Journal of Photogrammetry and Remote Sensing*, 56(1), 29-41.

Hannah, M. J. (1989). "A system for digital stereo image matching." *Photogrammetric Engineering and Remote Sensing*, 55(12), 1765-1770.

Hapke, B., DiMucci, D., Nelson, R., and Smythe, W. (1996). "The cause of the hot spot in vegetation canopies and soils: Shadow-hiding versus coherent backscatter." *Remote Sensing of Environment*, 58(1), 63-68.

Hapke, B. W. (1981). "Bidirectional reflectance spectroscopy 1. Theory." *Journal of Geophysical Research*, 86, 3039-3054.

Heikkila, J. (2000). "Geometric camera calibration using circular control points." *IEEE Transactions on Pattern Analysis and Machine Intelligence*, 22(10), 1066-1077.

Heipke, C. (1997). "Automation of interior, relative, and absolute orientation." *ISPRS Journal of Photogrammetry and Remote Sensing*, 52, 1-19.

Hong, G., Luo, M. R., and Rhodes, P. A. (2001). "A study of digital camera colorimetric cCharacterization based on polynomial modeling." *Color Research and Application*, 26(1), 76-84.

Jacobsen, I. K., and Mostafa, M. M. R. (2001). "Direct georeferencing." *Photogrammetric Engineering and Remote Sensing*, 67(12), 30-36.

King, D. J. (1995). "Airborne multispectral digital camera and video sensors: a critical review of system designs and applications." *Canadian Journal of Remote Sensing*, 21(3), 245-273.

Krupnik, A., and Schenk, T. (1997). "Experiments with matching in the object space for aerotriangulation." *ISPRS Journal of Photogrammetry and Remote Sensing*, 52(4), 160-168.

Lenz, R., Meer, P., and Hauta-Kasari, M. (1999). "Spectral-Based Illumination Estimation and Color Correction." *Color Research and Application*, 24(2), 98-111.

Light, D. L. (1992). "The new camera calibration system at the U.S. Geological Survey." *Photogrammetric Engineering and Remote Sensing*, 58(2), 185-188.

Lillesand, T. M., and Kieffer, R. W. (1994). *Remote Sensing and Image Interpretation*, John Wiley and Sons, Inc., New York.

Lipson, S. G., Lipson, H., and Tannhauser, D. S. (1995). *Optical Physics, 3rd Edition*, Cambridge Univeristy Press, Cambridge.

MacCue, F. (2001). "USGS Aerial Camera Calibration Program." G. Teasdale, ed., Optical Science Laboratory, U.S. Geological Survey, Reston, VA.

Manzer, G. (1996). "Avoiding digital orthophoto problems." Digital Photogrammetry--An Addendum to the Manual of Photgrammetry, C. Greve, ed., American Society for Photogrammetry and Remote Sensing, Bethesda, ML, 158-162.

Mason, S., Rüther, H., and Smit, J. (1997). "Investigation of the Kodak DCS460 digital camera for small-area mapping." *ISPRS Journal of Photogrammetry and Remote Sensing*, 52(5), 202-214.

Mikhail, E. M., Bethel, J. S., and McGlone, J. C. (2001). *Introduction to Modern Photogrammetry*, Wiley, New York.

Morovic, J., and Morovic, P. (2003). "Determining colour gamuts of digital cameras and scanners." *Color Research and Application*, 28(1), 59-68.

Mostafa, M. M. R., and Schwarz, K. P. (2001). "Digital image georeferencing from a multiple camera system by GPS/INS." *International Journal of Photogrammetry and Remote Sensing*, 56, 1-12.

Mustaffar, M., and Mitchell, H. L. (2001). "Improving area-based matching by using surface gradients in the pixel co-ordinate transformation." *ISPRS Journal of Photogrammetry and Remote Sensing*, 56, 42-52.

Philipson, W. R. (1997). "Manual of Photographic Interpretation, Second Edition." American Society for Photogrammetry and Remote Sensing, Bethesda, ML, 689.

Pinty, B., Verstraete, M. M., and Dickinson, R. E. (1989). "A physcial model for predicting bidirectional reflectances over bare soil." *Remote Sensing of Environment*, 27, 273-288.

Ray, S. F. (2002). *Applied Photographic Optics, 3rd Edition*, Focal Press, Oxford.

Rees, W. G. (2001). *Physical Principles of Remote Sensing*, Cambridge University Press, Cambridge.

Robson, S., and Shortis, M. R. (1998). "Practical influences of geometric and radiometric image quality provided by different digital camera systems." *Photogrammetric Record*, 16(92), 225-248.

Sandmeier, S. R. "Acquisition of bidirectional reflectance factor data with field goniometers." *Remote Sensing of Environment*, 73(3), 257-269.

Schwarz, K. P., Chapman, M. A., Cannon, M. E., and Gong, P. (1993). "Integrated INS/GPS approach to the georeferencing of remotely sensed data." *Photogrammetric Engineering and Remote Sensing*, 59(11), 1667-1674.

Shannon, R. R. (1997). *The Art and Science of Optical Design*, Cambridge University Press, Cambridge.

Short, N. M. (1998). "Remote Sensing Tutorial, http://rst.gsfc.nasa.gov." Goddard Space Flight Center National Aeronautics and Space Adiministration.

Shortis, M. R., Robson, S., and Beyer, H. A. (1998). "Principal point behaviour and calibration parameter models for Kodak DCS cameras." *Photogrammetric Record*, 16 (92), 165-186.

Shortis, M. R., Robson, S., and Beyer, H. A. (1998). "Principal Point Behaviour and Calibration Parameter Models for Kodak DCS Cameras." *Photogrammetric Record*, 16(92), 165-186.

Slama, C. C., Theurer, C., and Henricksen, S. W. (1980). "Manual of Photogrammetry." American Society of Photogrammetry, Bethesda, MD.

Susaki, J., Hara, K., Kajiwara, K., and Honda, Y. (2004). "Robust estimation of BRDF model parameters." *Remote Sensing of Environment*, 89(1), 63-71.

Tang, L., Braun, J., and Debitsch, R. (1997). "Automation of interior, relative, and absolute orientation." *ISPRS Journal of Photogrammetry and Remote Sensing*, 52(4), 122-131.

Tsai, R. Y. (1987). "A versatile camera calibration technique for high-accuracy 3D machine vision metrology using off-the-shelf TV cameras and lenses." *IEEE Journal of Robotics and Automation RA*, 3(4), 323-344.

Walthall, C. L., Norman, J. M., Welles, J. M., Campbell, G., and Blad, B. L. (1985). "Simple equation to approximate the bidirectional reflectance from vegetative canopies and bare soil surfaces." *Applied Optics*, 24(3), 383-387.

Wang, X., and Clarke, T. A. (2001). "Separate adjustment in close-range photogrammetry." *ISPRS Journal of Photogrammetry and Remote Sensing*, 55(5-6), 289-298.

Wang, Y. (1998). "Principles and applications of structural image matching." *ISPRS Journal of Photogrammetry and Remote Sensing*, 53, 154-165.

Wolf, P. R., and Brinker, R. C. (1994). *Elementary Surveying*, HarperCollins, New York.

Wolf, P. R., and Dewitt, B. A. (2000). *Elements of Photogrammetry*, McGraw-Hill, New York.

Zhang, Z. " Flexible camera calibration by viewing a plane from unknown orientations." *International Conference on Computer Vision*, Corfu, Greece, 666-673.

Zhang, Z. (2000). "A flexible new technique for camera calibration." *IEEE Transactions on Pattern Analysis and Machine Intelligence*, 22(11), 1330-1334.

Appendix 3.1
Least Squares Analysis

Least squares analysis is used frequently in many operations of photogrammetry. A simple, but non-trivial example illustrates the development of the least squares matrix equations.

Elevation differences between three points are measured stereoscopically by parallax methods. The elevation difference between point A and B is 10.5 m, the elevation difference between B and C is 8.9 m and the difference between A and C is 19.2 m. This is a practical exercise because parallax measurements have a finite precision dependent on image resolution and the ratio of the sensor height to the separation between images (height to base ratio). Re-measurement of the parallax difference between points accomplishes little if the original measurement is made carefully. Least squares analysis should give a better estimation of the true elevation differences A to B and B to C. These height differences are designated *x* and *y*.

The three measurement equations including residual terms are:

$$\begin{aligned} x + y &= 19.2 + v_1 \\ x &= 10.5 + v_2 \\ y &= 8.9 + v_3 \end{aligned} \qquad \text{A.3.1.1}$$

Least squares analysis minimizes the square difference between the measured values and the final estimates for *x* and *y*. The squared difference equation to minimize is:

$$\sum_{i=1}^{m} v_i = (x + y - 19.2)^2 + (x - 10.5)^2 + (y - 8.9)^2 \qquad \text{A.3.1.2}$$

Taking the partial derivatives with respect to *x* and *y* gives the normal equations:

$$\frac{\partial \sum v^2}{\partial x} = 0 = 2(x + y - 19.2) + 2(x - 10.5)$$
$$\frac{\partial \sum v^2}{\partial y} = 0 = 2(x + y - 19.2) + 2(x - 8.9) \qquad \text{A.3.1.3}$$

Collecting terms the normal equations become,

$$2x + y = 29.7$$
$$x + 2y = 28.1 \qquad \text{A.3.1.4}$$

Solving for either x and y in one of the equation in A.3.1.4 and substituting into the other gives the final estimated values x = 10.43 m and y = 8.83 m.

In general a large system of observations of equal weight has the form (Wolf and Dewitt 2000):

$$\begin{aligned}
&a_{11}X_1 + a_{12}X_2 + a_{13}X_3 + \cdots + a_{1n}X_n - L_1 = v_1 \\
&a_{21}X_1 + a_{22}X_2 + a_{33}X_3 + \cdots + a_{2n}X_n - L_2 = v_2 \\
&a_{31}X_1 + a_{32}X_2 + a_{33}X_3 + \cdots + a_{3n}X_n - L_3 = v_3 \\
&\cdots\cdots\cdots\cdots\cdots\cdots\cdots\cdots\cdots\cdots\cdots\cdots\cdots\cdots\cdots\cdots\cdots\cdots \\
&a_{m1}X_1 + a_{m2}X_2 + a_{m3}X_3 + \cdots + a_{mn}X_n - L_m = v_n
\end{aligned} \qquad \text{A.3.1.5}$$

where the a_{ij}'s are the coefficients of the unknown variables X_j's, L_i's are the observations, and v_i's are the residuals.

In matrix form the system of equations become,

$${}_m\mathbf{A}^n\,{}_n\mathbf{X}^1 = {}_m\mathbf{L}^1 + {}_m\mathbf{V}^1 \qquad \text{A.3.1.6}$$

where

$${}_m\mathbf{A}^n = \begin{bmatrix} a_{11} & a_{12} & a_{13} & \cdots & a_{1n} \\ a_{21} & a_{21} & a_{21} & a_{21} & a_{2n} \\ a_{31} & a_{31} & a_{31} & a_{31} & a_{3n} \\ a_{41} & a_{41} & a_{41} & a_{41} & a_{4n} \\ \vdots & \vdots & \vdots & \vdots & \vdots \\ a_{m1} & a_{m1} & a_{m1} & a_{m1} & a_{mn} \end{bmatrix} \quad {}_n\mathbf{X}^1 = \begin{bmatrix} X_1 \\ X_2 \\ X_3 \\ X_4 \\ \vdots \\ X_5 \end{bmatrix} \quad {}_m\mathbf{L}^1 = \begin{bmatrix} L_1 \\ L_2 \\ L_3 \\ L_4 \\ \vdots \\ L_m \end{bmatrix} \quad {}_m\mathbf{V}^1 = \begin{bmatrix} V_1 \\ V_2 \\ V_3 \\ V_4 \\ \vdots \\ V_m \end{bmatrix} \qquad \text{A.3.1.7}$$

Squaring the system of Equations A.3.1.5 and setting the partial derivatives of the variables ($X_1, X_2, X_3 \ldots X_n$) equal to zero results in the normal equations:

$$
\begin{array}{l}
\sum_{i=1}^{m}(a_{i1}a_{i1})X_1+\sum_{i=1}^{m}(a_{i1}a_{i2})X_1+\sum_{i=1}^{m}(a_{i1}a_{i3})X_3+\cdots+\sum_{i=1}^{m}(a_{i1}a_{in})X_n=\sum_{i=1}^{m}(a_{i1}L_i)\\
\sum_{i=1}^{m}(a_{i2}a_{i1})X_1+\sum_{i=1}^{m}(a_{i2}a_{i2})X_1+\sum_{i=1}^{m}(a_{i2}a_{i3})X_3+\cdots+\sum_{i=1}^{m}(a_{i2}a_{in})X_n=\sum_{i=1}^{m}(a_{i2}L_i)\\
\sum_{i=1}^{m}(a_{i3}a_{i1})X_1+\sum_{i=1}^{m}(a_{i3}a_{i2})X_1+\sum_{i=1}^{m}(a_{i3}a_{i3})X_3+\cdots+\sum_{i=1}^{m}(a_{i3}a_{in})X_n=\sum_{i=1}^{m}(a_{i3}L_i) \qquad \text{A.3.1.8}\\
\cdots\cdots\cdots\cdots\cdots\cdots\cdots\cdots\cdots\cdots\cdots\cdots\cdots\cdots\cdots\cdots\cdots\cdots\cdots\cdots\cdots\cdots\cdots\cdots\cdots\cdots\\
\sum_{i=1}^{m}(a_{in}a_{i1})X_1+\sum_{i=1}^{m}(a_{in}a_{i2})X_1+\sum_{i=1}^{m}(a_{in}a_{i3})X_3+\cdots+\sum_{i=1}^{m}(a_{in}a_{in})X_n=\sum_{i=1}^{m}(a_{in}L_i)
\end{array}
$$

There is much uncomplicated, but tedious algebra between the systems of equations in A.3.1.5 and A.3.1.8. Even a simple system of three variables and observations (X_1, X_2, X_3, L_m) produces a polynomial with 16 terms when squared for each observation. All the terms of all the observation equations are added together after squaring to construct the full least squares equation. Before collecting, the full least squares equation will have 16 times *m* terms where *m* is the number of observations. Taking the derivatives of the full least squares equation with respect to each variable (X_1, X_2, X_3) produces the three new equations of the form in Equation A.3.1.8. For example, the final expression for the derivative with respect to X_1 for a three variable system of linear equations is:

$$
\begin{array}{l}
\left(a_{11}{}^2+a_{21}{}^2+a_{31}{}^2\right)X_1+\left(a_{11}a_{12}+a_{21}a_{22}+a_{31}a_{32}\right)X_2+\cdots\\
\qquad\qquad\left(a_{11}a_{13}+a_{21}a_{23}+a_{31}a_{33}\right)X_3-a_{11}L_1-a_{21}L_2-a_{31}L_3=0
\end{array}
\qquad \text{A.3.1.9}
$$

Equation A.3.1.9 corresponds to the first equation in the system of equations in A.3.1.8. The symmetry of the system of equations is apparent and agrees with the summation notation in Equations A.3.1.8.

Further study of the system of equations in A.3.1.8 leads to the recognition that the entire system of equations can be represented in matrix form as,

$$\left(\mathbf{A}^T\mathbf{A}\right)\mathbf{X} = \mathbf{A}^T\mathbf{L} \qquad \text{A.3.1.10}$$

where $\mathbf{A}^T$ is the transpose of the **A** matrix. Equation A.3.1.10 can be manipulated to produce a matrix equation that determines the unknown elements of **X** from the observed elements of **L**. Multiplying Equation A.3.1.10 by $(\mathbf{A}^T\mathbf{A})^{-1}$ gives:

$$\left(\mathbf{A}^T\mathbf{A}\right)^{-1}\left(\mathbf{A}^T\mathbf{A}\right)\mathbf{X} = \left(\mathbf{A}^T\mathbf{A}\right)^{-1}\left(\mathbf{A}^T\mathbf{L}\right)$$

$$\mathbf{I}\mathbf{X} = \left(\mathbf{A}^T\mathbf{A}\right)^{-1}\left(\mathbf{A}^T\mathbf{L}\right) \qquad \text{A.3.1.10}$$

where **I** is the identity matrix. Since the identity matrix is merely multiplies each element in X by one, the least squares matrix equation becomes:

$$\mathbf{X} = \left(\mathbf{A}^T\mathbf{A}\right)^{-1}\left(\mathbf{A}^T\mathbf{L}\right) \qquad \text{A.3.1.11}$$

For the elevation difference example, the original system of equations and matrices are:

$$1x + 1y - 19.2 = v_1$$
$$1x + 0y - 10.5 = v_2$$
$$0x + 1y - 8.9 = v_3$$

$$\mathbf{A} = \begin{bmatrix} 1 & 1 \\ 1 & 0 \\ 0 & 1 \end{bmatrix} \qquad \mathbf{X} = \begin{bmatrix} x \\ y \end{bmatrix} \qquad \mathbf{L} = \begin{bmatrix} 19.2 \\ 10.5 \\ 8.9 \end{bmatrix} \qquad \mathbf{V} = \begin{bmatrix} v_1 \\ v_2 \\ v_3 \end{bmatrix}$$

The transpose of **A** multiplied by **A** is:

$$\mathbf{A}^T\mathbf{A} = \begin{bmatrix} 1 & 1 & 0 \\ 1 & 0 & 1 \end{bmatrix} \begin{bmatrix} 1 & 1 \\ 1 & 0 \\ 0 & 1 \end{bmatrix} = \begin{bmatrix} 1\cdot 1 + 1\cdot 1 + 0\cdot 1 & 1\cdot 1 + 0\cdot 1 + 0\cdot 1 \\ 1\cdot 1 + 0\cdot 1 + 1\cdot 0 & 1\cdot 1 + 0\cdot 0 + 1\cdot 1 \end{bmatrix} = \begin{bmatrix} 2 & 1 \\ 1 & 2 \end{bmatrix}$$

Finding the inverse of $\mathbf{A}^T\mathbf{A}$ by the cofactor method is completed in several steps:

1. Find the cofactor of each element in $\mathbf{A}^T\mathbf{A}$;
2. Replace each element by its cofactor
3. Find the transpose of the matrix of cofactors;
4. Multiply the transposed matrix by one divided by the determinant of $\mathbf{A}^T\mathbf{A}$.

Cofactors for each element are the minors of each element (determinant after deleting rows and columns intersecting the element). Since the determinant of a 1 by 1 array is simply the value of the element, the cofactors are:

$$\mathbf{C} = \begin{bmatrix} (-1)^{1+1}(2) & (-1)^{1+2}(1) \\ (-1)^{2+1}(1) & (-1)^{2+2}(2) \end{bmatrix} = \begin{bmatrix} 2 & -1 \\ -1 & 2 \end{bmatrix}$$

Transposing rows and columns gives the transpose of **C**. In this case the transpose of **C** is equivalent to **C**:

$$\mathbf{C}^T = \begin{bmatrix} 2 & -1 \\ -1 & 2 \end{bmatrix}$$

The determinate of $\mathbf{A}^T\mathbf{A}$ is:

$$\left|\mathbf{A}^T\mathbf{A}\right| = \begin{vmatrix} 2 & 1 \\ 1 & 2 \end{vmatrix} = (2\cdot 2) - (1\cdot 1) = 3$$

The transpose of **A** multiplied by **A** is then,

$$\left(\mathbf{A}^T\mathbf{A}\right)^{-1} = \begin{bmatrix} 2 & 1 \\ 1 & 2 \end{bmatrix}^{-1} = \left(\frac{1}{3}\right)\begin{bmatrix} 2 & -1 \\ -1 & 2 \end{bmatrix} = \begin{bmatrix} 0.6667 & -0.3333 \\ -0.3333 & 0.6667 \end{bmatrix}$$

Multiplying the transpose of **A** by **L** gives,

$$\mathbf{A}^T\mathbf{L} = \begin{bmatrix} 1 & 1 & 0 \\ 1 & 0 & 1 \end{bmatrix}\begin{bmatrix} 19.2 \\ 10.5 \\ 8.9 \end{bmatrix} = \begin{bmatrix} 29.7 \\ 28.1 \end{bmatrix}$$

Solving for **X** gives:

$$\mathbf{X} = \left(\mathbf{A}^T\mathbf{A}\right)^{-1}\left(\mathbf{A}^T\mathbf{L}\right) = \begin{bmatrix} 0.6667 & -0.3333 \\ -0.3333 & 0.6667 \end{bmatrix}\begin{bmatrix} 29.7 \\ 28.1 \end{bmatrix} = \begin{bmatrix} 10.43 \\ 8.83 \end{bmatrix}$$

The final estimated values are x = 10.43 m and y = 8.83 m, the same result as the algebraic computations.

Generating least squares solutions by hand computation is a formidable task for most problems of interest in photogrammetry and geomatics. Fortunately, least squares computations may be fairly directly implemented in computer code or performed with mathematical software. Matrix Equation A.3.1.11 is easily solved in Excel or Matlab.

References for Appendix 3.1

Wolf, P. R., and Dewitt, B. A. (2000). *Elements of Photogrammetry*, McGraw-Hill, New York.

Appendix 3.2

Development of the Hemispherical Radiance Equation

A surface intercepts radiation from all directions of exposure. The intensity of the radiation (radiance) striking the surface is a vector quantity having a direction and magnitude. It is of interest in many remote sensing applications to determine the total radiation (irradiance) received at the surface from the radiation field. For a planar surface element, irradiance is computed by integrating the incoming radiation across the hemisphere of exposure. The following develops the expression for irradiance from the geometry of the hemisphere.

The solid angle is defined as the ratio of the area α of a spherical surface intercepted by a cone projected from the center of the sphere to the square of the radius:

$$\Omega = \frac{\alpha}{r^2} \qquad \text{A.3.2.1}$$

The unit of a solid angle is the steradian (sr). Since the surface area of a sphere is $4\pi r^2$, there are 4π steradians in the complete sphere.

The differential elemental solid angle is defined as:

$$d\sigma = (r d\theta)(r \sin\theta \, d\phi) \qquad \text{A.3.2.2}$$

where r is the hemisphere radius, θ is the angle between the hemispherical zenith axis and the radius line to the differential element on the surface of the hemisphere, and ϕ is the azmithal angle from a horizontal reference radius line to the projection of the differential element radius projected to the horizontal plane. The polar geometry convention adopted in Equation A.3.2.2 is common to many geomatics analyses.

From Equation A.3.2.1 and A.3.2.2, the differential solid angle is:

$$d\Omega = \frac{d\sigma}{r^2} = \frac{(rd\theta)(r\sin\theta\, d\phi)}{r^2} = \sin\theta\, d\theta\, d\phi \qquad \text{A.3.2.3}$$

Radiation intensity is defined by radiance *L*, the specific intensity (W m^{-2} sr^{-1}) of radiation at a given wavelength incident upon a surface from a specific direction. It is useful to visualize a ray (vector) having an intensity *L* inclined to the planar surface at angle θ as having components normal and tangential to the surface. Only the normal component of this ray contributes to energy received at the surface. Restricting development to a single wavelength, the monochromatic flux density or monochromatic irradiance (W m^{-2}) is determined by integrating the the normal component of radiance over the entire solid angle of the hemisphere.:

$$E = \int_{\Omega} L\cos\theta\, d\Omega \qquad \text{A.3.2.4}$$

Substituting Equation A.3.2.3 into A.3.2.4 , the irradiance integral in polar coordinates becomes:

$$E = \int_0^{2\pi}\int_0^{\frac{\pi}{2}} L(\theta,\phi)\cos\theta\sin\theta\, d\theta\, d\phi \qquad \text{A.3.2.5}$$

This integral may be solved most easily with the trigonometric identity:

$$\sin\theta\cos\theta = \frac{1}{2}\sin 2\theta \qquad \text{A.3.2.6}$$

Assuming isotropic radiance so that *L* does not change with direction and substituting Equation A.3.2.6 into A.3.2.5 gives:

$$E = L\int_0^{2\pi}\int_0^{\frac{\pi}{2}}\frac{1}{2}\sin 2\theta \, d\theta \, d\phi \qquad \text{A.3.2.7}$$

The integral of sin *u* d*u* is –cos u + C so the inner integral of Equation A.3.2.7 is,

$$\int_0^{\frac{\pi}{2}}\frac{1}{2}\sin 2\theta \, d\theta = -\frac{1}{4}\cos 2\theta\Big|_0^{\frac{\pi}{2}} = -\frac{1}{4}(-1) - \left(-\frac{1}{4}(1)\right) = 0.5$$

The full integral is then,

$$E = L\int_0^{2\pi} 0.5 \, d\phi = 0.5L\phi\Big|_0^{2\pi} = L(\pi) - L(0) = L\pi \qquad \text{A.3.2.8}$$

Thus, the expression for irradiance of a planar element from radiation incident from the full exposure hemisphere is:

$$E = L\pi \qquad \text{A.3.2.9}$$

The integration for incoming irradiance is equally valid for reflected energy. These relationships arise frequently in radiation transfer computations. One example is in the quantitative expression for reflectance:

$$\rho_{s,\lambda} = \frac{\pi \cdot L_{s,\lambda}}{E_{dir,\lambda} + E_{dif,\lambda}} \qquad \text{A.3.2.10}$$

Appendix 3.3

Development of the Photometric Exposure Equation

The basic concepts of photometry are lacking in standard references of solar engineering and remote sensing. The design and functioning of most digital cameras are based on principles of photometry not radiometry. Given the importance of digital cameras to the dissertation research, small format aerial imagery in general, and close range photogrammetry, a brief synopsis of the most relevant principles is beneficial and a foundation for future work.

Photometry

Photometry is the measurement of light as it is seen by a human observer. This is a distinctly different principal than radiometry which studies the relationship between light and energy. Photometry uses different units and detectors that have a spectral response similar to that of the CIE Standard Observer. The sensitivity of human vision is standardized in the CIE spectral luminous efficiency function V(λ) in Figure A.3.3.1.

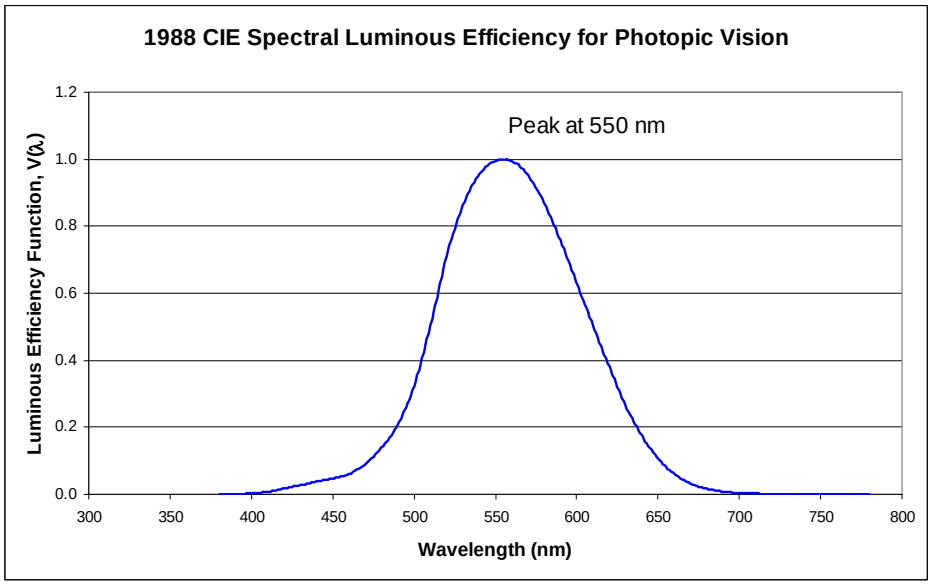

Figure A.3.3.1 Spectral Luminous Efficiency Function.

Radiometric Quantities and Units

Energy is measured in joules (J). The recommended symbol for energy is Q or W. Power (radiant flux) is the derivative of energy with respect to time, $d\boldsymbol{Q}/dt$, and the unit is the watt (W). The recommended symbol for power is Φ or P. Irradiance (flux density) is power per unit area (W m^{-2}) incident from all directions in a hemisphere onto a surface that coincides with the base of that hemisphere. Radiant exitance is power per unit area leaving a surface into a hemisphere whose base is that surface. The symbol for irradiance is E and the symbol for radiant exitance is M. Radiant intensity is power per unit solid angle (W/sr) and has the symbol is I. Radiance is power per unit projected area per unit solid angle (W m^{-2} sr^{-1}). The recommended symbol for radiance is L. Radiance is the derivative of power with respect to solid angle and projected area, $d\Phi /d\omega\ d\boldsymbol{A}\cos(\theta)$ where θ is the angle between the surface normal and the specified direction.

Photometric Quantities and Units

Photometric quantities corresponding directly to those in radiometry (Table A.3.3.1) and have the same symbols, but with a subscript v denoting visual. The lumen is an SI unit for luminous flux and is derived from the SI base unit candela (BIPM 1998). A lumen is the luminous flux emitted into unit solid angle (1 sr) by an isotropic point source having a luminous intensity of 1 candela. The lumen is the product of luminous intensity and solid angle (cd sr) and has the symbol is Φ_v. It corresponds to radiant power but is spectrally weighted to the standard spectral luminous efficiency function. The relationship between lumens and candelas is 1 cd = 4π lm for an isotropic source. It is permissible to state that 1 cd = 1 lm sr^{-1}.

Standard human vision has peak sensitivity at 555 nm ($V(\lambda) = 1.0$) . At this point 1 watt of radiant power corresponds to a luminous flux of 683 lumens. The value of 683 lm W^{-1} is abbreviated by the symbol K_m for photopic (color) vision. Luminous efficiency is 0.631 at 600 nm, so 1 W of radiant power corresponds to (0.631)(683) = 431 lm. Sources producing electromagnetic energy at wavelengths less than 380 nm and greater than 780 nm emit no luminous flux. An important point to recognize is that radiant power and luminous flux are directly related by the spectral luminous efficiency function. There is no mathematical ambivalence in this standardized relationship. Any subjectivity is in how well the luminous efficiency function represents human vision, but not in the conversion from radiometric to photometric quantities.

QUANTITY	RADIOMETRIC	PHOTOMETRIC
Power	Watt (W)	Lumen (lm)
Power per unit area	Irradiance (W m^{-2})	Illuminace (lm m^{-2} = lux)
Power per unit solid angle	W sr^{-1}	Lm sr^{-1} = candela (cd)
Power per area per solid angle	Radiance (W m^{-2} sr^{-1})	Luminance (Lm m^{-2} sr^{-1} = cd m^{-2})

Table A.3.3.1 Corresponding radiometric and photometric units.

Illuminance is luminous flux density (lm m^{-2}). It also called lux (lx) and has the symbol $\boldsymbol{E_v}$. It corresponds to irradiance. Luminance is the rate of flow of radiant energy producing visual sensation in a specific direction and has units of lumens per square meter per steradian (lm m^{-2} sr^{-1} or cd m^{-2}). It has the symbol is $\boldsymbol{L_v}$. Luminance corresponds to radiance and is also expressed in the unit, **nit.** Luminance is not specified in the SI system.

To convert a radiometric value X_λ for monochromatic light at wavelength λ to photometric units, all that is necessary is to multiply the radiometric quantity by the

corresponding spectral luminous efficiency function value $V(\lambda)$ for the particular wavelength. Conversion of radiometric quantities of mixed wavelengths requires numerical integration of the spectral luminous efficiency function:

$$X_v = K_m \int_0^\infty X_\lambda V(\lambda) d\lambda \qquad \text{A.3.3.1}$$

The conversion from photometric to radiometric quantities is more difficult because the final spectral distribution is not known. Standard spectral distributions such as the CIE illuminant curves for indoor and outdoor lighting may be assumed to facilitate the conversion.

Development of the photometric exposure equation

The amount of light incident on any point in the image plane can be determined from the geometry in Figure A.3.3.2 for a single lens with no spherical aberration or coma (aplanatic). A small area G_o of a uniformly diffusing surface at distance u from the lens emits luminance L_G (lm m^{-2} sr^{-1}) into the solid angle cone subtended by the lens of area A_L. The luminance reaching the image plane is reduced by the transmittance coefficient T_L of the lens material. The principal ray from object area G_o is at angle θ with the optical axis of the lens. The image of the object area G_I is formed on the image plane at distance v from the lens.

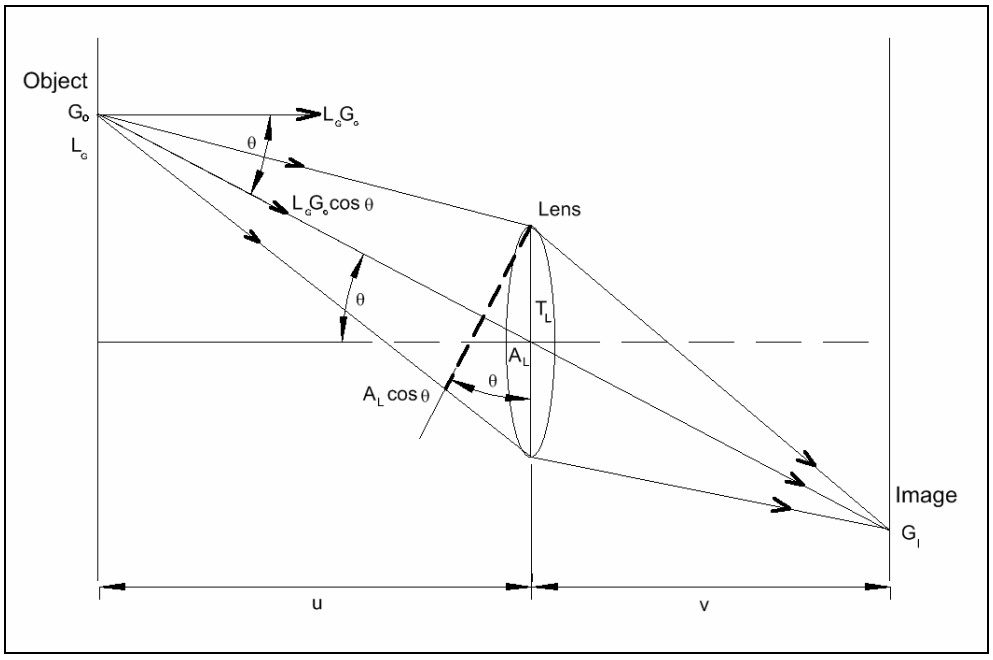

Figure A.3.3.2 Geometry of single lens illuminance.

The solid angle η between G_o and lens area A_L is:

$$\eta = \frac{A_L \cos\theta}{\left(\frac{u}{\cos\theta}\right)^2} = \frac{A_L \cos^3\theta}{u^2} \qquad \text{A.3.3.2}$$

The luminous intensity L_G (lm sr^{-1}) from G at angle θ is $L_G G_o \cos\theta$, so the luminous flux K (lm) entering the lens is:

$$K = L_G G_o \cos\theta \frac{A_L \cos^3\theta}{u^2} = \frac{L_G G_o A_L \cos^4\theta}{u^2} \qquad \text{A.3.3.3}$$

The amount of luminous flux is decreased by the transmittance coefficient T, so the image illuminance E_I (lm m^{-2}) at the image the small area G_I is:

$$E_I = \frac{T L_G G_o A_L \cos^4\theta}{G_I u^2} \qquad \text{A.3.3.4}$$

Right triangle geometry in Figure A.3.3.2 gives the relationship:

$$\frac{G_o}{G_I} = \frac{u^2}{v^2} \qquad \text{A.3.3.5}$$

Substituting this relationship into Equation A.3.3.5 gives the illumination at a point in the image due to light reflected from small area G_o:

$$E_I = \frac{TL_G A_L \cos^4 \theta}{v^2} \qquad \text{A.3.3.6}$$

Assuming infinite focus so image distance v equals the focal length f and substituting the area of a circular aperture ($\pi d^2/4$) into Equation A.3.3.6 gives:

$$E_I = \frac{\pi TL_G \cos^4 \theta}{4\left(\frac{f}{d}\right)^2} \qquad \text{A.3.3.7}$$

Equation A.3.3.7 is an important equation in camera sensor photometry. It reveals that the light energy at a point on the image sensor is proportional to the lens area, indirectly proportional to the square of the focal distance, and directly proportional to the fourth power of the cosine of the radial angle from the center of the image. Illuminance is maximum at the center of the image and decreases non linearly towards the edge. Focal length divided by aperture diameter is the f number N so Equation A.3.3.7 is conveniently expressed:

$$E_I = \frac{\pi TL \cos^4 \theta}{4N^2} \qquad \text{A.3.3.8}$$

The subscript G on luminance L is dropped because image points uniquely correspond to object points. Illuminance at the center of the image where $\cos^4 \theta = 1.0$ simplifies to:

$$E = \frac{\pi TL}{4N^2} \qquad \text{A.3.3.9}$$

Sensor illuminance is directly related to object luminance by Equation A.3.3.8 and A.3.3.9. Exposure H at the center of the sensor is the product of illuminance and exposure time t (s):

$$H = \frac{\pi TLt \cos^4 \theta}{4N^2} \qquad \text{A.3.3.10}$$

A constant k may be defined by the lens properties that are fixed with respect to a point on the image:

$$q = \frac{\pi T \cos^4 \theta}{4} \qquad \text{A.3.3.11}$$

Substituting constant q into Equation A.3.3.10 Exposure becomes:

$$H_{sensor} = \frac{qLt}{N^2} \qquad \text{A.3.3.12}$$

It is necessary to transform illuminance incident on sensor to that recorded by the sensor. Sensor recording sensitivity S (film speed) may be defined by two constants (Ray 2002)

$$S = \frac{H_0}{H_m} \qquad \text{A.3.3.13}$$

where H_0 is a constant and H_m is a speed point or minimum necessary exposure. Since H_m is defined as a minimum exposure, the actual desired exposure of the sensor or film H can be represented by an empirical factor k multiplied by the minimum necessary exposure:

$$H_{image} = kH_m = \frac{kH_0}{S} \qquad \text{A.3.3.14}$$

The factors k and H_0 define the sensitivity and response of the digital sensor or film and can only be determined by calibration.

Equating incident exposure (Equations A.3.3.12) to recorded exposure (Equation A.3.3.14) and solving for exposure time t gives:

$$H = k\frac{H_0}{S} = \frac{qLt}{N^2}$$

$$t = \frac{kH_0N^2}{qLS} \qquad \text{A.3.3.15}$$

Defining a new constant K can be defined by the fixed lens and sensitivity parameters:

$$K = \frac{kH_0}{q} = \frac{4kH_0}{\pi T\cos^4\theta} = \frac{tLS}{N^2} \qquad \left[\frac{\text{s}\cdot\text{lm}}{\text{m}^2\cdot\text{sr}}\right] \qquad \text{A.3.3.16}$$

The relationship between scene illuminance L, aperture number N, exposure time t and sensitivity S (film speed) in Equation A.3.3.16 is a fundamental equation of camera control. The illuminance of a scene can be determined by rearranging Equation A.3.3.17:

$$L = \frac{KN^2}{tS} \qquad \text{A.3.3.17}$$

Equation A.3.3.17 is a useful result. It relates camera settings to scene luminance with an empirical constant K. Measured luminance or radiance should plot as a straight line with N^2/tS.

In general, it is expected that for constant lens parameters and sensitivity a calibration equation would have the form:

$$E = a\left(\frac{N^2}{t}\right) + b \qquad \text{A.3.3.18}$$

Doubling the sensitivity (film speed) in Equation A.3.3.17 requires a compensating reduction in aperture area by decreasing aperture diameter by the multiplicative factor $\sqrt{1/2}$ or reducing the exposure time by half. Digital camera controls are conveniently scaled so that permissible adjustments of aperture, exposure time (shutter speed) and film speed produce doubling or halving of the amount of light on the focal plane. For example, if the exposure time of a camera set at *f* number 8.0 is reduced from 1/250 to 1/500 s the *f* number must be to $\sqrt{1/2}(8.0) = 5.7$. By definition the reduction in *f* number is an increase in aperture diameter.

Conventional camera control defines exposure settings in terms of exposure value *EV*. By definition *EV* is:

$$2^{EV} = \frac{N^2}{t} \qquad \text{A.3.3.19}$$

Exposure value is more conveniently expressed:

$$EV = \log_2\left(\frac{N^2}{t}\right)$$
$$EV = \frac{1}{\log_{10}(2)}\log_{10}\left(\frac{N^2}{t}\right) = 3.32\log_{10}\left(\frac{N^2}{t}\right) \qquad \text{A.3.3.20}$$

Substituting Equation A.3.3.20 into Equation A.3.3.17 gives:

$$L = \frac{K}{S}2^{EV} \qquad \text{A.3.3.21}$$

or

$$\log_{10}(L) = \frac{EV - 3.32\log_{10}\left(\frac{K}{S}\right)}{3.32} \qquad \text{A.3.3.22}$$

Equation A.3.3.22 shows that for a constant sensitivity or film speed and lens parameters (except aperture) the log of scene luminance should plot as a straight line with exposure value. An example in the main dissertation demonstrates the utility of this relationship.

References for Appendix 3.3

Asner, G. P., Braswell, B. H., Schimel, D. S., and Wessman, C. A. (1998). "Ecological research needs from multiangle remote sensing data." *Remote Sensing of Environment*, 63(2), 155-165.

ASPRS. (1995). *1995 DRAFT Standards for Aerial Photography, Online at http://www.asprs.org/asprs/resources/standards.html*, ASPRS Professional Practice Division Specifications and Standards Committee, American Society of Photogrammetry and Remote Sensing, Bethesda, ML.

ASTM (1998). *G159-98 Standard Tables for References Solar Spectral Irradiance at Air Mass 1.5: Direct Normal and Hemispherical for a 37° Tilted Surface*, Committee G03 on Weathering and Durability, American Society for Testing and Materials International, Bethesda, MD.

Barnard, K., and Funt, B. (2002). "Camera characterization for color research." *Color Research and Application*, 27(3), 152-163.

Beiser, A. (1973). *Physics*, Cummings, Menlo Park, CA.

BIPM (1998). The International System of Units (S I), 7th Ed., English Translation. Paris, Organisation Intergouvernementale de la Convention du Mètre, Bureau International des Poids et Mesures: 152.

Brown, D. C. (1966). "Decentering Distortion of Lenses." *Photogrammetric Engineering*, 32(3), 444-463.

Brown, D. C. (1971). "Close range camera calibration." *Photogrammetric Engineering*, 37(8), 855-866.

Campbell, H. E., and Dierker, P. F. (1978). *Calculus with Analytic Geometry*, Prindle, Weber and Schmidt, Inc, Boston.

Campbell, J. B. (1996). *Introduction to Remote Sensing*, The Guilford Press, New York.

Chandler, J. H., Fryer, J. G., and Jack, A. (2005). "Metric capabilities of low-cost digital cameras for close range surface measurement." *Photogrammetric Record*, 20(109).

Clarke, T. A., and Fryer, J. G. (1998). "The development of camera calibration methods and models." *Photogrammetric Record*, 16 (91), 51-66.

Clarke., T. A., and Wang, X. (1998). "The principal point and CCD cameras." *Photogrammetric Record*, 16(92), 293-312.

Dymond, J. R., Shepherd, J. D., and Qi, J. (2001). "A Simple Physical Model of Vegetation Reflectance for Standardising Optical Satellite Imagery." *Remote Sensing of Environment*, 77(2), 230-239.

Farrell, J. A., and Barth, M. (1999). *The global positioning system and inertial navigation*, McGraw-Hill, New York.

Fraser, C. S. (1997). "Digital camera self-calibration." *ISPRS Journal of Photogrammetry and Remote Sensing*, 52(4), 149-159.

Fryer, J. G., and Goodin, H. J. (1989). "In-flight aerial camera calibration from photography of linear features." *Photogrammetric Engineering and Remote Sensing*, 55(12), 1751-1754.

Habib, A., and Kelle, D. (2001). "Automatic relative orientation of large scale imagery over urban areas using Modified Iterated Hough Transform." *ISPRS Journal of Photogrammetry and Remote Sensing*, 56(1), 29-41.

Hannah, M. J. (1989). "A system for digital stereo image matching." *Photogrammetric Engineering and Remote Sensing*, 55(12), 1765-1770.

Hapke, B., DiMucci, D., Nelson, R., and Smythe, W. (1996). "The cause of the hot spot in vegetation canopies and soils: Shadow-hiding versus coherent backscatter." *Remote Sensing of Environment*, 58(1), 63-68.

Hapke, B. W. (1981). "Bidirectional reflectance spectroscopy 1. Theory." *Journal of Geophysical Research*, 86, 3039-3054.

Heikkila, J. (2000). "Geometric camera calibration using circular control points." *IEEE Transactions on Pattern Analysis and Machine Intelligence*, 22(10), 1066-1077.

Heipke, C. (1997). "Automation of interior, relative, and absolute orientation." *ISPRS Journal of Photogrammetry and Remote Sensing*, 52, 1-19.

Hong, G., Luo, M. R., and Rhodes, P. A. (2001). "A study of digital camera colorimetric cCharacterization based on polynomial modeling." *Color Research and Application*, 26(1), 76-84.

Jacobsen, I. K., and Mostafa, M. M. R. (2001). "Direct georeferencing." *Photogrammetric Engineering and Remote Sensing*, 67(12), 30-36.

King, D. J. (1995). "Airborne multispectral digital camera and video sensors: a critical review of system designs and applications." *Canadian Journal of Remote Sensing*, 21(3), 245-273.

Krupnik, A., and Schenk, T. (1997). "Experiments with matching in the object space for aerotriangulation." *ISPRS Journal of Photogrammetry and Remote Sensing*, 52(4), 160-168.

Lenz, R., Meer, P., and Hauta-Kasari, M. (1999). "Spectral-Based Illumination Estimation and Color Correction." *Color Research and Application*, 24(2), 98-111.

Light, D. L. (1992). "The new camera calibration system at the U.S. Geological Survey." *Photogrammetric Engineering and Remote Sensing*, 58(2), 185-188.

Lillesand, T. M., and Kieffer, R. W. (1994). *Remote Sensing and Image Interpretation*, John Wiley and Sons, Inc., New York.

Lipson, S. G., Lipson, H., and Tannhauser, D. S. (1995). *Optical Physics, 3rd Edition*, Cambridge Univeristy Press, Cambridge.

MacCue, F. (2001). "USGS Aerial Camera Calibration Program." G. Teasdale, ed., Optical Science Laboratory, U.S. Geological Survey, Reston, VA.

Manzer, G. (1996). "Avoiding digital orthophoto problems." Digital Photogrammetry--An Addendum to the Manual of Photgrammetry, C. Greve, ed., American Society for Photogrammetry and Remote Sensing, Bethesda, ML, 158-162.

Mason, S., Rüther, H., and Smit, J. (1997). "Investigation of the Kodak DCS460 digital camera for small-area mapping." *ISPRS Journal of Photogrammetry and Remote Sensing*, 52(5), 202-214.

Mikhail, E. M., Bethel, J. S., and McGlone, J. C. (2001). *Introduction to Modern Photogrammetry*, Wiley, New York.

Morovic, J., and Morovic, P. (2003). "Determining colour gamuts of digital cameras and scanners." *Color Research and Application*, 28(1), 59-68.

Mostafa, M. M. R., and Schwarz, K.-P. (2001). "Digital image georeferencing from a multiple camera system by GPS/INS." *ISPRS Journal of Photogrammetry and Remote Sensing*, 56(1), 1-12.

Mostafa, M. M. R., and Schwarz, K.-P. (2001). "Digital image georeferencing from a multiple camera system by GPS/INS." *International Journal of Photogrammetry and Remote Sensing*, 56, 1-12.

Mustaffar, M., and Mitchell, H. L. (2001). "Improving area-based matching by using surface gradients in the pixel co-ordinate transformation." *ISPRS Journal of Photogrammetry and Remote Sensing*, 56, 42-52.

Philipson, W. R. (1997). "Manual of Photographic Interpretation, Second Edition." American Society for Photogrammetry and Remote Sensing, Bethesda, ML, 689.

Pinty, B., Verstraete, M. M., and Dickinson, R. E. (1989). "A physcial model for predicting bidirectional reflectances over bare soil." *Remote Sensing of Environment*, 27, 273-288.

Ray, S. F. (2002). *Applied Photographic Optics, 3rd Edition*, Focal Press, Oxford.

Rees, W. G. (2001). *Physical Principles of Remote Sensing*, Cambridge University Press, Cambridge.

Robson, S., and Shortis, M. R. (1998). "Practical influences of geometric and radiometric image quality provided by different digital camera systems." *Photogrammetric Record*, 16(92), 225-248.

Sandmeier, S. R. "Acquisition of bidirectional reflectance factor data with field goniometers." *Remote Sensing of Environment*, 73(3), 257-269.

Schwarz, K. P., Chapman, M. A., Cannon, M. E., and Gong, P. (1993). "Integrated INS/GPS approach to the georeferencing of remotely sensed data." *Photogrammetric Engineering and Remote Sensing*, 59(11), 1667-1674.

Shannon, R. R. (1997). *The Art and Science of Optical Design*, Cambridge University Press, Cambridge.

Short, N. M. (1998). "Remote Sensing Tutorial, http://rst.gsfc.nasa.gov." Goddard Space Flight Center National Aeronautics and Space Adiministration.

Shortis, M. R., Robson, S., and Beyer, H. A. (1998). "Principal point behaviour and calibration parameter models for Kodak DCS cameras." *Photogrammetric Record*, 16 (92), 165-186.

Shortis, M. R., Robson, S., and Beyer, H. A. (1998). "Principal Point Behaviour and Calibration Parameter Models for Kodak DCS Cameras." *Photogrammetric Record*, 16(92), 165-186.

Slama, C. C., Theurer, C., and Henricksen, S. W. (1980). "Manual of Photogrammetry." American Society of Photogrammetry, Bethesda, MD.

Susaki, J., Hara, K., Kajiwara, K., and Honda, Y. (2004). "Robust estimation of BRDF model parameters." *Remote Sensing of Environment*, 89(1), 63-71.

Tang, L., Braun, J., and Debitsch, R. (1997). "Automation of interior, relative, and absolute orientation." *ISPRS Journal of Photogrammetry and Remote Sensing*, 52(4), 122-131.

Tsai, R. Y. (1987). "A versatile camera calibration technique for high-accuracy 3D machine vision metrology using off-the-shelf TV cameras and lenses." *IEEE Journal of Robotics and Automation RA*, 3(4), 323-344.

Walthall, C. L., Norman, J. M., Welles, J. M., Campbell, G., and Blad, B. L. (1985). "Simple equation to approximate the bidirectional reflectance from vegetative canopies and bare soil surfaces." *Applied Optics*, 24(3), 383-387.

Wang, X., and Clarke, T. A. (2001). "Separate adjustment in close-range photogrammetry." *ISPRS Journal of Photogrammetry and Remote Sensing*, 55(5-6), 289-298.

Wang, Y. (1998). "Principles and applications of structural image matching." *ISPRS Journal of Photogrammetry and Remote Sensing*, 53, 154-165.

Wolf, P. R., and Brinker, R. C. (1994). *Elementary Surveying*, HarperCollins, New York.

Wolf, P. R., and Dewitt, B. A. (2000). *Elements of Photogrammetry*, McGraw-Hill, New York.

Zhang, Z. " Flexible camera calibration by viewing a plane from unknown orientations." *International Conference on Computer Vision*, Corfu, Greece, 666-673.

Zhang, Z. (2000). "A flexible new technique for camera calibration." *IEEE Transactions on Pattern Analysis and Machine Intelligence*, 22(11), 1330-1334.

Appendix 3.4
Matlab Codes for Analytical Photogrammetry

Exterior Orientation of Camera or Sensor Geometry

```
% Exgeo.m
% Exterior orientation of a single aerial image by least squares resection
% of the collinearity equations.
% This code is algorithmic. It purposely omits standard devices, such
% as error trapping and checks on singularity, in favor of clarity.
% The intent of the code is educational.  There is no guarantee of suitability or accuracy.
%
% G.N. Teasdale copyright 2004, 2005
%
% Example for Genesee, ID aerial 22 Feb 04
%   Note that the ellipses (...) is a line continuation in Matlab and
%   is used to break long equations. The percent sign % leads comments.
%
% Set digital camera parameters
focl = 17.00  %calibrated lens focal length, mm
xo = 0;  % calibrated principal point x direction, mm
yo = 0;  % calibrated principal point y direction, mm
%
% Initialize counter and allowable error for least squares iteration
itcount = 0;
allowdelrot = 0.001*pi/180  % radians, allowable rotation error (0.001 degrees)
maxdelrot = 0.1;                % initial value or check error
%Load ground control point data of form:
%ID, image_x,image_y,gcp_X,gcp_Y,gcp_Z
% Image coordinantes in mm, gcp coordinates in m
% Image coordinate origin is at principal point of image.
%
%Read input from text file
[ID,x,y,X,Y,Z]=textread('genesee.dat','%s %f %f %f %f %f');
numpts = length(x)
%
%Compute the initial approximations for the external geometry parameters:
% omega (roll), phi (pitch), kappa (yaw), sensor X, sensor Y
% A good assumption is vertical geometry.  Not good for oblique imagery.
%  With vertical imagery there is no pitch or roll so,
omeg = 0;    %radians
phi = 0;       %radians
%Approximate height from vertical photo geometry and sequential control points
%  This is not all possible combinations, but good enough for the approximation
% f/H = image_length/ground_length
```

```
for i = 1:numpts-1
   imgleng = ((x(i+1)-x(i))^2+(y(i+1)-y(i))^2)^0.5...
           /((X(i+1)-X(i))^2+(Y(i+1)-Y(i))^2)^0.5;
   Hi(i) = focl/imgleng + (Z(i)+Z(i+1))/2;
end
TZ = mean(Hi);  % Initial estimate of sensor elevation
%Compute approximate GCP image centered coordinates assuming vertical geometry
%  X = x(H-ha)/f and Y = y(H-ha)/f
for i=1:numpts
   3(i)=x(i)*(TZ-Z(i))/focl;
   YY(i)=y(i)*(TZ-Z(i))/focl;
end
%Compute a two-dimensional conformal transformation of the GCPs
% to find the approximate sensor coordinates.
%  Xs = ax - by + Tx
%  Ys = ay + bx +Ty
% Develop the A matrix from image coordinates at ground scale
j = 1;
for i=1:numpts
   A(j,:)=[3(i),-YY(i),1,0];
   A(j+1,:)= [YY(i),3(i),0,1];
   j = j+2;
end
% Develop the L matrix from GCP ground coordinates
j = 1;
for i=1:numpts
   L(j)=X(i);
   L(j+1)=Y(i);
   j = j+2;
end
L = L';
% Compute the least squares solution
%   Note that the single quote charcter is the transpose operator in Matlab
   T2D = (A'*A)^-1*(A'*L);
% Compute the residuals matrix (not necessary, but good to check).
   V = L - A*T2D;
% Compute the initial estimate of yaw rotation
kap = atan2(T2D(2),T2D(1));    %radians, atan2 is full circle inverse tangent
% Compute scale (not necessary, but good to check).
scale = (T2D(1)^2+T2D(2)^2)^0.5;
% Compute the initial estimates of the sensor (camera) real world coordinates
TX = T2D(3);   % Initial estimate of sensor X
TY = T2D(4);   % Initial estimate of sensor Y
%
% Form the initial rotation matrix. Begin iteration while loop here.
while maxdelrot > allowdelrot  % check on allowable error (radians)
```

```
M = zeros(3,3);
M(1,1) = cos(phi)*cos(kap);
M(1,2) = sin(omeg)*sin(phi)*cos(kap) + cos(omeg)*sin(kap);
M(1,3) = -cos(omeg)*sin(phi)*cos(kap) + sin(omeg)*sin(kap);
M(2,1) = -cos(phi)*sin(kap);
M(2,2) = -sin(omeg)*sin(phi)*sin(kap) + cos(omeg)*cos(kap);
M(2,3) = cos(omeg)*sin(phi)*sin(kap) + sin(omeg)*cos(kap);
M(3,1) = sin(phi);
M(3,2) = -sin(omeg)*cos(phi);
M(3,3) = cos(omeg)*cos(phi);
%
B = zeros(numpts*2,6);
E = zeros(numpts*2,1);
% Compute the parameters of the Taylor series expansion
% of the collinearity equations
j = 1;
for i = 1:numpts
delX = X(i)-TX;
delY = Y(i)-TY;
delZ = Z(i)-TZ;
q(i) = M(3,1)*delX + M(3,2)*delY + M(3,3)*delZ;
r(i) = M(1,1)*delX + M(1,2)*delY + M(1,3)*delZ;
s(i) = M(2,1)*delX + M(2,2)*delY + M(2,3)*delZ;
%
B(j,1) = focl/q(i)^2*(r(i)*(-M(3,3)*delY...
       + M(3,2)*delZ)- q(i)*(-M(1,3)*delY + M(1,2)*delZ));
B(j,2) = focl/q(i)^2*(r(i)*(cos(phi)*delX + sin(omeg)*sin(phi)*delY...
       - cos(omeg)*sin(phi)*delZ)...
       + q(i)*(sin(phi)*cos(kap)*delX - sin(omeg)*cos(phi)*cos(kap)*delY...
       + cos(omeg)*cos(phi)*cos(kap)*delZ));
B(j,3) = focl/q(i)*(-M(2,1)*delX - M(2,2)*delY - M(2,3)*delZ);
B(j,4) = focl/q(i)^2*(-r(i)*M(3,1) + q(i)*M(1,1));
B(j,5) = focl/q(i)^2*(-r(i)*M(3,2) + q(i)*M(1,2));
B(j,6) = focl/q(i)^2*(-r(i)*M(3,3) + q(i)*M(1,3));
%
B(j+1,1) = focl/q(i)^2*(s(i)*(-M(3,3)*delY...
         + M(3,2)*delZ)- q(i)*(-M(2,3)*delY + M(2,2)*delZ));
B(j+1,2) = focl/q(i)^2*(s(i)*(cos(phi)*delX + sin(omeg)*sin(phi)*delY...
         - cos(omeg)*sin(phi)*delZ)...
       + q(i)*(-sin(phi)*sin(kap)*delX + sin(omeg)*cos(phi)*sin(kap)*delY...
       - cos(omeg)*cos(phi)*sin(kap)*delZ));
B(j+1,3) = focl/q(i)*(M(1,1)*delX + M(1,2)*delY + M(1,3)*delZ);
B(j+1,4) = focl/q(i)^2*(-s(i)*M(3,1) + q(i)*M(2,1));
B(j+1,5) = focl/q(i)^2*(-s(i)*M(3,2) + q(i)*M(2,2));
B(j+1,6) = focl/q(i)^2*(-s(i)*M(3,3) + q(i)*M(2,3));
%
```

```
E(j,1) = x(i) - xo + focl*r(i)/q(i);
E(j+1,1) = y(i) - yo + focl*s(i)/q(i);
j = j + 2;
end
%
% Solve for the Delta matrix
DEL = (B'*B)^-1*(B'*E);
%
% Add corrections to the external geometry parameters
omeg2 = omeg + DEL(1);
phi2 = phi + DEL(2);
kap2 = kap + DEL(3);
TX2 = TX + DEL(4);
TY2 = TY + DEL(5);
TZ2 = TZ + DEL(6);
% Repeat above steps with corrected external geometry parameters
% beginning with the M matrix.
% Iterate until acceptable error.
maxdelrot= max(DEL(1:3));
itcount = itcount + 1;
omeg = omeg2;
phi = phi2;
kap = kap2;
TX = TX2;
TY = TY2;
TZ = TZ2;
i = 1;
j = 1;
end   % end of while loop
%
% Display external geometry parameters in degrees and meters
itcount
format short;
omega = omeg*180/pi
phi = phi*180/pi
kappa = kap*180/pi
format bank;
CameraX = TX
CameraY = TY
CameraZ = TZ
% Print external geometry parameters to text file
fid = fopen('Exgeo.txt','wt');
     fprintf(fid,' Omega Phi Kappa  CameraX  CameraY CameraZ\n');
     fprintf(fid,'%12.4f  ',omega,phi,kappa,TX,TY,TZ);
     fclose(fid);
```

Space Intersection by Collinearity

```
% Spaceintersect.m
% Space intersection by the collinearity equations to determine ground coordinates
% and elevation of a target point measured in image space.
% This code is algorithmic. It purposely omits standard devices, such
% as error trapping and checks on singularity, in favor of clarity.
% The intent of the code is educational.  There is no guarantee of suitability or accuracy.
%
% G.N. Teasdale Copyright 2004, 2005
%
% Example of Genesee aerial 22 Feb 04
%
% Set digital camera parameters
focl = 17.00;  %calibrated lens focal length, mm
xo = 0;  % calibrated principal point x direction, mm
yo = 0;  % calibrated principal point y direction, mm
%
% Initialize counter and allowable error for least squares iteration
itcount = 0;
%Read external orientation parameters of both images from text file
% Rotation angles in degrees
[ID,omega,phi,kappa,XL,YL,ZL]=textread('Gen_exgeo.dat','%s %f %f %f %f %f %f');
%
%Read image coordinates of target point in overlap area from text file
% First element is measured in the left image.
[ID,xa,ya]=textread('Gen_target1.dat','%s %f %f');
%
% Convert the external orientation parameters to radians
omega = omega * pi/180;
phi = phi * pi/180;
kappa = kappa * pi/180;
%
nimages = length(ID);
% Compute initial estimates of ground coordinates of point
% assuming vertical geometry.
% Compute x-parallax of the target point
pa = xa(1)-xa(2);
%
% Compute air base
pbase = ((XL(2)- XL(1))^2 + (YL(2) - YL(1))^2)^0.5;
% Compute the approximate ground coordinates in image
% centered system from parallax relationship.
XI = pbase*xa(1)/pa;
YI = pbase*ya(1)/pa;
ZI = (ZL(1)+ZL(2))/2 - pbase*focl/pa;
```

```
% By definition the image space coordinates of the camera centers
% are zero values except for the x value of the right camera center.
% This is because the left cameras points at origin of the image
% coordinate system and the right camera points at the x axis at a
% distance equal to the photobase away from the origin.
xL = [0 pbase];
yL = [0 0];
%
% Transform ground coordinates from image centered coordinates
% used for parallax computations to UTM system.
% Camera center points are known so two equations ( x and y)
% can be written for each camera center.
% This gives four equations to solve for the three unknown
% transformation parameters.
%  Xs = ax - by + Tx
%  Ys = ay + bx +Ty
% Develop the A matrix from image coordinates at ground scale
j = 1;
for i=1:2
   A(j,:)=[xL(i),-yL(i),1,0];
   A(j+1,:)= [yL(i),xL(i),0,1];
   j = j+2;
end
% Develop the L matrix from GCP ground coordinates
j = 1;
for i=1:2
   L(j)=XL(i);
   L(j+1)=YL(i);
   j = j+2;
end
L = L';
% Compute the solution
%   Note that the single quote charcter is the transpose operator in Matlab
   T2D = (A'*A)^-1*(A'*L);
% Compute the residuals matrix (not necessary, but good to check).
   V = L - A*T2D;
% Compute the initial approximation UTM coordinates of the target point
XA1 = T2D(1)*XI - T2D(2)*YI + T2D(3);
YA1 = T2D(2)*XI + T2D(1)*YI + T2D(4);
ZA1 = ZI;   % No transformation of elevation. This is established by the
%           known external orientation.
%
% Form the initial rotation matrix for each image.
M = zeros(3,3,nimages);
for i = 1:nimages;
M(1,1,i) = cos(phi(i))*cos(kappa(i));
```

```
M(1,2,i) = sin(omega(i))*sin(phi(i))*cos(kappa(i))...
        + cos(omega(i))*sin(kappa(i));
M(1,3,i) = -cos(omega(i))*sin(phi(i))*cos(kappa(i))...
        + sin(omega(i))*sin(kappa(i));
M(2,1,i) = -cos(phi(i))*sin(kappa(i));
M(2,2,i) = -sin(omega(i))*sin(phi(i))*sin(kappa(i))...
        + cos(omega(i))*cos(kappa(i));
M(2,3,i) = cos(omega(i))*sin(phi(i))*sin(kappa(i))...
        + sin(omega(i))*cos(kappa(i));
M(3,1,i) = sin(phi(i));
M(3,2,i) = -sin(omega(i))*cos(phi(i));
M(3,3,i) = cos(omega(i))*cos(phi(i));
end
%
% Compute the parameters of the Taylor series expansion of the collinearity equations
%  The system of equations is:
%     b14 dXa + b15 dYa + b16 dZa = J + vxa
%     b24 dXa + b25 dYa + b26 dZa = K + vya
%  Write these equations for the target point for each each image
%  so there are four equations total.
%
Zdif = 10;
while Zdif > 0.1
for i = 1:nimages
delX(i) = XA1 - XL(i);
delY(i) = YA1 - YL(i);
delZ(i) = ZA1 - ZL(i);
q(i) = M(3,1,i)*delX(i) + M(3,2,i)*delY(i) + M(3,3,i)*delZ(i);
r(i) = M(1,1,i)*delX(i) + M(1,2,i)*delY(i) + M(1,3,i)*delZ(i);
s(i) = M(2,1,i)*delX(i) + M(2,2,i)*delY(i) + M(2,3,i)*delZ(i);
%
BB(1,4,i) = focl/q(i)^2*(-r(i)*M(3,1,i) + q(i)*M(1,1,i));
BB(1,5,i) = focl/q(i)^2*(-r(i)*M(3,2,i) + q(i)*M(1,2,i));
BB(1,6,i) = focl/q(i)^2*(-r(i)*M(3,3,i) + q(i)*M(1,3,i));
%
BB(2,4,i) = focl/q(i)^2*(-s(i)*M(3,1,i) + q(i)*M(2,1,i));
BB(2,5,i) = focl/q(i)^2*(-s(i)*M(3,2,i) + q(i)*M(2,2,i));
BB(2,6,i) = focl/q(i)^2*(-s(i)*M(3,3,i) + q(i)*M(2,3,i));
%
EE(1,i) = xa(i) - xo + focl*r(i)/q(i);
EE(2,i) = ya(i) - yo + focl*s(i)/q(i);
end
%
% Construct the combined B matrix (not elegant, but clear)
B = [BB(1,4,1) BB(1,5,1) BB(1,6,1)
    BB(2,4,1) BB(2,5,1) BB(2,6,1)
```

```
    BB(1,4,2) BB(1,5,2) BB(1,6,2)
    BB(2,4,2) BB(2,5,2) BB(2,6,2)];
% Construct the combined E matrix
E = [EE(1,1)
    EE(2,1)
    EE(1,2)
    EE(2,2)];
% Solve for the Delta matrix (delX, delY, delZ)
DEL = (B'*B)^-1*(B'*E);
%
% Add corrections to the initial estimates
XA1 = XA1 - DEL(1);
YA1 = YA1 - DEL(2);
ZA1 = ZA1 - DEL(3);
% Check allowable error
Zdif = abs(DEL(3));
itcount = itcount + 1
%
end  % end of while loop
%
% Check the result by substituting result back into the collinearity equations
%  Should be exact for two images except for truncation and roundoff error.
for i = 1:2;
delX(i) = XA1 - XL(i);
delY(i) = YA1 - YL(i);
delZ(i) = ZA1 - ZL(i);
testxa(i) = xo - focl*((M(1,1,i)*delX(i) + M(1,2,i)*delY(i) + M(1,3,i)*delZ(i))...
                /(M(3,1,i)*delX(i) + M(3,2,i)*delY(i) + M(3,3,i)*delZ(i)));

testya(i) = xo - focl*((M(2,1,i)*delX(i) + M(2,2,i)*delY(i) + M(2,3,i)*delZ(i))...
                /(M(3,1,i)*delX(i) + M(3,2,i)*delY(i) + M(3,3,i)*delZ(i)));
%
end
check_error = [xa - testxa' ya - testya']
%
% Display target point real world coordinates
TargetX = XA1
TargetY = YA1
TargetZ = ZA1
```

4. Analytical Aerial Survey

Many features of interest in watershed assessment are difficult to measure at an appropriate level of accuracy on a large scale. Current data about hydrologically important parameters such as land use and land cover type, drainage channel density, road density, potential point source discharge locations, and disturbance areas are seldom available at the onset of a hydrologic study. Ground-level sampling of these features over large areas is cost prohibitive or prevented by access restrictions.

Satellite and aerial remote sensing is an efficient alternative for collecting information about certain types of watershed features. Medium resolution satellites such as Landsat regularly image the surface of the earth to monitor changes in vegetation and some aspects of hydrologic condition over multiple seasons and years. Aerial transects, especially with simultaneous acquisition of high-resolution aerial imagery, reveal watershed and stream characteristics impossible to quantify by other means. An aircraft can acquire hundreds of miles of moderately spaced aerial imagery transects within a few days to capture a synoptic view of current watershed conditions.

Aerial transect sampling techniques generally fall under the general rubric of cluster sampling and distance sampling. Statistical theory related to cluster sampling is relatively well developed and follows familiar procedures from random and systematic sampling. Three main types of transect sampling are encountered when sampling with aerial image transects: line intersect sampling, line interval sampling and strip transect sampling. Each will be discussed below with illustrative examples from the Potlatch study region.

Distance sampling (Buckland et al. 2001) is a relatively new extension of conventional transect sampling with strong, but mostly undeveloped potential for even more efficient forms of aerial sampling of watershed characteristics, especially under rapidly changing conditions.

4.1 Aerial Line Intersect Sampling

Line intersect sampling (LIS) is an efficient method to estimate properties of ground surface features in aerial imagery or by direct aerial observation (Buckland et al. 2001; de Vries 1986). In line intersect (or intercept) sampling the properties of an element of a population are recorded when objects intersect lines or transects that pass through the study region. In this research LIS methods are used to estimate the total length of gullies and drainage channels with a series of flight lines arranged across the study region. A practical advantage of LIS for total object length is that no dimension measurements of the objects are necessary, only a count of the number objects that intersect transect lines. Counts may be made directly from sequential non-georeferenced aerial images, reducing cost and sampling effort.

A typical experimental design is to randomly select transect lines perpendicular to a base line across the region. Transects are traversed and the total number of object intercepts counted. Long objects have a higher probability of inclusion than short objects. In the current research, more numerous lower order channels have a higher probability of inclusion than higher order channels. In general, unbiased estimation of population quantities depends on determining the size dependent probabilities of inclusion (Thompson 1992). This holds for general LIS, but the dependency is removed for density estimates when feature length is the property of interest.

De Vries (1986) developed a general theory of line intersect sampling in which any quantifiable property x_i of a randomly placed object i of axis length, l_i could be estimated with a fixed line of Length L. An unbiased estimate of property density (quantity per unit area) is:

$$\hat{X} = \frac{\pi}{2L} \sum_n \frac{x_i}{l_i} \qquad 4.1$$

where $\hat{X}$ is the estimate of the quantity of the property of interest per unit area (specific property or areal density), x_i is the measured property of object i, n is the total number of objects that intersect the transect line of total length L. The constant $\pi/2$ and length parameters in Equation 4.1 derive from the arbitrary angular orientation of objects. This very useful relationship is derived from probability theory in Appendix 4.1.

When total object length is the property of interest, the summation in Equation 4.1 reduces to a simple count n of the intersected objects,

$$\hat{D} = \frac{\pi}{2L} \sum_n \frac{l_i}{l_i} = \frac{\pi}{2L} n \qquad 4.2$$

where $\hat{D}$ is the length of objects per unit area. De Vries reports that Matern (1964) and others employed Equation 4.2 to estimate lengths of waterways and channels. Skidmore and Turner (1992) adapted the technique to assess map accuracy and measure perimeters of vegetation patches. It is advantageous that Equation 4.2 holds even when some assumptions of the theoretical development are not met. Unfortunately, this is not the case for estimates of variance and estimator precision.

Variance of a quantifiable property of randomly distributed objects in an area with k fixed transect lines may be estimated (de Vries 1986):

$$\hat{\text{var}}\ \hat{X}_w = \left(\frac{\pi}{2\sum_k L_j} \right)^2 \sum_j^k \sum_i^{n_j} \left(\frac{x_{ij}}{l_{ij}} \right)^2 \qquad 4.3$$

where $\hat{\text{var}}\ \hat{X}_w$ is the estimate of the variance of the specific property (quantity per unit area) across all transect lines. When length is the property of interest Equation 4.3 simplifies to:

$$\hat{\text{var}}\ \hat{D} = \left(\frac{\pi}{2L_T} \right)^2 n = \left(\frac{\pi \cdot n}{2L_T \cdot n} \right)^2 n = \left(\frac{\hat{D}}{n} \right)^2 n = \frac{\hat{D}^2}{n} \qquad 4.4$$

Equation 4.4 is the expression for variance adapted by Skidmore and Turner (1992) to compute the number of transects required to achieve a desired level of precision. However, de Vries (1986) emphasized that Equation 4.3 was developed assuming objects are randomly distributed over *fixed* transect lines, such as fibers scattered on a counting grid, and not the alternative of transect lines randomly placed over a fixed unordered population of objects. In theory, Equation 4.3 cannot be applied to randomly (or systematically) placed transect lines because of unknown covariances between the transect lines and object lengths due to unknown object angular orientation.

Fortunately de Vries offers a practical suggestion. He suggests that quantifiable properties may be estimated from *k* randomly placed transects of varying length with:

$$\hat{X}_w = \frac{\sum_k L_j \hat{X}_j}{\sum_k L_j} \qquad 4.5$$

where the property estimate $\hat{X}_j$ along transect *j* is:

$$\hat{X}_j = \frac{\pi}{2L} \sum_i^{n_j} \frac{x_{ij}}{l_{ij}} \qquad 4.6$$

When length is the property of interest, Equation 4.5 reduces to Equation 4.2 where L is replaced by total length L_T:

$$\hat{D}_w = \frac{\pi}{2L_T} n \qquad 4.7$$

In application of the Central Limit Theorem, variance of the specific property may be estimated with:

$$\hat{\text{var}}\ \hat{X}_w = \frac{\sum_k L_j \left(\hat{X}_j - \hat{X}_w\right)^2}{(k-1)\sum_k L_j} \qquad 4.8$$

The *k-1* term in the denominator makes Equation 4.8 equivalent to the square of the standard error of the mean. Subsequently, confidence intervals with *k-1* degrees of freedom are approximated as:

$$\hat{X}_w - t^{\alpha}_{k-1}\sqrt{\hat{\text{var}}\ \hat{X}} < X < \hat{X}_w + t^{\alpha}_{k-1}\sqrt{\hat{\text{var}}\ \hat{X}} \qquad 4.9$$

Equation 4.8 indicates that multiple transects are necessary to compute an estimate of variance and precision of the property mean. In practical applications, appropriately long transects may be subjectively subdivided into multiple transects to approximate variance and confidence intervals (Buckland et al. 2001).

An appropriately long transect would be one in which the subdivided transects each provide a representative sample of the target population. For example, in an aerial survey of agricultural land cover types the observation is made at the scale of an agricultural field. Agricultural fields in the eastern Palouse region are about 1 km across, so a flight line 30 km long would be expected to sample about 30 agricultural fields – a reasonable representation. The 45 flight lines (transects) in the March 2004 aerial survey of the Potlatch River basin averaged 33 km in length. It would probably not

be appropriate to subdivide these flight lines to increase the number of transects used in the computation of the variance for land cover area estimates. On the other hand, a continuous aerial survey flight between Pullman, WA and Walla Walla, WA would sample a straight line distance of approximately 125 km. The outbound flight line could be divided into 4 or 5 sub-transects for variance computations. The return flight survey would be offset from the outbound flight path to provide a total of 8 or 10 sub-transects.

Line intersect sampling theory assumes random distribution of objects through the population region. Ordered arrangements, such as drainage channel networks and road systems, introduce bias into estimates. Estimates become biased when objects are clumped or angularly oriented along general trends. Objects parallel to sampling transects have the least probability of intercept (zero) while perpendicular elements have the greatest probability of inclusion, possibly 100% if the object is as long as the separation of transects.

Transects may be arranged to offset the effect of orderliness when direction bias is detected prior to sampling. Possible transect schemes include two-way grids and radial line clusters (de Vries 1986). Innovative sampling plans may be developed to take advantage of aircraft maneuverability and global positioning system tracking. With aircraft, sampling strategies may easily include aerial transects composed of meandering tracks, circular and spiral tracks, transects along contour lines, transects along drainages, tracks along and across environmental gradients, and feature avoidance tracks. Though not much discussed in the literature, clumping of elements (spatial autocorrelation) might be offset by grouped parallel transects arranged systematically across the study region. Strict random placement of transect lines may be relaxed and good results obtained with a

systematic grid originating from a random starting position as long as the line spacing does not coincide with regular spatial features (Buckland et al. 2001).

It should be remembered that the approaches suggested by de Vries for practical estimates in Equations 4.5 through 4.9 are partly subjective, though experience shows not unreasonably so. The stronger effect on estimate reliability in the current research likely comes from channel orientation bias. Considering the partly subjective nature of the variance estimator and the strong possibility of biased orientation of high order channels, it is prudent to test the LIS estimation technique by comparison with known population properties. A digital channel network derived from a digital elevation model DEM of the study region provides this opportunity.

4.2 LIS Estimate of Digital Drainage Channel Length

Testing the accuracy of an extensive sampling technique such as aerial LIS is conceptually simple, but difficult in practical application because there are no accurate and spatially extensive datasets for comparison. For example, an LIS estimate of total drainage channel length determined from aerial images might be compared to "blue line" channels on the USGS 7.5 minute topographic quadrangles. However, stream channels on the topographic maps are scale dependent (USGS 1997) and experience with high-resolution aerial imagery shows the topographic quadrangles exclude many low order and intermittent streams of significance in erosion modeling.

A practical test that simulates aerial LIS can be made with a digital drainage channel network of the Potlatch basin extracted from the USGS 10-meter resolution DEM. The simulated test will be followed by demonstration of an actual LIS sampling

of ephemeral gullies and persistent channels from aerial images acquired along transects across the study region. Ephemeral gullies are channels formed by concentrated flow erosion on annually tilled or disturbed soils that are later obliterated by normal tillage operations. Ephemeral gullies are important erosion features in the assessment of watershed sediment production and are discussed in detail in Section 8.

It is necessary to examine the simulated test first to better understand factors that might influence the accuracy of the LIS estimate of real channels. The digital channel network represents real terrain variability and should provide a reasonable model for testing the efficiency of aerial transect (flight line) spacing and orientation. The development of a digital channel network for the Potlatch basin is omitted from the discussion, but is not a trivial exercise and is detailed in Appendix 4.4.

4.2.1 Orientation of Aerial Transects

Transects are placed across the digital channel network in GIS at the same spacing and orientation as the aerial survey flight lines of the Potlatch basin study region. Counts of the intersections between the transect lines and digital channels and transect lengths provide the necessary data for an LIS estimate. Differences between estimated lengths and actual digital channel lengths demonstrate the accuracy of LIS techniques. Potential sampling bias is indicated by comparing estimated and actual digital channel lengths for different stream orders.

Aerial imagery transects in the research were required to satisfy multiple sampling and interpretation objectives. A total of 45 flight lines (Figure 4.1) were oriented north to south and spaced at one kilometer intervals across the region to give systematic coverage of the study area and provide efficient image interpretation and

geoprocessing. The easting coordinate of the first flight line was randomly selected. North-south extent of the flight lines passed beyond the study area boundaries. Total flight line length within the watershed boundaries of the six primary subbasins of the study region was 723 km (450 mi).

Straight north-south flight lines likely bias estimates of the length of high order stream channels. High order channels tend to flow southerly in most of the study region. Flight line orientation likely does not bias estimates of lower order channels that are more randomly oriented by erosion processes and drainage patterns of the loess hill topography.

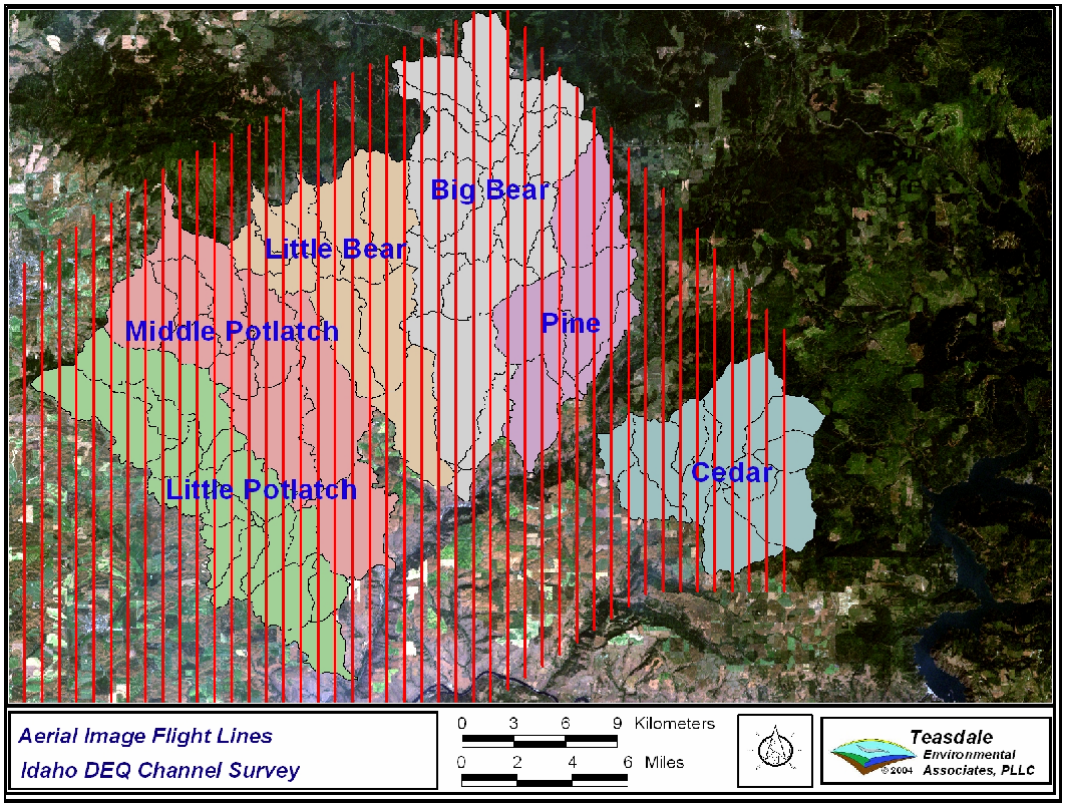

Figure 4.1 Flight lines over the primary subbasins of the lower Potlatch River basin.

4.2.2 Assessment of Orientation Bias

Direction azimuths of the 7,040 channel links were determined by GIS processing. Each channel link is composed of multiple line segments, yielding a total of over 80,000 elements. Histograms of direction azimuths (Figures 4.2 through 4.5) show increased bias with a southerly tendency in higher Horton-Strahler order channels. The histogram for first order channels approaches a uniform distribution of channel directions indicating near random orientation of the channel segments. Extending the trend means gullies are expected to be more randomly oriented than first order channels. Estimates of the length of low order channels (and gullies) by line intercept sampling will likely be the most reliable because of the reduced orientation bias. The effect of spatial bias likely persists because locations of clusters of first and second order channels are constrained by the locations and orientation of higher order channels.

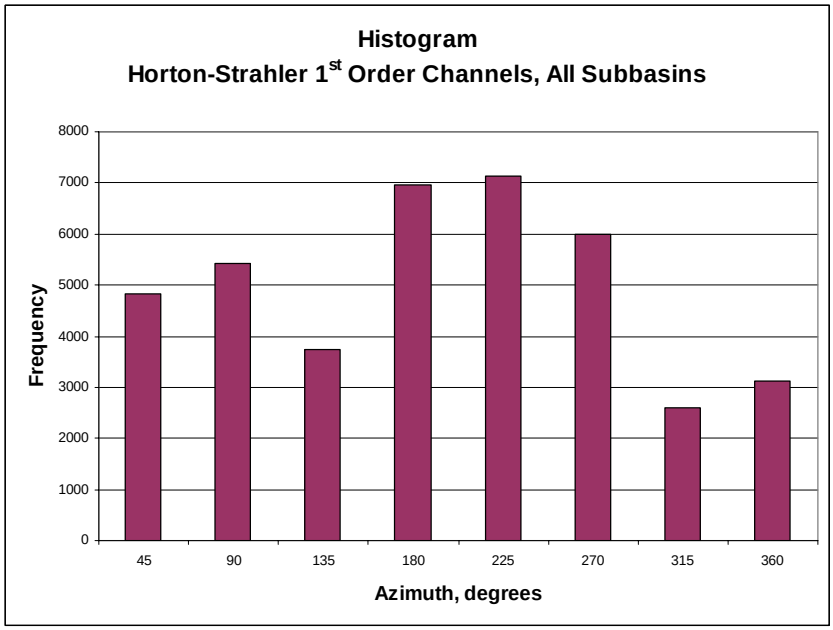

Figure 4.2 Histogram of first order channel direction azimuths.

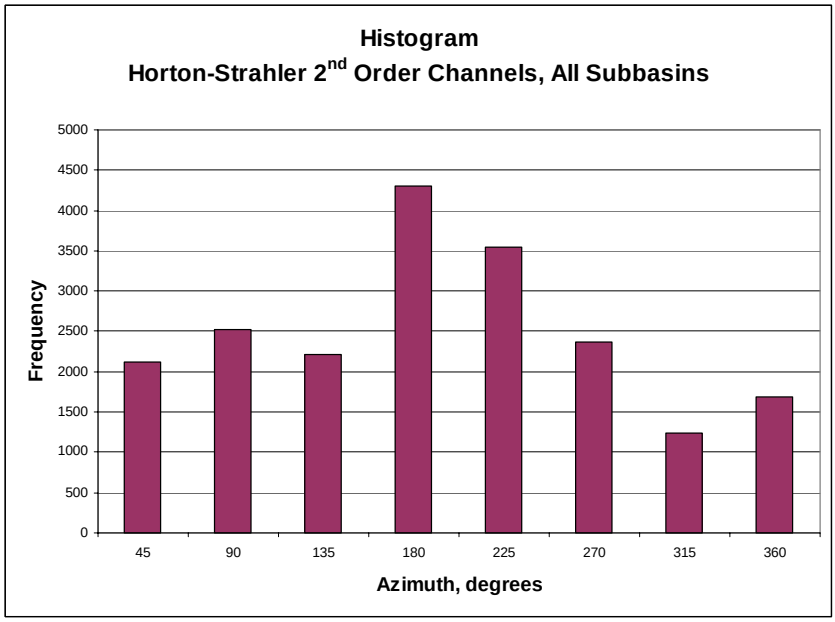

Figure 4.3 Histogram of second order channel direction azimuths.

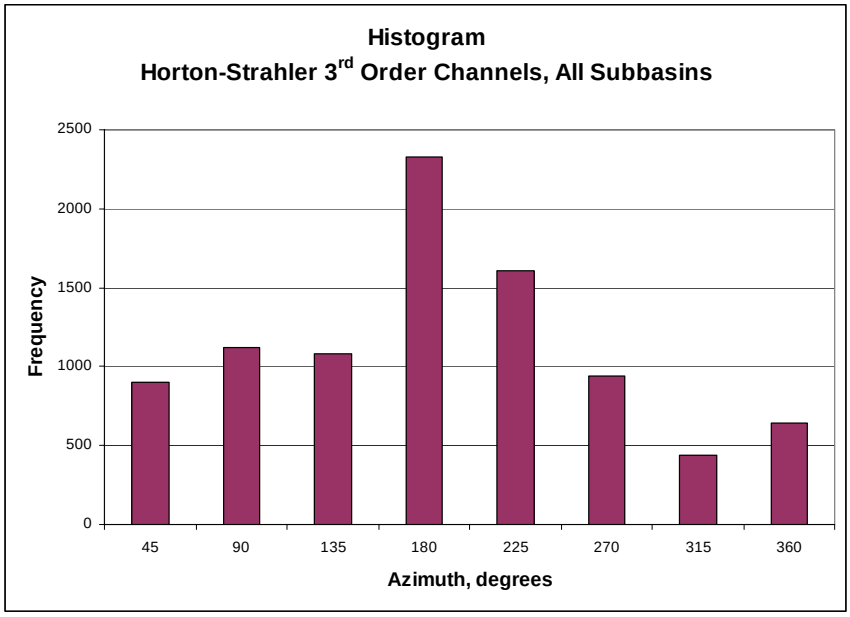

Figure 4.4 Histogram of third order channel direction azimuths.

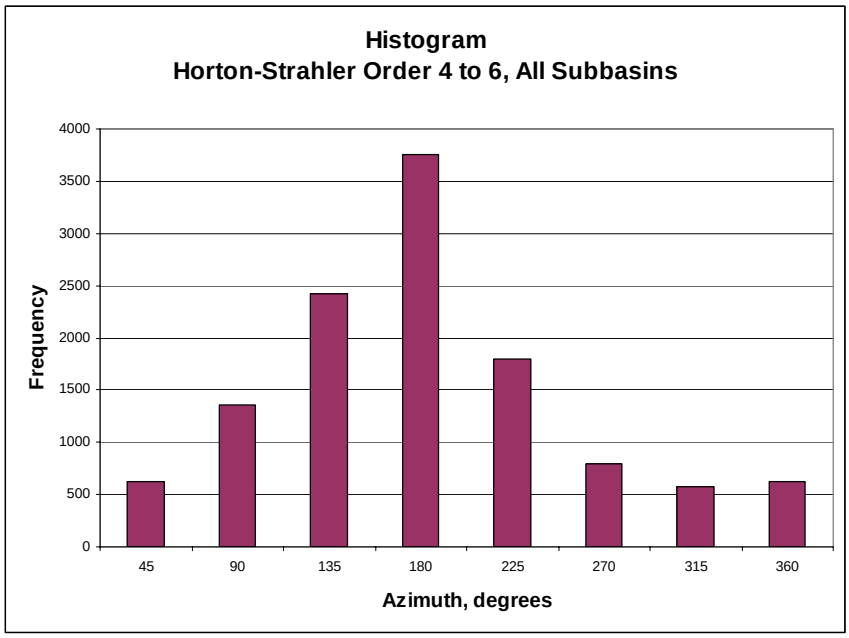

Figure 4.5 Histograms of higher order channel direction azimuths.

4.2.3 LIS Estimates of Channel Length and Theoretical LIS Variance

Flight line transect lengths within the perimeters of the subbasins were extracted with a GIS clipping operation. Point intersections between the flight line transects and the digital channel network were identified generated in GIS with a polyline-intersect operation (Figure 4.6). Channel intersections summarized in Table 4.1 were counted and tabulated by subbasin and Horton-Strahler channel order with a spreadsheet analysis. The steep canyons of the lower elevations of the Potlatch River basin were formed in prehistoric times in a wetter climate and now constrain development of middle order channels. This most noticeable in the low number of 4^{th} order channels intersected in the Little Bear Creek subbasin.

Drainage channel density for each order and subbasin was computed by Equation 4.7 from the intersect counts. Channel densities were converted to total channel lengths in each order by multiplying the channel density by the subbasin areas or total area.

Transect lengths and subbasin areas are tabulated in Table 4.2. Transect density, also in Table 4.2, provides a measure of sampling intensity and is nearly equivalent among the subbasins. Cedar Creek transect density is slightly less because there were no flight lines over forested terrain in the eastern margin of the subbasin.

Line Intercept Counts of Drainage Channels in the Potlatch Basin							
Order	Big Bear	Cedar	Little Bear	Little Potlatch	Middle Potlatch	Pine	Total
1	169	70	97	140	131	72	679
2	75	36	33	55	53	32	284
3	26	11	11	21	30	16	115
4	12	11	4	16	10	4	57
5	14	2	18	10	14	4	62
6	12	7	5	0	0	0	24
Total	308	137	168	242	238	128	1221

Table 4.1 Channel line intercept counts by subbasin and Horton-Strahler order.

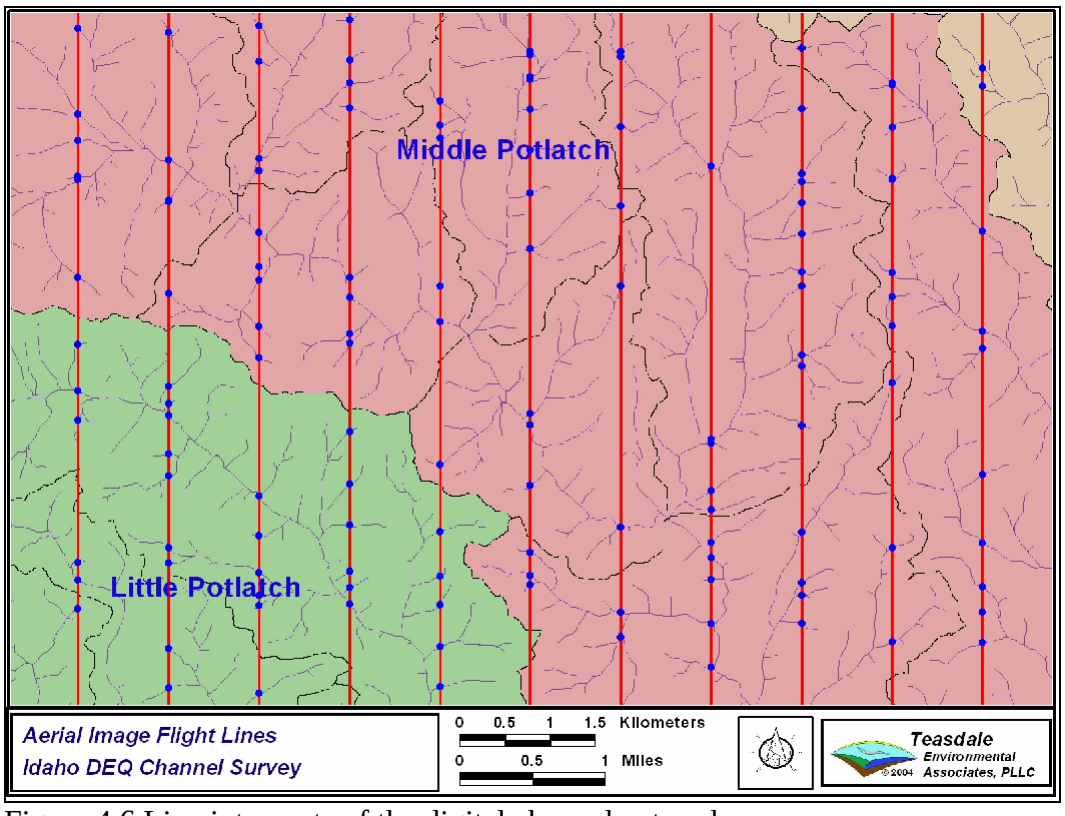

Figure 4.6 Line intercepts of the digital channel network.

Transect Length and Subbasin Areas							
	Big Bear	Cedar	Little Bear	Little Potlatch	Middle Potlatch	Pine	Total
Transect length, m	171,319	90,383	107,348	128,514	144,162	81,691	723,417
Subbasin area,ha	17,049	10,184	10,841	13,061	14,311	8,202	73,648
Transect density, m/ha	10	9	10	10	10	10	10

Table 4.2 Line intercept transect lengths and subbasin areas.

Equations 4.2 and 4.4 are readily incorporated into spreadsheet analysis of line intercept counts and watershed data. Example computations for first order channels in the Middle Potlatch demonstrate the spreadsheet formulas. Channel density and total length are computed:

$$\hat{D}_c = \frac{\pi \cdot m}{2 \cdot L_T} = \frac{\pi(131)}{2(144{,}162)} = 0.0014 \frac{\text{m}}{\text{m}^2}$$

$$\hat{L}_1 = \left(0.0014 \cdot \frac{\text{m}}{\text{m}^2}\right)(14{,}311 \cdot \text{ha})\left(10{,}000 \cdot \frac{\text{m}^2}{\text{ha}}\right)\left(\frac{1 \cdot \text{km}}{1000 \cdot \text{m}}\right) = 204.3\,\text{km}$$

The actual length of first order channels in the digital channel network of the Middle Potlatch basin is 222.7 km (excess precision is carried for clarity). Deviation and percent error is:

$$\left(\hat{L}_1 - L_{actual}\right) = 204.3 - 222.7 = -19\,\text{km}$$

$$\text{Error}\,\% = \frac{204.3 - 222.7}{222.7} \cdot 100 = -8\%$$

Expected mean deviation from the LIS estimator in Equation 4.4 is,

$$\left(\hat{L}_1 - \overline{L}\right) = \sqrt{\frac{\hat{L}_1^{\,2}}{m}} = \sqrt{\frac{(204.3)^2}{131}} = 18\,\text{km}$$

The close agreement between the expected deviation and the actual deviation indicates that random placement of transects (flight lines) only weakly violates LIS theoretical assumptions for low order channels in the study region. Actual total digital channel length, estimated total channel length, expected mean deviation, actual deviation, and percent error for the other subbasins and channel orders were similarly computed by spreadsheet and tabulated in Tables 4.3 through 4.8.

Actual deviations for first order channels ranged from -18 to 30 km. Percent differences for first order channels ranged from -10 to 16 percent. Percent differences for low channels orders (1, 2 and 3) ranged from -34 to 16 percent. Differences are much larger for higher order classes, as much as -89% for 5th order channels in Cedar Creek, as orientation bias increases. Total channel length across all orders tends to be underestimated. Variance estimates by the theoretical LIS estimator likely understate actual deviation, but still seem to offer a reasonable first approximation of the test data even though theoretical assumptions are violated by placement of the sample transects.

Total Digital Drainage Channel Length						
Order	Big Bear	Cedar	Little Bear	Little Potlatch	Middle Potlatch	Pine
	Channel Length, km					
1	261	137	155	193	223	111
2	107	79	70	97	99	58
3	49	30	25	42	45	29
4	22	21	10	26	27	13
5	23	33	32	20	25	16
6	30	9	8			
Total	492	308	300	377	419	227

Table 4.3 Total digital channel length by subbasin and channel order.

Line Intercept Estimate of Total Drainage Channel Length						
Order	Big Bear	Cedar	Little Bear	Little Potlatch	Middle Potlatch	Pine
	Channel Length, km					
1	264	124	154	223	204	114
2	117	64	52	88	83	50
3	41	19	17	34	47	25
4	19	19	6	26	16	6
5	22	4	29	16	22	6
6	19	12	8			
Total	492	219	268	386	380	204

Table 4.4 LIS estimate of total channel length by subbasin and channel order.

Expected Mean Deviation of Total Drainage Channel Length						
Order	Big Bear	Cedar	Little Bear	Little Potlatch	Middle Potlatch	Pine
	Mean Deviation, km					
1	20	15	16	19	18	13
2	14	11	9	12	11	9
3	8	6	5	7	9	6
4	5	6	3	6	5	3
5	6	3	7	5	6	3
6	5	5	4			

Table 4.5 LIS expected mean deviation of total channel length by subbasin and channel order.

Actual Deviation of Total Drainage Channel Length						
Order	Big Bear	Cedar	Little Bear	Little Potlatch	Middle Potlatch	Pine
	Mean Deviation, km					
1	3	-13	-1	30	-18	3
2	11	-16	-18	-9	-16	-7
3	-8	-10	-7	-8	2	-3
4	-4	-1	-4	0	-12	-7
5	-1	-29	-3	-4	-3	-10
6	-11	3	0	0	0	0

Table 4.6 Actual deviation of total channel length by subbasin and channel order.

Error of Line Intercept Estimate of Total Drainage Channel Length						
Order	Big Bear	Cedar	Little Bear	Little Potlatch	Middle Potlatch	Pine
	Percent Difference					
1	1	-10	-1	16	-8	2
2	10	-20	-26	-9	-17	-13
3	-17	-34	-30	-20	4	-12
4	-16	-5	-37	0	-43	-53
5	-3	-89	-11	-18	-11	-61
6	-37	39	2			

Table 4.7 Percent difference between LIS estimates of total channel length and actual digital channel lengths.

4.2.4 Practical Estimates of Variance and Confidence Intervals

Variance estimates and confidence intervals following the practical equations suggested by de Vries require a different computation procedure than described above. Each transect (flight line) is treated as an independent sample that contributes to the overall estimate of variance in proportion to its length. Computations are best carried out for each order to isolate directional bias. Squared deviation of the transect estimate of channel density from the full order estimate is computed and weighted before conversion to total length. Results of preliminary computations for first order channels are summarized in Table 4.8. Variance computations for each transect are tabulated in Appendix 4.2 Table 4A.2.1.

Preliminary Computations of First Order Channel Variance		
Total transect (flight line)	723,416	m
Number of transects, *k*	44	
Degrees of freedom (*k*-1)	43	
Two tailed t statistic, α = 0.05	2.0168	
Total Area	73,648	ha
Sum of weighted squared deviations	0.0840	$m^2 m^{-4}$
Count of first order intercepts	679	

Table 4.8 Preliminary computations of first order channel density by the equations suggested de Vries.

Final steps in the computational procedure after summation of weighted squared deviation proceeds as follows:

Channel density (Equation 4.7),

$$\hat{D}_1 = \frac{\pi \cdot n}{2 \cdot L_T} = \frac{\pi(679)}{2(723{,}416)} = 0.00147 \frac{\text{m}}{\text{m}^2}$$

Total first order channel length,

$$\hat{L}_1 = \left(0.00147 \frac{\text{m}}{\text{m}^2}\right)(73{,}648 \text{ ha})\left(10{,}000 \frac{\text{m}^2}{\text{ha}}\right)\left(\frac{1 \text{ km}}{1000 \text{ m}}\right) = 1083 \text{ km}$$

Total variance (squared standard error) of first order channel density (Equation 4.8),

$$\hat{\text{var}}\ \hat{D}_1 = \frac{\sum_k L_j \left(\hat{D}_j - \hat{D}_1\right)^2}{(k-1)\sum_k L_j} = \frac{0.0840}{(44-1)(723{,}416)} = 2.70 \times 10^{-9} \frac{\text{m}^2}{\text{m}^4}$$

Confidence interval for the estimate of channel density (Equation 4.9),

$$\hat{D}_1 - t_{k-1}^{\alpha} \sqrt{\hat{\text{var}}\, \hat{D}_1} < D_1 < \hat{D}_1 + t_{k-1}^{\alpha} \sqrt{\hat{\text{var}}\, \hat{D}_1}$$

$$0.00147 - 2.0168\sqrt{2.7 \times 10^{-9}} < D_1 < 0.00147 + 2.0168\sqrt{2.7 \times 10^{-9}}$$

Confidence interval converted to total channel length,

$$1083 - 76.3 < D_1 < 1083 + 76.3$$

$$1008 \text{ km} < D_1 < 1160 \text{ km}$$

Actual total length of first order channels measured by GIS in the digital channel network is 1081 km. The confidence intervals computed above confirm that the remarkably close estimate of total first order channels is valid. Similar computations can

be performed for other orders of channels by subbasin, but likely with less precision because of directional bias and fewer numbers of transects.

The test of LIS estimation with digital channel lengths indicates that reasonable estimates of total length of ephemeral gullies and channels can be obtained from aerial LIS sampling with moderate flight line spacing, at least for low order channels having low directional orientation bias in the study region. It appears that LIS theoretical assumptions are not strongly violated by placement of systematically spaced north-south flight lines in the experimental design. The practical approach for computing variances and confidence intervals suggested by de Vries (1986) for sampling with randomly placed transects appear to be appropriate and reliable for low order channel length determinations in the Potlatch basin study region.

4.2.5 Sampling with Grouped Line Transects

As discussed above, directional bias of high order channels affects precision of channel density estimates and estimates of total channel length. Spatial autocorrelation and clumping of low order channels in the drainage network may also bias length estimates. This aspect of line transect sampling appears to have drawn little attention, yet is likely important for developing efficient aerial LIS sampling plans of ordered networks. Grouped transects may have potential for offsetting spatial autocorrelation.

Expected variance of total channel length in Equation 4.4 depends on the summed length of transects and intercept counts. In spatially uniform ensembles, it is reasonable to assume intercept counts are likely proportional to transect length by a constant factor *k.*

Increasing the number of transects then decreases the total variance in direct proportion to total transect length:

$$\hat{\text{var}}\ \hat{D}_c = \left(\frac{\pi}{2L_T}\right)^2 m = \left(\frac{\pi}{2L_T}\right)^2 kL_T = k\frac{\pi^2}{4}\frac{1}{L_T} \qquad 4.10$$

Aerial imagery provides an efficient opportunity to increase the number of line transects when features of interest are smaller than the image coverage. A continuous aerial image swath samples a strip of ground surface of a width dependent on sensor size, lens focal length and flight altitude. The Potlatch basin aerial survey acquires images swaths with approximate widths of 650 meters on a 1 km spacing. Total coverage is about 65 percent of the study region area. The relatively wide image swath allows sampling along a cluster of parallel transects within each image swath. Analysis of the digital channel network indicates the average channel link is about 300 meters long. Since channel links are significantly less than swath width, multiple transects within a single image swath are likely to intercept unique channel links. This is an important consideration for assessing channel link properties and estimating channel lengths by channel order.

Additional transects within an image swath are not strictly random because they are contingent on the location of the central flight line. Though more rigorous statistical theory should be applied to formally evaluate the variance of the transect clusters, a first approximation of potential improvement in length estimates and variance can be made with the basic Equations 4.2 and 4.4. Practical reliability of the improved estimate can be further judged by comparison to the actual lengths of the digital channel network.

A group of three parallel transects in each image swath was evaluated to test improvement potential. The group consists of the central flight line transect plus two transects offset 250 meters on each side. This spacing was selected in keeping with the objective to systematically sample the study region. An alternative is to randomly select parallels within the image swath. Pure random selection may be less desirable if discovery and sampling of rare or sparse features is important. The additional transect lengths and intercepts were derived and analyzed as discussed above. Figure 4.7 shows the arrangement of the grouped transects and additional intercepts with the digital channel network.

Total channel length and variance by subbasin and channel order were computed by spreadsheet as discussed above. Line intersect counts, total channel length, expected mean deviations, actual deviations, and percent error of the estimated total channel length are tabulated in Tables 4.9 through 4.13. As indicated by the form of the line intercept equation, expected mean deviations were considerably reduced with the additional transects. The improvement in variance is likely overstated because of the clustering of the transect lines. Percent errors between estimated total channel lengths and actual channel lengths reduced for some channel orders and subbasins, but not consistently. There was a general improvement in estimates of lengths of higher order channels.

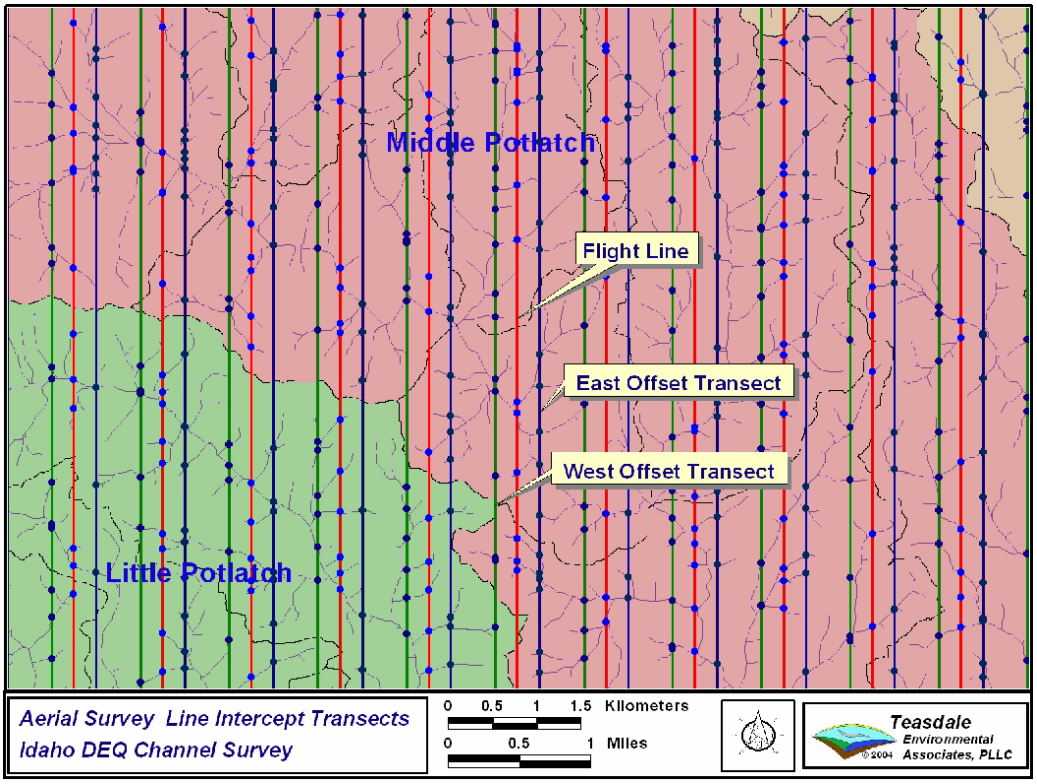

Figure 4.7 Line intercept transect clusters.

Line Intercept Counts of Drainage Channels in the Potlatch Basin							
Order	Big Bear	Cedar	Little Bear	Little Potlatch	Middle Potlatch	Pine	Total
1	476	197	298	399	441	203	2014
2	205	112	104	178	168	98	865
3	89	37	27	66	85	50	354
4	34	35	16	52	36	18	191
5	38	7	46	38	44	15	188
6	40	21	13				74
Total	882	409	504	733	774	384	3686

Table 4.9 Grouped transect line intercept counts.

Line Intercept Estimate of Total Drainage Channel Length						
Order	Big Bear	Cedar	Little Bear	Little Potlatch	Middle Potlatch	Pine
	Channel Length, km					
1	248	116	158	212	229	107
2	107	66	55	95	87	52
3	46	22	14	35	44	26
4	18	21	8	28	19	9
5	20	4	24	20	23	8
6	21	12	7			
Total	469	218	268	390	412	204

Table 4.10 Grouped transect estimate of total channel length.

Expected Mean Deviation of Total Drainage Channel Length						
Order	Big Bear	Cedar	Little Bear	Little Potlatch	Middle Potlatch	Pine
	Mean Deviation, km					
1	11	8	9	11	11	7
2	7	6	5	7	7	5
3	5	4	3	4	5	4
4	3	3	2	4	3	2
5	3	2	4	3	3	2
6	3	3	2	0	0	0

Table 4.11 Grouped transect expected mean deviation of total channel length.

Actual Deviation of Total Drainage Channel Length						
Order	Big Bear	Cedar	Little Bear	Little Potlatch	Middle Potlatch	Pine
	Mean Deviation, km					
1	-13	-21	2	19	7	-4
2	0	-13	-15	-2	-12	-6
3	-2	-8	-11	-7	-1	-2
4	-5	0	-2	2	-8	-4
5	-3	-29	-8	1	-2	-8
6	-9	3	-1			

Table 4.12 Grouped transect actual deviation of total channel length.

Error of Line Intercept Estimate of Total Drainage Channel Length						
Order	Big Bear	Cedar	Little Bear	Little Potlatch	Middle Potlatch	Pine
	Percent Difference					
1	-5	-15	2	10	3	-4
2	0	-17	-22	-2	-12	-11
3	-5	-27	-42	-16	-2	-8
4	-21	1	-16	9	-31	-29
5	-12	-87	-24	4	-7	-51
6	-31	39	-12			

Table 4.13 Percent difference between line intercept estimates of total channel length from grouped transects and actual digital channel lengths.

The analysis demonstrates that within-swath grouped transects likely improve the reliability of line intercept estimates of total channel length. It is uncertain whether the improvement is due to the increase in the number of transects or whether close spacing of transects in the group offsets spatial autocorrelation. It is likely a combination of both. Multiple transects within an image swath provide checks that help guard against mistakes in interpretation, feature classification and computations. The increased interpretive effort (no additional flight cost) of multiple within-image transects is likely warranted based both on improvements in statistical reliability and quality control.

4.3 LIS Estimate of March 2004 Ephemeral Gully Length

The test of simulated aerial LIS sampling of the digital channel network in the Potlatch Basin demonstrated good agreement between LIS estimates and actual digital channel lengths. This indicates that LIS should yield reasonable estimates of real ephemeral gully lengths in the Potlatch River study region. The accuracy of LIS estimates of real channels depends on the ability to observe and count channel intersections. Vegetation often obscures the overhead view of small channels in summer and early autumn aerial imagery. Ephemeral gullies are readily observed on high-resolution digital aerial images of agricultural land acquired during late winter and spring in the Palouse region. This section briefly describes the aerial assessment of ephemeral gullies necessary to support a LIS estimate of total ephemeral gully channel length. An expanded discussion of the aerial assessment of ephemeral gully characteristics is in Section 8.

Approximately 7,000 digital aerial images were acquired between March 13 and March 20, 2004 along the 45 flight lines described above (Figure 4.1). Ground pixel resolution averages about 0.21 m with a standard deviation of 0.02 m determined from a sample of 353 georeferenced images distributed throughout the coverage area. The GPR ranges from 0.31 m in the canyons to 0.18 m on hilltops. The digital aerial frame images are natural color with three non-radiometrically calibrated 8-bit color bands in Joint Photographic Experts Group (jpeg) format. Images of test grids show that lens geometric distortion is minimal. Raw images are 3072 by 2048 pixels oriented with the longer dimension approximately perpendicular to the direction of flight.

Figure 4.8 is a full frame image of fall-tilled agricultural fields showing gullies eroded during winter and spring 2004. Incised gullies, sediment deposition plaques and connections to the permanent channel system can be readily identified in the image. Figure 4.9 is a magnified view of the rectangular area identified in Figure 4.8.

Figure 4.8 Full frame aerial image from 13 March 2004.

Figure 4.9 Magnified view of ephemeral gullies in Figure 4.8.

Images were acquired in a timed sequence to produce approximately 60% overlap along the flight line. The camera system was passively stabilized so aircraft pitch and roll may tilt the images away from true vertical. Departures from vertical are most often induced by roll of the aircraft in turbulent air. Roll departures are momentary and usually less than 10 degrees. Features in significantly tilted images can often be viewed in adjacent overlapping aerial images that may be more nearly vertical.

4.3.1 Counts of Gully Intersections

Aerial images along a particular flight line are sequential and overlapping. Gully intersections were counted along a group of three transects on or parallel to the aircraft GPS ground track. As noted above, grouped transects increase confidence in LIS estimates without significantly increasing sampling effort. An accurate, but costly and

slow procedure is to georeference each overlapping image in a flight line sequence and count gully intersections with the ground track line and parallel offsets in GIS. This technique is best used for verification and accuracy assessment.

A more cost-effective sampling technique for large numbers of images is to view the continuous sequence of non-georeferenced aerial images in a browser or image processing program and count intersections observed along the transect line. To be most accurate the observer must visualize the ground track of the aircraft through the series of images and mentally adjust position of the transect line to compensate for minor roll departures.

Minor roll departures have little effect on the count of long gullies that cross at oblique angles to the transect line. Gullies that are short, nearly parallel to the transect line or cross at very acute angles required careful observation of the apparent position of the transect line through the sequence of images to confirm valid intersections.

Guidelines that are digitally superimposed on non-georeferenced images aid in visualization of the ground track and position of lateral transect lines (Figure 4.10). The "sweep" of the superimposed guideline along a sequence of images indicates the location of the true ground transect line. Gully intersections near points A and B on the middle transect and point C on the right transect were counted. No gullies intersect the left transect line.

Figure 4.10 Digital aerial image with superimposed transect lines.

An image interpretation key of valid gully intersections should be developed to guide new observers and maintain consistency among several observers. Magnified views of the gully intersections in Figure 4.10 are in Figure 4.11. Multiple intersections of a curving gully channel are counted as independent intersections.

Figure 4.11 Digital aerial image with superimposed transect lines.

Intersection counts must be tallied separately for each transect. Only a total count of intersections along each transect is necessary for computing an LIS estimate. Counts for individual subbasins are recorded for portion of the transect line that passes over the subbasin. It is not necessary to record the image number of a particular intersection though this may be desirable to check consistency among several observers.

Observers should not rely on a mental tally. Counts along individual transects can be conveniently accumulated with mechanical counters. Figure 4.12 illustrates an inexpensive and easily constructed device consisting of three manual counters fixed to plastic laminate or white board with double sided mounting tape. The observer depresses the counter button for each intersection and resets the counter to zero at the beginning of another transect line. Temporary identifiers for multiple transects or specific features along a single transect may be labeled on the laminate with a dry erase marker or written on masking tape.

Figure 4.12 Mechanical tally counter for three transects or three features.

4.3.2 LIS Ephemeral Gully Length Accuracy

Accuracy of an LIS estimate of ephemeral gully length can be judged by comparison with actual lengths of ephemeral gullies digitized in a swath of georeferenced aerial images. As a test, flight line number 7 of the Little Potlatch subbasin was selected at random from aerial transects crossing the Little Potlatch and Middle Potlatch subbasins (Figure 4.13). Overlapping areal images were georeferenced to produce a continuous imagery swath. Ephemeral gullies were digitized in GIS from the georeference images, a few of which are in Figure 4.14. Total length of the digitized gullies in the swath was 3,815 meters. The total imagery swath area covered by the georeferenced aerial images was 428.5 ha. Total length of the aerial transect length is 6,936 m.

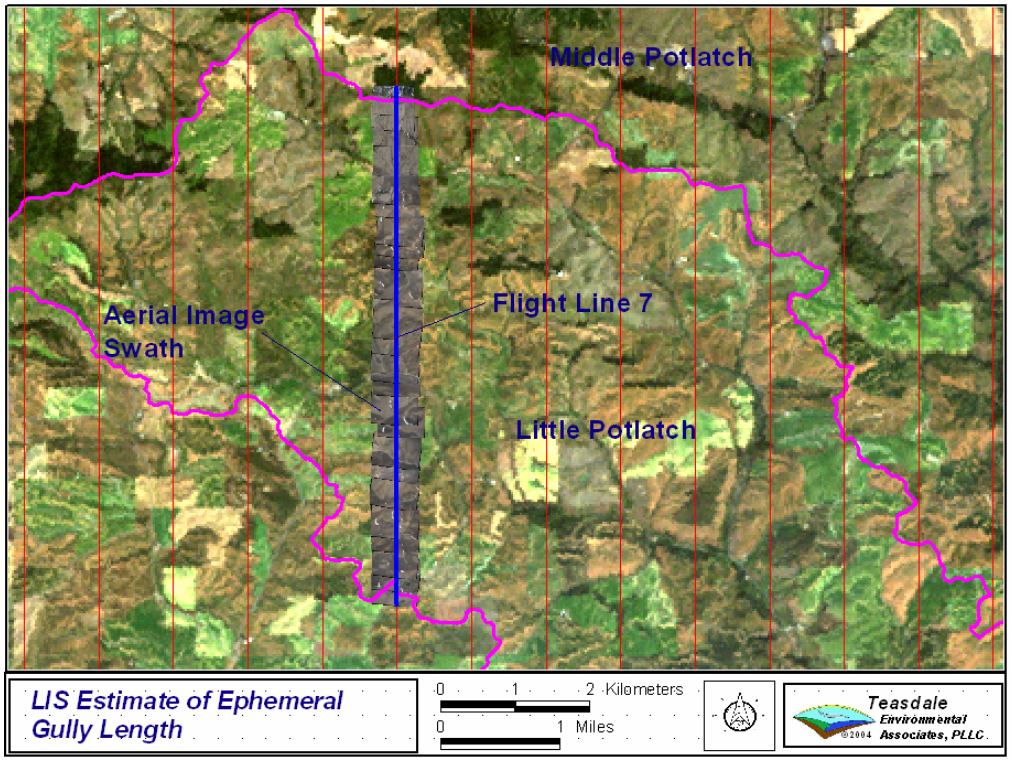

Figure 4.13 Aerial transect along flight line 7 of Little Potlatch Creek subbasin.

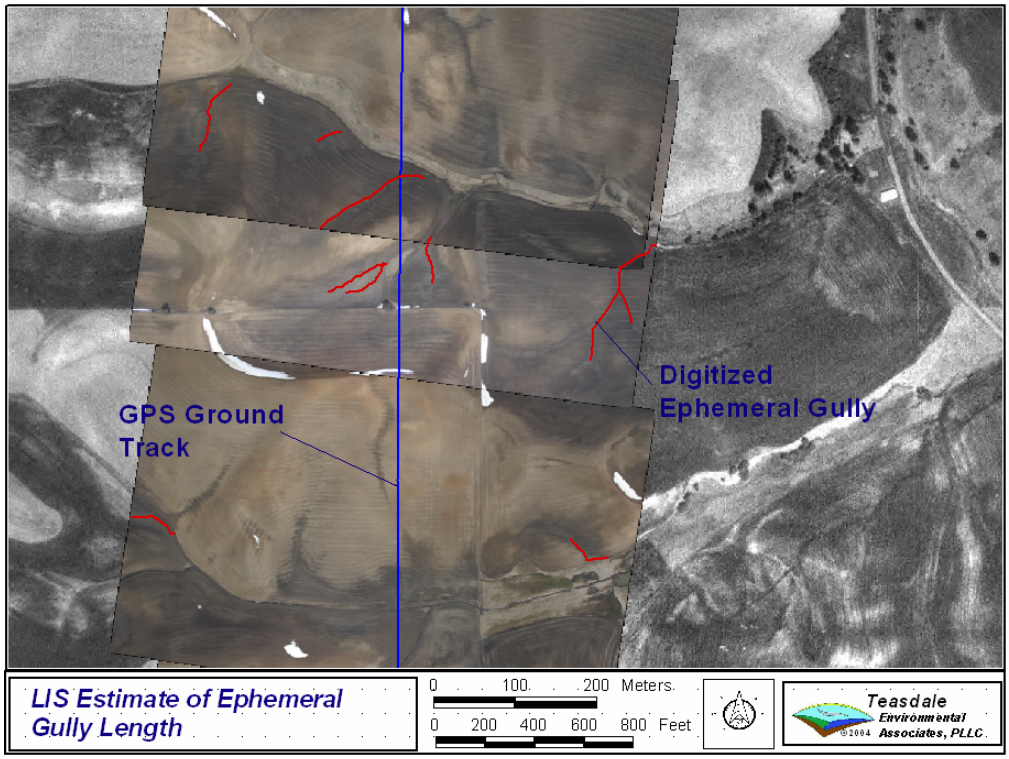

Figure 4.14 Digitized ephemeral gullies along flight line 7.

Transect 7 of the Little Potlatch subbasin is a sequence of 36 aerial images. Ephemeral gully intersection counts were 5, 4 and 4 for the left, middle and right transects. The LIS estimate of ephemeral gully density for the middle transect is computed by Equation 4.2,

$$\hat{D}_c = \frac{\pi}{2L} n = \frac{\pi}{2(6936)}(4) = 9.06 \times 10^{-4} \frac{\text{m}}{\text{m}^2}$$

An estimate of total gully length is computed by multiplying the computed gully density by the area of the image swath A_T along the transect,

$$L_e = \hat{D}_c \, A_T = 9.06 \times 10^{-4} \frac{\text{m}}{\text{m}^2} \left(428.5 \text{ ha} \times \frac{10{,}000 \text{ m}^2}{\text{ha}} \right) = 3881 \text{ m}$$

The percent difference between the estimated and actual length is,

$$E\% = \frac{3881 - 3815}{3815} \times 100\% = 2\%$$

A higher estimate of total ephemeral gully length is computed from the higher count on the left transect. With 5 intersections the estimated length is 4852 m, a 27 % difference from the actual length. An average of counts from three transects (4.33 intersections) gives an estimated length of 4,205 m, a 10% difference from the actual length.

The test indicates aerial line intersect sampling can produce remarkably accurate estimates of ephemeral gully length if intersections are counted carefully. A miscount changes estimated length in direct proportion to the error in number of intersections. Practical aerial surveys would seldom be based on a single short transect. The aerial survey of Little Potlatch subbasin consists of 18 flight lines with a total length of 138 km. The error from a miscount of gully intersections is likely greatly reduced with more and longer transects. It may be beneficial to keep a separate count of uncertain intersections to produce high and low estimates of total length.

Sometimes it is difficult to determine if an ephemeral gully exactly intersects a transect line in aerial imagery collected under turbulent conditions. Lateral discontinuity between images may be too pronounced to effectively visualize the location of the transect line. Ambiguity can be resolved by georeferencing the sequence of three overlapping images at the location of the gully in question and measure the distance of the feature from the GPS ground track. If the ground track crosses the gully it is counted as an intersection of the middle transect. If the perpendicular distance of any point on a gully to either side of the ground track equals the transect offset distance, then the gully intersection is counted in the tally of the respective lateral transect.

Figure 4.15 shows the location of the GPS ground track and offset transect lines on a sequence of georeferenced aerial images from Little Potlatch subbasin flight line 7.

Gully intersections at A, B and C were uncertain from observation of the non-georeferenced aerial images. Georeferencing shows that intersection A should be counted on the middle transect; a single branch of the gully system should be counted on the right transect at B; and both gully branches should be counted on the left transect at C. Georeferencing of the images confirmed 5 intersections on the left transect line, 4 intersections on the middle transect line and 4 intersections on the right transect line.

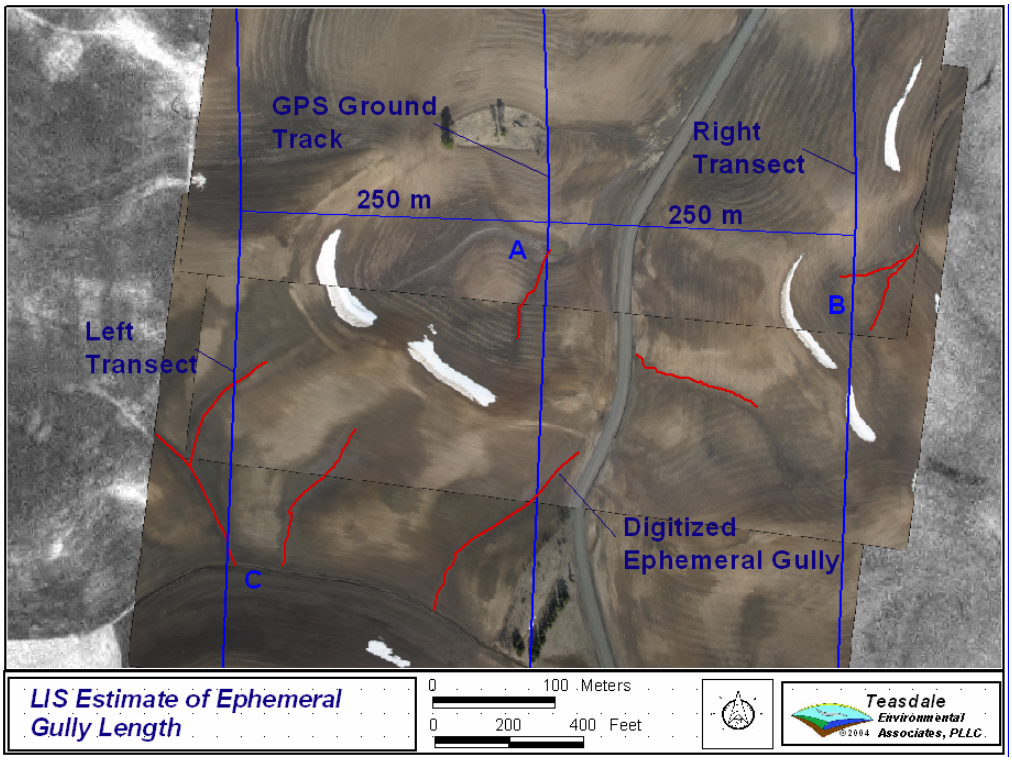

Figure 4.15 Resolving intersection ambiguities with georeferenced images.

It should be emphasized that transect lines are real ground lines established by the GPS ground track of the aircraft and need not be straight. Guidelines superimposed on the non-georeferenced aerial images only indicate the approximate location of the true transect lines. For best accuracy gully intersections should not be decided based solely on intersections with superimposed guidelines. However, guideline intersections can be

rapidly tallied and may provide sufficient accuracy for preliminary estimates. Guideline intersections for Little Potlatch flight line 7 are 5, 5 and 3 for the left, middle and right guidelines producing an average of 4.33 intersections per guideline, the same as the average value for the ground transects.

4.3.3 Total Ephemeral Gully Length for all Subbasins

Total length of ephemeral gullies for the six primary agricultural subbasins in the study region can be estimated by the LIS technique demonstrated for flight line 7. This provides a very cost effective and efficient method to estimate ephemeral gully erosion over extensive areas with rapid aerial survey methods. To the best of my knowledge this has not been done elsewhere or even discussed conceptually in the soil erosion literature.

Ephemeral gully intersections were counted along all flight lines of the six primary agricultural subbasins in the study region with the techniques discussed above. The aerial images showed that ephemeral gullies only occurred on tilled agricultural land. A more realistic estimate of ephemeral gully density is therefore based on only the length of transects across tilled agricultural land and the area within a subbasin classified as tilled agricultural land. Classification of tilled agricultural land from joint analysis of Landsat and aerial imagery is discussed in Sections 5 and 8.

Computations of ephemeral gully density are the same as the example for flight line 7 except that the total intersection count for a particular subbasin is applied to the total length of transect across the subbasin. The computations are summarized in Table 4.14. Total length of ephemeral gullies for the six subbasins is estimated to be 339 km. The Middle Potlatch subbasin had the greatest length of ephemeral gullies (106 km) and Pine Creek Subbasin had the least (26 km). Total ephemeral gully erosion volume can

be estimated by multiplying the LIS estimate of length by a typical channel width of 0.5 m and depth of 0.2 m. Assuming a bulk soil unit weight of 70 lb ft^{-3} (1120 kg m^{-3}), the ephemeral gully erosion is about 0.5 tons per acre (1.1 metric tons per ha) of tilled agricultural land.

Aerial Line Intercept Estimate of March 2004 Ephemeral Gully Length - Based on Tilled Crop Area							
	Big Bear	Cedar	Little Bear	Little Potlatch	Middle Potlatch	Pine	Total
Transect length, km	39.2	30.9	34.4	100.3	89.2	23.8	317.8
Tilled crop area, ha	4,777	4,298	3,914	9,695	8,310	2,444	33,438
ac	11,803	10,621	9,670	23,957	20,534	6,038	82,624
Intersection counts							
Left transect	22	15	31	37	78	13	196
Middle transect	32	19	41	31	68	17	208
Right transect	37	12	29	42	72	19	211
Gully density, m/m^2							
Left transect	0.00088	0.00076	0.00141	0.00058	0.00137	0.00086	0.00097
Middle transect	0.00128	0.00097	0.00187	0.00049	0.00120	0.00112	0.00103
Right transect	0.00148	0.00061	0.00132	0.00066	0.00127	0.00125	0.00104
Average	0.00122	0.00078	0.00154	0.00057	0.00128	0.00108	0.00101
Total gully length, km							
Left transect	42.1	32.8	55.4	56.2	114.2	20.9	323.9
Middle transect	61.3	41.5	73.2	47.1	99.6	27.4	343.8
Right transect	70.9	26.2	51.8	63.8	105.4	30.6	348.7
Average	58.1	33.5	60.1	55.7	106.4	26.3	338.8
Average gully width, m	0.5	0.5	0.5	0.5	0.5	0.5	0.5
Average gully depth, m	0.2	0.2	0.2	0.2	0.2	0.2	0.2
Total gully volume, m3	5,811	3,350	6,013	5,567	10,639	2,631	33,881
ft3	205,189	118,284	212,336	196,573	375,682	92,925	1,196,446
Soil unit weight, lb/ft3	70	70	70	70	70	70	70
LIS gully erosion, ton/ac	0.61	0.39	0.77	0.29	0.64	0.54	0.51

Table 4.14 Aerial line intercept sampling estimate of March 2004 ephemeral gullies.

Variance and confidence intervals are computed for the LIS estimate of ephemeral gully length by Equations 4.8 and 4.9. It is uncertain if the three grouped transect estimates can be aggregated without bias into the variance estimate, so the confidence intervals are computed only with data from the middle transect. Preliminary computations are performed by spreadsheet because of the large number of transects. As

before, the contribution of any particular transect to the total variance is weighted by the length of the particular transect to the total length of transects within a subbasin. For example, the confidence interval for the Middle Potlatch subbasin is computed by the following procedure.

Compute the weighted squared deviation of the estimate of length from flight line 14:

Flight line 14 transect length = 8007 m

Number of gully intersections = 5

Gully density estimate for flight line 14, $\hat{D}_c = \frac{\pi \cdot m}{2 \cdot L_T} = \frac{\pi(5)}{2(8007)} = 0.00098 \frac{\text{m}}{\text{m}^2}$

Squared deviation from subbasin total estimate = $8007(0.00098 - 0.00120)^2$

$= 3.8 \times 10^{-4} \frac{\text{m}^3}{\text{m}^4}$

Thus, flight line 14 contributes this amount to the summation in the numerator of Equation 4.8 in a computation of total variance for the Middle Potlatch subbasin. Contributions of the other flight lines in the Middle Potlatch subbasin are computed similarly. The total variance (squared standard error) of the Middle Potlatch subbasin is computed by Equation 4.8:

$$\hat{\text{var}}\ \hat{D}_1 = \frac{\sum_k L_j \left(\hat{D}_j - \hat{D}_1\right)^2}{(k-1)\sum_k L_j} = \frac{0.1517}{(17-1)(89{,}163)} = 1.063 \times 10^{-7} \frac{\text{m}^2}{\text{m}^4}$$

The 95 % confidence interval for the estimate of channel density by Equation 4.9 is then:

$$\hat{D}_1 - t^{\alpha}_{k-1}\sqrt{\hat{\text{var}}\,\hat{D}_1} < D_1 < \hat{D}_1 + t^{\alpha}_{k-1}\sqrt{\hat{\text{var}}\,\hat{D}_1}$$

$$0.00120 - 2.120\sqrt{1.063 \times 10^{-7}} < D_1 < 0.00120 + 2.120\sqrt{1.063 \times 10^{-7}}$$

$$0.00051\frac{\text{m}}{\text{m}^2} < D_1 < 0.00189\frac{\text{m}}{\text{m}^2}$$

The 95 percent confidence interval is converted to total channel length by multiplying by the area of tilled agricultural land in the Middle Potlatch subbasin (Table 4.14). For example the lower bound is computed:

$$L_{-mp} = 0.00051\frac{\text{m}}{\text{m}^2} \times \mathbf{8}310\ \text{ha} \times 10{,}000\frac{\text{m}^2}{\text{ha}} \times \frac{1\,\text{km}}{1000\,\text{m}} = 42.4\,\text{km}$$

The upper bound is computed similarly to give the confidence interval in units of length

$$42.4\,\text{km} < L_{mp} < 157.1\,\text{km}$$

$$L_{mp} = 96.6 \pm 57.4\,\text{km}$$

The estimate of ephemeral gully length in the Middle Potlatch subbasin based on the intersection count along the middle transect is 96.6 km plus or minus 60 percent. Confidence intervals for the middle transect count for other subbasins are summarized in Table 4.15. Confidence intervals varied from plus or minus 38 percent for the Big Bear Creek subbasin to plus or minus 79 percent for the Little Bear Creek subbasin. The overall estimate of ephemeral gully length and confidence interval for the six subbasins combined were 344 km plus or minus 19 percent.

Confidence interval widths reduce with inclusion of the left and right offset transects. For example, the estimate of ephemeral gully length and confidence interval for the Middle Potlatch Creek subbasin becomes 106 km plus or minus 22 percent. The overall estimate of ephemeral gully length and confidence interval for the six subbasins combined becomes 339 km plus or minus 7 percent. Again, it should be recognized that the statistical validity of this is uncertain because intersection counts along the two offset transects are made from the same set of aerial images and are contingent upon the

location of the primary (middle) transect. Statistics of LIS estimates produced by offset transects and extension of the de Vries equations should be pursued in future research.

March 2004 Ephemeral Gully Density and LIS Confidence Intervals for Middle Transect							
	Big Bear	Cedar	Little Bear	Little Potlatch	Middle Potlatch	Pine	Total
Gully density, m m^{-2}	0.00128	0.00097	0.00187	0.00049	0.00120	0.00112	0.00103
Flight line count, k	8	10	12	17	17	6	42
Transect length, km	39	31	34	100	89	24	318
Variance	4.15178E-08	6.0299E-08	4.46938E-07	2.62099E-08	1.06328E-07	3.00274E-08	9.51209E-09
t, 0.05, k-1	2.365	2.262	2.201	2.120	2.120	2.571	2.020
Lower CI, m m^{-2}	0.00080	0.00041	0.00040	0.00014	0.00051	0.00068	0.00083
Upper CI, m m^{-2}	0.00177	0.00152	0.00334	0.00083	0.00189	0.00157	0.00123
Estimate +- this %	37.5%	57.5%	78.6%	70.7%	57.7%	39.7%	19.2%
Tillage crop area, ha	4,777	4,298	3,914	9,695	8,310	2,444	33,438
Gully length, km	61.3	41.5	73.2	47.1	99.6	27.4	344
Lower CI, km	38	18	16	14	42	17	278
Upper CI, km	84	65	131	80	157	38	410

Table 4.15 Confidence intervals for middle transect LIS estimate of ephemeral gully length.

The width of the LIS confidence intervals for ephemeral gully length can be further reduced by stratification of the study region to reduce variance to due field type and tillage treatment. Ephemeral gullies form most often in recently tilled fields having little surface cover that exceed a critical combination of tributary area and ground steepness. This line of investigation is pursued in Sections 5 and 8 and resulted in the concept of an initiation regime for ephemeral gully development. The simple stratification adopted in the above example includes all agricultural fields, many of which have little or no potential to produce ephemeral gullies. This leads to increased variance between transect lines.

The above examples demonstrate the efficiency and robustness of the aerial survey techniques of line intercept sampling. Total ephemeral gully length is rapidly and economically estimated with aerial LIS. It is important to realize that the method does not require time consuming manual georeferencing of aerial images and digitization of

gully lengths. This is a significant new method that has much potential application in the study of soil erosion.

4.4 LIS Estimate of Persistent Intermittent and Perennial Channels

Channel length, slope and connectivity are the most important network parameters for channel erosion modeling in otherwise homogeneous bed and bank materials. Lengths determine the amount of bank exposure and slopes determine the erosive power of the water discharge. Connectivity determines how eroded sediment is routed. In hydrologic modeling, true horizontal and vertical positions of the channel segments are mostly irrelevant. The only existing dataset that partially satisfies this need is the USGS 1:24,000 hydrography digital line graph (DLG) coverages produced during compilation of 7.5 minute topographic maps. Most existing digital hydrography, such as the National Hydrography Dataset, evolved from the original USGS hydrography. Appendix 4.4 demonstrates that the existing digital datasets do not accurately represent the large scale channel detail important for high-resolution simulation.

4.4.1 Estimate of Persistent Channel Length by DEM Analysis

An alternative approach is to estimate channel length from a digital channel network derived from a DEM. The digital channel network of the lower Potlatch basin developed from the USGS 10-meter DEM in Appendix 4.4 is the best that can be produced with available elevation data at a reasonable cost. There are unavoidable errors in the digital representation of channels. The analysis of high-resolution stereo aerial imagery in Section 3 showed there are errors of definition and location in the

USGS DEM representation of relief. These errors will extend through to the digital channel network.

There are few alternatives for improving or even quantifying the error in a digital channel network derived from the USGS DEM. Higher resolution channel data is usually obtained by field survey and digitization of channels observed in aerial photography. Extensive ground survey is logistically difficult and costly. Direct digitization of channels in orthorectified or georeferenced high-resolution aerial imagery is time consuming and costly. A more precise channel network might be produced from LIDAR data (Hodgson and Bresnahan 2004; Hodgson et al. 2003; White and Wang 2003), but the cost of data acquisition puts LIDAR beyond most budgets.

4.4.2 Estimate of Persistent Channel Length by Aerial LIS

A rapid and cost effective method to define the high-resolution drainage channel network is needed. The unique approach investigated in this research combines the digital channel network extracted from readily available, but relatively low resolution, USGS DEM with verification and adjustment with aerial LIS.

Topology of real channels observed in high-resolution aerial images in the Palouse region usually compares well with the digital drainage channel network extracted from a 10-meter resolution USGS DEM. However, digital lines from 10-meter DEM cannot precisely define the actual channel geometry or even the existence of low order channels. Morphological parameters such as persistence, floodplain location, reach length, channel width, channel depth, sinuosity, bank type, sediment structures, and shading must be determined by field or aerial survey. Deriving channel morphology

from aerial imagery is discussed in detail in Section 6. Only the development of a refined estimate total channel network length by aerial LIS survey is discussed here.

The previous example demonstrated that ephemeral gullies are relatively easy to identify in late winter and early spring high-resolution aerial images. Crop canopy during this time of year does not obscure gully channels. Low order channels that persistent from year to year such as drainage ditches, classical gullies, and headwater streams are often partially obscured by perennial vegetation in an aerial view. It may even be impossible to discern small channels in dense timber or thick riparian vegetation. Interpretation of context and ancillary detail becomes important when identifying and assessing permanent channels in aerial imagery. An example demonstrates the interpretive process.

4.4.3 Aerial LIS estimate of Channel Lengths in an Aerial Image Sample

A section of the digital channel network is superimposed on georeferenced March 15, 2004 natural color aerial images in Figure 4.16. In this case, every digital channel represents a real channel. There are 5 first order channels and 2 second order channels joining Little Potlatch Creek which is a fourth order channel at this location. The red leader lines indicate correspondence between real channels and digital representatives. The DEM represents the fourth order channel fairly well, but is inaccurate for most first order channels. Channel junctions in the digital network are imprecise and miss the short second order channel created by the 2 first order channels in the lower right of the image. Figure 4.17 is the 2004 USGS/State of Idaho DOQ. It is difficult to distinguish first and second order channels in this summer image without support from high-resolution aerial imagery and/or the digital channel network.

The persistent channels are digitized from the aerial images in Figure 4.18. Both the DEM channels and the digitized aerial image channels are shown. Channels are labeled with order number. Large letters signify locations where characteristics of the real channels had to be interpreted from the aerial images but may not be obvious to the reader from the scale of the figure.

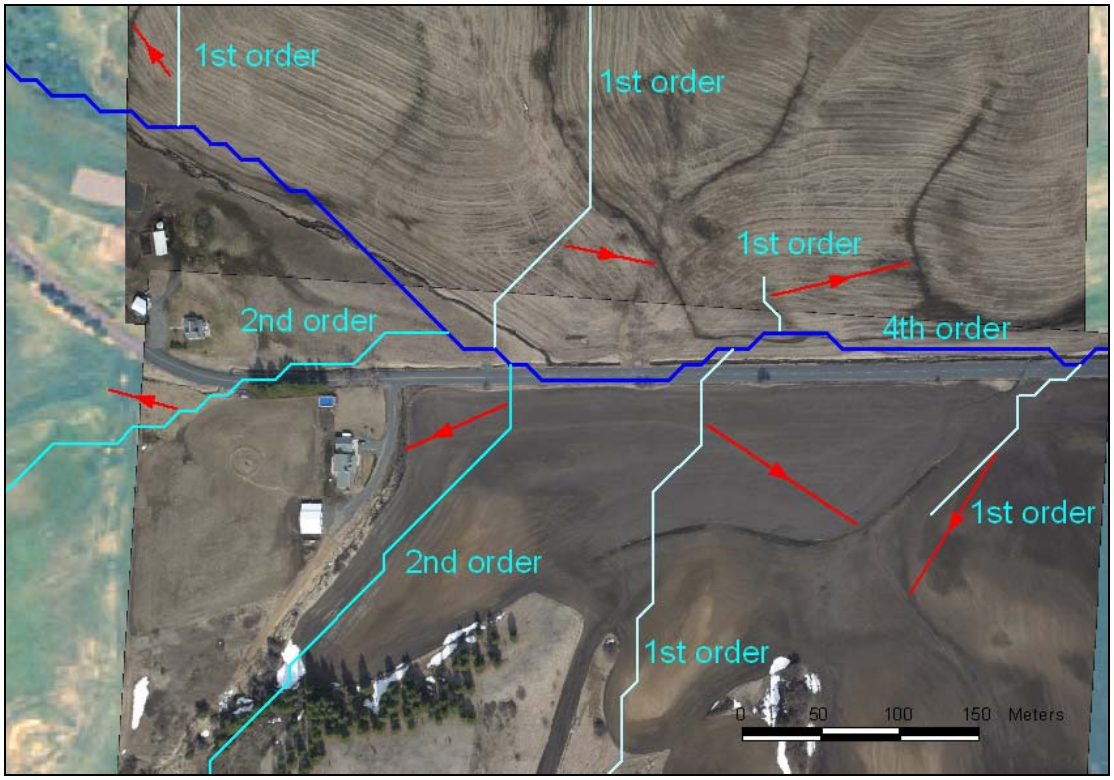

Figure 4.16 Comparison of actual channels and streams with DEM digital channels.

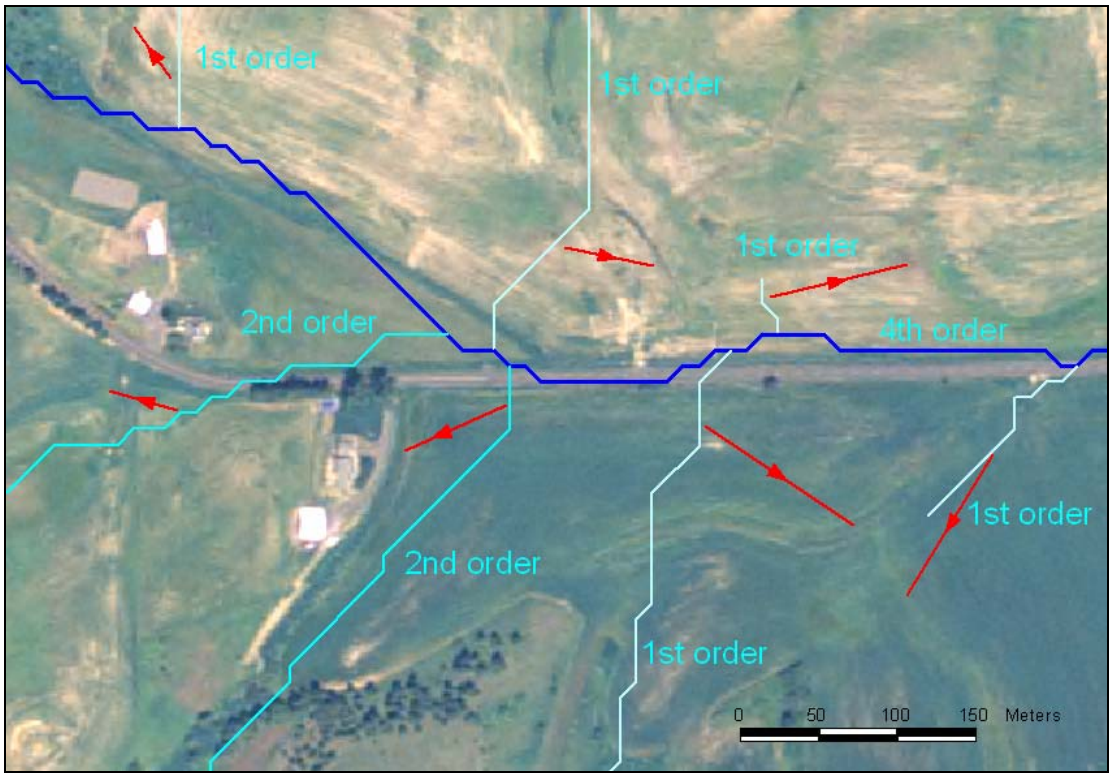

Figure 4.17 Digital channels superimposed on the 2004 USGS/State of Idaho DOQ.

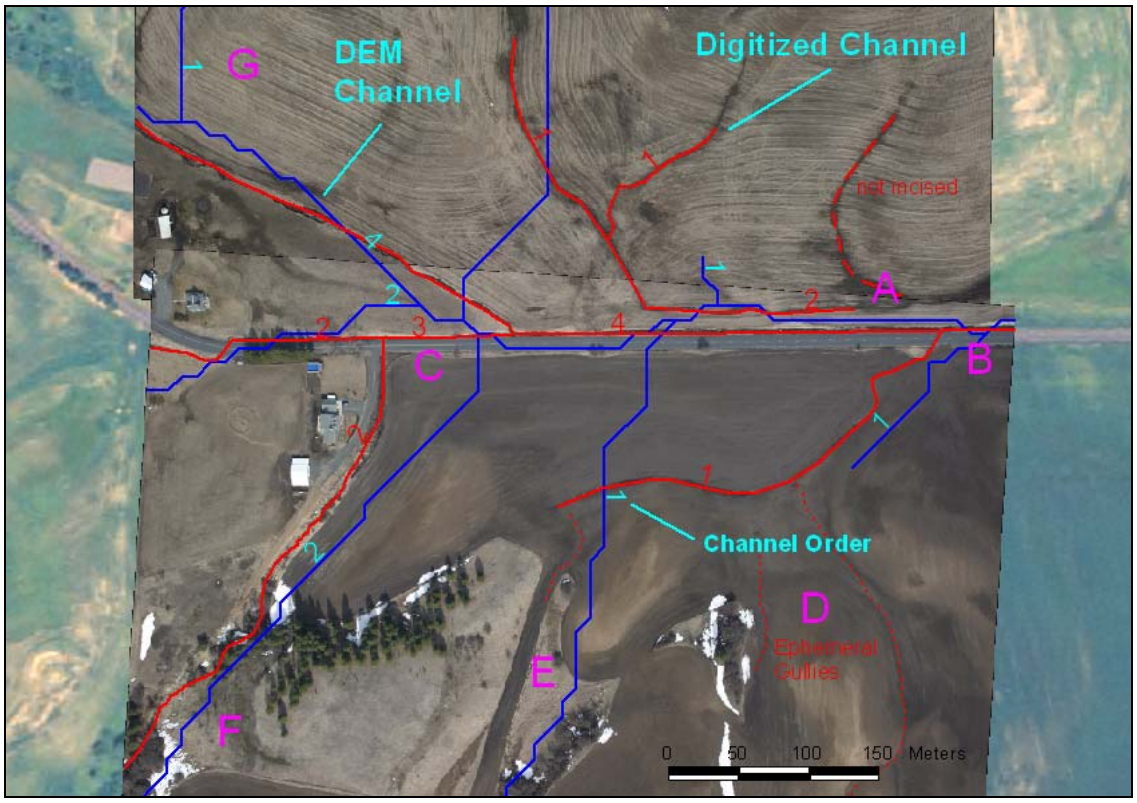

Figure 4.18 Digitized aerial image channels compared to DEM channels.

The topographic drainage path at location **A** is not incised so is not counted as a persistent channel. The outlet of the second order channel at **A** is not incised, but stereo observation shows there is no topographic barrier that prevents flow into the fourth order channel, so these channels are counted as part of the channel system. Two second order channels join to form a third order channel at **C**. This third order channel was not represented in the DEM channels. Ephemeral gullies at **D** are not considered part of the persistent channel system. Road crossing culverts are located at **C** and **B**. The DEM first order channel at **E** is protected by a grassed waterway so does not produce an actual incised channel. The position and alignment of the second order channel at **F** is obscured by shrubs so is inferred from elevation differences observed in a stereo view of the image. The first order DEM channel at location **G** is not observed in the aerial images, but likely would be seen if adjacent images were available.

Total channel lengths by channel order for the DEM channels and digitized aerial image channels are compared in Table 4.16. The DEM channel network overestimates the total length of channels by 20 percent. Overestimation is greatest for the first order channels (88 percent) because some first order channel length is actually second order length in the aerial image channels or protected by the grassed waterway at **E.**

	Total Length of Channel Order (m)				
	1	2	3	4	Total
DEM channel network	1171	670	0	719	2559
Digitized aerial	623	753	90	667	2134
DEM network error (percent)	187.8	88.9		107.8	120.0

Table 4.16 Comparison of total channel lengths for DEM channels and digitized aerial image channels.

In general, overestimation in DEM channels is caused by false extension of channels and artificial sinuosity. False extension is partially controlled by selection of a catchment threshold size in extraction of the digital channel network from the DEM. Figure 4.19 is a smaller scale (larger area) view of the vicinity of the channels in Figure 4.18. A catchment threshold area of 5 ha was selected by trial and error until digital channels agreed fairly well with real channels observed in medium scale aerial imagery. Appendix 4.4 provides additional discussion of the selection of catchment threshold and alternative approaches.

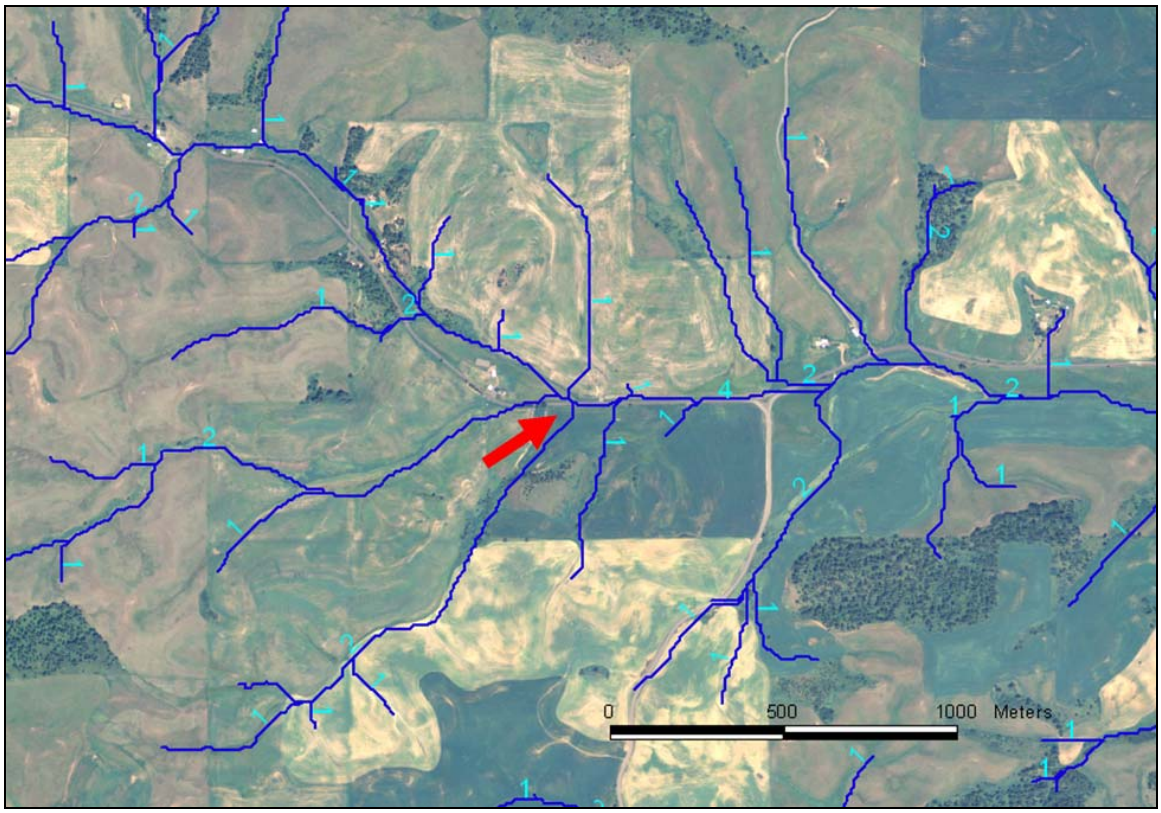

Figure 4.19 DEM channel network superimposed on the 2004 USGS/Idaho DOQ.

It is interesting to compare the length of channels estimated in the aerial image with an LIS estimate of channel length. A middle transect line is superimposed on the digitized aerial image channel network in Figure 4.20. The transect line has a total length

L_T of 795 m intersects 2 first order and 1 fourth order channels. The area A_T covered by the aerial images is 48.4 ha. By Equation 4.7 the LIS estimate of the total length of first order channels is:

$$L_1 = \frac{\pi n}{2L_T}\frac{1}{A_T} = \frac{\pi(2)}{2(795\,\text{m})}\frac{1}{484{,}000\,\text{m}^2} = 1913\,\text{m}$$

The LIS estimate is much higher than the 623 m length of digitized aerial image first order channels. The LIS estimate of fourth order channels is 957 m compared to 667 m for digitized aerial image fourth order channels. The LIS estimates of second and third order channels are both zero because channels of these orders were not intercepted by the middle transect line. Total LIS estimate of the length of channels of all orders from the middle transect is 2870 m is compared to 2134 m for the digitized aerial image channels, a 34 percent difference. The estimate of total length is fairly good considering that the estimate can be made in a fraction of the time required for georeferencing of aerial images and manual digitizing of channels. The LIS estimate improves with an increased number of transects at different orientations.

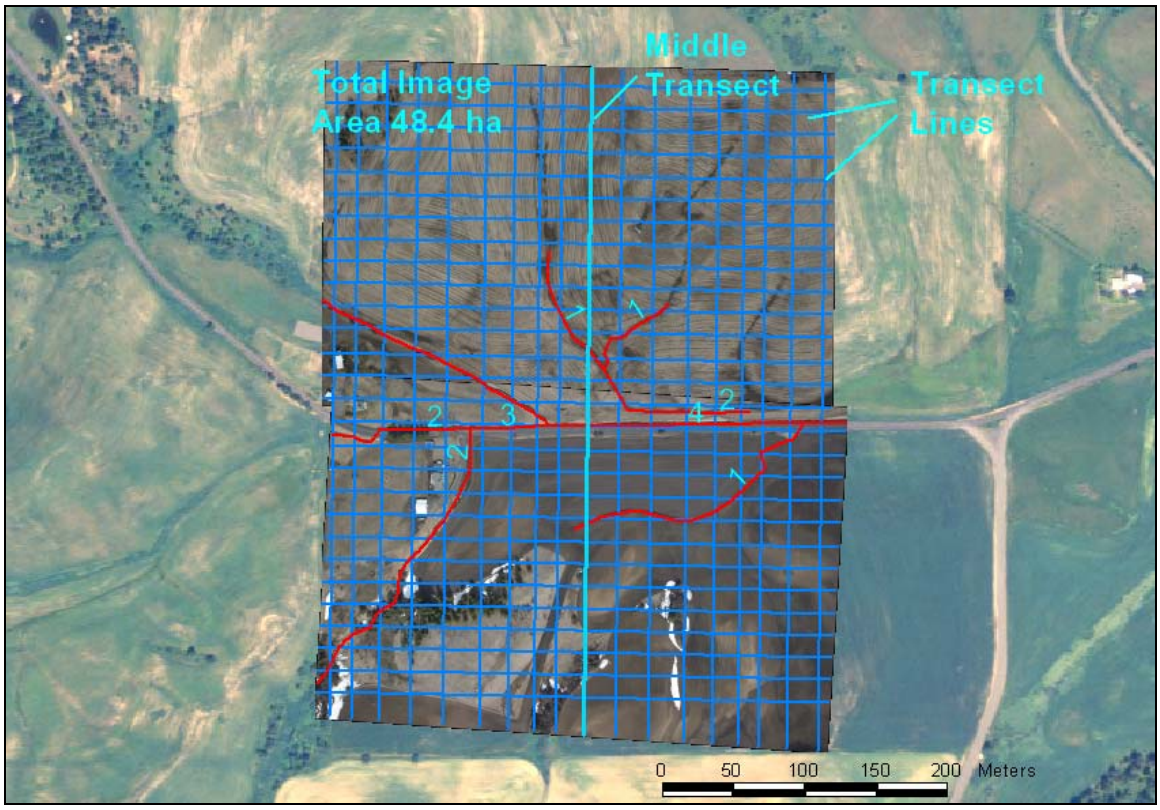

Figure 4.20 Transect lines for Aerial LIS estimate of channel length.

A transect grid is superimposed on Figure 4.20. Intersections of the horizontal and vertical transect lines are counted to produce 46 individual LIS estimates of the length of channels in each order. The averages of the LIS estimates for the grid of transect lines for each order are given in Table 4.17. Errors in the LIS estimate are less than 20 percent except for third order channels. The LIS estimate of total channel length for all orders is within 7 percent of the length digitized on the aerial images. An increased number of transects improves the accuracy of the LIS estimate for two images in this example and would be expected to similarly improve the LIS estimate of the full study region.

This example illustrated typical aerial image interpretations made while digitizing persistent channels in a georeferenced aerial image sample and identifying transect line

channel intersections. It also helps reinforce an impression of the accuracy inherent in the aerial LIS technique.

	Total Length of Channel Order (m)				
	1	2	3	4	Total
Middle transect	1913	0	0	957	2870
All transects	696	665	63	565	1989
Digitized aerial	623	753	90	667	2134
All transects error (percent)	111.7	88.3	69.6	84.7	93.2

Table 4.17 Multiple transect LIS estimate of channel length.

At this point it should be fairly obvious that aerial LIS estimates can be applied directly to the DEM channel network to refine the estimate of the lengths of channels in each order and the total length of channels in the full system. This is the key concept underlying the channel length estimation technique developed in the dissertation research. Length adjustment factors for the DEM channels are computed assuming the LIS estimate is accurate. Adjustment factors for the example are computed from the example information by dividing the LIS estimate of channel length by the digital channel length. Adjustment factors for the example data are listed in Table 4.18.

	Total Length of Channel Order (m)				
	1	2	3	4	Total
DEM channel network	1171	670	0	719	2559
LIS estimate for all transects	696	665	63	565	1989
Adjustment factor	0.59	0.99		0.79	0.78

Table 4.18 Channel length adjustment factors for example data.

4.4.4 Aerial LIS estimate of Total Channel length for the Potlatch Basin

The adjustment factors in Table 4.18 are based on too small of an aerial image sample to produce a reliable estimate of channel length for the full study region. More images and more transects from across the basin must be included in the analysis of

adjustment factors. This was done by a method similar to those for the LIS estimate of total ephemeral gully channel length. The count of intersections of all persistent channels proceeds quickly because images need not be georeferenced. Table 4.19 summarizes the computations for an aerial LIS estimate of total channel length in each subbasin and for the entire project area.

March 2004 Persistent Channel Density and LIS Confidence Intervals for a Single Transect Each Flight Line							
	Big Bear	Cedar	Little Bear	Little Potlatch	Middle Potlatch	Pine	Total
Intersection count	262	119	122	193	296	135	1127
Channel density, m m^{-2}	0.00294	0.00255	0.00201	0.00222	0.00303	0.00265	0.00261
Flight line count, k	10	10	12	17	17	6	42
Transect length, km	140	73	95	137	154	80	678
Variance	2.42068E-08	3.9104E-08	5.71019E-08	5.5054E-08	1.2925E-07	1.32463E-07	1.11126E-08
t, 0.05, k-1	2.262	2.262	2.201	2.120	2.120	2.571	2.020
Lower CI, m m^{-2}	0.00259	0.00211	0.00148	0.00172	0.00227	0.00172	0.00240
Upper CI, m m^{-2}	0.00330	0.00300	0.00254	0.00272	0.00379	0.00359	0.00282
Estimate +- this %	12.0%	17.5%	26.2%	22.4%	25.2%	35.3%	8.2%
Subbasin area, ha	17,441	9,202	10,929	13,083	14,677	8,317	73,649
Channel length, km	**513**	**235**	**220**	**290**	**444**	**221**	**1922**
Lower CI, km	452	194	162	225	333	143	1765
Upper CI, km	575	276	277	356	556	298	2079
DEM channel length, km	**492**	**308**	**300**	**377**	**419**	**227**	**2123**
Adjustment factor	**1.04**	**0.76**	**0.73**	**0.77**	**1.06**	**0.97**	**0.91**

Table 4.19 Aerial LIS estimate of total persistent channel length.

Table 4.19 shows that the LIS estimate of total channel length (1922 km) is close to the total channel length of the digital channel network (2123). The estimates for total channel length for all subbasins combined are within about 9 percent. These methods provide completely independent estimates of the total length of real persistent channel length in the study region. The close agreement between the two methods indicates that the LIS estimates of total channel length should be very reliable even though there may be some directional bias due to the north-south orientation of the aerial transect lines. Reliability is also indicated by the plus and minus 8 percent confidence interval (α = 0.05) of the LIS estimate of total channel length for all subbasins. LIS estimates of individual subbasins vary between 73 and 106 percent of the length of digital channels

extracted from the DEM. Confidence intervals for the individual subbasins vary between 12 and 35 percent. Confidence intervals of the individual subbasins are greater because of the fewer numbers of transects and variability of channel intersection counts within the subbasins due to the inclusion of canyon terrain.

Aerial LIS estimates of channel length for the Big Bear Creek, Middle Potlatch Creek and Pine Creek are very close to the DEM channel lengths. Aerial LIS estimates for the Cedar Creek, Little Bear Creek and Little Potlatch Creek average 25 percent less the DEM channel lengths. There are several possible reasons for observing fewer distinct channels than extracted from the elevation model:

- Observed channels are counted in the tally of ephemerally gullies, thus not counted as persistent channels.
- The channel is protected from incision by surface cover such as a grassed waterway.
- Precipitation or rate of snowmelt is less intense so erosion force and channel incision is less for a given catchment size.
- The watershed threshold assumed for extraction of DEM channels is too small for a particular watershed. This relates to the previous reason.
- Errors in the DEM create false digital channels.

Further research is needed to determine the dominant causes of the differences between channel lengths simulated by DEM analysis and those estimated by aerial LIS. In this particular study, there appears to be no clear relationship between ephemeral gullies and the DEM overestimation of channel length. Table 4.20 compares persistent channel density with ephemeral gully density. Density ratios varied from 0.12 to 0.28 for

the subbasins and averaged 0.18 for the entire study region. Densities in Table 4.20 are expressed as kilometers per square kilometer. Ephemeral gully densities in Table 4.20 are based on the full subbasin area, so will be less than the values in Table 4.14 based on tilled crop area.

Subbasin	Big Bear	Cedar	Little Bear	Little Potlatch	Middle Potlatch	Pine	Total
Channel density, km km^{-2}	2.94	2.55	2.01	2.22	3.03	2.65	2.61
Ephemeral gully density, km km^{-2}	0.34	0.29	0.55	0.42	0.74	0.32	0.47
Gully density/channel density	0.12	0.12	0.28	0.19	0.25	0.12	0.18

Table 4.20 Comparison of ephemeral gully density and channel density.

Aerial LIS in combination with digital terrain analysis is a very efficient and reliable method to estimate total channel length for conservation planning and hydrologic modeling. In practical application, the aerial LIS channel densities can be used directly or the adjustment factors in Table 4.19 are applied to refine the DEM channel lengths. The aerial LIS results for the lower Potlatch basin study region may be somewhat transportable to basins of similar land use, soils and climate. Further research is necessary to regionalize LIS estimates and develop watershed factors that correlate with channel density. The aerial LIS methods could easily be adapted to a broader study, opening an opportunity for beneficial hydrologic research heretofore impractical because of cost and logistics.

4.4.5 Example of the Use of an Aerial LIS Estimate of Channel Length

An uncomplicated example from hydrologic modeling demonstrates the practical usefulness of an aerial LIS estimate of channel length. A very important parameter in stormwater runoff modeling is the overland flow distance. This is the distance that runoff

flows down slope before concentrating in a topographic channel. It is very difficult to reliably estimate over an extensive area so rules of thumb are usually applied.

Horton (1945) is acknowledged as the first hydrologist to suggest that a drainage basin could be conceptualized as a single channel down the middle of a long narrow catchment of uniform width. Average overland flow distance is then one half the width of the catchment. With this conceptual model, average overland flow distance is computed from channel density by the relationship:

$$W_o = \frac{A}{2L_c} = \frac{A}{2D_c A} = \frac{1}{2D_c}$$

where W_o is the average overland flow distance, A is the total subbasin area, D_c is the combined density of persistent and ephemeral gully channels, and L_c is the total length of channels. From the data in Table 4.20, the average overland flow distance for the Middle Potlatch Creek basin is:

$$W_o = \frac{1}{2D_c} = \frac{1}{2(3.03 + 0.74)\frac{\text{km}}{\text{km}^2}} \times \frac{1000\,\text{m}}{\text{km}} = 133\,\text{m}$$

An overland flow distance of 133 m is reasonable value for the climate and topography of the eastern Palouse region.

Hydrologic engineers engaged in watershed modeling will appreciate the significance of a cost effective and reliable method of estimating this important parameter for a particular set of soil, terrain and climate conditions. Overland flow distance computed by this method represents the distance to well defined channels and is appropriate for the analysis of time-of-concentration as in the USGS TR55 methodology. Flow often becomes concentrated before reaching a main channel as evidenced by formation of rills in eroded soil. Actual overland flow distances observed in specific

high-resolution aerial images of eroded soil may be as short as 10 or 15 meters and are influenced by peak runoff intensity of a particular event.

The presence of grassed waterways increases the overland flow distances determined from aerial LIS. The increase in overland flow distance accompanies a legitimate increase in flow time caused by greater flow resistance in grassed channels. As demonstrated in the LIS example involving aerial images on Little Potlatch Creek, aerial LIS methods can be extended to the analysis of specific channel orders and channels resistance to erosion. Further research is needed to directly relate flow travel time to aerial LIS channel estimates.

4.5 Aerial Line-Interval Sampling

Areas of features, such as agricultural fields and flood plains can be estimated from aerial images with line interval sampling. Line interval sampling is similar to line intersect sampling except that the length of line in contact with a feature of interest, such as an agricultural field, is measured instead of a count of point intersections. As with line intersect sampling, an advantage of aerial line interval sampling is that a sequence of non-georeferenced aerial images can be used to make interval measurements if image-to-image scale does not vary drastically. Aerial images with minor lens distortion produced by flights at constant altitude over moderately level terrain are usually acceptable. Relative measures of land surface areas, such as percent cover, may be made completely without ground scale measurements. Line interval estimates from image swaths are readily converted to dimensional areas when image swath length and mean image width are known.

Percent cover estimates for each surface type are computed from the relative proportion of the full transect line in contact with the surface type. The percent cover equation is:

$$\%P_i = \frac{\sum L_i}{L_T} \cdot 100 \qquad 4.11$$

where $\%P_i$ is the percent cover of surface type i, L_i is the sum of line intervals in contact with surface type i, and L_T is the total length of the transect line. Attribution of the original form of the equation is uncertain, but Canfield (1941) appears to be among the first users in natural resource work to recognize its application with aerial photography. Ground level line interval sampling is widely applied in measurements of vegetative cover (Canfield 1941; Mitchell and Hughes 1995), agricultural residue (Li and Chaplin 1995) and habitat variables (Hays et al. 1981).

4.5.1 Estimate of Area by Line Interval Sampling

An uncomplicated example of line interval sampling is the estimation of subbasin area with line transect lengths. This is an artificial example, but it tests the method. A more practical demonstration follows. Subbasin and transect data for the example are in Table 4.21.

The percent cover and area of the Big Bear subbasin is computed:

$$\%P_{bb} = \frac{\sum L_i}{L_T} \cdot 100 = \frac{171{,}319}{723{,}417} \times 100 = 23.7\%$$

$$A_{basin} = P_{bb} \cdot A_T = (0.237)(73{,}648\ \text{ha}) = 17{,}441\ \text{ha}$$

where A_b is the dimensional area of the subbasin, P_{bb} is the line interval proportion of transect length in contact with the subbasin, and A_T is the total area of the study region.

The actual area of the subbasin is 17,049 ha. Percent difference from the actual subbasin area is computed:

$$\%E = \frac{17{,}441 - 17{,}049}{17{,}049}(100) = 2.3\%$$

Estimates of other subbasins areas are tabulated in Table 4.21. Percent difference ranges from -9.6 to 2.6%. The Cedar Creek subbasin estimate is low because there was no transect over the eastern margin of the subbasin.

Estimate of Subbasin Area by Line Interval Sampling							
	Big Bear	Cedar	Little Bear	Little Potlatch	Middle Potlatch	Pine	Total
Transect length, m	171,319	90,383	107,348	128,514	144,162	81,691	723,417
Actual area,ha	17,049	10,184	10,841	13,061	14,311	8,202	73,648
Percent cover	23.7%	12.5%	14.8%	17.8%	19.9%	11.3%	100.0%
Estimated area, ha	17,441	9,202	10,929	13,083	14,677	8,317	73,648
Percent difference	2.3	-9.6	0.8	0.2	2.6	1.4	

Table 4.21 Line interval estimate of subbasin area.

Conversion of percent cover estimates to dimensional areas was simplified in the above example because total area of the study region (73,648 ha) was known. Coverage area can be estimated solely from aerial transect length obtained from GPS track length, average image swath width scaled to actual ground dimensions, and flight line spacing. Average image swath width may be obtained from a representative sample of georeferenced images. Dimensional areas of surface type are computed from the line interval cover proportion with:

$$A_i = P_i \frac{L_s \cdot W_s}{W_s / S_s} = P_i(L_s \cdot S_s) \qquad 4.12$$

where A_i is the area of the surface type i, P_i is the percent cover of surface type i, L_s is the total swath length, W_s is the average width of the swath, and S_s is the swath (flight line) spacing. Swath width cancels in Equation 4.12 so that dimensional areas are

dependent only on cover proportion, swath length and flight line spacing. Swath width is retained in this equation to lend clarity to subsequent discussion.

Continuing with the example of the Big Bear subbasin, an estimate of the subbasin area from percent cover, image swath area and flight line spacing is computed:

$$A_{bb} = P_{bb}\frac{L_s \cdot W_s}{W_s / S_s} = P_i\left(L_s \cdot S_s\right) = 0.237 \times \frac{171{,}319\,\text{m} \times 650\,\text{m}}{650\,\text{m}/1000\,\text{m}} \times \frac{1\,\text{ha}}{10{,}000\,\text{m}^2} = 17{,}132\,\text{ha}$$

Percent error of estimated subbasin area compared to the actual subbasin area is 0.5%. Differences among the subbasins varied from 1.6 to 0.7%. The difference for Cedar Creek was not computed because part of the full basin was not sampled with line interval transects. Estimates for the other subbasins areas based on swath length are in Table 4.22.

Estimate of Subbasin Area by Line Interval Sampling and Swath Area							
	Big Bear	Cedar	Little Bear	Little Potlatch	Middle Potlatch	Pine	Total
Transect length, m	171,319	90,383	107,348	128,514	144,162	81,691	723,417
Percent cover	23.7%	12.5%	14.8%	17.8%	19.9%	11.3%	100.0%
Transect area, ha	11,136	5,875	6,978	8,353	9,371	5,310	47,022
Spacing ratio	0.65	0.65	0.65	0.65	0.65	0.65	
Estimated area, ha	17,132	9,038	10,735	12,851	14,416	8,169	72,342
Actual area,ha	17,049	10,184	10,841	13,061	14,311	8,202	73,648
Difference	0.5%		-1.0%	-1.6%	0.7%	-0.4%	

Table 4.22 Line interval estimate of subbasin area with swath area.

This example, though artificial, demonstrates a very practical concept – the area of any distinct land cover type, such as forest, urban or cropland can be easily measured by aerial survey techniques. This is particularly useful for measuring transient cover types such as fall tilled agricultural land or snow cover where ground survey is prohibited

or too time consuming. The method allows determination of confidence intervals on the estimate as will be demonstrated in the next example.

4.5.2 Area of Land Cover Type by Line Interval Sampling

The previous example demonstrated that line interval sampling can efficiently estimate the size of well-defined contiguous regions. Many watershed characteristics, such as land cover type, are not contiguous and may be sparsely represented. This example tests the line interval sampling method with a digital dataset of land cover types. Again, this is a rather artificial example that tests the accuracy of the method against known data. This approach is necessary because no extensive real datasets of land cover exist that were determined by methods more accurate than the proposed aerial survey method.

The 1992 National Land Cover Dataset (NLCD) in Figure 4.21 was developed by USGS from Landsat imagery and other sources. It is the most extensive and current national land cover dataset available and is appropriate for initial assessments of watershed characteristics. Land use and land cover types are separated into 21 classes (Anderson Type II) at a grid resolution of 30 meters. Small grains (class 83) and fallow land (class 84) predominate the agricultural lands of the Potlatch basin. Land cover patches are irregular with clusters of varying size. The NLCD coverage of the Potlatch study region is a realistic spatially heterogeneous dataset to test the efficiency of line interval sampling as means to interpret land cover classes from satellite and aerial images where actual cover class areas are not known.

Land cover areas in Table 4.23 were obtained from the gridded NLCD dataset for each class and subbasin. Area values were converted to percent cover for each class and

tabulated in Table 4.24. This data provides a reference for judging the accuracy of line interval area estimates. Line intervals of each cover class present were measured by standard GIS processing techniques along the flight lines transects spaced at 1 km intervals. Percent cover line interval estimates were computed by spreadsheet as described in the previous example and summarized in Table 4.25.

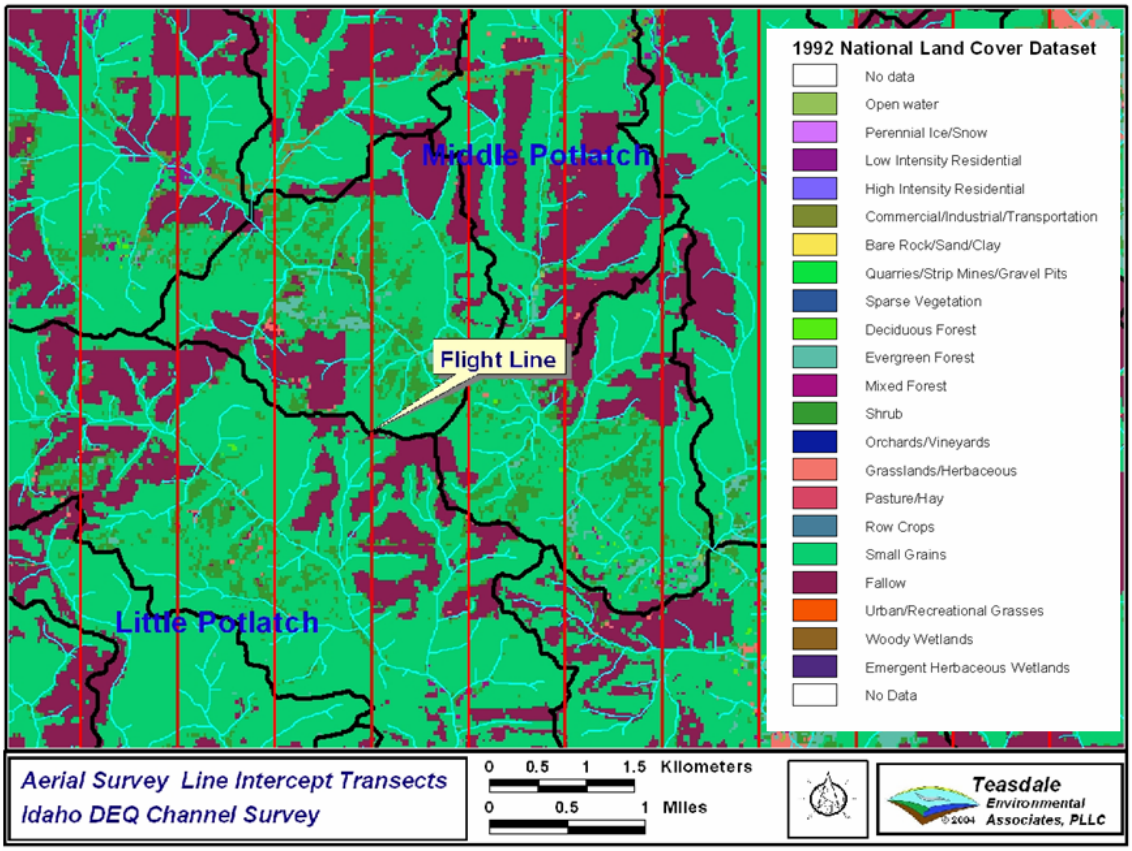

Figure 4.21 National Land Cover Data in the Potlatch study regions.

NLCD 1992 Area by Subbasin and Cover Class (actual NLCD grid areas)							
Type	Big Bear	Cedar	Little Bear	Little Potlatch	Middle Potlatch	Pine	Total
			Area, ha				
11 Open Water	61	10	38	4	21	26	160
21 Low Intensity Residential	170	16	85	0	34	69	375
23 Commercial/Industrial/Transportation	110	23	115	9	82	84	421
31 Bare Rock/Sand/Clay	14	1	13	0	1	5	34
33 Transitional	34	42	0	2	2	0	80
41 Deciduous Forest	39	291	16	126	104	81	657
42 Evergreen Forest	5,499	4,325	1,681	117	540	1,683	13,846
43 Mixed Forest	169	276	117	29	101	148	839
51 Shrubland	120	287	800	1,063	1,475	2	3,746
71 Grasslands/Herbaceous	152	85	471	861	695	11	2,276
81 Pasture/Hay	14	13	0	0	1	0	28
83 Small Grains	7,779	3,716	5,607	7,758	7,679	4,059	36,599
84 Fallow	2,885	1,098	1,897	3,094	3,575	2,031	14,580
91 Woody Wetlands	1	0	0	0	1	0	1
92 Emergent Herbaceous Wetlands	1	0	1	0	1	3	6
Total	17,049	10,183	10,840	13,063	14,312	8,201	73,648

Table 4.23 1992 National Land Cover Dataset classes in the Potlatch study region.

NLCD 1992 Percent Cover by Subbasin and Cover Class (actual NLCD grid areas)							
Type	Big Bear	Cedar	Little Bear	Little Potlatch	Middle Potlatch	Pine	Total
			% Cover				
11 Open Water	0.4%	0.1%	0.3%	0.0%	0.1%	0.3%	0.2%
21 Low Intensity Residential	1.0%	0.2%	0.8%	0.0%	0.2%	0.8%	0.5%
23 Commercial/Industrial/Transportation	0.6%	0.2%	1.1%	0.1%	0.6%	1.0%	0.6%
31 Bare Rock/Sand/Clay	0.1%	0.0%	0.1%	0.0%	0.0%	0.1%	0.0%
33 Transitional	0.2%	0.4%	0.0%	0.0%	0.0%	0.0%	0.1%
41 Deciduous Forest	0.2%	2.9%	0.1%	1.0%	0.7%	1.0%	0.9%
42 Evergreen Forest	32.3%	42.5%	15.5%	0.9%	3.8%	20.5%	18.8%
43 Mixed Forest	1.0%	2.7%	1.1%	0.2%	0.7%	1.8%	1.1%
51 Shrubland	0.7%	2.8%	7.4%	8.1%	10.3%	0.0%	5.1%
71 Grasslands/Herbaceous	0.9%	0.8%	4.3%	6.6%	4.9%	0.1%	3.1%
81 Pasture/Hay	0.1%	0.1%	0.0%	0.0%	0.0%	0.0%	0.0%
83 Small Grains	45.6%	36.5%	51.7%	59.4%	53.7%	49.5%	49.7%
84 Fallow	16.9%	10.8%	17.5%	23.7%	25.0%	24.8%	19.8%
91 Woody Wetlands	0.0%	0.0%	0.0%	0.0%	0.0%	0.0%	0.0%
92 Emergent Herbaceous Wetlands	0.0%	0.0%	0.01%	0.0%	0.0%	0.0%	0.0%
Total	100.0%	100.0%	100.0%	100.0%	100.0%	100.0%	100.0%

Table 4.24 Percent cover of 1992 NLCD classes in the Potlatch study region.

NLCD 1992 Percent Cover from Transect Interval by Subbasin and Cover Class (1 km spacing)							
Type	Big Bear	Cedar	Little Bear	Little Potlatch	Middle Potlatch	Pine	All Subbasins
			% Cover				
11	0.2%	0.2%	0.5%	0.1%	0.1%	0.1%	0.2%
21	0.8%	0.0%	0.5%	0.0%	0.4%	0.9%	0.5%
23	0.8%	0.1%	0.7%	0.0%	0.3%	0.7%	0.4%
31	0.0%	0.0%	0.2%	0.0%	0.0%	0.1%	0.0%
33	0.3%	0.3%	0.0%	0.0%	0.0%	0.0%	0.1%
41	0.3%	2.7%	0.2%	1.0%	0.6%	1.5%	0.9%
42	32.0%	36.3%	13.7%	1.0%	3.7%	18.7%	17.2%
43	0.9%	2.3%	1.0%	0.4%	0.4%	1.5%	1.0%
51	1.0%	2.8%	6.5%	7.8%	10.5%	0.0%	5.0%
71	0.9%	0.8%	3.8%	7.1%	4.3%	0.1%	3.0%
81	0.0%	0.1%	0.0%	0.0%	0.0%	0.0%	0.0%
83	45.3%	39.7%	53.5%	59.5%	54.6%	49.3%	50.6%
84	17.4%	14.8%	19.2%	23.1%	25.1%	27.1%	21.0%
91	0.0%	0.0%	0.1%	0.0%	0.0%	0.0%	0.0%
92	0.0%	0.0%	0.0%	0.0%	0.0%	0.0%	0.0%
Total	100.0%	100.0%	100.0%	100.0%	100.0%	100.0%	100.0%

Table 4.25 Percent cover of by line interval sampling of NCLD grid.

Line interval estimates agree with actual NLCD percent cover within 1 to 2 percent even for sparse classes. This example demonstrates that line interval sampling is an efficient method for determining the area of spatially heterogeneous land cover.

The line interval estimate of the area of land cover types was developed with aerial transects spaced at 1 km across the study region. Close agreement between estimated and actual percent cover indicates that fewer flight lines might provide acceptable accuracy. This is of practical interest because flight line spacing and total flight distance controls much of the cost and time commitment of aerial surveys.

Flight line transects were removed from the line interval dataset to observe the effect of fewer transects on estimate accuracy. Transects were spaced at intervals between 2 and 6 km. Accuracy of most class and subbasin percent cover estimates remained within a few percent up to a flight line spacing of 5 to 6 km. Percent cover remained within 3% of the actual values for the full study region even at the 6 km spacing. As a further test, a line interval estimate was made from a single transect line

passing through the centroid of each subbasin (Figure 4.22). The largest deviation for the centroid transect was 7% from the actual values for the full study region. Percent cover deviations for some subbasins were larger than the overall estimates, but not markedly. Percent cover deviations for the full study region are tabulated in Table 4.25. Percent cover deviations for the Middle Potlatch subbasin are in Table 4.26.

These demonstrations and comparisons with simulated aerial transects show that aerial line interval transects can be an efficient sampling technique that yields reliable estimates of the area of land cover at a watershed scale. The analysis of the effect of increased flight line spacing (reduced total transect length) suggests a practical approach for determining the appropriate spacing for actual flight lines in an assessment of the areas of spatially heterogeneous land cover types. Other factors affect the actual accuracy of aerial survey transect sampling including distinctiveness of features, vegetation phenology at the time of image acquisition, image resolution, image radiometric characteristics, sun angle, and interpreter skill.

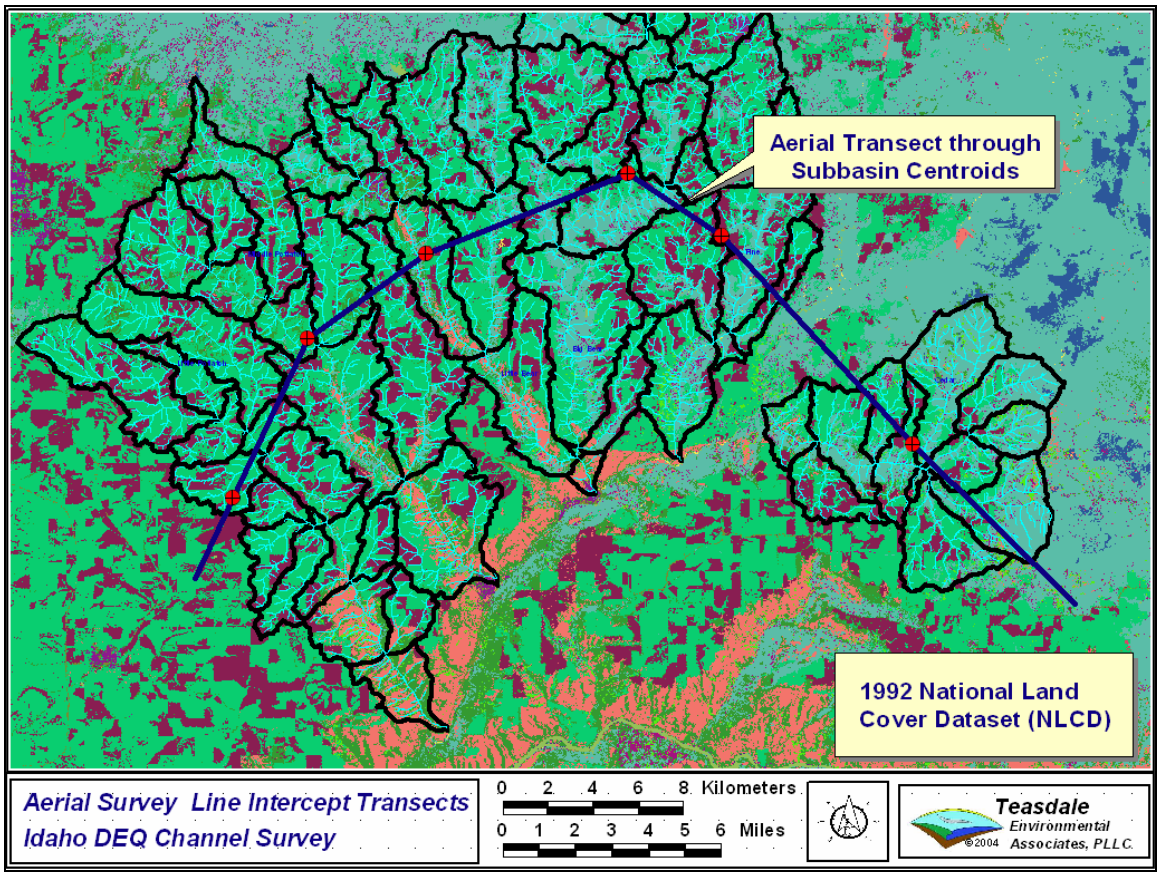

Figure 4.22 Line interval transect through subbasin centroids of area.

All Subbasins Difference in Percent Cover for NLCD Types by Subbasin and Cover Type							
	Spacing of Transects, km						Centroid
Type	1	2	3	4	5	6	Transect
11 Open Water	0.0%	0.0%	0.0%	0.0%	-0.1%	0.1%	-0.2%
21 Low Intensity Residential	-0.1%	-0.1%	0.0%	0.2%	0.2%	-0.1%	-0.5%
23 Commercial/Industrial/Transportation	-0.1%	-0.3%	-0.1%	-0.1%	-0.3%	-0.2%	-0.1%
31 Bare Rock/Sand/Clay	0.0%	0.0%	0.0%	0.1%	0.1%	0.0%	0.0%
33 Transitional	0.0%	0.0%	-0.1%	0.0%	-0.1%	-0.1%	-0.1%
41 Deciduous Forest	0.0%	0.0%	-0.2%	0.1%	-0.2%	0.0%	-0.6%
42 Evergreen Forest	-1.6%	-1.8%	-1.4%	-0.1%	-0.9%	2.4%	-3.9%
43 Mixed Forest	-0.2%	-0.1%	-0.1%	-0.1%	0.0%	0.0%	-0.1%
51 Shrubland	-0.1%	0.3%	-0.4%	0.7%	-0.9%	-0.7%	-0.4%
71 Grasslands/Herbaceous	-0.1%	-0.3%	-0.3%	-0.3%	-0.3%	-0.8%	-2.8%
81 Pasture/Hay	0.0%	0.0%	0.0%	0.0%	0.0%	0.0%	0.0%
83 Small Grains	0.9%	1.4%	1.6%	1.4%	-1.5%	-1.2%	6.4%
84 Fallow	1.2%	0.9%	1.1%	-1.8%	3.9%	0.8%	2.4%
91 Woody Wetlands	0.0%	0.0%	0.0%	0.0%	0.0%	0.0%	0.0%
92 Emergent Herbaceous Wetlands	0.0%	0.0%	0.0%	0.1%	0.1%	0.0%	0.0%

Table 4.26 Deviation of percent cover of NLCD classes with flight line spacing for the Potlatch study region.

Middle Potlatch Creek Difference in Percent Cover for NLCD Types by Subbasin and Cover Type						
	Spacing of Transects, km					
Type	1	2	3	4	5	6
11 Open Water	0.0%	0.0%	0.0%	-0.1%	-0.1%	0.1%
21 Low Intensity Residential	0.2%	0.3%	-0.1%	0.8%	0.9%	0.0%
23 Commercial/Industrial/Transportation	-0.2%	-0.2%	-0.3%	0.0%	-0.1%	-0.3%
31 Bare Rock/Sand/Clay	0.0%	0.0%	0.0%	0.0%	0.0%	0.0%
33 Transitional	0.0%	0.0%	0.0%	0.0%	0.0%	0.0%
41 Deciduous Forest	-0.2%	-0.3%	0.0%	-0.7%	-0.7%	0.4%
42 Evergreen Forest	-0.1%	0.5%	-0.5%	-0.5%	0.2%	-2.1%
43 Mixed Forest	-0.3%	-0.4%	0.1%	-0.2%	-0.4%	-0.4%
51 Shrubland	0.2%	0.5%	-1.2%	-1.1%	-1.2%	-3.4%
71 Grasslands/Herbaceous	-0.5%	-1.9%	-0.9%	-2.6%	-1.3%	-0.3%
81 Pasture/Hay	0.0%	0.0%	0.0%	0.0%	0.0%	0.0%
83 Small Grains	0.9%	2.5%	1.4%	1.0%	-5.5%	5.7%
84 Fallow	0.1%	-0.9%	1.5%	3.4%	8.2%	0.3%
91 Woody Wetlands	0.0%	0.0%	0.0%	0.0%	0.0%	0.0%
92 Emergent Herbaceous Wetlands	0.0%	0.0%	0.0%	0.0%	0.0%	0.0%

Table 4.27 Deviation of percent cover of NLCD classes with flight line spacing for the Middle Potlatch Creek subbasin.

4.5.3 Variance and Confidence Intervals of Line Interval Sampling

Line interval sampling is a form of cluster sampling (Buckland et al. 2001; Freeze 1962; Thompson 1992). Cluster sampling requires that transects (flight lines) be treated as individual sampling units. In this example, each transect is a sample unit, so the sample size is equal to the number of transects *k* across the study area. Unequal length transects are typical in aerial surveys because natural features are irregular. Unequal transects complicate statistical analysis of transect data. Two alternatives exist; apply a simple average of transect values in statistical computations or weight the transect values by transect length. Both approaches will be demonstrated.

In the weight-by-length approach, estimated mean percent cover is computed from the total length of transects in contact with a particular cover class divided by the total length of transects over all classes:

$$\hat{P}_c = \frac{L_c}{L_T} \times 100 \qquad 4.13$$

where $\hat{P}_c$ is the mean percent cover for a particular cover class, L_c is the total length of transects in contact with the cover class and L_T is the total length of transects. Equation 4.13 implicitly produces a mean percent cover weighted by transect length across all transects, though transects may be unequal. Estimates from Equation 4.13 will be different from a simple average of percent cover values unless transects are equal in length. Variance estimates weighted by transect length may be computed following the approach suggested by de Vries (1986) for line intersect sampling,

$$\hat{\text{var}}\ \hat{P}_c = \frac{\sum_k L_j \left(\hat{P}_j - \hat{P}_c\right)^2}{(k-1)\sum_k L_j} \qquad 4.14$$

where $\hat{\text{var}}\,\hat{P}_c$ is the variance of the mean proportional cover (percent or decimal), $\hat{P}_j$ is the mean proportional cover for transect *j*, L_j is the length of transect *j*, and *k* is the total number of transects. The weighting length L_j is the full length of transect and should not be confused with the length of transect interval in contact with the particular surface class. The variance of Equation 4.14 is recognized as the squared standard error of mean percent cover $\hat{P}_c$. Confidence intervals are determined with the *t* statistic.

Estimated mean proportional cover for small grains (class 83) for all subbasins is computed from the length of line in contact with class 83 divided by the total length of transects:

$$\hat{P}_{83} = \frac{L_{83}}{L_T} = \frac{366{,}397}{723{,}587} = 0.506 = 50.6\%$$

Actual percent cover of the small grains class from the NLCD grid was 49.7%. Results of preliminary computations for the weighted transect approach of Equation 4.14 are in Table 4.28. Total transect length is slightly longer than in previous computations because

of a slight overextension of flight line coverage by GIS processing. The difference is not significant to the variance computations.

Preliminary Computations of Class 83 Percent Cover Variance		
Total transect (flight line) length	723,587	m
Number of transects, *k*	44	
Degrees of freedom (*k*-1)	43	
Two tailed t statistic, α = 0.05	2.0168	
Total Area	73,648	ha
Sum of weighted squared deviations	10417	unitless
Estimated percent cover	50.6%	
Actual percent cover	49.7%	

Table 4.28 Preliminary computations for variance estimate with transects weighted by length.

Total variance (squared standard error) of the mean proportional (decimal) cover for class 83 is computed with Equation 4.14:

$$\hat{\text{var}}\ \hat{P}_{83} = \frac{\sum_k L_j \left(\hat{P}_j - \hat{P}_{83}\right)^2}{(k-1)\sum_k L_j} = \frac{10{,}417}{(44-1)(723{,}587)} = 3.35\times10^{-4}$$

The 95% confidence interval for the estimate of percent cover is,

$$\hat{P}_{83} - t^{\alpha}_{k-1}\sqrt{\hat{\text{var}}\,\hat{P}_{83}} < P_{83} < \hat{P}_{83} + t^{\alpha}_{k-1}\sqrt{\hat{\text{var}}\,\hat{P}_{83}}$$

$$50.6\% - 2.0168\sqrt{3.35\times10^{-4}}\times100 < P_{83} < 50.6\% + 2.0168\sqrt{3.35\times10^{-4}}\times100$$

$$50.6\% - 3.7\% < P_{83} < 50.6\% + 3.7\%$$

$$46.9\% < P_{83} < 54.3\%$$

Estimated percent cover of the small grains can be transformed into an area estimate by multiplying the decimal cover by the total area of the subbasins:

$$\hat{P}_{83} = \frac{L_{83}}{L_T} = \frac{366{,}397}{723{,}587}(73{,}648\ \text{ha}) = 0.506(73{,}648) = 37{,}292\ \text{ha}$$

The 95% confidence intervals in units of area is:

$$34{,}500 \text{ ha} < P_{83} < 40{,}000 \text{ ha}$$

The alternative statistical analysis applies no length weights to transect values and follows standard computations for random samples without replacement. Transect values are again treated as sample units. The estimate of mean percent cover is an arithmetic average of the transect values:

$$\hat{P}_{83} = \frac{\sum_k \frac{L_{83}}{L_j}}{k} = \frac{\sum_k \hat{P}_j}{k} = \frac{23.417}{44} = 0.532 = 53.2\%$$

Table 4.29 gives the results of the preliminary computations necessary to estimate variance and confidence intervals.

Preliminary Computations of Class 83 Percent Cover Variance		
Sum of transect proportional cover	23.4174	unitless
Sum of squared deviations from mean	1.1523	unitless
Number of transects, *k*	44	
Degrees of freedom (*k*-1)	43	
Two tailed t statistic, α = 0.05	2.0168	
Total Area	73,648	ha
Actual percent cover	49.7%	

Table 4.29 Preliminary computations for variance estimate with no length weighting.

Variance of the sample mean is computed is computed with the convention expression for random samples,

$$s_{83}{}^2 = \frac{\sum \left(\hat{P}_j - \hat{P}_{83}\right)^2}{k-1} = \frac{1.1523}{44-1} = 0.0268$$

The 95% confidence interval for the estimate of percent cover is,

$$\hat{P}_{83} - t_{k-1}^{\alpha}\sqrt{\frac{{s_{83}}^2}{k}\left(1-\frac{k}{K}\right)} < P_{83} < \hat{P}_{83} + t_{k-1}^{\alpha}\sqrt{\frac{{s_{83}}^2}{k}\left(1-\frac{k}{K}\right)}$$

The term $\left(1-\frac{k}{K}\right)$ is the finite population correction factor. The factor is 1.0 because there is an infinite number of possible parallel transects *K*. Substitution of previously computed values gives the 95% confidence interval,

$$53.2\% - 2.0168\sqrt{\frac{0.0268}{44}(1)}\times 100 < P_{83} < 53.2\% + 2.0168\sqrt{\frac{0.0268}{44}(1)}\times 100$$

$$53.2\% - 5.0\% < P_{83} < 53.2\% + 5.0\%$$

$$48.2\% < P_{83} < 58.2\%$$

Both the estimated mean percent cover and confidence intervals are slightly larger by the unweighted transect analysis approach. The actual small grains proportional cover from the NLCD grid still lies within the confidence interval. It appears the length-weighted transect approach produces a slightly better estimate of mean percent cover. Unweighted confidence intervals are more conservative.

4.6 Line Interval Sampling of Land Cover with High-Resolution Aerial Images

Line interval sampling with aerial images is a rapid and cost effective method to acquire land cover proportions over extensive areas. Development of a method to quickly characterize land cover into hydrologically relevant types was a primary interest in this research. Hydrologic cover classes are necessary for modeling stormwater runoff and water balances of watersheds. In the study region, significant land cover types such as fall-tilled agricultural fields and snow cover are transient in time and are not

represented by existing static land cover classification maps and digital datasets. A rapid technique for determining the seasonal variation of hydrologically relevant cover types would be beneficial for hydrologic and erosion modeling on the Palouse. Line interval sampling by aerial survey provides such a technique.

There are several methods to develop a line interval sample of cover along an aerial image transect. The most accurate method is to georeference all images along the transect as in Figure 4.13, then measure the total length of transect that contacts each land cover type. This method is time consuming. A second method is to scale or approximately georeference the aerial images with flight and terrain data, then measure land cover intervals on each image; adjusting the final estimates for image overlap. This method requires less time than the first, but still requires manual measurement of transect lines. A third method, the one demonstrated here, is very rapid and results in acceptable accuracy for hydrologic modeling.

Vertical aerial images acquired at a constant altitude above ground will cover approximately the same dimensional area on the ground. A transect through the center of the image along the direction of flight has a relatively constant length that may be determined from flight parameters, elevation data and the field of view of the camera. Some variation in coverage occurs because of terrain undulation, but in aggregate this has a minor influence on the accuracy of line interval estimates. Figure 4.13 shows that georeferenced aerial images of a typical flight line are about the same size indicating consistent ground coverage.

High-resolution low altitude aerial images sample a small length along the direction of flight (about 400 m) relative to the land cover types significant in a

watershed scale hydrologic analysis. A transect line through the center of an image usually contacts a single, or at most two, land cover types. Total length of transect that contacts a particular land cover type can be rapidly estimated by multiplying the average image transect length by the number of images of each land cover type along a flight line. No georeferencing or digitizing of the images is necessary.

The estimate can be refined by recording the percentage of each land cover type observed in each image. Only the forward "new" interval in overlapping stereo images is counted in the tabulation. Figure 4.23 is three sequential aerial images. Overlap lines (blue) and the mean location of the central transect line (red) are superimposed on the images. Neglecting sparse cover types such as road pavement, the forward transect interval in first image is 70 percent tilled crop and 30% grass; all grass in the second image; and 60 percent grass and 40 percent forest in the third image. Image observation and tabulation is readily performed with an image browser and spreadsheet. On-screen pixel measurements can be made in the image browser to determine land cover percentages in images with mixed cover, but with practice relative interval lengths can be visually estimated within ten percent.

The percent covers of five hydrologically significant land cover classes were estimated with the aerial line interval sampling technique for the Potlatch basin study region. Classes included tilled crops, canyon, grass, forest, and other. Total lengths of each cover type are listed by flight line in Table 4.30. Percent cover is computed by dividing the total transect length of a particular class by the grand total of transect length. The Potlatch basin study region in March 2004 was 46 percent tilled agriculture, 21 percent grass (pasture and CRP), 19 percent canyon land, 12 percent forest, and 1% other.

The actual area of each cover is computed by multiplying percent cover by the 73,648 ha total area of the study region.

Figure 4.23 observation of land cover type in sequential aerial images.

Land cover types are determined for any particular subbasin from the length of transect of a cover type and the total length of transect in that subbasin. This was how the area of tilled agricultural land was determined for the estimate of ephemeral gully length by line intercept sampling. Table 4.31 summarizes the line interval computations for the estimate of tilled agricultural land by subbasin.

Flight Line	Total Transect Length in meters					
	Tilled	Forest	Grass	Canyon	Other	Total
1	1,049	150	300	0	0	1,499
2	1,938	0	529	0	0	2,467
3	1,332	166	1998	0	0	3,496
4	2,974	0	2578	0	0	5,552
5	7,862	374	1872	0	374	10,483
6	9,266	908	182	0	727	11,083
7	9,105	743	2044	0	557	12,450
8	10,085	395	6723	395	198	17,797
9	7,609	2203	6208	1001	400	17,421
10	13,173	1769	1769	590	590	17,891
11	14,450	1297	2779	2964	371	21,861
12	15,701	1108	1662	2586	554	21,611
13	18,063	1304	1862	1676	372	23,277
14	12,395	572	2860	7246	381	23,455
15	11,553	3329	1958	8420	0	25,260
16	16,431	1292	2769	7015	923	28,431
17	14,682	773	2705	7921	386	26,466
18	10,262	1466	2749	10262	183	24,923
19	12,017	1479	2773	6656	555	23,479
20	13,398	0	1600	4799	0	19,797
21	8,231	2297	2297	9762	383	22,969
22	8,928	1116	3906	2232	0	16,181
23	9,444	741	3333	4630	0	18,148
24	3,699	0	2959	11837	0	18,496
25	3,897	4872	2533	7795	195	19,292
26	10,119	5644	4865	4281	0	24,909
27	10,249	4448	6382	1547	0	22,626
28	6,640	4296	9960	1172	0	22,067
29	3,451	6136	7286	4410	0	21,284
30	5,221	1934	7348	4254	0	18,757
31	9,791	1152	5375	1920	0	18,238
32	3,947	3750	3750	2368	592	14,407
33	0	1114	9097	3156	0	13,368
34	767	5947	6715	959	0	14,389
35	3,525	588	6071	1175	0	11,358
36	2,843	812	812	1218	0	5,686
37	2,054	0	2054	1494	0	5,602
38	2,999	0	1599	1799	0	6,397
39	4,448	387	1354	1934	0	8,122
40	4,159	1871	3951	832	0	10,812
41	3,611	5512	760	2091	0	11,975
42	4,503	1638	1842	0	0	7,983
43	2,975	2789	2417	0	0	8,182
44	0	8729	0	0	0	8,729
Total	318,849	85,101	144,587	132,399	7,742	688,678
Percent Cover	46.3	12.4	21.0	19.2	1.1	100.0
Land area, ha	34,098	9,101	15,462	14,159	828	73,648

Table 4.30 Percent cover of the Potlatch Basin study area by aerial line interval sampling.

	Big Bear	Cedar	Little Bear	Little Potlatch	Middle Potlatch	Pine
Total Transect length, km	139.8	73.2	95.3	136.6	153.5	80.0
Tillage transect length, km	39.2	30.9	34.4	101.4	89.2	23.8
Percent Tilled cover	28.0%	42.2%	36.1%	74.2%	58.1%	29.8%
Total subbasin area, ha	17,049	10,184	10,841	13,061	14,311	8,202
Tillage crop area, ha	4,777	4,298	3,914	9,695	8,310	2,444

Table 4.31 Aerial line interval estimate of tilled area for the study region subbasins.

4.7 Strip Transect Sampling

Estimates of the density of objects or features (objects per unit area) can be estimated by strip transect sampling. Strip transect sampling is an extension of quadrat sampling in which all objects within a sample area are counted. Density of the objects is estimated:

$$\hat{D} = \frac{n}{WL} \qquad 4.15$$

where $\hat{D}$ is the estimated density of the objects, n is the count of objects within the transect strip (swath), W is the mean width of the swath, and L is the length of transect. The total number of objects within a region is estimated by multiplying the density estimate by the area of a region. As with line interval sampling, strip intersect sampling is a form of cluster sampling in which transects are treated as sample units. Estimates of object density and confidence intervals are computed as described for line interval sampling.

Strip transect sampling is applied in both ground level and aerial surveys. A critical assumption is that all objects within a strip are counted, though generally no data are collected to test this assumption (Buckland et al. 2001). Unlike visual sampling, aerial image swaths increase assurance that all objects of interest are counted because the

data in the image is persistent. A permanent image record provides data for testing performance of interpreters and software detection algorithms.

Strip transect sampling can estimate the density of many distinct point features of interest in watershed assessment, such as buildings, ephemeral gully systems, landslides, and active construction sites. The actual geographic location of the point feature is unimportant. Only observation of its existence within the transect width is needed.

4.7.1 Density of Channel Encroachments

Density of channel encroachments is a measure of the potential impact of a road system on stream habitat and water quality. Encroachments are either *crossings* where the road passes over or through the stream channel or *incursions* where the road enters within a specified distance of the channel. Road encroachments are features that are readily identified in high-resolution aerial imagery. The following example demonstrates the aerial strip transect sampling method with an analysis of road encroachments observed in the aerial imagery of the Potlatch basin.

A GIS assessment of the number of intersections between roads and the channel network is a useful preliminary analysis that guides experimental design and provides data for comparison with the aerial strip transect sampling results. The GIS assessment of road encroachments is simply a count of the number of intersections between a road system polyline theme and the digital channel network. The road system polyline was developed from the U.S. Bureau of Statistics road coverage obtained from the USGS National Map dataset. A total of 1929 intersections (crossings and encroachments) were found within the 73,648 ha total area of the primary subbasins. Only intersections and not proximity incursions were counted to simplify the analysis. The road and channel

polylines do not have defined widths so the intersection count is likely a good estimate of total encroachments. Increased exposure because of co-alignment of roads and channels can be addressed by counting protocols implemented during the imagery assessment.

Density of the encroachments in the GIS data is computed:

$$D_e = \frac{N}{A} = \frac{1929}{73{,}648\ \text{ha} \times \dfrac{1\ \text{km}^2}{100\ \text{ha}}} = 2.62\ \text{ encroachments per km}^2 \qquad 4.16$$

Channel encroachments may also be expressed in terms of channel length. Total channel length of all orders in the six primary subbasins is 2094 km. The stream encroachment ratio is computed:

$$E_s = \frac{N}{L_c} = \frac{1929}{2094} = 0.92\ \text{encroachments per km} \qquad 4.17$$

Imagery transects described in previous examples provide a framework for judging the potential accuracy of imagery assessment of channel encroachments. The strip transects are 650 m wide and centered on the north-south flight lines across the study area (Figure 4.24). A total of 1211 intersections were counted in the 44 unequal length strip transects using the on-screen image observation and feature counting techniques previously described.

Length-weighted mean encroachment density is computed from the total area of the transects:

$$\hat{D}_e = \frac{N}{L_T W} = \frac{1211}{723{,}416\ \text{m} \times 650\ \text{m} \times \dfrac{1\ \text{km}^2}{10^6\ \text{m}^2}} = 2.58\ \text{ encroachments per km}^2$$

Length-weighted variance and 95% confidence intervals are computed as before in line intersect sampling:

$$\hat{\text{var}}\ \hat{D}_e = \frac{\sum_k L_j \left(\hat{D}_j - \hat{D}_e\right)^2}{(k-1)\sum_k L_j} = \frac{712.791 \frac{1}{\text{km}^3}}{(44-1)\,723.416\,\text{km}} = 0.02291\ \frac{1}{\text{km}^4}$$

$$\hat{D}_e - t^{\alpha}_{k-1}\sqrt{\hat{\text{var}}\,\hat{D}_e} < D_e < \hat{D}_e + t^{\alpha}_{k-1}\sqrt{\hat{\text{var}}\,\hat{D}_e}$$

$$\hat{D}_e - 2.0179\sqrt{0.02291} < D_e < \hat{D}_e + 2.0179\sqrt{0.02291}$$

$$2.58 - 0.31 < D_e < 2.58 + 0.31$$

$$2.27 < D_e < 2.89 \text{ intersections per km}^2$$

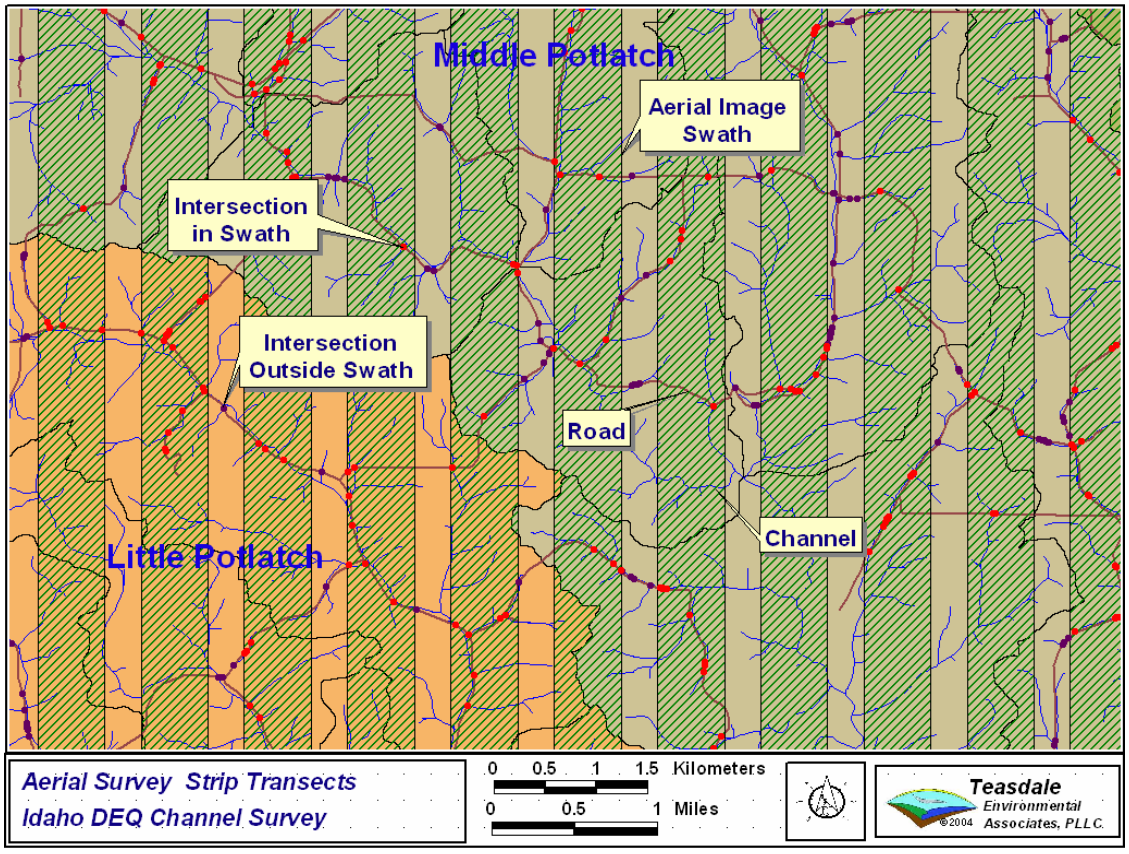

Figure 4.24 Strip transect sampling of road-channel intersections.

The strip transect sampling estimate of encroachment density of 2.58 encroachments per km^2 agrees well with the 2.62 encroachments per km^2 measured in GIS. Percent error between the estimate and the actual value was -1.5 percent. The actual value lies well within the 95 percent confidence interval computed by the length-weighted transect approach.

Transects were removed from the test data to judge of accuracy of estimates at decreased flight line spacing. Accuracy of the estimates degrades at transect intervals of more than 3 km. A single 44 km by 0.65 km transect through the subbasin centroids produced an estimate within -9 percent of the actual value. Results of varying transect spacing are in Table 4.32.

Estimates of Channel Encroachments at Various Transect Spacing							
	Transect (Flight Line) Spacing						Centroid
	1	2	3	4	5	6	Transect
Number of transects	44	22	15	11	9	8	1
Intersection count	1211	584	364	324	223	205	69
Total length of transects, km	723	359	237	175	143	122	44
Estimate of encroachment density, n/km^2	2.58	2.50	2.36	2.85	2.40	2.58	2.40
Actual encroachment density, n/km^2	2.62	2.62	2.62	2.62	2.62	2.62	2.62
Percent difference of estimate	-1.5%	-4.4%	-9.8%	8.6%	-8.5%	-1.4%	-8.4%
Lower confidence interval bound, n/km^2	2.27	2.11	1.79	2.29	1.63	1.67	
Upper confidence interval bound, n/km^2	2.89	2.89	2.93	3.40	3.16	3.50	

Table 4.32 Estimates of channel encroachments by strip transect sampling with varying transect lengths.

Accuracy of aerial strip transect sampling at moderate spacing likely yields good estimates of even relatively sparse visible features of interest in watershed characterization. Even a single flight line across the study area should yield a respectable first approximation of feature density appropriate for reconnaissance level investigations. The analysis of the effect of increased flight line spacing (reduced total transect length) again suggests a practical approach for determining the appropriate

spacing for actual flight lines in an assessment of the density of spatially heterogeneous point features.

4.8 Summary

This section introduced and adapted the line transect theory of de Vries (1986) to the aerial survey of hydrologic characteristics of watersheds and channel networks. The methods of aerial line intersect sampling, line interval sampling and strip transect sampling were applied to several simulated and real datasets and demonstrated to be efficient and reliable. The research presented here appears to be entirely original and will likely find wide application in hydrologic modeling and soil erosion analysis. Several possibilities for further research were suggested.

References for Section 4

Buckland, S. T., Anderson, D. R., Burnham, K. P., Laake, J. L., Borchers, D. L., and Thomas, L. (2001). *Introduction to Distance Sampling, Estimating Abundance of Biological Parameters*, Oxford University Press, Oxford.

Canfield, R. H. (1941). "Application of the line interception method in sampling range vegetation." *Journal of Forestry*, 39, 388-394.

de Vries, P. G. (1986). *Sampling Theory for Forest Inventory*, Springer Verlag, New York.

Freeze, F. (1962). *Elementary Forest Sampling, Agricultural Handbook No. 232*, U.S. Department of Agriculture, U.S. Forest Service.

Hays, R. L., Summers, c., and Seitz, W. (1981). *Estimating Wildlife Habitat Variables*, Office of Biological Services, U.S. Fish and Wildlife Service, Washington, DC.

Hodgson, M. E., and Bresnahan, P. (2004). "Accuracy of Airborne Lidar-Derived Elevation: Empirical Assessment and Error Budget." *Photogrammetric Engineering and Remote Sensing*, 70(3), 331-340.

Hodgson, M. E., Jensen, J. R., Schmidt, L., Schill, S., and Davis, B. (2003). "An evaluation of LIDAR- and IFSAR-derived digital elevation models in leaf-on conditions with USGS Level 1 and Level 2 DEMs." *Remote Sensing of Environment*, 84(2), 295-308.

Horton, R. E. (1945). "Erosional development of streams and their drainage basins: hydrophysical approach to quantitative morphology." *Bulletin of the Geological Society of America*, 56, 275-370.

Li, F., and Chaplin, J. (1995). "Analysis of random and systematic sampling methods for residue cover measurements." *Transactions of the American Society of Agricultural Engineers*, 38(5), 1353-1361.

Matern, B. (1964). "A method of estimating the total length of roads by means of a line survey." *Studia Forestalia Suecica*, 18, 68-70.

Mitchell, W. A., and Hughes, H. G. (1995). *Line Intercept: Section 6.2.5, U.S. Army Corps of Engineers Wildlife Resources Manual, Technical Report EL-95-22*, U.S. Army Corps of Engineers Waterways Experiment Station, Vicksburg, MS.

Skidmore, A. K., and Turner, B. J. (1992). "Map accuracy assessment using line transect sampling." *Photogrammetric Engineering and Remote Sensing*, 58(10), 1453-1457.

Thompson, S. K. (1992). *Sampling*, Wiley-Interscience, New York.

USGS. (1997). *Part 2: Hydrography, Standards for 1:24,000-Scale Digital Line Graphs - 3 Core (DLG-3)*, U.S. Geological Survey, Reston, VA.

White, S. A., and Wang, Y. (2003). "Utilizing DEMs derived from LIDAR data to analyze morphologic change in the North Carolina coastline." *Remote Sensing of Environment*, 85(1), 39-47.

Appendix 4.1

Derivation of the Line Intersect Sampling Formula

Transect line of length L is randomly placed over a fixed linear object (needle) of length λ_i in area A as in Figure A.4.1.1. The orientation angle β of the transect line is referenced to a fixed frame which for convenience in the derivation is aligned with fixed linear object. The transect line intersects the needle only if its endpoint E lies within the parallelogram of area λ_i L sin β. Placement of the transect line at a particular location E and orientation angle β are independent random variables.

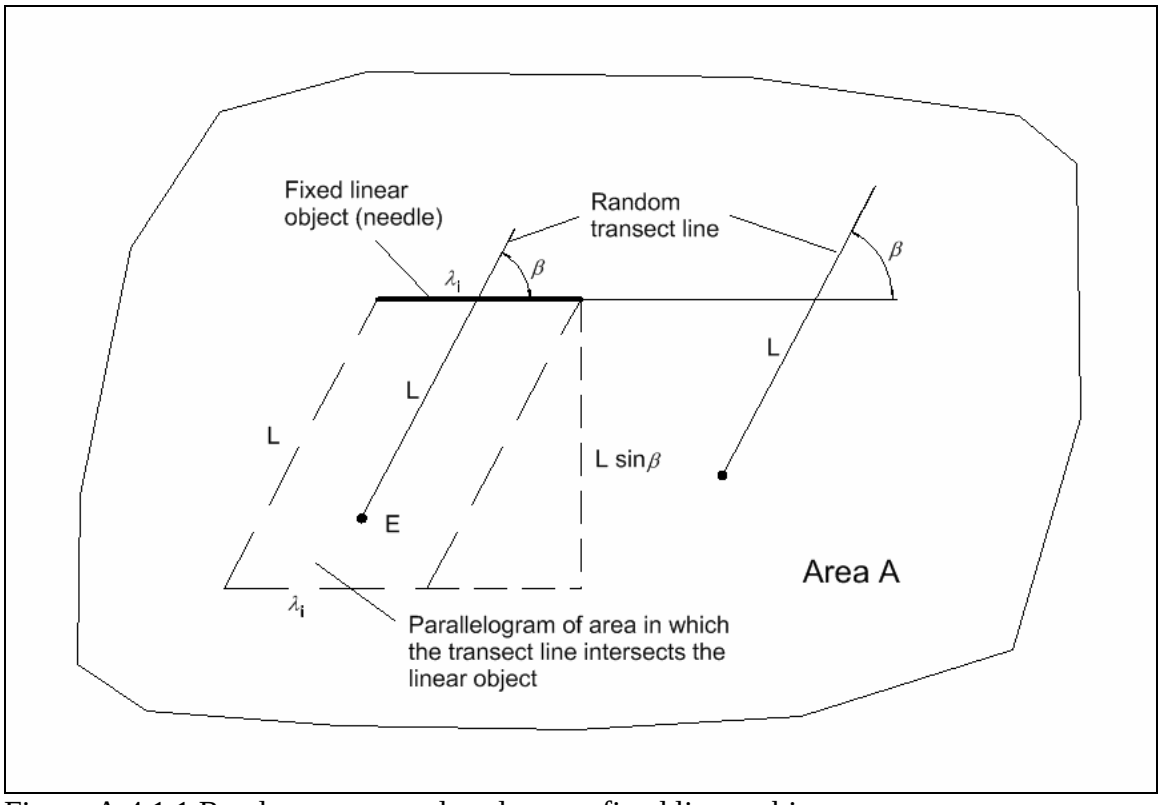

Figure A.4.1.1 Random transect placed over a fixed linear object.

The transect line orientation angle β is uniformly distributed on the interval 0 to 2π, so has a probability density of $1/2\pi$. The conditional probability that the transect line

intersects the needle is the probability of that the orientation angle is β multiplied by the probability that transect line is placed so it intersects the needle. The probability that the transect line is placed so it intersects the needle is equivalent to the probability that E lies within the parallelogram. The transect line could be placed anywhere in Area A so the probability of intersection is defined by the area of the parallelogram divided by area A. The conditional probability of is therefore defined as (de Vries 1986):

$$\mathrm{p_i}\left|\beta = \left(\frac{1}{2\pi}d\beta\right)\left(\frac{\lambda_i L \sin\beta}{A}\right) = \frac{\lambda_i L}{2\pi\ A}\sin\beta\ d\beta\right. \qquad \text{A.4.1.1}$$

The unconditional probability of intersection is the sum of the probabilities at all possible orientation angles β:

$$\mathrm{p_i} = \int_{\beta=0}^{2\pi} \mathrm{P_i}\left|\beta = 2\int_0^{\pi} \frac{\lambda_i L \sin\beta}{2\pi\ A} d\beta = \frac{\lambda_i L}{\pi\ A}\int_0^{\pi} \sin\beta d\beta\right. \qquad \text{A.4.1.2}$$

Integrating Equation A.4.2 gives the rather elegant result:

$$\mathrm{p_i} = \frac{\lambda_i L}{\pi\ A}\int_0^{\pi} \sin\beta d\beta = \frac{\lambda_i L}{\pi\ A}\left(-\cos\beta\right)\Big|_0^{\pi} = \frac{2\lambda_i L}{\pi\ A} \qquad \text{A.4.1.3}$$

The probability of intersection increases directly with the length of linear objects and transects, and is inversely proportional to the area being sampled.

Nothing in the de Vries development restricts the orientation or length of the fixed linear object. Nor does it require that the transect line be straight, just that its orientation angle be defined as it crosses the fixed object. A curved transect line simply adds a second level of integration to Equation A.4.1.3 for the differential elements of the transect line that vanish in the expression of unconditional probability. It is implied that

the transect line is entirely within area A, otherwise there is no restriction on the size of A.

If N number of linear objects having a quantifiable property x_i are randomly placed in area A, only n objects will intersect a transect line. Intersection and non-intersection can be described by a stochastic variable t_{-i}, that takes on a value of one or zero. The expected value of property x_i t_{-i} along the transect is:

$$E(x_i t_{-i}) = x_i E(t_{-i}) = x_i(1)\mathrm{p_i} + x_i(0)(\mathrm{p_i} - 1) = x_i \mathrm{p_i} = x_i \frac{2L\lambda_i}{\pi A} \qquad \text{A.4.1.4}$$

The total quantity of property x that intersects the transect line is:

$$\sum^{n} x_i = \sum^{N} x_i t_{-i} \qquad \text{A.4.1.5}$$

The expected value of property x intersecting the transect line is then:

$$E\left(\sum^{n} x_i\right) = E\left(\sum^{N} x_i t_{-i}\right) = \sum^{N} E(x_i t_{-i}) = \frac{2L}{\pi A}\sum^{N} x_i \lambda_i$$

or

$$E\left(\frac{\pi}{2L}\sum^{n} x_i\right) = \frac{1}{A}\sum^{N} x_i \lambda_i \qquad \text{A.4.1.6}$$

Dividing both sides of Equation A.4.1.6 by λ_i gives:

$$E\left(\frac{\pi}{2L}\sum^{n} \frac{x_i}{\lambda_i}\right) = \frac{1}{A}\sum^{N} x_i \qquad \text{A.4.1.7}$$

It is seen that the right hand side of Equation A.4.1.7 is the total quantity of property x per unit area. This gives the very useful unbiased estimator of the density of property x:

$$\hat{X} = \frac{\pi}{2L}\sum^{n} \frac{x_i}{\lambda_i} \qquad \text{A.4.1.8}$$

Equation A.4.1.8 provides that the area density of any property associated with a linear object can be estimated by measuring the magnitude of x_i and length λ_i of all linear objects that intercept a transect line of length L.

When total length per unit area of the linear objects is the property of interest, such as with the length of stream channels, Equation A.4.1.8 becomes:

$$\hat{X} = \frac{\pi}{2L} \sum^{n} \frac{\lambda_i}{\lambda_i} = \frac{\pi\, n}{2L} \qquad \text{A.4.1.9}$$

Equation A.4.1.9 is very useful in aerial survey and is utilized in many practical applications in the dissertation research.

Reference

de Vries, P. G. (1986). *Sampling Theory for Forest Inventory*, Springer Verlag, New York.

Appendix 4.2

LIS Variance Computations

Preliminary Computations for Practical Estimate of Variance for First Order Channels					
Transect (Flightline)	Intersect Counts	Length m	Channel Density $m\ m^{-2}$	Squared Deviation $m^2\ m^{-4}$	Squared Deviation x Length $m^3\ m^{-4}$
2	2	1,180	0.00266	1.4112E-06	1.6652E-03
3	0	2,380	0.00000	2.1737E-06	5.1736E-03
4	3	3,300	0.00143	2.1531E-09	7.1054E-06
5	5	4,840	0.00162	2.1999E-08	1.0648E-04
6	8	8,400	0.00150	4.6645E-10	3.9183E-06
7	8	10,680	0.00118	8.8663E-08	9.4694E-04
8	10	12,240	0.00128	3.6504E-08	4.4683E-04
9	19	16,330	0.00183	1.2481E-07	2.0381E-03
10	14	17,070	0.00129	3.4617E-08	5.9091E-04
11	14	16,190	0.00136	1.3463E-08	2.1796E-04
12	20	21,240	0.00148	2.2418E-11	4.7615E-07
13	21	20,660	0.00160	1.4955E-08	3.0897E-04
14	24	21,830	0.00173	6.3798E-08	1.3927E-03
15	20	24,700	0.00127	4.0990E-08	1.0125E-03
16	23	24,890	0.00145	5.2173E-10	1.2986E-05
17	31	27,760	0.00175	7.8269E-08	2.1728E-03
18	22	28,280	0.00122	6.3698E-08	1.8014E-03
19	38	28,070	0.00213	4.2523E-07	1.1936E-02
20	27	24,640	0.00172	6.0946E-08	1.5017E-03
21	19	21,720	0.00137	1.0056E-08	2.1843E-04
22	14	17,550	0.00125	4.8975E-08	8.5952E-04
23	19	19,610	0.00152	2.2628E-09	4.4374E-05
24	26	23,040	0.00177	8.8940E-08	2.0492E-03
25	23	24,970	0.00145	7.5632E-10	1.8885E-05
26	27	25,400	0.00167	3.8170E-08	9.6952E-04
27	28	26,850	0.00164	2.6798E-08	7.1953E-04
28	26	25,120	0.00163	2.2938E-08	5.7620E-04
29	22	22,530	0.00153	3.5373E-09	7.9696E-05
30	20	22,490	0.00140	6.0040E-09	1.3503E-04
31	24	21,540	0.00175	7.6076E-08	1.6387E-03
32	19	19,470	0.00153	3.4236E-09	6.6657E-05
33	8	17,937	0.00070	5.9874E-07	1.0740E-02
34	11	14,920	0.00116	1.0002E-07	1.4924E-03
35	17	13,000	0.00205	3.3612E-07	4.3696E-03
36	9	11,010	0.00128	3.6224E-08	3.9883E-04
37	3	6,000	0.00079	4.7470E-07	2.8483E-03
38	3	5,750	0.00082	4.2881E-07	2.4657E-03
39	8	6,620	0.00190	1.7962E-07	1.1892E-03
40	4	7,070	0.00089	3.4301E-07	2.4252E-03
41	8	11,040	0.00114	1.1299E-07	1.2474E-03
42	4	12,310	0.00051	9.2922E-07	1.1439E-02
43	11	12,030	0.00144	1.4518E-09	1.7466E-05
44	13	11,580	0.00176	8.3517E-08	9.6717E-04
45	4	9,170	0.00069	6.2282E-07	5.7115E-03
Total	679	723,416		9.2312E-06	8.4024E-02
All transects			0.00147		

Table A.4.2.1 Preliminary computations for practical variance estimation of first order channels.

Appendix 4.3

LIS Count of 2004 Ephemeral Gullies

LIS Intersection Count of March 2004 Ephemeral Gullies					
			2004 Ephemeral Gullies Transect		
Flight Line	Subbasin	Transect Length	Left	Middle	Right
2	Little Potlatch	1,499	0	0	0
3	Little Potlatch	2,467	2	2	2
4	Little Potlatch	3,496	0	1	0
5	Little Potlatch	5,552	6	3	10
6	Little Potlatch	6,883	6	8	3
6	Middle Potlatch	3,600	1	3	6
7	Little Potlatch	6,785	5	4	4
7	Middle Potlatch	4,298	6	9	5
8	Little Potlatch	7,211	2	2	3
8	Middle Potlatch	5,239	9	9	9
9	Little Potlatch	9,383	2	5	4
9	Middle Potlatch	8,414	2	8	5
10	Little Potlatch	9,359	5	1	6
10	Middle Potlatch	8,062	5	4	0
11	Little Potlatch	10,026	3	4	1
11	Middle Potlatch	7,866	3	1	6
12	Little Potlatch	13,627	3	0	2
12	Middle Potlatch	8,233	8	2	1
13	Little Bear	1,631	0	0	0
13	Little Potlatch	10,173	2	0	1
13	Middle Potlatch	9,808	10	7	4
14	Little Bear	2,063	1	1	0
14	Little Potlatch	10,638	0	0	0
14	Middle Potlatch	10,576	5	5	6
15	Little Bear	2,972	1	1	2
15	Little Potlatch	9,971	0	0	0
15	Middle Potlatch	10,512	4	2	7
16	Little Bear	5,067	0	1	0
16	Little Potlatch	9,391	0	0	2
16	Middle Potlatch	10,802	5	6	7
17	Little Bear	6,286	0	6	3
17	Little Potlatch	9,487	1	1	0
17	Middle Potlatch	12,658	10	5	10
18	Little Bear	5,426	2	8	0
18	Little Potlatch	8,542	0	0	3
18	Middle Potlatch	12,499	4	6	4
19	Little Bear	8,935	3	4	1
19	Little Potlatch	3,562	0	0	1
19	Middle Potlatch	12,426	3	1	2
20	Little Bear	12,245	3	1	6
20	Middle Potlatch	11,235	0	0	0
21	Little Bear	9,507	5	4	2
21	Middle Potlatch	10,290	0	0	0
22	Little Bear	15,938	2	1	1
22	Middle Potlatch	7,031	3	0	0
23	Little Bear	16,181	8	9	9
24	Big Bear	10,578	4	6	5
24	Little Bear	7,570	6	5	5
25	Big Bear	16,970	6	4	8
25	Little Bear	1,526	0	0	0
26	Big Bear	19,292	5	2	3
27	Big Bear	24,909	1	9	10
28	Big Bear	22,626	5	10	7
29	Big Bear	16,756	1	0	3
29	Pine	5,312	2	3	5
30	Big Bear	10,747	0	0	0
30	Pine	10,537	2	1	3
31	Big Bear	8,963	0	0	1
31	Pine	9,794	7	4	6
32	Big Bear	8,322	0	1	0
32	Pine	9,916	0	6	2
33	Big Bear	642	0	0	0
33	Pine	13,765	1	3	3
34	Pine	13,368	0	0	0
35	Cedar	2,558	2	0	0
35	Pine	11,830	0	0	0
36	Cedar	5,911	2	1	1
36	Pine	5,448	1	0	0
37	Cedar	5,686	2	1	1
38	Cedar	5,602	1	0	1
39	Cedar	6,397	1	4	0
40	Cedar	8,122	1	6	2
41	Cedar	10,812	1	2	2
42	Cedar	11,975	0	0	0
43	Cedar	7,983	3	3	2
44	Cedar	8,182	2	2	3
45	Cedar	8,729	0	0	0

Table A.4.3.1 Line intersect sampling count of March 2004 ephemeral gullies.

Appendix 4.4

Digital Channel Network of the Potlatch Drainage

A reasonably accurate assessment of the total length of drainage and stream channels in the agricultural lands of the Potlatch River Basin is essential for estimation of channel erosion. A channel reach has a potential bank erosion surface on both sides of the channel, thus an error in the estimate of channel length amounts to twice the error in bank length. Erosion estimates will unavoidably be sensitive to length determinations. An accurate estimate of the lengths of low order channels is difficult to determine for an area as large as the Potlatch basin with conventional map analysis techniques. This section demonstrates how to develop a better estimate of drainage channel length with digital terrain analysis and aerial line intersect sampling.

Lengths of moderately sized perennial streams can be obtained with reasonable effort from existing sources including USGS 7.5 minute series topographic maps, USGS Digital Line Graph (DLG) Hydrography, U.S. EPA Reach Files and most recently the USGS National Hydrography Dataset. The digital hydrography datasets may be analyzed with common GIS procedures to rapidly produce an estimate of total length for a given subbasin. However, each of these datasets has a scale of applicability, usually not larger than 1:24,000. Lengths (and existence) of smaller (low order) channels, of vital concern in this research because of high erosion potential, will be largely underestimated.

The original and best existing source of hydrography and topographic information for the Potlatch River basin are the USGS 7.5 minute series topographic maps developed from aerial photography acquired about 50 years ago. The newer digital sources of hydrography are based on the original topographic map contours. Blue hydrography

lines on the 7.5 minute topographic maps in the agricultural lands of the Potlatch basin generally only extend into the 3rd order channel network. Lower order channels must be inferred from analysis of digital elevation data or mapped from georeferenced (orthorectified) high-resolution aerial imagery.

Stream Network Models

Stream network models are idealized link and node topological representations of the connected channels of a drainage basin (Horton 1945). Source channel initiation points, tributary junctions and the basin outlet are represented as nodes in the network connected by links representing the channels. Stream network models appealed to hydrologic researchers well before GIS software made network analysis of all types a common operation. Stream network analysis reveals a remarkable degree of orderliness of form between basins (Horton 1945; Shreve 1969; Strahler 1957). Many empirical stream order laws are proposed that relate stream order to dimensional properties such as link length, link number, contributing area, and link slope. Complex watershed topology is thereby reduced to a simple self-scaling power law relationship that is easy to apply and aids discussion of watershed hydrologic characteristics.

Stream order, in the downstream sense applied by Horton and Strahler (1957), is the hierarchical arrangement of connected drainage channels, from smallest to largest, in the direction of flow. First order channels are farthest upstream in the network. Upstream nodes of first order channels represent initiation points in headwater source areas. A second order channel begins at the confluence node of two first order channels. A third order channel begins at the junction of two second order channels, and so on until reaching the highest order channel(s) just upstream from the network basin outlet. The

junction of a higher order channel with a lower order channel does not change the order of either. Stream order may be numbered in the upstream sense, as in the National Hydrography Dataset, with the first order channel at the outlet and higher order channels at source areas (USGS 2001). Upstream ordering is less convenient for geomorphological analysis where characteristics of headwater channels are of interest, because channels of equivalent landscape position can vary in order across the network. Upstream ordering has the advantage in that stream order for a given channel remains fixed even if finer scale channels are added to the network in source areas.

Hydraulically correct stream network models provide one-to-one mapping of idealized links to real stream segments or reaches. Links can be assigned attributes such as length, width, slope, discharge, pollutant loads and habitat metrics for hydrologic and environmental modeling. Stream networks also provide a spatial template for management of watershed information. The national stream network embodied in the U.S. EPA digital Reach File datasets, Versions 1.0 and 3.0 were developed from USGS digital line graph (DLG) hydrography to support watershed management and initial hydrological modeling at a scale of 1:100,000 or less (Horn and Grayman 1993). Both reach file versions are distributed in the EPA BASINS model dataset. The two reach file versions differ in resolution. Reach file Version 1.0 (RF1) includes only higher order streams (Figure A.4.4.1). Reach File Version 3.0 includes more lower order streams (Figure A.4.4.2) though still lacks the smallest channels observed in aerial images of the Potlatch basin (Figure A.4.4.3). Some channels in RF3 are disconnected from the stream network. While discharge and hydraulic geometry values in the EPA Reach files for

lower order streams of the Pacific Northwest should not be taken too literally, the HUC level networks support rapid development of initial and conceptual hydrologic models.

Much of the EPA Reach file information and DLG structure has been incorporated into the improved and more fully functional USGS National Hydrography Dataset (NHD). The NHD goes beyond the original reach file concept to include representation of two-dimensional features including riverbanks, lakes and ponds, and point features such as springs and wells. There may be one or more scaled (resolution) versions of the NHD for a given location.

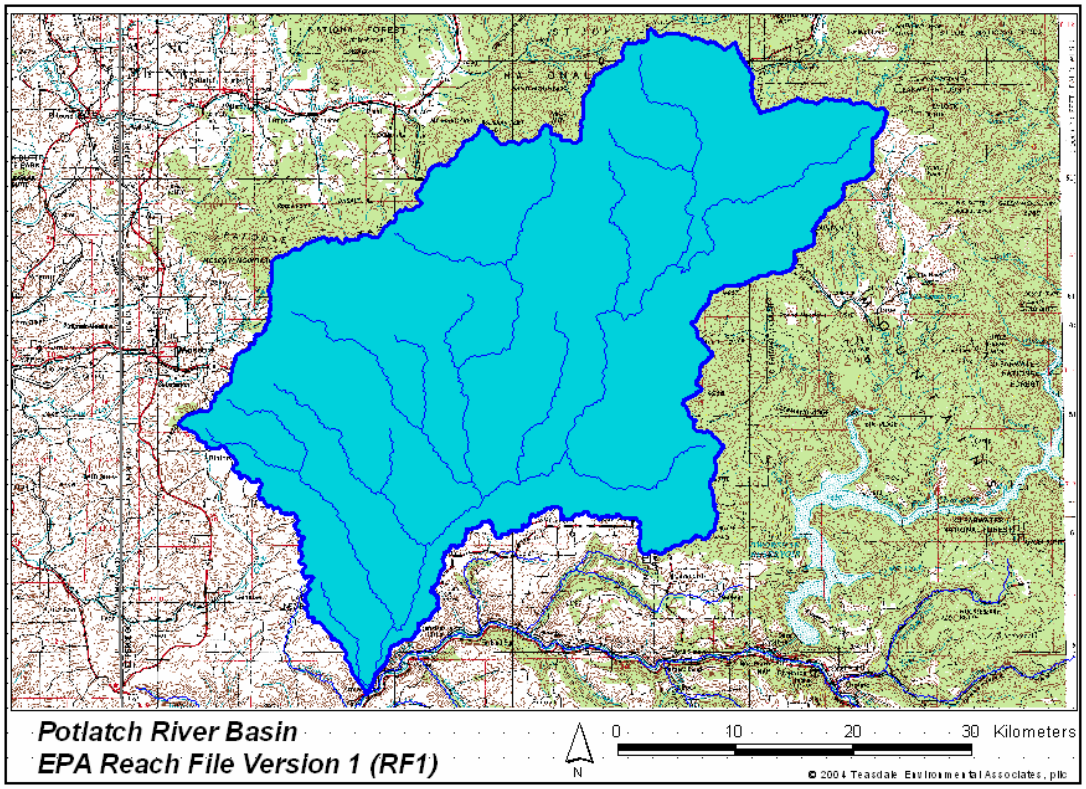

Figure A.4.4.1 U.S. EPA Reach File Version 1.0 of the Potlatch River basin.

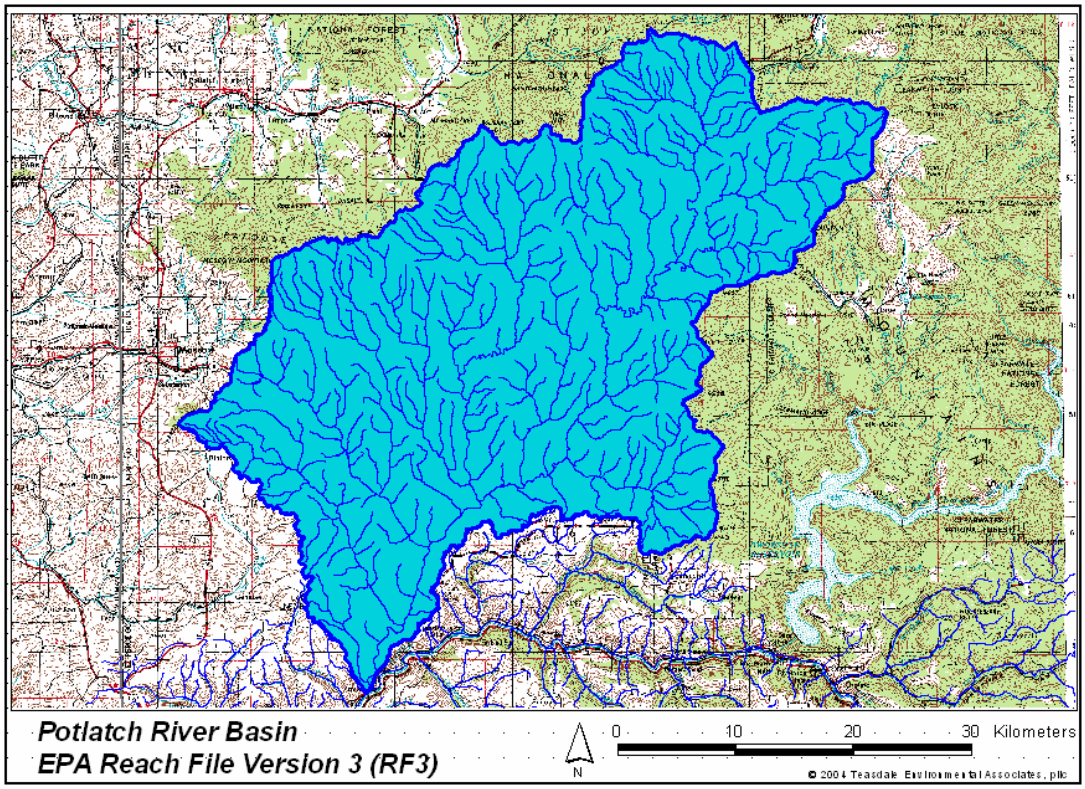

Figure A.4.4.2 U.S. EPA Reach File Version 3.0 of the Potlatch River basin.

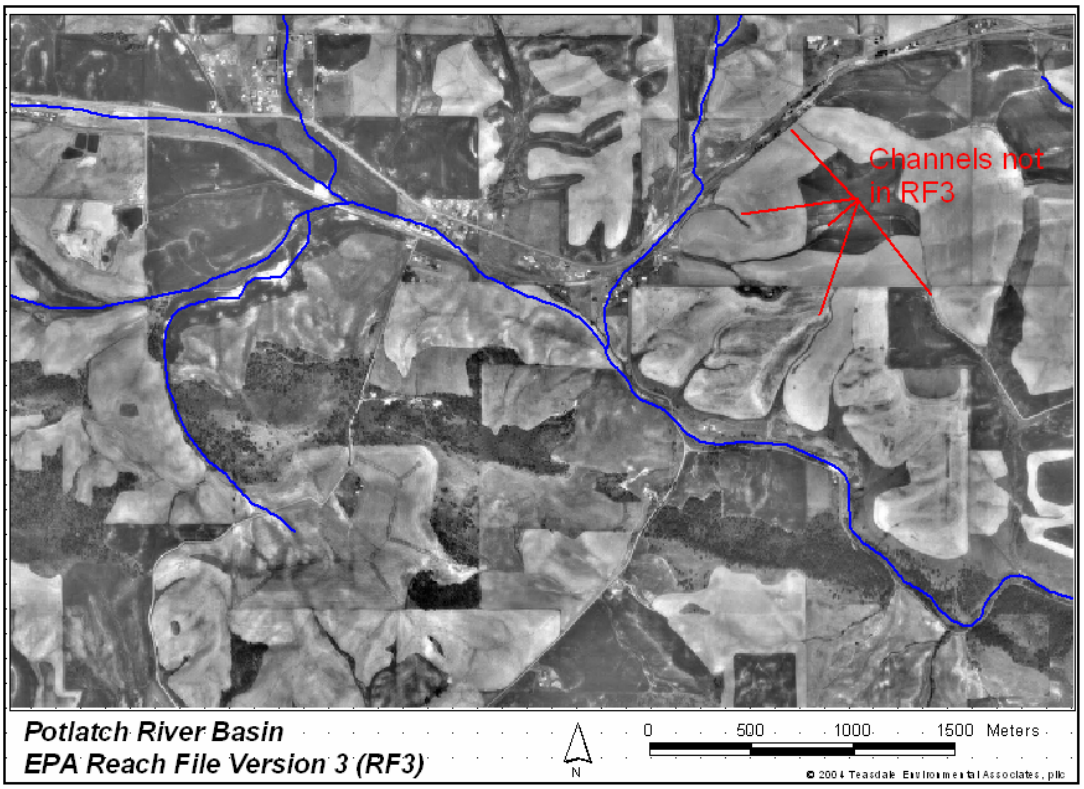

Figure A.4.4.3 Missing channels in U.S. EPA Reach File Version 3.0.

A flexible coding scheme in the NHD allows incorporation of locally derived, perhaps higher resolution, information and hydrography into the NHD framework. Higher resolution stream networks can be generated from digital elevation data with widely available software. Links in the NHD are upstream ordered. Digital streamlines of the medium resolution NHD (Figure A.4.4.4) and its predecessor EPA Reach File Version 3 (RF3) are identical in resolution and position the Pacific Northwest, though the network (topological) coding of the NHD is generally more hydraulically correct. U.S. EPA recommends use of NHD networks in current BASINS model applications (Lahlou et al. 1998). The high-resolution NHD (Figure A.4.4.5) extends the drainage network further into some source areas, but still lacks channels seen on aerial photography (Figure A.4.4.6). Some channels are disconnected from the network.

Existing national hydrography networks lack the resolution and completeness for analysis of channels in the lower Potlatch River basin. Desirable qualities of the digital channel network include,

- Resolution of the channel network should be such that first order links represent real first order permanent channels seen in high-resolution aerial imagery.
- Channel ordering should be topologically consistent and follow a downstream numbering convention.
- Links should correspond to real channel reaches with nodes at tributary junctions and at approximate channel initiation point in source areas.

- Channel links should be identified with a unique channel number in each major subbasin to allow assignment of real channel properties as feature attributes to corresponding links.
- Digital (arc) link lengths should be approximately equal to real channel lengths and its attribute length easily corrected by proportional factors.
- It should be possible to extrapolate characteristics measured or observed on a subset of real channels to the whole subbasin based on proportional representation in the digital channel network.
- It should be possible for others to reproduce the digital channel network given equivalent source materials and parametric constraints.

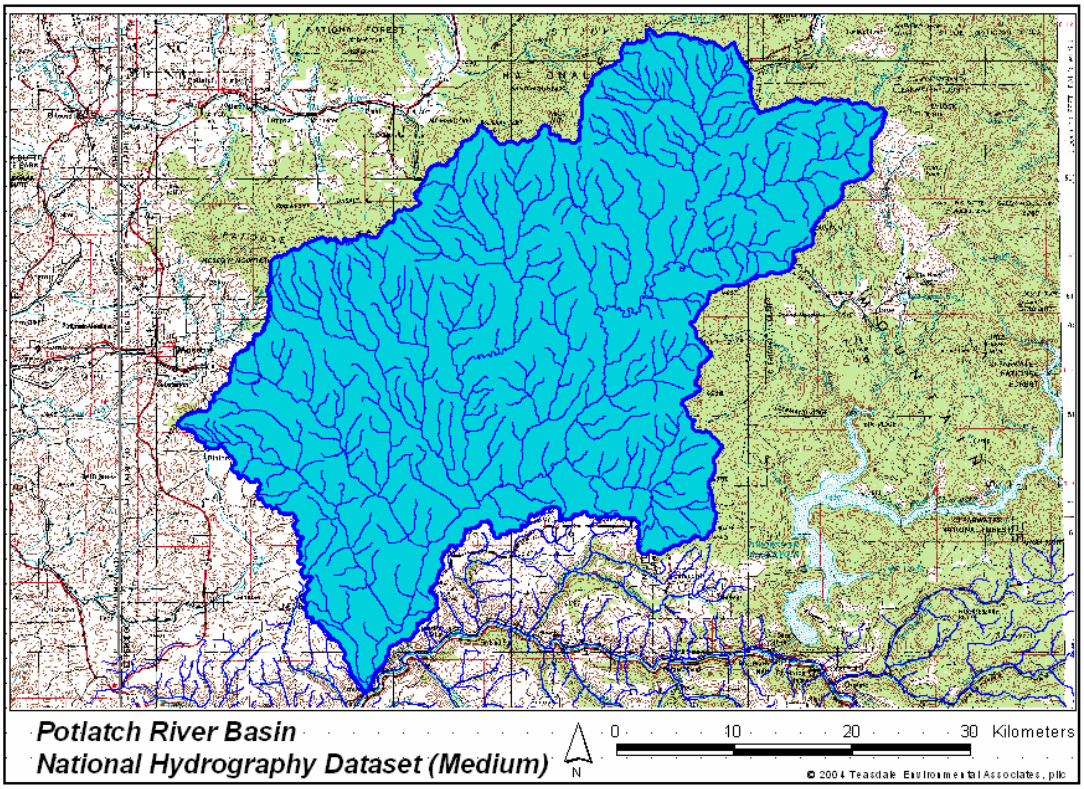

Figure A.4.4.4 Medium resolution National Hydrography Dataset reach lines of the Potlatch River basin.

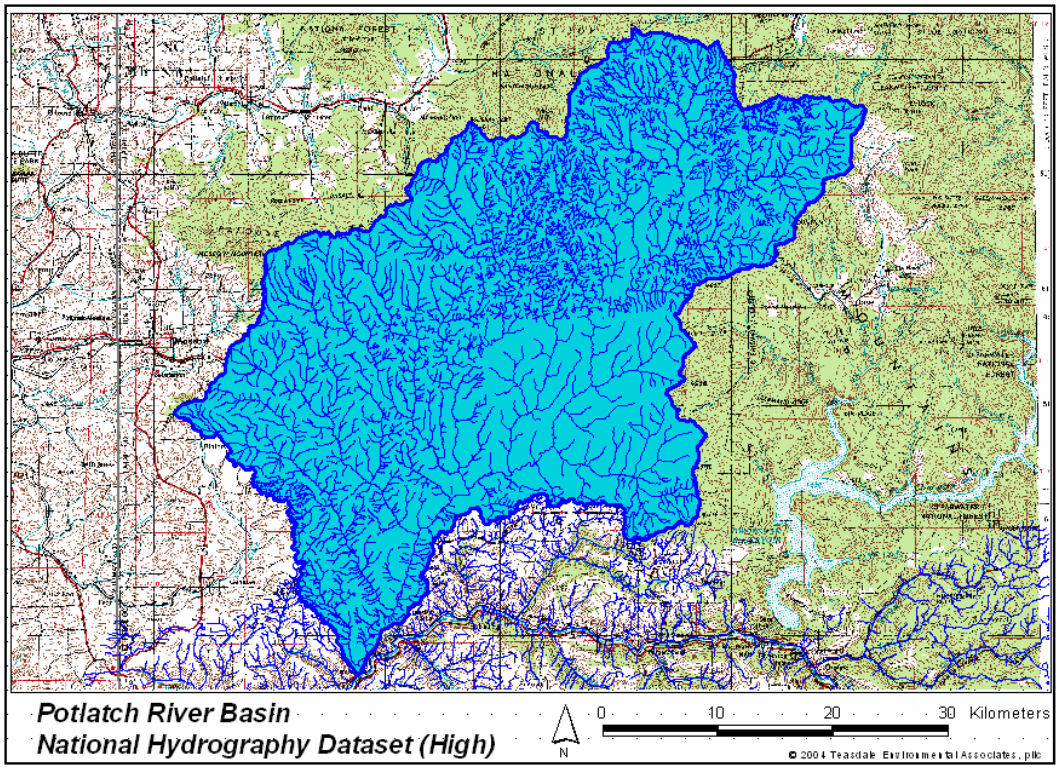

Figure A.4.4.5 High-resolution National Hydrography Dataset reach lines of the Potlatch River basin.

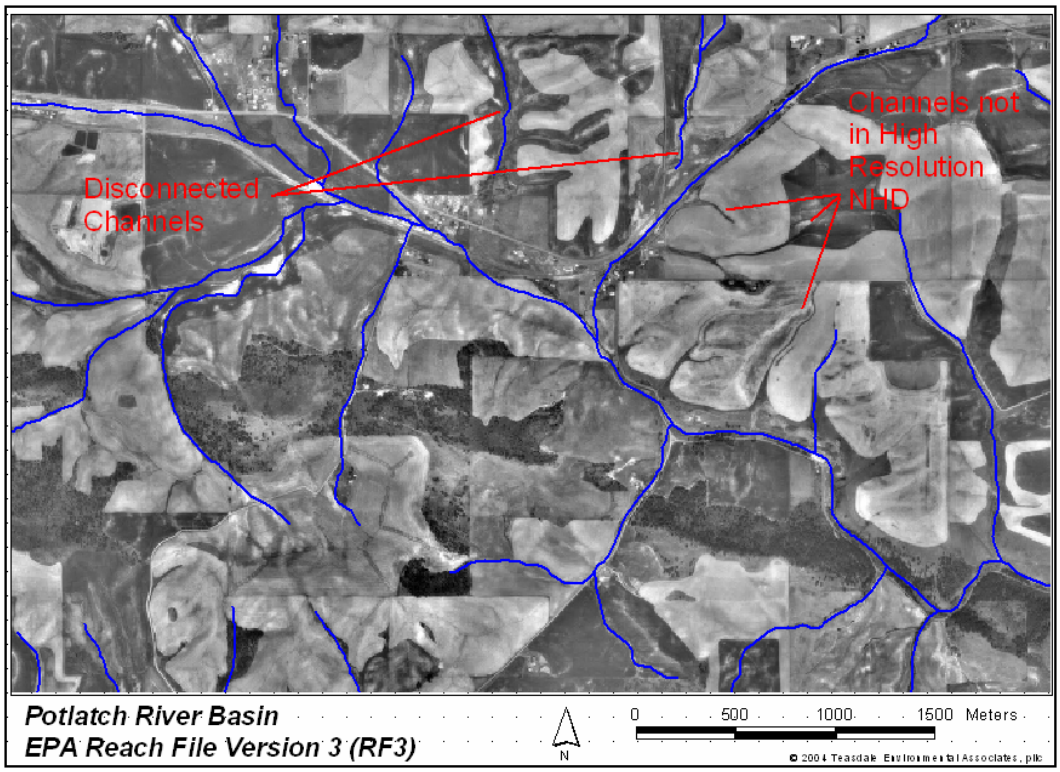

Figure A.4.4.6 Missing and disconnected channels in the high-resolution National Hydrography Dataset.

Drainage Line Template

Conceivably, the criteria listed above could be satisfied by completion and extension of the high-resolution National Hydrography Dataset. However, this would be a significant effort well outside the objectives of the current research. Fortunately digital terrain analysis offers a much more efficient and equally functional alternative for developing the digital channel network.

Digital terrain analysis has become an integral part of watershed analysis (Band 1986; Maidment and Djokic 2000; Martz and Garbrecht 1995). Terrain modeling is closely linked to advanced forms of distributive hydrologic and hydraulic analysis. Elevation gradients across the watershed landscape provide energy for water erosion and sediment transport. Many hydrologic processes are influenced by the spatial gradients of elevation including precipitation patterns, snow retention, vegetation type, soil type, landslide activity, temperature regime, and evapotranspiration. Geospatial representation of elevation and spatially correlated physical, chemical and biological processes are the empowering characteristics of hydrologic analysis with GIS.

Digital elevation data is available online. Several DEM coverages at different resolutions are typically available for the U.S. The 10-meter resolution (100 m^2 cells) Level 2 DEMs produced by USGS are the highest resolution DEMs available for the Potlatch River Basin. These DEMs are reproduced from digital contour lines of the USGS 7.5 minute series topographic maps originally derived by analog photogrammetric techniques from 1957 aerial photography. Nominal absolute vertical accuracy is about 7 meters root mean square error (RMSE).

Original Level 2 10-meter DEMs were obtained from USGS in the Spatial Data Transfer Standard (SDTS) format. These DEMs are projected in the UTM NAD27 coordinate system and are available in blocks corresponding to the USGS 7.5 topographic map coverages. Elevation data in SDTS format were converted to ESRI grid format before use in ArcView 3.x with the Spatial Analyst extension. A few state and federal websites offer processed and reprojected versions of the original SDTS DEMs. Reprocessed DEMs, especially those offered by the USGS National Map Seamless Data Distribution System (http://seamless.usgs.gov/), are convenient for some applications, but appear to undergo mathematical smoothing during processing. Elevation smoothing can reduce depiction of small order channels, so only original SDTS 10-meter DEMS were used in this research. The individual quad sheet DEM coverages for the Potlatch basin were mosaicked to form a seamless basin wide coverage (Figure A.4.4.7).

Topographic drainage lines extracted from the DEM by terrain processing provide a template for the digital channel network. Extraction of drainage lines from DEMs is a multi-step process that is more or less standardized (Garbrecht et al. 2003; Maidment and Djokic 2000; Tarboton et al. 1991). In general, it consists of the following steps,

- Preprocess the original DEM to remove internally draining low spots to produce a "filled" DEM that is free draining from all points in the basin to the outlet.
- Produce a flow direction grid from the filled DEM in which cell values are indicate the direction of flow to the next lowest grid cell that borders on a side or corner (8 directions possible), the so called D8 flow direction scheme. A variation is the D-infinity method of Tarboton (1997).

- Generate a flow accumulation grid from the flow direction grid in which cell values are the accumulated contributing area draining to that cell.
- Extract contributing drainage lines for a specified threshold subbasin area.
- Convert grid based subbasins and drainage lines to vector shapefiles for further processing into the digital channel network.

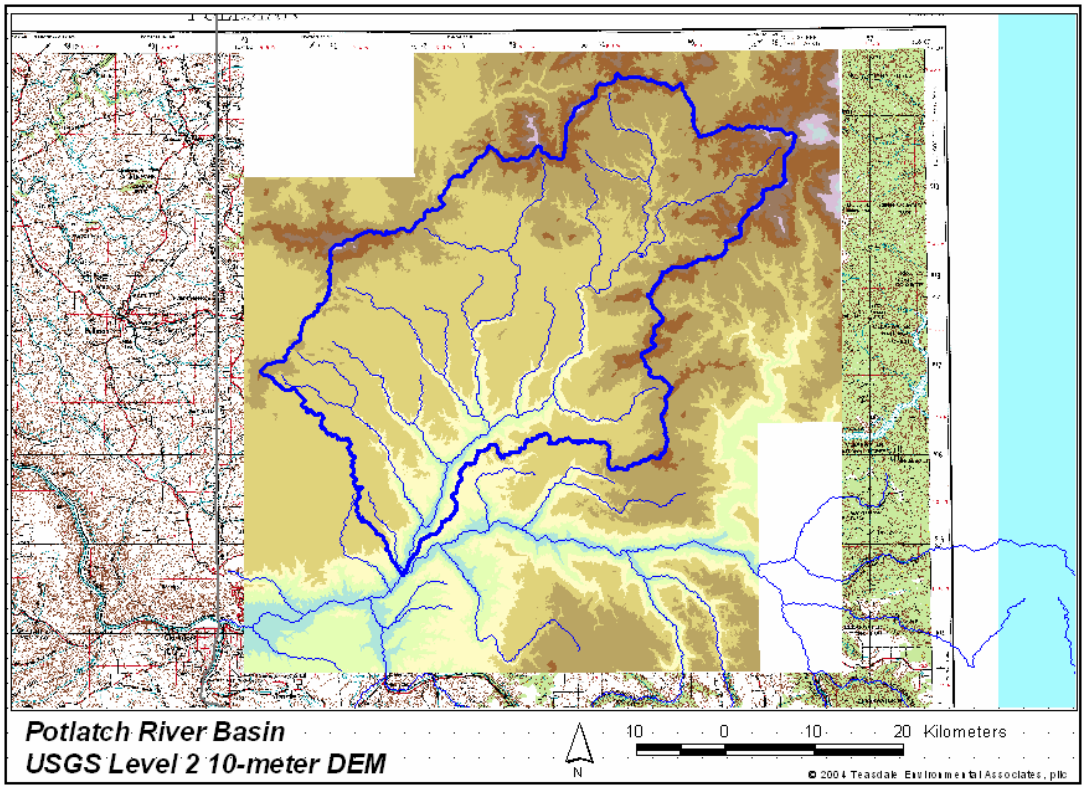

Figure A.4.4.7 Mosaicked USGS Level 2 10-meter DEM of Potlatch River basin.

Selection of an optimal subbasin threshold size is mostly a trial and error procedure. Experimentation showed that real first order channels observed in aerial photography of the agricultural land of the Potlatch basin were best matched when selecting a 5 ha (500 cells) watershed and drainage line threshold. This threshold size tends to over designate first order channels in steeper terrain and under represent the

length of first order channels in flatter terrain. Drainage lines generated with a 5 ha threshold for in the Little Bear Creek subbasin are in Figure A.4.4.8. Forested canyon land on the right side of the image is much steeper than the agricultural fields. DEM generated drainage lines align well with the actual channels. Drainage lines for the six predominantly agricultural subbasins were generated with the Hydrologic Modeling Extension Version 1.1 included with the ESRI Spatial Analyst Extension. Experimentation shows this extension to produce results similar to those obtained with delineation tools in EPA BASINS and SWAT ArcView interfaces. Results are also acceptably similar to those obtained with Tarboton's (1997) DEM processing techniques.

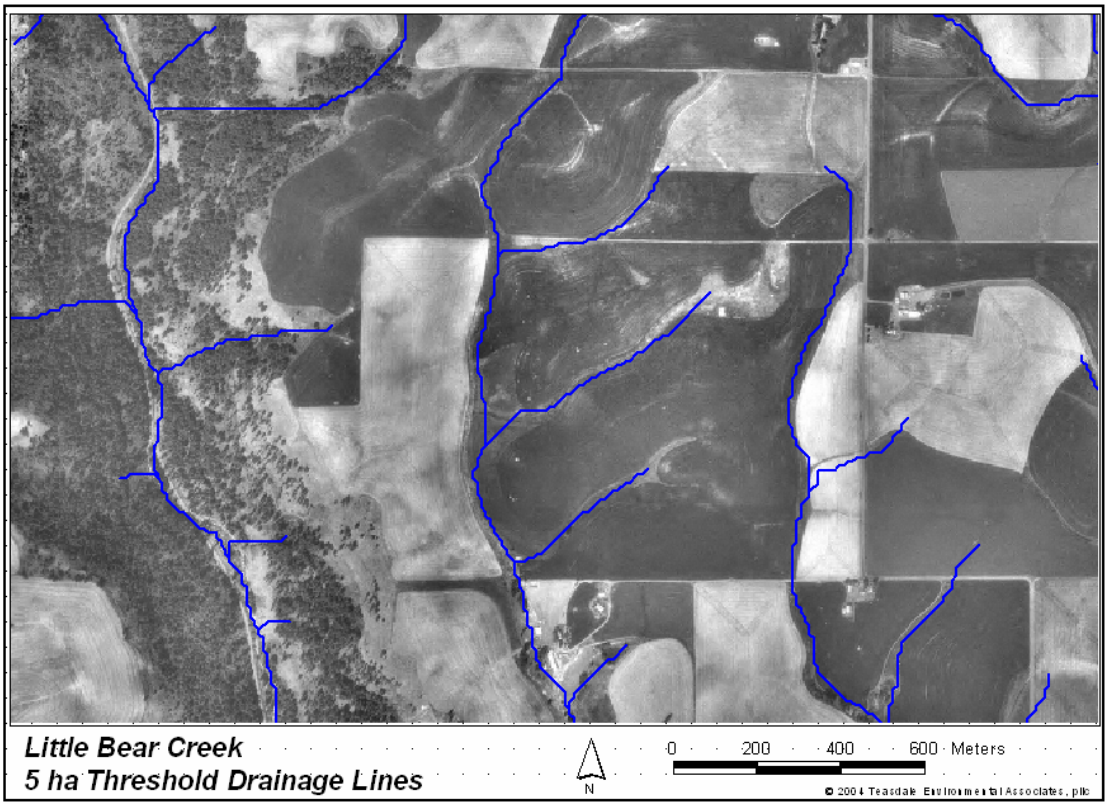

Figure A.4.4.8 Drainage lines generated with a 5 ha watershed threshold.

For consistency and convenience, a constant 5 ha threshold size was selected for all subbasins within the research area, though this is not a necessary condition. A unique threshold area could have been selected for each subbasin or parts of subbasins to obtain a better match to real first order channels, but reproduction of the drainage lines would become more effort for subsequent investigators. Future research could develop a rational approach for selection of channel network extraction in complex Palouse prairie topography.

Digital Channel Network

Drainage line attributes produced by the ESRI Hydrologic Modeling extension are limited to an arc (link) identification number, to node, from node, link length, and corresponding subbasin grid identification number. Horton-Strahler channel order must be determined for each link and added to the drainage line attribute table. The Hydrologic Modeling extension ArcView does not perform stream order determination. Channel orders were determined with a custom FORTRAN code. Channel orders were added to the drainage line template attribute file with the ArcView table joining procedure. Commercial ArcView scripts are available to determine channel order completely within the ArcView environment. Channel orders are labeled in Figure A.4.4.9 for a portion of the Little Bear Creek drainage. The most downstream channel in Little Bear Creek is 6^{th} order.

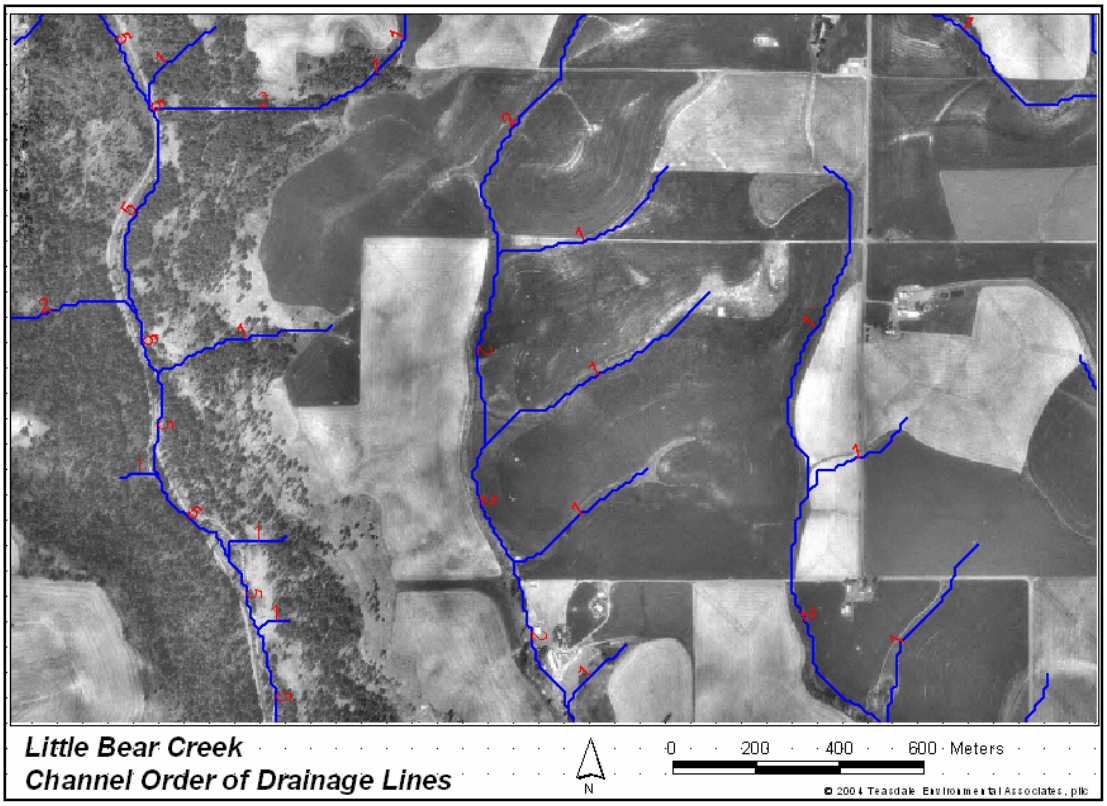

Figure A.4.4.9 Horton-Strahler channel order of drainage lines.

Maximum elevation, minimum elevation and average elevation of each link were extracted from the filled 10-meter DEM with standard functions of the ArcView Spatial Analyst extension. Overall link slope was computed with the ArcView field calculator as the difference of maximum and minimum elevations divided by the link length. Coordinates of link midpoints were determined with a custom ArcView Avenue script. Midpoint coordinates can be uploaded to a field GPS to locate real channels that correspond to the network links. The final drainage channel network shapefile attribute table includes the fields listed in Table A.4.4.1.

Field	Description
Chan_ID	Unique identification number of the link
From_node	Upstream node number
To_node	Downstream node number
Length_L	Length of link (m)
Strahler	Horton-Strahler channel order number
Elev_mean	Mean elevation of link (m)
Slope	Overall slope tangent of link, (m/m)
Xcoord	UTM 11 NAD83 easting coordinate of link midpoint (m)
Ycoord	UTM 11 NAD83 northing coordinate of link midpoint (m)

Table A.4.4.1 Digital channel network attribute fields.

Overall channel statistics are easily computed with GIS algorithms. Total length of the digital channel network is 2904 km (1301 mi). Table A.4.4.2 summarizes the total channel length in each subbasin by Horton-Strahler order. Figure A.4.4.10 is a log-linear plot of the total length of stream channel by stream order for each subbasin. Channel orders 1 through 4 plot along straight lines, exhibiting the power law relationship common to many naturally eroded channel systems. The break in the relationship at fifth order channels is because higher order channels are constrained and lengthened by the ancient canyon morphology formed under very different climate conditions.

Potlatch Basin Digital Channel Network (5 ha Threshold)							
	Channel Length (km) by Horton-Strahler Order						
Subbasin	1	2	3	4	5	6	Total
Big Bear	261.5	106.5	48.8	22.4	22.6	30.0	491.8
Cedar	137.0	79.5	29.7	20.5	3.3	8.9	278.9
Little Bear	155.3	70.4	24.8	10.1	32.0	7.8	300.5
Little Potlatch	193.2	97.0	41.7	25.5	19.5		377.0
Middle Potlatch	223.0	99.1	45.0	27.2	24.6		418.9
Pine	110.9	57.7	28.6	13.3	16.0		226.7
Total	1081.0	510.3	218.6	119.0	118.0	46.7	2093.7

Table A.4.4.2 Digital channel network length by subbasin and Horton-Strahler order.

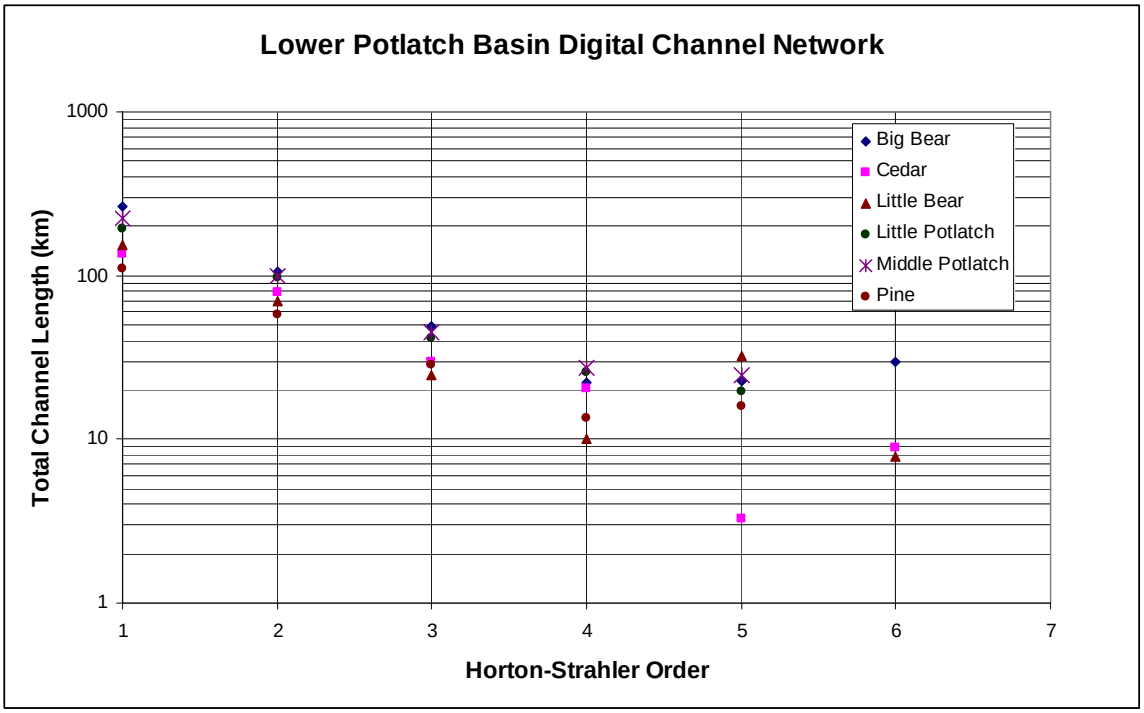

Figure A.4.4.10 Plot of total channel length by stream order for the lower Potlatch basin.

References for Appendix 4.4

Band, L. E. (1986). "Topographic Partition of Watersheds with Digital Elevation Models." *Water Resources Research*, 22(1), 15-24.

Buckland, S. T., Anderson, D. R., Burnham, K. P., Laake, J. L., Borchers, D. L., and Thomas, L. (2001). *Introduction to Distance Sampling, Estimating Abundance of Biological Parameters*, Oxford University Press, Oxford.

Canfield, R. H. (1941). "Application of the line interception method in sampling range vegetation." *Journal of Forestry*, 39, 388-394.

de Vries, P. G. (1986). *Sampling Theory for Forest Inventory*, Springer Verlag, New York.

Freeze, F. (1962). *Elementary Forest Sampling, Agricultural Handbook No. 232*, U.S. Department of Agriculture, U.S. Forest Service.

Garbrecht, J., Martz, L. W., and Starks, P. J. (2003). "Technological advances in automated surface parameterization from digital elevation models." GIS for Water Resources and Watershed Management, J. G. Lyon, ed., Taylor and Francis, New York, 207-218.

Hays, R. L., Summers, c., and Seitz, W. (1981). *Estimating Wildlife Habitat Variables*, Office of Biological Services, U.S. Fish and Wildlife Service, Washington, DC.

Hodgson, M. E., and Bresnahan, P. (2004). "Accuracy of Airborne Lidar-Derived Elevation: Empirical Assessment and Error Budget." *Photogrammetric Engineering and Remote Sensing*, 70(3), 331-340.

Hodgson, M. E., Jensen, J. R., Schmidt, L., Schill, S., and Davis, B. (2003). "An evaluation of LIDAR- and IFSAR-derived digital elevation models in leaf-on conditions with USGS Level 1 and Level 2 DEMs." *Remote Sensing of Environment*, 84(2), 295-308.

Horn, C. R., and Grayman, W. M. (1993). "Water-Quality Modeling with EPA Reach File System." *Journal of Water Resources Planning and Management*, 119(2), 262-274.

Horton, R. E. (1945). "Erosional development of streams and their drainage basins: hydrophysical approach to quantitative morphology." *Bulletin of the Geological Society of America*, 56, 275-370.

Lahlou, M., Shoemaker, L., Choudury, S., Elmer, R., Hu, A., Manguerra, H., and Parker, A. (1998). *Better Assessment Science Integrating Point and Nonpoint Sources BASINS, Version 2.0, EPA-823-R-98-006*, Office of Water, U.S. Environmental Protection Agency, Washington, D.C.

Li, F., and Chaplin, J. (1995). "Analysis of random and systematic sampling methods for residue cover measurements." *Transactions of the American Society of Agricultural Engineers*, 38(5), 1353-1361.

Maidment, D., and Djokic, D. (2000). "Hydrologic and Hydraulic Modeling." Environmental Systems Research Institute (ESRI), Redlands, CA, 216.

Martz, L. W., and Garbrecht, J. (1995). "Automated Recognition of Valley Lines and Drainage Networks from Grid Digital Elevation Models: A Review and a New Method-Comment." *Journal of Hydrology*, 167, 393-396.

Matern, B. (1964). "A method of estimating the total length of roads by means of a line survey." *Studia Forestalia Suecica*, 18, 68-70.

Mitchell, W. A., and Hughes, H. G. (1995). *Line Intercept: Section 6.2.5, U.S. Army Corps of Engineers Wildlife Resources Manual, Technical Report EL-95-22*, U.S. Army Corps of Engineers Waterways Experiment Station, Vicksburg, MS.

Shreve, R. L. (1969). "Stream Lengths and Basin Areas in Topologically Random Channel Networks." *Journal of Geology*, 77(4), 397-414.

Skidmore, A. K., and Turner, B. J. (1992). "Map accuracy assessment using line transect sampling." *Photogrammetric Engineering and Remote Sensing*, 58(10), 1453-1457.

Strahler, A. N. (1957). "Quantitative analysis of watershed geomorphology." *Eos, Transactions, American Geophysical Union*, 38, 912-920.

Tarboton, D. G. (1997). "A New Method for the Determination of Flow Directions and Contributing Areas in Grid Digital Elevation Models." *Water Resources Research*, 33(2), 309-319.

Tarboton, D. G., Bras, R. L., and Rodriguez-Iturbe, I. (1991). "On the Extraction of Channel Networks from Digital Elevation Data." *Hydrological Processes*, 5(1), 81-100.

Thompson, S. K. (1992). *Sampling*, Wiley-Interscience, New York.

USGS. (1997). *Part 2: Hydrography, Standards for 1:24,000-Scale Digital Line Graphs - 3 Core (DLG-3)*, U.S. Geological Survey, Reston, VA.

USGS. (2001). "National Hydrography Dataset Web Page, http://nhd.usgs.gov." U.S. Geological Survey.

White, S. A., and Wang, Y. (2003). "Utilizing DEMs derived from LIDAR data to analyze morphologic change in the North Carolina coastline." *Remote Sensing of Environment*, 85(1), 39-47.

5. Satellite Imagery in Hydrologic Assessment

Satellite imagery gives the hydrologist, environmental scientist and water resources engineer a view and perspective of the physical watershed that is nearly impossible to obtain otherwise. Difficult analytical characterizations such as determination of the actual proportion of erosion susceptible land cover prior to onset of winter precipitation or the acreage of canyon land exposed by wildfire in a sensitive watershed can be made with almost trivial ease. The availability of relatively inexpensive, repeated and moderately high-resolution satellite imagery data has fundamentally change the way that many scientists approach land surface assessment (Lauer et al. 1997). There is much opportunity for practical application and applied research of satellite imagery in watershed science. This dissertation research explores a few of the possibilities and demonstrates that satellite imagery is indispensable in contemporary hydrologic analysis and soil erosion modeling.

This section does not pretend to present a comprehensive review of satellite remote sensing. Full breadth of the science and engineering of satellite imaging encompasses an astounding amount of detail – orbital mechanics, atmospheric radiation transfer, meteorology, electronic sensor design, data transmission, image archiving, data distribution, remote sensing politics, and much more. Only topics found essential to the practical use and understanding of satellite imagery for watershed assessment and aquatic resource evaluation in this work are discussed. Standard undergraduate texts of remote sensing provide qualitative overviews of sensor configuration and satellite systems operation, so this type of detail will not be repeated here. Instead, the discussion

emphasizes what was learned and what might be learned from satellite imagery in the physical characterization of watersheds.

As with the discussion of aerial imaging, selected examples from the research will demonstrate the capabilities and limitations of particular sensors by extraction of spatial information for applications of practical interest. Spaceborne and aerial sensors share many of the principles of optics and photogrammetry described in Section 3, so only aspects unique to satellite sensors will be added. Even these are brief and necessarily incomplete.

5.1 Satellite Imagery in the Dissertation Research

Six spaceborne sensors were applied in various phases of this research: the USGS/NASA Landsat 5 and Landsat 7 satellites, the NASA Advanced Spaceborne Thermal Emission and Reflection Radiometer (ASTER) on board the Terra and Aqua satellites, the Moderate Resolution Imaging Spectroradiometer (MODIS) onboard Aqua and Terra, Ikonos commercial satellite imagery (SpaceImaging, LLC), and the Department of Energy Multispectral Thermal Imager (MTI). These satellites and sensors will be featured, but much of the discussion applies to satellite data from other sensors and sources. This research does not suggest that the suite of satellite systems studied are exclusive or perhaps even the best for characterizing the complete range of physical, biological and demographical characterization tasks in watershed assessment. Their selection was mostly dictated by access and funding. However, the satellite systems selected do fairly represent the current range and capabilities of image data available for hydrologic characterization.

Recognition of proprietary, private and security interests is unavoidable in remote sensing. The discussion here has strived to the utmost to protect these interests without sacrificing hard earned insights. Both the commercial Ikonos images and Department of Energy MTI datasets have stringent copyright and national security restrictions against public distribution. These are absolutely respected. It is unfortunate for the reader that details and capabilities of the multispectral MTI datasets cannot be shared, but such was the inviolable condition of use.

Likewise, products and capabilities of the high-resolution Ikonos visible and near infrared satellite purchased and evaluated in the Bonneville Power Administration project will not be demonstrated with a few exceptions to avoid infringement of a rather restrictive licensing agreement. It is difficult to discuss and demonstrate the capabilities of this amazing instrument without sharing full resolution images.

It is with regret that the reader should be made aware that the most useful satellite for routine watershed characterization, Landsat 7, has experienced a partial failure of onboard optical instruments. Compensating for the degraded image greatly increases the work of preparing land classifications demonstrated later in this section. Nonetheless, a motivated analyst must work with the quantity and quality of the satellite data available.

5.2 Satellite Imagery in Watershed Hydrologic Characterization

The promise of satellite imagery is not so much in the resolution of the images, but in the spectral information carried by the pixels. It is important to understand the meaning of this statement. Most introductions to satellite remote sensing texts begin by a review of the electromagnetic spectrum and a discussion of the transmission of light waves through the atmosphere. This material is likely overly general for most readers of

this dissertation. Only the essentials will be covered in this section. Expanded treatments are by Lillesand and Kieffer (1994), Campbell (1996), and Jensen (1996).

While the "top down" material is essential core knowledge of remote sensing science, it lacks immediate use for an analyst interested in the hydrologic characterization of watershed land cover using commonly available satellite images and derived products. An intimate knowledge of atmospheric radiation transfer and atmospheric transmission windows is not necessary for operational use of satellite imagery as demonstrated in the dissertation work. This information is vital to instrument designers and producers of satellite imagery, but as an end user, *you get what you get, and work with what you have.*

The practical user may find a "bottom up" perspective more instructive. Figure 5.1 is a terrestrial view of the approximate coverage of a 30 m ground pixel resolution (GPR) Landsat 7 image. Several land cover types – grass, maturing wheat and rough disked dry soil are within the coverage of the pixel. The corresponding pixel in the Landsat 7 image records the combined energy reflected from each surface type in each separate spectral band. A pixel to the left may record only the reflected energy of the wheat and a pixel to the right may record mostly grass. There probably is not enough exposed soil to record a homogeneous pixel of energy reflected from the soil.

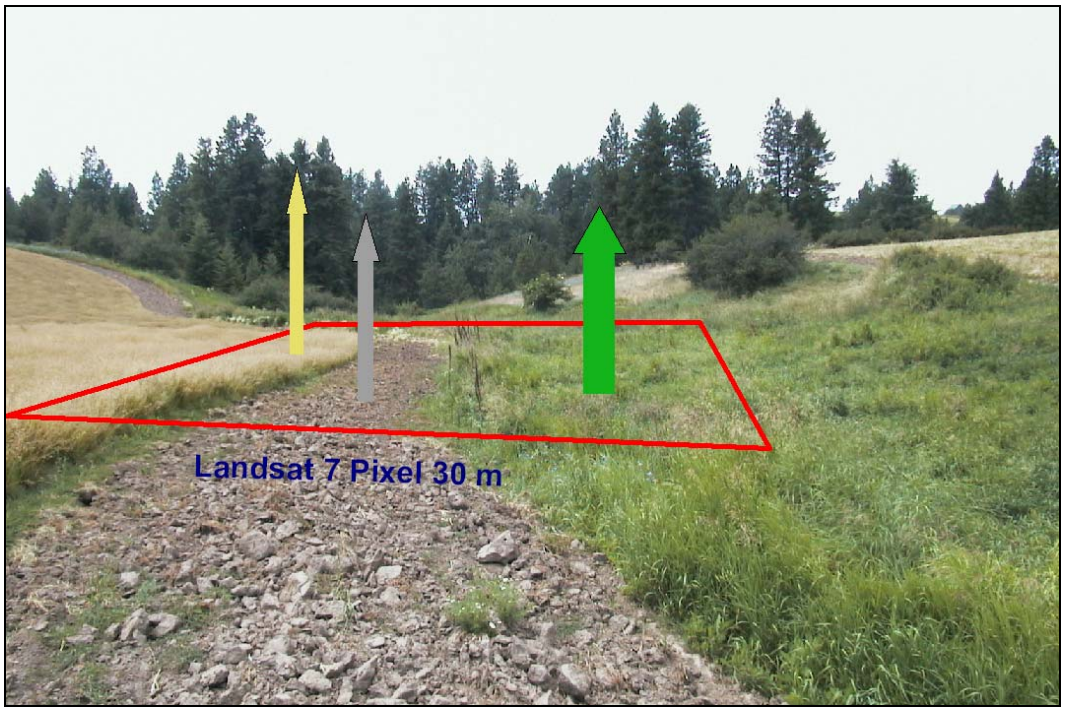

Figure 5.1 Mixed reflectance in the area covered by a Landsat 7 pixel.

Similarly, a mixture of winter wheat, spring wheat infested with dog fennel and a recently mowed grass waterway is covered by the 250 GPR MODIS pixel in Figure 5.2. Though the ground level image clearly distinguishes the grassed waterway and the boundary between the wheat fields by form and color (reflectance), the MODIS sensor could not, and would instead record a mixture of reflected energy having the characteristics of wheat, dog fennel flowers and close cropped hay. It is likely difficult to obtain many homogeneous MODIS pixels that would record reflectance solely from the dog fennel infestation.

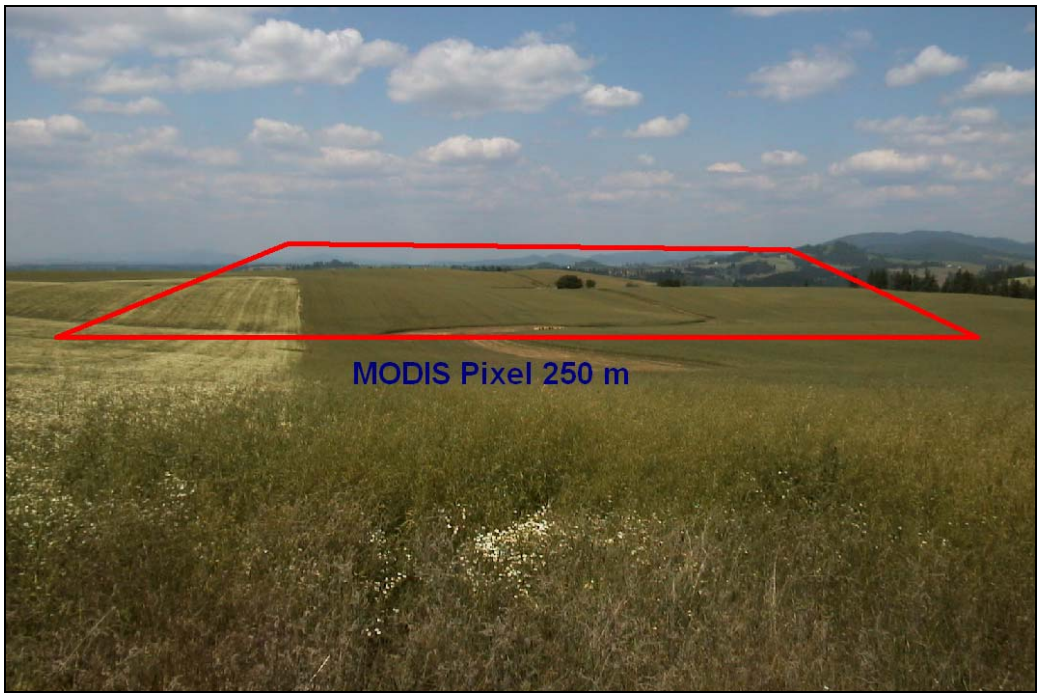

Figure 5.2 Mixed reflectance in the area covered by a MODIS sensor pixel.

Landsat 7 might have a better chance of capturing a homogeneous pixel of dog fennel, but chances are that the peak of dog fennel inflorescence would be missed in the 16 day interval between overpasses. The MODIS sensor with its 2-day interval might be able to detect an indication of peak inflorescence but could only provide rough information about spatial distribution.

Many features of interest in watershed hydrologic characterization occur at higher resolution or change more rapidly than can be recorded with certainty at the temporal frequency of medium and low resolution satellite images. The example illustrates three inescapable facts of satellite-based watershed hydrologic characterization:

- Pixels of mixed land cover are more the rule than the exception,
- Features will likely not be imaged at opportune times,
- Higher resolution sources of information are usually necessary to interpret information recorded by satellite images.

Such frankness is mostly missing from the remote sensing literature. Having laid bare the primary, but certainly not the only, difficulties with satellite remote sensing for watershed hydrologic characterization, perhaps the following statement is not too exuberant:

> *Contemporary land surface characterization for hydrologic modeling of medium to large size watersheds would be prohibitively difficult, expensive, and in final analysis, incredible without the use of current visible and shortwave infrared satellite imagery.*

This statement evolved from hard earned personal experience and agrees in principle with the views of long term experts in the field of water resource remote sensing (Engman and Schultz 2000). The balance of this section is intended to lead the reader to the same conclusion. However, the three reality-checks above should be kept in mind so as not to be deceived by seemingly precise technical details.

5.3 Watershed Characterization Strategy

Watershed characterization is an essential step in hydrologic modeling and many environmental assessments. This was the primary motivation for evaluating satellite imaging in the dissertation work. Operational hydrologic watershed and stream water quality models all require some form of watershed conceptualization and characterization including the U.S. EPA BASINS model, the Soil and Water Assessment Tool (SWAT), the Hydrologic Simulation Program in Fortran (HSPF), and the Corps of Engineers Hydrologic Engineering Center Hydrological Modeling System (HECHMS). It has been well documented from the beginnings of satellite remote sensing that hydrologically relevant characteristics of land cover can be efficiently and accurately characterized with

satellite imagery (Bondelid et al. 1982; Chery and Jensen 1982; Dallam et al. 1975; Schultz 1988; Shih 1988; Slack and Welch 1980), but this efficient resource is much under-exploited by hydrologic modelers (Schultz and Engman 2000). One reason may be the lack of an explicit watershed characterization strategy that compares alternative sources of information.

Watershed hydrological characterization should be defined in context of the dissertation research in as:

> *Watershed hydrologic characterization is the identification, qualitative description, and quantification of land surface hydrologic variables relevant to an analysis of hydrologic response within the spatial, temporal and process domains of the hydrologic model or environmental simulation.*

A more precise definition is presumptuous and restrictive, but most hydrologic modeling requires data on the following characteristics:

- Terrain parameters including catchment area and spatial distribution, hillslope lengths, hillslope gradients, topographic convergence, and elevation. Terrain shading and slope aspect may be necessary for snowmelt modeling.
- Drainage system channel lengths and topology,
- Physical characteristics and spatial distribution of surface and subsurface soils,
- Areas and spatial distribution of land cover types and land uses that have different characteristics of hydrologic response (magnitude, timing and duration) and quality of surface water and quickflow (interflow), and
- Antecedent moisture status at the beginning of the hydrological simulation.

In the dissertation work terrain parameters were extracted from digital elevation models (DEM) or measured by photogrammetric techniques, drainage system attributes

were determined by DEM analysis or observation of aerial imagery, soil information was obtained from the USDA soils databases, and antecedent moisture status was inferred from the appearance of surface soils. Land cover and land use types are determined efficiently by joint use of satellite and aerial imagery and the techniques described in this section. A method of determining land cover and land use over an extensive area based solely on aerial imagery is described in Section 4. Existing gridded land cover data, notably the National Land Cover Dataset (NLCD), provide a reasonable starting point for initial hydrologic modeling, but should be verified with current satellite and aerial imagery.

Selection of satellite imagery for watershed characterization should not be haphazard or ad hoc. If it is, image derived results will generally be misleading or have poor accuracy. For example, a hydrologic modeler in the Palouse region is likely interested in watershed response during the peak runoff season in winter and spring. A mid-summer Landsat 7 scene acquired at the time of crop maturity would incorrectly indicate the proportion of land surface covered with low vegetative that is susceptible to winter erosion. Land cover classifications based on the summer scene would under-represent the hydrologically sensitive cover types.

Combined and sustained use of high-resolution aerial imagery and satellite imagery over many seasons and many watersheds in the interior Pacific Northwest during the course of the dissertation research and other work has shown that best results are preceded by preparation of a watershed characterization strategy. Failure to prepare a characterization strategy for all but the simplest projects usually results in less than an

optimum assessment and needless expense. An imaging strategy for watershed characterization should include most of the following elements:

- A statement of the watershed characterization objectives
- A statement of imaging objectives and expectations
- A review of candidate satellite and aerial imaging sources
- A search of the imagery archive
- Analysis of local meteorological conditions that affect image acquisition
- Assessment of native plant and crop phenological stage
- Expectation of cultural activities, such as field burning, that affect image acquisition
- A statement of proprietary, private or security interests.
- Description and schedule of related field data collection
- Evaluation of user remote sensing and image processing capabilities.
- Imagery cost analysis
- Schedule for image acquisition
- Recommendation of the preferred imaging alternative
- Development of quantifiable criterion for judging conformance with the image acquisition plan
- Preparation of imagery specifications and bid documents or acquisition of vendor quotes
- Selection of imagery vendor or imaging contractor
- Evaluation of user technical support needs

In addition to the above, inexperienced users may require significant educational support and incur expense for software and computing resources during imagery planning and before image acquisition.

Many aspects of watershed characterization planning are outside the dissertation objectives and best reserved for a future publication. The most important aspects of satellite imagery that guide selection and use of satellite imagery will be discussed.

5.4 Operational Characteristics of Land Imaging Satellites

The suitability of a space-based sensor depends on the imaging objectives. Four general attributes of remote sensing imagery guide understanding of a remote sensing instrument's potential for application in environmental assessment tasks: 1) areal coverage, 2) radiometric resolution, 3) spatial resolution, and 4) temporal repeatability. Perhaps the key distinction between satellite and aerial imagery is that unlike aerial imagery, the user has no control over satellite imaging parameters and must work with the image data available. Even contracted Ikonos satellite imaging services cannot be scheduled for a specific time or sensor angle; SpaceImaging, LLC must be given a 60 day window for acquisition unless the user pays a substantial priority surcharge. This is not a limitation of satellite imagery, just a significant operational aspect that must be accommodated when planning the watershed characterization strategy.

5.4.1 Satellite Orbits and Operating Schedule

Standard remote sensing texts lack adequate discussion of relationships between orbits, image availability and coverage. A practical understanding is necessary to differentiate between possible sources of satellite data for specific watershed characterization tasks. Orbits and operating schedules determine the extent and coverage of satellite imagery available in the image archive.

Satellites are differentiated as having continuous imaging capabilities or acquire images on demand (tasking satellites). Some sensors, such as those on board the Landsat and Terra satellites acquire continuous imagery of the U.S. during daylight hours and intermittently at night and in other locations outside North America. Others, such as the highly specialized sensors on board shuttle missions and the ASTER satellite perform one-time imaging tasks with very specific objectives. Commercial satellites such as SPOT, IRS, RadarSat, Ikonos, and Quickbird acquire images under contract with the user or are collected by the operator in anticipation of need.

Orbit paths and altitudes generally control image scene coverage and resolution. Many land remote sensing satellites, including Landsat and MODIS, are placed in circular sun-synchronous near-polar orbits to consistently image a specific area at the same time of day on subsequent passes. In fact, the Terra satellite that carries a MODIS and ASTER sensor follows so closely behind Landsat 7 that for practical purposes their orbital paths and timing are essential the same. Consistent overpass time helps reduce scene differences due to illumination effects and allows direct comparisons between images.

Table 5.1 lists the orbit inclination and equatorial crossing time for the satellites evaluated in the dissertation research. Orbital paths and imaging schedules must be understood to coordinate ground data collection with satellite image acquisition. Satellite orbital paths and flyover schedules are published in satellite program documentation and technical references. It is advisable that researchers and watershed characterization planners locate and become familiar with this documentation. Internet addresses are very volatile, so will not be cited. They are best located with internet search engines using the satellite name as a keyword.

Satellite/Sensor	Altitude km	Orbit Inclination deg	Orbit Period min	Sensor Orientation	Equatorial Crossing	Scene Width km	Potential Revisit Time d	Maximum Resolution
Landsat 7	705	98.3	99	Nadir	10:30 AM	183	16	15
ASTER (Terra)	705	98.3	99	Nadir	10:30 AM	60	16	15
MODIS (Terra)	705	98.3	99	Nadir	10:30 AM	2330	1-2	250
IKONOS	680	98	98	Pointable	10:30 AM	13	2-3	1
MTI	555	NA	NA	Pointable	NA	Classified	Classified	5

Table 5.1 Orbital characteristics of satellites and sensors.

5.4.1.1 Orbital Geometry

A basic understanding of orbital geometry helps to better interpret satellite imagery metadata and anticipate possible limitations of satellite acquisitions. Figure 5.3 depicts the geometry of a satellite in an elliptical orbit around the earth. The size and shape of an ellipse are defined by the semi-major axis a and semi-minor axis b. A satellite is at the point of *perigee* when closest to the earth and furthest from the earth at the opposite point of *apogee*. The position of the satellite along the orbital path with respect to the center of the earth E is defined by angle θ from perigee and altitude (radius) r.

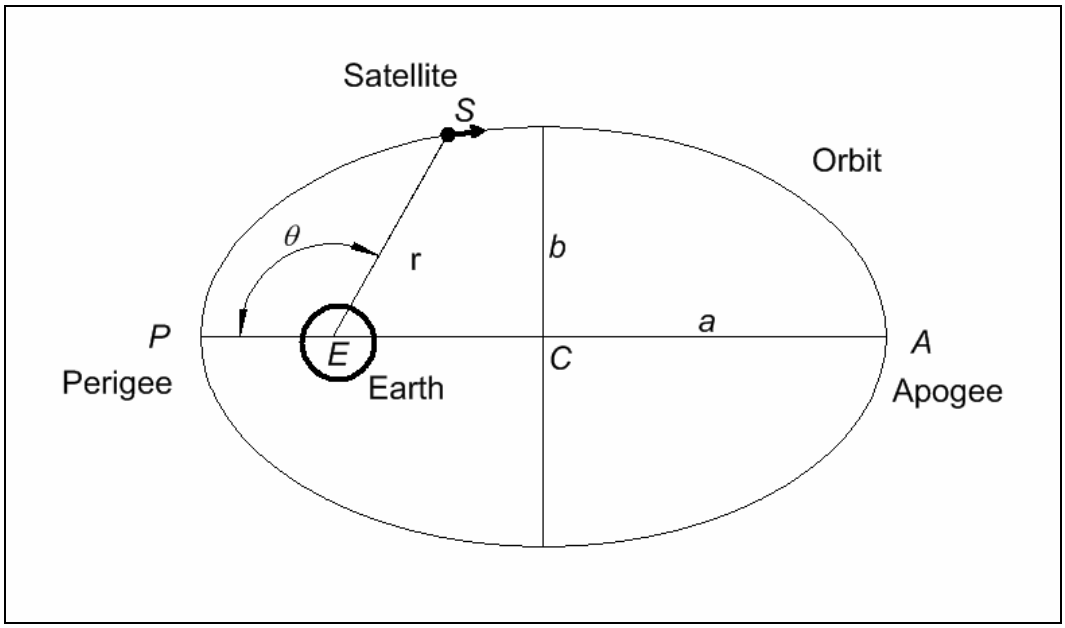

Figure 5.3 Satellite elliptical orbit geometry.

Essential parameters of orbital geometry are computed from relationships developed from Newtonian physics (Rees 2001). Eccentricity *e* of the ellipse is the ratio of lengths *CE* and *CA* and is related to the semi-axes by:

$$b^2 = a^2\left(1 - e^2\right) \qquad 5.1$$

The orbital period according to Newton's law of gravitation is:

$$P_o = 2\pi\left(\frac{a^3}{GM}\right)^{0.5} \qquad 5.2$$

where *G* is the gravitational constant and *M* is the mass of the Earth. The product *GM* has been determined very accurately to be:

$$GM = \left(3.98600434 \pm 0.00000002\right) \times 10^{14} \text{ m}^3 \text{ s}^{-2} \qquad 5.3$$

Satellite overpass time may be computed with Equations 5.2 and 5.3. For example, the orbit of Landsat 7 is nearly circular at an altitude 705 km so the semi axes of the orbit may be assumed equal to the mean radius of the Earth plus the altitude of the

satellite above the mean ground surface. Assuming the mean radius of the Earth is 6371 km, the orbital period of the Landsat 7 is approximately:

$$P_o = 2\pi\left(\frac{a^3}{GM}\right)^{0.5} = 2\pi\left(\frac{\left[(6371+705)\text{km}(1000)\frac{\text{m}}{\text{km}}\right]^3}{3.986\times10^{14}\,\frac{\text{m}^3}{\text{s}^2}}\right)^{0.5}\left(\frac{1\,\text{min}}{60\,\text{s}}\right) = 98.7\ \text{min}$$

This value agrees with published orbital periods.

5.4.1.2 Time of Landsat 7 Image Acquisition

Landsat 7 crosses the equator from north to south at approximately 10:30 am local solar time. Overpass time at any other latitude may be estimated by assuming a polar orbit and angular velocity of 360°/98.7 min or 3.64° per minute. Overpass at Pullman, WA at 46.74 degrees north latitude is then approximately:

$$T_c = 10:30\ \text{am} - \frac{46.74\ \text{min}}{3.64\,\frac{\text{deg}}{\text{min}}} = 10:30\ \text{am} - 13\ \text{min} \approx 10:17\ \text{am}$$

The nominal Landsat 7 crossing time varies by about 15 minutes, so the overpass time in Pullman will vary between 10:00 am and 10:30 am solar time. Overpass time computation is useful for planning field data collection or aerial image acquisitions simultaneously with satellite image collection. Satellite image acquisition times are usually recorded in the image metadata. Some archived satellite images lack metadata so it is useful to be able to ascertain approximate sun angles from orbit parameters and equatorial crossing time.

The orbit of the satellite is relatively fixed in space as the earth rotates within the orbital plane at its angular rate of 360 degrees in 24 hours, or about 0.25 degrees per minute. The earth rotates about 25 degrees of longitude during a 99 minute orbit period,

so the orbital path of Landsat 7 offsets about 1900 km to the west on successive passes at the latitude of Pullman, an offset well beyond the width of a Landsat scene. This is why Landsat scenes on adjacent orbital paths must be collected on different days, possibly to the frustration of analysts seeking a synoptic coverage of areas near the edge of the scene. This is another unavoidable attribute of satellite imaging that must be accommodated in watershed characterization planning.

According to Equation 5.2 Landsat 7 satellite should repeat an overpass once every 14.5 days (1440 min/98.7 min), but the orbital plane actually slowly rotates ahead (precesses) about the axis of the earth so that the repeat pass occurs every 16 days. It is not necessary to determine overpass dates and times by computation. Overpass schedules for operational satellites are prepared by the producer of the imagery and can be accessed through the internet. The Landsat 7 overpass schedule is at http://landsat.usgs.gov/l7flashcal.html which seems to be a stable address. A yearly schedule of Landsat 7 overpass dates for quick reference may be prepared for a particular path as in Table 5.2 simply by adding successive increments of 16 days to an overpass date obtained from the USGS Landsat schedule.

Landsat 7 2005 Schedule for Path 42					
January	February	March	April	May	June
14	15	03	04	06	07
30		19	20	22	23
July	August	September	October	November	December
09	10	11	13	14	16
25	26	27	29	30	

Table 5.2 Landsat 7 2005 overpass schedule for 2005.

5.4.2 Satellite Image Coverage

Most satellite images are acquired with scan-line or pushbroom sensors (Lillesand and Kieffer 1994). Pushbroom and scan-line images are acquired in a continuous swath across the landscape, so the along path (longitudinal) extent of the image coverage is conceptually continuous. Longitudinal extent is realistically limited by image storage capacity, lighting conditions and other operational constraints. Transverse coverage along a single orbital path is determined by the field of view of the sensor. An example of a field of view computation was presented in Section 3.

Swath widths of the primary satellites used in the dissertation work vary from 13 km for the Ikonos satellite to 2330 km for the MODIS sensor. Most of the dissertation work was with Landsat 5 and Landsat 7 images. A single Landsat 7 image width is about 183 km. Landsat images are normally delivered as approximately square images centered on the intersection of a path and row grid. Adjacent scenes overlap both along the path and between rows. Along-the-path overlap in central Idaho and eastern Washington is about 20 km or 11 percent of the scene width. Overlap between paths is about 66 km or 36 percent of scene width. The swath width and coverage for ASTER images are much smaller, about 60 km. Coverages of MODIS, ASTER and Landsat scenes are superimposed on a GIS image of the Columbia River Basin in Figure 5.4.

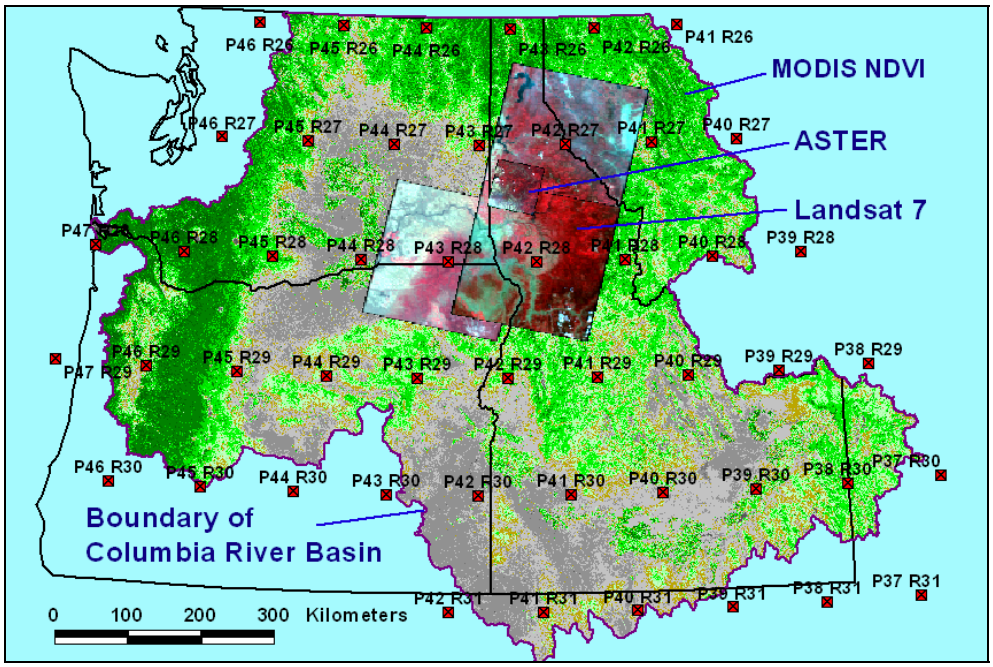

Figure 5.4 Coverage of Landsat 7, ASTER and MODIS images.

5.4.3 Landsat 7 World Reference System

The key to satellite imagery coverage, at least for Landsat and ASTER, is to understand the Landsat World Reference System. Satellites orbits are predictable and regular. A satellite can be operated to image the same area of the surface of the earth on a regular schedule. An area of the earth's surface that is consistently and repeatedly imaged is called a scene. Satellite images may be identified and archived according to scene designations. Landsat 7 images are identified and procured based on scene position within a path and row system known as the World Reference System 2 (WRS2). Path and row intersections of WRS2 are identified in Figure 5.4. The WRS is unique to the Landsat system, but other satellite images such as MODIS and some commercial satellite imagery may be referenced approximately by the WRS2 grid. The most general and unambiguous method to specify satellite image coverage is by latitude and longitude of the image center and bounding corners.

There is nothing particularly difficult or technical about finding the location, time and coverage satellite images. Satellite image producers and distributors have a stake in making this process uncomplicated. Most producers have internet based search and ordering systems that are well designed and efficient. Each one is different, but motivated users quickly learn specific procedures. Final procurement of commercial satellite imagery is usually discussed with a sales agent who may request latitudes and longitudes of the bounding area.

The USGS EarthExplorer (http://edcsns17.cr.usgs.gov/EarthExplorer/) search and order system is very functional and reliable. An amazing amount of preliminary research can be conducted with the high quality browse images available in EarthExplorer. I produced a step-by-step tutorial of the EarthExplorer system as part of the BPA project materials. New users might find this helpful.

There are 48 WRS2 path and row nodes in the Landsat 7 coverage of the Columbia River basin in Figure 5.4. Compiling historic and current watershed characterization maps of the entire basin from Landsat images are no small tasks. There are over 500 possible Landsat 5 and Landsat 7 images for each node in the WRS2. Such efforts require extraordinary resources and commitment, but are conceptually possible.

Land cover mapping from Landsat images at the national scale is performed by a partnership of federal agencies led by USGS and USEPA (Loveland and Shaw 1996). This effort produced the 1992 digital National Land Cover Dataset (NLCD) introduced in Section 4 (Vogelmann et al. 2001). An NLCD coverage for 2001 is being prepared (http://www.mrlc.gov/index.asp). The 1992 NLCD is a suitable starting point for hydrologic characterization for watershed modeling, but must be refined with techniques

demonstrated in Section 5.8. Another effort is the Gap Analysis Program (http://www.gap.uidaho.edu/). This work produced gridded land cover classification coverages for many states intended for assessing the extent to which native animal and plant species are being protected.

5.4.4 ASTER Image Coverage

The Terra and Aqua orbital platforms carry a suite of sensors with much proven and potential use in earth imaging and hydrology. The instrument of most interest in the dissertation work is ASTER. ASTER images are acquired for specific locations to meet imaging goals established by NASA. A high priority has been to acquire a cloud-free coverage of the world for analysis of the status land surface vegetation. Most locations in the Pacific Northwest are covered by at least one ASTER image acquired since May 2000, but they are often acquired at times not useful for hydrologic characterization. Figure 5.5 is an overlay of the outlines of ASTER images processed in the dissertation and BPA project work. ASTER images are higher resolution than Landsat images so sometimes provide extra detail to confirm interpretations of persistent features observed in Landsat images acquired on other dates. ASTER image products may be obtained without charge through the Earth Observing System Data Gateway at (http://edcimswww.cr.usgs.gov/pub/imswelcome/). The USGS GloVis internet satellite image browser is convenient for searches of ASTER images at (http://glovis.usgs.gov/ImgViewer/ImgViewer.html).

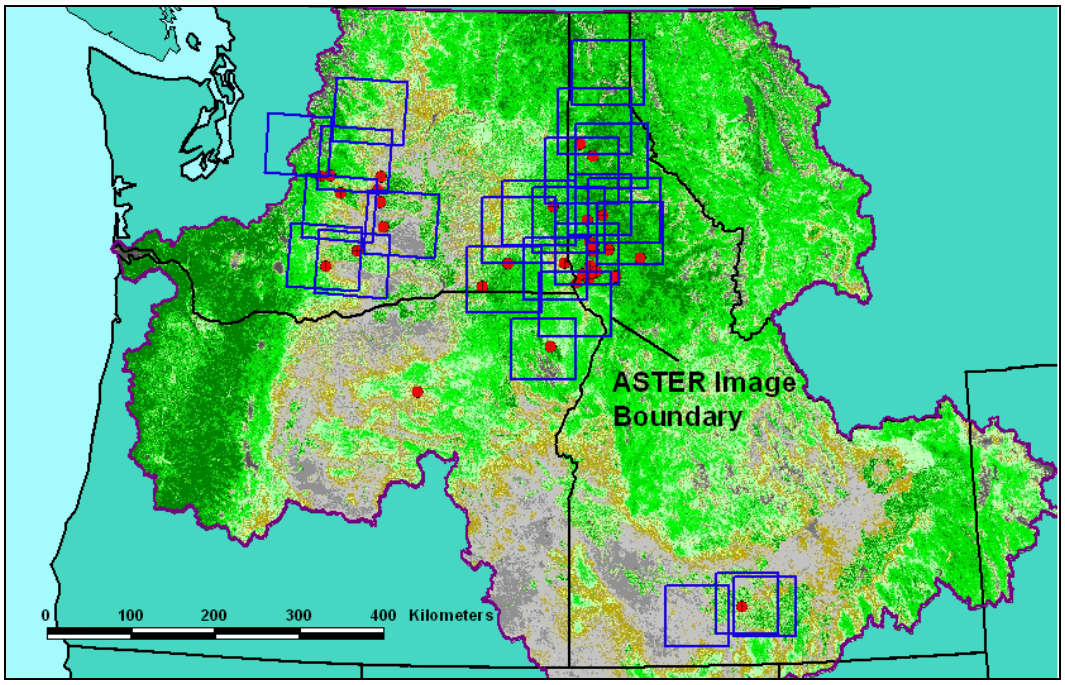

Figure 5.5 ASTER images acquired and processed for dissertation work the BPA project.

5.4.5 MODIS Imagery Coverage

The MODIS sensors onboard the Terra and Aqua satellites provide a nearly constant stream of images products since May 2000 with resolutions from 250 m to 1000 m. New MODIS images are available every one to two days through the Earth Observing System Data Gateway. Orbital graphics and overpass schedules for MODIS are available on several websites. Perhaps the best site is the University of Wisconsin Space Science and Engineering Center (http://eosdb.ssec.wisc.edu).

Many derived products are routinely produced by NASA and its collaborators that greatly reduce the work of using MODIS images. The algorithms that generate these products receive a fair amount of scientific scrutiny and occasionally appear in the peer reviewed literature (Gao and Kaufman 1998; Hall et al. 2002; Liang et al. 2002). The resolutions of MODIS products are mostly too coarse for detailed hydrologic analysis

without ancillary data, but offer a perspective on the temporal variability of large watersheds that is truly enlightening. The Normalized Difference Vegetation Index (NDVI) image in Figure 5.4 and Figure 5.5 is from MODIS 16-day composites produced September 13, 2002. Much research work can be done to increase the relevance of MODIS data to hydrologic modeling of moderately sized watersheds.

A unique feature of MODIS is its Direct Broadcast capability. MODIS broadcasts raw data that is immediately available to user-operated ground stations. The data stream is free of procurement fees. The broadcast carries data from all 36 spectral bands for the entire MODIS field of view. MODIS Direct Broadcast stations are at the University of Wisconsin – Madison's Space Science and Engineering Center (SSEC), the University of Miami's Rosenstiel School of Marine and Atmospheric Science (RSMAS), the Goddard Space Flight Center's Direct Readout Portal, and the Oregon State University MODIS Direct Broadcast Site.

5.4.6 Spatial Resolution of Satellite Imagery

Technical aspects of aerial image resolution discussed in Section 3 also apply to satellite imagery. The discussion here will emphasize qualitative aspects of satellite imagery resolution important in watershed characterization. Like satellite coverage, the practical meaning of satellite image resolution to the user is not technically complicated. The user cannot change the resolution of the satellite to suit a particular imaging objective as he or she might when contracting for aerial imaging services. From the user perspective, satellite image resolution is fixed for a particular sensor. Assessment techniques must be developed to make best use of the available resolution.

Table 5.3 lists the spatial and spectral resolution of sensors used in the dissertation research and includes the typical resolution and spectral bands of the Teasdale Environmental Associates color infrared aerial imaging system for comparison. Broad generalities about the suitability of satellite imagery for watershed characterization can be made based on resolution. Tables referenced in Section 2 categorize satellite imagery and ancillary data sources in low, medium and high-resolution suitability classes and suggest numerous assessment tasks that may be performed with each source. Numerous examples in the BPA project materials demonstrate the features that may be resolved and characterized with the different satellite sensors. Practical demonstrations of imagery use in this section further demonstrate the practical effect of satellite image resolution.

Spectral Regions		Landsat 5	Landsat 7	ASTER	MODIS	IKONOS	MTI	TEA CIR
Visible - Near Infrared	Panchromatic, μm GPR, m	None	0.52 - 0.90 15	None	None	0.5258 - 0.9285 1	None	None
	Blue, μm GPR, m	0.45 - 0.52 30	0.45 - 0.52 30	None	0.459 - 0.470 500	0.4447 - 0.5160 4	0.45 - 0.52 5	0.44 - 0.50 0.5
	Green, μm GPR, m	0.52 - 0.60 30	0.53 - 0.61 30	0.52 - 0.60 15	0.545 - 0.565 500	0.5064 - 0.5950 4	0.52 - 0.60 5	0.51 - 0.58 0.5
	Red, μm GPR, m	0.63 - 0.69 30	0.63 - 0.69 30	0.63 - 0.69 15	0.620 - 0.670 250	0.6319 - 0.6977 4	0.62 - 0.68 5	0.63 - 0.70 0.5
	Near-IR, μm GPR, m	0.76 - 0.90 30	0.78 - 0.90 30	0.78 - 0.86 15	0.841 - 0.876 250	0.7573 - 0.8527 4	0.76 - 0.86 5	0.75 - 0.90 0.5
Infrared	IR 1, μm GPR, m	1.55 - 1.75 30	1.55 - 1.75 30	1.60 - 1.70 30	1.628 - 1.652 500	None	1.54 - 1.75 20	None
	IR 2, μm GPR, m	2.08 - 2.35 30	2.09 - 2.35 30	Several 30	2.105 - 2.155 500	None	2.08 - 2.37 20	None
	IR 3, μm GPR, m	None	None	Several 30	1.230 - 1.250 500	None	Several 20	None
Thermal	TIR 1, μm GPR, m	10.4 - 12.5 90	10.4 - 12.5 60	10.95 - 11.65 90	2 bands 1000	None	None	None
	TIR 2, μm GPR, m	None	None	Several 90	Several 1000	None	Several 20	None

Table 5.3 Spatial resolution and visible-near infrared satellite sensor bands.

Hydrologic characterization of medium (greater than about 1000 ha) to large basins is most efficiently performed with medium scale satellite imagery such as Landsat. Hydrologic characterization for municipal stormwater modeling or farm conservation planning should be characterized with high-resolution satellite imagery such as Ikonos or aerial imagery. Very large basins such as the Columbia River basin can be efficiently

characterized with MODIS imagery products. ASTER imagery falls between Landsat and Ikonos in interpretive capability, but is often acquired during seasons inappropriate for hydrologic characterization. The MTI imagery is very similar to Ikonos multispectral images.

5.4.7 Satellite Image Spectral Resolution

The satellite sensors utilized and evaluated most in the dissertation work record reflected energy in the visible and near infrared region of the spectrum (Figure 5.6).

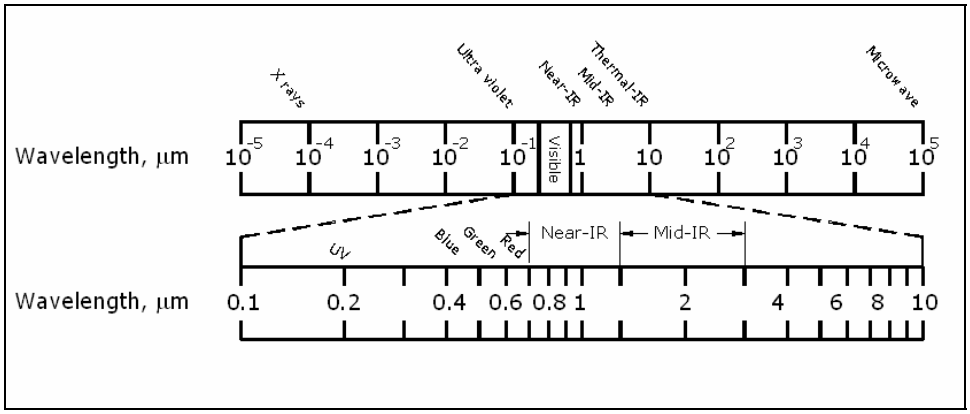

Figure 5.6 Electromagnetic spectrum for remote sensing.

Operational satellite sensors for earth surface imaging are fairly consistent in the selection of spectral band intervals. Table 5.3 compares the band intervals and resolution of the satellite sensors evaluated in the dissertation work including band intervals for the Teasdale Environmental Associates color infrared imaging system. All sensors except for ASTER have blue, green, red and near infrared bands. Since ASTER has no blue sensor, this means that natural color images cannot be produced with ASTER image datasets. Natural color images can be produced from MODIS data, but the blue and green bands are lower resolution than the red band. ASTER and MODIS designers place decreased importance on blue and green bands because of greater atmospheric scattering

in these wavelengths and instead emphasized red and near infrared bands because these have greater sensitivity to vegetation.

Landsat 7 and Ikonos have panchromatic bands that cover a wide range of visible and near infrared light. These bands are at higher resolution and increase discrimination of structural details. Panchromatic data can be merged with lower resolution bands in a process called image fusion to increase the interpretability of multispectral image composites.

Visible and near infrared (VIR) composite images are viewed by assigning the green, red and near infrared band values to the blue, green and red colors of the display system. VIR images enhance interpretability of vegetation characteristics. They also can discriminate some types of water quality differences such as chlorophyll reflectance from algae on or near the surface of lakes (see Figure 5.12). Numerous examples are in the BPA project materials. Access to these materials must be requested directly from the Bonneville Power Administration office in Portland, Oregon (800-282-3713).

All satellite instruments except Ikonos have bands in the shortwave infrared region beyond 1.0 μm. These bands are particularly useful for discerning differences in soil and rock surfaces. The Landsat bands are generally too broad to identify specific minerals, as is done in hyperspectral imaging, but they often can help discriminate bare soils. This capability of Landsat imagery is demonstrated in hydrological land cover classification developed in Section 5.8.

Thermal emissions are recorded in various intervals by all the satellite instruments evaluated in this research except Ikonos. Blackbody thermal radiation is emitted by the earth's surface and atmosphere and is very useful for remote sensing of meteorology and

atmospheric chemistry. Thermal images produced by the satellite sensors evaluated in the dissertation work are not very useful for watershed hydrologic characterization because they are either too coarse in resolution (MODIS) or to infrequently collected (all others). Thermal imagery has great potential in watershed hydrological and surface water imaging, but the imagery must be collected by aircraft. Acquisition and evaluation of aerial thermal imagery was beyond the resources available for the dissertation work.

The spectral response of a sensor describes the sensitivity of the sensor material and supporting architecture to a particular interval of electromagnetic radiation. Spectral response was introduced in context of aerial imagery in Section 3, but must be further described for satellite imagery because of its relationship to computation of reflectances. Spectral response of satellite imagery is best described while examining actual sensor data.

The spectral responses of the Enhanced Thematic Mapper Plus (ETM+) bands are plotted in Figure 5.7, Figure 5.8 and Figure 5.9. Spectral response indicates the relative sensitivity of a detector as a function of wavelength. Greater spectral response values indicate that more energy of the corresponding wavelengths is recorded. The maximum value of any spectral response curve is one.

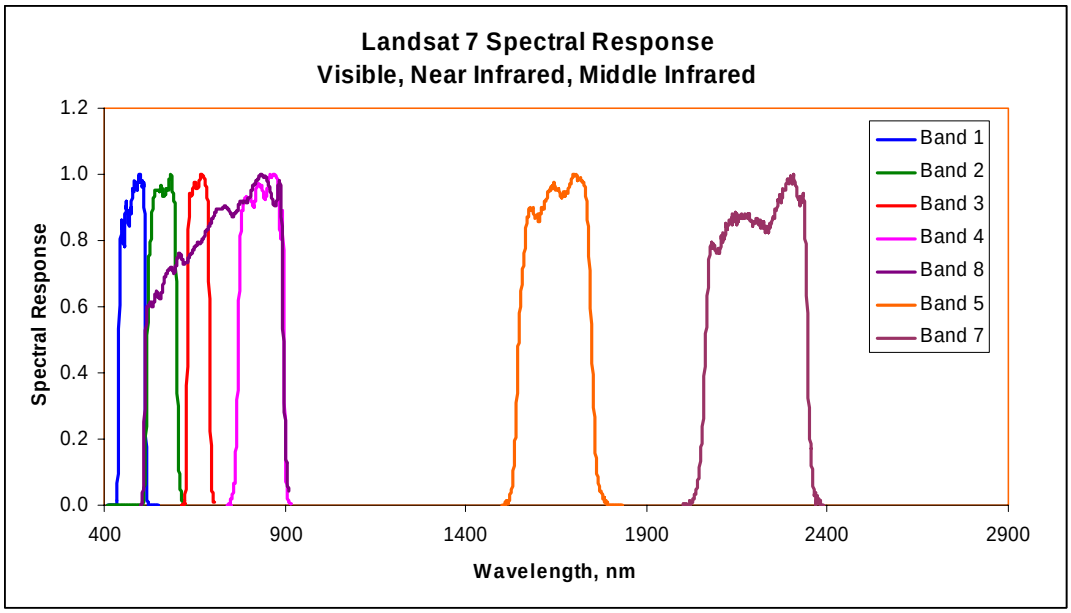

Figure 5.7 Spectral response of the Landsat 7 ETM+.

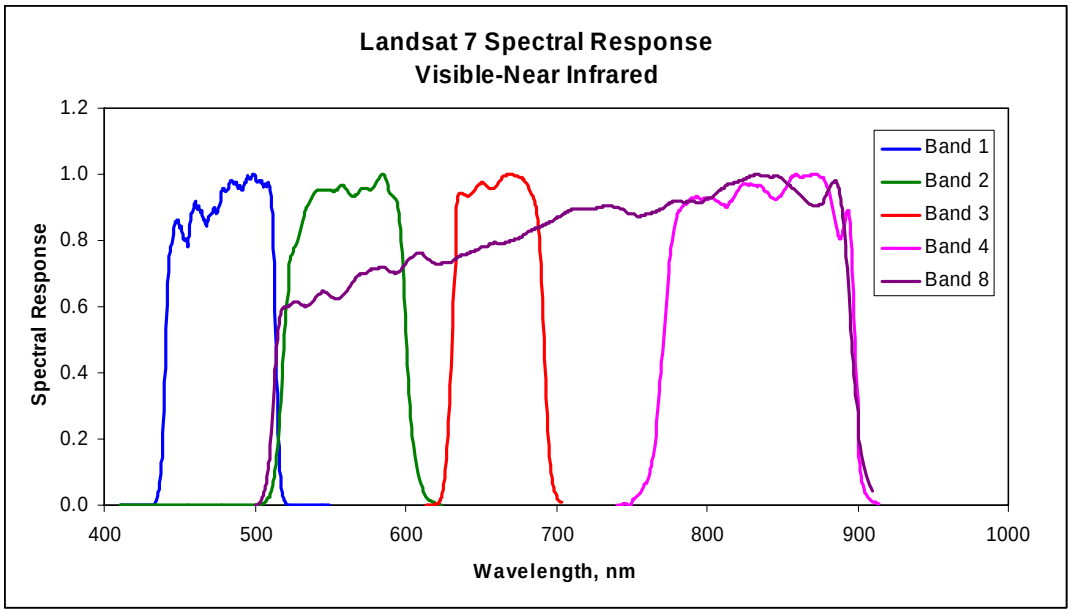

Figure 5.8 Visible and near infrared spectral response of the Landsat 7 ETM+.

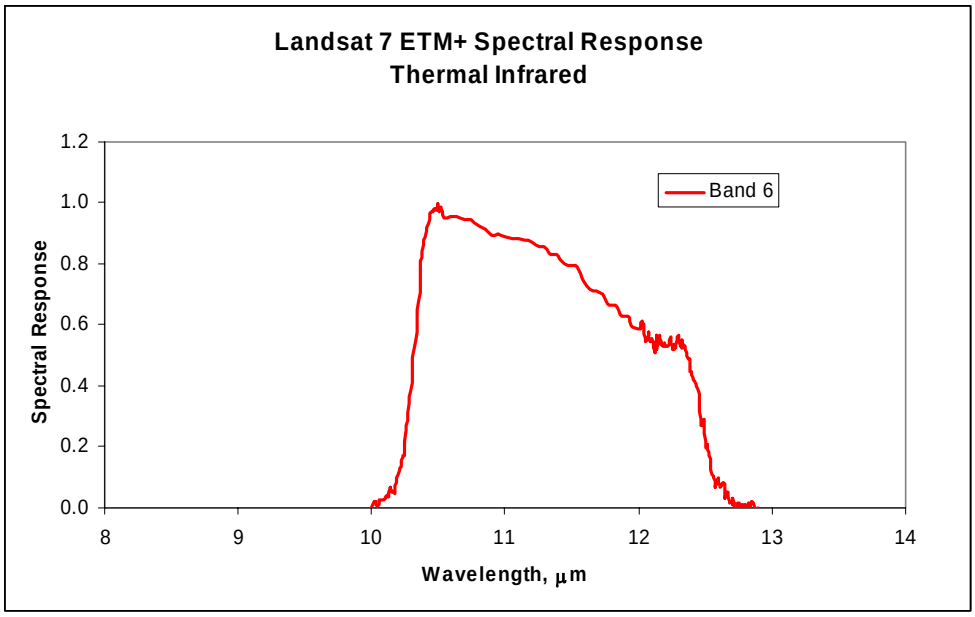

Figure 5.9 Spectral response of the Landsat ETM+ thermal sensor.

Wavelengths outside the spectral response region are not detected. For example, band 4 (near infrared) does not record green light, but band 8, the panchromatic band, records light through the green, red and near infrared regions. Distinct separation of band wavelengths gives the sensor the ability to "see" spectral reflections of features on the earth surface. Emitted thermal energy has a wavelength about 300 times longer than visible light. The band 6 thermal spectral response is usually plotted against wavelength in microns (µm).

Spectral response curves are sometimes described by three parameters, upper and lower values of the Full Width Half Maximum (FWHM) and the band center. The FWHM is the range of wavelengths corresponding to points on either edge of the spectral response plot that are one-half the maximum value (i.e., 0.5 since the maximum value is always 1). The band center is the mid point of the FWHM. The FWHM range for the band 4 spectral response is plotted in Figure 5.10. The limits of the band 4 FWHM are

approximately 0.77 μm and 0.90 μm, and the band center is about 0.84 μm. This spectral response plot was developed from USGS spectral response data and gives slightly different values than the nominal parameters reported in the Landsat 7 Users Handbook (USGS 1998) in the Table 5.4. Extraterrestrial solar irradiance values (E_o) for each band interval from the handbook are also in Table 5.4. Band centers and E_o values are important parameters for atmospheric correction of satellite imagery. Extraterrestrial solar irradiance is discussed in Section 5.5.2.

	Landsat 7 ETM+ Band						
	1	**2**	**3**	**4**	**5**	**7**	**8**
FWHM lower, μm	0.45	0.53	0.63	0.78	1.55	2.09	0.52
FWHM upper, μm	0.52	0.61	0.69	0.9	1.75	2.35	0.9
Band center, μm	0.49	0.57	0.66	0.84	1.65	2.22	0.71
Irradiance, Eo, mW cm^{-2} μm^{-1}	196.9	184	155.1	104.4	22.57	8.207	136.8

Table 5.4 Full width half maximum band intervals and band center for ETM+.

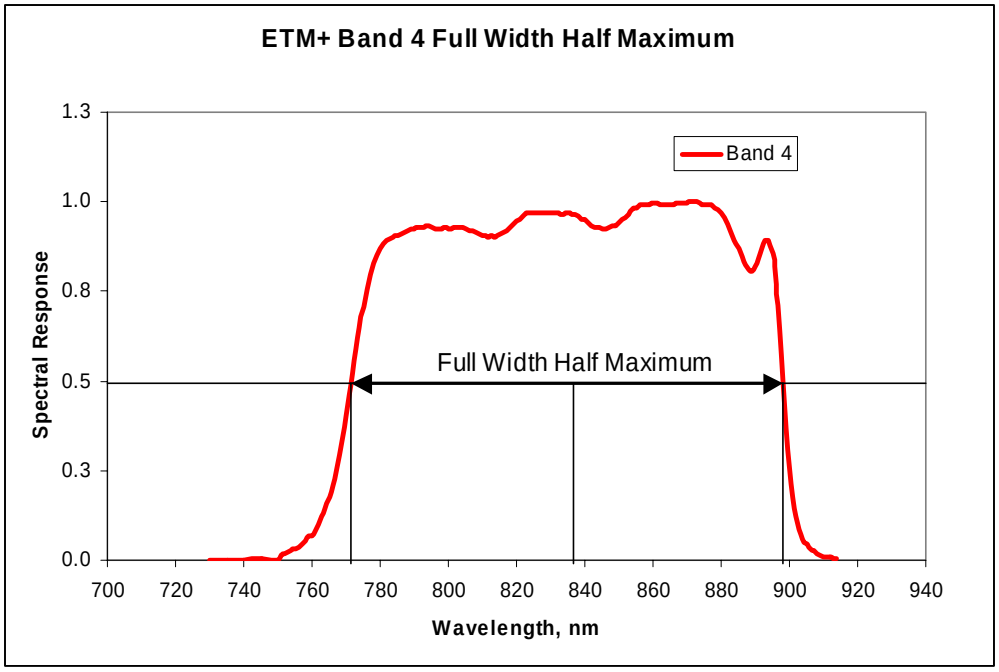

Figure 5.10 Full width half maximum band interval of ETM+ band 4.

5.4.8 Satellite Image Exterior Orientation

Sensor attitude or orientation determines whether a satellite image is vertical or tilted. Landsat, ASTER and MODIS are oriented so that their imaging telescopes are pointed vertically towards the center of the earth so that the center of the image coincides with the nadir point on the surface of the ground. Operators of nadir pointing satellites maintain the attitude of the satellite with onboard thrusters throughout the life of the spacecraft. The attitudes of pointable satellites are purposely controlled by operators to aim the imaging telescope at target areas beneath or to the side of the orbital path. This is a delicate operation. Sensors on board the MTI satellite were destroyed when the imaging telescope was mistakenly pointed at the sun during an orbital maneuver.

Importance and effect of image tilt were evaluated in Section 3 for aerial imagery. Much of that discussion is relevant to satellite imagery. Image geometry and rectification of pushbroom or scan line sensors are more complex than for the aerial camera frame images. Each pixel of a scan line imager or each line of a pushbroom sensor is exposed at different instants in time while the spacecraft transits the orbit. Therefore, each pixel or line must be individually rectified for the exterior orientation that existed at the instant of exposure. The exterior orientation parameters are familiar: the rotation angles of roll, pitch and yaw; and the position of the perspective center. Interior orientation parameters include lens focal length, the principal point location, the lens distortion coefficients, and other parameters are specific to the physical design of the sensor.

Conceptually, the collinearity equations can be applied to each image element, but they are so closely related that the multitude of orientation parameters cannot be independently estimated and must be modeled as low order polynomials in the matrix

solution (Mikhail et al. 2001). Geometrically corrected and orthorectified imagery can always be obtained from vendors of operational satellite imagery. Typical users do not need to apply rectification parameters for common applications. Users and researchers who desire to control the rectification process and have capable software can obtain correction parameters for specific sensors and rectify original images (Grodecki and Dial 2003; USGS 2000).

5.5 Operational Characteristics and Use of Satellite Imagery

In many ways the requirements for effective use of satellite imagery are less technically demanding than those for acquisition and use of aerial imagery. Expectations and uses of the two types of imagery are very different. Aerial images after orthorectification or georeferencing are typically expected to be dimensionally accurate so that direct measurement can be made of the features of interest. Satellite imagery users usually do not expect satellite imagery to be georeferenced to the accuracy of a single pixel. Satellite images are used more for characterization of representative areas or regions and monitoring the change in general attributes over time rather than precise measurement of linear and area features. There are of course exceptions, and functional differences between aerial imagery and satellite imagery all but disappear with very high-resolution satellite imagery such as Ikonos and Quickbird.

Generally less technical expectations of satellite imagery have encouraged a more or less common approach to land surface satellite image processing and analysis. This view is not meant to dismiss the real technical complexities of acquiring and producing satellite imagery, but is intended to suggest a practical perspective to the potential user.

Well designed and reliable software systems have made the processing and analysis of satellite imagery easy compared to other technical demands facing environmental scientists and water resource engineers.

It is reasonable for the user to expect that effective use of satellite imagery in watershed characterization can be self-taught or learned in focused seminars. However, that realization is not easily gained by reading the journal literature of remote sensing or standard remote sensing texts. To help encourage the consideration of satellite imagery in hydrologic analysis, this section emphasizes the core knowledge and techniques that are essential in the operational use of satellite imagery in hydrologic characterization. These techniques were routinely applied in the dissertation work. This treatment assumes familiarity with GIS operations including basic image manipulation.

5.5.1 Satellite Imagery Interpretation

As discussed in Section 3, nominal resolutions do not fully convey the resolving power of an image because of scene contrast and lighting conditions. Information extraction from images, especially by manual interpretation, is a subjective process that depends on the user's skill. Users eventually find that the most important aspect of satellite image resolution is not the size of the pixel in ground dimensions, but the size of the pixel relative to the desired interpretation of the feature of interest. This can only be learned by experience. An extreme example pertinent to snowmelt modeling is that 1-meter ground pixel resolution (GPR) Ikonos satellite images are not necessary to determine if most of a watershed the size of the Potlatch River basin is covered with snow. A single clear sky MODIS image (possibly a rare event) at a GPR of 250 m or 500 m is better suited to the task.

Written guidance and rating schemes (Leachtenauer et al. 1997) are not very useful in hydrologic assessment and do not significantly shorten the learning process. Ultimately, the best method for a user to gain a working knowledge of the resolving power and utility of a particular satellite sensor is to observe many images of different scenes under various atmospheric conditions and seasons. It was for this reason that I devoted an extraordinary effort to assembling numerous easily accessed comparative imagery training datasets for the BPA Project.

An example of a BPA project comparative dataset is in Figures 5.11, 5.12 and 5.13. The full dataset is collection of linked web pages and images. The user clicks on an image of interest in the site level screen (Figure 5.11) and is delivered a full resolution snippet (granule) of the image for viewing. A user can easily interpret algae chlorophyll reflectance in Manson Lakes in July 1988 (Figure 5.12) and July 2000 (Figure 5.13). Other image snippets show the middle infrared reflectance of the same scene. Landsat image resolution is sufficient to develop historical and seasonal estimates of the surface area of the Lake Chelan. Many other instructive examples are in the dataset. The full dataset compiled to date is included in the digital resource compact disc that accompanies the dissertation document.

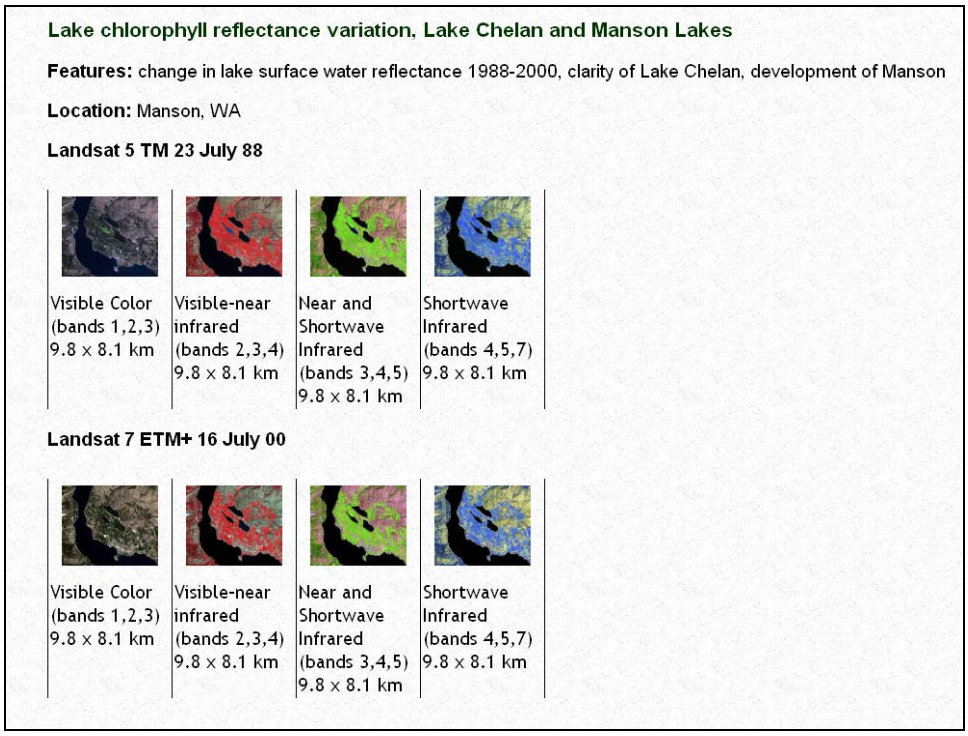

Figure 5.11 Comparison of Landsat images of Lake Chelan and Manson Lakes, WA


Figure 5.12 Chlorophyll reflectance in a Landsat 5 visible-near infrared image of Manson Lakes, July 23, 1988

Figure 5.13 Chlorophyll reflectance in a Landsat 7 visible-near infrared image, July 16, 2000 Mason Lakes.

A second type of training dataset in the BPA Project materials is sequence of Landsat, ASTER, sometimes MODIS, and high-resolution aerial images of the same location and feature. Most of the subjects are aquatic as in Figures 5.14, 5.15 and 5.16 of the Yakima River near Buena, WA. This type of dataset is very instructive and quickly gives the viewer a solid impression of the resolving capabilities of the sensor. Many other comparative datasets are in the BPA project materials. These materials would be valuable resource for a course related to remote sensing of freshwater aquatic resources and watershed analysis.

Figure 5.14 High-resolution digital aerial image of the Yakima River near Buena, WA.

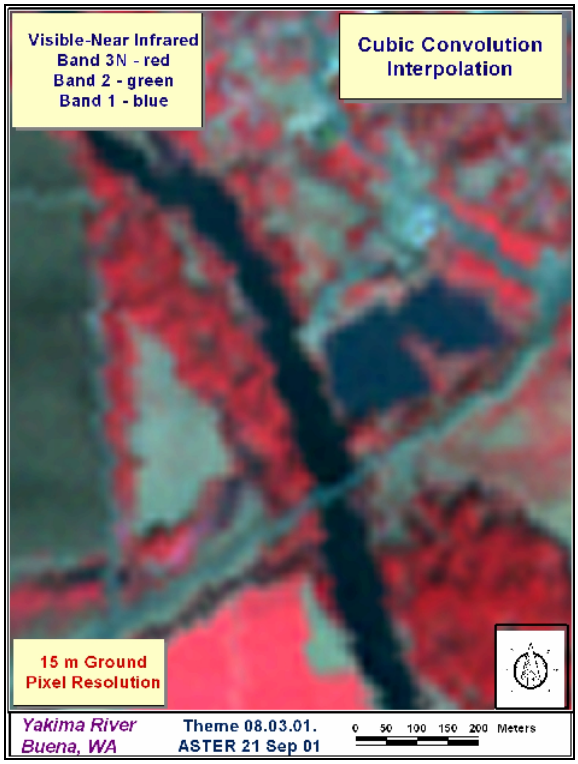

Figure 5.15 ASTER satellite image of the Yakima River near Buena, WA.

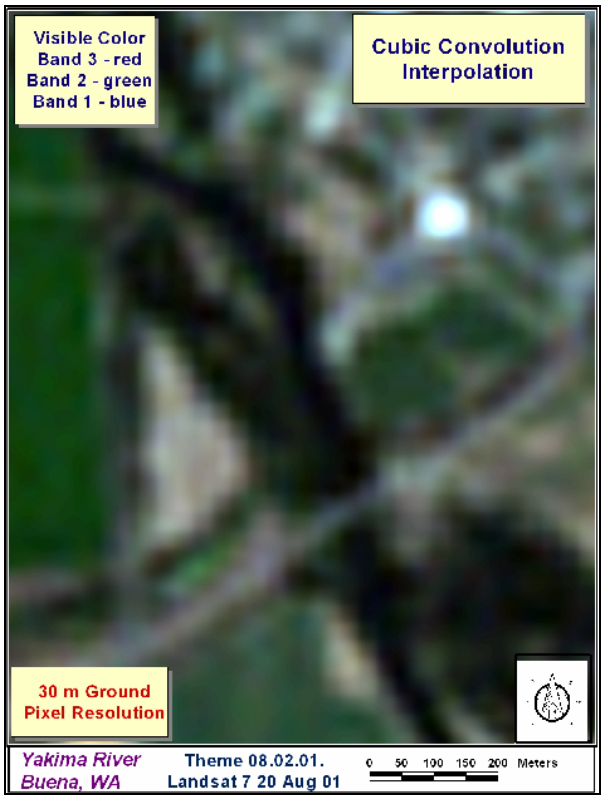

Figure 5.16 Landsat 7 natural color satellite image of the Yakima River near Buena, WA.

Figure 5.17 Landsat 7 color infrared satellite image of the Yakima River near Buena, WA.

Experience with numerous satellite images of the interior Pacific Northwest suggests that reasonably accurate hydrologic feature delineation and direct interpretation is possible in satellite images if the feature of interest is five to ten times larger than the nominal resolution of the image. Accuracy of the interpretation depends on the skill of the image interpreter and familiarity with the content of the image, but many features are intuitively obvious. Most environmental scientists and water resources engineers would have little difficulty identifying the Yakima River in Figure 5.17, though the river at this point is less than 150 meters in width. Even the position of the roadway and bridge is evident. The linear nature of these features greatly aids in the interpretation (Philipson 1997). Intuitive interpretation supported by technical judgment takes on greater importance in hydrologic studies of areas of the world where detailed topographic maps do not exist or are withheld for security reasons. Personal experience with satellite imagery classifications in the country of Jordan and the Commonwealth of Puerto Rico confirmed this.

The ability to interpret detail in satellite images is a skill acquired through practice with training datasets and experience with applied problems. The recently updated 700 page ASPRS Manual of Photographic Interpretation (Philipson 1997) includes a mere eight page glance at non-photographic remote sensing. Much work remains to be done in the important and growing field of satellite imagery interpretation. The often cited internet based overview by Short (1998) is interesting, but is necessarily of a very general nature. An accessible and motivating introduction to meteorological satellite imagery is given by Conway (1997). A similar work for land surface imaging would be useful and would help promote use of the satellite imagery archive.

5.5.2 Radiance and Reflectance

The concepts of radiance and reflectance are essential to an understanding of all but the most purely interpretive uses of satellite imagery. Reflectance was discussed in Section 3 in context of aerial imagery. The reflectance Equation 3.33 is repeated below as Equation 5.4. This is the single most important relationship in operational use of satellite imagery:

$$\rho_{s,\lambda} = \frac{\pi \cdot L_{s,\lambda}}{E_{dir,\lambda} + E_{dif,\lambda}} \qquad 5.4$$

where $L_{s,\lambda}$ is the reflected energy expressed as radiance (W m^{-2} sr^{-1} μm^{-1}), $E_{dir,\lambda}$ is the incoming direct irradiance (W m^{-2} μm^{-1}), and $E_{dif,\lambda}$ is the incoming diffuse irradiance (W m^{-2} μm^{-1}). Reflectance of a surface by Equation 5.4 has a specific magnitude defined by the ratio of reflected irradiance to the sum of the direct and diffuse irradiance incident upon the surface. Reflectance values may change due to illumination direction and measurement direction with respect to the surface as described in the discussion of bidirectional reflectance distribution in Section 3, but measured or computed reflectance is not a relative quantity, it has precise meaning.

It is necessary to describe the terms of 5.4 in an operational sense to understand the technical meaning of reflectance. Radiance and irradiance are sometimes confused in the literature, so it is instructive to examine their origin in the physics of solar radiation. Plank's law of black body radiation is:

$$M_{B,\lambda}(T) = \frac{2\pi hc^2}{\lambda^5} \cdot \frac{1}{\exp\left(\frac{hc}{\lambda kT}\right) - 1} \qquad 5.5$$

where M_B is *spectral exitance* or *emittance*, W m^{-2} μ m^{-1}, h is Planck's constant (6.623 x 10^{-34} J s), c is the speed of light (2.998 x 10^8 m s^{-1}), k is the Boltzmann constant (1.38 x 10^{-23} W s K^{-1}), λ is the wavelength, m, T is the temperature of the radiating body (°K). Solar exitance in Figure 5.18 peaks in visible green light at approximately 8.4 x 10^7 W m^{-2} μ m^{-1}. The peak wavelength is computed according to Wein's displacement law:

$$\lambda_{\max} = \frac{A}{T} = \frac{2.898 \times 10^{-3}\ ^\circ\text{K m}}{5800\ ^\circ\text{K}} \times \frac{1 \times 10^6\ \mu\text{m}}{1\,\text{m}} = 0.4996\ \mu\text{m} \qquad 5.6$$

where A is Wein's constant (2.898 x 10^{-3} °K m). The sun's radius is about 6.96 x 10^5 km and the distance from the sun to the earth is about 1.5 x 10^8 km, so by the inverse square law, the *irradiance* of green light at the outer atmosphere of the earth is approximately:

$$E_\lambda = 8.4 \times 10^7 \times \left(\frac{6.96 \times 10^5}{1.5 \times 10^8} \right)^2 = 1800\ \text{W m}^{-2} \mu\text{m}^{-1}$$

The entire blackbody solar exitance curve in Figure 5.18 can be similarly adjusted for the distance to the sun to compute an approximate distribution of extra terrestrial (ET) solar irradiance. The approximate solar ET irradiance is plotted in Figure 5.18 and scaled to the right axis. The current ASTM standard (ASTM 2000) spectral distribution of solar ET irradiance for air mass zero (AM0), is also plotted in Figure 5.18. The main point here is that irradiance is simply the solar exitance incident upon the outer atmosphere of the earth and the earth's surface after attenuation by the atmosphere, and that this term has precise meaning defined by solar radiant energy relationships.

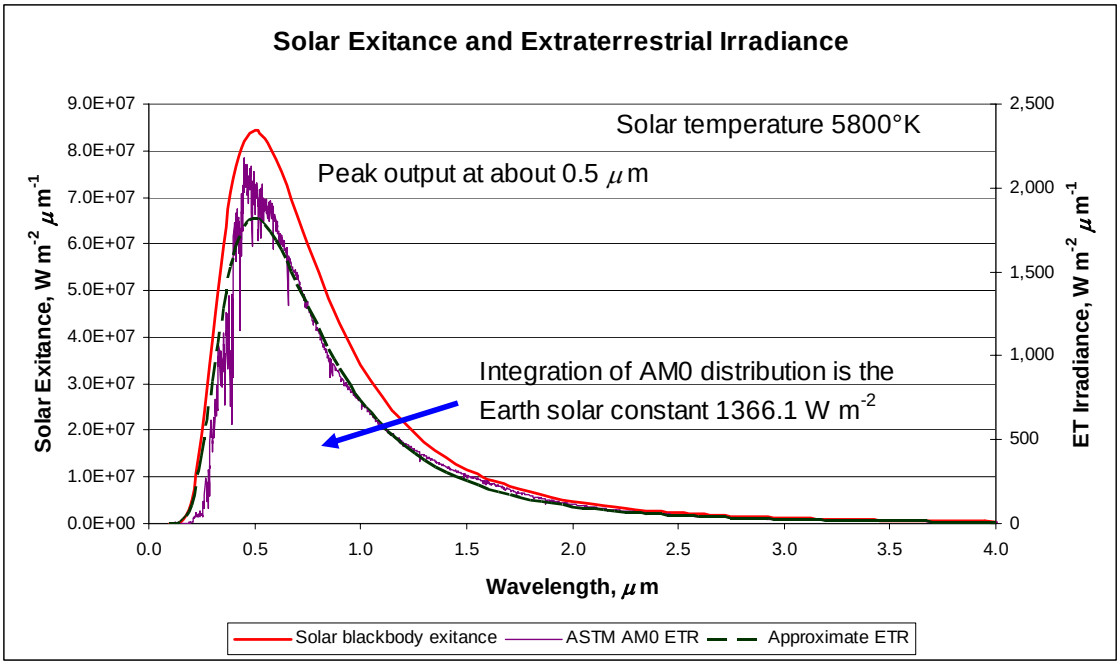

Figure 5.18 Spectral distribution of solar blackbody exitance, extraterrestrial irradiance and solar constant.

Radiation intensity is defined by *radiance L* or the specific intensity (W m^{-2} sr^{-1}) of radiation at a given wavelength incident upon a surface from a specific direction. Irradiance is computed by multiplying radiance by π:

$$E_\lambda = \pi L_\lambda \qquad 5.7$$

This simple relationship has a more complicated origin fully developed in Appendix 3.2.

A necessary condition for specifying a value of radiance and irradiance is the location and receiving direction in the electromagnetic field of the measurement point. These are vertically up or down at the surface of the earth for the reflectance relationship in Equation 5.4. Downwelling extraterrestrial irradiance at the top of the atmosphere is not equivalent to downwelling irradiance at the surface of the earth because of scattering and absorption in the atmosphere. Upwelling reflected irradiance measured above the

earth surface is reduced from downwelling irradiance because of scattering, adsorption and transmittance of the surface.

Integration of the solar exitance curve across all wavelengths gives the total exitance of the sun. Total exitance is most easily calculated with the Stefan's law:

$$M_B = \sigma \cdot T^4 \qquad 5.8$$

where σ is the Stefan-Boltzmann constant (5.67×10^{-8} Wm^{-2} K^{-4}). Total solar exitance by the Stefan's law is about 6.4×10^7 W m^{-2} for a solar temperature of 5800 °K. Very approximate total irradiance at the outer atmosphere of the earth by the inverse square law is:

$$E_s = 6.4 \times 10^7 \times \left(\frac{6.96 \times 10^5}{1.5 \times 10^8} \right)^2 = 1388 \text{ W m}^{-2}$$

The approximate value approaches the thoroughly measured, much analyzed, crucially important, and almost agreed upon standard solar constant of 1366.1 W m^{-2} (ASTM 2000; Lean and Rind 1998). The solar constant is an important parameter in radiometric calibration of satellite imagery, meteorology and solar engineering.

The ASTM AM0 spectral irradiance distribution in Figure 5.18 has been adjusted so that integration of the distribution results in a solar constant of 1366.1 W m^{-2}. Another cited value for the solar constant is 1367 W m^{-2} (Duffie 1991) and some authors suggest values as high as 1368 W m^{-2} (Stull 1995). Figure 13 of the reconstructed historical solar irradiance in Lean and Rind (1998) is particularly enlightening and shows an increasing trend in solar output since the year 1700. That figure also clearly indicates the fallacy of implying a precision in reflectance computations to less than the equivalent of 3 W m^{-2} and possibly 4 or 5 W m^{-2}. Remote sensing computations should utilize the

ASTM standard 1366.1 W m^{-2} solar constant for consistency, but not necessarily for increased accuracy.

5.5.3 User Processing of Satellite Imagery

The dissertation research found that hydrologic characterization of medium to large size watersheds (10 km^2 to 1000 km^2) is most efficient and cost effective with Landsat 5 and Landsat 7 imagery. Characteristics of the Landsat 7 satellite and imagery are described in Appendix 5.1. User processing of satellite imagery for watershed hydrologic characterization will be described and demonstrated with a relatively current Landsat 7 scene of the lower Potlatch River study area. Basic processing of other satellite images is similar.

Many remote sensing tasks can be accomplished with Level 1G Landsat 7 images (see Appendix 5.1) without further geometric rectification or manipulation of pixel values. Pixel values are often called digital numbers (DN) or brightness values (BV). Simple measurements such as approximate areas of distinct land surface classes can be made directly from Level 1G images without much concern by the user for positional accuracy or spectral characteristics. Some scientific users derive spectral indices such as the Normalized Vegetation Difference Index (NDVI) from original Level 1G images knowing that atmospheric effects remain (Huang et al. 2000). This may provide comparable results for clear atmospheres if a consistent method is applied among images.

Other remote sensing tasks require a higher level of geometric precision and place more importance on spectral differences. Objectives such as the analysis of the changes in vegetative cover between seasons or over several years require that images be comparable and that extraneous influences be removed. The scientific and academic

community has developed numerous approaches of image correction and normalization. This section describes the basics of a popular and useful technique—conversion of at-sensor radiances to surface reflectances. Another popular approach is to compute of spectral indices from various band combinations such as the Normalized Difference Vegetation Index (NDVI).

5.5.4 Conversion of Satellite Image Digital Numbers to Radiance

Pixel values in Landsat images produced by USGS are scaled radiances measured at the satellite and must normally be processed by the user into land surface radiances and reflectances. In USGS production of Level 1G images, digital numbers of absolute radiance are rounded off and scaled to integers values between byte values 0 and 255 (USGS 1998). This allows most GIS and remote sensing software to easily read Landsat image data and reduces the image file size. Byte scaling is controlled by ETM+ sensor gain settings and can vary between images. The conceptual relationship between image DN and radiance is illustrated in Figure 5.19.

Landsat 7 managers electronically increase or decrease the sensitivity of the ETM+ sensors to compensate for varying light conditions. Prior to image acquisition each band in the ETM+ sensor is set to low or high gain depending on the expected brightness of the land cover within the scene. The goal is to maximize the sensor's 8-bit radiometric resolution without saturating the detectors. Bright scenes are imaged at low gain settings and lower light scenes at high gain. The low gain setting is preferred because it has a dynamic range approximately 1.5 times that of high gain. Gain setting parameters are applied in the conversion of Landsat DN images to reflectance images. Gain settings are reported in the metadata that accompanies the Landsat image.

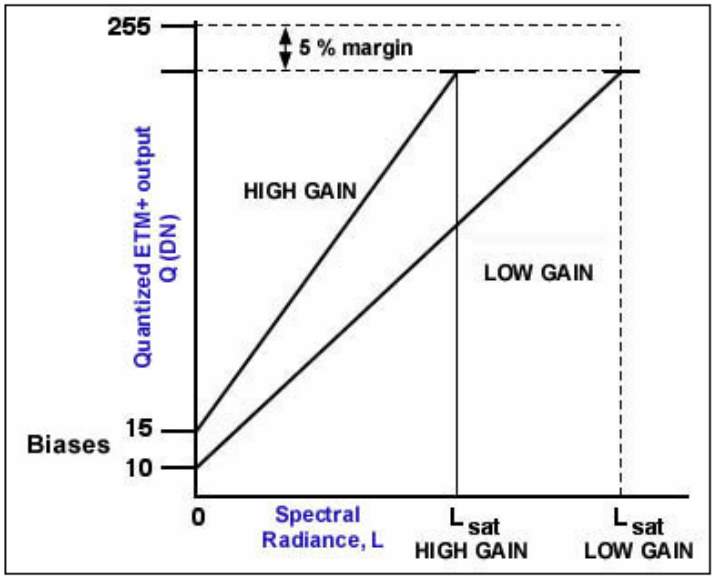

Figure 5.19 Relationship between Landsat 7 digital number and radiance (USGS).

Gain settings vary depending on the type of terrain and time of year. For example, in desert regions USGS protocols require the following gain settings:

- Bands 1, 2 and 3 (visible color bands) are set to low gain where sun elevation is greater than 28 degrees to avoid bright desert target (reflectance >0.65 in band 3, >0.66 in band 1, >0.71 in band 2) saturation.
- Band 4 (near infrared) is set to low gain where sun elevation is greater than 45 degrees to avoid bright desert (reflectance > 0.66) saturation.
- Band 5 and 7 (shortwave infrared bands) are set to low gain where sun elevation is greater than 38 to avoid bright desert target (reflectance >0.70 in band 5 and >0.68 in band 7) saturation.
- Band 8 (panchromatic) set to low gain.

Other typical gain settings are listed in the Landsat 7 Science Date Users Handbook (USGS 1998).

Scaled at-satellite DN are converted to units of absolute radiance with the equation:

$$L_\lambda = Gain \times Qcal + Offset \qquad 5.9$$

In terms of image metadata parameters the equation becomes:

$$L_\lambda = \frac{L\max_\lambda - L\min_\lambda}{Qcal_{\max} - Qcal_{\min}}\left(Qcal - Qcal_{\min}\right) + L\min_\lambda \qquad 5.10$$

where L_λ is the spectral radiance at the sensor aperture ($W \cdot m^{-2} \cdot sr^{-1} \cdot \mu m^{-1}$); *Gain* is the rescaled gain (the data product "gain" contained in the Level 1 product header or ancillary data record, $W \cdot m^{-2} \cdot sr^{-1} \cdot \mu m^{-1}$); *Offset* is the rescaled bias (the data product offset" contained in the Level 1 product header, $W \cdot m^{-2} \cdot sr^{-1} \cdot \mu m^{-1}$); *Qcal* is the quantized calibrated pixel value (digital number); $Lmin_\lambda$ is the spectral radiance that is scaled to $QCAL_{MIN}$ ($W \cdot m^{-2} \cdot sr^{-1} \cdot \mu m^{-1}$); $Lmax_\lambda$ is the spectral radiance that is scaled to $QCAL_{MAX}$ ($W \cdot m^{-2} \cdot sr^{-1} \cdot \mu m^{-1}$); $QCAL_{MIN}$ is the minimum quantized calibrated pixel value (corresponding to $Lmin_\lambda$, digital number); and $QCAL_{MAX}$ is the maximum quantized calibrated pixel value (corresponding to $Lmax_\lambda$, digital number). $QCAL_{MIN}$ is takes on a value is 1 for LPGS processed products and 0 for NLAPS products. $QCAL_{MAX}$ takes on a value of 255 for both LPGS and NLAPS processed products

For example, a patch of homogeneous pixels of a maturing wheat field might have a band 4 (near infrared) DN of 100. Image metadata lists the following parameters:

$Lmin_\lambda = -5.1$, $W \cdot m^{-2} \cdot sr^{-1} \cdot \mu m^{-1}$

$Lmax_\lambda = 241$, $W \cdot m^{-2} \cdot sr^{-1} \cdot \mu m^{-1}$

The image was produced by NLAPS so,

$QCAL_{MIN} = 0$

$QCAL_{MAX} = 255$

Absolute radiance is computed:

$$L_\lambda = \frac{L\max_\lambda - L\min_\lambda}{Qcal_{\max} - Qcal_{\min}} \cdot (Qcal - Qcal_{\min}) + L\min_\lambda$$

$$L_\lambda = \frac{241 - (-5.1)}{255 - 0} \cdot (100 - 0) + (-5.1) = 91.4 \quad \mathrm{W \cdot m^{-2} \cdot sr^{-1} \cdot mm^{-1}}$$

This computation is repeated by remote sensing software for every pixel in the image to produce the at-sensor radiance image. Gain settings differ for each band, so the user must be careful to select the correct parameters for each band.

5.5.5 Correction of Satellite Images for Atmospheric Effects.

Landsat 7 images produced by USGS have pixel values in scaled units of radiance as measured by the satellite sensor outside the earth's atmosphere. The previous section described how the scaled digital numbers are converted to physically meaningful radiance in units of W m^{-2} sr^{-1} μm^{-1}. The next step in producing a surface reflectance image is to transform the at-sensor (exoatmospheric) pixel radiance values to ground surface radiance or reflectance values. The transformation must take into consideration the position of the sun and attenuation of reflected and emitted radiation by the atmosphere between the satellite and surface.

Molecules of atmospheric gas scatter shorter wavelength radiation (Rayleigh scattering). This causes the sky to appear blue to a surface observer. Blue light has a shorter wavelength than green, red or infrared light, thus is scattered more. Certain atmospheric gases including oxygen, carbon dioxide, ozone and water vapor also selectively absorb specific wavelengths of light drastically reducing the transmission of these wavelengths. Light is also non-selectively scattered by airborne particulates and aerosols (Mie scattering). Particulates are the primary cause of haze. Theoretical details

of scattering and absorption are in atmospheric radiation transfer texts. Among the best is the recent work by Liou (2002). The acknowledged seminal work is by Chandrasekhar (1950).

Several practical approaches for correcting satellite imagery for atmospheric effects evolved from the science of atmospheric light attenuation. Most remote sensing software packages have semi-automated algorithms that combine simplified atmospheric correction techniques with illumination corrections to directly compute ground surface reflectances from exoatmospheric radiances. It is only necessary for the user to supply appropriate orbital, sun position and atmospheric parameters from the image metadata. Two popular approaches – the Dark Object Subtraction method and the Chavez Cos(t) model (Chavez 1996), do not even require atmospheric parameters. Both will be briefly discussed.

5.5.6 Dark Object Subtraction (DOS) Model

Particulate induced scatter (haze) slightly increases light energy received by the satellite sensor because of backscatter of solar radiation. The effect is relatively uniform across a scene in the absence of significant local emissions of particulates such as smoke from wildfire or urban air pollution. In the Dark Object Subtraction (DOS) method a uniform haze $Lhaze_{\lambda}$ value is subtracted from each pixel in each band in the image. The correction value is estimated from pixel values of objects in the scene that should reflect little or no light in a given wavelength band (i.e., the dark object). Good dark objects (actually areas) are bodies of deep clear water and very dark shadows. Some analysts assume more realistically that a dark object has a reflectance value of 1 percent in reflectance computations (Chavez 1986).

An analyst finds dark objects by exploring the image and observing pixel values in each band for several candidate objects. The lowest pixel value for each band is the haze correction value if it is not an obvious image artifact or sensor fault. Band haze correction values are subtracted from each pixel in the image during final processing. The result of this process is an image with reduced values of radiance that may be helpful when visually comparing scenes taken at different times or locations or when computing relatively robust band indices such as the NDVI. Dark object subtraction by itself does not produce a reflectance value and does not correct for sun angle or solar intensity effects, although adaptations of the DOS approach can accommodate the other effects.

The amount of solar energy received on a unit surface varies with the distance between the earth and sun (intensity) and the angle between the sun and the surface. When the sun is directly overhead (0 degrees solar zenith angle θ) a unit area on the surface receives the full irradiance of the sun. As the sun elevation angle decreases, the direct rays of the sun are spread over a larger area, decreasing the irradiance on a unit surface of the tangent plane by a factor equivalent to the cosine of the solar zenith angle. Reflectance computations typically account for these effects.

5.5.7 Cos(t) Model Transformation to Reflectance

The Cos(t) model (Chavez 1996) is a useful technique to produce a reflectance image from sensor (at-satellite) radiances when atmospheric parameters are not readily available. It works well with Landsat images acquired through a clear atmosphere. Chavez developed the Cos(t) model from the more generalized equation given by Moran et al. (1992) that was based on the derivations of Chadresekhar (1950):

$$\rho_\lambda = \frac{\pi\left(Lsat_\lambda - Lhaze_\lambda\right)}{TAUv_\lambda\left(\frac{Esun_\lambda}{d^2}\cos\theta \cdot TAUz_\lambda + Edown_\lambda\right)} \qquad 5.11$$

where ρ_λ is the spectral reflectance of the surface (dimensionless decimal), $Lsat_\lambda$ is the at-satellite spectral radiance for a given spectral band (W m^{-2} sr^{-1} μm^{-1}), $Lhaze_\lambda$ is the upwelling atmospheric spectral radiance scattered in the direction of the sensor (path radiance), (W m^{-2} sr^{-1} μm^{-1}), $TAUv_\lambda$ is the atmospheric transmittance along the path from the ground surface to the sensor (dimensionless), $TAUz_\lambda$ is the atmospheric transmittance along the path from the sun to the ground surface (dimensionless), $Esun_\lambda$ is the solar spectral irradiance on a surface perpendicular to the sun's rays outside the atmosphere (exoatmospheric) (W m^{-2} μm^{-1}), $Edown_\lambda$ is the downwelling spectral irradiance at the surface due to scattered solar flux in the atmosphere (W m^{-2} μm^{-1}), d is the earth to sun distance in astronomical units (au), and θ is the solar zenith angle (degrees).

Chavez (1996) found that good first order approximations for the atmospheric transmittance coefficients are the cosine of the solar zenith angle for $TAUz_\lambda$ and a value of 1.0 for $TAUv_\lambda$ for the nadir viewing Landsat sensor. With these approximations and assuming that downwelling spectral irradiance is zero the reflectance equation becomes,

$$\rho_\lambda = \frac{\pi\, d^2\left(Lsat_\lambda - Lhaze_\lambda\right)}{Esun_\lambda \cos^2\theta} \qquad 5.12$$

This equation is called the Cos(t) model. The subscript λ refers to spectral band λ. For each Landsat7 ETM+ image the gains, biases and sun elevation angle (90-θ) are provided in the header file that accompanies the image. Solar irradiance for each band interval Eo_λ is obtained from the Landsat 7 Science Data Users Handbook (USGS 1998). These values can also be obtained by integration of the ASTM AM0 spectral distribution in

Figure 5.18. The normalized Sun-Earth distance *d* in astronomical units for any day of the year may be interpolated from a data table in the Landsat 7 Science Data Users Handbook or computed directly from astronomical equations. The necessary data tables are reproduced here as Table 5.5 and Table 5.6.

Band	$Esun_{\lambda}$ W m^{-2} sr^{-1} μm^{-1}
1	1969
2	1840
3	1551
4	1044
5	225.7
7	82.07
8	1368

Table 5.5 Landsat 7 band interval extraterrestrial irradiances.

Earth-Sun Distance in Astronomical Units									
Julian Day	Distance	Julian Day	Distance	Julian Day	Distance	Julian Day	Distance	Julian Day	Distance
1	0.9832	74	0.9945	152	1.014	227	1.0128	305	0.9925
15	0.9836	91	0.9993	166	1.0158	242	1.0092	319	0.9892
32	0.9853	106	1.0033	182	1.0167	258	1.0057	335	0.986
46	0.9878	121	1.0076	196	1.0165	274	1.0011	349	0.9843
60	0.9909	135	1.0109	213	1.0149	288	0.9972	365	0.9833

Table 5.6 Earth - Sun distance in astronomical units for representative Julian dates.

Cos(t) model image transformations are produced relatively easy with the Idrisi© remote sensing software package. At-satellite reflectance values can be computed by excluding the haze correction and atmospheric transmission coefficient in Equation 5.12. This approach was adopted for development of the 2000 Multi-resolution Land Cover Dataset (MRLC) of the U.S. from Landsat 7 data (Huang et al. 2002). At-satellite reflectance values in the MRLC procedure are further processed with an image transformation algorithm called the "tasseled cap" transformation to produce derivative images for use in land cover classification.

All Landsat 7 images used in land cover classification in the dissertation work were corrected for sun and atmospheric effects with the Chavez Cos(t) model approach.

A detailed step-by-step tutorial for processing Landsat 7 imagery and computing reflectances with Idrisi© software was prepared for the Advanced Watershed Tools training class presented to technical staff of the Jordanian Water Ministry (Teasdale and Barber 2003).

5.5.8 Spectral Signatures

Visual interpretation of the information in multipsectral satellite images becomes more challenging as the number of image bands increases. Many analytical procedures have been developed to convert spectral data recorded by satellite images to meaningful interpretations of the identity and character of features in the image (Jensen 1996; Richards 1993). The essential concept among all these techniques is the spectral signature. Several land cover types in the lower Potlatch River basin are identified in the July 17, 2002 Landsat 7 reflectance image in Figure 5.21, Figure 5.22 andFigure 5.23. Figure 5.21 is a visual color composite image of bands 1, 2 and 3 represented as blue, green and red in the image display. Bands 2, 3, and 4 are displayed as blue, green and red in the visual-near infrared image in Figure 5.22. The shortwave infrared image in Figure 5.23 is a composite of bands 4, 5 and 7 displayed as blue, green and red.

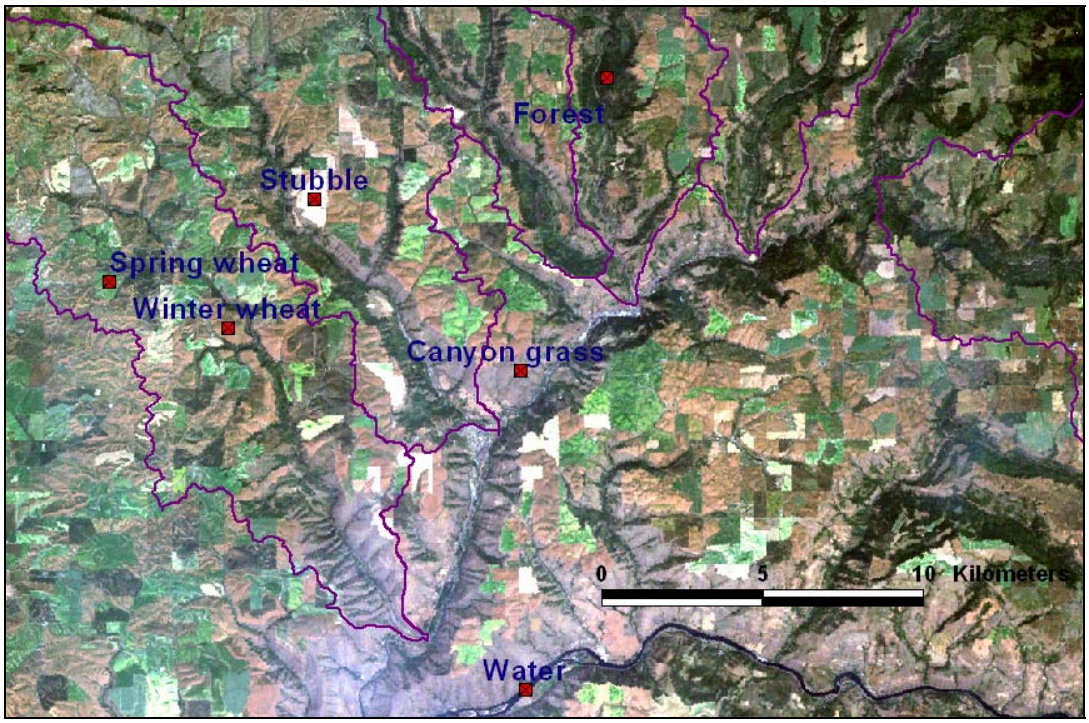

Figure 5.20 Land cover types in July 17, 2002 Landsat 7 image (bands 1,2,3).

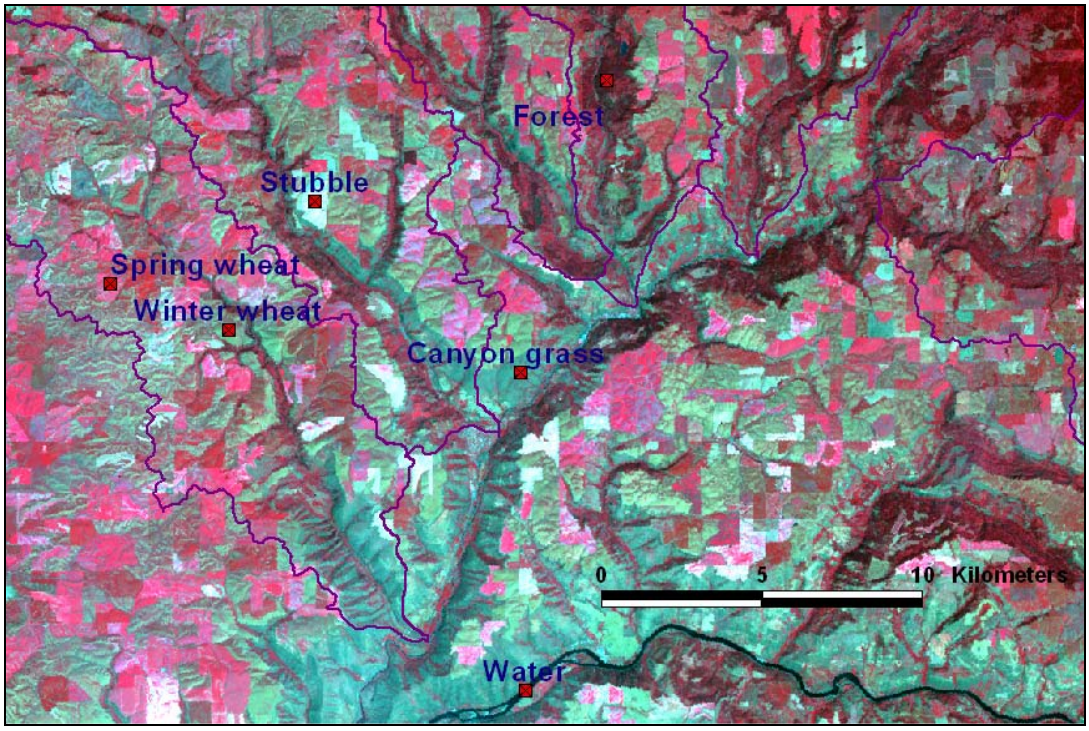

Figure 5.21 Land cover types in July 17, 2002 Landsat 7 image (bands 2,3,4).

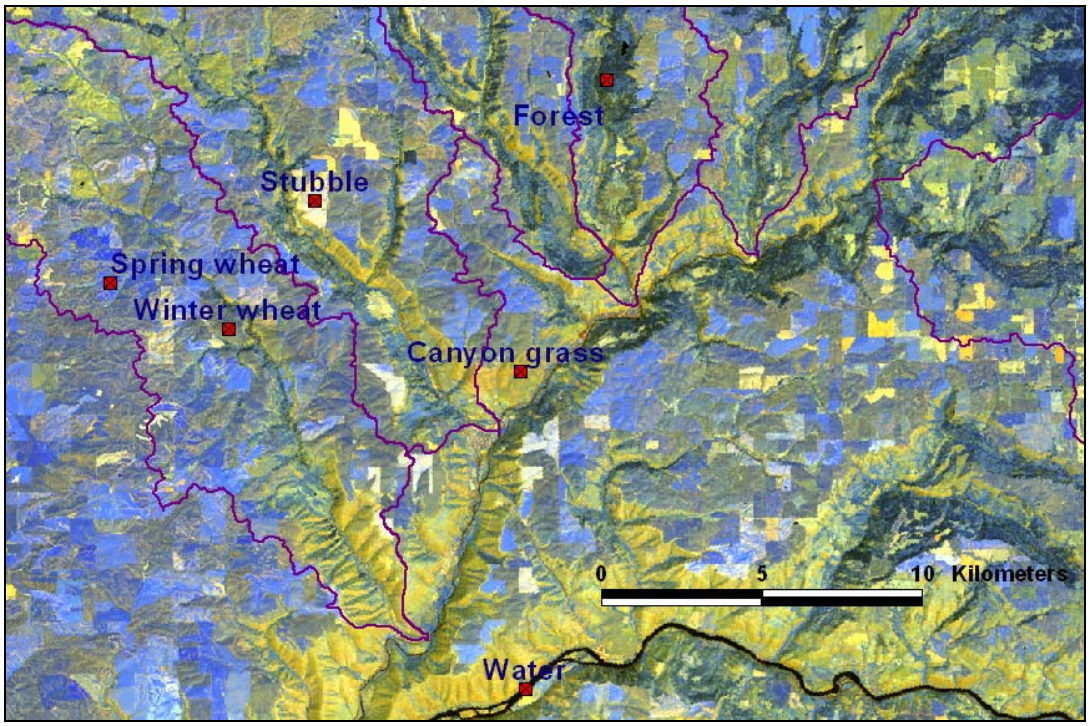

Figure 5.22 Land cover types in July 17, 2002 Landsat 7 image (bands 4,5,7).

Reflectance values for each land cover type are plotted in Figure 5.23. The reflectance values have been scaled over a range of 255 to reduce image file size. For example the infrared reflectance of spring wheat is 175/255 = 0.68. Each of the land cover types has a unique spectral signature. Reflectance values vary the most in the red, infrared and shortwave infrared bands (3, 4, 5, and 7) while the blue and green bands (1 and 2) are much less discriminating. Lack of distinctive information in blue and green bands is common in scenes of natural land cover.

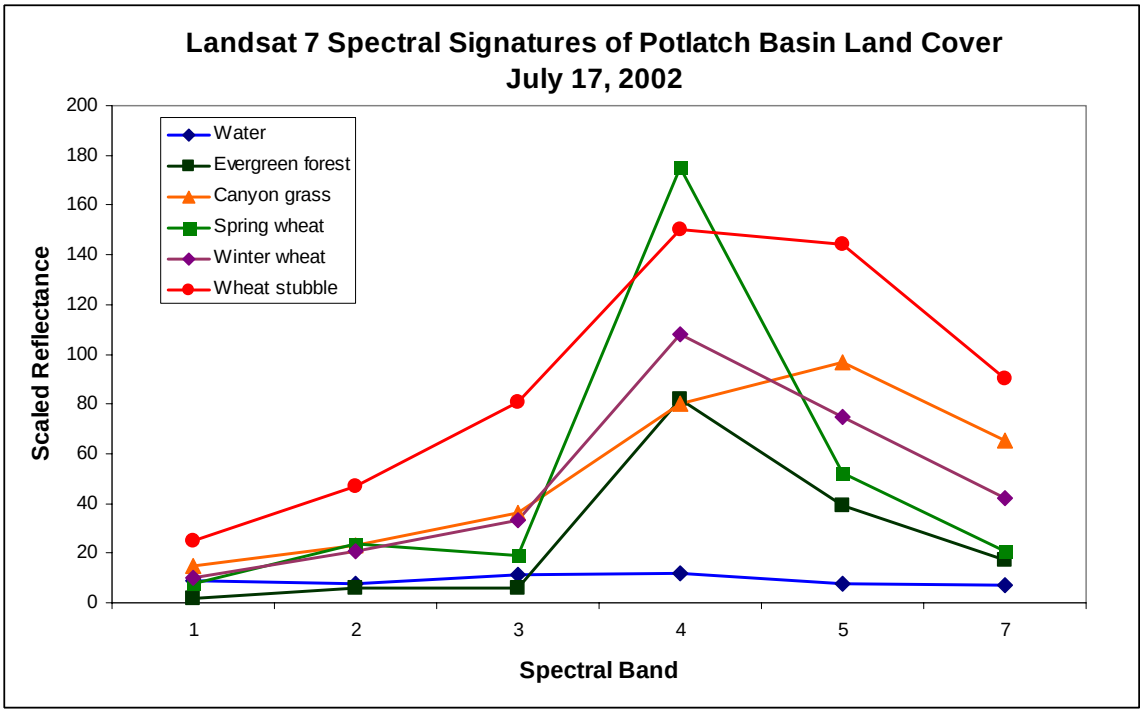

Figure 5.23 Spectral signatures of land cover types in Landsat 7 image July 17, 2003.

Close study of the images and plot show that each band carries information that helps the observer discriminate land cover types, but that the information content is somewhat redundant between bands. For example, the plotting order of the magnitudes of reflectance values of bands 5 and 7 are the same, indicating these bands carry redundant information.

Band redundancy is a well-recognized property of multispectral imagery datasets that has motivated the development of many procedures and algorithms, such as the "tasseled cap" transformation and principal component analysis, that attempt to reduce the full multispectral dataset to three or four unique data layers. Many such algorithms were tested in the course of the dissertation work. None seemed to work as efficiently for discriminating hydrologically relevant land cover types as well as the standard classification methods discussed in Section 5.8.

5.6 Vegetation Indices

Image indices combine the information from two or more bands into an artificial single band image or gridded dataset. Indices are widely applied in the study of vegetated land cover to compare vegetation characteristics among several images, usually a series of seasonal or annual images. Vegetation index images are easily constructed with remote sensing software. Some analysts use vegetation indices to "normalize" an image to reduce atmospheric effects.

Vegetation and soil indices are derived from satellite and aerial images by algebraically combining the digital numbers or reflectances of one or more wavelength bands. Vegetation indices take advantage of the information in the relationships between bands that might not otherwise be evident. There are many different vegetation indices. Vegetation indices can be divided into two categories: slope based and distance based. Slope based indices are computed from band ratios and are the simplest. Distance based indices incorporate a measure of the distance of the digital numbers from the soil line.

There are literally hundreds of journal articles related to vegetation indices. A good recent article that discussed the limitations of vegetation indices in semi-arid environments is by Elmore et al. (2000). Steven and Mathus (2003) discuss techniques for comparing vegetation indices among data sources. The Idrisi© software includes nineteen different indices as options in the VEGINDEX module and includes an excellent overview of vegetation indices in the program manual. Vegetation indices should be computed with surface reflectance rather than at-satellite radiances. A few of the most common indices are briefly described below.

The simplest vegetation index is the Ratio Vegetation Index (RVI) which is a ratio of infrared and red reflectance:

$$RVI = \frac{\rho_{nir}}{\rho_{red}} \qquad 5.13$$

where ρ_{nir} is the reflectance of the near infrared band and ρ_{red} is the reflectance of the near infrared band. The RVI is a slope-based index that divides the near infrared band by the red band. Values range from about 1 for bare soil to more than 20 for dense vegetation.

The Normalized Difference Vegetation Index (NDVI) is a very common index that emphasizes vegetation reflectance in satellite and aerial imagery. It is computed from red and infrared reflectance by:

$$NDVI = \frac{\rho_{nir} - \rho_{red}}{\rho_{nir} + \rho_{red}} \qquad 5.14$$

Standard NDVI products are routinely developed from images acquired by the NOAA AVHRR sensor and the NASA MODIS. The difference in the reflectances is divided by the sum of the two reflectances. The typical range of actual values is about -0.01 for open water surfaces and wet soils to 0.9 for dense vegetation. NDVI is more sensitive to low levels of vegetative cover than the RVI, but tends to maximize as the canopy closes even though biomass may still increase.

The Soil-Adjusted Vegetation Index (SAVI) adds a soil calibration factor L to compensate for soil background influences:

$$SAVI = \frac{\rho_{nir} - \rho_{red}}{\rho_{nir} + \rho_{red} + L}(1 + L) \qquad 5.15$$

The soil calibration factor can vary from 0 to 1 depending on the amount of visible soil. A value of 0.5 is a good approximation when the amount of visible soil is unknown. The most important reference for the SAVI is by Huete (1988).

In practical application, vegetation indices require no technical analysis and only minimal processing effort. Vegetation index algorithms are automatic in most remote sensing software packages. Vegetation indices developed from archive imagery are usually worth a quick review when planning a watershed characterization strategy. Depending on imaging objectives, a simple vegetation index may provide the needed land cover information and save considerable time performing more complicated classifications. Figure 5.24 is a NDVI grid computed from the July 17, 2002 Landsat 7 image of the lower Potlatch River basin. The NDVI correctly indicates the general trend in green vegetation – least in stubble and highest in spring wheat and forest cover. The NDVI may be sufficient to indicate the status of the wheat harvest. Permanent, grass, shrub and forest vegetation are clearly distinguished in the NDVI grid of the October 24, 2003 Landsat 7 image in Figure 5.25.

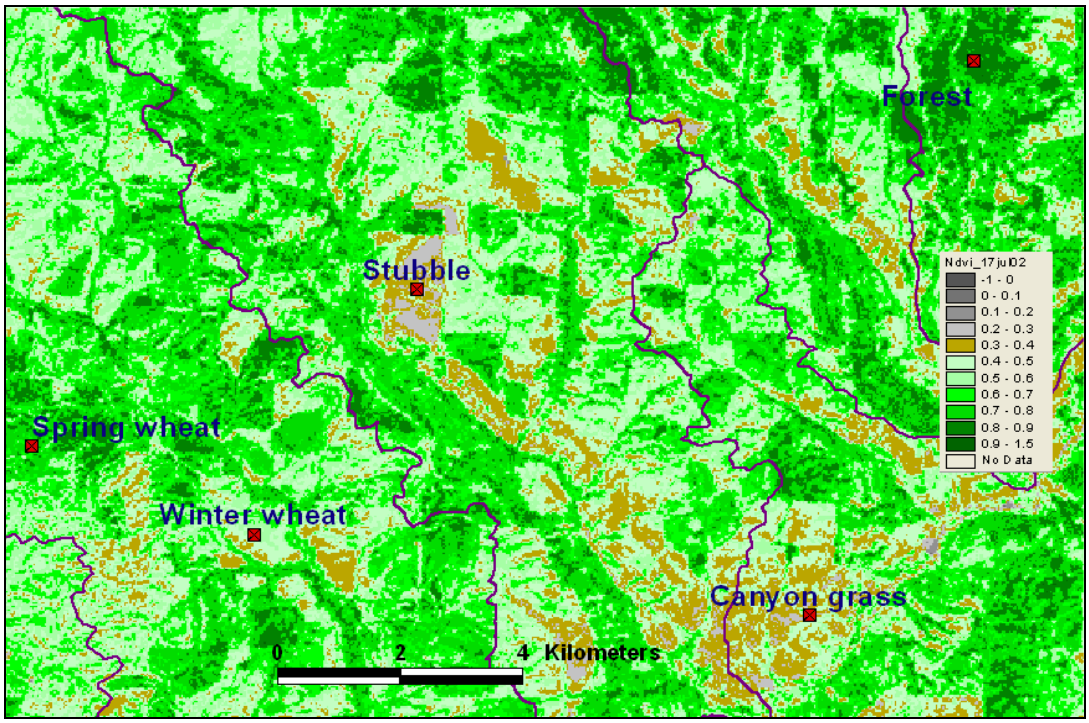

Figure 5.24 NDVI of July 17, 2002 Landsat 7 image.

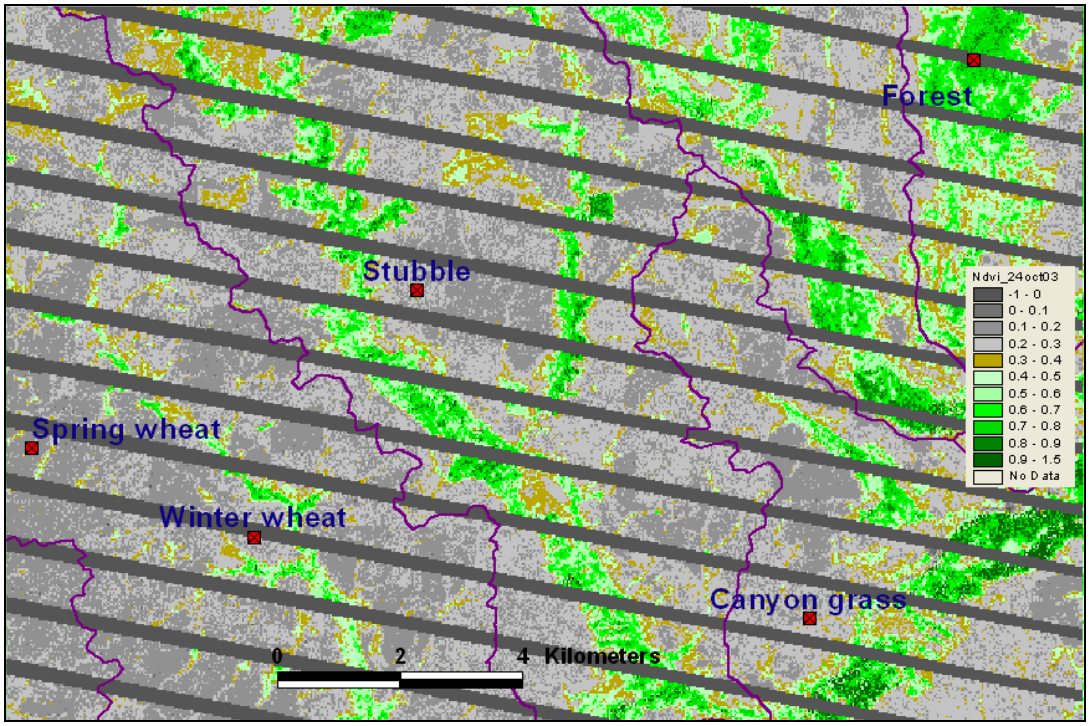

Figure 5.25 NDVI of October 24, 2003 Landsat 7 image.

5.7 Identification and Indexing of Hydrologically Sensitive Land Cover

The combined use of satellite and aerial imagery in the dissertation work culminated in techniques to classify land cover of multiple use watersheds in north central Idaho and eastern Washington. This effort has clear applications in hydrologic modeling and soil erosion assessment described in Sections 7 and 8. These procedures are primarily software based and can only be conveyed in a general way in this dissertation document. Fortunately, the work is not technically complicated and the main points of the procedure could be learned in one or two days of computer based training.

The first serious effort in the dissertation research to characterize watershed land cover with satellite imagery began with the acquisition of three images: a July 17, 2002 Landsat 7 image, a September 10, 2002 ASTER image and an October 12, 2002 Landsat 7 image. High-resolution digital aerial color infrared images (CIR) were acquired on October 8, 2002 along 16 north-south aerial transects spaced at 5 km intervals across the lower Potlatch River watershed to provide ground truth data for land cover classifications. The aerial image acquisition had been planned based on the good quality of the July 2002 Landsat 7 image and the likelihood of a favorable Landsat collection on October 12. The ASTER acquisition was fortuitous, but very beneficial.

Soil erosion, and therefore phosphorous export, is sensitive to antecedent moisture content so it is important to locate agricultural fields that are fallowed in the current season to store soil moisture. Fallowed fields should be bare preceding the general harvest and apparent in the July 17, 2002 Landsat 7 in Figure 5.26 either by NDVI analysis or by shortwave infrared response in Figure 5.27.

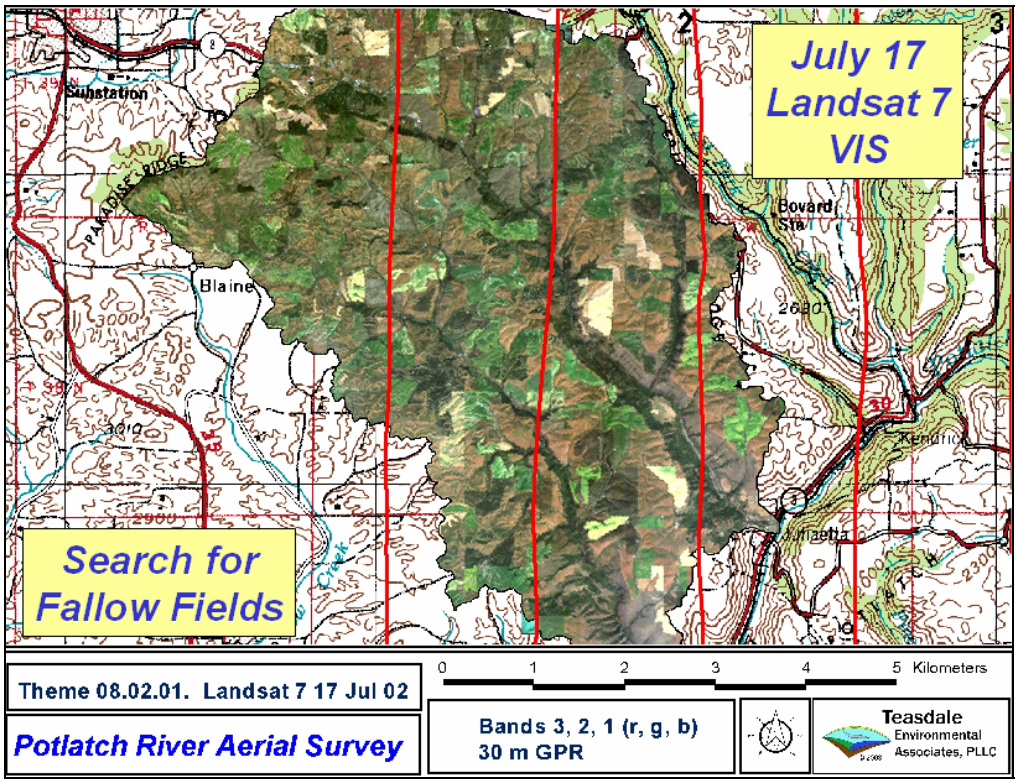

Figure 5.26 Search for fallow fields in the July 17, 2002 Landsat 7 visible color image.

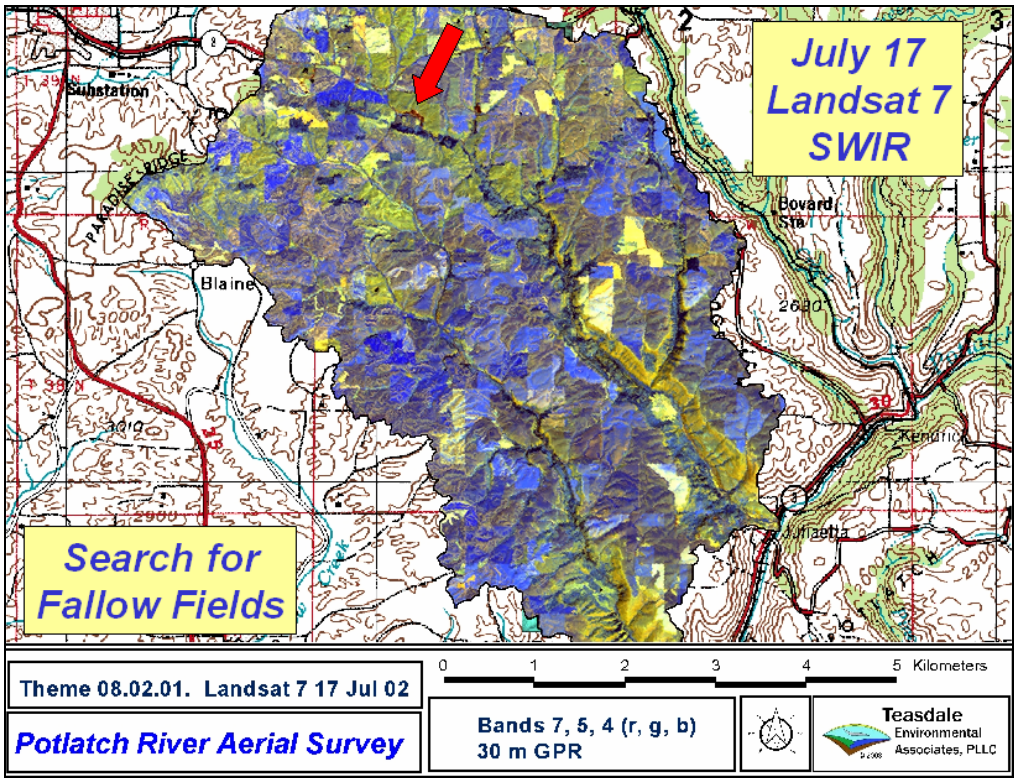

Figure 5.27 Search for fallow fields in the July 17, 2002 Landsat 7 shortwave infrared image.

No fallowed fields of significant size were detected in the study region. The red arrow on Figure 5.27 marks the position of a quarry. The very dark brown color in this shortwave image is very distinctive compared to fields with vegetation, indicating that fallow fields should have been easily detected. The brown field to the right of the arrow is burned grass.

Dark brown tilled low residue fields and light brown fields with moderate residue are easy to identify in the September 8 ASTER image and October 12 Landsat image in Figure 5.28Figure 5.29. Bright white land cover is standing small grain stubble. The progress of fall tillage operations can be monitored by the differences between the September ASTER and October Landsat images. The red arrow in Figure 5.28 marks the location of a controlled burn in a stubble field. Smoke from the fire is seen in the magnified view of the field in Figure 5.30.

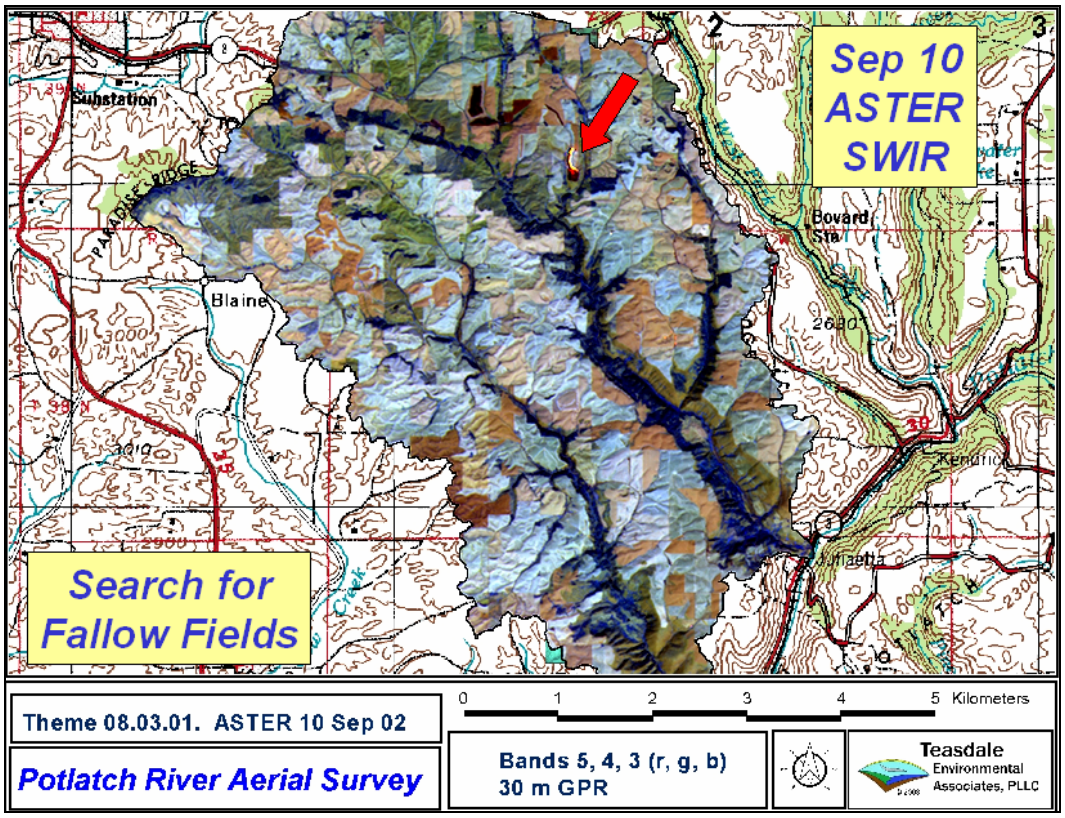

Figure 5.28 Harvested and tilled fields in the ASTER September 8, 2002 image.

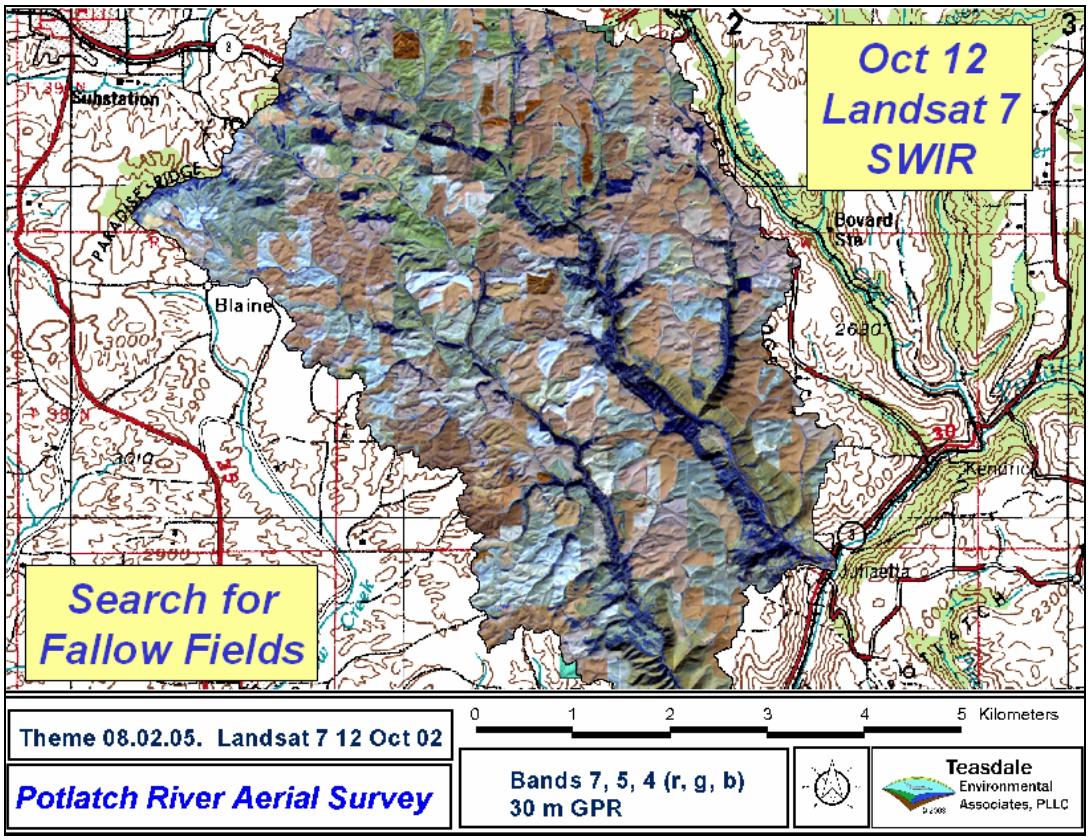

Figure 5.29 Harvested and tilled fields in the Landsat 7 October 12, 2002 image.

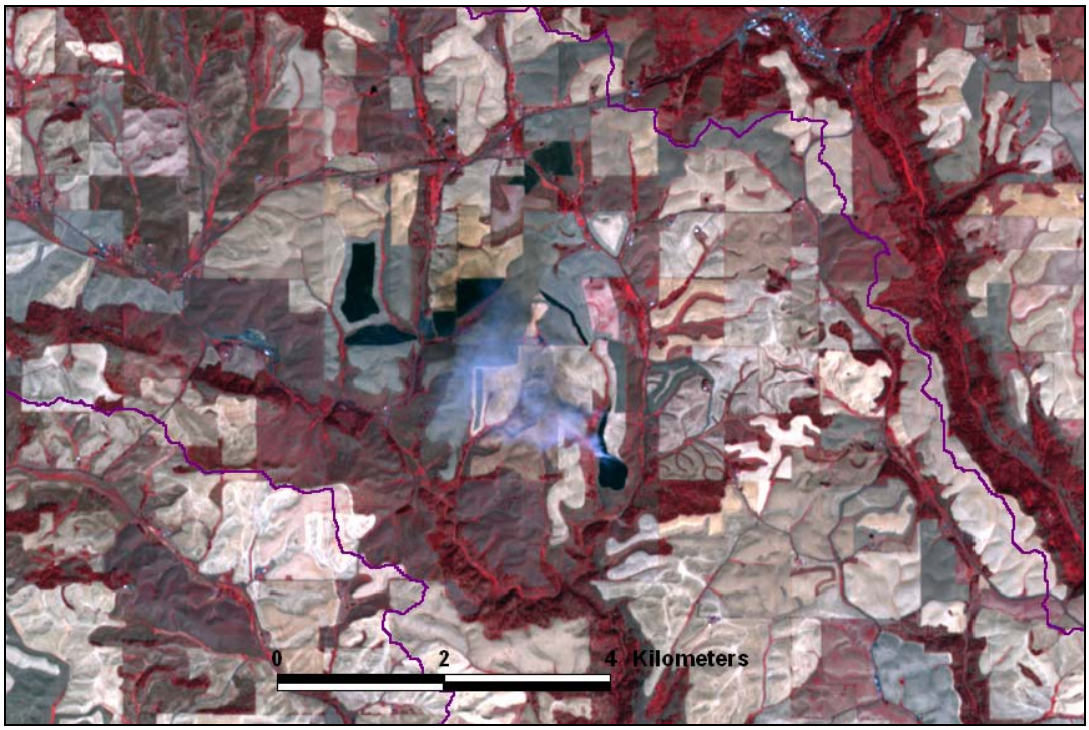

Figure 5.30 Burning stubble field in the ASTER September 8, 2002 image.

Land cover type interpretation in the October Landsat 7 was verified with the high-resolution digital aerial CIR images acquired on October 8, 2002. Figure 5.31 through Figure 5.34 illustrate the ground truthing process. A feature area is selected along a flight line (Figure 5.31) and the aerial images in this location are georeferenced to the same datum as the Landsat image (Figure 5.32). Hydrologically relevant land cover types are identified in the high-resolution aerial image (Figure 5.33) and the spectral and textural characteristics of the Landsat image are analyzed (Figure 5.34). A selection of ground truth areas are digitized to provide training site data for software classification algorithms.

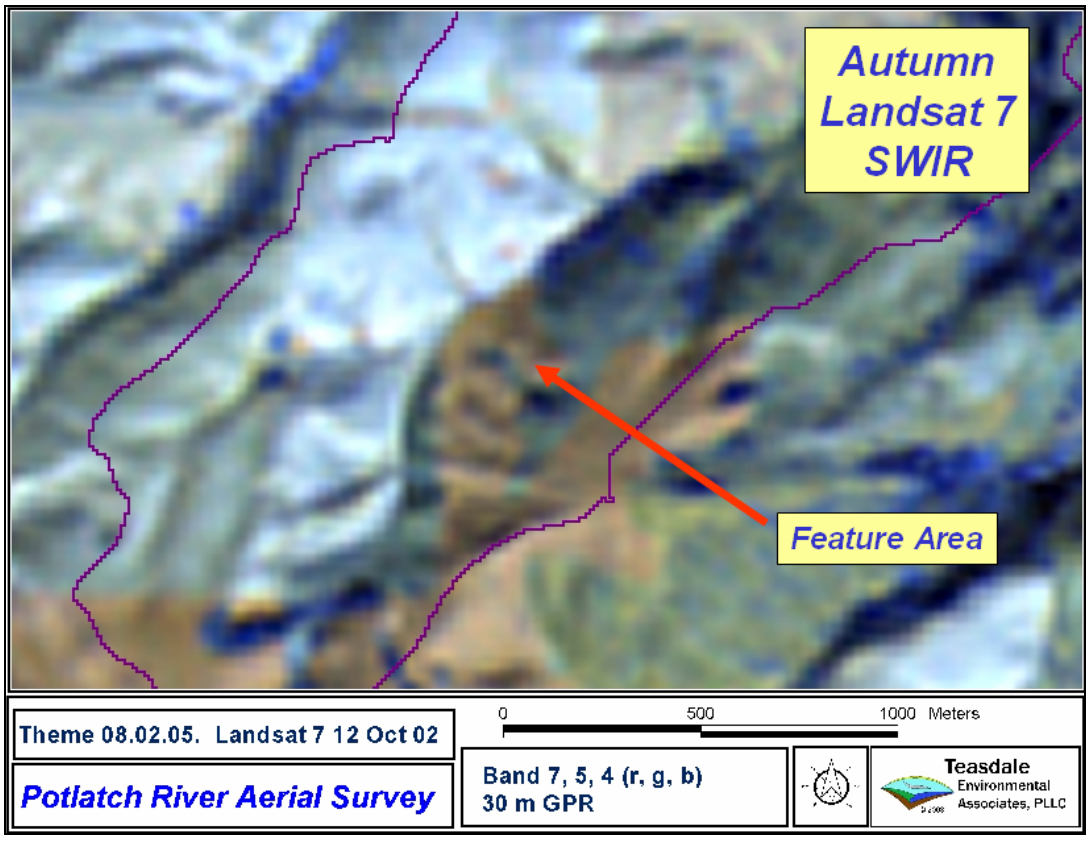

Figure 5.31 Ground truth area along aerial image transect

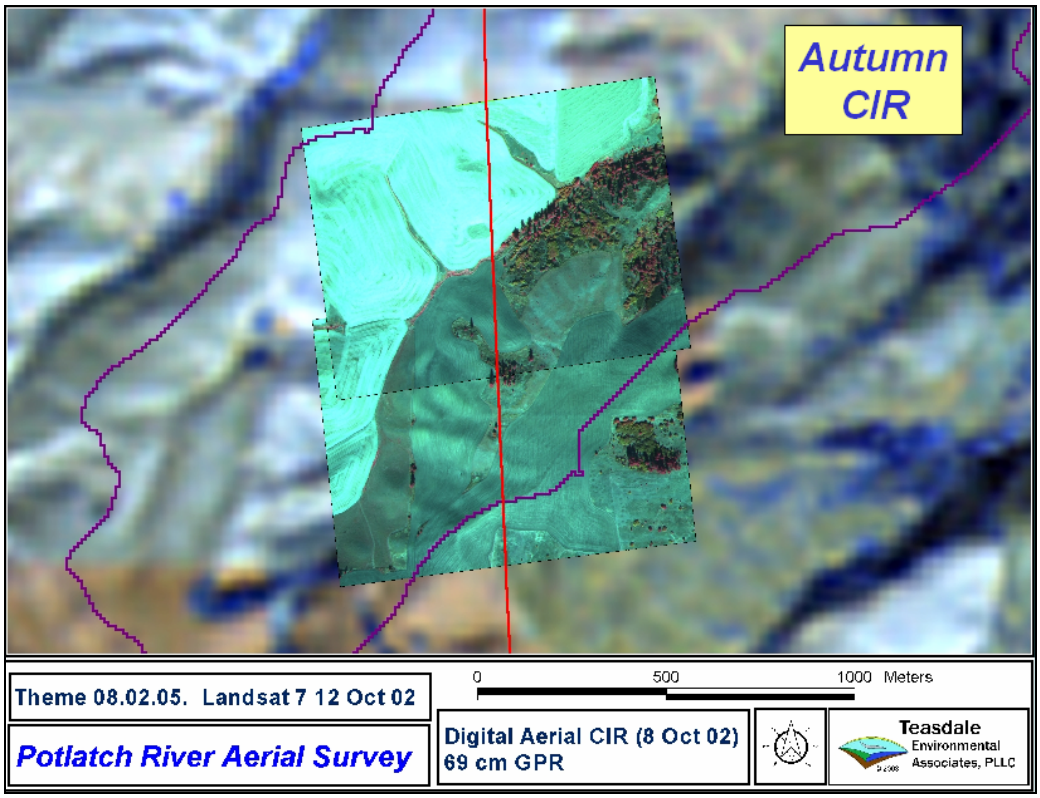

Figure 5.32 High-resolution digital CIR aerial image transect.

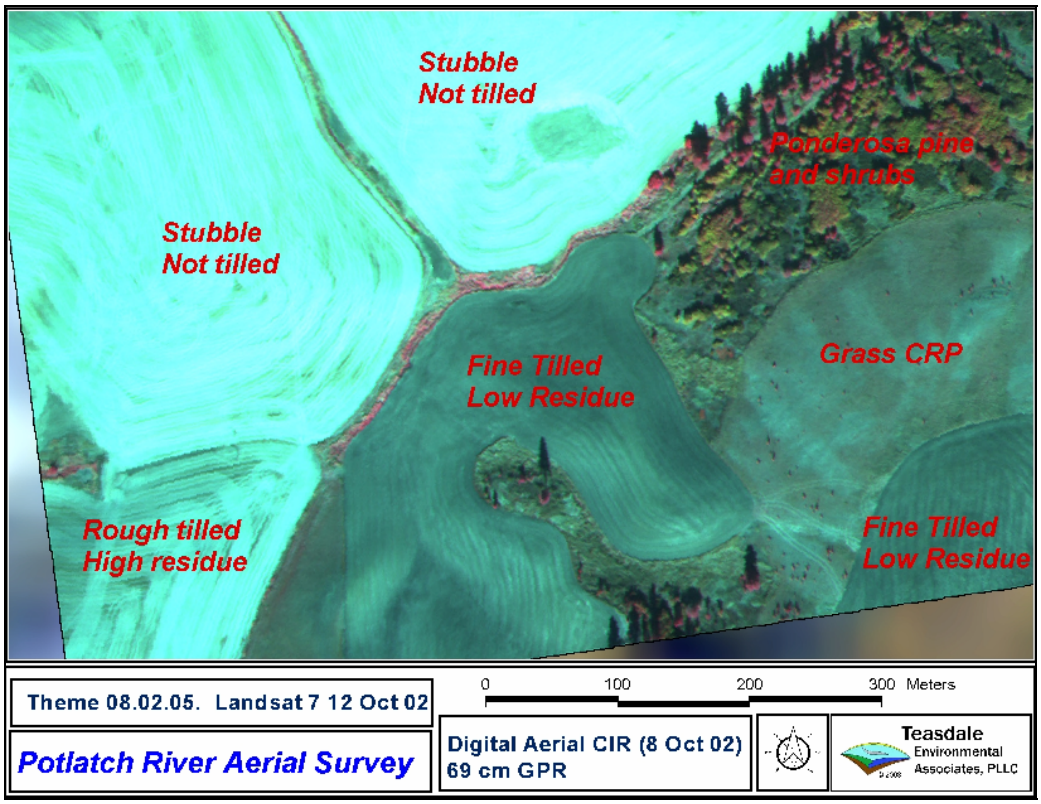

Figure 5.33 Land cover types identified in the aerial CIR image.

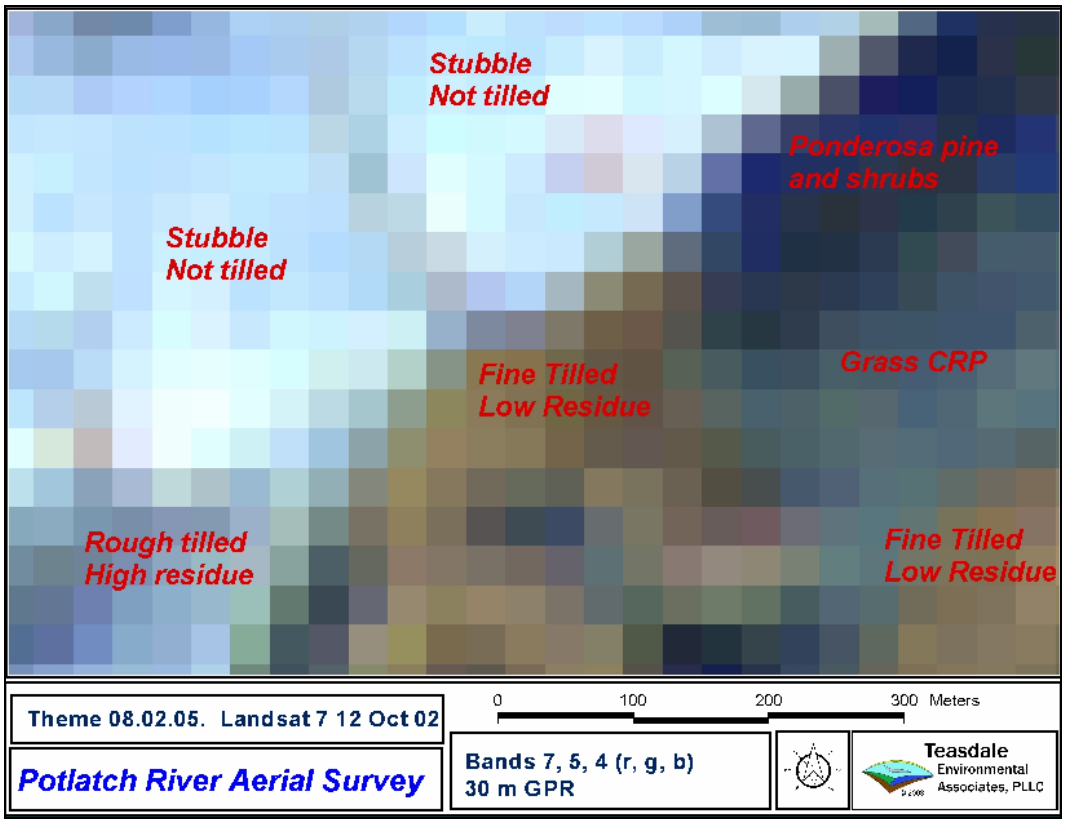

Figure 5.34 Magnified view of the land cover types in the October Landsat 7 image.

The GIS and image processing required to perform the above analysis are routine and well within the capabilities of moderately experienced GIS users. The ground truthing analysis is relatively rapid. On-the-ground verification should be performed for some sites as further documentation of the interpretation, but is not absolutely necessary if the analyst is familiar with land cover types in the area. A visual survey along roads in the project may be sufficient. It is important that the satellite and aerial images be collected after most of fall tillage operations are complete.

This preliminary investigation showed that late fall Landsat 7 imagery gives a good indication of the location and extent of agricultural fields that have been tilled and have low surface residue. These fields are the most hydrologically sensitive.

Experimentation with various indices showed that low-residue fall-tilled fields could be identified with a normalized difference index (NDI) using the October Landsat 7 shortwave infrared bands (5,7). This index is computed:

$$NDI = \frac{B5 - B7}{B5 + B7} \qquad 5.16$$

where *B5* and *B7* are the Landsat 7 band 5 and band 7 reflectances. A threshold NDI value of 0.15 in Figure 5.35 discriminated the low residue fields from other land cover types reasonably well throughout the study region. The NDI threshold value is determined by trial and error comparison of the Landsat image, a trial NDI grid and the high-resolution aerial images. A NDI threshold value of 0.15 may not be appropriate for other regions.

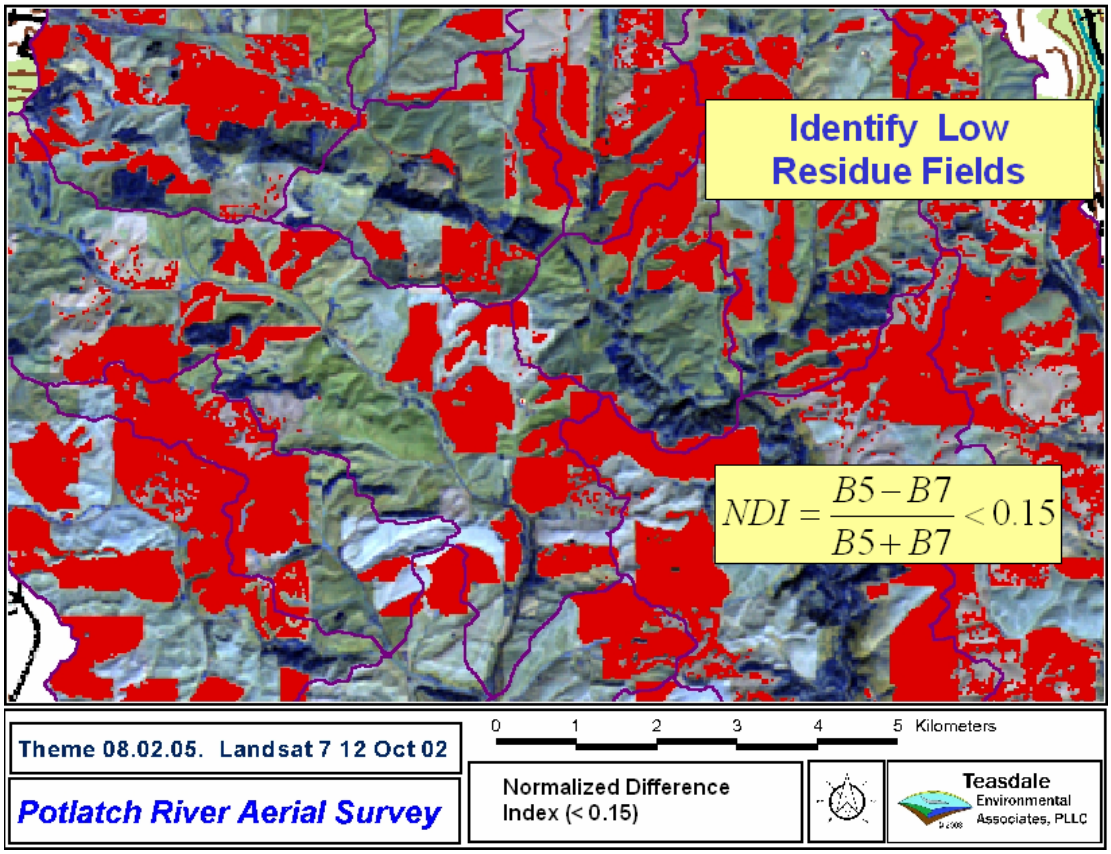

Figure 5.35 Identification of low residue fields with a normalized difference index.

The NDI only indicates the presence of low surface-residue soils. It is not a complete indicator of erosion susceptibility. Two other important factors: soil erodibility and slope were included in a composite index. Soil erodibility for the study regions were obtained from the NRCS Soil Survey Geographic database. Terrain slope was determined by digital analysis of the USGS 10-meter DEM. The Erosion Potential Index (EPI) is determined by the criteria:

1) Normalized Difference index greater less than 0.15,
2) DEM ground slope greater than 15 percent,
3) Soil erodibility greater than 0.4.

Threshold values for slope and soil erodibility were preliminary estimates. The area of land surface identified by the EPI in Figure 5.36 is much reduced from the NDI.

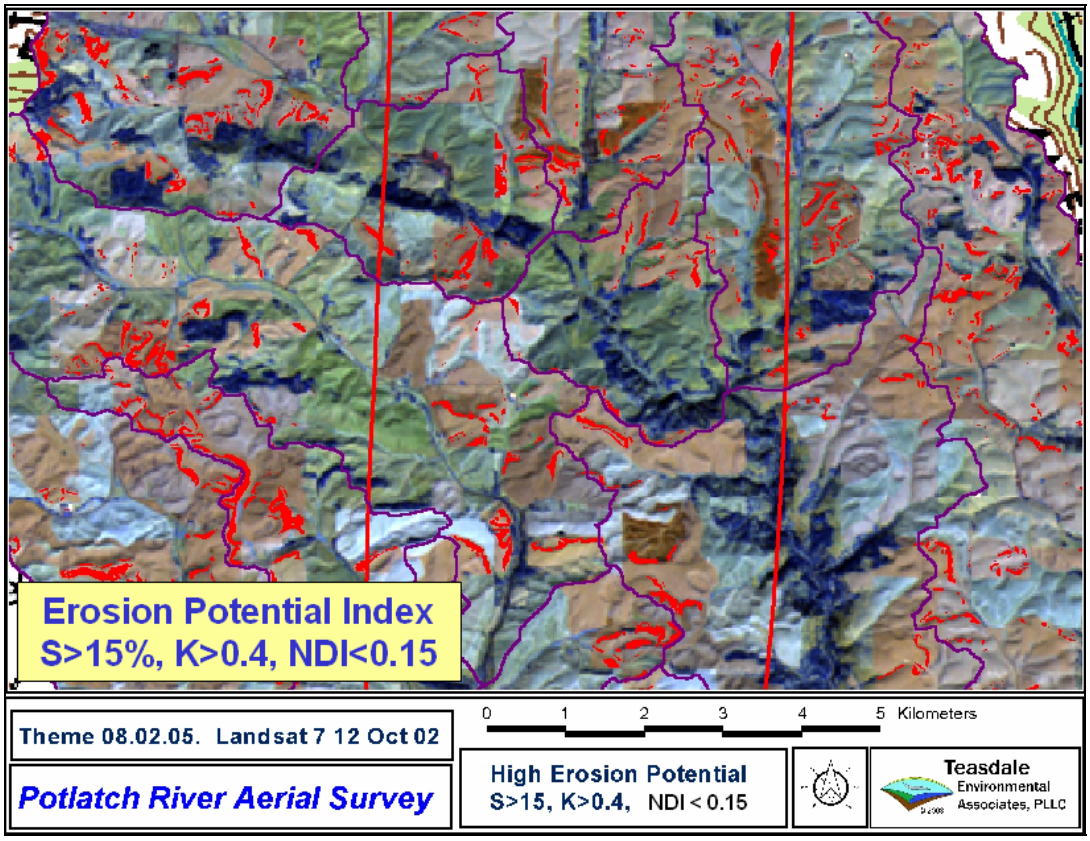

Figure 5.36 Erosion susceptible soils identified by the Erosion Potential Index.

High-resolution digital natural color aerial images were acquired along a single transect on April 19, 2003 to observe the performance of the EPI index. Several observation sites are identified in Figure 5.37. Soil erosion observed in the aerial imagery and indicated by ephemeral gullies corresponded reasonably well to the EPI in Figure 5.38 and Figure 5.39. The EPI did not predict the ephemeral gully erosion in Figure 5.40 because the ground slope is flatter than 15 percent and the EPI does not account for topographic flow convergence.

This initial research indicates the EPI is a reasonable predictor of soil erosion susceptibility. Future research should further test and adapt the EPI for operational use.

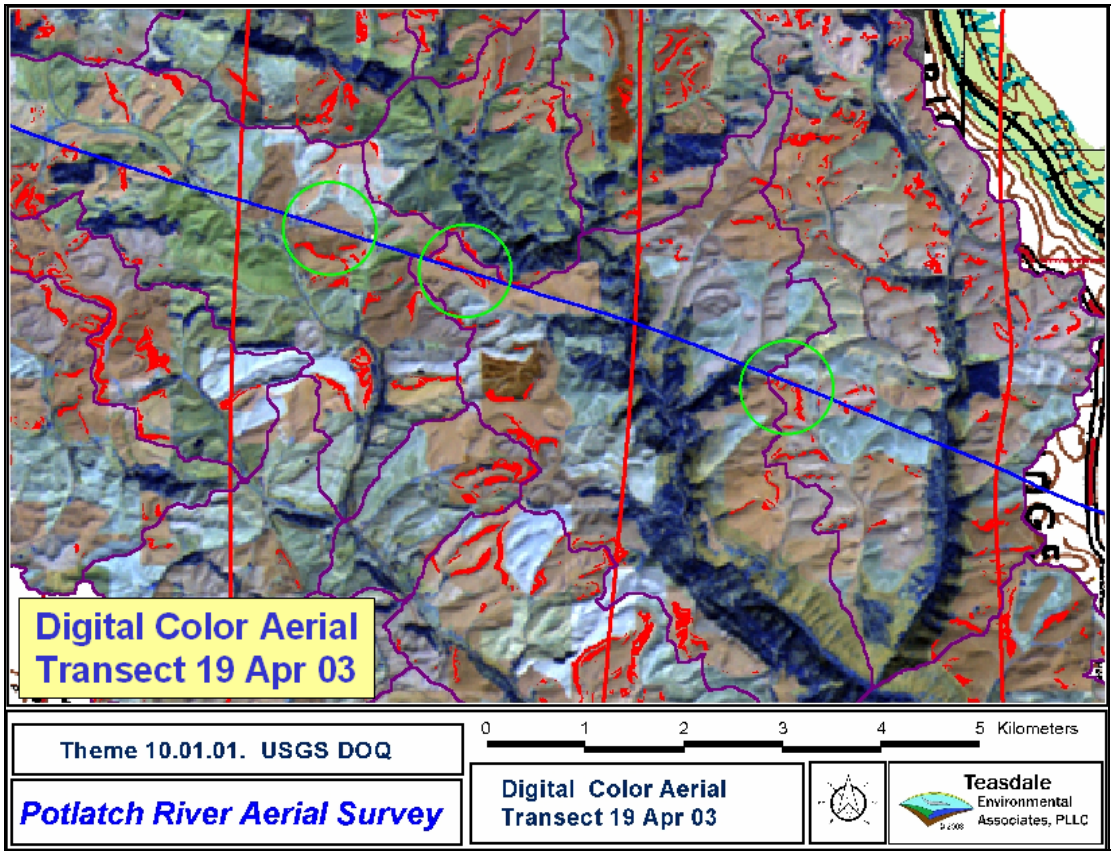

Figure 5.37 EPI verification sites along the April 19, 2003 aerial image transect.

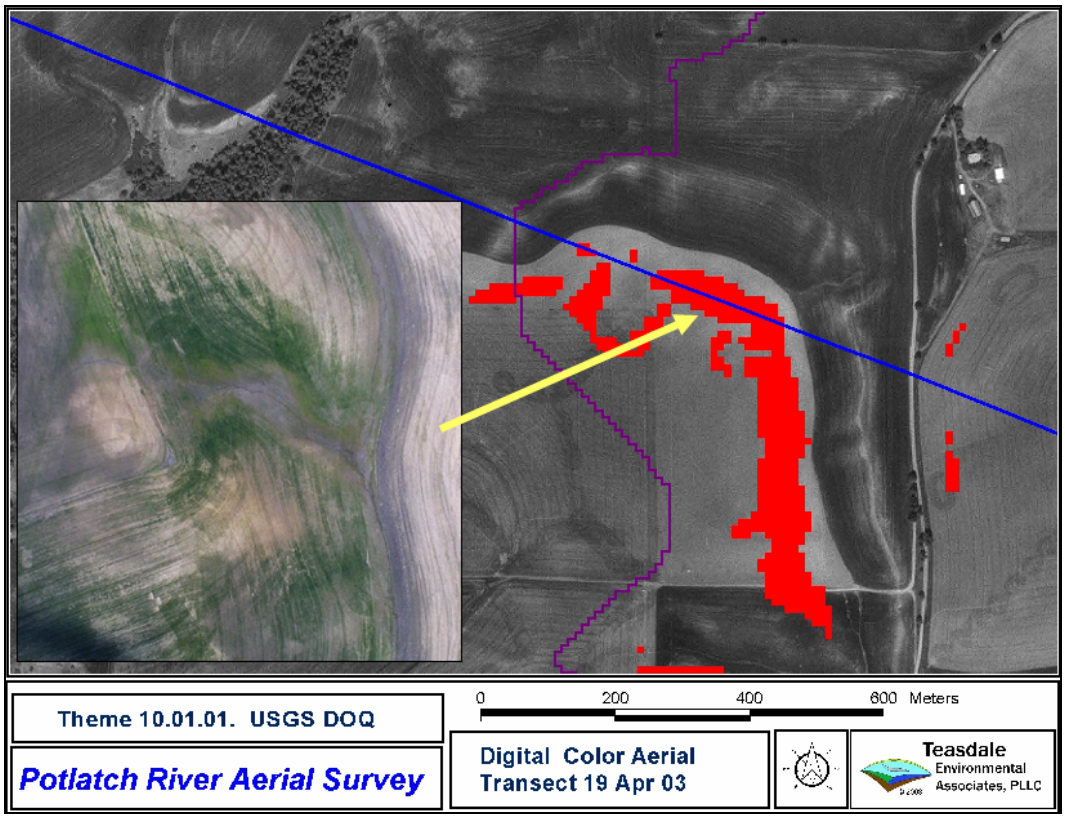

Figure 5.38 Observed soil erosion in a location identified by the EPI.

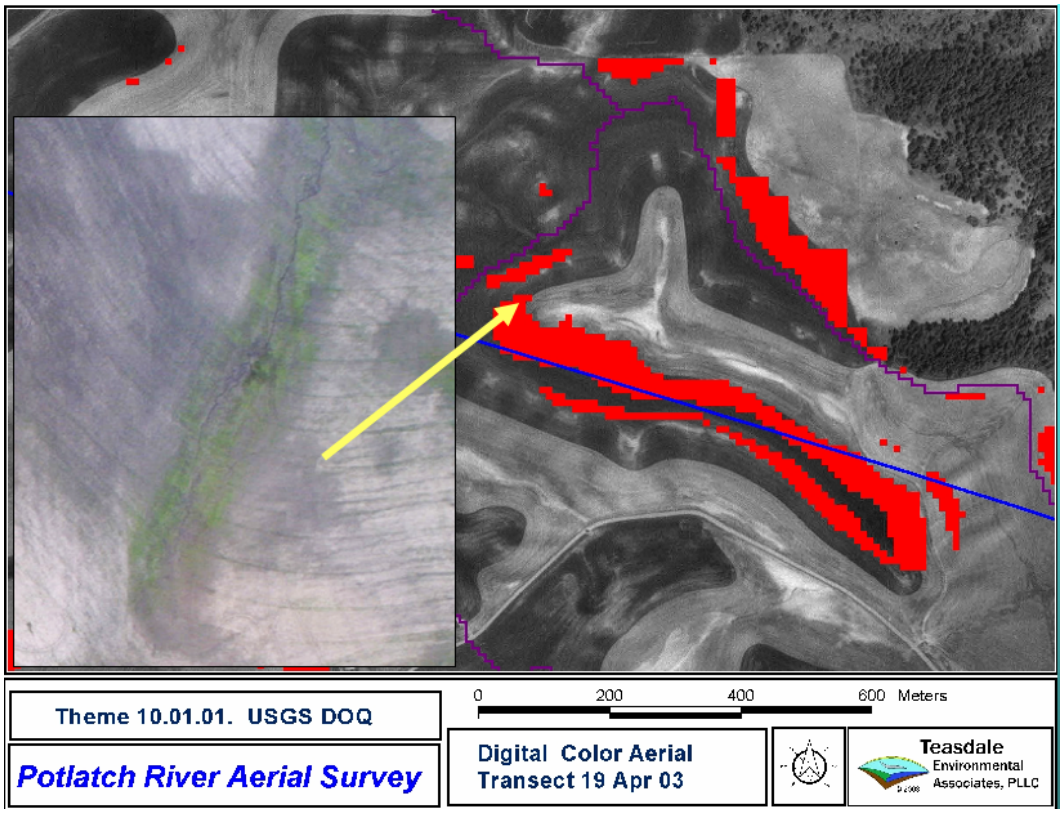

Figure 5.39 Observed soil erosion in a location identified by the EPI.

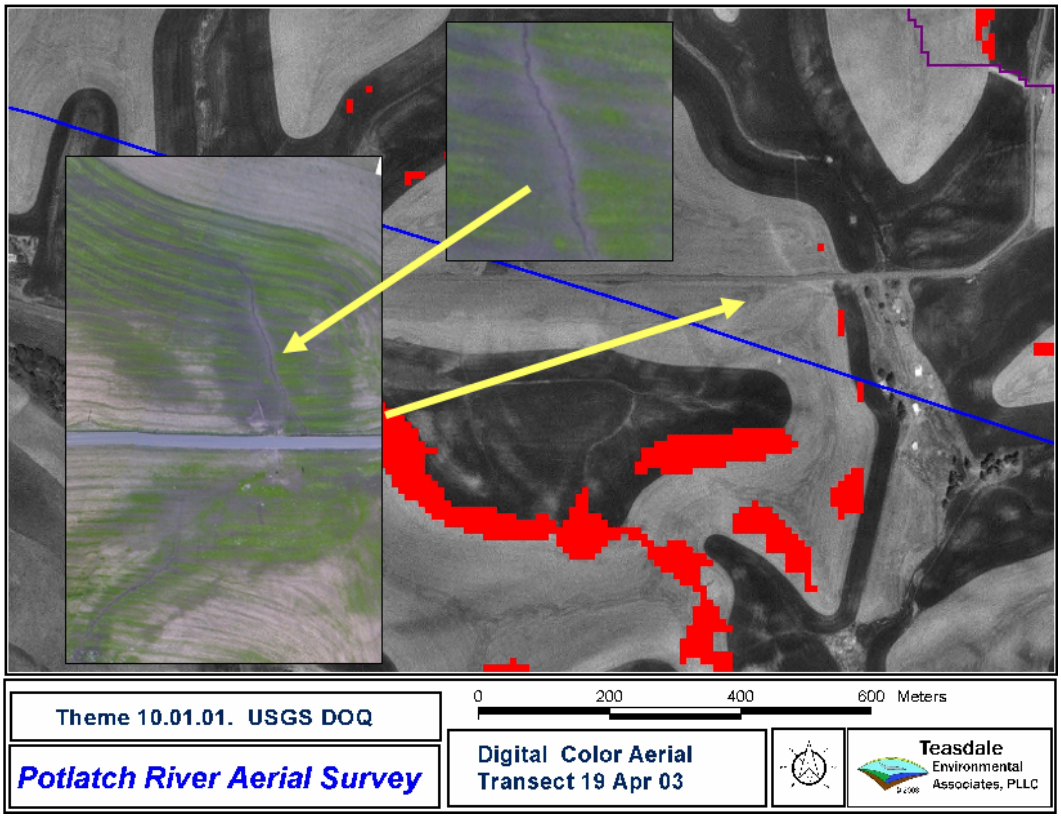

Figure 5.40 Observed soil erosion in a location identified by the EPI.

5.8 Classification of Hydrologic Land Cover Types

Current land cover and land use information are prerequisites to efficient natural resource and environmental management (Anderson et al. 1976; Campbell 1996). Accurate land cover information is also a central data requirement of runoff and erosion modeling. Two of the most widely adopted hydrologic equations, the Soil Conservation Service TR55 runoff equation and the Revised Universal Soil Loss Equation (RUSLE), are formulated with land cover derivatives as primary variables. Watershed scale hydrologic models including SWAT, HECHMS and HSPF require land cover data aggregated at the subbasin level. Land cover is a key prediction variable in USGS flood magnitude and frequency regression equations including those in Idaho (Berenbrock

2002). Contemporary watershed modeling practice requires accurate and current land cover information, but dependable data is usually lacking at the onset of model development.

Some watershed characterization objectives, such as the analysis of seasonal soil erosion, require very current land cover data, so it is questionable to depend on aged land cover data without supplemental verification. The soil erosion and sedimentation study of the lower Potlatch River basin motivated the development of a hydrologically relevant digital land cover map of the Potlatch Basin study region. Though not part of the formal products required by the project contract, the current land cover classification is an essential component of the related research. It also offers a good opportunity to demonstrate the joint use of satellite and aerial imagery in hydrological assessment.

The land cover classification was developed primarily from the October 24, 2003 Landsat 7 image. Landsat 7 sensors were designed for efficient discrimination of land cover and vegetation detail over large areas (Goward and Masek 2001). It remains the most cost effective choice for evaluation of the current land cover despite failure of a sensor component that results in gapped coverage in the Potlatch Basin area. A late fall season land cover map better describes hydrologic condition and erosion susceptibility prior to the winter-spring erosion period.

Land cover information is extracted from satellite imagery through the process of image classification. Image classification proceeds through several steps to produce a final classified land cover map or digital coverage:

- Identify desired land cover classes
- Select the satellite or aerial images
- Preprocess the satellite image

- Identify reference sites for each land type within the image coverage area
- Develop final classification rules
- Select an image classifying technique
- Classify the satellite image with image processing software
- Assess the accuracy of the classified map (coverage)
- Develop final land cover map products

Image classification procedures vary in complexity depending on classification objectives, image quality and analyst preference. A large body of literature addresses the technical aspects of satellite image classification. Basic approaches and techniques are presented in standard remote sensing texts. The procedural steps above are briefly discussed to give an overview of the rationale and methods adopted to produce the 2003 fall land cover map of the Potlatch basin study region.

5.8.1 Existing Digital Land Cover

Existing land cover data for the Potlatch Basin is limited. The best existing is the 1992 National Land Cover Dataset (Figure 5.41) derived from satellite imagery collected nearly 20 years ago, which does not contain detail that adequately describes current land cover during the non-growing season. Only two classes of tilled agricultural land are classified in the 1992 NLCD, small grains and fallow, representing 50 and 20 percent of the area of the primary agricultural subbasins (Table 5.7). These classes might indicate general erosion susceptibility, but the distribution, proportion, time of year represented, and applicability to the current state of land cover are unknown. In addition, accuracy of the NLCD Level II classification is about 65 percent (Stehman et al. 2003).

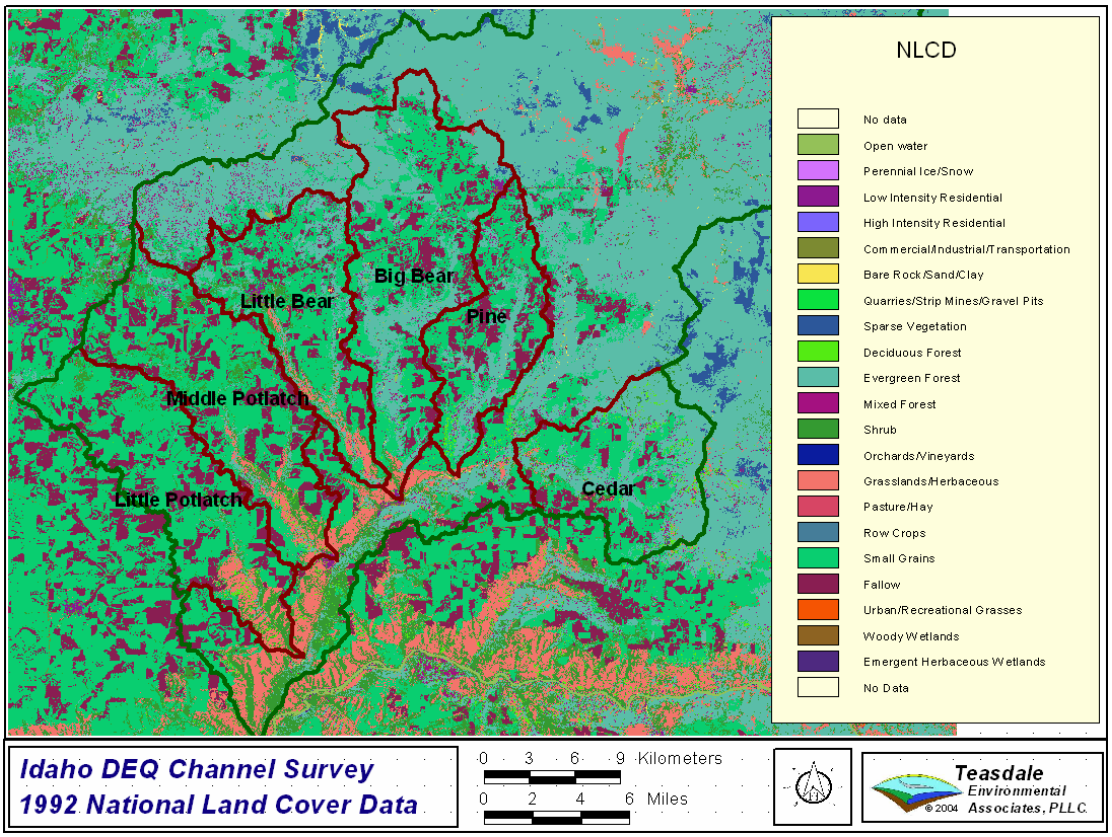

Figure 5.41 1992 digital National Land Cover Data of Potlatch River Basin study area.

NLCD 1992 Percent Cover by Subbasin and Cover Class (actual NLCD grid areas)							
Type	Big Bear	Cedar	Little Bear	Little Potlatch	Middle Potlatch	Pine	Total
			% Cover				
11 Open Water	0.4%	0.1%	0.3%	0.0%	0.1%	0.3%	0.2%
21 Low Intensity Residential	1.0%	0.2%	0.8%	0.0%	0.2%	0.8%	0.5%
23 Commercial/Industrial/Transportation	0.6%	0.2%	1.1%	0.1%	0.6%	1.0%	0.6%
31 Bare Rock/Sand/Clay	0.1%	0.0%	0.1%	0.0%	0.0%	0.1%	0.0%
33 Transitional	0.2%	0.4%	0.0%	0.0%	0.0%	0.0%	0.1%
41 Deciduous Forest	0.2%	2.9%	0.1%	1.0%	0.7%	1.0%	0.9%
42 Evergreen Forest	32.3%	42.5%	15.5%	0.9%	3.8%	20.5%	18.8%
43 Mixed Forest	1.0%	2.7%	1.1%	0.2%	0.7%	1.8%	1.1%
51 Shrubland	0.7%	2.8%	7.4%	8.1%	10.3%	0.0%	5.1%
71 Grasslands/Herbaceous	0.9%	0.8%	4.3%	6.6%	4.9%	0.1%	3.1%
81 Pasture/Hay	0.1%	0.1%	0.0%	0.0%	0.0%	0.0%	0.0%
83 Small Grains	45.6%	36.5%	51.7%	59.4%	53.7%	49.5%	49.7%
84 Fallow	16.9%	10.8%	17.5%	23.7%	25.0%	24.8%	19.8%
91 Woody Wetlands	0.0%	0.0%	0.0%	0.0%	0.0%	0.0%	0.0%
92 Emergent Herbaceous Wetlands	0.0%	0.0%	0.01%	0.0%	0.0%	0.0%	0.0%
Total	100.0%	100.0%	100.0%	100.0%	100.0%	100.0%	100.0%

Table 5.7 1992 National Land Cover Data for the Potlatch River Basin study area.

5.8.2 Desired land cover classes

Factors heightening erosion susceptibility of agricultural soils in the Palouse region have been investigated for nearly thirty years and have been unequivocally identified in research reports and agricultural practice guidance (Michalson et al. 1999). A primary conclusion of the research and practical trials is that "cropping practices that leave the largest amount of (crop) residues on the soil surface generally will provide the most protection against soil erosion" (Elliot et al. 1999). Since sediment production was the focus of the Potlatch Basin research, a land cover classification that emphasizes differences in hydrologic condition and erosion susceptibility during the winter-spring period when most erosion occurs would best serve the objectives of the study. Soil erosion in the lower Potlatch basin is discussed in greater detail in Section 7.

Erosion susceptibility is not a discrete phenomenon, but grades across a continuum of soil and terrain. It varies with landscape position at less than first order channel scale. Semi-empirical models can sometimes avoid the scale limitations of physically based models. They attempt to predict watershed sediment yield by empirical relationships with land cover properties, storm hydrology and other variables. A good representative is the Modified Universal Soil Loss Equation (MUSLE) developed by Williams and Berndt (1977).

A continuous grid cell-based assessment might be usefully adopted at field or farm scale, but would tend to obscure management associations at watershed or basin scale. Discrimination of hydrologic condition and erosion susceptibility at approximately the scale of a typical agricultural field is a necessary simplification for this study. Ideal land cover classes would represent a consistent inter-annual stratification of vegetative

cover and crop residue associated with specific land management practices (e.g. conventional fall tillage, conservation tillage, CRP). Actual classes, however, are conditioned on constraints of spectral separability of the selected satellite imagery and logistics of reference site identification and assessment. The initial research discussed in Section 5.7 demonstrated that selection of an appropriate late fall satellite image and acquisition of ground reference data by aerial survey methods improves classification reliability.

Hydrologically relevant land cover classes that could be discriminated in the fall Landsat 7 image in the initial research included:

- Low residue tilled agricultural land
- Medium residue tilled agricultural land
- High residue tilled agricultural land
- Untilled stubble
- Burned fields
- Perennial grass (pasture, hay, grass CRP, canyon grassland)
- Dense shrubland
- Open shrubland
- Dense forest
- Open forest
- Surface water
- Barren nonvegetated, disturbed and constructed sites

The classes represent the full range of biomass and residue variation across the study region during fall and winter. The classes are compatible with the USGS modified Anderson Level II classification system developed for the National Land Cover Dataset (NLCD). The NLCD classification system could not be adopted exclusively because Level II classifications are too broad in some categories for effective hydrologic

characterization. The Anderson Level II classes and extended level III subclasses are listed in Table 5.8.

Fall - Spring Land Cover Classifications for the Potlatch Basin				
Anderson Level II (NLCD) Classes			Level III Classes	
Category	Code	Class	Code	Subclass
1 Water				
	11	Open Water		
	12	.Perennial Ice/Snow		
2 Developed				
	21	Low Intensity Residential		
	22	High Intensity Residential		
	23	Commercial/Industrial/ Transportation		
3 Barren				
	31	Bare Rock/Sand/Clay Quarries/Strip Mines/Gravel		
	32	Pits		
	33	Transitional		
4 Forested upland				
	41	Deciduous Forest		
	42	Evergreen Forest		
			421	Dense Forest
			422	Open Evergreen Forest
	43	Mixed Forest		
5 Shrubland				
	51	Shrubland		
6 Non-natural wooded				
	61	Orchards/Vineyards/ Other		
7 Herbaceous Upland				
	71	Grasslands/Herbaceous		
8 Herbaceous Planted/Cultivated				
	81	Pasture/Hay		
			811	Pasture
			812	Hay
			813	Grass dominated transitional (CRP)
			814	Bluegrass
			815	Burned grass
	82	Row Crops		
	83	Small Grains		
			831	Tilled Low Residue
			832	Tilled Medium Residue
			833	Tilled High Residue
			834	Stubble
			835	Burned stubble
	84	Fallow		
		Urban/Recreational		
	85	Grasses		
9 Wetlands				
	91	Woody Wetlands		
		Emergent Herbaceous		
	92	Wetlands		

Table 5.8 Fall – Spring land cover classes for the Potlatch River Basin study region.

5.8.3 Selection of a Fall 2003 Landsat 7 Image

The Potlatch Basin study region is predominantly agricultural land, grassland and forest. These main types are readily differentiated in the late October and early November Landsat 7 imagery (Figure 5.42). During this period spectral differences between coniferous forest, harvested agricultural land and perennial grass cover are greatest. Soil exposure by fall tillage in the Potlatch Basin is mostly complete at this time, yet fall seeded crops have little foliar mass to contribute to spectral reflectance.

The October 24, 2003 path 42 row 28 Landsat 7 image was the most cloud-free image that covered the study region. Earlier images showed more small grain stubble (thus incomplete fall tillage) while later images were significantly obscured by clouds. Lower sun angle and longer shadows in later images also tend to inhibit image classification in the canyons and hilly Palouse terrain. Spatial and proportional distribution of over-winter land cover types in the Potlatch Basin persist from late fall to start of spring tillage operations, around the middle of March in 2004. The October 24 Landsat 7 image well represents the maximum amount of low residue soil exposed to winter erosion.

Striping in the Landsat 7 image is caused by failure of the scan line corrector (SLC) component of the Enhanced Thematic Mapper Plus (ETM+) sensor in May 2003. The SLC is inoperative resulting in linear gaps in the image plane across all bands. Images produced after the malfunction are designated as SLC-Off and are available from USGS at a reduced price to encourage their use. Spectral information missing in the gaps is not recoverable and the sensor malfunction appears to be permanent. Further discussion of the SLC problem is in Appendix 5.1.

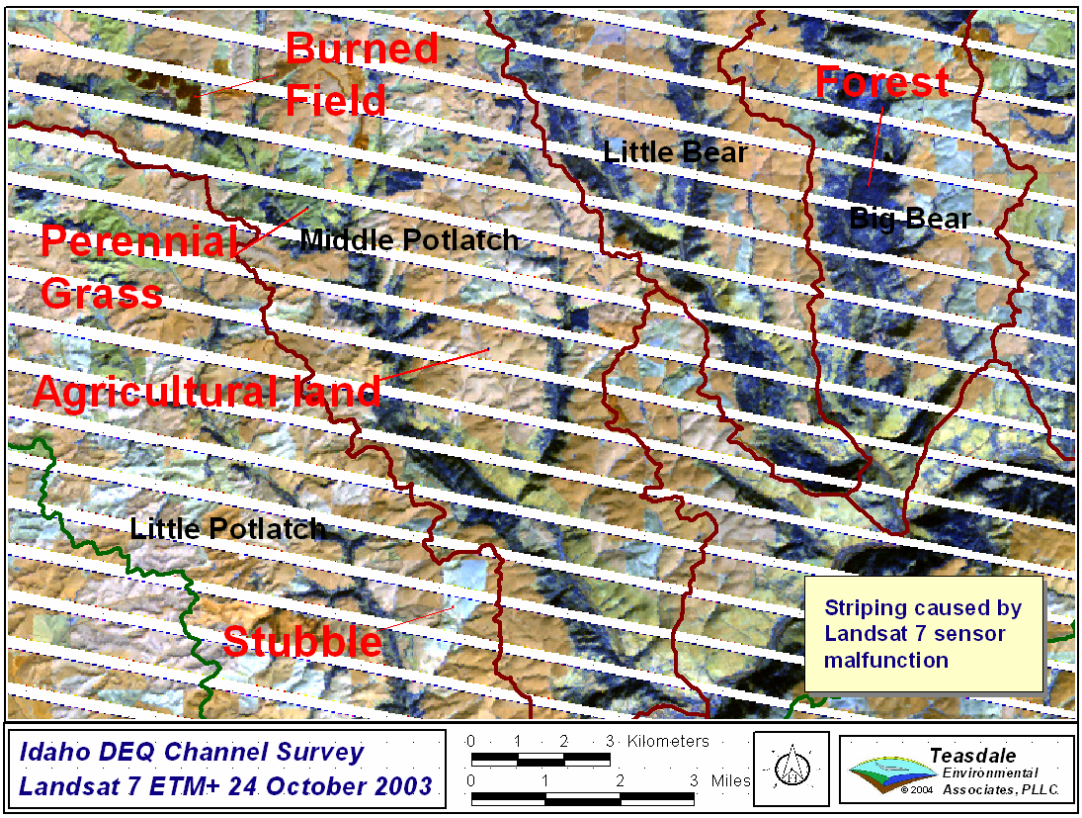

Figure 5.42 Landsat 7 image from October 24, 2003; bands 4,5,7 as blue, green and red.

Gap locations are systematically random as determined by orbital position of the satellite at the time of image acquisition. Approximately 80 percent of the study region is imaged when gaps are excluded. The SLC-Off gaps have little statistical effect on estimates of proportional coverage at the subbasin level. Information missing in the gaps could be inferred from adjacent stripes or determined from ancillary data if a continuous thematic coverage is desired. USGS offers a modified image product with gaps filled with comparable images from previous years. The modified product was not selected for use in this study because of the unknown bias introduced into proportional estimates and measures of classification accuracy.

5.8.4 Reference Site Selection

High-resolution natural color digital aerial images acquired on October 21 and November 6, 2003 provide reference sites for classification of the October 24, 2003 Landsat 7 image. Ideally reference imagery should be obtained on the same day as a Landsat 7 overpass, but that was not possible in this case because of other aerial imaging commitments. The aerial image flight dates bracket the Landsat 7 acquisition and provided an opportunity to evaluate the rate of land cover conversion by late season tillage. The reference aerial images were acquired along four north-south flight lines spaced 5 kilometers apart across the Little Potlatch, Middle Potlatch and Little Bear subbasins (Figure 5.43). These flight lines nearly coincide with flight lines number 5, 10, 15, and 20 of the March 2004 digital aerial imagery acquired for the ephemeral gully assessment.

Ground pixel resolution (GPR) of the reference site aerial images is approximately 20 cm. The level II and III land cover classes listed in Table 5.8 are directly interpreted from the aerial images. Figure 5.44 is one of the October 21 aerial images showing several Level III classes.

Agricultural residue and forest density classes adopted in this study are qualitative. Quantitative relationships between image reflectance and biomass and surface cover have not been determined, but merit investigation in future research.

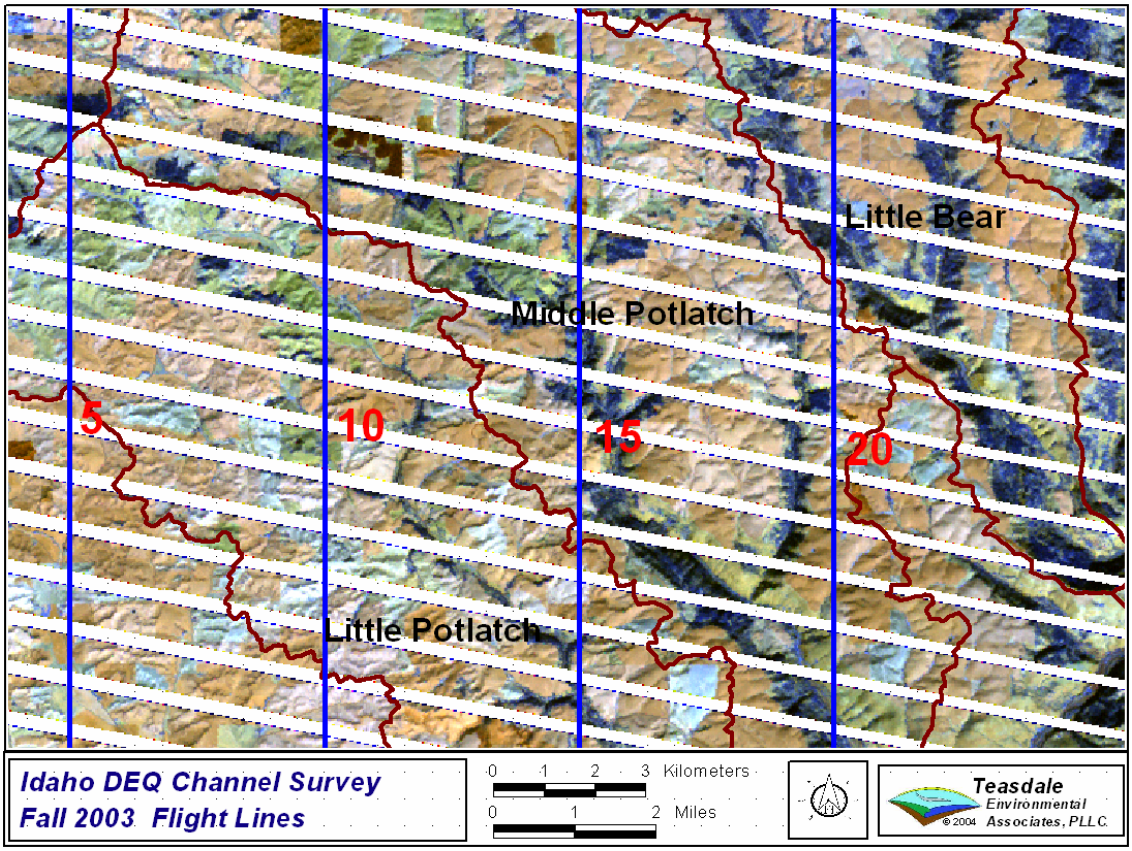

Figure 5.43 Flight lines for October and November 2003 reference site aerial imagery.

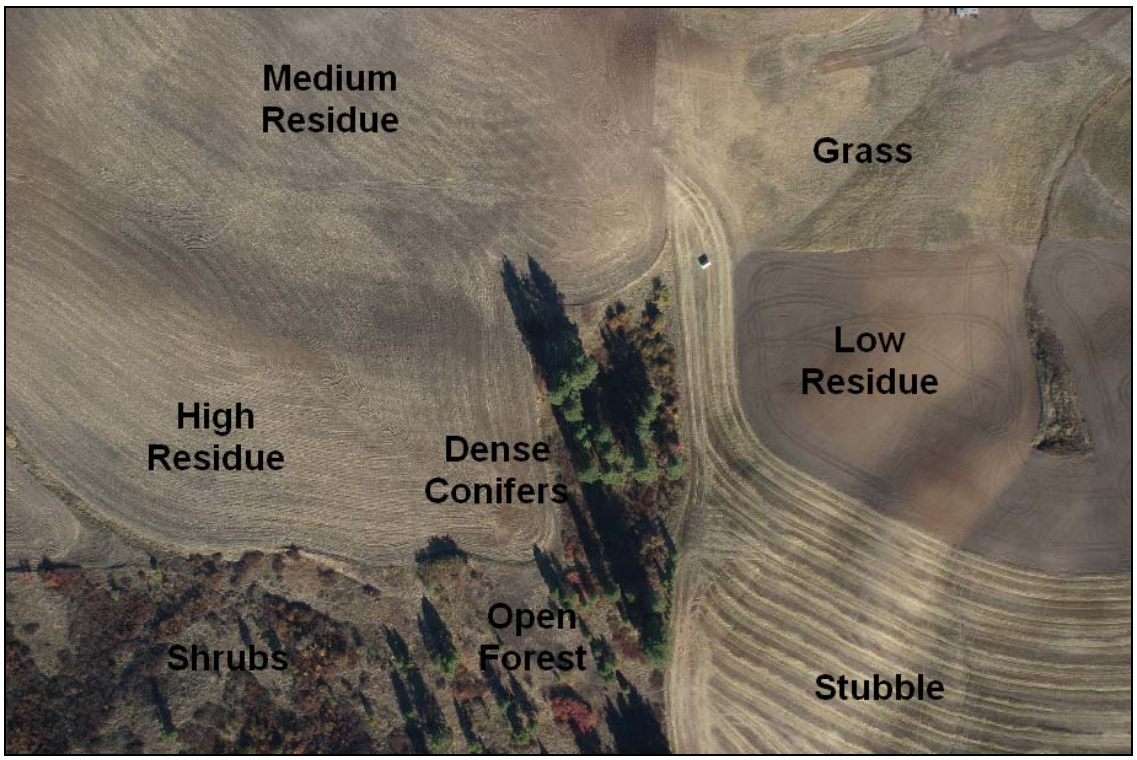

Figure 5.44 Natural color digital aerial reference site image, October 21, 2004.

Systematic randomly sampled image locations were selected along the flight lines of the October 21 aerial imagery and georeferenced to the same projection as the October 24 Landsat 7 image. Reference sites employed in the development phase of image classification are called training sites. Training site polygons were delineated for representative patches within the major land cover types. Training polygons were delineated from the interiors of relatively homogeneous patches to reduce the occurrence of bimodal spectral signatures (Campbell 1996). Selection of training sites for the actual classification process is iterative. Training site polygons may be eliminated from classification computations if they later prove to contribute conflicting spectral information. The continuous aerial image swaths provide a surplus of potential reference sites so the analyst has latitude to seek an optimum suite of sites.

Spectral confusion was evident with some training polygons selected from the October 21 aerial images. Confusion arises because of the three day separation between the aerial image flight and the Landsat 7 overpass. Some fields were still being tilled during late October. Confusion was most apparent between training polygons of stubble fields that were tilled after the October 21 aerial image flight but before the October 24 Landsat 7 overpass. The stubble land cover conversion was easily recognized by comparing the Landsat (bands 4,5,7) image with the October 21 and November 6 aerial images. Confusion from fields burned during the intervening period were also readily identified. Confusion arising from secondary tillage operations that more subtly affect surface residue were harder to identify, but appear not to have unduly influenced the land cover classification.

Reference sites for assessment of the accuracy of the classified land cover map were selected from the November 6, 2003 aerial images.

5.8.5 Development of Classification Rules

Rules for assigning land cover to classes should be mutually exclusive and exhaustive (Congalton and Green 1999), meaning that classes should not overlap and all pixels in the image should be assigned to a class. Classification rules for this study were purposely uncomplicated and take advantage of an analyst's intuitive ability to recognize common land types in high-resolution natural color aerial imagery. During preliminary research images like Figure 5.44 were shown to a variety of imagery users. Most could quickly identify the general hydrologic classes adopted in this study with a high degree of confidence.

Rules for NLCD classes are primarily interpretive and described with simple narrative. Classification rules for the NLCD modified Anderson Level II classes are included in Appendix 5.2. Classification rules for the extended Level III classes in this study are also interpretive and described with narrative:

421. **Dense Forest** – stands of conifer trees (Douglas fir, ponderosa pine, grand fir, western red cedar, western larch) with canopy cover greater than 75 percent. Understory of shrubs or herbaceous plants. Many included cultivated evergreens such as Christmas tree plantations.

422. **Open Forest** – areas dominated by conifer trees (Douglas fir, ponderosa pine, grand fir, western red cedar, western larch) with canopy cover less than 75 percent.

Understory of shrubs or herbaceous plants. This class does not include areas with widely spaced trees fewer than about three trees per acre.

811. **Pasture** – areas dominated with smooth textured short grass lacking uniform tillage or harvest tracks. Fields are usually irregular in shape and located near farm buildings with indications of fence rows and livestock trails. Green color is lacking in November aerial imagery.

812. **Hay** – Areas dominated with smooth textured short grass with indications of uniform tillage or harvest tracks. Bales and windrows may be visible. Green color may be visible in November imagery.

813. **Grass Dominated Transitional** – areas dominated with mottled texture medium to tall grass lacking recent tillage or harvest tracks. Invasive or planted trees and shrubs may be present. Green color is lacking in November imagery. Large acreages in northern portions of the study area may be enrolled in the Conservation Reserve Program (CRP). Grass dominated transitional may be difficult to separate from grazing land or low use pasture. Confusion with these classes is not particularly hydrologically significant.

813. **Bluegrass** – cultivated short to medium grass often with a bunched texture and indications of tillage or harvest tracks. Green color is usually visible in November images.

814. **Burned grass** – recently burned grass fields are characteristically black in November images. Burning usually does not obscure the grass texture so burned grass may be separated from burned small grain stubble fields. Burned grassed waterways may be identified by shape and landscape position. A black charcoal surface layer may be visible in emergent grass in spring aerial imagery.

831. **Tilled Low Residue** – recently tilled fields with less than 20 percent surface crop residue. Crop residue is identified by light brown to yellow to white color and contrast with exposed soils. Crop residue patterns follow tillage tracks. Surface area of crop residue is estimated visually.

832. **Tilled Medium Residue** – recently tilled fields with between 20 and 70 percent surface crop residue. Crop residue is identified by color contrast with exposed soils and textured appearance. Crop residue patterns follow tillage tracks. Surface area of crop residue is estimated visually. Small grain and legume residue is estimated similarly though soil protection characteristics may be different. Tilled medium residue fields usually have rougher texture than tilled low residue fields.

833. **Tilled High Residue** – recently tilled fields with greater than 70 percent surface crop residue. Surface area of crop residue is estimated visually. Tillage tracks are visible and suppress, but may not eradicate, harvest tracks. Very high residue tilled fields may be difficult to separate from some stubble fields. Confusion with stubble is not hydrologically significant.

834. **Stubble** – untilled small grain and legume fields with high surface residue. Harvest tracks are visible. Color varies from light brown to yellow to white. Stubble is the most easily identified of the Level III agricultural classes.

835. **Burned Stubble** – recently burned stubble fields are characteristically black in October and November images. Burning usually does not completely suppress stubble texture and harvest tracks, so burned stubble may be separated from burned grass fields.

5.8.6 Selection of a Classifying Technique

Thematic land cover datasets are commonly produced from satellite imagery with two broad categories of digital image classification techniques: unsupervised and supervised classification. Both are performed with commercial image analysis software such as Idrisi© or ERDAS Imagine©. In unsupervised classification, the software automatically groups pixels into categories of like signatures without an analyst providing information about potential land cover types. After completion of the pixel categorization, the user identifies what cover types those categories represent. With supervised classification, the user develops the spectral signatures of known categories, such as urban and forest, and then the software assigns each pixel in the image to the cover type to which its signature is most similar. Concepts and algorithms of supervised and unsupervised classification are thoroughly discussed in standard texts of remote sensing and geographic information systems analysis. Step-by-step computer based tutorials that demonstrate supervised and unsupervised classification techniques with the Idrisi© software were produced as part of the Advanced Watershed Tools training materials for the Jordanian Water Ministry (Teasdale and Barber 2003).

Several classification techniques were attempted including unsupervised isodata clustering, tasseled-cap transformations, principal component analysis, and several supervised classification methods. The maximum likelihood supervised classifier in the Idrisi© software package performed best among those tried with this particular Landsat image. The tests of possible techniques were not exhaustive or conclusive. Future research should examine classification methods in detail and include textural classifiers, segmentation algorithms and fuzzy logic classifiers.

5.8.7 Selection of Training Sites

Training sites for maximum likelihood classification were selected by observation of the aerial image transects and the October 24 Landsat 7 image. Some of the training site polygons are superimposed on the 2004 USGS/State of Idaho DOQ in Figure 5.45. This new DOQ was not used in the classification or acquisition of training site data because it was developed from aerial imagery acquired during the summer of 2004 when mature crop cover makes it difficult to evaluate the extent of erosion susceptible fall-tilled fields. Also the GPR of the 2004 DOQ is a 1.0 meter, too low to judge relative concentrations of surface residue. Though all the classes in Table 5.8 could be identified, the relative proportion of area was small. A reduced set of land cover classes were selected for final classification work. These classes are listed in Table 5.9.

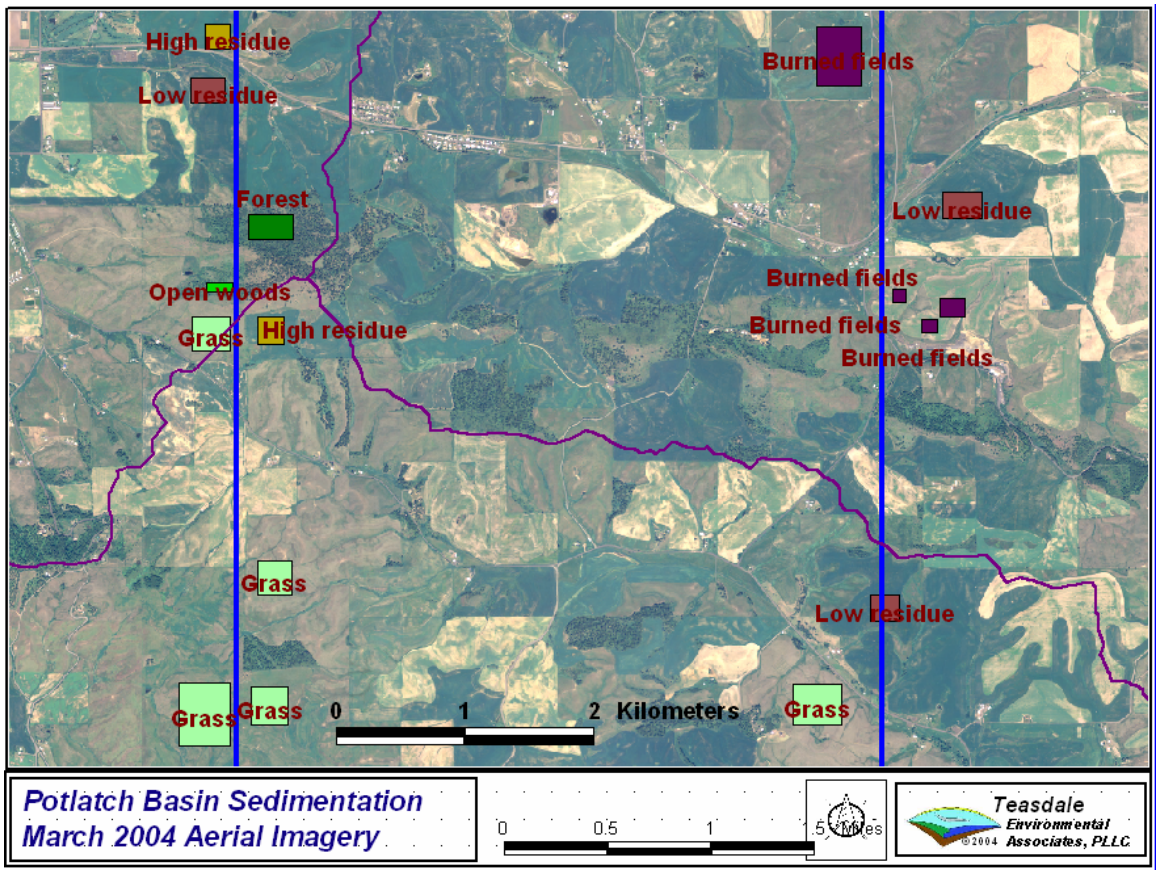

Figure 5.45 Classification training sites along the October 21, 2003 aerial transects.

Code	Class Name
1	Low residue
2	Medium residue
3	High residue
4	Stubble
6	Burned fields
7	Grass
11	Forest
13	Open woods and shrubs
15	Water

Table 5.9 Fall 2003 hydrologic land cover classifications.

5.8.8 Final 2003 Hydrologic Land Cover Dataset

All bands of the October 24, Landsat 7 image except the thermal band were used in the Idrisi MAXLIKE classification procedure. The Idrisi classified image was exported to tif format and converted to an ESRI grid. Initial inspection of the grid classes

showed many small isolated pixels that were not hydrologically relevant. The classified grid was generalized with a 3 by 3 pixel median filter. No further processing was performed except to subset the grid to fit the boundaries of the study watersheds. The final classified dataset is shown in Figure 5.46.

The hydrologic land cover classes are compared with the October 21 natural color aerial images in Figure 5.47,Figure 5.48 and Figure 5.49. Ground pixel resolution of the aerial images in Figure 5.47 is about 17 cm. The background for Figure 5.47 is the summer 2004 USGS/State of Idaho DOQ.

The original maximum likelihood hydrologic classification is superimposed over the aerial images in Figure 5.48. Permanent grass cover is well represented down to the about the size of a single Landsat pixel. The tilled soil residue classes exhibit some confusion, but generally agree with the observed classifications. A small area of medium residue soil was classified as low residue may have been influenced by higher soil moisture from recent tillage. Only a few pixels classified as forest and open woods with shrubs are present in the area covered by Figure 5.48, but these are mostly representative of the actual land cover. Classifications at the transitions between cover types are irregular with many mismatched pixels, typical of hard classifiers.

The filtered and generalized maximum likelihood classifications are superimposed over the aerial images in Figure 5.49. The 3 by 3 pixel window eliminated most of the isolated pixels and produced a more a field scale classification. However, the filtering algorithm may have eliminated some real differences in surface residue. Apparent surface density is observed in the aerial images to vary within many fields. Classification results are summarized in Table 5.10.

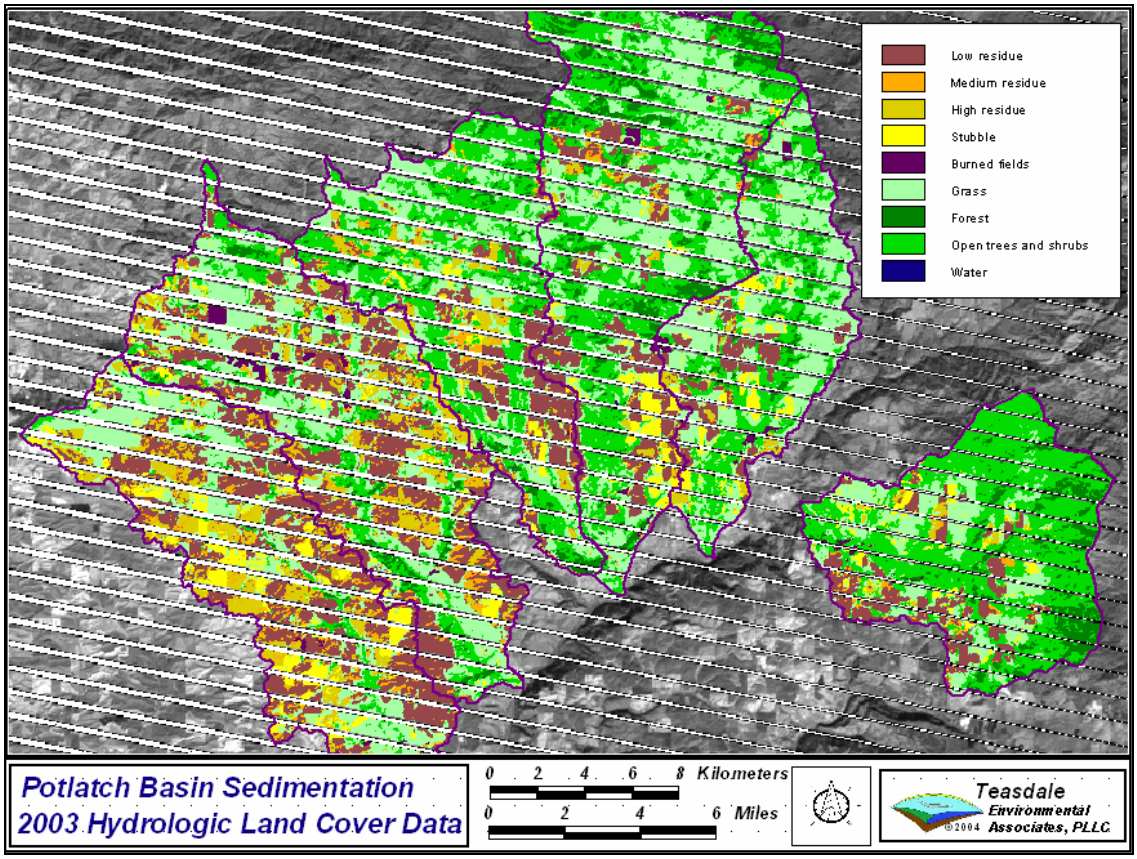

Figure 5.46 Final fall 2003 hydrologic land cover classification.

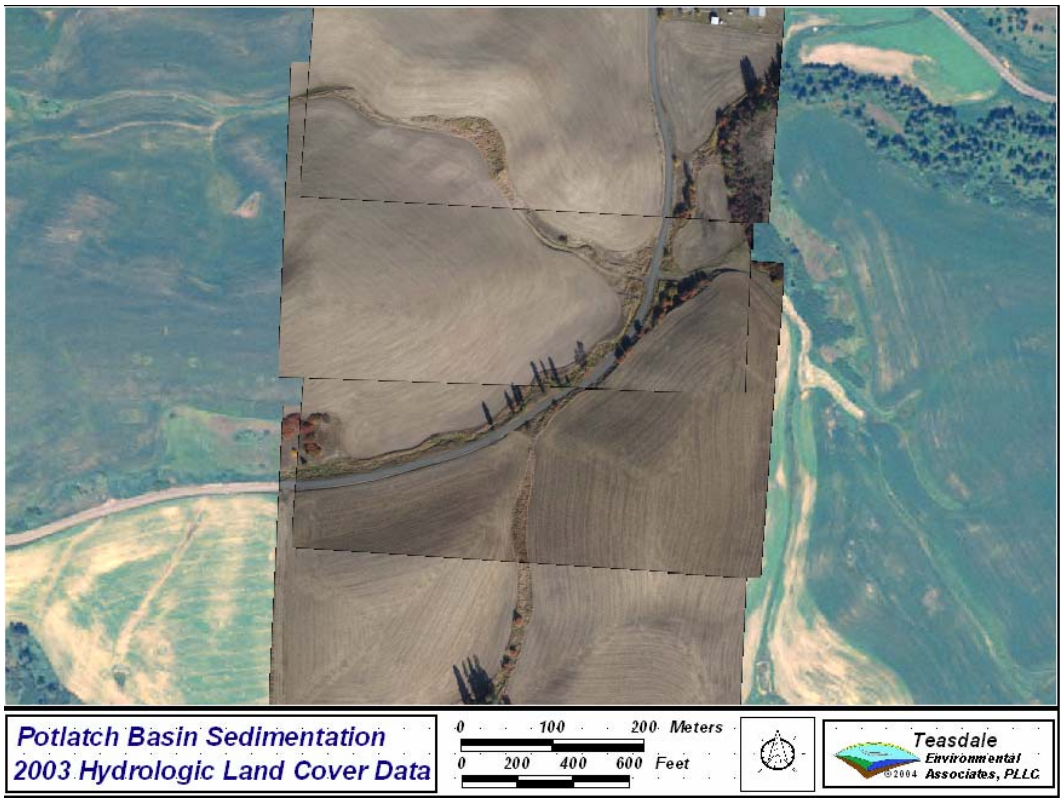

Figure 5.47 October 21, 2004 aerial images in the Little Potlatch Creek basin.

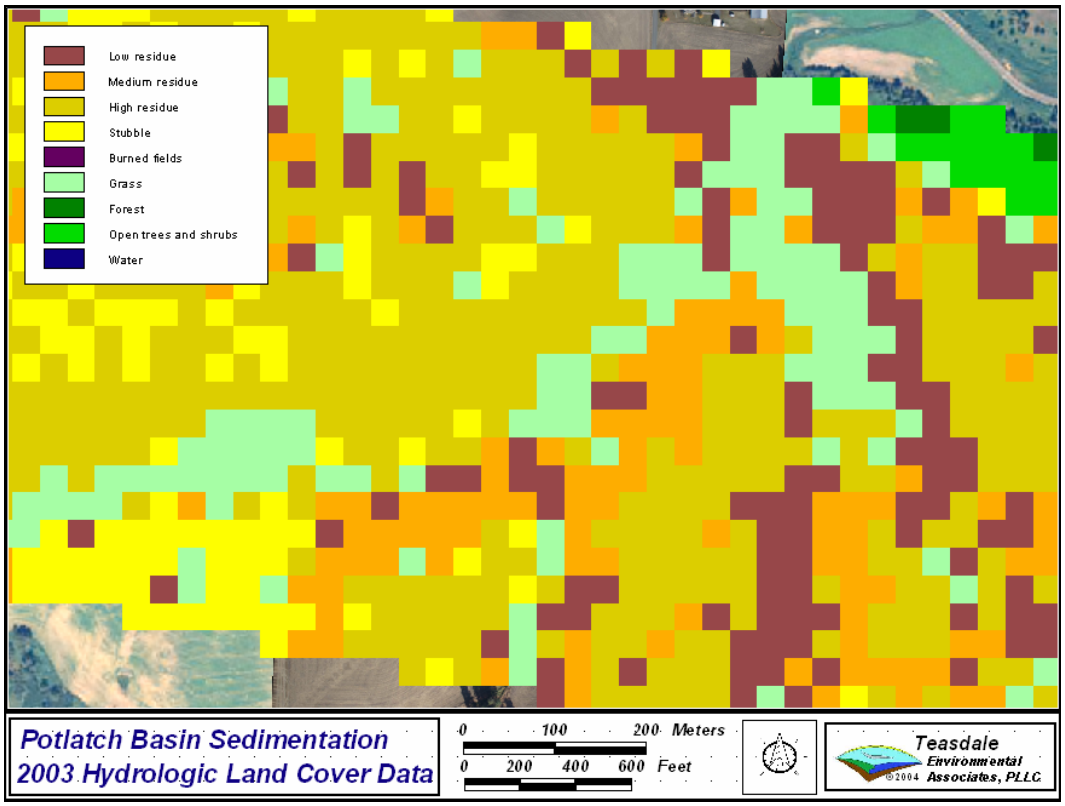

Figure 5.48 Original maximum likelihood hydrologic classification.

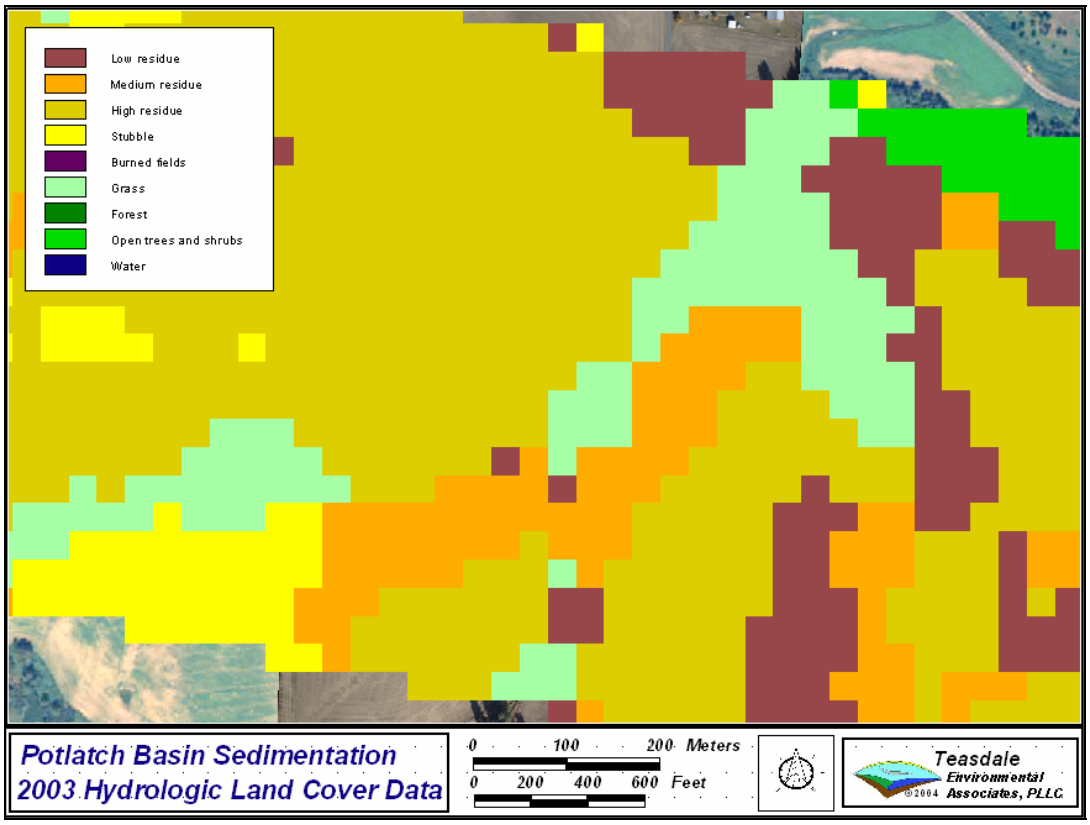

Figure 5.49 Final filtered and generalized maximum likelihood hydrologic classification.

	Area of Land Cover (ha)							
Land Cover Type	Big Bear	Cedar	Litte Bear	Little Potlatch	Middle Potlatch	Pine	Total	Percent Cover
Low residue	1,390	994	1,280	3,049	3,287	662	10,661	18.6%
Medium residue	165	124	205	641	635	38	1,809	3.2%
High residue	256	171	614	1,433	1,246	210	3,930	6.9%
Stubble	492	307	244	1,047	326	391	2,806	4.9%
Burned fields	91	28	20	75	213	78	504	0.9%
Grass	4,337	1,690	2,340	2,834	3,102	3,004	17,307	30.2%
Forest	1,304	868	365	37	331	245	3,150	5.5%
Open woods	5,388	4,593	3,134	482	1,522	2,037	17,156	29.9%
Water	1.6	0	0.5	0	0	0	2	0.0%
Total	13,424	8,775	8,200	9,599	10,662	6,664	57,325	100.0%

Table 5.10 Summary of hydrologic land cover classification.

Approximated 19 percent of the area within the study region is classified as low residue tilled agricultural field. Fields classified as medium, high and stubble residue comprise about 15 percent of the total area. Grass and open woodland and shrub cover are each about 30 percent of the area. Forest and burned fields were 6 and 1 percent. There was almost no land cover classified as water. The total area covered by the classification (57,325 ha) is less than the area of the study basins (73,649 ha) because of

the gaps in the Landsat 7 image. The Landsat 7 image covers about 78 percent of the study region.

Classification results in Figure 5.47, Figure 5.48 and Figure 5.49 are typical of the observed accuracy along the aerial image transects. Accuracy is worse in areas of fragmented land cover and better in homogeneous areas. The accuracy of thematic classifications can be assessed by several techniques including the line transect sampling technique discussed in Section 4. A common approach is to construct an error matrix as discussed in the next section.

5.8.9 Classification Accuracy Assessment

Accuracy assessment is an integral part of thematic classification (Congalton and Green 1999) and some form of accuracy assessment should be performed on all image classifications intended for operational use. Doing so allows a degree of confidence to be attached to the results and indicates whether the analysis objectives were achieved (Richards 1993). The most common forms of accuracy assessment for remote sensing derived classifications are the error matrix and Kappa statistic (Congalton 1991). A preliminary accuracy assessment of the 2003 hydrologic land cover classification data was developed with these techniques.

The error matrix compares a sample of actual land cover types with the land cover designations assigned by the classification algorithm. Reference sites, also called ground truth sites, should be selected in a statistically valid manner (if possible) throughout the coverage area of the classification. A two dimensional error or confusion matrix is constructed of the test site data versus the designated classifications.

The sample unit is typically a 3 by 3 block of pixels distributed throughout the area to avoid spatial autocorrelation. Congalton and Green (1999) suggest a minimum of 50 samples for each land cover category. Formulas for determining sample size are available. The suggested minimum amounts to 450 samples for the nine categories in the hydrologic land cover classification.

The suggested minimum sample size was not satisfied in this preliminary accuracy assessment. The primary motivation for performing the accuracy assessment was to judge how well the relatively simple classification techniques utilized performed at the scale of a typical agricultural field. A total of 125 reference polygons were digitized in georeferenced November 2003 and March 2004 aerial images along four aerial transects located in the western part of the study region. Typical polygons are superimposed on the 2004 DOQ in Figure 5.50. Average polygon size was 7000 m^2, somewhat less than the 8100 m^2 size of a 3 by 3 block of 30 meter Landsat pixels.

The polygons were selected by moving along a transect of georeferenced images and digitizing *homogeneous* patches of land cover types. Reference sites were not selected from transition areas between types. The homogenous patches were selected solely by observing the aerial image. The selection process was not influenced by the original satellite image or the classification grid. Admittedly, this is a somewhat biased technique, but it gave a better understanding of how well the classification technique worked at the field level. An analysis of the reference data yields the error matrix in Table 5.11. A more strict and formal accuracy assessment could be conducted if desired in future research.

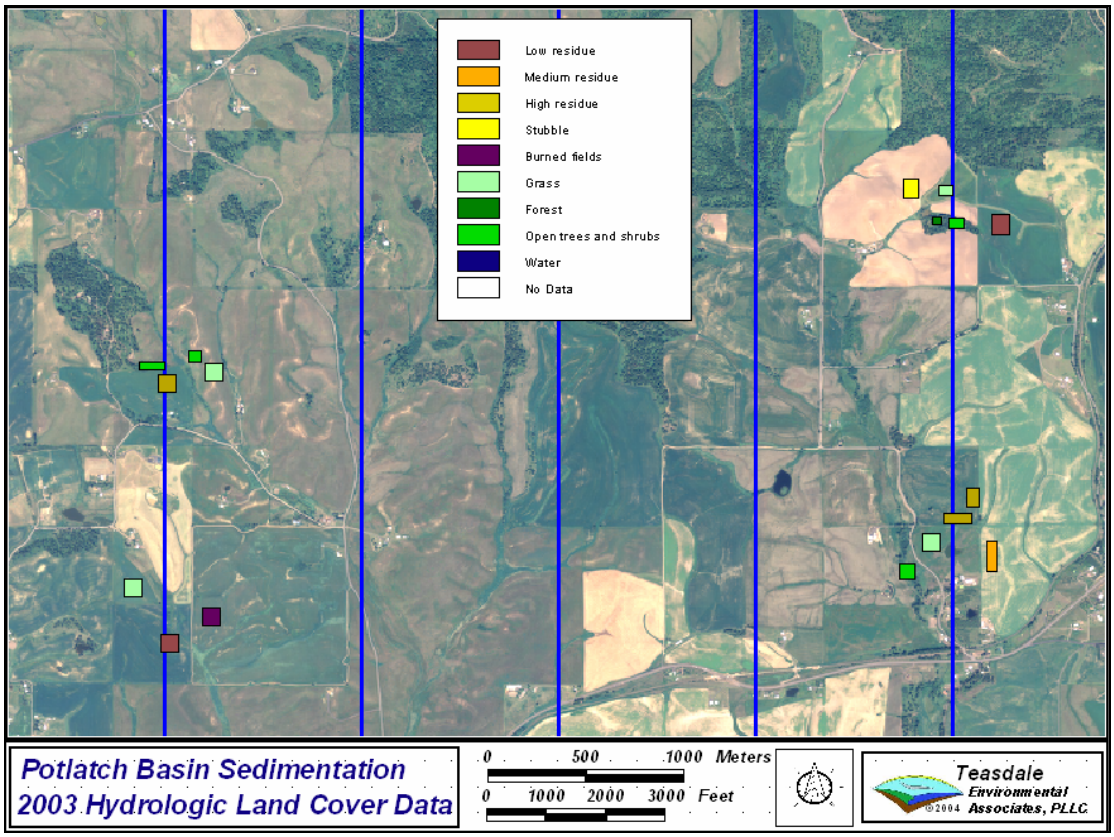

Figure 5.50 Reference site polygons used in accuracy assessment computations.

		Ground Truth Reference											
	Cover Type	Low Residue	Medium Residue	High Residue	Stubble	Burned Fields	Grass	Forest	Open Woods	Water	Marginal Total	Errors of Commission	Consumers Accuracy
Classification Grid	Low residue	265	78	17	0	0	0	0	0	0	360	26.4%	73.6%
	Medium residue	10	31	1	0	1	0	0	0	0	43	27.9%	72.1%
	High residue	0	35	36	0	0	0	0	0	0	71	49.3%	50.7%
	Stubble	0	0	21	24	0	0	0	0	0	45	46.7%	53.3%
	Burned fields	0	0	0	0	10	0	0	0	1	11	9.1%	90.9%
	Grass	0	0	11	4	0	209	2	30	0	256	18.4%	81.6%
	Forest	0	0	0	0	0	0	19	1	0	20	5.0%	95.0%
	Open woods	0	0	0	0	0	0	25	119	0	144	17.4%	82.6%
	Water	0	0	0	0	0	0	0	0	9	9	0.0%	100.0%
	Marginal total	275	144	86	28	11	209	46	150	10	959		
	Errors of Omission	3.6%	78.5%	58.1%	14.3%	9.1%	0.0%	58.7%	20.7%	10.0%			
	Producer accuracy	96.4%	21.5%	41.9%	85.7%	90.9%	100.0%	41.3%	79.3%	90.0%			

Table 5.11 Error matrix for 2003 hydrologic land cover classification

The overall accuracy of the classification is 75 percent and was computed by dividing the sum of the diagonal in Table 5.11 by the total number of grid cells involved in the accuracy assessment:

$$\text{Overall accuracy} = \frac{\sum_{i=1}^{k} n_{ii}}{n} = \frac{722}{959} = 0.75$$

where n is the total number of grid cells in the assessment, n_{ii} is the number of grid cells in each element along the error matrix diagonal and k is the number of unique classes. The subscript *ii* indicates that row and column classes are the same. For example, the error matrix element with subscript 33 has a value of 36 grid cells and represents the intersection of high residue column and the high residue row.

Producer accuracy for each class is computed by dividing the number of correctly classified cells in each class by the number of reference data cells in that class. Producer accuracies for the low residue class were very high at 96 percent. All grass cover reference cells were correctly classified. As illustrated by the 21.5 percent accuracy, the medium residue class was incorrectly classified as low residue and high residue more than it was correct. The high residue class faired better, but was confused with low residue and stubble. These results suggest the difficulty of classifying residue solely by Landsat 7 data. Forest cover was understandably confused with open woods and shrubs. Open woods cover was correctly classified with 79 percent producer accuracy.

It is common practice to compute the kappa statistic which is a measure of agreement based on the difference between the actual agreement in the error matrix and the chance agreement indicated by the row and column totals (Congalton and Green 1999). The kappa statistic is estimated with $\hat{\kappa}$ (called κ hat) in computational form:

$$\hat{\kappa} = \frac{n\sum_{i=1}^{k} n_{ii} - \sum_{i=1}^{k} n_{i+} n_{+i}}{n^2 - \sum_{i=1}^{k} n_{i+} n_{+i}} \qquad 5.17$$

where n is the total number of samples (grid cells); $n_{i+} = \sum_{j=1}^{k} n_{ij}$ is the marginal row total (class total); $n_{+j} = \sum_{i=1}^{k} n_{ij}$ is the marginal column total (reference total); and $n_{i+}n_{+i}$ is the multiplication of the marginal row total for class i by the marginal column total for class i. (i.e., the correct designations).

Analysis of the marginal totals in Table 5.11 provides the values for the $\hat{\kappa}$ computation:

$$\hat{\kappa} = \frac{n\sum_{i=1}^{k} n_{ii} - \sum_{i=1}^{k} n_{i+}n_{+i}}{n^2 - \sum_{i=1}^{k} n_{i+}n_{+i}} = \frac{959(722) - (188793)}{959^2 - (188793)} = 0.69$$

The accuracy assessment suggests that the major hydrological cover types: low to medium residue agricultural fields, high residue and stubble agricultural fields, permanent grass cover, and wooded cover can be successfully classified with late fall Landsat 7 imagery using standard classification techniques. Additional research is necessary to refine the techniques of satellite assessment hydrologically relevant land cover. The main shortcoming of the demonstrated method is the likely inability to consider antecedent soil moisture in the classification process.

5.9 Summary

This section discussed topics found essential to the practical use and understanding of satellite imagery for watershed assessment and aquatic resource evaluation. It presented operational characteristics of satellite imaging and a practical

perspective on the use of satellite imagery in hydrologic characterization of watersheds for hydrologic modeling. Two significant applications of hydrologic assessment were demonstrated with sufficient detail to motivate additional research. A consistent thread throughout the discussion and examples was that aerial imagery and satellite imagery are compatible data sources that can be used jointly to enhance watershed assessment methods.

References for Section 5

Anderson, J. R., Hardy, E. E., Roach, J. T., and Witmer, R. E. (1976). *A Land Use and Land Cover Classification System for Use with Remote Sensor Data*, U.S. Geological Survey, Washington D.C.

ASTM. (2000). *E490-00a Standard Solar Constant and Zero Air Mass Solar Spectral Irradiance Tables*, Committee E21 on Space Simulation and Applications of Space Technology, American Society for Testing and Materials International, Bethesda, MD.

Berenbrock, C. (2002). *Estimating the Magnitude of Peak Flows at Selected Recurrence Intervals for Streams in Idaho; Water Resources-Investigations Report 02-4170*, U.S. Geological Survey, Boise, ID.

Bondelid, T. R., Jackson, T. J., and McCuen, R. H. (1982). "Estimating runoff curve numbers using remote sensing data." Applied Modeling in Catchment Hydrology, V. P. Singh, ed., Water Resources Publications, Littleton, CO, 511-528.

Campbell, J. B. (1996). *Introduction to Remote Sensing*, The Guilford Press, New York.

Chandrasekhar, S. (1950). *Radiative Transfer*, Oxford Univ. Press, New York.

Chavez, P. S., Jr. (1996). "Image-based atmospheric corrections- revisited and improved." *Photogrammetric Engineering and Remote Sensing*, 62(9), 1025-1036.

Chery, D. L., Jr., and Jensen, J. R. (1982). "Lumped water balance mode using cover areas determined by Landsat remote sensing." Applied Modeling in Catchment Hydrology, V. P. Singh, ed., Water Resources Publications, Littleton, CO, 529-544.

Congalton, R. G. (1991). "A review of assessing the accuracy of classifications of remotely sensed data." *Remote Sensing of Environment*, 37, 35-46.

Congalton, R. G., and Green, K. (1999). *Assessing the accuracy of remotely sensed data: Principles and Practices*, Lewis, Boca Raton.

Conway, E. D. (1997). *An Introduction to Satellite Image Interpretation*, John Hopkins Univeristy Press, Baltimore.

Dallam, W. C., Rango, A., and Shima, L. (1975). "Hydrologic Land Use Classification of the Patuxent River Watershed Using Remotely Sensed Data."

Duffie, J. A. B. W. A. (1991). *Solar Engineering of Thermal Processes*, Wiley, New York.

Elliot, L. F., Stott, D. E., Douglas, C. L., Papendick, R. I., Campbell, G. S., and Collins, H. (1999). "Residue management issues for conservation tillage systems." Conservation Farming in the United States: The Methods and Accomplishments of the STEEP Program, E. L. Michalson, R. I. Papendick, and J. E. Carlson, eds., CRC Press, Boca Raton.

Elmore, A. J., Mustard, J. F., Manning, S. J., and Lobell, D. B. (2000). "Quantifying Vegetation Change in Semiarid Environments: Precision and Accuracy of Spectral Mixture Analysis and the Normalized Difference Vegetation Index." *Remote Sensing of Environment*, 73(1), 87-102.

Engman, E. T., and Schultz, G. A. (2000). "Future Perspectives." Remote Sensing in Hydrology and Water Management, G. A. Schultz and E. T. Engman, eds., Springer, New York, 446-457.

Gao, B.-C., and Kaufman, Y. J. (1998). "The MODIS Near-IR Water Vapor Algorithm, Product ID: MOD05 - Total Precipitable Water." National Aereonautics and Space Administration, Greenbelt, MD.

Goward, S. N., and Masek, J. G. (2001). "Landsat--30 Years and Counting." *Remote Sensing of Environment*, 78(1-2), 1-2.

Grodecki, J., and Dial, G. (2003). "Block adjustment of high-resolution satellite Images described by rational polynomials." *Photogrammetric Engineering and Remote Sensing*, 69(1), 59-68.

Hall, D. K., Riggs, G. A., Salomonson, V. V., DiGirolamo, N. E., and Bayr, K. J. (2002). "MODIS snow-cover products." *Remote Sensing of Environment*, 83(1-2), 181-194.

Huang, C., Wylie, B., Yang, L., Homer, C., and Zylstra, G. (2000). *Derivation of a tasseled cap transformation based on Landsat 7 at-satellite reflectance*, U.S. Geological Survey EROS Data Center.

Huete, A. R. (1988). "A Soil-Adjusted Vegetation Index (SAVI)." *Remote Sensing of Environment*, 25(295-309).

Jensen, J. R. (1996). *Introductory Digital Image Processing: A Remote Sensing Perspective*, Prentice-Hall, Upper Saddle River, NJ.

Lauer, D. T., Morain, S. A., and Salomonson, V. V. (1997). "The Landsat Program: Its Origins, Evolution, and Impacts." *Photogrammetric Engineering and Remote Sensing.*, 63(7), 831-838.

Leachtenauer, J. C., Malila, W., Irvine, J., Colburn, L., and Salvaggio, N. (1997). "General image-quality equation: GIQE." *Applied Optics*, 36(32), 8322-8328.

Lean, J., and Rind, D. (1998). "Climate forcing by changing solar radiation." *Journal of Climate*, 11, 3069-3094.

Liang, S., Fang, H., Chen, M., Shuey, C. J., Walthall, C., Daughtry, C., Morisette, J., Schaaf, C., and Strahler, A. (2002). "Validating MODIS land surface reflectance and albedo products: methods and preliminary results." *Remote Sensing of Environment*, 83(1-2), 149-162.

Lillesand, T. M., and Kieffer, R. W. (1994). *Remote Sensing and Image Interpretation*, John Wiley and Sons, Inc., New York.

Liou, K. N. (2002). *An Introduction to Atmospheric Radiation, 2nd Ed.*, Academic Press, Boston.

Loveland, T. R., and Shaw, D. M. " Multiresolution land characterization: Building collaborative partnerships, Gap Analysis: A Landscape Approach to Biodiversity Planning." *Proceedings of the ASPRS/GAP Symposium*, Charlotte, North Carolina, 83-89.

Michalson, E. L., Papendick, R. I., and Carlson, J. E. (1999). *Conservation Farming in the United States: The Methods and Accomplishments of the STEEP Program*, CRC Press, Boca Raton.

Mikhail, E. M., Bethel, J. S., and McGlone, J. C. (2001). *Introduction to Modern Photogrammetry*, Wiley, New York.

Moran, M. S., Jackson, R. D., Slater, P. N., and Teillet, P. M. (1992). "Evaluation of simplified procedures for retrieval of land surface reflectance factors from satellite sensor output." *Remote Sensing of Environment*, 41, 169-184.

Philipson, W. R. (1997). "Manual of Photographic Interpretation, Second Edition." American Society for Photogrammetry and Remote Sensing, Bethesda, ML, 689.

Rees, W. G. (2001). *Physical Principles of Remote Sensing*, Cambridge University Press, Cambridge.

Richards, J. A. (1993). *Remote Sensing Digital Image Analysis*, Springer, Berlin.

Schultz, G. A. (1988). "Remote Sensing in Hydrology." *Journal of Hydrology*, 100(1/3), 239-265.

Schultz, G. A., and Engman, E. T. (2000). "Remote Sensing in Hydrology and Water Management." Springer, New York, 483.

Shih, S. F. (1988). "Satellite Data and Geographic Information System for Land Use Classification." *Journal of Irrigation and Drainage Engineering*, 114(3), 505-519.

Short, N. M. (1998). "Remote Sensing Tutorial, http://rst.gsfc.nasa.gov." Goddard Space Flight Center National Aeronautics and Space Adiministration.

Slack, R. B., and Welch, R. (1980). "Soil Conservation Service Runoff Curve Number Estimates from Landsat Data." *Water Resources Bulletin*, 16(5), 887-893.

Stehman, S. V., Sohl, T. L., and Loveland, T. R. (2003). "Statistical sampling to characterize recent United States land-cover change." *Remote Sensing of Environment*, 86(4), 517-529.

Steven, M. D., Malthus, T. J., Baret, F., Xu, H., and Chopping, M. J. (2003). "Intercalibration of vegetation indices from different sensor systems." *Remote Sensing of Environment*, 88(4), 412-422.

Stull, R. B. (1995). *Meteorology Today for Scientists and Engineers*, West Publishing, Mineapolis/St. Paul.

Teasdale, G. N., and Barber, M. E. (2003). "Advanced Watershed Tools - Introduction to Landsat 7." Washington Water Research Center, Amman, Jordan.

USGS. (1998). "Landsat 7 Science Data Users Handbook." U.S. Geological Survey and National Aeronautics and Space Administration.

USGS. (2000). "Landsat 7 Image Assessment System (IAS) Geometric Algorithm Theoretical Basis Document." U.S. Geological Survey, Denver, CO.

Vogelmann, J. E., Howard, S. M., Yang, L., Larson, C. R., Wylie, B. K., and Driel, N. V. (2001). "Completion of the 1990s National Land Cover Data Set for the Conterminous United States from Landsat Thematic Mapper Data and Ancillary Data Sources." *Photogrammetric Engineering and Remote Sensing*, 67(6), 650-662.

Williams, J. R., and Berndt, H. D. (1977). "Sediment Yield Prediction Based on Watershed Hydrology." *Transactions of the American Society of Agricultural Engineers*, 20, 1100-1104.

Appendix 5.1

Landsat 7 Satellite, ETM+ Sensor and Image Products

Landsat 7 acquires repetitive, synoptic coverage of continental surfaces with multispectral images in the visible, near infrared, shortwave, and thermal infrared regions of the electromagnetic spectrum. Visible, near infrared and shortwave infrared bands (bands 1,2,3,4,5,7) have a spatial resolution of 30 meters (98-feet) and the thermal band (band 6) has a 60-meter resolution. The spectral and spatial characteristics of Landsat 7 are nearly equivalent to that of Landsat 5 so images of both series may be readily compared. Landsat 7 also has a panchromatic sensor (band 8) that produces images with a 15-meter resolution that greatly enhances feature identification and interpretation. Main imaging components of Landsat 7 are in Figure A.5.1.1.

Landsat 7 is part of NASA's Earth Science Enterprise (ESE) and is the latest in a series of land observing satellites that provide global change information to users worldwide. Scientists use Landsat satellites to gather remotely sensed images of the land surface and surrounding coastal regions for global change research, regional environmental change studies and other civil and commercial purposes. Over thirty years of Landsat images offer a mostly unexplored resource for the study and assessment of aquatic resources in the Columbia River Basin.

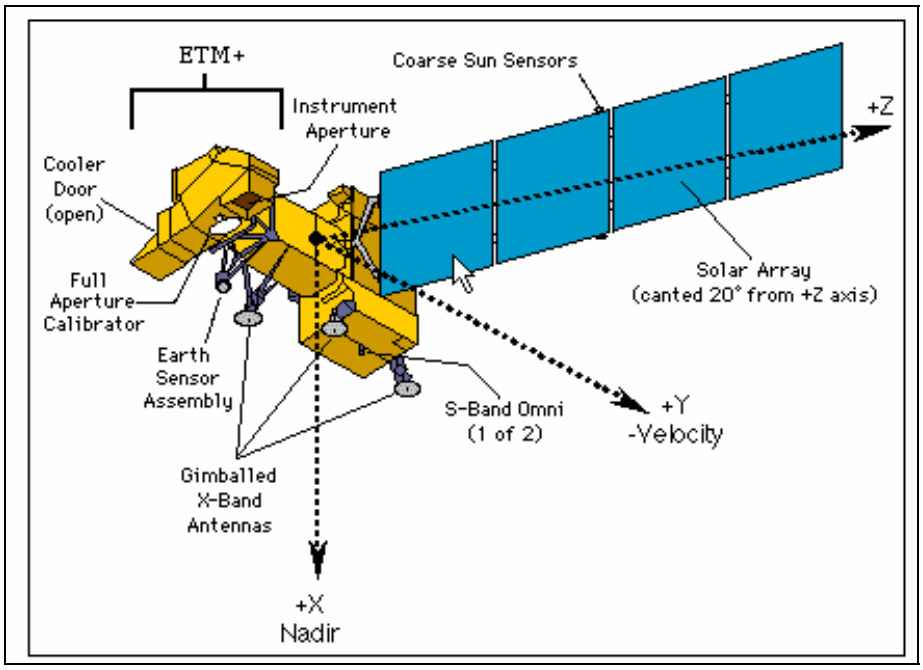

Figure A.5.1.1 Landsat 7 Satellite components (USGS).

Landsat History

Images acquired by Landsat satellites were used to produce the first composite multi-spectral mosaic of the 48 contiguous United States. Landsat imagery serves a broad user scientific community. Landsat imagery are being used for monitoring agricultural productivity, water resources, urban growth, deforestation, and natural change due to fires and insect infestations. Landsat images are applied in commercial activities including mineral exploration, forest cover assessment, and monitoring of mining operations.

The first Landsat satellites were originally called ERTS for Earth Resources Technology Satellite and were developed and launched by NASA between July 1972 and March 1978. An improved Landsat 4 was launched in July 1982 with Landsat 5 following in March 1984. Amazingly, Landsat 5 is still transmitting images. Landsat 6 failed shortly after launch. Landsat 7 was launched on April 15, 1999.

Enhanced Thematic Mapper Plus

The Enhanced Thematic Mapper Plus (ETM+) imaging instrument is an eight-band multispectral scanning radiometer. It detects radiation at visible, near-infrared, short wave, and thermal infrared frequency bands from the sun-lit Earth in a 183 kilometer-wide swath when orbiting at an altitude of 705 kilometers. Nominal ground sample distances (GSD) or "pixel" sizes are 15 meters in the panchromatic band; 30 meters in the six visible, near and short-wave infrared bands; and 60 meters in the thermal infrared band. Figure A.5.1.2 identifies the main component of the ETM+.

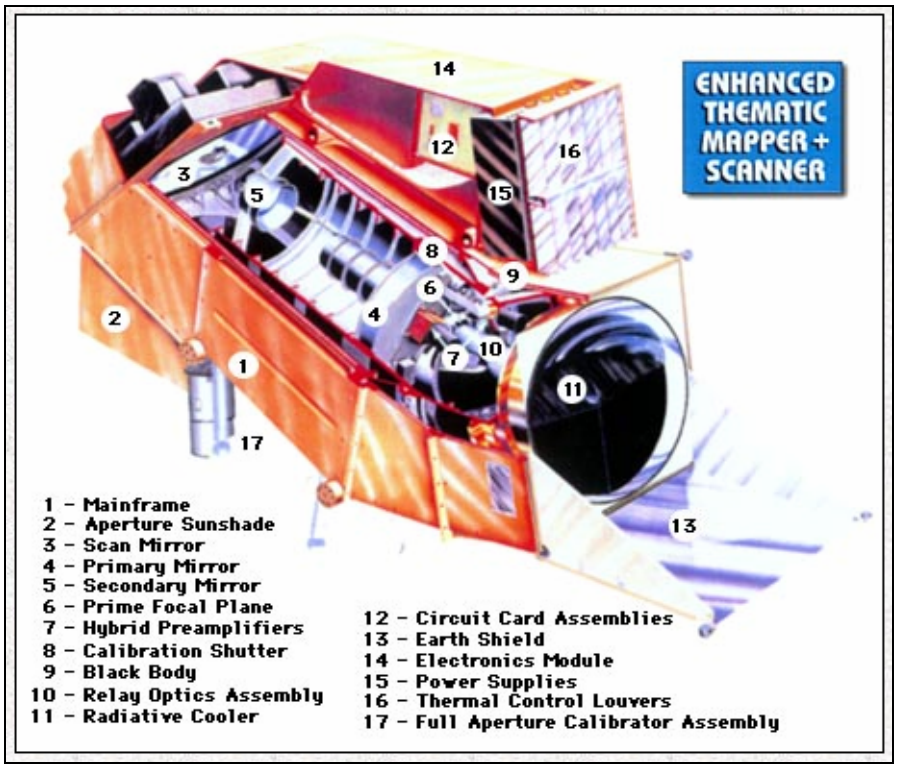

Figure A.5.1.2 ETM+ system components (USGS).

Landsat 7 sensors are routinely calibrated to preserve radiometric accuracy. The Landsat 7 full-aperture-solar-calibrator and a partial-aperture-solar-calibrator use the sun, with its known exo-atmospheric irradiance, as an absolute radiometric calibration source.

On-board solar calibration procedures in conjunction with an internal calibration lamp and ground-based validation experiments, permit calibration to an uncertainty of less than five percent.

World-Wide-Reference system

The Landsat 7 satellite orbits the Earth with a sun-synchronous 98-degree inclination and a descending equatorial crossing time of 10:30 a.m. local solar time. The orbit is maintained with periodic adjustments for the life of the satellite. A three-axis attitude control subsystem stabilizes the satellite keeps the instrument pointed toward Earth to within 0.05 degrees.

Landsat images are catalogued according to the Landsat World-Wide-Reference system (WRS). The WRS divides the Earth's surface into 57,784 scenes, 233 paths by 248 rows, each 183 kilometers wide by 170 kilometers long. Orbit swaths are repeated once every 16 days. Landsat 7 overflights adhere to a fixed schedule. The swath to the west of a particular swath is collected 7 days later. Landsat 7 images are identified and ordered by WRS coordinates.

Adjacent swaths overlap at the equator by 7.3 percent. Moving from the Equator toward either pole the sidelap increases because the fixed 185 km swath width. Overlap is about 20% at 30° latitude, increasing to about 30% at 40° latitude.

Two Landsat 7 scenes cover most of the Lower Clearwater Basin. These scenes are in the same orbital path are identified by the WRS designations Path 42 Row 27 and Path 42 Row 28. Daytime Landsat 7 are collected as the satellite orbits from north to south (descending) so Scene P42R27 is acquired a few minutes before scene P42R28.

Endlap between scenes in Figure A.5.1.3 is 13 percent. The dashed line shows the edge of the underlying image.

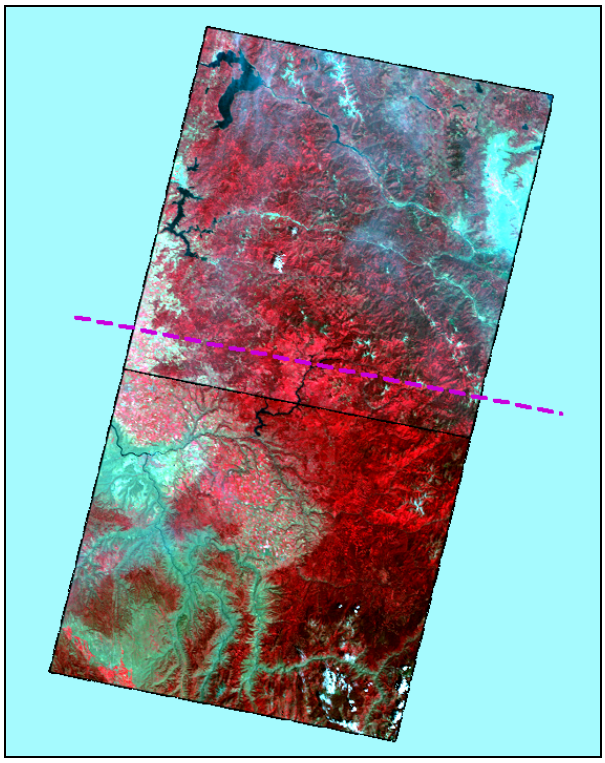

Figure A.5.1.3 Endlap between scenes of Path 42 Row 27 and 28.

Acquisition and Coverage

Landsat 7 has acquired approximately 300,000 daytime images through January 2003. The densest coverage is over the U.S., but repeat coverage is available worldwide. The Landsat-7 Long Term Acquisition Plan (LTAP) selects scenes to update a global archive of sunlit, substantially cloud-free land images. A foremost objective is to monitor changes in vegetation across the planet. The LTAP schedules acquisitions more frequently during periods of change, such as growth and senescence of vegetation, and less frequently during relatively stable periods, such as when full growth canopy exists or

during the winter. The density of the Landsat 7 archived image collection is greatest in the U.S. in Figure A.5.1.4.

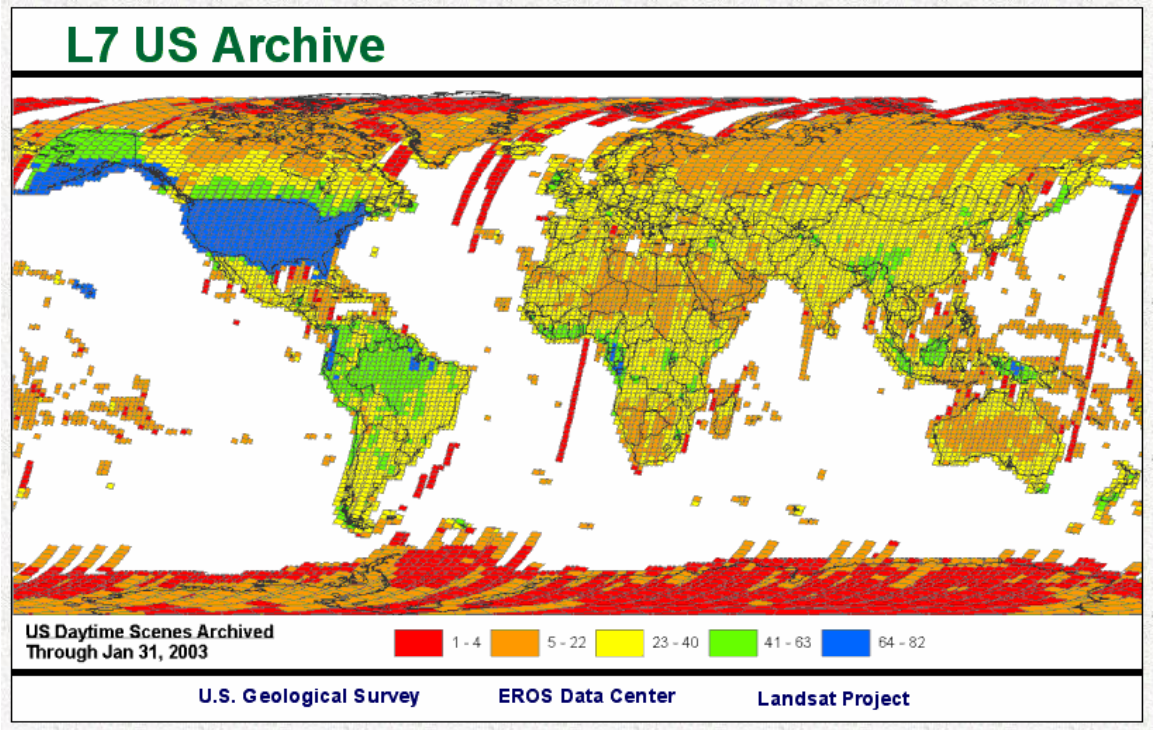

Figure A.5.1.4 Density of Landsat 7 coverage (USGS).

Approximately 70 percent of the 250 scenes per day acquired by Landsat 7 are routine acquisitions to support vegetation analysis. The other 30 percent of collection capacity is devoted to other scientific "niche" requests, including about 3 percent for night images or special high-priority acquisitions (natural disasters, national needs, etc). Identified annual scientific priorities include:

- 282 scenes for agricultural monitoring and research
- 35 scenes for instrument calibration
- 896 scenes of reefs (acquired 2 – 6 times each year)
- 30 scenes of wildfire
- 1392 scenes of land ice (acquire once during certain months)

- 3601 scenes of Antarctica (acquire once during Jan-Feb)
- 60 scenes of oceanic islands (acquire twice each year)
- 1175 scenes of rainforest
- 352 scenes of sea ice (acquired 1 – 3 times each year)
- 11 scenes of Siberia (annual)
- 72 scenes of volcanoes (acquired 2 – 12 times each year)

Landsat Ground and Archive System

The Landsat ground system includes a spacecraft control center, ground stations for uplinking commands and receiving data, a data handling facility and a data archive developed by the Goddard Space Flight Center, Greenbelt, Md., in conjunction with the U.S. Geological Survey (USGS) EROS Data Center (EDC), Sioux Falls, SD. These facilities, augmented by existing NASA institutional facilities, communicate with the Landsat 7 satellite, control all spacecraft and instrument operations, and receive, process, archive, and distribute ETM+ data. The USGS manages the primary ground station, the data handling facility and archive at the EROS Data Center. NASA managed flight operations from the control center at the Goddard Space Flight Center until October 1, 2000 then passed responsibility for flight operations to the USGS.

The ground system at the data center can capture and process 250 Landsat scenes per day and deliver at least 100 of the scenes to users each day. The ground system is capable of distributing raw ETM+ data within 24 hours of its reception at the EROS Data Center. All 100 of these scenes can be radiometrically corrected to within five percent and geometrically located on the Earth to within 250 meters of true location.

Spectral and spatial resolution

Spectral and spatial resolution of satellite and aerial imagery indicate the suitability of imagery for particular remote sensing tasks. Landsat-7 collects seven bands (channels) of reflected energy and one band of emitted (thermal) energy. The ETM+ sensor converts solar energy to radiance. Radiance is the flux of energy (primarily irradiant or incident energy) per solid angle leaving a unit surface area in a given direction. Conventional units of radiance are watts per square meter per steradian[1] per micron of wavelength ($W\ m^{-2}\ sr^{-1}\ \mu m^{-1}$). Radiance is different from reflectance, which is the dimensionless ratio of reflected versus total power energy. Land surface reflectance may be computed from at-sensor radiance by adjusting for sun angle, satellite orientation, atmospheric effects, and normalizing by assumed values of total solar energy incident on the earth within a wavelength interval. Table A.5.1.1 lists the Landsat 7 band numbers and wavelength intervals along with spatial resolution and sensor type. Bands 1 through 5 and band 7 record reflected solar energy and are called the visible, near infrared and shortwave infrared bands. Band 8 responds to a wide spectral region in the visible and near infrared and is called the panchromatic band. Band 6 records emitted thermal energy and is called the thermal band. Together these bands cover the portion of solar spectrum found to be scientifically useful for studying the characteristics of the earth surface.

[1] A steradian is a cone shaped unit solid angle. There are 4π steradians in a full sphere.

Band	Interval	Resolution	Detector
1	0.45 - 0.52 µm	30	SiPD
2	0.52 - 060 µm	30	SiPD
3	0.63 - 069 µm	30	SiPD
4	0.76 - 0.90 µm	30	SiPD
5	1.55 - 1.75 µm	30	InSb
6	10.4 - 12.5 µm	60	HgCdTe
7	2.08 - 2.35 µm	30	InSb
8	0.50 - 0.90 µm	15	SiPD

Table A.5.1.1 Landsat 7 Spectral and spatial resolution.

Different surface materials reflect and emit varying levels of radiation. Land cover can often be identified by reflectance characteristics. A basic premise of the science of remote sensing is that spectral signatures of similar objects or classes of objects will reflect or emit similar levels electromagnetic radiation at any given wavelength under constant conditions of illumination or temperature. If this were not true, then it would be impossible to interpret irrigated crops from water or desert vegetation in band composite images in Figure A.5.1.5.

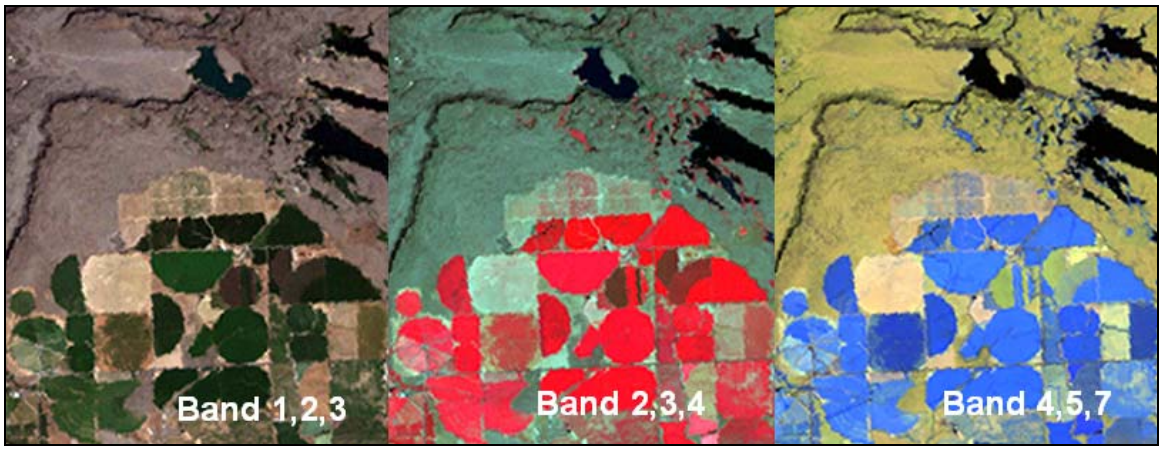

Figure A.5.1.5 Different band composites of a portion of a Landsat 7 scene in central Washington State.

Unique spectral signatures of reflected and emitted energy can be identified by laboratory spectrometer measurements or by interpretation of calibrated satellite and aerial imagery. The seven bands of Landsat 7 imagery give seven points on the spectral reflectance curve. Each band is defined by its mid point and width on the electromagnetic spectrum. Landsat 7 bands are relatively broad. Hyperspectral sensors may collect hundreds of individual spectral bands each just a few micrometers wide. Hyperspectral images yield highly detailed spectral signatures.

More detailed spectral signatures improve the ability of imagery to discriminate surface materials. The spectral signatures developed Landsat 7 imagery often overlap among materials because of the relatively few bands. Even so, many general surface types such as open water, forest, desert, agricultural land, bare soil, rock, ice and urbanized areas may be identified in Landsat 7 images. It is usually more difficult or impossible to distinguish individual species plants within a particular vegetative community with Landsat imagery, for example discriminating wheat from barley or pine from fir. Seasonal changes in imagery characteristics because of plant phenology and agricultural practices can assist in discriminating land surface types.

Spatial Resolution

Common descriptive terms for spatial resolution encountered by imagery users are instantaneous field of view (IFOV), ground sample distance (GSD) and ground pixel resolution (GPR). The IFOV, or pixel size, is the area of surface covered by the field of view of a single electronic detector in the sensor. The IFOV can be thought of as a discrete sample of energy reflected or emitted from the Earth surface. The ETM+ on board Landsat 7 samples at three different resolutions; 30 meters for bands 1-5, and 7, 60

meters for band 6, and 15 meters for band 8. The multispectral visible and near infrared bands 1-5 are most often used in watershed characterization. Satellite image interpretation is a skill best learned by experience, but many features are easily recognized such as the irrigated fields along the Columbia River in Figure A.5.1.6. Interpretation becomes increasingly more difficult as the size of the feature relative to GPR decreases.

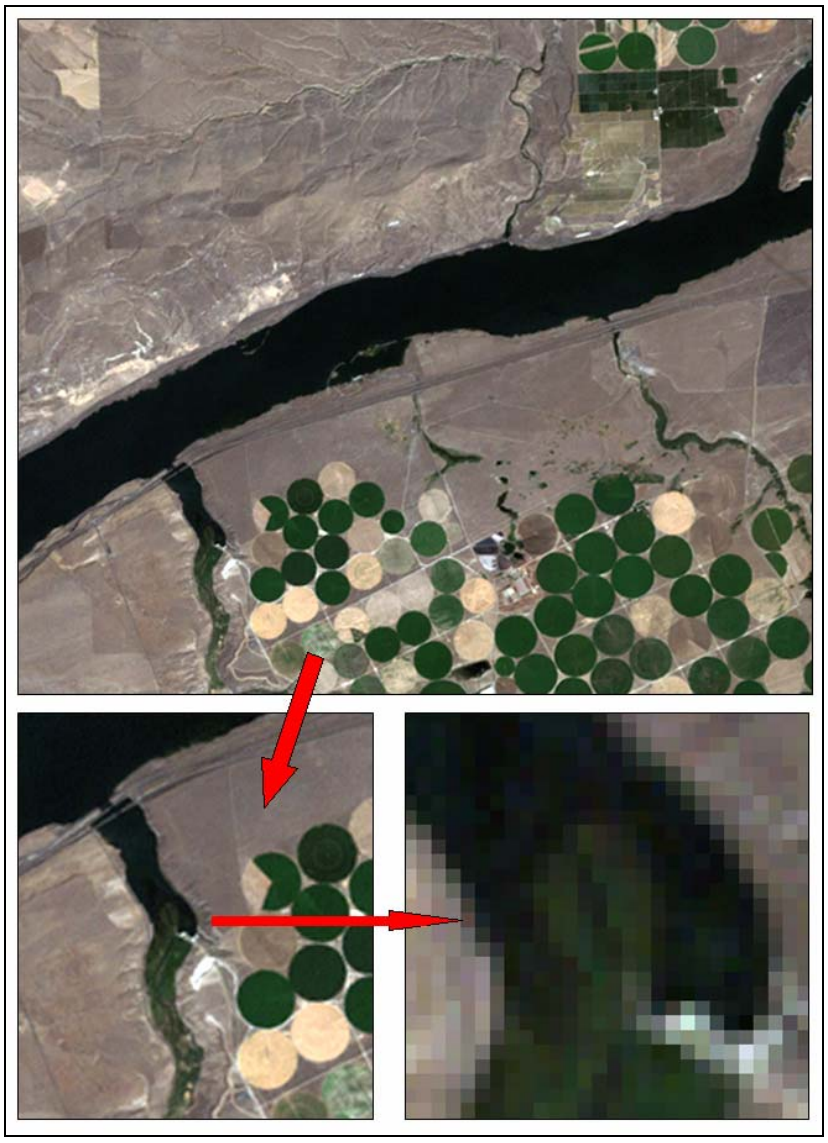

Figure A.5.1.6 Relative spatial resolution of Landsat 7.

The IFOV of a sensor may be described as an angle, usually in radians, in the longitudinal and transverse directions of the sensor. It is necessary to know the distance from the earth surface to compute the spatial coverage of an individual detector from IFOV in degrees or radians. The term IFOV is more commonly used to describe sensors on board aircraft because images can be acquired at a range of flight altitudes.

Satellite orbital altitudes are relatively constant, so the terms Ground sampling distance (GSD) and ground pixel resolution (GPR) are widely adopted by satellite imagery users. The two terms have essentially the same meaning: the linear dimension of the square surface area sampled by an individual detector in the sensor. The preferred term among scientific users is GSD. Many imagery suppliers and GIS companies use the term GPR, especially if imagery is resampled to a different resolution than the original satellite product. The figure below compares the nominal spatial resolution and coverage width of several satellites.

It should be noted that none of these terms adequately or consistently describe the size of the smallest feature that may be discerned in an image. Many factors affect the appearance of spatial detail in an image including scene contrast, atmospheric effects, processing methods, and sensor settings. Techniques from spatial resolution theory, such as the development of the modulation transfer function (MTF) must be employed to gain a more precise description of true resolving power of a sensor-image combination. Fortunately, most users do not need to apply complex techniques to understand what can likely be discerned in an image. Users quickly learn by examining images whether a particular satellite imagery product will support an intended analysis.

There is a trade-off between spatial resolution and the area covered by a single image (scene). High spatial resolution satellites cover less area with each image than medium or low-resolution satellites. High-resolution satellites available to civilian users offer fewer spectral bands than Landsat 7. Higher spatial resolution is not always better, especially when project areas are large (regional scale) and or must be evaluated quickly at least cost. High-resolution satellite imagery is justifiable both in initial cost and processing time when critical remote sensing tasks require images with high spatial resolution, especially for inaccessible locations not routinely imaged or impractical to image by airborne sensors.

Landsat 7 Image Products

Three Landsat 7 image products are routinely available from USGS: the Level 0R, Level 1R and Level 1G products. These are produced from the same scene acquisition so have equivalent image content. They differ by the level of processing USGS applies to prepare the image for use. Raw satellite imagery must be corrected for geometric and radiometric (spectral) bias of the satellite optical assembly and electronic sensor components.

The Level 0R product is a raw data form that is marginally useful prior to radiometric and geometric correction. A Level 0R product includes ancillary data required to perform geometric and radiometric corrections. Specialized users with appropriate software may prefer Level 0R products to allow greater control of image processing. The figure to the left is an example of a Level 0R image. Pixels from one scan line to the next are offset. Most users would find it difficult or impossible to use

without further processing. The Level 0R product is only available in the Hierarchical Data Format (HDF), a self-describing gridded data format only partially supported by common remote sensing and GIS software packages. Figure A.5.1.7 is portion of a Landsat 7 Level 0R image of an agricultural field.

Figure A.5.1.7 Landsat 7 Level 0R image (bands 1,2,3).

Level 1R Products

Level 1R products are radiometrically corrected with sensor calibration data. Image artifacts such as banding, striping, and scan correlated shift are removed prior to radiometric correction. Image pixels are converted to units of absolute radiance calculations during 1R product processing. The Level 1R product, like Level 0R is not geometrically corrected. Again, most users would find it difficult or impossible to use Level 1R products without further processing.

Level 1G Products

Most users will likely prefer the Level 1G product for routine remote sensing tasks. Level 1G products are radiometrically and geometrically (systematically) corrected. Correction algorithms model the spacecraft and sensor using data recorded by onboard computers during image acquisition. Geometric parameters include satellite attitude and ephemeris profiles. During processing the image data is resampled to user-specified parameters including output map projection, rotation angle, pixel size, and resampling kernal. USGS supports several map projections. The most popular for general use is the Universal Transverse Mercator. The full list of projections include:

- Universal Transverse Mercator
- Lambert Conformal Conic
- Polyconic
- Transverse Mercator
- Polar Stereographic
- Hotine Oblique Mercator A
- Hotine Oblique Mercator A
- Space Oblique Mercator

Level 1G image products are ready for use in many remote sensing tasks. Figure A.5.1.8 is the Level 1G version of the image in Figure A.5.1.7. Compared to the Level 0R figure above, scan lines are correctly registered to each other and angular orientation closely approximates true surface geometry.

Figure A.5.1.8 Landsat 7 Level 1G image (bands 1,2,3).

USGS employs the WGS84 ellipsoid for coordinate transformation and resampling. The Level 1G product is a geometrically rectified and free from distortion related to the sensor (e.g. jitter, view angle effects), satellite (e.g. attitude deviations from nominal), and Earth geometry (e.g. rotation, curvature). The systematic Level 1G correction process does not use ground control or elevation data during processing. Accuracy of the systematically corrected Level 1G product is approximately 250 meters (1 sigma) in flat areas at sea level.

Other geometric correction processes may be applied by USGS for additional cost. Precision correction employs ground control points to reduce geodetic error of the output product to approximately 30 meters. This accuracy is attained in areas where relief is moderate. Terrain correction processing employs both ground control points and digital elevation models to reduce geodetic error of the output product to less than 30 meters in areas where terrain relief is substantial. Online archives of Landsat imagery may

contain images produced with any of the correction processes. Image metadata and header files usually, but not always, describe the level of processing.

Partial Failure of the Landsat 7 Sensor

The scan line mirror assembly partially failed onboard Landsat 7 on May 31, 2003. The problem was caused by failure of the Scan Line Corrector (SLC), which compensates for the forward motion of the satellite. Without an operating SLC, the ETM+ instantaneous field of view now traces a zig-zag pattern along the satellite ground track in Figure A.5.1.9. Landsat 7 images acquired after July 14, 2003 have gaps within each scene. Technical details are of the failure are described at the USGS website: http://landsat.usgs.gov/slc_enhancements/slc_off_background.php.

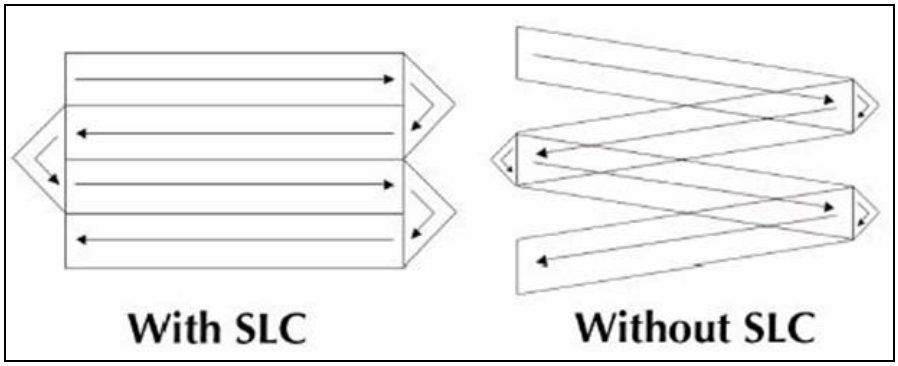

Figure A.5.1.9 Pattern of ETM+ field of view across the ground (USGS).

The ETM+ still produces useful image data with the SLC turned off, particularly within the central portion of any given scene. USGS continues to acquire Landsat 7 imagery in the "SLC-off" mode. Radiometric and geometric quality of the SLC-off images are the same as those before the SLC failure. Image gaps are widest along the edge of the scene and diminish toward the center of the scene. Gaps are approximately

200 meters wide on an spacing of 1.2 km in the October 24, 2003 Landsat 7 SLC-off image in Figure A.5.1.10. The gaps increase image processing and GIS analysis work, but do not seriously impair the use of Landsat 7 images for watershed hydrologic characterization.

Figure A.5.1.10 October 24, 2003 Landsat 7 SLC-off image (bands 2,3,4) of Potlatch River basin study area.

USGS offers modified products to partially correct for the missing image data. The **Level 1G Gap-filled** product provides a gapless image, in which all of the missing image pixels in the original SLC-off image have been replaced with histogram-matched data values derived from one or more alternative acquisition dates. The **Level 1G Interpolated** is a gapless image, in which all missing pixels have been filled with digital number values interpolated from neighboring scan lines. All replacement data values are derived from within the current SLC-off image.

Appendix 5.2

Narrative Descriptions of Level II NLCD Classes

Water - areas of open water or permanent ice/snow cover.

11. Open Water - areas of open water, generally with less than 25 percent or greater cover of water (per pixel).

12. Perennial Ice/Snow - areas characterized by year-long cover of ice and/or snow.

Developed - areas characterized by high percentage (approximately 30% or greater) of constructed materials (e.g. asphalt, concrete, buildings, etc).

21. Low Intensity Residential - areas with a mixture of constructed materials and vegetation. Constructed materials account for 30-80 percent of the cover. Vegetation may account for 20 to 70 percent of the cover. These areas most commonly include single-family housing units. Population densities will be lower than in high intensity residential areas.

22. High Intensity Residential - heavily built up urban centers where people reside in high numbers. Examples include apartment complexes and row houses. Vegetation accounts for less than 20 percent of the cover. Constructed materials account for 80-100 percent of the cover.

23. Commercial/Industrial/Transportation – infrastructure (e.g. roads, railroads, etc.) and all highways and all developed areas not classified as High Intensity Residential.

Barren - areas characterized by bare rock, gravel, sad, silt, clay, or other earthen material, with little or no "green" vegetation present regardless of its inherent ability to support life. Vegetation, if present, is more widely spaced and scrubby than that in the "green"vegetated categories; lichen cover may be extensive.

31. Bare Rock/Sand/Clay - Perennially barren areas of bedrock, desert, pavement, scarps, talus, slides, volcanic material, glacial debris, and other accumulations of earthen material.

32. Quarries/Strip Mines/Gravel Pits - Areas of extractive mining activities with significant surface expression.

33. Transitional - Areas of sparse vegetative cover (less than 25 percent that are dynamically changing from one land cover to another, often because of land use activities. Examples include forest clearcuts, a transition phase between forest

and agricultural land, the temporary clearing of vegetation, and changes due to natural causes
(e.g. fire, flood, etc.)

Forested Upland - areas characterized by tree cover (natural or semi-natural woody vegetation, generally greater than 6 meters tall); tree canopy accounts for 25-100 percent of the cover.

41. Deciduous Forest - areas dominated by trees where 75 percent or more of the tree species shed foliage simultaneously in response to seasonal change.

42. Evergreen Forest - areas characterized by trees where 75 percent or more of the tree species maintain their leaves all year. Canopy is never without green foliage.

43. Mixed Forest - Areas dominated by trees where neither deciduous nor evergreen species represent more than 75 percent of the cover present.

Shrubland - areas characterized by natural or semi-natural woody vegetation with aerial stems, generally less than 6 meters tall with individuals or clumps not touching to interlocking. Both evergreen and deciduous species of true shrubs, young trees, and trees or shrubs that are small or stunted because of environmental conditions are included.

51. Shrubland - areas dominated by shrubs; shrub canopy accounts for 25-100 percent of the cover. Shrub cover is generally greater than 25 percent when tree cover is less than 25 percent. Shrub cover may be less than 25 percent in cases when the cover of other life forms (e.g. herbaceous or tree) is less than 25 percent and shrubs cover exceeds the cover of the other life forms.

Non-natural Woody - areas dominated by non-natural woody vegetation; non-natural woody vegetative canopy accounts for 25-100 percent of the cover. The non-natural woody classification is subject to the availability of sufficient ancillary data to differentiate non-natural woody vegetation from natural woody vegetation.

61. Orchards/Vineyards/Other - Orchards, vineyards, and other areas planted or maintained for the production of fruits, nuts, berries, or ornamentals.

Herbaceous Upland - Upland areas characterized by natural or semi- natural herbaceous vegetation; herbaceous vegetation accounts for 75-100 percent of the cover.

71. Grasslands/Herbaceous - areas dominated by upland grasses and forbs. In rare cases, herbaceous cover is less than 25 percent, but exceeds the combined cover of the woody species present. These areas are not subject to intensive management, but they are often utilized for grazing.

Planted/Cultivated - herbaceous vegetation that has been planted or is intensively managed for the production of food, feed, or fiber; or is maintained in developed settings for specific purposes. Herbaceous vegetation accounts for 75-100 percent of the cover.

81. Pasture/Hay - grasses, legumes, or grass-legume mixtures planted for livestock grazing or the production of seed or hay crops.

82. Row Crops - crops such as corn, soybeans, vegetables, tobacco, and cotton.

83. Small Grains - crops such as wheat, barley, oats, and rice.

84. Fallow - areas used for the production of crops that are temporarily barren or with sparse vegetative cover as a result of being tilled in a management practice that incorporates prescribed alternation between cropping and tillage.

85. Urban/Recreational Grasses - vegetation (primarily grasses) planted in developed settings for recreation, erosion control, or aesthetic purposes. Examples include parks, lawns, golf courses, airport grasses, and industrial site grasses.

Wetlands - areas where the soil or substrate is periodically saturated with or covered with water.

91. Woody Wetlands - areas where forest or shrubland vegetation accounts for 25-100 percent of the cover and the soil or substrate is periodically saturated with or covered with water.

92. Emergent Herbaceous Wetlands - areas where perennial herbaceous vegetation accounts for 75-100 percent of the cover and the soil or substrate is periodically saturated with or covered with water.

6. Assessment of Stream Morphology with Aerial Imagery

Free-flowing natural streams form in response to water and sediment inflow. Self-formed channels are broadly comparable among similar regimes of flow and sediment load. Over 100 years of observation and empirical study have found that near-term channel form may be predicted from discharge (flow duration), channel boundary material properties, overall valley slope, and sediment load, though predictions are often imprecise and have poorly defined limits of certainty. Empirical study of rivers and streams has evolved into the science and practice of analytical channel morphology (morphodynamics). This science attempts to predict the form and response of stream channels to varying environmental conditions associated with climate change and watershed land cover conversion.

There is great motivation for the study of stream channels and morphodynamics. Channels and floodplains may change rapidly to threaten life and property during extreme hydrological events. In-stream alterations and changes in basin characteristics may induce channel changes that impair stream biological communities and threaten habitat integrity. Navigable channels scour and fill in response to altered hydrologic regime and sediment load – incurring costs to maintain infrastructure. Thus the characterization, cause and prediction of channel evolution is of keen societal interest.

Stream channel assessment for the purposes of this dissertation is limited to physical characteristics of the channel cross section and alignment – width, depth, length, discharge, sinuosity, macrostructure, bed and bank material properties, and sediment load. Biological and chemical aspects of streams, while essential for a complete

characterization of stream channel condition and ecological integrity, are not treated extensively in this present research except when these factors dominate the physical form and hydraulic response of the channel system (e.g. vegetative bank reinforcement, large woody debris). The importance of biotic and chemical characteristics of streams was affirmed in the literature review.

Extensive engineering and biological literature relates to stream channel assessment and morphological analysis. Analytical channel morphology incorporates the engineering sciences of sediment transport and fluvial hydraulics (Chang 1988) and inherits much from the historical study of geomorphology (Morisawa 1968; Schumm 1972). No attempt will be made here to critically review this vast multidisciplinary body of literature. Practice oriented syntheses exist (Chang 1988; Hey et al. 1982; Knighton 1998; Lagasse et al. 2001; Richards 1982; Richardson et al. 1990; Richardson et al. 2001; Thorne et al. 1987; Thorne et al. 1997; Vanoni 1975; Yang 1996). A scarce few of these references note the engineering utility of aerial imagery for description and monitoring of alluvial channels. None adequately discuss or demonstrate the potential of aerial images in stream assessment and morphological characterization. That is the objective of this research.

6.1 Aerial Imagery Research Datasets of Rivers and Streams

Since beginning development of aerial imaging techniques and research in 1998, I have acquired natural color and color infrared aerial images of over 2000 stream miles within the Columbia River Basin in Washington, Idaho and Oregon including all high-resolution aerial images used in this research. A portion of this work was funded by the

Bonneville Power Administration (BPA) in a project that demonstrated the basic use of satellite and aerial imagery in aquatic assessment and watershed characterization. Primary aerial imaging project locations are shown in Figure 6.1. Work products for this extensive and unique project juxtapose current satellite and high-resolution aerial imagery in various aquatic and watershed settings. The imagery dataset provides a guide to selection of imagery for particular uses along with focused tutorials on the use and analysis of images. To the best of my knowledge it is the most extensive educational imagery dataset of its kind in the world. These materials are available directly from the BPA office in Portland, Oregon (800-282-3713).

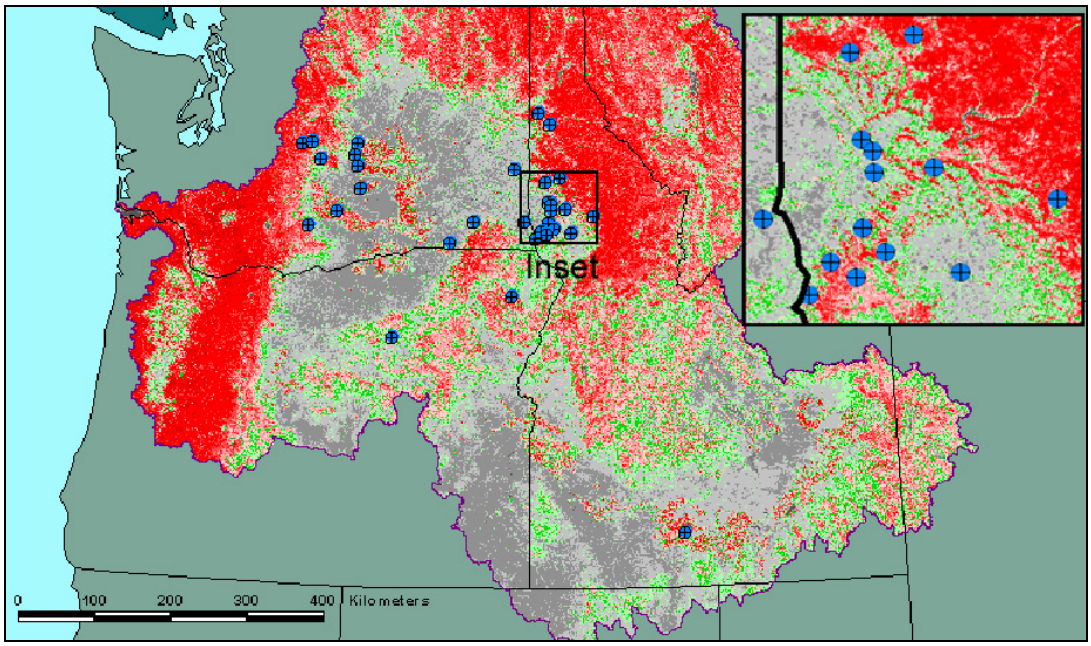

Figure 6.1 Locations of aerial imaging projects in the Columbia River Basin.

Rivers and streams imaged in the BPA work covered the full range of types and sizes—from headwater streams in forested watersheds such as Corral Creek in Latah County, Idaho to the mainstems of the Snake and Columbia Rivers. Table 6.1 lists the primary rivers, streams, lakes and reservoirs imaged in the BPA project. Site summaries

and descriptions of the assembled datasets are included in the digital resource of that project.

The BPA work products are not recapitulated in this dissertation, but are none-the-less indispensable for developing a comprehensive and solid basis for interpretation of stream corridor images in the Columbia River Basin. Essential excerpts from the BPA work products are included in the digital resource to assist users of this dissertation to gain quick familiarity with the broader context of satellite and aerial remote sensing. Much work remains to be done to fully explore and illuminate the large imagery dataset assembled for BPA.

The aerial image datasets for many projects are mostly single acquisitions, imaged once to meet specific objectives. A few project areas, such as the Mid Snake River, Teanaway River and Potlatch River were imaged more often to enable seasonal or interannual comparisons. The Potlatch River imagery dataset is unique. I have imaged the lower Potlatch River several times each year since 1999 to monitor recovery and redevelopment of the fluvial system after the 1996 extreme flood. The Potlatch River dataset is a primary research aerial imagery dataset analyzed and demonstrated in this dissertation. Aerial images of the Palouse River in Idaho provide a complementary analysis. Selected features of other imagery datasets are introduced to the discussion when doing so clarifies elements of channel morphology not apparent in the primary datasets.

River, Stream or Lake	Basin	USGS HUC Code
Big Canyon Creek	Clearwater River. ID, WA	170603061001
Clearwater River	Clearwater River. ID, WA	170603060801
Corral Creek	Clearwater River. ID, WA	170603060702
Cottonwood Creek	Clearwater River. ID, WA	170603062701
Jim Ford Creek	Clearwater River. ID, WA	170603061403
Lapwai Creek	Clearwater River. ID, WA	170603062901
Lawyer Creek	Clearwater River. ID, WA	170603062403
Potlatch River	Clearwater River. ID, WA	170603060301
Soldiers Meadow Creek	Clearwater River. ID, WA	170603063003
Spring Valley Reservoir	Clearwater River. ID, WA	170603060403
Winchester Lake	Clearwater River. ID, WA	170603062802
Coeur d'Alene River	Couer D'Alene Lake. ID	170103030403
Micabay inlet	Couer D'Alene Lake. ID	170103030101
Asotin Creek	Lower Snake River. ID, OR, WA	170601030702
Snake River in Hells Canyon	Lower Snake River. ID, OR, WA	170601030303
Waha Lake	Lower Snake River. ID, OR, WA	170601033005
Yakima River near Buena, WA	Lower Yakima River. WA	170300032401
Starvation Flats	Lower Yakima River. WA	170300031402
North Fork John Day River	North Fork John Day River. OR	170702020201
Palouse River	Palouse. ID, WA	170601081401
Columbia River at Crescent Bar	Upper Columbia River, WA	170200100501
Columbia River at Sunland Estates	Upper Columbia River, WA	170200100204
Columbia River at Vantage	Upper Columbia River, WA	170200100104
Columbia River at Desert Aire	Upper Columbia River, WA	170200160101
Mid Snake River	Upper Snake River, ID	170402121501
Cle Elum River	Upper Yakima River. WA	170300011002
Teanaway River	Upper Yakima River. WA	170300011901
Yakima River	Upper Yakima River. WA	170300010602
Touchet River at Dayton	Walla Walla River. WA	170701020809
Walla Walla River	Walla Walla River. OR, WA	170701020403
Wallowa River	Wallowa River. OR	170601050501

Table 6.6.1 Primary rivers, streams and lakes aerial imagery sites.

6.1.1 Reconnaissance Aerial Image Surveys

Most of the streams surveyed in this research are mid-elevation gravel-bed streams, a stream type common to the Columbia River Basin. Virtually all the aerial images acquired for these streams are overhead (vertical) high-resolution natural color and color infrared. Technical analysis of these images comprises a large part of this section. Spatial measurements are made directly from the images to assess stream

morphological parameters and sediment transport. The technical analysis makes use of the principles of photogrammetry and imagery characterization described in Sections 3 and 4.

Aerial imagery need not always be acquired for immediate technical assessment to be useful. Reconnaissance aerial imaging surveys provide rapid familiarization and monitoring of streams and riparian zones. A reconnaissance aerial image dataset is a permanent record of the condition and extent of the stream at a particular point in time. Reconnaissance surveys can be repeated to reveal critical trends. Reconnaissance aerial surveys were conducted for many purposes during the course of the research including stream and lake macrophyte surveys, fuel spill emergency response, pollution source identification, burn area characterization, forest fuel loading, and habitat assessment.

Two unique stream corridor aerial image datasets from outside the Columbia River Basin illustrate the nature and potential of aerial reconnaissance surveys: aerial imagery of streams in the Apostle Islands National Lakeshore (AINL) in Lake Superior, Wisconsin; and aerial images from the Manati and Arecibo River basins in Puerto Rico.

In November 2002, I conducted a reconnaissance aerial survey of sand bed and bedrock streams (Figure 6.2 and Figure 6.3) in and around the AINL. The aerial images were acquired at a high oblique angle from the side door of the aircraft. Oblique imagery gives more natural perspectives that some viewers find easier to interpret. Geographical position system (GPS) equipment on board the aircraft recorded the time and location of the aerial images.

The AINL holds a strong personal interest arising from my work there as an environmental research technician in the early 1970's. Much of this unique region was

(finally!) afforded permanent wilderness protection in 2004. The AINL aerial imaging work demonstrated the practicality of early winter aerial surveys in closed deciduous canopies to identify stream types and channel modifications maintained by an extensive beaver (*Castor canadensisis*) population (Figure 6.4). My engineering interest lay in the possibility of reducing sediment yield and phosphorus export from eroding landscapes by simultaneous introduction of beaver and cultivated hybrid poplar (food and material source) in degraded low order stream channels. I knew from my early work in the AINL that its fine soils and natural state afforded a good opportunity to observe the influence of beaver on stream channel morphology. Figure 6.4 shows two closely spaced beaver dams on a moderate-gradient third-order stream. Beaver dams were observed on even higher gradient streams. The quick survey was not conclusive, no in-stream surveys were possible at that time, but it indicated that the *Castor-Populus* stabilization approach merits further consideration. This stabilization technique may have application on other forestland depending on seasonal water availability.

Figure 6.2 Aerial oblique image of a sand-bed channel in the AINL, November 8, 2002.

Figure 6.3 Aerial oblique image of a bedrock channel in the AINL, November 8, 2002.

Figure 6.4 Aerial oblique image of two beaver dams on a third order stream in the AINL, November 8, 2002.

In October 2002, I flew reconnaissance surveys of coastal waters (Figure 6.5) and the Rio Grande de Manati (Figure 6.6) and Rio Grande de Arecibo watersheds (Figure 6.7) in Puerto Rico. These basins were hard hit by Hurricane Georges in 1998. The primary purpose of this flight was to demonstrate that satellite imagery and a rapid reconnaissance flight could greatly enhance development of hazard assessment capabilities with the USEPA Basins watershed modeling system in remote and unfamiliar regions having minimal existing data. I assembled cartographic and satellite imagery datasets for the region, developed a preliminary watershed model, and verified land cover classifications with the high-resolution aerial images. I made presentations of this work and approach to USEPA water quality personnel in Washington D.C. and Seattle. The technique is viable, but needs to be more fully developed to increase information

acquisition and exploitation efficiency. A lasting value of this project is that it showed it is practical and cost-effective to plan and execute a high-resolution aerial reconnaissance survey in a cooperative overseas location by use of a compact aerial camera system and chartering of a local aircraft and pilot.

The AINL and Puerto Rico aerial image datasets demonstrate the general potential of aerial imaging reconnaissance surveys to rapidly and efficiently document the nature and condition of critical stream channels and riparian zones. Reconnaissance aerial imaging datasets provide a foundation for initial assessments and planning of more detailed investigations.

Figure 6.5 Vertical aerial image of near shore shallow water bed structure, October 29, 2002.

Figure 6.6 Vertical aerial image of a boulder – pool stream in the Rio Grande de Manati basin, October 29, 2002.

Figure 6.7 Aerial oblique image of karst topography lacking distinct stream channels in the Rio Grande de Arecibo basin, October 29, 2002.

6.2 Acquisition of Stream Channel Aerial Image Datasets

The aerial image datasets discussed in the preceding section were acquired to provide a quick familiarization of streams in relatively inaccessible settings for initial assessment and planning. Extensive technical analysis of the images was not intended so the acquisition parameters (resolution, camera settings, orientation, altitude, image overlap, sun angle) were flexible and not tightly controlled to enhance the measurement of stream morphological details. The aerial images discussed in the balance of this section were mostly acquired for technical analysis of stream morphology. Aerial image acquisition parameters gain increasing importance as the level of detail to be measured in the images increases. The importance of aerial acquisition parameters will be discussed in context of the measurements and analyses demonstrated.

A distinction needs to be made between aerial images that happen to contain a portion of a stream channel and a stream channel aerial imagery dataset. Four types of technical aerial surveys are typically produced in hydrologic aerial imaging: point locations, transects, area coverage, and alignments. Images of point locations are acquired on one or more overpasses from various directions or altitudes and usually provide stereo coverage. I often use the point location method when acquiring very-high-resolution images of specific features such as the surface of the gravel bar in Figure 6.8.

Figure 6.8 Very high-resolution aerial image of a gravel bar on the Potlatch River at Centennial Park, October 22, 2002.

Aerial transects are continuous image swaths across a watershed flown on a regular grid or along a curvilinear track. Images along the transect overlap end to end, but do not overlap with adjacent transects. Aerial transects are typically flown to sample landcover characteristics of large areas, such as for verification of satellite image classifications. Aerial image swaths for the Potlatch River Basin Sediment Study were 650 meters wide and acquired along 45 north-south oriented flight lines spaced at one kilometer intervals across the study region.

Aerial images acquired for complete area coverage overlap end to end and between adjacent flight lines. This is the most common type of aerial survey. Aerial image collections such as the U.S. Geological Survey National Aerial Photography

Program (NAPP) are acquired as complete area coverages for a given state or geographic region.

The Potlatch River and Palouse River aerial image datasets are alignment acquisitions. The aerial images were acquired in continuous sequence as the aircraft follows the alignment of the stream channel. A user can view the images as a continuous traverse along the stream in a consistent upstream or downstream direction without the need for special software to sort the image sequence. Some archived aerial images datasets, such as those commissioned by the U.S. Army Corps of Engineers (USACE), may be alignment acquisitions. Few of these imagery databases are documented with searchable references by the archiving agency. Stream channel aerial image datasets acquired by federal agencies are best located by contacting the aerial photography department of the specific agency. Some imagery datasets are copyrighted by the original aerial photography contractor and cannot be used without explicit permission.

A word of caution is in order for readers contemplating conducting their own aerial stream surveys. Acquisition of low altitude stream channel images requires special piloting skills and can be hazardous in the steep canyons of the Columbia River Basin. It is advisable to utilize experienced commercial pilots who are familiar with the demands of maneuvering in close terrain at low altitudes. Under Federal Aviation Administration (FAA) rules aerial survey, in general, is considered a commercial flight activity and subject to commercial flight regulations.

6.3 Formats and Types of Stream Channel Aerial Images

High resolution aerial images of rivers and streams are commonly of three types: panchromatic (black and white), natural color and color infrared. Formats may be large (9 inch by 9 inch film), medium (70 mm film), small (35 mm film size), digital frame, and digital video. The most advanced aerial mapping cameras are now fully digital and may acquire imagery in continuous swaths (e.g. Leica ADS40). Panchromatic photographs were typically acquired during the aerial film era and still may be acquired depending on project requirements. Figure 6.9 is a historical panchromatic image of the Potlatch River near Juliaetta acquired by the USACE in November 1972.

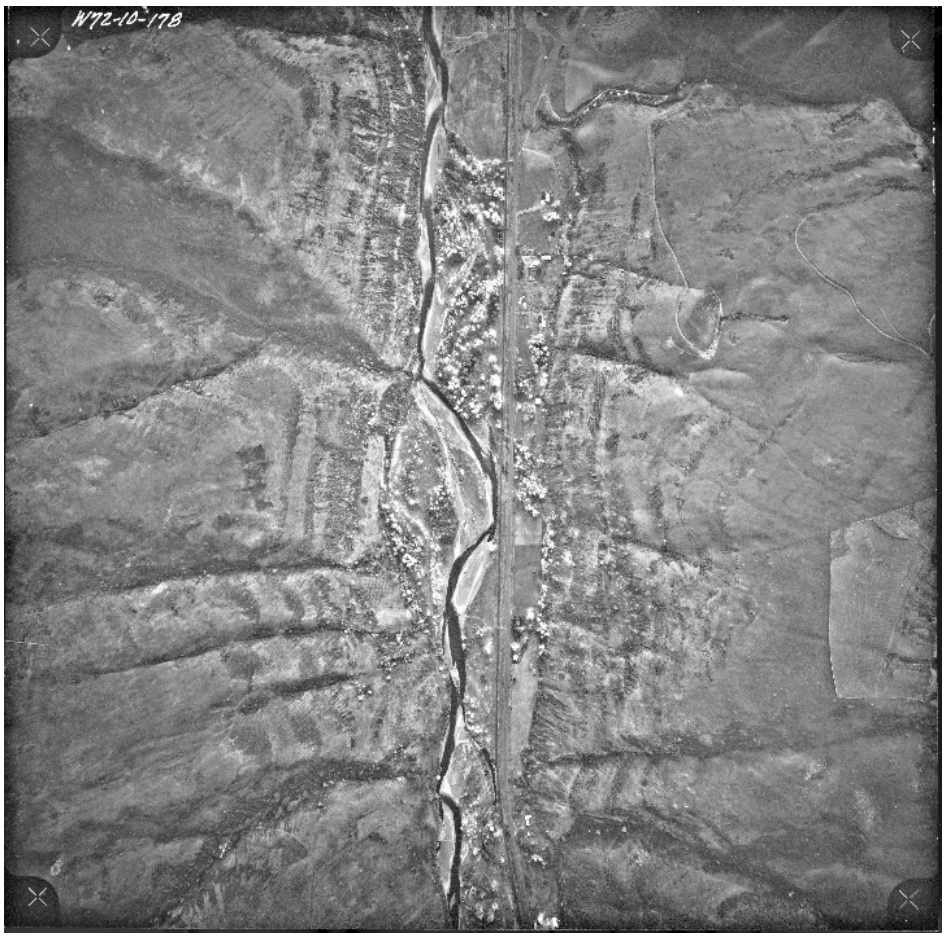

Figure 6.9 USACE aerial photo of Potlatch River, November 13, 1972.

Some of the first aerial images I produced were with 35 mm panchromatic film and developed with personal darkroom equipment. I did this in an effort to control the quality of film processing. It is possible to achieve very high quality aerial images from small format film, but extensive use of 35mm film is impractical for routine imaging of stream channels. Film roll capacity of 35 mm cameras is limited, film is expensive to process, and film negatives or prints must be scanned for practical use. I occasionally use 35 mm color film cameras for high quality aerial landscape photographs such as realty images. Availability of high-resolution professional grade digital cameras has now reduced incentives for the use of film.

Natural color professional quality digital video in the mini-DV^{tm} format is a very practical media for rapid acquisition and delivery of stream aerial imagery datasets. Before high-resolution professional digital frame cameras were available, I acquired many miles of digital aerial video of streams and watersheds in the north Idaho region. Figure 6.10 is a single frame from natural color digital aerial video of a migrating bend of the Palouse River near Harvard, Idaho. The image has acceptable quality for many types of reconnaissance level assessments.

Figure 6.10 Digital aerial video image of the Palouse River near Harvard, ID, July 11, 2000.

My digital video aerial imaging system was eventually interfaced to flight GPS equipment so that latitude and longitude could be encoded directly on the image. The video image frame was then self-geolocated, a great savings in time and processing. The main limitation of the mini-DV format is its resolution compared to high quality digital still cameras. Special software and connections are necessary to convert mini-DV video into single images, but this is not as problematic as it once was now that many desktop computers come equipped with IEEE 1394 Firewire ports.

Most remote sensing texts mention that a near infrared image can accentuate the appearance of a free water surface (Campbell 1996; Lillesand and Kieffer 1994; Schultz and Engman 2000) rendering the water surface very dark or black compared to dry surfaces. This occurs because very little infrared light is reflected from a wet surface and penetrating infrared light is absorbed by moderately deep water so that only a small

amount is reflected from the stream channel bottom. Figure 6.11 is a visible-near infrared aerial image of the Yakima River near Ellensburg, WA acquired on April 2, 2004. The lower half of the image is the natural color band set (blue, green, red) while the upper half is the set of color infrared bands (green, red, near-infrared). Water does indeed appear darker in the color infared image. Isolation of the infrared band in Figure 6.12 shows that almost no infrared light is reflected from the bed in shallow water near the lower end of the island.

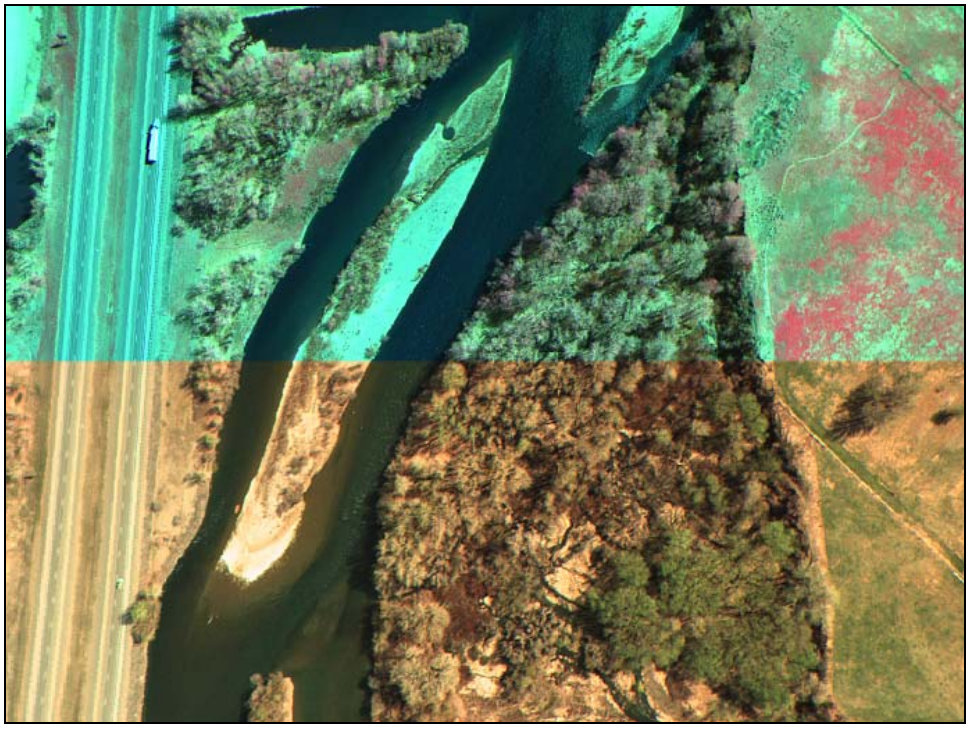

Figure 6.11 Visible-near infrared aerial image of the Yakima River near Ellensburg, WA acquired on April 2, 2004.

Despite this rather dramatic effect, I have found infrared images to be of little benefit and more often detrimental when studying stream morphology with my visible-near infrared aerial imaging system. In stream morophology work it is usually desirable to observe submerged details and use of the visible-near infrared camera system makes

this harder. This is because when I acquire visible near infrared images for a stream channel dataset it is usually for analysis of riparian and aquatic vegetation. I optimize the camera control settings for recording infrared reflectance from vegetation and avoid oversaturation in the green and red bands. This produces a less than optimum setting for depth penetration or recording details of highly reflective sand and gravel bar surfaces. An exception is found when attempting automatic software-based extraction of water surfaces as in Figure 6.13. The low infrared reflectance from the water surface usually gives good results with extraction operations such as those employing the Image Analyst seed tool. The island was purposely excluded from the extraction operation so is not outlined in Figure 6.13.

Figure 6.12 Infrared single band image of Yakima River, April 2, 2004.

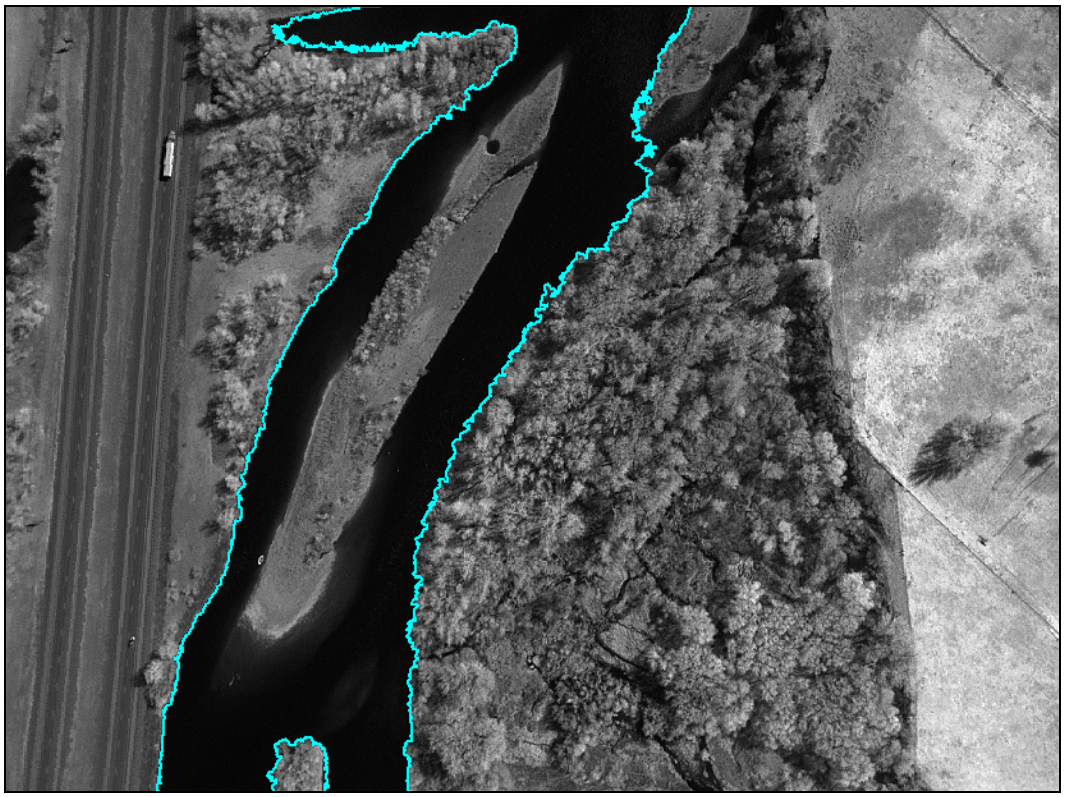

Figure 6.13 Automatic extraction of water surface boundary (light blue) from a single band infrared image.

6.4 Stream Channel Aerial Image Resolution and Interpretation

Information in stream channel aerial images can be separated somewhat arbitrarily into interpreted (qualitative) information and dimensional (metric) information. The distinction is blurred because, for example, points defining the edge-of-water must be interpreted before a channel width may be measured. After producing and viewing well over 100,000 aerial images of streams, it becomes clear that working stream channel images should offer the following essential elements for morphological work:

- Clearly delineated water surface;
- Visible bottom structure (thalweg) in shallow clear water conditions;

- Discrimination of macrostructure (e.g. pools and riffles);
- Normal limits of high water;
- Bank lines in incised channels;
- Discrimination of the various types of deposition structures (gravel and sand bars);
- Interpretation of bed material (silt, sand, gravel, cobble, boulder, bedrock);
- Interpretation of the life form and density of near bank and in-channel vegetation (e.g. shade analysis);
- Discrimination of accumulations of large wood debris;
- Adequate details for interpretation of in-stream constructed features such as dams, diversions, crossings, encroachments, bank stabilization, and barbs;
- Near natural color for best interpretation of vegetation characteristics;
- Stereo coverage for enhanced interpretation of features.

The optimum frame coverage is relative to the size of the stream. There are no absolute rules, but I generally prefer to produce low altitude aerial images in which the normal limits of high water occupy the middle 1/3 to 2/3 of the image width. This typically results in stereo overlapped images with a ground pixel resolution (GPR) between 20 to 30 centimeters with my aerial imaging equipment. I sometimes give priority to including visible ground control points for manual georeferencing of individual aerial images to an existing lower resolution base image, but this becomes less important with newer DOQ coverages.

It is sometimes difficult to image the full active width of braided or highly meandering stream channels while retaining sufficient resolution to interpret bed and bar materials. In this situation I often acquire dual coverage – a low altitude pass at a GPR between 20 and 30 centimeters in which the thalweg is centered as much as practical in the middle of the image, and a medium altitude coverage to capture the normal limits of high water in a single frame. A higher altitude pass may be necessary if full floodplain coverage is desired. Medium or high altitude coverages can greatly assist manual georeferencing of lower altitude smaller footprint images.

Large rivers may be imaged using the same technique as those for medium sized streams if it is acceptable to occasionally miss one of the edge-of-water lines as the river widens beyond the limits of the low altitude image frame. It is sometimes necessary with very large rivers and reservoirs to fly along each shore in separate passes. This was the case in a flight of the mid Columbia River reservoirs near Vantage. Mid river features of interest such as islands and shoals can be imaged as point features or small area coverages.

A typical georeferenced high-resolution aerial image is in Figure 6.14. It is a natural color near-vertical aerial image of the Potlatch River at Centennial Park near Juliaetta acquired during a low discharge of 19 $ft^3\ s^{-1}$ (0.54 $m^3\ s^{-1}$) on July 22, 2004. GPR of the image is 0.28 m. Many of the essential morphological characteristics can be observed and measured at this resolution including water surface width, water surface area, locations and size of channel macrostructure (e.g. pools, riffles, sediment bars), relative water depth, texture of the gravel bar surface, extent and forms of riparian vegetation, stream bank protection, channel encroachments, and floodplain structures.

An image comparison illustrates the strong influence on the type and quality of information that may be discerned from an aerial image. Figure 6.15 is a 1.0 meter resolution natural color digital orthophotoquadrangle (DOQ) aerial image acquired by the National Aerial Photography Program (NAPP) in early July 2004. Many channel features and characteristics can still be identified, but the uncertainty of interpretation is much greater. Though lower in resolution, the DOQ image is a convenient and sufficiently accurate base image for georeferencing higher resolution aerial images. Georeferencing of uncontrolled high-resolution aerial images is usually cost-prohibitive without a relatively recent orthorectified base aerial image. An aerial image is uncontrolled if precise camera position (GPS) and orientation (roll, tilt, crab) are not collected at the time of image acquisition, or if coordinates of observed ground control points are unknown.

Figure 6.14 Natural color aerial image of Potlatch River July 22, 2004.

Figure 6.15 Natural color orthorectified aerial image of Potlatch River July 22, 2004.

Even higher resolution images provide more detail of in-stream channel structure and bar surfaces. Figure 6.16 is a natural color image acquired of the Centennial Park reach on September 27, 2003. Channel bed texture of the and gravel/cobble bar surface are more apparent. Size of the largest cobbles and particle clusters can be estimated in the georeferenced image, about 1 foot (0.3 m) on the top of the bar. This is useful because the largest predominant surface elements control the grain friction contribution to overall channel hydraulic roughness (rugosity). The size distribution of smaller particles cannot be estimated quantitatively, but a qualitative feel for the particle distribution can be obtained by observing the variation in texture associated with particle sorting in bar and channel features. The gravel on the surface of the bar shows some signs of lateral fining. Fine gravel in the bermed play area at the left center of the image is clearly distinguishable from the bar sediment. Both gravels developed from weathered basalt so appear about the same color when dry. An even higher resolution image of this

location was presented in Figure 6.8. The analysis of bar surface texture in aerial images is considered further in the sediment transport discussion below.

Figure 6.16 Natural color aerial image of Potlatch River September 27, 2003.

Relative water depth is also more clearly interpreted in very-high-resolution images. With practice, relative width to depth ratios can be estimated with good reliability in shallow clear water, especially when overlapping images are viewed stereoscopically. The main visual clues for depth interpretation are brightness of the submerged bed particles (indicating relative light extinction) and protruding bed elements. This skill is worth cultivating because it allows relatively rapid development of an initial stream channel hydraulic model with little or no on-the-ground channel measurements. Development of such a model will be demonstrated below.

Ultimately, the optimum resolution for stream and river aerial images depends on the imaging objective. In general, it is most cost effective to acquire the lowest resolution image that allows reliable detection and measurement of the desired features. Planimetric morphology such as water surface width, wetted surface area, and stream centerline of small and medium size channels can usually be determined with good accuracy from aerial images having a GPR of between 30 and 50 centimeters. Horizontal dimensions more precise than about 0.3 meter are seldom needed for natural channel hydraulic analysis. Detailed structure interpretation and analysis is better served with a GPR between 20 and 30 centimeters. Standard 1-meter resolution DOQ aerial images and IKONOS satellite images are suitable for measurements of medium to large rivers. Dimensions of very large rivers, reservoirs and medium size lakes may be measured in the 15-meter resolution Landsat 7 panchromatic (band 8) image.

Timing of the aerial survey controls much of the information content in the aerial image in seasonally variable streams and rivers. Stream discharge in the Pacific Northwest varies dramatically depending on season. Figure 6.17 is natural color image of the Centennial Park reach acquired on March 15, 2004 during a discharge of 1130 $ft^3 s^{-1}$ (32.0 $m^3 s^{-1}$). The 0.33 m GPR image was acquired under light overcast skies. Diffuse light afforded by uniform cloudy skies suppresses terrain shadows and helps offset the effect of low sun angle. The width of the active channel is easily delineated. Tonal differences along the water edge result from soil moisture retained by interstitial sediment. This indicates recent higher water. The width of the high-water surface could be estimated based on this evidence.

Figure 6.17 Natural color aerial image of Potlatch River March 15, 2004.

The effect of aerial image resolution on stream channel feature interpretation is more thoroughly evaluated and documented with numerous examples in my BPA work products and digital resource of satellite and aerial imagery that accompanies this dissertation. Geometry and photogrammetric analysis of the near vertical aerial image and procedures for measurement of dimensions and areas in georeferenced aerial images were discussed in Section 2.

6.5 Morphological Measurements from Stream Channel Aerial Images

Making measurements from digital aerial images is not particularly complicated and is now a routine GIS or photogrammetric operation. The ease of making measurements from digital aerial images with common software and the widespread

familiarity of people with consumer digital cameras now makes some aspects of image processing and measurement seem too basic to include in a dissertation discussion. This was not the case when I began this line of research seven years ago. Digital photogrammetric software was then prohibitively expensive and high-resolution images had to be scanned from aerial photography. At that time I performed basic image processing and rectification with commercial photoprocessing software (Adobe Photoshop™) and had worked out elaborate procedures for scanning images and construction of rectified and seamless image mosaics. These procedures had much practical significance at that time but have little value now.

Relatively inexpensive image processing packages such as Lieca's (ERDAS) Image Analyst and Stereo Analyst extensions are now available and have good explanatory documentation. I am purposefully limiting the routine details of image processing and manipulation to the minimum necessary to illuminate the work flow. Still it is important for a user of this dissertation to understand the main steps in the digital process to appreciate the efficiency of acquiring stream morphology information with aerial survey techniques. I will describe the essential steps.

While some of the morphological information I will extract from aerial images seems basic and simple, it is appropriate to remark that only a handful of articles in the literature discuss the derivation of stream morphology data from aerial imagery (Mount et al. 2003; Winterbottom and Gilvear 1997). If I illustrate aerial imagery based morphological assessments that seem very basic, it is because they are mainstays of the procedures I developed over a period of years with little guidance and have repeated hundreds of times. I have helped many environmental scientists, engineers,

academicians, and field biologists learn to apply these techniques in their work as part of numerous other projects. I will illustrate procedures that are reliable and useful.

6.5.1 Basic Stream Morphology Measurements

Several basic stream cross section and planform measures are common to nearly all stream assessment methods (e.g. USGS National Water Quality Program protocols and USEPA Rapid Bioassessment Protocols). These are reach length, reach average width, reach average depth, and reach average slope. A stream reach has been variously defined (Armantrout 1998; Frissell et al. 1986). Its working definition depends on context and available information. A reach usually signifies a segment of a stream with approximately homogeneous properties of discharge, geology, sediment type, riparian vegetation, groundwater exchange, and pollutant load. A single reach should probably not extend through a main tributary junction and should not be shorter than a single pool-riffle sequence. I usually define reaches from the viewpoint of flow modeling and set reach endpoints at tributary junctions, points of water withdrawal, major breaks in channel slope, significant changes in width, hydraulic control sections, discontinuities in boundary roughness, impoundments, changes in channel confinement, pollutant discharge points, significant changes in sediment storage, bridge and road encroachments, and changes in dominant riparian vegetation (among others).

An exact definition of a stream reach is probably not worth debating. In flow modeling the computational cost for over-specifying reaches is not very harsh. Appropriate locations to begin and end stream reaches are usually obvious in high-resolution stream images. A fisheries manager would probably not find my reach

identification rationale completely suitable, but could probably agree where a reach ends by examining the aerial image. It is usually not wise to accept coded reach breaks such as those in the National Hydrography Dataset (NHD) without verification. The NHD datasets in Idaho and Washington were prepared from much smaller scale information than that afforded by high-resolution aerial imagery.

Real stream reach morphology cannot in general be established by digital terrain analysis of digital elevation models (DEM) commonly available in the Columbia River Basin. The elevation data is too coarse and imprecise within the active channel. A special procedure was developed for the Potlatch River Basin Sediment Project whereby an automatically extracted digital drainage network was corrected with high-resolution aerial imagery. This procedure is discussed in the Potlatch River study work products.

6.5.2 Digitizing of Edge-of-Water Lines

Water surface area of stream channel is the least ambiguous morphological parameter that can be interpreted and measured in a georeferenced high-resolution aerial image. Even in very complex channels, the boundary between water and shore is almost always distinct because of tone and color changes across a very narrow zone. Ambiguity in the location of the edge-of-water (EOW) in Figure 6.18 is due to the gradual emergence of coarse bed material at the shore. The ambiguity at this resolution (GPR 0.31 m) is not significantly greater than that faced by a worker measuring the water surface width with a tape or total station on the ground. Most image analysts could confidently digitize a line demarking the averaged EOW and reject any residual

uncertainty as insignificant in practical analysis (Figure 6.19). I have found that demarking a locally averaged EOW is often easier on the image than on the ground.

Figure 6.18 Edge-of-water indicated by tone and color variation.

Figure 6.19 Digitized edge-of-water lines.

It is generally just as efficient to manually digitize EOW lines as it is to attempt automatic extraction of a water surface with GIS or remote sensing software. Automatic extraction does not always work with natural color images of shallow and clear water because of bottom reflectance. Manual digitizing gives the analyst greater flexibility in choosing the morphological significance of the EOW lines. In flow modeling, the active channel width is often of more interest than the true wetted width, so I would usually digitize EOW lines to the off-shore side of the locus of emergent bed materials. Admittedly, this introduces subjectivity, but the simplified modeling of complex hydrodynamics is always partially subjective. Stereo viewing often improves interpretation of the active channel.

When sharing digitizing work among several analysts, it is best to establish criteria for digitizing of EOW lines to be sure the process is efficient and compatible with analysis objectives. I have found the following criteria to be helpful when digitizing streams the size of the Potlatch River in ArcView for flow modeling.

- Set the view scale to about 1:1500;
- Space digitizing points about one quarter of the stream width. Do not erase line segments unless absolutely necessary, use the vertex edit tools instead;
- Ignore minor EOW crenulations and dead-end side channels;
- Digitize branching active channels and around islands and medial bars;
- Reflectance of light from riffle surfaces indicate channels with significant discharge;

- View overlapping images to discriminate between reflectance of the water surface on riffles and light colored bed materials. The reflectance from the riffle surface will change with camera view angle;

- Be cognizant of overhanging vegetation and digitize the probable location of the EOW;

- Begin digitizing at the lowest reach and proceed upstream, extending both EOW lines as work progresses from one aerial image to the next. Use the endpoint snap functions to avoid gaps and hanging nodes. The thalweg line can be digitized at the same time as the EOW lines;

- Save the EOW line theme often and make temporary backup copies. Digitizing is laborious, so protect your time investment.

The digitized EOW lines provide sufficient and necessary information for a highly precise estimate of the length and average width of a reach. Reach average length is estimated as the shorter of the two EOW lines. Reach average width is the total area enclosed within the EOW lines divided by the reach average length. The only ambiguity in these computations is in the digitizing of the EOW lines and the accuracy of the aerial image georeferencing.

All other techniques of estimating reach average width and length of reaches longer than about 500 meters are much less precise and have poorly defined uncertainties. If desired, the uncertainty of the EOW digitizing can be partially assessed by comparing the products from several analysts. There is no practical or reasonable way to evaluate digitizing uncertainty by comparison with field measurements over an extensive length of stream. The task of performing an unbiased random statistically valid sample of ground based stream measurements over a meaningful length of stream is daunting. Any

implementable accuracy assessment based on comparison with ground measured data will be unavoidably biased to sites with easy measurement access. Except during low base flow, it is likely that discharge rates will change significantly before all field measurements can be completed. Ad hoc measurements are only valid for the immediate location and aerial image and could not be extended to the full reach or all images. Variance estimates would almost certainly be biased because of autocorrelation within a particular image or sub reach. In practice it is seldom necessary to evaluate the uncertainty of the EOW lines. They are simply accepted as factual.

6.6 Lower Potlatch River Fluvial Morphology Study Reach

A practical test of these procedures was developed for the lower Potlatch River over a length 25 kilometers from the confluence of the Potlatch River with the Clearwater River to the County Highway P1 bridge above Kendrick, ID (Figure 6.20). The lower Potlatch River is a near ideal study reach consisting of a gravel-cobble bed stream that exhibits meandering and braiding characteristics. High gravel and cobble sediment loads originate in the steep basalt canyons and there is significant washload from agricultural land above the canyonlands. Average slope of the study reach is 0.005 m m^{-1}.

There is highway access along most of its length and an old railroad grade has been converted to a public walkway between Juliaetta and Kendrick. Wastewater treatment plants at Kendrick and Juliaetta both discharge to the river and the City of Juliaetta operates a surface water treatment plant that withdraws water from an infiltration gallery in a lateral gravel bar. Several bridges cross the river and a new USGS discharge gaging station was recently installed upstream from the confluence.

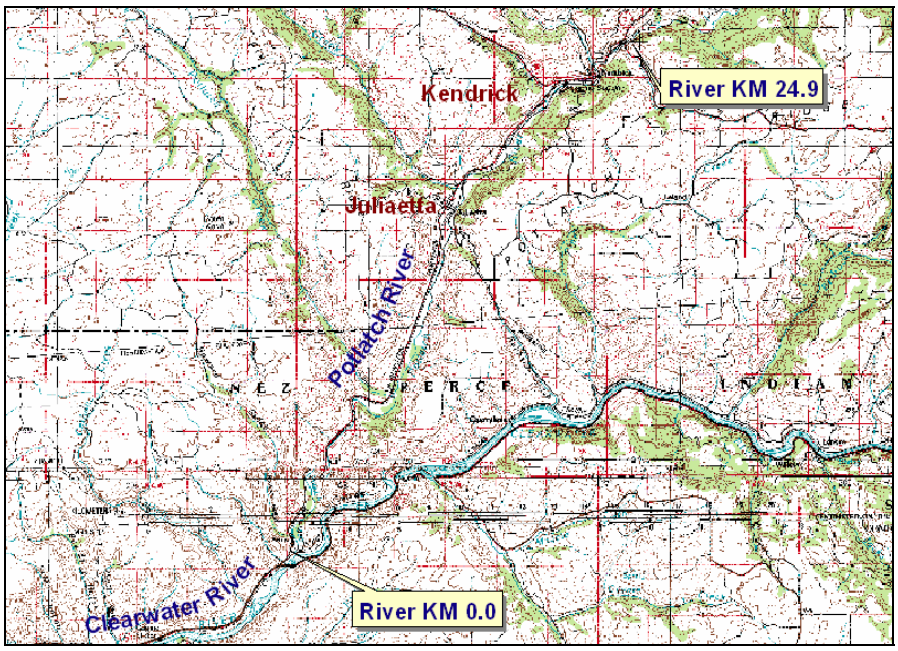

Figure 6.20 Lower Potlatch River morphological research reach.

As will be seen in subsequent analysis, the Lower Potlatch River channel is highly mobile within constraints imposed by the canyon. Some segments of the channel have been reinforced with bank protection, levees and spur dikes. Approximately 2000 people live along the study reach. The lower end of the study reach is in the Nez Perce Reservation.

6.6.1 EOW lines, Water Surface Area, Reach Length, and Reach Average Width

Edge-of-water lines were digitized along the full length of the stream from the confluence to County Highway P1 bridge. The entire study reach was covered by 47 georeferenced aerial images acquired on July 22, 2004 having an average GPR of about 0.3 meters. Georeferencing was completed in about 8 hours and edge-of-water digitizing was completed in about 2 hours. Initial setup of the ArcView project took less than 15 minutes. River stationing was set to 0.0 kilometers at the railroad bridge at the

confluence. As will be discussed below, river stationing was established by digitizing the low flow thalweg line. The right and left EOW lines were 24,953 m and 25,032 m long. The low flow thalweg line will usually be slightly shorter than the shortest EOW line when digitized as described above; but not always. The right bank is established in the conventional sense in the downstream viewing direction. Close agreement between the lengths of right and left EOW are typical.

Water surface area is determined by enclosing the area bounded by the EOW lines with polylines, converting the set of polylines into a polygon, then subtracting out polygons around islands and medial bars. Conversion of the polylines and measurement of area is performed with conventional GIS operations and takes about 15 minutes on a 2.4 Ghz Pentium 4 processor. The total area enclosed within the EOW lines of the full study reach excluding islands and medial bars is 407,552 m^2 (40.8 ha). Reach average stream width is computed:

$$W_{avg} = \frac{A_{surface}}{L_{avg}} = \frac{407{,}552\,\text{m}}{24{,}953\,\text{m}} = 16.33\,\text{m} \qquad 6.1$$

The estimate of reach average width is not particularly sensitive to the assumption that the reach average length is equal to the shortest EOW line. Reach lengths much shorter than the EOW lines would be suspect. The procedure is highly efficient even if other practical means for making the width estimate were available. Total office time to produce the estimate for the 25 kilometer reach is about 10 hours.

Estimates of reach length and average width can be made for any sub-reach from the original EOW polylines and surface water area polygons with conventional GIS operations. The georeferenced aerial imagery dataset can facilitate many other analyses

and habitat evaluations, so the cost of image acquisition and georeferencing should be allocated to all dependent assessments.

Traversing cobble bedded streams for field measurement is hard and sometimes hazardous work – impossible during high water. Access is often difficult and resisted by adjacent land owners. Field measurements take a significant amount of time and can hardly be considered synoptic. Aerial survey methods avoid these difficulties.

6.6.2 Channel Thalweg

The channel centerline or thalweg is an important morphological feature that is necessary to compute parameters such as sinuosity and meander length. The thalweg is defined as the continuous line along the deepest part of the channel, thus the thalweg is a planform representation of a three dimensional feature. Thalwegs can often be identified in high-resolution aerial images acquired during low flow when water is clear. A portion of the thalweg of the lower Potlatch River is in Figure 6.21. At some points the thalweg is poorly interpreted because of reflectance from the surface of riffles. The thalweg may be digitized at the same time as EOW lines, but is not dependent on them.

Figure 6.21 Thalweg of the lower Potlatch River in July 22, 2004 aerial images.

It is not conceptually valid to "split the distance" between EOW lines to determine the location of the thalweg. This would produce what is more properly called the channel centerline. Thalweg digitizing requires the analyst to judge the relative depth of the channel. Thalwegs cannot be digitized if relative depth cannot be interpreted in the aerial image. Depth cannot be judged in the 1992 DOQ images of the Potlatch River in Figure 6.22, so the digitized red line signifies the approximate channel centerline. A channel centerline produced in this manner has no morphological significance, except that it usually is a good estimator of reach length and may approximate thalweg at the time of aerial image acquisition.

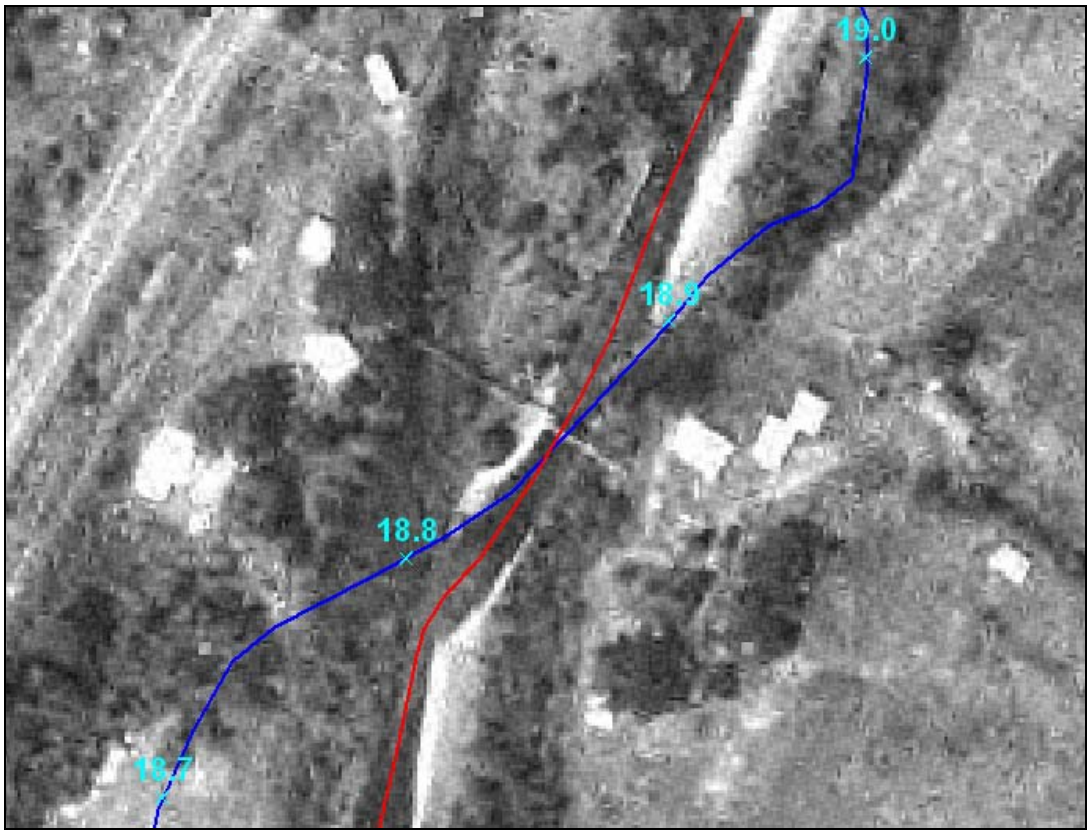

Figure 6.22 Thalweg of the lower Potlatch River in the May 22, 1992 DOQ.

I almost always digitize the channel thalweg or channel centerline. I prefer to use the low-flow thalweg as the basis of establishing river station distance because the summer low-flow condition has the widest window of opportunity for aerial image acquisition, and aerial images acquired during this time the greatest comparative value. This method of stationing is contrary to procedures adopted by USGS for topographic quadrangle maps that attempt to infer channel centerlines from indications of the normal limits of high water or rely on stations established by a local water authority (USGS 2001). Intervals of 0.1 kilometers mark river stations on the July 22, 2004 in Figure 6.21 and Figure 6.22. The station marks are easily produced with a GIS divide or set-node operations and requires less than 0.3 hours.

Comparison of channel thalweg lines or centerlines observed in a time sequence of aerial images is perhaps the simplest and most illuminative method of channel change analysis. Alteration of the Potlatch River channel is obvious in Figure 6.21 and Figure 6.22. This method of change analysis will be discussed more in a subsequent section.

6.6.3 Assessment of Channel Structure

Morphological assessment of alluvial channels usually includes some form of classification of the channel into type and channel units following from the propensity of alluvial channels to exhibit common characteristics (Church 1996; Leopold and Wolman 1957; Montgomery and Buffington 1993; Thorne et al. 1997). Early work recognized that high-resolution aerial imagery is useful for channel classification (Greentree and Aldrich 1976) and the use of aerial imagery has been evaluated in stream assessment work in the State of Washington (Somers et al. 1991). These findings are confirmed by my investigations in a much broader context.

Channels are classified into types by overall planform and profile shape and dominance. Montgomery and Buffington (1993) recognized six alluvial channel types in gravel bed streams of the Pacific Northwest: cascade, step-pool, plane-bed, pool-riffle, regime, and braided channels. A variety of morphological structures or channel units are observed within these general channel types. Channel units are morphologically distinct areas of one to many channel widths in length. Common channel unit types in the Pacific Northwest are pools, riffles, cascades, step-pool cascades, slip-face cascades, glides, runs, and rapids (Montgomery and Buffington 1993; Montgomery and Buffington 1997). Distinctions can be made based on organization and areal density of particles

(clasts), local slope, flow depth, flow velocity, and particle size. An alternative channel classification system that is based on reach averaged cross sectional geometry more than in-channel flow structure is the Rosgen stream classification system (Rosgen and Silvey 1998; Rosgen 1994).

Channel units in pool-riffle streams are easily discriminated in high-resolution aerial images by reflectance of riffle surfaces. The GIS process for creating a channel unit polygon is uncomplicated. In ArcView, the water surface area polygon is segmented at appropriate locations with the polygon-splitting tool and the classification of the "child" polygon is noted in an attribute field. Figure 6.23 Figure 6.24 represent a pool-riffle (pool-riffle-bar) sequence on the Potlatch River and the resulting channel unit polygons. Formal criteria, such as minimum unit length, could be established to ensure consistent classifications between analysts. The small run on the right side of the island in Figure 6.21 (flow direction is from top to bottom) was included with the riffle unit because of emergent bed elements and short length.

Summary statistics are readily computed from channel unit polygons. Table 6.2 summarizes morphological characteristics of the channel units for the 25 km study reach. There were 96 pools, 106 riffles and 19 runs in this segment of the Lower Potlatch River on July 22, 2004. Runs mostly replaced pools in the sequence, in agreement with observations in other streams (Montgomery and Buffington 1993). Mean pool length and width are 101 m and 17.6 m respectively. The semi-braided nature of the lower Potlatch River is seen in the channel unit morphology summary statistics: the average spacing between pools is 16 widths of the channel. Pools are typically spaced between 5 and 7 channel widths in fully developed meandering pool-riffle streams (Leopold 1982).

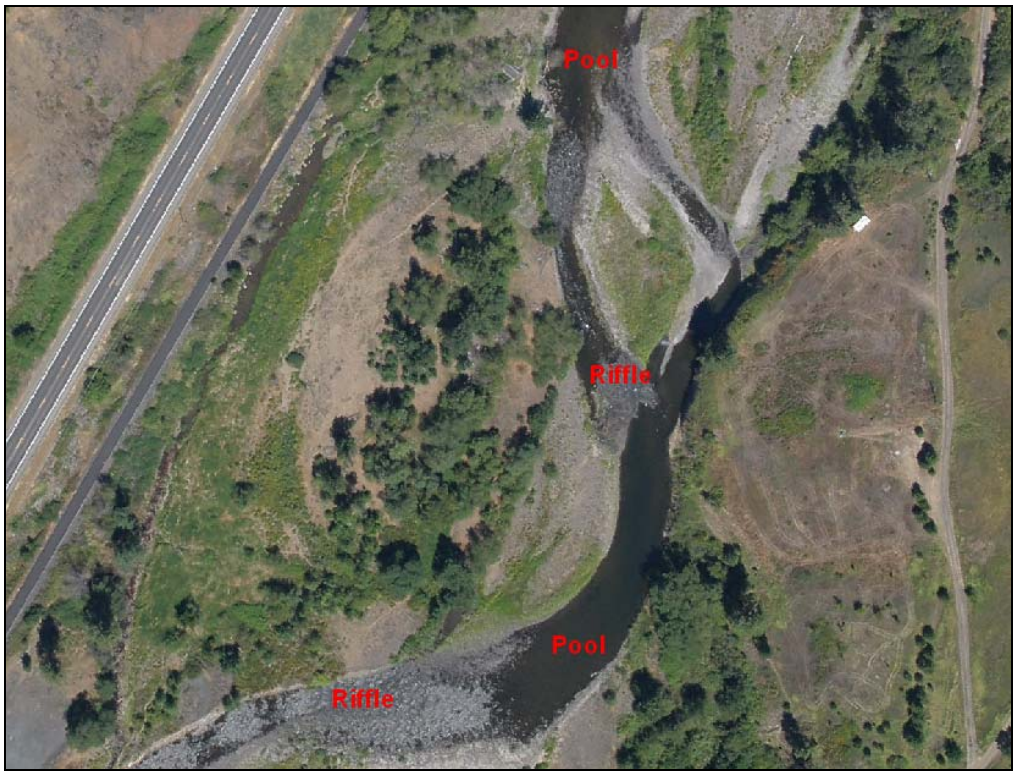

Figure 6.23 Pool-riffle channel unit in the Potlatch River.

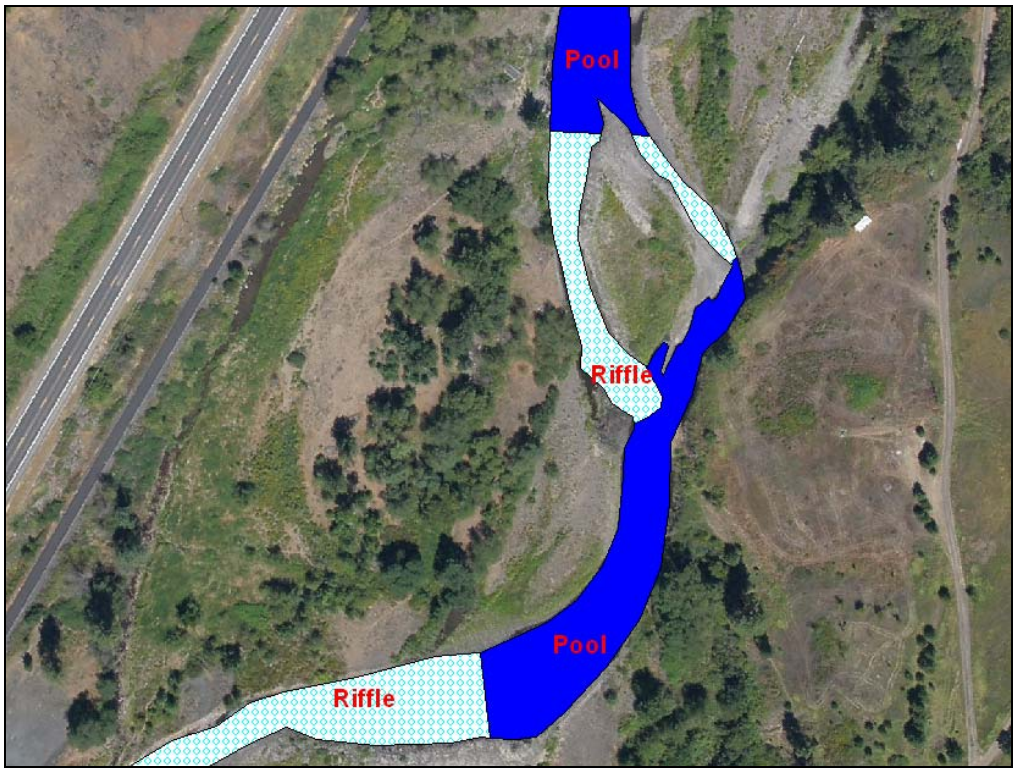

Figure 6.24 Pool-riffle channel unit polygons.

Morphological Parameter	Channel Unit		
	Pool	Riffle	Run
Total number	96	106	19
Mean length, m	101	105	238
Mean width, m	17.6	17.2	14.6
Mean area, m^2	1773	1540	3898
Average spacing, m	259	235	--
Average spacing, widths	16	14	--

Table 6.2 Lower Potlatch River channel unit summary statistics.

Segmentation of the full 25 km long water surface polygon into this annotated channel units was completed in about 2 hours. The channel unit attribute table was imported into Excel and the statistical summaries were completed in about 0.5 hour. More complex classification schemes would require more time.

An advantage of the georeferenced aerial image dataset is that specific channel units can be located by river station or other streamwise addressing system. This is generally known as development of linear events in geographical system science. A simple scheme is to uniquely identify each channel unit by the river kilometer nearest its polygon feature centroid. This becomes a permanent reference point for future monitoring and change analysis. Other spatial descriptors such as accumulated watershed area to the centroid or distance from nearest upstream point discharge could be added with more effort. Spatial context descriptors can help identify probable stressors and the likely effect of management intervention. River kilometer designators were assigned to the channel unit centroids for the lower Potlatch River and completed in about 0.2 hours with conventional GIS spatial context operations.

The high-resolution aerial image dataset is self documenting and provides a transparency of analysis that should increase confidence in management actions taken based on summary professional judgments. This advantage of aerial image datasets

seems not to have been recognized in stream assessment work, though the principles of imagery induced transparency are well known in political and defense matters (Baker et al. 2001; Hays 2001). With appropriate legal and copyright protections, a reasonably sized aerial imagery dataset can be easily shared among researchers and managers so that the level of abstraction is greatly reduced and the potential for collaborative decision making and concurrence is increased. The entire georeferenced aerial imagery dataset for the Lower Potlatch River is about 1.67 gigabytes without image compression.

6.7 Channel Change Detection and Analysis

The most often cited and long-standing use of aerial imagery in stream morphology work is detection and measurement of stream channel migration over time (Brice 1982; Bryant and Gilvear 1999; Graf 1984; Gurnell 1997; Hickin and Nanson 1984; Leopold 1973; Leopold 1982; Leys and Werritty 1999; Miller 1986; Neill and Galay 1967; Philipson 1997; Winterbottom and Gilvear 1997). The stream course is the most easily recognized morphological feature in an aerial or satellite image. One gains an immediate visual impression of channel change when comparing historic images at suitable scales. Two analysts are not likely to dispute that channel migration has occurred. Development of a meaningful quantification of the rate and significance of change between image dates is much more illusive.

Quantitative approaches to assessment and prediction of channel migration are not numerous. Graf (1984) recognized the ineffectual nature of deterministic channel migration theories and developed a probabilistic approach to the spatial assessment of river channel instability. This approach has received some recent attention

(Winterbottom and Gilvear 2000). The method proposed that bank erosion probability could be determined for a location on a floodplain as a power function of its distance from the active channel in the lateral and upstream direction, and a value representing flood magnitudes for the given period. Coefficients for the probability expression are developed from analysis of the historic channel change and climate record. Graf (1984) recommended basing the analysis on a record of aerial photos or channel survey maps of at least once every 10 years for 50 years or longer. High resolution aerial photography of streams of this extent and duration do not often exist in the Pacific Northwest. Adaptation of this methodology to the Pacific Northwest is a subject for future research.

Fortunately, elaborate quantification is probably not necessary to derive meaningful stream management information from historic and current aerial imagery record. In my view there are three primary questions to be addressed for any given stream location:

1) Has the channel migrated significantly in a consistent direction in the recent past?

2) Has upstream discharge or sediment load changed or is expected to change significantly?

3) Are there barriers or impediments (natural or artificial) to further channel migration at a given location?

A historic satellite and aerial imagery database provide a basis to evaluate questions 1) and 2). Recent high-resolution aerial imagery is an efficient source of information to assess question 3).

The simplest, and perhaps most convincing technique, that yields an answer to 1) is to compare historic thalwegs or channel centerlines. This procedure is relatively

unbiased and merely abstracts the visual impression of channel change seen in the imagery record to a more convenient cartographic form that facilitates basic one-dimensional analysis. As seen in the demonstration above, the alignment of the channel is easily represented by a single line digitized along the thalweg or apparent channel centerline. A change in channel alignment of any significance is readily apparent by the offset of the digitized thalweg or centerlines.

6.7.1 Potlatch River Channel Change

The apparent channel centerline for the lower Potlatch River was digitized from the May 22, 1992 USGS digital orthophotoquadrangle (DOQ) and compared to the thalweg digitized from the July 22, 2004 aerial imagery dataset. A portion of the two channel lines is seen in Figure 6.22. Figure 6.25 is another segment of the Potlatch River upstream from Juliaetta. Also shown is the channel centerline from the National Hydrography Dataset GIS coverage developed by USGS probably from small scale aerial images from the 1960's. Channel alignment changes are prevalent throughout the 25 km study reach between 1992 and 2004. It appears that most of the realignment occurred during the extreme floods of 1996 and 1997. Unfortunately, no aerial photos are available for these years. Relatively large floods in the Potlatch basin in 1965, 1972 and 1974, as evidenced by the lower Clearwater River discharge records, likely contributed to the changed channel alignment observed between the date aerial photography used to develop the NHD hydrography and the 1992 DOQ.

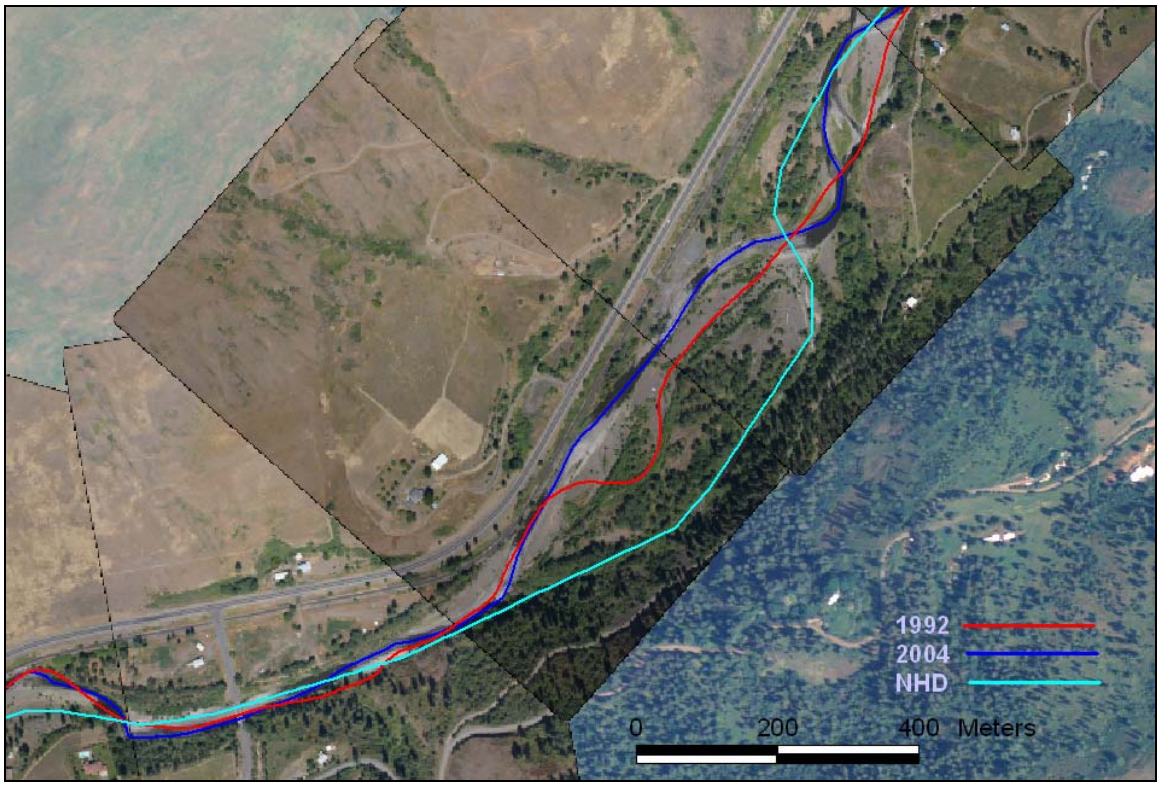

Figure 6.25 Comparison of channel alignments for 1992, 2004 and the National Hydrography Dataset.

A question of some importance is whether the total length of channel in a highly active alluvial channel changes significantly through the geomorphological cycle between significant floods. Important related questions that are fundamental to the field of morphodynamics are where changes in alignment are likely to occur and how much channel movement can be expected at a particular location. A time sequence of high-resolution aerial imagery provides a fairly definitive answer to the first question and meaningful insights that help answer the latter questions. These latter questions are treated in detail in subsequent sections and led to a unique concept of stream morphology called the morphological transport segment described in Section 6.11.

Significant changes in channel length have implications for validity of water quality and flood modeling, and emergency spill response. The channel centerline

comparison answers this convincingly. Total length of the 1992 and 2004 channel centerlines are 24.55 km and 24.97 km. Overall sinuosity (channel length divided by valley length) of the 2004 thalweg is 1.08. The 420 meter difference is not significant for either water quality modeling or spill response. It is interesting to note that the length of the NHD centerline for the study reach is 24.02 km, also not a particularly significant departure from the 2004 channel length.

A rapid channel migration hazard assessment can be made by viewing the historic and current channel centerlines superimposed over current high-resolution aerial imagery. Figure 6.26 is the segment of the lower Potlatch River at the Juliaetta Wastewater Treatment facility. The narrow channel migration band indicates that the wastewater facility is in a relative secure location though it is in the historic floodplain. The aerial photograph in Figure 6.27 by the USACE in November 1972 taken after a large spring flood supports the judgment that the wastewater facility is probably not threatened by floods with greater than a one percent (100 year) chance of occurrence.

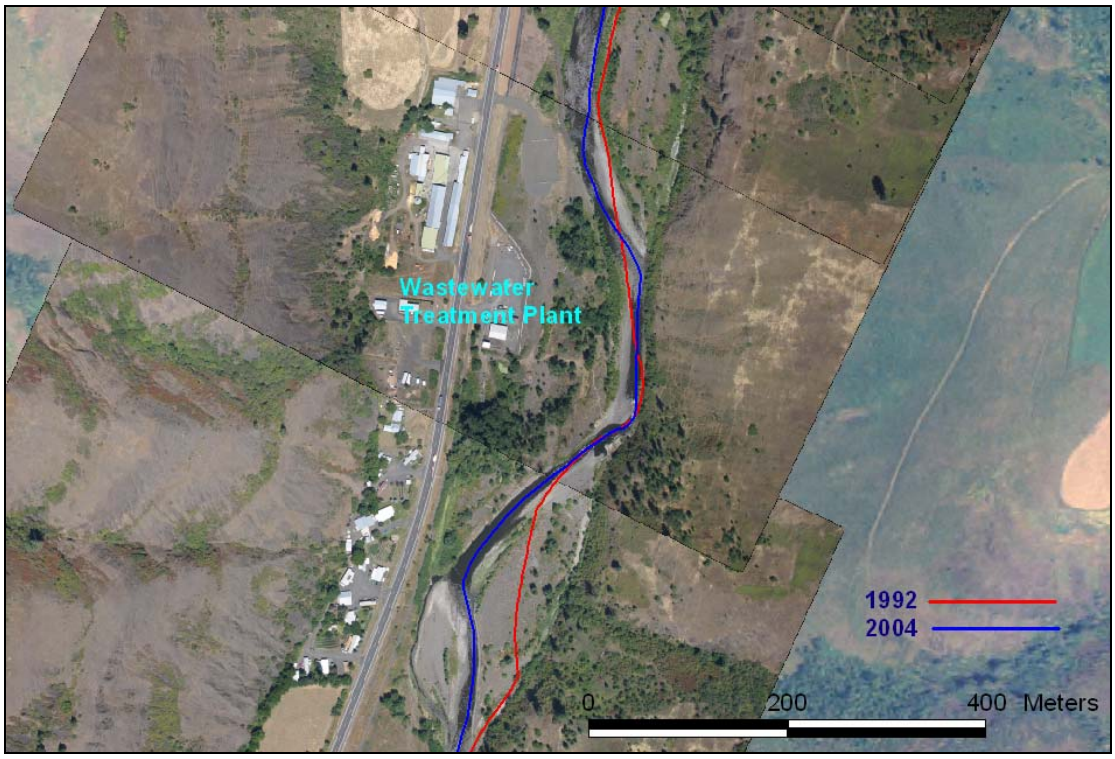

Figure 6.26 Channel migration near the Juliaetta Wastewater Treatment plant.

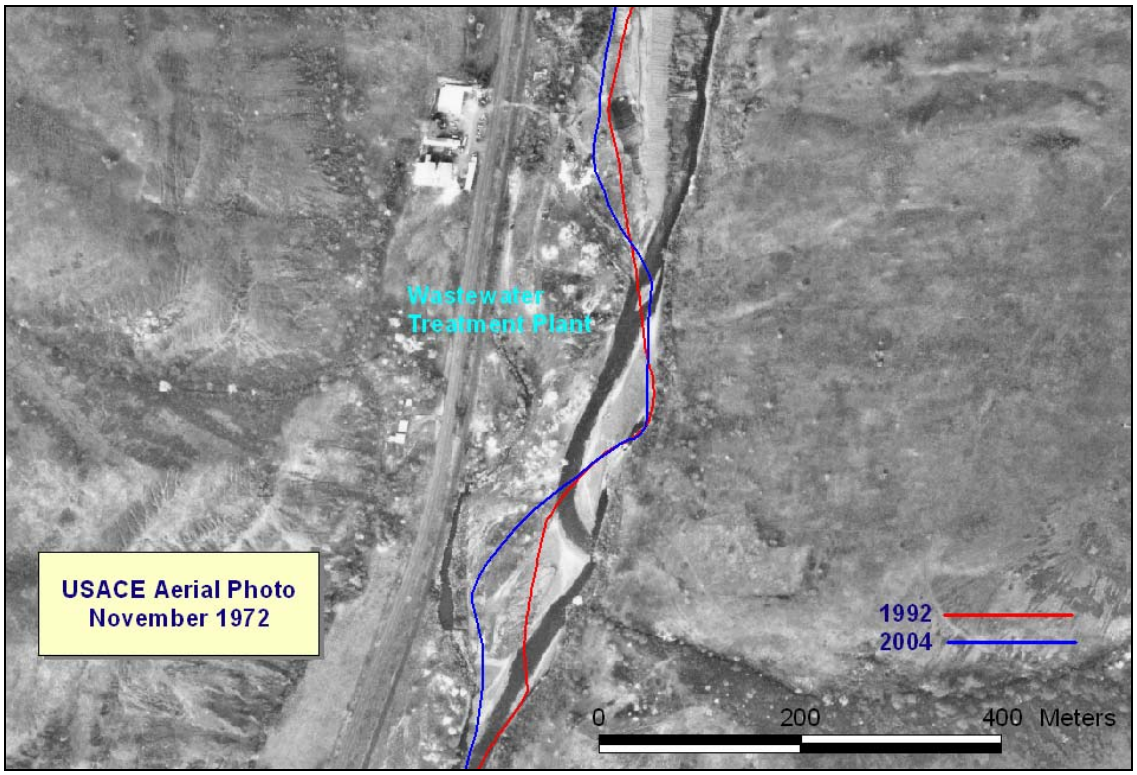

Figure 6.27 1972 aerial photo of the lower Potlatch River near the site of the Juliaetta Wastewater Treatment plant.

Elsewhere on the lower Potlatch River, the river appears ready to reclaim a portion of the historic floodplain with significant hazard to private property. Figure 6.28 shows that residential buildings and equipment storage facilities are in a zone where the migration band is wide and active.

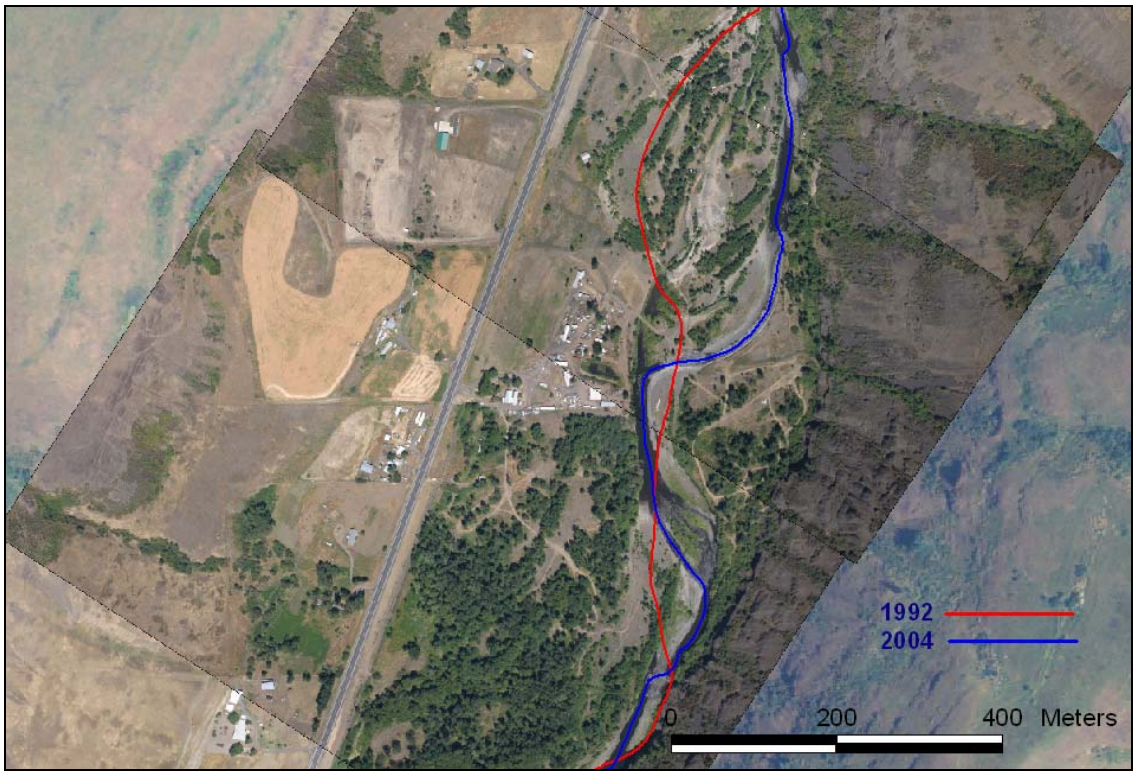

Figure 6.28 Residential buildings and equipment storage facilities in the active floodplain of the Potlatch River.

The 1972 USACE aerial photo in Figure 6.29 shows that the active channel used to occupy the building site. A closer inspection of the high-resolution aerial images in stereo view reveals that some of the building site has been filled to raise the ground level above the surrounding floodplain. The fill material seems to be local alluvial material indicating that the river might reoccupy the site by lateral erosion rather than flooding and avulsion. A detailed site survey would be necessary to judge actual flood and channel erosion hazard at the site.

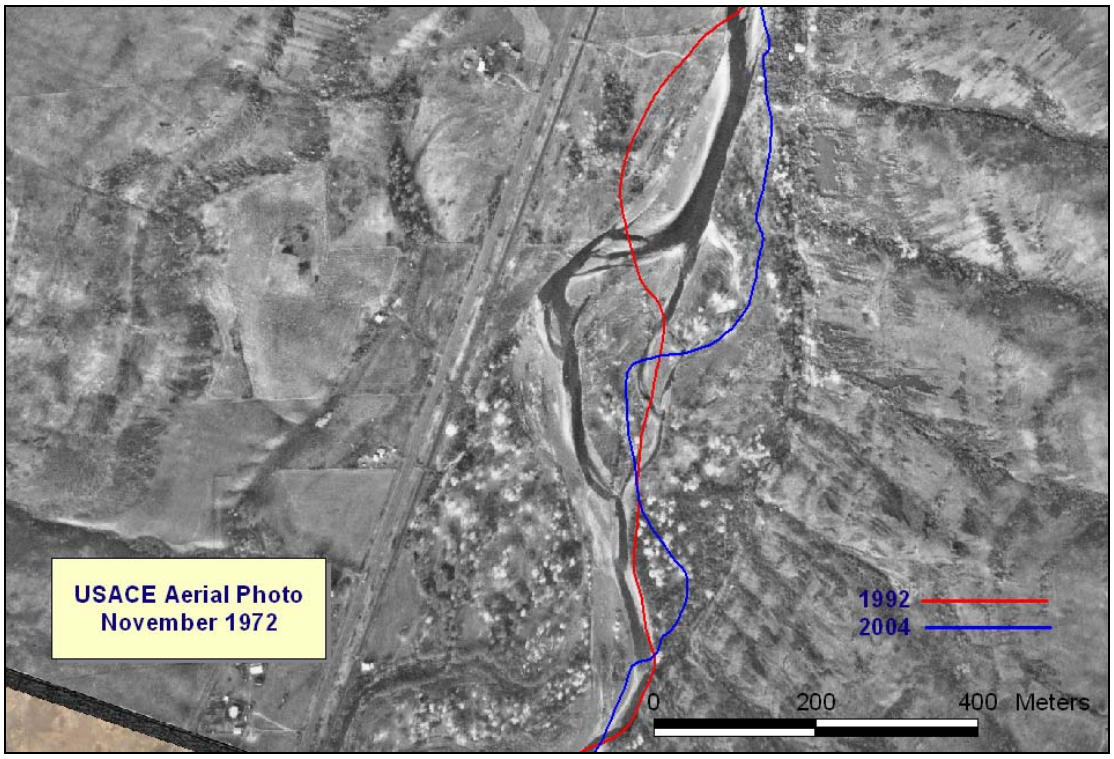

Figure 6.29 1972 aerial photo of the lower Potlatch River near the residential building site in Figure 6.28.

Recent low-flow and high-flow high-resolution aerial images provide important visual clues and hydraulic data that indicate the potential for a channel to migrate laterally at a particular location. Locations of relatively mobile gravel bars and flow impingement points are readily visible. Resistant channel forms such as bedrock outcrops, high-roughness vegetated banks, and artificial revetments are usually apparent. Relative sediment sizes of bar and bed materials can be judged in very high-resolution aerial images to provide further evidence of resistance to fluvial action. The overall best indicator of likely channel change is the trend observed in time sequence of high-resolution aerial images. The aerial image-based analysis is compatible with mechanistic computational approaches to assessment of channel mobility and provides valuable

corroborating evidence. These aspects of the use of high-resolution aerial in the assessment of stream morphology will be discussed further in subsequent sections.

Channel change between 1992 and 2004 can be quantified in a one dimensional sense by measuring the area occluded as the channel sweeps from its 1992 to 2004 position. This is a relatively uncomplicated GIS procedure that is somewhat awkward to describe without a software demonstration. The procedure involves the following steps:

- Convert each channel centerline into complementary enclosed area polygons. The conversion must be made in both directions to produce complementary areas for each channel centerline (four polygons total);
- Intersect the right complementary polygon for 1992 with the left complementary polygon for 2004;
- Intersect the left complementary polygon for 1992 with the right complementary polygon for 2004;
- Union the two intersection polygons.

For example, the right complementary polygon for 1992 and the left complementary polygon for 2004 are in Figure 6.30. The overlap between the polygons identify the area "swept out" by the channel alignment change. The resulting 1992-2004 channel change polygon for the segment of the lower Potlatch River near Little Potlatch Creek is in Figure 6.31. Total area of the channel change polygon is 57.99 ha or 2.3 ha per km. Dividing this area by the 2004 thalweg length of 24.97 km gives an average channel migration of 23 meters per meter of channel, about 1.4 channel widths.

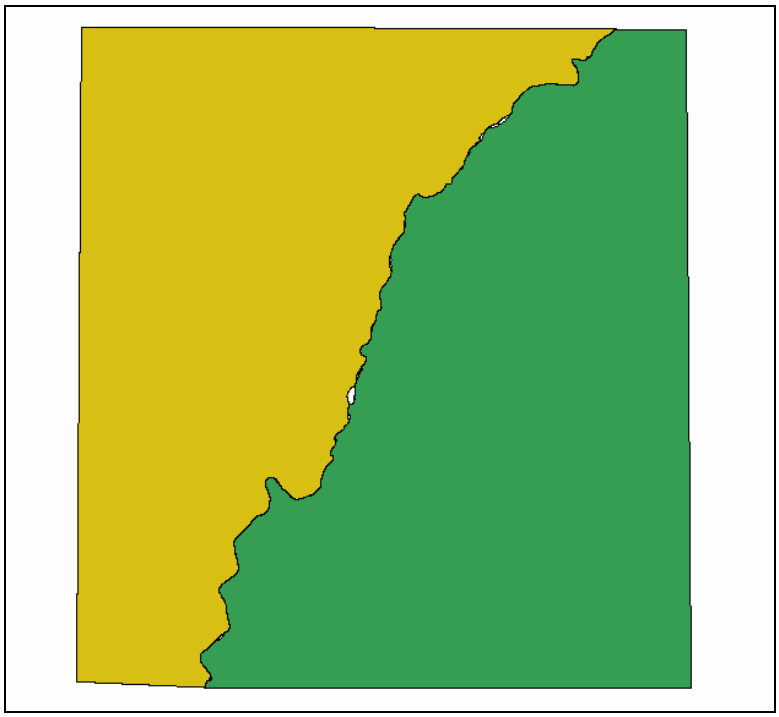

Figure 6.30 Right complementary polygon for 1992 (yellow) and the left complementary polygon (green) for 2004.

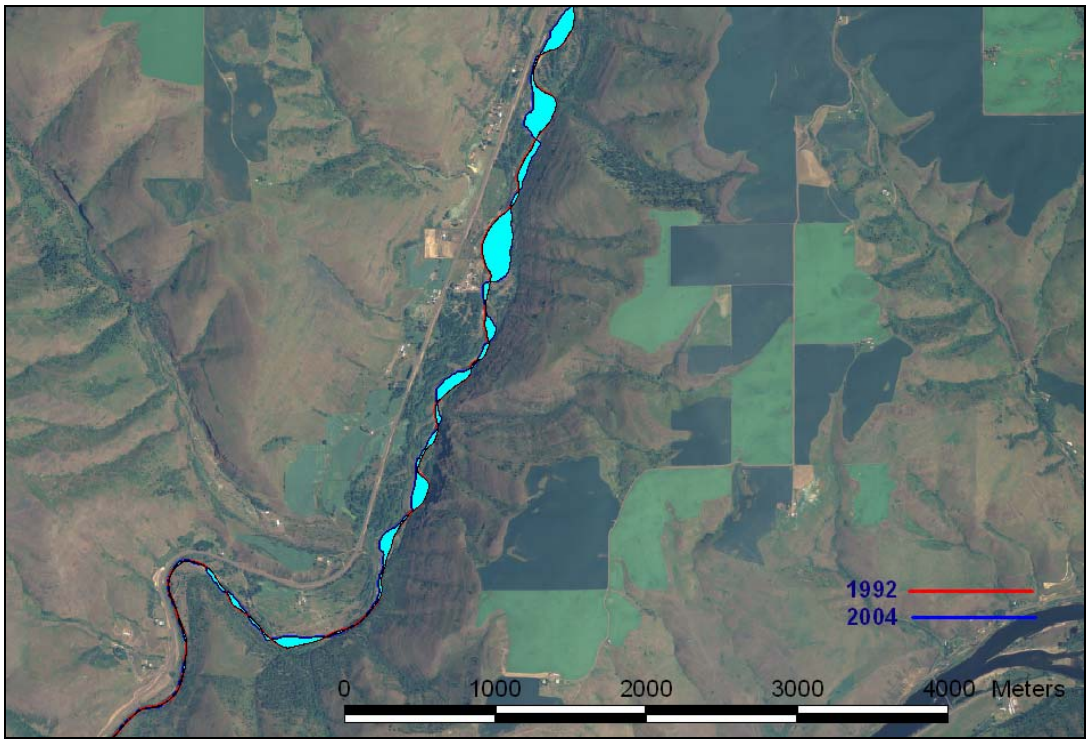

Figure 6.31 Channel change between 1992 and 2004 in the lower Potlatch River near Little Potlatch Creek.

The spatial distribution of the channel change polygon can be further analyzed for comparison with other streams or time periods. A simple representation is to plot the cumulative area that the channel centerline occupies with distance along the channel. Steep slopes on the cumulative occupancy plot indicate significant channel movement and sediment load due to channel lateral adjustment. Another reduction of much practical significance is to plot the average channel shift with distance along the channel. Both these morphological parameters are plotted in Figure 6.32. The plot shows that the lower Potlatch River channel is highly active between river kilometers 10 and 15.

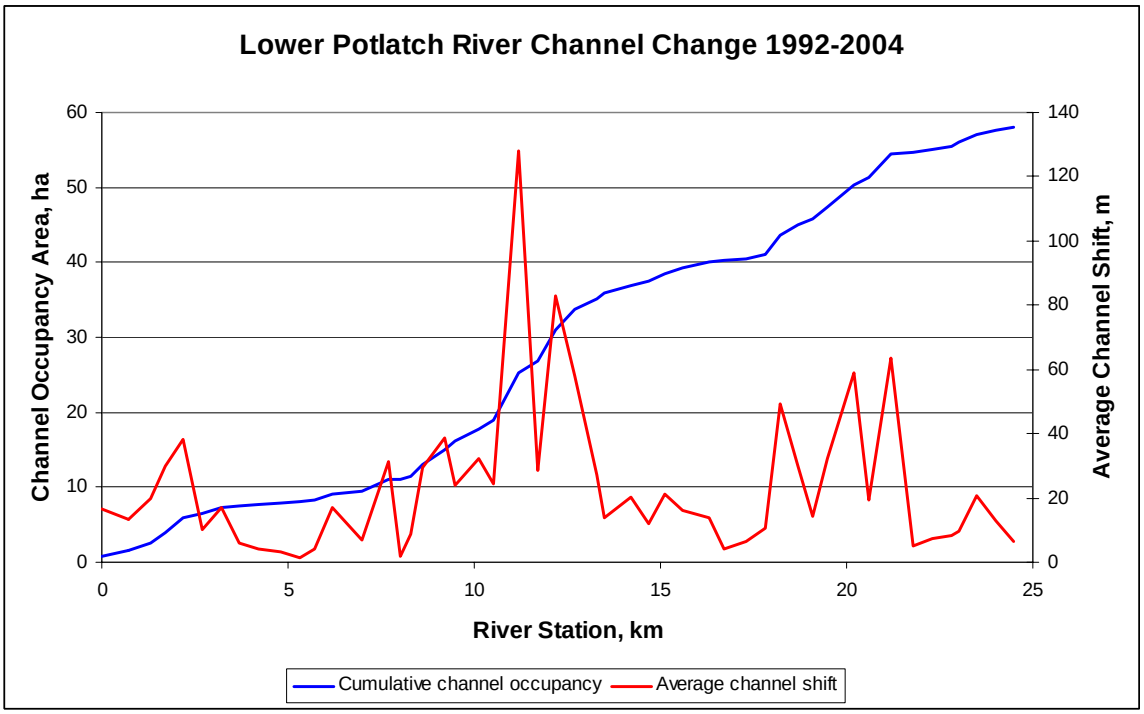

Figure 6.32 Lower Potlatch River channel change morphology 1992-2004.

The channel change plot was produced by splitting the channel change polygon into separate segments at convenient or uniform locations along the channel. Average width for a segment is determined by dividing the segment polygon area by the channel length through the segment. The average width is added to the attribute table of the

segmented channel change polygon and imported into Excel for analysis and plotting. Development and analysis of the channel change polygon was completed in about 1.0 hour.

The channel change polygon in Figure 6.31 and the plot in Figure 6.32 hint at periodicity in the spatial distribution of channel change where migration is not constrained laterally by non-fluvial factors. Given the periodicity observed for meanders and channel units (Leopold and Wolman 1957), it seems reasonable to expect that given a sufficiently long record, the amplitude and spatial and temporal frequencies of meander oscillations would bear some relationship to mean channel width, valley slope, and median particle size. The Potlatch River record is insufficient to support this analysis.

6.7.2 Palouse River Channel Change

A similar analysis was developed for a 17 km reach of the upper Palouse River between the forest products mill near Harvard, ID to the abandoned dam at Laird Park. Figure 6.33 is a portion of active channel near the bridge on State Highway 6 east of Harvard. Water flows from the top (north) of the figure to the bottom. The channel is actively encroaching on pastureland south of the highway and migrating into the home site north of the bridge.

Landowners at these locations consider the channel migration to be highly destructive. The owner of the home site has attempted to stabilize the channel with large riprap. Total channel migration was between 1992 and 2004 for the 17 km reach was 13.6 ha or 0.8 ha per km. The average channel shift was 7.9 m per meter of channel length. This is loss in property value of about $85,000 or $8000 per mile if river

frontage is conservatively estimated at $2500 per acre. A more precise economic analysis would consider interest and the residual value of channel area reverting to adjacent property owners. A plot of the one dimensional channel change morphology is in Figure 6.34. The most intense channel change activity occurs between 6 and 10 km upstream from the county road bridge near the forest products mill.

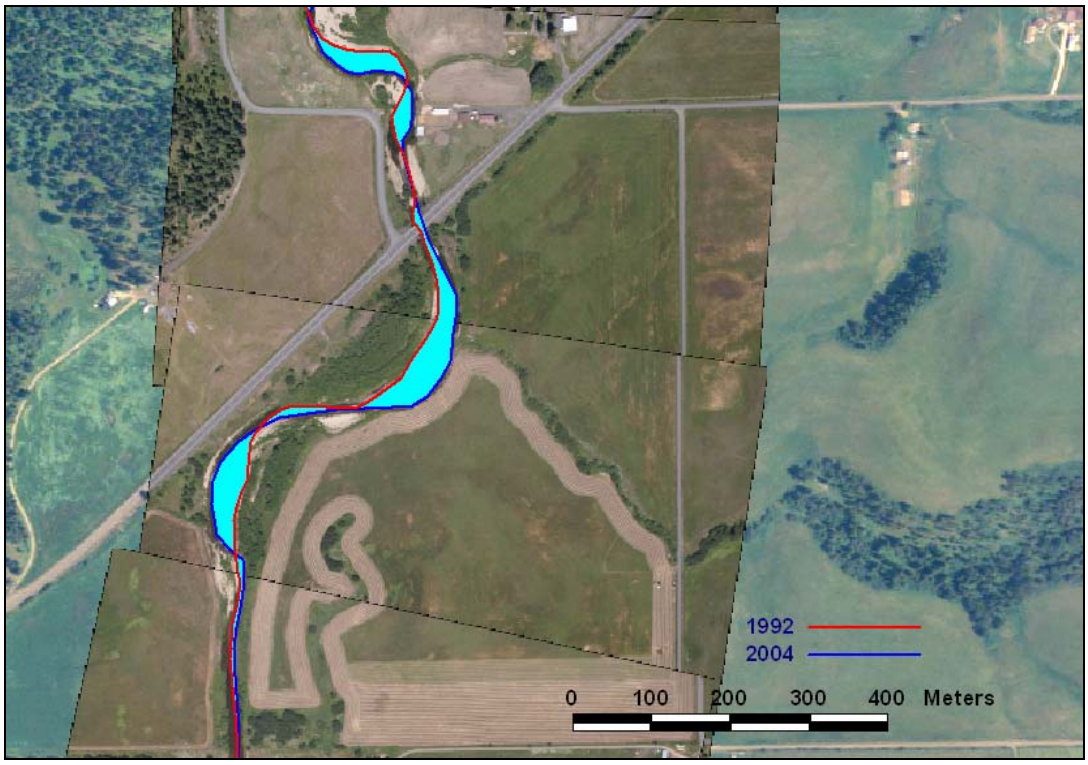

Figure 6.33 Channel change 1992-2004 on the upper Palouse River near Harvard, ID.

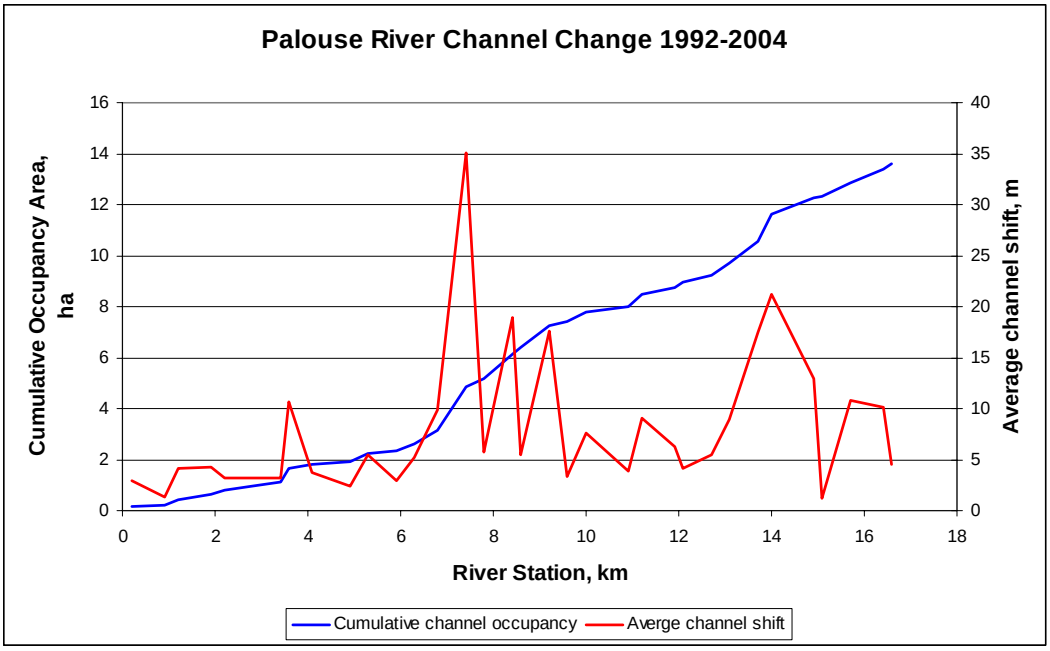

Figure 6.34 Upper Palouse River channel change morphology 1992-2004.

Older aerial photography shows that the upper Palouse channel has been actively migrating for at least half a century. Figure 6.35 is the channel change between 1957 and 2004. Arrows show the direction of bend migration. This simple analysis offers fairly convincing evidence that the bends will continue to migrate into the pasture and will eventually encroach on the highway right-of-way. Very interesting features of Figure 6.34 are the apparent stability of the channel in the segment below the lower bend and the cross over point between bends. This stability seems to be unrelated to bank material properties and is associated with a riffle channel unit as seen in the July 21, 2004 aerial imagery (Figure 6.36). Stability of this type is significant and will be discussed later in this section. A more sophisticated analysis would be to superimpose bend migration vector arrows on the the current aerial image. Direction of a bend vector arrow indicates the predominant direction of movement and the length of the vector the magnitude of change during a particular increment of the analysis period.

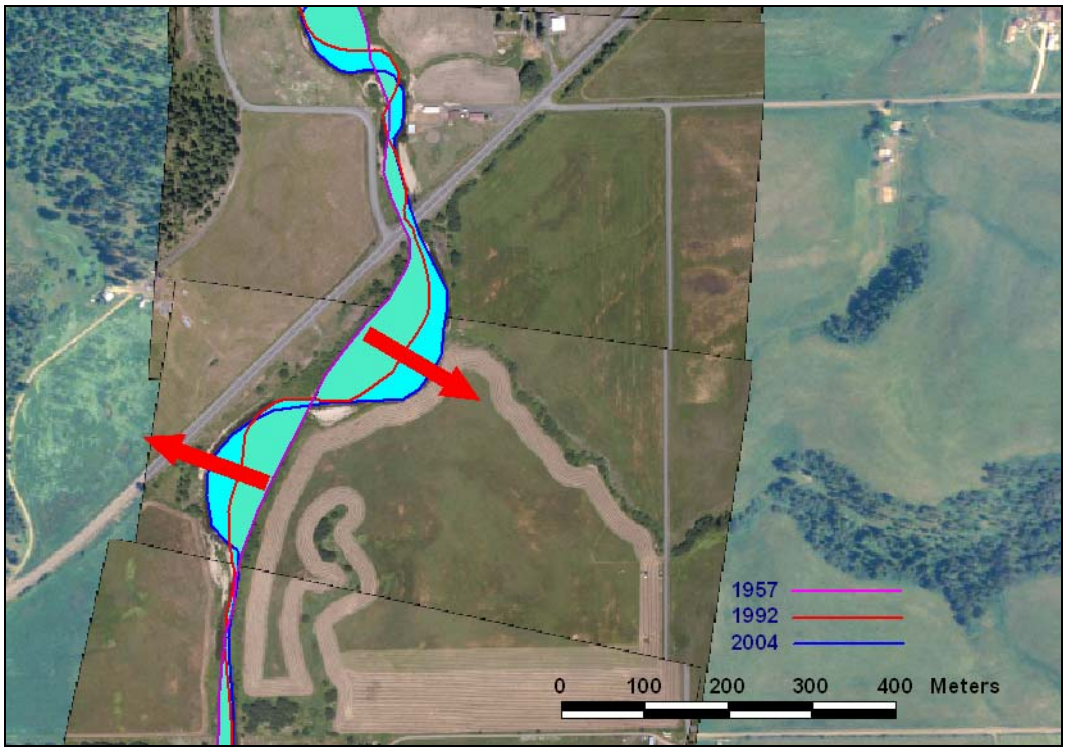

Figure 6.35 Channel change 1957-2004 on the upper Palouse River near Harvard, ID.

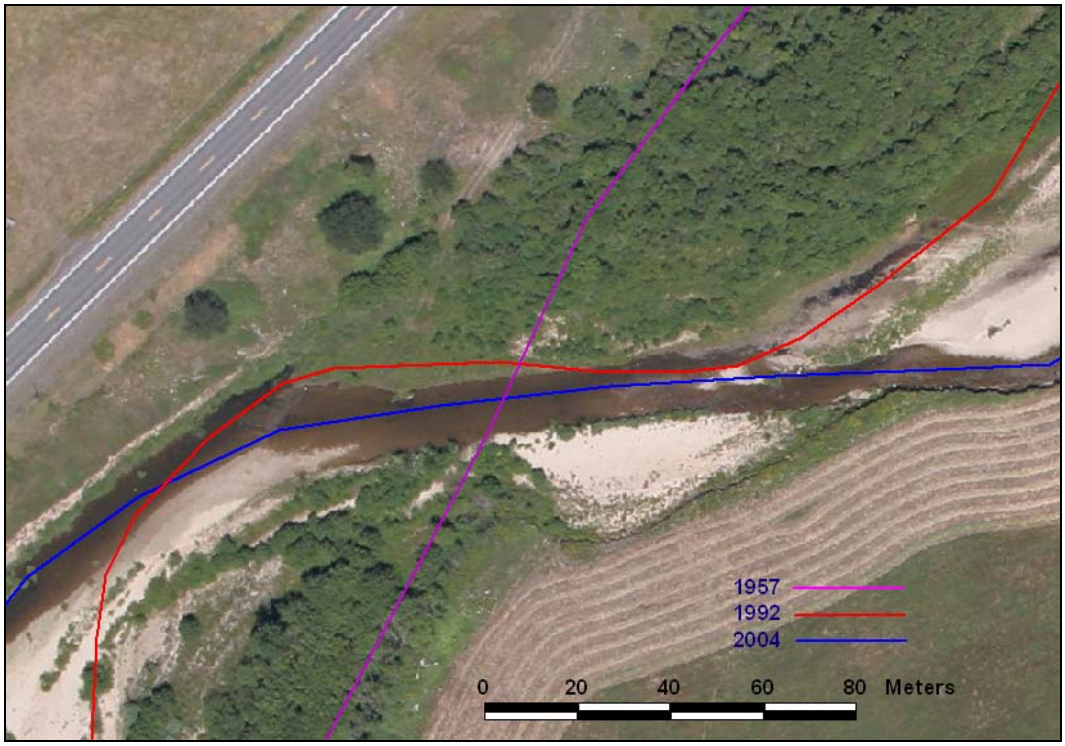

Figure 6.36 Geomorphically stabilized channel anchor point on the upper Palouse River.

Total channel migration was between 1957 and 2004 for the 17 km reach was 47.5 ha or 2.8 ha per km. Total property value loss is approximately $1.24 million assuming a uniform loss of 1.01 ha per year over the 47 year period, a property value that increases linearly from $300 per acre in 1957 to $2500 per acre in 2004, no residual value of land occupied abandoned by the stream channel, and an interest rate of 9 percent per year. Annual future value computations are summarized in Table 6.3.

Year	Period n	Cumulative Land loss ha	Annual Land Loss ha	Property Value $/ha	Annual Loss $	2004 Future Value[1] $	Year	Period n	Cumulative Land loss ha	Annual Land Loss ha	Property Value $/ha	Annual Loss $	2004 Future Value[1] $
1957		0.0					1981	24	24.3	1.01	3,459	3,496	25,375
1958	1	1.0	1.01	741	749	39,465	1982	25	25.3	1.01	3,578	3,616	24,075
1959	2	2.0	1.01	859	869	41,978	1983	26	26.3	1.01	3,696	3,735	22,817
1960	3	3.0	1.01	978	988	43,807	1984	27	27.3	1.01	3,814	3,854	21,602
1961	4	4.0	1.01	1,096	1,107	45,048	1985	28	28.3	1.01	3,932	3,974	20,433
1962	5	5.1	1.01	1,214	1,227	45,786	1986	29	29.3	1.01	4,050	4,093	19,309
1963	6	6.1	1.01	1,332	1,346	46,094	1987	30	30.3	1.01	4,168	4,213	18,231
1964	7	7.1	1.01	1,450	1,466	46,040	1988	31	31.3	1.01	4,287	4,332	17,200
1965	8	8.1	1.01	1,569	1,585	45,680	1989	32	32.3	1.01	4,405	4,452	16,215
1966	9	9.1	1.01	1,687	1,705	45,066	1990	33	33.4	1.01	4,523	4,571	15,275
1967	10	10.1	1.01	1,805	1,824	44,241	1991	34	34.4	1.01	4,641	4,691	14,380
1968	11	11.1	1.01	1,923	1,944	43,246	1992	35	35.4	1.01	4,759	4,810	13,529
1969	12	12.1	1.01	2,041	2,063	42,113	1993	36	36.4	1.01	4,878	4,929	12,720
1970	13	13.1	1.01	2,159	2,182	40,873	1994	37	37.4	1.01	4,996	5,049	11,952
1971	14	14.1	1.01	2,278	2,302	39,550	1995	38	38.4	1.01	5,114	5,168	11,225
1972	15	15.2	1.01	2,396	2,421	38,167	1996	39	39.4	1.01	5,232	5,288	10,536
1973	16	16.2	1.01	2,514	2,541	36,743	1997	40	40.4	1.01	5,350	5,407	9,884
1974	17	17.2	1.01	2,632	2,660	35,294	1998	41	41.4	1.01	5,468	5,527	9,269
1975	18	18.2	1.01	2,750	2,780	33,834	1999	42	42.4	1.01	5,587	5,646	8,687
1976	19	19.2	1.01	2,869	2,899	32,374	2000	43	43.5	1.01	5,705	5,765	8,138
1977	20	20.2	1.01	2,987	3,018	30,924	2001	44	44.5	1.01	5,823	5,885	7,621
1978	21	21.2	1.01	3,105	3,138	29,494	2002	45	45.5	1.01	5,941	6,004	7,134
1979	22	22.2	1.01	3,223	3,257	28,088	2003	46	46.5	1.01	6,059	6,124	6,675
1980	23	23.2	1.01	3,341	3,377	26,714	2004	47	47.5	1.01	6,177	6,243	6,243
Subtotal						900,620							338,527
Grand total													$1,239,147
[1]Interest rate is 9 percent compounded annually													

Table 6.3 Future value of property lost because of channel migration in the upper Palouse River.

There may be some recovery in land value as the abandoned stream channel recovers (slowly) to a condition that supports agricultural use. It is unlikely that planning and building authorities would allow a higher use, such as new residential construction, in close proximity to an abandoned stream channel adjacent to a morphologically active stream. Riparian habitat values should be included in a more detailed analysis, but would likely not be considered particularly relevant by private landowners.

Bank erosion sediment load can be estimated from the one dimensional channel migration morphology. Average bank height observed in the 2004 high-resolution aerial images is about 1.5 meters. Bank erosion volume for the period 1992 to 2004 is estimated at 204,000 m^3 by multiplying the total channel occupancy area 13.6 ha by the average bank height 1.5 m. Assuming a bulk density of 1.5 metric tons per cubic meter, annual bank erosion load is 25,500 metric tons per year for the upper Palouse River.

The one-dimensional morphological analysis in itself offers no explanation of why the Upper Palouse River may be experiencing accelerated bank erosion and channel migration. Anecdotal statements by residents suggest that the river once had “holes as deep as 30 feet”. The satellite imagery record offers some indication of why the river may be subject to higher peak discharges and increased sediment load. Figure 6.37Figure 6.38 are visible-near infrared Landsat images from 1990 and 2002. The outline of the upper Palouse watershed determined by DEM terrain analysis is superimposed on both satellite images. Land cover in the upper basin is dominated by forest, a mix of National Forest and industrial forestland. A high proportion of the area has been harvested, probably causing increased peak flow and sediment loads to the Palouse River over historic levels. Peak daily discharges at the USGS gage near Potlatch, ID (Figure 6.39) are subdued during the period 1985-1995. January and February peak flows have increased significantly since then, even discounting the extreme flood in 1996. The satellite images or gage records are not conclusive evidence of a causative effect, but provide a good starting point for further hydrological analysis.

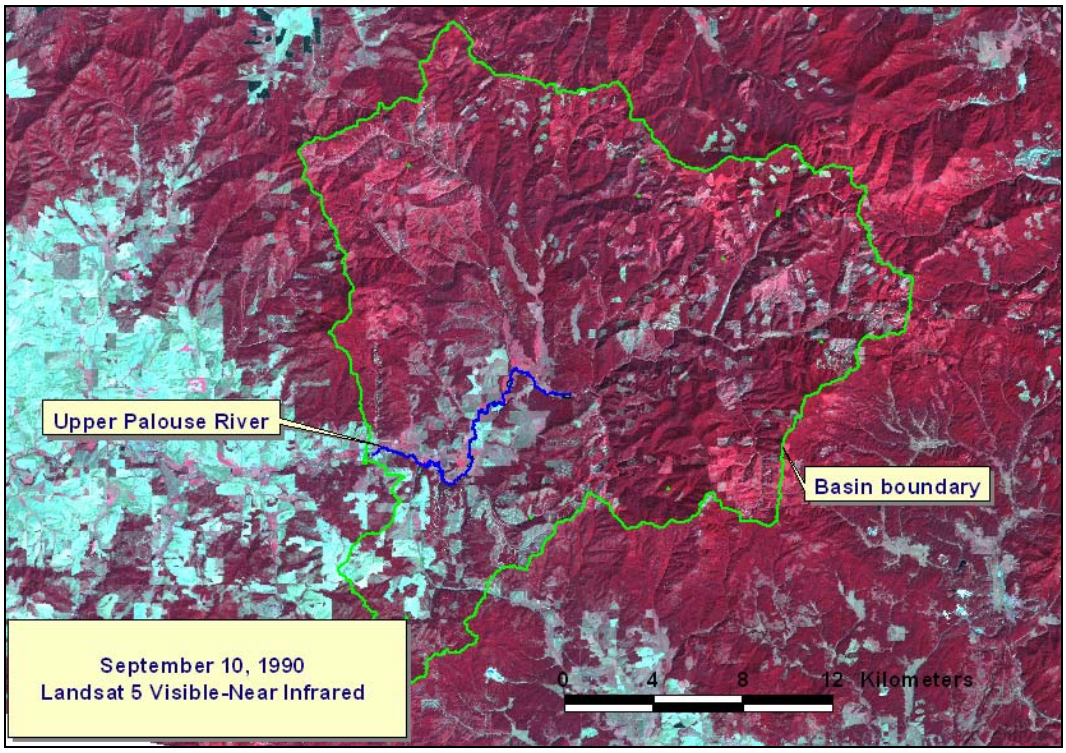

Figure 6.37 1990 Landsat 5 visible-near infrared image of the upper Palouse basin.

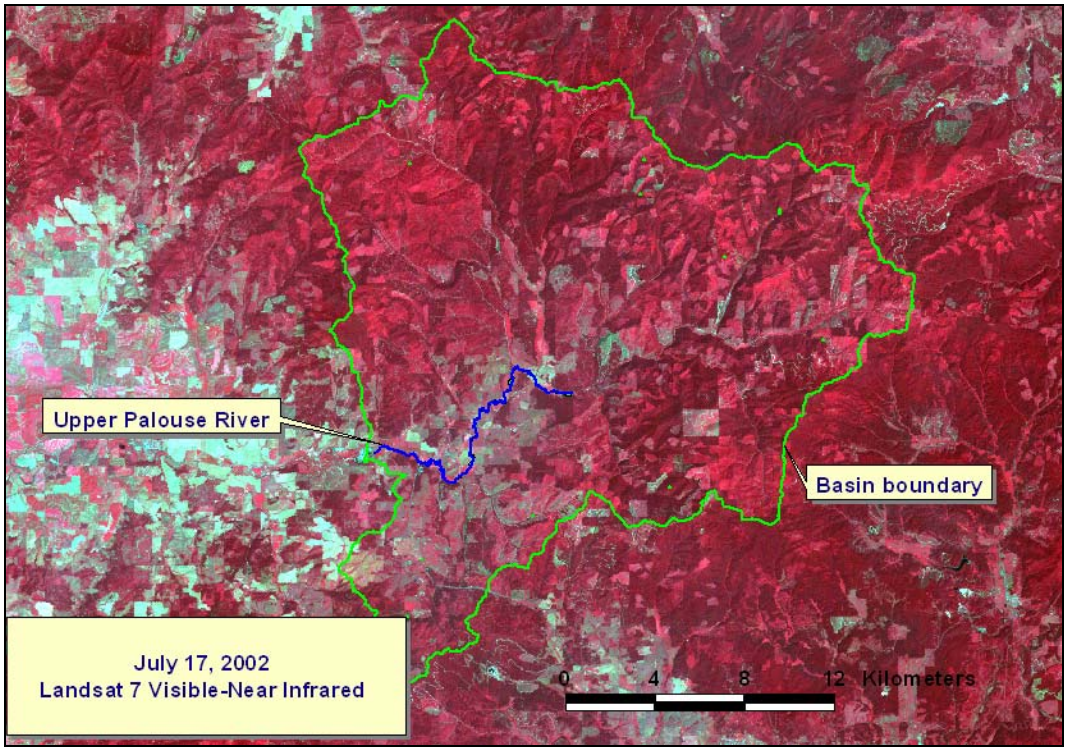

Figure 6.38 2004 Landsat 7 visible-near infrared image of the upper Palouse basin.

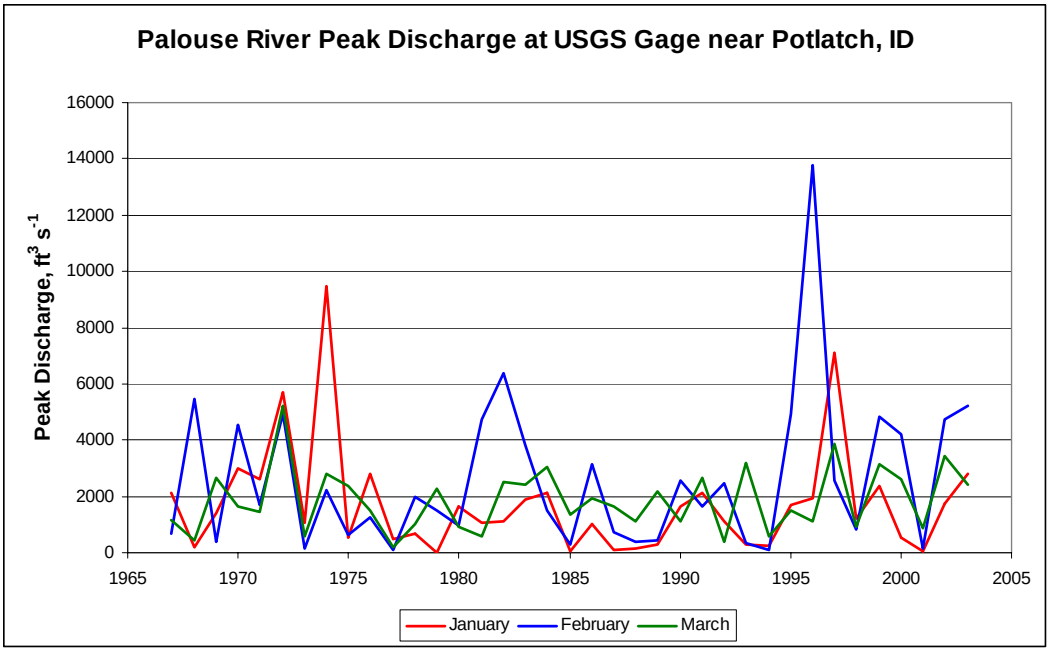

Figure 6.39 Potlatch River peak daily discharge 1966-2003 at USGS gage near Potlatch, Idaho.

The property loss and bank erosion computations illustrate an advantage of aerial and satellite imagery based analysis: potentially controversial computations are based on observed conditions and uncomplicated and highly transparent analysis. There are no untenable appeals to professional judgment arising from the application of flume derived bedload transport equations or assumptions of bank stability strength factors. The analysis is almost as accessible to the lay public as it is to managers and technical professionals.

Channel change polygons indicate the net movement of the channel between the dates of the centerlines represented, this was a 12 year period from 1992 to 2004 in the Potlatch River and Palouse River examples. During this time the channel may have occupied and surrendered some portions of floodplain several times. Absolute channel movement must be determined by annual analysis, possibly more often if two or more

channel forming discharges occur in a particular year. The frequency of analysis might be reduced if ancillary evidence, such as discharge records, indicates little potential for channel migration or bedload movement in a given year. A short term channel change analysis for the Potlatch River is presented in the next section.

6.8 Short Term Change Analysis with High Resolution Aerial Imagery

Gravel-bed streams display a fascinating complexity of form and process. They possess at least nine degrees of freedom: average bankfull width, average bankfull depth, maximum depth, slope, velocity, sinuosity, meander arc length, bedform height, and bed form wavelength (Hey 1978; Hey 1982). These variables manifest themselves in an ever-changing spatial and temporal continuum in response to water discharge, sediment load, bed sediment size, bank material type, valley slope, vegetative recruitment, and anthropogenic disturbance.

The pursuit of the rational and mathematical foundation of fluvial complexity has engaged geomorphologists and water engineers for well over a century. It has not been an easy task and many issues of engineering interest have yet to be resolved (ASCE 1998). It is reported that Albert Einstein commiserated with his son Hans, a renowned fluvial scientist, for having chosen a field of study more intractable than his own (Wolman 1977). This context should be kept in mind through the following discussion of the application of high-resolution aerial imagery to various aspects of stream morphological assessment.

A time sequence of high-resolution aerial images of low-flow stream channels reveals abundant detail of stream morphology and sediment movement that cannot be obtained by other means. Even a casual observer of the low flow paired images in Figure 6.40 can readily detect subtle changes in channel structure, bank erosion and sediment storage. When coupled with an aerial image acquired at high discharge (Figure 6.41), a strong sense of the morphodynamics emerges.

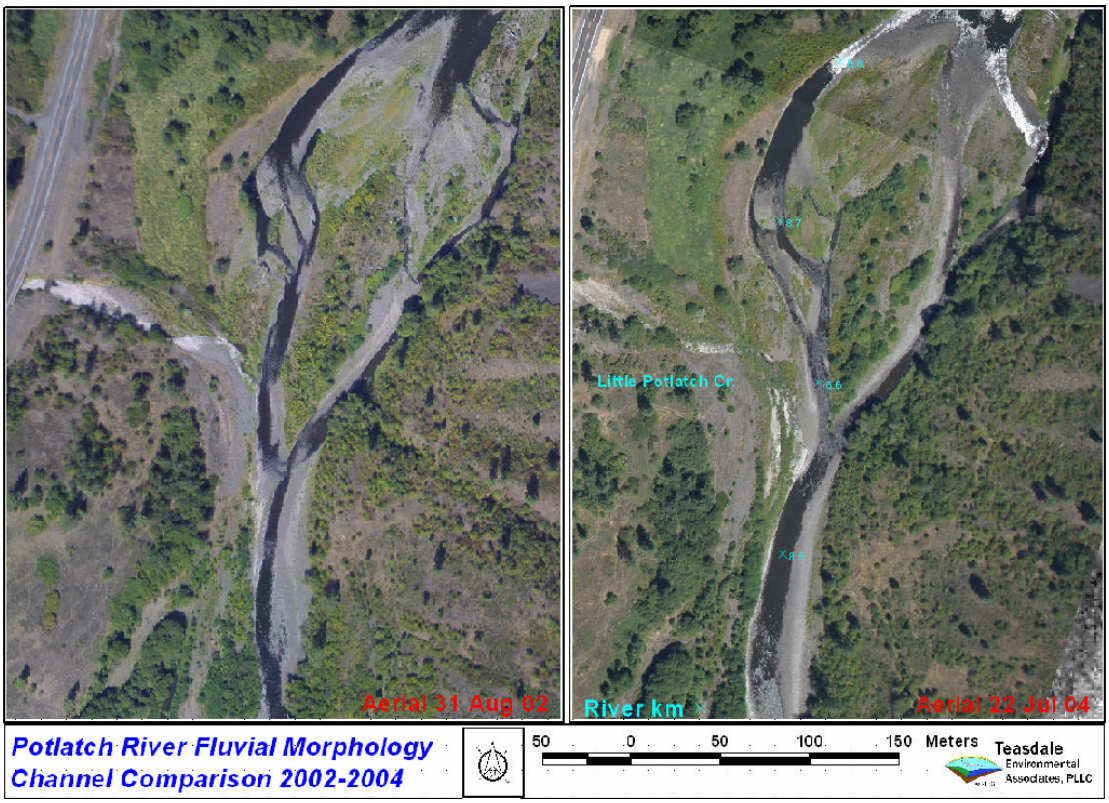

Figure 6.40 Paired high-resolution aerial images of the lower Potlatch River, August 31, 2002 and July 22, 2004.

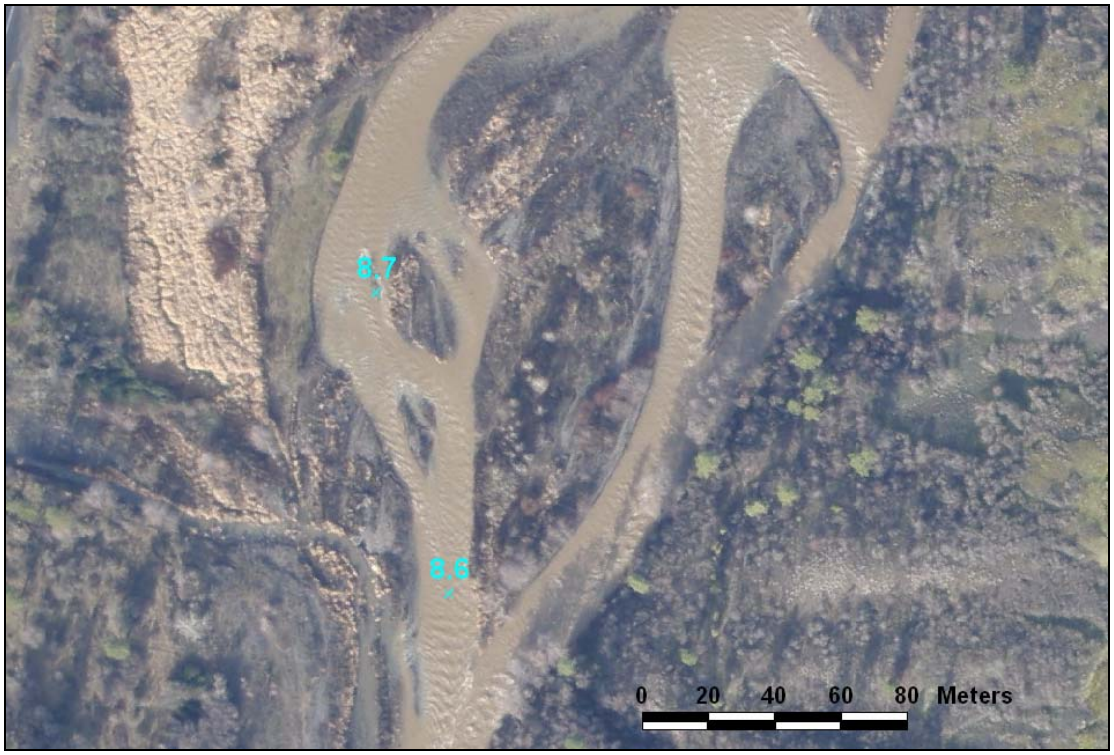

Figure 6.41 Lower Potlatch River slightly below channel forming discharge, January 19, 2005.

The science and art of extracting morphodynamic information from aerial images of real streams is mostly undeveloped and has received scant research attention (Lane 2000). The subtle pattern of regular surface waves and their spacing, amplitude, angle, convergence, and divergence must contain all or most of the information necessary to map velocities and shear stress throughout the reach, especially when grain and form roughness characteristics can be observed in antecedent and subsequent low flow images.

Even without detailed physics, empirical observation and causative association tells us that the dissipating impinging flow on the vertical bank at river kilometer 8.7 in Figure 6.41 will not cause as much bank recession at this discharge as it did in the spring of 2003. On the other hand, a high energy impingement is probably continuing to erode the upper end of the medial bar on the right side of the image. Detailed photogrammetric analysis would give us a relatively precise estimate of the net change in sediment stored within the reach – a much more accurate estimate than the best bed material transport equation or theoretical bend migration relationship.

6.8.1 Morphological Investigation

Quantification of reach scale morphological change in high-resolution aerial image datasets should be approached systematically. The principles of morphological investigation in context of the analysis of river regime were illuminated in an insightful article by Neill and Galay (1967). Their inquiry produced a standardized list of data requirements that suggests the most efficient means to acquire data of streams of various

sizes. They recognized aerial photography as an indispensable data source for analysis of planform, channel cross section and even velocity measurement.

The essential elements of the Neil and Galay (1967) data are listed in Table 6.4 with the addition of a rating of the potential use of high-resolution aerial imagery in characterizing the data element. In the rating ++ indicates an effective and proven capability, + indicates less precise capability and - indicates poor capability. Discussion of the data elements most relevant to my research follows.

	Use of Aerial Imagery	
Morphological Data Element	**Quantitative[1]**	**Qualitative[1]**
Geographic Features		
Location	++	++
Climate	+	+
Geologic setting	+	++
Vegetation	+	++
Channel pattern	++	++
Drainage area	-	+
Hydrologic and Hydraulic Data		
Discharge and stage spectrum	-	++
Water temperature	-	-
Ice phenomena	+	++
Channel slope	+	++
Channel cross sections	++	++
Velocities	+	++
Hydraulic roughness	+	++
Materials and Sediment		
Bed material	+	++
Subbed and subsurface materials	-	-
Bank material	-	+
Suspended sediment	-	+
Bed load	-	+
Channel processes		
Channel lateral shift and bank erosion	++	++
Bed morphology	++	++
Degradation and aggradation	+	++

[1] - + Potential use of aerial imagery in stream morphology assessment

Table 6.4 Essential data requirements for detailed stream morphology assessment adapted from Neil and Galay (1967) and rating of aerial imagery usefulness as a data source.

6.8.1.1 Geographic Features

Vegetation and landform characteristics provide evidence for interpretation of climate and geologic setting. This is a long standing and proven use of aerial photography in the fields of geology, forestry, wildlife management, and range science. Techniques and specific examples are well documented in standard manuals of imagery interpretation (Philipson 1997) and remote sensing texts (Campbell 1996; Jensen 1996; Lillesand and Kieffer 1994). Drainage area can sometimes be interpreted from channel patterns and stereo observation of terrain in small scale aerial images (e.g. NAPP aerial photography) but ancillary elevation data such as topgraphic maps or digital elevation models are need for practical applications. Virtually all extensive elevation datasets and contour maps of the recent past were derived from photogrammetric analysis of aerial photography. Laser altimetry and radar imaging are now operational alternatives for acquisition of elevation data.

Neil and Galay (1967) included vegetation in the geographic features category. Riparian and in-stream vegetation should be in a separate category given the effect of vegetation recruitment on stream stability and the importance of large woody debris accumulation. Seasonal high-resolution aerial images are a very effective data source for discrimination of vegetation life form (herb, shrub, tree) and some species identification. Deciduous and evergreen trees are easily distinguished in the October 27, 2004 aerial image in Figure 6.42 by color and crown pattern.

Figure 6.42 October 27, 2004 aerial image of the Potlatch River at the mouth of Little Potlatch Creek.

Upon closer examination the evergreens trees are mostly Ponderosa pine and the deciduous trees and shrubs are cottonwood and alder respectively. Trees can be distinguished from shrubs by shadows in this image. Botanists, foresters and vegetation ecologists could identify other species and reduce spatial distribution information to a meaningful appraisal of the status of the vegetation. I am ignoring riparian vegetation classification issues (Muller 1997) and assume that remotely sensed data has intrinsic value in the effort.

6.8.1.2 Hydrology and Hydraulic Data

Hydraulic analysis of open channel flow in natural channels invariably requires the measurement of the geometric properties of representative cross sections. The most precise hydraulic computations rely on conventional ground survey measurements with transit, tape, level or total station. Acquisition of cross-section data by aerial photogrammetric techniques for extensive floodplain mapping and modeling is a practical and less expensive alternative firmly established in practice. The Federal Emergency Management Agency (FEMA) has published standard specifications for national flood modeling (FEMA 2003). The FEMA aerial photography mapping standards summarized in Table 6.5 were adapted from guidelines developed by the American Society for Photogrammetric Engineering and Remote Sensing (ASPRS) for maps with scales of 1 inch equals 500 foot. Class 1 surveys require a horizontal accuracy of 5 feet and a vertical accuracy of 0.67 feet. These standards can be routinely met with precision aerial mapping cameras and aerotriangulation reduction.

Horizontal Accuracies			
for 1" = 500' maps	Class 1	Class 2	Class 3
Limiting RMSE in X and Y	5 ft	10 ft	15 ft
Horiz. Survey Standards (Order/Class)	3rd/Cl I	3rd/Cl II	3rd/Cl II
Relative Accuracies	1:9,000	1:4,500	1:3,000
Vertical Accuracies			
RMSE for well defined features			
interpolated between workmap contours	1.33 ft	2.67 ft	4.0 ft
Spot heights, ERMs, ERPs	0.67 ft	1.33 ft	2.0 ft
Vertical Survey Standards (Order)	3rd order	3rd order	3rd order

Table 6.5 FEMA Aerial photography mapping standards for floodplain mapping.

Non-optical remote sensing is an increasingly viable alternative for elevation acquisition. Standards for airborne Light Detection and Ranging (LIDAR) were added as

an appendix to the FEMA standards. The standards specify that LIDAR techniques must be capable of producing DEMs on a 5-meter point spacing and with vertical accuracy of 0.3 meters. The operational precision of the photogrammetric and LIDAR techniques indicated by the FEMA standards is sufficient to conduct a wide variety of rigorous morphological investigations.

Increased availability and relative ease of use of digital photogrammetry software has encourage the use of digital imagery in the study of fluvial morphology (Lane et al. 2000; Lane et al. 1993). Section 2 provided a summary of a few reported uses of aerial imaging in the assessment of streams and stream corridors. Recent literature not cited before includes a comparison of the accuracy of imagery derived bankfull width measurements (Mount et al. 2003), further river bank erosion monitoring (Pyle et al. 1997), studies of sandbar movement in Grand Canyon (Dexter and Cluer 1999) and an European perspective on digital imagery in assessment of stream morphology (Lane 2000) that illuminates research needs. Recent developments in digital image techniques and soft-copy photogrammetry merit reporting as Lane (2000) has done, but reviewers will also benefit from earlier experience with aerial imagery of channel morphology (Anderson et al. 1993; Brabets 1994; Buttle 1995; Collins 1979; Doiron and Whitehurst 1978; Greentree and Aldrich 1976; Kesser 1976; Lo and Wong 1973; Neale et al. 1995; Ray 1960; Tator 1958; Thompson 1958; Welch and Jordan 1983). In my view the extraordinary work of Lueder (1959) still stands out as one of the finest references for photointerpretation of stream morphology.

The aerial survey techniques employed in my research cannot routinely achieve the Class 1 FEMA floodplain mapping standards mostly because precise aircraft position

and orientation are not recorded simultaneously with image acquisition. However such accuracy is usually not necessary in hydrologic modeling for natural resource and environmental assessment work. The rapid and lower cost aerial imaging techniques I have employed support development of initial one-dimensional flow models and morphological assessments with a reasonable amount of effort and expense. These procedures are described in Section 6.9.

6.8.2 Discharge Estimation from Water Surface Area

It is well established that aerial imagery, commercial satellite imagery, and synthetic aperture radar (SAR) imagery of flooded waterways are rapidly acquired and provide detailed information for damage assessment and emergency management (Frazier and Page 2000; Guo 2000; Schultz 1988; Schultz and Engman 2000; Townsend and Walsh 1998). Improved and repeatable satellite and radar imaging techniques have encouraged attempts to estimate discharge from remotely sensed water levels and water surface area (Alsdorf et al. 2000; Birkett 2000; Smith 1997; Smith et al. 1996; Smith et al. 1995). High resolution aerial imagery can also serve this purpose.

There is a sound basis for estimating discharge from observed water surface area in rivers and streams. A simple explanation is seen in the Mannings uniform flow equation:

$$Q = \frac{1}{n} A R^{2/3} S^{1/2} \qquad 6.2$$

where Q is discharge ($m^3\ s^{-1}$), A is the cross section area (m^2), R is the hydraulic radius (m), S is the channel slope ($m\ m^{-1}$), and n is the Mannings friction factor. This relationship shows that discharge increases with increased cross sectional area and

hydraulic radius. In self-forming alluvial channels an increase in depth increases cross sectional area, hydraulic radius, and usually surface width and wetted surface area. Evidence that surface width and surface area increases with discharge in seen in cross section measurements for gravel bed streams and empirical relationships of hydraulic geometry (e.g. Figure 11, Rosgen 1994). Conventional stage-discharge relationships estimate discharge based on a measurement of depth at the gage section. An equally valid relationship can be developed between reach surface area or reach average width and discharge.

Such a relationship is implied in the equations of hydraulic geometry where effective width of the stream is commonly expressed as a power law relationship (Leopold and Maddock 1953) with discharge:

$$B = aQ^b \qquad 6.3$$

where B is the effective stream width, Q is discharge, and a and b are empirical constants. Alternatively, Williams (1978) found reasonable hydraulic geometry relationship for bankfull discharge of active floodplain channels:

$$Q_b = 3.7 A_b^{1.15} S^{0.23} \qquad 6.4$$

where Q_b is bankfull discharge ($m^3\ s^{-1}$), A_b is bankfull cross sectional area, and S is slope of the water surface at the point of estimation.

Monotonic relationships between discharge and stream are also seen in hydraulic geometry relationships of mobile gravel-bed streams. Hey (1982b) derived empirical expressions for wetted perimeter P, hydraulic radius R, maximum depth dm, and channel slope for gravel bed streams in the U.K. The Hey expression for wetted perimeter is a reasonable approximation of observed width:

$$B \approx P = 2.20 Q_b^{0.54} Q_s^{-0.05} \qquad 6.5$$

where Q_s is the bankfull volumetric bed load (m^3 s^{-1}). Width of the alluvial stream in Equation 6.5 varies by approximately the square root of discharge.

An aerial image analysis of the variation of water surface area with discharge is easily developed. Water surface areas are digitized from the georeferenced aerial images as described previously. Aerial images of the lower Potlatch River were acquired on July 22, 2004 at a discharge of 19 ft^3 s^{-1} and on January 31, 2004 at a discharge of 1820 ft^3 s^{-1}. Figure 6.43. shows water surface area polygons for a segment of the lower Potlatch River near Juliaetta.

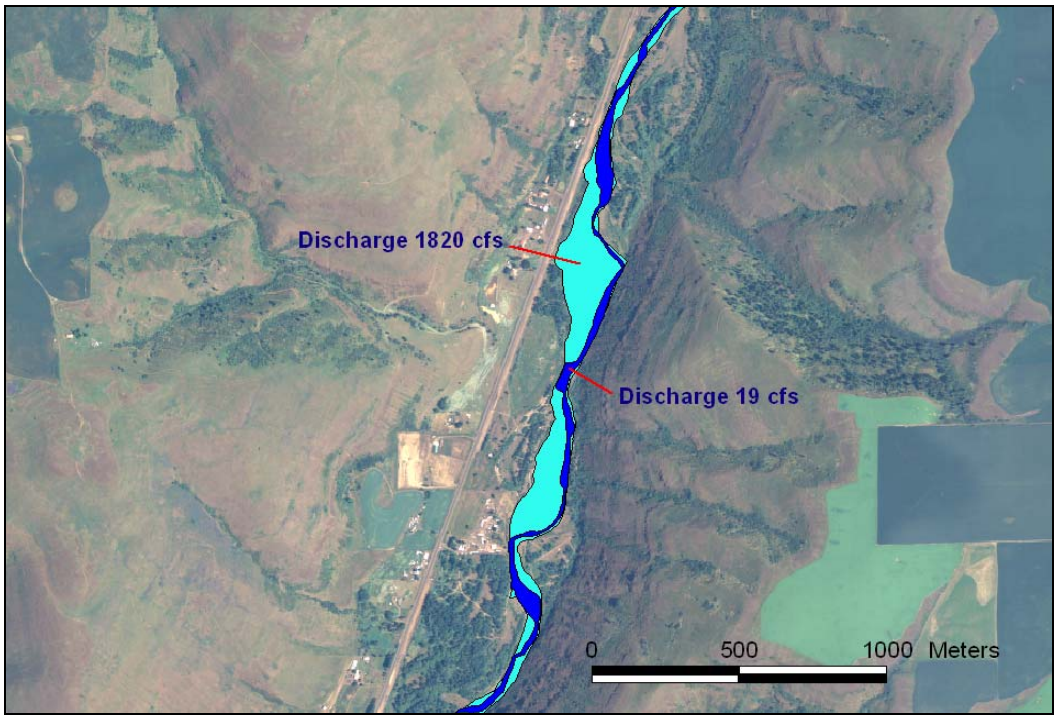

Figure 6.43 Water surface area for two discharges in the lower Potlatch River.

Water surface area at 19 ft^3 s^{-1} (0.54 m^3 s^{-1}) was 1.63 ha per kilometer of stream length (effective width of 16.3 m), and 3.09 ha per kilometer (effective width of 30.9 m) at the discharge of 1820 ft^3 s^{-1} (51.54 m^3 s^{-1}). This is an increase of 0.026 ha per

kilometer per cubic meter per second. The difference is certainly sufficient to develop a correlation between water surface area and discharge with additional measurements.

It is very probable given the morphological similarity of streams in similar geologic settings that a discharge water surface area relationship for one stream could enable reliable estimation of discharge on a similar ungaged stream. Smith (1996) found estimates of the discharge of braided streams in Alaska accurate within two hundred percent when estimated with SAR measurements of surface area.

Transferability is probably best for discharges near bankfull as indicated by the alluvial hydraulic geometry relationships. The bankfull discharge is often of the most interest in morphology assessment. An estimate of near bankfull discharge, or effective discharge, correlates well with bedload discharge in gravel bed rivers (Emmett and Wolman 2001). Discharge estimates would likely improve with inclusion of other morphological information, such as catchment area or effective width of riffle channel units. As of yet, I have an insufficient database of aerial images of small to medium sized gaged streams to enable confirmation and practical testing of this hypothesis.

Widespread availability of digital orthophoto quadrangles and the large National Aerial Photography Archive may support another approach: measure water surface area in aerial images of rivers and streams in the USGS stream gage database and develop new hydraulic geometry relationships based on water surface area or observed reach effective width. This approach is mostly an office exercise, but would require funding to purchase aerial photography and a considerable time commitment (six months to a year). Preliminary work has indicated this is feasible, but that the analysis is biased towards lower flows because NAPP images are typically acquired in late spring and early

summer. Supplemental aerial image surveys during high discharge would greatly enhance the analysis.

6.8.3 Channel Processes and Morphology

The introduction to this section remarked on the richness of morphological details apparent in aerial imagery such as Figure 6.39Figure 6.40. A morphological link between alluvial channel widths and parallax depths observed in aerial images can be found in the hydraulic geometry relationships developed for alluvial channels. The Hey (1982b) expression for wetted perimeter presented above is one example. More recent examples developed from a larger database than Hey are the relationships of Parker et al. (2003) and Julien and Wargadalam (1995). The expression for bankfull width developed by Parker et al. may be recast in the form:

$$B_{bf} = 4.698 \frac{Q_{bf}^{2/5}}{g^{1/5}} \left(\frac{Q_{bf}}{\sqrt{g D_{s50}}\, D_{s50}^2} \right)^{0.0661} \qquad 6.6$$

where B_{bf} is bankfull width (m), Q_{bf} is bankfull discharge ($m^3\ s^{-1}$), D_{s50} is the median surface particle size (m), and g is the acceleration of gravity ($m\ s^{-2}$). The Parker et al. relationship was developed by empirical reduction of field data against dimensionless channel geometry. Parker et al. also developed equations for bankfull depth and channel slope.

The relationship of Julien and Wargadalam (1995) was developed from theoretical three- dimensional particle stability analysis expressed in the form of hydraulic exponents:

$$B_{bf} = 0.512 Q_{bf}^{(2m+1)/(3m+2)} D_{s50}^{(-4m-1)/(6m+4)} \tau_{\theta}^{*(-2m-1)/(6m+4)} \quad 6.7$$

where B_{bf} is the bankfull width (m) and τ_{θ}^{*} is the dimensionless Shields parameter at incipient motion. The parameter m is computed by:

$$m = \frac{1}{\ln\left(12.2 \frac{h}{D_{s50}}\right)} \quad 6.8$$

where h is the bankfull depth of flow (m) computed from the

$$h = 0.133 Q_{bf}^{1/(3m+2)} D_{s50}^{(6m-1)/(6m+4)} \tau_{\theta}^{*-1/(6m+4)} \quad 6.9$$

The bankfull depth is computed by iteration until m and h converge. The coefficients 0.512 and 0.133 were developed from empirical analysis of river data. The value of parameter m is substituted into Equation 6.7 to compute bankfull width. Julien and Wargadalam also developed relationships for channel slope and average velocity.

The relationships of Parker et al. (2003) and Julien and Wargadalam (1995) are remarkable not for their differences in formulation, but for their similarity of results. Figure 6.44 compares bankfull width computed for both relationships for a range of flows and constant value of median particle size and Shields parameter.

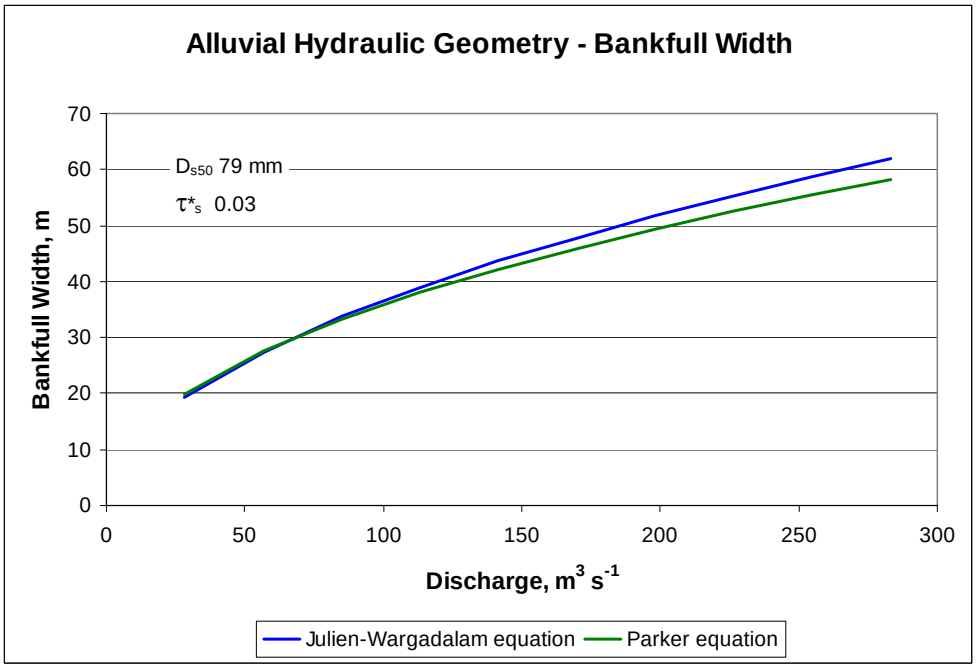

Figure 6.44 Comparison of alluvial hydraulic geometry relationships.

The value of median particle size adopted for the comparison is typical of active lateral bars in the lower Potlatch River. A Shields parameter value of 0.03 is recommended in Parker et al. (2003) for fully turbulent flow in coarse material and is noted as being less than the 0.047 value from the bed load transport analysis of Meyer-Peter and Muller (1948) value often quoted in sediment transport texts. Hey (1982b) also adopted a Shields parameter of 0.03 for threshold and low transport rates in gravel-bed streams.

The monotonic relationships of Parker et al. (2003) and Julien and Wargadalam (1995) alluvial hydraulic geometry support a hypothesis that water surface areas and morphological structures observed in aerial images provide an efficient basis for estimation of discharge and assessing channel morphology, particularly at bankfull discharge. It was stated in the introduction to this section that I did not intend to critically review the full breadth of fluvial hydraulics and geomorphology literature in

support of the dissertation hypothesis; a truly formidable task. Initial review of the diverse literature reveals consistent and convincing support that spatially and temporarily extensive high-resolution aerial imagery datasets of stream channels would further the engineering and ecological analysis of alluvial streams. Of particular interest for future work would be aerial survey investigation of the very complex morphological relationships of braided channels (Bridge 1993) and development of imagery derived precursors to imminent channel avulsion (Richards et al. 1993).

6.8.4 Sediment Transport and Sediment Characterization

Movement of sediment along a stream channel often manifests itself in the spatial and temporal variation of morphological structures. Sediment transport rates can be estimated by an analysis of the time variation of channel form and sediment storage structures. Derivation (inversing) of sediment transport rates from channel structures has been called a new paradigm of fluvial morphology (Ashmore and Church 1995). Morphology-based sediment transport is of considerable practical interest and was a primary motivation for my interest and research in aerial survey of stream channels. I explore it in detail in Section 6.10.

One of the earliest uses of high-resolution aerial photography in stream channel assessment was characterization of bed sediment (Greentree and Aldrich 1976). With a few exceptions this avenue of research has been virtually untouched (Lyon et al. 1992). An investigation that approaches the subject of sediment characterization for sediment transport analysis is that of Hassan and Church (1998) who acquired overhead images of a stream channel with a tethered balloon in an investigation of particle clustering.

Ground-based techniques of acquiring overhead stream channel imagery (balloons, poles, kites, remote controlled motorized airborne platforms) may have a place in research investigations, but have limited application in extensive surveys because of deployment logistics and legal access restrictions.

Other more portable ground based imaging techniques are useful and effective in the study of fluvial morphology such as those that employ photogrammetric analysis of terrestrial oblique images (Heritage et al. 1998; Lane et al. 1995) or close range imagery of bar surfaces for particle distributions analysis or sediment movement (Adams 1979; Butler et al. 2001; Carbonneau et al. 2003; Chandler et al. 2001; Ibbeken and Schleyer 1986; Kellerhals and Bray 1971). I have found this latter technique very useful in my morphological field work.

Imagery analysis of gravel bar surfaces has been limited to terrestrial techniques. My investigations have shown that bar surface properties can be characterized with very high-resolution aerial imagery. I believe this is an original approach with excellent prospects. My initial research is presented in Section 6.13.

6.9 Development of a Hydrologic Flow Model with High Resolution Aerial Imagery

Section 2 demonstrated that stream cross-section geometry can be determined from analytical photogrammetry of high-resolution digital aerial images. A flow model of the Potlatch River at Centennial Park near Juliaetta, ID was developed from aerial images acquired on July 22, 2004. Cross sections of less accuracy can be measured in a stereo model constructed by manual methods without sophisticated photogrammetric

software. The procedure is similar to the elementary photogrammetry techniques for large format photographic prints taught in many natural resources aerial photography courses. The primary difference is that the images are viewed side-by-side on a computer monitor instead of with a stereoscope.

Many observers find it difficult to view on-screen images in stereo without special equipment such as red-blue anaglyph or LCD shuttered glasses. This is unfortunate, because the low cost devices that new users are likely to purchase invariably alter the color and reduce the interpretability of the aerial images. I encourage observers to persist in their efforts and train themselves to view on-screen images in stereo without the assistance of stereo vision devices—the benefits are worthwhile. Once accustomed, an observer should be able to easily and comfortably switch back and forth between monoscopic and stereo views. This skill greatly enhances the utility of aerial images.

When tilt in aerial images is minor, the images can be treated as vertical images. It is known from Section 2 that this greatly simplifies the parallax height computations. Flight data provides the sensor height and ground elevation can be determined from sensor focal length, sensor pixel size and image georeferencing statistics. A typical stereo model setup of the Centennial Park reach is in Figure 6.45. All parallax measurements were made in Adobe Photoshop©.

Locations for representative cross sections were selected by inspection of the aerial imagery and were generally located at points of flow convergence and divergence, breaks in the longitudinal profile, and changes in channel roughness. The full channel including the submerged bed could be observed in the low flow aerial imagery. This is a key requirement of the technique. Elevation differences along the cross sections were

measured and computed using the floating mark principle and the standard parallax equation. Locations of a few of the cross sections are seen in Figure 6.46 after importing into the HECRAS (USACE 1995) modeling system.

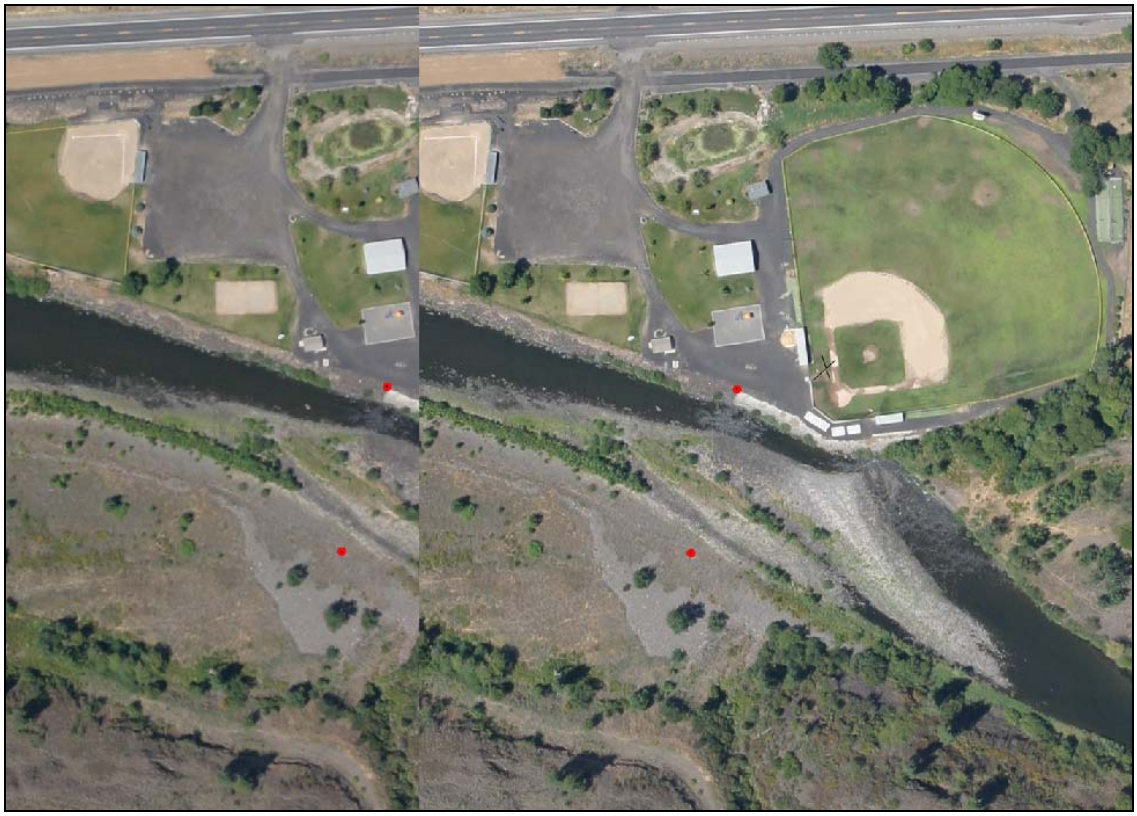

Figure 6.45 Stereo model of the Centennial Park Reach of the Potlatch River.

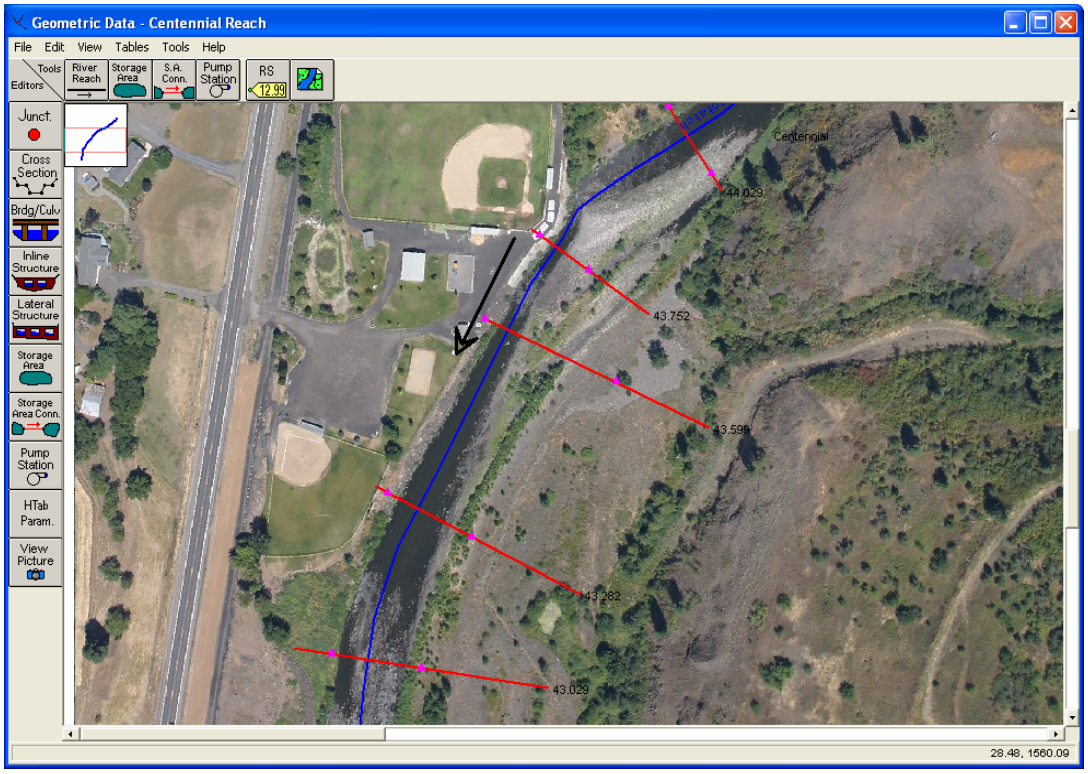

Figure 6.46 Locations of channel cross sections after importing into the HECRAS modeling system.

Channel friction factors were initially estimated at 0.03 to 0.04 based on experience and published guidelines (Arcement and Schneider 1984; ASCE and USACE 1996). A steady mixed flow analysis was performed in HECRAS for a discharge of 1820 $ft^3\ s^{-1}$ (55.5 $m^3\ s^{-1}$). A three dimensional representation of the simulated water surface and longitudinal profile produced by the HECRAS modeling system are in Figure 6.47Figure 6.48.

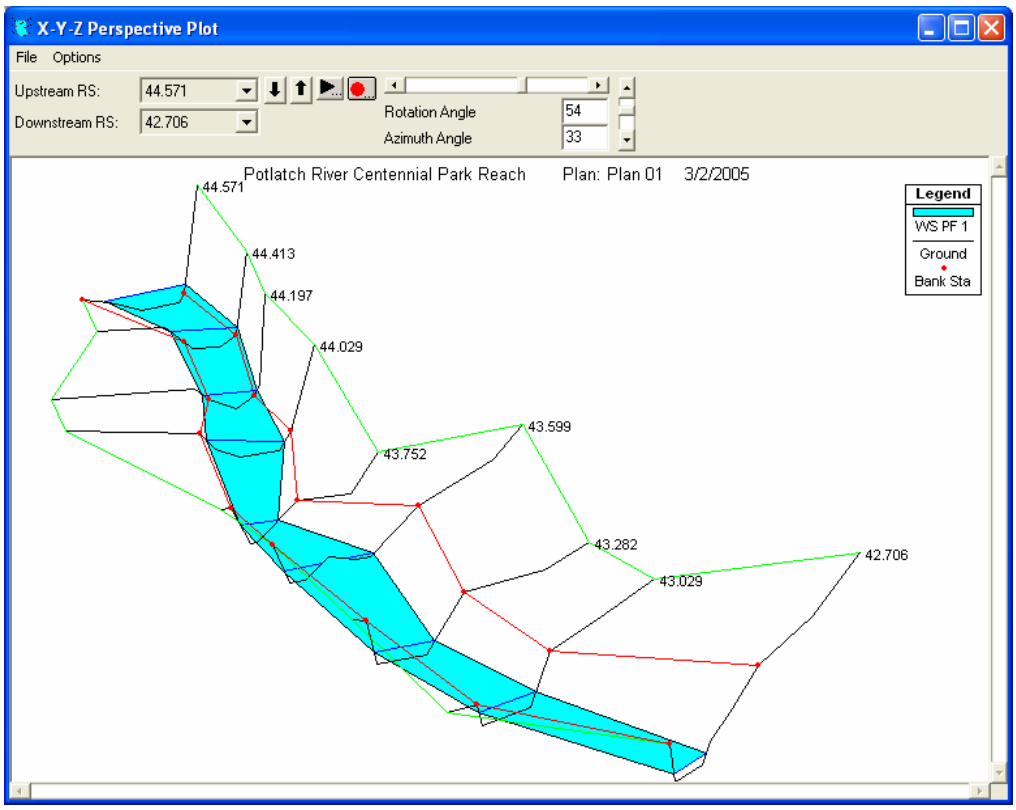

Figure 6.47 Three dimensional flow surface from a HECRAS simulation of the Potlatch River at Centennial Park, discharge 1820 $ft^3\ s^{-1}$.

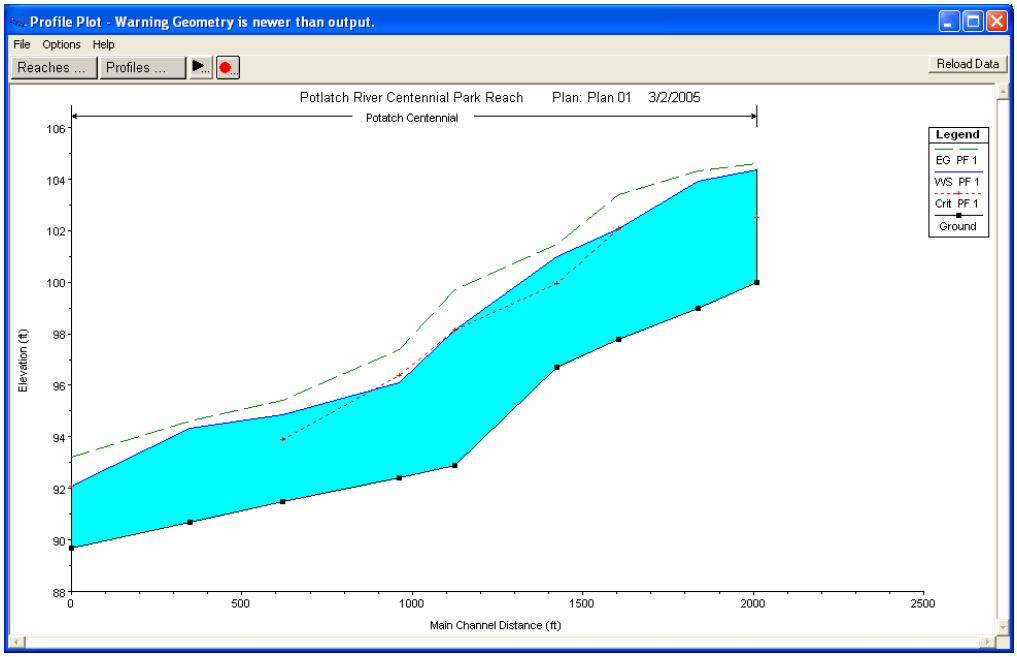

Figure 6.48 Longitudinal profile from a HECRAS simulation of the Potlatch River at Centennial Park, discharge 1820 $ft^3\ s^{-1}$.

The planform geometry of the simulated flow surface was exported from HECRAS and superimposed on aerial images of the Potlatch River acquired on January 31, 2004. Discharge at the time of image acquisition was 1820 ft^3 s^{-1} as reported by the USGS stream gage on the Potlatch River. The high flow aerial images and superimposed simulated water surface are in Figure 6.49Figure 6.50.

Figure 6.49 Aerial image of Potlatch River at Centennial Park, January 31, 2004.

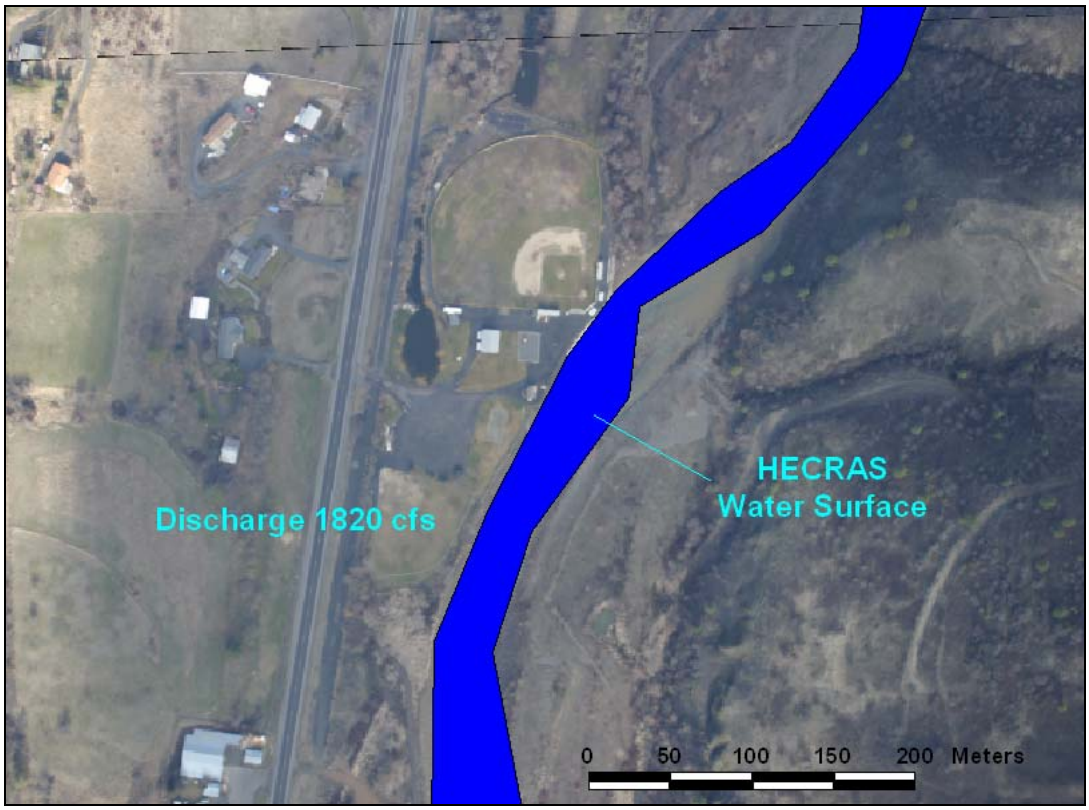

Figure 6.50 Simulated water surface superimposed on the January 31, 2004 aerial image.

The initial simulated water surface coincided with the actual water surface reasonably well without calibration. Supercritical velocities downstream from the ball field appear to have been correctly simulated as evidenced by indications of a hydraulic jump in the aerial image in Figure 6.51.

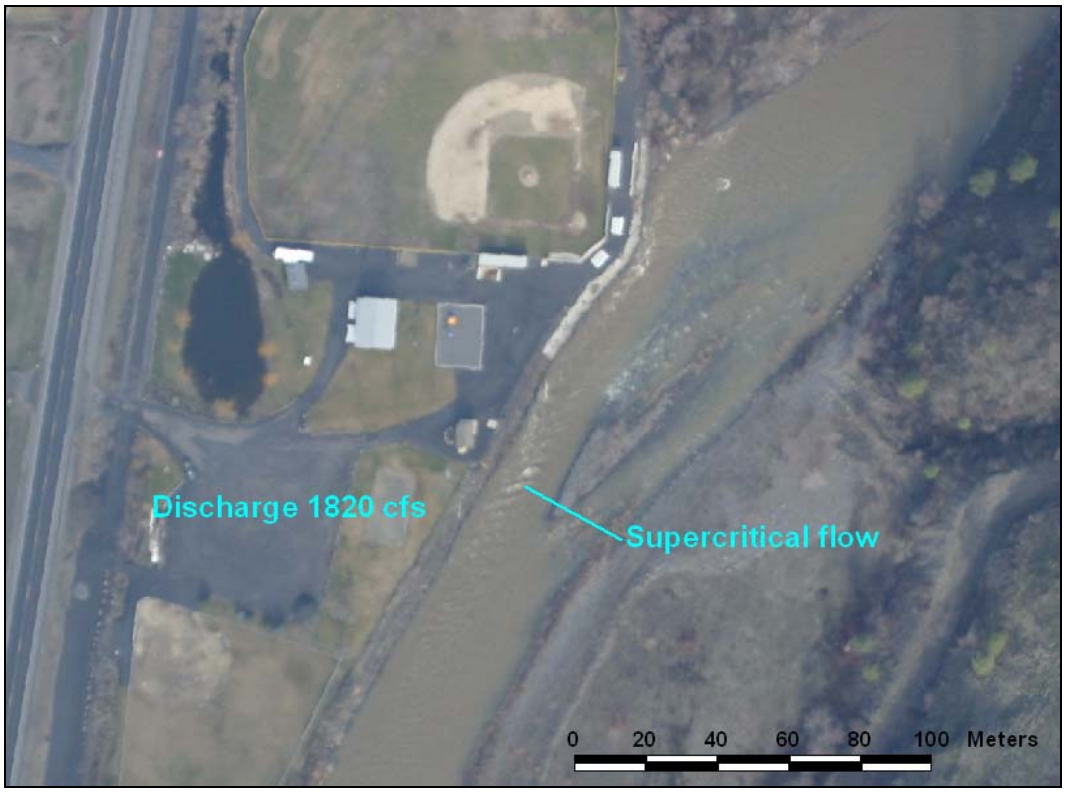

Figure 6.51 Supercritical flow and hydraulic jump in the January 31, 2004 aerial image.

A better match to the high flow aerial image is achieved by adjustment of the preliminary cross sections and friction values. This is the essence of the hydrologic flow model technique: given one or more high-flow aerial images of known discharge, the one-dimensional flow simulation model can be calibrated to match the observed surface. Field measurements are not absolutely necessary. Conversely, given measured cross section data, a discharge may be estimated from the high-flow aerial image.

The approach described above derived preliminary cross-section data from approximate photogrammetric measurements. Preliminary work indicates that it is possible to interpret reasonable cross section shapes from the aerial images without resorting to stereo models, then calibrate the cross sections based on high flow imagery. This produces a tremendous savings in time and cost for development of an initial hydrologic flow model. I have not yet developed a standardized approach to compare to

more exact techniques. I intend to pursue this in future research. Conceptually, the entire procedure might be semi-automated within a software modeling system.

Initial two-dimensional and three dimensional flow models can likely be developed with multi-temporal high-resolution aerial imagery. Initial work with relatively coarse resolution serendipitous satellite imagery supports the possibility (Bates et al. 1997). A serious effort of hydrodynamic model development must include the purposeful acquisition of aerial images during flow conditions that are optimum for model calibration. Ultimately this may be the best method to match flow structures with morphological forms in high-resolution aerial images. Developing this procedure for operational use would require a substantial research investment.

6.10 Morphology Based Sediment Transport

Interest is revitalized in monitoring and measurement of gravel-bed forms as a means to estimate sediment transport (Ashmore and Church 1995; Ashmore and Church 1998; Lane 1997; Lane et al. 1995). This approach may be characterized somewhat loosely as morphology based sediment transport. Marin and Church (1995) and Lane (1997) noted early research suggested that sediment transport rates in rivers could be inferred from observed changes of channel morphology (Hubbell 1964; Neill 1969; Popov 1962). As noted by Ashmore and Church (1995), morphology based transport has origins at the roots of morphodynamics in the Exner equation (Exner 1925; Neill 1987; Parker et al. 2000; Yang 1996). It is also implied in the qualitative relationships of E.W. Lane (1955).

Investigations at reach scale have long recognized the utility of aerial photography in mapping channel morphology and monitoring change (Heimes et al. 1978; Komura 1986; Miller 1986; Neale et al. 1995; Neill 1971; Odgaard 1987; Popov 1962; Ruff et al. 1975; Thorne 1981). Few (none) of the reported investigations have attempted to study morphological change over an extensive length of channel (tens of kilometers) with annual and seasonal acquisitions of high-resolution aerial imagery. This was my objective.

6.10.1 Morphodynamics

Some discussion of the fundamentals of morphology-based transport is necessary to place my research in context. The Exner equation is the basis of the study of morphodynamics. Its most basic differential form is (Yang 1996):

$$\gamma_s \frac{\partial \eta}{\partial t} + \frac{\partial q_s}{\partial x} = 0 \qquad 6.9$$

where γ_s is the specific weight of sediment, η is bed elevation, q_s is the sediment discharge per unit width of channel, x is the downstream distance, and t is time.

The Exner equation may be expressed in terms of a volumetric sediment discharge and bed porosity to develop the concept of an active layer of bed material (Parker et al. 2000):

$$(1-\lambda_p)\frac{\partial \eta}{\partial t} = -\frac{\partial q}{\partial x} \qquad 6.10$$

where flow is unidirectional in the x direction over an erodible bed, η is bed elevation, q is the volume transport rate of bed material load per unit width, λ_p is bed porosity and t is

time. Both η and q are interpreted to be averaged over local fluctuations associated with bedforms. Conceptualizing the exchange of transported bedload and the temporarily dormant bed material substrate as an active layer of finite thickness, the Exner formulation for the evolution of the grain-size distribution of the active layer is:

$$\left(1-\lambda_p\right)L_a\frac{\partial F_a}{\partial t}=-\frac{\partial q_\psi}{\partial x}+F_I\frac{\partial q}{\partial x} \qquad 6.11$$

where L_a is the active layer depth, F_a is the mass fraction of a particular particle size class in the active layer, F_I is the mass fraction of a particular particle size class at the interface between the active layer and the bed material substrate, q_ψ is the mass transport rate of a particular size class.

Parker et al. (2000) note that the active layer formulation of Equation 6.10 has been a mainstay of morphodynamic investigation for over 30 years. Hotchkiss and Parker (1991), Hoey and Ferguson (1994) and Toro-Escobar et al. (1996) demonstrate use of this equation in the analysis of the long profile and sediment sorting of gravel-bed channels. Ballamudi and Chaudhry (1991) demonstrate numerical techniques for solving the Saint-Vernant and sediment continuity equations for an alluvial channel.

Parker et al. (2000) develop a more general probabilistic embodiment of Equation 6.10. It is not necessary to repeat the complete derivation of the probabilistic formulation that is clearly developed in Parker et al. (2000). A key concept of the probability analysis is that the instantaneous elevation of the bed $p_e(z)$ is defined by the derivative:

$$p_e(z)=-\frac{\partial P_s}{\partial z} \qquad 6.12$$

where z is a coordinate that is oriented upward normal to the local mean bed elevation, and $P_s(z)$ is the mean fraction of a line at elevation z perpendicular to the z-coordinate

that falls within the sediment. The parameter $P_s(z)$ should approach unity for as z approaches negative infinity (deep in the deposit) and zero as z approaches positive infinity (in the water column well above the deposit). Parker et al. (2000) state that $P_s(z)$ can be interpreted as the probability that the instantaneous bed is higher than elevation z.

The utility of the Parker et al. (2000) assumption is that the right side of Equation 6.12 equals unity when integrated, a requirement of probability density functions. Parker et al. (2000) further transforms the probability assumption by requiring P_s to be a function of the deviation of the bed elevation about its mean value. Ultimately all probabilities of bed elevation change should derive from the time history of velocity at the bed and the sediment discharge carried by the flow. It is difficult to fully accept that this is represented in Equation 6.12.

Further, I it seems that probability analysis requires that segments of the line that intersect particles (rather than pass through empty space external to bedforms or gravel particles) be randomly distributed to support the probability transform, which is most certainly not the case as bedforms and particle clustering would introduce large amounts of autocorrelation of the line segments.

Parker et al. (2000) appears to addresses this by requiring the instantaneous bed elevation be statistically *uniform* in a region of influence that is large compared to the elevation fluctuation, but small compared to local bedforms. Again, I have an intuitive difficulty with this assumption when visualizing the movement of cobble material that may occupy a large portion of the depth of flow while in motion and significantly change the local bed elevation upon deposition, especially when participating in formation of a local cluster group.

Lastly, the coupling of sediment mass continuity to flow hydrodynamics required by the Exner equation through the sediment discharge is tenuous. Natural channels exist as a non-homogeneous state space because of channel discontinuities imposed by boundary constraints (e.g. bedrock outcrops) and semi-permanent channel structures (e.g. pools, riffles, bars). This is a scale effect that cannot be evolved from the original partial differential equations. The practical result of this condition is that all positions in the channel are not equally available for particle deposition even with changes in initial conditions.

A recent analysis of particle travel distance data supports this assertion (Pyrce and Ashmore 2003) and casts serious doubt in the stochastic view of particle travel distance entrenched in the literature since Einstein's experiments (Einstein 1950). Natural gravel-bed channels almost always exhibit zones of semi-permanent preferential deposition. It might be argued that expressing the Exner equation in three dimensions with appropriate initial boundary geometry can address this problem, but the inability of the partial differential equations to evolve scale structure remains. The semi-permanent nature of scale structures suggests a spatial transform that alleviates some of the difficulties of the non-homogeneous state space. Theoretical development of the spatial transform is a subject for future research.

Apparently the hydraulic engineering community accepts the probabilistic development of Parker et al. (2000). Subsequent literature discussion raised no new issues. Despite my reservations, which perhaps may be dispelled by further analysis of the formulation, Parker et al. (2000) appears to be a significant development in

morphodynamics which opens the way for integrated analysis of sediment transport and morphological change.

The Parker et al. (2000) formulation for sediment mixtures may be summarized in three relationships:

$$\bar{c}_b \frac{\partial \eta}{\partial t} = D - E \tag{6.13}$$

$$c_b = P_s \frac{\partial F}{\partial t} = p_e \left[D\left(\beta_{\psi D} F_t - \frac{c_b}{\bar{c}_b} F \right) - E\left(\beta_{\psi E} F - \frac{c_b}{\bar{c}_b} F \right) \right] \tag{6.14}$$

$$\frac{c_b}{\bar{c}_b}(D - E) = \beta_D D - \beta_E E \tag{6.15}$$

where c_b is the volume concentration of sediment within bed (1 -λ_p), $\bar{c}_b$ is the vertically averaged volume concentration of sediment, D is the volume rate of sediment deposition per unit time per unit bed area, E is the volume rate of sediment entrainment per unit time per unit bed area, F is the probability density of grain size ψ at elevation z or distance above bed y = z - η, F_t is the volume probability density of grain size c in transport, P_s is the probability distribution such that bed elevation is higher than level z or variation of bed elevation about mean level is higher than level (y = z - η), p_e is the probability density of bed elevation z or variation of bed elevation about mean level (y = z - η), β_D is the bias function associated with elevation-specific density of deposition, β_E is the bias function associated with elevation-specific density of entrainment, $\beta_{\psi D}$ is the bias function associated with elevation-specific and grainsize–specific density of deposition, and $\beta_{\psi E}$ is the bias function associated with elevation-specific and grainsize–specific density of entrainment,

Parker et al. (2000) note that is not possible at present to implement the probabilistic formulations for mass conservation of sediment as proposed. This is principally because they found that general predictors for the probability distribution of bed elevation and elevation-specific densities for erosion and deposition (grain-size specific or otherwise) of sediment have not yet been developed. They further recognized that rivers contain bed variations at multiple scales, including those at the level of the size of the grains themselves, ripples, dunes, bars, and bends. The probabilistic formulation to be used becomes a function of the scale of the phenomenon of interest.

Parker et al. (2000) challenged the research community to investigate these probability distributions and so open the window for development of more sophisticated models of morphological response and bed stratigraphy. This theoretical underpinning and challenge enhanced my desire to investigate the morphology of gravel-bed streams with multitemporal high-resolution aerial imagery. An investigation with high-resolution aerial imagery has merit because the key development in the Parker et al. (2000) approach is its linkage between bed elevation dynamics and spatial distribution of sediment. I suggest that given a sufficiently detailed spatial and temporal coverage of morphological change in a gravel-bed stream, it should be possible to develop the sediment entrainment and deposition rates and spatial probability distribution required by Equations 6.13 through 6.15. High resolution aerial imagery may be the most efficient method to acquire this information in complex channels (Davies 1987; Popov 1962), especially when supported by intensive field surveys of representative channel reaches (Fuller et al. 2003). Progress towards this goal will be discussed in context of an example from the lower Potlatch River.

6.10.2 Morphological Bedload Transport

The morphodynamic approach described by Parker et al. (2000) is what may by analogy with stream flow routing be called the "hydraulic" approach to morphology-based bedload transport. It is founded on partial differential equations of mass continuity with a solid physical basis. It appears to be the best theoretical approach to morphology-based bedload transport at present suggested in the hydraulic engineering and sediment transport literature. An alternative is the **morphological** bedload transport analogous to the "hydrologic" methods of stream flow routing.

Neill (1987) describes the setting of the morphological transport analysis with clarity,

"In most alluvial rivers, the morphology-transport relationships are complicated by several factors, including: the continuously 3-D nature of the flow; the presence at times of hierarchy of bed forms ranging from large-scale bars to small ripples; the wide range of flow conditions such that (especially in gravel rivers) most of the bed-sediment transport takes place in short flood episodes widely spaced in time; and, most importantly, the process of sediment exchange between bed and banks whereby the channel, or channels, continually shift their location and planform".

Estimation of sediment transport by changes in channel morphology is practical and has a firm conceptual basis. Fundamental equations of morphological transport may be derived from mass continuity. Beginning with the conventional hydrologic routing equation:

$$\frac{dS}{dt} = Q_{s_{in}} - Q_{s_{out}} \tag{6.16}$$

where $Q_{s_{in}}$ and $Q_{s_{out}}$ are the total sediment inflow and outflow (mass per unit time) at the boundaries of a channel segment, S is the sediment mass stored in the channel segment, and t is time. Expressing Equation 6.16 in finite form and dividing each by the bulk density of the channel bed gives:

$$\frac{\Delta S}{\rho_s(1-\lambda_b)\Delta t} = \frac{\Delta Q_s}{\rho_s(1-\lambda_b)} \tag{6.17}$$

where ρ_s is sediment density (mass per unit volume) and λ_b is bed porosity (dimensionless). The change in elevation of the bed is obtained by dividing by the channel width B and the length of the channel segment Δy:

$$\frac{\Delta S}{\rho_s(1-\lambda_b)B\Delta y\Delta t} = \frac{\Delta z}{\Delta t} = \frac{\Delta Q_s}{\rho_s(1-\lambda_b)B\Delta y} \tag{6.18}$$

Sediment discharge is typically expressed as a mass rate per unit width of channel so Equation 6.18 may be expressed:

$$\frac{\Delta z}{\Delta t} = \frac{\Delta q}{\rho_s(1-\lambda_b)\Delta y} \tag{6.19}$$

Rearranging Equation 6.19 gives,

$$\frac{\rho_s(1-\lambda_b)\Delta z}{\Delta t} = \frac{\Delta q}{\Delta y} \tag{6.20}$$

In absence of an input of sediment load to the channel segment a positive sediment transport rate q_s will erode the bed and decrease bed elevation. In other words, ΔQ_s of Equation 6.18 is negative. Imposing this convention on Equation 6.20 produces a common form of the morphological bed material transport equation:

$$\frac{\rho_s(1-\lambda_b)\Delta z}{\Delta t} = \frac{-\Delta q_s}{\Delta y} \qquad 6.21$$

Morphological bed material transport has been discussed and applied in numerous investigations (Ashmore and Church 1998; Beschta 1987; Davies 1987; Ferguson et al. 1992; Fuller et al. 2003; Goff and Ashmore 1994; Jackson and Beschta 1982; Lane 1997; Lane et al. 1995; Martin and Church 1995; Neill 1987).

It is important to realize that the development of the morphological transport relationship implies the existence of a control volume. The amount of sediment stored within the control volume changes if there is an imbalance between sediment inflow and outflow. A change in sediment storage must be expressed as a change in observed morphology (however difficult that may be). Morphological transport does not preclude steady state through-flow of sediment during which the amount of sediment within the control volume does not change. But, even steady state sediment discharge could very well change the morphology of the sediment structures. In fact, given the well documented observations of the threshold nature of gravel bed mobility, altered morphology is quite probable. These realizations motivated this question:

> *Does a control volume (reach) exist in which all sediment transport is expressed as morphological change that may be observed between cycles of high and low flow?*

This question is explored in the next section.

6.11 The Morphological Transport Segment

The morphological bed material transport relationship in Equation 6.21 is not a theory of bed material movement, it simply indicates a method to measure it. After

viewing thousands of aerial images of gravel-bed streams, it became apparent that many streams exhibit a shared reach scale structural organization. Some alluvial channel segments, such as in Figure 6.40, show altered channels, banks, bars and islands at the end of almost every flow cycle – even when peak flows in the cycle are well below the nominal formative (bankfull) discharge. Furthermore, these expressive morphological segments occur in distinct segments that persist over long periods of time.

Reach-scale morphological structures are observed in two very different alluvial streams examined during the research: the upper Palouse River and the Teanaway River in Washington State near Cle Elum. Stable channel centerline locations observed in historic aerial photos in Figure 6.52 indicate 12 reach scale morphological structures over a 15 km segment of the upper Palouse River. Heavy red arrows Figure 6.53 mark the approximate locations of what might be called strong singularity points in the alluvial morphology. Smaller magenta arrows mark locations of weak singularity points. The stable channel sections appear to be unrelated to bank or bed material, though landowner permission was not obtained for field inspection. The Teanaway River in Figure 6.54Figure 6.55 exhibits 12 reach-scale morphological structures over an 18 km segment. Stability of the channel sections appears to be unrelated to bank or bed material. Landowner permission again was not obtained for field inspection to confirm material properties. Length of the reach scale structures varies by about 50 percent and appears somewhat correlated to mean stream width at between 40 to 50 bankfull channel widths. Reach-scale structures also occur in the lower Potlatch River and will be analyzed in detail.

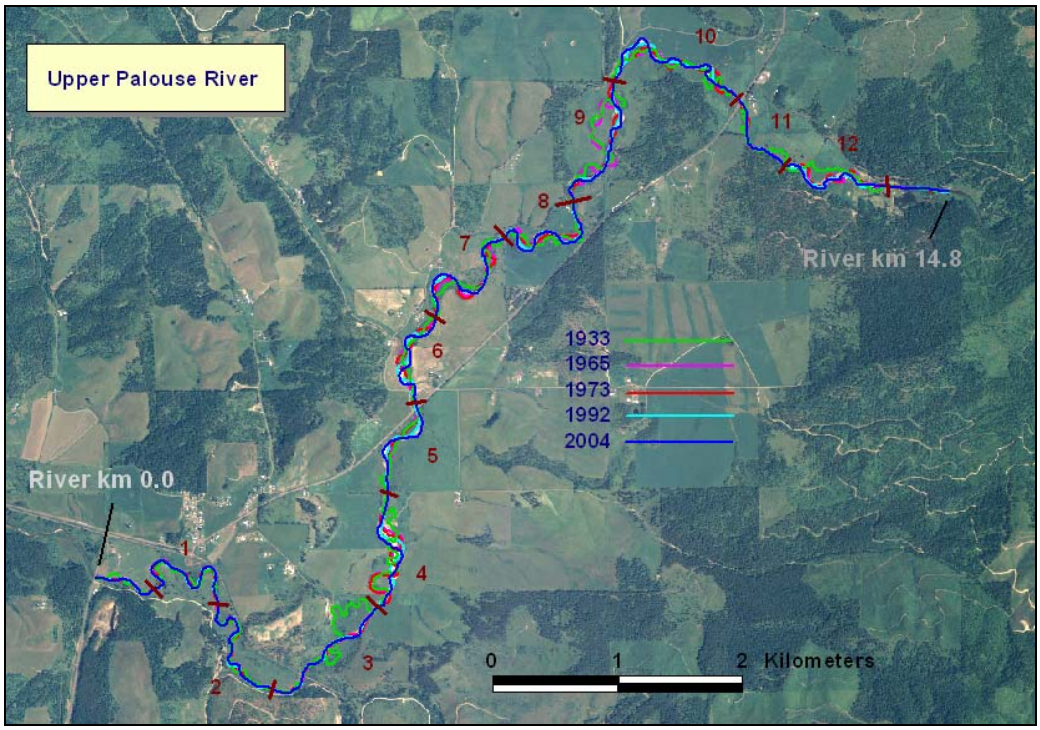

Figure 6.52 Reach scale morphological structures in the upper Palouse River.

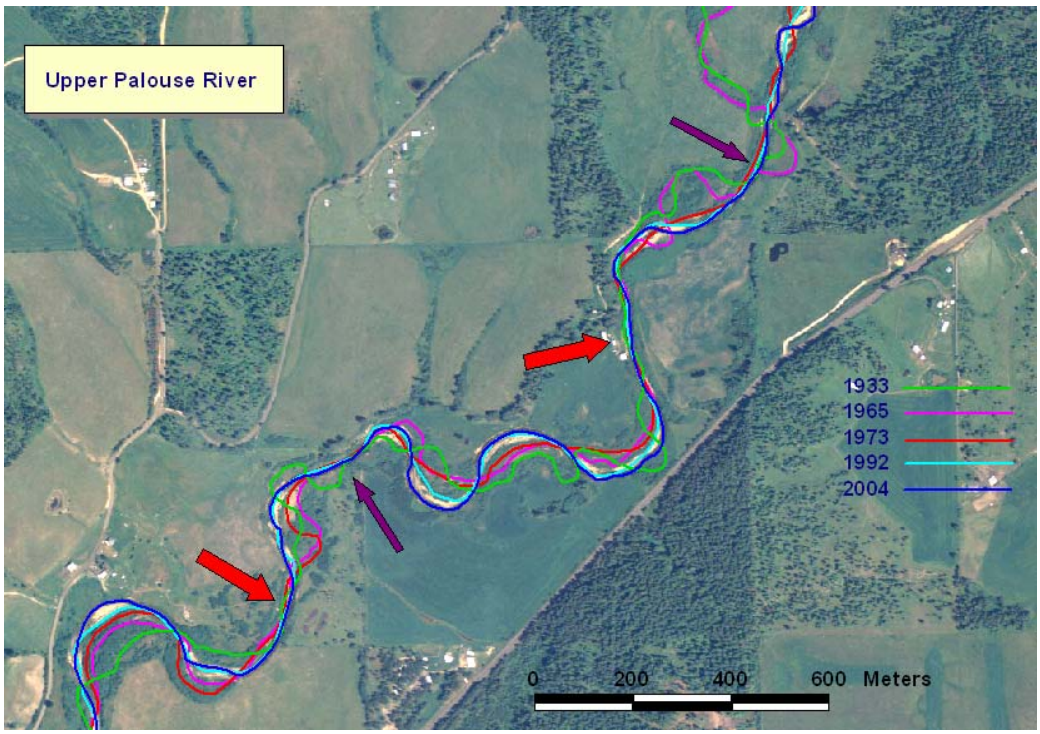

Figure 6.53 Stable centerline locations in the upper Palouse River.

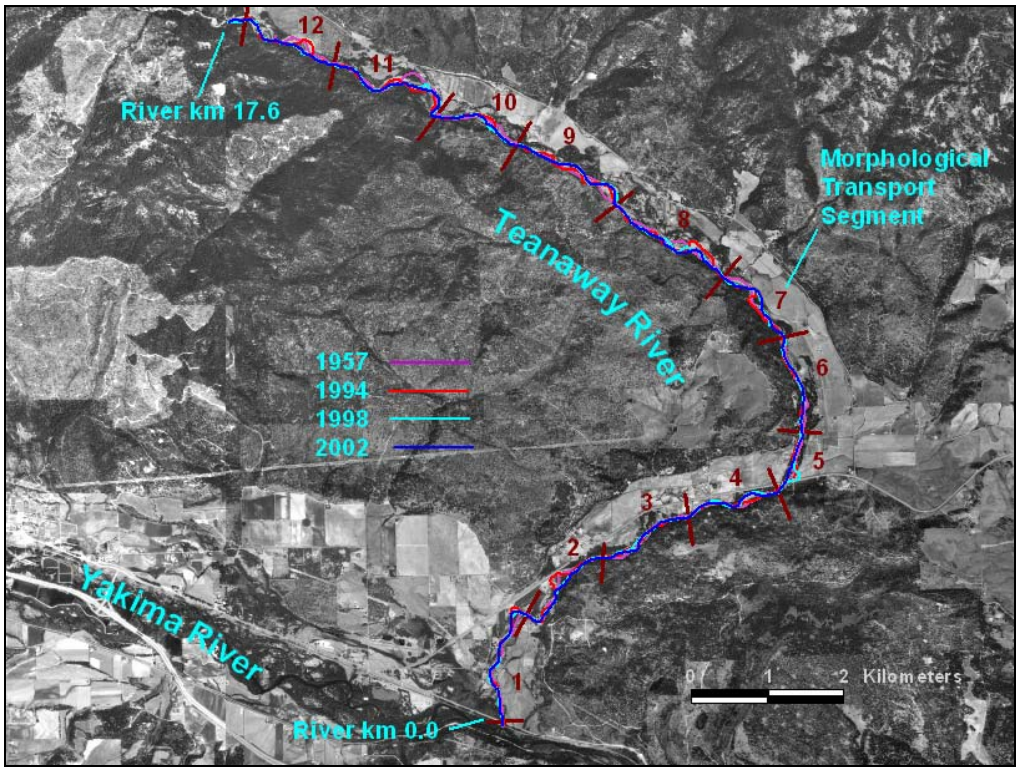

Figure 6.54 Reach scale morphological structures in the lower Teanaway River.

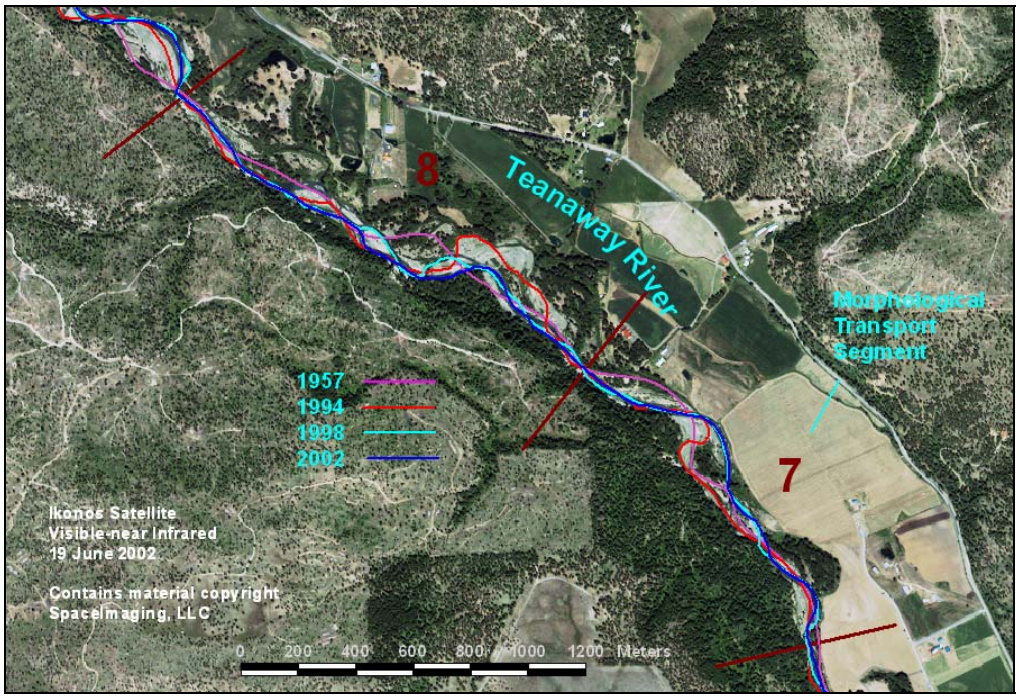

Figure 6.55 Stable centerline locations in the lower Teanaway River.

The remarkable stability of the more or less regularly spaced sections along freely alluvial channels leads me to posit the existence in many natural alluvial channels of a morphological transport segment in which total bed material transport may be determined solely by measurement of the differences in channel form and structure between cycles of high and low discharge. This is not simply a restatement of the concept of morphological transport so well described by Neill (1987) and Ashmore and Church (1995), but asserts the existence of a channel scale structure not previously recognized. I suggest this is an original concept in the study of fluvial morphology and sediment transport that has practical significance and research merit. I must admit I reserve a measure of healthy engineering skepticism of this concept in lieu of a rational physical explanation for the existence of the morphological transport segment. Arguments against the existence of the morphological transport segment should offer an explanation for the singularity points observed in Figure 6.52Figure 6.55.

6.11.1 Principles of the Morphological Transport Segment

The concept of a morphological transport segment suggests several idealized principles at work:

1) **Principle of downstream transport** – evacuated (entrained) material is transported to a downstream morphological structure. Bed material that is temporarily entrained, but is not transported to a downstream morphological structure does not contribute to morphological bed material transport. The transit of bed material along the length of a bar certainly occurs, but is not morphological transport. Sediment from a hydraulic perspective only becomes of real

importance when it participates in the formation or translocation of a morphological structure (channels, bars, banks), possibly with damaging or unexpected consequences.

2) **Principle of morphological separability** – translocation of the channel boundaries and/or evacuation and emplacement structures during the flow cycle is such that distinct evacuation and emplacement volumes may be observed and measured. All sediment movement is associated with the formation and translocation of morphological structures. No (negligible) sediment transits the segment without residing in temporary and observable morphological structures. Each particle signifies its entry to or departure from the segment by contributing to an observable change in the morphological structure at the end of the flow cycle.

3) **Principle of least flowpath work** – translocation of sediment is governed by criteria of least work along the flow path as defined by history of velocity vectors during the flow cycle. Channel patterns observed at the end of the flow cycle are initiated at the beginning of the cycle and progressed to their final form. This principle is closely related to principle 1).

4) **Principle of discharge scaling** – dimensions of evacuation and emplacement structures are scaled to discharge;

5) **Principle of independence** – channel structures within the morphological transport segment are independent of the morphological structure of upstream or downstream segments;

6) **Principle of persistence** – morphological transport segments persist between extreme discharge events.

7) **Principle of flow correlation** – evacuation of the channel is primarily during the rising limb of the discharge hydrograph and emplacement primarily during the falling limb of the hydrograph;

Evacuation and emplacement are terms with special meaning in the concept of a morphological transport segment and are distinguished from erosion and deposition. Evacuations and emplacements are distinct volumes at a point in time. Erosion and deposition are processes and rates of entrainment and settling of surficial material by hydraulic force. Evacuation is the creation of a void in the channel boundary scaled to the magnitude and duration of discharge and correlated to the flow macro structure. Examples of evacuation are the creation of the low flow channel, bank recession and pool scour. Emplacements fill antecedent evacuations or fill previously unoccupied space (rare). Examples of emplacements are creation of island and bars, infilling of low flow channels, and the increase in volume of existing emplacement structures.

Not all channel segments need be morphological transport segments. Stable and constrained channels pass bed material without significant change in structure or dimension. Only freely alluvial channels possess the stochastic variability necessary for the separation of evacuation and emplacement structures. Some alluvial channels exhibit no morphological change during periods of low sediment loads and when peak discharges are well below threshold mobility for the size of the dominant bed material. These channels may have the appearance of stability, but are not in equilibrium with the

contemporary discharge and sediment regime. With increased sediment load, these channels would again show active morphology.

I want to emphasize an aspect of morphological transport in gravel-bed channels that has not been clearly stated by others. If a reach is sufficiently long and transport ceases between flow cycles, then all bed material sediment transits the reach only by manifesting in the end-of-cycle morphological structure. There is no other possibility. The few studies of tracers in gravel-bed streams indicate particle travel distances during a flow cycle (epoch) are scaled to discharge, but are typically only a few tens of meters long, with all reported distances less than 100 – 200 meters (Church and Hassan 1992; Hassan and Church 1991; Pyrce and Ashmore 2003). This indicates that morphological transport segments are of reasonable size and provides an empirical basis for their existence.

6.11.2 Theoretical Development of the Morphological Transport Segment

I have not sufficiently developed a stochastic-hydrodynamic theory of the morphological transport section to offer a proof of its existence. However, I see no physical principles that would bar existence of a morphological transport segment. I have observed their probable existence on a sufficient number of gravel-bed streams to be convinced of the generality of the concept. If stable segments exist that show no morphological transport, then freely alluvial segments may also exist that exhibit nearly perfect morphological transport. Support for assertion of a morphological transport segment might be found in the theory of minimum rate of energy dissipation (Yang and Song 1979), theory of minimum entropy production (Leopold and Langbein 1962) and

the theory of minimum variance (Langbein and Leopold 1966). Further review of these and other so called extremal hypotheses (Bettes and Wright 1987) is warranted.

I realize that proposing a new unit of spatial organization for fluvial channels within the mature fields of geomorphology and sediment transport should be viewed critically, especially without having developed a firm theoretical foundation and a large body of empirical evidence. I am emboldened by the fact that other channel scale structures, such as pool and riffle sequences, are admitted by empirical observation, but have not been explained by theory. The implication of the morphological transport segment is that it is unnecessary to measure bed material transport with in-stream contrivances and portable samplers – it is only necessary to move to an appropriate location and measure the change in morphological dimensions. No bed material sediment escapes unnoticed in the morphological transport segment.

6.11.3 Analytical Development of the Morphological Transport Segment

I have not avoided analytical considerations altogether. The following probabilistic treatment seems plausible. As discharge increases, the proportion of the channel exposed to the surficial velocity field increases (i.e. wetted perimeter increases). Since Einstein (1950) it has been recognized that near the threshold of bed movement, particle entrainment and displacement are stochastic phenomenon. This suggests sediment transport within the morphological transport segment might be described by a Poisson probability distribution. The Poisson distribution estimates the probability that a specified outcome will occur exactly x times in a standardized unit when the average rate of occurrence per unit is a constant λ. Einstein adopted the Poisson distribution in

his analysis. The Poisson distribution is a discrete probability distribution; appropriate because sediment transport in gravel bed streams is the culmination of discrete displacements of individual particles (this may not be true for sand bed streams).

The Poisson probability density function is (Blank 1980):

$$P(x;\lambda) = \frac{e^{-\lambda}\lambda^{x}}{x!} \qquad 6.22$$

Assumptions of the Poisson distribution are (Blank 1980):

1) There are *n* independent trails where *n* is very large.
2) Only one outcome is of interest in each trial.
3) There is a constant probability of occurrence on each trial.
4) The probability of more than one occurrence per trial is negligible.

In morphological transport, trails may be viewed as excursions of velocity transients (possibly carrying previously entrained sediment) across the surficial bed material exposed to flow. Autocorrelation between velocity transients is ignored. The only outcome of interest is the displacement of bed material – it does or does not move. The probability that movement is not triggered by velocity transients is negligible, ignoring rare events such as subsurface and bank slope failures (mass displacements).

The requirement for constant probability on each trial is the weakest assumption. The probability of occurrence should be dependent on discharge and sediment load through the morphologic transport section, since discharge is the primary control on the magnitude and number of velocity transients prior to channel deformation. It seems reasonable that constant probabilities could be assigned to discrete intervals of discharge

magnitude. Velocity transients at low discharges should have a lower probability of triggering bed material movement than velocity transients at higher discharges. This suggests that the probability of sediment displacement within the morphological transport segment can be represented by a discharge dependent family of Poisson distribution curves. Hypothetical probability distributions for low and high discharges are presented in Figure 6.56Figure 6.57.

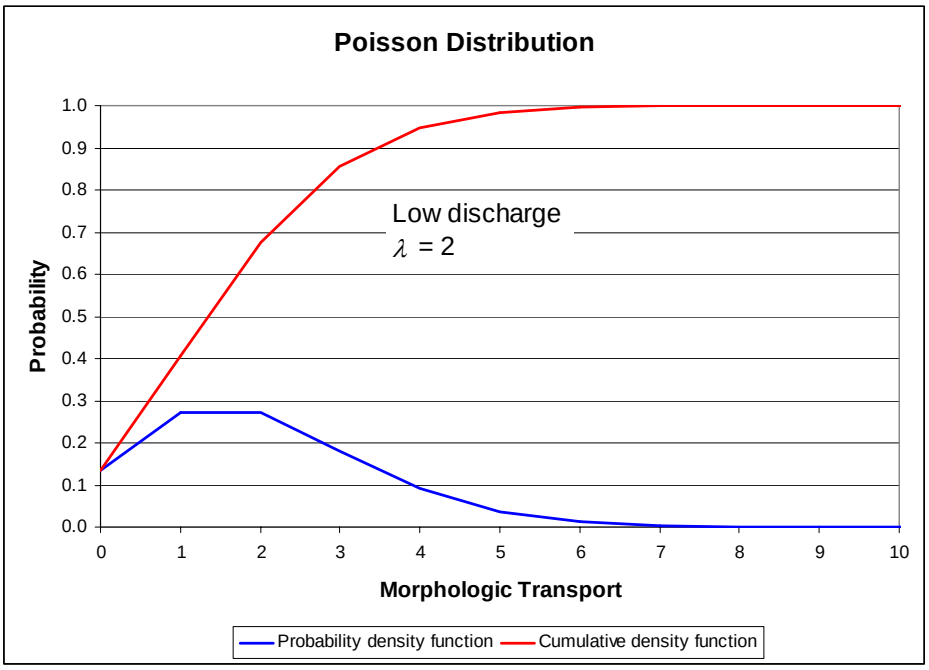

Figure 6.56 Poisson probability distribution of evacuation for low discharge.

The Poisson event outcome rate x was replaced by a conceptual morphologic transport scale when generating the curves in Figure 6.56Figure 6.57. Increasing the value of λ models the effect of increasing flow by increasing the relative rate of morphological transport. I can assign no definite magnitude to the morphological transport scale, which could be logarithmic. At this point I assume the physical dimensions of the morphological transport scale are volume or mass moved by a velocity

transient. Much further work is necessary to relate the Poisson parameter λ to real transport rates and evacuation volumes. The effects of particle size are implicit in λ and the scaling of morphological transport.

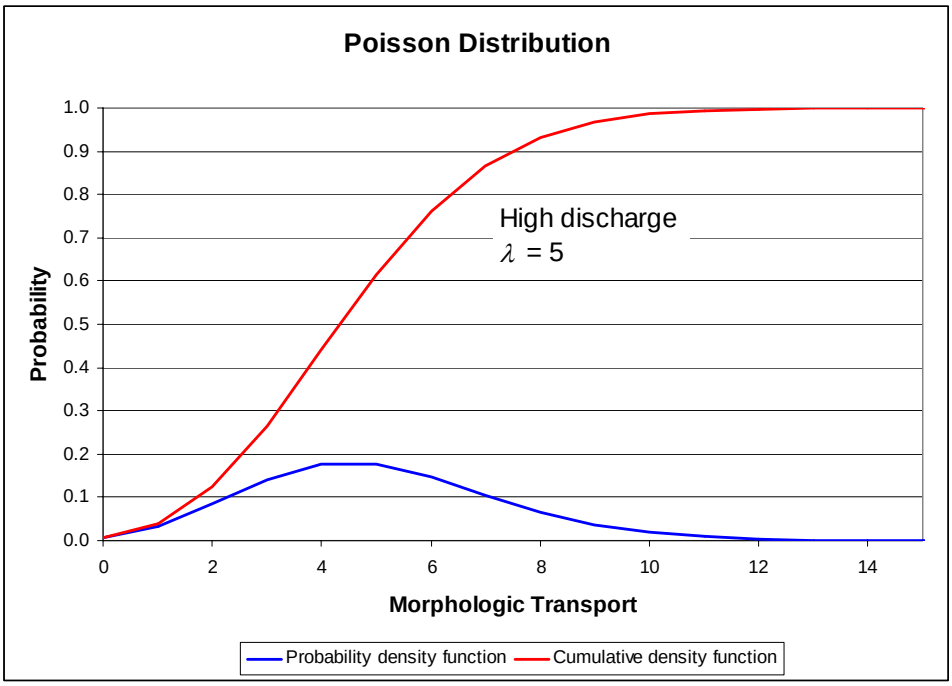

Figure 6.57 Poisson probability distribution of evacuation at high discharge.

It is also plausible that a Poisson distribution describes the probability of emplacement within the morphological transport segment since velocity transients and sediment load control both the process of entrainment and deposition. A simple reversal of the evacuation probability curve may be a reasonable starting point, but full development must account for Shields stress disparity. Sediment settles on the bed at a significantly lower Shields stress than that required for entrainment.

The Poisson probability distribution suggests that time variation of sediment evacuation and emplacement within the morphological transport segment may be conceptualized by a gamma probability distribution. A gamma distribution gives the

probability of the time to observe n events that have an average rate of occurrence of λ. The gamma probability density function is (Blank 1980):

$$P(t;n;\lambda)=\frac{\lambda^n}{\Gamma(n)}t^{n-1}e^{-\lambda t} \qquad 6.23$$

Where Γ is the gamma function integral,

$$\Gamma(n)=\int_0^\infty x^{n-1}e^{-x}dx \qquad 6.24$$

A hypothetical gamma probability distribution for evacuation in a morphological transport segment is in Figure 6.58. As with the Poisson distribution, the abscissa is a conceptual scale, in this case transport time. I cannot assign a meaningful magnitude to the time scale at this point in the conceptual development. The gamma distribution should similarly apply to the probability of emplacement volume. Discharge scaling also applies.

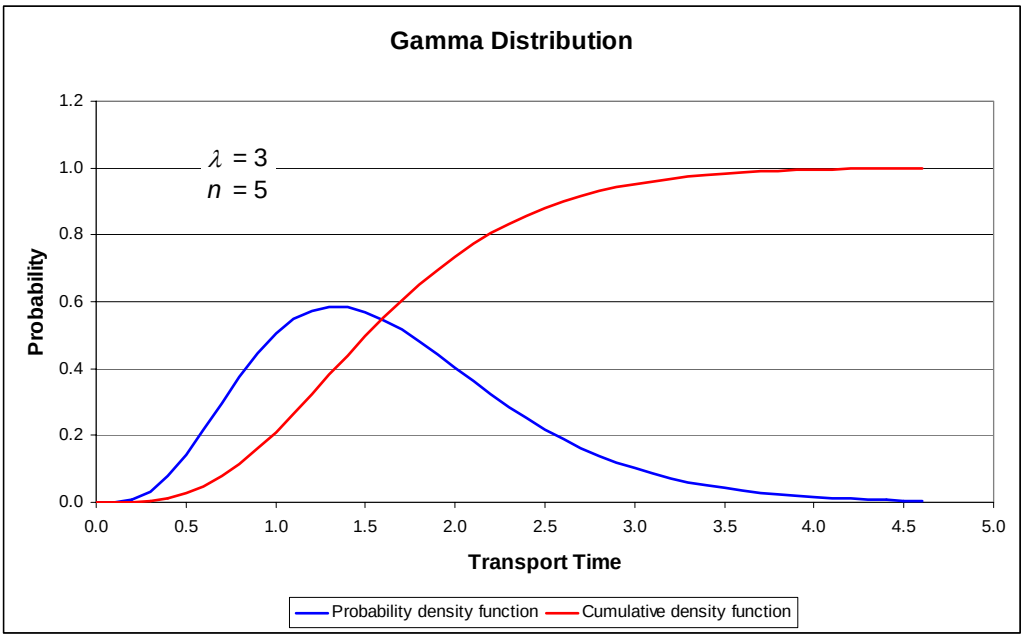

Figure 6.58 Gamma distribution of time variable evacuation.

Higher probabilities of the occurrences of evacuation and emplacement should transform to higher volumes of transport. Transforms of this type are commonly applied in flood frequency analysis and simulation of storm discharge hydrographs (Gupta 1995; McCuen 1998) both of which are dependent on the characteristics and size of tributary area. One would expect the gamma distribution to be similarly useful in modeling sediment transport in the area-based concept of the morphological transport segment.

The Poisson and gamma probability distributions also suggest that higher probabilities of at-a-point detection of dimensional change in the morphological transport segment should relate to the sediment transport rate. This concept is quite intuitive. If one does not see (detect) morphological change then the sediment transport rate must have been very low or non existent during the previous epoch. Conversely, if the channel is drastically altered and change is detected at many points in the morphological transport segment, then sediment transport must have been great. I hypothesize the existence of a relationship between probability of detection and sediment transport such as in Figure 6.59. The utility of such a relationship is that it is no longer necessary to measure morphological dimensions, just detect that a particular point experienced change. I note the similarities between this hypothesis and the probabilistic assertion of Parker et al. (2000). Furthermore, the bounds of a morphological transport segment should be found where the probability of detection ceases to be zero, passes through a local maximum then reduces again to zero (i.e. the calculus of the morphological transport segment).

Development of a direct relationship between the probability of the detection of morphological change and sediment transport is an objective for future work. This work

is beneficial because it should reduce the need for the effort and expense of photogrammetric or tacheometric analysis of morphological dimensions. Less expensive and more automated remote sensing techniques such as the analysis of spectral reflectance and textural classification may be sufficient to detect morphological change and construct the necessary probability distributions.

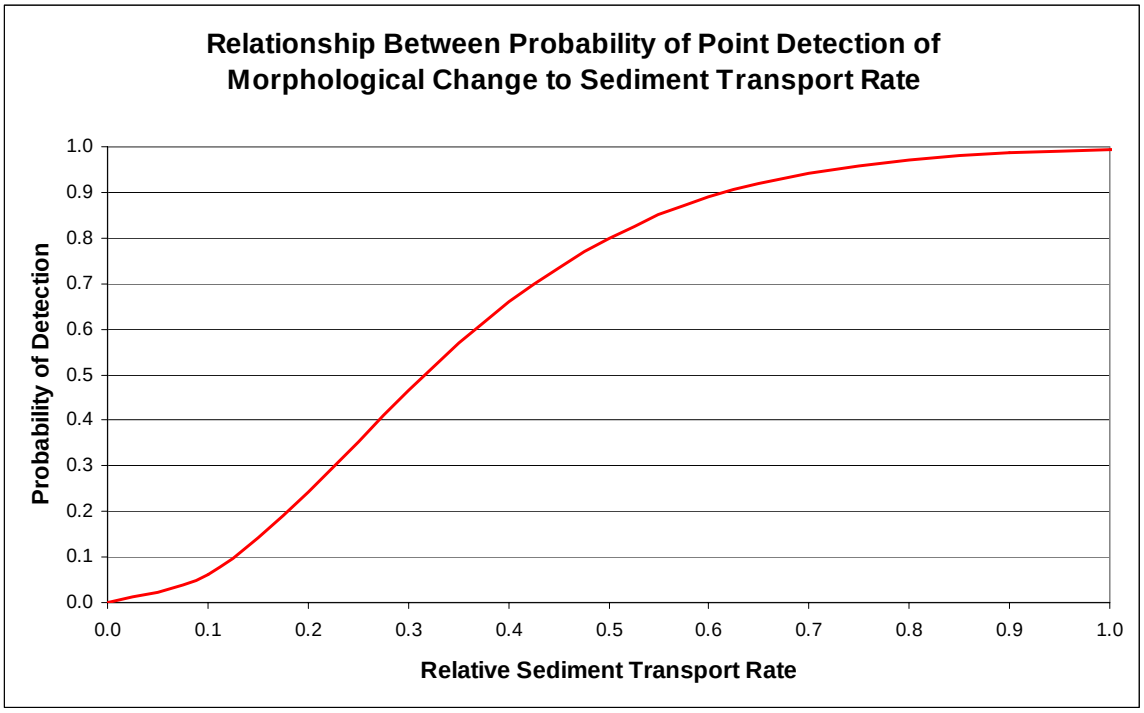

Figure 6.59 Conceptual relationship between the at-a-point probability of detection of morphological transport and sediment transport rate.

A single probability curve such as Figure 6.59 is likely insufficient to describe the transformation to sediment transport for the full morphological transport segment because resistance to movement is dependent on numerous factors including particle size, bed form and position in the channel. Spatially dependent families of probability curves or probability surfaces are likely necessary, the analysis of which requires application of

geostatistics. An alternative would be to develop a composite curve based on detection of sediment movement at representative points in the channel.

One other aspect of the morphological transport segment should be introduced. If the morphological transport segment exists, then it constitutes a statistically independent member of a larger sampling population of morphological transport segments. This opens the possibility for statistical sampling of like channel units among morphological transport segments to determine reach-averaged sediment transport rates and trends (i.e. sediment waves). This aspect of morphological transport segments may be the most beneficial for extensive surveys of the magnitude and variability of sediment transport within a basin.

The cumulative gamma distribution is easily adapted to simulate varying rates of evacuation and emplacement. Figure 6.60 is one possible combination of the time sequence of evacuation and emplacement. A greater volume of material is evacuated from the morphological transport segment than emplaced. The start of emplacement follows evacuation by a slight time delay. The water discharge that drives the morphological transport is also shown on the figure. The end of cycle morphological transport volume (positive or negative) is the difference between the asymptotic values of the evacuation and emplacement volumes. The nominal rate of morphological transport is the total morphological transport volume divided by the time base of the discharge hydrograph. Segment average rates of net transport are determined from the difference of the evacuation and emplacement curves over a finite period. Hydrologists will recognize similarities between the morphological transport curves and hydrographs employed in the hydrologic analysis of stormwater detention.

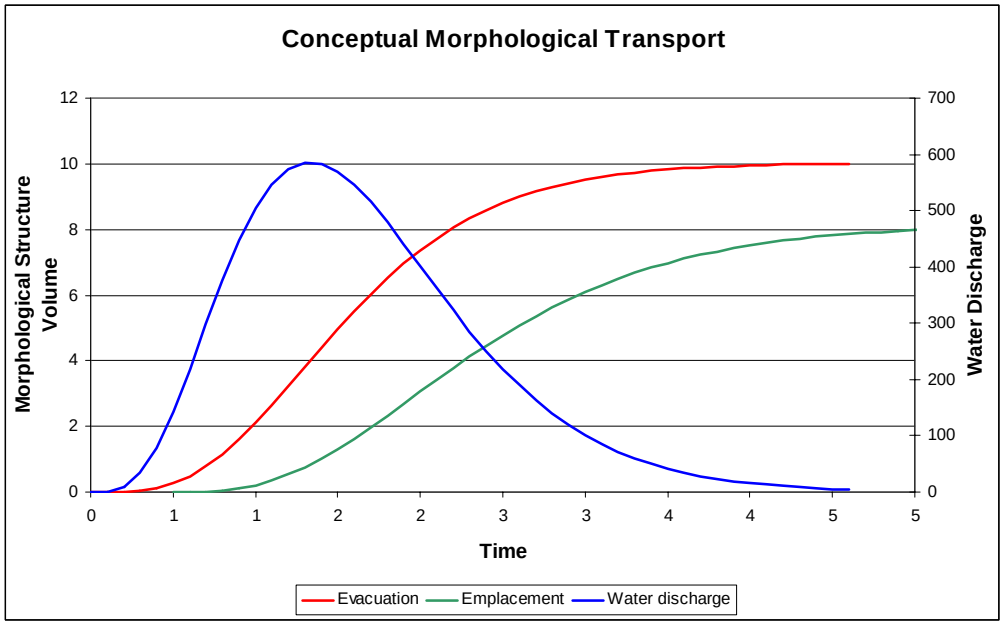

Figure 6.60 Conceptual morphological Transport Curves.

6.11.4 Lower Potlatch River Morphological Transport Segment

The most convincing argument is often a practical demonstration. An analysis of the lower Potlatch River shows how a morphological transport segment is applied to estimate bed material export. The analysis is made efficient by high-resolution aerial imagery I acquired since 1999. Only the aerial imagery datasets from 2001 and later are of sufficient quality to support high-resolution morphological analysis. The natural color near-vertical aerial images were acquired during low discharges on September 20, 2001, August 31, 2002, September 27, 2003, July 31, 2004, October 27, 2004, and March 10, 2005. Winter high flow images were acquired on several dates, but the January 31, 2004 images provide the best observance of falling stage flow.

Export of bed material from the Potlatch River to the Clearwater River is of practical interest. Figure 6.61 identifies the location of a morphological transport

segment at river kilometer 2.0 well above the potential backwater zone of the Clearwater River, but sufficiently close to the confluence to provide a meaningful estimate of basin export. The historic aerial imagery record since 1965 indicates ten other potential morphological transport sections over a 21.5 kilometer stretch of the lower Potlatch River between the confluence and Kendrick, ID. The average length of the potential morphological transport segments is 890 meters, much longer than the probable transport distances of gravel and cobble material for the discharges experienced by the lower Potlatch River. Though the research on particle transport distance is not extensive or conclusive, it indicates that sediment does not transit the full length of a typical morphological transport segment on the Potlatch River during a single flow cycle and so avoids incorporation into the end-of-cycle morphological structure.

High flows during February and March 2003 significantly altered the channel; producing significant changes in bank lines, channel position and the gravel bars between the 2002 and 2003 aerial images. A smaller discharge slightly altered the segment during spring 2004. A side-by-side comparison of 2002 and 2004 aerial images is in Figure 6.62. Flow is from top to bottom of the image. The approximate limits of the morphological transport segment are indicated by red transverse lines. The secondary channel along the left side of the image carries a small flow during normal high water, but is geomorphically inactive for the range of flows observed.

Side-by-side images are a very effective means of locating potential morphological transport segments and documenting morphological change. Analytical comparisons must be made in a GIS or Remote Sensing software system. Morphological transport segments seem to be most often associated with abrupt longitudinal changes in

high flow stream power either above or below the segment. The complete sequence of side-by-side images of the lower Potlatch River is in the accompanying digital resource.

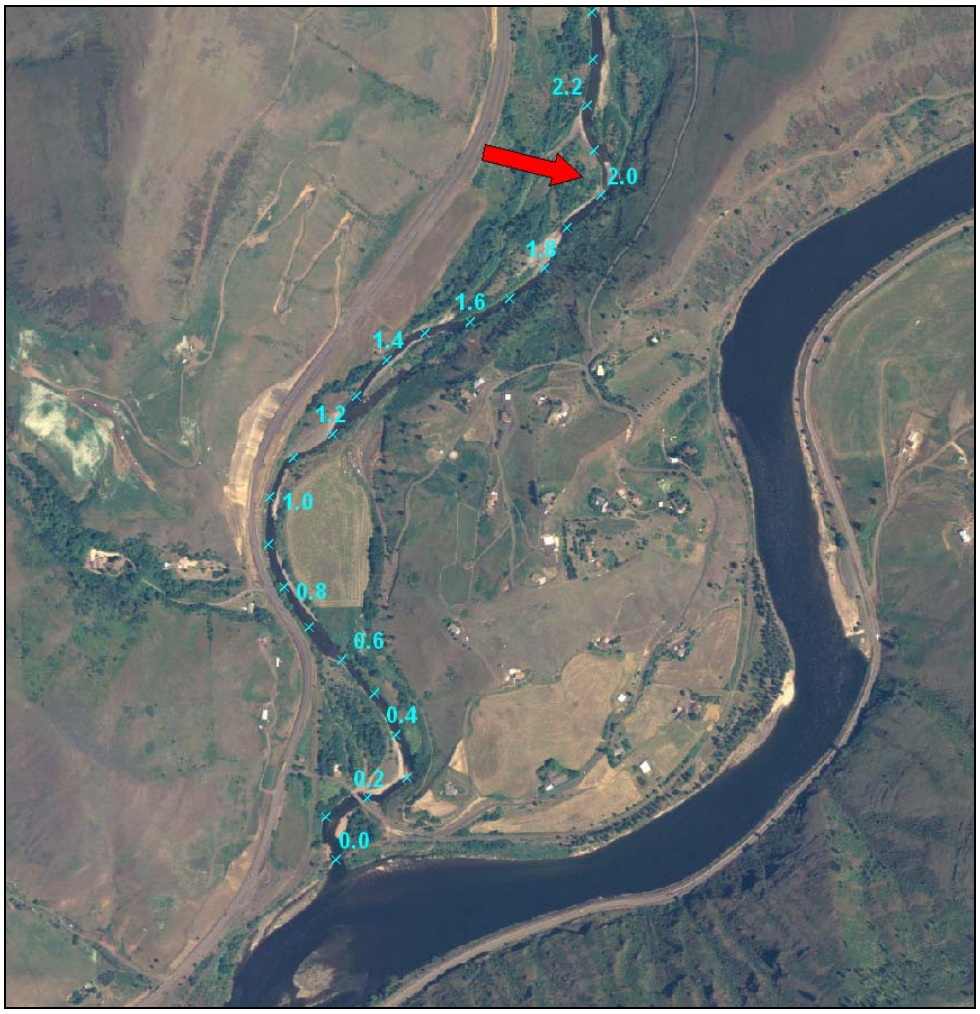

Figure 6.61 Location of the analyzed morphological transport section on lower Potlatch River.

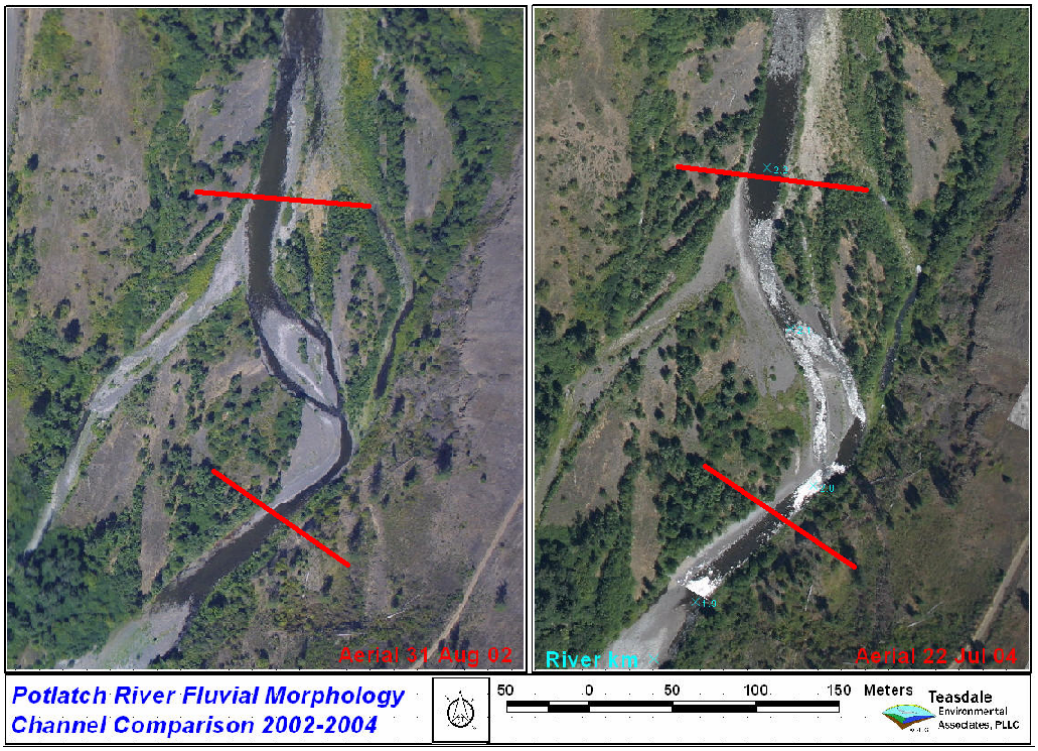

Figure 6.62 Comparison of aerial images from 2002 and 2004.

Morphological change was significant between 2002 and 2003. The 2002 and 2003 aerial images in Figure 6.63 indicate the downstream translocation of bar sediment. Figure 6.64 is a higher magnification view of the evacuated medial bar and a residual clump of cottonwood trees. The cottonwoods succumbed to erosion in 2004. The right bank line migrated laterally and large woody vegetation was dislodged from the relic bar.

Figure 6.63 2002 – 2003 side-by-side aerial images indicating downstream translocation of bar sediment.

Figure 6.64 Magnified view of resistant residual bar vegetation in 2002 – 2003 side-by-side aerial images.

It is useful to examine the historic aerial imagery record for persistence of the morphological transport segment. Figure 6.65 is a comparison of aerial images from 1965, 1992, 1998 and 2004. The images show maintenance of the morphological transport segment between kilometer 1.0 and 3.0. Stable channels bound the morphological transport segment. Alluvial change within the segment is scaled to the

magnitude of discharge. The active portion of the morphological transport segment lengthens and shortens from year to year depending on the magnitude and duration of the flow cycle. It is obvious that sediment transiting the segment manifests its presence by altering channel morphology. The principle of morphological separability holds that it is unlikely that a significant volume of bed material transits the morphological transport segment in an inexpressive conveyor-belt like fashion as it does through the bounding stable channel segments.

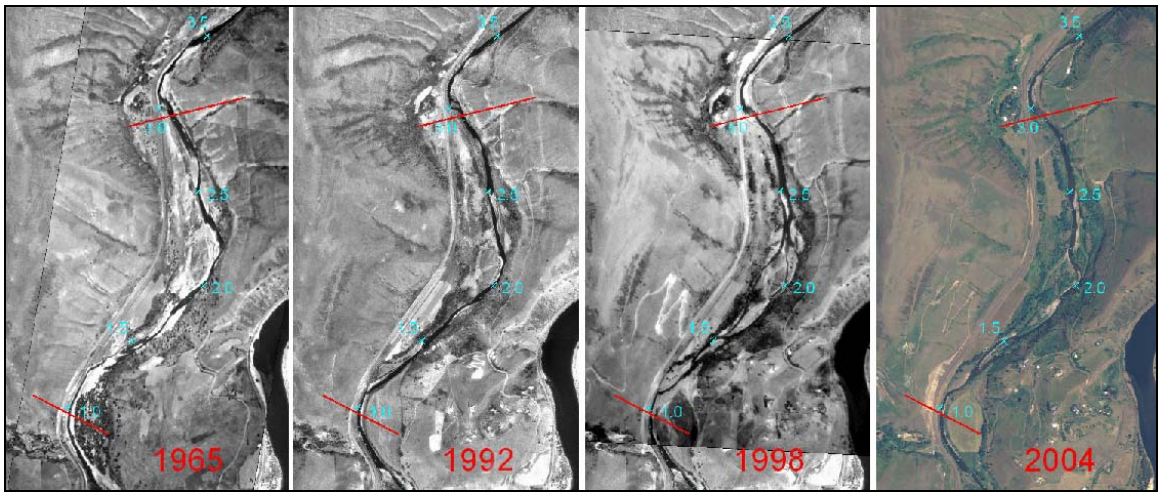

Figure 6.65 Historical persistence of the Morphological Transport Segment.

Inscriptions of extreme floods in the winter and spring of 1965 and 1996 are evident in the 1965 and 1998 aerial images. The 1992 and 2004 aerial images record more quiescent periods in the fluvial cycle. According to the principle of discharge scaling, the 1998 aerial image shows significantly more sediment transiting the reach, and is also an indication of the passing of a sediment wave originating in earlier floods. Estimated peak discharges over 10,000 $ft^3 s^{-1}$ are listed in Table 6.6. Development of the historic Potlatch River hydrograph is discussed in a separate report on the hydrology of the Potlatch River basin.

Date	Peak Discharge $ft^3 s^{-1}$	$m^3 s^{-1}$
12/23/1964	14,200	402
1/29/1965	21,500	609
1/6/1969	13,700	388
2/28/1972	15,900	450
1/16/1974	19,200	544
5/16/1979	10,134	287
2/19/1982	14,456	409
2/24/1986	14,000	396
2/9/1996	29,190	827
1/1/1997	12,380	351

Table 6.6 Estimated historic peak discharges over 10,000 $ft^3 s^{-1}$ of the lower Potlatch River.

6.11.5 Measurement of Morphological Bed Material Transport

The process of evacuation, translocation and emplacement is intuitively obvious in the above images. A more detailed analysis of morphological transport may be performed with annual comparison of high-resolution aerial images. Horizontal and vertical changes in the dimensions of sediment structures can be made with analytical photogrammetric techniques discussed in Section 2. The most exact analysis would measure morphological change by differencing annual digital elevation models (DEM), but is not absolutely necessary for a preliminary analysis. The following sequence of images demonstrates a GIS-based approach augmented by point measurements of elevation change made by stereo observation. The example computes the morphological transport in 2002-2003 for the lower Potlatch River segment because the amount of change within the morphological transport segment was relatively dramatic and easier for the reader to follow.

The first step in the analysis is to georeference the annual aerial image sequence to a common scale and geographic datum. It is convenient to georeference uncontrolled

aerial images to an existing georeferenced base image such as a DOQ. An alternative is to designate one of the images as a local base image and establish its scale from flight data and approximate ground elevations. All other aerial images are rectified to the local base image. This latter alternative may be the only practical alternative when working with high-resolution images of streams in forested terrain where visual ground control is sparse in existing lower resolution DOQs.

The preferred next step is to digitize bank lines in each aerial image of the sequence. This gives an overall indication of magnitude of morphological change and helps constrain the analysis area. Bank lines often demonstrate support for the principles of persistence and discharge scaling. Bank lines for each year in the five year sequence are superimposed on the aerial image of September 20, 2001 in Figure 6.66. Transverse red lines indicate the approximate boundaries of the morphological transport segment analyzed in this image sequence. The color of the dashed bank lines identifies the image year. Erosion of the relic bar and channel margin was steady during the five year period.

Figure 6.66 September 20, 2001 aerial image with digitized bank lines.

The volume of new sediment supplied to the channel may be measured from the area and depth evacuated by the migrating bank lines. Bank lines in this sequence move a different amount each year (principle of discharge scaling). Monoscopic interpretive

indicators of bank migration are bank shadow lines, changes in surface texture and removal of vegetation. Bank line migrations across relic bars and at channel margins are good indicators of a freely alluvial channel and a possible morphological transport segment.

Bank lines are superimposed on the other images in the sequence from 2002, 2003, 2004, and 2005 aerial images in Figures 6.67 through 6.71. The October 27, 2004 aerial image is included because it is at a slightly higher resolution than the July 22, 2004 image and it demonstrates the wide acquisition window for low flow aerial imagery in the inland Pacific Northwest.

A central premise of the existence of a morphological transport segment (MTS) is that evacuation and emplacement structures are primarily separate and distinct (principle of separability). It is revealing to observe flow structures in an aerial image acquired during the declining hydrograph that support the principle of translocation. Figure 6.72 is an aerial image acquired on January 31, 2004 at a discharge of 1820 ft^3 s^{-1}. A peak 15 minute discharge of 4100 ft^3 s^{-1} had occurred 35 hours earlier. Channel evacuations observed in the 2003 aerial image and the July and October 2004 aerial images (Figures 6.68, 6.69 and 6.70) are mostly complete and are being deepened by the strong flow structure. A second independent peak discharge of 4040 ft^3 s^{-1} occurred on February 19, but the nearly equivalent peak discharge in February did not significantly alter channel morphology, demonstrating support for the principle of least work. The hydrograph of the January and February discharge at the USGS Potlatch River gage records is in Figure 6.73.

Figure 6.67 August 31, 2002 aerial image with digitized bank lines.

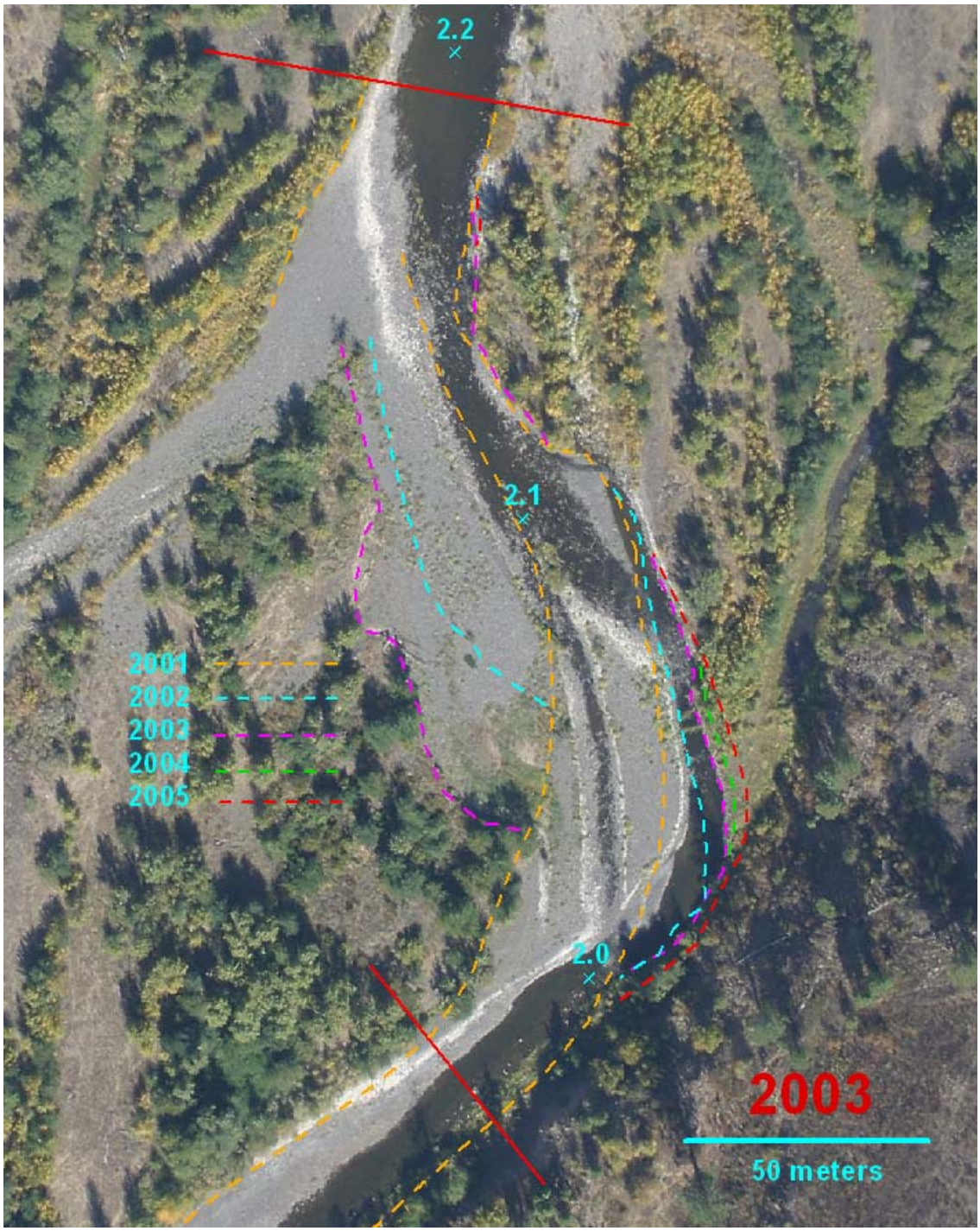

Figure 6.68 September 27, 2003 aerial image with digitized bank lines.

Figure 6.69 July 22, 2004 aerial image with digitized bank lines.

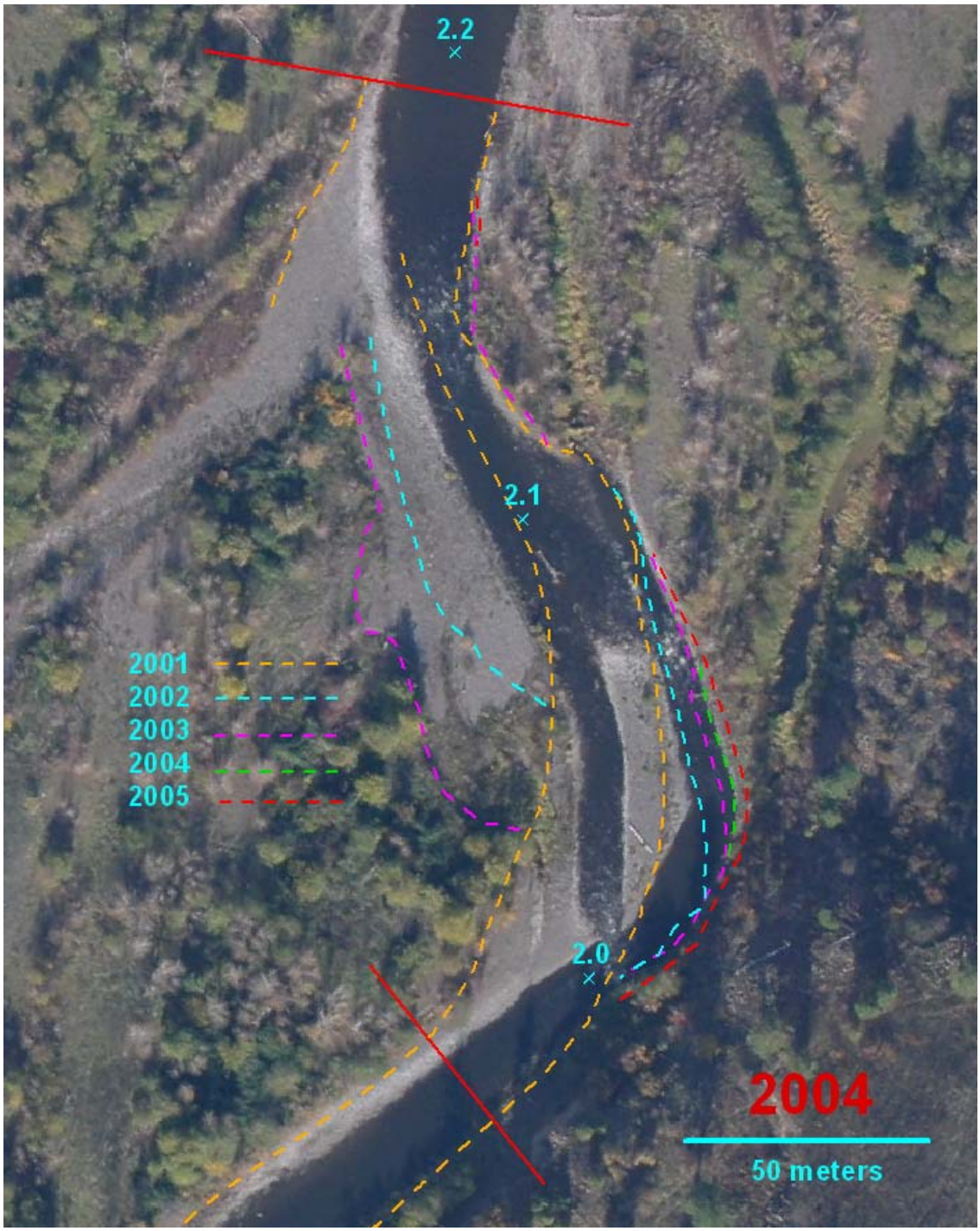

Figure 6.70 October 27, 2004 aerial image with digitized bank lines.

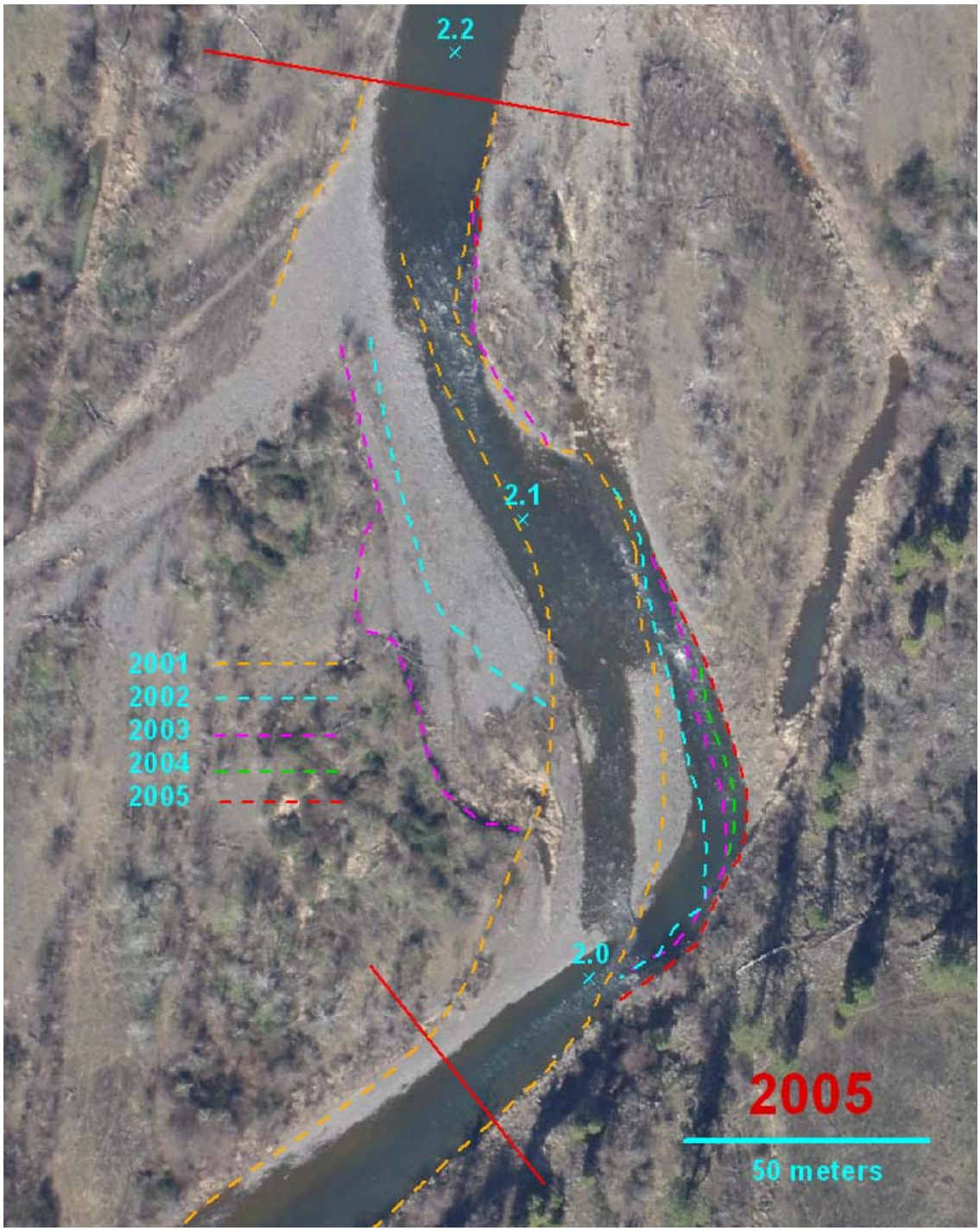

Figure 6.71 March 10, 2005 aerial image with digitized bank lines.

It is interesting to note that the cottonwood trunk on the medial bar in Figure 6.69 indicates the direction of the shoaling flow across the top of the bar during high flow. Prompted by this and similar observations, I have begun research and development of

neutrally weighted and positively weighted “ball and chain” indicators scaled to discharge that visually record the history of velocity vectors during a flow cycle.

Figure 6.72 High flow aerial image January 31, 2004.

The January and February 2004 peak discharges are well below the conventionally defined bankfull discharge for this channel of approximately 9000 ft^3 s^{-1}. Even though experiencing a discharge less than bankfull, the morphological transport segment was further matured in spring 2004. A scouring flow at B in Figure 6.72 is eroding the bank and further excavating the pool at this location when compared to the 2003 image. The turbulent flow surface indicates deepening of the channel at location A. Disturbance at the cottonwood tree root wad is seen at D, indicating further excavation of

the relic bar. Since the toppled cottonwood is observed and exposed in the summer and fall images, it possible to infer that not much evacuation or emplacement occurred on the relic bar during the February flow cycle. A small discharge bypasses the main channel at E and a temporary hard point of resistant vegetation is at C. An obviously shallower and less turbulent zone above D is continuation of an emplacement site initiated in 2003.

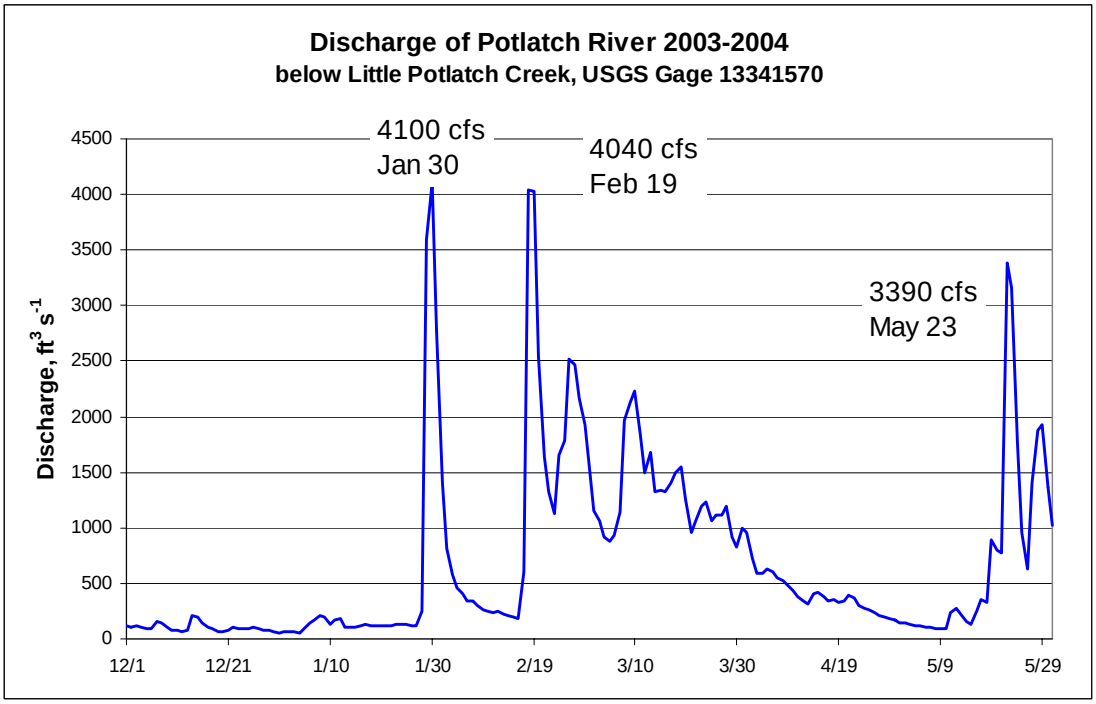

Figure 6.73 Lower Potlatch River hydrograph 2003-2004.

The next step in the GIS analysis process is to digitize the water surface area of the low flow channels in each year of the aerial image time sequence. This was done for all years of the record in Figure 6.74. Translocation of the low flow channel between flow cycles defines the dominant areas of evacuation and emplacement. Net evacuation and emplacement areas are extracted with a GIS intersection operation. Net evacuation and emplacement polygons for 2002 and 2003 are in Figure 6.75.

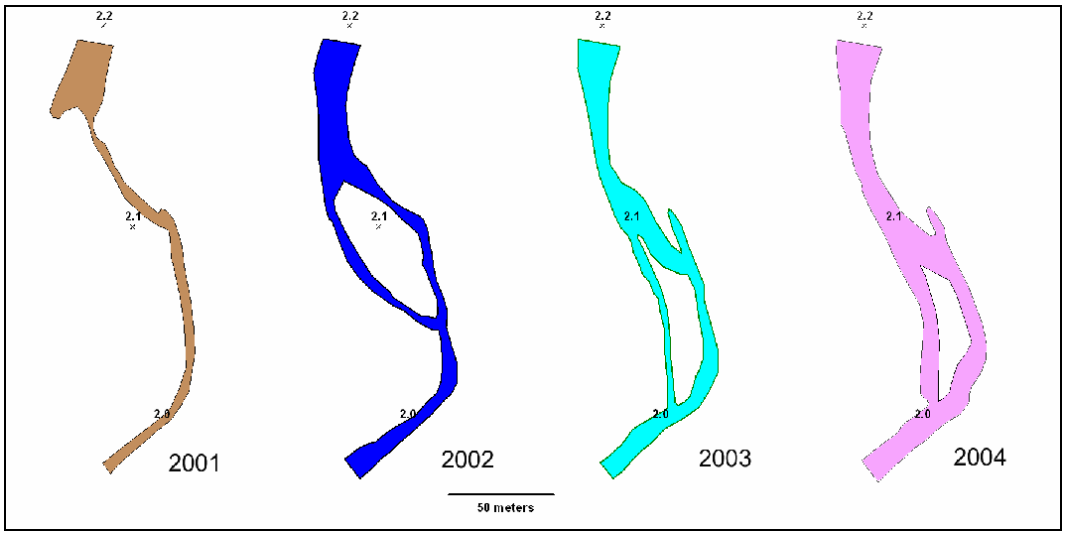

Figure 6.74 Low flow water surface areas of the morphological transport segment.

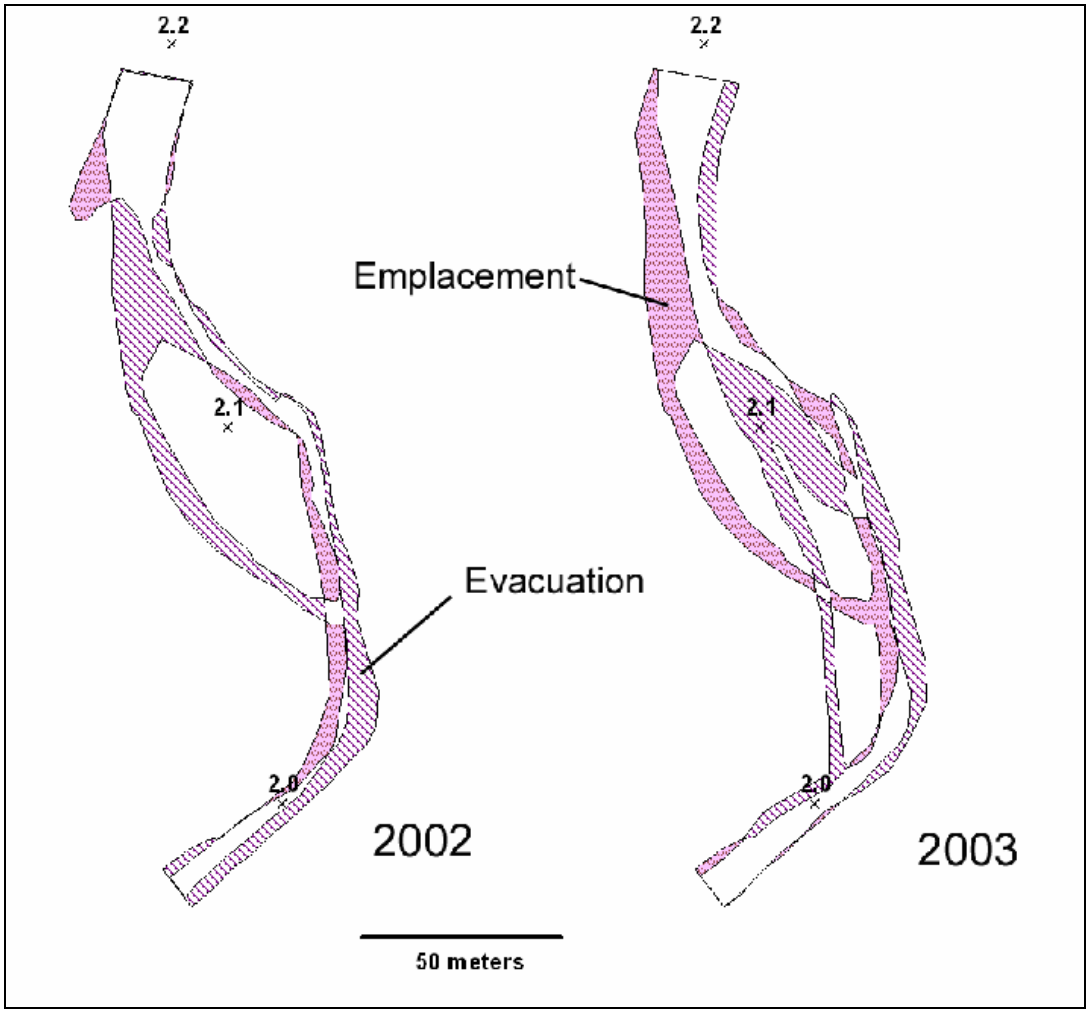

Figure 6.75 Net evacuation and emplacement zones of the morphological transport segment.

6.11.6 Level-One Estimate of Morphological Bed Material Transport

In 2003 the net evacuation area of 1445 m^2 exceeds the net emplacement area of 1324 m^2. Average channel depth observed in the stereo aerial imagery was 1.5 meters, so a first or level-one approximation of the net change in bed material stored in the segment is:

$$Ev_{net} = (1445 - 1324)\,\mathrm{m} \times 1.5\,\mathrm{m} = 182\,\mathrm{m}^3$$

It is clear that this is the volume of net transport; the 2003 channel that was excavated by the seasonal flows exceeded the amount of 2002 channel that was filled. Values are reported to the nearest cubic meter for computational clarity. An estimate of precision will be given with final results. The level-one estimate is the easiest approximation to compute from basic aerial imagery measurements of bed form area and estimated mean depth.

Total throughput of bed material is approximated by a mass balance accounting that acknowledges that evacuated sediment cannot move laterally across flow vectors (principle of downstream transport). An approximate analysis is to conceptualize the stream channel as a sequence of channel cells linked by a minimum downstream transport distance. Evacuated material from an upstream cell must move downstream the minimum distance before emplacement. Upstream evacuated material that exceeds a cell emplacement volume moves further downstream to the nearest available emplacement cell (principle of minimum flowpath work). By inspection of the probable flowpaths of this reach, the minimum downstream transport distance is about 30 meters in Figure 6.76.

Cumulative volumes of evacuation and emplacement as a function of downstream distance are determined by splitting the net evacuated and emplacement polygons at

selected intervals along the average channel centerline. The channel cell areas were determined by splitting the evacuation and emplacement area polygons every 10 meters in Figure 6.76. Volumes of emplacement and the *offset* evacuation as a function of downstream distance are plotted as in Figure 6.77.

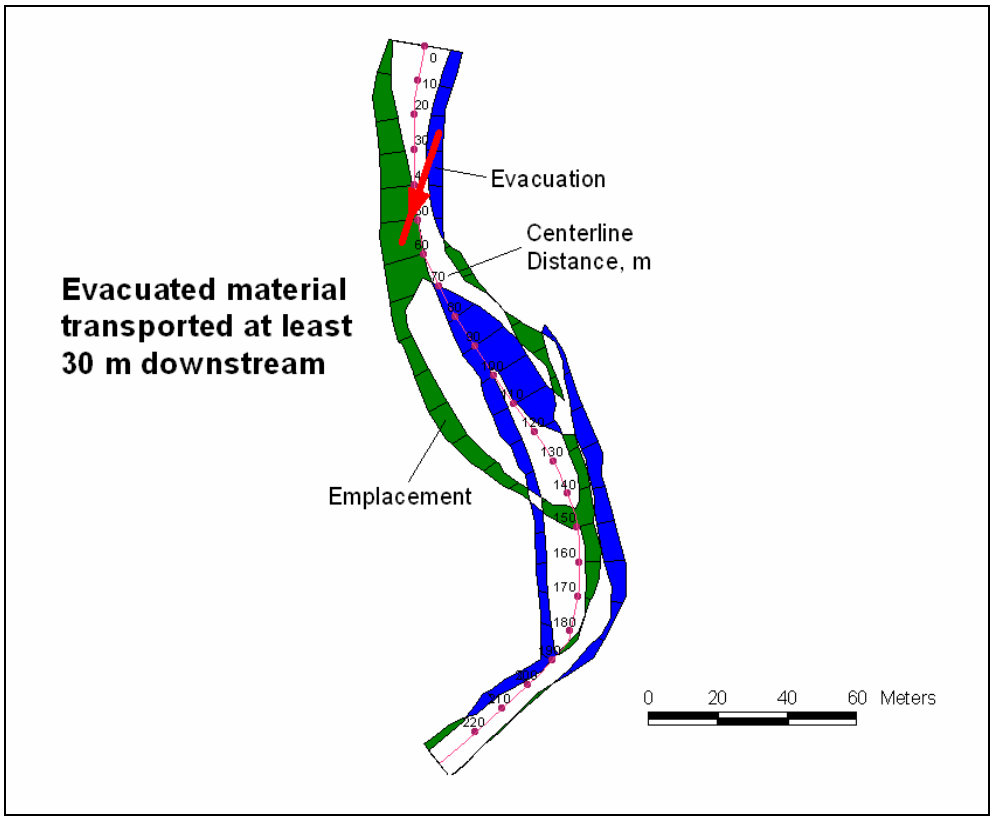

Figure 6.76 Minimum downstream transport distance of evacuated material.

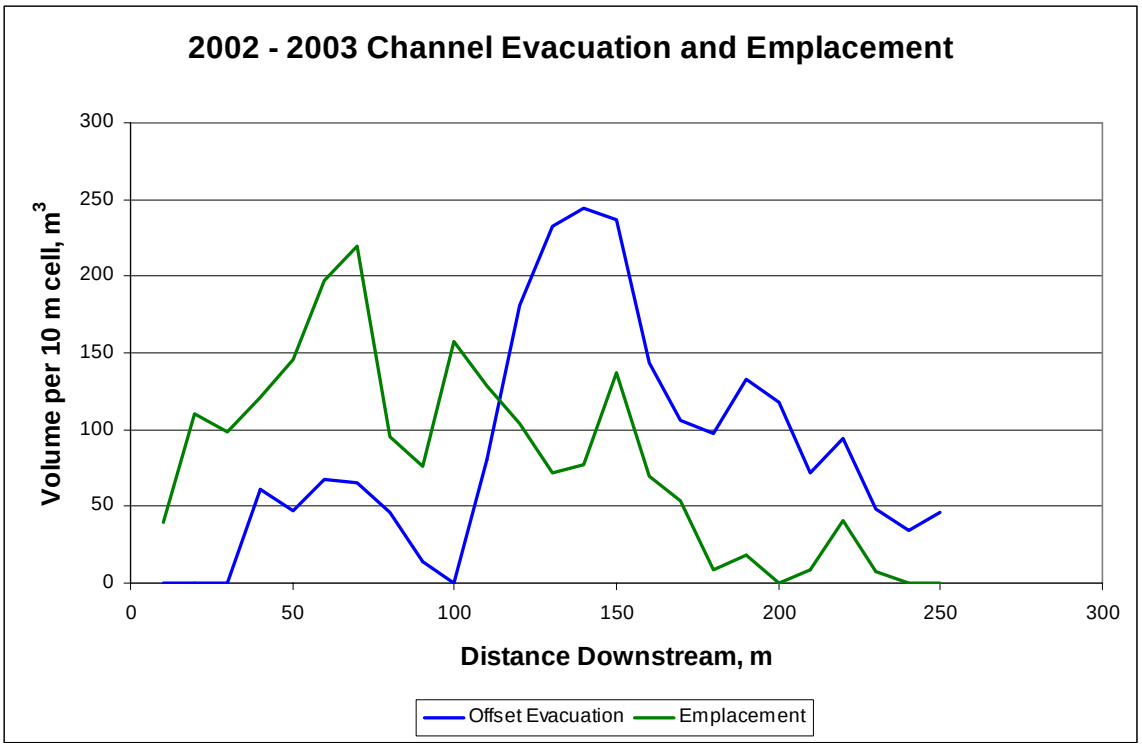

Figure 6.77 Channel excavation and emplacement volumes of channel cells.

Emplacement cell volumes exceed offset evacuation cell volumes for the first 110 m of channel length. Bed material must be transported into the morphological transport segment from upstream to fill excess emplacement volume. Cumulative bed material imported into example morphological transport segment is shown by the mass balance in Table 6.7 is 1009 m^3. Offset evacuated material exceeds emplacement volume in cells further than 110 m along the channel. Cumulative excess evacuated bed material exported downstream of the morphological transport segment is 1191 m^3. The difference between net import and net export is -182 m^3 (exported from the reach), the change in bed material stored in the morphological transport segment.

A	B	C	D	E	F	G	H
Downstream Distance m	Measured Evacuated Volume m^3	Measured Emplaced Volume m^3	Transport Offset Evacuated Volume m^3	Emplacement less offset Evacuated Volume m^3	Cumulative Emplacement Volume filled from upstream m^3	Excess Evacuated Volume Exported Downstream m^3	Cumulative Excess Evacuated Volume Exported Downstream m^3
10	61	39	0	39	39		
20	47	111	0	111	150		
30	67	99	0	99	249		
40	65	122	61	61	309		
50	46	146	47	99	408		
60	14	197	67	130	538		
70	0	219	65	154	692		
80	81	96	46	49	741		
90	181	76	14	63	804		
100	232	157	0	157	961		
110	244	129	81	48	**1009**		
120	237	103	181	-77		77	77
130	143	72	232	-161		161	238
140	106	77	244	-167		167	405
150	98	138	237	-99		99	504
160	133	69	143	-74		74	578
170	118	54	106	-52		52	630
180	71	9	98	-89		89	720
190	95	18	133	-115		115	834
200	48	0	118	-118		118	952
210	34	9	71	-63		63	1015
220	46	41	95	-54		54	1069
230	0	7	48	-41		41	1110
240	0	0	34	-34		34	1144
250	0	0	46	-46		46	**1191**

Table 6.7 Approximate mass balance of the morphological transport segment.

Average channel depth may be determined by field measurement if resources and access restrictions allow, or by photogrammetric analysis of the low flow aerial images as indicated in Figure 6.78. Stereoscopic height measurements are made as discussed in Section 2. Access to this channel location was not permitted, so no field measurements were possible. The precision of the relative height differences is 0.3 to 0.5 meters based on stereo observation of the cottonwood trunk on top of the medial bar. Several locations along the channel banks and gravel bars were measured to obtain an average channel depth of about 1.5 meters.

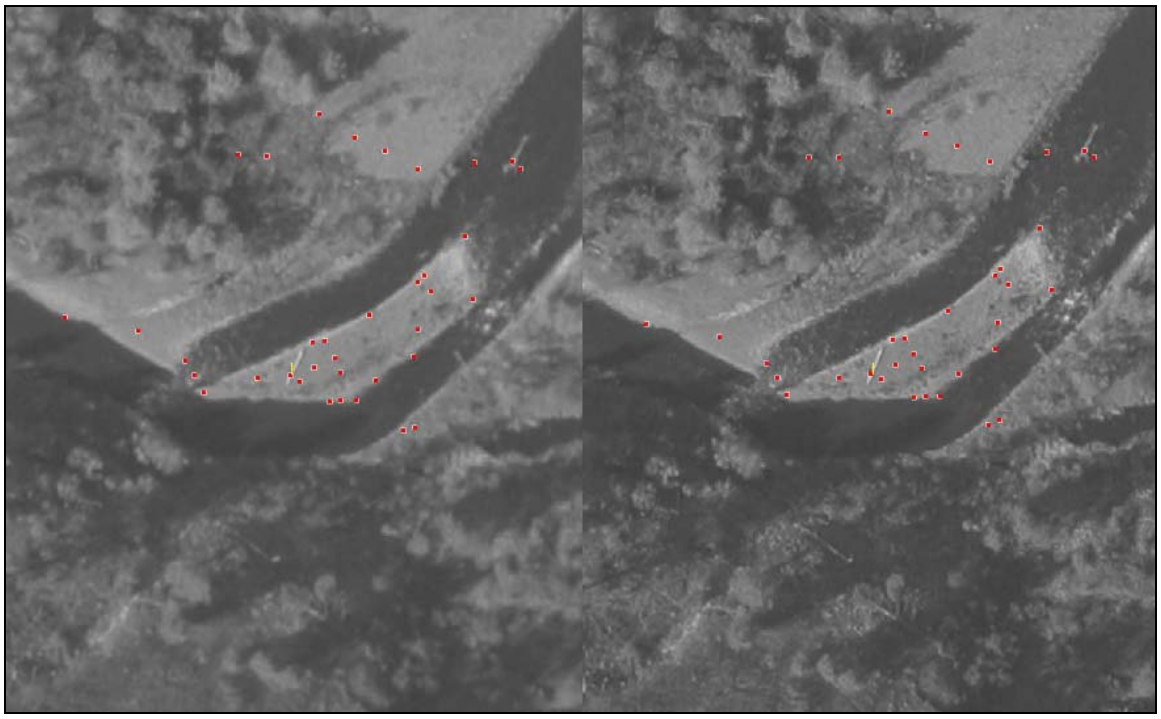

Figure 6.78 Photogrammetric analysis of average channel depth.

6.11.7 Level-Two Estimate of Morphological Bed Material Transport

A refined or level-two estimate of bed material transport includes evacuation volumes caused by stream bank erosion during the flow cycle. Bank erosion can be harder to detect in aerial images because of obscuration by vegetation and shadows. Bank erosion in this morphological transport segment is easily recognized in Figures 6.67 and 6.68. Surface area polygons for bank evacuation in 2003 are in Figure 6.79. Bank evacuation polygons are compared with the emplacement and channel polygons. Only bank evacuation not previously included in channel evacuation is added to the downstream export estimate. It is unlikely that material eroded from the stream banks was deposited in the emplacement volume, because of location and timing in the discharge hydrograph, with the possible exception of larger cobbles. Bank erosion occurs near the peak discharge; emplacement likely occurs during the receding hydrograph. It

was observed in more accessible reaches of the lower Potlatch River that median particle size of bank material is generally smaller than material forming the main channel bed and bars.

The surface area of the large bank evaluation cell in Figure 6.79 is 1376 m^2 and the average eroded depth is about 0.5 m. The bank evacuation volume exported from the morphological transport segment is 688 m^3. The level-two estimate of bed material export from the morphological transport segment is the sum of the level-one export and the bank evacuation export or 1879 m^3. Bed material import is unchanged. The estimate of bank erosion depth in this example is near the precision of the photogrammetric methods so is more uncertain than the level-one analysis.

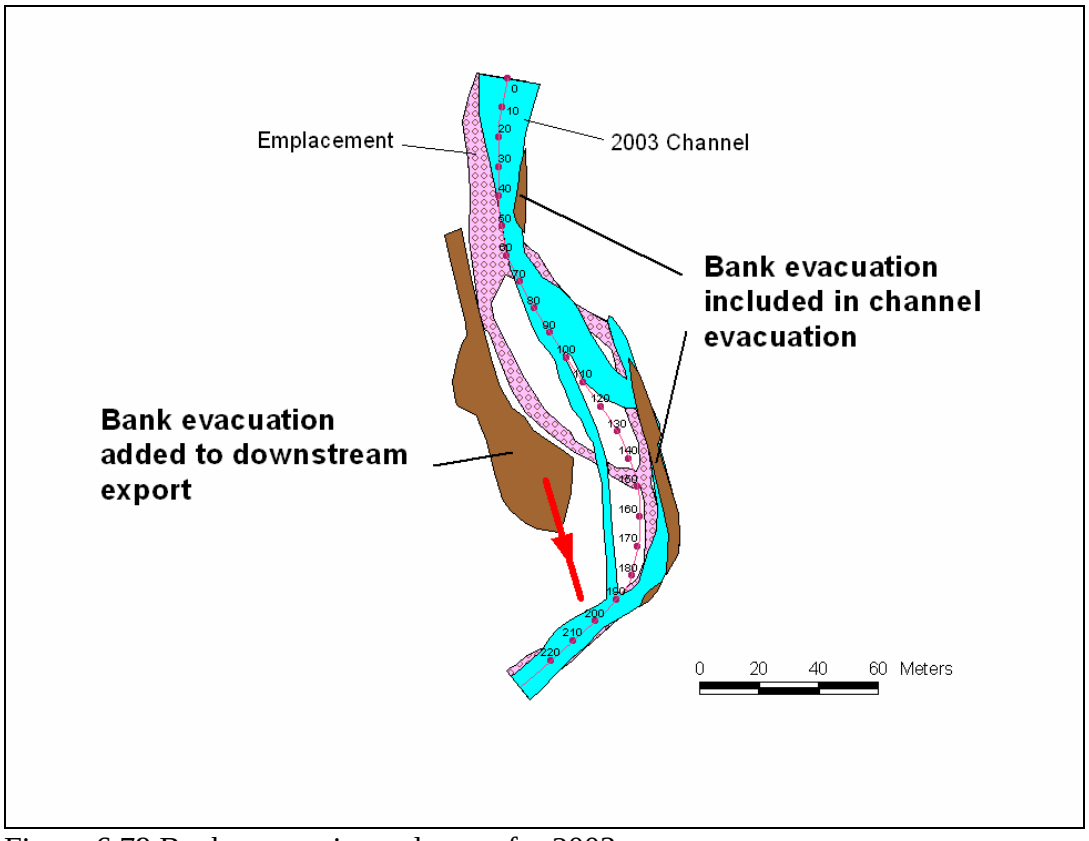

Figure 6.79 Bank evacuation polygons for 2003.

6.11.8 Level-Three Estimate of Morphological Bed Material Transport

The estimate of bed material transport import and export of the morphological transport segment can be further refined by adding emplacement and evacuation volumes for deposition and erosion of the surface of gravel bars not included in the level-one and level-two estimates. This is a more difficult aerial image and flow interpretation. The depths of deposition and erosion of the relic bars cannot be measured with much certainty with photogrammetry in this example because the depths appear to be less than the stereoscopic precision. Depths must be estimated from interpretive clues such as removal of vegetation and changes in the texture of bar surfaces indicating fining and coarsening of surface gravels. Knowing that bar deposition and erosion appears less than the stereoscopic precision is useful information and places a limit on the maximum likely depth. Bar emplacement and evacuation polygons are evaluated qualitatively in Figure 6.80.

Assuming an average disturbed depth of 0.3 m, the emplacement and evacuation volumes for the relic bars are 306 m^3 and 416 m^3, respectively. All bar excavation volume is exported downstream because of its position in the lower portion of the morphological transport segment. About half the bar emplacement volume, 153 m^3, likely is imported into the segment from upstream. The other half of the bar emplacement volume reduces downstream channel evacuation export. Since this is more than offset by the gross bar excavation volume, the net bar excavation volume is 416 minus 153 or 263 m^3.

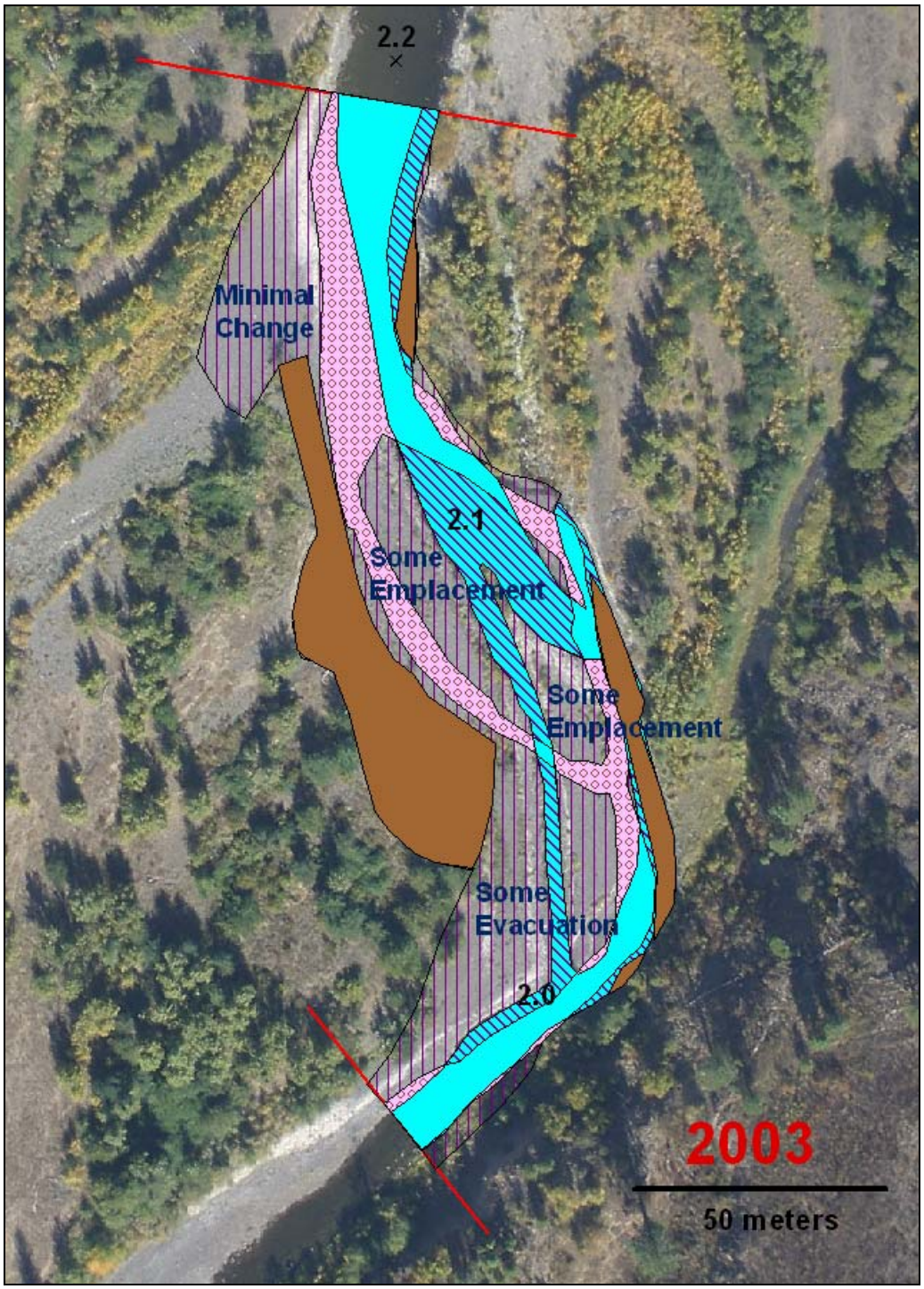

Figure 6.80 Qualitative relic bar emplacement and evacuation.

The level-three estimates for the Potlatch River morphological transport section are summarized in Table 6.8. Net downstream export from morphological transport

section is 980 m^3. Precision in the net export estimate is likely plus or minus 50 cubic meters. Precise confidence intervals cannot be computed because the accuracy of the photogrammetric measurements of height cannot be verified with field measurements.

Source	Import Emplacement Volume m^3	Export Evacuation Volume m^3
Channels (level 1)	1009	1191
Banks (level 2)	0	688
Bars (level 3)	153	263
Total	1162	2142

Table 6.8 Level-three estimate of bed material import and export.

Bed material transport of the morphological transport segment can be expressed as the sum of the components of the level-one, level-two and level-three analyses:

$$Ev_{bm} = Ev_{chan} - Em_{chan} + \varepsilon_1 + Ev_{bank} - Em_{bank} + \varepsilon_2 + Ev_{bar} - Em_{bar} + \varepsilon_3 + \varepsilon_4 \qquad 6.25$$

where Ev_{bm} is the downstream bed material export, Ev_{chan} is the net channel evacuation volume (level-one), Em_{chan} is the net channel emplacement volume (level-one), and ε_1 is the error in the level-one estimate; terms for bank evacuation and bar evacuation and emplacement are denoted by the subscripts *bank* and *bar*. Error terms for all three levels are necessary because the precision of the measurements likely decreases with increasing level because of image interpretation difficulty and stereoscopic precision. A fourth error term is included to account for bed material that transits the morphological transport segment during the flow cycle and is undetected as a change in morphological structure. Hidden throughput should be minimal according to the morphological transport segment principle of morphological separability. Some undetected throughput of smaller grain sizes might be expected at the beginning and end of the flood hydrograph

or during flow cycles having smaller peak discharges that do not significantly alter channel morphology.

The net bed material volume export estimate is all that is usually necessary for many practical applications of sediment transport. It is valid and sufficient to state,

> "Approximately 2100 m^3 of bed material was transported past river kilometer 2.0 on the lower Potlatch River during winter and spring 2002-2003. Of this about 1000 m^3 was sediment eroded from bars and banks between river kilometer 2.0 and 2.2."

This type of statement is seldom possible with conventional sediment transport analysis based on formulas extrapolated from flume and field studies. It is not even necessary to estimate discharge. An assessment of the accuracy of the sediment transport volume by the aerial imagery method is open to evaluation by anyone with GIS and photogrammetry skills.

The volume estimates from the morphological transport segment analysis can be converted to sediment transport rates by assuming, or measuring, bulk sediment density and partitioning the transport volume to a measured or assumed hydrograph by stream power or excess Shields stress. Preliminary work indicates that a productive approach is to compute excess Shields stress from a composite hydraulic model (before, transition and after channels) calibrated with high flow aerial imagery. This is a subject for future research.

6.11.9 Hydraulic Geometry of Morphological Transport Segments

Many readers may not have access to photogrammetry software or the patience and time to learn to use it. Another method of estimating channel depth can be

employed — depths of gravel bed channels may be estimated from the hydraulic geometry relationships of Parker et al. (2003) and Julien and Wargadalam (1995).

Particle size distributions were measured at several locations along the lower Potlatch River. Figure 6.81 is a typical grain size distribution. Median gravel particle size is 79 mm. The width of the water surface B_{bf} at the maximum discharge during winter and spring 2003 was 58 meters and is the measured distance between the eroded bank lines in the September 27, 2003 aerial image in Figure 6.82. By trail and error, a peak discharge Q_{bf} of 9900 $ft^3\ s^{-1}$ (280 $m^3\ s^{-1}$) is computed from the Parker et al. expression for bankfull width in Equation 6.6 and repeated in the set of Equations 6.26:

$$H_{bf} = 0.3785\frac{Q_{bf}^{2/5}}{g^{1/5}}$$

$$B_{bf} = 4.698\frac{Q_{bf}^{2/5}}{g^{1/5}}\left(\frac{Q_{bf}}{\sqrt{gD_{s50}}\,D_{s50}^2}\right)^{0.0661} \qquad 6.26$$

$$S = 0.1003\left(\frac{Q_{bf}}{\sqrt{gD_{s50}}\,D_{s50}^2}\right)^{-0.3438}$$

With the peak discharge, an average bankfull depth H_{bf} of 2.29 m is computed from the first relationship in the set of Equations 6.26. The depth of the low flow channel relative to the main bars is less than the average bankfull depth. This is because the main bars are inundated during peak flow with sufficient depth to cause displacement of surface gravels. Assuming a Shields parameter of 0.03 for full mobility of gravel bed streams, the minimum depth over the main bars is approximately:

$$H_s = \frac{\tau_s^* g(\rho_s - \rho_w)D_{50}}{\gamma_w S} = \frac{0.03(9.81)(1800)(0.079)}{9810(0.00241)} = 1.77\ \text{m} \qquad 6.27$$

where τ^*_s is the Shields parameter, g is the acceleration of gravity (m s^{-2})ρ_s is the density of the gravel and cobble particles (kg m^{-3}), ρ_w is the density of water (kg m^{-3}), D_{50} is the median particle size (m), γ_w is the specific weight of water (N m^{-3}), and S is the channel slope from the hydraulic geometry relationship in Equation 6.26. The gravel and cobble material is primarily basalt with a specific gravity of about 2.8.

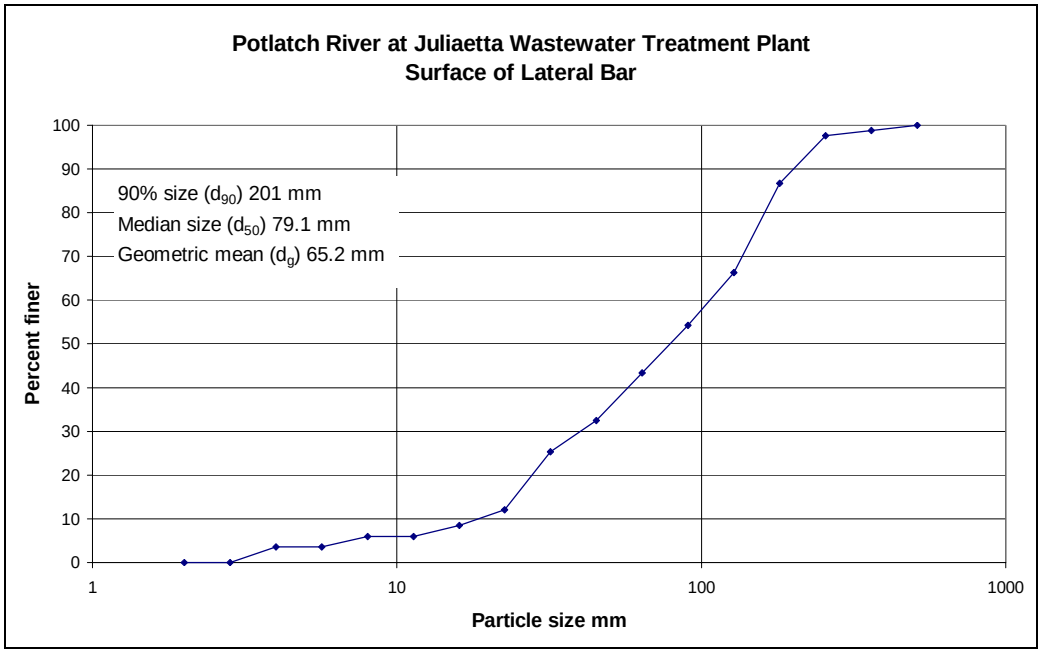

Figure 6.81 Typical gravel particle distribution of lower Potlatch River.

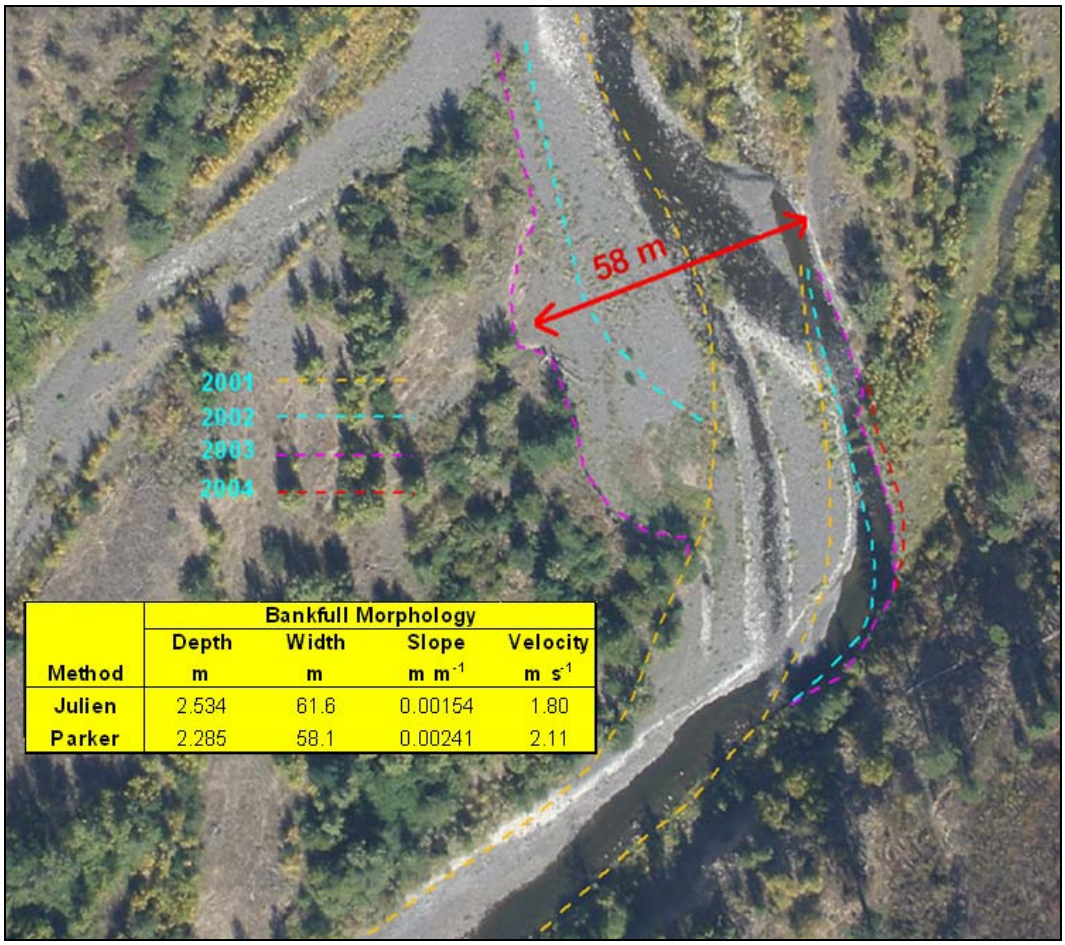

	Bankfull Morphology			
	Depth	Width	Slope	Velocity
Method	m	m	m m^{-1}	m s^{-1}
Julien	2.534	61.6	0.00154	1.80
Parker	2.285	58.1	0.00241	2.11

Figure 6.82 Maximum surface water width during 2002-2003 flow cycle.

The average height of main gravel bars can be approximated assuming the channel geometry in Figure 6.83. Total channel cross section area at bankfull discharge is bankfull width multiplied by the average depth. Total channel cross section area in Figure 6.83 is the minimum depth computed by the Shields stress relationship multiplied by bankfull width plus the width of the low flow channel multiplied by the average bar height. Solving the channel area relationship for average bar height (H_b) gives:

$$H_b = \frac{B_{bf}\left(H_{bf} - H_s\right)}{B_{lf}} \qquad 6.28$$

where B_{lf} is the width of the low flow channel and H_b is the bar height.

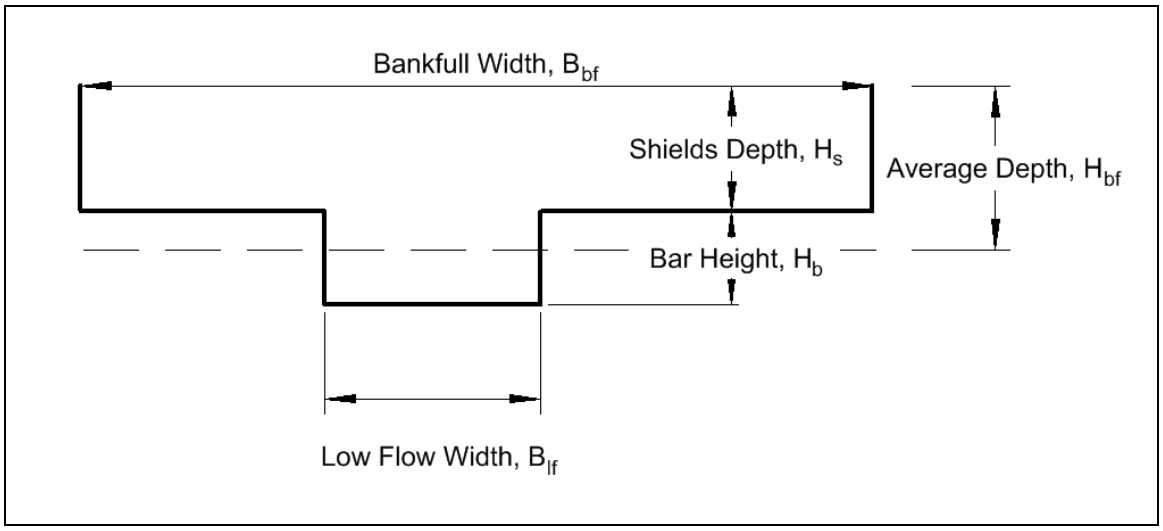

Figure 6.83 Hydraulic geometry for computation of approximate bar height.

The width of the water surface at low flow at the hydraulic geometry section in Figure 6.82 is 23 m so the average bar height is:

$$H_b = \frac{B_{bf}\left(H_{bf} - H_s\right)}{B_{lf}} = \frac{58\,\text{m} \times (2.3 - 1.8)\,\text{m}}{23\,\text{m}} = 1.3\,\text{m}$$

A level-one analysis of morphological bed material transport can then be based on this estimate of mean channel depth. The computed average bar height agrees well with the bar height measured in the stereo aerial images. Users should be aware that the Shields parameter for gravel bed streams is highly variable (Buffington and Montgomery 1997; Lisle et al. 2000) and that computations of bar height by hydraulic geometry methods are very approximate. Mean channel depth can also be estimated with the Julien and Wargadalam (1995) relationships of hydraulic geometry. Results of hydraulic geometry computations are compared on Figure 6.82 and are in good agreement.

The USGS gage on the Potlatch River was not installed until autumn of 2003. Discharge in the lower Potlatch River can be estimated by analysis of the USGS gage records for Peck and Spalding on the Clearwater River and is developed in a separate publication. Figure 6.83 indicates that the peak discharge on the lower Potlatch River was about 9500 $ft^3 s^{-1}$ (269 $m^3 s^{-1}$) in February followed by a lesser peak of about 8600 $ft^3 s^{-1}$ (244 $m^3 s^{-1}$) in March. The hydraulic geometry computations agree very well with estimated discharges.

This example demonstrates a little acknowledged aspect of the gravel bed hydraulic geometry relationships. These relationships can estimate channel geometry at discharges less than the nominal bankfull width if the section of channel is freely alluvial and the discharge is above the threshold of bed material motion. By definition the channel within the morphological transport segment is freely alluvial. In this example, the hydraulic geometry relationships of Parker et al. (2003) and Julien and Wargadalam (1995) gave a good estimate of peak discharge from the width measured in the low flow aerial imagery. No field measurements of channel slope are required, only a reasonable estimate of median particle size. The gravel bed hydraulic geometry relationships appear to provide an expedient confirmation of a morphological transport segment. A discussion of this possibility would make a useful journal article and warrants further research.

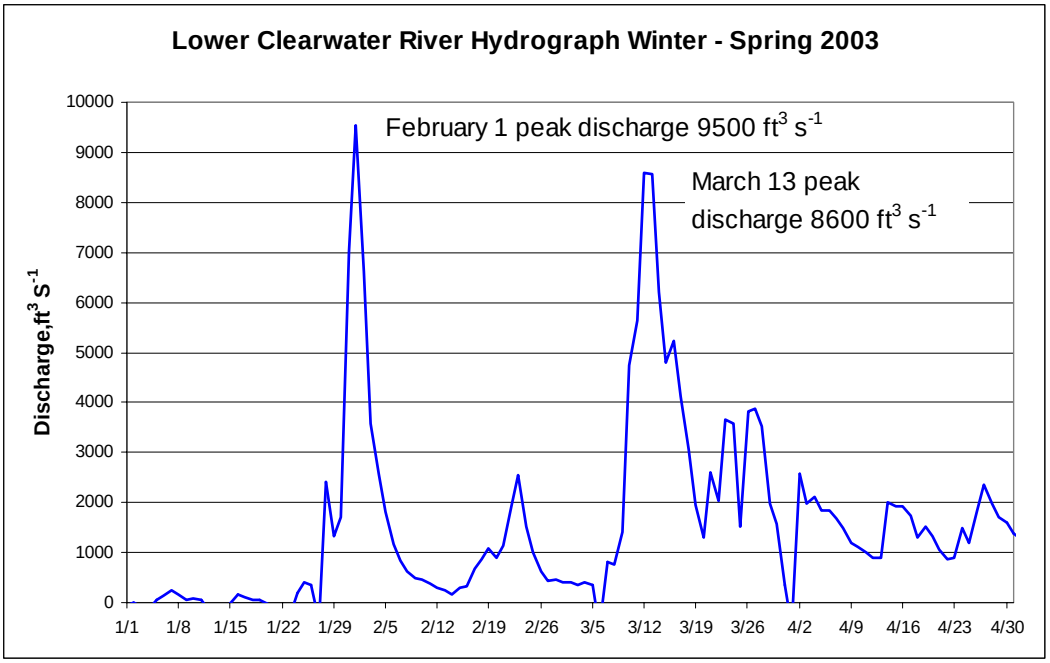

Figure 6.84 Hydrograph of the lower Potlatch River approximated from Clearwater River discharge records.

6.11.10 Importance of Flow Cycles

The two flow cycles during winter and spring of 2003 in Figure 6.83 have peak discharges that produce Shields stresses in excess of the threshold of bed material movement. Aerial images were acquired in August 2002 and again in September 2003. There were no aerial images acquired between the February and March flow cycles. Different embankment and evacuation volumes were probably produced by the February discharge and reworked during the March discharge. The magnitude of the undetected bed material transport cannot be determined. There is no way to recover this lost information and it would be difficult to partition the transport volume. It is very important to acquire aerial images of morphological transport segments between every

flow cycle. This is not an onerous or unreasonable effort in a serious study of sediment transport over an extensive channel system.

6.11.11 Undetected Bed Material Transport

A reasonable question is: how much bed material movement is undetected in a morphological transport segment? The method presumes that it is minimal. However, there has been surprisingly little investigation of this question. The sparse data on particle transport distances mentioned above indicate that gravel and cobble sized particles do not travel very far during a single flow cycle, probably much less than the typical length of morphological transport segment identified in this research. Peak discharges do not persist for long periods of time. Sediment in motion during the peak of the hydrograph must be deposited again in the channel when flows diminish. If the sediment is not in the observed morphological structures, then where is it?

It is unreasonable and contrary to sediment transport physics to expect transiting bed material to be spread evenly across the bottom of the low flow channels or that morphological structures maintain a constant size and shape while exchanging significant quantities of sediment with the flow. Doing so would preclude the existence of sediment waves in gravel bed streams. Certainly some sediment passes undetected, but numerous observations aerial images over a range of flows indicate that gravel bed morphology is fairly expressive once the threshold of motion is exceeded. There is no completely satisfactory answer to questions and criticisms of the morphological transport segment concept. The magnitude of morph-invariant bed material transport in gravel bed streams is a challenging and important topic for further research.

6.12 Naive Model of Morphological Bed Material Transport

Looking ahead at what might be achieved with further study of morphological transport segments, there seems to be an opportunity to develop a family of spatially aware sediment transport models. One possibility is to explicitly recognize the influence of upstream distance on the bed material residing in the morphological transport segment between flow cycles. Initial thoughts suggest that morphological transport can be modeled conceptually as:

$$M_{\psi x_o} = \int_{t_o}^{t}\int_{x_o}^{x} G_{\psi}\left(\gamma Q_x S_x\right)_x^{m_\psi} B_{x\psi} \cdot \left(\beta_\psi e^{-\beta_\psi x}\right) \cdot \left(\gamma Q_{x_o} S_{x_o}\right)_{x_o}^{n_\psi} dxdt \qquad 6.29$$

Where $M_{\psi x_o}$ is the mass of bed material (kg) of a particular size class deposited and stored at location x_o in the channel, x is the upstream distance, t is precedent time (backwards from time t_o), $G_{\psi x}$ is the potential mass entrainment rate (kg m^{-2} s^{-1}) of bed material of a particular size or size class generated (eroded) at distance x upstream at time precedent time t, $\gamma Q_x S_x$ is streampower per unit length of channel at distance x upstream at precedent time t (kg m s^{-1} m^{-1}), $B_{x\psi}$ is the active width of bed material deposit of a particular size class at distance x upstream at precedent time t (m), $\gamma Q_{x_o} S_{x_o}$ is streampower per unit length at location x_o in the channel upstream at time precedent time t, m_ψ and n_ψ are entrainment and deposition stream power exponents for a particular size class, and $\beta_\psi e^{-\beta_\psi x}$ is a dimensionless primogeniture term for a particular size class that diminishes the contribution of sediment to a particular location with distance upstream.

The primogeniture concept holds that for episodic transport during any finite period the further a source is upstream, the less likely that it will have contributed to sediment stored at a particular location. Entrainment and deposition of sediment is modeled as a function of stream power; other formulations are possible. The stream power term for entrainment should be lagged by the time of transport, but this is probably an unnecessary complication except when discharge is changing rapidly. There are three groups of variables in Equation 6.27: a source or entrainment term, a reach transport term and a sink or deposition term. These types of terms are common, one way or another, in most water quality simulation models.

The difficulty with Equation 6.29 is that the exponents and entrainment coefficient cannot be determined from sediment transport physics and must be evaluated by empirical analysis for each particle size class. It may follow from the principles of similarity collapse (Parker 1990) that a single set of exponents and coefficient would suffice for all particle size classes. Despite its empirical nature, the appeal of Equation 6.27 is that it offers a plausible relationship that explains the orderly variation in bed material accumulation observed in a time sequence of aerial images. It should be noted that all current models of incipient motion and bed material transport are at best semi-physically based and heavily dependent on empirical constants.

The primogeniture transport equation is most practical when evaluated in discrete form:

$$M_{\psi x_o} = \sum_{t=t_o}^{T} \sum_{x=x_o}^{L} G_\psi \left(\gamma Q_x S_x\right)_x^{m_\psi} \cdot \left(\beta_\psi e^{-\beta_\psi x}\right) \cdot \left(\gamma Q_{x_o} S_{x_o}\right)_{x_o}^{n_\psi} \qquad 6.30$$

The discrete distance steps in Equation 6.28 would be defined by channel units and sediment accumulations (bars and riffles) observed in the aerial imagery. Time steps would be set by the shape and duration of the discharge hydrograph.

Further work on this model is a subject for future research.

6.13 Very High Resolution Aerial Imagery Analysis of Gravel Bar Surfaces

I have begun a line of original research that appears to have significant potential in the study of gravel bed streams. Results are very preliminary and can only be highlighted. Figure 6.85 is a very high-resolution image of a gravel bar on the Clearwater River. Image tone and texture clearly varies with particle size and particle cluster organization at this image resolution. Area **A** is sand, Area B is fine gravel and **C** is medium coarse gravel. A plot of median particle size with various measures of image texture showed a near linear relationship.

This opens the possibility of assessing the spatial heterogeneity of the surface particle size of gravel and cobble bed streams by aerial survey techniques with more or less generalized image correlations. Success in this effort would greatly improve the ability to develop sediment transport models of alluvial gravel bed streams. It could also provide a rational basis for estimating hydraulic roughness over extensive reaches.

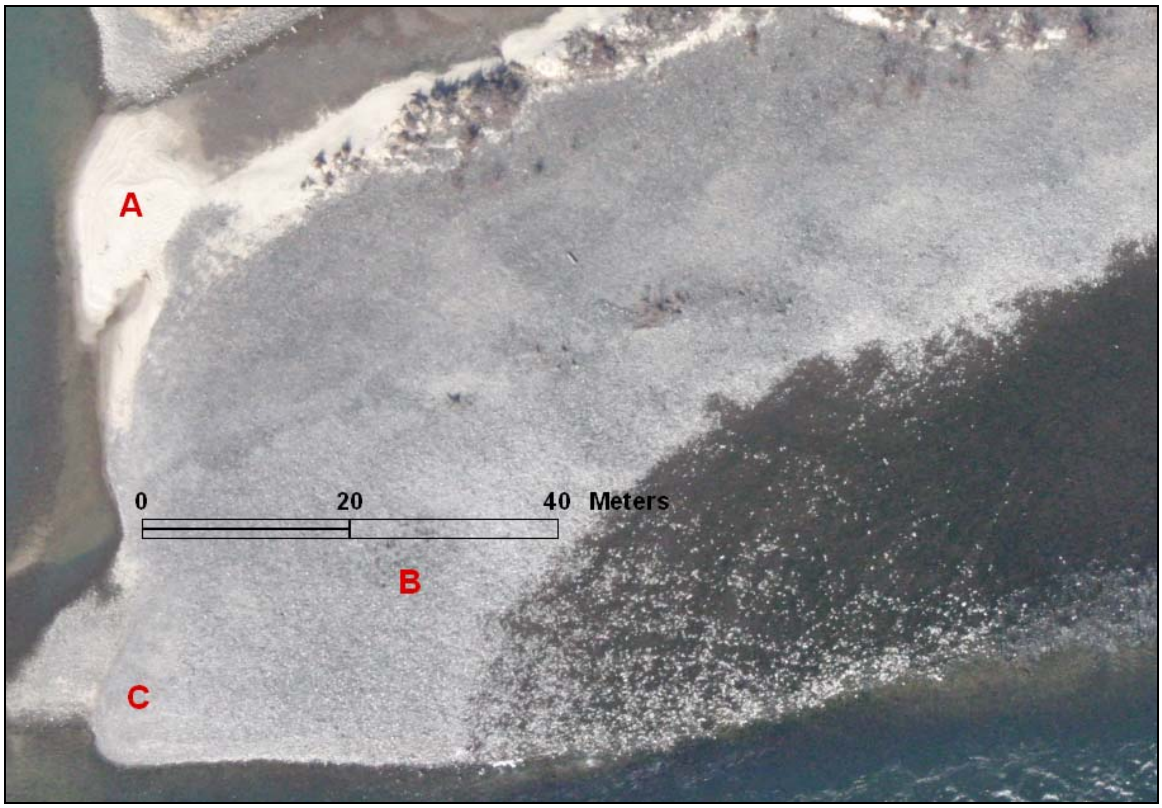

Figure 6.85 Very high-resolution aerial image of a gravel bar surface.

6.14 Summary

Reid et al. (1997) clearly expressed the difficulty faced by geomorphologists and sediment transport engineers:

"Here, researchers are faced with a familiar problem and one that has bedeviled successful prediction of bedload discharge: obtaining adequate field data poses major logistical difficulties. The upshot is that there are no databases that allow us to follow river behavior over a wide range of flow conditions. "

This dissertation research has begun an exploration of the possibilities of aerial survey and high-resolution aerial imagery in the analytical assessment of the morphology, hydraulics and sediment transport of alluvial rivers and streams. Numerous examples

have demonstrated the practicality of these methods. Several possibilities for future research were suggested. This work appears to be a unique contribution and may help alleviate the paucity of data encountered in the practice of river engineering and fluvial geomorphology research.

References for Section 6

Adams, J. (1979). "Gravel size analysis from photographs." *Journal of the Hydraulics Division*, 105(HY10), 1247-1255.

Alsdorf, D. E., Melack, J. M., Dunne, T., Mertes, L. A. K., Hess, L. L., and Smith, L. C. (2000). "Interferometric radar measurements of water level changes on the Amazon flood plain." *Nature*, 404(6774), 174-177.

Anderson, P. C., Hardy, T. B., and Neale, C. M. U. "Application of multispectral videography for the delineation of riverine depths and mesoscale hydraulic features." *Proceedings of the 14th Biennial Workshop on Color Aerial Photography and Videography for Resource Monitoring*, Logan, UT, 154-163.

Arcement, G. K., and Schneider, J. R. (1984). "Guide for Selecting Manning's Roughness Coefficients for Natural Channels and Flood Plains, Report FHWA-TS-84-204." Federal Highway Administration, Washington, DC.

Armantrout, N. B. (1998). *Glossary Aquatic Habitat Inventory Terminology*, American Fisheries Society, Bethesda, MD.

ASCE. (1998). "River Width Adjustment. I: Processes and Mechanisms: report of the Task Committee on Hydraulics Bank Mechanics and Modeling of River Width Adjustment." *Journal of Hydraulic Engineering*, 124(9), 881-902.

ASCE, and USACE. (1996). *River Hydraulics: Technical Engineering and Design Guides as Adapted from the U.S. Army Corps of Engineers, No. 18*, American Society of Civil Engineers, New York.

Ashmore, P., and Church, M. "Sediment transport and fiver morphology: a paradigm for study." *4th Gravel-bed Rivers Conference Gravel-bed Rivers and the Environment*, August 20-26, 1995, Gold Bar, Washington.

Ashmore, P. E., and Church, M. A. (1998). "Sediment transport and river morphology: a paradigm for study." Gravel-Bed Rivers in the Environment, P. C. Klingemann, R. L. Beschta, P. D. Komar, and J. B. Bradley, eds., Water Resources Publications, Highlands Ranch, Colorado.

Baker, J. C., O'Connel, K. M., and Williamson, R. A. (2001). *Commercial Observation Satellites: at the leading edge of global transparency*, Rand, Santa Monica, CA.

Bates, P. D., Horritt, M. S., Smith, C. N., and Mason, D. (1997). "Integrating remote sensing observations of flood hydrology and hydraulic modelling." *Hydrological Processes*, 11(14), 1777-1795.

Beschta, R. L. (1987). "Conceptual models of sediment transport in streams." Sediment Transport in Gravel-Bed Rivers, C. R. Thorne, J. C. Bathurst, and R. D. Hey, eds., Wiley, Chichester, 387-419.

Bettes, R., and Wright, W. R. (1987). "Extremal hypothesis applied to river regime." Sediment transport in gravel bed rivers, C. R. Thorne, J. C. Bathurst, and R. D. Hey, eds., Wiley, Chichester, 767-778.

Bhallamudi, S. M., and Chaudhry, M. H. (1991). "Numerical modeling of aggradation and degradation in alluvial channels." *Journal of Hydraulic Engineering*, 117(9), 1145-1163.

Birkett, C. M. (2000). "Synergistic Remote Sensing of Lake Chad: Variability of Basin Inundation." *Remote Sensing of Environment*, 72(2), 218-236.

Blank, L. (1980). *Statistical Procedures for Engineering, Management, and Science*, McGraw-Hill, New York.

Brabets, T. P. (1994). "Scour assessment at bridges from flag point to Million Dollar Bridge, Copper River Highway, Alaska, Water-Resources Investigations Report: 94-4073." U.S. Geological Survey, Denver.

Brice, J. C. (1982). "Stream Channel Stability Assessment, Report No. FHWA/RD-82-021." Federal Highway Administration, Washington, DC.

Bridge, J. S. (1993). "The interaction between channel geometry, water flow, sediment transport and deposition in braided rivers." Braided Rivers, Geological Society Special Publication No. 75, J. L. Best and C. S. Bristow, eds., The Geological Society, London, 13-71.

Bryant, R. G., and Gilvear, D. J. (1999). "Quantifying geomorphic and riparian land cover changes either side of a large flood event using airborne remote sensing: River Tay, Scotland." *Geomorphology*, 29(3-4), 307-321.

Buffington, J. M., and Montgomery, D. R. (1997). "A systematic analysis of eight decades of incipient motion studies, with special reference to gravel-bedded rivers." *Water Resources Research*, 33(8), 1993-2029.

Butler, J. B., Lane, S. N., and Chandler, J. H. (2001). "Automated extraction of grain-size data from gravel surfaces using digital image processing." *Journal of Hydraulic Research*, 39(4), 1-11.

Buttle, J. M. (1995). "Channel changes following headwater reforestation; the Ganaraska River, Ontario, Canada." *Geografiska Annaler. Series A: Physical Geography*, 77(3), 107-118.

Campbell, J. B. (1996). *Introduction to Remote Sensing*, The Guilford Press, New York.

Carbonneau, P. E., LANE, S. N., and Bergeron, N. E. (2003). "Cost-effective non-metric close-range digital photogrammetry and its application to a study of coarse gravel river beds." *International Journal of Remote Sensing*, 24(14), 2837-2854.

Chandler, J. H., Shiono, K., Rameshwaren, P., and Lane, S. N. (2001). "Measuring Flume Surfaces for Hydraulics research using a Kodak DCS460." *Photogrammetric Record*, 17(97), 39-61.

Chang, H. H. (1988). *Fluvial Processes in River Engineering*, Wiley, New York.

Church, M. (1996). "Channel Morphology and Typology." River Flows & Channel Forms, G. Petts and P. Calow, eds., Blackwell Science, Incorporated, London, 185-202.

Church, M., and Hassan, M. A. (1992). "Size and distance of travel of unconstrained clasts on a streambed." *Water Resources Research*, 28(1), 299-303.

Church, M., and Hassan, M. A. (1998). "Stabilizing self-organized structures in gravel-bed stream channels: field and experimental observations." *Water Resources Research*, 34(11), 3169-3179.

Collins, S. H. (1979). "Stereometric measurement of streambank erosion." *Photogrammetric Engineering and Remote Sensing*, 45(2), 183-190.

Davies, T. H. R. (1987). "Problems of bedload transport in braided gravel-bed rivers." Sediment Transport in Gravel-Bed Rivers, C. R. Thorne, J. C. Bathurst, and R. D. Hey, eds., Wiley, Chichester, 793-828.

Dexter, L. R., and Cluer, B. L. (1999). "Cyclic erosional instability of sandbars along the colorado river, Grand Canyon, Arizona." *Annals of the Association of American Geographers*, 89(2), 238-266.

Doiron, L. N., and Whitehurst, C. A. (1978). "Channel Erosion in Southwestern Louisiana Canal." *Journal of the Waterway Port Coastal and Ocean Division*, 104(2), 201-213.

Einstein, H. A. (1950). *The Bed-Load Function for Sediment Transportation in Open Channel Flows*, U.S.D.A, Soil Conservation Service, Washington, D.C.

Emmett, W. W., and Wolman, M. G. (2001). "Effective discharge and gravel-bed rivers." *Earth Surface Processes and Landforms*, 26, 1369-1380.

Exner, F. M. (1925). "Uber die Weschselwirkung Zwischen Wasser and Geschiebe in Flussen." *Sitzenberichts der Akademic der Wissenschaften, Wein*, Heft 3-4.

FEMA. (2003). *Guidelines and Specifications for Flood Hazard Mapping Partners, Appendix A: Guidance for Aerial Mapping and Surveying*, Federal Emergency Management Agency, Washington, D.C.

Ferguson, R. I., Ashmore, P. E., Ashworth, P. J., Paola, C., and Prestegaard, K. L. (1992). "Measurements in a braided river chute and lobe, I, flow pattern, sediment transport and channel change." *Water Resources Research*, 28, 1877-1886.

Frazier, P. S., and Page, K. J. (2000). "Water Body Detection and Delineation with Landsat TM Data." *Photogrammetric Engineering and Remote Sensing*, 66(12), 1461-1467.

Frissell, C. A., Liss, W. J., Warren, C. E., and Hurley, M. D. (1986). "A hierarchial framework for stream habitat classification: view streams in a watershed context." *Environmental Management*, 10, 199-214.

Fuller, I. C., Large, A. R. G., Charlton, M. E., Heritage, G. L., and Milan, D. J. (2003). "Reach-scale sediment transfers: an evaluation of two morphological budgeting approaches." *Earth Surface Processes and Landforms*, 28(8), 889-903.

Goff, J. R., and Ashmore, P. E. (1994). "Gravel transport and morphological change in braided Sunwapta river, Alberta, Canada." *Earth Surface Processes and Landforms*, 19(195-213).

Graf, W. L. (1984). "A probabilistic Approach to the Spatial Assessment of River Channel Stability." *Water Resources Research*, 20(7), 953-962.

Greentree, W. J., and Aldrich, R. C. (1976). "Evaluating Stream Trout Habitat on Large-Scale Aerial Color Photographs. USDA Forest Service Research Paper PSW-123." U.S. Forest Service, Pacific Southwest Forest and Range Experiment Station, Berkeley, California.

Guo, H. (2000). "Spaceborne and Airborne SAR for Target Detection and Flood Monitoring." *Photogrammetric Engineering and Remote Sensing*, 66(5), 611-618.

Gupta, R. S. (1995). *Hydrology and Hydraulic Systems*, Waveland Press, Prospect Heights, IL.

Gurnell, A. M. (1997). "Channel change on the River Dee meanders, 1946-1992, from the analysis of air photographs." *Regulated Rivers: Research & Management*, 13(1), 13-26.

Hassan, M. A., and Church, M. (1991). "Distance of movement of coarse particles in gravel bed streams." *Water Resources Research*, 27(4), 503-511.

Hays, L. C. P. L. "Transparency, stability, and deception: military implications of commercial high resolution imaging satellites in theory and practice." *International Studies Association Annual Convention*, Chicago, 26.

Heimes, F. J., Moore, G. K., and Steele, T. D. (1978). "Preliminary applications of Landsat images and aerial photography for determining land-use, geologic, and hydrologic characteristics: Yampa River basin, Colorado and Wyoming, Water resources investigations 78-96." U.S. Geological Survey, Denver, Colo.

Heritage, G. L., Fuller, I. C., Charlton, M. E., Brewer, P. A., and Passmore, D. P. (1998). "CDW photogrammetry of low relief fluvial features: accuracy and implications for reach-scale sediment budgeting." *Earth Surface Processes and Landforms*, 23, 1219–1233.

Hey, R. D. (1978). "Determinate Hydraulic geometry of river channels." *Journal of the Hydraulics Division*, 104(6), 869-885.

Hey, R. D. (1982). "Gravel-bed rivers: form and processes." Gravel-Bed Rivers, R. D. Hey, J. C. Bathurst, and C. R. Thorne, eds., Wiley, New York, 5-13.

Hey, R. D. (1982b). "Design equations for mobile gravel-bed rivers." Gravel-Bed Rivers, R. D. Hey, J. C. Bathurst, and C. R. Thorne, eds., Wiley, New York, 553-580.

Hey, R. D., Bathurst, J. C., and Thorne, C. R. (1982). "Gravel-Bed Rivers." Wiley, New York, 875.

Hickin, E. J., and Nanson, G. C. (1984). "Lateral Migration Rates of River Bends." *Journal of Hydraulic Engineering*, 110(11), 1557-1567.

Hoey, T. B., and Ferguson, R. (1994). "Numerical simulation of downstream fining by selective transport in gravel bed rivers: model development and illustration." *Water Resources Research*, 30(7), 2251-2260.

Hotchkiss, R. H., and Parker, G. (1991). "Shock fitting of aggradational profiles due to backwater." *Journal of Hydraulic Engineering*, 117(9), 1129-1144.

Hubbell, D. W. (1964). "Apparatus and techniques for measuring bedload. U.S. Geological Survey Water-Supply Paper, 1748." U.S. Geological Survey, Washington, D.C.

Ibbeken, H., and Schleyer, R. (1986). "Photo sieving: a method for grainsize analysis of coarse-grained, unconsolidated bedding surfaces." *Earth Surface Processes and Landforms*, 11, 59-77.

Jackson, W. L., and Beschta, R. L. (1982). "A model of two phase bed load transport in an Oregon Coast Range stream." *Earth Surface Processes and Landforms*, 7, 517-527.

Jensen, J. R. (1996). *Introductory Digital Image Processing: A Remote Sensing Perspective*, Prentice-Hall, Upper Saddle River, NJ.

Julien, P. Y., and Wargadalam, J. (1995). "Alluvial Channel Geometry: Theory and Applications." *Journal of Hydraulic Engineering*, 121(4), 312-325.

Kellerhals, R., and Bray, D. I. (1971). "Sampling Procedures for Coarse Fluvial Sediments." *Journal of the Hydraulics Division*, 97(HY8), 1165-1180.

Kesser, N. (1976). *Interpretation of Landforms from Aerial Photographs*, Ministry of Forests, Province of British Columbia, Victoria, BC.

Knighton, D. (1998). *Fluvial Forms and Processes*, Arnold and Oxford University Press, London and New York.

Komura, S. (1986). "Method for Computing Bed Profiles during Floods." *Journal of Hydraulic Engineering*, 112(9), 833-846.

Lagasse, P. F., Schall, J. D., and Richardson, E. V. (2001). "Stream Stability at Highway Structures, FHWA NHI 01-002 HEC-20." National Highway Institute, Federal Highway Administration, Washington, DC.

Lane, E. W. (1955). "The importance of fluvial morphology in hydraulic engineering." *American Society of Civil Engineers, Proceedings*, 81(Paper 795), 1-17.

Lane, S. N. (1997). "The reconstruction of bed material yield and supply histories in gravel-bed streams." *Catena*, 30, 183-196.

Lane, S. N. (2000). "The measurment of river channel morphology using digital photogrammetry." *Photogrammetric Record*, 16(96), 937-961.

Lane, S. N., James, T. D., and Crowell, M. D. (2000). "The application of digital photogrammetry to complex topography for geomorphological research." *Photogrammetric Record*, 16(95), 793-821.

Lane, S. N., Richards, K. S., and Chandler, J. H. (1993). "Developments in photogrammetry; the geomorphological potential." *Progress in Physical Geography*, 17(3), 203-328.

Lane, S. N., Richards, K. S., and Chandler, J. H. (1995). "Morphological estimation of the time-integrated bedload transport rate." *Water Resources Research*, 31, 761-772.

Langbein, W. R., and Leopold, L. B. (1966). *River meanders--theory of minimum variance, U.S. Geol. Surv. Prof. Pap. 422H*, U.S. Geological Survey, Washington D.C.

Leopold, L. B. (1973). "River channel change with time: an example." *Geological Society of American Bulletin*, 84(6), 1845-1860.

Leopold, L. B. (1982). "Water surface topography in river channels and implications for meander development." Gravel-Bed Rivers, Wiley, New York, 359-388.

Leopold, L. B., and Langbein, W. R. (1962). *The concept of entropy in landscape evolution, U.S. Geol. Surv. Prof. Pap. 500A*, U.S. Geological Survey, Washington D.C.

Leopold, L. B., and Maddock, T., Jr. (1953). *The hydraulic geometry of stream channels and some physiographic implications*, U.S. Geological Survey, Washington D.C.

Leopold, L. B., and Wolman, M. G. (1957). *River Channel Patterns: Braided, Meandering and Straight*, U.S. Geological Survey, Washington D.C.

Leys, K. F., and Werritty, A. (1999). "River channel planform change: software for historical analysis." *Geomorphology*, 29(1-2), 107-120.

Lillesand, T. M., and Kieffer, R. W. (1994). *Remote Sensing and Image Interpretation*, John Wiley and Sons, Inc., New York.

Lisle, T. E., Nelson, J. M., Pitlick, J., Madej, M. A., and Barkett, B. L. (2000). "Variability of bed mobility in natural, gravel-bed channels and adjustments to sediment load at local and reach scales." *Water Resources Research*, 36(12), 3743-3755.

Lo, C. P., and Wong, F. Y. (1973). "Micro-scale geomorphology features." *Photogrammetric Engineering and Remote Sensing*, 39(12), 1289-1296.

Lueder, D. R. (1959). *Aerial Photographic Interpretation*, McGraw-Hill, New York.

Lyon, L. J., Lunneta, R. S., and Williams, R. S. (1992). "Airborne multispectral scanner data for evaluating bottom sediment types and water depths in the St. Marys River Michigan." *Photogrammetric Engineering and Remote Sensing*, 57, 951-956.

Martin, Y., and Church, M. (1995). "Bed-material transport estimated from channel surveys -- Vedder River British Columbia." *Earth Surface Processes and Landforms*, 20, 347-361.

McCuen, R. H. (1998). *Hydrologic Analysis and Design*, Prentice-Hall, Upper Saddle River, NJ.

Meyer-Peter, E., and Muller, R. (1948). "Formulas for bed-load transport." *International Association for Hydraulic Research*, 2, 39-64.

Miller, A. J. "Photogrammetric analysis of channel adjustment." *Proceedings of the Fourth Federal Interagency Sedimentation Conference March 24-27, 1986*, Las Vegas, Nevada, 5.11-5.20.

Montgomery, D. R., and Buffington, J. M. (1993). *Channel classification, prediction of channel response, and assessment of channel condition, TFW-SH10-93-002*, Prepared for the Washington State Dept. of Natural Resources under the Timber, Fish, and Wildlife Agreement.

Montgomery, D. R., and Buffington, J. M. (1997). "Channel-reach morphology in mountain drainage basins." *Geological Society of America Bulletin*, 109(5), 596-611.

Morisawa, M. (1968). *Streams: Their dynamics and Morphology*, McGraw-Hill, New York.

Mount, N. J., Louis, J., Teeuw, R. M., Zukowskyj, P. M., and Stott, T. (2003). "Estimation of error in bankfull width comparisons from temporally sequenced raw and corrected aerial photographs." *Geomorphology*, 56, 65-77.

Muller, E. (1997). "Mapping riparian vegetation along rivers: old concepts and new methods." *Aquatic Botany*, 58, 411-437.

Neale, C. M. U., Vest, G. K., and O'Neill, M. P. "Monitoring streambank erosion using multispectral video imagery in a GIS." *Proceedings of the 15 th Biennial Workshop on Color Photography and Videography in Resource Assessment*, Terre Haute, IN, 210-223.

Neill, C. R. (1969). "Bedforms in the Lower Red Deer River Alberta." *Journal of Hydrology*, 7, 58-85.

Neill, C. R. (1971). "River bed transport related to meander migration rates." *Journal of the Waterways, Harbors and Coastal Engineering Division*, 97(WW7), 783-786.

Neill, C. R. (1987). "Sediment balance considerations linking long-term transport and channel processes." Sediment Transport in Gravel-Bed Rivers, C. R. Thorne, J. C. Bathurst, and R. D. Hey, eds., Wiley, Chichester, 225-240.

Neill, C. R., and Galay, V. J. (1967). "Systematic evaluation of river regime." *Journal of the Waterways and Harbors Division*, 93(WW1), 25-53.

Odgaard, A. J. (1987). "Streambank erosion along Two Rivers Iowa." *Water Resources Research*, 23(7), 1225-1236.

Parker, G. (1990). "Surface-based bedload transport relation for gravel rivers." *Journal of Hydraulic Research*, 28(4), 417-436.

Parker, G., Paola, C., and LeClair, S. (2000). "Probabilistic form of Exner equation of sediment continuity for mixtures with no active layer." *Journal of Hydraulic Engineering*, 126(11), 818-826.

Parker, G., Toro-Escobar, C. M., Ramey, M., and Beck, S. (2003). "Effect of floodwater extraction on mountain stream morphology." *Journal of Hydraulic Engineering*, 129(11), 885-895.

Philipson, W. R. (1997). "Manual of Photographic Interpretation, Second Edition." American Society for Photogrammetry and Remote Sensing, Bethesda, ML, 689.

Popov, I. V. (1962). "Application of morphological analysis to the evaluation of the general channel deformations of the River Ob." *Soviet Hydrology*, 3(267-324).

Pyle, C. J., Chandler, J. H., and Richards, K. S. (1997). "Digital photogrammetric monitoring of river bank erosion." *Photogrammetric Record*, 15, 753-764.

Pyrce, R. S., and Ashmore, P. E. (2003). "The relation between particle path length distributions and channel morphology in gravel-bed streams: a synthesis." *Geomorphology*, 56, 167-187.

Ray, R. G. (1960). "Aerial Photographs in Geologic Interpretation and Mapping, Geological Survey Professional Paper 373." U.S. Geological Survey, Washington D.C.

Reid, I., Bathurst, J. C., Carling, P. A., Walling, D. E., and Webb, B. W. (1997). "Sediment Erosion, Transport and Deposition." Applied Fluvial Geomorphology for River Engineering and Management, C. R. Thorne, R. D. Hey, and M. D. Newson, eds., Wiley, New York, 95-135.

Richards, K. (1982). *Rivers: Forms and process in alluvial channels*, Methuen, London.

Richards, K., Chandra, S., and Friend, P. (1993). "Avulsive channel systems: characteristics and examples." Braided Rivers, Geological Society Special Publication No. 75, J. L. Best and C. S. Bristow, eds., The Geological Society, London, 195-203.

Richardson, E. V., Simons, D. B., and Julien, P. Y. (1990). "Highways in the River Environment, FHWA-HI-90-016." National Highway Institute, Federal Highway Administration, Arlington, VA.

Richardson, E. V., Simons, D. B., and Lagasse, P. F. (2001). "River Engineering for Highway Encroachments, FHWA NHI 01-004 HDS 6." National Highway Institute, Federal Highway Administration, Arlington, VA.

Rosgen, D., and Silvey, H. L. (1998). *Field Guide to Stream Classification*, Wildland Hydrology Books, Pagosa Springs, CO.

Rosgen, D. L. (1994). "A classification of natural rivers." *Catena*, 22(3), 169-199.

Ruff, J. F., Skinner, M. M., Winkley, B. R., Simons, D. B., and Dorratcague, D. E. "Remote Sensing of Mississippi River Characteristics." *NASA Earth Resources Survey Symposium*, Houston, Texas, 2299-2315.

Schultz, G. A. (1988). "Remote Sensing in Hydrology." *Journal of Hydrology*, 100(1/3), 239-265.

Schultz, G. A., and Engman, E. T. (2000). "Remote Sensing in Hydrology and Water Management." SpringerVerlag, Berline, 483.

Schumm, S. A. (1972). "River Morphology." Benchmark Papers in Geology, R. W. Fairbridge, ed., Dowden, Hutchinson and Ross, Stroudsburg, PN, 429.

Smith, L. C. (1997). "Satellite remote sensing of river inundation area, stage, and discharge: A review." *Hydrological Processes*, 11(10), 1427-1439.

Smith, L. C., Isacks, B. L., Bloom, A. L., and Murray, A. B. (1996). "Estimation of discharge from three braided rivers using synthetic aperture radar satellite imagery: Potential application to ungaged basins." *Water Resources Research*, 32(7), 2021-2034.

Smith, L. C., Isacks, B. L., Forster, R. R., Bloom, A. L., and Preuss, I. (1995). "Estimation of discharge from braided glacial rivers using ERS 1 synthetic aperture radar: First results." *Water Resources Research*, 31(5), 1325-1329.

Somers, D., Smith, J., and Wissmar, R. (1991). "Watershed and Stream Channel Cumulative Effects Analysis Using Aerial Photography and Ground Survey Data - Interim Report, TFW-SH8-91-001." Washington Department of Natural Resources, Olympia, WA.

Tator, B. A. (1958). "The aerial photograph and applied geomorphology." *Photogrammetric Engineering and Remote Sensing*, 24(4), 549-562.

Thompson, M. M. (1958). "Photogrammetric mapping of sand beds in a hydraulic flume test." *Photogrammetric Engineering and Remote Sensing*, 24(3), 468-475.

Thorne, C. R. "Field Measurements of Rates of Bank Erosion and Bank Material Strength." *Erosion and Sediment Transport Measurement: Symposium, IAHS Publication No. 133*, Florence, Italy, 503-512.

Thorne, C. R., Bathurst, J. C., and Hey, R. D. (1987). "Sediment Transport in Gravel-Bed Rivers." Wiley, New York, 995.

Thorne, C. R., Hey, R. D., and Newson, M. D. (1997). *Applied Fluvial Geomorphology for River Engineering and Management*, Wiley, New York.

Toro-Escobar, C. M., Paola, C., and Parker, G. (1996). "Transfer function for the deposition of poorly sorted gravel in response to streambed aggradation." *Journal of Hydraulic Research*, 34(1), 35-53.

Townsend, P. A., and Walsh, S. J. (1998). "Modeling floodplain inundation using an integrated GIS with radar and optical remote sensing." *Geomorphology*, 21(3-4), 295-312.

USACE. (1995). *HEC-RAS River Analysis System Hydraulic Reference Manual*, U.S. Army Corps of Engineers, Davis, CA.

USGS. (2001). *Standards for 1:24,000-Scale Digital Line Graphs and Quadrangle Maps (DLG-F/Quadrangle Maps), Revision April 2001*, U.S. Geological Survey, Reston, VA.

Vanoni, V. A. (1975). *Sedimentation Engineering, ASCE Manuals and Reports on Engineering Practices, No. 54*, American Society of Civil Engineers, New York.

Welch, R., and Jordan, T. R. (1983). "Analytical non-metric close-range photogrammetry for monitoring stream channel erosion." *Photogrammetric Engineering and Remote Sensing*, 49(3), 367-374.

Winterbottom, S. J., and Gilvear, D. J. (1997). "Quantification of channel bed morphology in gravel-bed rivers using airborne multispectral imagery and aerial photography." *Regulated Rivers: Research & Management*, 13(6), 489-499.

Winterbottom, S. J., and Gilvear, D. J. (2000). "A GIS-based approach to mapping probabilities of river bank erosion: regulated River Tummel, Scotland." *Regulated Rivers: Research & Management*, 16(2), 127-140.

Wolman, M. G. (1977). "Changing needs and opportunities in the sediment field." *Water Resources Research*, 13(1), 50-54.

Yang, C. T. (1996). *Sediment Transport: Theory and Practice*, McGraw Hill, New York.

Yang, C. T., and Song, C. C. S. (1979). "Theory of minimum rate of energy dissipation." *Journal of the Hydraulics Division*, 105, 769-784.

7. Assessment of Soil Erosion with High-Resolution Aerial Imagery

Control of soil erosion in excess of geomorphic replacement is of paramount importance to human survival and environmental protection. Food and fiber production is inexorably dependent on the availability and quality of soil resources. Governments have large political and administrative structures to oversee and assure protection of soil resources and the security of food production. Much public money is spent on soil conservation programs and related agricultural research. Alternative techniques of measuring soil loss are necessary to improve soil loss estimates for extensive areas It is surprising that organized soil conservation makes little or no use of aerial survey and high-resolution aerial imagery analysis in soil conservation planning and erosion assessment. This section begins to amend the lacuna.

Over 20 years ago Frazier et al. noted in an introduction to the potential use of aerial photography in soil erosion assessment (1983),

> "While many conservation practices were implemented during the first 50 years of work in the Palouse, erosion continues because of the lack of an integrated effort throughout the basin. Erosion rates could be reduced 40 to 60 percent without adversely affecting farm income. Conservation tillage alone would reduce soil loss by about 35 percent."

A pertinent question is, what has been the real reduction in soil loss during the ensuing period? This question is difficult to answer precisely, but the aerial survey methods described in this section and Section 8 reveal ample opportunity for further adoption of conservation tillage to reduce soil loss.

The dissertation research described in this section has been developed by a civil water resources engineer and not an agricultural engineer or soil conservationist. I have confronted the effects of waterborne sediment both as a city engineer faced with the threat of flooding from sediment deposition and as a regulatory engineer who set design criteria for public drinking water treatment plants supplied by streams impacted by agricultural runoff. The research emphasis and description in the dissertation reflects that viewpoint.

7.1 Use of Aerial Imagery in Assessment of Soil Erosion

Aerial imagery has a long record of use in conservation planning and studies of soil characteristics (Belcher 1997; Lueder 1959; Reybold 1997; White 1977). Perhaps the earliest analytical treatment of aerial photography in soil erosion assessment in the English language journals is by Bergsma (1974). Though the imaging technology is dated, this work remains an excellent introduction to the erosion assessment process. Researchers at Washington State University were among the first to recognize the value of aerial imagery in quantitative studies of soil erosion (Frazier and McCool 1981) and its potential to reveal the complexities of winter erosion on the Palouse (Frazier et al. 1983).

Other researchers and conservationists have advocated the use of aerial imagery and satellite derived information in soil erosion modeling (Fraser et al. 1995; Morgan et al. 1980; Morgan and Nalepa 1982; Pelletier and Griffin 1988; Stephens et al. 1985; Thomas et al. 1986; Whiting et al. 1987). In practice, the use of aerial imagery in soil erosion modeling is limited because of the scale, timing and characteristics of film type aerial photography. Digital aerial imaging is removing this limitation.

Advances in lower cost digital imaging technology have enabled the development and deployment of reliable aerial imaging systems in cost-efficient light aircraft (King 1995; Quackenbush et al. 2000). Aerial imaging systems routinely acquire a thousand or more high-resolution true color or color infrared images in a single flight covering thousands of acres. Aerial imaging light aircraft can accomplish multiple imaging objectives during a single flight by making repeated passes at variable zoom settings or by employing secondary cameras to acquire close up aerial oblique images of critical areas. Digital aerial images can be available for analysis soon after the flight.

7.2 Soil Erosion of the Eastern Palouse Prairie

The Palouse Prairie agricultural region of the Pacific Northwest experiences among the highest erosion rates in the U.S. Much of the eroded soil is eventually carried by stream flow and deposited in the lower Snake River reservoirs (Figure 7.1). Average annual erosion ranges from 10 to 30 tons per acre (1/8 inch of topsoil) on conventionally tilled agricultural land (Michalson et al. 1999). Losses of over 150 tons per acre are not uncommon on steep slopes during a single winter season (Veseth et al. 1986). Average annual sheet and rill erosion from all cultivated lands in north central Idaho was 6.7 tons per acre per year (Nrcs 2003).

Most precipitation in the inland Northwest comes during winter when warm, moisture-laden storms move in from the Pacific Ocean. Precipitation and rapid snowmelt on partially frozen soils that have little or no surface residue produces significant surface runoff and soil erosion. Most severe erosion occurs on fields seeded to winter wheat on fine conventionally tilled soils with low amounts of surface residue (Veseth et al. 1986).

Water and soil losses are especially high after summer fallow due to higher residual soil moisture and soil compaction. Stubble burning followed by low or no till planting removes protective residue and also increases erosion susceptibility (Michalson et al. 1999).

Figure 7.1 Sediment discharge from Potlatch River January 31, 2004.

Approximately 9 percent of the agricultural land in Latah, Nez Perce, Lewis and Idaho Counties was conventionally tilled and fall seeded to small grains during 2000 (Conservation Technology Information 2003). Potential exists for additional cultivated land to be released from the Conservation Reserve Program (CRP) some of which is likely to be classified as highly erodible land (HEL). Retirement of HEL lands accounted for 53 percent of the erosion reduction on agricultural lands in Idaho from 1982 to 1997 though HEL lands only comprise 10 percent of the land area (Nrcs 2003).

Waterborne sediment, both mineral and organic, is caused primarily by erosion of surface soils and detachment of bed and bank materials in flowing channels. Erosion is a natural process that can be accelerated by land use. Water erosion of soils disturbed by agricultural and site development is typically identified by type: erosion of hillslopes by rill and interrill erosion, and erosion along topographically concentrated pathways by ephemeral and classic gully erosion. Stream bed and bank erosion also produce significant amounts of sediment at the scale of the full watershed. Wind erosion appears not to be a significant source of sediment in the eastern Palouse and is not measured in the NRCS Natural Resources Inventory for north central Idaho.

7.2.1 Validity of Soil Loss Estimates

Soil loss estimates by conventional techniques have been questioned and have become controversial. Trimble and Crosson (2000) questioned the validity of soil loss estimates produced by existing soil erosion models and noted:

> "Little physical, field-based evidence (other than anecdotal statements) has been offered to verify the high estimates. It is questionable whether there has ever been another perceived public problem for which so much time, effort, and money were spent in light of so little scientific evidence."

They further suggest that the general impression of severe soil erosion and attendant deterioration of associated resources is questionable in most regions. They advocate field studies and monitoring of sediment mass budgets for entire watersheds based on ground surveys augmented with cosmogenic isotopic dating and high-precision remote sensing techniques.

Parsons et al. (2004) found conventional soil loss estimates to greatly exceed long term rates of continental lowering. They cite three lines of evidence that suggest that erosion volume is not proportional to area:

- Observed rates of erosion become smaller as the area over which they are measured increases.
- Travel distances of individual particles are typically small and inversely related to particle size.
- Rates of soil detachment decrease with distance down slope as flow depths increase.

This dissertation work demonstrates that soil erosion on the Palouse can be directly evaluated by a systematic aerial survey and measurements made from high-resolution digital aerial images. Aerial surveys provide the data necessary to reduce the uncertainty between actual and predicted rates of soil erosion.

7.2.2 Rill and Interrill Erosion

Erosion rills in Figure 7.2 and Figure 7.3 are small incised channels that form on laterally uniform slopes at locations initiated by random microrelief after accumulation of sufficient flow to overcome soil erosion resistance and transport sediment. Erosion rills are observed in high-resolution aerial images of tilled agricultural fields having low canopy density acquired in late winter and spring (Frazier and McCool 1981). Rills in areas A and B in Figure 7.4 were formed by snowmelt and precipitation runoff in late winter 2004 on fall tilled winter wheat in silt loam soils. Soil between the rills is dislodged by rain splash and transported by shallow sheet flow to adjacent rills. This interrill erosion, also called sheet erosion, is a relatively minor source under melting

snowpacks. Interrill erosion cannot be directly observed in aerial images, but can be inferred by the presence of rills and deposition areas.

Figure 7.2 Rills formed in conventionally tilled winter wheat, March 12, 2003.

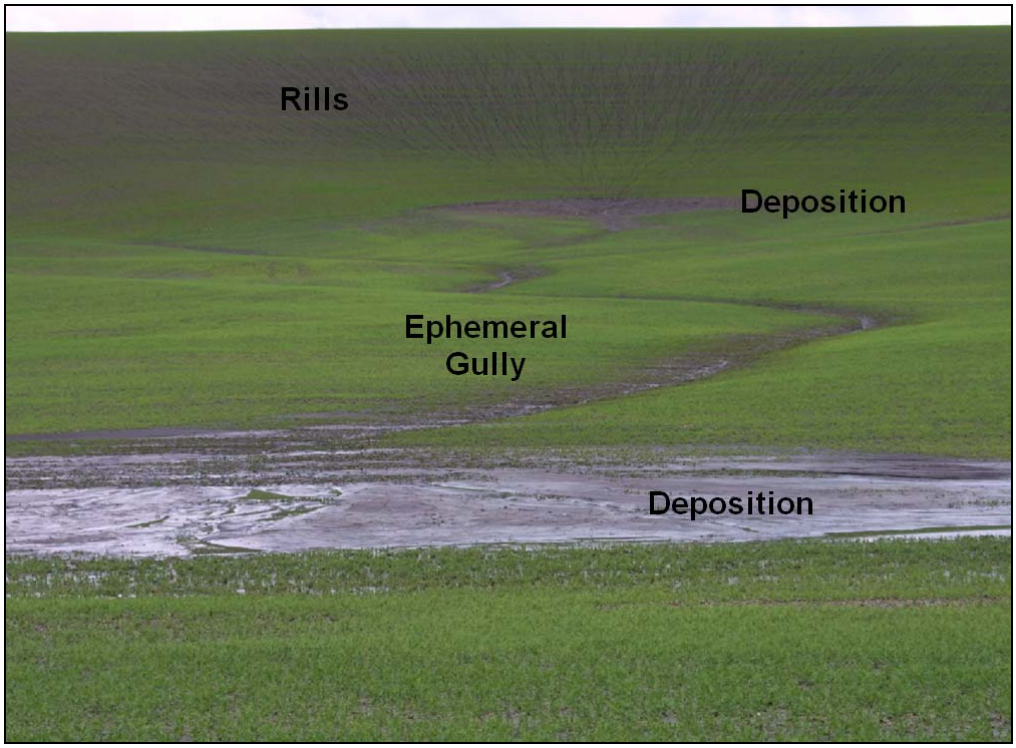

Figure 7.3 Rills, ephemeral gully and deposition in spring seeded peas, May 28, 2004.

Figure 7.4 Natural color vertical aerial image of an ephemeral gully system, March 13, 2004.

Rill erosion in Figures 7.2 through 7.4 is spatially heterogeneous even on similar hillslopes and soils. Erosion rates vary because soil moisture, subsurface drainage, snow load, soil bulk density, soil erosivity, and microtopography change over small distances. Large scale (small area) spatial heterogeneity leads to difficulties in extrapolating soil loss estimates based on plot measurements and hillslope methods to applications for larger areas. Spatial heterogeneity can be evaluated in the high-resolution aerial images.

7.2.3 Sediment Deposition and Storage

Not all eroded sediment contributes immediately to stream channel sediment load. Some sediment, most under certain conditions, is deposited on lower terrain before

reaching natural waterways (Figure 7.3). Deposition occurs when the amount of sediment flowing into a segment of a hillslope or channel exceeds the carrying capacity of the flow through the segment. The rate of deposition is governed by the velocity and turbulence of the flow, and in free surface flow is primarily dependent on flow rate and slope gradient. Sediment deposition is labeled in Figure 7.3 and is observed at area E in aerial image in Figure 7.4.

Deposition areas temporarily store sediment eroded from upstream hillslopes and channels. Residence time of sediment in storage zones varies from minutes between surges of unsteady runoff to millennia between cycles of climatic change. The sediment deposited in the culvert barrel in Figure 7.5 likely has a residence time of one flow cycle (one year) and will be transported to downstream storage sites during the next flow cycle. Over long periods of time all eroded sediment is eventually exported from a watershed (Harvey et al. 1985). Changed sediment load is expressed as altered in channel morphology and sediment storage structures. Section 6 discussed the aerial assessment of morphological bed material transport in a medium sized stream. Aerial imagery is much less effective for determining sediment resident time in small channels primarily because of image resolution and greater potential for obscuration by vegetation and terrain. For example, it is not possible to proportion sediment load between seasonally eroded sources and sediment remobilized from stream channels deposited in previous flow cycles in a single image.

Figure 7.6 is a March 15, 2004 aerial image of the channel of a fourth order tributary of the Middle Potlatch Creek. Bank erosion is often observable, but sediment structures are not normally visible during the relatively high discharges in spring

imagery. Figure 7.7 is a July 22, 2004 aerial image of the same stream reach. Additional bed detail is observed, but vegetation obscures some portions of the channel. Bed material in Figure 7.7 is mostly gravel and cobble. There are no large accumulations of fine sediment. Ground pixel resolution of these images is about 23 cm.

Figure 7.8 is a higher resolution aerial image (19 cm GPR) of the junction of two tributaries of Little Bear Creek acquired on September 27, 2003. Two low flow pools are visible. Bed material is cobble and gravel. There are no significant accumulations of fine sediment or recent origin. The medial bar is likely a relic of the extreme 1996 flood and is now stabilized with vegetation.

Figure 7.5 Temporary sediment storage in a culvert barrel, Little Bear Creek.

Figure 7.6 March 15, 2004 aerial image of a tributary of Middle Potlatch Creek.

Figure 7.7 July 22, 2004 aerial image of a tributary of Middle Potlatch Creek.


Figure 7.8 September 27, 2003 aerial image of a tributary junction on Little Bear Creek.

The best approach to estimating transient sediment volume is often with seasonal stream reach sediment inventories (Reid and Dunne 1996; Thorne 1998). The sediment in the culvert barrel on a tributary of Little Bear Creek in Figure 7.5 is obviously of recent origin and transient. The discharge that transported sediment into the culvert will likely occur again. Repeated surveys of a representative reach above or below the culvert would determine if the volume of stored sediment is increasing, decreasing or in dynamic equilibrium. It is difficult to measure the seasonal change in sediment stored at the bottom hillslopes such as in Figure 7.3 because the newly deposited sediment is incorporated into surrounding soils by tillage operations. It is often difficult to proportion sediment load between seasonally eroded sources and sediment remobilized from stream

channels that may have been deposited in previous years. The importance of deposition in a watershed sediment balance is discussed more in Section 7.2.5.

7.2.4 Ephemeral Gully and Classical Gully Erosion

Gullies form when surface runoff and subsurface flow concentrate into existing topographic flow lines and overcome the soil resistance to erosion, transport and subsurface piping. Ephemeral gully systems are readily observed in late winter and early spring high-resolution aerial images. Assessment of ephemeral gully systems by aerial survey techniques was a primary objective of the dissertation work and is discussed in Section 8. Mechanisms and modeling of ephemeral gully systems will be developed in this section.

Topographic convergence of rills into ephemeral gullies observed in aerial images usually occurs in a relatively small transition zone and may be very abrupt. The upper end of the ephemeral gully system is represented by a gully initiation point in GIS analysis and erosion modeling. Two gully initiation points are identified in Figure 7.9. The gully initiation zone near area C in Figure 7.4 is much less distinct. Once initiated, gullies incise and widen rapidly to approach an equilibrium shape (Foster 1982). Gullies accumulate flow and sediment from rills formed on adjacent hillslopes. Ephemeral gullies are small enough to be obliterated by normal tillage operations and often reappear in the same location year after year.

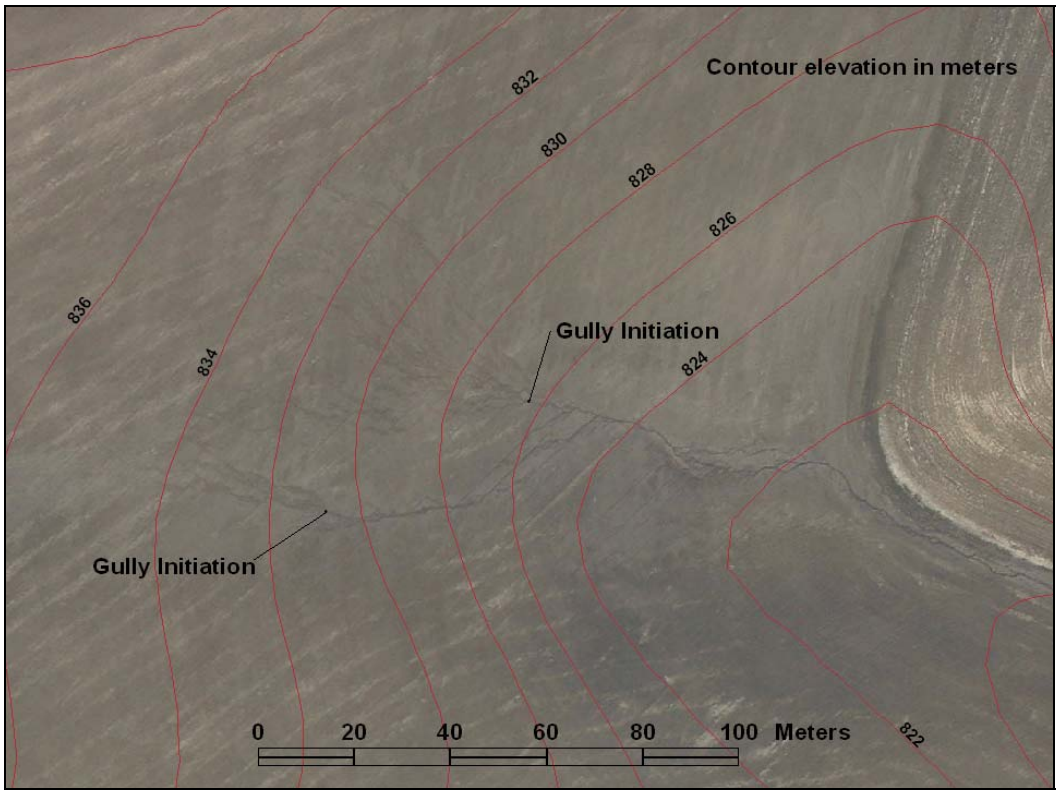

Figure 7.9 Vertical aerial of an ephemeral gully system, March 16, 2004.

Larger classical gullies incise to a depth not easily removed by tillage and become permanent features of the landscape. Classical gullies may continue to lengthen by upslope advancement of headwalls and widening by sloughing of channel sides. Gully formation is unsteady and proceeds in pulses as hydrologic processes and erosion mechanisms interact (Foster 1982). Figure 7.10 is a vertical aerial image of a headcut in classical gully system formed on a grassed slope. The headcut will likely continue to progress upstream to widen and deepen the gully channel. Classical gully extension and widening can be monitored in aerial images acquired over a period of several years, but is not explicitly considered in this dissertation research.

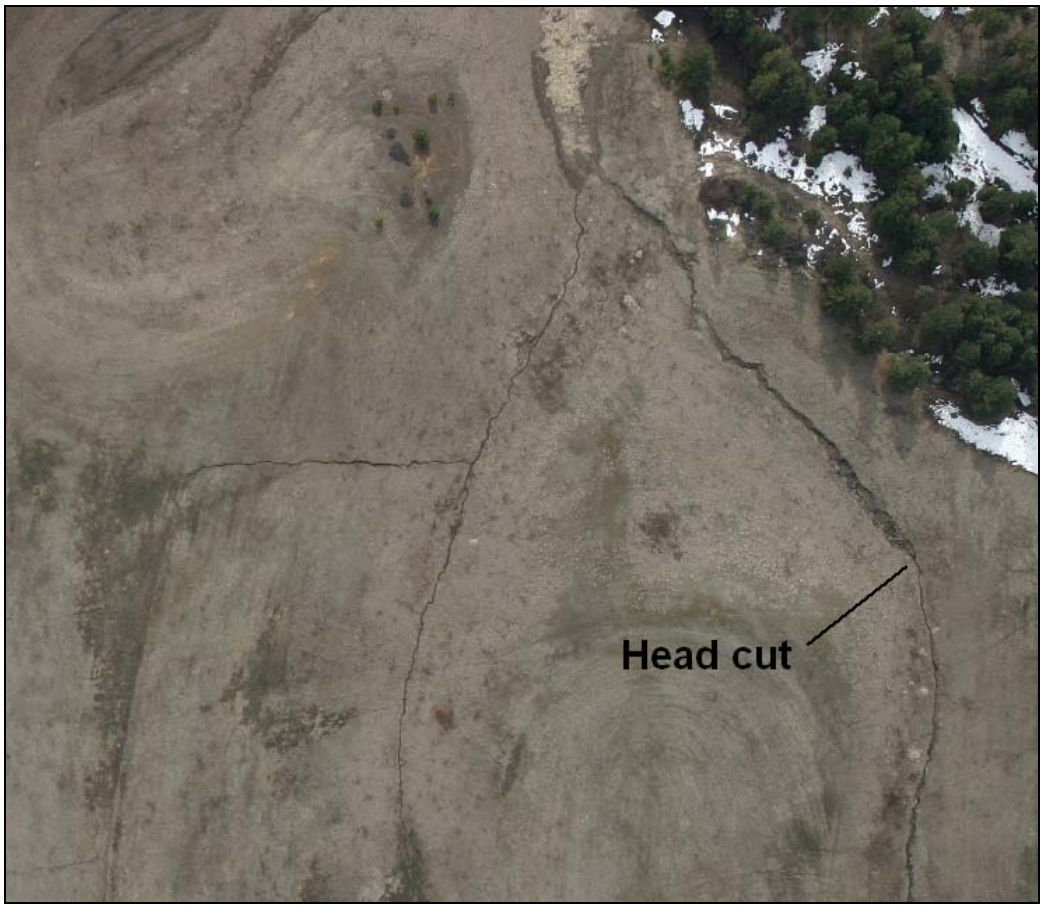

Figure 7.10 Vertical aerial of a classical gully system with head cut, March 13, 2004.

7.2.5 Sediment Yield

Sediment delivered to surface waters is the net result of a dynamic interaction of erosion, transport and deposition processes. Net sediment exported from a watershed is known as its sediment yield. More specifically sediment yield is the total sediment carried by stream flow beyond a given location (such as a stream gaging station) expressed as mass or volume over a period of time (Vanoni 1975). A related concept, the sediment delivery ratio, expresses sediment yield as a proportion of gross erosion. Delivery ratios are usually less than one unless channel erosion is the dominant source. Models that estimate soil loss from a field slope, such as the RUSLE2 model do not

directly estimate watershed sediment yield. Other techniques must be applied to adjust field erosion for transit deposition in lower terrain and the channel system. Because of the numerous variables that affect transport and deposition, prediction of sediment yield is more uncertain than other aspects of sedimentation (Haan et al. 1994). Simple measures of basin characteristics and hydrology such as basin area and runoff volume often do not correlate well with sediment yield (Verstraeten and Poesen 2001) and may be confounded by longer term cycles of alluviation involving geomorphic thresholds (Harvey et al. 1985).

Sediment yield must take into account transient and permanent storage of sediment in downstream landscape positions or sediment structures within the channel system and floodplain. This requires a higher level of geomorphic detail than is commonly available for soil erosion modeling. Sediment yield is best determined by direct measurement of sediment discharge and surveys of stream morphology as advocated by Trimble and Crosson (2000).

Sediment yield has been estimated by various means including sediment delivery ratios (Haan et al. 1994; Vanoni 1975), adaptations of the USLE method (Neitsch et al. 2002; Williams and Berndt 1972), regression of measured sediment data with basin characteristics (USACE 1995), physically based modeling with channel routines (Flanagan and Nearing 1995). Less tested methods appear in the literature (Ferro and Porto 2000; Lee and Singh 1999; Mashriqui and Cruise 1997; Simons et al. 1976) The most cited method is the application of an assumed delivery ratio to USLE/RUSLE estimates of soil erosion.

Sediment yield computed with an assumed delivery ratio is very approximate (USACE 1989; Vanoni 1975; Walling 1983), though this approach is accepted in practice (USACE 1995) when measured sediment data are not available. The theoretical concept of a sediment delivery ratio is questionable since given sufficient time all eroded sediment is eventually exported from a watershed (Harvey et al. 1985; Parsons et al. 2004; Schuum 1973).

Sediment delivery ratios typically decrease with watershed size. A representative example is Figure 7.11 from the ASCE Sedimentation Engineering Manual (Vanoni 1975). Discussion of sediment yield data for the upper Mississippi River basin in Vanoni (1975) suggests that the sediment delivery ratio declines by approximately -1/8 power of drainage area and that the estimate of gross erosion should be based on an representative area of about 0.001 mi^2 (0.26 ha). According to this relationship the sediment delivery ratio for the 284 mi^2 (736 km^2) agricultural portions of the Potlatch River basin would be about 21 percent. Figure 7.11 is based on a different set of data and indicates sediment delivery ratio of about 7 percent. Figure 7.11 gives similar values as Figure 8.25 in Haan et al. (1994) suggested for use with the USLE and RUSLE soil loss equations.

If the soil loss estimate of 6.7 tons ac^{-1} a^{-1} cited in Section 7.2 and these sediment delivery ratios are approximately correct for the 80 year history of agriculture in the Potlatch Basin, then a massive amount of sediment has been relocated to lower landscape positions or stored in channel structures. High-resolution aerial imagery provides a method to check the validity of these long term estimates.

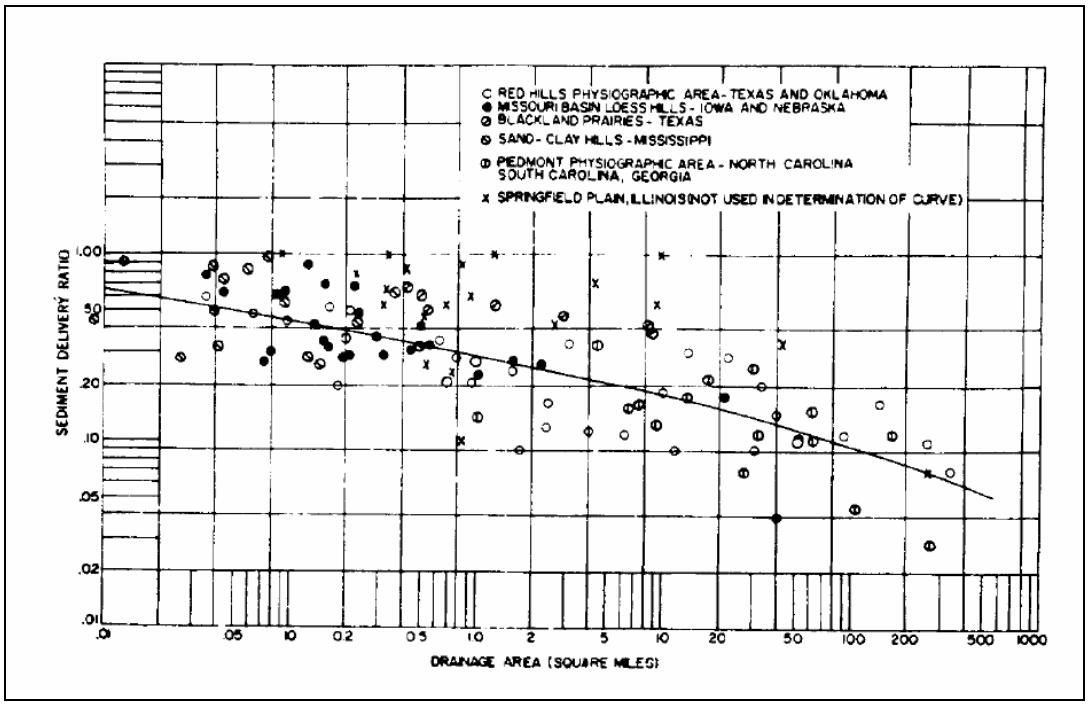

Figure 7.11 Relationship between drainage basin size and sediment delivery ratio (Vanoni 1975).

Assuming a bulk density of 75 lb ft^{-3} (1200 kg m^{-3}) for deposited sediment, the total volume of eroded sediment for 80 years is:

$$Vol = 6.7 \frac{\text{ton}}{\text{ac} \cdot \text{yr}} \times 284\,\text{mi}^2 \frac{640\,\text{ac}}{\text{mi}^2} \times 80\,\text{yr} \times \frac{2000\,\text{lb}}{\text{ton}} \times \frac{\text{ft}^3}{75\,\text{lb}} = 2.59 \times 10^9\ \text{ft}^3$$

If 7 percent of the sediment is exported from the Potlatch basin, then 93 percent must be transported off hillslopes and deposited in flatter terrain or stored in drainage channels. Approximately 5 percent of the area of the agricultural portions of the Potlatch River basin has a slope of less than 2 percent based on an analysis of the USGS 10-meter DEM. If all deposition is assumed to occur on slopes that are now flatter than 2 percent, the average depth of deposited sediment is:

$$Sed_{depth} = (1-.07) \times 2.59 \times 10^9 \text{ ft}^3 \times \frac{1}{0.05\left(284\text{mi}^2 \times \frac{640 \text{ ac}}{\text{mi}^2} \times \frac{43{,}560 \text{ ft}^2}{\text{ac}}\right)} = 6 \text{ ft}$$

Widespread deposition of sediment 6 feet (1.8 m) deep should be clearly evident in landscape morphology observed in high-resolution aerial imagery. This amount of sediment would bury tree trunks, roads, bridges, and buildings that occupy flatter terrain. It would be declared an ongoing catastrophe. Since this not the general case, it likely the sediment delivery ratio is much higher.

Figure 7.12 is a March 13, 2004 aerial image of a headwater catchment in the Little Potlatch Creek basin. This fall seeded winter wheat field is in a portion of the watershed that has been farmed for many decades. Several ephemeral gullies indicate active and significant erosion. Water and sediment flows to the grassed waterway in the upper part of the figure. Catchment area is 12.7 ha (31.4 ac) and the area of land with less than 2 percent ground slope is 0.9 ha (2.3 ac).

Applying a higher sediment delivery ratio of 0.15 for the 50 mi^2 Little Potlatch basin the volume and sediment depth for this catchment would be:

$$Vol = 6.7 \frac{\text{ton}}{\text{ac} \cdot \text{yr}} \times 31.4 \text{ ac} \times 80 \text{ yr} \times \frac{2000 \text{ lb}}{\text{ton}} \times \frac{\text{ft}^3}{75 \text{ lb}} = 4.49 \times 10^3 \text{ ft}^3$$

$$Sed_{depth} = (1-.15) \times 4.49 \times 10^3 \text{ ft}^3 \times \frac{1}{2.3 \text{ ac} \times \frac{43{,}560 \text{ ft}^2}{\text{ac}}} = 3.8 \text{ ft}$$

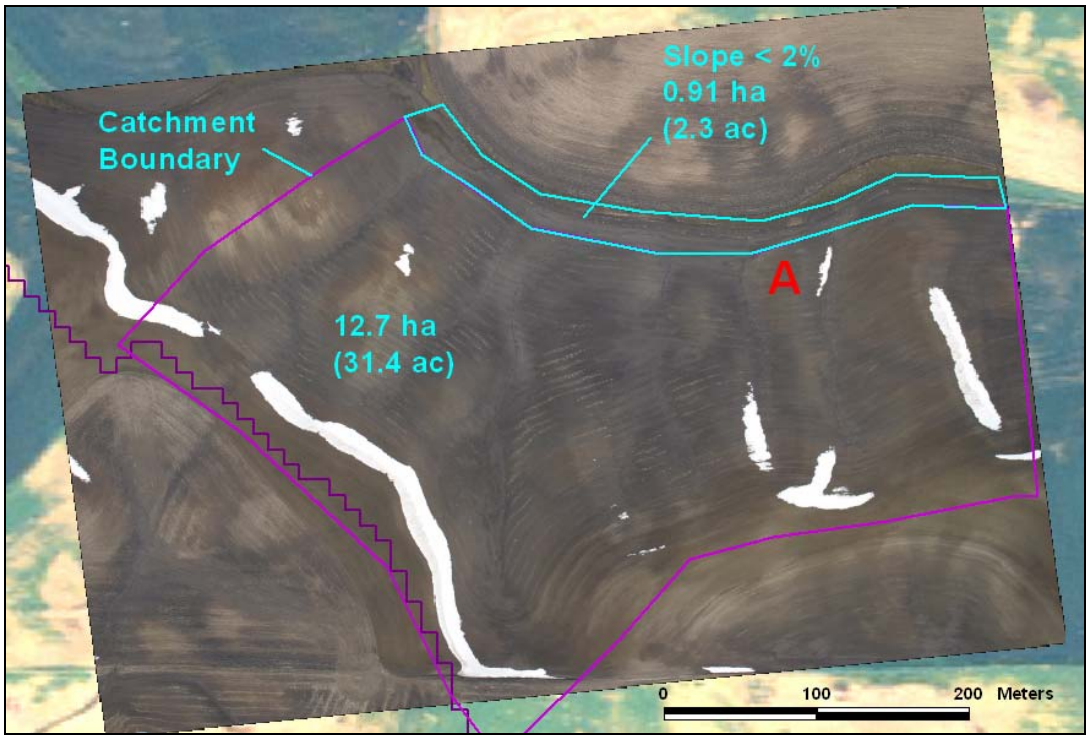

Figure 7.12 Potential deposition area in an eroding catchment.

A sediment accumulation of 4 ft (1.2 m) should be observable in the magnified view of area A in Figure 7.13. Some seasonal deposition is evident at the outlet of the ephemeral gully, but morphological indicators of persistent and ongoing deposition are lacking. In fact, the upper end of the grassed waterway shows signs of concentrated flow erosion. Moreover, if this was a persistent sediment storage area *it would be stable and aggrading.* There would be no need for a grassed waterway to protect the channel.

It might be argued that this particular location is not typical and that sediment is stored downstream in the channel system. If this is the case, then the requirement for sediment storage increases progressively downstream and the expected depths of sediment accumulation are proportionally greater. Sediment eroded from this catchment cannot be redistributed upstream to other portions of the basin as implied by the statistical

concept of the sediment delivery ratio. Mass balance of routed sediment must be preserved.

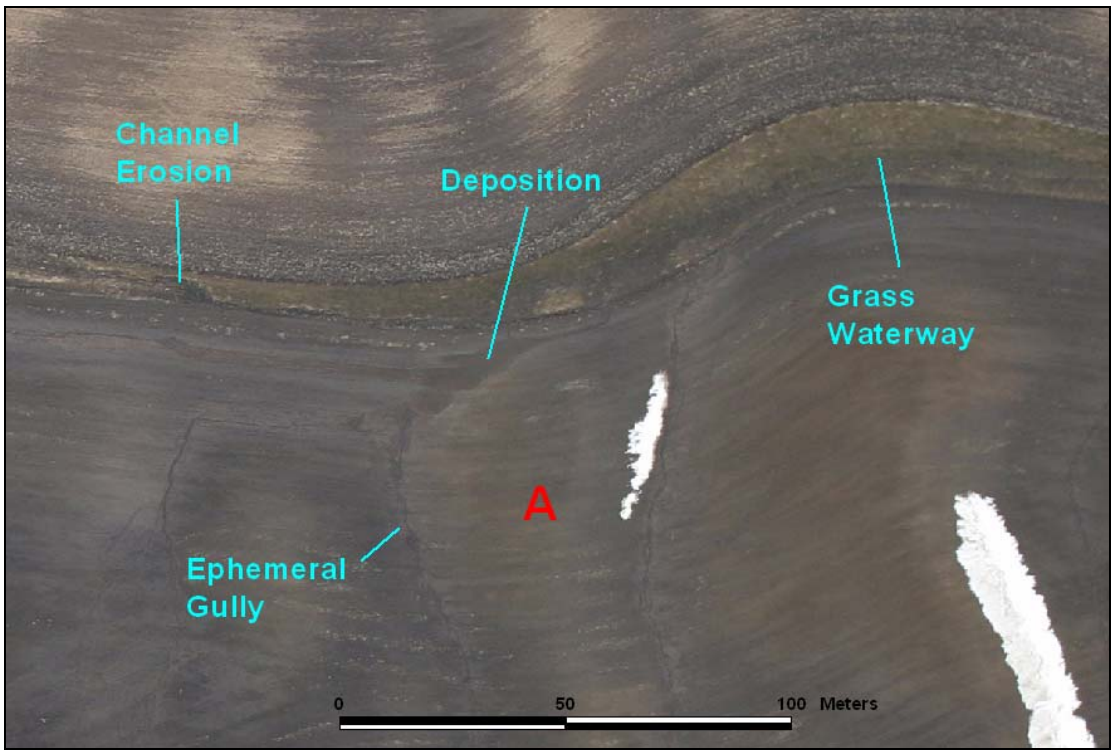

Figure 7.13 Magnified view of a potential deposition area.

If the hillslope morphology of Figure 7.13 is typical of many agricultural fields in the Potlatch basin (it is), then a massive amount of sediment must be permanently stored in the channel system and this ongoing accumulation of channel sediment should be very evident in high-resolution aerial images. It is not, based on observation of numerous aerial images of agricultural land of the lower Potlatch basin and the stream channel system. Clearly, either the original estimate of the soil erosion rate or the sediment delivery ratio is substantially in error. It is likely a combination of both – lower actual soil loss and higher sediment delivery ratios.

Taking the prevalence of grassed waterways throughout the basin as a sign of unstable (non-aggrading) low order channels and recognizing the lack of significant

ongoing accumulation of *fine* sediment in main channels, it is probable that the sediment delivery ratio for the lower Potlatch basin is quite high, approaching 100 percent. It would also indicate it is unwise to base fine sediment total maximum daily load analyses (TMDL) on conventional soil conservation planning models and literature value delivery ratios in the Palouse region.

7.3 Soil Loss Estimation and Erosion Modeling

Erosion, sediment transport and sedimentation modeling encompasses the full continuum of scale from interrill soils to large rivers and reservoirs. Aerial assessment of main channel erosion and sediment transport were discussed in Section 6. Pond and reservoir sedimentation was not explicitly considered in the dissertation research, but aerial survey techniques could easily be adapted to identify likely locations for sedimentation structures in watershed conservation planning and monitor best management practice implementation. Best practice soil loss estimation techniques must be evaluated to understand how high-resolution aerial imagery can be usefully applied in the analysis of soil erosion. Best practice means the methods and procedures will likely have the most credibility in a regulatory and legal setting.

Prediction of soil erosion and sedimentation receives sustained attention by research organizations and resource agencies worldwide. Soil erosion research became a national priority following the dust bowl era of the 1930's in the U.S. (Michalson et al. 1999). This gave initial impetus to efforts to develop methods of estimating soil erosion for conservation planning. Soil erosion models that evolved can be separated into two general categories: physically-based and empirical. Numerous models have been

developed in the U.S. and Europe following both approaches. In the U.S. the premiere erosion models are the empirical USDA Revised Uniform Soil Loss Equation (RUSLE) model and the physically-based USDA Water Erosion Prediction Project (WEPP) model. Both models and their adaptations are widely applied in practice. These models are described in detail in hydrology and sedimentation engineering texts (Foster 1982; Haan et al. 1994), soil conservation texts (Michalson et al. 1999; Troeh et al. 1980) and model documentation (Flanagan and Nearing 1995; Foster et al. 2003).

7.3.1 Water Erosion Prediction Project Model

The Water Erosion Prediction Project (WEPP) model estimates watershed sediment yield as a process of detachment, transport, and deposition of sediment on overland (rill and interrill) flow areas and channel flow areas. Movement of suspended sediment on rill, interrill, and channel flow areas is based on a steady-state erosion model developed by Foster and Meyer (1972). Simulated channel elements include grassed waterways, terrace channels, and ephemeral gullies. Channel hydrology runoff processes include infiltration, depression storage, rainfall excess (runoff), and transmission losses.

WEPP is best suited to small agricultural watersheds less than 260 ha (1 mi^2) where sediment yield at the outlet is primarily influenced by hillslope and channel processes (Flanagan and Nearing 1995). Sufficiently detailed hillslope topographic data is normally not available to implement WEPP for larger watersheds and sediment routing is not suitable for watershed scale analysis. Standard USGS digital elevation model (DEM) data of the Palouse region does not represent first order terrain well enough for high-resolution soil erosion modeling. USGS DEM data can be augmented with high-

resolution topographic data developed with the analytical photogrammetry techniques demonstrated in Section 3 for individual fields and farms.

The winter hydrology component in WEPP does not realistically simulate winter erosion in the Palouse region. Table 7.1 is a summary of erosion events for a typical agricultural field in the Little Potlatch Creek basin generated by a simulation of 100 years of climate data by the WEPP modeling system (version 2004.7). Having observed soil erosion on the Palouse for 30 years, the simulated late winter and early spring sediment delivery is well below expectations compared to high values for late spring and early fall. Part of the distortion may be due to the climate generation component of WEPP. The exact cause is difficult to determine. Difficulties of the WEPP winter hydrology are recognized and are receiving modest attention (Pannkuk et al. 2000; Van Klaveren and McCool 1998).

Month	Number of Events	Average Precipitation mm	Average Runoff mm	Average Detachment kg m^{-2}	Sediment Delivery kg m^{-1}	Sediment Yield ton ha^{-1} y^{-1}
1	132	9.7	4.4	0.04	2.4	0.32
2	274	5.9	6.8	0.05	4.1	1.13
3	104	13.7	3.1	0.07	6.0	0.64
4	113	14.3	1.2	0.10	9.9	1.13
5	144	18.2	3.0	0.21	21.1	3.08
6	121	17.5	2.9	0.20	19.2	2.36
7	28	15.9	1.0	0.03	2.6	0.07
8	58	21.6	2.3	0.01	0.9	0.05
9	34	17.8	1.1	0.02	2.1	0.07
10	102	15.7	1.6	0.22	20.7	2.14
11	125	14.7	3.1	0.23	20.5	2.59
12	99	13.3	4.4	0.14	11.0	1.10
Total						14.70

Table 7.1 Results of 100 year WEPP simulation with Moscow, ID climate data.

Local break point climate data can be admitted to the WEPP simulation by a rather obtuse process. Unfortunately, this does not resolve the poor simulation of winter erosion in the Palouse region by WEPP. The WEPP model has capability for physically

realistic simulation of erosion, but until the winter hydrology and erosion components are refined, it should not be used to develop best practice estimates of soil loss in the Palouse region for periods of snowmelt and thawing soils.

As a physically-based model, WEPP requires numerous soil parameters and a spatially accurate representation of soil variability. Soil color transitions observed in high-resolution aerial images indicate that SSURGO soils data may not provide the detail necessary to properly characterize soil profiles in eroded Palouse terrain. This aspect of soil erosion modeling was not formally investigated in the current research, but it casts additional doubt on the practical ability to estimate soil loss with a physically-based model over an extensive area of the Palouse.

7.3.2 Uniform Soil Loss Equation

The Uniform Soil Loss Equation (USLE) was introduced in the early 1960's and has been applied worldwide to estimate erosion of agricultural lands and natural lands. It is an empirical model derived from more than 12,000 plot years of data (Foster et al. 2003). The basic USLE equation estimates long term average annual erosion rates as the product of six factors:

$$A = R \cdot K \cdot L \cdot S \cdot C \cdot P \qquad 7.1$$

where A is the average annual soil loss (mass per unit area per unit time), R is the rainfall erosivity factor, K is the soil erodibility factor, L is the soil slope length factor, S is the slope steepness factor, C is the cover-management factor, and P is the supporting practices factor. The USLE is intended for conservation planning. It estimates gross erosion and does not explicitly account for deposition of sediment on complex slopes, so cannot directly estimate sediment yield.

The USLE in the form of Equation 7.1 estimates total mass (weight) of erosion per unit area per unit time along a slope length originating at the beginning of overland flow and ending at start of net deposition or concentrated flow. One year is the typical time period, but other periods, such as seasonal, may be used if the rainfall erosivity and other factors are appropriate.

A modified form of the USLE estimates erosion at a point (Foster and Wischmeier 1974). Mass continuity requires that sediment transport at a point on the slope be governed by:

$$D = \frac{dG}{dx} \qquad 7.2$$

where D is the detachment or deposition rate at a point (mass per unit area per unit time), G is the sediment load (mass per unit width per unit time), and x is the down-slope distance. Assuming a unit slope width Equation 7.1 provides an estimate of the sediment load at the end of the slope length profile if multiplied by the slope length:

$$G = A\lambda_e = RKLSCP(\lambda_e) \qquad 7.3$$

where λ_e is the slope length for which the USLE in Equation 7.1 is determined. When slope length is in feet the slope length factor L is computed from (Wischmeier and Smith 1976):

$$L = \left(\frac{\lambda_e}{72.6}\right)^m \qquad 7.4$$

where m is the USLE slope length exponent. Substitution of Equation 7.4 into Equation 7.3 and exchanging down slope distance x for λ_e gives the sediment load at any point along the slope profile:

$$G = RKx^{m+1}SCP\frac{1}{72.6^m} \qquad 7.5$$

Taking the first derivative of Equation 7.5 gives the estimate of erosion rate at any location along the slope profile:

$$D = \frac{dG}{dx} = (m+1)RKSCPx^m\frac{1}{72.6^m} \qquad 7.6$$

where x (ft) is the profile distance from the beginning of overland flow. This form of the USLE equation is convenient for estimating erosion at points selected in a sampling strategy. Point erosion values from Equation 7.6 may be analyzed statistically and extended to estimate erosion for representative areas. For example, a series of estimates computed by Equation 7.6 for points along a slope profile would average, if spaced sufficiently close, to about the same soil loss computed by Equation 7.1 for the total profile length.

The continuing appeal of the USLE is its relative simplicity and broadly applicable soil and crop factors. USLE erosion estimates should only be developed for situations considered during development of the USLE factors (Renard et al. 1996; Wischmeier and Smith 1976). Accuracy of USLE estimates is acceptable for many practical applications (Haan et al. 1994) and appears as accurate (or better) than the more complex Revised Uniform Soil Loss Equation (RUSLE) and WEPP model when compared to long term erosion plot data within the scope of the USLE factors (Tiwari et al. 2000). Sediment yield at watershed scale has been estimated from USLE gross erosion by application of secondary empirical relationships (Haan et al. 1994) or enhancements of the basic USLE equation (Neitsch et al. 2000).

7.3.3 Revised Uniform Soil Loss Equation

The Revised Uniform Soil Loss Equation (RUSLE) was developed to comply with federal legislation in the 1980's that required erosion estimation methods for additional cropland uses not considered during development of the USLE (NRCS 1996). The crop management factor was redefined as the product of several subfactors that could be estimated from physical characteristics of a broader range of land uses. Process-based equations were added to estimate the values for the support practice factor *P* so that soil loss could be estimated for modern strip cropping systems. The RUSLE factors may vary throughout a year and over multiyear crop rotations. Like the USLE, RUSLE computes erosion along a one-dimensional hillslope. Hillslope estimates must be aggregated to estimate total erosion for farms and watersheds. The USLE and RUSLE do not estimate gully or channel erosion or provide for sediment transport in channel systems.

The first version of Revised Uniform Soil Loss Equation (RUSLE1) is primarily a manual computation method assisted by spreadsheet or programmed computations (Renard et al. 1996). The latest version, RUSLE2 has increased sophistication and is fully implemented in a Windows software application. RUSLE2 explicitly considers sediment transport capacity and computes detachment and deposition along the slope profile (Foster et al. 2003). The Windows interface facilitates easy comparison of conservation planning alternatives. RUSLE2 retains the empirical philosophy of the USLE, so can utilize experience gained with USLE, but better accounts for seasonal variation by disaggregating computations to bimonthly (possibly daily) intervals.

The uncertainties of soil erosion predictions for watersheds are large. Validation data is expensive and difficult to collect (McCool and Busacca 1999). Developers of the original USLE found the error of long term predictions to be less than 1 ton per acre per year for 53 percent of the estimates and less than 2 tons per acre per year for 84 percent of the estimates when compared to the original plot data (Wischmeier and Smith 1976). Average soil loss of the comparison plot data was 11.3 tons per acre per year so estimates could be expected to be within 20 percent for 80 percent of estimates. Uncertainties for single storm or single season estimates are much greater. Expectations presented in recent RUSLE2 training suggest that long term estimates are within 25 percent when annual erosion is between 4 and 30 tons per acre per year. Uncertainty increases to 50 percent for annual soil loss between 30 and 50 tons per acre per year. Uncertainty greater than 100 percent is expected for very low or very high soil loss rates (Kuenstler 2004).

7.3.4 Accuracy of Soil Loss Estimates

A recent comparison of the USLE, RUSLE and WEPP average annual estimates with soil plot data found Nash-Sutcliffe model efficiency R^2 values to be 0.80, 0.72 and 0.71 respectively (Tiwari et al. 2000). Efficiencies of yearly estimates were lower; 0.58 for USLE, 0.60 for RUSLE, and 0.40 for WEPP. The data included about 1,600 plot years of natural runoff erosion data at 20 locations in the south and midwest. None of the sites were in the Pacific Northwest.

Nash-Sutcliffe (1970) model efficiencies are computed:

$$R^2 = 1 - \frac{\sum_{i=1}^{n} (Q_{mi} - Q_{ci})^2}{\sum_{i=1}^{n} (Q_{mi} - Q_m)^2} \qquad 7.7$$

where R^2 is the efficiency of the model, Q_{mi} is the measured soil loss, Q_{ci} is the estimated soil loss, and Q_m is the average of the measured values. Model efficiencies are hard to interpret in practical terms so the actual summaries were converted to U.S. Customary units and given in Table 7.2 Table 7.3 for the average annual and yearly soil loss comparisons. Prediction errors cancelled to give a reasonable overall accuracy for the models. However, the average magnitudes of the errors for the individual plots varied from 33 to 54 percent for the average annual estimates and 57 to 78 percent for the yearly estimates.

Estimates of Average Annual Soil Loss			
	Soil Loss Model		
Parameter	USLE	RUSLE	WEPP
Average measured soil loss, ton ac^{-1}	16.4	16.4	16.5
Average estimated soil loss,ton ac^{-1}	16.8	14.7	16.2
Average magnitude of error, ton ac^{-1}	6.3	5.5	9.0
Average percent error	38%	33%	54%

Table 7.2 Comparison of model estimates with measured average annual soil loss (after Tiwari 2000).

Estimates of Average Annual Soil Loss			
	Soil Loss Model		
Parameter	USLE	RUSLE	WEPP
Average measured soil loss, ton ac^{-1}	15.7	15.7	15.7
Average estimated soil loss,ton ac^{-1}	14.4	14.4	14.7
Average magnitude of error, ton ac^{-1}	9.5	8.9	12.2
Average percent error	61%	57%	78%

Table 7.3 Comparison of model estimates with measured yearly soil loss (after Tiwari, 2000).

In another study, USLE and RUSLE estimates were compared to 206 natural runoff plots representing a broad range of conditions and not used in the development of RUSLE (Rapp et al. 2001). Model efficiency R^2 for annual average soil loss was 0.73 with an average magnitude of error of 5.2 tons ac^{-1} (1.17 kg m^{-2}) for an average of 7.9 years per plot. Predictions of 1638 individual annual soil loss events had an average

model efficiency R^2 of 0.58 with an average magnitude of error of 9.3 tons ac^{-1} (2.08 kg m^{-2}). RUSLE did not estimate soil loss better than the USLE.

Soil loss estimates from WEPP and RUSLE were compared to six years of measured data at three sites in Austria (Klik and Zartl 2001). WEPP mostly underestimated soil erosion (86%) while RUSLE overestimated long-term average annual soil loss (148 %).

Measured soil loss from the Tillage, Runoff, Agricultural Chemical Erosion (TRACE) research plots located at the North Carolina Agricultural and Technical State University research farm in Greensboro, North Carolina were compared with estimates from RUSLE and WEPP (Reyes et al. 2004). RUSLE over-predictions of soil loss for various tillage treatments ranged between 261 to 419 percent. WEPP under predictions were between 14 and 46 percent. Plot data was only collected for two seasons.

Few studies of the accuracy of soil loss estimates have been completed under the unique climate conditions of the Pacific Northwest. An exception is the investigation by Pannkuk et al. (2000). Runoff and soil loss estimates from WEPP were compared with 8 years of runoff plot data under various crop managements at the Palouse Conservation Field Station (PCFS) near Pullman, WA. The slopes of the soil erosion plots varied from 15 to 22 percent and measured 22.2 meters long by 3.7 meters wide. Treatments included tilled bare fallow, winter wheat/fallow rotation, winter wheat/spring pea rotation, and continuous winter wheat. The comparison for the continuous tilled bare fallow was reported. WEPP under-predicted total runoff by 38 percent and over-predicted total soil loss by 126 percent.

Neither RUSLE or WEPP have clear advantage in predicting soil loss accurately without calibration to measured data. Uncertainties in soil loss estimates are high, especially for single seasons or storm events, even under conditions similar to the research plots from which these methods were derived. Uncertainty increases even more when sediment yield must be included in estimates of sediment export from fields or watersheds. It seems improbable that uncalibrated WEPP or RUSLE2 technology will be able to adequately estimate sediment production from upland sources at a degree of precision expected for development of engineering project sediment budgets (for example reservoir sedimentation) or determining compliance with regulatory numeric water quality protection standards as in Total Maximum Daily Load (TMDL) analyses.

7.3.5 Advantages of WEPP and RUSLE2 Technology

It would be unfair and dismissive of larger issues involved in sediment control to discard RUSLE2 and WEPP technology as simply being too inaccurate for development of sediment budgets. The true efficacy of these tools is their ability to reveal relative differences among land use and management practices, a function vital to developing effective sediment reduction plans. The most recent versions of RUSLE2 and WEPP facilitate conservation planning with unprecedented efficiency.

For the current research, RUSLE2 has an advantage because it requires less data to initialize and can more easily accommodate larger watersheds. In best practice soil loss estimation, an analyst may have to defend the value selected for each parameter in the model. This becomes difficult in a complex physically based model where field data are lacking and default or literature values must be assumed. The new core databases available with RUSLE2 offer a reasonably well documented and wide selection of cover

management options that are particularly suited to agricultural land of the Potlatch basin. As discussed below, RUSLE2 has also been specifically adapted for the unique climate of northern Idaho and eastern Washington with data collected at the Palouse Conservation Field Station near Pullman, WA.

7.4 Estimating Soil Loss with USLE and RUSLE2

The USLE and RUSLE compute soil loss for a user selected one-dimensional hillslope profile that extends from the initial point of overland flow to the point of net deposition or a concentrated flow channel. In RUSLE1 (and conceptually RUSLE2) the daily contribution to average annual soil loss on each i^{th} day for a *uniform slope* with *constant factors* is computed:

$$a_i = r_i \; k_i \; l_i \; S \; c_i \; p_i \qquad 7.8$$

where a_i is the contribution to average annual soil loss (tons ac^{-1} y^{-1}), r_i is the rainfall erosivity factor (ft tonsf in ac^{-1} hr^{-1} yr^{-1}), k_i is the soil erodibility factor (tons $acre^{-1}$ per unit erosivity) , l_i is the soil slope length factor (dimensionless), S is the slope steepness factor (dimensionless) , c_i is the cover-management factor (dimensionless), and p_i is the supporting practices factor (dimensionless), all on the i^{th} day. The slope steepness factor S is the constant throughout the year. Equation 7.8 is the same as Equation 7.1 but has been defined for a daily time step.

Soil loss is affected by the shape of the slope. Soil loss computed for a uniform averaged gradient underestimates erosion on convex slopes (steeper towards the bottom) and overestimates erosion on concave slopes (flatter towards the bottom). Soil loss on irregular slopes cannot be computed as the sum of losses from uniform segments because

of the effect of upslope flow and sediment transport capacity. An effective *LS* factor can be computed for an irregular slope by weighting individual *LS* factors for length segments on the irregular slope by the fraction of erosion occurring in similarly positioned length segment on a uniform slope (Wischmeier and Smith 1976). This procedure assumes that changes in gradient do not cause deposition of upslope sediment.

The basic USLE method assumes net erosion along the profile and does not compute sediment transport capacity or deposition. The user must terminate the profile at the likely point of deposition. Complex slopes with varying soil loss potential could be accommodated with a procedure for manual computations outlined in USLE guidance (Foster and Wischmeier 1974; Wischmeier and Smith 1976). Erosion was proportioned for equal length intervals with the relationship:

$$f_i = \frac{i^{m+1} - (i-1)^{m+1}}{N^{m+1}} \qquad 7.9$$

where f_i is the fraction of erosion occurring in the equal length slope segment, i is the number of a particular equal length segment ordered from top to bottom of the slope, m is the exponent of the USLE slope length relationship, and N is the total number of equal length segments along the slope.

In RUSLE2, complex slopes or slopes with varying soil and land use factors are divided into representative segments (Foster et al. 2003; Griffin et al. 1988). RUSLE2 routes sediment down slope with a steady state mass balance from Equation 7.2:

$$g_{out} = g_{in} + D\Delta x \qquad 7.10$$

where g_{out} is the sediment load leaving the lower end of a slope segment, g_{in} is the sediment load entering the upper end of the segment, Δx is the length of sediment, and D is the net detachment or deposition within the segment.

Detached sediment within a slope length segment is computed with a numerical integration of Equation 7.6 resulting in the equation:

$$D = r \cdot k \cdot S \cdot c \cdot P_c \cdot \frac{x_i^{m+1} - x_{i-1}^{m+1}}{\lambda_u^m (x_i - x_{i-1})} \qquad 7.11$$

where D is the detachment (mass per unit area per time), r is the erosivity factor, k is the soil erodibility factor, S is the slope steepness factor, c is the cover management factor, P_c is the contouring factor, x_i is the distance to lower end of the segment, x_{i-1} is the distance to the upper end of the segment, λ_u is the length of the unit plot (either 72.6 feet or 22.1 meters), and m is the slope length exponent. The slope length exponent is function of the ratio of rill to interrill erosion in all regions except the Northwestern Wheat and Range Region (NWRR) where plot data shows m to be nearly a constant value of 0.5 (McCool and Busacca 1999). All variables are assumed to apply for the i^{th} day and for a particular segment without explicitly showing subscripts except for segment number.

RUSLE2 computes deposition when sediment load exceeds transport capacity by:

$$D_p = \frac{V_f}{q}(T_c - g) \qquad 7.12$$

where D_p is the deposition, V_f is the fall velocity of the sediment in still water, q is the overland flow (runoff) rate per unit width of flow, T_c is the transport capacity, and g is the sediment load. RUSLE2 computes runoff rate using the 10-year-storm erosivity, the NRCS curve number method, and a runoff index computed using cover management variables.

RUSLE2 computes transport capacity with:

$$T_c = K_T \; q \sin\alpha \qquad 7.13$$

where K_T is a transport coefficient computed as a function of cover-management variables and α is the slope angle. Specific formulations for q and T_c cannot be determined from the RUSLE2 documentation.

7.4.1 Precipitation and Snowmelt Erosivity

Erosion processes in the NWRR are dominated by rainfall and/or snowmelt on thawing soils. Rainfall erosivity values, (R in Equation 7.1) are higher than expected compared to other regions in the U.S. (McCool and Busacca 1999). Equivalent R-values (R_{eq}) have been developed for the NWRR (Figure 7.14) from data collected in eastern Washington and northern Idaho. Values for R_{eq} are computed from annual precipitation with the simple relationship:

$$R_{eq} = 7.86V_{rf} - 50.5 \qquad 7.14$$

where R_{eq} is the equivalent erosivity (U.S. erosivity units) and V_{rf} is average annual precipitation (in). This equation was developed primarily for conditions across eastern Washington and west central Idaho. It is limited to values less than 200 U.S. erosivity units.

The seasonal distribution of erosivity is unique to the NWRR. Erosivity in Figure 7.15 from the RUSLE2 database is concentrated in winter and early spring. While the monthly fluctuations are questionable for estimates of long-term soil loss, the general trend agrees with know precipitation and snowmelt patterns in Clearwater region. Almost all erosivity occurs December through March when agricultural soils are least protected by vegetative cover.

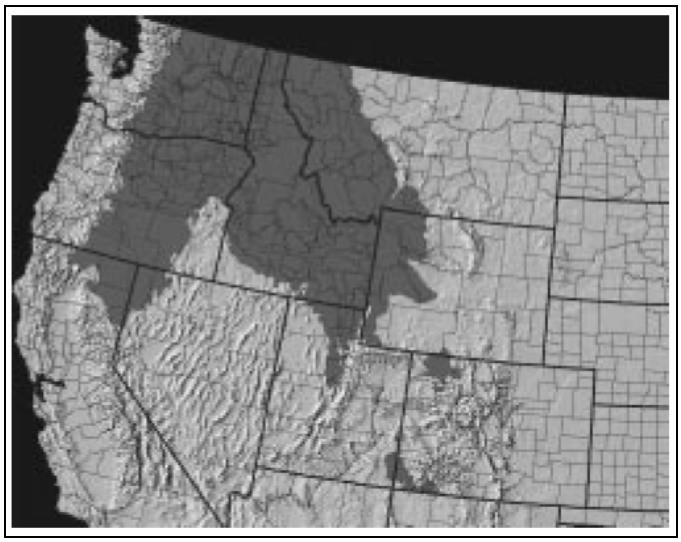

Figure 7.14 Area of applicability of R_{eq} in the Northwestern Wheat and Range Region (NWRR).

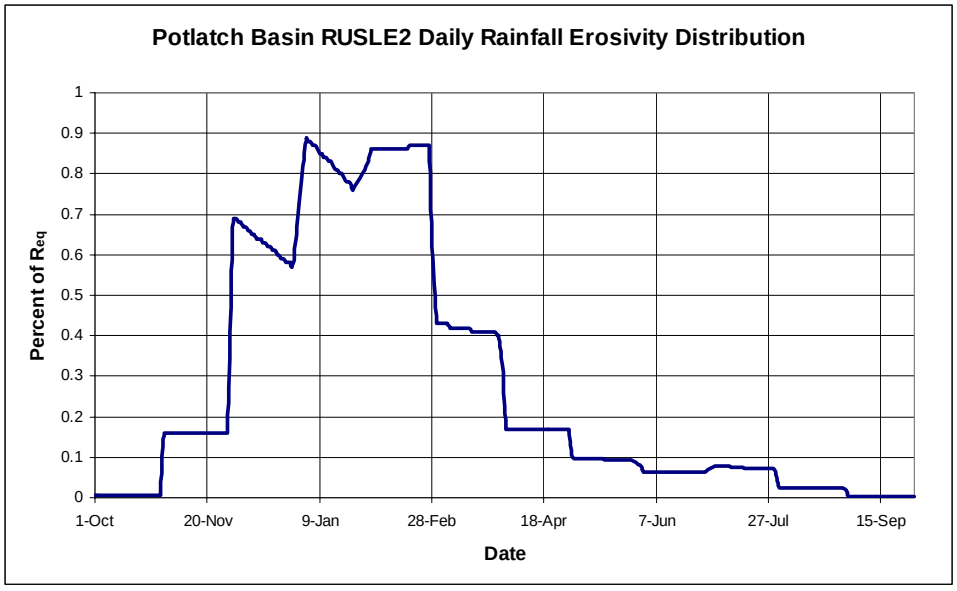

Figure 7.15 Seasonal R_{eq} distribution for Potlatch Basin.

Dominance of winter and spring erosivity in the Potlatch basin reduces the importance of growing season crop cover parameters in soil loss computations when compared to other regions of the U.S. It is not crucial to precisely define crop rotations and secondary tillage treatments to estimate winter soil loss in the Potlatch basin.

Emphasis should be placed on topographic variables (profile length, gradient), the division of land cover into general types (forest, permanent grass, tilled agriculture) and variation in dormant season surface cover (forest density, crop residue, field burning, tillage roughness).

The R_{eq} relationships apply to freshly disturbed and unconsolidated soils such as cropland where tillage occurs annually, and disturbed construction sites, reclaimed land, and disturbed forest lands within one year after disturbance. The R_{eq} relationships should not be applied to undisturbed lands like pasture and rangelands (Foster et al. 2003). Soils that are infrequently disturbed, such as hay and possibly bluegrass fields consolidate with time and a recommended approach is to assume that the transition time between the R_{eq} effect and standard erosivity effect equals the time to soil consolidation (Foster et al. 2003). Soil loss is interpolated between values using the R_{eq} relationships and the standard erosivity relationships depending on the disturbance frequency.

Appropriate options in RUSLE2 must be selected for R_{eq} computations. The program should be allowed to adjust for soil moisture when erosion is computed with the R_{eq} relationships. Soil moisture adjustment may be necessary with some management practices and crops grown ahead of the winter season, such as fall seeded winter wheat. The option to vary soil erodibility with climate should not be selected for R_{eq} computations, but should be selected when computing erosion with standard erosivity.

7.4.2 Soil Erodibility

Soils are characterized by an erodibility factor *K* for USLE and RUSLE erosion computations. Erodibility is determined empirically from erosion plot data and is

primarily dependent on soil texture, organic matter content, permeability, soil structure, and presence of coarse fragments. The soil erodibility factor is defined as the soil loss rate per erosion index unit for a specified soil as measured on a unit plot (Wischmeier and Smith 1976). A unit plot is 22.1 m (72.6 ft) long, with a uniform slope of 9 percent, in continuous fallow, tilled up and down the slope. Continuous fallow is defined as land that has been tilled and kept free of vegetation for more than 2 years.

The USLE and RUSLE documentation includes nomographs and equations for estimating erodibility from these factors (Foster et al. 2003; Wischmeier and Smith 1976). In practical applications, erodibility can be obtained from USDA-Natural Resources Conservation Service (NRCS) digital Soil Survey Geographic Database (SSURGO) based on county level field soil surveys. Mapping scales generally range from 1:12,000 to 1:63,360; SSURGO and is the most detailed level of soil mapping by the NRCS. Soil survey erodibility factors are included in the RUSLE2 downloaded databases of state and county agricultural soils. Erodibility factors are normally not available for soils on construction sites, landfills, or reclaimed surface mines because of the mixing of naturally developed soil and soil-like materials associated with surface mining. A soil erodibility nomograph in RUSLE2 can estimate *K* values for these soils from measured soil properties.

Soil erodibility is seasonable variable. It is highest when soils are wet, particularly after thaw. RUSLE2 can compute a seasonally variable erodibility adjusted by precipitation and temperature. Seasonally variable *K* values should not be used in the NWRR. Freeze and thaw effects on erodibility are absorbed by the R_{eq} factor (McCool and Busacca 1999).

Erodibility reduces as soils consolidate on disturbed sites converted to permanent cover. RUSLE2 assumes that soil erodibility is 2.2 times more erodible immediately after mechanical disturbance and that a soil will become fully consolidated seven years after disturbance where mean precipitation exceeds 20 inches (500 mm). An exponential decay curve describes the decrease in erodibility. Erodibility reductions from consolidation are additive to land cover effects and are likely appropriate for bluegrass rotations in the Potlatch basin.

7.4.3 Hydrologic Soil Group

RUSLE2 computes runoff with the NRCS curve number method. Runoff volume is an empirical function of land cover, land treatment, antecedent moisture conditions and soil properties. Soil properties for runoff computations are represented by the Hydrologic Soil Group (HSG) designations. Soils are separated into four groups depending on the infiltration rate of water ponded on bare soil. HSG descriptions from the NRCS Soil Survey Manual (NRCS 1993) are given in Table 7.4 based on the saturated hydraulic conductivity criterion in Table 7.5. HSG designations for U.S. soils are included in the NRCS Soil Surveys and the RUSLE2 database.

HSG	Description
A	Saturated hydraulic conductivity is very high or in the upper half of high and internal free water occurrence is very deep
B	Saturated hydraulic conductivity is in the lower half of high or in the upper half of moderately high and free water occurrence is deep or very deep.
C	Saturated hydraulic conductivity is in the lower half of moderately high or in the upper half of moderately low and internal free water occurrence is deeper than shallow.
D	Saturated hydraulic conductivity is below the upper half of moderately low, and/or internal free water occurrence is shallow or very shallow and transitory through permanent.

Table 7.4 NRCS Soil Survey Handbook Hydrologic Soil Group descriptions.

Class	Ksat (µm/s)
Very High	$\geq$ 100
High	10 - 100
Moderately High	1 - 10
Moderately Low	0.1 - 1
Low	0.01 - 0.1
Very Low	< 0.01

Table 7.5 Saturated hydraulic conductivity classes.

7.4.4 Topographic Variables

Even casual observation of the Palouse hills in winter and spring reveals that terrain relief– steepness, slope length and aspect greatly influence soil erosion. Steepness (gradient) and slope length are directly represented in the USLE and RUSLE by the slope factor S and length variables (L, m, λ). Few aspects of USLE and RUSLE application have received as much attention in the literature as determination of the topographic variables slope length and slope gradient (Castro and Zombeck 1986; Desmet and Govers 1996; Di Stefano et al. 2000; Griffin et al. 1988; Wang et al. 2000).

Original USLE plot data showed average soil loss per unit area along a slope to be proportional to a power of slope length because of increased flow (greater depth and velocity) as slope length increases (Wischmeier and Smith 1976). Low intensity rainfall

and snowmelt erosion on thawing soils of the Palouse Region were recognized during development of the USLE and RUSLE. Gradient and length effects are less pronounced in this region warranting special equations for slope gradient and length factors (McCool and Busacca 1999; Wischmeier and Smith 1976).

Original USLE plot data and new data were reevaluated during development of RUSLE2 to define updated relations for the *L* and *S* factors. The RUSLE2 slope factor *S* in the R_{eq} zone is computed (McCool and Busacca 1999):

$$S = 10.8\sin\theta + 0.03 \qquad \tan\theta < 0.09 \quad (9\%\,\text{slope}) \qquad 7.15$$

$$S = \left(\frac{\sin\theta}{0.0896}\right)^{0.6} \qquad \tan\theta \geq 0.09 \quad (9\%\,\text{slope}) \qquad 7.16$$

where the slope angle θ is in degrees. Cover management also affects how slope steepness affects soil loss, but plot data and theory are sufficient for incorporating those effects into RUSLE2 (Foster et al. 2003).

The slope length factor *L* in the USLE and RUSLE1 implicitly integrates the effect of slope position on soil loss. Soil loss can then be distributed along the slope with Equation 7.3. Soil loss in RUSLE2 is determined by explicitly integrating Equations 7.4, 7.5, and 7.6 along the slope profile. Direct integration along the profile eliminates the need to determine the length factor separately. The length exponent *m* retains its meaning and importance in the effect of position in the profile. Unlike other regions where the length exponent is partially dependent on slope gradient, ground cover and rill to interrill erosion ratios, *m* in the NWRR is assumed to be a constant value of 0.5 (McCool and Busacca 1999). The RUSLE1 and RUSLE2 treatment of slope position is functionally equivalent for uniform slopes.

An equivalent combined *LS* factor may be computed for uniform slopes with:

$$LS = \left(\frac{\lambda}{72.6}\right)^{0.5} 10.8\sin\theta + 0.03 \qquad \tan\theta < 0.09 \quad (9\%\ \text{slope}) \qquad 7.17$$

$$LS = \left(\frac{\lambda}{72.6}\right)^{0.5} \left(\frac{\sin\theta}{0.0896}\right)^{0.6} \qquad \tan\theta \geq 0.09 \quad (9\%\ \text{slope}) \qquad 7.18$$

where the slope angle θ is in degrees and slope length λ is in feet.

There are an infinite number of possible hillslope profiles in any given drainage basin. Soil loss for fields and catchments is estimated by selecting representative hillslope profiles for analysis. A profile that represents the one-fourth to one-third most erodible part of the area is suggested for conservation planning (Foster et al. 2003). Selection of even a single profile is constrained by limitations of the USLE and RUSLE plot data. Documentation for RUSLE2 program offers the following guidelines for selecting profiles (Foster et al. 2003):

1) Profiles (flow paths) are traced perpendicular to contour lines assuming the surface is even without regard to how microtopography, such as ridges left by tillage, affects flow direction.

2) Overland flow path lengths are best determined by visiting the site, pacing flow paths and making measurements directly on the ground.

3) Contour maps having intervals greater than 2 feet (1 meter) should be used cautiously, if at all, to determine profile lengths.

4) Contour maps based on 10 foot (3 meter) intervals should not be used to determine profile lengths because deposition and concentrated flow areas that identify the ends overland flow paths cannot be adequately delineated. Profile lengths are generally overestimated when contour maps are used to determine profile length.

5) Slope length and steepness values have, in some cases, been assigned to soil mapping units. These values may be acceptable for large scale regional conservation planning, but they should not be used for local conservation planning.

6) Profile lengths on many landscapes generally are less than 250 feet (75 meters), and usually do not exceed 400 feet (125 meters).

7) Profile lengths longer than 1,000 feet (300 meters) should also not be used in RUSLE2 because the reliability of RUSLE2 at these long slope lengths is questionable—and overland flow often becomes concentrated on most landscapes before such lengths are reached. The longest plot used in the derivation of RUSLE2 was about 650 feet (200 meters).

8) Maximum slope steepness that can be entered in RUSLE2 is 100 percent, well beyond the 30 percent maximum steepness of the plots used to derive RUSLE2. (Plots with slopes up to 56 percent were included in NWRR data (McCool and Busacca 1999)).

9) Profile lengths should be entered as horizontal distances in RUSLE2.

It is very clear from the RUSLE2 guidance that an accurate and relatively high-resolution representation of the landscape is necessary for best practice applications of the technology. The recommendation that overland flow distances be measured by field survey all but precludes a best practice RUSLE2 analysis of an extensive area. It will be demonstrated below that an erosion analysis with high-resolution aerial imagery can relax this guideline.

The RUSLE guidance does not directly address use of gridded elevation datasets such as the USGS 1/3-arc-second (10 meter) grid digital elevation model (DEM) in the National Elevation Dataset (NED). As of June 2004, the 1/3-arc-second NED covers

80% of the United States excluding Alaska (USGS 2004). The 1/3-arc-second NED for Idaho, Washington and Oregon was produced from source data with a resolution of 10-meters or higher. The NED spatial metadata delivered with each order from the Seamless Data Distribution System (http://seamless.usgs.gov/) can be queried to determine the source data used to produce 1/3-arc-second NED over any given area. USGS has begun producing higher resolution 1/9-arc-second (approximately 3 meters) elevation data from LIDAR. Some of the first is for the Puget Sound region in Washington. The NED is a very convenient source of good quality elevation data and should not be discarded lightly. Section 3 demonstrated photogrammetry techniques that can augment the NED for soil erosion modeling.

Slope aspect receives no attention in the USLE and RUSLE documentation and little discussion in the literature with the notable exception of Frazier et al. (1983). Slope aspect may not have significant influence on soil loss rates for locations in humid regions where snowmelt is not the primary generator of erosion, but snow accumulation can have a dramatic influence on soil erosion in the annual cropping zones of the eastern Palouse. Figure 7.16 is an aerial oblique image of the loess hills in the Little Potlatch Creek drainage acquired on December 17, 2003. Snow is retained longer and at greater depths on north facing slopes increasing the amount of effective precipitation available for runoff during periods of rapid snowmelt. Over geologic time this effect has eroded cirque shaped basins on many north and east facing slopes (Kirkham et al. 1941).

Figure 7.16 Snow accumulation on north facing slopes and erosion cirques in Middle Potlatch Creek basin, December 17, 2003.

The USLE and RUSLE methodology provide no means to incorporate slope aspect into soil loss computations except perhaps by application of differential precipitation depths. While the profile and erodibility of a complex north or east facing slope could be represented, there is no method to proportion the snowmelt component of erosivity. It seems against the modeling philosophy of USLE and RUSLE, that is based on a locally parameterized hillslope profile, to assume that the effects of locally variable erosivity average out at basin scale by use of a regional erosivity value. Several methods might be proposed to adjust a regional erosivity value for aspect:

- Proportion erosivity by slope aspect obtained by digital terrain analysis.
- Proportion erosivity by shaded terrain analysis.
- Develop basin specific erosivity values.

- Develop basin specific snow accumulation and depletion curves to augment or replace regional erosivity curves. This may be appropriate since rainfall energy has diminished importance in the Palouse region.

- Develop curve numbers adjusted for aspect.

These suggestions require data not likely collected under the current USLE and RUSLE research agenda, but would nonetheless be beneficial for extending the soil loss technology to a watershed scale.

7.4.5 Cover Management Factor

Vegetative cover, organic residue and surface roughness reduce soil loss compared to continuously smooth tilled fallow soil. In the USLE and RUSLE the effect of vegetative cover is represented by the cover management factor *C*. It is a dimensionless ratio of the soil loss from the given cover-management condition to the soil loss from a fallow plot at the same location on the same soil and slope length and steepness as the site-specific field condition. Cover management is the most complex RUSLE2 component.

Crop growth is not modeled in the USLE or RUSLE, so seasonal changes in the cover management factor are specified at intervals in a seasonal cycle or multi-year rotation. Cover management factors for the intra-season intervals are called soil loss ratios (SLR) in older USLE and RUSLE documentation. The average annual cover (crop) management factor *C* is computed as the sum of interval SLR values weighted by the proportion of rainfall erosivity that occurs during the interval:

$$C_{annual} = \frac{\sum_{i=1}^{n} EI_i \cdot SLR_i}{\sum_{i=1}^{n} EI_i} \qquad 7.19$$

Research at the WSU Palouse Conservation Field Station indicates that the RUSLE soil loss ratio relationship for cover management should be modified to include a soil moisture subfactor for the NWRR region (McCool and Busacca 1999).

$$SLR_i = PLU_i \cdot CC_i \cdot SC_i \cdot SR_i \cdot SM_i \qquad 7.20$$

where SLR_i is the soil loss ratio, PLU_i is prior land use factor, CC_i is the crop canopy subfactor, SC_i is the surface cover subfactor, SR_i is the surface roughness subfactor, and SM_i is the soil moisture subfactor.

This research indicates the soil moisture subfactor depends on soil moisture depletion by the previously grown crop and rainfall replenishment up to the time of the computation interval. The soil moisture subfactor varies from 0.0 when the upper six feet of soil is at wilting point to 1.0 when the soil is at field capacity. The relationship for *SM* is not necessarily linear with soil moisture content. Suggested growing season soil moisture depletion rates are listed in Table 7.6.

Growing Season Soil Moisture Depletion Rates

Crop	Depletion Rate
Winter wheat	1.00
Sping wheat and barley	0.75
Spring peas and lentils	0.67
Shallow rooted crops	0.50
Summer fallow	0.00

Table 7.6 Growing season soil moisture depletion rates for crops in the Palouse Region.

Approximately 33% of the previous season soil moisture remains when winter wheat is planted following spring peas and lentils (McCool and Busacca 1999). Residual soil

moisture prior to the winter season increases erosion susceptibility because less precipitation is required to bring the soil to saturation (field capacity).

Rough tilled winter wheat stubble has very little residual soil moisture and low erosion potential until significant rainfall or snowmelt replenishes soil moisture. Summer fallow depletes none of the previous season's soil moisture so has the highest erosion susceptibility for a given fall seeded crop. The RUSLE2 soil moisture subfactor indicates it is important to account for antecedent soil moisture for reliable soil loss estimates in the Palouse region. As a first approximation, antecedent moisture can be represented by the crop type preceding the winter erosion period.

Detailed data were not available from runoff plots at the Palouse Conservation Field Station to evaluate the other subfactors (McCool and Busacca 1999). Cover management factors for the Potlatch basin must be estimated with standard relationships in the RUSLE1 or RUSLE2 methodology. Like all USLE and RUSLE parameters, no error bounds or uncertainty can be established from the published methods.

RUSLE2 expanded the number of terms in the cover management SLR relationship to include tillage ridge height, soil biomass and soil consolidation subfactors. Previous land use effects are mostly represented in the soil biomass and soil consolidation factors:

$$c = C_c G_c S_r R_h S_b S_c A_m \qquad 7.21$$

where c is the interval cover management factor (SLR), C_c is the canopy subfactor, G_c is the ground cover subfactor, S_r is the soil roughness subfactor, R_h is the ridge height subfactor, S_b is the soil biomass subfactor, S_c is the soil consolidation subfactor and A_m is the antecedent soil moisture subfactor.

At first it seems the cover management factor is over parameterized for use in the NWRR given uncertainties in the erosivity factor and other variables. This is likely true for watershed scale soil loss estimates, but RUSLE is primarily intended for conservation planning where the relative differences between alternative cover management operations are of main interest (Foster et al. 2001). An effort was made in RUSLE2 to relate cover management subfactors to measurable physical variables and account for seasonal variation. Descriptions, relationships and basis of cover management subfactors are incomplete and contain editing mistakes in the draft RUSLE2 documentation (Foster et al. 2003), but are sufficient to review data requirements and probable importance to soil loss estimates in the Potlatch basin.

Vegetative canopies intercept raindrops, slowing impact velocity and reducing interrill erosion. Cover proportion and canopy height are the primary variables. The canopy subfactor is computed:

$$C_c = 1 - f_c \exp\left(-0.1 h_f\right) \qquad 7.22$$

where f_c is the canopy cover (fraction) and h_f is the effective raindrop fall height (feet). Canopy cover has a minor influence on winter and spring erosion of annually tilled cropland in the Potlatch basin. The portion of the canopy that is above ground cover is assumed to have no effect.

RUSLE2 adjusts the canopy subfactor proportional to the square root of crop yield. Values of ground biomass at maximum canopy cover are specified by the user. RUSLE adjusts for reduced canopy and increased ground residue after harvest, shredding, mowing, grazing, burning and frost are operations. Canopy factors should have a minor effect on soil loss on cropland during the winter and early spring period in

the Potlatch basin when fall seeded crops have little above ground biomass. Canopy cover will have a significant influence on soil loss during middle and late spring rainfall erosion events.

Ground cover protects the soil surface from direct raindrop impact and slows runoff velocity. Ground cover includes all material in contact with the soil surface such as crop residue, rock fragments, portions of live vegetation; applied materials including manure, mulch and manufactured erosion control products. Ground cover reduces soil loss for rill and interrill areas by different mechanisms, so the relationship between rill and interrill erosion becomes an important variable when computing the overall ground cover subbfactor. RUSLE2 tracks and accounts for ground cover on a mass per unit area basis and converts mass values to the proportion of the soil surface covered.

The main equation used in RUSLE2 that computes the ground cover subfactor is:

$$G_c = \exp(-b \cdot f_g) \qquad 7.23$$

where b is a coefficient that describes the relative effectiveness of ground cover and f_g is the proportional ground cover. The corresponding expression in the RUSLE2 documentation has editing mistakes. Equation 7.23 given here was interpreted from RUSLE1 documentation.

Coefficient b is computed from a complex secondary expression that contains editing mistakes and cannot be interpreted from RUSLE1 documentation. Coefficient b is dependent on the relative amounts of rill and interrill erosion. It is adjusted seasonally and reduced for steep slopes with little biomass. It is also adjusted for how elements of residue and rock fragments conform to the ground surface and the interaction of ground cover with canopy biomass, random surface roughness, infiltration, and soil

consolidation. Relationships for these interactions are not given in the RUSLE2 documentation.

RUSLE2 converts residue mass to proportional surface cover with the expression:

$$f_g = 1 - \exp(\alpha \cdot M_g) \qquad 7.24$$

where α is an empirical coefficient derived from residue measurements and M_g is dry residue mass per unit area. Proportional ground cover increases rapidly and the relationship is nearly linear for wheat residue up to about 2000 pounds per acre at about 70 percent cover (Figure 7.17).

Ground cover may be the single most important variable in RUSLE2 because it has more effect on soil loss than almost any other variable (Foster et al. 2003). Figure 7.18 is the relative effect of ground cover on rill and interrill erosion. Ground cover is very important when computing soil loss estimates for the winter-spring and late spring seasons in the Potlatch basin. Relative differences of residue ground cover can be inferred in high-resolution aerial imagery from color and surface texture.

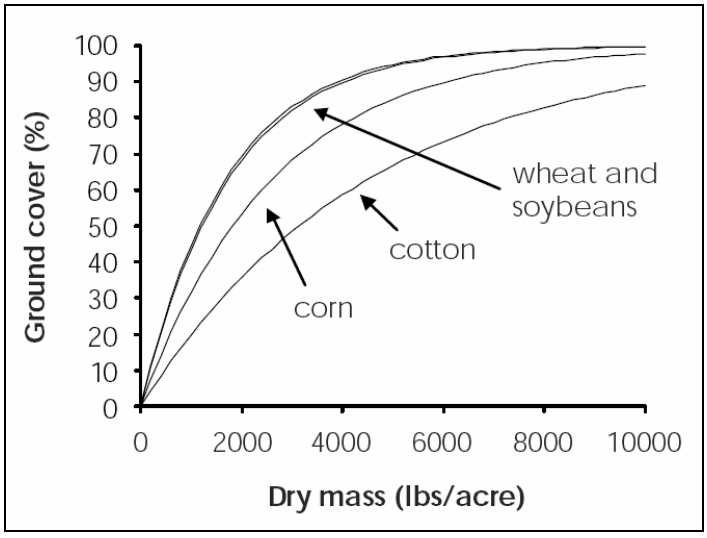

Figure 7.17 Proportional ground cover by crop type and residue mass (Foster et al. 2003).

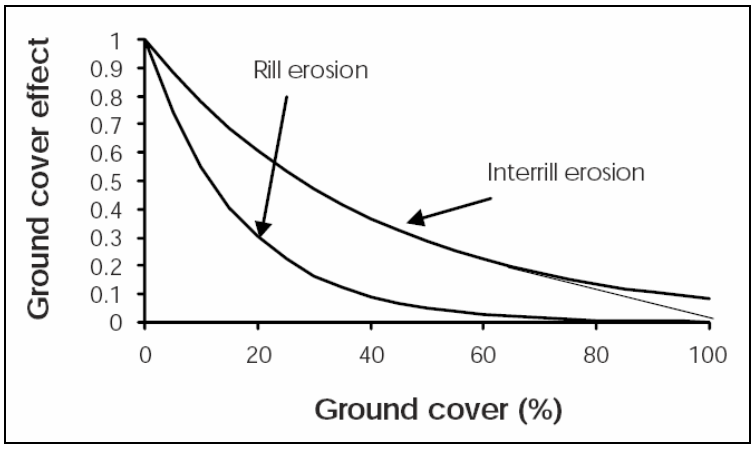

Figure 7.18 Reduction of rill an interrill erosion by ground cover (Foster et al. 2003).

Surface random roughness represents the effect of surface irregularity produced by tillage (disturbance) operations that is superimposed on spatially ordered (systematic) ridges and furrows. Random roughness does not redirect the runoff in a specific direction. Roughness from disturbance depends on soil properties, primarily texture soil moisture and biomass, and the type of soil-disturbing operation. Different types of soil disturbance produce widely differing distributions of aggregates and clod sizes depending on soil conditions. Surface roughness decays over time to a smooth surface, except for a few persistent clods on some soils.

In RUSLE2 random surface roughness is computed by:

$$S_r = \exp\left[-0.66\left(R_a - 0.24\right)\right] \qquad 7.25$$

where R_a is a roughness index value that has been adjusted for soil texture and soil biomass and decayed from an initial roughness value to account for weathering of the roughness elements. Adjustments for soil texture and biomass are necessary because initial roughness values for all soils are based on those for a silt loam soil subject to equivalent disturbance. Soil texture adjustments are multiplicative factors that range

from 0.69 for sand soils to 1.39 for clay soils. The texture adjustment for silt loam soils common to the Potlatch study region is 1.05.

The roughness index is adjusted for soil biomass by:

$$R_a = 0.24 + (R_{it} - 0.24)[0.8[\exp(-0.0012 B_{ta})] + 0.2] \quad 7.26$$

where R_{it} is the initial roughness value (in) after adjustment for soil texture and B_{ta} is the total mass of buried residue and dead roots averaged over the soil disturbance depth after the operation (lbs/acre per inch depth).

Surface roughness is an important factor for computing soil loss estimates in the Potlatch basin. It is suggested that initial roughness values for soil disturbing operations be selected from the RUSLE2 database to help assure consistence among RUSLE2 estimates (Foster et al. 2003). Relative differences of surface roughness can be inferred in high-resolution aerial imagery from surface texture.

Ridges formed by tillage equipment increase interrill erosion because the sides of the ridges are steeper than overall slope of the field. Measured soil loss can be as much as twice the soil loss from a level soil surface for land slopes up to 6 percent (Foster et al. 2003). The increase in soil loss caused by ridges is related to relative ridge sideslope steepness with the relationship:

$$K_r = 3(\sin\theta_i)^{0.8} + 0.56 \quad 7.27$$

where K_r is the proportional increase in interrill erosion due to ridges and θ_i is the amount the ridge side slope angle exceeds the overall field slope angle. The relative steepness of ridge side slopes becomes less as the overall field slope angle increases. RUSLE2 represents the combined effect of ridge side slope length and steepness with a single measure of ridge height. Ridge heights are more easily measured. The ridge subfactor

converges to 1.0 on steep slopes (Figure 7.19). Computational forms of the ridge subfactor relationships are not given in the RUSLE2 documentation. Ridge height is reduced by weathering throughout the season depending on rainfall and amount of interrill erosion.

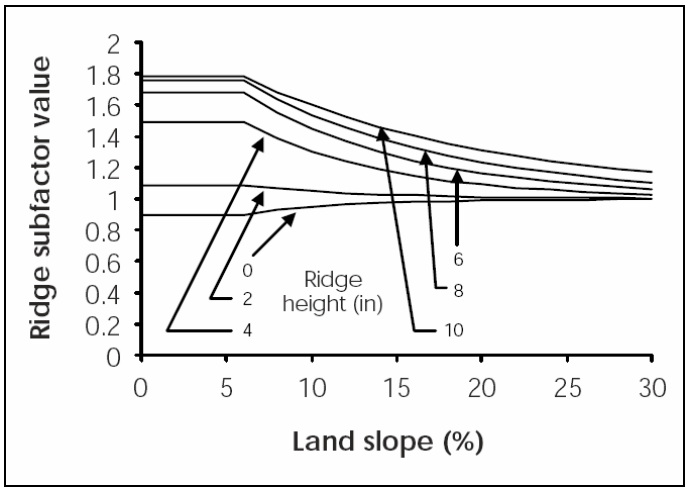

Figure 7.19 Ridge subfactor relationship to ridge height and land slope (Foster et al. 2003).

Initial values for ridge height should be selected from the RUSLE2 database to preserve the relationship with RUSLE2 contouring practice factors. The ridge subfactor is likely important for computing soil loss estimates in the Potlatch basin for both fall and spring seeded crops.

Buried soil biomass mechanically reinforces soil aggregates and resists surface erosion when exposed. Live roots are more effective in soil reinforcement than dead roots and buried residue. Decomposing residue releases organic compounds that help bind and give structure to the soil that decreases soil erodibility and increases infiltration. Live roots are also a measure of plant transpiration that reduces soil moisture. Soil biomass has a much greater effect on rill erosion than interrill erosion and is computed:

$$S_b = 0.951\exp\left(-0.00696B_{rt} - 0.000866\frac{B_{rs}}{S_c^{0.5}}\right) \qquad 7.28$$

where S_b is the soil biomass subfactor, B_{rt} is the sum of the live and dead root biomass averaged over a 10 inch (250 mm) depth (pounds per acre per inch of depth), B_{rs} is the amount of buried residue averaged over a depth that linearly ranges from 3 inches if the soil is not consolidated to 1 inch if the soil is fully consolidated. The coefficients within the brackets are specific to the R_{eq} zone so apply to the Potlatch basin.

Soil disturbance redistributes soil biomass through the soil profile and brings buried residue to the surface. Redistribution relationships in RUSLE2 are complex because of the wide variety of tillage operations and climatic effects on rates of decomposition. Harvest (killing) operations transfer soil biomass from the live to dead biomass pools. Redistribution and transfer of soil biomass is parameterized by selection of a sequence of tillage operations in a management scenario.

Soil biomass input values and tillage scenarios should be obtained from the RUSLE2 database to conform to values used to derive Equation 7.22 (Foster et al. 2003). Early season soil biomass is likely important for soil loss computations in the Potlatch basin because of the greater relative amount of rill erosion.

Mechanical disturbance loosens soil and increases erodibility. Following disturbance, seasonal moisture cycles and soil chemistry processes encourage consolidation of the soil by cementing of soil particles and aggregates. Consolidation of the soil reduces erodibility. RUSLE2 assumes that soil erodibility is 2.2 times more erodible immediately after mechanical disturbance and that a soil will become fully consolidated. The soil consolidation subfactor S_c varies by an inverse exponential relationship from 1.0 to 0.45 after seven years (Figure 7.20). Full consolidation (95%) is

assumed to occur over seven years where annual precipitation is greater than 20 inches and over 25 years where precipitation is less than 20 inches.

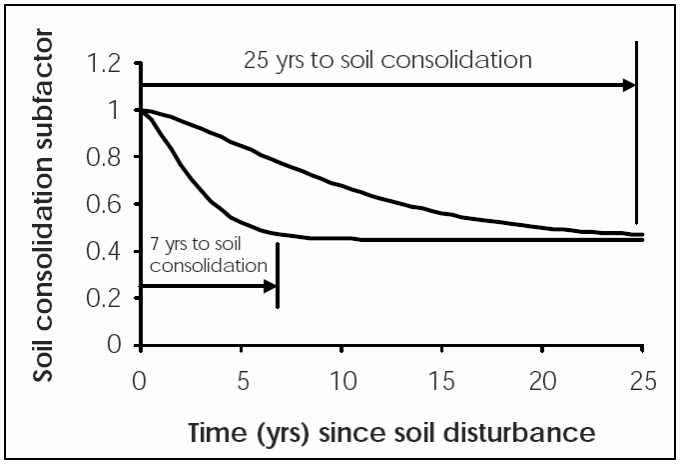

Figure 7.20 Soil consolidation relationship (Foster et al. 2003).

Some tillage operations only disturb a portion of the soil. Partial disturbance is represented by selection and description of tillage appropriate operations in the cover management scenario. Soil consolidation is likely important for long term estimates of soil loss in the Potlatch basin for land converted from annual tillage to bluegrass, pasture or retired in the conservation reserve program.

RUSLE2 includes a soil moisture subfactor for the R_{eq} zone. Subfactor values are 1.0 when the soil profile is "filled" relative to the unit plot, and less than 1.0 when the soil profile is depleted of moisture relative to the unit plot. The RUSLE2 docmentation does not describe how the soil moisture subfactor is distributed throughout the season if soil moisture is allowed to carry over between years in a crop rotation. A general relationship for the moisture subfactor in a winter wheat – spring pea rotation at Walla Walla, Wa and Pullman, WA is in Figure 7.21.

Soil moisture effects are significant in the estimation of soil loss in the Potlatch basin. The average value of the soil moisture factor during the January through March

period following seeding of winter wheat is about 0.98. Crops and crop cycle can be interpreted from seasonal multi-year high-resolution aerial images or inferred from surface texture of tilled soils during the winter erosion period. Soil color changes caused by relative differences in soil moisture content can be observed in winter and spring aerial images. Gamma radiation, thermal, radar and microwave remote sensing techniques show potential for operational estimation of soil moisture content (Carroll 2001; Engman 2000; Houser et al. 1998; Hutchinson 2003; Ottle et al. 1996; Price 1980).

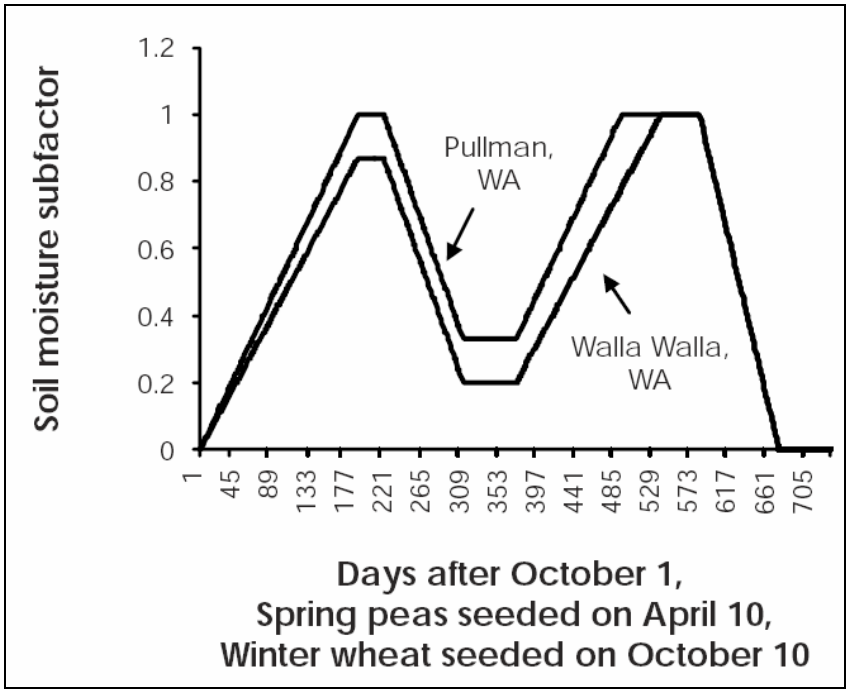

Figure 7.21 Soil moisture subfactor for a winter wheat – spring pea rotation in the R_{eq} zone (Foster et al. 2003).

7.5 Topographic Parameters from Digital Elevation and Aerial Imagery

This dissertation work suggests that conventional digital elevation data is not sufficient for soil erosion modeling and best practice soil loss estimation. This section demonstrates a relatively simple method of augmenting digital elevation data with a

semi-quantitative analysis of high-resolution aerial imagery to confirm topographic parameters derived by DEM analysis. Doing so relieves some of the concerns in the RUSLE2 guidance and more convincingly extends the RUSLE technology to large areas. A fairly detailed discussion of the extraction of representative profiles from digital elevation data is necessary to understand the role of aerial imagery.

Much of the work to produce soil loss estimates for large areas has been the development of representative topographic variables for hillslopes. Many methods have been investigated to derive spatially averaged topographic variables for representative hillslope profiles from elevation data for USLE, RUSLE and WEPP (Cochrane and Flanagan 2003; Desmet and Govers 1996; Griffin et al. 1988; Mitasova et al. 1996; Moore and Burch 1986; Quinn et al. 1991; Williams and Berndt 1972; Wilson 1986). Geographic Information System (GIS) interfaces that extract topographic variables from digital elevation models (DEM) greatly assist the development of soil loss and sediment yield estimates for large areas. Popular GIS interfaces include the Agricultural Research Service (ARS) GeoWEPP ArcView^{tm} interface for the WEPP program, the ARS ArcView interface for Soil and Water Assessment Tool (SWAT), and the ARS ArcView utility for the Agricultural Nonpoint Source (AGNPS).

Methods of deriving slope profiles from digital elevation data vary in complexity and accuracy. Techniques for analysis of digital elevation data have proliferated as accessible and reasonably accurate data became available. Several DEM analysis software applications are available including the Hydro version 1.1 included with ESRI ArcView Spatial Analyst, the Topographic Parameterization (TOPAZ) software (Garbrecht and Martz 1997), TauDEM (Tarboton 1997), MicroDEM (Gluth 2004),

Jensen's algorithms (Jenson and Domingue 1998), and LandSurf (Woods 2004). Full function GIS and Remote Sensing software packages include digital elevation analysis functions icluding ESRI ArcInfo, Leica Geosystem's Imagine, Clark Lab's Idrisi, ERMapper, and RSI's Envi. It is beyond the scope of this research to perform an extensive comparison of terrain analysis algorithms.

Three key applications have been widely accepted in watershed hydrologic analysis: ESRI ArcView Spatial Analyst, TOPAZ and TauDEM. The EPA BASINS program and the ArcView interface for SWAT adopt the ESRI terrain analysis algorithms that appear to have evolved from work by Maidment (Maidment et al. 1990). GeoWEPP and the ArcView utility for AGNPS evaluate terrain variables with algorithms from TOPAZ. Tarboton's TauDEM is in a class by itself and offers a variety of useful hydrologic analysis functions.

7.5.1 Semi-Quantitative Assessment of Terrain with Aerial Imagery

Erosion flow lines and erosion severity are often very clearly observed in late winter and spring aerial images. Qualitative and quantitative erosion information in the aerial images may confirm or question the accuracy of topographic parameters extracted from digital elevation data. These data sources are independent and highly compatible. Augmentation with current seasonal aerial images greatly extends the usefulness of the USGS 10 meter DEM data. A semi-quantitative example from Middle Potlatch basin illustrates the benefits of aerial imagery in terrain assessment for erosion modeling and orients the reader to the subsequent discussion.

High-resolution aerial imagery transects in this area of the Potlatch basin were acquired on March 15, 2004. The 10.78 ha (26.6 ac) first order subbasin in Figure 7.22

was derived with the TOPAZ software from the USGS 10 meter DEM. The aerial image was manually georeferenced to the 1992 USGS digital orthophotoquadrangle (DOQ). Soils are silt loam with an eodibility of 0.32 tons ac^{-1} per unit rainfall index. The field was tilled fall 2003 and seeded to winter wheat. A grass waterway protects most of the first order channel. Ephemeral gullies eroded in several topographic swales.

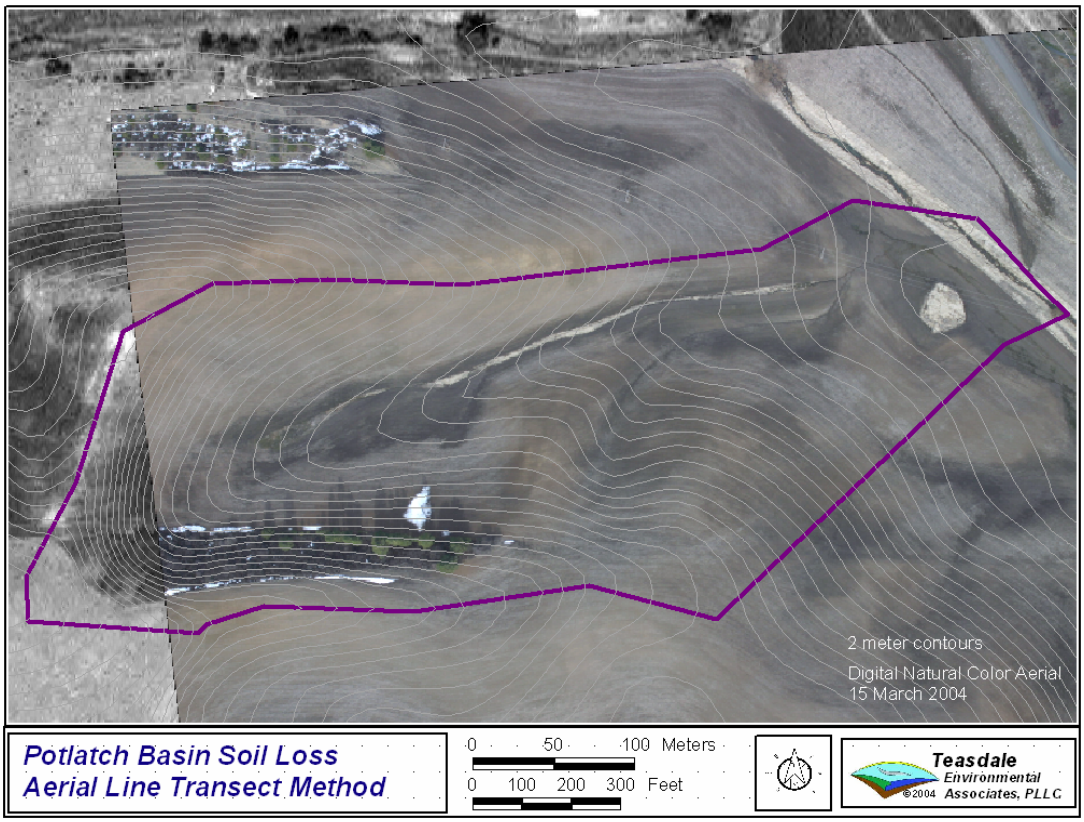

Figure 7.22 First order subbasin in the Middle Potlatch Creek basin.

The aerial image reveals exposed subsoils on ridge tops, wet soils along the drainage channels, and indications of sediment deposition at the upper end of the grass waterway. A patch of snow remains on the north slope of the shrub and tree protected "eyebrow". Tillage marks indicate that the DEM and DOQ are misaligned by about 15 meters in a northwest direction. The contour lines were derived with the Spatial Analyst Hydro extension.

In this particular example the superimposed contours of the USGS 10 meter DEM in Figure 7.22 agrees well with terrain relief observed in overlapping aerial images. Moreover, a soil erosion analyst who observes the late winter aerial images knows precisely which slopes are critical to the accuracy of the soil loss estimate. This is the essence of the simple, but very powerful technique of qualitative augmentation with aerial imagery. It is not possible to convey all nuances of stereo observation of the aerial images. Even monoscopic analysis is beneficial. The approach can be summarized as a series of questions that the erosion analyst might ask:

1) Do the superimposed contours match terrain variation observed in the imagery?

2) If not, which slopes are incorrect? If the incorrect slopes are covered with trees, shrubs or other permanent dense vegetation, then the incorrect slope is not meaningful for soil loss estimation in agricultural settings.

3) Are incorrect bare soil slopes concave or convex compared to the DEM contours?

4) Could a more accurate concave slope profile be estimated by using the DEM contours as starting reference? Even spacing between contours indicates a uniform slope?

5) Do ephemeral gullies indicate the actual slope length?

6) Is slope length indicated by soil color and texture changes caused by deposition in topographic low points?

7) Does soil color change on terrain high points or slopes? If so, this probably indicates exposure of subsoil with different erosion characteristics.

7.5.2 Effective Subasin Slope Gradient

Soil loss computed with average subbasin terrain slope ignores nonlinearities in erosion computations and the effect of hillslope profile (Foster et al. 2003). Nonetheless, models that adopt a lumped parameter approach for subbasins and hydraulic response units (England and Holtan 1959) require representative average slopes for computation. Models of this type include the ArcView interface for the U.S. Army Corps of Engineers Hydrologic Modeling System HEC-GeoHMS (USACE 2003), the Soil and Water Assessment Tool – SWAT (Neitsch et al. 2000) and HSPF (Becknell et al. 1993). A technically more correct method for computing slopes for soil loss estimation is discussed in the next section. Further discussion of the development of model subbasin parameters from aerial imagery satellite imagery is given in Section 7.7.

Again, the primary use of the high-resolution aerial imagery in the example above was to confirm that the USGS 10 meter DEM represents the actual terrain well enough for soil loss computations. Having confirmed that it does, the effective subbasin slope may be computed with GIS operations. Spatial Analyst computes slopes by the D8 method of steepest descent for each grid cell in the subbasin. For the example basin, an average terrain slope of 20.9 percent and maximum slope of 58.2 percent were computed with the ArcView Spatial Analyst function SLOPE. All slopes in this comparison are reported as percent slope.

An average flow vector slope (fvslop) of 21.2 percent and maximum slope of 61.00 percent were computed by TOPAZ. TauDEM computed average and maximum slopes of 21.2 and 61.8 percent. Differences are likely caused by rounding in the

elevation values and treatment of boundary cells. The differences are insignificant for watershed hydrologic computations.

The average hydraulic slope computed by TOPAZ is 21.6 percent with a maximum of 57.0 percent. The TOPAZ hydraulic slope (hslope) is the mean of all flow vector slopes entering and leaving the grid cell and is preferred for hydraulic computations. It differs from the flow vector slope only at flowpath intersections. Subbasin slope derived by the ArcView interface for SWAT (AvSWAT) was 21.4 percent. GIS algorithms are encrypted in the AvSWAT interface and cannot be verified (Di Luzio et al. 2002), but it appears that HRU slopes are simple basin average slopes.

TauDEM computes a more hydraulically relevant slope by the D-infinity method (Tarboton 1997) in which flow direction is not constrained to only the eight sides and corners of the grid cell. The D-infinity average and maximum slopes for the subbasin are 21.7 and 62.0. Again, differences are not particularly significant for hydrologic computations.

Topographic effects due to slope gradient for the USLE and RUSLE soil loss computations in the NWRR are best represented by the *S* factor computed from Equations 7.15 and 7.16 (McCool and Busacca 1999). The slope gradient factor can vary by 300 percent across the range of slopes typical in Palouse topography (Figure 7.23).

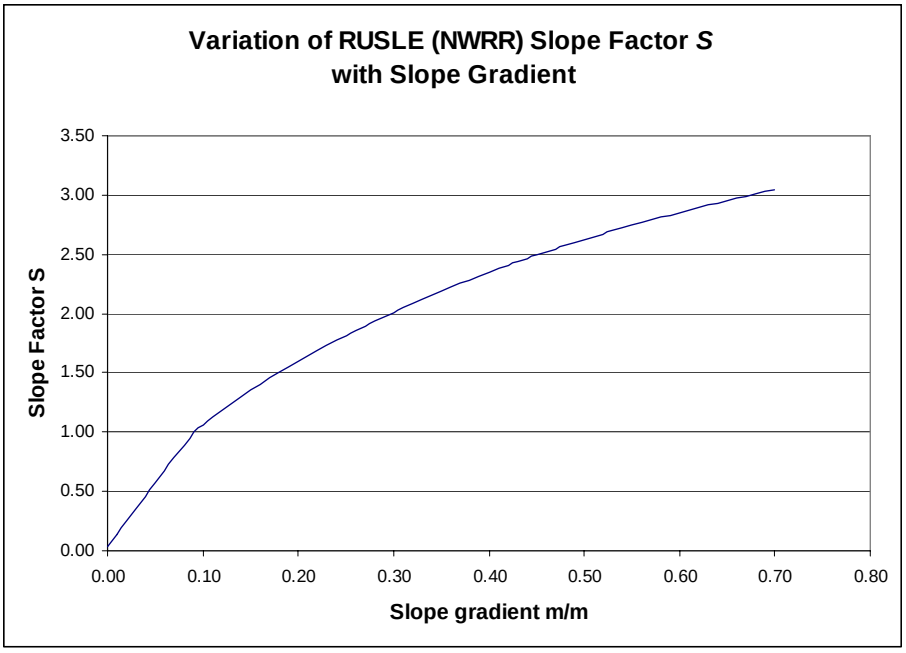

Figure 7.23 Variation of RUSLE slope factor for the NWRR with slope gradient.

For the example subbasin, the slope factor computed from the average hydraulic slope is:

$$S = \left(\frac{\sin(\text{atan}(0.2157))}{0.0896} \right)^{0.6} = 1.67$$

Slope gradient factors can also be computed for each grid cell then averaged for the subbasin to better represent the slope effect on soil loss. Applying Equations 7.15 or 7.16 to each cell in the TOPAZ hslope grid gives an average S factor of 1.58. With all other factors being equal, the difference in S factors produces an error in the erosion estimate of:

$$E\% = \frac{1.67 - 1.58}{1.58} \times 100 = 5.7\%$$

A 6 percent conservative error is not particularly meaningful compared to typical overall RUSLE uncertainties ten times this amount. Inversion of Equation 7.16 gives an equivalent subbasin slope of 19.6 percent. Best practice estimates of soil loss for lumped

parameter models should be computed with an *S* factor equivalent subbasin slope rather than an *S* factor computed from the basin average slope. It should be noted that the SWAT model does not provide and option to compute *S* factors with the NWRR Equations 7.15 and 7.16, so basin USLE factors must be adjusted manually for use of SWAT in the Palouse region. The SWAT model will be discussed more in a subsequent section.

7.5.3 Representative Hillslope Flowpaths for Erosion Modeling

The effective subbasin slope method in the preceding section should not be used for best practice estimates of soil loss. Recent developments in DEM processing for soil erosion appear to increase the precision of terrain representation for soil loss estimation. These are reviewed to better understand the potential use of high-resolution aerial imagery in soil erosion modeling. The representative slope profile or flowpath is a key concept of the USLE and RUSLE approach to estimating soil erosion. Even the more physically-based WEPP model relies on a composite profile to representative each of three hillslopes in its standard triplex configuration (Flanagan and Livingston 1995). Distributive grid models such as Annual AGNIPS do not rely on representative profiles, but route sediment from cell to cell in the full grid.

A flowpath for erosion computation purposes is the steepest route beginning at a source point on a hillslope and ending in a concentrated flow channel or the point where deposition begins. Source points have no tributary inflow. Watershed boundaries are a locus of source points, but an interior point such as the top of a hillock (small isolated terrain highpoint) can also be a source point when it receives no flow from adjacent terrain. There are an infinite number of flowpaths on a continuous surface. Grid cell

digital elevation models (DEMs) simulate the flow field of real surfaces with a finite set of flowpaths.

Flowpaths are different from drainage networks composed of links and nodes. Codependent flowpaths that converge share part of a common route. To use a municipal storm drainage analogy, each catch basin in a storm drainage system eventually connects to the main drainage outlet. So does every other catch basin in the system. The flow path for a particular catch basin traverses a route from the catch basin to the main outlet, mostly through a common system of pipes and channels. Total length of the pipes and channels in the system will be substantially less than the sum of all possible flow paths. Soil loss computations are most representative when based on actual field measurements of flowpaths (Haan et al. 1994; Renard et al. 1996).

The slope length factor *L* in USLE and RUSLE incorporates the effect of increasing volume of flow as tributary area increases along the flowpath. Flowpath profiles for soil loss computations are simply characterized as uniform, concave, convex, and complex (Wischmeier and Smith 1976) to help caution analysts to use interval computations for combined *LS* factors on irregular slopes. More realistic representations of erosion and deposition in complex terrain must consider convergence of flow and slope shape (Di Stefano et al. 2000; Moore and Burch 1986).

Slope length exerts a strong influence on USLE and RUSLE soil loss estimates. The slope length factor from Equations 7.17 and 7.18 in metric form is:

$$L = \left(\frac{\lambda}{22.13} \right)^{m} \qquad 7.29$$

where λ is the length of slope (m) from the beginning of overland flow to a concentrated flow channel or the point where net deposition begins, and *m* is the slope length

exponent, recommended to be 0.5 in the NWRR (McCool and Busacca 1999). The slope length exponent is influenced by slope gradient, surface conditions (Wischmeier and Smith 1965) and the ratio of rill to interrill erosion . Slope length factor varies by 300 percent over the range of slopes lengths expected in Palouse watersheds (Figure 7.24). Arbitrary or unrealistic slope lengths can greatly bias soil loss estimates. Profile lengths on many landscapes generally are less that 75 meters, and usually do not exceed 125 meters (Foster et al. 2003).

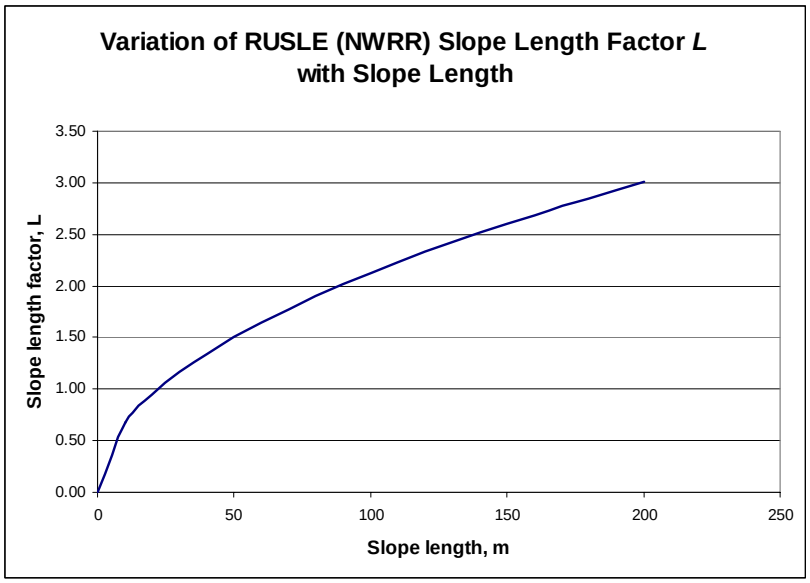

Figure 7.24 Variation of RUSLE length factor for the NWRR with slope length.

Slope length should not be a calibration variable. Plot lengths (and slopes) in the USLE and RUSLE empirical studies are unambiguous (Foster et al. 2001). Slope lengths for best-practice estimates of soil erosion should be as realistic and representative as possible. In large watershed applications representative profiles require considerable effort to select, measure and verify (Cochrane and Flanagan 2003; Haan et al. 1994). As noted in the RUSLE2 guidance, slope lengths should be determined by direct observation whenever possible (Foster et al. 2003).

It is not always possible or practicable to measure slope lengths in the field, especially at times when runoff can be observed. Access may be restricted, areas too extensive and expensive to survey; or in the case of land conversion and regrading, flow profiles may not yet exist. Various strategies for establishing representative profiles have evolved of necessity and convenience. The may be characterized as:

- Selection of slope lengths based on literature values
- Selection of slope lengths based on local experience
- Extracting flow profiles from digital elevation data
- Estimating average slope length from subbasin area and concentrated flow channel length
- Observation of slope length in high-resolution aerial imagery
- Combination methods

Average slope lengths for subbasins or HRU's may have to be assumed to begin erosion model development and prioritize modeling efforts. The ArcView interface for SWAT (AvSWAT) automatically assigns initial values of slope length to assist preliminary model development (Di Luzio et al. 2002). Values assigned by the ArcView interface version of SWAT for a preliminary model of the Middle Potlatch basin averaged around 15 meters, a plausible length. The ArcView scripts that compute subbasin parameters are encrypted and algorithms are not described in the model documentation. Lacking other information, RUSLE and RUSLE2 manuals offer some starting guidance (Foster et al. 2003; Renard et al. 1996). Section 4 demonstrated a method to estimate overland flow length using aerial line intersect sampling.

7.5.4 Representative Flow Paths from Digital Elevation Data

Profiles extracted from topographic contour maps or digital elevation models only approximate actual conditions. The accuracy of the representation depends on the resolution and quality of the DEM. Several comparative studies have reported that DEM's can provide sufficient detail to infer the location and gradient of *probable* hillslopes and flowpaths that are sufficiently representative to support realistic hydrologic assessment (Band 1986; Endreny et al. 2000; Kenward et al. 2000; Wang and Hjelmfelt 1998). When combined with digital climate, soils and land cover data, digital terrain data provides an unprecedented opportunity to investigate erosion and sedimentation in locations, and at frequencies, not before possible.

Each cell in the DEM grid is a segment in at least one flowpath. Terrain analysis algorithms trace the grid, extracting information such as total flowpath length and tributary area during the traverse (Jenson and Domingue 1998). Terrain algorithms in ESRI-Hydro and TauDEM both generate a secondary grid of the length of the longest flowpath upstream from each grid cell. A grid of upstream flowpath lengths is very useful for computing USLE and RUSLE slope length factors for each cell in the grid. TauDEM also computes a grid of the total length of all flowpaths upstream from each cell, a useful measure of flow path redundancy. TOPAZ generates a table of flowpath statistics, but not a grid.

Flowpaths for the example subbasin are superimposed on the triplex of hillslopes in Figure 7.25. The triplex was created with GeoWepp ArcView extension with a critical source area (threshold) of 1.5 ha. Flowpath grid cells have been converted to a shapefile with ESRI-Hydro to aid visualization. Vector shapefiles are not ordinarily used in

erosion simulation. The shapefile flowpaths in Figure 7.25 converge together as they approach the main drainage channel. Long parallel lines show the effect of the finite resolution of the DEM grid and the grid accumulation algorithm. A query of the accumulation (upslope area) grid cell at the outlet of the subbasin is equal to the total area of the subbasin (10.78 ha), as it should be. Total accumulation of the source hillslope (green) is 1.47 ha.

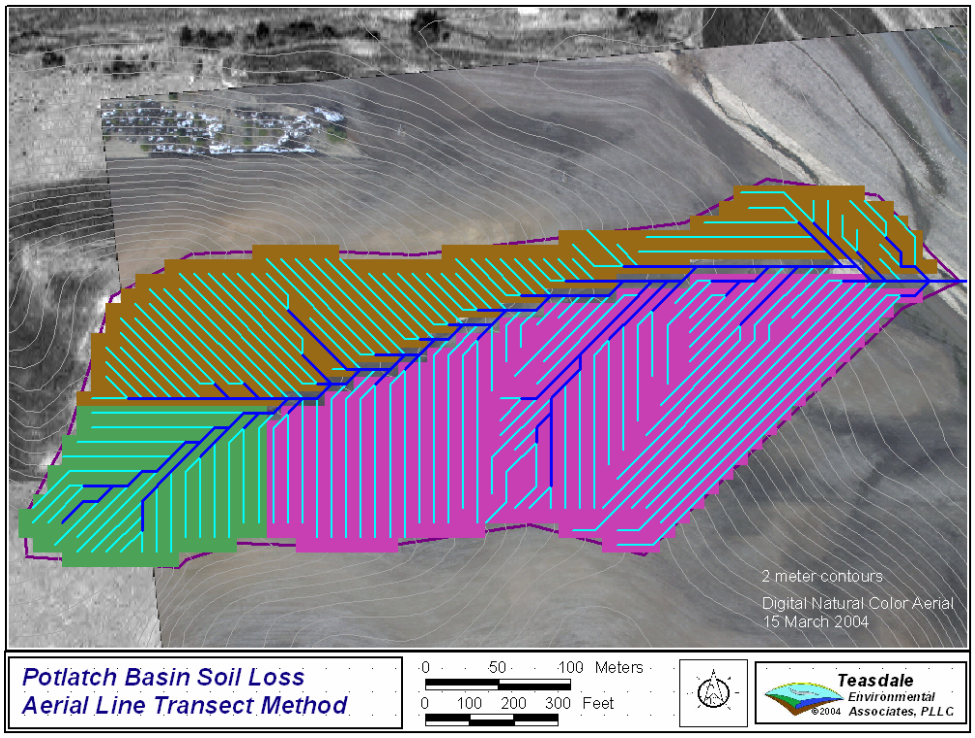

Figure 7.25 Hillslope triplex and flowpaths.

Conventional USLE and RUSLE soil loss estimates are determined as an average over an entire flowpath; *L* and *S* factors are computed from the total length. Upper ends of flowpaths can be determined directly by querying the grid to identify all cells with no tributary area. Downstream locations of erosion flowpaths may be determined from the accumulation grid by adopting a termination criteria, such as "the longest flowpath

cannot be longer than 120 meters", or "the total tributary area of converging flowpaths cannot exceed 1500 m^2".

Flowpath termination criteria should not be arbitrary. High-resolution aerial imagery acquired soon after the dominant erosion period often reveals surface features that indicate sediment deposition, ephemeral gullies, permanent channels, and evidence of concentrated flow. Figure 7.26 marks the location and upslope area of flowpaths that terminate at probable concentrated flow swales, the upper end of the grass waterway, and an ephemeral gully.

Figure 7.27 is a magnified view of two termination points in Figure 7.26. The red leaders show the corresponding locations on the flow the hillslope flowpath. The DEM is slightly offset from the base imagery so an automated termination cannot be performed in GIS without a fairly sophisticated radial search algorithm. It is an easy matter to visually and logically match the termination point indicated in the aerial imagery to the corresponding location on the DEM flowpath. Statistical justification for erosion flowpath termination criteria is obtained by extending the termination point analysis to a number of aerial images and hillslopes. Stereo views of the overlapping aerial images, difficult to show here, greatly aid image interpretation.

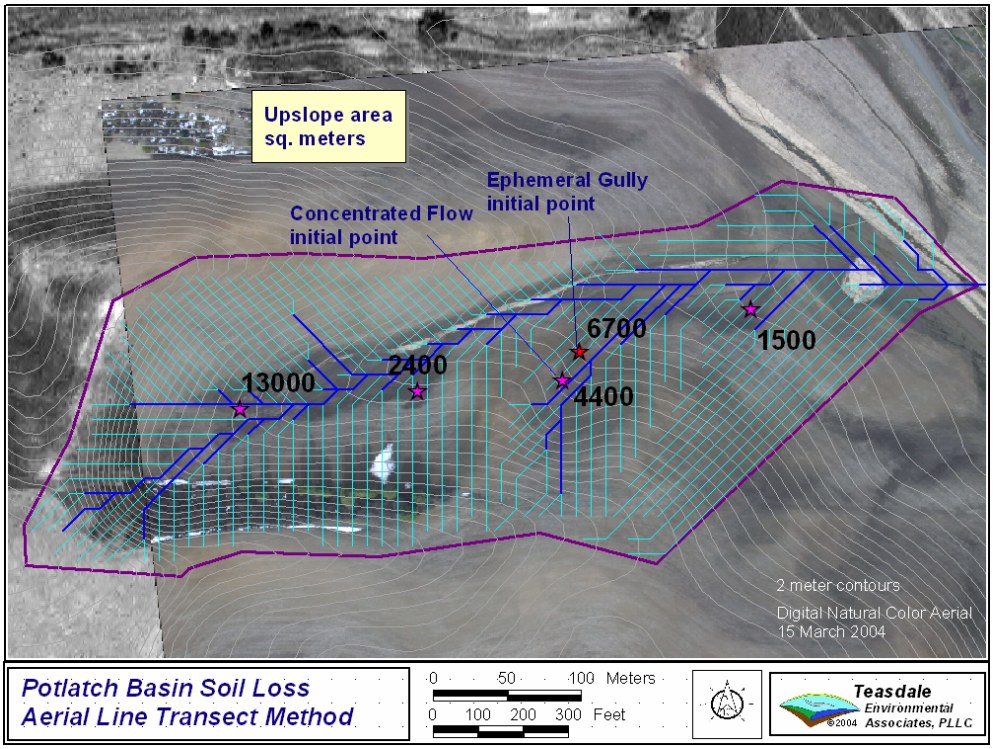

Figure 7.26 Tributary areas of concentrated flow and ephemeral gully initiation points.

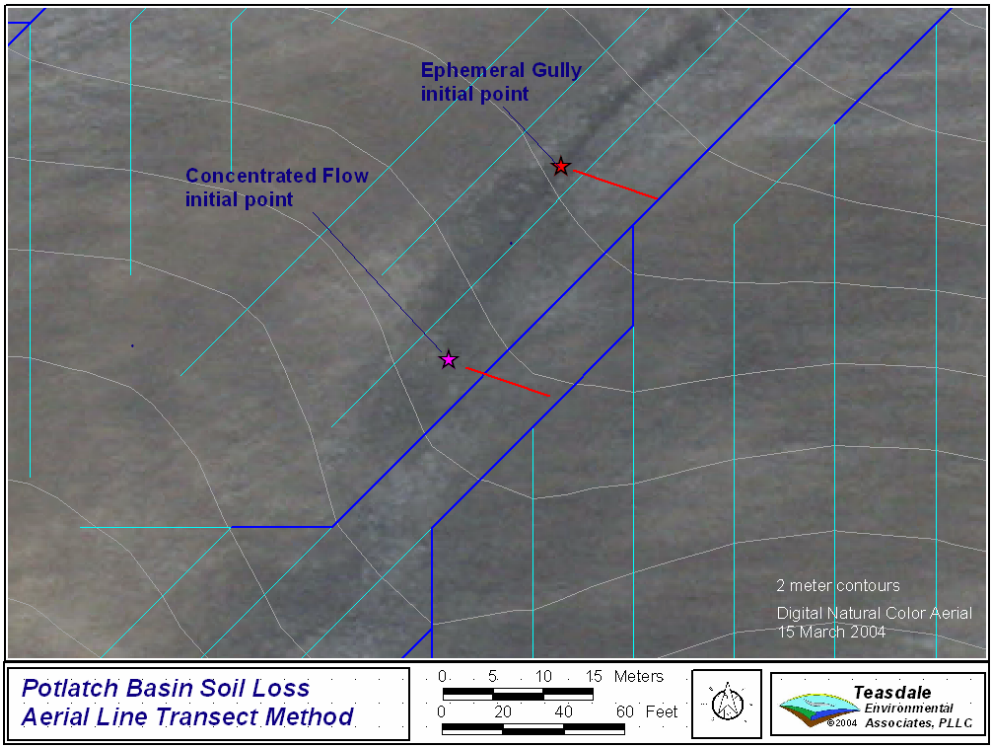

Figure 7.27 Flowpath termination points for hillslope soil loss computation.

Flowpath upslope areas marked in Figure 7.26 vary widely though single line flowpaths are roughly the same length. Upslope area at the flowpath terminating at the upper end of the grass waterway is 3 times more than the termination point near the ephemeral gully. The differences are real, as evidenced by the aerial image. No ephemeral gully erosion is seen at the end of the grassed waterway even though the accumulation area is much larger than that of the observed ephemeral gully. Soils, slope angle and tillage treatment are about the same at each location, yet there is no deeply incised gully at the end of the waterway as might be expected based on the existence of the observed gully.

The incongruence observed in the image demonstrates an inherent difficulty with USLE and RUSLE modeling in the Palouse region. Erosivity of precipitation of all forms in USLE-RUSLE is represented completely by the R_{eq} factor. Though R_{eq} has been developed to represent long term climate effects on a regional basis (McCool and Busacca 1999), it does not well represent local variation caused by differential snowmelt in the Palouse topography.

Snowmelt was delayed and prolonged on the northerly slopes in the Potlatch Basin during winter 2003-04. Some snow can still be seen in the March 15, 2004 image on the north facing slope below the “eyebrow” that drains to the upper end of the grass waterway. Slower melt results in lower peak runoff and erosion energy. In other years the effect could reverse if snow stored on north slopes was rapidly melted by warm winds and rain on snow events when more exposed slopes had previously shed snow cover at a slower pace. Freeze and thaw cycling undoubtedly influences the slope aspect effect (McCool et al. 1995).

Flowpaths in Figure 7.26 converge and merge in complex terrain. Evaluation of flowpath convergence has led to an alternative method to evaluate the USLE-RUSLE slope length factor. Tributary area is actually two-dimensional; single hillslope profiles only approximate the hydraulic action of converging sheet and rivlet flow passing through the tributary region (Moore and Burch 1986). Erosion that is not transport-limited is primarily driven by water flow, so it makes sense that a slope length factor based directly on tributary area might be more representative of actual terrain conditions. Desmet and Govers (1996) analyzed the accumulation grid and derived an alternative slope length factor based on tributary area and flow direction:

$$L_{i,j} = (m+1)\left(\frac{A_{i,j-in} + \frac{D^2}{2}}{D \cdot x_{ij}}\right)^m \frac{1}{\lambda_u{}^m} \qquad 7.30$$

where $L_{i,j}$ is the USLE or RUSLE slope length factor at grid cell i,j, $A_{i,j\text{-}in}$ is the tributary area to the cell exclusive of its cell area, D is the width of a grid cell, m is the USLE slope length exponent, and λ_u is the USLE unit plot slope length. Comparison with Equation 7.6 shows that the term in the brackets in Equation 7.30 is an equivalent slope length. The factor x_{ij} is a variable to account for the direction of flow (aspect) through the cells in the rectangular grid and is computed:

$$x_{i,j} = \sin\alpha_{i,j} + \cos\alpha_{i,j} \qquad 7.31$$

where $\alpha_{i,j}$ is the aspect of the flow direction in degrees of azimuth.

Equation 7.30 may be modified for computations in the NWRR with a 10 meter resolution DEM by adopting a slope length exponent of 0.5 (McCool and Busacca 1999),

$$L_{i,j} = 0.101\left(A_{i,j-in} + 50\right)^{0.5} \quad \text{for cardinal directions} \qquad 7.32$$

$$L_{i,j} = 0.057\left(A_{i,j-in} + 50\right)^{0.5} \quad \text{for noncardinal directions} \qquad 7.33$$

where tributary area is in square meters and cardinal flow directions are 0°, 90°, 180°, 270°. The slope length factor computed from tributary area varies by several hundred percent for tributary areas expected in Palouse topography (Figure 7.28).

A comparison of Equations 7.32 and 7.33 shows that the effect of non-orthogonal flow is to reduce the *L* factor to about half that of orthogonal flow. Some studies assume only orthogonal flow (Fernandez et al. 2003; Fu et al. 2002; Mitasova et al. 1996), but the reason is not clear. An orthogonal only version of Equation 7.30 was not offered by Desmet and Govers, but it does simplify GIS analysis because x_{ij} is equal to 1.0 for orthogonal directions; no conditional processing is required. Figure 7.26 shows that many of the flowpaths in typical Palouse topography flow in non-orthogonal directions so the effect is not insignificant.

A grid surface of slope length factors can be computed in ArcView Spatial Analyst with Equations 7.32 and 7.33. This surface gives the *L* value for each grid cell point in the DEM coverage. The original Desmet and Govers study (1996) indicated significant differences in *L* factors computed from tributary area compared with single flowpath selection techniques. An exclusive recommendation is not yet supportable. The tributary area method offers analytical advantages when processing DEMs and probably assures more representative assessments of large areas.

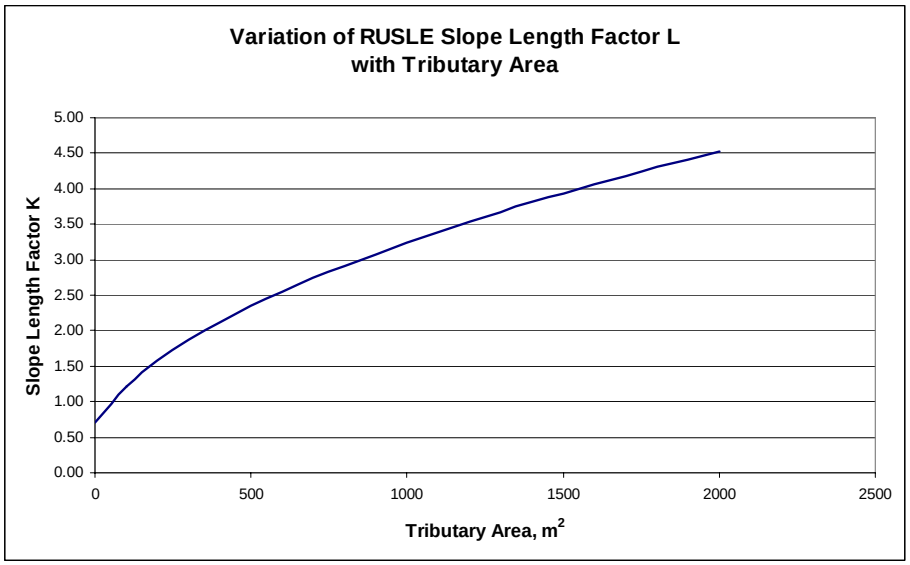

Figure 7.28 Variation of slope length factor with tributary area.

The ArcView interface for the WEPP model, GeoWepp offers a selection of techniques to derive representative flowpaths described as the flowpath method (Cochrane and Flanagan 1999) and the hillslope methods (Cochrane and Flanagan 2003). In the hillslope method, a representative flowpath length is computed by an area-weighted-average of all possible flowpaths on the hillslope.

Converging (codependent) flowpaths are weighted by applying a representative width for a particular flowpath computed from the total tributary area of the set of codependent flowpaths. In an analysis of grid cells the representative width for a particular flowpath is the total drainage area of the codependent flowpaths divided by the length of the particular flowpath. The representative area for all codependent flowpaths in the Cochrane and Flanagan method is always the total drainage area of the set of codependent flowpaths. Only the top part of a particular flow path, from its source point to its first intersection with another flowpath, is an independent contribution to the overall

estimate. Information from the lower part of a codependent flowpath is redundant with other codependent flowpaths.

Redundancy at the lower end of codependent flowpaths is important when contemplating flowpath averaging methods. In WEPP, the flowpath method computes a final erosion estimate for a set of codependent flowpaths as a simple average of the particular flowpath erosion estimates. This method always underestimates erosion by diminishing the effect of flow accumulation. The amount of bias depends on the redundancy or length of profile shared by codependent flowpaths. On uniform slopes that are not transport limited, soil erosion increases with flow rate. Erosion along a grid cell flowpath increases as flow accumulates in successive cells. Flow can be contributed by cells along the flow path or added at junctions with other flowpaths. An averaging scheme is biased if does not represent the effect of the actual cumulative flow through the network of cells.

A simple example of the flowpath method demonstrates the bias. A grid cell representation of three codependent flowpaths is shown in Figure 7.29. This example is fairly realistic of hillslopes in Palouse terrain represented by 10 meter DEM grid cells. Terrain gradient is nearly uniform such that flow is routed along the flowpaths as indicated on the left side of the figure. Total drainage area is 10 cells (0.1 ha). Assuming uniform precipitation, flow is proportional to tributary area. Since erosion increases with cumulative flow, a measure of total erosion is the sum of the individual cumulative flow values of all cells. The right side of the figure shows the true accumulation of flow (tributary area) for the network of cells. Adding all the cumulative values noted in the

grid cells of the right side of Figure 7.29 gives a value of 44. This value represents the combined erosion effect of all cells in the network.

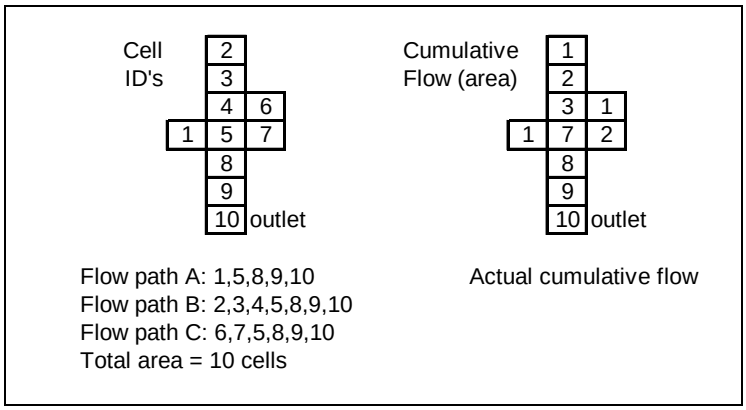

Figure 7.29 Grid cell representation of codependent hillslope flowpaths.

Computations in Table 7.7 show how total erosion is estimated for each codependent flowpath by apportioning the total tributary along the length of the flowpath in the Cochrane and Flanagan method. Flow in flowpath A is 5 cells long (50 meters) and is routed through cells 1, 5, 8, 9, and 10. Assumed drainage area for flowpath A is the total area of 10 cells. The representative width is the total area divided by the number of cells in the flow path, 10 divided by 5 or 2 cells for flowpath A. Tributary area to each cell along flowpath A is the representative width times the cell length, or 2 cells of tributary area per cell of length.

For simplicity a uniform precipitation depth of one unit is assumed for all cells, so the cumulative flow (the erosion effect) is the sum of the cumulative tributary area. The erosion estimate for flow path A is then the total sum of cumulative flows to each cell in the flowpath; 2 + 4 + 6 + 8 + 10 or 30. Since the actual erosion effect is 44, the estimate from flowpath A underestimates the erosion effect by -32 percent. Similarly, the bias of flow paths B and C are -9 and -20 percent. The overall estimate is the simple average of

the three flowpath estimates, 105 divided by 3 or 35. The bias of the overall estimate is then -20 percent. Biases of the Cochrane and Flanagan method will always be negative because flowpath redundancy always diminishes the cumulative flow effect.

	Flowpath A			Flowpath B			Flowpath C		
	Cell ID	Tributary Area	Cumulative Flow	Cell ID	Tributary Area	Cumulative Flow	Cell ID	Tributary Area	Cumulative Flow
				2	1.43	1.43			
Grid				3	1.43	2.86	6	1.67	1.67
Cells	1	2.00	2.00	4	1.43	4.29	7	1.67	3.33
in	5	2.00	4.00	5	1.43	5.71	5	1.67	5.00
Flowpath	8	2.00	6.00	8	1.43	7.14	8	1.67	6.67
	9	2.00	8.00	9	1.43	8.57	9	1.67	8.33
	10	2.00	10.00	10	1.43	10.00	10	1.67	10.00
Number of cells	5			7			6		
Representative width	2.00			1.43			1.67		
Total tributary area		10.0			10.00			10.00	
Total cumulative flow			30.00			40.00			35.00
Bias			-32%			-9%			-20%

Table 7.7 Example of Cochrane and Flanagan flowpath weighting method.

The consistent reduction in predicted hillslope erosion is seen in data presented by Cochrane and Flanagan (1999). Table 7.8 is a summary of three methods of determining representative hillslopes for WEPP: the manual method, a representative hillslope area method, and the flowpath method. The flowpath method estimates are negatively biased except for one comparison with the manual method. Negative bias of the flow path method is about 20 percent averaged across the sites. Cochrane and Flanagan (1999) recognized the data suggested the flowpath method consistently underestimated erosion and attributed it to “the large amount of weighting involved in the method”. The flowpath method is still an option in GeoWEPP.

To summarize, hillslope methods of determining representative erosion flowpaths for WEPP soil loss computations evolved from practical field techniques (Renard et al. 1996; Wischmeier and Smith 1965; Wischmeier and Smith 1976) and were adapted to utilize digital elevation data (Cochrane and Flanagan 2003). The WEPP hillslope

methods are consistent with the assertion that erosion characteristics of a homogeneous two-dimensional hillslope area can be adequately represented by a single one-dimensional composite flowpath. This assumption may not be proven theoretically for real surfaces composed of converging flowpaths, but it is sufficient for practical use.

WEPP predicted hillslope erosion					
Site	Manual method kg	Hillslope method kg	Flowpath method kg	Deviation Manual method	Deviation Hillslope method
Watkinsville, P1	160,900	118,500	107,700	-33%	-9%
Watkinsville, P2	37,300	35,700	21,900	-41%	-39%
Holly Springs, WC1	300,600	546,300	449,100	49%	-18%
Holly Springs, WC3	136,700	146,700	122,200	-11%	-17%
Holly Springs, WC3	111,000	81,100	64,800	-42%	-20%
Trynor, W2	2,173,100	1,946,100	1,547,200	-29%	-20%
Average				-18%	-20%

Table 7.8 Comparison of WEPP profile determination methods (Cochrane and Flanagan 1999).

The discussion in this section shows that digital elevation data have become an important component of soil loss estimation procedures and soil erosion modeling. The research of digital terrain assessment for soil erosion modeling is far from complete. It is not possible at this point to define best practice use of digital elevation data in soil loss estimation. Future research should investigate the conditions in which the USGS NED does not adequately represent large scale terrain variation for soil erosion modeling. The examples and discussion in this section and Sections 3, 4 and 8 suggest a realistic approach for such a study using seasonal high-resolution aerial imagery.

7.6 Soil Loss Estimates for Large Areas

Soil loss computed for the USLE and RUSLE one-dimensional profile has dimensions of mass per unit area. No information collected during parameterization of

the profile suggests how well the profile represents the hillslope in the vicinity of the profile. USLE and RUSLE parameters were developed from erosion plots about 40 feet wide. The plot-based soil loss estimation methodology must be extended to develop best practice estimates of soil loss for large areas.

Watershed scale soil erosion modeling is usually performed with computer models such as SWAT, WEPP, HSPF, AGNPS and more recently the Kinematic Runoff and Erosion model (KINEROS). As noted above WEPP is usually applied to small watersheds. These GIS-enabled models provide a convenient means to compute soil loss and route sediment through a drainage network. There is a large gap in the soil loss estimation technology between the profile-based best practice estimates of soil loss and the watershed scale models. The gap is significant because at present it appears only the USLE/RUSLE methods are acceptable for federal soil conservation planning under the enabling legislation. This dissertation research suggests how this gap may be bridged with a combination of aerial survey techniques, high-resolution aerial imagery and medium resolution satellite imagery.

Statistical sampling methods can extend RUSLE soil loss for profiles to larger areas. Several methods have been suggested (Foster et al. 2003; Griffin et al. 1988). One method is to estimate erosion at a selection of sample points. Erosion computations are based on a one foot long segment, slope length to the point and values for steepness, soil, and cover and management at the point. This approach is likely most compatible with the intent and design of RUSLE2.

An alternative approach is to determine slope length through the point that extends to the location of initial deposition or to a concentrated flow area. Erosion

computations are based on conditions along the slope length, so are representative of the full slope length not just the sampling point. A third approach, adopted by the NRCS for the National Resources Inventory (NRI), computes soil loss based on the slope length through the point to either the location of deposition or a concentrated flow area and conditions at the point. This approach also does not provide a true estimate of soil loss at the sampling point. It is more difficult, perhaps impossible, to correctly aggregate the sample soil loss estimates to the full area with these later two approaches.

Nonlinearities in the RUSLE equations make it unjustifiable to compute average soil loss for large areas from simple averaged values for slope length and steepness, soil, and cover-management conditions within the inventory area (Foster et al. 2003). The previous section discussed techniques to extract spatially-averaged values of slope gradient and slope length from digital elevation data with GIS software. The effective subbasin slope method (Section 7.4.2) and the digital terrain flow path methods (Section 7.4.4) by themselves do not result in best practice estimates of soil loss because they cannot reliably represent actual soil erosion slope lengths or discriminate invalid flow paths. Assessment of slope length and flow path validity must be made with other information. The only practical source of this information for extensive areas is high-resolution aerial imagery. Techniques for assessing slope profile attributes from high-resolution aerial imagery were suggested in the preliminary example in Section 7.4. The techniques will be more explicitly demonstrated in this section.

7.6.1 Aerial Image Estimate of Soil Loss for a Hillslope Profile

High-resolution natural color aerial images were acquired along parallel north-south transects across the agricultural subbasins of the Potlatch River basin between

March 13 and March 21, 2004. Figure 7.30 shows profiles of first order catchments of fall seeded winter wheat in the Middle Potlatch Creek basin. Aerial images 964 and 965 acquired March 16 overlap to provide stereo coverage. Ground pixel resolution is 20 cm. The aerial images were georeferenced in ArcView© GIS. Contours at 1-meter intervals were derived from the USGS 10-m DEM and superimposed on the image. The catchment divide observed in the stereo view marked with a blue dashed line coincides with the DEM.

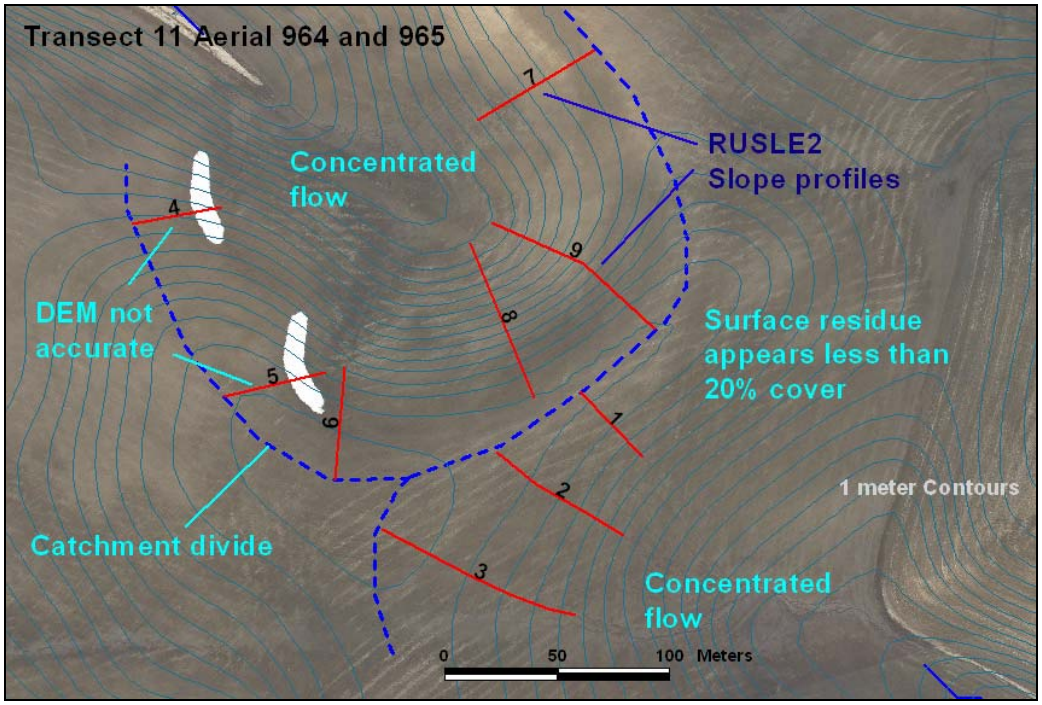

Figure 7.30 Potential RUSLE2 Profiles in a March 16, 2004 aerial image.

Soil color and texture changes indicate locations of recent concentrated flow. This is more apparent under higher magnification. Several ephemeral gullies are observed in the areas of topographic convergence. Potential RUSLE2 hillslope profile lines are superimposed on the aerial image in a polyline shapefile. The upper end of a profile line begins at the catchment divide and is relatively unambiguous, especially when observed in the stereo view. Profile lines extend through areas of rills and end at the likely

beginning of concentrated flow. Selection of the end point is more subjective, but is constrained by indications in the aerial image. A histogram-stretch enhancement of the aerial image in Figure 7.31 accentuates soil color changes and assists in locating the beginning of concentrated flow areas.

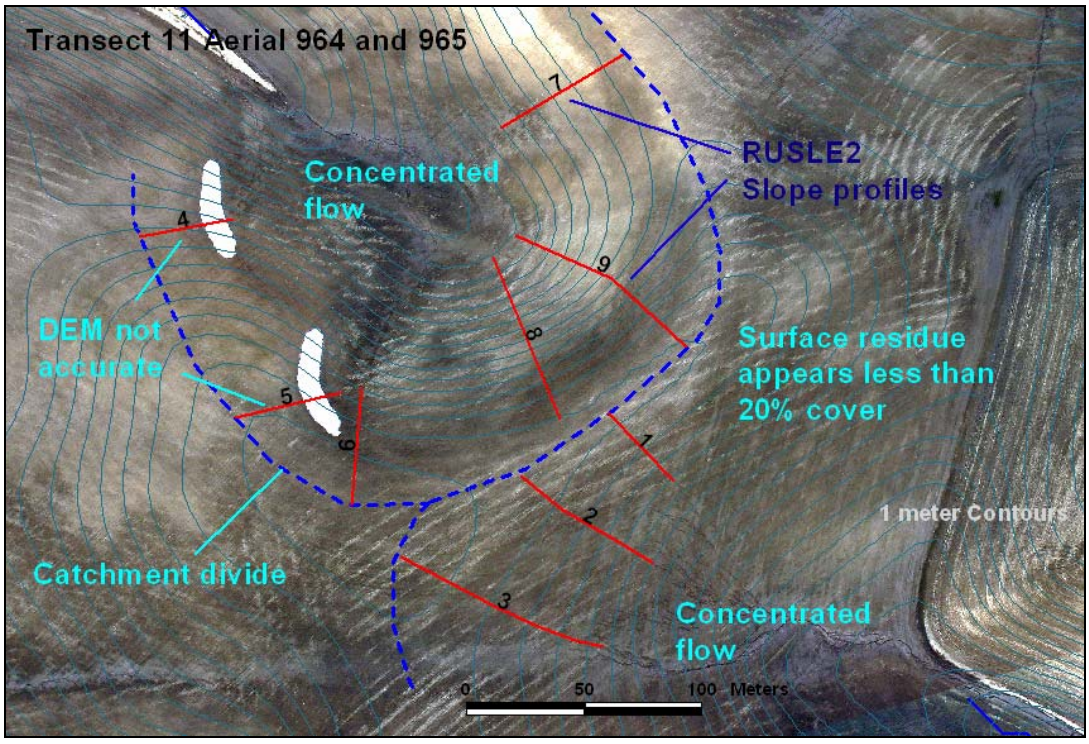

Figure 7.31 Image processed to accentuate rills and ephemeral gullies.

The March 16 aerial images recorded the effects of the preceding runoff cycle. The analyst must judge how far to extend the profile lines (overland flow distances) to represent average conditions assumed by the RUSLE method. In other words, the analyst may truncate the profile line before the observed beginning of concentrated flow if it is thought the current runoff cycle is significantly less than the long-term climatic average. This points out a hydraulic reality not acknowledged in the RUSLE2 guidance: the length of the effective overland flow distance varies with the magnitude of runoff and

it is nearly impossible to define the average profile length in a field survey conducted under benign conditions.

Potential profile lines are placed to represent the range of slopes in the catchments. Profile lines may be placed to represent equal areas in a detailed analysis, but this was not done in this example for clarity. A flowpath analysis of the DEM, such as that provided by GeoWEPP may be performed to *guide* placement of profile lines. As repeatedly stated throughout the dissertation discussion, the USGS 10-meter DEM does not sufficiently represent large scale terrain variation, so final placement and acceptance of hillslope profile lines should be based on interpretation of the high-resolution aerial imagery.

Slope gradient measurements are made from DEM contours and should not be made by querying the DEM grid or automatically generated DEM slope surface. Contouring algorithms smooth errors in the digital elevation data. Potential profile lines are rejected from the analysis if stereo observation or monoscopic interpretive clues indicate that DEM contours do not conform to the actual terrain. Profile lines nos. 4, 5 and 6 in Figure 7.30 are rejected because the actual terrain is steeper than indicated by the contour lines. This is clearly indicated by the snow drifts at the top of the small erosion cirques. Hillslope profile lengths and slope gradients are summarized Table 7.9. The measurements or method do not justify more than two significant digits.

Profile	Soil	Profile Length		Average Slope
		m	ft	Percent
1	Southwick silt loam	40	130	10
2	Southwick silt loam	68	220	8
3	Southwick silt loam	94	310	6
4	Taney silt loam	41		
5	Taney silt loam	46		
6	Taney silt loam	50		
7	Southwick silt loam	61	200	8
8	Taney (Southwick)	74	240	18
9	Taney (Southwick)	87	290	15

Table 7.9 Hillslope profile lengths and slope gradients.

An analyst might wish to estimate the actual slopes for the questionable profile lines in a strict statistical analysis to avoid bias against significant terrain features. It is assumed in this method that slope gradients obtained from the DEM are accurate where the contour lines conform to the observed terrain. The analytical photogrammetry techniques discussed in Section 3 could be utilized for a more precise measurement of slope gradient.

Soil information is obtained from the 1:24,000 scale NRCS SSURGO soil database (http://soildatamart.nrcs.usda.gov/State.aspx). Mapping unit polygons are superimposed over the aerial image in Figure 7.32. Most of the profiles are across Southwick silt loam. Only profiles no. 8 and 9 are across the more erosive Taney silt loam.

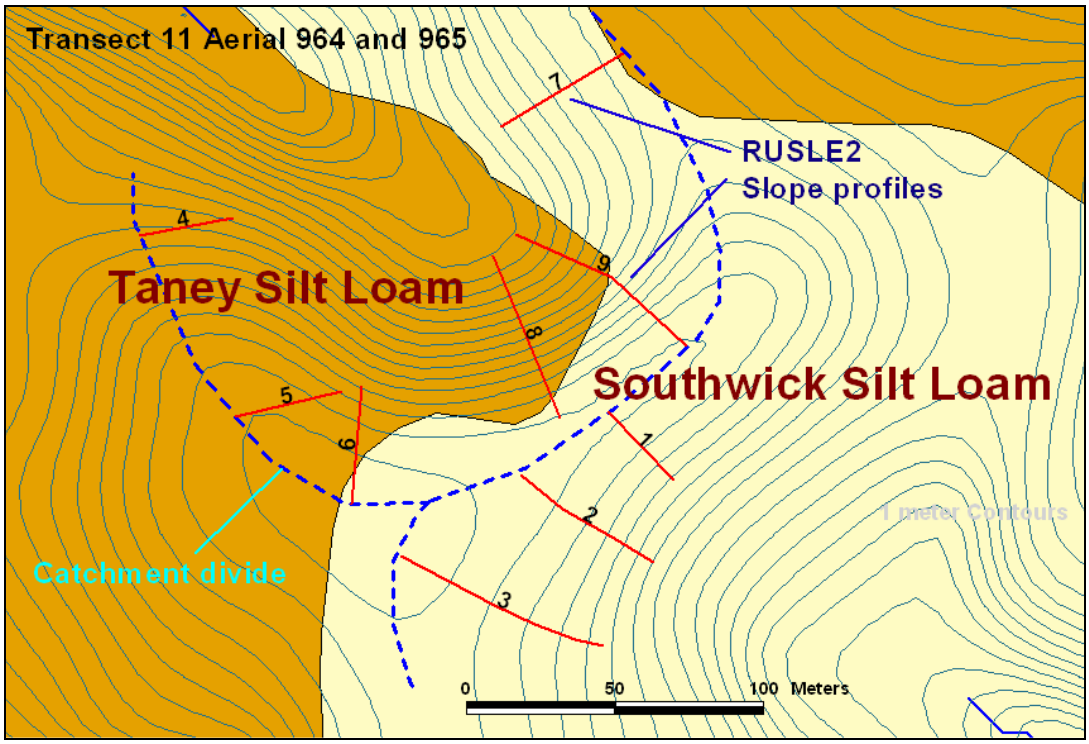

Figure 7.32 Soil types from the SSURGO soils database.

Soil loss for the individual hillslope profiles is evaluated with the RUSLE2 Windows-based software (version 1.18.4.1.0). The site is within the R-equivalent region of Latah County, ID and the mean annual precipitation is between 25 and 30 inches per year. An unmodified crop rotation of conventionally tilled winter wheat – spring wheat – spring barley in Crop Zone 47 was selected from the RUSLE2 database. Normal crop residue and tillage contouring at an absolute gradient of 2 percent is assumed. Uniform hillslope profiles were assumed for simplicity, but could have been represented in segments. The accuracy of the USGS 10-meter resolution DEM probably does not warrant other than an assumption of uniform slope. Profile curvature significantly affects soil loss, so should be represented in best practice estimates if more precise elevation data is available.

Figure 7.33 is the RUSLE2 data entry and computation window for profile no. 1. The slope profile is 130 ft (40 m) long and the gradient is 10 percent. Sediment delivered by the hillslope is 8.7 tons per acre per year (20 Mg ha^{-1} a^{-1}). Soil loss tolerance (T value) specified for Southwick silt loam in the SSURGO database is 4 ton ac^{-1} a^{-1}. Soil loss computations for the other profiles are summarized in Table 7.10. Long term soil loss for conservation planning is estimated at 14.1 ton ac^{-1} a^{-1} for an average T-ratio of 3.5.

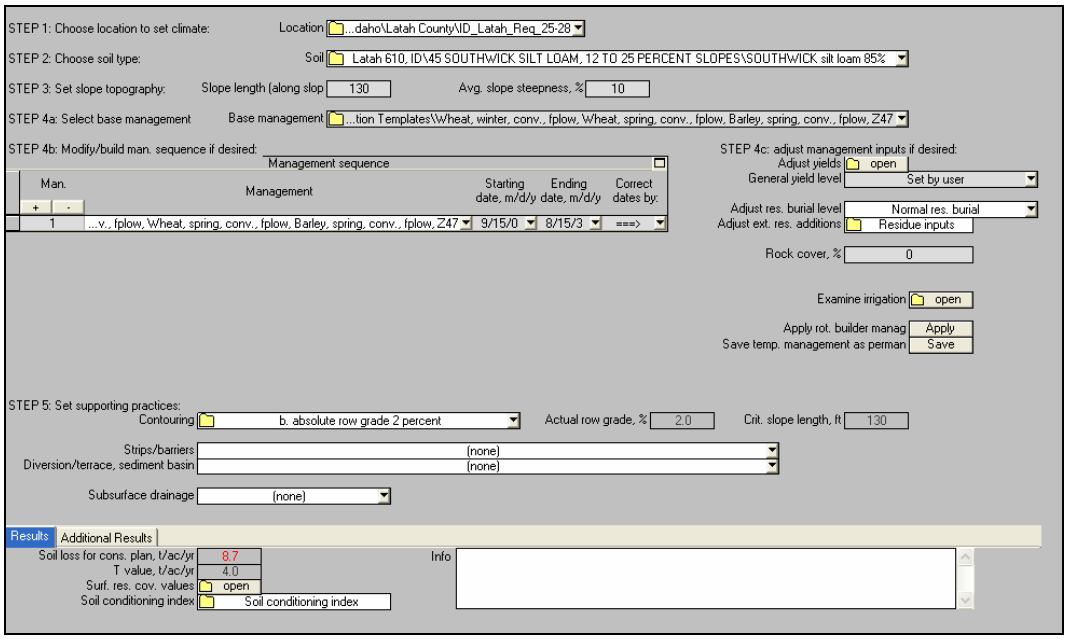

Figure 7.33 RUSLE2 data entry and computation window.

Profile	Soil	Profile Length m	Profile Length ft	Average Slope Percent	Soil Loss ton ac^{-1} y^{-1}	Soil T Value ton ac^{-1} y^{-1}	Ratio
1	Southwick silt loam	40	130	10	8.7	4.0	2.2
2	Southwick silt loam	68	220	8	9.7	4.0	2.4
3	Southwick silt loam	94	310	6	9.1	4.0	2.3
4	Taney silt loam	41					
5	Taney silt loam	46					
6	Taney silt loam	50					
7	Southwick silt loam	61	200	8	9.3	4.0	2.3
8	Taney (Southwick)	74	240	18	24 (15)	4.0	6.0
9	Taney (Southwick)	87	290	15	24 (16)	4.0	6.0
Average					14.1	4.0	3.5

Table 7.10 RUSLE2 Soil loss estimates for Transect 11 Aerial Image 964-965.

It is important to emphasize the relative ease of computing soil loss estimates for alternative conservation scenarios with the RUSLE2 software and digital resources. National elevation data (NED), SSURGO soil data and the state specific RUSLE2 databases are dependably available from federally maintained internet sites. The USDA is committed by legislative mandate to maintain the RUSLE2 technology, so upgrades and extension of the methods should continue to be available. The example analysis was completed in about one hour after initial databases and GIS coverages were prepared. Soil losses for alternative conservation practices can be quickly compared. For example, 10 percent more residue on the surface of profile no. 1 reduces the soil loss estimate to 5.4 ton ac^{-1} a^{-1}. A switch to a no-till rotation of tilled winter wheat – spring wheat – spring barley decreased the soil loss estimate to 1.0 ton ac^{-1} a^{-1}.

A conservation planning estimate of soil loss is almost as easily computed with the WEPP Windows-based hillslope software (version 2004.7). Figure 7.34 is the data entry and computation window for profile no. 1. Climate data for the nearby University of Idaho climate station is included in the CliGen database. Physical parameters for Southwick silt loam are included in the WEPP soils database for Idaho. A conventional

till winter wheat – spring pea rotation was developed from information in the WEPP guidance and example rotations. Average annual sediment yield for this rotation in a 100 year climate simulation is 2.0 ton ac^{-1} a^{-1}.

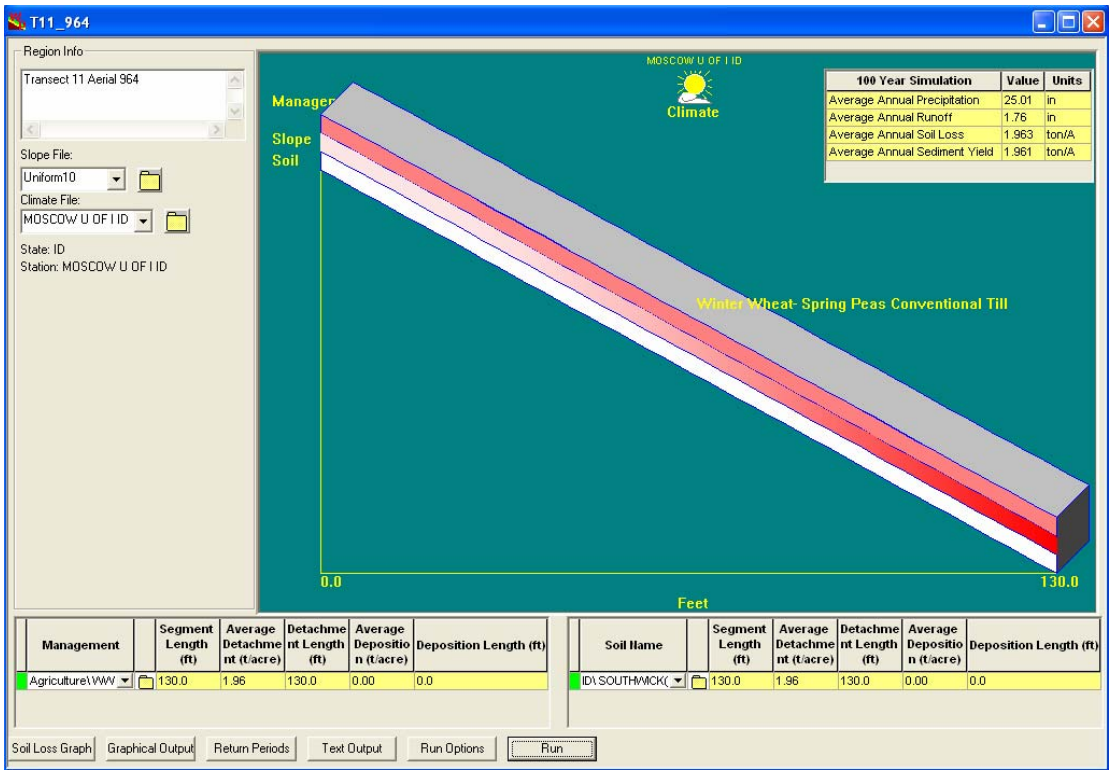

Figure 7.34 WEPP Soil loss estimate for profile no. 1 Transect 11 Aerial 964-965.

The single image analysis can be extended to more image samples from the full set of flight transects. A statistically valid sampling strategy can be developed for individual subbasins or the entire basin using techniques described in Section 4. Formal documentation and testing of a complete aerial survey method of estimating basin wide soil loss and sediment yield would be a very beneficial subject for future research.

7.7 Estimation of Subbasin Soil Erosion Parameters

Semi-empirical lumped parameter watershed models such as the Soil and Watershed Assessment Tool (SWAT) partially avoid the scale limitations of physically based models. They attempt to predict watershed sediment yield by empirical relationships with land cover properties, storm hydrology and other variables. The modeled watershed is subdivided into small relatively homogeneous subbasins commonly called a representative elementary area (REA) or hydrologic response units (HRU) (Kouwen et al. 1993; Maidment and Djokic 2000; Manguerra and Engel 1998; Wood et al. 1988).

Values for relevant hydrologic characteristics are estimated for each HRU and are then treated as independent computational units in the full model linked by a channel system. Subbasin parameters are adjusted to match basin response to measured flow and water quality. Subbasin parameters should accurately represent the actual physical characteristics of the subbasin for best practice modeling or the modeling effort degenerates into a data matching exercise of questionable validity. Such modeling efforts have been severely criticized by the scientific community (Oreskes et al. 1994). Physically realistic and more accurate subbasin parameters can be determined with the aerial survey and satellite imagery techniques demonstrated in this dissertation work.

Soil erosion routines in SWAT adopt the Modified Universal Soil Loss Equation (MUSLE) developed by Williams (1977) which takes the form:

$$sed = a\left(Q_{surf}\ q_{peak}\ area_{hru}\right)^{b} K_{USLE}\ C_{usle}\ P_{USLE}\ LS_{USLE}\ CFRG \qquad 7.34$$

where *sed* is the sediment yield on a given day (metric tons), Q_{surf} is the surface runoff volume (mm H_2O/ha), q_{peak} is the peak runoff rate (m^3/s), $area_{hru}$ is the area of the

hydrologic response unit (ha), K_{USLE} is the Uniform Soil Loss Equation (USLE) soil erodibility factor (0.013 metric ton m^2 hr/(m^3-metric ton cm)), C_{USLE} is the USLE cover and management factor, P_{USLE} is the USLE support practice factor, LS_{USLE} is the USLE topographic factor and *CFRG* is the coarse fragment factor. This approach bypasses computation of the sediment delivery ratio. The MUSLE hydrologic parameter group, $a\left(Q_{surf}\ q_{peak}\ area_{hru}\right)^b$, represents runoff energy and replaces the rainfall erosivity factor in the USLE and Revised USLE.

Williams developed constants a =11.8 and b=0.56 for the hydrologic parameter group with sediment yield data from 778 storms in *Texas and Nebraska* for watersheds ranging from 3 to 4380 acres and on slopes between 1 and 6 percent. These constants have been incorporated into the SWAT sediment yield computations. Research with the Revised USLE (Michalson, Papendick et al. 1999) has shown that standard rainfall energy factor is inadequate to represent the winter hydrologic response of soils within the Wheat and Range Region of the interior Pacific Northwest. The standard rainfall energy factor was modified in the RUSLE model to account for the rain on thawing soil events that produce the most significant erosion. Undoubtedly the SWAT hydrologic parameter group (runoff energy factor) must also be modified or replaced to best represent hydrologic conditions within the interior Pacific Northwest. The constants of the hydrologic parameter group should be modified based on local research (Blaszczynski 2003).

An initial SWAT model is relatively rapid to develop with the AVSWAT ArcView© GIS extension. Figure 7.35 is the main SWAT window for the Middle Potlatch Creek basin. The outlined and numbered subbasins were extracted from a NED

30-meter DEM with a watershed threshold size of 400 ha. Multple HRU's were initially defined for each unique combination of SSURGO soil type and land cover type from the USGS National Land Cover Dataset (NLCD). The HRU's within each subbasin are not routed separately. Flow routing is performed at the subbasin level.

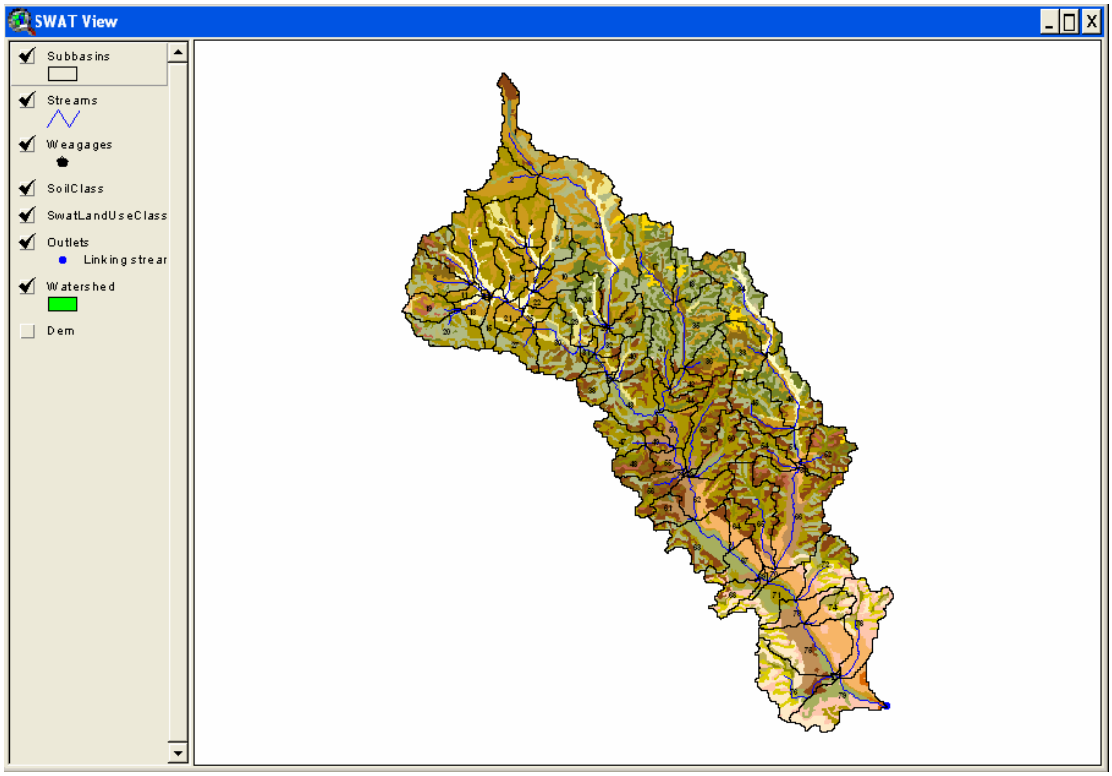

Figure 7.35 Initial SWAT Model of the Middle Potlatch Creek basin

Ultimately, the SSURGO soil data polygon shapefile defines the level of detail to be ascertained from satellite and aerial imagery. March 2004 flight lines and two aerial images acquired on March 16, 2004 are superimposed on the SWAT soil theme in Figure 7.36. Different procedures for incorporating the high-resolution aerial image information into SWAT are possible. One of the most direct is to modify the subbasin HRU files (text or dbf) based on an evaluation of the aerial image. An expedient method is to examine the automatically generated SWAT model input and modify it as needed

with current information from the aerial image. In other words, the analyst compares and "challenges" the automatically generated parameters with observations from the aerial and satellite imagery. The automatically generated parameters are changed only if the analyst judges the difference to be hydrologically significant.

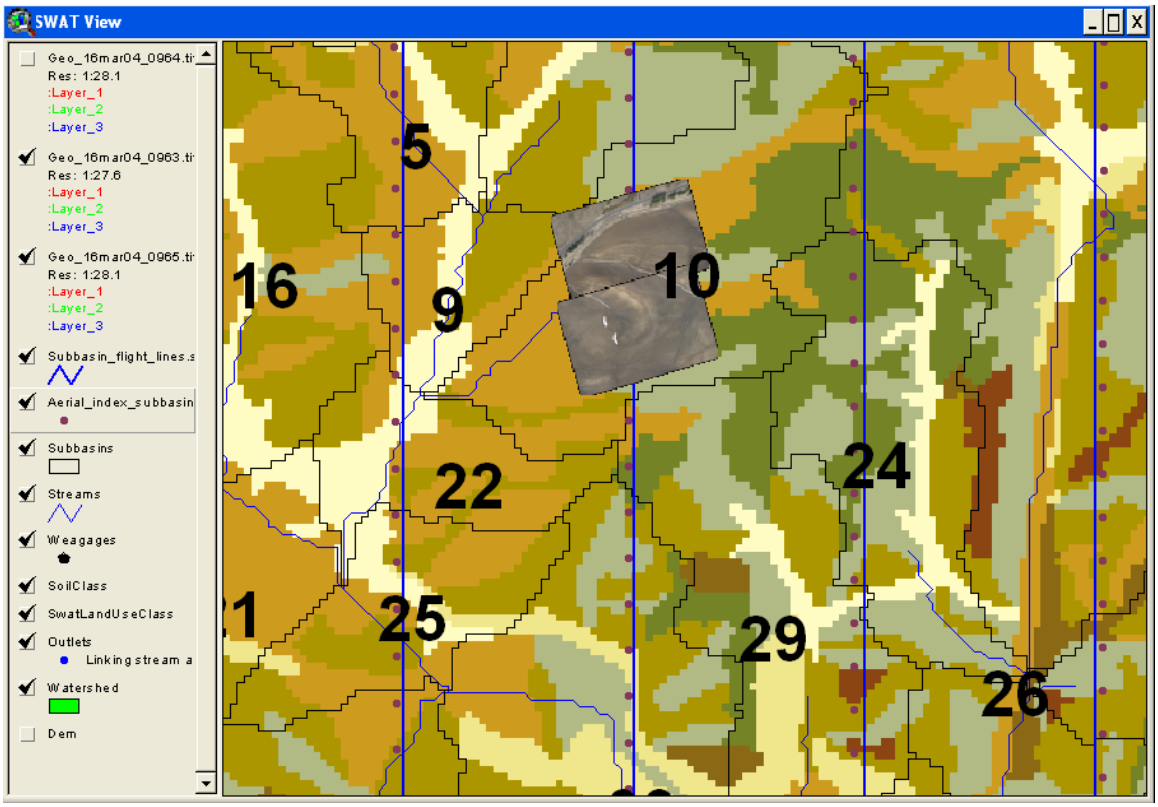

Figure 7.36 March 2004 flightlines and aerial images superimposed on the SWAT data themes.

An excerpt from the SWAT model HRU file for HRU 2 in subbasin 10 of the Middle Potlatch basin is given in Figure 7.37. The average slope length and slope would be changed if the methods of Section 7.5 indicated a significant difference. There are three HRU's in subbasin 10; by default each has the same slope and slope length.

```
.hru file Subbasin:10 HRU:2 Luse:AGRC Soil:A79542 Tue Dec 23 21:21:26 2004
AVSWAT2000 - SWAT interface MDL
     0.0056630    | HRU_FR : Fraction of total watershed area contained in HRU
       60.976     | SLSUBBSN : Average slope length \
        0.080     | SLOPE : Average slope stepness (m/m)
        0.140     | OV_N : Manning's "n" value for overland flow
```

Figure 7.37 SWAT input file for HRU 2 in subbasin 10 of the Middle Potlatch basin.

The relative area of the land use type, in this case close seeded winter wheat (AGRC), could be changed if a joint analysis of the satellite and aerial imagery as demonstrated in Section 5 indicated a change was warranted. A decrease in the fraction of watershed in one HRU of a subbasin must be compensated by increase in the fraction area of another HRU in the same subbasin. The fractional area of SSURGO soil type would not normally be changed unless it was hydrologically isolated or converted to an impervious land type.

The process of modifying the subbasin parameters to reflect observed reality is not difficult, but does take effort. There are 79 subbasins and a total of 411 HRU's that must be challenged and verified in the Middle Potlatch Creek basin. It is important to realize that prior to examining the aerial imagery, the modeler has no real proof that the default model based on SSURGO, NED and NLCD data is an accurate representation of the actual physical characteristics of the watershed. Even a modest effort of comparing a sample of automatically generated subbasins with corresponding aerial images greatly increases a modeler's knowledge of how well the model represents reality.

Development and description of the full SWAT model procedure is unnecessary in this discussion and would be mostly redundant to model documentation and training materials (Neitsch et al. 2000). It is important to emphasize that the coefficients on the MUSLE formulation in SWAT have not been adapted to snowmelt runoff conditions of

the Palouse region, thus any SWAT model output for the Palouse region is questionable. Further, crop rotation management files have not been developed for the Palouse region and default values are difficult to verify from references cited in the documentation. Both these aspects of watershed modeling in the Palouse region would be beneficial subjects for future research.

7.8 Summary

This section examined current methods of estimating soil loss and sediment yield from mixed use and agricultural watersheds with the objective of identifying where and how aerial survey methods and high-resolution aerial imagery measurements can enhance existing approaches. The discussion emphasized technical aspects of soil loss computations and avoided discussion of difficult soil conservation and economic issues. The perspective offered is one of sediment production and estimation of soil loss on a watershed scale.

Aerial survey and high-resolution aerial imagery analysis are clearly underutilized in current soil erosion modeling practice. There are no technical barriers to wider use of the techniques discussed and demonstrated. The limited use of high-resolution aerial imagery in soil erosion assessment is most likely due to the perception that seasonal high-resolution aerial images are difficult to acquire, process and analyze. Digitization of aerial imagery and the analysis techniques have removed this limitation. Aerial imaging survey methods and analyses are relatively easy to apply and are efficient for soil erosion evaluation over extensive areas. The science and engineering of soil conservation and soil erosion modeling would benefit from wider adoption of these methods.

References for Section 7

Band, L. E. (1986). "Topographic Partition of Watersheds with Digital Elevation Models." *Water Resources Research*, 22(1), 15-24.

Becknell, B. R., Imhoff, J. C., Kittle, J. L., Donigian, A. S., and Johanson, R. C. (1993). *Hydrological simulation program: FORTRAN. User's manual for release 10.*

Belcher, D. J. (1997). "Chapter 4 Soils." Manual of Photographic Interpretation, W. R. Philipson, ed., American Society for Photogrammetry and Remote Sensing, Bethesda, 167-223.

Bergsma, E. (1974). "Soil erosion sequences on aerial photographs." *ITC Journal*, 1974(3), 342-376.

Carroll, T. (2001). *Airborne gamma radiation airborne gamma radiation snow survey program snow survey program: A User's Guide A User's Guide Version 5.0*, National Operational Hydrologic Remote Sensing Center, Office of Climate, Water, and Weather Services,National Weather Service, NOAA, Chanhassen, MN.

Castro, C. D., and Zombeck, T. M. (1986). "Evaluation of the topographic factor in the universal soil loss equation on irregular slopes." *Journal of Soil & Water Conservation*, 41, 113-116.

Cochrane, T. A., and Flanagan, D. C. (1999). "Assessing water erosion in small watersheds using WEPP with GIS and digital elevation models." *Journal of Soil & Water Conservation*, 54(4), 678-685.

Cochrane, T. A., and Flanagan, D. C. (2003). "Representative hillslope methods for applying the WEPP Model with DEMs and GIS." *Transactions of the American Society of Agricultural Engineers*, 46(4), 1041-1049.

Conservation Technology Information, C. (2003). "National Crop Residue Management Survey, Conservation Tillage Data. Online at http://www.ctic.purdue.edu/CTIC/CRM.html."

Desmet, P. J. J., and Govers, G. (1996). "A GIS procedure for automatically calculating the USLE LS factor on topgraphically complex landscape units." *Journal of Soil & Water Conservation*, 51(5), 427-433.

Di Luzio, M., Srinivasan, R., Arnold, J. G., and Neitsch, S. L. (2002). *ArcView Interface for SWAT2000*, USDA Agricultural Research Service, Temple, TX.

Di Stefano, C., Ferro, V., Porto, P., and Tusa, G. (2000). "Slope curvature influence on soil erosion and deposition processes." *Water Resources Research*, 36(2), 607-617.

Endreny, T. A., Wood, E. F., and Lettenmaier, D. P. (2000). "Satellite-derived digital elevation model accuracy: hydrological modelling requirements." *Hydrological Processes*, 14(2), 177-194.

England, C. B., and Holtan, H. N. "Geomorphic grouping of soils in watershed engineering." *Annual meeting of the Americal Society of Agronomy*, Washington, DC.

Engman, E. T. (2000). "Soil Moisture." Remote Sensing in Hydrology and Water Management, G. A. Schultz and E. T. Engman, eds., Springer, New York, 197-216.

Fernandez, C., Wu, J. Q., McCool, D. K., and Stockle, C. O. (2003). "Estimating water erosion and sediment yield with GIS, RUSLE and SEDD." *Journal of Soil & Water Conservation*, 58(3), 128-136.

Ferro, V., and Porto, P. (2000). "Sediment delivery distributed (SEDD) model." *Journal of Hydrologic Engineering*, 5(4), 411-422.

Flanagan, D. C., and Livingston, S. J. (1995). "WEPP User Summary, NSERL Report No. 11." National Soil Erosion Research Laboratory, West Lafayette, IN.

Flanagan, D. C., and Nearing, M. A. (1995). "Water Erosion Prediction Project (WEPP) Hillslope Profile and Watershed Model Documentation, NSERL Report No. 10." National Soil Erosion Research Laboratory, West Lafayette, IN, 142.

Foster, G. R. (1982). "Modeling the Erosion Process." Hydrologic Modeling of Small Watersheds, C. T. Haan, H. P. Johnson, and D. L. Brakensiek, eds., American Society of Agricultural Engineers, St. Joseph, MO, 297-380.

Foster, G. R., and Meyer, L. D. "A closed-form soil erosion equation for upland areas." *Sedimentation: Symposium to honor Professor H.A. Einstein*, Ft. Collins, CO.

Foster, G. R., and Wischmeier, W. H. (1974). "Evaluating irregular slopes for soil loss prediction." *Transactions of the American Society of Agricultural Engineers*, 17(2), 305-309.

Foster, G. R., Yoder, D. C., Weesies, G. A., McCool, D. K., McGregor, K. C., and Bingner, R. L. (2003). *User's Guide: Revised Universal Soil Loss Equation Version 2(RUSLE2), January 2003*, USDA-Agricultural Research Service, Washington, DC.

Foster, G. R., Yoder, D. C., Weesies, G. A., and Toy, T. J. "The Design Philosophy Behind RUSLE2: Evolution of an Empirical Model." *Soil Erosion Research for the 21st Century, Proc. Int. Symp.*, Honolulu, HI, 95-98.

Fraser, R. H., Warren, M. V., and Barten, P. K. (1995). "Comparative evaluation of land cover data sources for erosion prediction." *Water Resources Bulletin*, 31(6), 991-1000.

Frazier, B. E., and McCool, D. K. (1981). "Aerial Photography to Detect Rill Erosion." *Transactions of the ASAE*, 24(5), 1168-1171.

Frazier, B. E., McCool, D. K., and Engle, C. F. (1983). "Soil Erosion in the Palouse: An Aerial Perspective." *Journal of Soil and Water Conservation*, 38(2), 70-74.

Fu, G., Chen, S., and McCool, D. K. "Soil erosion and its response to no-till practice estimated with ArcView GIS, Paper No: 032288." *2002 ASAE Annual International Meeting*, Las Vegas, NV, 15.

Garbrecht, J., and Martz, L. W. (1997). *TOPAZ: an Automated Digital Landscape Analysis Tool for Topographic Evaluation, Drainage Identification, Watershed Segmentation, and Subcatchment Parameterization: Overview. ARS-NAWQL 95-1*, U.S.D.A. Agricultural Research Service, El Reno, OK.

Gluth, P. (2004). "MicroDEM analysis software, on line at http://www.usna.edu/Users/oceano/pguth/website/microdem.htm." Oceanography Department, U.S. Naval Academy.

Griffin, M. L., Beasley, D. B., Fletcher, J. J., and Foster, G. R. (1988). "Estimating soil loss on topographically nonuniform field and farm units." *Journal of Soil & Water Conservation*, 43, 326-331.

Haan, C. T., Barfield, B. J., and Hayes, J. C. (1994). *Design Hydrology and Sedimentology for Small Catchments*, Academic Press, San Diego, CA.

Harvey, M. D., Watson, C. C., and Schumm, S. A. (1985). *Gully Erosion, Technical note 366*, Bureau of Land Management, U.S. Department of Interior, Denver Services Center, Denver, CO.

Houser, P. R., Shuttleworth, W. J., Famiglietti, J. S., Gupta, H. V., Syed, K. H., and Goodrich, D. C. (1998). "Integration of soil moisture remote sensing and hydrologic modeling using data assimilation." *Water Resources Research*, 34(12), 3405-3420.

Hutchinson, J. M. S. (2003). "Estimating near-surface soil moisture using active microwave satellite imagery and optical sensor inputs." *Transactions of the American Society of Agricultural Engineers*, 46(2), 225-236.

Jenson, S. K., and Domingue, J. O. (1998). "Extracting Topographic Stucture from Digital Elevation Data for Geographic Information System Analysis." *Photogrammetric Engineering and Remote Sensing*, 54, 1593-1600.

Kenward, T., Lettenmaier, D. P., Wood, E. F., and Fielding, E. (2000). "Effects of Digital Elevation Model Accuracy on Hydrologic Predictions." *Remote Sensing of Environment*, 74(3), 432-444.

King, D. J. "Development of an airborne multispectral digital frame camera sensor." *15th Biennial Workshop on Videography and Color Photography in Resource Assessment*, Terre Haute, Indiana, 13-21.

Kirkham, V. R. D., Johnson, M. M., and Holm, D. (1941). "The origin of the Palouse Hills topography." *Science*, 73, 207-209.

Klik, A., and Zartl, A. S. "Comparison of Soil Erosion Simulations Using WEPP and RUSLE with Field Measurements." *Soil Erosion Research for the 21st Century, Proc. Int. Symp.*, Honolulu, HI, 350-353.

Kouwen, N., Soulis, E. D., Pietroniro, A., Donald, J., and Harrington, R. A. (1993). "Grouped Response Units for Distributed Hydrologic Modeling." *Journal of Water Resources Planning and Management*, 119(3), 289-305.

Kuenstler, B. (2004). "RUSLE2 Training materials, online at http://fargo.nserl.purdue.edu/rusle2_dataweb." USDA-Agricultural Research Service.

Lee, Y. H., and Singh, V. P. (1999). "Prediction of sediment yield by coupling Kalman filter with instantaneous unit sediment graph." *Hydrological Processes*, 13(17), 2861-2875.

Lueder, D. R. (1959). *Aerial Photographic Interpretation*, McGraw-Hill, New York.

Maidment, D., and Djokic, D. (2000). "Hydrologic and Hydraulic Modeling." Environmental Systems Research Institute (ESRI), Redlands, CA, 216.

Maidment, D. R., Wright, S. G., and Jones, N. L. (1990). "Watershed Delineation with Triangle-Based Terrain Models."

Manguerra, H. B., and Engel, B. A. (1998). "Hydrologic parameterization of watersheds for runoff prediction using SWAT." *Journal of the American Water Resources Association*, 34(5), 1149-1162.

Mashriqui, H. S., and Cruise, J. F. (1997). "Sediment yield modeling by grouped response units." *Journal of Water Resources Planning and Management*, 123(2), 95-104.

McCool, D. K., and Busacca, A. J. (1999). "Measuring and modeling soil erosion and erosion damages." Conservation Farming in the United States: The Methods and Accomplishments of the STEEP Program, CRC Press, Boca Raton, 23-56.

McCool, D. K., Walter, M. T., and King, L. G. (1995). "Runoff index values for frozen soil areas in the Pacific Northwest." *Journal of Soil and Water Conservation*, 50(5), 466-469.

Michalson, E. L., Papendick, R. I., and Carlson, J. E. (1999). *Conservation Farming in the United States: The Methods and Accomplishments of the STEEP Program*, CRC Press, Boca Raton.

Mitasova, H., Hofierka, J., Zlocha, M., and Iverson, L. R. (1996). "Modeling topographic potential for erosion and deposition using GIS." *Journal of Geographical Information Science*, 10(5), 629-641.

Moore, I. D., and Burch, G. J. (1986). "Modelling erosion and deposition: topographic effects." *Transactions of the ASAE*, 29(6), 1624-1630.

Morgan, K. M., Morris-Jones, D. R., Lee, G. B., and Kiefer, R. W. (1980). "Airphoto analysis of erosion control practices." *Photogrammetric Engineering and Remote Sensing*, 46(5), 637-640.

Morgan, K. M., and Nalepa, R. (1982). "Application of Aerial Photographic and Computer Analysis to the Usle for Areawide Erosion Studies." *Journal of Soil and Water Conservation*, 37(6), 347-350.

Nash, J. E., and Sutcliffe, J. E. (1970). "River flow forecasting through a conceptual model." *Journal of Hydrology*, 10, 282-290.

Neitsch, S. L., Arnold, J. G., Kiniry, J. R., Williams, J. R., and King, K. W. (2002). *Soil and Water Assessment Tool Theoretical Documentation, Version 2000*, Agricultural Research Service, Grassland Soil and Water Research Laboratory, Temple, TX.

Neitsch, S. L., Arnold, J. G., and Williams, J. R. (2000). *Soil and Water Assessment Tool User's Manual, Version 2000*, Agricultural Research Service, Grassland Soil and Water Research Laboratory, Temple, TX.

NRCS. (1993). *Soil Survey Manual, 3rd Ed., Handbook No. 18*, Agriculture Dept., Soil Survey Division.

NRCS. (1996). "Federal Register, Vol. 61, No. 108 of Tuesday, June 4, 1996." Natural Resource Conservation Service, Washington, DC.

Nrcs. (2003). *Findings From 1997 NRI (Idaho), On-line at http://www.id.nrcs.usda.gov/technical/nri/find97.html*, Natural Resources Conservation Service, U.S. Department of Agriculture, Boise.

Oreskes, N., Shrader-Frechette, K., and Belitz, K. (1994). "Verification, validation, and confirmation of numerical models in the earth sciences." *Science*, 263(5147), 641-646.

Ottle, C., Vida-Madjar, D., Cognard, A. L., Loumagne, C., and Normand, M. (1996). "Radar and optical remote sensing to infer evapotranspiration and soil moisture." Scaling up in Hydrology using Remote Sensing, J. B. Stewart, E. T. Engman, R. A. Feddes, and Y. Kerr, eds., Wiley, New York, 221-234.

Pannkuk, C. D., McCool, D. K., and Laflen, J. M. (2000). "Evaluation of WEPP for Transient Frozen Soil." Soil Erosion and Dryland Farming, J. M. Laflen, J. Tian, and C.-H. Huang, eds., CRC Press, Boca Raton, 567-571.

Parsons, A. J., Wainwright, J., Powell, D. M., Kaduk, J., and Brazier, R. E. (2004). "A conceptual model for determining soil erosion by water." *Earth Surface Processes and Landforms*(29), 1293-1302.

Pelletier, R. E., and Griffin, R. H., II. (1988). "An evaluation of photographic scale in aerial photography for identification of conservation practices." *Journal of Soil and Water Conservation*, 43(4), 333-337.

Price, J. C. (1980). "The Potential of Remotely Sensed Thermal Infrared Data to Infer surface Soil Moisture and Evaporation." *Water Resources Research*, 16(4), 787-795.

Quackenbush, L. J., Hopkins, P. F., and Kinn, G. J. (2000). "Developing Forestry Products from High Resolution Digital Aerial Imagery." *Photogrammetric Engineering and Remote Sensing*, 66(11), 1337-45.

Quinn, P., Beven, K., Chevallier, P., and Planchon, O. (1991). "The Prediction of Hillslope Flow Paths for Distributed Hydrological Modelling Using Digital Terrain Models." *Hydrological Processes*, 5(1), 59-79.

Rapp, J. F., Lopes, V. L., and Renard, K. G. "Comparing Soil Erosion Estimates from RUSLE and USLE on Natural Runoff Plots." *Soil Erosion Research for the 21st Century, Proc. Int. Symp.*, Honolulu, HI, 24-27.

Reid, L. M., and Dunne, T. (1996). *Rapid Evaluation of Sediment Budgets*, Catena Verlag, Reiskirchen, Germany.

Renard, K. G., Foster, G. R., Weesies, G. A., McCool, D. K., and Yoder, D. C. (1996). *Predicting soil erosion by water: a guide to conservation planning with the*

Revised Universal Soil Loss Equation (RUSLE), Agricultural Handbook 703, U.S. Department of Agriculture, Agricultural Research Service, Tucson, AZ.

Reybold, W. U. (1997). "The Use of Aerial Photography in the U.S. National Cooperative Soil Survey Program." Manual of Photographic Interpretation, Second Edition, W. R. Philipson, ed., American Society for Photogrammetry and Remote Sensing, Bethesda, ML, 219-223.

Reyes, M. R., Raczkowski, C. W., Gayle, G. A., and Reddy, G. B. (2004). "Comparing the soil loss predictions of GLEAMS, RUSLE, EPIC, and WEPP." *Transactions of the American Society of Agricultural Engineers*, 47(2), 489-493.

Schuum, S. A. (1973). "Geomorphic Thresholds and Complex Response of Drainage Systems." Fluvial Geomorphology, M. Morisawa, ed., State University of New York, Binghamtop, New York, 11.

Simons, D. B., Reese, A. J., Li, R.-M., and Ward, T. J. (1976). "A simple method for estimating sediment yield." Soil Erosion Prediction and Control, Soil Conservation Society of America, Ankeny, Iowa, 234-241.

Stephens, P. R., MacMillan, J. K., Daigle, J. L., and Cihlar, J. (1985). "Estimating Universal Soil Loss Equation Factor Values with Aerial Photography." *Journal of Soil and Water Conservation*, 40(3), 293-296.

Tarboton, D. G. (1997). "A New Method for the Determination of Flow Directions and Contributing Areas in Grid Digital Elevation Models." *Water Resources Research*, 33(2), 309-319.

Thomas, A. W., Welch, R., and Jordan, T. R. (1986). "Quantifying Concentrated-Flow Erosion on Cropland with Aerial Photogrammetry." *Journal of Soil and Water Conservation*, 41(4), 249-251.

Thorne, C. R. (1998). *Stream Reconnaissance Handbook*, Wiley, West Sussex, England.

Tiwari, A. K., Risse, L. M., and Nearing, M. A. (2000). "Evaluation of WEPP and its comparison with USLE and RUSLE." *Transactions of the American Society of Agricultural Engineers*, 43(5), 1129-1135.

Trimble, S. W., and Crosson, P. (2000). "U.S. Soil Erosion Rates--Myth and Reality." *Science*, 289(14 July), 248-250.

Troeh, F. R., Hobbs, J. A., and Donahue, R. L. (1980). *Soil and Water Conservation*, Prentice-Hall, Englewood Cliffs, NJ.

USACE. (1989). "Sedimentation Investigations of Rivers and Reservoirs, EM 1110-2-4000." Hydrologic Engineering Center, U.S. Army Corps of Engineers, Davis, CA.

USACE. (1995). "Applications of Methods and Models for Prediction of Land Surface Erosion and Yield, TD-36." Hydrologic Engineerin Center, U.S. Army Corps of Engineers, Davis, CA.

USACE. (2003). *Geospatial Hydrologic Modeling Extension, HEC-GeoHMS*, U.S. Army Corps of Engineers, Davis, CA.

USGS. (2004). "NED Release Notes, June 2004, online at http://edc.usgs.gov/products/elevation/ned.html." U.S. Geological Survey.

Van Klaveren, R. W., and McCool, D. K. (1998). "Erodibility and critical shear of a previously frozen soil." *Transactions of the American Society of Agricultural Engineers*, 41(5), 1315-1321.

Vanoni, V. A. (1975). *Sedimentation Engineering, ASCE Manuals and Reports on Engineering Practices, No. 54*, American Society of Civil Engineers, New York.

Verstraeten, G., and Poesen, J. (2001). "Factors controlling sediment yield from small intensively cultivated catchments in a temperate humid climate." *Geomorphology*, 40, 123-144.

Veseth, R., Vomocil, J., McDole, B., and Engle, C. (1986). "Effective conservation Farming Systems." Pacific Northwest Conservation Tillage Handbook, R. Veseth and D. Wysocki, eds., Plant, Soil and Entomological Sciences Dept., University of Idaho, Moscow, ID, 12.

Walling, D. E. (1983). "The sediment delivery problem." *Journal of HYdrology*, 65, 209-237.

Wang, G., Gertner, G., Parysow, P., and Anderson, A. (2000). "Spatial prediction and uncertainty assessment of topographic factor for revised universal soil loss equation using digital elevation models." *Journal of Soil & Water Conservation*, 55, 374-384.

Wang, M., and Hjelmfelt, A. T. (1998). "DEM based overland flow routing model." *Journal of Hydrologic Engineering*, 3(1), 1-8.

White, L. P. (1977). *Aerial photography and remote sensing for soil survey*, Clarendon Press, New York.

Whiting, M. L., DeGloria, S. D., Benson, A. S., and Wall, S. L. (1987). "Estimating conservation tillage residue using aerial photography." *Journal of Soil and Water Conservation*, 42(2), 130-132.

Williams, J. R., and Berndt, H. D. (1972). "Sediment yield computed with universal equation." *Journal of the Hydraulics Division*, 98, 2087-2098.

Wilson, J. P. (1986). "Estimating the topographic factor in the universal soil loss equation for watersheds." *Journal of Soil & Water Conservation*, 41(3), 179-184.

Wischmeier, W. H., and Smith, D. D. (1965). *Predicting Rainfall-Erosion Loses from Cropland East of the Rocky Mountains*, U.S. Department of Agriculture Agricultural Research Service, Washington, DC.

Wischmeier, W. H., and Smith, D. D. (1976). *Predicting rainfall erosion losses - a guide to conservation planning, Agricultural Handbook 537*, U.S. Department of Agriculture, Washington DC.

Wood, E. F., Sivapalan, M., Beven, K., and Band, L. (1988). "Effects of spatial variability and scale with implications to hydrologic modeling." *Journal of Hydrology*, 102, 29-47.

Woods, J. (2004). "LandSerf, online at http://www.soi.city.ac.uk/~jwo/landserf/landserf200." University of Leicester.

8. Analysis of Ephemeral Gullies with High Resolution Aerial Imagery

Ephemeral gully erosion is a readily visible component of concentrated flow erosion in the continuum of processes that perpetually reform a disturbed landscape. Ephemeral gullies originate and assume forms largely dependent on climatic agents and upslope surface and subsurface properties (Beer and Johnson 1963; Begin and Schumm 1979; Foster 1982; Harvey et al. 1985; Peterson et al. 2003; Schumm 1973). Ephemeral gullies are small enough to be obliterated by normal tillage operations and often reappear in the same location year after year. Differences between ephemeral gullies and persistent classical gullies were discussed in Section 7.2.4. Bennett et al. (2000) found that estimated ephemeral gully erosion rates vary widely and may account for between 30 and 100 percent of total soil loss from arable land.

Several broad conclusions can be drawn from numerous investigations into gully erosion (Haan et al. 1994; Harvey et al. 1985):

- Gullies may develop in a short time due to exceeding an intrinsic or extrinsic geomorphic threshold.
- Gully initiation and development is a complex physical process.
- Gully initiation thresholds for homogeneous regions may be estimated from empirical data.
- Gullies evolve by following a similar trend of initiation, channel slope reduction, reduction of bank angle, sediment deposition and vegetation establishment.
- Gully morphology is influenced by the properties of the sediment eroded and transported.
- Onsite effects of gully erosion can be quantified more easily than offsite (sediment yield) effects.

The USGS identified gully erosion as a research priority to support national soil conservation work (Bernard 1997). USGS concluded:

- Ephemeral gully erosion is a significant source of sediment where this type of erosion occurs and affects the processes of sediment transport off the field.
- Ephemeral gully erosion predictive techniques need to be refined.
- A procedure is needed to identify the extent and/or location of ephemeral gullies.
- Mechanics of ephemeral gully erosion need to be refined.

Computation of ephemeral gully erosion and yield is conceptually simple. Eroded volume of an ephemeral gully is computed by multiplying the length of the gully channels by its average width and depth. Total watershed ephemeral gully erosion volume is the sum of the eroded volumes of all the ephemeral gullies within the watershed. Mean annual ephemeral gully erosion volume is the long term average of annual erosion volumes. Sediment yield of ephemeral gullies to the main channel system approaches unity because most ephemeral gullies connect directly to the main channel system. This conceptual simplicity is deceiving.

Conventional techniques of field reconnaissance and land surveying type (e.g. cloth tape or total station) measurements of gully position, length and volume are appropriate for field scale research, but cumbersome and expensive to implement on a watershed basis. Extensive measurement field survey of ephemeral gullies would be logistically difficult, costly, intrusive of private property, and not synoptic for a basin the size of the lower Potlatch River. Moreover, a single season field measurement of ephemeral gully erosion, however costly and difficult, would likely poorly represent the

long term average for the watershed. Direct measurement of watershed ephemeral gully erosion is practically impossible. Aerial survey is the only practical alternative.

This section describes the dissertation work related to the measurement, analysis and modeling of ephemeral gully erosion with high-resolution digital aerial imagery as the primary data source. This research found that aerial survey is an efficient and accurate means to detect and measure the morphology of ephemeral gullies and estimate ephemeral gully erosion over extensive area. Two approaches evolved: 1) estimation of seasonal ephemeral gully erosion volume from measurement of ephemeral gully channel dimensions in the aerial imagery and, 2) a prediction of ephemeral gully erosion volume with a watershed scale model derived from physical erosion processes and parameters in the aerial imagery.

The first approach is fully operational and was the basis of the applied research effort for the Idaho Department of Environmental Quality study of erosion and sediment in the lower Potlatch River basin (Teasdale and Barber 2005). The aerial image measurement approach is discussed in Sections 8.1 to 8.4. The ephemeral gully modeling approach diverges somewhat from the dissertation objectives and is preliminary, although the modeling approach is of sufficient practical value to merit presentation in this dissertation. The watershed modeling approach is discussed in Sections 8.5 to 8.16.

Ephemeral gully erosion has received comparatively little attention in the fields of soil erosion and hydrologic modeling. The fundamental concepts, mathematical formulations, and primary research studies are not widely distributed in the literature of erosion modeling, water resources, fluvial morphology, and landscape evolution. It is

necessary to review and summarize the primary research to construct a foundation for the watershed ephemeral gully erosion model.

It became very clear during the research that ephemeral gullies belong to the continuum of erosion from the finest rills and interrills on headwater hillslopes to deposition in reservoirs and ocean. Each larger scale of observation carries information about preceding ones: reservoir deposition reveals sediment borne by rivers and streams, suspended sediment and bed load in streams evidence channel and upland erosion, and ephemeral gullies indicate rill and interrill erosion. As a whole we are not very proficient at inverting the sediment continuum. It is hoped this section contributes to a better understanding with the aid of aerial imagery.

8.1 Objectives of an Aerial Survey of Ephemeral Gullies

Characterization of ephemeral gullies with high-resolution aerial imagery is both a technical and interpretive analysis. Some characteristics such as gully length are easily obtained after georeferencing of the aerial images. Other characteristics such as gully channel form and channel connectivity must be interpreted from the images. Interpretive judgments are more qualitative and contingent upon the skills and experience of the analyst. Interpretation keys can help reduce differences among analysts (Lillesand and Kieffer 1994). It is often advantageous to perform image interpretation directly from original digital aerial images as georeferencing rectification sometimes obliterates fine detail. Observing features in stereo view greatly aids interpretation, but is not absolutely necessary.

The feature characterization process should begin with thorough consideration of the information to be derived and the prospects for successfully obtaining this information from the aerial images and supporting data sources. An extensive project area and limited budget also constrain data collection methods. Narrative objectives can help focus consideration of desired feature characteristics, data sources and methods.

Several objectives for the lower Potlatch River ephemeral gully characterization by aerial survey techniques including:

- The primary objective of ephemeral gully characterization was to estimate the volume of sediment eroded during the winter and spring 2003-2004.
- Characterization methods should be primarily based on aerial image and GIS analysis with on-the-ground fieldwork mostly assuming a supporting and confirmation role.
- Provide a benchmark dataset for future analyses and comparisons.
- The erosion characterization and supporting data may be applied in development of a Total Maximum Daily Load (TMDL) analysis for regulatory purposes.
- Permanent channel bed and bank erosion estimates are of secondary importance and are recognized as being difficult to determine accurately with both direct and indirect methods.
- Meteorological data should be collected to characterize the erosion season in perspective of long-term climate data.
- Field and GIS procedures should be effective, but not overly complicated, so that technical personnel with backgrounds in environmental science, water resources engineering, geology, and fisheries science could quickly learn and apply the techniques.

- Methods, particularly fieldwork, should be unobtrusive to landowners and nondestructive.

- Privacy should be respected in the handling and disposition of the high-resolution aerial images of private property.

- The methods should not require the purchase of expensive and extraordinary equipment or expensive software systems.

It is sometimes useful to identify false or anti-objectives that initially seem beneficial, but can mislead or misdirect progress towards the true objectives. Important anti-objectives for this project include:

- The purpose of the project was not to identify locations of ephemeral gullies to target implementation of best management practices or characterize site (land owner) specific land use practices for regulatory purposes. This, however, is a possible use of the aerial survey technique.

- It was not necessary to estimate agricultural rill and interill erosion or develop parameterization for soil erosion models. While the acquired data could support this type of work, it was beyond the intended scope of the dissertation research.

- Fieldwork did not collect water quality data or data for sediment transport analysis. Though this would be very beneficial, there were insufficient funds and mobilization time for this work.

8.2 Ephemeral Gully Morphological Parameters

There are many morphological parameters of interest in the assessment of channel erosion and sediment transport. The most important parameters for ephemeral gully channel assessment and the methods of assessment are listed and prioritized in Table 8.1 and Table 8.2. The four highest priority parameters in Table 8.1: presence, length,

width, and depth are sufficient to estimate the volume of soil eroded from ephemeral gullies. Lower priority primary parameters and the secondary parameters help characterize the observed erosion and contribute to an understanding of the factors influencing the development of ephemeral gullies.

From the viewpoint of estimating soil erosion, the initiation or presence of a gully system is the most important indication that ephemeral gully erosion is a source of sediment in the channel system. The term *initiation* has special meaning in the study of ephemeral gullies and will be explained in the modeling discussion. If many ephemeral gullies are observed, then this source of sediment has greater importance and is larger in magnitude. If the observed gully system density, computed from aerial survey counts as described in Section 4 is below a selected value, then further evaluation may not be necessary. An initial aerial gully system count can be made visually in a systematic manner, eliminating the need to acquire and process digital aerial imagery.

Measurement/Characteristic	Priority	Method
Initiation (Presence)	1	Gully system counts by aerial observation or counts in aerial images
Length	2	Aerial line transect sampling or digitized from georeferenced aerial images
Mean incised width	3	Random sample of widths from georeferenced aerial images or estimated from erosion models
Depth	4	Estimated from field observation or estimated from channel erosion models.
Connection type	5	Image interpretation
Mean disturbance width	6	Random widths from georeferenced aerial image
Downstream sediment basin	7	Image interpretation (2004 aerial, 1992 DOQ, 1998 NAPP)
Channel form	8	Image interpretation
Tillage	9	Image interpretation
Soil type	10	Extracted from SSURGO shapefile
Slope aspect	11	Interpreted from DEM or DRG
Elevation of initiation point	12	Interpreted from DEM or DRG
DEM channel correspondence	12	Order and measured length comparison
Persistence of channel	14	Image interpretation (1992 DOQ, 1998 NAPP)

Table 8.1 Primary Ephemeral Gully Measurements and Characteristics.

Measurement/Characteristic	Priority	Method
Channel order (Strahler)	1	Topology of digitized channels
Channel initiation area	2	Digitized from georeferenced aerial image
Channel initiation distance	3	Measured on georeferenced aerial image
DEM correspondence	4	Visual comparison with stereo images
Slope at point of channel initiation	5	Interpreted from DEM or DRG
Gully slope profile	6	Interpreted from DEM or DRG
Outlet deposition area	7	Digitized from georeferenced aerial image
Buffer filter width	8	Measured on georeferenced aerial image
Exposed subsoil	9	Digitized from georeferenced aerial image
National Hydrography Dataset ID	10	Analysis of NHD digital datasets

Table 8.2 Secondary Ephemeral Gully Measurements and Characteristics.

The next most important morphological parameter is the length of the ephemeral gully channels. As discussed in the next section, total channel length is required by the common ephemeral gully erosion estimation methods and explains most of the variability in ephemeral gully volume. Georeferencing techniques demonstrated in Section 3 provide sufficiently accurate measurements of linear features aerial images. Section 4 demonstrated that reliable estimates of total ephemeral gully can be measured with aerial line transect sampling (LIS). Measuring total ephemeral gully length with aerial LIS saves a large amount of time and expense over manual digitizing. I have come to view aerial LIS as the preferred method.

Width of ephemeral gullies can be measured on georeferenced or orthorectified aerial images, estimated from a statistical sample of widths measured by field survey, or estimated with gully erosion models. The precision of the width measurement in aerial images is dependent on the ground pixel resolution (GPR) of the aerial image and contrast of the gully soil with adjacent soils. Timing and weather conditions of the aerial image acquisition are important. Ephemeral gully width can be estimated by the gully erosion models discussed in the next section.

Depths of ephemeral gullies cannot be reliable measured by the stereo photogrammetric techniques discussed in Section 3 and must be estimated from a statistical sample of gully channels measured by field survey or estimated with gully erosion models. A statistically valid sample of gully depth was not obtained in the research work, even after a disappointingly arduous and costly public relations campaign. Very few landowners within the study area permitted access for field measurements. Ephemeral gully measurements that were obtained by field survey are therefore indisputably biased.

Observation of the aerial imagery reveals that ephemeral gully widths and depths are remarkably consistent between gully systems on similar soils. This characteristic offsets the need for extensive statistical sampling of gully widths and depths. The most variable parameters, thus most important, are gully initiation and length. These parameters are very reliably discerned and measured on late winter and early spring high resolution aerial imagery of the lower Potlatch basin.

8.3 Digital Aerial Images for Ephemeral Gully Assessment

Ephemeral gully morphology is measured in aerial images by sensor (camera) and image geometrical relationships. The science and technology of this analysis is called photogrammetry. Very accurate measurements can be made from aerial images with sophisticated digital photogrammetric software. High accuracy requires cameras with high quality optics and precise information about aircraft position and orientation. Such high accuracy is necessary for critical engineering design applications such as roadway design. Highly precise aerial imaging systems are not necessary for the natural resource

quality measurements and sufficient accuracy is obtained with the georeferencing techniques discussed in Section 3.

Ephemeral gullies form when concentrated runoff erodes surface soils. Erosion potentially exposes soils with varying properties including color and light reflectance (albedo). Figure 8.1 shows the main elements of the reflectance of a conceptual gully cross section. Light reflectance of fine textured soils, such as the silt loams found in most of the study area, lessens as moisture content increases, appreciably darkening the apparent color of the soil (Bowers and Hanks 1965). Soil moisture gradients form as tilled soils drain and dry following precipitation or snowmelt. Surface soils outside the gully channel are typically drier, thus lighter in appearance, than soils in the channel. Subsurface drainage patterns may maintain higher moisture contents in channel bottom soils. Sun shadows can also lessen the amount of light reflected from gully soils depending on the depth and orientation of the gully channel.

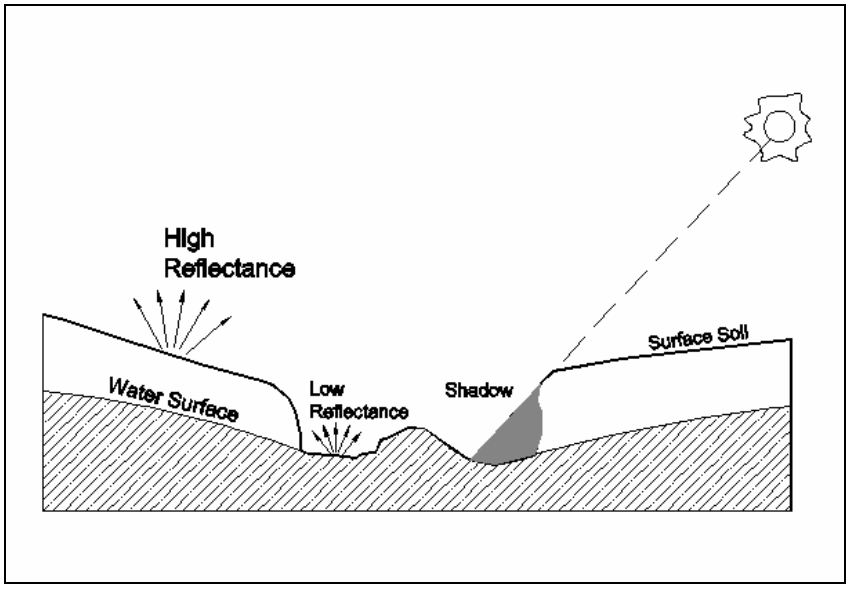

Figure 8.1 Ephemeral gully channel light reflectance.

Aerial images for ephemeral gully assessment of the winter erosion period in the Palouse region are best acquired following snowmelt and before spring tillage operations in mid March and early April (Figure 8.2 and Figure 8.3).

Figure 8.2 Ephemeral gully in the Little Potlatch Creek basin (31 March 2004).

Figure 8.3 Ephemeral gully in the Middle Potlatch Creek basin (24 April 2004).

Aerial images acquired later in the spring show ephemeral gullies eroded in spring seeded cropland and may show ephemerally gullies on fall seeded cropland that have been enlarged by spring rain showers and thunderstorms. The duration of the time period available for acquiring images of ephemeral gullies is limited by the closure of crop canopies, but large ephemeral gullies can usually be detected and measured in imagery acquired up until the start of primary tillage operations in early fall. Late spring aerial imagery should be acquired following a period of wet weather to obtain images that exhibit increased soil contrast (Figure 8.4)

Figure 8.4 Ephemeral gully after rainfall in mid May 2004.

Solar radiation reflected from soils carries information about soil properties and moisture content (Bowers and Hanks 1965). Interpretation of soil properties from natural color, panchromatic (black and white), and color infrared aerial imagery has a confirmed scientific basis and is widely practiced by natural resource organizations worldwide

(Belcher 1997). The marked color contrast between moist and dry soils indicates the pattern of concentrated flow erosion in agricultural fields. Length and width of even small gullies and rills can be discerned in very high resolution aerial images (Frazier and McCool 1981) . Current research in the multispectral and hyperspectral reflectance of soil and minerals indicate that remote sensing data and analysis techniques will continue to improve the ability to assess soil over large areas under different environmental conditions (Clark et al. 2003).

The dissertation research showed that ephemeral gully systems in tilled fields could be reliably observed monoscopically in three band (blue, green and red) natural color digital aerial imagery having a ground pixel resolution (GPR) of about 0.2 meters. The aerial imaging system used in this dissertation research is not radiometrically calibrated, but image colors closely match the observed color of soil and vegetation (Section 3).

Ephemeral gullies are linear features that are relatively easy to identify in aerial images across a broad range of image resolution. Figure 8.5 is a small section of a natural color aerial image acquired on November 6, 2003. It shows a single thread ephemeral gully eroded the previous winter at decreasing image resolution. The original ground pixel resolution (GPR) is 15 cm. Resolution was decreased by resampling the pixel array of the original image. Length and angular alignment of the ephemeral gully are distinct and consistent across the range of resolutions. Further processing shows the gully begins to disappear at resolution of about 0.5 meter GPR.

The effect of decreasing resolution on width interpretation and measurement is seen more readily in a highly magnified section of the gully channel. Figure 8.6 is the

same section of the gully at the various resolutions. The dashed red line along the interpreted channel centerline was superimposed to provide a visual reference. Mean interpreted width of the gully channel is between 0.2 and 0.3 meters. Uncertainty of the width interpretation increases markedly beyond 0.25 meter GPR for this particular section.

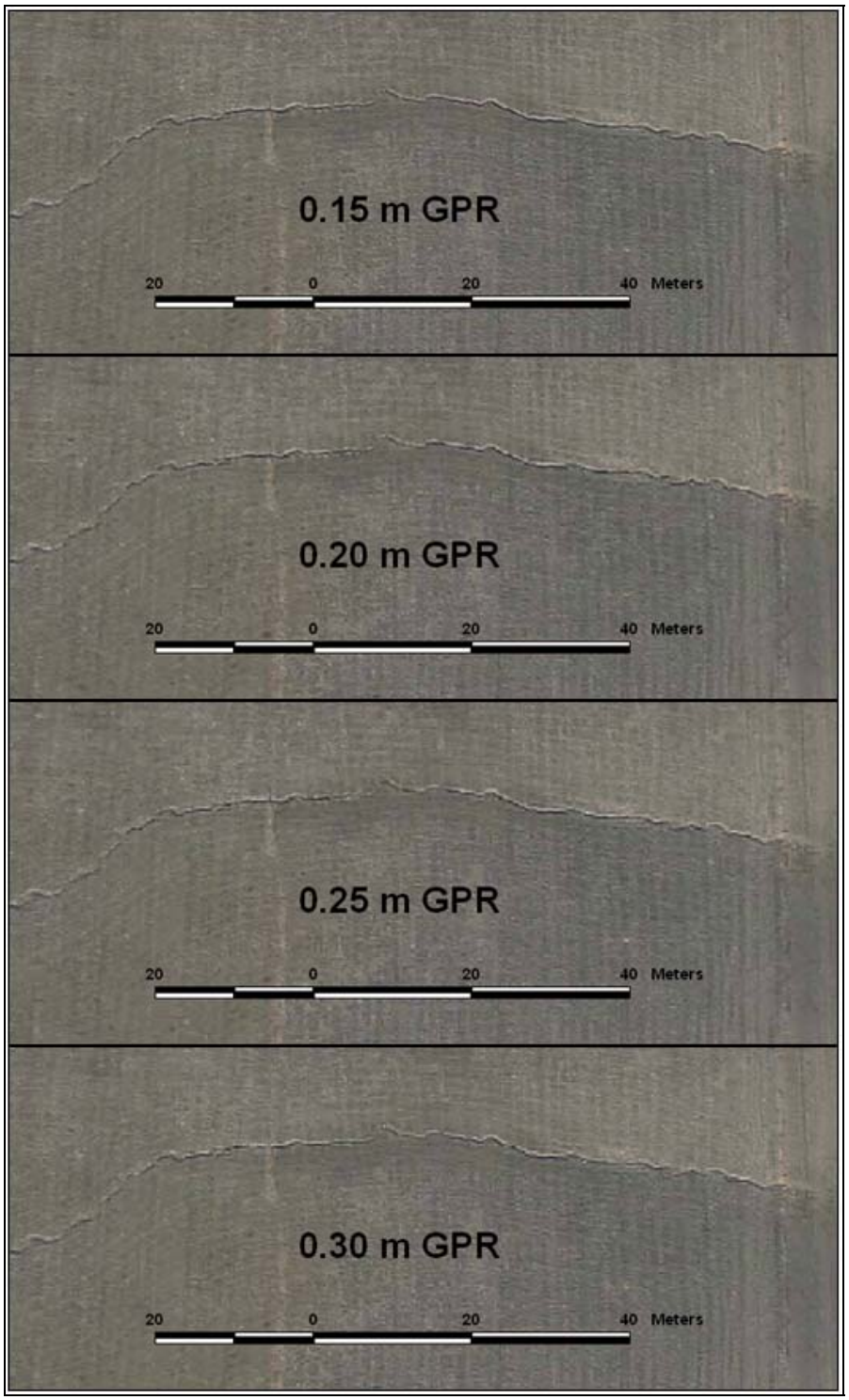

Figure 8.5 Resolution comparison for length and alignment precision.

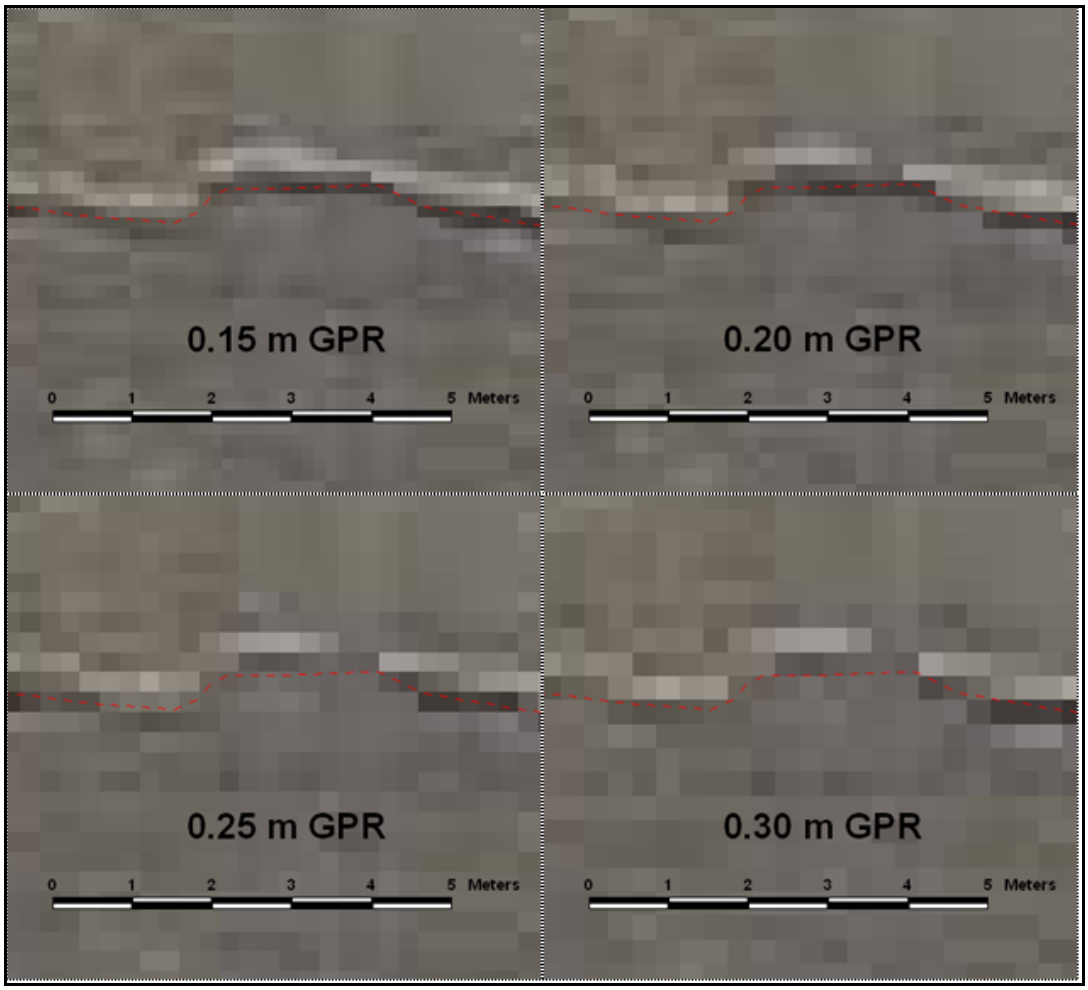

Figure 8.6 Resolution comparison for gully channel width interpretation.

It is usually best to interpret channel width from an unaltered display image as this is the truest representation of the actual image data. However, image display techniques can sometimes improve interpretation of images at high magnification relative to GPR. Figure 8.7 is the same image as Figure 8.6, but is displayed with a cubic convolution algorithm. The smoothing of the color and contrast of display pixels gives the appearance of a more defined and slightly wider channel. A cubic convolution display can make manual digitizing of channel centerlines more efficient. Cubic convolution and other smoothing display algorithms tend to encourage a wider interpretation of width.

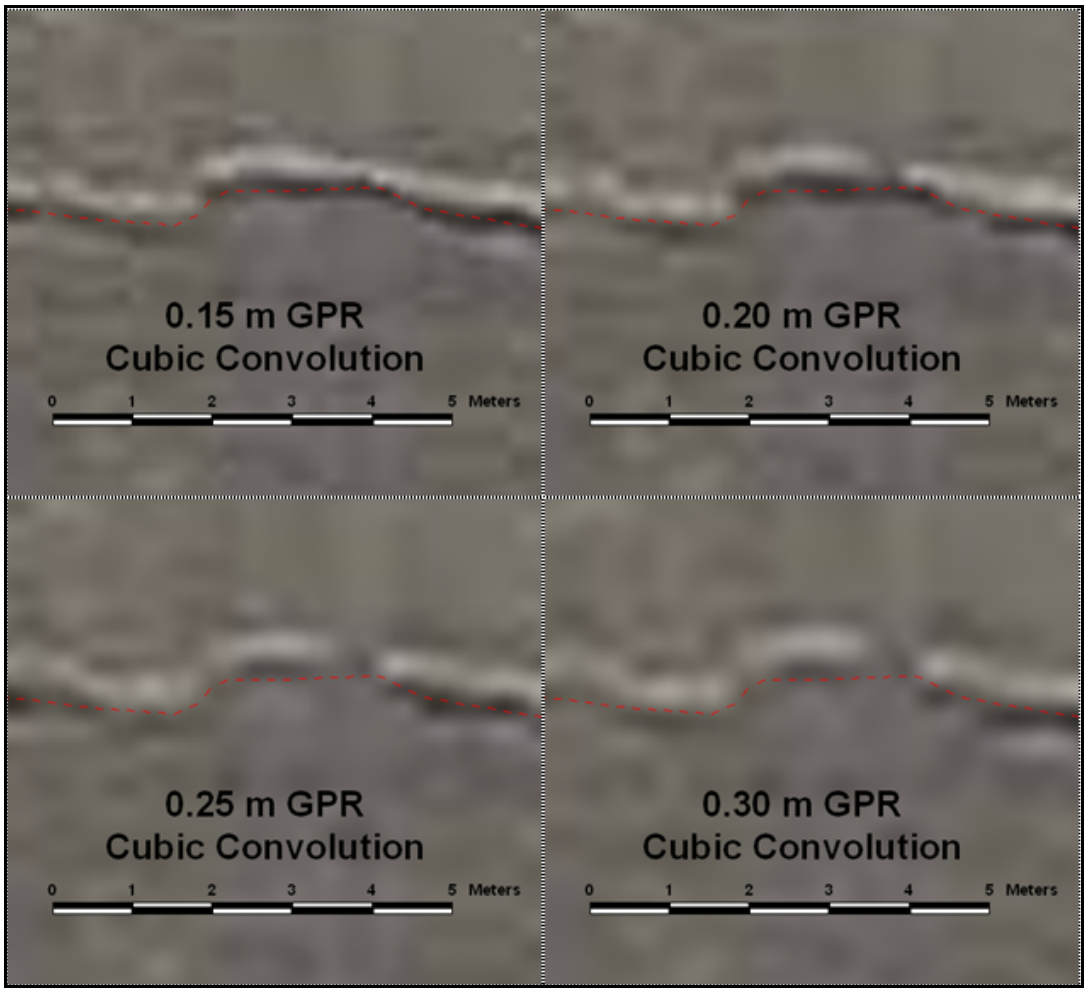

Figure 8.7 Cubic convolution display of an ephemeral gully section at various resolutions.

Resolution comparisons were made with November 6, 2003 aerial images along several aerial transects in the Potlatch basin. These comparisons and previous experience indicated that an image resolution between 0.20 and 0.25 meter GPR would provide reliable measurements of ephemeral gullies with widths greater than about 0.3 meters (1 foot). Although the minimum measurable dimension is generally twice the GPR, extra precision is gained in this case because the interpreter is able view a length of channel and infer a smaller width from the distinctiveness and discontinuous presentation of the

linear feature. It is odd that a description of this effect was not found in the photointerpretation literature.

Approximately 10 percent of the 3600 March 2004 digital aerial images were manually georeferenced for digitizing of ephemeral gully channels. Additional aerial images were georeferenced to support stream and drainage channel assessment. Mean GPR of the georeferenced aerial images was 0.21 meters. A frequency histogram of the GPR recorded georeferencing statistics is given in Figure 8.8.

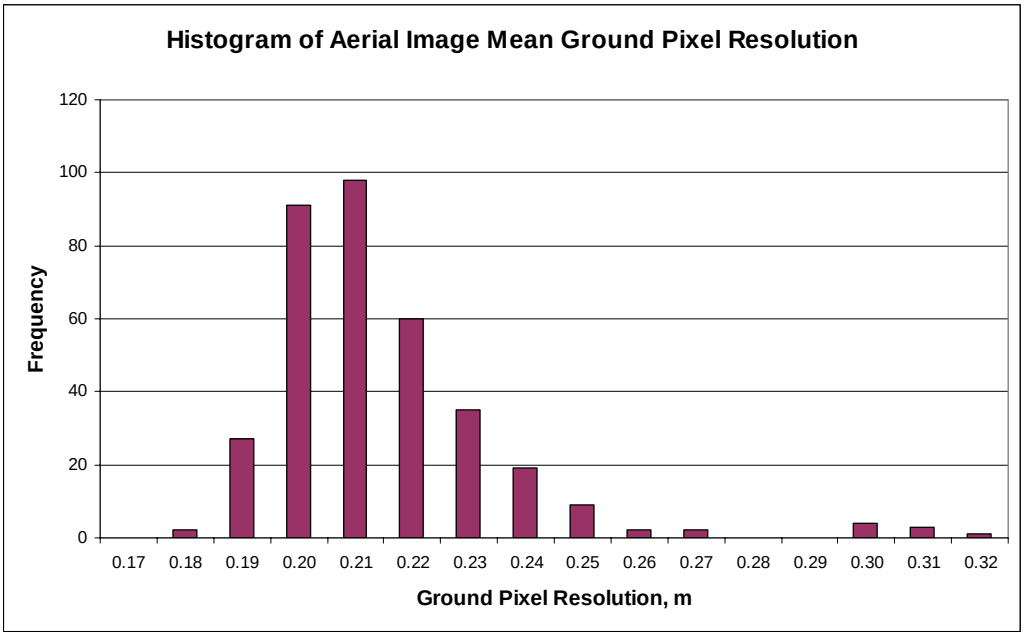

Figure 8.8 Histogram of georeferenced aerial image GPR values.

The left-skewed distribution is mostly due to terrain elevation variation. The GPR of a specific image is dependent on height of the sensor above the surface of the ground. Flight altitude was held approximately constant for all imaging flights, though air turbulence in low altitude flights invariably caused transient and minor departures. Georeferenced GPR values are greater for images of steep canyons and less for images of

higher elevation terrain. The distribution of GPR is well within the 0.20 – 0.25 meter criteria set for the acquisition.

8.4 Estimate of the Number of 2004 Ephemeral Gullies

Approximately 3600 aerial images were acquired along flight lines across the six primary agricultural subbasins of the Potlatch River basin. In this study the percentage of area surveyed is relatively large, about 62 percent of the total area of the six primary agricultural subbasins after adjusting for georeferencing scale variation. Figure 8.9 shows the aerial image transect swath for a portion of Little Potlatch Creek and Middle Potlatch Creek basins.

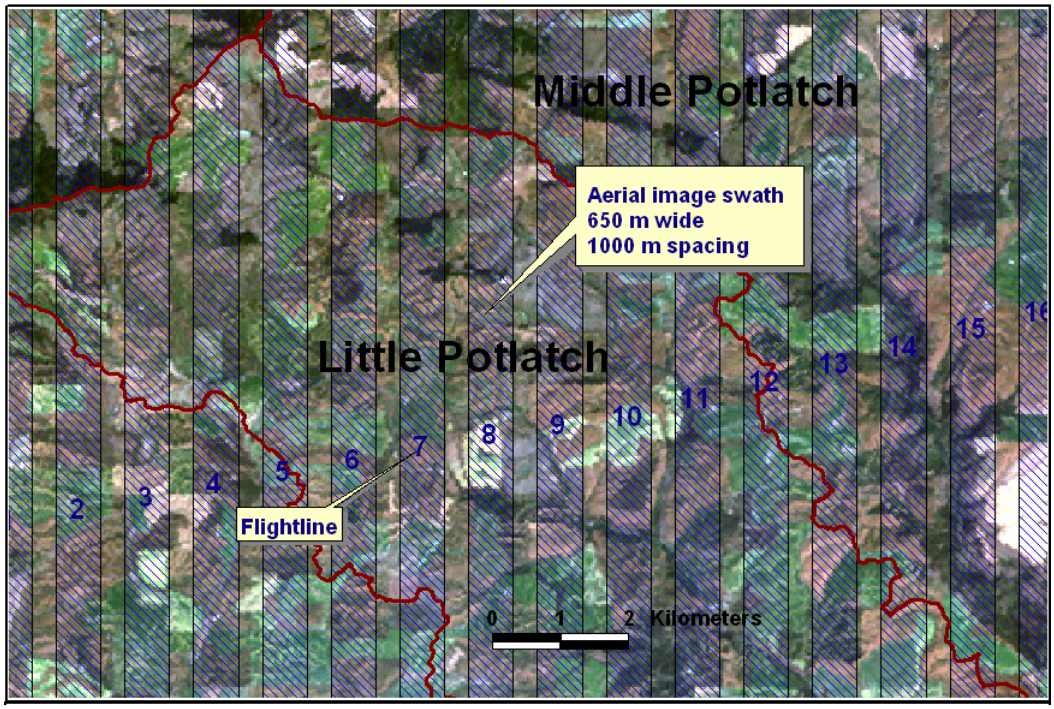

Figure 8.9 March 2004 aerial image transects.

The total number of ephemeral gully systems was estimated by inspection of the aerial imagery. Non-georeferenced aerial images were viewed simultaneously with the USGS 1-meter resolution DOQQ in ArcView©. Approximate locations of ephemeral

gully systems were identified by manually placing a point in an ESRI shapefile. Configurations of the ArcView© view windows are in Figure 8.10.

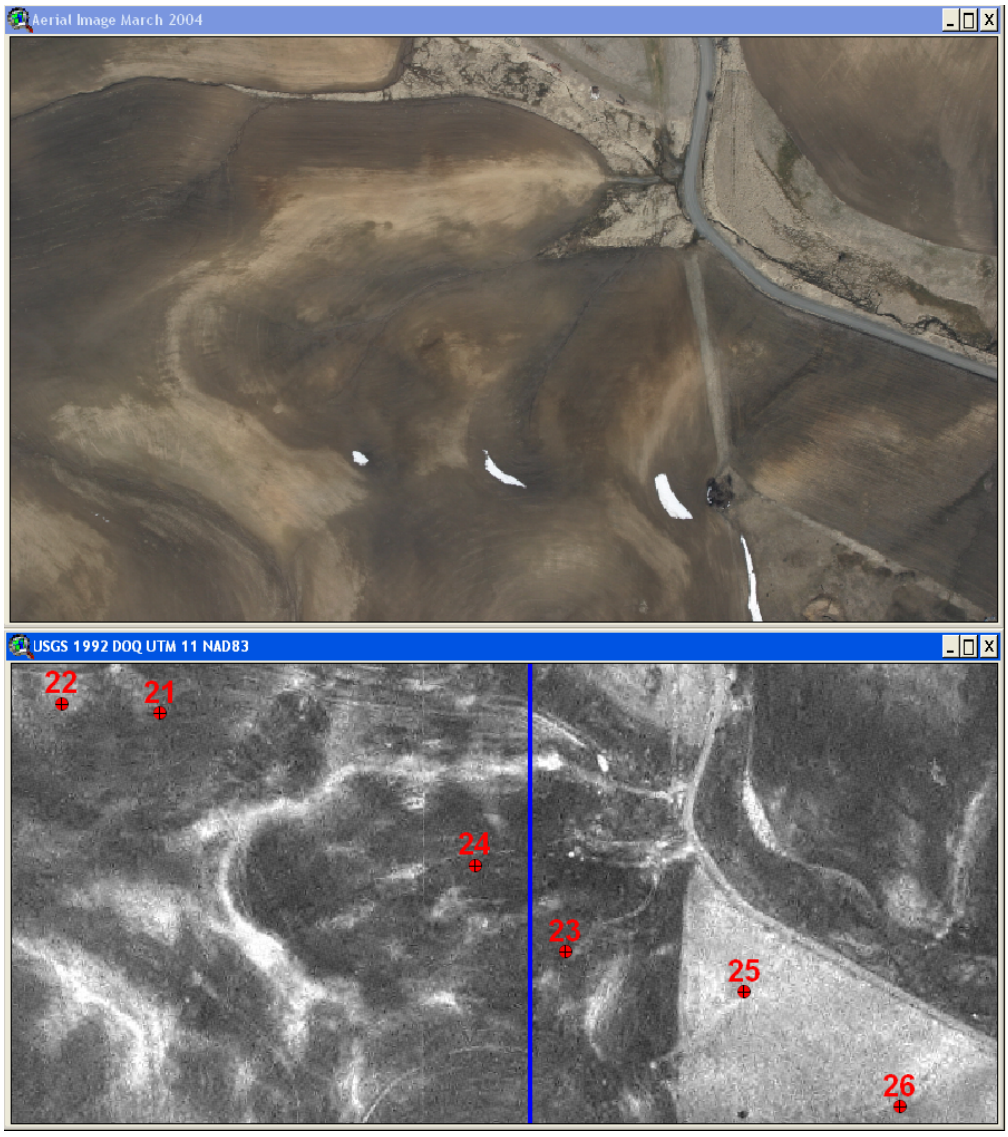

Figure 8.10 Identification of ephemeral gully locations in ArcView.

Over 1000 ephemeral gully systems were identified across the six primary subbasins. A summary by subbasin is in Table 8.3. The initial count of ephemeral gully systems was made relatively rapidly, and was completed within a few days following acquisition of the aerial imagery. It is not necessary to georeference aerial images to

conduct the count. This technique is relatively simple and efficient, yet provides important information for prioritization of soil conservation work. Table 8.3 shows that the Middle Potlatch Creek subbasin has about twice the density of ephemeral gully systems (3.7 per square kilometer) as most other subbasins. The count was made from approximately 62 percent area (the aerial image coverage) so estimates of gully-system density are projected to the full basin by dividing raw counts by 0.62.

Subbasin	Ephemeral Gully Count on 62% of Area	Percent of Total Count	Subbasin Area, ha	Percent of Total Area	Gully Systems per km^2
Big Bear	171	17%	17,049	23.1%	1.62
Cedar	107	11%	10,184	13.8%	1.69
Little Bear	156	16%	10,841	14.7%	2.32
Little Potlatch	133	13%	13,061	17.7%	1.64
Middle Potlatch	343	34%	14,311	19.4%	3.87
Pine	94	9%	8,202	11.1%	1.85
Total	1004	100%	73,648	100.0%	2.20

Table 8.3 Summary of ephemeral gully system counts and density by subbasin.

An ephemeral gully system for purposes of this method of identification is a continuous network of concentrated flow erosion channels having a single and unique terminal outlet in a permanent channel, deposition zone or conservation feature such as a grassed waterway or sedimentation pond. Ephemeral gully systems are distinguished from areas of rill erosion by indications of topographic convergence. Total length and width of the ephemeral gully channel are not discriminating factors. The point locations of ephemeral gullies were primarily intended to prioritize georeferencing work and guide analysis.

The March 2004 ephemeral gully systems in Figure 8.11 are well distributed across the agricultural subbasins, indicating that relatively uniform hydrological conditions produced a widespread erosion event. No estimate of ephemeral gully soil loss was made from the spatial distribution of ephemeral gully system points, though

correlations with conservation practices and hydrometeorological factors (e.g. snowmelt) are expected. Ephemeral gully system count methods could be refined to produce an initial estimate of erosion volume in future research. Ideally, ephemeral gully counts would be referenced to occupancy potential.

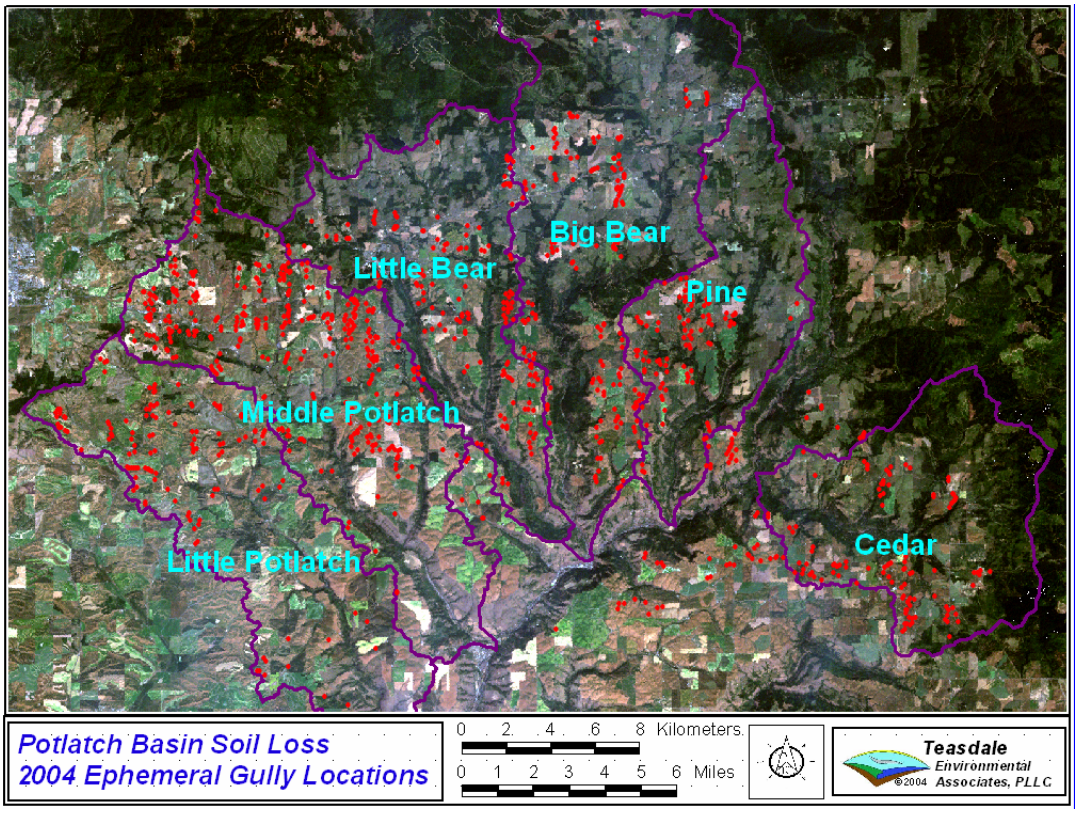

Figure 8.11 Spatial distribution of March 2004 ephemeral gully systems.

8.4.1 Digitization and Measurement of Ephemeral Gully Length

Ephemeral gullies exhibit a morphology that is consistent and measurable. Figure 8.12 is a typical unbranched single thread ephemeral gully eroded along the locus of topographic convergence in a north facing catchment. Erosion was caused by rainfall and snowmelt by two runoff events of nearly the same magnitude in late January and mid February 2004.

Figure 8.12 Ephemeral gully in the Little Potlatch Creek basin, March 15, 2004.

The length of an ephemeral gully is measured by digitizing the centerline of the eroded channel between the gully initiation point and gully outlet. The gully endpoints and digitized length for this gully are marked in Figure 8.13. Total length of this gully is 79 meters. Digitized gully lengths are computed by GIS analysis and recorded in an ESRI polyline shapefile of the gully centerlines.

Elevation contour lines and catchment area for the gully system are superimposed on Figure 8.13. The critical support area defines the tributary area at the beginning of the well defined eroded channel. The catchment area was determined by stereo observation. Individual catchment areas help in understanding ephemeral gully development, but are not needed for soil loss estimation.

Ephemeral gully outlets are generally easy to identify. Ephemeral gullies terminate at 1) conservation structures (Figure 8.14 and Figure 8.15), 2) permanent drainage channels (Figure 8.16), 3) sediment deposition zones (Figure 8.17), or 4) at the edge of a more resistant land surface which may also be a deposition zone. Based on observation of the March 2004 aerial imagery, termination of ephemeral gullies in deposition zones are infrequent and limited to very small catchments. This is in agreement with sediment transport principles that require downcutting through deposition zones when critical slopes to the baseline drainage channel are exceeded by build up of deposited material. Very fine suspended sediment is washed through deposition zones even when the gully channel appears disconnected from the permanent drainage system. Support for this assertion was presented in the sediment yield analysis in Section 7.

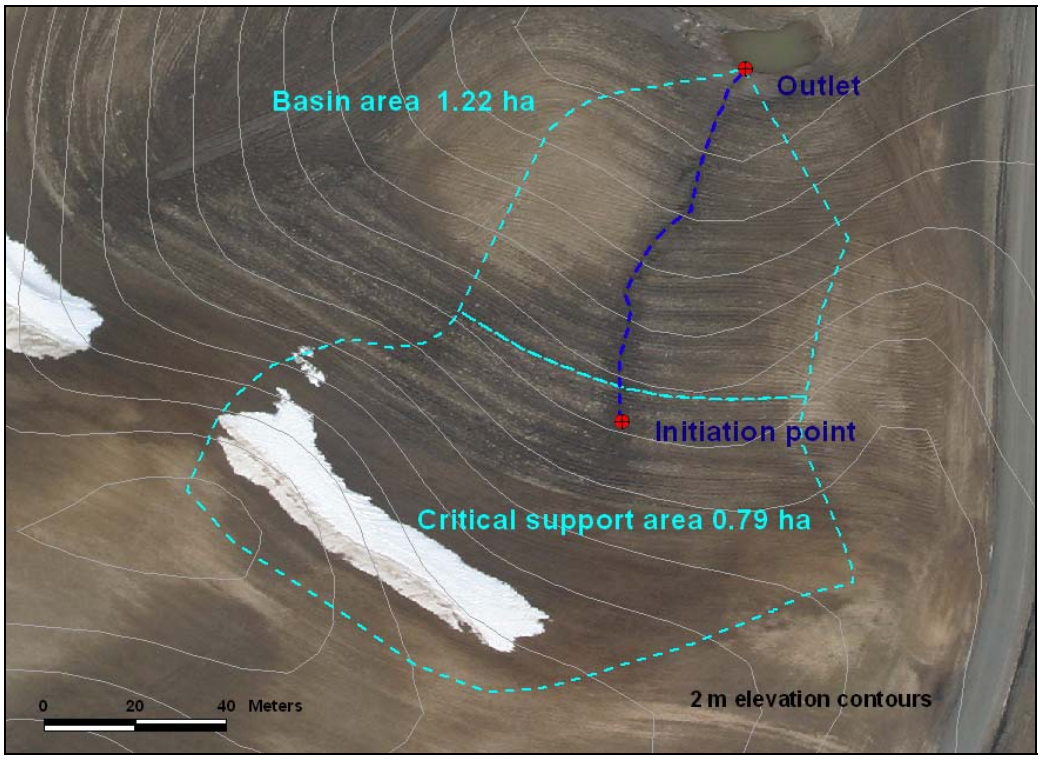

Figure 8.13 Digitized ephemeral gully and catchment area.

Figure 8.14 Outlet of the ephemeral gully in Figure 2.29.

Figure 8.15 Termination of a multiple thread ephemeral gully in a grassed waterway.

Figure 8.16 Termination of a multi-thread ephemeral gully in a permanent drainage channel (road ditch).

Figure 8.17 Apparent termination of a small ephemeral gully in a deposition zone.

There is some uncertainty in defining where an ephemeral gully channel begins for digitized length determination. Ephemeral gullies are part of the continuum of erosion. The upper end of a first order (headwater) channel is a transition from hillslope rill erosion channels to a topographically convergent concentrated flow erosion channel. The zone of uncertainty is typically between 2 and 10 meters in length. Figure 8.18 shows the zone of uncertainty for the initiation point of the ephemeral gully in Figure 8.13. Gully initiation point uncertainty zones are elliptical because of slope curvature, but can be approximated with a circle. The effect of the uncertainty zone is to place an error bound on the length of the ephemeral gully channel. Initiation zones are not proportional to gully length and only affect first order channels.

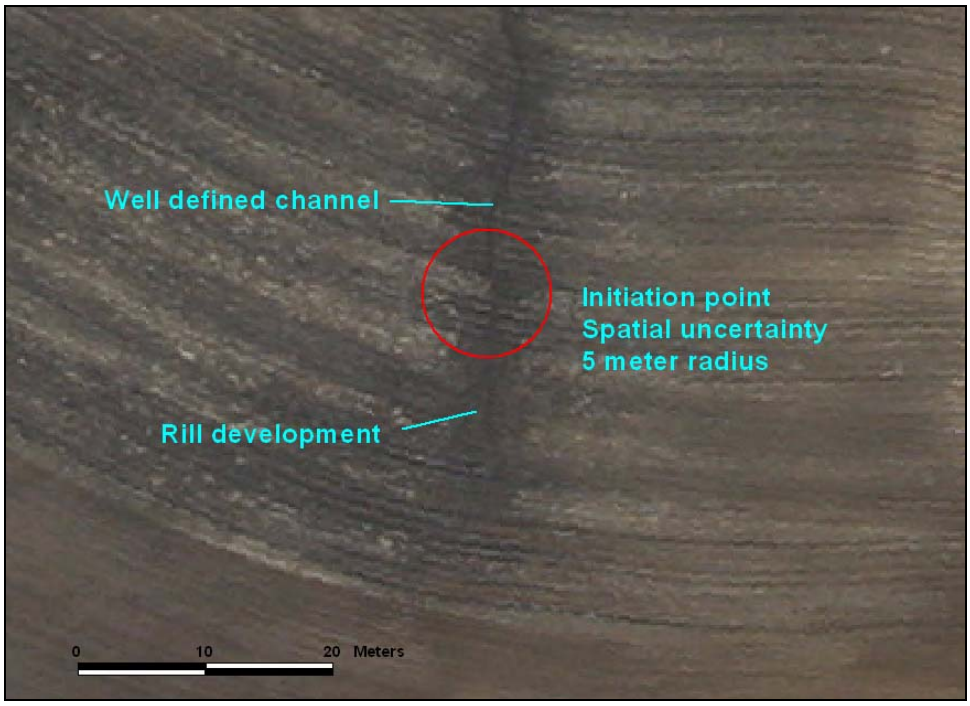

Figure 8.18 Spatial uncertainty of the initiation point of gully in Figure 2.29.

Branched gully systems are digitized as connected segments (links) as shown in Figure 8.19. A branched system has two or more initiation points, two or more channel links, one or more junctions, and a single outlet. Figure 8.20 shows the digitized representation of the branched gully system in Figure 8.19. Total length of the gully system in Figure 8.19 is 418 meters.

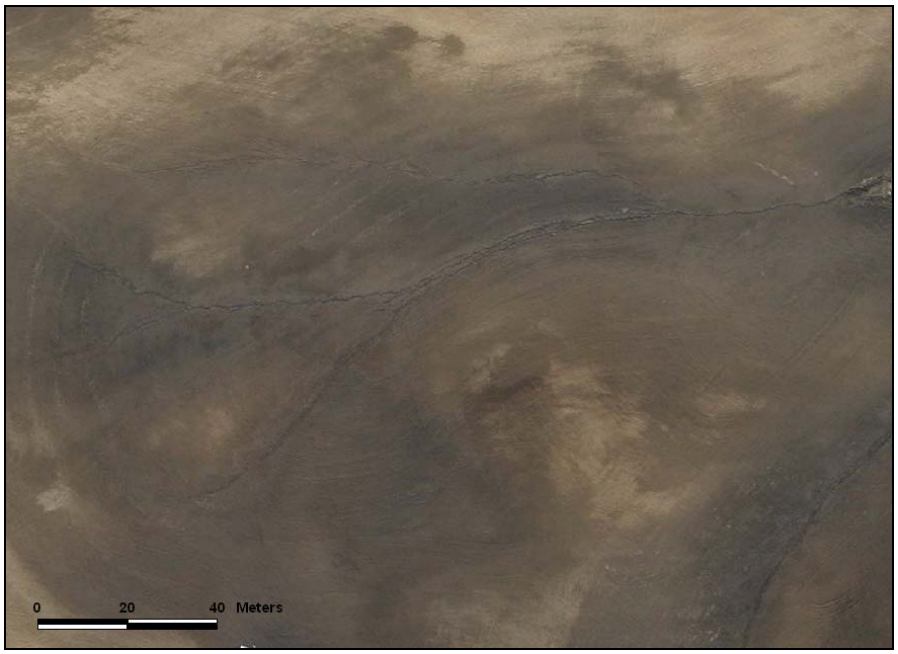

Figure 8.19 Branched ephemeral gully system, March 15,2004.

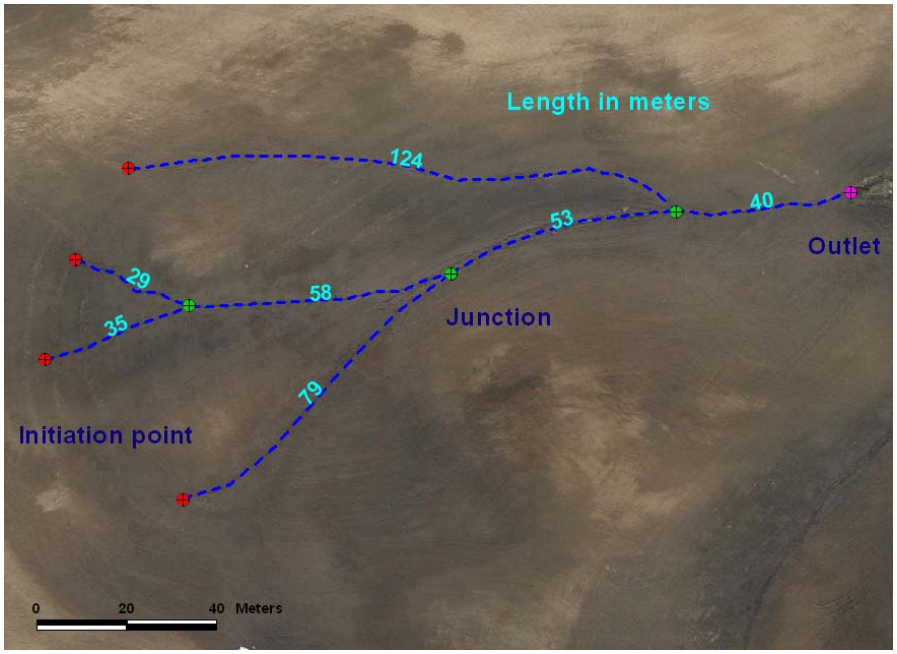

Figure 8.20 Digitization of the branched ephemeral gully digitization.

Some ephemeral gullies have no headwater initiation points as in Figure 8.21 where concentrated flow from an area of perennial cover passes into an annually tilled

surface. Ephemeral gullies of this type are digitized beginning at the edge of the perennial cover.

Figure 8.21 Ephemeral gully with no initiation point, March 15, 2004.

Ephemeral gullies are distinguished from excavated or plowed field drainage channels by the tortuosity of the channel. Constructed field drainage channels are curvilinear and often are accompanied by equipment tracks and ridge marks as in Figure 8.22. Field drainage channels should not be digitized as ephemeral gullies unless edges of the channel have an irregular appearance indicating significant recruitment of sediment by side wall erosion.

Figure 8.22 Constructed field drainage channels, March 15, 2004.

Over 118 km and 1300 gully segments were digitized from georeferenced high-resolution digital aerial images acquired in March 2004. Total digitized lengths of ephemeral gullies in each subbasin are summarized in Table 8.4. Digitized gully centerlines for a portion of the Little Potlatch Creek and Middle Potlatch Creek basin are in Figure 8.23. Gullies can only be digitized from the aerial imagery coverage, about 62 percent of the total basin area after adjusting for georeferencing scale variation.

Total length of ephemeral gullies expected for a subbasin is estimated in Table 8.4 by dividing the digitized length by the aerial image coverage factor of 0.62 and the completeness factor 0.75. Estimated ephemeral gully density in a subbasin is computed by dividing the estimated basin gully length in km by the subbasin area in km^2. The overall average ephemeral gully density is computed as an area weighted average of the subbasin values.

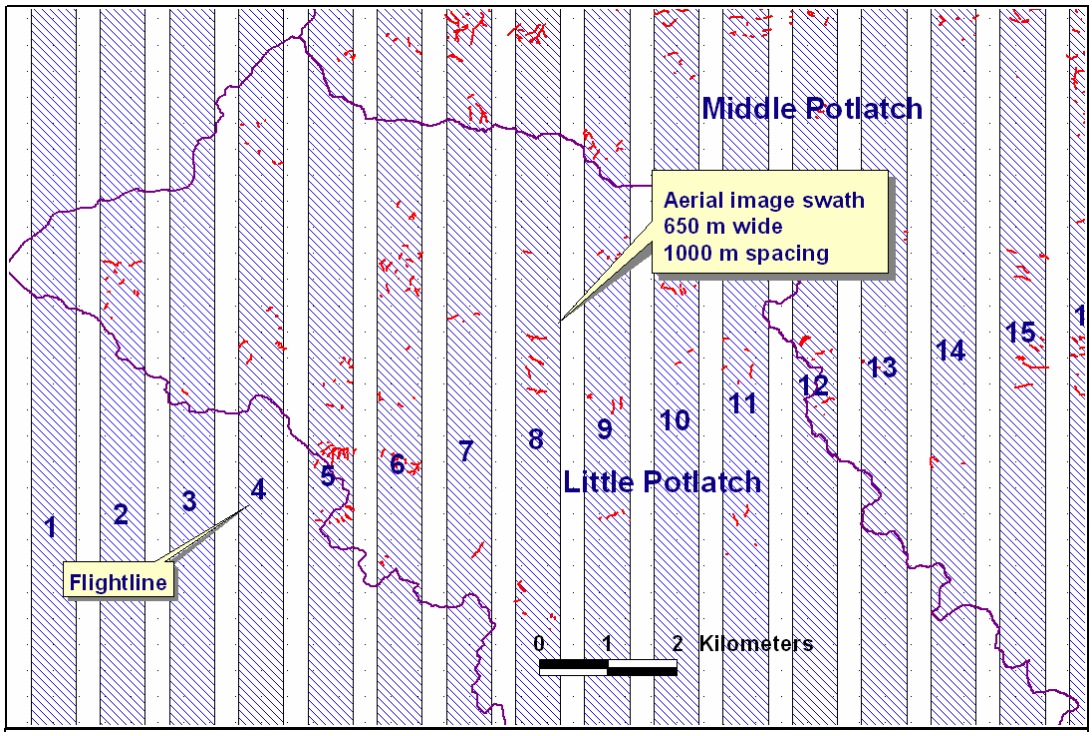

Figure 8.23 Ephemeral gully centerlines digitized from March 2004 aerial imagery.

Subbasin	Digitized Ephemeral Gully Length, km	Estimated Basin[1,2] Gully Length, km	Subbasin Area, ha	Percent of Total Area	Ephemeral Gully Density km/km^2
Big Bear	18.5	39.8	17,049	23.1%	0.23
Cedar	13.3	28.6	10,184	13.8%	0.28
Little Bear	19.0	40.8	10,841	14.7%	0.38
Little Potlatch	15.1	32.6	13,061	17.7%	0.25
Middle Potlatch	40.9	87.9	14,311	19.4%	0.61
Pine	11.9	25.5	8,202	11.1%	0.31
Total	118.6	255.1	73,648	100.0%	0.35

[1]Aerial image coverage is approximately 62% of the total basin area.
[2]Digitizing completeness is approximatel 75% of the gully systems.

Table 8.4 Summary of ephemeral gully digitized length and estimated subbasin ephemeral gully density.

Digitization of the ephemeral gully systems was approximately 75 percent complete across all subbasins. There are several reasons for this. Primarily, this is the only study of the prevalence and spatial distribution of ephemeral gullies in the Palouse region and is likely the largest study of ephemeral gullies in a contiguous area with high resolution aerial imagery ever attempted. Many more ephemeral gullies were found than expected during development of the research proposal. This became apparent after the

initial count of ephemeral gully systems. A contributing factor is that most of the digitizing was performed by undergraduate engineering students involved in course work and other research. Productivity was reduced because the students did not have previous experience with GIS and required training and close supervision during initial georeferencing and digitizing work.

The partial nature of the ephemeral gully digitization does not significantly impair statistical validity of the ephemeral gully estimation of mean length per unit area. Faced with the amount of digitizing, ephemeral gully systems were selected for digitizing by a random process. A random number was assigned to each point in the ephemeral gully system point coverage. Gully systems were selected for digitizing by descending order of the assigned random numbers. Since a large part of the digitizing effort is in georeferencing of aerial images, for efficiency and greater productivity, all ephemeral gullies observed in a georeferenced image were digitized even if they did not belong to the randomly selected gully system.

It is believed this introduces a minor bias, which could be removed by a simple GIS process if desired, but doing so would reduce the sample size. In addition, readily identifiable subsets of area (i.e. the area georeferenced images) were completely digitized and could be sampled for further statistical analysis. A practical judgment, supported further in Section 7.5, is that the 2004 ephemeral gully soil loss estimate per unit area is significantly less than the nominal soil loss tolerance value. Errors in soil loss estimates due to statistical inexactness have little practical impact. The total gully system count could provide conditioning of the statistical analysis, but this was not explored.

Absolute error bounds cannot be assigned to the estimates of digitized gully length because the accuracy of the USGS DOQ is unknown. Approximate values of the most significant sources of error in the overall estimate of ephemeral gully length are listed in Table 8.5. These subjective estimates are based on experience, observation of the digitizing process, and supplemental measurements.

Source of Error	Effect on length Estimate
Gully overlooked in the aerial image or wrong type of channel digitized	5%
Uncertainty in initiation point position	3%
Georefencing scale error	3%
Digitizing gully centerline	1%
Overshoot/undershoot of gully outlet	1%
Aerial image coverage estimate	2%
Digitizing completeness	3%
Total	18%

Table 8.5 Sources and expected magnitude in errors of the ephemeral gully length estimates.

An attempt was made to digitize all concentrated flow erosion channels in positions of topographic convergence. Smaller channels might be classified as extensions of rill erosion channels. Some classical or multi-year gullies may be incorrectly identified as ephemeral gullies eroded during the 2003-2004 season. Some constructed channels appear to have been eroded after construction and may be incorrectly classified as ephemeral gullies when sidewall erosion might have occurred in previous years. Some ephemeral gullies might be overlooked or mistaken for large rills, especially at the edge of aerial images where downstream connectivity cannot be determined. Overall, these interpretation errors appear to have a magnitude of plus or minus 5 percent of the total estimated length. Reasonable assumptions are that the first and last two sources of error in

Table 8.5 are additive and other sources cancel, resulting in an error bound of plus or minus 8 percent.

One aspect of ephemeral gully interpretation that merits consideration in future research is the treatment of constructed field drainage channels. Unlined drainage channels undoubtedly erode by mechanisms that depend on discharge rate. The amount of this erosion is difficult to ascertain in aerial imagery. The undergraduate GIS technicians were directed to digitize field drainage channels if they looked slightly irregular, indicating sidewall erosion. This is a difficult interpretation. Results of one quality control check by the author are summarized in Table 8.6.

Random Selection of 30 Digitized Gully Segments	
Original digitized length, m	2,919
Original without field drainage channels, m	2,571
Corrected gully channel lengths, m	2,552
Adjustment factor, field drainage channels excluded	0.874
Adjustment factor, field drainage channels retained	0.993

Table 8.6 Summary of a quality control check on digitized gully length.

A low estimate of ephemeral gully erosion would exclude any channel that looked like a constructed field drainage channel; total ephemeral gully lengths would be multiplied by the adjustment factor 0.874. Sediment from this source would then have to be added to the permanent channel bank erosion estimate. A higher estimate of ephemeral gully erosion would retain the field drainage channels and assume that field drainage channels widened by an amount equal to the ephemeral gully average width. In the latter case the total digitized length would be multiplied by an adjustment factor of 0.993. The latter approach seems reasonable because field drainage channels are reconstructed after tillage and are most easily assessed during ephemeral gully evaluation. In future work it would be advisable to include an attribute field that

identifies a digitized segment as a possible field drainage channel. This was not done in this study.

It should be emphasized that the spatial distribution and length of ephemeral gullies over large areas are the most uncertain and most difficult ephemeral gully soil loss parameters to determine by other techniques. Estimation of total ephemeral gully length by aerial survey methods is efficient and offers an order of magnitude improvement over estimates by other means. In fact, it is difficult to conceive how it might reasonably be done otherwise. More precise estimates might be made by direct measurement in individual fields, but would be impractical or impossible to obtain for large areas and in locations where ground access is restricted.

8.4.2 Interpretation and measurement of Ephemeral Gully Width

Widths of ephemeral gullies may be interpreted in high-resolution aerial images from differences in color and brightness along the gully channel. Aerial images should be acquired when moisture differences between surface soils and channel bottoms are greatest to take best advantage of this effect. This section will describe techniques of width interpretation and measurements for ephemeral gully erosion volume estimation.

Idealized gully channels are often represented as more or less rectangular in cross section as in Figure 8.1. Actual ephemeral gully channels are seldom prismatic. The process of channel downcutting and widening is not steady or uniform, but occurs as innumerable boundary failures, discontinuous in space and time. Concentrated flow scours the channel bottom, collapses sidewalls, and avulses around temporary hard points. An erosion episode can begin and end abruptly in the hydrodynamic interaction of shear thresholds and sediment transport. What remains to be imaged is a gully channel

that records the total erosion process, downcut and widened in steep sections where sediment supply did not exceed transport capacity, recovered channels partially refilled during flow recession on low slopes, and planar deposition plaques and delta features on flattened toe slopes. The final channel form can be single threads, multiple threads, or fully braided; all within the same gully system. Ground level images of some of the ephemeral gully channels forms observed in this study are in Figure 8.24 through Figure 8.28.

Figure 8.24 Single thread ephemeral gullies.

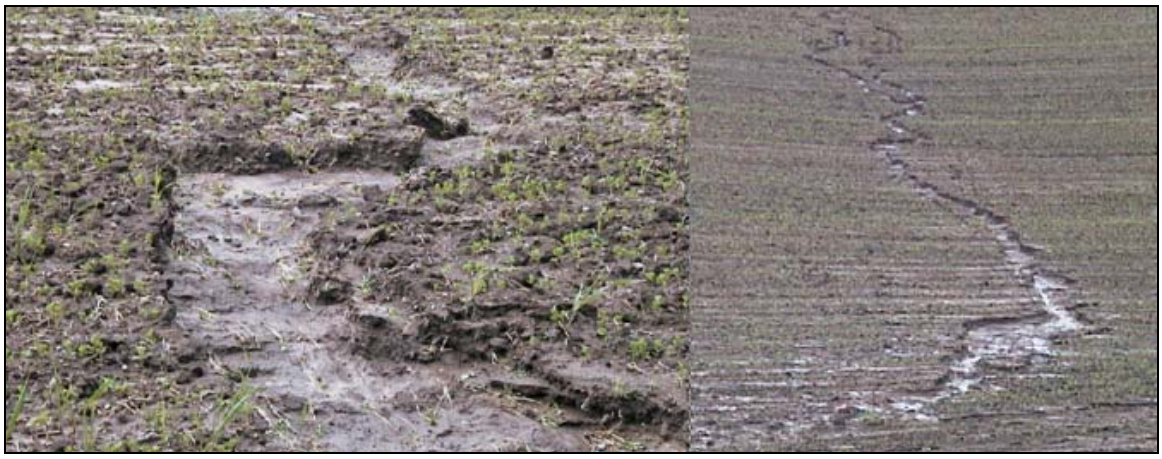

Figure 8.25 Single thread ephemeral gully – almost rectangular.

Figure 8.26 Multiple thread ephemeral gully.

Figure 8.27 Channel eroded through a deposition plaque.

Figure 8.28 Distinctive self-armored single thread ephemeral gully.

The linear forms of ephemeral gullies are easily recognized in aerial images by most interpreters because of the extraordinary pattern recognition capabilities of human vision (Teng 1997). Figure 8.29 is a natural color image of the March 2004 ephemeral gully system in Figure 8.12. This is a good image for analysis because some sections of the gully channel are distinct and incised while others are vague and dispersive – typical of gullies in complex topography. The average slope of the channel profile is about 12 percent and total length is 79 meters. The gully is mostly aligned with the sun azimuth at the time of acquisition so terrain shadows in the channel are minimized. Variation in digital brightness values in this image are mostly a result of soil moisture differences.

Soil moisture differences in natural color imagery are best recorded by the visible red component of the three-band image. Figure 8.30 is the red color band of the image in Figure 8.29. Brightness values have been adjusted (histogram stretch) in the display of the image to emphasize moisture differences. A moisture gradient that increases towards the channel can be inferred from the darkening of the soil.

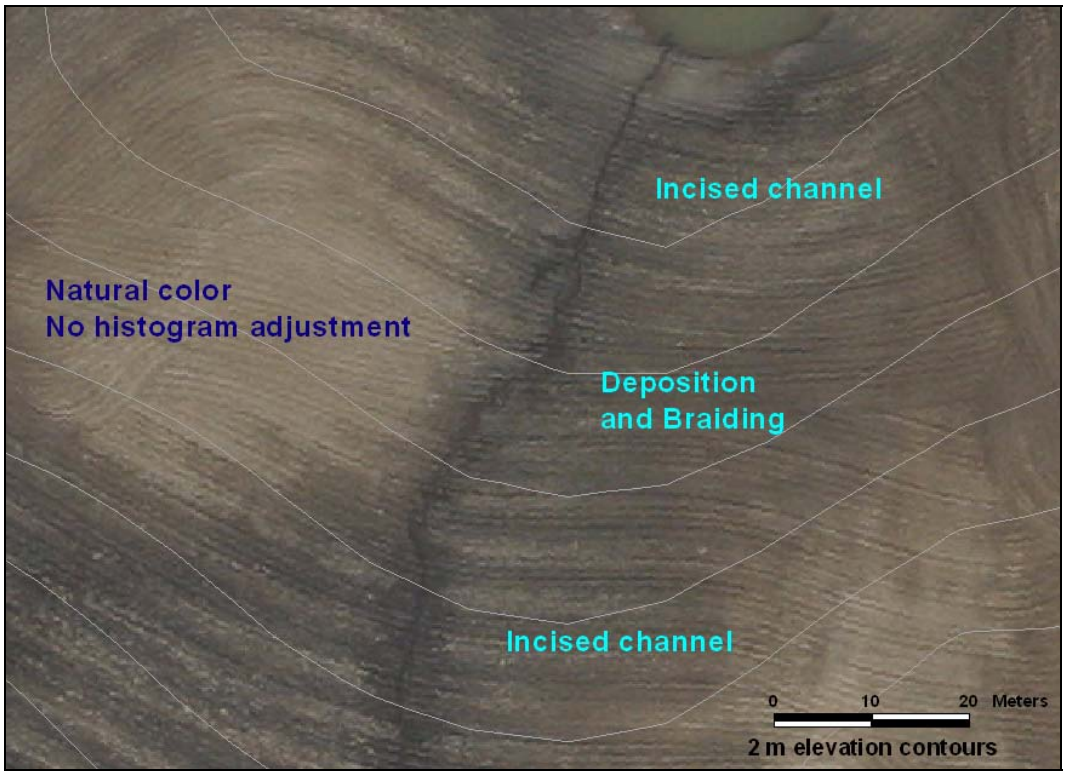

Figure 8.29 Typical unbranched ephemeral gully, March 15, 2004.

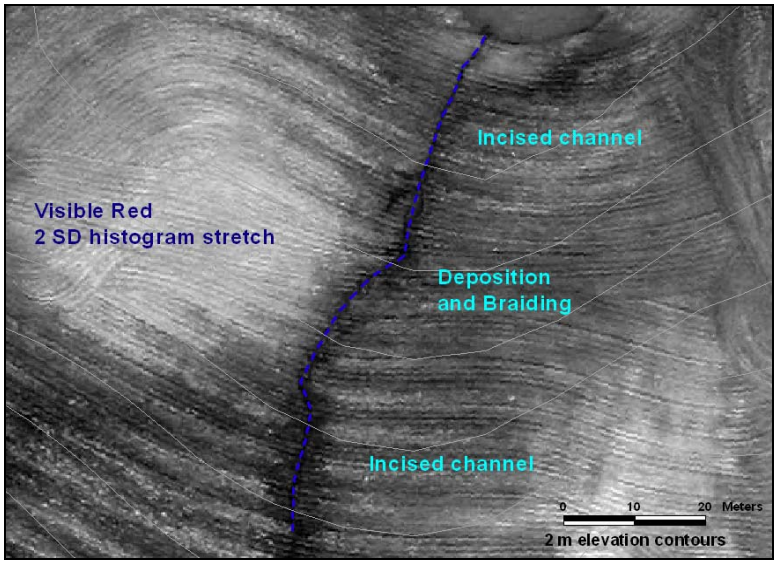

Figure 8.30 Visible red band of the ephemeral gully in Figure 2.46.

Much of the science of remote sensing is based upon the fundamental principle that image brightness values (digital numbers) relate to physical characteristics consistently across the imaged scene. With knowledge and analysis of the

correspondence, physical characteristics can be inferred from the image. Red band brightness value profiles taken at 10 meter long cross sections in Figure 8.31 and plotted in Figure 8.32 indicate strong correlation with gully position and width. A mean gully width of less than 0.5 meter can be inferred from the plots.

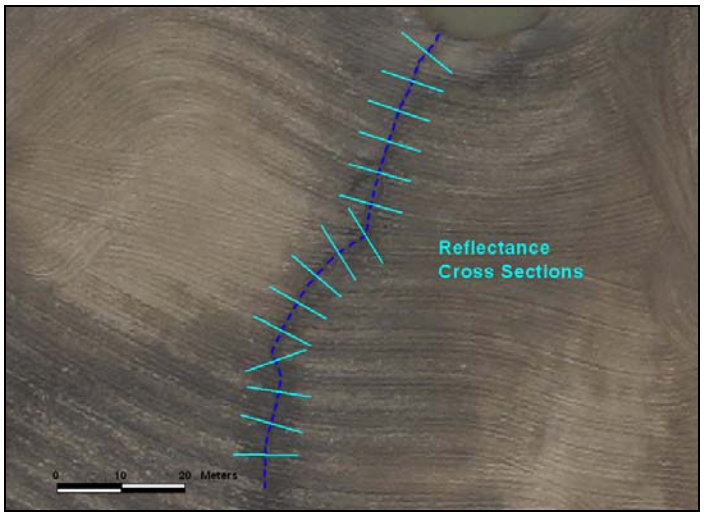

Figure 8.31Cross sections for visible red band digital number profiles.

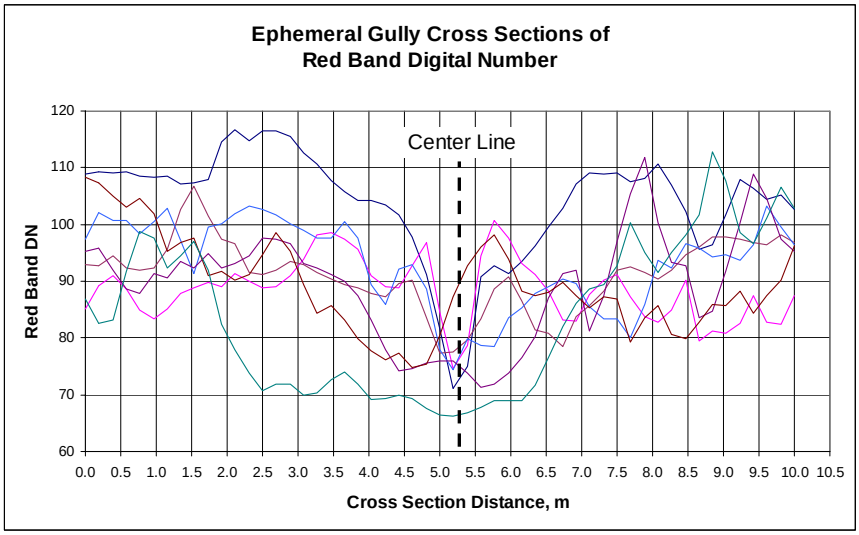

Figure 8.32 Plots of selected visible red band DN profiles.

Human vision interpretation of ephemeral gully width essentially duplicates and enhances the analysis of brightness value profiles in a greatly accelerated and intuitive

psycho-visual process. It is not difficult for an image interpreter to magnify a section of gully in Figure 8.29 and measure inferred widths as in Figure 8.33. The width inferred by this interpretation is the disturbed width of the channel which includes the horizontal projection of moist sloping channel sidewalls. The width of the equivalent rectangular excavated volume is somewhat less than the disturbed width, generally between 0.1 and 0.3 m. The average disturbance width of this incised section of channel is 0.4 m. Its equivalent excavated width is likely about 0.3 m.

An alternative approach is the compute the average width of an ephemeral gully channel from the surface area of the channel and the channel length. Figure 8.34 is a five-class unsupervised isodata classification of the natural color image constrained to a 10 meter corridor along an ephemeral gully. Class 1 of this image in Figure 8.35 is strongly correlated with the gully channel.

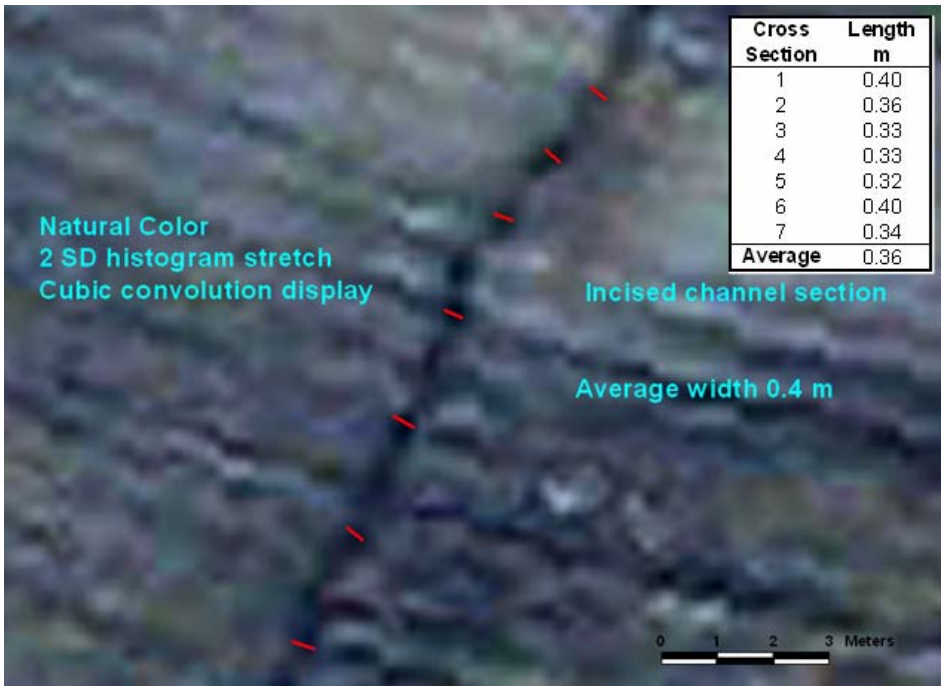

Cross Section	Length m
1	0.40
2	0.36
3	0.33
4	0.33
5	0.32
6	0.40
7	0.34
Average	0.36

Figure 8.33 Measurement of inferred ephemeral gully width.

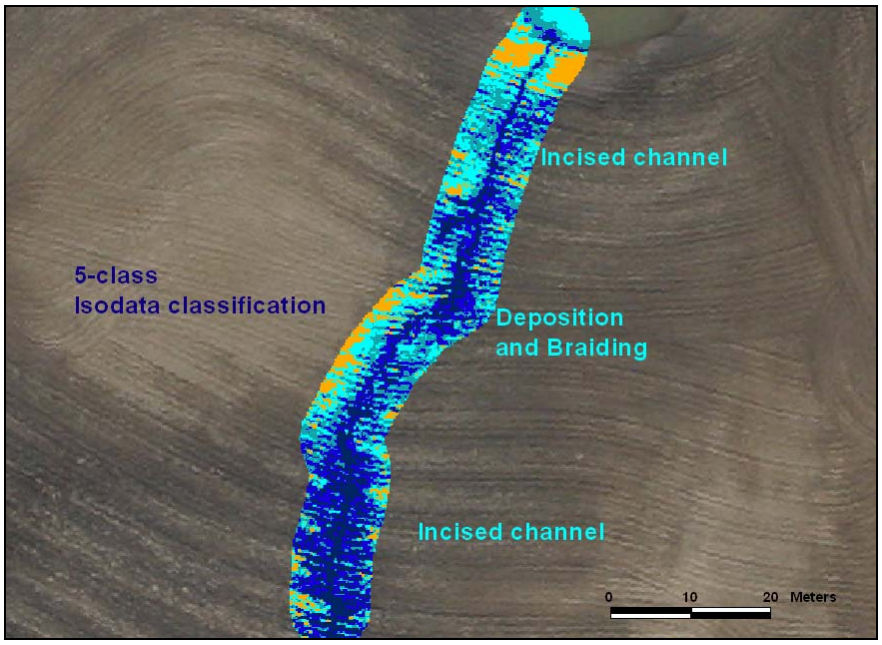

Figure 8.34 Isodata classification of the ephemeral gully corridor.

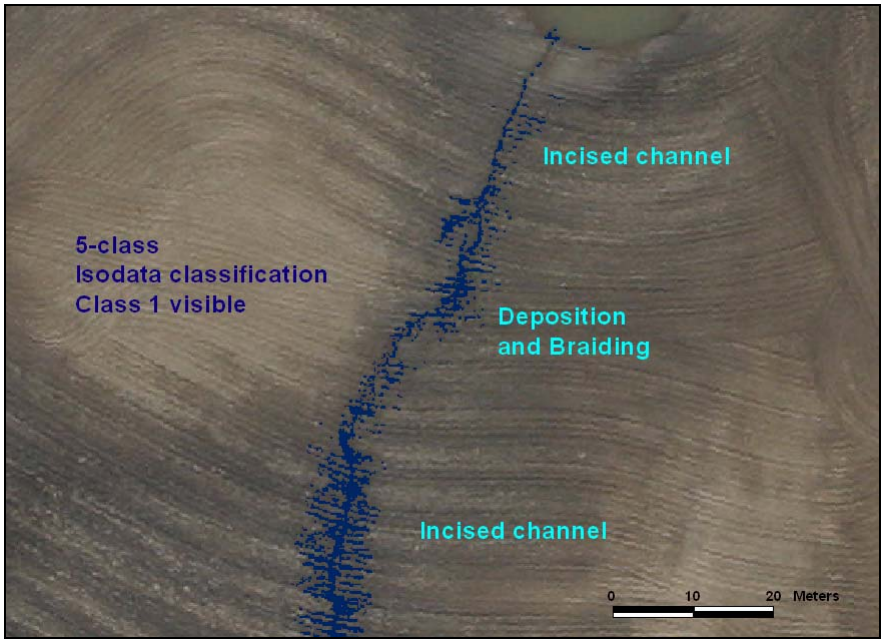

Figure 8.35 Class 1 of the isodata classification of the ephemeral gully corridor.

For this particular gully the reflectance of the moist soil between the tillage ridges cannot be adequately separated from the reflectance of the soil of the channel. The average width computed from the area of Class 1 cells (0.015 ha) divided by the 79 m

total channel length is 1.9 meters, clearly unrealistic. However, this simple analysis indicates good potential for extracting gully morphology from multispectral or hyperspectral imagery of Palouse soils. The additional information from narrow near-infrared and middle-infrared bands (perhaps even thermal) may also support automated extraction of gully widths. Image textural classifiers may also support semi-automated extraction of gully morphology. Investigation of these techniques is a subject for future research.

The study area is too large, and ephemeral gullies are too numerous, to apply brightness profile and image classification techniques routinely in this study. Instead, gully widths were interpreted directly from the natural color images by the undergraduate GIS technicians and the author at prescribed locations along randomly selected ephemeral gullies. Preliminary analysis showed a remarkable consistency in gully width from one location to another and a weak correlation of gully width with total length. Statistically it is unnecessary to measure widths of every ephemeral gully for reliable estimation of mean width for soil loss computation. Widths were measured at three points along randomly selected gully channels at 25, 50 and 75 percent total length (Figure 8.36).

Digitized cross section lines were recorded in an ESRI polyline shapefile for later analysis. The three digitized widths for the example gully are in Figure 8.37. The aerial image is displayed with a two standard deviation histogram stretch and cubic convolution display for clarity. In practice, the interpreter zooms in and out of the image to help in the interpretation of the width. The interpreters were directed to not mechanistically

digitize the line, but to visually interpret the width of the gully system in the vicinity of the measurement point. This process is difficult to convey in a report with static figures.

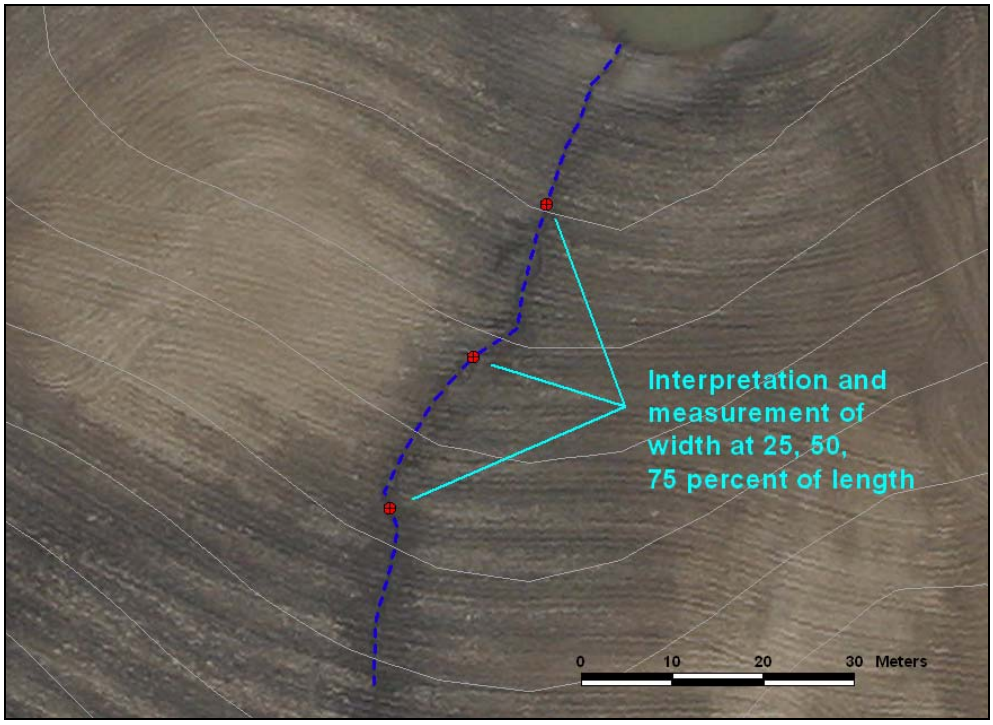

Figure 8.36 Points of gully width interpretation and measurement.

Interpreted widths of ephemeral gully channels are best when channels are incised so that soil moisture differences are accentuated by the linear form of the channel. Multiple thread channels present no great difficulty. The gully width is assumed to be the sum of the separate channels across the disturbed width as depicted in Figure 8.38.

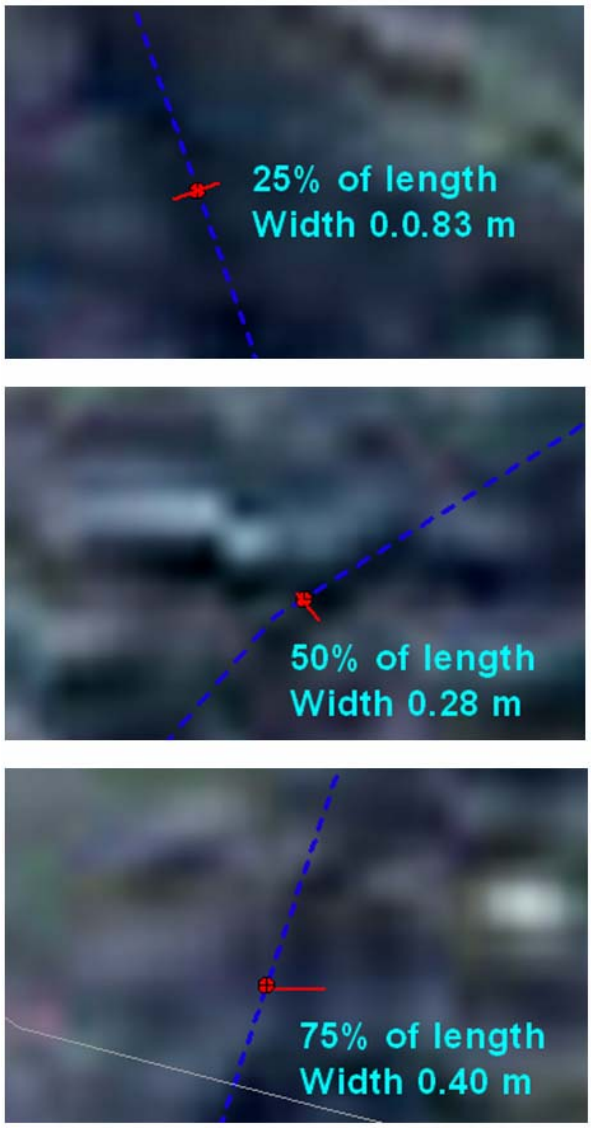

Figure 8.37 Measurements of interpreted ephemeral gully widths.

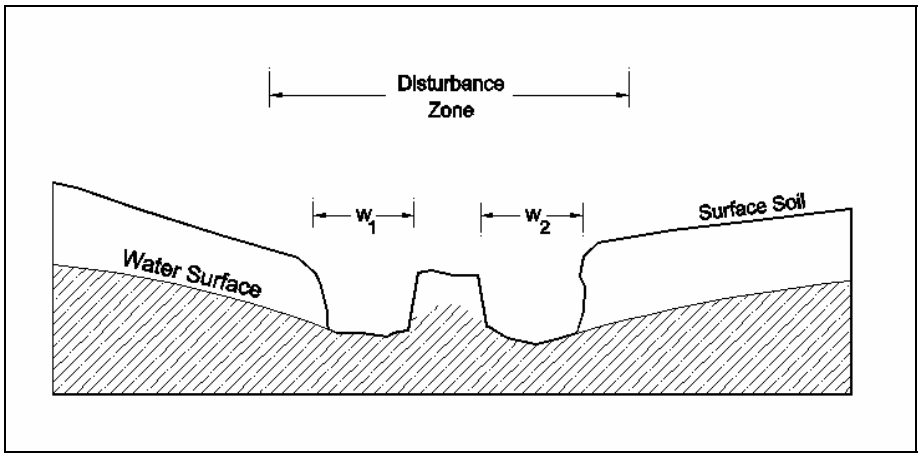

Figure 8.38 Measurement of width in a multiple thread ephemeral gully channel.

Discontinuous gully channels must be interpreted somewhat differently. It is important to realize that the lack of indications of an incised channel is in itself valuable information about the ephemeral gully profile. It is a strong indication of a change of sediment transport capacity (reduced slope) causing deposition of sediment eroded from hillslopes and rills upstream, likely during hydrograph recession. It probably does not indicate a change in soil erosion resistance at the scale of a typical ephemeral gully, especially when the gully channel is incised further downstream. As a first approximation it is reasonable to carry the average incised gully channel width through intermittent sections where the gully channel is indistinct. Indistinct sections of gully channels were noted as such in the ephemeral gully width attribute file.

Average ephemeral gully disturbance width measured on the March 2004 aerial imagery is 0.6 meters (2 feet). This width was estimated from a random sample of 229 cross sections. Interpreted widths ranged from 0.2 to 1.6 m. The standard deviation was 0.24 m. The 95 percent confidence interval of the mean is 0.56 ± 0.03 m. The relative frequency histogram in Figure 8.39 is left skewed because it is harder to distinguish narrow widths as they approach the image resolution.

There was some difference between interpreters. The average gully width measured by the undergraduate GIS technician tended to be wider by about 0.1 m than quality control measurements by the author.

There was very little variation in the disturbance width of incised channels with distance along the channel beyond the zone of initiation point uncertainty. Variation was less than 0.1 m. The narrow range of ephemeral gully widths appears consistent with concentrated flow erosion theory that holds that gullies widen quickly to an initial width

then incise at constant width until reaching a resistive soil layer (Foster and Lane 1983). Once a resistive layer is encountered, the gully widens until shear forces in the flow are insufficient to cause further widening. It appears that peak rates of runoff during the significant runoff events in 2004 did not provide sufficient flow to reach the widening stage. Mechanics of ephemeral gully erosion will be discussed more in the modeling discussion.

Interpreted disturbance widths of ephemeral gullies must be converted to an average incised width for ephemeral gully erosion volume estimation. Average incised width appears to be about 0.1 meter less than the interpreted disturbance width. While this reduction is believed to reasonable, as discussed in the next section, it is based on solely on observation of available ephemeral gullies and should be confirmed with statistically valid sampling in future research.

Also, it must be remembered that aerial images record the final form of the flow erosion channel after sediment deposition during the recession hydrograph. It is conceivable that some channels reach a maximum width during peak flow then narrow as sediment is deposited during recession. This appears to be the case in Figure 8.25.

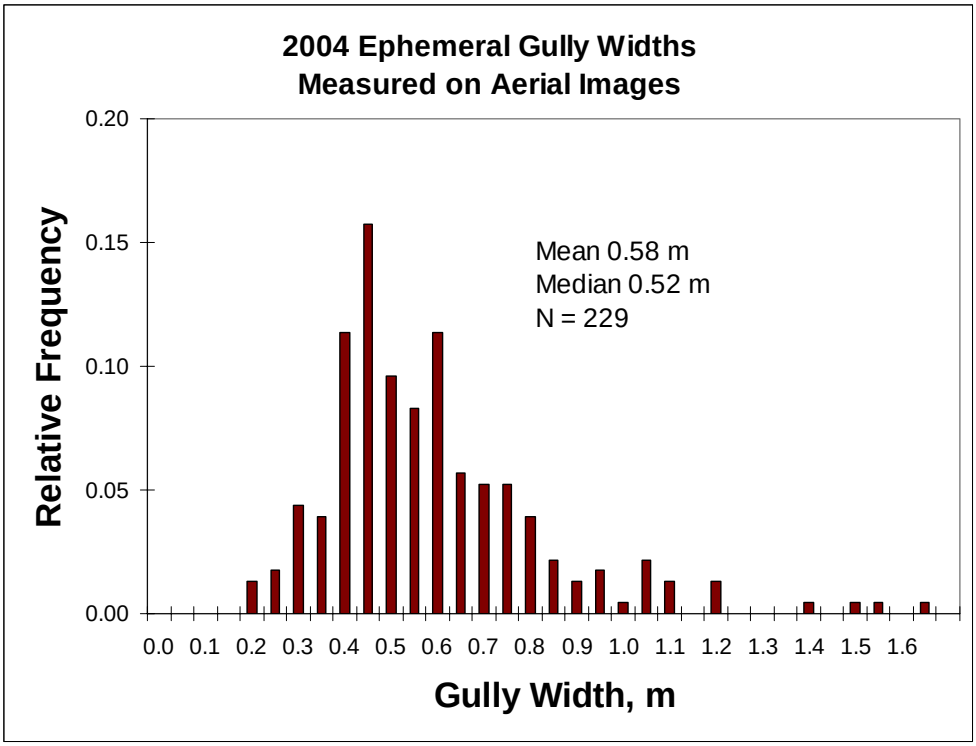

Figure 8.39 Histogram of ephemeral gullies widths measured on March 2004 aerial imagery.

Refinements or alternative methods of measuring ephemeral gullies in aerial imagery should be investigated in future research to increase the efficiency and reliability of image based soil loss estimates. Average width inferred from distinct sections is believed to be a reasonable approach, and likely slightly under-estimates concentrated flow erosion in braided sections of small ephemeral gullies.

8.4.3 Estimation of Ephemeral Gully Depth and Erosion Volume

A watershed estimate of the volume of soil eroded by ephemeral gullies is computed from values of three morphological parameters: total length of gully channels, average channel width and average channel depth. An idealized ephemeral gully cross section is in Figure 8.40. Total ephemeral gully length is highly variable between watersheds. Section 8.4.1 demonstrated that an accurate estimate of total ephemeral

gully length can be measured from aerial images. This is the key parameter that represents the overall severity of ephemeral gully erosion. Section 8.4.2 demonstrates that measurement of the width of ephemeral gullies from aerial images is less precise, but is offset by a remarkable uniformity of gully widths across the study region. Varying the average gully width by 0.1 m should acceptably bound the error in the estimate of soil loss due to this parameter.

Ephemeral gully channel depth cannot be estimated directly from aerial imagery acquired in this study, but it has been observed in many investigations (see modeling discussion) that ephemeral gully depths are also very uniform in similar soils and tillage treatments. Uniformity in depth is expected because ephemeral gully widening and downcutting at a section result from the same hydrodynamic erosion processes acting on relatively isotropic material. In other words, the uniformity of width corresponds with uniformity of depth. Tillage homogenizes soil properties so there is little difference in soil erosion resistance in the horizontal and vertical directions. Possible exceptions that should be investigated in future research are the effect of a consolidation gradient and differential resistance due to residue incorporation.

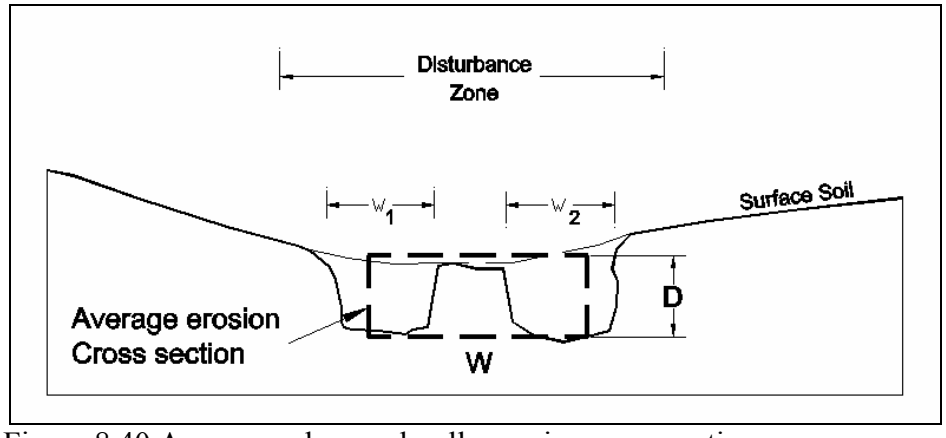

Figure 8.40 Average ephemeral gully erosion cross section.

Ground level photographic observations of numerous ephemeral gullies show that ephemeral gully depths during the winter of 2003-2004 are mostly between 0.1 and 0.2 m deep. Several ephemeral gullies were observed and measured in the field to support the general observation, but as a whole the campaign to field-survey ephemeral gullies was a failure and did not produce statistically meaningful averages of measured ephemeral gully width and depth. Figure 8.41 compares an aerial image of a small ephemeral gully with its ground level photograph. The estimated erosion volume for the total gully is 4.5 m^3 computed from an average width of 0.3 m and an average depth 0.1 m.

The planned field survey effort failed because the investigators did not anticipate landowner reluctance to permit access for field measurements. An extraordinary effort was made to secure access to privately owned agricultural fields to measure ephemeral gullies after commencement of the study. Nearly all property owners contacted were reluctant or refused to grant permission to conduct field work. The most cited reason was the potential that erosion measurements might be used for regulatory purposes. This reasoning tends to agree with previous research findings (Kerns and Krammer 1985).

Landowner and operator reluctance is understandable because the presence of ephemeral gullies can be taken as a sign of ineffective soil conservation practices and poor land stewardship. A few land owners permitted access to measure ephemeral gullies, but the gully systems tended to be small compared to those observed remotely on surrounding ownerships. When viewed as a whole, it must be assumed that the ephemeral gully field measurements are statistically invalid because they include no measurements of large gully systems. Future research must take this into account and

secure permission to measure ephemeral gullies while protecting landowners from undue criticism, regulatory threat and public scrutiny.

While apparently more dimensional precision can be obtained from field measurements, it is likely unjustifiable in a study of this nature to imply a precision in any measurement of ephemeral gully morphology less than 0.1 meter with measurements made with conventional field techniques. It is very problematic in field surveys to objectively determine mean gully width and depth accurately without resorting to devices such as displacement pin frames or laser profilers. Use of these types of devices in a scientifically valid manner was beyond the resources of the dissertation work.

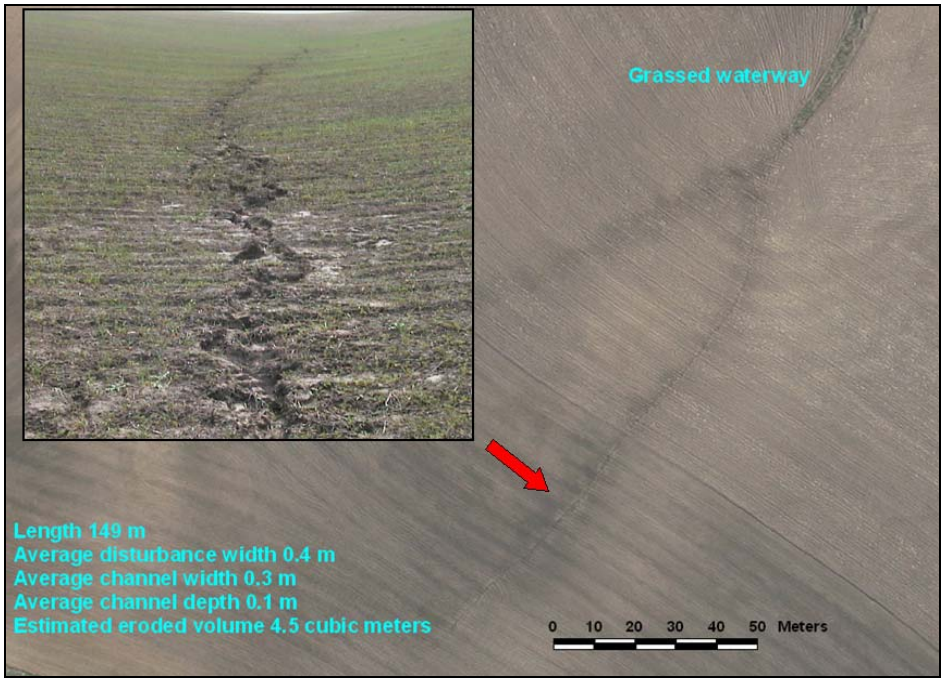

Figure 8.41 Aerial and terrestrial images of a March 2004 ephemeral gully system in the Middle Potlatch basin.

Despite the weak statistical validity of the ephemeral gully depth measurements, an estimate of the average depth of ephemeral gullies in the March 2004 aerial images can be reasoned from the following:

- The average width of ephemeral gullies measured in the aerial images is about 0.5 m. It is highly unlikely, because of tilled soil structure, that larger ephemeral gullies in the study region would have a width to depth ratios approaching 1.0. Therefore the upper bound of possible average ephemeral gully depth is 0.5 m.

- None of the observed gullies, either in the field surveys, or by photographic observation from public roads had apparent mean depths greater than 0.3 m.

- Field measurements of smaller ephemeral gullies averaged 0.1 m or less in depth.

- Smaller ephemeral gullies have shallower depths than larger gullies.

- Ephemeral gully measurements by conventional techniques are probably no more precise than 0.1 meter

Based on the above observations and judgments, the schedule of estimated average gully depths in Table 8.7 can be developed.

Average Ephemeral Gully Width, m	Average Ephemeral Gully Depth, m
0.2 – 0.4	0.1
0.4 – 0.6	0.2
>0.6	0.3

Table 8.7 Schedule of estimate ephemeral gully depth.

A high estimate of watershed ephemeral gully erosion for the winter erosion period of 2003-2004 would adopt an average depth of 0.2 m and a low estimate would use a depth of 0.1 m. High and low estimates of the 2003-2004 ephemeral gully erosion can now be computed from watershed average values for the ephemeral gully total length, mean width and mean depth with the equation:

$$V_{EG} = L_{total} \times W_{avg} \times D_{avg}$$

where V_{EG} is the watershed average erosion volume (m^3), L_{total} is the total length of ephemeral gullies (m), W_{avg} is the average gully width (m), and D_{avg} is the average gully depth (m).

Table 8.8 summarizes the computation for the total area of the six primary agricultural subbasins in the Potlatch basin. Overall average ephemeral gully erosion estimated by aerial survey techniques was 0.22 tons per acre per year (0.50 Mg ha^{-1}).

Subbasin	Gully[1,2] Density km/km^2	Average Width, m	Average Depth, m	Erosion Volume, m^3/km^2	Soil Unit Weight, kg/m^3	Gully Erosion mton/km^2	Gully Erosion Erosion, ton/ac
Big Bear	0.23	0.6	0.2	28.0	1200	33.6	0.15
Cedar	0.28	0.6	0.2	33.7	1200	40.4	0.18
Little Bear	0.38	0.6	0.2	45.2	1200	54.2	0.24
Little Potlatch	0.25	0.6	0.2	29.9	1200	35.9	0.16
Middle Potlatch	0.61	0.6	0.2	73.7	1200	88.4	0.39
Pine	0.31	0.6	0.2	37.4	1200	44.8	0.20
All	0.35	0.6	0.2	41.6	1200	49.9	0.22

[1]Aerial image coverage is approximately 62% of the total basin area.
[2]Digitizing completeness is approximatel 75% of the gully systems.

Table 8.8 Estimate of 2003-2004 ephemeral gully erosion in the Potlatch basin.

High estimates of 2003-2004 ephemeral gully erosion would be 150 percent of the erosion values in Table 8.8. A low estimate of erosion would be 50 percent of the values in Table 2.13 based on an average gully depth of 0.1. It can be seen from the U.S. customary unit conversion of areal erosion that the 2003-2004 erosion is much less than the USDA soil loss tolerance values of 4 to 5 tons per acre per year for soils in the study area. The areal erosion estimates in Table 8.8 are computed using the full subbasin area regardless of land cover types.

If the precipitation and runoff cycle for 2004-2005 is typical and if the hydrologic condition of the watershed is representative of long term conditions, then it appears that the 0.22 tons per acre per year of ephemeral gully erosion is a relatively minor source of sediment in the lower Potlatch River basin compared to the 6.7 tons per acre per year estimate of rill and interrill erosion cited in Section 7. However, as discussed in Section

7, the rill and interrill soil loss estimate is seriously questioned and may be too high. Moreover, ephemeral gullies act as the conveyance structure for much of the rill and interrill erosion and would act to increase sediment delivery. As such, farm plans should use this information when selecting best management practices or conservation tillage practices.

8.5 Ephemeral Gully Prediction and Modeling

Ephemeral gully erosion assessed by a single aerial survey and measured in aerial images, however accurate, only provides a point-in-time estimate. Aerial surveys must be repeated over several seasons under different hydrologic conditions to estimate long term mean annual ephemeral gully erosion. While this is a practical and achievable strategy for serious long term studies of watershed sediment yield, short term records must be augmented with erosion modeling to estimate average sediment yield and predict response to changed land surface conditions. This section discusses the current status of ephemeral gully erosion modeling and presents initial work on an original watershed ephemeral gully erosion model.

8.5.1 Current status of Ephemeral Gully Prediction and Modeling

Researchers note the difficulty modeling erosion and transport processes of ephemeral and classical gullies especially at a watershed scale (Desmet et al. 1999; Ogden et al. 2001). Many models avoid explicit estimation of gully erosion. Ephemeral gully erosion is not estimated by the RUSLE method (Foster et al. 2003). The WEPP model (Flanagan and Nearing 1995) and the Ephemeral Gully Erosion Model (EGEM)

(Woodward 1999) predict ephemeral gully erosion with physical process algorithms but only after topographic position and gully length are input.

Recent literature indicates that existing physical process models may not estimate ephemeral gully erosion accurately in deep loess soils (Nachtergaele et al. 2001a) or steep terrain (Istanbulluoglu et al. 2003). Other research suggests it may be impractical to model the full physical process of ephemeral gully erosion in larger watersheds due to spatial variability in topographic relief, heterogeneity in soil characteristics, temporally varying land use practices, and low temporal and spatial resolution of meteorological data (Nachtergaele et al. 2001b) . Difficulties arise because gully initiation appears to be triggered by a complex interaction of several variables including microrelief (Takken et al. 2002), topographic position and tributary area (Desmet et al. 1999; Vandekerckhove et al. 1998), variations of precipitation intensity (Woodward 1999), and possibly infringement of a geomorphic threshold (Harvey et al. 1985).

Research findings indicate that ephemeral gully length and density are likely the most significant parameters for estimating gully erosion volume. Investigations of gully erosion on loess soils in Belgium and in the Mediterranean (Nachtergaele et al. 2001b) showed that an accurate measurement of ephemeral gully length was the key variable necessary to reliably predict ephemeral gully volumes. These studies found that gully length statistically explained over 90 percent of the observed variation in ephemeral gully volumes.

Gully erosion as estimated by the WEPP model represents the current status of operational models employing the physical processes of channel type rill and ephemeral gully erosion. Channel erosion routines for WEPP were adapted from the CREAMS

model channel component (Knisel 1980). Erosion is based on a steady-state sediment continuity equation in which flow shear stress is calculated using regression equations developed by Foster (Foster 1982; Foster and Lane 1983). Channel elements in the WEPP routines can model flow in terrace channels, diversions, ephemeral gullies, grass waterways, and other similar channels. The channel element does not describe classical gully or stream channel erosion.

The length of the eroding channel (element) and maximum erosion depth must be specified to run the WEPP model. Channel elements are divided into ten segments of equal length. Homogeneous slope segments are computed for each channel segment by interpolating the channel topographic data. All slope segments within a channel element are assumed to have identical parameter values (e.g., Manning's roughness coefficient). Sediment detachment of ephemeral gullies is assumed to occur initially from the channel bottom until reaching a nonerodible layer (usually the primary tillage depth). After reaching the nonerodible layer the erosion channel widens until flow is too shallow to cause detachment. In extended simulation the ephemeral gully cross-section is updated after each precipitation event to calculate channel hydraulics for subsequent events.

8.5.2 Ephemeral Gully Channel Processes

Opposing processes of sediment detachment and deposition control the time dependent shape and size of eroded concentrated flow channels (Foster 1982). Channels incise and widen when discharge boundary forces (represented by shear stress, velocity or stream power) overcome channel material detachment resistance (represented by erodibility and critical shear stress). Erosion continues if the flow is competent to

transport sediment. Sediment settles from the flow and deposits on the channel boundary when sediment load exceeds flow transport capacity. Deposited sediment may be eroded by later discharges of greater magnitude or those with less sediment inflow from source areas.

Soil and surface characteristics affect the severity of channel erosion. Major factors identified by Foster (1982) for upland and channel erosion are contrasted in Table 8.9. Subsurface factors gain importance in channel erosion. In particular, the subsurface nonerodible layer will tend to limit channel incision.

Uplands	Channels
Hydrology	Inflow from upstream areas
Topography	
Soil erodibility	Soil erodibility
Soil transportability	Soil transportability
Cover	Cover
Incorporated residue	
Residual land use	
Subsurface effects	
Tillage	Tillage
Roughness	
Tillage marks (micro channels)	
	Presence of nonerodible layer
	Channel control
	Channel sidewall stability
	Channel adjustment

Table 8.9 Major factors affecting upland erosion and concentrated flow erosion processes (after Foster 1982).

8.6 Foster and Lane Model

Flow and sediment interactions are complex stochastic phenomena difficult to define (Einstein 1950). Process simplifications are necessary in order to model channel erosion in practical applications. A common starting point for soil erosion modeling is

the shallow flow one-dimensional continuity equation for sediment (Foster 1982; Haan et al. 1994):

$$\frac{dq_s}{dx} = D_r + D_i \qquad 8.1$$

where q_s is the sediment load, x is the down slope distance, D_r is the channel (rill) detachment or deposition rate, and D_i is the lateral inflow of sediment. Foster and Meyer (1982) simplified the detachment-deposition process with a first order reaction coefficient:

$$D_r = C\left(T_c - q_s\right) \qquad 8.2$$

where C is the rate coefficient and T_c is the sediment transport capacity. The deposition rate and transport capacity may be defined for separate particle size classes. A further simplification is to assume that the maximum detachment capacity is proportional to transport capacity to give the relationship:

$$\frac{D_r}{D_{rc}} + \frac{q_s}{T_c} = 1 \qquad 8.3$$

where D_{rc} is the maximum detachment capacity. Observations show that the transition from erosion to deposition is indistinct (Foster et al. 1984) and primarily dependent on channel slope.

Foster and Lane (1982; 1983; 1980) developed equilibrium geometry for small channels eroded by a steady discharge based on critical shear stress and a two stage erosion process of incision and widening. Incision stops at a specified depth to a non-eroding layer. Widening commences until shear stress decreases to the critical soil stress. Potential equilibrium channel geometry is computed for a steady discharge of infinite duration, and reduced to a final eroded width for a storm of finite duration. The decrease

in widening rate is an exponential function of time under steady flow. Flow resistance is based on Manning's equation.

The incision stage assumes instantaneous widening of the channel to an initial equilibrium width. The channel then degrades at a rate defined by the maximum shear stress until it reaches the non-erodible layer. Non-erodible layers have higher critical stresses than surface soils and are typically encountered at the bottom of the primary or secondary tillage. In the widening stage, the channel ceases deepening and erodes laterally to the final channel width depending on the duration of flow. Hydraulic geometry of the potential initial equilibrium and final potential widths is determined from a graphical conveyance function. Conceptual incision and lateral erosion channels employed in the model are shown in Figure 8.42.

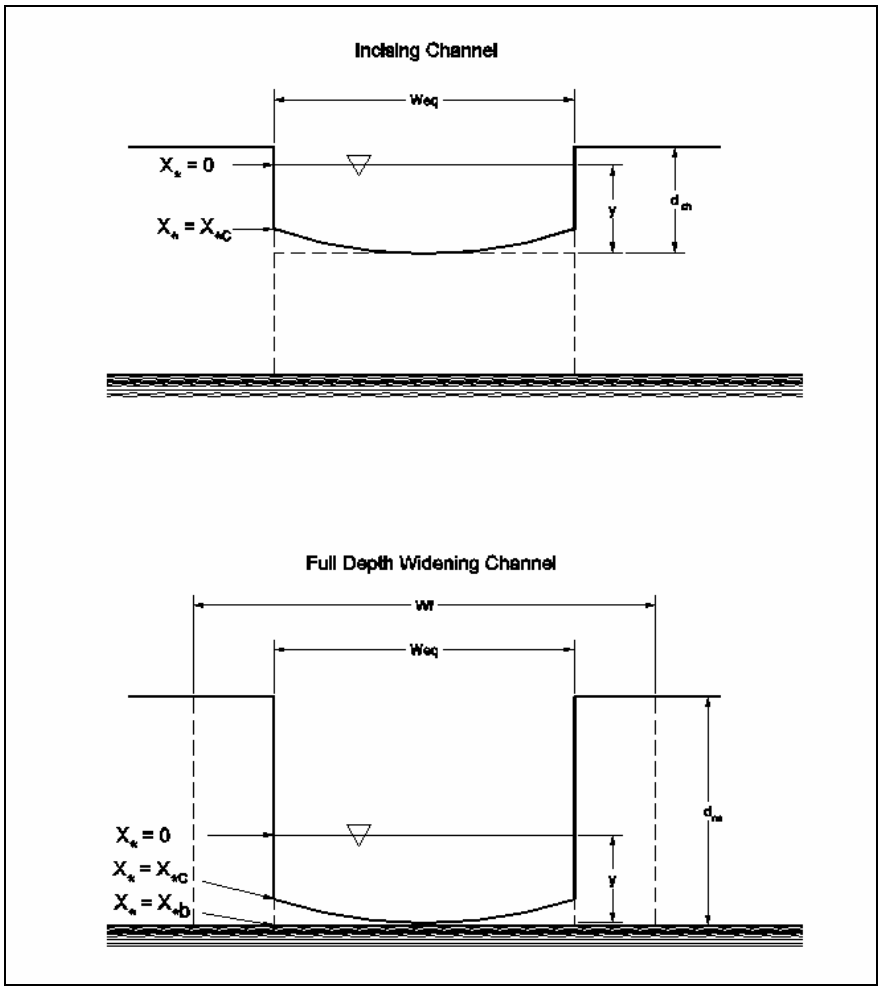

Figure 8.42 Foster and Lane Channel Geometry (After Haan 1984).

8.6.1 Equilibrium Channel Geometry

Tractive force at the wetted perimeter of a channel varies with channel shape and width-to-depth ratio. A channel erodes to a particular shape given a shear stress distribution, critical shear stress of the channel boundary material, discharge, slope, and roughness. Channel erosion can be modeled assuming detachment is proportional to the difference between the actual shear stress and the critical shear stress. Detachment is computed:

$$D_{rc} = K_r\left(\tau - \tau_c\right)^m \qquad 8.4$$

where D_{rc} is the detachment rate potential (kg m^{-1} sec^{-1}), τ is actual shear stress (Pa), τ_c is the critical shear stress (N m^{-2}), K_r is the rill erodibility (m s^{-1}), m is a calibration exponent typically assumed to be 1.0 or 1.05 (Foster 1983). Critical shear stress may be assumed to be negligible and may be removed from Equation 8.1 in high shear stress applications where critical shear stress is very low compared to actual shear stress (Hanson 1991). The rate of channel incision and widening can be determined if D_{rc} is known.

Actual shear in Equation 8.4 at any point on the channel boundary is a function of the boundary shear stress distribution. Foster and Lane (1980, 1982) developed a normalized shear stress distribution from observed data. Shear stress at any point on the wetted perimeter of the channel is computed with a normalized shear force ratio:

$$\tau_* = \frac{\tau}{\tau_a} = \exp\left[0.127 - 0.516 \cdot \ln(X_*) - 0.408 \cdot \ln(X_*)^2 - 0.0344 \cdot \ln(X_*)^3\right] \qquad 8.5a$$

or

$$\tau_* = \frac{\tau}{\tau_a} = 1.35\left[1 - (1 - 2 \cdot X_*)^{2.9}\right], \qquad \text{limited to } X_* < 0.5 \qquad 8.5b$$

where τ_* is the dimensionless shear, τ is the actual shear force (N m^{-2}), τ_a is the average shear force (N m^{-2}), and X_* is the normalized wetted perimeter distance. Equation 8.5a is the original form of the equation (Foster 1982). Equation 8.5b (Foster 1983) is a close approximation. Critical dimensionless shear τ_c occurs where τ is equal to τ_c. Average shear channel shear stress is:

$$\tau_a = \gamma \cdot R \cdot S \qquad 8.6$$

where γ is the unit weight of water, R is the hydraulic radius and S is the channel friction slope, maximum shear stress is 1.35 τ_a at X_* equal to 0.5.

The method utilizes several other normalized parameters. Dimensionless distance along the wetted perimeter X_* starting at the water surface is:

$$X_* = \frac{X}{P_w} \tag{8.7}$$

where X is the distance along the wetted perimeter from the water surface in the channel to a point on the wetted perimeter and P_w is the total length of the wetted perimeter. A dimensionless perimeter distance X_{*c} can be defined for the point on the channel boundary where actual shear stress is equivalent to the material critical shear stress τ_c.

Dimensionless hydraulic radius is:

$$R_* = \frac{R}{P_w} \tag{8.8}$$

where R is the hydraulic radius, and dimensionless equilibrium width is,

$$W_* = \frac{W_{eq}}{P_w} \tag{8.9}$$

where W_{eq} is the equilibrium width of the channel.

Foster and Lane applied the shear stress distribution in Equation 8.5 to the two stage erosion model and expressed the resulting normalized equilibrium channel geometry as a graphical function. The normalized equilibrium geometry function gives values of W_* and R_* for values of X_{*c}. Both W_* and R_* are only functions of X_{*c} , so equilibrium geometry for a particular discharge, roughness and slope can be determined from a conveyance function:

$$g(X_{*c}) = \frac{1}{\tau_{*c} \cdot R_*^{3/8}} = \frac{\gamma \cdot S}{\tau_c}\left(\frac{nQ}{\sqrt{S}}\right)^{3/8} \tag{8.10}$$

where γ is the unit weight of water (N m^{-3}), Q is the peak discharge (m^3 s^{-1}), n is the Manning's friction coefficient, and S is the channel slope (m m^{-1}). The conveyance function value $g(X_{*c})$ is related to the dimensionless critical distance X_{*c} by a second graphical relationship. Haan et al. (1984) recommend that high values of $g(X_{*c})$ be limited to 35 and provide a tabulation of the normalized equilibrium geometry and graphical conveyance function with this restriction. Values of X_{*c} are undefined for $g(X_{*c})$ less than 1.8 because actual shear stress would be less than critical shear stress.

Once W_* is determined from the conveyance function, the initial equilibrium width is computed:

$$W_{eq} = W_* \cdot P_w . \qquad 8.11$$

The initial equilibrium width is the width of the incising channel through the first stage of channel formation. Channel width remains constant until incision reaches the non-erodible layer.

The average flow shear stress is expressed in terms of dimensionless hydraulic radius as:

$$\tau_a = \gamma \cdot S \cdot \left(\frac{nQR_*}{\sqrt{S}} \right)^{3/8} \qquad 8.12$$

The steady state mass erosion rate E_{rc} per unit length of channel during initial incision (kg s^{-1} m^{-1}) when *transport capacity is not limiting* is computed from Eq. 8.4 multiplied by the equilibrium width:

$$E_{rc} = K_r \left(1.35\tau_a - \tau_c\right) \cdot W_{eq} . \qquad 8.13$$

Since equilibrium width does not change during incision, the vertical degradation rate is,

$$M_{rc} = \frac{E_{rc}}{W_{eq} \cdot \rho_b} \qquad 8.14$$

where M_{rc} is the channel incision rate (m s^{-1}) and ρ_b is the soil bulk density (kg m^{-3}). Time to reach the non-erodible layer is computed from the incision rate and depth to the non-erodible layer:

$$t_{ne} = \frac{d_{ne}}{M_{rc}} \qquad 8.15$$

where t_{ne} is the erosion time (s) and d_{ne} is the depth to the non-erodible layer (m) that must be determined by other means.

Depth of water in the channel (based on steady discharge) when incision reaches the non-erodible layer is:

$$y = \frac{P_w - W_{eq}}{2} \qquad 8.16$$

where y is the water depth (m). This water depth defines the initial shear stress on the non-erodible layer or at the toe of the channel wall before lateral widening.

Lateral erosion occurs if the storm duration exceeds the time to reach the non-erodible layer. The initial rate of lateral erosion is controlled by the shear stress at the toe of the channel wall just as incision reaches the non-erodible layer:

$$\frac{dW}{dt} = K_r \frac{\tau_b - \tau_c}{\rho_b} \qquad 8.17$$

where dW/dt is the initial channel widening rate (m) and τ_b is the shear at the toe of the wall (N m^{-2}) computed from Equation 8.10 for a value X_* determined for y in Equation. 8.16. The mass erosion rate per unit length of channel (kg s^{-1} m^{-1}) is:

$$E_{rc} = \rho_b \frac{dW}{dt} d_{ne} . \qquad 8.18$$

The potential final channel width eroded under a steady discharge of infinite duration is computed from the conveyance function (Equation 8.10):

$$g\left(X_{*cf}\right) = \frac{1}{\tau_{*cf} \cdot R_{*f}{}^{3/8}} = \frac{\gamma \cdot S}{\tau_c} \left(\frac{nQ}{\sqrt{S}} \right)^{3/8} \qquad 8.19$$

where the subscript ***cf*** indicates the limiting condition when shear stress at the toe of the wall just equals the critical shear stress. The dimensionless wetted perimeter distance X_{*cf} at the limiting condition is:

$$X_{*cf} = \frac{y_f}{P_w} \qquad 8.20$$

Recognizing that the wetted perimeter is $W_f + 2y_f$ and that dimensionless hydraulic radius R_* is $W_f\, y_f / P_w^2$, the dimensionless hydraulic radius for the limiting condition is:

$$R_{*f} = X_{*cf} \cdot \left(1 - 2X_{*cf}\right). \qquad 8.21$$

Equation 8.19 is solved by iteration for the unknown value of X_{*cf}. The graphical conveyance function is not used to solve for X_{*cf}, nor is the $g(X_{*c})$= 35 limit imposed for the right hand side of Equation 8.19.

The potential final channel width is computed with the known value of X_{*cf}:

$$W_f = \left[\frac{nQ}{\sqrt{S}} \cdot \frac{1 - 2X_{*cf}}{X_{*cf}{}^{5/3}} \right]^{3/8} \qquad 8.22$$

Foster (1982) found that actual channel width approached the potential final channel width at a decreasing rate as shear stress diminished and could be expressed with an exponential function:

$$W_*^{'} = 1 - e^{-t_*}$$

or the first derivative:

$$\frac{dW_*^{'}}{dt_*} = e^{-t_*} \qquad 8.23$$

where W_*' is the dimensionless width and t_* is the dimensionless time. Dimensionless width and time are computed:

$$W_*^{'} = \frac{W - W_{in}}{W_f - W_{in}} \qquad 8.24$$

and

$$t_* = \frac{t\left(dW/dt\right)_{in}}{W_f - W_{in}} \qquad 8.25$$

where W is the actual width at any time t, W_f is the potential final channel width, W_{in} is the initial incision width W_{eq} in a continuous steady flow erosion event or last eroded width in a subsequent storm, and $(dW/dt)_{in}$ is the initial rate of lateral erosion computed with Eq. 8.17. The time t for channel widening begins after incision is complete and is limited to the flow duration.

Application of the dimensionless width and dimensionless time in Equations 8.21 – 8.23 gives the definition of the rate of lateral erosion:

$$\frac{dW}{dt} = \frac{dW}{dW_*^{'}} \frac{dW_*^{'}}{dt_*} \frac{dt_*}{dt} = \left(\frac{dW}{dt}\right)_{in} e^{-t_*} \qquad 8.26$$

Total channel widening from lateral erosion is computed by integration of Equation 8.26:

$$W_{Lat} = \int_0^t \left(\frac{dW}{dt}\right)_{in} e^{-t_*} dt \qquad 8.27$$

Initial rate of channel widening $(dW/dt)_{in}$ for a continuous erosion event is computed with Equation 8.17 so Equation 8.63 becomes:

$$W_{Lat} = \int_0^t K_r \frac{\tau_b - \tau_c}{\rho_b} \cdot e^{-t_*} dt \qquad 8.28$$

where

$$t_* = \frac{K_r \frac{\tau_b - \tau_c}{\rho_b} \cdot t}{W_f - W_{in}}.$$

Integration of 8.28 gives a direct expression for the amount of channel widening for any time *t*:

$$W_{Lat} = \left(W_{eq} - W_f\right) \cdot \exp\left[- K_r \cdot \frac{\tau_b - \tau_c}{\rho_b \left(W_f - W_{eq}\right)} \cdot t \right] + W_f - W_{eq} \qquad 8.29$$

Total eroded width is the sum of the initial equilibrium width from the incision stage of erosion and the lateral widening:

$$W_{total} = W_{eq} + W_{Lat}$$

Total erosion for the duration of the steady flow discharge is computed:

$$E_{rc} = \rho_b \cdot W_{total} \cdot d_{ne} \cdot L_c \qquad 8.30$$

8.6.2 Reconstruction and Approximation of the Foster and Lane Equilibrium Geometry

The graphical functions of Foster and Lane (1980) must be converted to numeric form before use in simulation. Foster and Lane assumed that an equilibrium channel existed such that under steady flow it eroded vertically downward at the rate set by the maximum shear stress. Maintenance of a constant equilibrium channel shape requires that all points across the channel must erode downward at the same rate until encountering a more resistant layer. They also assumed that the rate of erosion at a point

on the channel boundary was controlled by the actual shear at the point and in a direction established by the angle α:

$$\cos\alpha = \left(\frac{\tau - \tau_c}{\tau_{\max} - \tau_c}\right)^m = \left(\frac{\tau_* - \tau_{*c}}{1.35 - \tau_{*c}}\right)^m . \qquad 8.31$$

Foster and Lane constructed the graphical functions by assuming values of X_{*c} (each X_{*c} uniquely determines a particular channel cross section); subdividing the active perimeter (distance X_{*c} to 0.5) into 50 computational elements; determining the angle α with Equation 8.31; computing the cross section coordinates of each element; and computing values of W_*, R_*, D_*, *and* $g(X_{*c})$ for each cross section.

The Foster and Lane geometry was reconstructed and tabulated for 100 values of X_{*c} ranging from .005 to 0.495 in Figure 8.43 and Figure 8.44 assuming m is 1.0. Tabulated values are in Appendix 8.1. The reconstructed tabulated values are slightly different than those referenced in Haan et al. (1994). A possible reason may be the empirical equation selected to approximate the shear stress distribution or the selection of m. The reconstructed tabulated values were computed with Foster's (1982) original equation (Equation 8.5a). The differences are insignificant for practical computations.

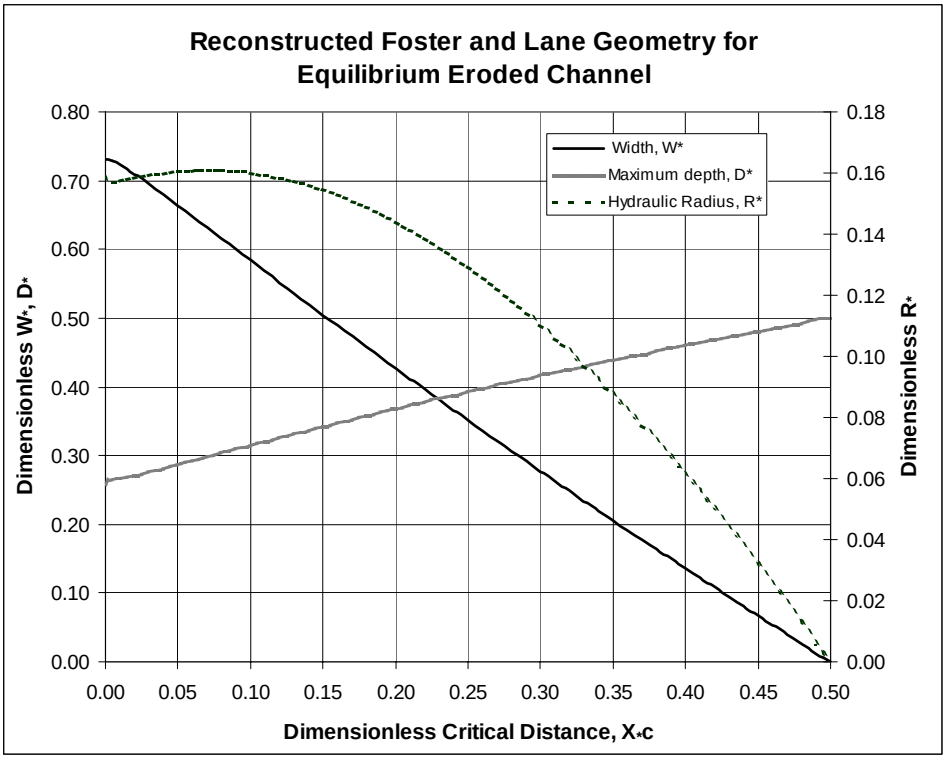

Figure 8.43 Reconstructed Foster and Lane channel geometry.

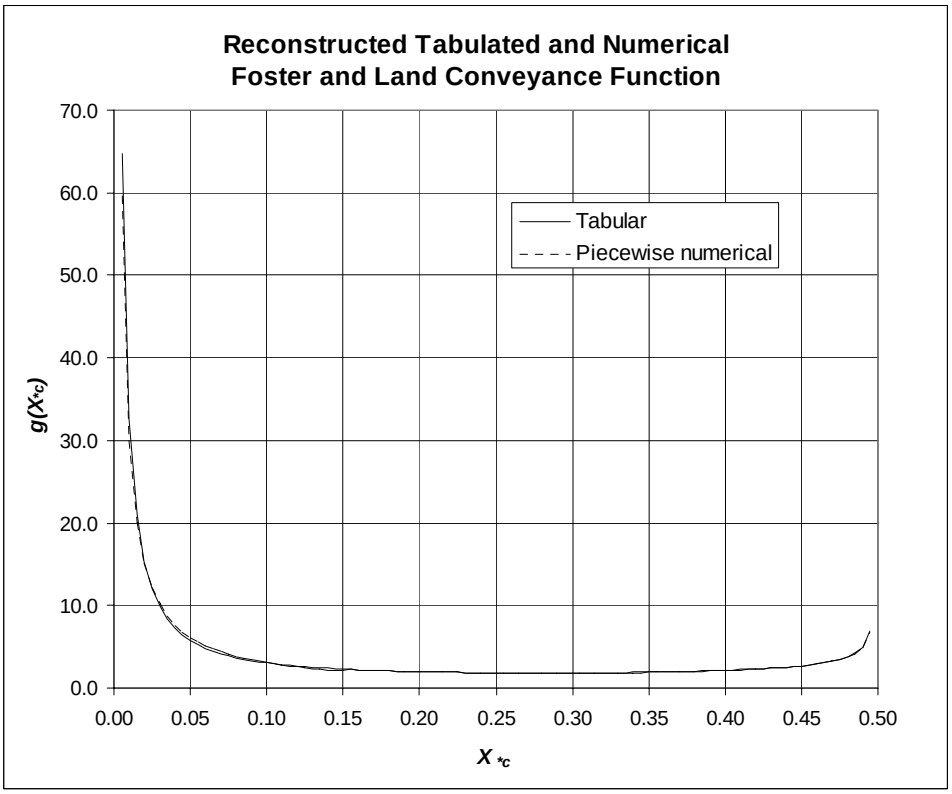

Figure 8.44 Reconstructed Foster and Lane Conveyance Function.

Numerical approximations for the equilibrium geometry and conveyance function were developed with standard curve fitting methods. Power functions or polynomials closely matched the tabulated values. These numerical approximations are intended for computer simulation of concentrated flow channels and may not be satisfactory for laboratory analysis. The numerical approximations are listed in Table 8.10. The piecewise numerical fit of the conveyance function $g(X_{*c})$ is plotted in Figure 8.44 with the tabulated curve.

Numerical Approximation of Foster and Lane Dimensionless Channel Geometry		
Parameter	Numerical Approximation	R^2
Eroded width, W_*	$-1.4895\ X_{*c} + 0.7308$	0.9992
Hydraulic Radius, R_*	$-0.8213\ X_{*c}^2 + 0.0885\ X_{*c} + 0.1584$	0.9996
Maximum depth, D_*	$-0.203\ X_{*C}^2 + 0.585\ X_{*c} + 0.2587$	0.9999
Conveyance Function, $g(X_{*c})$		
Interval 0.005 - 0.150	$0.3172\ X_{*c}^{-0.9883}$	0.9959
Interval 0.150 - 0.300	$28.919\ X_{*c}^2 - 15.79\ X_{*c} + 3.9873$	0.9971
Interval 0.300 - 0.450	$44.608\ X_{*c}^2 - 28.334\ X_{*c} + 6.3574$	0.9933
Interval 0.450 - 0.500	$1015.9\ X_{*c}^2 - 908.5\ X_{*c} + 205.84$	0.9959

Table 8.10 Numerical approximation of Foster and Lane eroded channel geometry.

8.7 Ephemeral Gully Erosion Model

The Ephemeral Gully Erosion Model (EGEM) model is derived from the Foster and Lane model and evolved from the Ephemeral Gully Erosion Estimator (EGEE) model by Laflen and Watson at the USDA Agricultural Research Service (Woodward 1999). Peak discharge and volume of runoff are estimated with standard SCS rainfall distributions and curve numbers. Single storm or annual average erosion can be estimated. The model assumes that a log normal distribution describes the annual

maximum erosion frequency with inputs from the 2-year and 25-year 24-hour rainfall distributions. Soil and crop conditions for up to three periods may be specified.

Incision erosion equilibrium width W_{eq} (m) and lateral erosion potential final width W_f (m) are estimated with regression equations constructed from selected widths generated by the Foster and Lane model,

$$W_{eq} = 2.66 \cdot Q^{0.396} \cdot n^{0.387} \cdot S^{-0.16} \cdot \tau_c^{-0.24} \quad 8.32$$

and

$$W_f = 179 \cdot Q^{0.552} \cdot n^{0.556} \cdot S^{0.199} \cdot \tau_c^{-0.476} \quad 8.33$$

where Q is peak discharge ($m^3\ s^{-1}$), n is Manning's friction coefficient, S is channel slope ($m\ m^{-1}$), and τ_c is soil critical shear stress ($N\ m^{-2}$). Steady flow at the peak discharge is assumed to act through the duration of the runoff volume. The widths computed with Equations 8.68 and 8.69 represent the gully outlet. Average gully width along the channel is assumed to be 66.4 percent of the eroded width at the outlet of the channel. Gully depth is assumed to be constant along the full length.

Maximum shear stress is estimated as 1.35 times the average shear stress (τRS) and is estimated with (Haan et al. 1994):

$$\tau = 4867 \cdot Q^{0.375} \cdot n^{0.375} \cdot S^{0.811}. \quad 8.34$$

Estimated gully volumes were compared with measured data from several states by Woodward (1999). The absolute difference between volumes estimated with the EGEM equation and volumes measured for single storms was 40 percent with no consistent bias above or below the measured values. State summaries are listed in Table 8.11.

Comparison of EGEM with Measured Gully Erosion					
State	Number of Gullies	Average Measured metric tons	EGEM Estimated metric tons	Difference %	Absolute Difference %
Maine	309	8.4	16.4	95.2	95.2
Michigan	12	7.2	9.7	34.7	34.7
Wisconsin	14	1.9	2.2	15.8	15.8
Kansas	21	3.5	1.0	-71.4	71.4
New York	32	48.3	33.4	-30.8	30.8
Louisiana	10	60.8	35.6	-41.4	41.4
Washington	30	11.7	11.2	-4.3	4.3
Delaware	10	5.6	6.9	23.2	23.2
Average		18.4	14.6	2.6	39.6

Table 8.11 Comparison of EGEM estimated gully volume with measured volumes for single storms (after Woodward, 1999).

The positive and negative signs on the slope exponents in Equations 8.32 and 8.33 reflect the incision and lateral widening stages of erosion. Widths of incising channels decrease with increasing slope. Final channels become wider with increasing slope after reaching a non-erodible layer. Variation of final potential gully width (Equation 8.32) with discharge and slope is plotted in Figure 8.45.

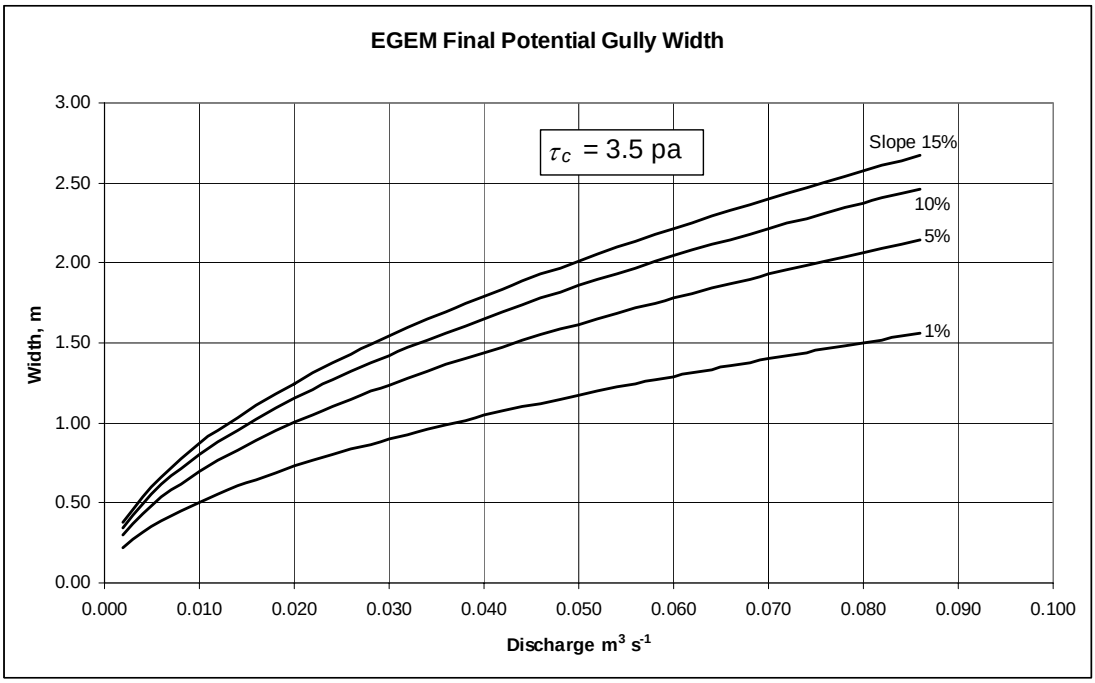

Figure 8.45 EGEM final potential gully width by slope and discharge.

8.8 Steep Slope Gully Model

The Foster and Lane erosion model was developed assuming typical channel geometry observed in agricultural soils on moderate slopes. Istanbulluoglu et al. (2003) examined gully formation on steep slopes in the Idaho Batholith after wildfire and developed a dimensionless expression for sediment discharge based on shear stress and a channel form. The sediment discharge expression is calibrated to measured data with two calibration parameters. Incision and widening occur simultaneously. The assumption of constant channel form leads to an expression for flow (channel) width that depends on discharge, slope, channel roughness, and channel shape:

$$W_f = k_s \cdot k_n \cdot C^{-0.25} \cdot Q^{0.375(1-m_n)} \cdot S^{-0.1875} \qquad 8.35$$

where W_f is the flow width (m), Q is discharge ($m^3\ s^{-1}$), S is channel slope ($m\ m^{-1}$), k_s and C are channel shape factors, and k_n is a discharge dependent Manning's roughness parameter that combines grain and form roughness.

The shape factors k_s and C for triangular channels are computed:

$$C = \frac{\left(z_1 - z_2\right)^{0.5}}{\left(z_1 - 2z_2\right) + 2\left(z_2{}^2 + 1\right)^{0.5}} \qquad 8.36$$

and

$$k_s = \frac{z_1}{\left(z_1 - z_2\right)^{0.5}} \qquad 8.37$$

where z_1 is the width to depth ratio and z_2 is the side slope ratio.

The roughness factor k_n must be selected guided by the relationship:

$$n = k_n Q^{-m_n} \qquad 8.38$$

where n is the combined Manning's roughness coefficient and m_n is an empirical coefficient. The authors chose k_n to be 0.045 for relatively unobstructed channels and 0.08 for channels with large roughness elements (boulders). They also selected a value of 0.2 for m_n based on information from Knighton (1998). This shape factor largely controls channel width and likely cannot be estimated with a high degree of confidence in absence of field observations.

8.9 Soil Properties for Ephemeral Gully Erosion Modeling

Concentrated flow erosion models are sensitive to channel (rill) erodibility and soil critical shear stress. Developers of the WEPP model examined soil erodibility and critical stress for a wide variety of agricultural and rangeland soils (Flanagan and Nearing 1995). WEPP requires baseline erodibility parameters that represent freshly-tilled soil and allows adjustments to account for seasonal variation through the crop cycle. WEPP defaults to a baseline soil erodibility K_{rb} of 0.0115 s m^{-1} and a critical stress τ_{cb} of 3.1 N m^{-2}. Elliott et al. (1989) developed equations to estimate baseline erodibility and critical shear. For cropland surface soils containing 30% or more sand, the equations:

$$K_{rb} = 0.00197 + 0.030 \cdot vfs + 0.03863 \cdot e^{-184\ orgmat} \quad 8.39$$

and

$$\tau_{cb} = 2.67 + 6.5 \cdot clay - 5.8 \cdot vfs \quad 8.40$$

where *vfs* is the fraction of very fine sand, *clay* is the fraction of clay, and *orgmat* is the fraction of organic matter in the soil.

For soils with less than 30% sand:

$$K_{rb} = 0.0069 + 0.134 \cdot e^{-20 clay} \quad 8.41$$

and

$$\tau_{cb} = 3.5 \quad 8.42$$

Rill erodibility is adjusted for several conditions with multiplicative factors:

$$K_{radj} = K_{rb} \cdot CK_{rbr} \cdot CK_{rdr} \cdot CK_{rlr} \cdot CK_{rsc} \cdot CK_{rft} \quad 8.43$$

where K_{radj} is the adjusted rill erodibility, K_{rb} is the baseline rill erodibility, CK_{rbr} is the rill erodibility adjustment for buried residue, CK_{rdr} is the adjustment for mass of dead roots, CK_{rlr} is the adjustment for mass of live roots, CK_{rsc} is the adjustment for soil surface sealing and crusting, and CK_{rft} is the adjustment for changes as the soil dries from saturation to field capacity during freeze and thaw.

Critical stress may also be adjusted:

$$\tau_{cadj} = \tau_{cb} \cdot C\tau_{rr} \cdot C\tau_{sc} \cdot C\tau_{cons} \cdot C\tau_{ft} \quad 8.44$$

where τ_{cadj} is the adjusted critical shear stress value, τ_{cb} is the baseline critical shear stress, $C\tau_{rr}$ is the adjustment for random roughness, $C\tau_{sc}$ is the adjustment for sealing and crusting , $C\tau_{cons}$ is the adjustment for consolidation , and $C\tau_{ft}$ is the adjustment for soil drying during freeze and thaw.

An extensive database of soil characteristics for the U.S. (Soils 5) is distributed with the WEPP program. Most agricultural soil series for Idaho and Washington are included. Table 8.12 lists the erodibility and critical shear values of the soil series' found within the agricultural subbasins of the Potlatch River basin. Soil erodibility ranged from 0.005449 to 0.020228 m s^{-1}. The most common soil erodibility value 0.007896 m s^{-1} occurs on 52 percent of the soil area. Soil critical shear stress ranged from 2.90 to 3.50 N m^{-2}. The most prevalent critical shear stress value, 3.50 N m^{-2}, occurred on 87 percent of the soil area.

Potlatch Basin Study Subasins (Latah County) Soil Erodibility and Critical Shear Stress (USDA-WEPP Soil 5)				
Soil Name	Area ha	Area ac	Erodibility K_r (m s^{-1})	Critical Shear τ_c (N m^{-2})
Agatha Gravelly Silt Loam, 35 To 65 Percent Slopes	965	2384	0.007896	3.50
Aquic Xerofluvents, Nearly Level	785	1939	0.007085	3.50
Athena-Palouse Silt Loams, 7 To 25 Percent Slopes	76	188	0.010498	3.50
Bluesprin-Flybow Complex, 35 To 65 Percent Slopes	2725	6734	0.005683	2.90
Bluesprin-Keuterville Complex, 35 To 65 Percent Slopes	3174	7843	0.005683	2.90
Crumarine Silt Loam, 0 To 3 Percent Slopes	849	2098	0.010498	3.50
Garfield Silt Loam, 3 To 30 Percent Slopes	1500	3707	0.007085	3.50
Helmer Silt Loam, 5 To 20 Percent Slopes	2089	5162	0.020228	3.50
Huckleberry Silt Loam, 35 To 65 Percent Slopes	31	77	0.010498	3.50
Joel Silt Loam, 3 To 7 Percent Slopes	548	1354	0.007896	3.50
Klickson Cobbly Loam, 35 To 65 Percent Slopes	3494	8633	0.010498	3.50
Klickson Silt Loam, 7 To 25 Percent Slopes	2560	6327	0.010498	3.50
Klickson-Bluesprin Complex, 35 To 65 Percent Slopes	2638	6519	0.010498	3.50
Larkin Silt Loam, 12 To 35 Percent Slopes	5284	13058	0.007896	3.50
Larkin Silt Loam, 3 To 12 Percent Slopes	2156	5327	0.007896	3.50
Latah Silt Loam, 0 To 3 Percent Slopes	331	817	0.007896	3.50
Latahco Silt Loam, 0 To 3 Percent Slopes	269	664	0.007896	3.50
Latahco-Thatuna Silt Loams, 0 To 5 Percent Slopes	1669	4124	0.007896	3.50
Lovell Silt Loam, 0 To 3 Percent Slopes	501	1239	0.007896	3.50
Minaloosa-Huckleberry Association, Very Steep	264	653	0.006983	3.12
Molly Silt Loam, 35 To 65 Percent Slopes	415	1026	0.005449	2.90
Naff-Palouse Silt Loams, 7 To 25 Percent Slopes	2302	5687	0.007896	3.50
Palouse Silt Loam, 3 To 7 Percent Slopes	1646	4068	0.007896	3.50
Palouse Silt Loam, 7 To 25 Percent Slopes	1583	3913	0.007896	3.50
Porrett Silt Loam, 0 To 3 Percent Slopes	1050	2596	0.020228	3.50
Santa Silt Loam, 2 To 5 Percent Slopes	1447	3575	0.020228	3.50
Santa Silt Loam, 20 To 35 Percent Slopes	2163	5345	0.020228	3.50
Santa Silt Loam, 5 To 20 Percent Slopes	8073	19949	0.020228	3.50
Schumacher Silt Loam, 10 To 35 Percent Slopes	146	360	0.007896	3.50
Southwick Silt Loam, 12 To 25 Percent Slopes	6117	15117	0.007896	3.50
Southwick Silt Loam, 25 To 35 Percent Slopes	243	601	0.007896	3.50
Southwick Silt Loam, 3 To 12 Percent Slopes	5170	12776	0.007896	3.50
Southwick Silt Loam, 7 To 35 Percent Slopes, Eroded	157	387	0.007896	3.50
Spokane Loam, 15 To 35 Percent Slopes	459	1133	0.005449	2.90
Spokane-Rock Outcrop Complex, 35 To 65 Percent Slopes	273	673	0.005449	2.90
Taney Silt Loam, 25 To 35 Percent Slopes	651	1608	0.007896	3.50
Taney Silt Loam, 3 To 7 Percent Slopes	2335	5769	0.007896	3.50
Taney Silt Loam, 7 To 25 Percent Slopes	5911	14607	0.007896	3.50
Thatuna Silt Loam, 3 To 7 Percent Slopes	21	53	0.020228	3.50
Thatuna-Naff Silt Loams, 25 To 40 Percent Slopes	50	123	0.020228	3.50
Tilma-Garfield Silt Loams, 7 To 25 Percent Slopes	964	2382	0.007896	3.50
Tilma-Naff Silt Loams, 7 To 25 Percent Slopes	414	1023	0.007896	3.50
Tilma-Thatuna Silt Loams, 7 To 25 Percent Slopes	552	1364	0.007896	3.50
Uvi Loam, 20 To 35 Percent Slopes	1126	2781	0.006033	3.12
Uvi Loam, 5 To 20 Percent Slopes	470	1162	0.006033	3.12
Uvi-Vassar Association, Very Steep	24	60	0.006033	3.12
Vassar Silt Loam, 20 To 35 Percent Slopes	101	249	0.010498	3.50
Vassar Silt Loam, 35 To 65 Percent Slopes	100	247	0.010498	3.50
Vassar Silt Loam, 5 To 20 Percent Slopes	48	119	0.010498	3.50

Table 8.12 Erodibility and critical shear stress of soils within the Potlatch Basin.

8.10 Physical Basis of the Initiation of Ephemeral Gullies

The process of gully formation falls within the scope of the study of landscape morphology. Two complementary theories of channel formation have evolved: landscape stability based on a change in dominance of erosion and sediment transport processes (Carson and Kirkby 1972; Gilbert 1907; Loewenherz-Lawrence 1994; Smith and Bretherton 1972; Tarboton et al. 1992) and channel initiation caused by exceedance of an erosion threshold (Begin and Schumm 1979; Dietrich et al. 1993; Dietrich et al. 1992; Horton 1945; Montgomery and Dietrich 1988; Montgomery and Dietrich 1989; Moore et al. 1988; Patton and Schuum 1975; Vandaele et al. 1996; Willgoose et al. 1991).

The landscape evolution theory holds that sediment transport at any topographical position in soil-covered terrain is the sum of diffusive and incisional (advective) erosion processes:

$$q_s = f(S) + f(q, S) \tag{8.45}$$

where q_s is the sediment flux, S is the local ground slope, and q is the overland flow rate. The first term on the right represents the diffusive processes and the second term the incisional processes. Smith and Bretherton (1972) showed by linear stability analysis that channels and valleys form where:

$$\frac{q_s}{q} < \frac{\partial q_s}{\partial q} \tag{8.46}$$

Solution of Equation 8.46 shows that when sediment transport capacity is limiting, stable slopes are convex and that rills and channels only form on concave slopes up to the point (inflection point) of meeting the concave slope. Since overland flow rate is proportional to specific catchment area under uniform precipitation excess or

snowmelt, Tarboton, Bras et al. (1992) (also see Kirkby (1993)) replaced overland flow rate with upslope catchment area and expressed landscape sediment continuity as:

$$A\frac{\partial q_s}{\partial S}\frac{dS}{dA_b} = q_s - A\frac{\partial q_s}{\partial A_b} \qquad 8.47$$

where A is the upslope catchment area. The right side of Equation 8.47 is equivalent to the Smith and Bretherton criteria. When the right side is less than 0 the landscape is unstable and will erode valleys and channels. Since A and $\partial q_s / \partial S$ are always positive in soil covered terrain, the left side of Equation 8.47 can only be less than zero when dS/dA is less than zero. The criterion $dS/dA < 0$ describes a concave slope. Break points in observed slope-area relationships of real landscapes can indicate locations where channel formation is expected.

Figure 8.46 is a plot of local ground slope versus upslope catchment area for several random transects across agricultural land in the Middle Potlatch Basin. It shows that dS/dA passes through zero (local maximum) at an upslope area of about 600 m^2. Slope profiles for upslope areas less than about 0.6 ha will generally be convex with few channels. Small catchments drain to larger catchments, so slope profiles in larger catchments will tend to be convex-concave and have most of the ephemeral and permanent channels on the concave portion of the profile. There are no upslope areas less than 100 m^2 because of the finite 10-meter resolution of the digital elevation model used in the analysis.

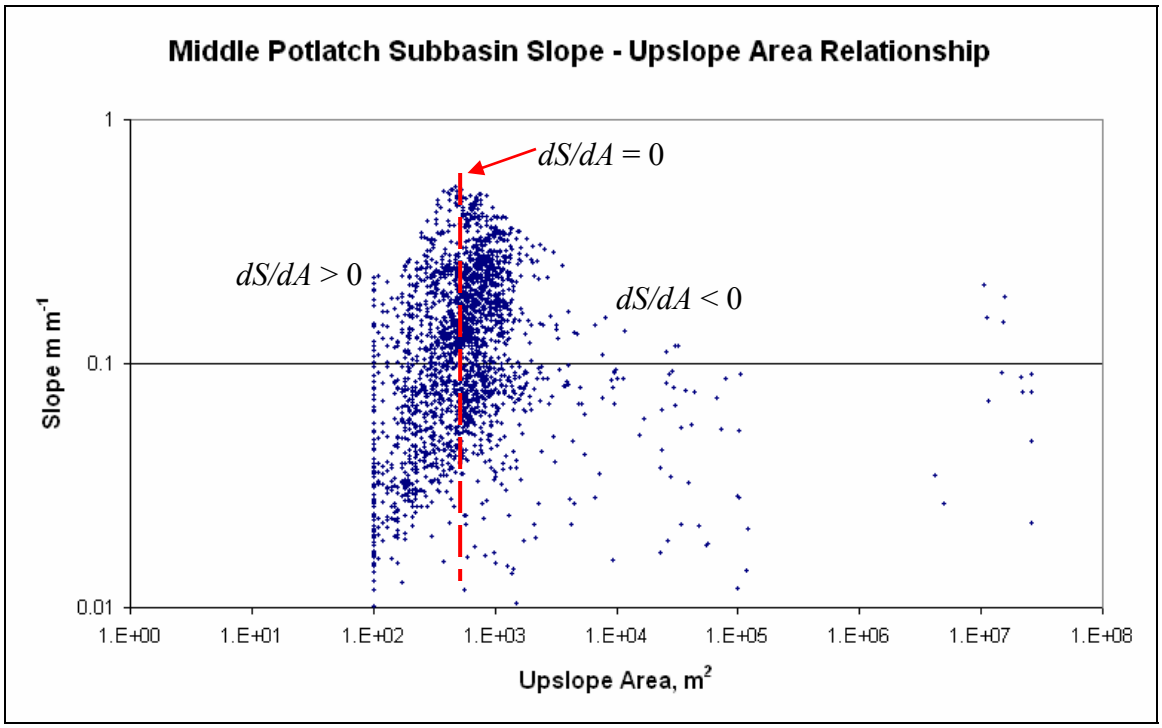

Figure 8.46 Local ground slope versus upslope catchment area in the Middle Potlatch Creek subbasin.

Willgoose, Bras et al (1994; 1991) extended the landscape sediment continuity approach by incorporating threshold initiation processes in a numerical model of catchment and channel evolution. Sediment flux is expressed as an empirical function of slope and flow rate. Channels originate and extend in accord with threshold initiation functions. Tucker and Bras (1998) explore the effect of different threshold models on landscape morphology with a numerical model of sediment continuity in a hypothetical drainage basin. Both models reveal erosion and channel initiation thresholds strongly influence the morphology of drainage basins. Further refinement of these models is needed to develop short term predictive capabilities for real landscapes.

Investigators have long sought criteria for the geomorphic threshold of channel incision. Horton (1945) viewed it as a critical slope length. Patton and Schumm (1975) deduced the existence of a threshold by examining the relationship between drainage area

and valley slope for stable and unstable channel systems. They observed that incising channel systems consistently plotted above a threshold line on a plot of valley slope versus drainage area. Begin and Schumm (1979) expressed this threshold as an exceedance of a constant shear stress indicator:

$$K_\tau = A^{rf} S \qquad 8.48$$

where K_τ is an observed shear stress indicator constant separating stable and unstable channel systems, A is the upslope drainage area, *rf* is an empirical exponent, and *S* is the valley slope tangent. The exponent *rf* is expected to vary between 0.2 and 0.4 based on a simple shear stress model proposed by Begin and Schumm (1979). Equation 8.48 can be rearranged to indicate a critical slope above which gully formation is expected:

$$S_c = K_\tau A^{-rf} \qquad 8.49$$

Numerous investigations have observed a relationship between upslope drainage area, local slope, and the occurrence of surface saturation, concentrated flow, and the locations of channel heads (Band 1986; Beven 1979; Beven and Kirkby 1993; Desmet et al. 1999; Dietrich and Dunne 1993; Montgomery and Dietrich 1989; Montgomery et al. 1993; O'Loughlin 1986; Vandekerckhove et al. 1998; Willgoose 1994; Zhang and Montgomery 1994).

Ephemeral gullies form when hydraulic forces exceed an erosion threshold (Dietrich et al. 1993; Horton 1945; Montgomery and Dietrich 1992; Patton and Schuum 1975; Schumm 1973). Ephemeral gullies begin incising at landscape positions where surface runoff overcomes erosion resistance or where seepage forces exceed soil shear strength causing local mass failure and subsurface piping channels. Both processes likely act jointly to initiate and propagate ephemeral gullies in Palouse terrain.

Convergence of surface and shallow subsurface flow to produce saturation of near surface soils promotes both processes. Simple physical processes can describe the threshold initiation of ephemeral gullies with accuracy sufficient to indicate the probable locations and extent of ephemeral gullies across the agricultural landscape.

Dietrich and Dune (1993) and Montgomery and Dietrich (1994) describe and further develop catchment scale threshold models of channel initiation for the analysis of soil-covered landscapes. Their channel initiation processes and models may be separated into basic types:

- Channel incision caused by the erosive force of laminar and turbulent overland flow.
- Channel initiation and headward extension caused by subsurface seepage forces.
- Channels initiated by landsliding.

Each of these channel erosion processes is observed in the Potlatch basin. Figure 8.47 shows a typical ephemeral gully system created by overland flow erosion. Rills at the upper ends of the gullies converge to provide increased flow for greater incision and widening. Figure 8.48 shows a classical gully on a grass-covered hillside. The abrupt deepening and widening of the channel indicates erosion by seepage. Figure 8.49 is a north facing erosion cirque with a recent shallow landslide. Grass cover did not protect the slope from landsliding and may have contributed by increasing infiltration and retention of water. Landslides in steep terrain are not unusual in agricultural catchments of the Potlatch basin, but appear to be a minor contributor of sediment compared to ephemeral gullies created by overland flow erosion.

Figure 8.47 Ephemeral gullies incised by overland flow erosion.

Figure 8.48 Classical gully extending upslope by seepage erosion

Figure 8.49 Steep north facing erosion cirque with landslide.

Selection of the appropriate model depends on the dominant channel initiation process. Most ephemeral gullies in the Potlatch basin appear to be caused by overland flow erosion. Montgomery and Dietrich (1994) developed a threshold channel initiation relationship for laminar and turbulent overland flow from familiar soil erosion principles. Their formulation appears well suited to modeling ephemeral gully initiation on tilled agricultural lands in the Potlatch basin.

The Montgomery and Dietrich relationship assumes a steady rainfall intensity R and uniform infiltration I, the discharge per unit contour length q with Hortonian overland flow is:

$$q = (R - I)\frac{A}{b} \qquad 8.50$$

where A is the upslope drainage area and b is the contour length at the downslope end of A. The term A/b appears frequently in channel initiation relationships and has been called the *specific catchment area* A_b. The term (R-I) is precipitation excess P_e as rainfall or snowmelt.

Discharge per unit contour length is the product of flow velocity u and flow depth h, so by the Manning equation (metric units):

$$q = \frac{1}{n} h^{5/3} S^{1/2} \qquad 8.51$$

where h is flow depth, n is the Manning resistance coefficient, and S is the water surface slope.

Hydraulic boundary shear stress overcomes soil resistance at the threshold of channel incision:

$$\tau_{cr} = \rho_w g (hS)_{cr} \qquad 8.52$$

where τ_{cr} is soil erosion resistance expressed as a critical shear stress, ρ_w is water density, and g is the acceleration of gravity. Substitution of Equation 8.52 into Equation 8.51 gives the critical discharge q_{cr}:

$$q_{cr} = \frac{\tau_{cr}^{5/3}}{(\rho_w g)^{5/3} n S^{7/6}} \qquad 8.53$$

Critical specific catchment area is obtained by equating Equations 8.50 and 8.53:

$$(A_b)_{cr} = \frac{\tau_{cr}^{5/3}}{(R-I)(\rho_w g)^{5/3} n S^{7/6}} \qquad 8.54$$

Equation 8.54 can be rearranged to obtain the critical slope at the threshold of channel initiation:

$$\left(S^{7/6}\right)_{cr} = \frac{{\tau_{cr}}^{5/3}}{(R-I)(\rho_w g)^{5/3} n A_b} \qquad 8.55a$$

$$S_{cr} = \left[\frac{{\tau_{cr}}^{5/3}}{(R-I)(\rho_w g)^{5/3} n}\right]^{6/7} \cdot {A_b}^{-6/7} \qquad 8.55b$$

Equation 8.55b is the key equation in assessment of watershed ephemeral gully erosion and indicates that the critical slope is approximately inversely proportional to the upslope drainage area and soil critical stress to the 3/2 power. There is no particular requirement that Equation 8.55b be restricted to turbulent flow conditions, though most tabulated values of Manning's resistance coefficient from alluvial channel research are developed for turbulent flow conditions. An appealing characteristic of Equation 8.55b is that the incorporated shear stress relationships and the physical meaning of soil critical stress and Manning's resistance coefficients are widely accepted and understood by practicing hydrologists and water resource engineers.

Montgomery and Dietrich (1989) and Dietrich et al. (1993; 1992) proposed a threshold equation for overland flow erosion under laminar flow conditions that may be more representative of vegetative surfaces that retard the velocity of flow. Flow velocity from the Darcy-Weisbach flow resistance equation modified for overland flow is:

$$u = \left(2gh\frac{S}{f}\right)^{1/2} \qquad 8.56$$

The dimensionless friction factor f is,

$$f = \frac{kv}{q} = \frac{kv}{uh} \qquad 8.57$$

where k is a dimensionless surface roughness coefficient, v is the kinematic viscosity, u is the flow velocity and h is the flow depth. Substitution of Equations 8.56 and 8.57 into Equation 8.52 gives the critical discharge for laminar flow:

$$q_{cr} = \frac{2\tau_{cr}^{\ 3}}{kv\rho_w^{\ 3} g^2 S^2} \qquad 8.58$$

Combining Equations 8.49 and 8.58 gives the laminar flow threshold criteria for critical area:

$$\left(A_b\right)_{cr} = \frac{2\tau_{cr}^{\ 3}}{(R-I)kv\rho_w^{\ 3} g^2 S^2} \qquad 8.59$$

Rearranging the terms in Equation 8.59 gives the threshold criteria for critical slope,

$$S_{cr} = \left[\frac{2\tau_{cr}^{\ 3}}{(R-I)kv\rho_w^{\ 3} g^2}\right]^{1/2} A_b^{-1/2} \qquad 8.60$$

Equation 8.60 indicates that critical slope is inversely proportional to the square root of upslope drainage area and soil critical stress to the 3/2 power. The relationship of critical slope to upslope drainage area is significantly different between the turbulent flow and laminar flow erosion process models. An exponent derived from plotted observations of critical slope and drainage area likely indicates the dominant erosion process, or if significantly different, more complex processes not considered by Equation 8.55b or 8.60. Many practitioners would lack an intuitive understanding of the dimensionless roughness coefficient k in Equations 8.57 and 8.60.

Soil, precipitation and topographic variables may be grouped in Equation 8.60 to give:

$$S_{cr} = \left[\frac{2\tau_{cr}^{\ 3}}{kv\rho_w^{\ 3} g^2} \right]^{1/2} \left(R - I\right)^{-1/2} A_b^{\ -1/2} \qquad 8.61a$$

$$S_{cr} = K\ P_e^{-0.5} A_b^{\ -0.5} \qquad 8.61b$$

where K is a constant representing soil erosion resistance (m $s^{-1/2}$), P_e is the effective peak rate of precipitation excess (m s^{-1}) and A_b is specific catchment area (m^2 m^{-1}).

Dietrich et al. (1993; 1992) and Montgomery and Dietrich (1989) also proposed a combined threshold relationship for saturated overland flow:

$$\left(A_b\right)_{cr} = \frac{2\tau_{cr}^{\ 3}}{Rkv\rho_w^{\ 3} g^2 S^2} + \frac{T}{R} S \qquad 8.62$$

where T is the transmissivity of the soil. Subsurface flow increases the drainage area required to initiate erosion. The left-hand term is dominant on low gradient slopes and the right-hand term becomes more important on steep slopes (Montgomery and Dietrich 1994). More general forms of Equation 8.59 and 8.62 were derived by Prosser and Abernethy (1996) and adapted to Hortonian (unsaturated) overland flow assuming the conventional Darcy-Weisbach flow resistance equation.

The processes embodied in the critical support area relationships of Equations 8.55b, 8.59 and 8.62 are all likely in effect in the Potlatch basin depending on the characteristics of particular catchments. Montgomery and Dietrich (1994) also developed shallow landsliding threshold relationships that may be important in isolated locations. Of these, the overland flow threshold initiation relationship in Equation 8.55b appears best suited to model ephemeral gully erosion in the Potlatch basin. Properly parameterized, this equation provides the basis for a watershed ephemeral gully erosion model.

8.11 Rainfall and Snowmelt Erosivity and Ephermal Gully Initiation Processes

Annual tillage renews a disturbed landscape upon which ephemeral gullies inscribe an observable record of seasonal erosivity. Extent and variability of channel erosion across a landscape carry information about the local climate (Begin and Schumm 1979; Kirkby 1993). The physically-based threshold channel initiation relationships provide a plausible linkage between precipitation as rainfall or snowmelt and observed locations of ephemeral gullies. Threshold channel initiation equations offer a means to characterize the erosivity of a particular season of rainfall and snowmelt and place the observed gully erosion in context of a longer meteorological record. Gully erosion volume in an extensive area is dependent on the number and location of gully initiation points, so with a proper meteorological context it should be possible to express ephemeral gully erosion in terms of a frequency distribution and return period. Doing so may allow reasonable predictions of long-term gully erosion from short-term observations.

Linkage of gully initiation to precipitation is clarified by grouping the soil, precipitation and topographic variables in the turbulent flow Equation 8.55b such that:

$$S_{cr} = \left[\frac{\tau_{cr}^{5/3}}{(\rho_w g)^{5/3} n} \right]^{6/7} (R - I)^{-6/7} \cdot A_b^{-6/7} \qquad 8.63a$$

$$S_{cr} = K \, P_e^{-0.857} A_b^{-0.857} \qquad 8.63b$$

where K is a constant representing soil erosion resistance of a particular soil and management practice, P_e is the effective peak rate of precipitation excess and A_b is specific catchment area.

Erosive effects of precipitation may be compared between seasons by examining the relationship between observed ephemeral gully initiations. Taking the ratio of critical slopes observed in two different years and assuming soil properties and management do not change:

$$\frac{(S_{cr})_1}{(S_{cr})_2} = \frac{\left(K\ P_e^{-.857} A_b^{-0.857}\right)_1}{\left(K\ P_e^{-0.857} A_b^{-0.857}\right)_2} \quad 8.64a$$

$$(P_e)_2 \left(A_b S_{cr}^{1.17}\right)_2 = (P_e)_1 \left(A_b S_{cr}^{1.17}\right)_1 \quad 8.64b$$

$$\frac{(P_e)_2}{(P_e)_1} = \frac{\left(A_b S_{cr}^{1.17}\right)_1}{\left(A_b S_{cr}^{1.17}\right)_2} \quad 8.64c$$

where the subscripts designate year 1 and year 2. Equation 8.64b demonstrates nearly an inverse relationship between precipitation and the observed topographic parameter $A_b S_{cr}$. This is reasonable because critical source areas for gully initiation should decrease with more intense precipitation for a given critical slope. Relative erosivity of two precipitation seasons is indicated by the ratio of the seasonal threshold initiation topographic parameters in Equation 8.64c.

An immediately apparent use of Equation 8.64c is to describe the spatial variability of precipitation excess across an agricultural landscape. The observed relationship between the threshold initiation topographic parameters is a direct measure of the difference in peak runoff. Equation 8.64c does not require that drainage areas be the same size to describe differences in precipitation excess, it only requires that soil and cover conditions be approximately equivalent, or in other words belong to the same *initiation regime*. The concept of an ephemeral gully initiation regime appears to be original and will be discussed in Section 8.13.3. It is likely possible to construct a continuous representation of precipitation excess across an agricultural landscape subject

to annual tillage. Understanding the distribution of precipitation excess would help avoid incorrectly attributing differences in suspended sediment measurements among basins during a particular season solely to differences in land management practices. Longer term comparisons could help conservationists target implementation practices to elevation zones or storm tracks that experience persistently higher levels of precipitation or snowmelt that cause erosion. Such an evaluation could help overcome weaknesses of the USLE/RUSLE rainfall erosivity factor discussed in Section 7.

Development of an ephemeral gully erosion frequency distribution requires that precipitation excess be related to variables in the meteorological record. Factors that influence the rate and timing of runoff have the most influence. For the Palouse region these include winter precipitation amounts, snow accumulation and rapidity of snowmelt. Peak precipitation excess rates also depend on time-to-concentration of the drainage basins, but these are generally very short in small tilled catchments (less than 0.1 ha) where ephemeral gullies develop.

Snow accumulation and rate of snowmelt are difficult aspects of estimating precipitation excess in the Potlatch basin; almost no reliable historical information is available. Winter and spring weather data were collected at three meteorological stations in the project area to support an estimate of precipitation and snowmelt. The meteorological data are discussed below.

Soil infiltration rates and antecedent moisture conditions are necessary for best estimates of precipitation excess, especially where frozen soils influence infiltration. Unfortunately, extensive infiltration data are seldom available. Estimations of precipitation excess from soil and management characteristics, such as the SCS curve

number technique, are very inaccurate in the Palouse region for individual runoff events even when gross precipitation is known with high certainty. McCool et al. (1995) computed runoff indexes (curve numbers) for common tillage practices on frozen and unfrozen soils under carefully controlled conditions at the Palouse Conservation Field Station near Pullman, WA. Runoff indexes were revised significantly upward from standard SCS curve numbers based on representative events from 13 years of data. The relative difference between estimates computed with the revised curve numbers and measured runoff for specific events was always greater than 60 percent and greater than 100 percent for all but two treatments. Agreement was better for annual runoff estimates, but annual values do not well represent the peak runoff conditions that produce ephemeral gully erosion.

It seems unlikely that precipitation excess can be computed from basin scale meteorological inputs in the Palouse region with sufficient accuracy to support direct application of the physically based relationships in Equations 8.55b and 8.63a for predictions of gully initiation on individual agricultural fields. Overall watershed predictions should be better as estimation errors are averaged. An alternative approach is to incorporate empirical evidence in a relationship between gully initiation and the topographic parameters. The physical relevance for this approach can be seen by rearranging the terms in Equation 8. 63b:

$$K\left(P_e\right)^{-0.857} = S_{cr} A_b^{\,0.857} \qquad 8.65$$

Terms on the left side of Equation 8.65 represent probabilistic meteorological and soil characteristics while terms on the right side represent catchment response and the likelihood of the appearance of one or more ephemeral gullies in a particular catchment.

In Equations 8.55b and 8.61b, the exponent for the specific catchment area A_b varied depending on the erosion process. It is reasonable and consistent with the physical basis of initiation thresholds that in general the exponent for A_b for a group of catchments in an initiation regime is variable among soils, climates and cover type. Equations 8.55b and 8.61b can be expressed in general form by:

$$S_{cr} = aA_b^{\ m} \qquad 8.66$$

where a is a coefficient representing meteorological and soil characteristics, A_b is the upslope specific catchment area and m is an exponent influenced most by erosion and threshold processes. This power law relationship has been recognized since early investigations (Leopold and Maddock 1953). The exponent m typically varies from -0.37 to -0.83 (Tarboton et al. 1992). Equation 8.66 can be formulated with specific catchment area A_b without affecting the value of the exponent m.

8.12 Empirical Analysis of Ephemeral Gully Initiation

The threshold channel initiation equations indicate possible locations of gully formation, but cannot predict exact locations with certainty. This is mostly because soil hydraulic parameters (T, τ_c, k, n) typically exhibit large spatial variation (Bloeschl et al. 1995; Bloschl et al. 1997; Merz and Plate 1997) even if total runoff were known with certainty.

A distinction is made between the point of initiation of an ephemeral gully and the trajectory or length of the gully. Gullies initiate at a point where the erosion threshold is exceeded. After initiation the gullies incise, widen and lengthen, possibly under the influence of different precipitation, snowmelt and soil frost conditions than existed during

initiation. Gullies may propagate upstream into steeper terrain with less tributary area by progressive failure of the gully headwall in response to the combined effects of seepage forces (headcutting). These factors may confuse identification the actual location of gully initiation points observed after a storm event or season.

Numerous investigators have shown that topographic variables, upslope area and local slope gradient, correlate reasonably well with observed locations of ephemeral gullies (Desmet et al. 1999; Dietrich et al. 1993; Montgomery and Dietrich 1989; Moore et al. 1988). Slope gradient and upslope drainage area are also primary topographic parameters in the theory of landscape evolution and drainage density (Smith and Bretherton 1972; Tarboton et al. 1992; Willgoose 1994; Willgoose et al. 1991). Upslope area and local slope gradient have been combined in various ways to describe the channel initiation threshold.

The topographic parameters in Equation 8.66 may be formulated as the topographic index or wetness index (Beven and Kirby 1979; Quinn et al. 1995):

$$\text{Wetness index} = \ln\left(\frac{A}{b\tan\theta}\right) = \ln\left(A_s\right) \qquad 8.67$$

This index is a primary topographic parameter of the distributive runoff model TOPMODEL (Beven 1997). The natural logarithm of the inverse relationship in Equation 8.19 avoids divide-by-zero problems in grid computations (Tarboton 1997).

Moore et al. (1988) found that locations of ephemeral gullies in an agricultural catchment could be indicated by a composite criteria of the wetness index and an erosion index. They observed that:

$$\ln\left(A_s\right) > 6.8 \qquad 8.68$$

$$\frac{A}{b}\tan\theta = A_b S > 18 \qquad 8.69$$

were reasonable criteria to indicated probable locations of the full length (trajectory) of eroded ephemeral gullies. Equation 8.68 tends to represent seepage influence on gully initiation on upper slopes of a catchment while Equation 8.69 represents surface flow erosion and further incision on lower slopes.

Following initial work by Begin and Schumm (1979), the gully initiation threshold has been expressed as a critical slope (Dietrich et al. 1993; Dietrich et al. 1992; Montgomery and Dietrich 1988; Vandaele et al. 1996),

$$S_{cr} = aA_b^{\ m} \qquad 8.70$$

where S_{cr} is the critical slope, and a and m are coefficients determined by observation of the locations of gully incision. Vandaele et al. (1996) found that coefficients reported in the literature varied significantly depending on climatic region, soils and land use. Coefficient a varied from 0.0035 to 0.35 and coefficient m varied from -0.60 to -0.25. They adopted values of 0.025 and -0.40 for a and m for GIS modeling of potential ephemeral gully locations. The reported values of the drainage area exponent are greater than those (less negative) in the physically-based threshold channel initiation relationships, indicating more complex erosion mechanisms or difficulty in determining the location of the channel initiation point.

Desmet et al. (1999) predicted ephemeral gully initiation with a slope and tributary area threshold criteria:

$$SA_b^{\ m} > t \qquad 8.71$$

where the optimal coefficients from a study of Belgium loess soils was 0.4 and 0.486 for *m* and *t*.

The dependency of ephemeral gully initiation on upslope area and local slope derived from the physical relationships described above is reinforced by empirical analysis of ephemeral gully initiation. It is therefore credible to expect that the threshold channel initiation relationships provide a physically reasonable basis to identify probable locations of ephemeral gully initiation points within the Potlatch basin. Identification of gully initiation points sets the probable lengths of ephemeral gully flowpaths to downslope permanent channels. Having established the probable length of a gully, gully erosion volume may be computed if gully width and depth are estimated by observation or modeling. Estimation of ephemeral gully erosion volume with the threshold channel initiation relationship Equation 8.55b requires the following data:

- Digital elevation model of sufficient accuracy
- Stratification of the basin into likely ephemeral gully initiation regimes
- Soil critical stress
- Manning's resistance coefficients appropriate for the initiation threshold
- Precipitation excess
- Digital representation of the permanent channel structure
- An estimate of ephemeral gully width as a function of channel flow rate
- An estimate of ephemeral gully depth

The USGS 10-meter resolution digital elevation model (DEM) of the Potlatch basin is assumed to be sufficiently accurate for computation of slopes, specific catchment area, and the permanent channel network. As discussed in previous sections, this is not true at all locations in Palouse topography, but use of the 10-meter DEM should be acceptable for demonstration of the watershed gully erosion model. Landsat 7 and aerial images was analyzed to stratify the land surface into initiation regimes by the procedures described in Section 5. Soil erosion research has reliably established critical stresses for soils in the Potlatch basin as discussed above. Precipitation excess and threshold Manning's resistance coefficients for most basins are not known, but as will be shown below, may be estimated by an analysis of observed ephemeral gully initiation points. Estimates of ephemeral gully width and depth can be obtained from the physical relationships discussed below.

8.13 Analysis of Gully Initiation Points in the Potlatch Basin

A subset of 106 gully initiation points were identified in digital high resolution aerial images of low residue tilled agricultural land acquired in March 2004 along flight lines 5, 6, 7 and 8 in the western part of the Little Potlatch and Middle Potlatch basins. Gully initiation points were visually identified in the images at the upstream end of single thread or multithread channels where rills converged. Gully initiation points were only selected from tilled agricultural fields with low to medium visible rates of residue. There is a small zone of uncertainty in the exact placement of a gully initiation point in GIS. This error is approximately 2 or 3 meters for most ephemeral gullies. Figure 8.50 shows four ephemeral gully initiation points. Uncertainty of the exact location of one of the

initiation points is indicated in Figure 8.51. Figure 8.51 also shows that tillage direction influences the formation of an initiation point by directing overland flow laterally to converge in the swale. The tillage concentration effect was also noted by Frazer et al. (1983). This shortens the drainage flowpath compared to that expected for randomly rough surfaces. The area darkened by soil moisture extends upslope from the gully initiation points and may indicate saturation at the time of incision.

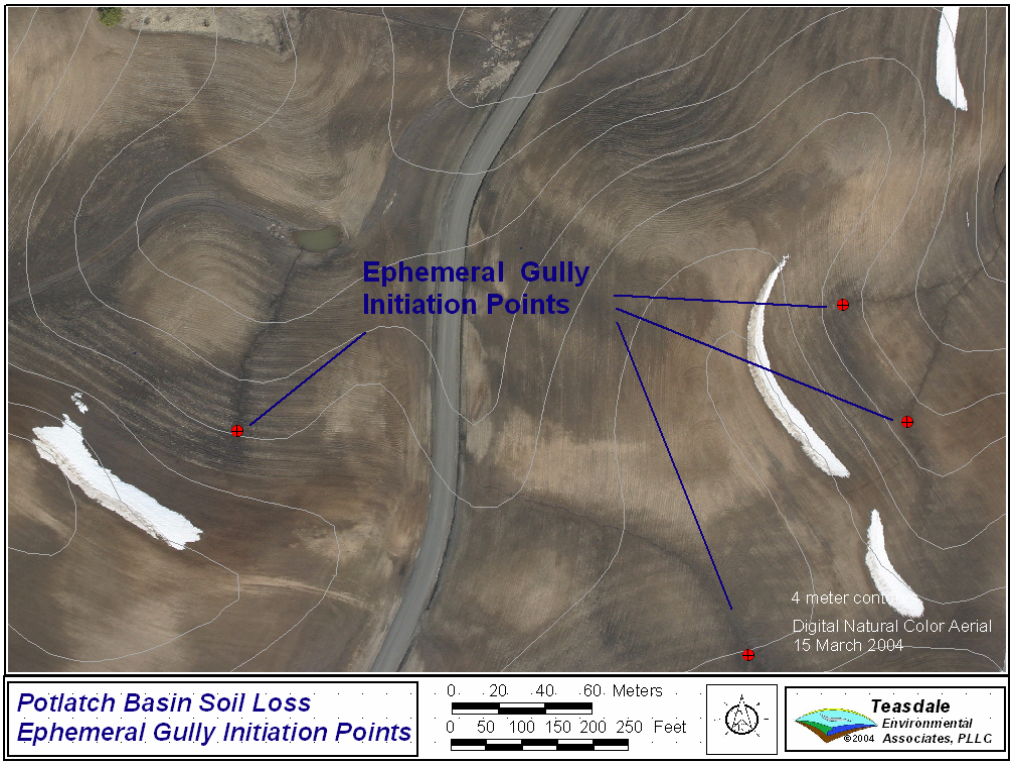

Figure 8.50 Ephemeral gully initiation points in a March 2004 aerial image of fall tilled small grain fields (Transect 7 Aerial 70).

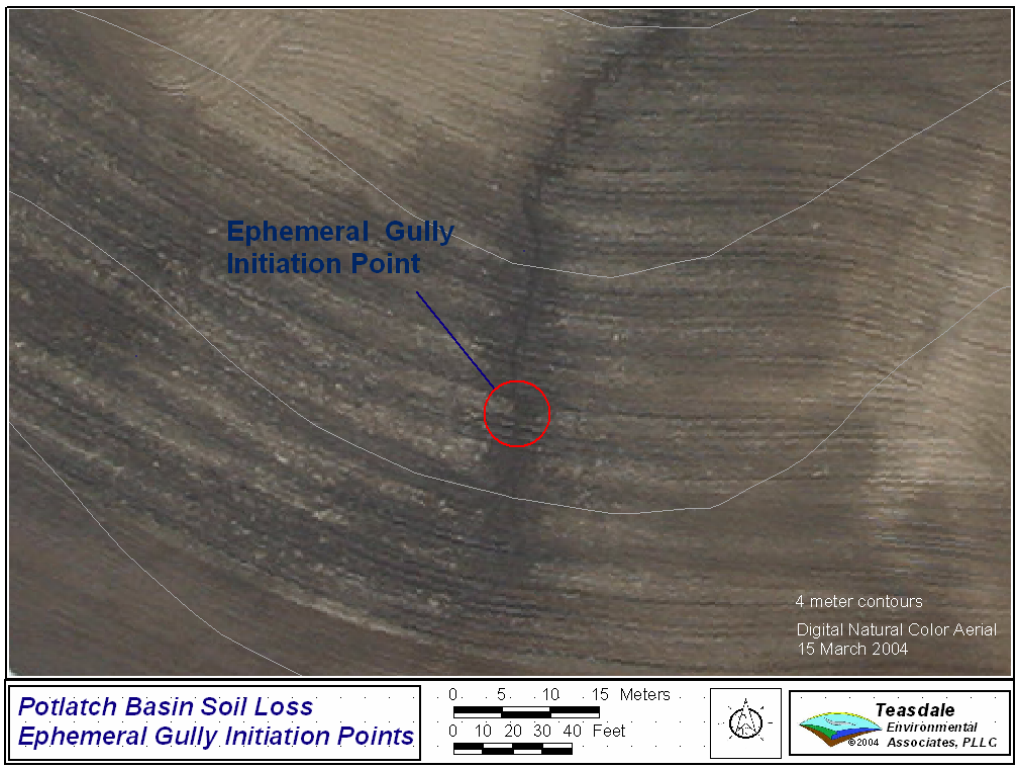

Figure 8.51 Magnified view of an ephemeral gully initiation point.

8.13.1 Gully Initiation Point Topographical Parameters

Many topographic parameters may be extracted from DEMs with terrain analysis techniques. Common parameters include upslope tributary area, local slope gradient, flow direction, upslope maximum flowpath length, upslope average flowpath length, and downslope distance to the watershed outlet. Upslope catchment area and local slope gradient are the most relevant in the analysis of ephemeral gully initiation. Figure 8.52 shows the upslope catchment area for the gully initiation points in Figure 8.50. Flowpath lines are superimposed on the flow grid, but are not necessary for the analysis of gully initiation points. The extracted topographic parameters are listed in Table 8.13.

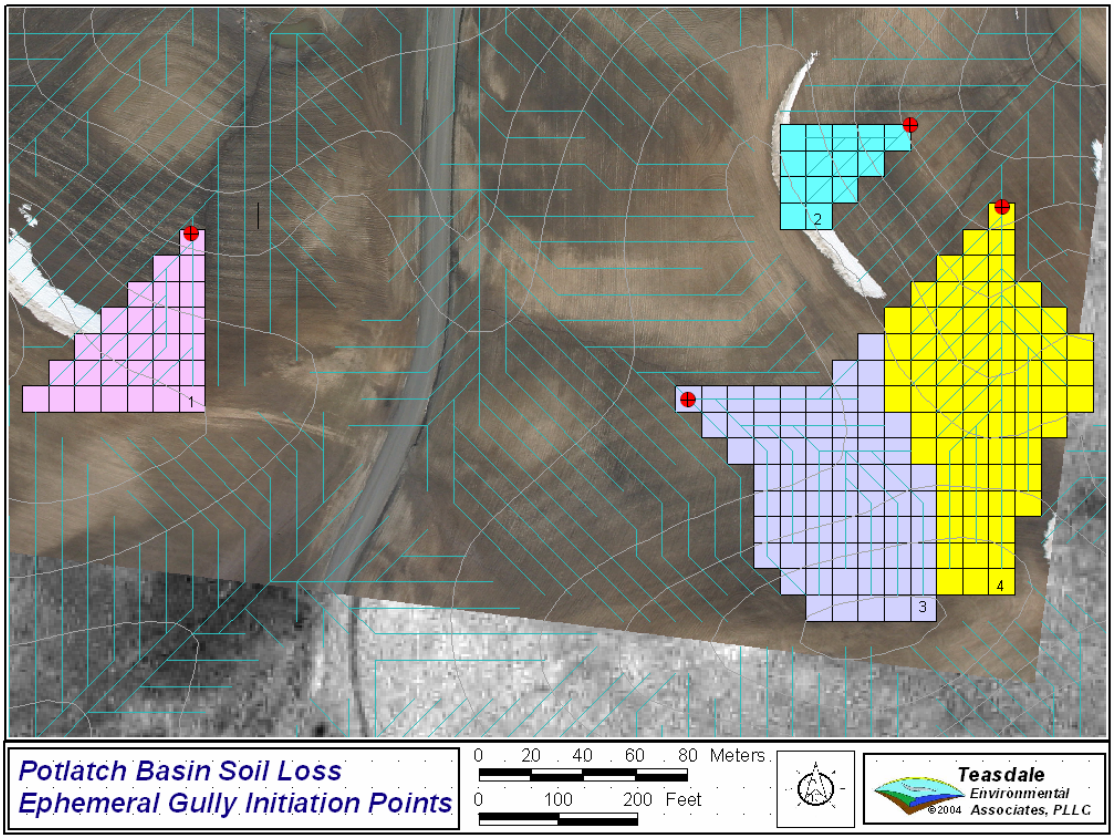

Figure 8.52 Grid representation of upslope catchment area the example gully initiation points.

Gully Initiation Point Topographic Parameters				
Gully Initiation Point	Upslope Catchment Area		Specific Catchment Area	Local Slope
	cells	m^2	$m^2\ m^{-1}$	$m\ m^{-1}$
1	28	2,800	280	0.1695
2	14	1,400	140	0.1844
3	65	6,500	650	0.0619
4	70	7,000	700	0.1287

Table 8.13 Topographic parameters for the gully initiation points.

8.13.2 Topographical Position Uncertainty

All imagery assessments and digital terrain analyses are subject to error and uncertainty. Uncertainty of gully initiation topographic parameters is primarily from inaccurate placement of gully initiation points in the horizontal plane and the accuracy of

the digital elevation model. Horizontal location error of a gully initiation point is composed of several factors and may be expressed:

$$E_{hp} = E_{obs} + E_{georef} + E_{dem} \qquad 8.72$$

where E_{hp} is the total horizontal error in the location of the ephemeral gully initiation point, E_{obs} is the observational error when interpreting the initiation point in the image, E_{georef} is the error associated with georeferencing of the aerial image with respect to the DEM, and E_{dem} is the error of the DEM representing the actual terrain. The uncertainty in interpreting the location of the gully initiation point in the image is usually small compared to the uncertainty in the accuracy of the USGS 10-meter resolution DEM and georeferencing of the aerial image with respect to the DEM. An exception may be when the gully has been significantly extended upstream from the point of initiation by headwall failure during hydrograph recession.

Georeferencing error may be locally significant in areas of high relief. Georeferencing error was assessed and compensated during initiation point selection by viewing overlapping aerial images in stereo and relocating the apparent initiation point in the image to the corresponding point in the DEM. This is an interpretive analysis which requires visual matching of the observed stereo topography with the DEM. Care must be taken to not arbitrarily relocate interpreted initiation points to the bottom of the nearest topographic swale. The aerial images show that some gully initiation points are located on the lower part of hillslopes near, but above, the bottom of the swale. Gully initiation points in Figure 8.52 are adjusted from their georeferenced locations in Figure 8.50.

Vertical error is associated with horizontal error. A horizontal shift of the initiation point will change the corresponding topographic parameters of elevation, local

slope and upslope tributary area extracted from the DEM. The DEM is likely the largest source of topographic parameter error. It is not practicable to quantify DEM errors over an extensive area in the Potlatch basin because there is no higher accuracy elevation data available for comparison. Select catchments might be surveyed with field instruments, but cost constraints and access difficulties would lead to statistical weakness. It may be possible to develop a correlation between topographic parameter error and horizontal position error, but this would be conditioned on the accuracy of the DEM. A more precise analysis would require orthorectification of aerial images to a higher accuracy DEM such as that produced by LIDAR.

Further investigation is needed to estimate uncertainty due to initiation point interpretation and DEM accuracy. However, the analysis of ephemeral gully initiation does not appear to be overly sensitive to terrain representation errors when the interpretive procedure described above is employed. Uncertainty and error propagation due to terrain representation were not formally considered in the dissertation work.

8.13.3 Ephemeral Gully Initiation Regimes

Empirical analysis of gully initiation points is best begun with a plot of local slope versus upslope specific catchment area. This plot can reveal relationships that have physical significance. Local slope versus specific catchment area is plotted in Figure 8.53 for the four example gully initiation points. Points 1, 2, and 4 very closely conform to a log-linear relationship while point 3 appears anomalous. A log-linear relationship is expected under homogenous conditions from the physically-based threshold model of Equation 8.11b and the empirical studies described above. It appears that points 1, 2,

and 4 belong to a common initiation regime while point 3 was developed under different conditions.

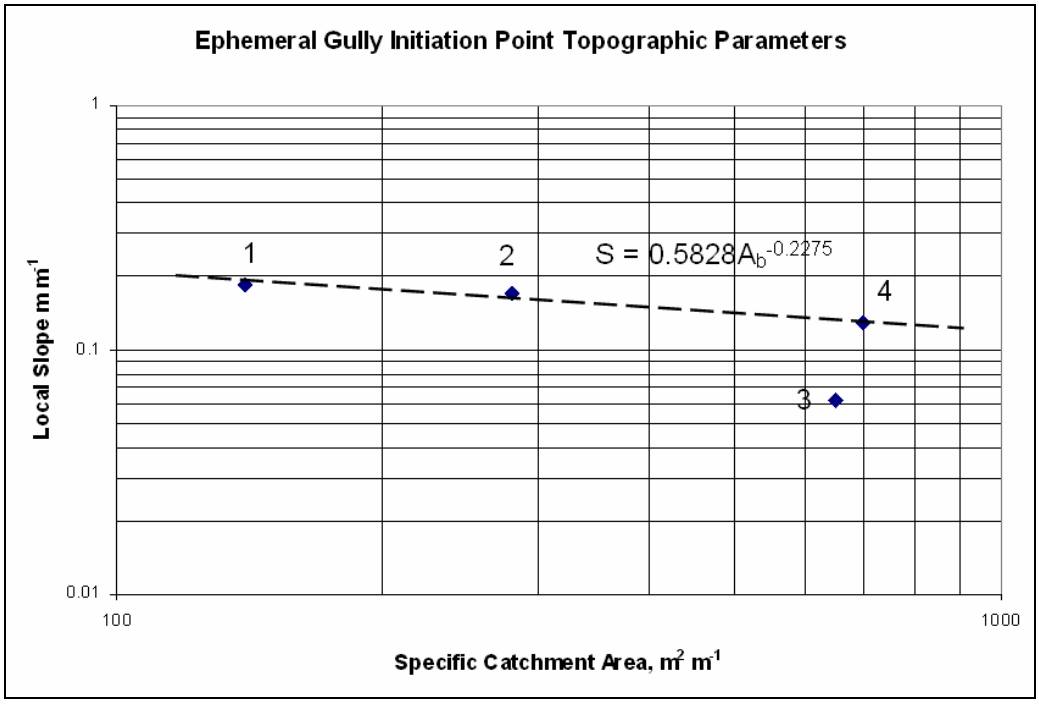

Figure 8.53 Plot of local slope versus specific catchment area for the ephemeral gully initiation points in aerial image 7-70.

The March 2004 aerial image provides evidence for a plausible explanation of initiation regime. An initiation regime may exist because of a combination of hydrologic, soil and cover characteristics that result in locally significant differences in ephemeral gully extent or density. More formally it can be defined as a locally unique stratification of catchments with similar soil, land cover, subsurface drainage, and meteorological characteristics so that a sample of threshold gully initiation points from the catchments follow a single log-linear relationship between slope and specific catchment area.

There is evidence of two regimes in the example gully initiation points. The catchments of points 1, 2, and 4 are on northeast facing slopes and have retained snow longer due to less direct insolation. They may also have had greater snow drift

accumulation. The catchment of point 3 has a more exposed westerly aspect. Snow likely melted at a higher rate over a shorter duration in the catchment for point 3. With a higher runoff rate (precipitation excess) less area is necessary to initiate a gully on a given slope. Extension of the log-linear line in Figure 8.53 indicates that a specific catchment area of about 19,000 m^2 m^{-1} is necessary to initiate a gully in the regime of points 1, 2, and 4 at the same slope as that of point 3; a 29 fold increase in area.

Four gully initiation points are not sufficient to establish a reliable quantitative relationship, but, the qualitative relationships between the gully initiation points indicate that variations in snowmelt likely cause differences in gully expression in Palouse terrain. Slope aspect and topographic shading may be significant variables for distinguishing gully initiation regimes.

8.13.4 Ephemeral Gully Initiation Regime Threshold

The empirical relationship between slope and specific catchment area is strengthened by inclusion of more gully initiation points. All 106 ephemeral gully initiation points are plotted in Figure 8.54. There is considerable scatter among the points. Soils are mostly silt loam with similar erosion resistance. Only gully initiation points from tilled fields with low to medium visible residue soils were included, so the scatter is mostly attributed to topographic parameter error, variations in surface roughness, and topographically variable snowmelt precipitation excess. A log-linear fit to the points gives an R^2 value of about 0.15.

Few gully initiation points in Figure 8.54 are observed in catchments with specific catchment areas less than about 50 m^2 m^{-1} (equivalent to an area of 500 m^2 for a DEM

with 10 meter wide grid cells). This agrees well with the break in the *dS/dA* relationship in Figure 8.46 and tends to support the application of the Smith and Bretherton (1972) criteria to loess hill topography of the eastern Palouse.

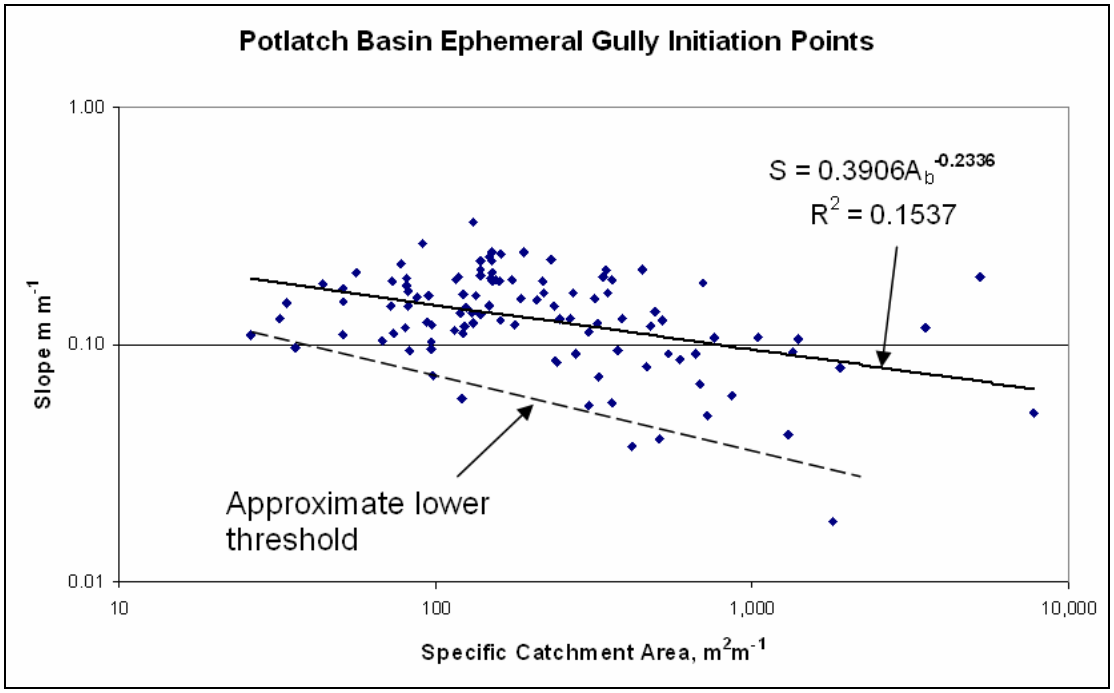

Figure 8.54 Plot of local slope versus catchment area for gully initiation points the Little Potlatch and Middle Potlatch basins, March 2004.

A striking feature of Figure 8.54 is that the lower boundary of the envelope is more or less log-linear as indicated by the dashed line when compared to the top boundary except for two outliers. The log-linear trend along the bottom boundary identifies the initiation threshold of the most sensitive initiation regime in the watershed. Log-linear threshold relationships in slope and catchment area plots have been observed by previous investigators (Begin and Schumm 1979; Dietrich et al. 1993; Dietrich et al. 1992; Montgomery and Dietrich 1988; Vandaele et al. 1996; Vandekerckhove et al. 1998; Willgoose et al. 1991). Following the method of Begin and Schumm (1979), the

threshold may be represented by a log-linear fit of selected points in the lower boundary. The selected threshold points and log-linear fit are plotted in Figure 8.55.

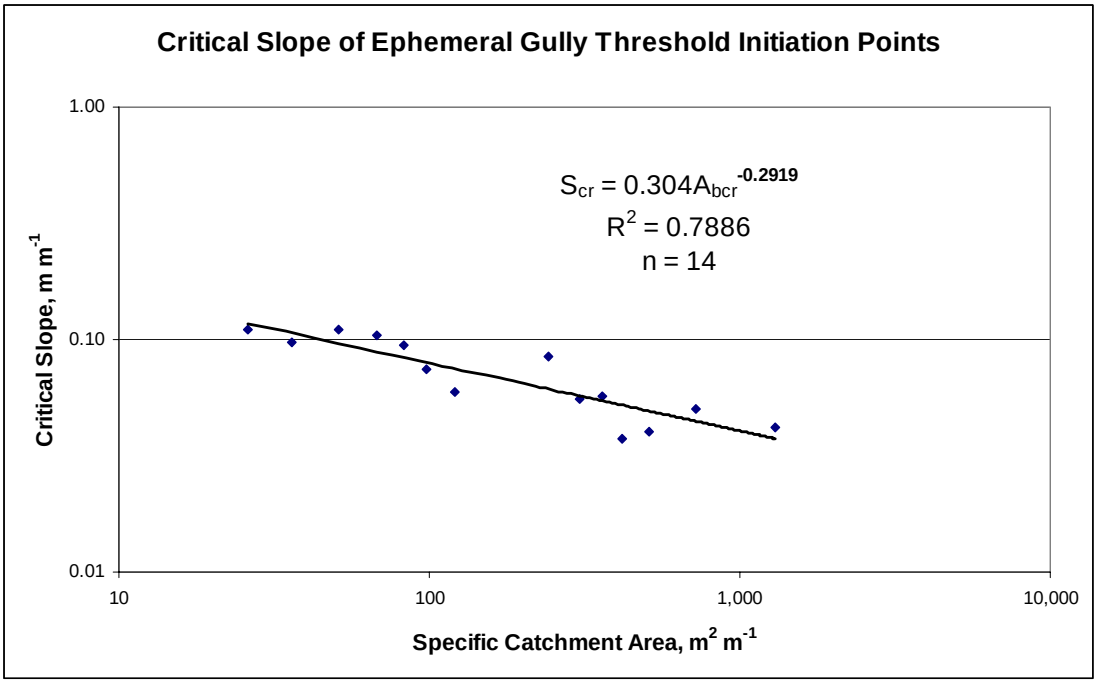

Figure 8.55 Critical slope of gully initiation points in the Little Potlatch and Middle Potlatch basins, March 2004.

The threshold log-linear regression relationship is:

$$S_{cr} = 0.304 A_{bcr}^{-0.29} \qquad 8.73$$

where S_{cr} is the critical slope for ephemeral gully initiation (m m^{-1}) and A_{bcr} is the critical specific catchment area (m^2 m^{-1}) for the initiation regime represented by the lower boundary. This regime is the most sensitive that occurred during the 2003-04 winter and spring erosion period in the Potlatch basin. Gullies in this regime were likely initiated in late February when temperatures warmed and melted most of the snowpack on exposed slopes.

Threshold gully initiation points were selected by visual inspection of Figure 8.54. No attempt was made to find an optimum set of boundary points, such as might be done by analyzing ancillary information related to initiation regimes. There is some hint of a second regime line above the first among the initiation points in Figure 8.54. Further research could examine appropriate techniques for selecting the optimum set of initiation points for the critical threshold relationship of specific initiation regimes.

8.14 Development of Parameters for the Turbulent Flow Threshold Initiation Regime Relationship

The -0.29 value of the exponent of the empirical critical specific catchment area relationship obtained above is greater than the -0.857 value obtained in the physically-based turbulent flow threshold Equation 8.55b, but it is within the range reported by Vandaele et al. (1996). The difference indicates that the threshold relationship of Equation 8.55b does not fully represent the gully initiation processes in Palouse terrain for the initiation regime as a whole in response to the specific hydrologic conditions of the winter and spring 2003-2004. Closer examination of the parameters of Equation 8.55b reveals how the relationship can be adapted for use in a watershed ephemeral gully erosion model.

The parameters of Equation 8.55b have well established physical meaning, but are necessarily simplifications of complex hydraulic processes. In particular, it is recognized that the Manning equation is an empirical relationship that represents complex overland flow hydraulics. Its use is prevalent in the practice of open channel flow hydraulics. Soil and surface properties are represented by the Manning's n and the soil critical stress τ_c. These are very important and control the response of catchments in a specific

initiation regime. These parameters jointly control channel initiation in response to the action of flow convergence.

8.14.1 Flow convergence

Flowpaths converge over short distances near most ephemeral gully initiation points. Resolutions of commonly available digital elevation models are too coarse to represent the actual surface area covered by flowing water. Evidence of flow convergence can be seen in the high resolution aerial images. The spread of converging rill flow paths, eradication of tillage patterns and moisture darkened soils indicate the width of the flow covered surface. Such evidence can be seen in Figure 8.46, Figure 8.50 and Figure 8.51. Numerous March 2004 aerial images of Potlatch basin ephemeral gullies show the convergence width to be between 1 and 2 meters, much less than the 10 meter resolution of the DEM.

The critical slope - specific catchment area relationship in Equations 8.70 and 8.73 can be adjusted for flow convergence with the factor:

$$a_c = a\left(\frac{b}{w_c}\right)^{-m} \qquad 8.74$$

where a_c is the adjusted coefficient for the, a and m are the coefficient and exponent from regression analysis of the DEM, b is the resolution of the DEM, and w_c is the average observed flow convergence width near ephemeral gully initiation points. Flow convergence of the grid cell does not change the exponent of the critical slope – specific catchment area relationship.

The adjustment factor in Equation 8.74 assumes that all flow entering the DEM grid cell is spread uniformly across the convergence width. The upper limit of the

convergence width is the DEM grid cell resolution. Convergence width can be no smaller than the observed width of the ephemeral gully disturbance zone, which averaged about 0.6 meters for the March 2004 ephemeral gullies. Flow convergence increases the boundary shear stress by increasing flow depth (Equation 8.52), so it significantly influences the relationship among excess precipitation, flow resistance and the location of gully initiation points. Adopting an average convergence width and uniform depth based on observation of the aerial images is reasonable lacking additional topographic detail around gully initiation points. Flow convergence near the gully initiation point might be better represented by a parabolic flow cross section deriving its properties from curvature of the DEM and subsurface drainage characteristics. Further research should investigate the hydraulic significance of variations in fine scale topography near gully initiation points.

8.14.2 Hydraulic Flow Resistance

The use of the Manning equation to represent the hydraulics of overland flow has long been questioned (Maheshwari 1992). Despite theoretical limitations, overland flow values for Manning's *n* have been widely studied and reported for numerous surfaces (Emmett 1970; Engman 1986; Liong et al. 1989; Weltz and Lane 1992). The main justification for continued use of the Manning's coefficient is its simplicity and familiarity. It is well known that Manning's *n* is not constant for a given channel or surface, but varies with flow hydraulics. In natural catchments, flow depths generally increase with increased catchment area because of larger contributing flow and decreasing local slope. It is reasonable to expect that relative submergence of roughness elements will increase with increasing catchment area.

Sediment stained snowmelt in the terrestrial and aerial images exhibit this effect in Figure 8.56 and Figure 8.57. The observed width of the flow widens and deepens from the hillslope swales to the permanent first order channels. Given that relative submergence increases with increasing catchment area, it is further likely that Manning's *n* will decrease with increasing catchment area among catchments with similar surface characteristics.

Figure 8.56 Snowmelt runoff in the Middle Potlatch Subbasin January 31, 2004.

Figure 8.57 Snowmelt runoff in the Middle Potlatch Subbasin February 22, 2004.

Flow dependency is easily recognizable in the Darcy Weisbach resistance factor and resistance factor – Reynolds number diagrams (Chow 1959). It is well documented that Darcy Weisbach resistance factors generally decrease in alluvial channels with increasing discharge as a larger proportion of flow is less influenced by roughness elements on the channel boundary (Meyer-Peter and Muller 1948; Simons and Richardson 1966; Simons and Senturk 1976).

Decreasing flow resistance with discharge and depth is documented in overland flow studies (Abrahams and Parsons 1991; Emmett 1970; Maheshwari 1992; Maheshwari and McMahon 1992; Ree and Crow 1977). Temple (1980) represented the Manning's coefficient for vegetated channel design with an exponential function that was, in part, dependent on flow rate. Decreased Manning's coefficients in irrigation overland flow are likely associated with submergence of non-soil roughness elements rather than soil surface roughness (Esfandiari and Maheshwari 1998). Manning's coefficients vary by two orders of magnitude depending on tillage operation and residue rates. Engman (1986) reported Manning's *n* values ranging from 0.4 to 0.7 for rough tilled plowed cropland. Chisel plow and disking operations produced Manning's *n* values in the range 0.006 to 0.53. Large variation and high Manning's *n* values approaching 1.0 are also reported for grassland and rangeland (Weltz and Lane 1992).

Gilley and Finkner (1991) measured hydraulic roughness coefficients of the surface of loess agricultural soils on a 6.4 percent ground slope prepared by various tillage operations. They applied a latex stabilizer to prevent erosion of soil surfaces and destruction of roughness elements. Regression analysis of plot data showed that Manning's *n* could be represented by a log-linear function that depended on roughness of

the microtopography produced by tillage and decreased with Reynolds number. Figure 8.58 is a plot of two values of tillage random roughness for a range of overland flow Reynolds number expected for gully initiation points in the Potlatch basin. Random roughness *Rr* is in millimeters and *Re* is the overland flow Reynolds number. The original plot data appeared to have significant scatter at low values of Reynolds number. Gilley and others (1992; 1994; 1991) generally found that Darcy Weisbach and Manning's resistance coefficients decreased with increasing Reynolds number in several other investigations of overland flow and rill erosion for agricultural soils and crop management practices. Gilley and Finkner (1991) cite other studies that found decreasing overland flow resistance with increasing Reynolds number.

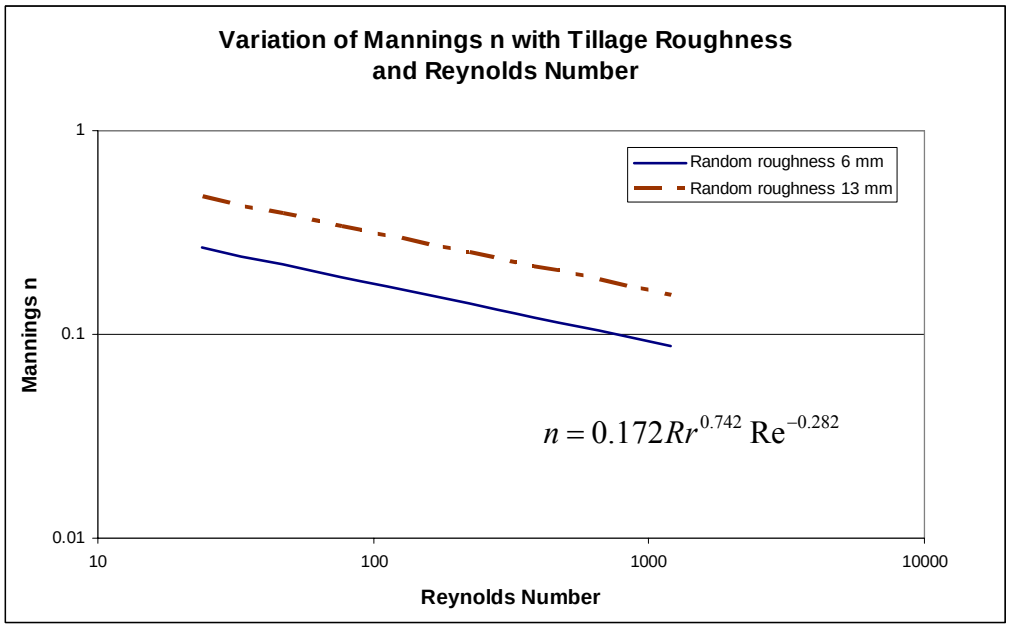

Figure 8.58 Variation of Manning's *n* with tillage roughness and Reynolds number - after Gilley and Finkner (1991).

Few, if any, studies have specifically examined the hydraulics of overland flow on low residue consolidated tilled agricultural soils prior to the onset of erosion and

exceedance of soil critical stress. These conditions are characterized by low Reynolds number and soils in which tilled microtopography is mostly intact and weathered by non-erosive precipitation and snowmelt. The Gilley and Finkner stabilized soil data appear to be the best available to represent this condition. The effect of slope steepness may not be completely represented by the Reynolds number (Gilley et al. 1991).

Hydraulics at the threshold of ephemeral gully initiation may be more similar to shallow rill flow than overland sheet flow or interrill flow. Gilley et al. (1990) measured rill flow hydraulics for representative soils and found Manning's n could be represented by an empirical function of the Reynolds number:

$$n = c_1 \, \mathrm{Re}^{c_2} \qquad 8.75$$

where Re is the Reynolds number, and c_1 and c_2 are empirical coefficients. For the three silt loam soils on moderate slopes (7 percent), the average coefficient c_1 and c_2 were 0.497 and -0.283. The negative sign of exponent C_2 shows that Manning's n decreases with increasing Reynolds number.

Van Klaveren and McCool (1987; 1993; 1998) measured the hydraulics, erodibility and critical shear of eroding rills in a flume study of thawed Palouse silt loam near Pullman, WA. The soil was screened to remove residue and leveled with a shallow V-shape to promote formation of the rill in the center of the flume. Random surface roughness was not reported, but was likely very low. Bed slope was fixed at 6.75 percent. The Manning's coefficient averaged 0.033 for rill flow rates from 0.97 to 4.01 L min^{-1}. Reported values of Manning's n plotted in Figure 8.59 increase with increased flow rate, probably because rill incision increased form roughness. Manning's n values were computed for upper and lower sections of the flume.

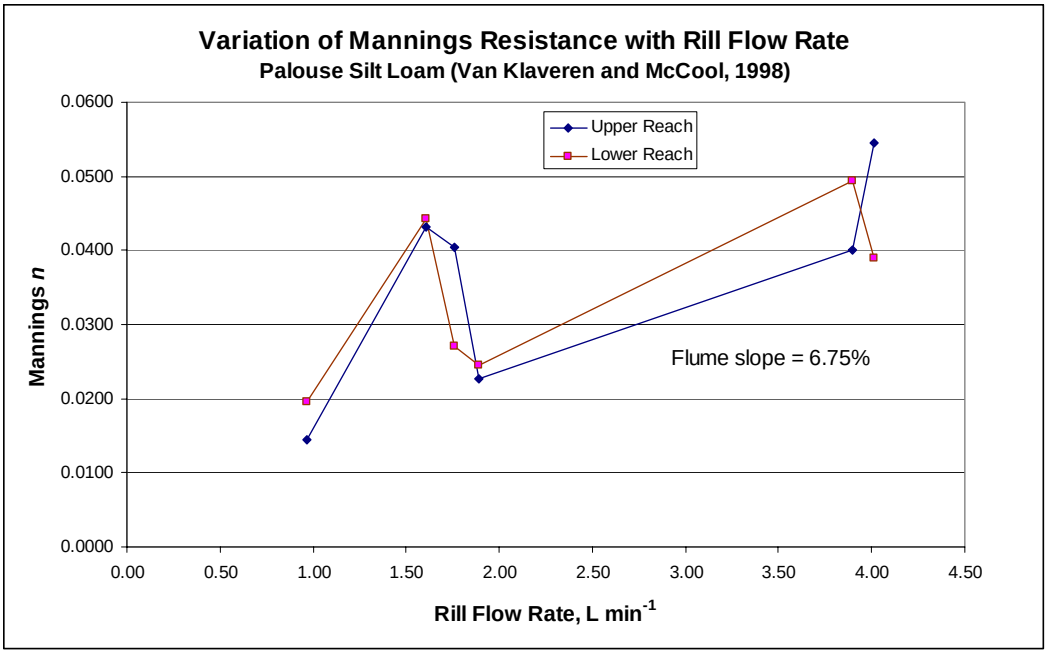

Figure 8.59 Variation of Manning's *n* with rill flow rate for thawed Palouse Silt loam.

Elliott et al. (1989) measured the hydraulics and erodibility of shallow rills in a field study of Palouse silt loam as part of the Watershed Erosion Prediction Project (WEPP). Excess surface residue was removed, and the sites were deep-tilled and lightly disked three to twelve months prior to erosion studies. Rills were preformed with a ridging tool mounted on a small tractor. Rill plots were each nine meters long, spaced at 460 mm. Surface slopes varied from 5.9 to 6.7 percent. Soil random roughness was not reported, but appears to represent typical low residue conventionally tilled field conditions. Manning's *n* values were computed from hydraulic parameters reported in the data and plotted in Figure 8.60.

Manning's n values in the WEPP study were similar to those reported by Van Klaveren and averaged about 0.037 with a range from 0.025 to 0.05. Interestingly, Manning's *n* initially decreased, then increased with increasing rill flow rate. This seems to indicate that initial surface roughness dominated resistance at the low flow rate, then

diminished as roughness elements were submerged. Resistance increased again as form roughness of the incising rills dominated.

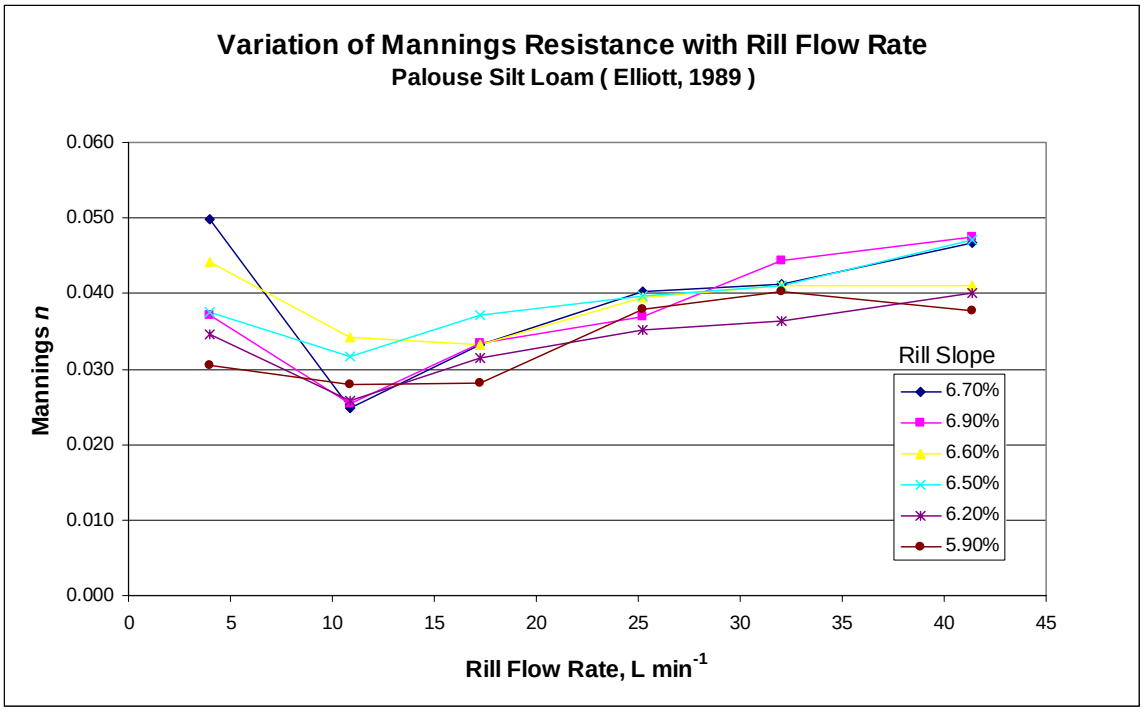

Figure 8.60 Variation of Manning's *n* with rill flow rate from WEPP soil data.

8.14.3 Manning Equation Formulation

The threshold overland flow initiation relationship of Equation 8.55b can be reformulated to express the Manning's resistance coefficient as a function of specific catchment area. The Manning equation for uniform overland flow as a function of unit discharge:

$$q = \frac{1}{n} h^{5/3} S^{1/2} \qquad 8.76$$

where q is the unit discharge (m^3 s^{-1}, m^{-1}), n is the Manning's coefficient, h is the overland flow depth (m), and S is the slope of the energy grade line (m m^{-1}) by definition parallel to the ground slope for uniform flow.

Assuming uniform precipitation excess across the catchment, the unit discharge is related to specific catchment area by:

$$q = P_e A_b \tag{8.77}$$

where P_e is excess precipitation or snowmelt ($R - I$), and A_b is the specific catchment area.

The critical slope and specific catchment area relationship in Equation 8.73 has the general form:

$$S_{cr} = a A_{bcr}{}^{m} \tag{8.78}$$

where a and m are empirical coefficients derived from log-linear fit of the lower threshold of gully initiation points in Figure 8.55.

Substitution of Equations 8.77 and 8.78 into Equation 8.76 gives the critical Manning's resistance coefficient as a function of specific catchment area:

$$n = \frac{a^{1/2}}{P_e} h^{10/6} A_{bcr}{}^{\frac{m}{2}-1} \tag{8.79}$$

For a given precipitation excess the Manning's resistance coefficient in Equation 8.79 depends on the value of overland flow depth as well as the critical slope - specific catchment area relationship observed among the gully initiation points. A second relationship is needed to define the overland flow depth at the threshold of gully initiation. A necessary assumption for the physical relationships of Equation 8.55b is that the boundary shear stress is equal to the soil critical stress so that:

$$h = \frac{\tau_{cr}}{\rho_w g S_{cr}} \tag{8.80}$$

where τ_{cr} is the critical soil stress and ρ_w is the density of water. Substitution of Equation 8.78 into Equation 8.80 gives:

$$h_{cr} = \frac{\tau_{cr}}{\rho_w g a A_{bcr}{}^{m}} \tag{8.81}$$

where h_{cr} is the critical threshold overland flow depth. Substitution of Equation 8.81 into Equation 8.79 gives the critical threshold Manning's resistance coefficient:

$$n_{cr} = \frac{a^{-7/6}}{P_e}\left(\frac{\tau_{cr}}{\rho_w g}\right)^{10/6} A_{bcr}{}^{-(\frac{7}{6}m+1)} \tag{8.82}$$

where n_{cr} is the critical threshold Manning's resistance coefficient. Equation 8.82 shows that for a given precipitation or snowmelt excess the Manning's resistance coefficient of the lower threshold boundary of a regime must follow a unique log-linear relationship if the physical relationships of Equation 8.55b correctly represent gully initiation in the initiation regime.

The critical Manning's resistance defined by Equation 8.38 may be expressed more generally:

$$n_{cr} = \alpha A_{bcr}{}^{\beta} \tag{8.83}$$

where

$$\alpha = \frac{a^{-7/6}}{P_e}\left(\frac{\tau_{cr}}{\rho_w g}\right)^{5/3} \tag{8.84}$$

and

$$\beta = -\left(\frac{7}{6}m + 1\right) \tag{8.85}$$

Substitution of Equation 8.83 into the turbulent flow threshold initiation relationship of Equation 8.55b gives:

$$S_{cr} = \left[\frac{\tau_{cr}^{5/3}}{P_e (\rho_w g)^{5/3} \alpha A_b^{\beta}} \right]^{6/7} \cdot A_b^{-6/7} \qquad 8.86$$

After substitution of Equations 8.84 and 8.85, Equation 8.86 simplifies to the critical slope – specific catchment area relationship observed among the threshold ephemeral gully initiation points, Equation 8.78.

It should be acknowledged that the use of Equation 8.82 and its general empirical form in Equation 8.83 will force the turbulent threshold initiation relationship to exactly fit the observed log-linear critical slope regime line as in Figure 8.55. The reason for doing this is not merely to better fit the observed data, but to reinforce the expected relationship between the physical variables at the threshold of initiation. Manning's *n* values at this complex threshold have been poorly investigated. There is no compelling reason at this point to reject the plausibility of Equation 8.83. It must be recognized that at the point of incipient gully initiation, that the channel has not yet incised and gully channel form does not affect hydraulic resistance. Threshold hydraulic resistance is primarily a static surface phenomenon subject to relative submergence effects noted above. It is reasonable to assume that if precipitation excess and soil critical shear stress are approximately constant within the sample region, the only variable remaining in Equation 8.55b that may change to produce the observed relationship is Manning's *n*, and this must vary in an orderly manner with increasing discharge according to Equation 8.83.

With precipitation excess and critical soil stress known, coefficient α can be computed directly from Equation 8.84. For example, assuming a precipitation excess of 3 mm h^{-1} and a soil critical stress of 1.5 N m^{-2}, the coefficient α in Equation 8.83 becomes:

$$\alpha = \frac{a^{-7/6}}{P_e}\left(\frac{\tau_{cr}}{\rho_w g}\right)^{10/6} = \frac{(0.304)^{-7/6}}{(3/1000/3600)}\left(\frac{1.5}{1000(9.81)}\right)^{10/6} = 2.105 \qquad 8.87$$

Exponent β is only dependent on exponent m of the critical slope – specific catchment area. The exponent β in Equation 8.83 becomes:

$$\beta = -\left(\frac{7}{6}m + 1\right) = -\left(\frac{7}{6}(-0.29) + 1\right) = -0.66 \qquad 8.88$$

Equations 8.83 through 8.88 have powerful meaning. They require all critical slope – specific catchment area threshold lines in a common initiation regime to plot parallel in log-linear space with slope β and separated by coefficient α. These equations have several potential uses:

1. Precipitation excess may be estimated from gully initiation point data by specifying an appropriate value of soil critical stress and a reasonable range of Manning's resistance coefficients. This allows assessment of the variability of precipitation and snowmelt patterns across landscapes having little or no meteorological data. Judging the validity of the range of critical resistance coefficients along the initiation threshold line is likely more reliable than choosing a Manning's *n* value for a particular gully initiation point as implied by Equation 8.55b. As will be discussed below, it is contrary to physical reasoning and empirical evidence to select a single value of Manning's *n* for computing all critical slopes along a threshold line.

2. Threshold lines for other values of precipitation excess may be directly computed without supplementary gully initiation point data so long as the Hortonian flow assumptions of Equation 8.55b hold. This allows modeling of the erosional response of a group of catchments in a common initiation regime to variable inputs of precipitation and snowmelt.

3. If precipitation excess is measured or estimated by hydrologic modeling, threshold flow resistance coefficients may be computed for observed threshold gully initiation points in an initiation regime.

4. Regime-averaged values of critical soil stress can be computed from measured precipitation data and gully initiation point data if threshold flow resistance relationships are known or assumed. This has forensic advantages because critical soil stress can be estimated following an erosion event because no soil erosion data is necessary. Since threshold flow resistance is independent of soil critical stress, effects of *insitu* tillage practices, crop rotation, residue rates and freeze-thaw cycling on soil critical stress can be directly assessed. Soil loss computations are very sensitive to soil critical stress, so field scale values may help improve erosion estimates.

5. Catchment infiltration rates may be estimated from gross precipitation or snowmelt measurements and gully threshold initiation data.

8.14.4 Soil Critical Shear Stress

Soil critical stress is the only soil parameter in the turbulent flow threshold relationship Equation 8.55b. Soil critical stress is primarily determined by soil texture and moisture content in non-cohesive soils (Haan et al. 1994). The WEPP model guidance suggests a base critical shear stress of 3.5 N m^{-2} for soil having a sand content less than 30% (Flanagan and Nearing 1995). Adjustments to the base critical shear stress

are made for random roughness, surface condition, soil consolidation, and freeze-thaw effects. The adjusted critical shear stress is computed:

$$\tau_{cadj} = \tau_{cb} \cdot C_{rr} \cdot C_{sc} \cdot C_{cons} \cdot C_{ft} \qquad 8.89$$

where τ_{cb} is the base critical shear stress, C_{rr} is a random roughness factor, C_{sc} is a sealing and crusting factor, C_{cons} is a soil consolidation factor, and C_{ft} is a freeze-thaw factor. Manipulation of the WEPP empirical equation shows the adjustment factors may increase or decrease the soil critical shear stress about 1 N m^{-2}. The default WEPP values appear too large.

Van Klaveren and McCool (1998) investigated erodibility and critical shear of thawed Palouse silt loam near Pullman, WA and found values ranging from 1.2 to 1.7 N m^{-2} at 50 mm moisture tension and 0.8 to 1.4 N m^{-2} at 150 mm moisture tension. The reason for the counter-intuitive decrease in critical shear stress for the drier condition was not known. Critical shear stress increased to between 1.9 and 2.4 N m^{-2} at a higher moisture tension of 450 mm. A reasonable value of critical stress for silt loam soils with the Potlatch basin study regions would be 1.5 N m^{-2} based on the Van Klaveren and McCool data. The Van Klaveren and McCool critical shear stress values agree well with the 1.1 N m^{-2} mean value for Palouse silt loam reported in the WEPP soil compendium (Elliott et al. 1989).

King et al. (1995) compared the effect of tillage treatment on rill erodibility of silt loam soils in Illinois. Critical shear stress varied less than 1 N m^{-2} between conventional tillage and no-till treatments. Residue rate appeared to have the most influence on the variation of critical stress. Critical stress values reported for the Illinois silt loams were about the same as those for Palouse silt loam.

8.15 Practical Use of the Ephemeral Gully Watershed Erosion Model

Examination of the parameters of Equation 8.55b reveals how it may be adapted to represent the threshold relationship for all catchments in an initiation regime. Equation 8.55b is repeated here:

$$S_{cr} = \left[\frac{\tau_{cr}^{5/3}}{(R-I)(\rho_w g)^{5/3} n} \right]^{6/7} \cdot A_b^{-6/7} \qquad 8.55b$$

The meaning of Equation 8.55b can be summarized as the critical combination of catchment area represented by A_b and the ground slope S_{cr} at the location where ephemeral gullies begin eroding for a given amount of runoff (R-I). The locations of the critical combinations of S_c and A_b can be determined by routine terrain analysis of a suitable DEM for an entire watershed composed of many catchments. The critical combination of S_c and A_b defines specific points (cells) in a DEM grid. These points are probable beginning points of ephemeral gullies.

Once the beginning points of the ephemeral gullies are identified, then the total length of ephemeral gullies can be determined by DEM flow path analysis to the nearest permanent channel. The locations of permanent channels can be estimated with the digital channel network methods demonstrated in Section 4. A watershed estimate of ephemeral gully erosion is then made by multiplying the total ephemeral gully channel length by reasonable values of width and depth, determined as described in Section 8.4 or from the ephemeral gully width models discussed in Sections 8.6 and 8.7. The utility of Equation 8.55b is that watershed ephemeral gully erosion can be predicted for varying runoff amounts and altered hydrologic conditions. It is a relatively direct procedure to implement Equation 8.5b in a watershed GIS model.

Equation 8.55b, here after called the ephemeral gully threshold model (EGTM), may be implemented in a spreadsheet based on a threshold critical slope - specific catchment area relationship defined by observed initiation point data (as in Figure 8.55). In the first example, an unknown magnitude of peak precipitation excess will be computed with the EGTM assuming constant values of Manning's n. The critical slope line is computed assuming a fixed value of Manning's n of 0.20 and a trial precipitation excess P_e of 5 mm h^{-1}. The EGTM critical slope in Figure 8.61 plots too low indicating the assumed precipitation excess rate is too high.

A precipitation excess of 0.5 mm h^{-1} is tried and the EGTM critical slope plots too high in Figure 8.62. After several trials, a precipitation excess of 1.0 mm h^{-1} produces a critical slope line that fits the observed data as well as possible in Figure 8.63. The EGTM plot and the log-linear fit of the observed data both have negative slopes, but the slope values differ significantly in magnitude. This is because the Manning n value is held constant for all specific catchment areas and thus not allowed to decrease with relative submergence as expected for increasing catchment areas. The plots show that even with a high value of Manning's n, the range of peak precipitation excess is reasonably constrained.

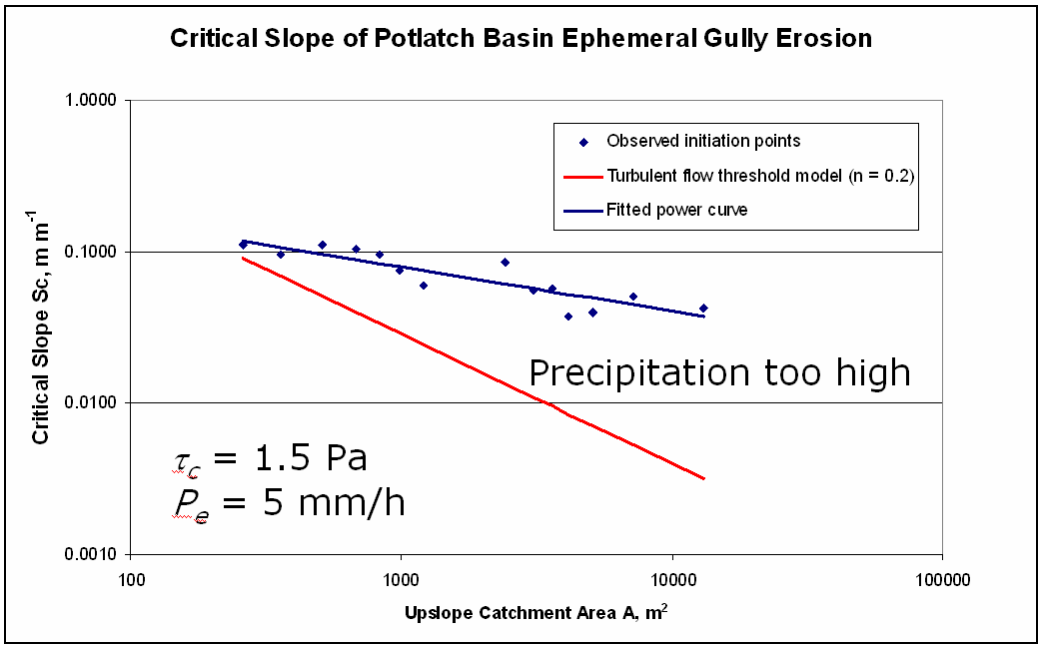

Figure 8.61 EGTM critical slope with too high of an assumed precipitation.

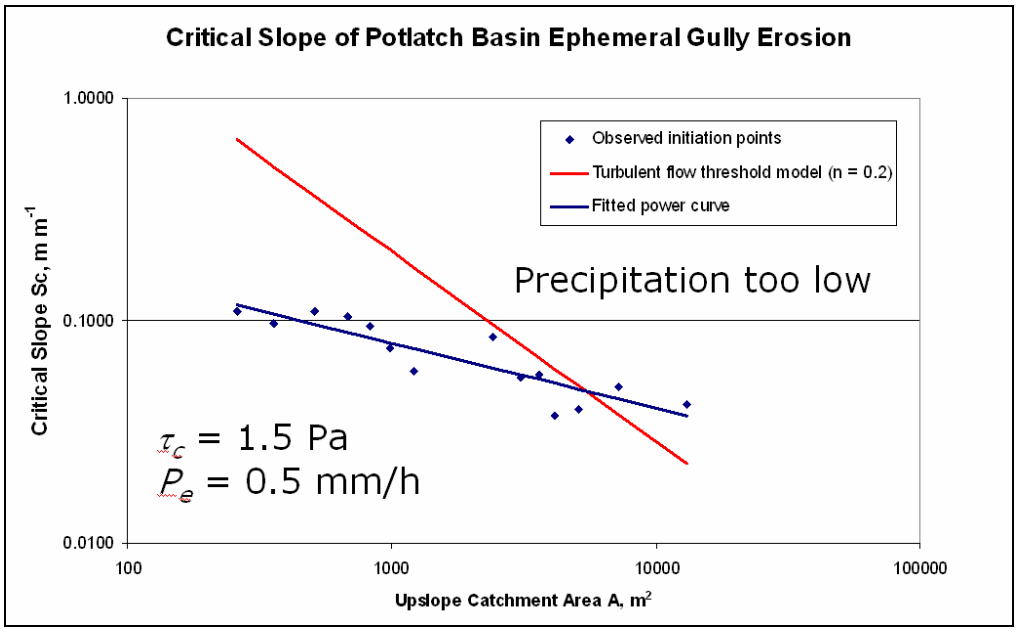

Figure 8.62 EGTM critical slope with too low of an assumed precipitation.

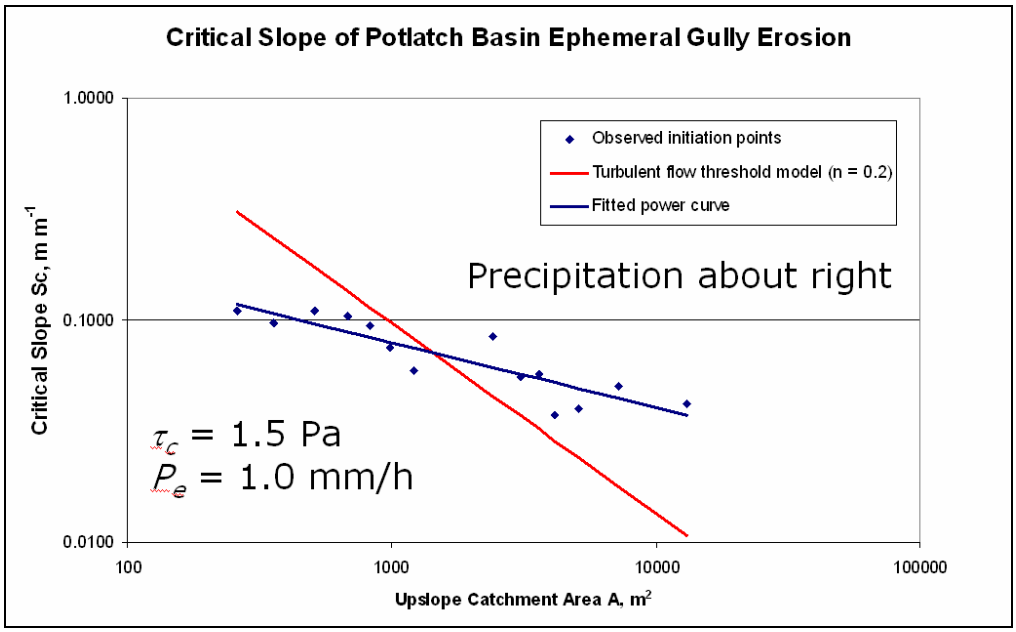

Figure 8.63 EGTM critical slope with a best fit of precipitation excess.

A range of physically reasonable Manning's *n* values can be assumed to demonstrate the effect on the estimate of precipitation excess. Precipitation excess is 2 mm h^{-1} in Figure 8.64 for an *n* value of 0.10 and 4 mm h^{-1} in Figure 8.65 for a value of 0.05. Again, the peak precipitation excess estimate is fairly well constrained to reasonable values.

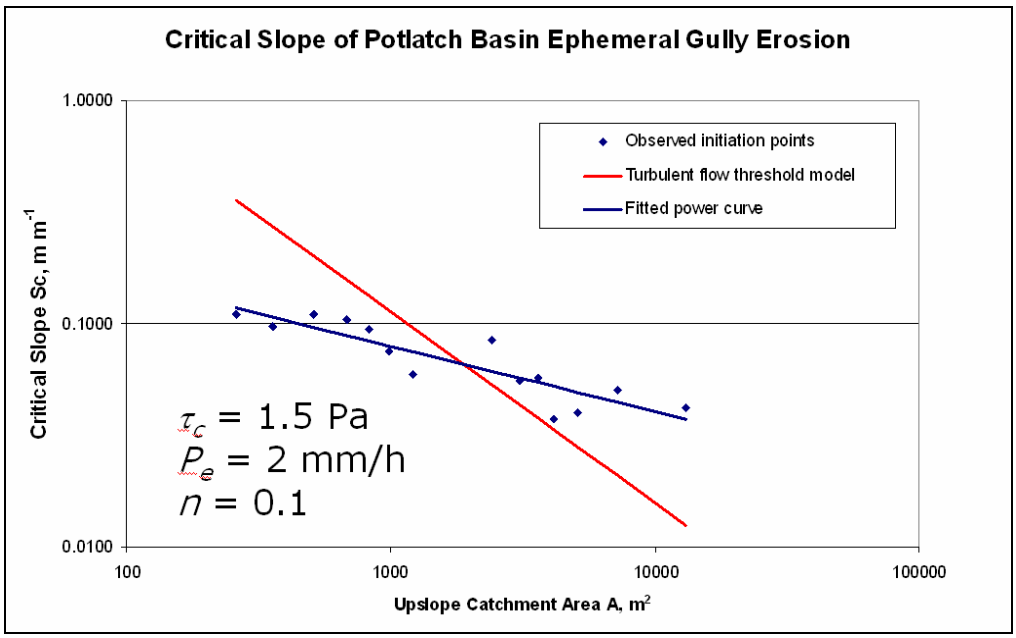

Figure 8.64 EGTM critical slope with *n* equals 0.10.

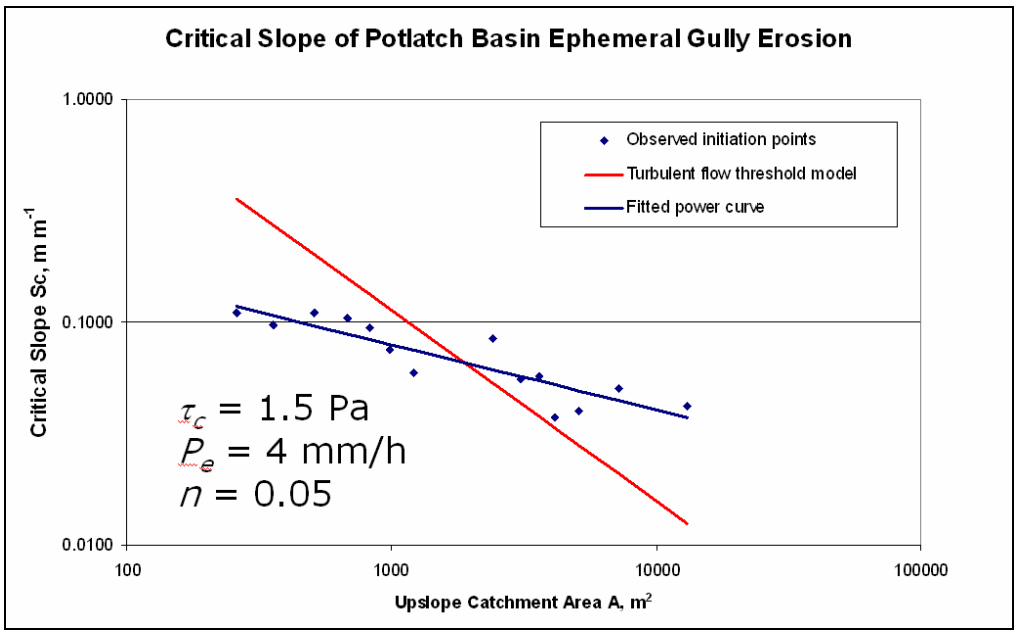

Figure 8.65 EGTM critical slope with *n* equals 0.05.

A variable Manning's *n* relationship can be derived for the EGTM if precipitation excess is measured or estimated by hydrologic modeling. Assuming a precipitation excess of 1.5 mm h^{-1}, the empirical coefficients are computed and Equation 8.83 becomes:

$$n_{cr} = \alpha A_{bcr}{}^{\beta} = 2.794 A_{bcr}{}^{-0.66} \qquad 8.89$$

The empirical coefficients for variable Manning's *n* (2.794, -0.66) were substituted in Equation 8.86 to give the EGTM critical slope plotted in Figure 8.66. The EGTM critical slope line exactly coincides with the log-linear fit to the gully initiation point data (as it must). The EGTM relationship for a fixed *n* of 0.04 is also plotted for reference.

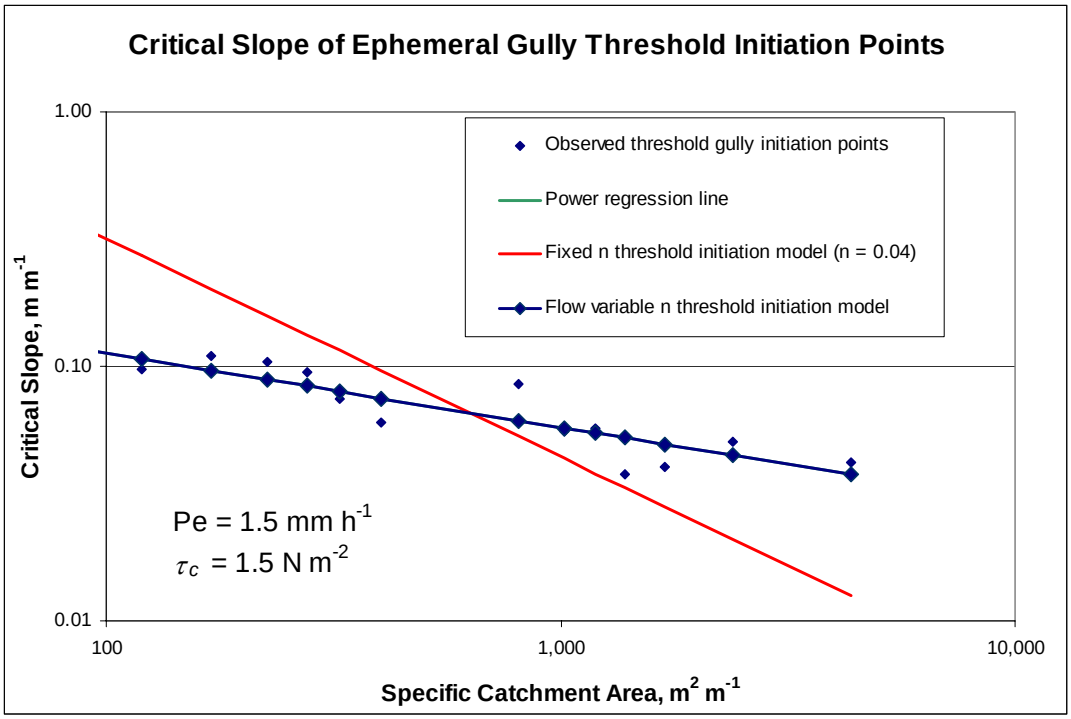

Figure 8.66 TFTM critical slope for variable Manning's *n*.

The variable Manning's *n* relationship with catchment area is plotted in Figure 8.67. The range of Manning's *n* values is in reasonable agreement with the reported data reviewed above.

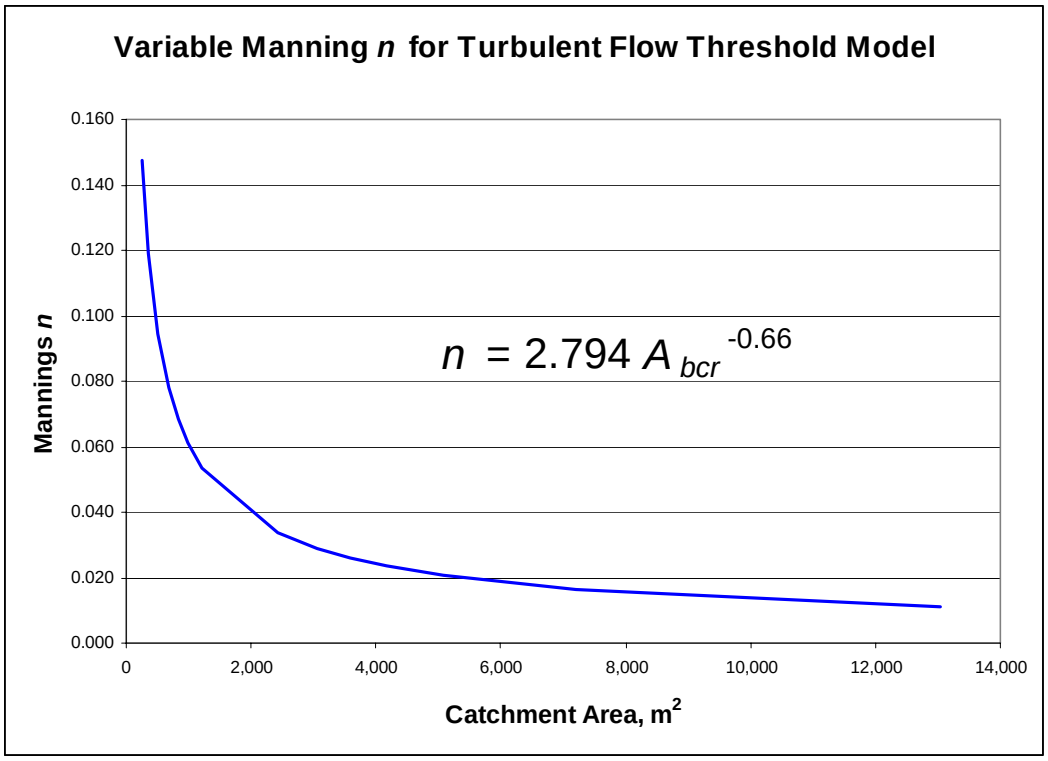

Figure 8.67 Variable Manning *n* relationship with catchment area.

It should again be acknowledged that the power relationship (Equation 8.83) adopted to represent the variation of Manning's *n* with relative flow submergence exactly fits the observed threshold critical slope – specific catchment area relationship because the parameters of the observed log-linear relationship are in turn used to define the parameters of the critical Manning's *n* relationship in Equation 8.83. The slope and specific catchment data of individual observed gully initiation points vary about this log-linear line as seen in Figure 8.66. The EGTM is an internally consistent physically-based model that is parameterized with observed critical slope – specific catchment area data and an estimate of precipitation excess. The EGTM model can then be applied to other catchments in the same initiation regime even though precipitation excess may be somewhat different.

The examples above illustrate the two most likely uses of use of observed gully initiation point data and the EGTM model. Either precipitation excess or Manning's *n* values must be known to compute the unknown variable. In many situations neither is known with high certainty as was the case with the peak snowmelt runoff events that produced the ephemeral gullies in the Potlatch basin during the winter 2003-2004. An advantage of a physically-based model is that reasonable values of the physical parameters may be assumed to estimate the state of the system in comparison with ancillary data. This was done with the analysis of Figure 8.67. The 1.5 mm h^{-1} peak precipitation excess is the best estimate of the actual value at the time of gully formation. Total precipitation excess for the Potlatch River basin was computed from gage records and is plotted in Figure 8.68.

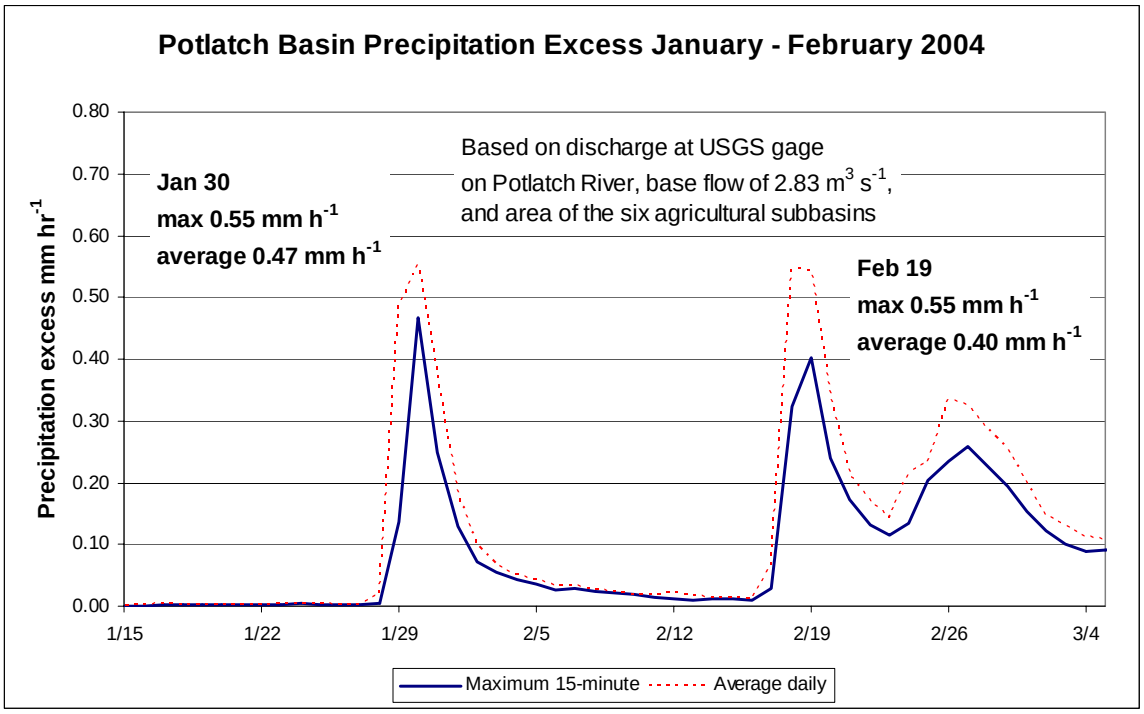

Figure 8.68 Potlatch basin precipitation excess during January and February 2004 runoff events.

In this analysis all stream discharge above a base flow of 2.83 m^3 s^{-1} is attributed to snowmelt in the agricultural subbasins. Peak 15-minute precipitation excess for the agricultural subbasins is 0.55 mm h^{-1} for each event. It is reasonable to expect the peak precipitation excess from the ephemeral gully catchments to be approximately three times this value before attenuation in the channel system.

Certainly, this is not full validation of the EGTM approach, but it does indicate a robustness and potential to derive extensive hydrologic data nearly impossible to obtain otherwise. Water resource engineers and soil erosion modelers should be enthused with the prospects.

8.16 GIS Implementation of the Ephemeral Gully Threshold Model

The EGTM model can be implemented in GIS with terrain processing algorithms discussed in Sections 3 and 7 and additional computations performed with map algebra formulas. It is possible, but not necessary, to develop the model in GIS scripting language such as ESRI Avenue© or Visual Basic©. The basic GIS processing steps to for an ephemeral gully analysis of the Potlatch River basin study area are:

1) Select an appropriate DEM, in this case the USGS 10-meter DEM available from the National Elevation Dataset (NED).

2) Generate a grid of specific catchment area (SCA) cells with terrain processing algorithms in Spatial Analyst extension or other software packages discussed in Section 7.

3) Generate a grid of land surface slopes with Spatial Analyst extension or other software package discussed in Section 7.

4) Using map algebra commands, generate a grid of EGTM critical slope cells by applying Equation 8.55b to each cell of the SCA grid. With the variable Manning's *n* method, the critical slope formula is numerically the same as the log-linear fit to the observed gully initiation points. Figure 8.69 is a portion of the SCA grid for the Little Potlatch Creek and Middle Potlatch Creek basins.

5) Identify the desired initiation regime by GIS processing. In this case the initiation regime of interest is the low and medium residue fall seeded agricultural fields. These fields were classified with the techniques demonstrated in Section 5. The hydrologic land cover map for the Potlatch River basin study area is in Figure 8.70.

6) Limit the analysis to catchments with areas from 0.03 to 1.3 ha as indicated by the analysis of ephemeral gully initiation point data.

7) Separate critical slope points for ephemeral gullies from those for rills by limiting selection to only areas of topographic convergence. Automatic extraction of convergence zones is a somewhat advanced terrain processing procedure that is specific to the DEM processing software utilized.

8) Create mask a mask grid(s) for the excluded areas identified in steps 5, 6 and 7.

9) Using map algebra commands, generate a binary grid of cells with actual slopes and specific catchment areas that exceed the EGEM criteria. A convenient method is to generate an intermediate grid of cells with values of SCA multiplied by the ground slope (A_bS). This useful topographic parameter was discussed earlier.

10) An ephemeral gully hazard potential index grid can be created at this point by assigning a numeric rating to the grid cells based on how much the actual A_bS value exceeds the critical A_bS value. Figure 8.71 is an example of an ephemeral gully hazard potential index grid. Darker colors indicate higher potential erosion. The grid cells should conform to topographic channels and swales if the grid masks are correct.

11) Using map algebra, compute a grid of runoff discharge from the assumed or known rainfall excess depth and the SCA grid.

12) Using map algebra, compute a grid of equilibrium or final ephemeral gully widths for each index grid cell with the EGEM model discussed above or simply assume a constant gully width based on aerial survey measurements. A more exact method is to use the Foster and Lane ephemeral gully width procedure, but this requires processing with Avenue or Visual Basic code. Representative widths computed with the EGEM model are marked on Figure 8.72. Light blue topographic convergence cells show that the EGTM cells are part of the topographic drainage structure and not hillslopes. An uncovered aerial image of the example area is in Figure 8.73. Channel connectivity is not assessed in this GIS implementation.

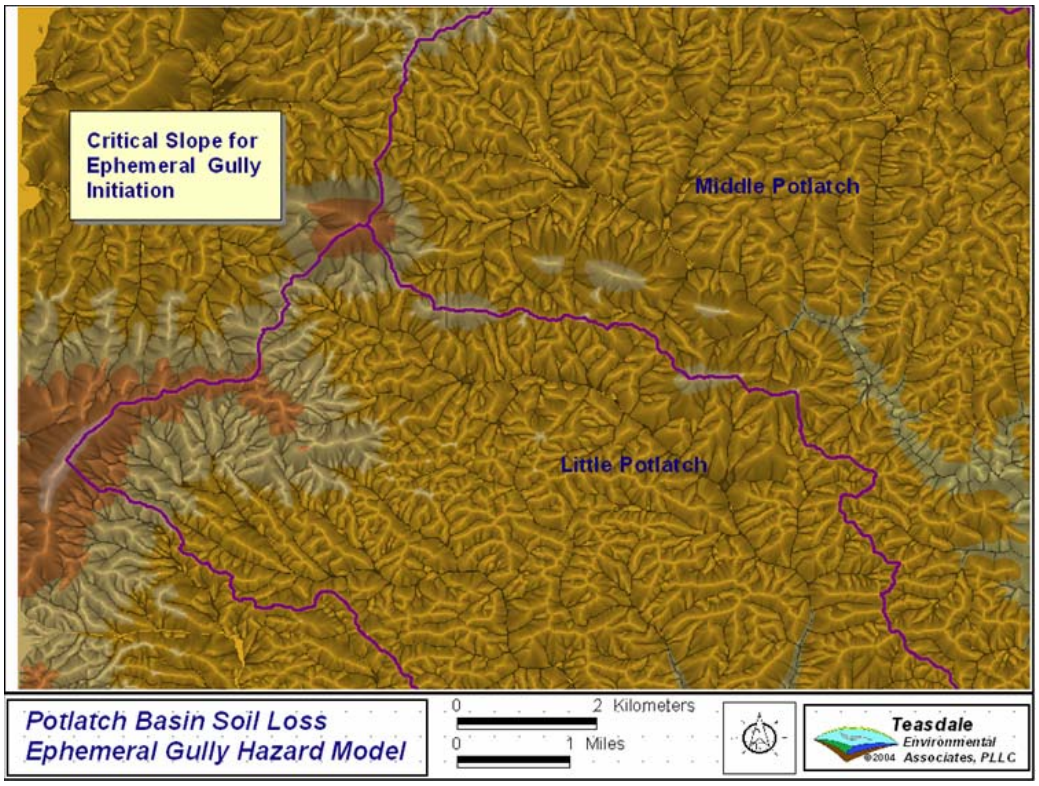

Figure 8.69 EGTM critical slope grid for a portion of the Little Potlatch Creek and Middle Potlatch Creek basins.

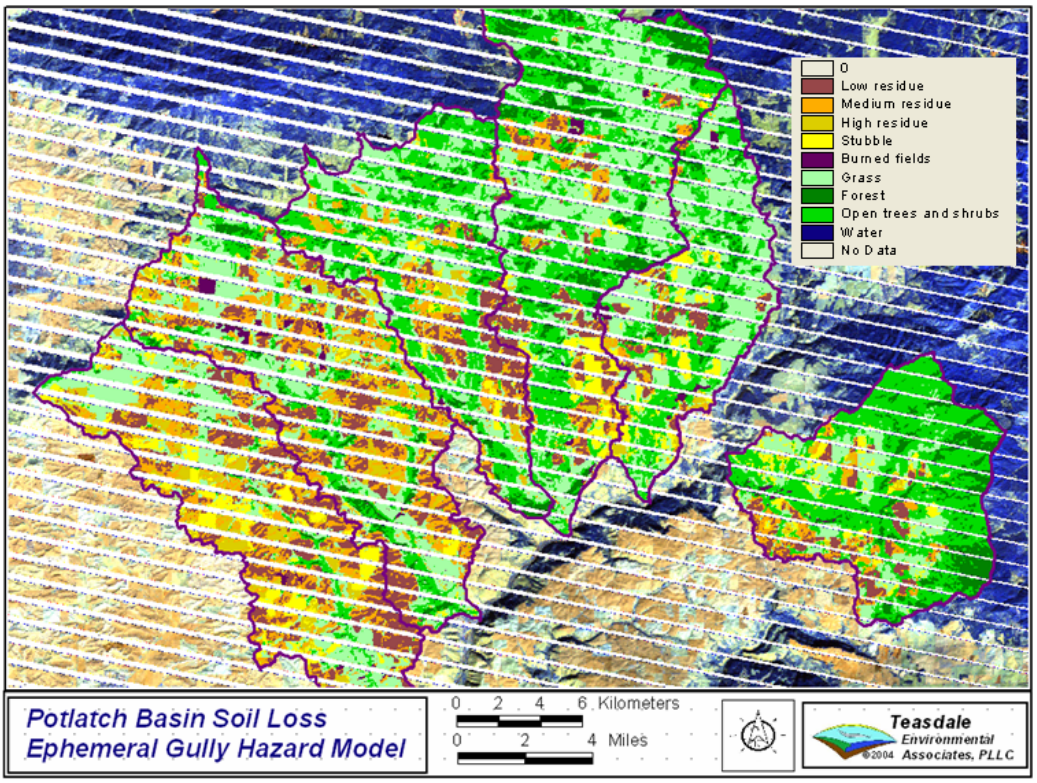

Figure 8.70 Hydrologic land cover classification of the Potlatch River study area.

Figure 8.71 Ephemeral gully hazard potential classification.

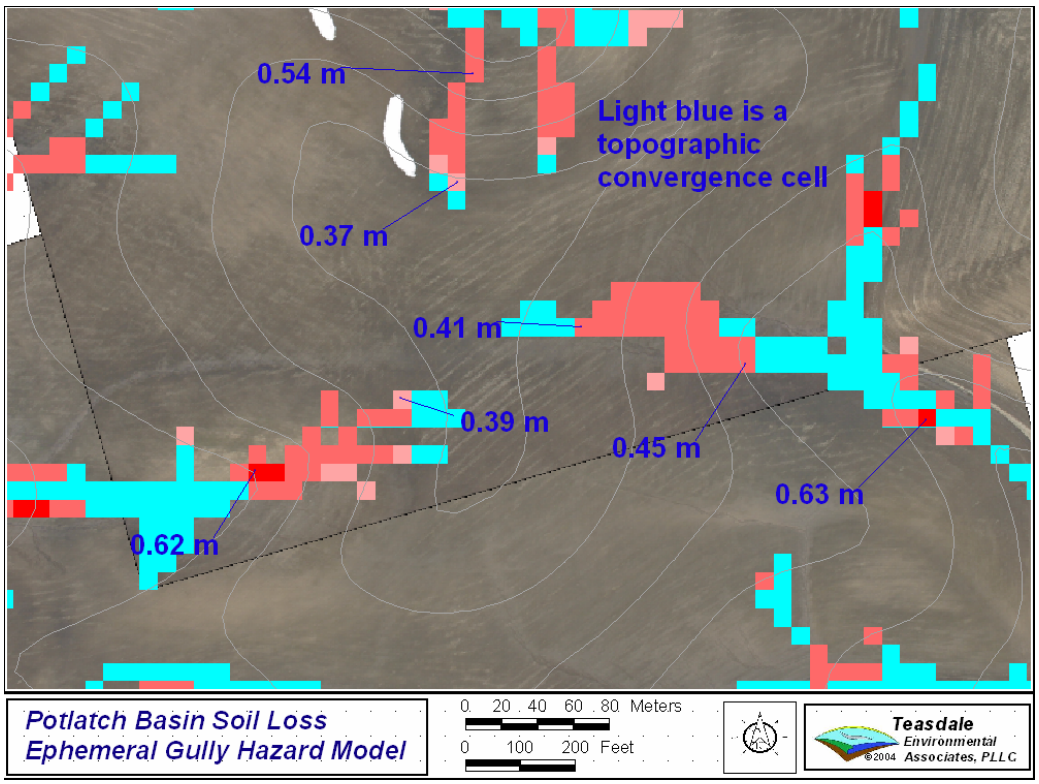

Figure 8.72 Ephemeral gully widths computed with EGEM and assigned to EGTM index cells.

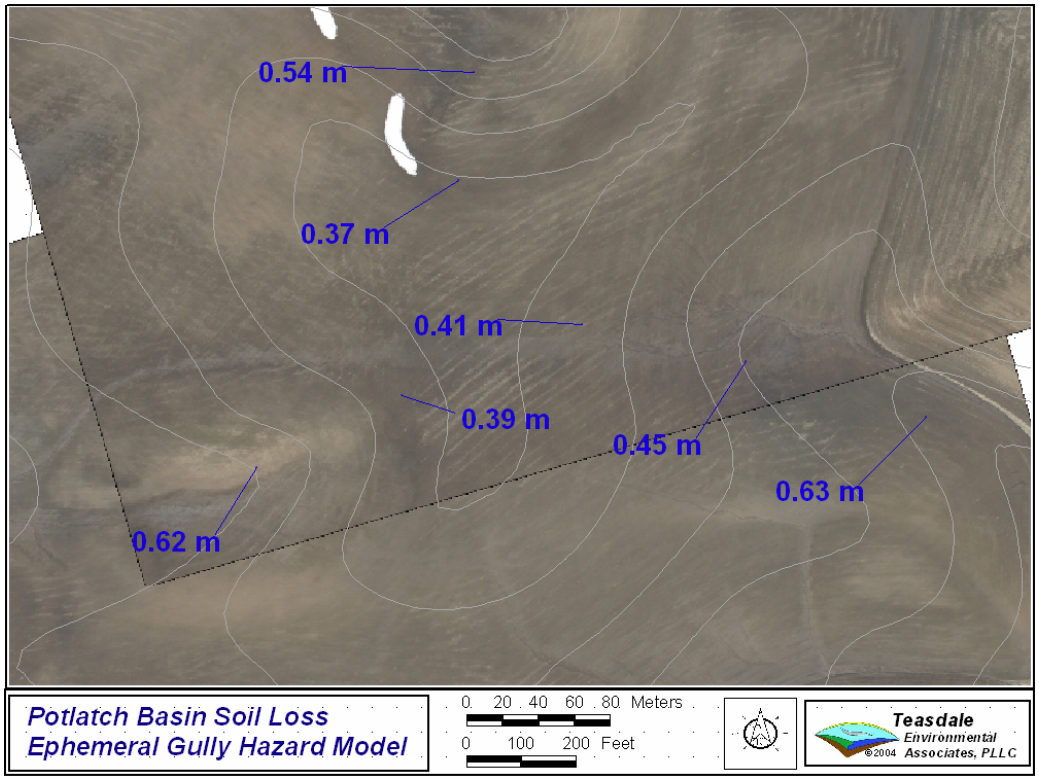

Figure 8.73 Uncovered aerial image of the example EGTM index coverage.

Predicted ephemeral gully locations in Figure 8.72 correspond reasonably well with observed ephemeral gully locations in Figure 8.73. Some isolated cells are not correctly located and is due in part to the accuracy of the DEM. It is also known from the RUSLE2 example that the USGS 10-meter DEM in this area does not fully represent the smallest catchments. These catchments are important in the EGTM analysis. Further development of GIS processing techniques is necessary to refine the grid model approach. Refinement of terrain and GIS procedures is a good subject for future research.

Total ephemeral gully erosion is estimated by multiplying the widths of each EGTM index cell by the length of the index cell and estimated gully depth. The length of an index cell is nominally the DEM grid size of 10 meters. An adjustment for diagonal flow paths could be made with more sophisticated GIS processing. As discussed in aerial image approach (Section 8.4), ephemeral gully depth must be estimated by other means.

An illustrative alternative to full GIS processing is to compute an average width of the EGTM cells by GIS techniques then complete the erosion computations manually. Manual computations are summarized in Table 8.14. The average final ephemeral gully width for the sampling region was 0.49 m. The average depth of ephemeral gullies is estimated to be 0.2 m. Total length of ephemeral gullies is the number of EGTM grid cells multiplied by the 10 m nominal cell length. Average width, average depth and total length are multiplied to compute the total volume of ephemeral gully erosion. The volume of erosion is multiplied by the soil bulk density of 1200 kg m^{-3} to produce an erosion estimate of 80,422 metric tons. The EGTM analysis covered 37,096 ha, so the estimated areal rate of erosion for the winter of 2004-2005 is 2.2 Mg ha^{-1} (1.0 ton ac^{-1}).

Average ephemeral gully width	0.49	m
Estimated channel depth	0.2	m
Number of cells in sample region	3,709,614	cells
Total area of sample region	37,096	ha
Number of EGTM cells	68,151	cells
Total area of EGTM cells	681.51	ha
Length of cell	10	m
Total Volume of erosion	67,019	m^3
Soil bulk density	1200	kg m^{-3}
Total mass of erosion	80,422	Mg or metric tons
EGTM erosion rate	2.17	Mg ha^{-1}
or	0.97	ton ac^{-1}

Table 8.14 Summary of EGTM erosion computations

It is noted that the EGEM (Watson 1996) model produced a value of average gully width that was within 0.1 m of the average width observed in the aerial imagery. This tends to validate the physically-based Foster and Lane ephemeral gully width model for use in the Palouse region.

Ephemeral gully erosion estimated by the EGTM GIS model is 4.4 times higher than the erosion estimated by measurement of ephemeral gullies on the aerial images in Table 8.8. There are plausible reasons for this. First, the gully initiation point sample data was obtained from an area in the study region that had a high density of ephemeral gullies, so was likely an area of greater snowmelt and runoff. A uniform value of 1.5 mm h^{-1} precipitation was estimated from the gully initiation point data and applied to the full region.

A precipitation and snow depth gradient was observed in the basin, but not considered in the demonstration GIS implementation. The values in Table 8.8 were computed from the full digitized sample across the study region including areas with few ephemeral gullies so would be expected to average lower than areas of higher runoff. This is seen in Table 8.8 in the 0.39 ton ac^{-1} estimated erosion for the Middle Potlatch

Creek subbasin. The EGTM estimate is 2.5 times the measured estimate for the Middle Potlatch Creek subbasin.

Another possible reason is that the initiation regime threshold line is too sensitive and does not represent the characteristics of the dominant initiation regime. It may be that soils in topographic convergence zones are consolidated more because of increased amplitudes of soil moisture cycles and have inherently higher soil critical shear stresses compared to soils in typical rill experiments. Further analysis of the initiation regimes and additional gully initiation point data should produce a more representative estimate of basin average ephemeral gully erosion. Lastly, the GIS processing techniques are relatively simple and do not exclude isolated and disconnected cells that would have been attributed to rill erosion in digitizing of ephemeral gullies. Refined GIS algorithms should be developed in future research.

The EGTM model even in its preliminary form should be useful for the estimation of ephemeral gully erosion and soil erosion research. It appears to produce a credible estimate of seasonal ephemeral gully erosion that is relatively easy and cost effective to produce. The main steps in the estimation process are:

1) Prepare an initiation regime classification of land surfaces that are susceptible to ephemeral gully erosion. These were low and medium residue fall-seeded agricultural fields in the Potlatch basin example.

2) Characterize the soil critical stress and possibly Manning's *n* for soils in the study region. These are usually obtained from the published sources described.

3) Acquire high resolution aerial imagery along a sample of transects in late winter or early spring.

4) Identify and analyze ephemeral gully initiation point data to determine precipitation excess and Equation 8.55b parameters.

5) Implement the EGTM model in GIS as demonstrated above or apply more sophisticated processing as suggested.

6) Develop predictive scenarios for other precipitation excess or altered land surface.

There is much opportunity for research related to the EGTM modeling approach, the results of which would benefit hydrologic analysis of agricultural watersheds and soil erosion investigations.

8.17 Summary

This section described research related to the measurement, analysis and modeling of ephemeral gully erosion with high-resolution digital aerial imagery as the primary data source. Aerial survey is an efficient and sufficiently accurate means to detect and measure the morphology of ephemeral gullies and estimate ephemeral gully erosion over an extensive area. Two different approaches were discussed and demonstrated. The most direct method of estimating seasonal ephemeral gully erosion is by measurement of ephemeral gully channel dimensions in the aerial imagery. Depending on area this technique is relatively rapid, cost effective and easily understood by soil erosion professionals and landowners.

The watershed ephemeral gully modeling approach (EGTM) is new method based on physical principles that appears to give credible estimates of ephemeral gully erosion with a minimum of aerial survey information. The model is relatively easy to parameterize from observed ephemeral gully initiation point data and implement in GIS.

Some field measurements should be made of ephemeral gully width and depth, but are not absolutely necessary for producing reasonable estimates. Both approaches should be useful in practical estimation of ephemeral gully erosion, soil erosion research and the study of the hydrology of agricultural watersheds.

References for Section 8

Abrahams, A. D., and Parsons, A. J. (1991). "Resistance to overland flow on desert pavement and its implications for sediment transport modeling." *Water Resources Research*, 27(8), 1827-1836.

Band, L. E. (1986). "Topographic Partition of Watersheds with Digital Elevation Models." *Water Resources Research*, 22(1), 15-24.

Beer, C. E., and Johnson, H. P. (1963). "Factors in gully growth in deep loess area of western Iowa." *Transactions of the American Society of Agricultural Engineers*, 6(3), 237-240.

Begin, Z. B., and Schumm, S. A. (1979). "Instability of Alluvial Valley Floors: A Method for its Assessment." *Transactions of the American Society of Agricultural Engineers*, 22(2), 347-350.

Belcher, D. J. (1997). "Chapter 4 Soils." Manual of Photographic Interpretation, W. R. Philipson, ed., American Society for Photogrammetry and Remote Sensing, Bethesda, 167-223.

Bennett, S. J., Casali, J., Robinson, K. M., and Kadavy, K. C. (2000). "Characteristics of actively eroding ephemeral gullies in an experimental channel." *Transactions of the American Society of Agricultural Engineers*, 43(3), 641-649.

Bernard, J. M. "Sediment research needs and related support for programs of the usda--natural resources conservation service." *Proceedings of the U.S. Geological Survey (USGS) Sediment Workshop, February 4-7, 1997*, Reston, VA, and Harpers Ferry, WV.

Beven, K. (1979). "A Sensitivity Analysis of the Penman-Monteith Actual Evapotranspiration Estimates."

Beven, K. (1997). "TOPMODEL: A critique." *Hydrological Processes*, 11(9), 1069-1085.

Beven, K., and Kirkby, M. J. (1993). "Channel Network Hydrology." Wiley, West Sussex, Enland, 320.

Beven, K. J., and Kirby, M. J. (1979). "A physically based variable contributing aera model of basin hydrology." *Hydrological Sciences Bulletin*, 24, 43-69.

Bloeschl, G., Grayson, R. B., and Sivapalan, M. (1995). "On the representative elementary area (REA) concept and its utility for distributed rainfall-runoff modelling." *Hydrological Processes*, 9(3-4), 313-330.

Bloschl, G., Sivapalan, M., Gupta, V., and Beven, K. (1997). "Preface to the special secton on scale problems in hydrology." *Water Resources Research*, 33(12), 2281.

Bowers, S. A., and Hanks, R. J. (1965). "Reflection of radiant energy from soils." *Soil Science*, 100(2), 130-138.

Carson, M. A., and Kirkby, M. J. (1972). *Hillslope Form and Process*, Cambridge University Press, Cambridge.

Chow, V. T. (1959). *Open-Channel Hydraulics*, McGraw-Hill, New York.

Clark, R. N., Swayze, G. A., Livo, K. E., Kokaly, R. F., Sutley, S. J., Dalton, J. B., McDougal, R. R., and Gent, C. A. (2003). "Imaging spectroscopy: Earth and planetary remote sensing with the USGS Tetracorder and expert systems." *Journal of Geophysical Research*, 108(E12), 5131-5141.

Desmet, P. J. J., Poesen, J., Govers, G., and Vandaele, K. (1999). "Importance of slope gradient and contributing area for optimal prediction of the initiation and trajectory of ephemeral gullies." *Catena*, 37, 377-392.

Dietrich, W. E., and Dunne, T. (1993). "The Channel Head." Channel Network Hydrology, K. Veven and M. J. Kirkby, eds., Wiley, New York, 175-219.

Dietrich, W. E., Wilson, C. J., Montgomery, D. R., and McKean, J. (1993). "Analysis of erosion thresholds, channel networks, and landscape morphology using a digital terrain model." *Journal of Geology*, 101, 259-278.

Dietrich, W. E., Wilson, C. J., Montgomery, D. R., McKean, J., and Bauer, R. (1992). "Erosion Thresholds and Land Surface Morphology." *Geology*, 20(8), 675-679.

Einstein, H. A. (1950). *The Bed-Load Function for Sediment Transportation in Open Channel Flows*, U.S.D.A, Soil Conservation Service, Washington, D.C.

Elliott, W. J., Liebenow, A. M., Laflen, J. M., and Kohl, K. D. (1989). *A Compendium of Soil Erodibility Data From WEPP Cropland Soil Field Erodibility Experiments 1987 & 1988. NSERL Report No. 3*, USDA-ARS National Soil Erosion Research Lab, West Lafayette, IN.

Emmett, W. W. (1970). "The Hydraulics of Overland Flow on Hillslopes, Geological Survey Professional Paper 662-A." U.S. Geological Survey, Wasington, DC.

Engman, E. T. (1986). "Roughness Coefficients for Routing Surface Runoff." *Journal of Irrigation and Drainage Engineering*, 112(1), 39-53.

Esfandiari, M., and Maheshwari, B. L. (1998). "Suitability of Selected Flow Equations and Variation of Manning□s n in Furrow Irrigation." *Journal of Irrigation and Drainage Engineering*, 124(2), 89-95.

Flanagan, D. C., and Nearing, M. A. (1995). "Water Erosion Prediction Project (WEPP) Hillslope Profile and Watershed Model Documentation, NSERL Report No. 10." National Soil Erosion Research Laboratory, West Lafayette, IN, 142.

Foster, G. R. (1982). "Modeling the Erosion Process." Hydrologic Modeling of Small Watersheds, C. T. Haan, H. P. Johnson, and D. L. Brakensiek, eds., American Society of Agricultural Engineers, St. Joseph, MO, 297-380.

Foster, G. R., Huggins, L. F., and Meyer, L. D. (1984). "A laboratory study of rill hydraulics: I. velocity relationships." *Transactions of the American Society of Agricultural Engineers*, 27, 790-796.

Foster, G. R., and Lane, L. J. "Erosion by concentrated flow in farm fields." *D.B. Simons Symposiun on Erosion and Sedimentation*, Colorado State University, Ft. Collins, CO, 9.65-9.82.

Foster, G. R., Lane, L. J., Nowlin, J. D., Laflen, J. M., and Young, R. A. (1980). "Chapter 3. A model to estimate sediment yield from field-sized areas: development of model." CREAMS: A field-scale model for chemicals, runoff, and erosion from agricultural management systems. Conservation Research Report No.26, W. G. Knisel, ed., U.S. Department of Agriculture, Washington, DC, 640.

Foster, G. R., Yoder, D. C., Weesies, G. A., McCool, D. K., McGregor, K. C., and Bingner, R. L. (2003). *User's Guide: Revised Universal Soil Loss Equation Version 2(RUSLE2), January 2003*, USDA-Agricultural Research Service, Washington, DC.

Frazier, B. E., and McCool, D. K. (1981). "Aerial Photography to Detect Rill Erosion." *Transactions of the ASAE*, 24(5), 1168-1171.

Frazier, B. E., McCool, D. K., and Engle, C. F. (1983). "Soil Erosion in the Palouse: An Aerial Perspective." *Journal of Soil and Water Conservation*, 38(2), 70-74.

Gilbert, G. K. (1907). "The convexity of hilltops." *Journal of Geology*, 17, 344-350.

Gilley, J. E., and Finkner, S. C. (1991). "Hydraulic roughness coefficients as affected by random roughness." *Transactions of the American Society of Agricultural Engineers*, 34(3), 897-903.

Gilley, J. E., Flanagan, D. C., Kottwitz, E. R., and Weltz, M. A. (1992). "Darcy-Weisbach roughness coefficients for overland flow." Overland Flow Hydraulics and Erosion Mechanics, A. J. Parsons and A. D. Abrahams, eds., Chapman & Hall, New York, 25-52.

Gilley, J. E., and Kottwitz, E. R. (1994). "Darcy-Weisbach roughness coefficients for selected crops." *Transactions of the American Society of Agricultural Engineers*, 37(2), 467-471.

Gilley, J. E., Kottwitz, E. R., and Simanton, J. R. (1990). "Hydraulic characteristics of rills." *Transactions of the American Society of Agricultural Engineers*, 33(6), 1900-1906.

Gilley, J. E., Kottwitz, E. R., and Wieman, G. A. (1991). "Roughness Coefficients for Selected Residue Materials." *Journal of Irrigation and Drainage Engineering*, 117(4), 503-514.

Haan, C. T., Barfield, B. J., and Hayes, J. C. (1994). *Design Hydrology and Sedimentology for Small Catchments*, Academic Press, San Diego, CA.

Hanson, G. J. (1991). "Development of a jet index method to characterize erosion resistance of soils in earthen spillways." *Transactions of the American Society of Agricultural Engineers*, 34(2015-2020).

Harvey, M. D., Watson, C. C., and Schumm, S. A. (1985). *Gully Erosion, Technical note 366*, Bureau of Land Management, U.S. Department of Interior, Denver Services Center, Denver, CO.

Horton, R. E. (1945). "Erosional development of streams and their drainage basins: hydrophysical approach to quantitative morphology." *Bulletin of the Geological Society of America*, 56, 275-370.

Istanbulluoglu, E., Tarboton, D. G., Pack, R. T., and Luce, C. H. (2003). "A sediment transport model for incision of gullies on steep topography." *Water Resources Research*, 39(4).

Kerns, W. R., and Krammer, R. A. (1985). "Farmers' attitudes toward nonpoint pollution control and participation in cost-share programs." *Water Resources Bulletin*, 21(2), 207-215.

King, K. W., Flanagan, D. C., Norton, L. D., and Laflen, J. M. (1995). "Rill erodibility parameters influenced by long-term management practices." *Transactions of the American Society of Agricultural Engineers*, 38(1), 159-164.

Kirkby, M. J. (1993). "Long term interactions between networks and hillslopes." Channel Network Hydrology, K. Beven and M. J. Kirkby, eds., Wiley, New York, 256-293.

Knighton, D. (1998). *Fluvial Forms and Processes*, Arnold and Oxford University Press, London and New York.

Knisel, W. G. (1980). *CREAMS: A Field-Scale Model for Chemicals, Runoff, and Erosion. From Agricultural Management Systems. Conservation Research Report No. 26*, USDA-SEA, Washington D.C.

Leopold, L. B., and Maddock, T., Jr. (1953). *The hydraulic geometry of stream channels and some physiographic implications*, U.S. Geological Survey, Washington D.C.

Lillesand, T. M., and Kieffer, R. W. (1994). *Remote Sensing and Image Interpretation*, John Wiley and Sons, Inc., New York.

Liong, S. Y., Selvalingam, S., and Brady, D. K. (1989). "Roughness Values for Overland Flow in Subcatchments." *Journal of Irrigation and Drainage Engineering*, 115(2), 203-214.

Loewenherz-Lawrence, D. S. (1994). "Theoretical constraints on the development of surface rills: mode, shapes, amplitude limitations and implications for non-linear evolution." Process Models and Theoretical Geomorphology, M. J. Kirby, ed., Wiley, New York, 315-333.

Maheshwari, B. L. (1992). "Suitability of different flow equations and hydraulic resistance parameters for flows in surface irrigation: a review." *Water Resources Research*, 28(8), 2059-2066.

Maheshwari, B. L., and McMahon, T. A. (1992). "Modeling Shallow Overland Flow in Surface Irrigation." *Journal of Irrigation and Drainage Engineering*, 118(2), 201-217.

McCool, D. K., Walter, M. T., and King, L. G. (1995). "Runoff index values for frozen soil areas in the Pacific Northwest." *Journal of Soil and Water Conservation*, 50(5), 466-469.

Merz, B., and Plate, E. J. (1997). "An analysis of the effects of spatial variability of soil and soil moisture on runoff." *Water Resources Research*, 33(12), 2909-2922.

Meyer-Peter, E., and Muller, R. (1948). "Formulas for bed-load transport." *International Association for Hydraulic Research*, 2, 39-64.

Montgomery, D. R., and Dietrich, W. E. (1988). "Where do channels begin?" *Nature*, 336, 232-234.

Montgomery, D. R., and Dietrich, W. E. (1989). "Source Areas, Drainage Density, and Channel Initiation." *Water Resources Research*, 25(8), 1907-1918.

Montgomery, D. R., and Dietrich, W. E. (1992). "Channel Initiation and the Problem of Landscape Scale." *Science*, 255, 826-830.

Montgomery, D. R., and Dietrich, W. E. (1994). "Landscape Dissection and Drainage Area-Slope Thresholds." Process Models and Theoretical Geomorphology, M. J. Kirby, ed., Wiley, New York, 221-246.

Montgomery, D. R., Dunne, T., and Dietrich, W. E. (1993). *Geomorphological Watershed Analysis Project, Biennial Report for the Period from 10/1/91 to 6/30/93, TFW-SH10-93-002*, Prepared for the Washington State Dept. of Natural Resources under the Timber, Fish, and Wildlife Agreement.

Moore, I. D., Burch, G. J., and Mackenzie, D. H. (1988). "Topographic effects on the distribution of surface soil water and the location of ephemeral gullies." *Transactions of the ASAE*, 31, 1098– 1107.

Nachtergaele, J., Poesen, J., Steegen, A., Takken, I., Beuselinck, L., Vandekerckhove, L., and Govers, G. (2001a). "The value of a physically based model versus an empirical approach in the prediction of ephemeral gully erosion for loess-derived soils." *Geomorphology*, 40(3-4), 237-252.

Nachtergaele, J., Poesen, J., Vandekerckhove, L., Wijdenes, D. O., and Roxo, M. (2001b). "Testing the ephemeral gully erosion model (EGEM) for two Mediterranean environments." *Earth Surface Processes and Landforms*, 26(1), 17-30.

O'Loughlin, E. M. (1986). "Prediction of surface saturation zones in natural catchments by topographic analysis." *Water Resources Research*, 22, 794-804.

Ogden, F. L., Garbrecht, J., Deberry, P. A., and Johnson, L. E. (2001). "GIS and Distributed Watershed Models. II: Modules, Interfaces, and Models." *Journal of Hydrologic Engineering*, 6(6), 515-523.

Patton, P. C., and Schuum, S. A. (1975). "Gully erosion, Northwestern Colorado: a threshold phenomenon." *Geology*, 3, 88-90.

Peterson, J. R., Flanagan, D. C., and Robinson, K. M. (2003). "Channel evolution and erosion in PAM-treated and untreated experimental waterways." *Transactions of the American Society of Agricultural Engineers*, 46(4), 1023-1031.

Prosser, I. P., and Abernathy, B. (1996). "Predicting the topographic limits to a gully network using a digital terrain model and process thresholds." *Water Resources Research*, 23(7), 2289-2298.

Quinn, P. F., Beven, K. J., and Lamb, R. (1995). "The ln(a/tanb)Index: How to Calculate it and how to use it Within the Topmodel Framework." *Hydrological Processes*, 9, 161-182.

Ree, W. O., and Crow, F. R. (1977). "Manning n and the overland flow equation." *Transactions of the American Society of Agricultural Engineers*, 20, 89-95.

Schumm, S. A. (1973). "Geomorphic Thresholds and Complex Response of Drainage Systems." Fluvial Geomorphology, M. Morisawa, ed., State University of New York, Binghamtop, New York, 11.

Simons, D. B., and Richardson, E. V. (1966). *Resistance to flow in Alluvial Channels*, U.S. Geological Survey, Washington D.C.

Simons, D. B., and Senturk, F. (1976). *Sediment Transport Technology*, Water Resources Publications, Fort Collins, CO.

Smith, T. R., and Bretherton, F. P. (1972). "Stability and the conservation of mass in drainage basin evolution." *Water Resources Research*, 8(6), 1506-1529.

Takken, n., Jetten, V., Govers, G., Nachtergaele, J., and Steegen, A. (2002). "The effect of tillage-induced roughness on runoff and erosion patterns." *Geomorphology*, 37, 1-14.

Tarboton, D. G. (1997). "A New Method for the Determination of Flow Directions and Contributing Areas in Grid Digital Elevation Models." *Water Resources Research*, 33(2), 309-319.

Tarboton, D. G., Bras, R. L., and Rodriguez-Iturbe, I. (1992). "Physical Basis for Drainage Density." *Geomorphology*, 5(1/2), 59-76.

Teasdale, G. N., and Barber, M. E. (2005). "Aerial Assessment of Ephemeral Gully Erosion and Channel Erosion in the Lower Potlatch River Basin." State of Washington Water Research Center, Pullman, WA.

Temple, D. M. (1980). "Tractive force design of vegetative channels." *Transactions of the American Society of Agricultural Engineers*, 23, 884-890.

Teng, W. L. (1997). "Chapter 2 Fundamentals of Photographic Interpretation." Manual of Photographic Interpretation, W. R. Philipson, ed., American Society for Photogrammetry and Remote Sensing, Bethesda, 49-113.

Tucker, G. E., and Bras, R. L. (1998). "Hillslope processes, drainage density, and landscape morphology." *Water Resources Research*, 34(10), 2751-2764.

Van Klaveren, R. W. (1987). "Hydraulic erosion resistance of thawing soils. Ph.D. diss." Washington State University, Pullman, WA.

Van Klaveren, R. W., and McCool, D. K. (1993). "Facility for hydraulic tests of a frozen soil." *Transactions of the American Society of Agricultural Engineers*, 36(6), 1721-1725.

Van Klaveren, R. W., and McCool, D. K. (1998). "Erodibility and critical shear of a previously frozen soil." *Transactions of the American Society of Agricultural Engineers*, 41(5), 1315-1321.

Vandaele, K., Poesen, J., Govers, G., and Van Wesemael, B. (1996). "Geomorphic threshold conditions for ephemeral gully incision." *Geomorphology*, 16, 161-173.

Vandekerckhove, L., Poesen, J., Oostwoud Wijdenes, D., and De Figueiredo, T. (1998). "Topographical thresholds for ephemeral gully initiation in intensively cultivated areas of the Mediterranean." *Catena*, 33, 271-292.

Weltz, M. A., and Lane, L. J. (1992). "Hydraulic Roughness Coefficients for Native Rangelands." *Journal of Irrigation and Drainage Engineering*, 118(5), 776-790.

Willgoose, G. (1994). "A physical explanation for an observed area-slope-elevation relationship for catchments with declining relief." *Water Resources Research*, 30(2), 151-160.

Willgoose, G., Bras, R. I., and Rodriguez-Iturbe, I. (1991). "A Physical Explanation of an Observed Link Area-Slope Relationship." *Water Resources Research*, 27(7), 1697-1702.

Willgoose, G., Bras, R. L., and Rodriguez-Iturbe, I. (1991). "A Coupled Channel Network Growth and Hillslope Evolution Model: 1. Theory." *Water Resources Research*, 27(7), 1671-1684.

Woodward, D. E. (1999). "Method to predict cropland ephemeral gully erosion." *Catena*, 37(3-4), 393-399.

Zhang, W., and Montgomery, D. R. (1994). "Digital elevation model grid size, landscape representation, and hydrologic simulations." *Water Resources Research*, 30(4), 1019-1028.

Appendix 8.1

Reconstructed Foster and Lane Channel Dimensionless Geometry

Foster and Lane Channel Dimensionless Geometry									
X_{*c}	W_*	R_*	D_*	$g(X_{*c})$	X_{*c}	W_*	R_*	D_*	$g(X_{*c})$
0.000	0.7308	0.1584	0.2587						
0.005	0.7293	0.1567	0.2640	64.7769	0.255	0.3437	0.1275	0.3949	1.8487
0.010	0.7234	0.1572	0.2660	32.5777	0.260	0.3363	0.1257	0.3973	1.8439
0.015	0.7169	0.1577	0.2683	21.0458	0.265	0.3289	0.1239	0.3996	1.8402
0.020	0.7099	0.1581	0.2707	15.3406	0.270	0.3215	0.1221	0.4020	1.8374
0.025	0.7027	0.1586	0.2733	12.0044	0.275	0.3141	0.1202	0.4044	1.8356
0.030	0.6952	0.1590	0.2759	9.8423	0.280	0.3067	0.1183	0.4067	1.8347
0.035	0.6876	0.1594	0.2786	8.3401	0.285	0.2994	0.1163	0.4091	1.8348
0.040	0.6798	0.1597	0.2813	7.2423	0.290	0.2920	0.1143	0.4114	1.8358
0.045	0.6720	0.1601	0.2840	6.4089	0.295	0.2847	0.1123	0.4137	1.8377
0.050	0.6641	0.1603	0.2868	5.7570	0.300	0.2774	0.1102	0.4160	1.8406
0.055	0.6562	0.1605	0.2896	5.2349	0.305	0.2702	0.1081	0.4183	1.8444
0.060	0.6482	0.1607	0.2924	4.8082	0.310	0.2629	0.1060	0.4206	1.8492
0.065	0.6402	0.1608	0.2952	4.4540	0.315	0.2557	0.1038	0.4229	1.8549
0.070	0.6322	0.1608	0.2980	4.1557	0.320	0.2484	0.1016	0.4251	1.8616
0.075	0.6242	0.1608	0.3008	3.9015	0.325	0.2412	0.0993	0.4274	1.8694
0.080	0.6162	0.1608	0.3036	3.6828	0.330	0.2341	0.0970	0.4296	1.8781
0.085	0.6081	0.1606	0.3064	3.4929	0.335	0.2269	0.0947	0.4318	1.8879
0.090	0.6001	0.1605	0.3091	3.3267	0.340	0.2198	0.0924	0.4341	1.8988
0.095	0.5921	0.1603	0.3119	3.1803	0.345	0.2126	0.0900	0.4363	1.9109
0.100	0.5841	0.1600	0.3147	3.0505	0.350	0.2055	0.0875	0.4385	1.9242
0.105	0.5761	0.1597	0.3175	2.9349	0.355	0.1984	0.0851	0.4407	1.9388
0.110	0.5681	0.1593	0.3202	2.8314	0.360	0.1913	0.0826	0.4428	1.9547
0.115	0.5601	0.1589	0.3230	2.7384	0.365	0.1843	0.0801	0.4450	1.9720
0.120	0.5521	0.1584	0.3257	2.6544	0.370	0.1772	0.0775	0.4472	1.9909
0.125	0.5441	0.1579	0.3284	2.5784	0.375	0.1702	0.0749	0.4493	2.0113
0.130	0.5362	0.1573	0.3311	2.5094	0.380	0.1632	0.0723	0.4515	2.0336
0.135	0.5283	0.1567	0.3338	2.4466	0.385	0.1562	0.0696	0.4536	2.0578
0.140	0.5204	0.1560	0.3365	2.3893	0.390	0.1492	0.0669	0.4557	2.0840
0.145	0.5125	0.1552	0.3392	2.3369	0.395	0.1423	0.0642	0.4579	2.1126
0.150	0.5046	0.1545	0.3418	2.2889	0.400	0.1353	0.0614	0.4600	2.1436
0.155	0.4967	0.1536	0.3445	2.2449	0.405	0.1284	0.0586	0.4621	2.1775
0.160	0.4889	0.1528	0.3471	2.2044	0.410	0.1215	0.0558	0.4642	2.2146
0.165	0.4811	0.1518	0.3498	2.1673	0.415	0.1146	0.0530	0.4663	2.2552
0.170	0.4733	0.1509	0.3524	2.1332	0.420	0.1077	0.0501	0.4683	2.2998
0.175	0.4655	0.1498	0.3550	2.1018	0.425	0.1008	0.0472	0.4704	2.3490
0.180	0.4577	0.1488	0.3576	2.0729	0.430	0.0940	0.0442	0.4725	2.4037
0.185	0.4500	0.1477	0.3601	2.0463	0.435	0.0872	0.0412	0.4745	2.4647
0.190	0.4423	0.1465	0.3627	2.0219	0.440	0.0803	0.0382	0.4766	2.5332
0.195	0.4346	0.1453	0.3652	1.9995	0.445	0.0735	0.0352	0.4786	2.6107
0.200	0.4269	0.1440	0.3678	1.9789	0.450	0.0667	0.0321	0.4806	2.6995
0.205	0.4192	0.1428	0.3703	1.9601	0.455	0.0600	0.0290	0.4827	2.8022
0.210	0.4116	0.1414	0.3728	1.9429	0.460	0.0532	0.0259	0.4847	2.9231
0.215	0.4040	0.1400	0.3753	1.9273	0.465	0.0464	0.0227	0.4867	3.0680
0.220	0.3964	0.1386	0.3778	1.9131	0.470	0.0397	0.0195	0.4887	3.2462
0.225	0.3888	0.1371	0.3803	1.9002	0.475	0.0329	0.0163	0.4908	3.4733
0.230	0.3812	0.1356	0.3827	1.8887	0.480	0.0261	0.0130	0.4928	3.7780
0.235	0.3737	0.1341	0.3852	1.8784	0.485	0.0193	0.0097	0.4949	4.2215
0.240	0.3662	0.1325	0.3876	1.8693	0.490	0.0124	0.0062	0.4970	4.9742
0.245	0.3587	0.1308	0.3900	1.8613	0.495	0.0052	0.0026	0.4991	6.8846
0.250	0.3512	0.1292	0.3925	1.8545	0.500	0.0000	0.0000	0.5000	

Table A8.1 Tabulation of reconstructed Foster and Lane eroded channel geometry.

SATELLITE AND AERIAL IMAGING IN CHARACTERIZATION, HYDROLOGIC ANALYSIS AND MODELING OF INLAND WATERSHEDS AND STREAMS

Section 9. Summary and Conclusions

By

GREGG N. TEASDALE

A dissertation to be submitted in partial fulfillment of
the requirements for the degree of

DOCTOR OF PHILOSOPHY
(Civil Engineering)

WASHINGTON STATE UNIVERSITY
Department of Civil and Environmental Engineering

December 2005

Section Table of Contents

9. Summary and Conclusions

Satellite and Aerial images provide spatial, spectral and temporal information necessary to observe, characterize and parameterize the physical nature of watersheds and streams. Aerial views give a perspective that makes clear the spatial continuity and dependency of distributive physical and ecological systems—a perspective difficult to obtain otherwise.

Remote sensing technology is changing the practice of hydrologic analysis. The link between hydrologic analysis and remote sensing is clear: practical hydrologic analysis requires an abundance of geospatial information that usually must be developed by remote sensing techniques for projects larger than a few hectares. Remote sensing provides a perspective of broad-scale, dynamic patterns that can be difficult to discern using only point measurements. Environmental scientists and water resource engineers are beginning to appreciate the value of geospatial data and imaging resources. Use and analysis of these resources for practical project work has lagged behind the development of remote sensing technology. Readers of this dissertation might ask why.

Schultz (1988) bluntly identified the main obstacle that inhibits more widespread use of remote sensing information in the practice of hydrology:

> *"When, however, hydrologists working in the field of remote sensing explain to their classical colleagues that data obtained from remote sensing can significantly improve our knowledge of precipitation, runoff, evaporation, soil moisture, snow, etc., the classical hydrologist, typically, accepts the information but continues to do what he always did, i.e. to squeeze out information from often*

more or less useless conventional field data by the most sophisticated mathematical techniques."

In a review of hydrological applications of remote sensing, Engman attributes part of this reluctance to the scattered nature of the literature (Engman 1993; Engman and Gurney 1991) and also faults traditional hydrological models developed from a point data concept (Engman 1982). Even now, relatively few reports of the hydrologic applications of remote sensing appear in the standard refereed publications of hydrologic and environmental engineering. But, professional acceptance of remote sensing information in the practice of hydrology is growing. Perhaps this research and dissertation contributes in a meaningful way to the effort to encourage the use of remote sensing methods in research and in the practice of watershed hydrologic characterization and engineering assessment of rivers and streams.

9.1 General Summary

It is difficult to encapsulate seven years of research work into a few summary statements. The most general realizations reached in this research include:

- Remote sensing technology and methods are under-utilized in hydrologic characterization of watersheds, hydrologic modeling, soil erosion modeling, and the assessment of stream morphology for engineering purposes.
- There are no significant technological barriers to wider adoption of remote sensing in hydrologic analysis.
- Effective application of imagery analysis and basic remote sensing principles are not restricted solely to specialists. Primary techniques can

be self-taught or learned in focused training with a reasonable investment in time and expense.

- Useful and innovative engineering analyses can be performed with remote sensing data.

- There are ample opportunities for beneficial research related to the disciplines of hydrologic modeling, soil erosion modeling, fluvial morphology and sediment transport using remote sensing information as primary or supporting data sources.

9.2 Conclusions

This dissertation explored, examined and demonstrated the use of satellite and aerial imagery in the characterization and hydrologic analysis of inland Pacific Northwest watersheds and streams as intended by the objectives listed in Section 1. The research clearly showed that hydrologically relevant watershed and stream characteristics can be efficiently monitored and evaluated with a variety of remote sensing methods. As demonstrated, these data and parameterizations have direct application in environmental assessment and hydrologic modeling work. The data and information derived by remote sensing methods presented are useful in both engineering research and practice.

The dissertation assembles the most relevant details of operational land surface imaging satellites in a form useful to environmental scientists and water resource engineers. Essential remote sensing principles are discussed and sources cited for further and supporting information. Satellite and aerial data preparation and analysis techniques are illustrated with hundreds of color images that convey the benefit and power of remote sensing methods. Fundamental principles are detailed for a highly efficient and

unrecognized method of water resources investigation – analytical aerial survey. This method is demonstrated in practical applications and may be the most significant contribution of the research.

Beyond fundamentals, the dissertation demonstrated how satellite and aerial remote sensing methods are applied in the analysis of critical water resources issues: best practice hydrologic modeling, soil erosion, sediment delivery, fluvial morphology, and sediment transport. New engineering models of morphological sediment transport and watershed ephemeral gully erosion were proposed and demonstrated. Numerous opportunities for further research are noted throughout the dissertation.

References for Section 9

Engman, E. T. (1982). "Remote sensing applications in watershed modeling." Applied Modeling in Catchment Hydrology, V. P. Singh, ed., Water Resources Publications, Littleton, CO, 473-494.

Engman, E. T. (1993). "Remote Sensing." Handbook of Hydrology, D. R. Maidment, ed., McGraw-Hill, New York, 24.1-24.23.

Engman, E. T., and Gurney, R. J. (1991). *Remote Sensing in Hydrology*, Chapman and Hall, London.

Schultz, G. A. (1988). "Remote Sensing in Hydrology." *Journal of Hydrology*, 100(1/3), 239-265.